coatings

Recent Trends in Coatings and Thin Film–Modeling and Application

Edited by
Rahmat Ellahi

Printed Edition of the Special Issue Published in *Coatings*

www.mdpi.com/journal/coatings

Recent Trends in Coatings and Thin Film–Modeling and Application

Recent Trends in Coatings and Thin Film–Modeling and Application

Editor

Rahmat Ellahi

MDPI • Basel • Beijing • Wuhan • Barcelona • Belgrade • Manchester • Tokyo • Cluj • Tianjin

Editor
Rahmat Ellahi
Fulbright Fellow University of
California
Riverside
USA

Editorial Office
MDPI
St. Alban-Anlage 66
4052 Basel, Switzerland

This is a reprint of articles from the Special Issue published online in the open access journal *Coatings* (ISSN 2079-6412) (available at: https://www.mdpi.com/journal/coatings/special_issues/model_appl).

For citation purposes, cite each article independently as indicated on the article page online and as indicated below:

LastName, A.A.; LastName, B.B.; LastName, C.C. Article Title. *Journal Name* **Year**, *Volume Number*, Page Range.

ISBN 978-3-0365-1014-9 (Hbk)
ISBN 978-3-0365-1015-6 (PDF)

Contents

About the Editor

Rahmat Ellahi, Ph.D. is an Ex-Chairperson and founder chairman (Mathematics and Statistics), accomplished researcher, teacher and a prolific scholar and has a key role in promotion of science at national and international levels. He has successfully reached great heights in academics, from the University of Punjab, Quaid-i-Azam University, Islamabad, Pakistan and University of California Riverside, USA as his Alma matter. He has published round 300 papers in the journals of the USA, Germany, the UK, Canada etc. His work has been cited more than 17,000 times on Google Scholar with an h-index of 74. He is editor/editorial board member for 19 international journals and referee for more than 350 international journals. Furthermore, he has edited 6 special issues for ISI impact factor journals. He has successfully supervised 30 research students (08 PhD and 22 MS). His leadership in academics is further reflected through the research collaboration with more than 80 international leading scientists all over the world. His research particularly upgraded the science capacity of several Universities of the world such as in the USA, Canada, Australia, the UK, France, China, Romania, Turkey, Iran, South Africa, Egypt, Saudi Arabia, Kuwait, India, Vietnam, Italy and Pakistan etc. He is an author of 6 books published at national and international levels. He has organized 8 international conferences, delivered 20 seminars and attended 25 conferences as key speaker and participant. As a referee he has evaluated more than 100 research and books projects submitted at United State Education Foundation Poland, USEFP Pakistan, European Science Foundation, PRESTIGE post-doc fellowships of French National Agency, Chilean National Science and Technology Commission Chile, HEC under NRUP, FWO Fellowships, Elsevier Book proposals and projects of European Commission etc. He has been honored as a Highly Cited Researcher for the years 2018, 2019 and 2020 by Clarivate Analytics. He was among the top 5 Productive Scientists of Pakistan in Category A. In addition, he has received 8 (4 international and 4 national) awards and several honors. He is actively involved in different professional and academia bodies/institutes at national and international levels. In summary, Dr. Rahmat Ellahi appears to be a superb individual encompassing all facets of a great educationist. As a matter of fact, he is an outstanding candidate and this is because of his remarkable contributions to society, teaching, research, development and promotion of scientific cooperation, international collaboration, human resource development and updating education systems with the latest trends. Inkeeping his excellent research work, the United State of Education Foundation has honored him as a Fulbright Fellow for the years 2011-2012, while King Fahd University of Petroleum and Minerals, Dhahran, Saudi Arabia, chose to honor him with the title of Chair Professor at Research Institute KFUPM in 2018.

Preface to "Recent Trends in Coatings and Thin Film–Modeling and Application"

This book contains twenty-seven chapters, whereas the Editorial is given in chapter twenty-eight. In this Special Issue total of 58 papers have been submitted for possible publication. After a comprehensive peer review, only 27 papers qualified accepted for final publication. Extensive uses of realistic applications are given in each chapter. To enable the readers' full understanding, a relevant list of references is also given at the end of each chapter for further study. I wish to thank all reviewers for their excellent suggestions and critical reviews on submitted manuscripts. I was fortunate enough to have prominent scholars who contributed with their original research work. I applaud all of them on successful completion of this Special Issue. Errors and omissions, if any are requested, will be gratefully acknowledged in the next possible Edition. Particularly, suggestions for improvement, scope and format of the book will be highly appreciated. I express my gratitude to MPDI for publishing this book and I also especially want to express my gratitude to the Section Managing Editor and my family and friends for their helpful cooperation. It is worth mentioning that this Special Issue has been cited more than 300 times in a very short period.

Rahmat Ellahi
Editor

coatings

MDPI

Editorial

Recent Trends in Coatings and Thin Film: Modeling and Application

Rahmat Ellahi [1,2,3]

[1] Fulbright Fellow, Department of Mechanical Engineering, University of California Riverside, Riverside, CA 92521, USA; rahmatellahi@yahoo.com or rellahi@alumni.ucr.edu
[2] Department of Mathematics & Statistics, Faculty of Basic and Applied Sciences, International Islamic University, Islamabad 44000, Pakistan
[3] Center for Modeling & Computer Simulation, Research Institute, King Fahd University of Petroleum & Minerals, Dhahran 31261, Saudi Arabia

Received: 3 August 2020; Accepted: 7 August 2020; Published: 10 August 2020

Abstract: This special issue took this opportunity to invite researchers to contribute their original research work and review articles to this Special Issue on "Recent Trends in Coatings and Thin Film: Modeling and Application" to be published in Coatings. The goal of this Special Issue was to address challenges and current issues that either advance the state-of-the-art of experimental, numerical, and theoretical methodologies, or extends the bounds of existing methodologies to new contributions that are related to coatings and thin film containing whichever, magnetic, multiphase, material science, nanotechnology, surfaces, interfaces, and mechanical sensing properties. In response to the call for papers, a total of 58 papers were submitted for possible publication. After comprehensive peer review, only 27 papers qualified for acceptance for final publication. The rest of 31 papers could not be accommodated. The submissions may have been technically correct, but were not considered appropriate for the scope of this special issue. The authors are from 17 geographically distributed countries, such as China, Spain, Romania, Turkey, Saudi Arabia, Pakistan, Malaysia, Abu Dhabi, UAE, Vietnam, Korea, Taiwan, Thailand, Lebanon, Egypt, India, and Kuwait, etc. This reflects the great impact of the proposed topic and the effective organization of the guest editorial team of this Special Issue.

Keywords: development and characterization of coatings; applications of thin films; nanostructured materials; surfaces and interfaces; applications of multiphase fluids; mathematical modeling on biological applications; electronics; magnetics and magneto-optics; droplet impact modelling; impedance analysis; rain erosion; ultrasound measurements; viscoelastic modelling; wind turbine blades; computational modelling

1. Introduction

The process of covering the surface of an object or substrate with a very thin layer is known as Coating. This layer can be of some sort of a thin polymer sheet, paint, or lacquer, which can be utilized for protective/decorative purposes. Most of industrial products get-up-and-go through the process of coating not only to prevent corrosion but to make them attractive. As the coating involves the development of a thin film layer that can be lacquer or polymeric on a fabric or substrate etc. Therefore, if the substrate starts and ends the process wound up in a roll, the process can be termed "roll-to-roll" or "web-based" coating. Due to multiple usages of coatings, several theoretical and experimental attempts have been devoted and this special issue is one of them. We hope that this issue will not only address the current challenges, but will also provide an overall picture and up-to-date findings to readers of the scientific community that ultimately benefits the industrial sector regarding its specific market niches and end users.

2. Methodologies and Usages

Two-dimensional, incompressible asymmetric peristaltic propulsion coated with Synovial fluid (non-Newtonian model) with mass transport was investigated in [1]. Because of the coating of the same base-fluid at the surface of the channel, the boundaries become non-porous and exert no slip on the fluid particles. Two illustrative models for the viscosity, namely, shear-thinning (Model 1) and shear-thickening (Model 2), are considered, which reveal the presence and integrity of coating. The perturbation method has been applied to linearize the complicated differential equations. Model 1 predicted higher viscosity values and more significant non-Newtonian behavior than Model 2. It is also observed that the shear-thinning model behaved in quite the opposite manner for the shear thickening model. The converse behavior of Models 1 and 2 occurs due to a curvature of the flow domain. Moreover, Model 1 is not able to capture the correct exponential viscosity dependence on concentration for the whole range of shear rates. On the other hand, the second model shows a strong relationship with accurate power. Solutions are attained for velocity field, concentration profile, and pressure gradient. The novelty of all the essential parameters is analyzed through graphical results. Furthermore, streamlines are also drawn in order to determine the trapping mechanism. The present analysis is beneficial in the study of intrauterine fluid dynamics; furthermore, it is applicable in vivo diagnostic; drug delivery; food diagnostics; protein chips; and, cell chips and packaging, i.e., smart sensors.

Ellahi et al. [2] devoted their efforts to investigate the shiny thin film with a metallic tactile covering of nanoparticles over the surface of a rotating disk. To decorate, glowing silver and gold particles were chosen. Four illustrative base liquids, namely (i) ethanol, (ii) methanol, (iii) ethylene-glycol, and (iv) water were considered with different geometries, which have great importance in industrial use. An emphasis on comparative multi nanofluid analysis was used to make a sound judgment on which one of the fluids best suited the metallic glittering process of spin coating. The film thickness process highly depends on the process of evaporation, which takes some time to settle on the disk's surface. It was found that of the base fluids, the best choices were ethanol alloys with silver. Hence, one can conclude that, from an experimental point of view, if silver alloy is used for coating, then only those liquids can be considered that exhibit ethanol-like properties. The impact of pertinent parameters with different aspects are graphically illustrated in each case

Lu et al. examined the flow of hybrid (nickel–zinc ferrite and ethylene glycol) nanoliquid with entropy optimization and nonlinear thermal radiation coatings past a curved stretching surface [3]. Analysis was carried out in the presence of magnetohydrodynamic, heat generation/absorption, and convective heat and mass flux conditions. A solution of the modeled problem was attained numerically using MATLAB built-in function bvp4c. Impacts of prominent parameters on betrothed distributions were depicted through graphs and they were well supported by requisite discussions. Numerically calculated values of Sherwood number were established in a tabulated form and were scrutinized critically. An excellent concurrence was achieved when the results of the presented model were compared with previously published result; hence, dependable results are being presented. It was observed that concentration field diminished with increasing values of curvature parameter, though the opposite trend was noticed for velocity and temperature distributions. Further, it was detected that Nusselt number decreased with augmented values of radiation and curvature parameters.

Investigation [4] is carried out on the thin film flow of Reiner-Philippoff fluid of boundary-layer type. We have analyzed the flow of thin films of Reiner–Philippoff fluid in the changeable heat transmission and radiation over a time-dependent stretching sheet in two-dimensions (2D). The time-dependent governing equations of Reiner–Philippoff fluid model are simplified with the help of transformation of similarity variables. To investigate the behavior of the Reiner-Philippoff fluid with variable stretching surface for different physical effects, we considered thermophoresis and Brownian motion parameters in the flow. The Homotopy Analysis Method is implemented in the reduced model in order to achieve a solution of the original problem. A numerical convergence of the implemented method is also analyzed. The behavior of temperature, velocity, and concentration profiles have been investigated with the variation of skin friction, Nusselt number, and Sherwood number. A comparative graphical

survey is presented for the velocity gradient, under different parameters. An analytical analysis is presented for the time-dependent parameter over thin film flow. The results that we obtained are better than the previously available results. For the survey, the physical representation of the embedded parameters, are discussed in detail and plotted graphically.

The thin film flow of micropolar fluid in a porous medium under the influence of thermophoresis with the heat effect past a stretching plate is analyzed in [5]. Micropolar fluid is assumed as a base fluid and the plate is considered to move with a linear velocity and subject to the variation of the reference temperature and concentration. The latitude of flow is limited to being two-dimensional and it is steadily affected by sensitive fluid film size with the effect of thermal radiation. The basic equations of fluid flow are changed through the similarity variables into a set of nonlinear coupled differential equations with physical conditions. The suitable transformations for the energy equation is used and the non-dimensional form of the temperature field are different from the published work. The effects of radiation parameter are shown graphically and discussed.

The modern optical fiber required a double-layer resin coating on the glass fiber to provide protection from signal attenuation and mechanical damage. The most important plastics resin used in the coating of fiber optics are plasticized polyvinyle (PVC), low/high density polyethylene (LDPE/HDPE), nylon, and polysulfone. Due to abounded application, the polymer flow during optical fiber coating in a pressure type coating die has been simulated under non-isothermal conditions in [6]. The flow dependent on the wire or fiber velocity, geometry of the die, and the viscosity of the polymer. The wet-on-wet coating process is an efficient process for two-layer coating on the fiber optics. In the present study, the constitutive equation of polymer flow satisfies viscoelastic Phan–Thien–Tanner (PTT) fluid, is used to characterize rheology of the polymer melt. Based on the assumption of the fully developed incompressible and laminar flow, the viscoelastic fluid model of two-immiscible resins-layers modeled for simplified-geometry of capillary-annulus where the glass fiber drawing inside the die at high speed. The equation describing the flow of the polymer melt inside the die was solved, analytically and numerically, by the Runge–Kutta method. The effect of physical characteristics in the problem has been discussed in detail through graphs by assigning numerical values for several parameters of interest. As a first attempt, the model PTT fluid as a coating material for double-layer optical fiber coating using the wet-on-wet coating process is considered. At the end, the present study is compared with the published work as a particular case, and good agreement is found.

The main objective of [7] is to elaborate the characteristics of heat transport and magneto-hydrodynamics finite film flow of human blood with Carbon Nanotubes (CNTs) nanofluids over a stretchable upright cylinder. Two kinds of CNTs nanoparticles, namely (i) SWCNTs (single walled carbon nanotubes) and (ii) MWCNTs (multi walled carbon nanotubes), are used with human blood as a base liquid. In addition, a uniform magnetic field has been perpendicularly conducted to the motion of nanoliquid. The transformation of the partial differential structure into a non-linear ordinary differential structure is made by using appropriate dimensionless quantities. The controlling approach of the Homotopy analysis method has been executed for the result of the velocity and temperature. The thickness of the coating film has been kept variable. The pressure distribution under the variable thickness of the liquid film has been calculated. The impacts of different variables and the rate of spray during coating have been graphically plotted. The coefficient of skin friction and Nusselt number have been presented numerically. In addition, it is noticed that the thermal field of a nanoliquid elevates with rising values of ϕ and this increase is more in SWCNTs nanofluid than MWCNTs nanofluid.

Lu et al. proposed the unsteady flow and heat transfer analyses of a viscous-based nanofluid over a moving surface emerging from a moving slot [8]. A new form of boundary layer flow resembles with the boundary layer flow over a stretching/shrinking surface depending on the motion of the moving slot. The governing partial differential equations are transformed to correct similar form using the Blasius–Rayleigh–Stokes variable. The transformed equations are numerically solved. The existence of dual solutions is observed for a certain range of moving slot parameter. The range of dual solution is strongly influenced by Brownian and thermophoretic diffusion of nanoparticles.

In [9], the three-dimensional nanofluid thin-film flow of Casson fluid over an inclined steady rotating plane is examined. A thermal radiated nanofluid thin film flow is considered with suction/injection effects. With the help of similarity variables, the partial differential equations are converted into a system of ordinary differential equations. The obtained ODEs are solved by the homotopy analysis method with the association of MATHEMATICA software. The boundary-layer over an inclined steady rotating plane is plotted and explored in detail for the velocity, temperature, and concentration profiles. Additionally, the surface rate of heat transfer and shear stress are described in detail. The impact of numerous embedded parameters, such as the Schmidt number, Brownian motion parameter, thermophoretic parameter, and Casson parameter, etc., were examined on the velocity, temperature, and concentration profiles, respectively. The essential terms of the Nusselt number and Sherwood number were also numerically and physically examined for the temperature and concentration profiles. It was observed that the radiation source improves the energy transport to enhance the flow motion. The smaller values of the Prandtl number, augmented the thermal boundary-layer and decreased the flow field. The increasing values of the rotation parameter decreased the thermal boundary layer thickness. These outputs are examined physically and numerically and are also discussed.

This study of [10] aims to scrutinize the thin film flow of a nanofluid comprising of carbon nanotubes (CNTs), single and multi-walled i.e., (SWCNTs and MWCNTs), with Cattaneo-Christov heat flux and entropy generation. The time-dependent flow is supported by thermal radiation, variable source/sink, and magneto hydrodynamics past a linearly stretched surface. The obtained system of equations is addressed by the numerical approach bvp4c of the MATLAB software. The presented results are validated by comparing them to an already conducted study and an excellent synchronization in both results is achieved. The repercussions of the arising parameters on the involved profiles are portrayed via graphical illustrations and numerically erected tables. It is seen that the axial velocity decreases as the value of film thickness parameter increases. It is further noticed that, for both types of CNTs, the velocity and temperature distributions increase as the solid volume fraction escalates.

The study [11] is about the pressure-driven heated bi-phase flow in two slippery walls. The non-Newtonian couple stress fluid is suspended with spherically homogenous metallic particles. The magnetic susceptibility of Hafnium allures is taken into account. The rough surface of the wall is tackled by lubrication effects. The nonlinear coupled partial differential equations along with the associated boundary conditions are first reduced into a set of ordinary differential equations using appropriate transformations and then numerical results were obtained by engaging the blend of Runge–Kutta and shooting techniques. The sway of physical quantities is graphically examined. Excellent agreement within graphical illustration and numerical results is achieved.

The aim of this research work [12] is to increase our understanding of the exhaustion of energy in engineering and industrial fields. The study of nanofluids provides extraordinary thermal conductivity and an increased heat transmission coefficient as compared to conventional fluids. These specific sorts of nanofluids are important for the succeeding generation of flow and heat transfer fluids. Therefore, the investigation of revolutionary new nanofluids has been taken up by researchers and engineers all over the world. In this article, the study of the thin layer flow of Darcy–Forchheimer nanofluid over a nonlinear radially extending disc is presented. The disc is considered as porous. The impacts of thermal radiation, magnetic field, and heat source/sink are especially focused on. The magnetic field, positive integer, porosity parameter, coefficient of inertia, and fluid layer thickness reduce the velocity profile. The Prandtl number and fluid layer thickness reduce the temperature profile. The heat source/sink, Eckert number, and thermal radiation increase the temperature profile. The suggested model is solved analytically by the homotopy analysis method. The analytical and numerical techniques are compared through graphs and tables, and they have shown good agreement. The influences of embedded parameters on the flow problem are revealed through graphs and tables.

In the analysis [13], peristaltic flow was discussed for magnetohydrodynamic Newtonian fluid through the gap between two coaxial tubes, where the viscosity of the fluid is treated as variable.

In addition, the inner tube was considered to be at rest, while the outer tube had the sinusoidal wave traveling down its motion. Further, the assumptions of long wave length and low Reynolds number were taken into account for the formulation of the problem. A closed form solution is presented for general viscosity while using the Adomian decomposition method. Numerical illustrations that show the physical effects and pertinent features were investigated for different physical included phenomenon. It was found that the pressure rise increases with an increase in Hartmann number, and frictional forces for the outer and inner tube decrease with an increase in Hartmann number when the viscosity is constant. It was also observed that the size of the trapping bolus decreases with an increase in Hartmann number, and it increases with an increase in amplitude ratio when the viscosity is parameter.

The magnetohydrodynamic flow of a micropolar nanofluid on an exponential sheet in an Extended–Darcy–Forchheimer porous medium have been considered by Lund et al. [14]. The Buongiorno's model is considered in order to formulate a mathematical model with different boundary conditions. The governing partial differential equations of the nanofluid flow are changed into a third order non-linear quasi-ordinary differential equation, using the pseudo-similarity variable. The resulting equation of the boundary value problems are renewed into initial value problems using a shooting method, and then the initial value problems are solved by a fourth order Runge–Kutta method. The effects of various physical parameters on the profiles of velocity, temperature, microrotation velocity, concentration, skin friction, couple stress coefficients, heat, and concentration transfer are graphically demonstrated. A stability analysis has been performed in order to show the stability of the solutions; only the first solution is stable and physically possible, whereas the remaining two solutions are not stable.

The magnetohydrodynamic flow over a shrinking sheet and heat transfer with viscous dissipation has been studied in [15]. The governing equations of the considered problem are transformed into ordinary differential equations while using similarity transformation. The resultant equations are converted into a system of fractional differential boundary layer equations by employing a Caputo derivative, which is then numerically solved using the Adams-type predictor-corrector method. The results show the existence of two ranges of solutions, namely, dual solutions and no solution. Moreover, the results indicate that dual solutions exist for a certain range of specific parameters which are in line with the results of some previously published work. It is also observed that the velocity boundary layer decreases as the suction and magnetic parameters increase.

The aim of [16] is to present an analytical and numerical treatment of a two-dimensional peristaltic channel along with the coating of laminar layers of nanoparticles with non-Newtonian (Williamson) base liquid. In addition to this, convective heat transfer and magnetic field effects also take into consideration. The geometry is considered as an asymmetric two-dimensional channel experiencing sinusoidal waves propagating across the walls. The walls are supposed to have heat convection at the upper wall and the lower wall is having no temperature gradient. The problem is manufactured under the theory of lubrication approach. The mathematical models are evolved using appropriate transformations. The obtained nonlinear differential equations are solved analytically. Graphical features are presented to find the influence of emerging physical parameters on the stream function, velocity of the nanofluid, heat transfer, nanoparticles concentration, pressure gradient, and pressure increase. It is found that the velocity decreases in the lower part while increasing in the upper side of the channel in the presence of nanoparticles. The temperature is becoming large with increasing amount of nanoparticles and heat convection at the boundaries. It is also observed that nanoparticle concentration is getting higher with Brownian motion parameter, but fluid becomes less thermal against the thermophoresis parameter. The streamlines phenomenon clearly reflects the asymmetry of the channel. The characteristics of viscous fluid can be recovered by switching the Weissenbureg number) to zero.

The impact of second-order slip with thermal and solutal stratification coatings on three-dimensional Williamson nanofluid flow past a bidirectional stretched surface and analytically envisages it by Ramzan et al. [17]. The novelty of the analysis is strengthened by Cattaneo–Christov

heat flux accompanying varying thermal conductivity. The appropriate set of transformations is implemented to get a differential equation system with high nonlinearity. The structure is addressed via the homotopy analysis technique. The authenticity of the presented model is verified by creating a comparison with the limited published results and finding harmony between the two. The impacts of miscellaneous arising parameters are deliberated through graphical structures. Some useful tabulated values of arising parameters versus physical quantities are also discussed here. It is observed that velocity components exhibit an opposite trend with respect to the stretching ratio parameter. Moreover, the Brownian motion parameter shows the opposite behavior versus temperature and concentration distributions.

The peristaltic flow of velocity second slip boundary conditions and inclined magnetic field of Jeffrey fluid by means of heat and mass transfer in asymmetric channel was inspected by Saleem et al. [18]. Leading equations that described the existing flow were then simplified under lubrication approach. Therefore, exact solutions of stream function, concentration and temperature were deduced. Further, the numerical solutions of pressure rise and pressure gradient were computed while using Mathematica software. Furthermore, the effect of the second slip parameter was argued via graphs. It has been depicted that this kind of slip is mandatory and very imperative to foresee the physical model. On the other hand, false results will be obtained.

The importance of Hall current coatings in the establishment of Cattaneo–Christov heat flux model in an unsteady aqueous-based nanofluid flow comprising single (SWCNTs) and multi-walled (MWCNTs) carbon nanotubes (CNTs) amid two parallel rotating stretchable disks in reported in [19]. The novelty of the presented model is strengthened with the presence of homogeneous-heterogeneous reactions and thermal stratification effects. The numerical solution of the system of coupled differential equations with high nonlinearity is obtained by applying the bvp4c function of MATLAB software. To corroborate the authenticity of the present envisioned mathematical model, a comparison table is added to this study in limiting case. An excellent harmony between the two results is obtained. The effects of numerous parameters on involved distributions are displayed graphically and are argued logically in the light of physical laws. Numerical values of coefficient of drag force and Nusselt number are also tabulated for different parameters. It is observed that tangential velocity (function of rotation parameter) is increasing for both CNTs. Further, the incremental values of thermal stratification parameter cause the decrease in fluid temperature parameter.

Alghmdi et al. [20] explored the magnetohydrodynamic stretched flow of viscoelastic nanofluids with heterogeneous–homogeneous reactions. Attention in modeling has been specially focused to constitutive relations of viscoelastic fluids. Thermophoresis and Brownian dispersion are utilized to explore the heat and mass transport process. Resulting nonlinear systems are computed for numerical solutions. Findings for temperature, concentration, concentration rate, skin-friction, local Nusselt, and Sherwood numbers are analyzed for both second grade and elastico-viscous fluids.

The role of mixed convective 3D nanoliquid flow by a rotating disk with activation energy and magnetic field is explored in [21]. Flow was created by a rotating disk. Velocity, concentration, and temperature slips at the surface of a rotating disk were considered. The impacts of Brownian diffusion and thermophoretic were additionally accounted for. The non-linear frameworks are simplified by suitable variables. The shooting method is utilized to develop the numerical solution of resulting problem. Plots were prepared just to explore that how concentration and temperature are impacted by different pertinent flow parameters. The Sherwood and Nusselt numbers were additionally plotted and explored. Furthermore, the concentration and temperature were enhanced for larger values of Hartman number. However, the heat transfer rate (Nusselt number) diminishes when the thermophoresis parameter enlarges.

A liquid coating of bubbly flow with peristaltic motion inside elastic walls was investigated by Ijaz et al. [22]. The proposed model is constructed using the two-fluid approach with the most distinctive collaboration among gas, fluid, pressure, and drag forces. The variation in pressure leads to a change in void fraction. The differential controlling conditions affected by the long wavelength of the

peristaltic wave and the slow movement are taken into account. Analytical results of the simplified governing equations are obtained using the homotopy perturbation method (HPM). The features of the significant parameters are shown and examined graphically.

As nanofluids have great potential to enhance thermophysical properties and heat transfer performance. Also double diffusion convection plays an important role in natural processes and technical applications. The effect of double convection by diffusion is not limited to oceanography, but is also evident in geology, astrophysics, and metallurgy. For such a vital role of such factors in applications, Alolaiyan et al. [23] have presented the analytical solutions of pumping flow of third-grade nanofluid and described the effects of double diffusion convection through a compliant curved channel. The model used for the third-grade nanofluid includes the presence of Brownian motion and thermophoresis. Additionally, thermal energy expressions suggest regular diffusion and cross-diffusion terms. The governing equations have been constructed for the incompressible laminar flow of the non-Newtonian nanofluid along with the assumption of long wavelength. The obtained analytical expressions for velocity, temperature, and nanoparticle concentration have been sketched for various considerable parameters. The effects of regular buoyancy ratio, buoyancy parameter, modified Dufour parameter, and Dufour-solutal Lewis number have been analyzed along with wall properties and pumping characteristics. This study concludes that fluid becomes hotter with an increase in regular buoyancy ratio and a modified Dufour parameter, but a decrease in temperature is observed for the buoyancy parameter. Moreover, the solutal concentration is behaving inversely against the Defour–Solutal Lewis number.

A mathematical illustration of an application to endoscopy by incorporating hybrid nanoparticles and an induced magnetic field with a rheological fluid model in inspected by Awais et al. [24] for more realistic results. Rheological fluid behavior is characterized by the Ostwald-de-Waele power-law model. A hybrid nanofluid mechanism is considered comprising platelet-shaped nanoparticles, since nanoparticles are potential drug transportation tools in biomedical applications. Moreover, ciliary activity is encountered regarding their extensive applications in performing complex functions along with buoyancy effects. An endoscope is inserted inside a ciliated tube and peristalsis occurred due to ciliary activity in the gap between tube and endoscope. A non-Newtonian model is developed by mathematical formulation, which is analytically tackled using homotopy analysis. The outcomes are interpreted graphically along with the pressure rise and streamlining configuration for the case of negligible inertial forces and long wavelength. A three-dimensional graphical interpretation of axial velocity is also studied. Moreover, tables are prepared and displayed for a more physical insight.

In [25], the authors developed the mathematical model for entropy generation analysis during the peristaltic propulsion of Jeffrey nanofluids passing in a midst of two eccentric asymmetric annuli. The model was structured by implementation of lubrication perspective and dimensionless strategy. Entropy generation caused by the irreversible influence of heat and mass transfer of nanofluid and viscous dissipation of the considered liquid was taken into consideration. A powerful analytical technique handled the governing equations. The comparison of total entropy with the partial entropy was also invoked by discussing Bejan number results. The influence of various associated variables on the profiles of velocity, temperature, nanoparticle concentration, entropy generation, and Bejan number was formulated by portraying the figures. Mainly from graphical observations, they analyzed that, in the matter of thermophoresis parameter and Brownian motion parameter, entropy generation is thoroughly enhanced while inverse readings were reported for the temperature difference parameter and the ratio of temperature to concentration parameters.

Top coating is usually moulded, painted, or sprayed onto the wind blade Leading-Edge surface to prevent rain erosion due to transverse repeated droplet impacts. Wear fatigue failure analysis based on Springer model has been widely referenced and validated to quantitatively predict damage initiation. The model requires liquid, coating, and substrate speed of sound measurements as constant input parameters to analytically define the shockwave progression due to their relative vibro-acoustic properties. The modelling assumes a pure elastic material behavior during the impact

event. Recent coating technologies applied to prevent erosion are based on viscoelastic materials and develop high-rate transient pressure build-up and a subsequent relaxation in a range of strain rates. In order to analyze the erosion performance by using Springer model, appropriate impedance characterization for such viscoelastic materials is then required and it represents the main objective of this work to avoid lack of accuracy. In [26], the authors have proposed a modelling methodology that allows one to evaluate the frequency dependent strain-stress behavior of the multilayer coating system under single droplet impingement. The computational tool ponders the operational conditions (impact velocity, droplet size, layer thickness, etc.) with the appropriate variable working frequency range for the speed of sound measurements. Moreover, this research defines in a complementary paper, the ultrasonic testing characterization of different viscoelastic coatings and the methodology validation. The modelling framework is then used to identify suitable coating and substrate combinations due to their acoustic matching optimization and analyze the anti-erosion performance of the coating protection system.

Under droplet impingement, surface leading edge protection (LEP) coating materials for wind turbine blades develop high-rate transient pressure build-up and subsequent relaxation in a range of strain rates. The stress-strain coating LEP behavior at a working frequency range depends on the specific LEP and on the material and operational conditions, as described in this research in a previous work. Wear fatigue failure analysis, based on the Springer model, requires coating and substrate speed of sound measurements as constant input material parameters. It considers a linear elastic response of the polymer subjected to drop impact loads, but it does not account for the frequency dependent viscoelastic effects for the materials involved. The model has been widely used and validated in the literature for different liquid impact erosion problems. In [27], an appropriate definition of the viscoelastic materials properties with ultrasonic techniques is investigated. It is broadly used for developing precise measurements of the speed of sound in thin coatings and laminates. It also allows accurately evaluating elastic moduli and assessing mechanical properties at the high frequencies of interest. In the current work, an investigation into various LEP coating application cases have been undertaken and related with the rain erosion durability factors due to suitable material impedance definition. The proposed numerical procedures to predict wear surface erosion have been evaluated in comparison with the rain erosion testing in order to identify suitable coating and composite substrate combinations. LEP erosion performance at rain erosion testing (RET) technique is used widely in the wind industry as the key metric, in an effort to assess the response of the varying material and operational parameters involved.

3. Future Trends in Fluid Mechanics

The material that advances the state-of-the-art experimental, numerical, and theoretical methodologies or extends the bounds of existing methodologies through new contributions in coatings is still insufficient, even with the completion of this Special Issue. The rheological characteristics with thin films under the influence of different nanoparticles and shapes can help with the development of better applications in industry.

Funding: This research received no external funding.

Acknowledgments: The guest editorial team of Coatings would like to thank all authors for contributing their original work to this special issue, no matter what the final decision on their submitted manuscript was. The editorial team would also like to thank all anonymous professional reviewers for their valuable time, comments, and suggestions during the review process. We also acknowledge the entire staff of the journal's editorial board for providing their cooperation regarding this Special Issue. We hope that this issue will, not only provide an overall picture and most up-to-date findings to readers from the scientific community working in the field, but would also benefit the industrial sectors in specific market niches and end users.

Conflicts of Interest: The author declares no conflict of interest.

References

1. Riaz, A.; AlOlayan, H.; Zeeshan, A.; Razaq, A.; Bhatti, M.M. Mass Transport with Asymmetric Peristaltic Propulsion Coated with Synovial Fluid. *Coatings* **2018**, *8*, 407. [CrossRef]
2. Ellahi, R.; Zeeshan, A.; Hussain, F.; Abbas, T. Study of Shiny Film Coating on Multi-Fluid Flows of a Rotating Disk Suspended with Nano-Sized Silver and Gold Particles: A Comparative Analysis. *Coatings* **2018**, *8*, 422. [CrossRef]
3. Lu, D.; Ramzan, M.; Ahmad, S.; Shafee, A.; Muhammad, S. Impact of Nonlinear Thermal Radiation and Entropy Optimization Coatings with Hybrid Nanoliquid Flow Past a Curved Stretched Surface. *Coatings* **2018**, *8*, 430. [CrossRef]
4. Ullah, A.; Alzahrani, E.O.; Shah, Z.; Ayaz, M.; Islam, S. Nanofluids Thin Film Flow of Reiner-Philippoff Fluid over an Unstable Stretching Surface with Brownian Motion and Thermophoresis Effects. *Coatings* **2018**, *9*, 21. [CrossRef]
5. Ali, V.; Gul, T.; Afridi, S.; Ali, F.; Alharbi, S.O.; Khan, I. Thin Film Flow of Micropolar Fluid in a Permeable Medium. *Coatings* **2019**, *9*, 98. [CrossRef]
6. Khan, Z.; Rasheed, H.U.; Alharbi, S.; Khan, I.; Abbas, T.; Chin, D.L.C. Manufacturing of Double Layer Optical Fiber Coating Using Phan-Thien-Tanner Fluid as Coating Material. *Coatings* **2019**, *9*, 147. [CrossRef]
7. Alsagri, A.S.; Nasir, S.; Gul, T.; Saeed, I.; Nisar, K.S.; Shah, Z.; Khan, I. MHD Thin Film Flow and Thermal Analysis of Blood with CNTs Nanofluid. *Coatings* **2019**, *9*, 175. [CrossRef]
8. Lu, D.; Mumtaz, S.; Farooq, U.; Ahmad, A. Analysis of Unsteady Flow and Heat Transfer of Nanofluid Using Blasius–Rayleigh–Stokes Variable. *Coatings* **2019**, *9*, 211. [CrossRef]
9. Saeed, A.; Shah, Z.; Islam, S.; Jawad, M.; Ullah, A.; Gul, T.; Kumam, P. Three-Dimensional Casson Nanofluid Thin Film Flow over an Inclined Rotating Disk with the Impact of Heat Generation/Consumption and Thermal Radiation. *Coatings* **2019**, *9*, 248. [CrossRef]
10. Lu, D.; Ramzan, M.; Mohammad, M.; Howari, F.; Chung, J.D. A Thin Film Flow of Nanofluid Comprising Carbon Nanotubes Influenced by Cattaneo-Christov Heat Flux and Entropy Generation. *Coatings* **2019**, *9*, 296. [CrossRef]
11. Ellahi, R.; Zeeshan, A.; Abbas, T.; Hussain, F. Thermally Charged MHD Bi-phase Flow Coatings with non-Newtonian Nanofluid and Hafnium Particles along Slippery Walls. *Coatings* **2019**, *9*, 300. [CrossRef]
12. Dawar, A.; Shah, Z.; Kumam, P.; Khan, W.; Islam, S. Influence of MHD on Thermal Behavior of Darcy-Forchheimer Nanofluid Thin Film Flow over a Nonlinear Stretching Disc. *Coatings* **2019**, *9*, 446. [CrossRef]
13. Akram, S.; Aly, E.H.; Afzal, F.; Nadeem, S. Aly Effect of the Variable Viscosity on the Peristaltic Flow of Newtonian Fluid Coated withMagnetic Field: Application of Adomian Decomposition Method for Endoscope. *Coatings* **2019**, *9*, 524. [CrossRef]
14. Lund, L.A.; Ching, D.L.C.; Omar, Z.; Khan, I.; Nisar, K.S. Triple Local Similarity Solutions of Darcy-Forchheimer Magnetohydrodynamic (MHD) Flow of Micropolar Nanofluid Over an Exponential Shrinking Surface: Stability Analysis. *Coatings* **2019**, *9*, 527. [CrossRef]
15. Lund, L.A.; Omar, Z.; Alharbi, S.O.; Khan, I.; Nisar, K.S. Numerical Investigation of Multiple Solutions for Caputo Fractional-Order-Two Dimensional Magnetohydrodynamic Unsteady Flow of Generalized Viscous Fluid over a Shrinking Sheet Using the Adams-Type Predictor-Corrector Method. *Coatings* **2019**, *9*, 548. [CrossRef]
16. Riaz, A.; Alolaiyan, H.; Razaq, A. Convective Heat Transfer and Magnetohydrodynamics across a Peristaltic Channel Coated with Nonlinear Nanofluid. *Coatings* **2019**, *9*, 816. [CrossRef]
17. Ramzan, M.; Liaquet, A.; Kadry, S.; Yu, S.; Nam, Y.; Lu, D. Impact of Second-Order Slip and Double Stratification Coatings on 3D MHD Williamson Nanofluid Flow with Cattaneo–Christov Heat Flux. *Coatings* **2019**, *9*, 849. [CrossRef]
18. Saleem, N.; Akram, S.; Afzal, F.; Aly, E.H.; Hussain, A. Impact of Velocity Second Slip and Inclined Magnetic Field on Peristaltic Flow Coating with Jeffrey Fluid in Tapered Channel. *Coatings* **2020**, *10*, 30. [CrossRef]
19. Ramzan, M.; Riasat, S.; Kadry, S.; Kuntha, P.; Nam, Y.; Howari, F. Numerical Analysis of Carbon Nanotube-Based Nanofluid Unsteady Flow Amid Two Rotating Disks with Hall Current Coatings and Homogeneous–Heterogeneous Reactions. *Coatings* **2020**, *10*, 48. [CrossRef]
20. Alghamdi, M. On Magnetohydrodynamic Flow of Viscoelastic Nanofluids with Homogeneous–Heterogeneous Reactions. *Coatings* **2020**, *10*, 55. [CrossRef]
21. Alghamdi, M. Significance of Arrhenius Activation Energy and Binary Chemical Reaction in Mixed Convection Flow of Nanofluid Due to a Rotating Disk. *Coatings* **2020**, *10*, 86. [CrossRef]

22. Ijaz, N.; Riaz, A.; Zeeshan, A.; Ellahi, R.; Sait, S. Buoyancy Driven Flow with Gas-Liquid Coatings of Peristaltic Bubbly Flow in Elastic Walls. *Coatings* **2020**, *10*, 115. [CrossRef]
23. Alolaiyan, H.; Riaz, A.; Razaq, A.; Saleem, N.; Zeeshan, A.; Bhatti, M. Effects of Double Diffusion Convection on Third Grade Nanofluid through a Curved Compliant Peristaltic Channel. *Coatings* **2020**, *10*, 154. [CrossRef]
24. Awais, M.; Shah, Z.; Perveen, N.; Ali, A.; Kumam, P.; Rehman, H.U.; Thounthong, P.; Parveen, N. MHD Effects on Ciliary-Induced Peristaltic Flow Coatings with Rheological Hybrid Nanofluid. *Coatings* **2020**, *10*, 186. [CrossRef]
25. Riaz, A.; Gul, A.; Khan, I.; Ramesh, K.; Khan, S.U.; Baleanu, D.; Nisar, K.S. Mathematical Analysis of Entropy Generation in the Flow of Viscoelastic Nanofluid through an Annular Region of Two Asymmetric Annuli Having Flexible Surfaces. *Coatings* **2020**, *10*, 213. [CrossRef]
26. Domenech, L.; Renau, J.; Šakalytė, A.; Sánchez, F. Top Coating Anti-Erosion Performance Analysis in Wind Turbine Blades Depending on Relative Acoustic Impedance. Part 1: Modelling Approach. *Coatings* **2020**, *10*, 685. [CrossRef]
27. Domenech, L.; García-Peñas, V.; Šakalytė, A.; Francis, D.P.; Skoglund, E.; Sánchez, F. Top Coating Anti-Erosion Performance Analysis in Wind Turbine Blades Depending on Relative Acoustic Impedance. Part 2: Material Characterization and Rain Erosion Testing Evaluation. *Coatings* **2020**, *10*, 709. [CrossRef]

coatings

MDPI

Article

Mass Transport with Asymmetric Peristaltic Propulsion Coated with Synovial Fluid

Arshad Riaz [1,*], Hanan A. Al-Olayan [2], Ahmad Zeeshan [3], Abdul Razaq [1] and Muhammad Mubashir Bhatti [4]

1 Department of Mathematics, University of Education, Lahore, Jauharabad Campus, Jauharabad 41200, Pakistan; makenqau@gmail.com
2 Department of Mathematics, King Saud University, Riyadh 11451, Saudi Arabia; holayan@ksu.edu.sa
3 Department of Mathematics & Statistics, FBAS, IIUI, Islamabad 44000, Pakistan; ahmad.zeeshan@iiu.edu.pk
4 Shanghai Institute of Applied Mathematics and Mechanics, Shanghai University, Shanghai 200072, China; muhammad09@shu.edu.cn
* Correspondence: arshad-riaz@ue.edu.pk

Received: 17 September 2018; Accepted: 13 November 2018; Published: 16 November 2018

Abstract: This article aims to model two-dimensional, incompressible asymmetric peristaltic propulsion coated with Synovial fluid ("non-Newtonian model") with mass transport. Due to the coating of the same base-fluid at the surface of the channel, the boundaries become non-porous and exert no slip on the fluid particles. Two illustrative models for the viscosity, namely, shear-thinning (Model 1) and shear-thickening (Model 2), are considered, which reveal the presence and integrity of coating. The perturbation method has been applied to linearize the complicated differential equations. Model 1 predicted higher viscosity values and more significant non-Newtonian behavior than Model 2. It is also observed that the shear-thinning model behaved in quite the opposite manner for the shear thickening model. The converse behavior of Models 1 and 2 occurs due to a curvature of the flow domain. Moreover, Model 1 is not able to capture the correct exponential viscosity dependence on concentration for the whole range of shear rates. On the other hand, the second model shows a strong relationship with accurate power. Solutions are attained for velocity field, concentration profile, and pressure gradient. The novelty of all the essential parameters is analyzed through graphical results. Furthermore, streamlines are also drawn to determine the trapping mechanism. The present analysis is beneficial in the study of intrauterine fluid dynamics; furthermore, it is applicable in vivo diagnostic; drug delivery; food diagnostics; protein chips; and cell chips and packaging, i.e., smart sensors.

Keywords: Synovial fluid; coating; shear-thinning and -thickening models; mass transport; asymmetric channel; analytical solution

1. Introduction

Synovial fluid is secreted to the cavity by its inner membrane called Synovial [1]. It is a biological fluid filling the Synovial joint-cavity's several-micrometers-thick layer between the interstitial cartilages [2]. The main component of Synovial fluid is ultrafiltration of the blood plasma devoid of high-molecular proteins, blood cells, and aggressors. Synovial fluid supports joints via high effective cartilage lubrication, while its essential component is an added lubricant called hyaluronan/hyaluronic acid [3]. Several studies showed that the viscoelastic features of Synovial fluid occur due to hyaluronic acid [4]. Hyaluronic acid is natively present in the Synovial fluid in relatively high concentrations [5]. It is experimentally [6] confirmed that the viscoelastic features of Synovial fluids strongly rely on a concentration of hyaluronic acid; therefore, the magnitude of

polymerization is substantial, because the volume of hyaluronic random coils exhibits a momentous role in the viscoelastic attributes of Synovial fluid [7,8].

Furthermore, Synovial fluid contains mixtures that reveal a viscoelastic fashion. When a Synovial fluid is propagating with versatile conditions where there is no instantaneous input, then it performs as a Stokesian fluid. When it is only subject to immediate input, then its viscoelastic charactersitics manifests itself. Hron et al. [9] examined the flow analysis of three separate models that could be referred to as Synovial fluid models. These models fit into the type of generalized viscous fluids, whereas only one goes fits into the class of a shear-thinning model in which the power-law exponent relies upon the concentration.

Moreover, incompressible non-Newtonian liquids have attracted great interest in recent years. Perhaps this is due to academic curiosity and their several industrial applications including synthetic lubricants, colloidal fluids, and liquid crystals. It is found that various physiological fluids reveal non-Newtonian behavior. Non-Newtonian characteristics produce satisfactory results when analyzing the mechanism of peristalsis propagating in lymphatic vessels, blood vessels, ductus afferents, intestines, the motion of urine in the human body, food bolus moving through esophagus, the movement of spermatozoa in a vas deferens, the blending of food material, Chyme motion, cilia propagation, blood circulation, and the propagation of bile in a bile duct. A peristaltic movement is a fluid transport that happens because of the contraction and extension of smooth walls. Recently, many authors have determined the peristaltic mechanism in various boundary and initial conditions. Notably, Mekheimer et al. [10] calculated the peristaltic phenomenon of magnetized couple-stress fluid along with the effects of the induced magnetic field. He further achieved the exact analytics solutions for the velocity profile. Srinivas and Kothandapani [11] examined the mass and heat transfer impact on the peristaltic transportation of viscous liquid. They formulated the governing flow using the lubrication approach and obtained the exact solution. Further, they assumed that fluid is travelling in a porous medium having compliant walls. Riaz et al. [12] modeled the unsteady peristaltic flow of Carreau fluid propagating through a small intestine and presented analytic solutions using the perturbation method. Akram et al. [13] explored the behavior of lateral walls on the non-uniform, peristaltic-propelled three-dimensional flow of the couple stress fluid model. Ellahi et al. [14] also discussed the three-dimensional motion of Carreau fluid with an external uniform magnetic field. They used the Homotopy perturbation scheme to obtain the solutions of the obtained non-linear partial differential equations. They determined that the magnetic field is a significant factor in the preservation of the flow field. Bhatti et al. [15] examined the behavior of the oblique magnetic field with heat transfer on the uniform peristaltic motion containing small particles. They presented the exact solutions for the fluid and particulate phases, whereas numerical integration was used to determine the pumping characteristics. Sinha et al. [16] presented the peristaltic motion of viscous liquid containing a variable viscosity under the inclusion of heat exchange and the static magnetic field with asymmetric geometry. They obtained the perturbation solutions under the slip conditions and temperature jump. Shit et al. [17] examined the asymmetrical motion of a micropolar fluid with the induced magnetic field. They obtained exact results for micro-rotation components, magnetic force function, the velocity profile, and the current density profile. A mathematical analysis of a micropolar fluid in an artery having composite stenosis was measured by Ellahi et al. [18]. Bhatti et al. [19] evaluated the peristaltic propulsion of magnetized solid particles in Biorheological fluids. They considered the model of Casson fluid and obtained the exact results for liquid and particulate phase against velocity and temperature profile. Peristaltic motion through a porous channel was presented by Maiti and Misra [20]. They discussed the bile flow with in ducts in the pathological state. Bhatti et al. [21] considered the combined electric and magnetic field impact on the propulsion of the peristaltic third-grade fluid model containing small particles. They further considered the heat transfer effects and obtained the analytical results using Homotopy perturbation methods.

Furthermore, Kabov et al. [22] experimentally discussed the two-phase flow propagating through a microchannel. Mekheimer and Elmaboud [23] addressed the impression of heat exchange and

magnetic field on the viscous-fluid model stimulated in peristaltic fashion. They explained the influence of endoscope and bioheat transfer. Elmaboud and Mekheimer [24] addressed the nonlinear peristaltic motion of second-grade fluid propagating through a porous geometry. They further applied the perturbation method to solve the velocity equations, whereas pumping features and friction forces were evaluated by numerical integration. Khan et al. [25] studied the behavior of changeable viscosity of the Jeffrey fluid model propagating through the asymmetric porous channel. Transient peristaltic flow through a permeable finite channel was determined by Tripathi [26]. Chaube et al. [27] discussed the peristaltic flow of the power-law model using the creeping flow regime. Shit et al. [28] also discussed the role of velocity slip on the wavy motion of the couple stress fluid model. They mainly focused on a peristaltic movement in the digestive system. Later, Shit et al. [29] governed the peristaltic biofluid flow through a microchannel. Moreover, they also considered the EMHD ("Electro-Magnetohydrodynamic") and velocity slip due to a hydrophobic/hydrophilic collision between negatively charged walls. Recently, Zeeshan et al. [30] addressed the behavior of the Sisko fluid model propagating across a non-uniform peristaltic channel. They obtained the second order solution using the Homotopy perturbation method. Some more useful studies related to the topic can be seen in [31,32].

According to literature surveyed, it is observed that no results have been presented yet to examine the behavior of Synovial fluid on peristaltic propulsion through an asymmetric channel. According to our knowledge, not a single mathematical model is given in the literature describing the behavior of Synovial fluid for peristaltic flow. The governing fluid holds the properties of incompressibility and irrotational and constant density. Furthermore, mass transport is also taken into account to discuss the present flow. Mass transportation is also an important phenomenon in the propagation of mass from one region to another region. Therefore, the primary theme of the current study is to present a theoretical and mathematical analysis of the said topic to fill this gap in the literature. The graphical results are presented for two different models of Synovial fluid.

2. Mathematical Modeling

The peristaltic (or "sinusoidal") motion of Synovial fluid described by generalized incompressible fluid possesses the Navier-Stokes equations with a viscosity depending on a shear rate and concentration. We must couple this system with one extra convection-diffusion equation for a concentration of hyaluronic acid. The fundamental equations of governing flow with synovial fluid model are described in reference [8] as follows:

$$\mathrm{div}V = 0 \tag{1}$$

$$\frac{\partial V}{\partial t} + V \cdot \nabla V + \frac{\nabla p}{\rho} = \frac{2}{\rho}\mathrm{div}(\Theta) \tag{2}$$

$$\frac{\partial C}{\partial t} = \mathrm{div}(F(C)) - \mathrm{V} \cdot \nabla C \tag{3}$$

in above equation:

$$F(C) = D_C \nabla C,\ \Theta = \mu(C,\ D)\ D \tag{4}$$

in which $\Delta V(U,V)$ is velocity, μ is viscosity, D is symmetric part of velocity gradient, P is pressure, ρ is density, F is concentration flux, C is concentration of hyaluronan/hyaluronic, and D_C is constant diffusivity.

Let us focus on two-dimensional peristaltic flows in an asymmetric channel containing width $d_1 + d_2$ due to wave traveling in direction of flow with constant velocity c. The flow is discussed in Cartesian coordinates. The mass concentrations upon the upper wall are C_0, whereas on the bottom wall they are C_1. Peristaltic motion on the upper and lower internal surfaces is recognized as

$$H_1(X,\ t) = Y = d_1 + b_1 \cos 2\pi(X - ct)\frac{1}{\lambda} \tag{5}$$

$$H_2(X,t) \;=\; Y \;=\; -d_2 - b_2\cos[(X-ct)2\pi+\lambda\phi]\frac{1}{\lambda} \tag{6}$$

To translate the coordinates, we use the same procedure that was used in [13].

The consequent relations of the boundaries of channel are described as

$$h_1(x) \;=\; y-1 \;=\; a\cos 2\pi x \tag{7}$$

$$h_2(x) \;=\; y \;=\; -b\cos(\phi+2\pi x) - d \tag{8}$$

Synovial Fluid Model

The peristaltic motion of viscous synovial fluid (see [33,34]) with thin film coating at the walls is considered in a two-dimensional channel. The flow patterns corresponding to Models 1 and 2 are markedly different. We shall ignore the detailed discussion here. However, fewer essential points associated with the model are presented. The models under consideration present exciting features. Model 1 is a simple generalized form of a power-law mathematical model for a shear-dependent viscosity that is helpful to define various non-Newtonian fluids in biological and polymer fluid mechanics, food rheology, and geology, to consider the basis of viscosity that affects the concentration of a reactant. Model 2 describes that exponent is a function of concentration.

Model 1: The generalized power-law model and the viscosity are exponentially dependent on concentration, then the Model 1 is written as:

$$\mu(C,\,D) \;=\; \mu_0 e^{\alpha C}\left(1+\gamma^2\left|D^2\right|\right)^n \tag{9}$$

Model 2: In this model, a shear-thinning index depends upon the concentration (i.e., zero concentration):

$$\mu(C,\,D) \;=\; \mu_0\left(1+\gamma^2\left|D^2\right|\right)^{n(C)} \tag{10}$$

in which,

$$|D| \;=\; \sqrt{2\left(\frac{\partial u}{\partial x}\right)^2 + 2\left(\frac{\partial u}{\partial y}\right)^2 + \left(\frac{\partial v}{\partial x}+\frac{\partial u}{\partial y}\right)^2} \tag{11}$$

and

$$n(C) \;=\; -\frac{e^{\alpha C}-1}{2e^{\alpha C}} \tag{12}$$

in which n is index of shear-thinning comprising values between -0.5 and 0. It is worth mentioning that results of Newtonian fluid are obtained as a particular case of current fluid when $n = 0$.

The governing equations are too arduous to be acquiescent to stability analysis. Therefore, it is necessary to simplify the modeled equations. Make sure that the simplification process is congruous for such problems. Henceforth, we shall assume the long wavelength constraint, i.e., $\delta \ll 1$ and less Reynolds number $\mathrm{Re} \approx O(1)$. Now, it is suitable to make the observing equations dimensionless by defining the following ratios:

$$\begin{gathered}\overline{y} \;=\; \frac{y}{d_1}, \alpha \;=\; \alpha^*(C_1-C_0),\; \sigma \;=\; \frac{C-C_0}{C_1-C_0}, \overline{\mu} \;=\; \frac{\mu}{\mu_0},\; \overline{h} \;=\; \frac{H}{d_1},\; \overline{p} \;=\; \frac{d_1^2 p}{\mu c\lambda}, \delta \;=\; \frac{d_1}{\lambda},\; a \;=\; \frac{b_1}{d_1},\\ b \;=\; \frac{b_2}{d_1}, d \;=\; \frac{d_2}{d_1},\; \mathrm{We} \;=\; \frac{\gamma c}{d_1},\; |\overline{D}| \;=\; \frac{d_1}{c}|D|, S_c \;=\; \frac{\mu}{\rho D_C},\; \overline{v} \;=\; \frac{v}{c\delta},\; \mathrm{Re} \;=\; \frac{\rho d_1 c}{\mu},\; \overline{u} \;=\; \frac{u}{c}, \overline{x} \;=\; \frac{x}{\lambda}\end{gathered} \tag{13}$$

In above expression, S_c denotes Schmidt number, R_e stands for Reynolds number, α represents concentration production, and γ is a material parameter.

The resulting non-dimensional governing equations along with Models 1 and 2 after exempting bar symbols in a wave frame will observe the following form:

$$\frac{\partial v}{\partial y} \;=\; -\frac{\partial u}{\partial x} \tag{14}$$

$$\frac{\partial p}{\partial x} = \begin{cases} \frac{1}{2}\frac{\partial}{\partial y}\left[(1+\alpha\sigma)\left\{1+n\mathrm{We}^2\left(\frac{\partial u}{\partial y}\right)^2\right\}\frac{\partial u}{\partial y}\right] & \text{(Model 1)} \\ \frac{\partial^2 u}{\partial y^2} - \frac{\alpha \mathrm{We}^2}{2}\frac{\partial}{\partial y}\left[\sigma\left(\frac{\partial u}{\partial y}\right)^3\right] & \text{(Model 2)} \end{cases} \tag{15}$$

Concentration equation for Models 1 and 2 is simplified to the following form:

$$\frac{1}{S_c}\frac{\partial^2 \sigma}{\partial y^2} = 0 \tag{16}$$

The no slip boundary conditions become:

$$u(h_1) = -1\, u(h_2) = -1,\ \sigma(h_1) = 0,\ \sigma(h_2) = 1 \tag{17}$$

3. Solution Procedure

The analytical solutions of Equations (15)–(17) have been determined by regular perturbation method. To solve the problem under consideration, we presented the flow quantities wherein the velocity, concentration, and pressure interns of small Weissenberg number (We) have the following form:

$$u(x,\, y) = u_{0,\,i} + (\mathrm{We})^2 u_{1,\,i} + (\mathrm{We})^4 u_{2,\,i} + \ldots,\ i = 1,\, 2. \tag{18}$$

$$\sigma = \sigma_0 + (\mathrm{We})^2\sigma_1 + (\mathrm{We})^4\sigma_2 + \ldots \tag{19}$$

$$K = (K)_{0,i} + (\mathrm{We})^2(K)_{1,i} + (\mathrm{We})^4(K)_{2,i} + \ldots,\quad i = 1, 2, \ldots \tag{20}$$

in which $K = \frac{\mathrm{d}p}{\mathrm{d}x}$. After the implementation of above expressions in Equations (15)–(17) and equating the exponents of We, one obtains the following systems of equations along with associated boundary conditions.

3.1. Model 1

- System of Order Zero

$$K_{0,\,1} = \frac{1}{2}\left(\alpha\frac{\partial\sigma_0}{\partial y}\frac{\partial u_{0,\,1}}{\partial y} + (1+\alpha\sigma_0)\frac{\partial^2 u_{0,\,1}}{\partial y^2}\right) \tag{21}$$

$$\frac{1}{S_c}\frac{\partial^2\sigma_0}{\partial y^2} = 0 \tag{22}$$

Along with the boundary conditions:

$$u_{0,\,1}(h_1) = -1,\ u_{0,\,1}(h_2) = -1,\ \sigma_0(h_1) = 0,\ \sigma_0(h_2) = 1 \tag{23}$$

- System of Order One

$$\begin{aligned} K_{1,\,1} = {} & \frac{1}{2}\left(\alpha\frac{\partial\sigma_0}{\partial y}\frac{\partial u_{1,\,1}}{\partial y} + (1+\alpha\sigma_0)\frac{\partial^2 u_{1,\,1}}{\partial y^2}\right) + \frac{n\alpha}{2}\frac{\partial\sigma_0}{\partial y}\left(\frac{\partial u_{0,\,1}}{\partial y}\right)^3 \\ & + \frac{3n}{2}(1+\alpha\sigma_0)\left(\frac{\partial u_{0,\,1}}{\partial y}\right)^2\frac{\partial^2 u_{0,\,1}}{\partial y^2} \end{aligned} \tag{24}$$

$$\frac{1}{S_c}\frac{\partial^2\sigma_1}{\partial y^2} = 0 \tag{25}$$

and the boundary conditions:

$$u_{1,\,1}(h_1) = 0,\ u_{1,\,1}(h_2) = 0,\ \sigma_1(h_1) = 0,\ \sigma_1(h_2) = 0. \tag{26}$$

Obtaining the solutions of the above sets of equations by making use of mathematical software Mathematica 7.0, we have the following results:

- Zeroth Order Solution

$$u_{0,1} = \frac{1}{\alpha(\ln(h_2-h_1) - \alpha\ln(h_2-h_1)\ (1+\alpha)} \begin{bmatrix} (2(h_1-h_2)\ K_{0,1}(h_2-y)-\alpha)\ \ln(h_2-h_1) \\ -(2(-h_2+h_1)\ K_{0,1}(h_1-y)-\alpha)(\alpha+1)\ \ln(h_2-h_1) \\ +2(h_1-h_2)^2 K_{0,1}\ln(h_2+y\alpha-h_1(1+\alpha)) \end{bmatrix} \quad (27)$$

$$\sigma_0 = \frac{1-y+a\cos(2\pi x)}{1+d+a\cos(2\pi x)+b\cos(2\pi x+\varphi)} \quad (28)$$

- First Order Solution

$$\begin{aligned} u_{1,1} = & \frac{2(h_2-h_1)}{\alpha^4}(h_1-h_2-h_1\alpha+y\alpha)\ \Big[4h_1^2 nK_{0,1}^3 - 8h_1h_2nK_{0,1}^3 + 4h_2^2nK_{0,1}^3 \\ & - K_{1,1}\alpha^2\Big] + \frac{4(h_2-h_1)^6 n}{\alpha(-h_1+h_2+h_1\alpha-y\alpha)^2(\ln[h_1-h_2]-\ln[(h_1-h_2)(1+\alpha)])^3}K_{0,1}^3 \\ & + \frac{24(h_2-h_1)^5 n}{\alpha^2(-h_1+h_2+h_1\alpha-y\alpha)(\ln[h_1-h_2]-\ln[(h_1-h_2)(1+\alpha)])^2}K_{0,1}^3 \\ & - \frac{2(h_2-h_1)\ C_1}{\alpha^4\Big((1+\alpha)^2(\ln[h_1-h_2]-\ln[(h_1-h_2)(\alpha+1)])^3(\ln[h_2-h_1]-\ln[(h_2-h_1)(1+\alpha)])\Big)}\times \\ & K_{0,1}^3 + \frac{1}{\alpha^4\Big((1+\alpha)^2(\ln[h_1-h_2]-\ln[(h_1-h_2)(1+\alpha)])^3(\ln[h_2-h_1]-\ln[(h_2-h_1)(1+\alpha)])\Big)} \\ & \Big[2(-h_1+h_2)\ \Big((-h_1+h_2)\Big(\Big(K_{0,1}^3C_2+K_{1,1}C_3\Big)\ \ln[h_2-h_1] \\ & + \Big(K_{0,1}^3C_4+K_{1,1}C_5\Big)\ (1+\alpha)^2\ln[(h_2-h_1)(1+\alpha)]\Big)\Big)\Big] \end{aligned} \quad (29)$$

$$\sigma_1 = 0 \quad (30)$$

here,

$$K_{0,1} = \frac{(1+d+h_2-Q-h_1)\alpha^2(\ln[h_2-h_1]-\ln[(h_2-h_1)(1+\alpha)])}{(-h_2+h_1)^3(2\alpha+(\alpha+2)\ln[h_2-h_1]-(2+\alpha)\ln[(h_2-h_1)(1+\alpha)])} \quad (31)$$

$$\begin{aligned} K_{1,1} = & -((1+d-Q)\alpha^2(\ln[h_1-h_2]-\ln[(h_1-h_2)(1+\alpha)]))/ \\ & ((h_1-h_2)^2(-2h_1\alpha+2h_2\alpha+(h_1+h_2)\alpha\ln[h_1-h_2]- \\ & 2(h_1-h_2+h_1\alpha)\ln[-h_1+h_2]-h_1\alpha\ln[(h_1-h_2)(1+\alpha)]- \\ & h_2\alpha\ln[(h_1-h_2)(1+\alpha)]+2h_1\ln[(-h_1+h_2)(1+\alpha)]- \\ & 2h_2\ln[(-h_1+h_2)(1+\alpha)]+2h_1\alpha\ln[(-h_1+h_2)(1+\alpha)])) \end{aligned} \quad (32)$$

In above-presented equations, C_1–C_5 are some lengthy calculations that have particular values by considering above-given boundary conditions and are defined in Appendix A.

3.2. Model 2

The same contrast as described for Model 1 along with solutions are summarized as:

- System of Order Zero

$$K_{0,2} = \frac{\partial^2 u_{0,2}}{\partial y^2} \quad (33)$$

- System of Order One

$$K_{1,2} = \frac{\partial^2 u_{1,2}}{\partial y^2} - \frac{\alpha}{2}\frac{\partial}{\partial y}\left(\sigma_0\left(\frac{\partial u_{0,2}}{\partial y}\right)^3\right) \quad (34)$$

- Zeroth Order Solution

$$u_{0,2} = \frac{1}{2}\Big(-2+h_1h_2K_{0,2}-h_1K_{0,2}y-h_2K_{0,2}y+K_{0,2}y^2\Big) \quad (35)$$

- First Order Solution

The solution of above equation is examined directly and is prescribed as:

$$\begin{aligned} u_{1,2} = \; & \tfrac{1}{160(h_1-h_2)}(h_1-y)(h_2-y)(-80h_2K_{1,2}+9h_1^3K_{0,2}^3\alpha-h_2^3K_{0,2}^3\alpha- \\ & 6h_2^2K_{0,2}^3y\alpha+14h_2K_{0,2}^3y^2\alpha-16K_{0,2}^3y^3\alpha-h_1^2K_{0,2}^3(h_2+26y)\alpha+ \\ & h_1\left(80K_{1,2}+K_{0,2}^3(9h_2^2-16h_2y+34y^2)\alpha\right)\Big) \end{aligned} \tag{36}$$

here,

$$K_{0,2} = -\frac{12(-1-d+h_1-h_2+Q)}{(h_1-h_2)^3} \tag{37}$$

$$\begin{aligned} K_{1,2} = \; & -\tfrac{1}{5(h_1-h_2)^7}12(-5h_1^4(1+d-Q)-5h_2^4(1+d-Q)+h_1^3(20h_2(1+d-Q) \\ & -27\alpha)+27h_2^3\alpha+81h_2^2(1+d-Q)\alpha+81h_2(1+d-Q)^2\alpha+27(1+d-Q)^3 \\ & \alpha+h_1^2(-30h_2^2(1+d-Q)+81h_2\alpha+81(1+d-Q)\alpha)+h_1(20h_2^3(1+d-Q) \\ & -81h_2^2\alpha-162h_2(1+d-Q)\alpha-81(1+d-Q)^2\alpha)) \end{aligned} \tag{38}$$

Pressure rise Δp over one wavelength in dimensionless format is obtained by

$$\Delta p = \int_0^1 K\mathrm{d}x \tag{39}$$

The integral in Equation (41) is evaluated numerically using software package Mathematica 7.0.

4. Graphical Analysis

This study describes a critical analysis with which to approach two different fluid models that can disclose the properties of Synovial fluid when there is no slip at the boundaries and thin-film coating with non-Newtonian thick fluid (Synovial) is applied the walls. A non-linear coupled system of partial differential equations subject to boundary conditions is solved for shear-thinning and thickening models (Models 1 and 2). The complicated equations are solved by a regular perturbation method. To analyze graphically, Figures 1–11 have been sketched to measure the behavior of emerging factors on velocity distribution, pressure gradient profile, pressure rise, and trapping phenomena. Figures 1 and 2 show the effect of concentration parameter α and Weissenberg number We on the velocity component u for both models, respectively. It is extracted that velocity behaves in an opposite manner to shear-thinning and thickening models against multiple values of α. The Weissenberg number is helpful to analyze viscoelastic flows. It is the ratio of elastic forces and viscous forces. In Figure 2, we can understand that the velocity distribution of Model 1 behaves as an increasing quantity for higher values of Weissenberg number. This behavior reveals that elastic forces are dominant over viscous forces. However, the reaction of Model 2 is opposite as matched to Model 1. In Model 2, it can be noticed that viscous forces are dominant over elastic forces. This implies that the nature of shear thinning (Model 1) and the thickening (Model 2) are entirely different. Figure 3 displays the dependence of velocity on the average volume flow rate, as expected increase in the value of Q increases the flow velocity in both models.

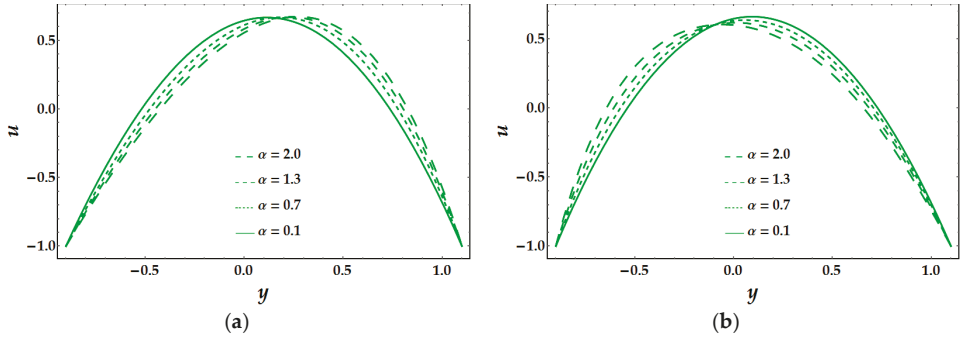

Figure 1. Effects of α on velocity profile with $n = -0.28$, $Q = 2$, $x = 0$, $a = 0.1$, $b = 0.1$, $d = 0.8$, $\varphi = 0.1$, We = 0.05 for (**a**) Model 1 and (**b**) Model 2.

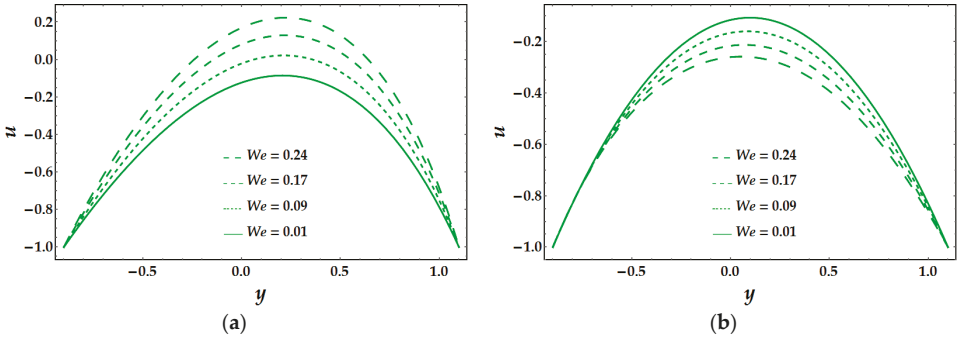

Figure 2. Effects of We on velocity profile with $n = -0.28$, $Q = 1$, $x = 0$, $a = 0.1$, $b = 0.1$, $d = 0.8$, $\varphi = 0.1$, $\alpha = 0.9$ for (**a**) Model 1 and (**b**) Model 2.

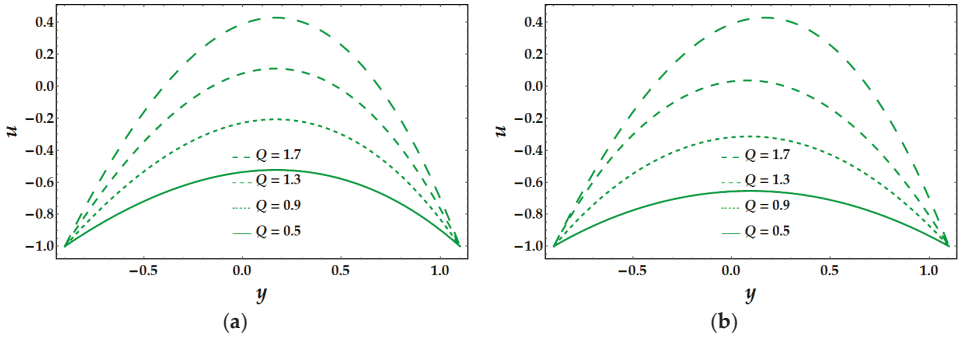

Figure 3. Effects of Q on velocity profile with $n = -0.28$, $\alpha = 0.5$, $x = 0$, $a = 0.1$, $b = 0.1$, $d = 0.8$, $\varphi = 0.1$, We = 0.05 for (**a**) Model 1 and (**b**) Model 2.

To compare the differences between two models, we include Figures 4–6 for pressure gradient dp/dx. In Figures 4 and 5, it is noted that with an excess of α and Q pressure gradient rises. As one can see, the prediction of the viscosity magnitude gets much larger values for the Model 2, unlike Model 1, whereas Weissenberg number We acts in an opposite way, that is, the change in pressure becomes larger throughout the flow and smaller for Model 2 than for Model 1 (see Figure 6).

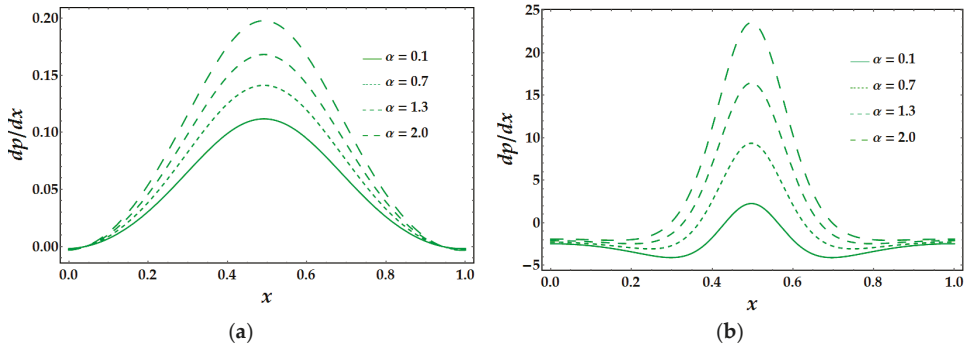

Figure 4. Effects of α on pressure gradient with $n = -0.28$, $Q = 0.1$, $a = 0.1$, $b = 0.1$, $d = 2$, $\varphi = 0.1$, We = 0.05 for (**a**) Model 1 and (**b**) Model 2.

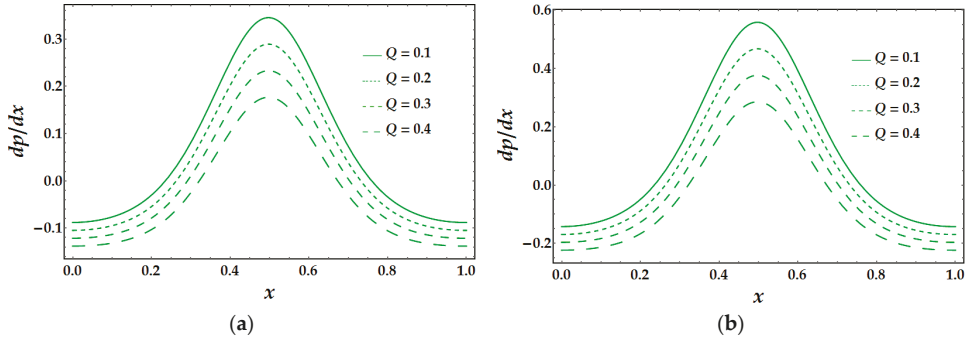

Figure 5. Effects of Q on pressure gradient with $n = -0.28$, $\alpha = 0.5$, $a = 0.5$, $b = 0.1$, $d = 2$, $\varphi = 0.1$, We = 0.05 for (**a**) Model 1 and (**b**) Model 2.

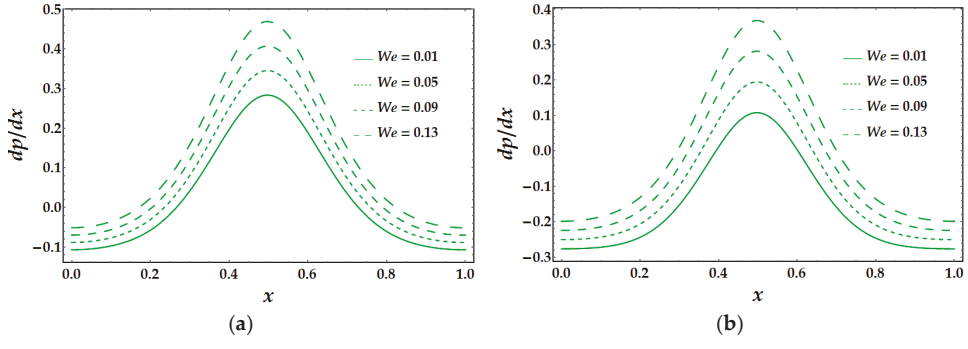

Figure 6. Effects of We on pressure gradient with $n = -0.28$, $Q = 0.1$, $a = 0.5$, $b = 0.1$, $d = 2$, $\varphi = 0.1$, $\alpha = 0.5$ for (**a**) Model 1 and (**b**) Model 2.

Figures 7–9 are plotted to determine the behavior of pumping rate in different regions. The pumping features can be examined by the pressure rise (Δp) versus the average volume flow rate/mean flux Q. The complete area is divided into four quarters [13]. Figure 7a describes the pressure rise Δp under the variety in values of α. It is observed that pressure rise is linearly dependent on flow rate, and free pumping is attained at $Q = 0$. It is evaluated here that while increasing α, the pressure rise Δp decreases in Region II, whereas it increases in Region III. Figure 7b is plotted for Model 2, and

one can easily infer from it that dependence is not linear other than in $\alpha = 0.1$. This figure indicates that with an increase in α, magnitude of Δp decreases in Region III and has opposite behavior in other two regions. The effects of phase angle φ on Δp are depicted in Figure 8. For Model 1, we can visualize that there is an increase of pressure rise in Region II when φ increases, while the reverse situation is found in Region II and remains consistent in Region I. It is entirely possible that the opposite behavior of Model 1 and Model 2 is due to the curvature in the flow domain. Figure 9a examines the influence of Weissenberg number We on Δp for Model 1. It is noticed that Δp increases by increasing We in Regions I and II, while the reduction in pressure rise is seen in Region III. On the other hand, the behavior of pressure gradient for We is also noted in Figure 9b. Model 2 shows a continuous increase in the Region I, hasty fall in Region II, and a drastic increase in Region III.

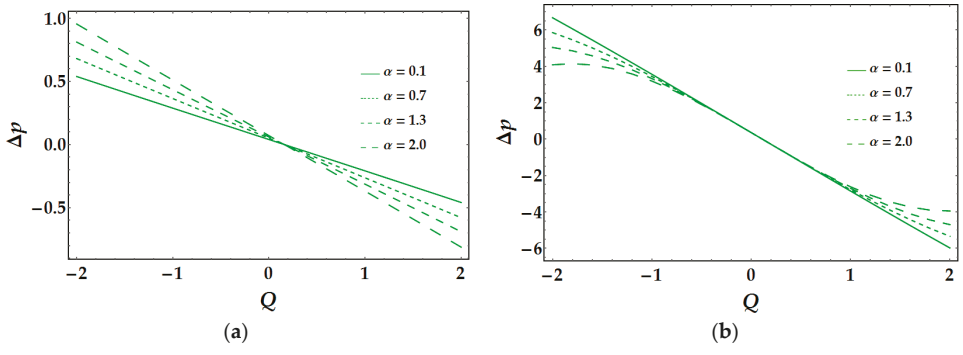

Figure 7. Effects of α on pressure rise with $n = -0.28$, $a = 0.1$, $b = 0.1$, $d = 2$, $\varphi = 0.1$, We = 0.05 for (**a**) Model 1 and (**b**) Model 2.

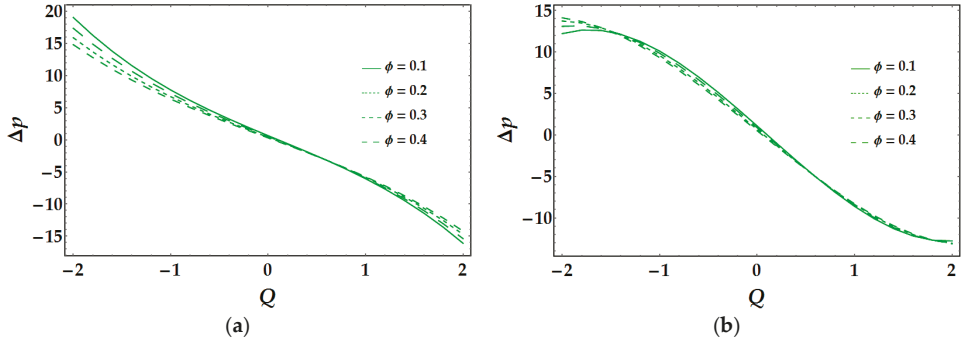

Figure 8. Effects of φ on pressure rise with $n = -0.28$, $a = 0.1$, $b = 0.1$, $d = 0.1$, $\alpha = 0.4$, We = 0.05 for (**a**) Model 1 and (**b**) Model 2.

Trapping scheme is another important mechanism for analyzing flow pattern. However, in peristaltic (or sinusoidal) motion, a closed contour of streamlines can be examined at time-averaged flow rate and different values of amplitude. This phenomenon is known as trapping. According to the physiological point of view, the fluids can be trapped due to continuing movements of smooth boundaries, which are beneficial to adequately propel the working biological liquid from one point to another point. Due to proper prorogation, the working organs can stay alive for a long time without any difficulty. Therefore, the trapping phenomena can be observed by sketching stream functions against the concentration parameter α and the volume flow rate Q. Figures 10 and 11 are drawn to show the trapping phenomena. Figure 10a–c is illustrated for Model 1. It is observed that for changing values of α, a large bolus is formed at the center that decreases in size and increases in α. For Model 2,

Figure 10d–f shows as α increases the bolus formed above $y = 0$ decreases in size, whereas below $y = 0$ it increases, and more boluses are obtained with large values of α. Figure 11 shows the effect of variation of Q on trapping. It can be analyzed that with an increase in Q, bolus decreases and increases in size above and below $y = 0$, respectively. The present investigation is also suggested for three-dimensional flow configuration with appropriate assumptions and modifications.

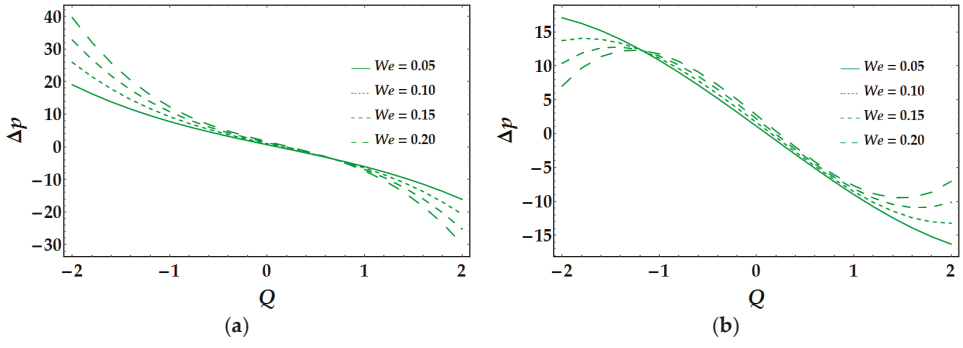

Figure 9. Effects of We on pressure rise with $n = -0.28$, $a = 0.1$, $b = 0.1$, $d = 0.1$, $\varphi = 0.1$, $\alpha = 0.4$ for (**a**) Model 1 and (**b**) Model 2.

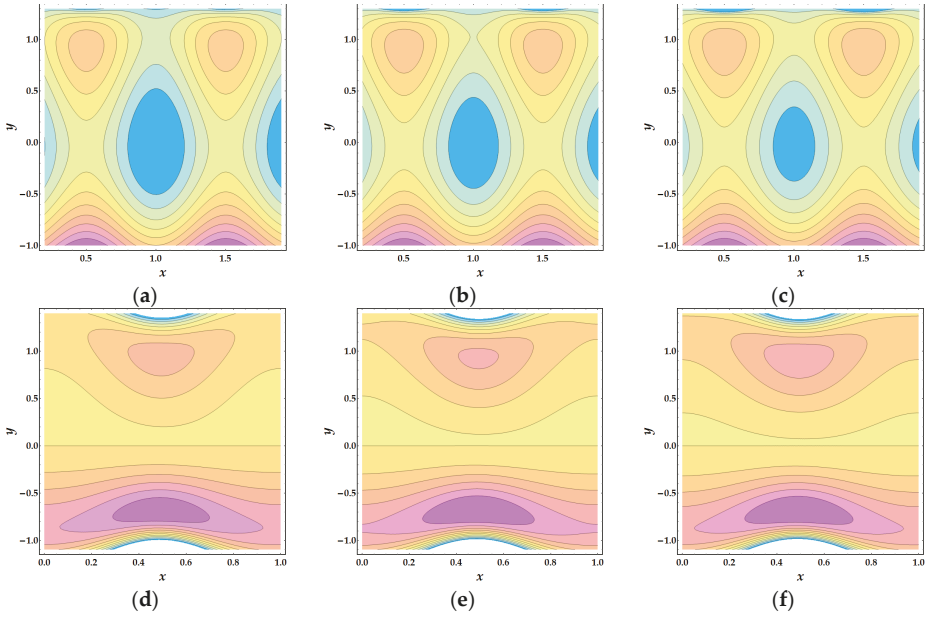

Figure 10. Stream lines for different values of α, $\alpha = 3, 3.2, 3.4$: (**a**–**c**) for Model 1, (**d**–**f**) for Model 2. The other parameters are $n = -0.2$, $a = 0.05$, $b = 0$, $d = 0.1$, $\varphi = 0.1$, We $= 0.05$, $Q = 5$.

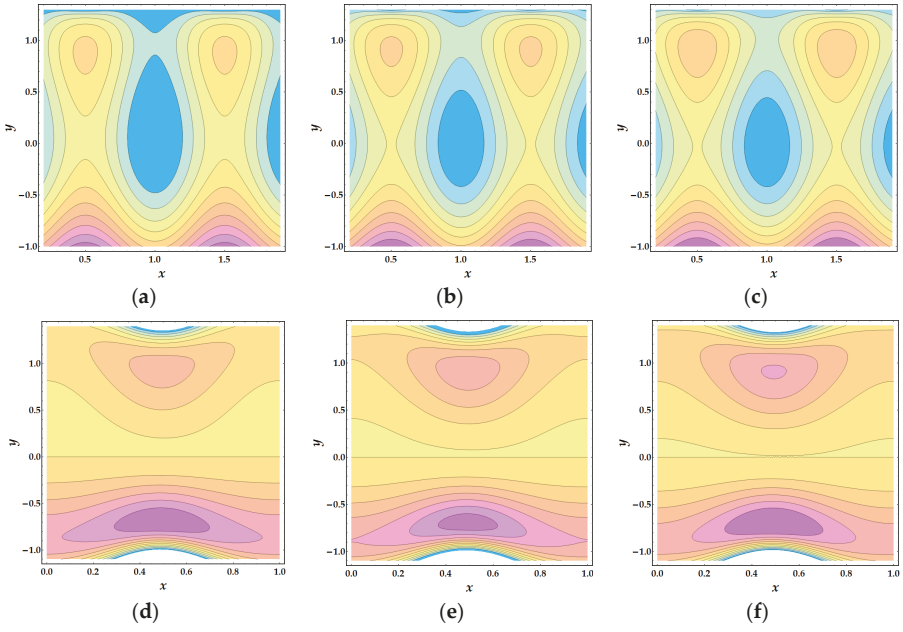

Figure 11. Stream lines for different values of Q = 2, 3, and 4: (**a**–**c**) for Model 1, (**d**–**f**) for Model 2. The other parameters are $n = -0.2$, $a = 0.05$, $b = 0$, $d = 0.1$, $\varphi = 0.1$, We = 0.05, $\alpha = 3$.

5. Conclusions

In the current analysis, we examined theoretically the peristaltic motion of Synovial fluid in the two-dimensional asymmetric channel in the presence of coating on the walls exposing thin-film layers. The Synovial fluid has viscoelastic material; it can be described under specific physical conditions such as non-Newtonian fluid. We have considered two models for viscosity to capture shear-thinning properties and viscosity dependence on the concentration of hyaluronic acid. Analytic solutions for velocity, concentration, and pressure gradient are first produced using the regular perturbation method, and then the behavior of pertinent parameters is examined and discussed graphically. The expression of pressure rise is obtained numerically. The contours have also been drawn to explain the action of the trapping bolus phenomenon. The model with the shear-thinning index is directly dependent on the concentration of hyaluronic acid, which seems to be appropriate. According to our knowledge, no studies have been presented before that can describe the concentration effects on shear-thinning and thickening models for the peristaltic flow of Synovial fluid. Solutions are carried out for velocity, concentration field, and pressure gradient. The behavior of all the governing parameters is shown and scrutinized. The present analysis is also applicable for experimental investigation and assurance to give reliance for the significance of the governing nonlinear-boundary value problem.

Author Contributions: Data Curation, M.M.B.; Formal Analysis, A.R.; Validation, H.A.A.-O.; Funding Acquisition, H.A.A.-O.; Methodology, A.R.; Resources, A.Z.

Funding: This research project was supported by a grant from the Research Center of the Center for Female Scientific and Medical Colleges, Deanship of Scientific Research, King Saud University.

Acknowledgments: The authors are very thankful to University of Education, Lahore, Jauharabad Campus for administrative and technical support.

Conflicts of Interest: The authors declare no conflict of interest.

Appendix A

$$
\begin{aligned}
C_1 = {} & -2{h_1}^2\, n\alpha^3 \ln[h_1 - h_2] + 4h^{1h_2} n\alpha^3 \ln[h^1 - h_2] - 2h_2 n\alpha^3 \ln[h^1 - h_2] - 12(h^1 - h_2)^2 n\alpha^2 \\
& (1+\alpha)\ln[h^1 - h_2]\ln[-h^1 + h_2] + 4{h_1}^2 n(1+\alpha)^3 \ln[h^1 - h^2]\ln[-h^1 + h^2]^3 - 8h^1 h^2 n(1+\alpha)^3 \\
& \ln[h1 - h2]\ln[-h1 + h2]^3 + 4h2^2 n(1+\alpha)^3 \ln[h_1 - h_2]\ln[-h_1 + h_2]^3 + 2(h_1 - h_2)^2 n\alpha^3(1+\alpha)^2 \\
& \ln[(h_1 - h_2)(1+\alpha)] + 12(h_1 - h_2)^2 n\alpha^2(1+\alpha)^2 \ln[-h_1 + h_2]\ln[(h_1 - h_2)(1+\alpha)] \\
& -4{h_1}^2 n(1+\alpha)^2 \ln[-h_1 + h_2]^3 \ln[(h_1 - h_2)(1+\alpha)] \\
& +8h_1 h_2 n(1+\alpha)^2 ln[-h_1 + h_2]^3 \ln[(h_1 - h_2)(1+\alpha)] \\
& -4h2^2 n(1+\alpha)^2 \ln[-h_1 + h_2]^3 \ln[(h1 - h2)(1+\alpha)] + 12h1^2 n\alpha^2 \ln[h1 - h2]\ln[(-h1 + h2)(1+\alpha)] \\
& -24h1h2n\alpha^2 \ln[h1 - h2]\ln[(-h1 + h2)(1+\alpha)] + 12h2^2 n\alpha^2 \ln[h1 - h2]\ln[(-h1 + h2)(1+\alpha)] \\
& +12h1^2 n\alpha^3 \ln[h1 - h2]\ln[(-h1 + h2)(1+\alpha)] - 24h1h2n\alpha^3 \ln[h1 - h2]\ln[(-h1 + h2)(1+\alpha)] \\
& +12h2^2 n\alpha^3 \ln[h_1 - h_2] ln[(-h_1 + h_2)(1+\alpha)] - 12{h_1}^2 n(1+\alpha)^3 \ln[h_1 - h_2]\ln[-h_1 + h_2]^2 \\
& +24h_1 h_2 n(1+\alpha)^3 \ln[h_1 - h_2]\ln[-h_1 + h_2]^2 \ln[(-h_1 + h_2)(1+\alpha)] - 12h2^2 n(1+\alpha)^3 \ln[h_1 - h_2] \\
& \ln[-h_1 + h_2]^2 \ln[(-h_1 + h_2)(1+\alpha)] - 12(h_1 - h_2)^2 n\alpha^2(1+\alpha)^2 \ln[(h_1 - h_2)(1+\alpha)] \\
& \ln[(-h_1 + h_2)(1+\alpha)] + 12{h_1}^2 n(1+\alpha)^2 \ln[-h_1 + h_2]^2 \ln[(h_1 - h_2)(1+\alpha)]\ln[(-h_1 + h_2)(1+\alpha)] \\
& -24h_1 h_2 n(1+\alpha^2)\ln[-h1 + h2]^2 \ln[(h1 - h2)(1+\alpha)]\ln[(-h1 + h2)(1+\alpha)] + \ln[-h_1 + h_2]^2 \\
& \ln[(h_1 - h_2)(1+\alpha)]\ln[(-h_1 + h_2)(1+\alpha)] + 12h1^2 n(1+\alpha)^3 \ln[h1 - h2]\ln[-h1 + h2]\ln[-h1 + h2] \\
& \ln[(-h1 + h2)(1+\alpha)]^2 - 24h_1 h_2 n(1+\alpha)^3 \ln[h_1 - h_2]\ln[-h_1 + h_2]\ln[(-h_1 + h_2)(1+\alpha)]^2 \\
& +12h_2^2 n(1+\alpha)^3 \ln[h_1 - h_2]\ln[-h_1 + h_2]\ln[(-h_1 + h_2)(1+\alpha)]^2 - 12{h_1}^2 n(1+\alpha)^2 \ln[-h_1 + h_2] \\
& \ln[(h_1 - h_2)(1+\alpha)]\ln[(-h_1 + h_2)(1+\alpha)]^2 + 24h_1 h_2 n(1+\alpha)^2 \ln[-h_1 + h_2]\ln[(h_1 - h_2)(1+\alpha)] \\
& \ln[(-h_1 + h_2)(1+\alpha)]^2 - 12h2^2 n(1+\alpha)^2 \ln[-h_1 + h_2]\ln[(h_1 - h_2)(1+\alpha)]\ln[(-h_1 + h_2)(1+\alpha)]^2 \\
& -4{h_1}^2 n\ln[h_1 - h_2]\ln[(-h_1 + h2)(1+\alpha)]^3 + 8h1h2n\ln[h1 - h2]\ln[(-h1 + h2)(1+\alpha)]^3 \\
& -4h2^2 n\ln[h1 - h2]\ln[(-h1 + h2)(1+\alpha)]^3 - 12h1^2 n\alpha\ln[h1 - h2]\ln[(-h1 \\
& +h2)(1+\alpha)]^3 + \\
& 24h1h2n\alpha\ln[h1 - h2]\ln[(-h1 + h2)(1+\alpha)]^3 - 12h2^2 n\alpha\ln[h1 - h2]\ln[(-h1 + h2)(1+\alpha)]^3 \\
& -12h1^2 n\alpha^2\ln[h1 - h2]\ln[(-h1 + h2)(1+\alpha)]^3 + 24h1h2n\alpha^2\ln[h1 - h2]\ln[(-h1 \\
& +h2)(1+\alpha)]^3 \\
& -12h2^2 n\alpha^2\ln[h1 - h2]\ln[(-h1 + h2)(1+\alpha)]^3 - 4h1^2 n\alpha^3\ln[h1 - h2]\ln[(-h1 + h2)(1+\alpha)]^3 \\
& +y8h1h2n\alpha^3\ln[h1 - h2]\ln[(-h1 + h2)(1+\alpha)]^3 - 4h2^2 n\alpha^3\ln[h1 - h2]\ln[(-h1 \\
& +h2)(1+\alpha)]^3 \\
& +4h1^2 n(1+\alpha)^2\ln[(h1 - h2)(1+\alpha)]\ln[(-h1 + h2)(1+\alpha)]^3 - 8h1h2n(1+\alpha)^2\ln[(h1 - h2)(1 \\
& +\alpha)]\ln[(-h_1 + h_2)(1+\alpha)]^3 \\
& +4h2^2 n(1+\alpha)^2\ln[(h_1 - h_2)(1+\alpha)]\ln[(-h_1 + h_2)(1+\alpha)]^3
\end{aligned}
\tag{A1}
$$

$$
\begin{aligned}
C2 = {} & -\alpha^2(1+\alpha)^3\ln[h1 - h2]\ln[-h1 + h2]^3 + \alpha^2(1+\alpha)^2\ln[-h1 + h2]^3\ln[(h1 - h2)(1+\alpha)] \\
& +3\alpha^2(1+\alpha)^3\ln[h1 - h2]\ln[-h1 + h2]^2\ln[(-h1 + h2)(1+\alpha)] - 3\alpha^2(1+\alpha)^2\ln[-h1 + h2]^2 \\
& \ln[(h1 - h2)(1+\alpha)]\ln[(-h1 + h2)(1+\alpha)] - 3\alpha^2(1+\alpha)^3\ln[h1 - h2]\ln[-h1 + h2] \\
& \ln[(-h1 + h2)(1+\alpha)]^2 + 3\alpha^2(1+\alpha)^2\ln[-h1 + h2]\ln[(h1 - h2)(1+\alpha)]\ln[(-h1 + h2) \\
& (1+\alpha)]^2 + \alpha^2\ln[h1 - h2]\ln[(-h1 + h2)(1+\alpha)]^3 + 3\alpha^3\ln[h1 - h2]\ln[(-h1 + h2)(1 \\
& +\alpha)]^3 + 3\alpha 4\ln[h1 - h2]\ln[(-h1 + h2)(1+\alpha)]^3 + \alpha^5\ln[h1 - h2]\ln[(-h1 + h2)(1+\alpha)]^3 \\
& -\alpha^2(1+\alpha)^2\ln[(h_1 - h_2)(1+\alpha)]\ln[(-h_1 + h_2)(1+\alpha)]^3
\end{aligned}
\tag{A2}
$$

$$
\begin{aligned}
C_3 = {} & 2(h1 - h2)^2 n\alpha^3(2+\alpha) + 12(h1 - h2)^2 n\alpha^2(1+\alpha)\ln[-h1 + h2] + 4h1^2 n(1+\alpha)^2\ln[-h_1 \\
& +h2]^3 - 8h1h2n(1+\alpha)^2\ln[-h1 + h2]^3 + 4h2^2 n(1+\alpha)^2 ln[-h1 + h2]^3 - 12(h1 \\
& -h2)^2 n\alpha^2(1+\alpha) \\
& \ln[(-h1 + h2)(1+\alpha)] - 12h1^2 n(1+\alpha)^2\ln[-h1 + h2]^2\ln[(-h1 + h2)(1+\alpha)] + 24h1h2n \\
& (1+\alpha)^2\ln[-h1 + h2]^2\ln[(-h1 + h2)(1+\alpha)] - 12h2^2 n(1+\alpha)^2\ln[-h1 + h2]^2\ln[(-h1 + h2) \\
& (1+\alpha)] + 12h1^2 n(1+\alpha)^2\ln[(-h1 + h2)]\ln[(-h1 + h2)(1+\alpha)]^2 - 24h1h2n(1+\alpha)^2 \\
& \ln[-h1 + h2]\ln[(-h1 + h2)(1+\alpha)]^2 + 12h2^2 n(1+\alpha)^2\ln[-h1 + h2]\ln[(-h_1 + h_2)(1+\alpha)]^2 \\
& -4{h_1}^2 n(1+\alpha)^2\ln[(-h_1 + h_2)(1+\alpha)]^3 + 8h_1 h_2 n(1+\alpha)^2\ln[(-h1 + h2)(1+\alpha)]^3 \\
& -4h2^2 n(1+\alpha)^2\ln[(-h_1 + h_2)(1+\alpha)]^3\ln[h_1 - h2 + h1\alpha - y\alpha]
\end{aligned}
\tag{A3}
$$

$$C_4 = \alpha(-\alpha^2(1+\alpha)^2 \ln[-h1+h2]^3 + 3\alpha^2(1+\alpha)^2 \ln[-h1+h2]^2 \ln[(-h1+h2)(1+\alpha)] - 3\alpha^2(1+\alpha)^2 \ln[-h_1+h_2] \ln[(-h_1+h_2)(1+\alpha)]^2 + \alpha^2(1+\alpha)^2 \ln[(-h_1+h_2)(1+\alpha)]^3 \ln[h1-h2+h1\alpha-y\alpha]) \quad \text{(A4)}$$

$$C_5 = (1+\alpha)\ln[(-h_1+h_2)(1+\alpha)] + 3(1+\alpha)^2(-4{h_1}^2\, n + 8h_1h_2n - 4{h_2}^2(1+\alpha)\ln[(-h_1 + h_2)(1+\alpha)](1+\alpha)\ln[(-h_1+h_2)(1+\alpha)] + 3(1+\alpha)^2(-4{h_1}^2\, n + 8h_1h_2n - 4{h_2}^2 + \alpha^2). \ln[-h_1+h_2]^2 \ln[(-h_1+h_2)(1+\alpha)] + (1+\alpha)^2(-4{h_1}^2\, n + 8h_1h_2n\alpha^2) + \alpha) + 3(\ln[-h_1 \ln[(-h_1+h_2)(1+\alpha)]^3 + h_2](4(h_1-h_2)^2 n\alpha^2 + (1+\alpha) \quad \text{(A5)}$$

References

1. Coleman, P.J.; Scott, D.; Ray, J.; Mason, R.M.; Levick, J.R. Hyaluronan secretion into the synovial cavity of rabbit knees and comparison with albumin turnover. *J. Physiol.* **1997**, *503*, 645–656. [CrossRef] [PubMed]
2. Fung, Y.C. *Biomechanics Mechanical Properties of Living Tissues*, 2nd ed.; Springer-Verlag: New York, NY, USA, 1993.
3. Voet, D.; Voet, J.G. *Biochemistry*, 4th ed.; John Wiley & Sons: Hoboken, NJ, USA, 2010.
4. Laurent, T.; Laurent, U.; Fraser, J. Functions of hyaluronan. *Ann. Rheum. Dis.* **1995**, *54*, 429–432. [CrossRef] [PubMed]
5. Decker, B.; McGuckin, W.F.; McKenzie, B.F.; Slocumb, C.H. Concentration of hyaluronic acid in synovial fluid. *Clin. Chem.* **1959**, *5*, 465–469.
6. Gibbs, D.A.; Merrill, E.W.; Smith, K.A. Rheology of hyaluronic acid. *Biopolymers* **1968**, *6*, 777–791. [CrossRef] [PubMed]
7. Morris, E.R.; Rees, D.A.; Welsh, E.J. Conformation and dynamic interactions in hyaluronate solutions. *J. Mol. Biol.* **1980**, *138*, 383–400. [CrossRef]
8. Pustejovska, P. Mathematical modeling of synovial fluids flow. In Proceedings of the 17th Annual Conference of Doctoral Students—WDS 2008, Prague, Czech Republic, 3–6 June 2008; pp. 32–37.
9. Hron, J.; Málek, J.; Pustějovská, P.; Rajagopal, K.R. On the modeling of the synovial fluid. *Adv. Tribol.* **2010**, *2010*, 104957. [CrossRef]
10. Mekheimer, K.S. Effect of the induced magnetic field on peristaltic flow of a couple stress fluid. *Phys. Lett. A* **2008**, *372*, 4271–4278. [CrossRef]
11. Srinivas, S.; Kothandapani, M. The influence of heat and mass transfer on MHD peristaltic flow through a porous space with compliant walls. *Appl. Math. Comput.* **2009**, *213*, 197–208. [CrossRef]
12. Riaz, A.; Nadeem, S.; Ellahi, R.; Akbar, N.S. Series solution of unsteady peristaltic flow of a Carreau fluid in small intestines. *Int. J. Biomath.* **2014**, *7*, 1450049. [CrossRef]
13. Akram, S.; Mekheimer, K.S.; Nadeem, S. Influence of lateral walls on peristaltic flow of a couple stress fluid in a non-uniform rectangular duct. *Appl. Math. Inf. Sci.* **2014**, *8*, 1127–1133. [CrossRef]
14. Ellahi, R.; Bhatti, M.M.; Khalique, C.M. Three-dimensional flow analysis of carreau fluid model induced by peristaltic wave in the presence of magnetic field. *J. Mol. Liq.* **2017**, *241*, 1059–1068. [CrossRef]
15. Bhatti, M.M.; Zeeshan, A.; Ijaz, N.; Ellahi, R. Heat transfer and inclined magnetic field analysis on peristaltically induced motion of small particles. *J. Braz. Soc. Mech. Sci. Eng.* **2017**, *39*, 3259–3267. [CrossRef]
16. Sinha, A.; Shit, G.C.; Ranjit, N.K. Peristaltic transport of MHD flow and heat transfer in an asymmetric channel: Effects of variable viscosity, velocity-slip and temperature jump. *Alex. Eng. J.* **2015**, *54*, 691–704. [CrossRef]
17. Shit, G.C.; Roy, M.; Ng, E.Y.K. Effect of induced magnetic field on peristaltic flow of a micropolar fluid in an asymmetric channel. *Int. J. Numer. Methods Biomed. Eng.* **2010**, *26*, 1380–1403. [CrossRef]
18. Ellahi, R.; Rahman, S.U.; Gulzar M., M.; Nadeem, S.; Vafai, K. A mathematical study of non-newtonian micropolar fluid in arterial blood flow through composite stenosis. *Appl. Math. Inf. Sci.* **2014**, *8*, 1567–1573. [CrossRef]
19. Bhatti, M.M.; Zeeshan, A.; Tripathi, D.; Ellahi, R. Thermally developed peristaltic propulsion of magnetic solid particles in biorheological fluids. *Indian J. Phys.* **2017**, *92*, 423–430. [CrossRef]
20. Maiti, S.; Misra, J.C. Peristaltic flow of a fluid in a porous channel: A study having relevance to flow of bile within ducts in a pathological state. *Int. J. Eng. Sci.* **2011**, *49*, 950–966. [CrossRef]

21. Bhatti, M.M.; Zeeshan, A.; Ellahi, R. Electromagnetohydrodynamic (EMHD) peristaltic flow of solid particles in a third-grade fluid with heat transfer. *Mech. Ind.* **2017**, *18*, 314. [CrossRef]
22. Kabov, O.A.; Chinnov, E.A.; Cheverda, V. Two-phase flow in short rectangular mini-channel. *Microgravity Sci. Technol.* **2007**, *19*, 44–47. [CrossRef]
23. Mekheimer, Kh. S.; Elmaboud, Y.A. The influence of heat transfer and magnetic field on peristaltic transport of a newtonian fluid in a vertical annulus: Application of an endoscope. *Phys. Lett. A* **2008**, *372*, 1657–1665. [CrossRef]
24. Elmaboud, Y.A.; Mekheimer, Kh.S. Non-linear peristaltic transport of a second-order fluid through a porous medium. *Appl. Math. Model.* **2011**, *35*, 2695–2710. [CrossRef]
25. Khan, A.A.; Ellahi, R.; Vafai, K. Peristaltic transport of Jeffrey fluid with variable viscosity through a porous medium in an asymmetric channel. *Adv. Math. Phys.* **2012**, *2012*, 169642.
26. Tripathi, D. Study of transient peristaltic heat flow through a finite porous channel. *Math. Comput. Model.* **2013**, *57*, 1270–1283. [CrossRef]
27. Chaube, M.K.; Tripathi, D.; Bég, O.A.; Sharma, S.; Pandey, V.S. Peristaltic creeping flow of power law physiological fluids through a non-uniform channel with slip effect. *Appl. Bionic Biomech.* **2015**, *2015*, 152802. [CrossRef] [PubMed]
28. Shit, G.C.; Ranjit, N.K. Role of slip velocity on peristaltic transport of couple stress fluid through an asymmetric non-uniform channel: Application to digestive system. *J. Mol. Liq.* **2016**, *221*, 305–315. [CrossRef]
29. Shit, G.C.; Ranjit, N.K.; Sinha, A. Electro-magnetohydrodynamic flow of biofluid induced by peristaltic wave: A non-newtonian model. *J. Bionic Eng.* **2016**, *13*, 436–448. [CrossRef]
30. Zeeshan, A.; Bhatti, M.M.; Akbar, N.S.; Sajjad, Y. Hydromagnetic blood flow of Sisko fluid in a non-uniform channel induced by peristaltic wave. *Commun. Theor. Phys.* **2017**, *68*, 103–110. [CrossRef]
31. Marin, M. Weak solutions in elasticity of dipolar porous materials. *Math. Prob. Eng.* **2008**, *2008*, 158908. [CrossRef]
32. Marin, M. An approach of a heat-flux dependent theory for micropolar porous media. *Meccanica* **2016**, *51*, 1127–1133. [CrossRef]
33. Ogston, A.G.; Stanier, J.E. The physiological function of hyaluronic acid in synovial fluid; viscous, elastic and lubricant properties. *J. Physiol.* **1953**, *119*, 244–252. [CrossRef] [PubMed]
34. Thurston, G.B.; Greiling, H. Viscoelastic properties of pathological synovial fluids for a wide range of oscillatory shear rates and frequencies. *Rheol. Acta* **1978**, *17*, 433–445. [CrossRef]

coatings

MDPI

Article

Study of Shiny Film Coating on Multi-Fluid Flows of a Rotating Disk Suspended with Nano-Sized Silver and Gold Particles: A Comparative Analysis

Rahmat Ellahi [1,2,*], Ahmed Zeeshan [1], Farooq Hussain [1,3] and Tehseen Abbas [4]

1 Department of Mathematics & Statistics, Faculty of Basic and Applied Sciences (FBAS), International Islamic University (IIUI), Islamabad 44000, Pakistan; ahmad.zeeshan@iiu.edu.pk (A.Z.); farooq.hussain@buitms.edu.pk (F.H.)
2 Department of Mechanical Engineering, University of California Riverside, Riverside, CA 92521, USA
3 Department of Mathematics, Faculty of Arts and Basic Sciences (FABS), Balochistan University of Information Technology, Engineering, and Management Sciences (BUITEMS), Quetta 87300, Pakistan
4 Department of Mathematics, University of Education Lahore, Faisalabad Campus, Faisalabad 38000, Pakistan; tehseen.abbas@ue.edu.pk
* Correspondence: rellahi@alumni.ucr.edu

Received: 14 September 2018; Accepted: 10 November 2018; Published: 24 November 2018

Abstract: The current effort is devoted to investigate the shiny thin film with a metallic tactile covering of nanoparticles over the surface of a rotating disk. To decorate, glowing silver and gold particles were chosen. Four illustrative base liquids, namely (i) ethanol, (ii) methanol, (iii) ethylene-glycol, and (iv) water were considered with different geometries, which have great importance in industrial usage. An emphasis on comparative multi nanofluid analysis was used to make a sound judgment on which one of the fluids best suited the metallic glittering process of spin coating. The film thickness process highly depends on the process of evaporation, which takes some time to settle on the disk's surface. It was found that of the base fluids, the best choices were ethanol alloys with silver. Hence, one can conclude that from an experimental point of view, if silver alloy is used for coating, then only those liquids can be considered that exhibit ethanol-like properties. The impact of pertinent parameters with different aspects are graphically illustrated in each case.

Keywords: thin film; spin coating; rotating disk; nanoparticles; Newtonian fluids

1. Introduction

The mechanical process of covering the surface of an object/substrate with the help of a very thin layer is known as "Coating". This layer can be of some sort of paint, lacquer or a thin polymer sheet, which may be used for protective or decorative purposes. Nowadays, most of the engineered products go through the process of coating to prevent corrosion and to make them attractive [1,2]. From an industrial point of view, coating involves the development of a thin film layer (which can be polymeric or lacquer) on a substrate or fabric etc. If the substrate starts and ends the process wound up in a roll, the process may be termed "roll-to-roll" or "web-based" coating. Apart from a process of simple coating, developing a uniform and thin film or covering to a spinning sample or substrate, is called "spin coating". In the latter sort of coating, a small amount of liquid solution is placed at the center of the highly rotating disk, with the help of a pipette or syringe, resulting in the solution spreading uniformly and evenly in all directions as elaborated in [3]. This is all because of centrifugal forces, which cause liquid solution to spread across the surface uniformly. Application of spin coating is mainly used to fabricate tiny structures, usually of micrometer size or even much smaller, known as the microfabrication process. Manufacturing of solar cells, integrated circuits, insulators, nanomaterials, compact disks, magnetic disk coating and microfluidic devices are a few examples of such technology,

which depend upon the process of high quality spin coating. The simplicity and relative ease that helps to process any set up is regarded as the main advantage of spin coating. The spinning causes fast airflow around the rotating substrates or disks which results in quick drying of a thin layer of coating. Hence, this saves time and reduces the consumption of energy but a consistent efficiency is also achieved at the scale of nanolength or macroscopic level. Surprisingly, spin coating deals with a process which involves single substrates. This leads to a major drawback of spin coating and puts this on the back foot as compared to the "roll-to-roll" coating process. This disadvantage causes low performance. Also, the fast-drying times mean the actual material usage in a spin coating process is typically very low, around 10% or less, with the rest being flung off the side and wasted. Despite these drawbacks, spin coating is usually the starting point and benchmark for most academic and industrial processes that require a thin and uniform coating. Moreover, nanofluids can simply be termed as the liquid containing the tiny metallic particles. These tiny particles are invisible to the naked eye, for these range between 1 nm and 100 nm. In the later phase of the twentieth century, the concept of nanoparticles was introduced by Choi and Eastman [4] as a supporting agent. The initial intention was to obtain immense thermal conductivity of the base fluid. However, Buongiorno [5,6] performed his role focusing on convective heat transfer involving nanoparticles in the concerned base liquids. However, he negated some previous conclusions inferred by different researchers in their investigations. Since then, nanoparticles are being in used in different ways by scientists in their endeavors [7–37]. One cannot deny the beneficial application of nanoparticles from electronics to electrical appliances, from the energy sector to medical sciences working towards the remedy of some fatal disease, it is all mainly due to the blessing of the perfect utility of nanoparticles. Primarily, nanoparticles were meant to enhance the thermal features of a phenomenon involved in it, but recently, nanofluids are being applied in a new dimension, which is in solar collectors. In this application, nanofluids are employed for their tunable optical properties. Consequently, graphene-based nanofluid increases the performance of polymerase chain reaction. As a matter of fact, in some cases nano-technology has improved the performance of spin coating, which requires time to self-assemble or crystallize as the nanoparticles such as gold, silver, zinc oxide, copper and aluminum have significant potential in conductive metal as compared to conventional conductive materials. Especially, incorporating the said nanomaterials into thin films would always pool together electrical and optical properties for multipurpose features that play a key role in fabricating stretchable conductive thin films and coatings, since their mechanical properties include greater flexibility, stretch ability and designed structures. These materials can be easily incorporated into thin films with simple inexpensive solution-based testimony techniques like spin coating, ink-jet printing and spray coating [38,39].

What makes this paper so special is that in this study more than one base fluids suspended with a couple of different nanoparticles have been comparatively studied altogether which, so far, is a novel innovation in the field of applying a thin film of spin coating. To form this shiny silver and gold metallic layer of coating, four different types of base liquids (i.e., water, ethanol, methanol and ethylene-glycol) were brought in to use. It was found that evaporation of the liquid suggested rapidly settling down a shiny metallic layer of silver or gold on the surface of a rotating disk.

2. Formulation

Let $V = [\overline{u}(\overline{t}, \overline{r}, \overline{\theta}, \overline{z})\ \overline{v}(\overline{t}, \overline{r}, \overline{\theta}, \overline{z})\ \overline{w}(\overline{t}, \overline{r}, \overline{\theta}, \overline{z})]$ be the velocity of unsteady, incompressible and viscous multi nanofluids axi-symmetrically rotating disk having an angular velocity $\overline{\Psi}$, as shown in Figure 1.

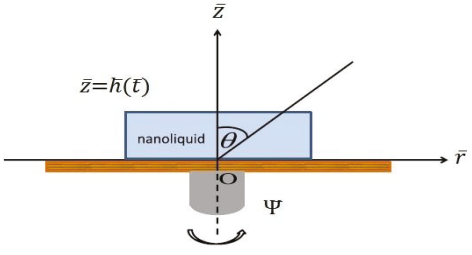

Figure 1. Physical configuration of the rotating disk.

The layer of nanofluid across the surface is evenly spread out; thus, appropriate assumptions can be enlisted as:

i. The nanofluid is assumed to be diluted and an impact of evaporation of a thin layer of the liquid is negligible as the solution is behaving "non-volatile".
ii. The nanoparticles and the base fluid are in equilibrium, therefore, no slip condition is considered.

The governing equations in components form are:

$$\frac{\partial \overline{u}}{\partial \overline{t}} + \frac{\overline{u}}{\overline{r}} + \frac{\partial \overline{w}}{\partial \overline{z}} = 0 \tag{1}$$

$$\overline{\rho}_{nf}\left(\frac{\partial \overline{u}}{\partial \overline{t}} + \overline{u}\frac{\partial \overline{u}}{\partial \overline{r}} + \overline{w}\frac{\partial \overline{u}}{\partial \overline{z}} - \frac{\overline{v}^2}{\overline{r}}\right) = -\frac{\partial \overline{p}}{\partial \overline{r}} + \overline{\mu}_{nf}\left\{\frac{\partial^2 \overline{u}}{\partial \overline{r}^2} + \frac{\partial}{\partial \overline{r}}\left(\frac{\overline{u}}{\overline{r}}\right) + \frac{\partial^2 \overline{u}}{\partial \overline{z}^2}\right\} \tag{2}$$

$$\overline{\rho}_{nf}\left(\frac{\partial \overline{v}}{\partial \overline{t}} + \overline{u}\frac{\partial \overline{v}}{\partial \overline{r}} + \overline{w}\frac{\partial \overline{v}}{\partial \overline{z}} + \frac{\overline{u}\overline{v}}{\overline{r}}\right) = -\frac{\partial \overline{p}}{\partial \overline{\theta}} + \overline{\mu}_{nf}\left\{\frac{\partial^2 \overline{v}}{\partial \overline{r}^2} + \frac{\partial}{\partial \overline{r}}\left(\frac{\overline{v}}{\overline{r}}\right) + \frac{\partial^2 \overline{v}}{\partial \overline{z}^2}\right\} \tag{3}$$

$$\overline{\rho}_{nf}\left(\frac{\partial \overline{w}}{\partial \overline{t}} + \overline{u}\frac{\partial \overline{w}}{\partial \overline{r}} + \overline{w}\frac{\partial \overline{w}}{\partial \overline{z}}\right) = -\frac{\partial \overline{p}}{\partial \overline{z}} + \overline{\mu}_{nf}\left\{\frac{\partial^2 \overline{w}}{\partial \overline{r}^2} + \frac{\overline{w}}{\overline{r}} + \frac{\partial^2 \overline{w}}{\partial \overline{z}^2}\right\} \tag{4}$$

$$\left(\overline{\rho}C_p\right)_{nf}\left(\frac{\partial \overline{T}}{\partial \overline{t}} + \overline{u}\frac{\partial \overline{T}}{\partial \overline{r}} + \overline{w}\frac{\partial \overline{T}}{\partial \overline{z}}\right) = \overline{k}_{nf}\left\{\frac{\partial^2 \overline{T}}{\partial \overline{r}^2} + \frac{1}{\overline{r}}\frac{\partial \overline{T}}{\partial \overline{r}} + \frac{\partial^2 \overline{T}}{\partial \overline{z}^2}\right\} \tag{5}$$

Initial and boundary conditions associated with Equations (1)–(5) are defined in the following sub sections:

2.1. Initial Conditions

$$\left.\begin{array}{c}(\mathrm{i}).\ \overline{u} = 0,\\ (\mathrm{ii}).\ \overline{v} = 0,\\ (\mathrm{iii}).\ \overline{w} = 0,\\ (\mathrm{iv}).\ \overline{T} = \overline{T}_0,\\ (\mathrm{v}).\ \overline{h}(\overline{t}) = h_0\end{array}\right\};\ \text{when } \overline{t} = 0 \tag{6}$$

here, $\overline{h}$, h_0 and $\overline{T}_0$ represent thickness of the film, initial thickness of the film and room temperature respectively.

2.2. Boundary Conditions

- At the surface of the rotating disk

$$\left.\begin{array}{c}(\mathrm{i}).\ \overline{u}=0,\\ (\mathrm{ii}).\ \overline{v}=\overline{r}\,\overline{\Psi},\\ (\mathrm{iii}).\ \overline{w}=0,\\ (\mathrm{iv}).\ \overline{T}=\overline{T}_a-\frac{\overline{T}_b}{2}\overline{r}^2\end{array}\right\};\ \text{when } \overline{z}=0 \tag{7}$$

- At the free surface of the rotating disk

$$\left.\begin{array}{c}(\mathrm{i}).\ \frac{\partial\overline{h}}{\partial\overline{t}}=\overline{w},\\ (\mathrm{ii}).\ \overline{p}+2\overline{\mu}_{nf}\frac{\partial\overline{w}}{\partial\overline{z}}=0,\\ (\mathrm{iii}).\ \overline{\mu}_{nf}\left(\frac{\partial\overline{u}}{\partial\overline{z}}+\frac{\partial\overline{w}}{\partial\overline{r}}\right)=\frac{\partial\overline{T}}{\partial\overline{r}}\frac{\partial\overline{\sigma}}{\partial\overline{T}},\\ (\mathrm{iv}).\ \overline{\mu}_{nf}\left(\frac{\partial\overline{v}}{\partial\overline{z}}\right)=\frac{\partial\overline{T}}{\partial\overline{z}}\frac{\partial\overline{\sigma}}{\partial\overline{T}},\\ (\mathrm{v}).\ \frac{\partial\overline{T}}{\partial\overline{z}}+L\left(\overline{T}-\overline{T}_g\right)=0.\end{array}\right\};\ \text{when } \overline{z}=\overline{h}(\overline{t}) \tag{8}$$

where L denotes heat transfer coefficient and $\overline{\sigma}$ stands for surface tension.

By using suitable transformations [40], the governing equations can be obtained as:

$$2F+\frac{\partial W}{\partial z}=0 \tag{9}$$

$$\mathrm{Re}\varnothing_1\left(\frac{\partial F}{\partial t}+F^2+W\frac{\partial F}{\partial z}\right)=\frac{\partial^2F}{\partial z^2}+G^2 \tag{10}$$

$$\mathrm{Re}\varnothing_1\left(\frac{\partial G}{\partial t}-G\frac{\partial W}{\partial z}+W\frac{\partial G}{\partial z}\right)=\frac{\partial^2G}{\partial z^2} \tag{11}$$

$$\mathrm{RePr}\varnothing_2\left(\frac{\partial\Gamma}{\partial t}-\Gamma\frac{\partial W}{\partial z}+W\frac{\partial\Gamma}{\partial z}\right)=\frac{k_{nf}}{k_f}\frac{\partial^2\Gamma}{\partial z^2} \tag{12}$$

$$\mathrm{RePr}\varnothing_2\left(\frac{\partial\tau}{\partial t}+W\frac{\partial\tau}{\partial z}\right)=\frac{k_{nf}}{k_f}\left(\frac{\partial^2\tau}{\partial z^2}+2\Gamma\right) \tag{13}$$

$$\left.\begin{array}{c}(\mathrm{i}).\ F(z,t)=0,\\ (\mathrm{ii}).\ G(z,t)=0,\\ (\mathrm{iii}).\ W(z,t)=0,\\ (\mathrm{iv}).\ \Gamma(z,t)=0,\\ (\mathrm{v}).\ \tau(z,t)=0,\\ (\mathrm{vi}).\ H(t)=1,\end{array}\right\};\ \text{at } t=0 \tag{14}$$

$$\left.\begin{array}{c}(\mathrm{i}).\ F(z,t)=0,\\ (\mathrm{ii}).\ G(z,t)=1,\\ (\mathrm{iii}).\ W(z,t)=0,\\ (\mathrm{iv}).\ \Gamma(z,t)=1,\\ (\mathrm{v}).\ \tau(z,t)=0,\end{array}\right\};\ \text{at } z=0 \tag{15}$$

here, Re is the Reynolds number and Pr denotes the Prandtl number, whereas $\varnothing_1$ and $\varnothing_2$ represent dimensionless constants.

For free surface

$$\left.\begin{array}{c}\text{(i). } \frac{\partial F}{\partial z} = \alpha(1-\phi)^{2.5}\Gamma, \\ \text{(ii). } \frac{\partial G}{\partial z} = 0, \\ \text{(iii). } \frac{\partial \Gamma}{\partial z} = 0, \\ \text{(iv). } \frac{\partial \tau}{\partial z} = 0, \\ \text{(v). } \frac{dH}{dt} = W.\end{array}\right\}; \text{ at } z = H(t) \tag{16}$$

2.3. Thermophysical Properties

The present investigation is concerned with the development of a thin film of liquid on a rotating disk with different metallic particles that require effective thermo-physical properties of nanofluids and nanoparticles. Two distinctive models proposed by Khanafer and Vafai [41] were chosen to analyze the density and specific heat of the nanofluids; whereas to estimate the thermal conductivity and viscosity of fluids, the thermophysical model [42] is utilized. In view of the thermophysical model in the presence of multi fluids containing two different types of nano-sized metallic particles, the realistic properties were developed as follows:

2.3.1. For Water as the Base Fluid

The most significant and highly utilized fluid on this planet is water that contains 997.1 kg·m^{-3}, density, 0.89 mPa·S. viscosity, 4179 J/Kg m heat capacity and 0.569 W·m^{-1}·K^{-1} thermal conductivity.

- For gold nanoparticles

The mathematical expressions that describe the thermophysical properties of water and gold nanofluids are given as:

$$\overline{\rho}_{nf} = (1-\phi)\overline{\rho}_f - \phi\overline{\rho}_p \tag{17}$$

$$\left(\overline{\rho}_{nf}\right)_{\text{water/gold}} = 997.1(1-\phi) - 19300\phi \tag{18}$$

$$\overline{\mu}_{nf} = \left(1.013 + 0.092\phi - 0.015\phi^2\right)\overline{\mu}_f \tag{19}$$

$$\left(\overline{\mu}_{nf}\right)_{\text{water/gold}} = 0.89\left(1.013 + 0.092\phi - 0.015\phi^2\right) \tag{20}$$

$$(\overline{\rho}C_P)_{nf} = (C_P)_f\overline{\rho}_f(1-\phi) - (C_P)_p\phi\overline{\rho}_p \tag{21}$$

$$(\overline{\rho}C_P)_{\text{water/gold}} = (4179)(997.1)(1-\phi) - (126)(19300)\phi \tag{22}$$

$$\overline{k}_{nf} = (1.0204 + 0.0249\phi)\overline{k}_f \tag{23}$$

$$\left(\overline{k}_{nf}\right)_{\text{water/gold}} = 0.569(1.0204 + 0.0249\phi) \tag{24}$$

where the gold density is 19,300 kg·m^{-3} and heat capacity and thermal conductivity are 126 J/kg m and 317 W·m^{-1}·K^{-1}, respectively.

- For silver nanoparticles

The thermophysical properties of water and silver nanofluids are given as:

$$\left(\overline{\rho}_{nf}\right)_{\text{water/silver}} = 997.1(1-\phi) - 10490\phi \tag{25}$$

$$\left(\overline{\mu}_{nf}\right)_{\text{water/silver}} = 0.89\left(1.013 + 0.092\phi - 0.015\phi^2\right) \tag{26}$$

$$(\overline{\rho}C_P)_{\text{water/silver}} = (4179)(997.1)(1-\phi) - (233)(10490)\phi \tag{27}$$

$$\left(\overline{k}_{nf}\right)_{\text{water/silver}} = 0.569(1.0204 + 0.0249\phi) \tag{28}$$

where the density of silver is 10,490 kg·m^{-3} while heat capacity and thermal conductivity are respectively 233 J/Kg m and 429 W·m^{-1}·K^{-1}

2.3.2. For Methanol as the Base Fluid

The features displayed by methanol at room temperature according to the System International (SI) units is of density 790 kg·m^{-3} whereas viscosity takes the numerical value 0.543 mPa·S, heat capacity is 2534 J/Kg m and thermal conductivity is 0.201 W·m^{-1}·K^{-1}.

- For gold nanoparticles

The mathematical expressions describing the thermophysical properties are given as:

$$\left(\overline{\rho}_{nf}\right)_{\text{methanol/gold}} = 790(1-\phi) - 19300\phi \tag{29}$$

$$\left(\overline{\mu}_{nf}\right)_{\text{methanol/gold}} = 0.543\left(1.013 + 0.092\phi - 0.015\phi^2\right) \tag{30}$$

$$(\overline{\rho}C_P)_{\text{methanol/gold}} = (2543)(790)(1-\phi) - (126)(19300)\phi \tag{31}$$

$$\left(\overline{k}_{nf}\right)_{\text{methanol/gold}} = 0.201(1.0204 + 0.0249\phi) \tag{32}$$

- For silver nanoparticles

For the methanol and silver nanofluids suspension, the physical properties of silver, heat capacity and thermal conductivity are 10,490,790 kg·m^{-3}, 233 J/Kg m and 429 W·m^{-1}·K^{-1} respectively. Thus, thermophysical properties corresponding to this model are:

$$\left(\overline{\rho}_{nf}\right)_{\text{methanol/silver}} = 790(1-\phi) - 10490\phi \tag{33}$$

$$\left(\overline{\mu}_{nf}\right)_{\text{methanol/silver}} = 0.543\left(1.013 + 0.092\phi - 0.015\phi^2\right) \tag{34}$$

$$(\overline{\rho}C_P)_{\text{methanol/silver}} = (2543)(790)(1-\phi) - (233)(10490)\phi \tag{35}$$

$$\left(\overline{k}_{nf}\right)_{\text{methanol/silver}} = 0.201(1.0204 + 0.0249\phi) \tag{36}$$

In order to make a methanol and gold nanofluids suspension, gold density is 19,300 kg·m^{-3}. The heat capacity and thermal conductivities are 126 J/Kg m and 317 W·m^{-1}·K^{-1} respectively.

2.3.3. For Ethanol as the Base Fluid

The features displayed by ethanol at room temperature have a density of 789 kg·m^{-3}. The viscosity is 1.074 mPa·S, heat capacity is 2500 J/Kg m and thermal conductivity is 0.0235 W·m^{-1}·K^{-1}.

- For gold nanoparticles

For an ethanol and gold nanofluids suspension, the density of gold is 19,300 kg·m^{-3}, and heat capacity and thermal conductivity are 126 J/Kg m and 317 W·m^{-1}·K^{-1}, respectively. Mathematically, it can be written as:

$$(\overline{\rho}_{nf})_{\text{ethanol/gold}} = 789(1-\phi) - 19300\phi \tag{37}$$

$$(\overline{\mu}_{nf})_{\text{ethanol/gold}} = 1.074\left(1.013 + 0.092\phi - 0.015\phi^2\right) \tag{38}$$

$$(\overline{\rho}C_P)_{\text{ethanol/gold}} = (2500)(789)(1-\phi) - (126)(19300)\phi \tag{39}$$

$$\left(\overline{k}_{nf}\right)_{\text{ethanol/gold}} = 0.0235(1.0204 + 0.0249\phi) \tag{40}$$

- For silver nanoparticles

To make an ethanol and silver nanofluids suspension, the density of silver is 10,490 kg·m^{-3}, heat capacity is 233 J/Kg m and thermal conductivity is 429 W·m^{-1}·K^{-1}. The mathematical expressions can be written as:

$$\left(\overline{\rho}_{nf}\right)_{\text{ethanol/silver}} = 789(1-\phi) - 10490\phi \tag{41}$$

$$\left(\overline{\mu}_{nf}\right)_{\text{ethanol/silver}} = 1.074\left(1.013 + 0.092\phi - 0.015\phi^2\right) \tag{42}$$

$$(\overline{\rho}C_P)_{\text{ethanol/silver}} = (2500)(789)(1-\phi) - (233)(10490)\phi \tag{43}$$

$$\left(\overline{k}_{nf}\right)_{\text{ethanol/silver}} = 0.0235(1.0204 + 0.0249\phi) \tag{44}$$

2.3.4. For Ethylene-Glycol as the Base Fluid

The density of ethylene-glycol at room temperature by System International (SI) units system is 1101 kg·m^{-3}. The viscosity takes the numerical value 0.0162 mPa·S, heat capacity and thermal conductivity are respectively 2400 J/Kg m and 0.256 W·m^{-1}·K^{-1}.

- For gold nanoparticles

For an Ethylene-glycol and Gold nanofluids suspension, the physical property of gold density is 19,300 kg·m^{-3}, heat capacity is 126 J/Kg m and thermal conductivity is 317 W·m^{-1}·K^{-1}. Accordingly, the mathematical expression can be written as:

$$\left(\overline{\rho}_{nf}\right)_{\text{ethylene/gold}} = 1101(1-\phi) - 19300\phi \tag{45}$$

$$\left(\overline{\mu}_{nf}\right)_{\text{ethylene/gold}} = 0.0162\left(1.013 + 0.092\phi - 0.015\phi^2\right) \tag{46}$$

$$(\overline{\rho}C_P)_{\text{ethylene/gold}} = (2400)(1101)(1-\phi) - (126)(19300)\phi \tag{47}$$

$$\left(\overline{k}_{nf}\right)_{\text{ethylene/gold}} = 0.256(1.0204 + 0.0249\phi) \tag{48}$$

- For silver nanoparticles

For the suspension of ethylene-glycol and silver nanofluids the physical property of silver density is 10,490 kg·m^{-3}. The heat capacity and thermal conductivity are 233 J/Kg m and 429 W·m^{-1}·K^{-1}, respectively. On the previous contrast, mathematical expression can be attained as:

$$\left(\overline{\rho}_{nf}\right)_{\text{ethylene/silver}} = 1101(1-\phi) - 10490\phi \tag{49}$$

$$\left(\overline{\mu}_{nf}\right)_{\text{ethylene/silver}} = 0.0162\left(1.013 + 0.092\phi - 0.015\phi^2\right) \tag{50}$$

$$(\overline{\rho}C_P)_{\text{ethylene/silver}} = (2400)(1101)(1-\phi) - (233)(10490)\phi \tag{51}$$

$$\left(\overline{k}_{nf}\right)_{\text{ethylene/silver}} = 0.256(1.0204 + 0.0249\phi) \tag{52}$$

For the best understating of readers, the realistic physical properties of base fluids and nanoparticles are offered in Tables 1 and 2.

Table 1. Thermo-physical properties of the base fluids.

Base Fluids	Density ρ (kg·m^{-3})	Viscosity μ (mPa·S)	Heat Capacity C_p (J·kg^{-1}·K^{-1})	Thermal Conductivity k (W·m^{-1}·K^{-1})
Water [43] (H_2O)	997	0.89	4179	0.569
Ethanol [44] (C_2H_6O)	789	1.074	2500	0.0235
Methanol [45] (CH_4O)	790	0.543	2534	0.200
Ethylene-Glycol [46] ($C_2H_6O_2$)	1101	0.0162	2400	0.256

Table 2. Physical properties of the nanoparticles.

Nano Particles	Density ρ (kg·m^{-3})	Heat Capacity C_p (J·kg^{-1}·K^{-1})	Thermal Conductivity k (W·m^{-1}·K^{-1})
Gold [47] (Au)	19300	126	317
Silver [48] (Ag)	10490	233	429

3. Analytical Results

Analytical solutions of nonlinear and coupled Equations (9)–(13) subject to (14)–(16) are obtained as:

$$\begin{aligned} F(z,t) = f_1(t)z \quad & +f_2(t)z^2 + f_3(t)z^3 + f_4(t)z^4 + f_5(t)z^5 + f_6(t)z^6 + f_7(t)z^7 + f_8(t)z^8 \\ & +f_9(t)z^9 + f_{10}(t)z^{10} + f_{11}(t)z^{11} + f_{12}(t)z^{12} + f_{13}(t)z^{13} + f_{14}(t)z^{14} \\ & +f_{15}(t)z^{15} \end{aligned} \tag{53}$$

$$\begin{aligned} G(z,t) = 1 + g_1(t)z \quad & +g_2(t)z^2 + g_3(t)z^3 + g_4(t)z^4 + g_5(t)z^5 + g_6(t)z^6 + g_7(t)z^7 \\ & +g_8(t)z^8 + g_9(t)z^9 \end{aligned} \tag{54}$$

$$\begin{aligned} W(z,t) = w_1(t)z \quad & +w_2(t)z^2 + w_3(t)z^3 + w_4(t)z^4 + w_5(t)z^5 + w_6(t)z^6 + w_7(t)z^7 + w_8(t)z^8 \\ & +w_9(t)z^9 + w_{10}(t)z^{10} + w_{11}(t)z^{11} + w_{12}(t)z^{12} \\ & +w_{13}(t)z^{13} + w_{14}(t)z^{14} + w_{15}(t)z^{15} + w_{16}(t)z^{16} \end{aligned} \tag{55}$$

$$\begin{aligned} \Gamma(z,t) = 1 + m_1(t)z \quad & +m_2(t)z^2 + m_3(t)z^3 + m_4(t)z^4 + m_5(t)z^5 + m_6(t)z^6 + m_7(t)z^7 \\ & +m_8(t)z^8 \end{aligned} \tag{56}$$

$$\begin{aligned} \tau(z,t) = n_1(t)z \quad & +n_2(t)z^2 + n_3(t)z^3 + n_4(t)z^4 + n_5(t)z^5 + n_6(t)z^6 + n_7(t)z^7 \\ & +n_8(t)z^8 + n_9(t)z^9 + n_{10}(t)z^{10} \end{aligned} \tag{57}$$

where the expressions $f_1, f_2 \ldots f_{15}, g_1, g_2 \ldots g_9, m_1, m_2 \ldots m_8, n_1, n_2 \ldots n_{10}$ and $w_1, w_2 \ldots w_{16}$ are given in the Appendix A.

4. Discussion

The process of coating heavily depends upon the time taken by any fluid to settle down on the surface of the material; a fluid can only be considered more suitable for the coating if it takes less time to leave its effects on the surface. Moreover, the engaged nanoparticles are of very small size and of a concentration of at most 2%. The effects on viscosity, thermal conductivity, density and heat capacity are evaluated experimentally in many communications. It is now a well-established fact that in the presence of such a small quantity of nanosized particles, the nature of fluid does not change but changes in physical properties are evident. For that, many correlations are presented for different situations and particles. To serve the purpose of this study, four different kinds of Newtonian fluids having diverse physical and chemical properties are considered instead of non-Newtonian fluids because coatings with such types of fluids would have a tremendous impact on the cost, volume, weight, and mechanical properties of electronic, optoelectronic, and photovoltaic devices; thus, this portion is dedicated to the parametric study of the proposed model in which four kinds of Newtonian fluids, such as water, ethanol, methanol and ethylene-glycol are opted for as the base fluids. The gold and silver nanoparticles are used to furnish the thin metallic and shiny coating on the surface of the

rotating disk. The main reason to carry out this graphical work is to confirm whether or not the obtained mathematical results are in complete coherence with the physical expectation of the spin coatings. Moreover, the graphic illustrations will help to make a sound judgement about the role and contribution of field variables. Major parameters which have been comprehensively focused on are the concentration of the metallic particles and the thermocapillary parameter. Furthermore, the presented parametric study unlike the customary results and discussion have been delicately divided into three following sub sections to make this comparative analysis more clear and fathomable.

4.1. Thickness of the Film

The key emphasis in this article is on furnishing a shiny metallic layer of nanoparticles, suspended with different base fluids displaying distinct physical and chemical features altogether. Here, the sole aim is to decide which one of the base fluids is the best suitable choice for this metallic covering over the disk with spin coatings that can quickly spread on the disk in a short span of time. As shown in Figure 2, it can clearly be seen that ethanol is the sole liquid which shows a rapid action with both metals as compared to the other base fluids. It is in accordance with their physical prospects, due to their densities, which help them evaporate quickly and results in a shiny metallic nanoliquids coating on the disk. On the other hand, silver particles' coating is much faster than gold, as Figure 3 shows.

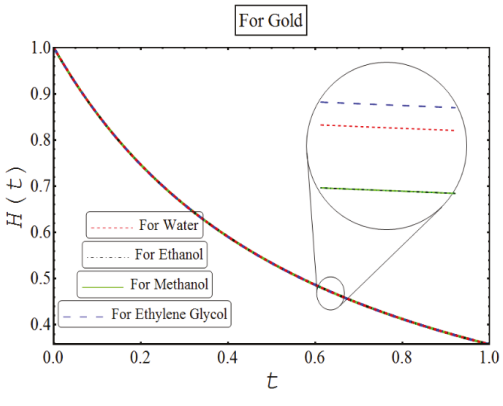

Figure 2. Behaviour of film thickness for different base fluids containing gold nanoparticles.

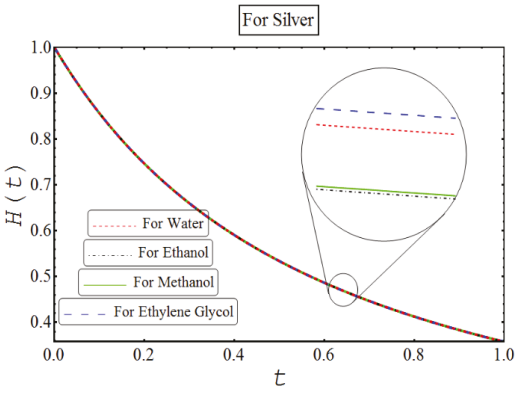

Figure 3. Behaviour of film thickness for different base fluids containing silver particles

In Figures 4–7, thermocapillary parameters and the concentration of the metallic particles' influence on nanofluid coating have been displayed. It is a well-recognized fact that the thicker solution yields to the thicker layer of the film. The thermocapillary parameter depletes and attenuates this metallic layer as shown in Figures 4 and 5. From the above given facts, it is inferred that ethanol and silver particles share a great deal of mutual compatibility. Thickness of the film increases in size upon the additional supply of metallic particles as shown in Figures 6 and 7. This confirms the above preceding claim that an increase of the particles will enlarge the film thickness in size. Therefore, it can be concluded that any fluids and particles which exhibit different characteristics like ethanol and silver are regarded as the most suitable option for this metallic process of coating. Consequently, to see the effects of thermal, radial and azimuthal velocity, ethanol was chosen as a base fluid.

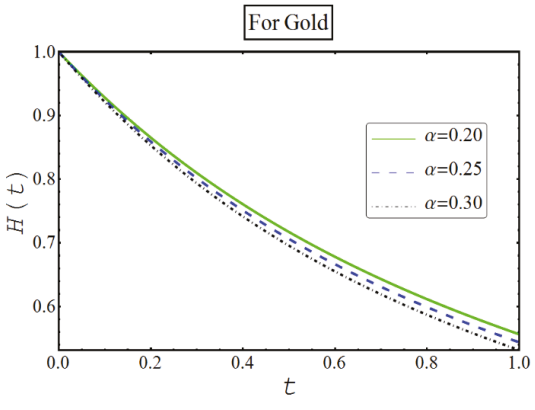

Figure 4. Behaviour of film thickness for thermocapillary parameter for gold particles.

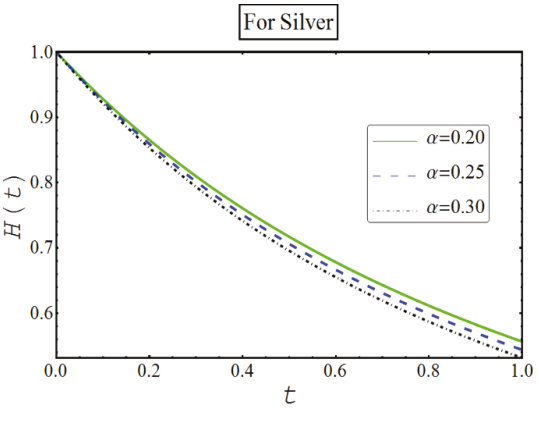

Figure 5. Behaviour of film thickness for thermocapillary for silver particles parameter.

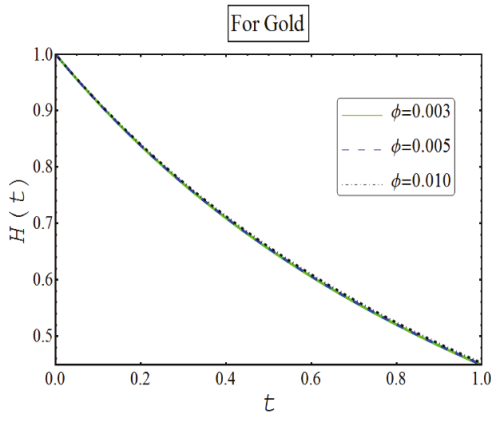

Figure 6. Effects of the concentration of particles on film thickness for the case of gold.

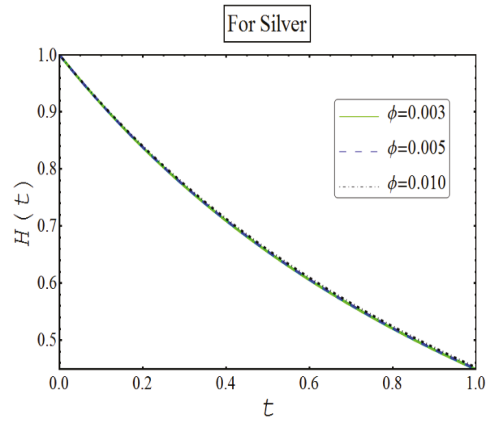

Figure 7. Effects of the concentration of particles on film thickness for the case of silver.

4.2. Radial Velocity and Azimuthal Velocity

In Figures 8–21, the radial and azimuthal velocities have been sketched for all base fluids, the thermocapillary parameter and the concentration of the particles. In view of suitable transformation, the mathematical expressions take the following final form:

$$U(z,t) = R\,F(z,t) \tag{58}$$

$$V(z,t) = R\,G(z,t) \tag{59}$$

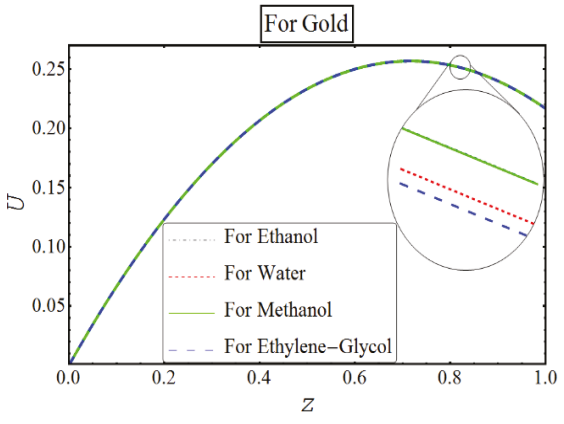

Figure 8. Behavior of radial velocity for each fluid comprising gold particles.

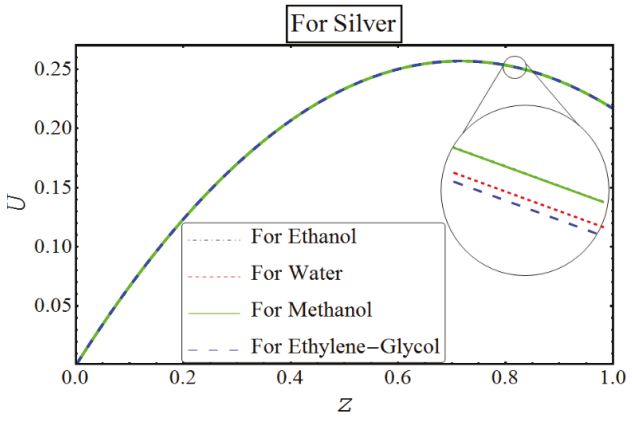

Figure 9. Behavior of radial velocity for each fluid comprising silver particles.

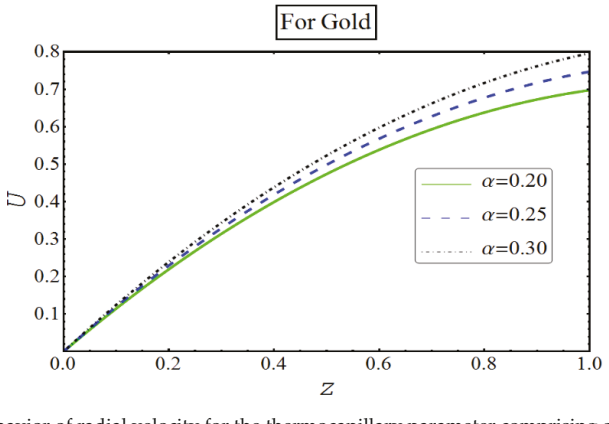

Figure 10. Behavior of radial velocity for the thermocapillary parameter comprising gold particles.

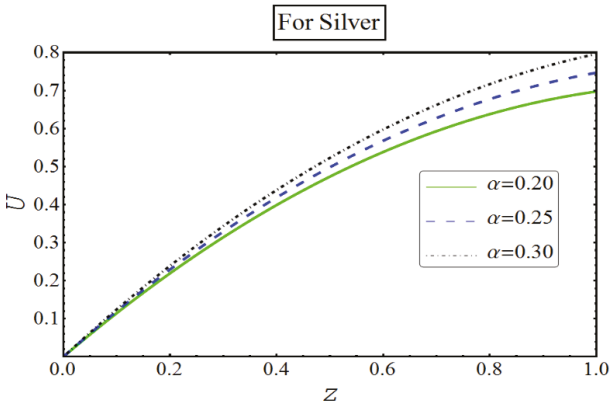

Figure 11. Behavior of radial velocity for the thermocapillary parameter comprising gold particles.

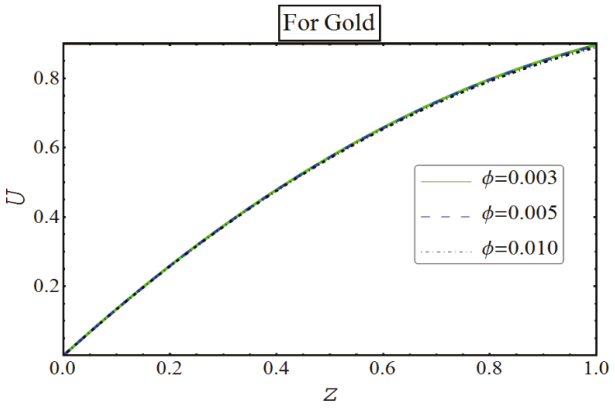

Figure 12. Effects of concentration particles on radial velocity with gold particles.

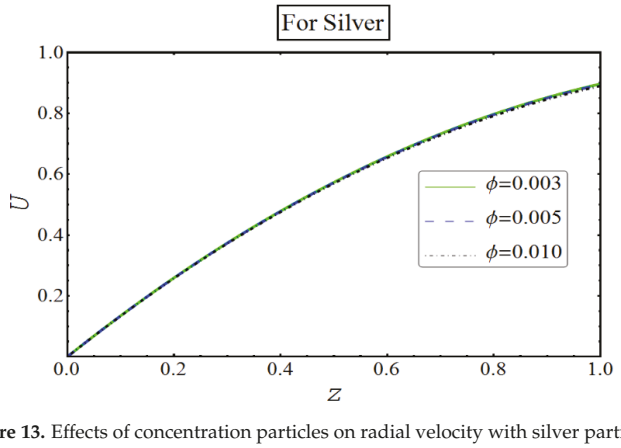

Figure 13. Effects of concentration particles on radial velocity with silver particles.

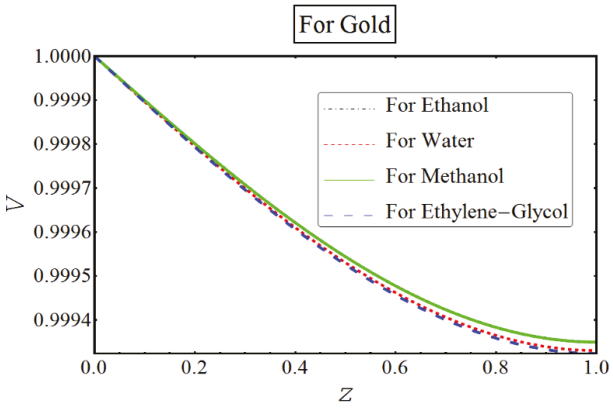

Figure 14. Behavior of azimuthal velocity for each fluid with gold particles.

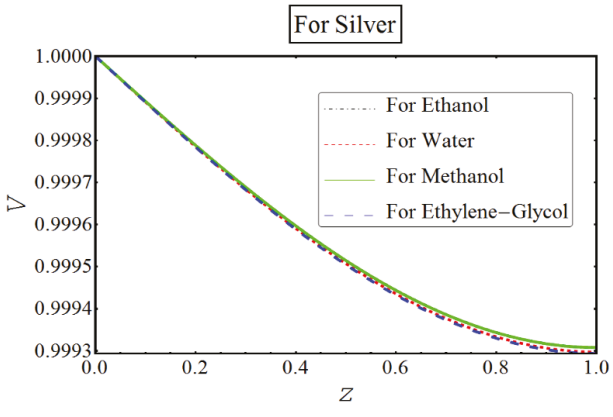

Figure 15. Behavior of azimuthal velocity for each fluid with silver particles.

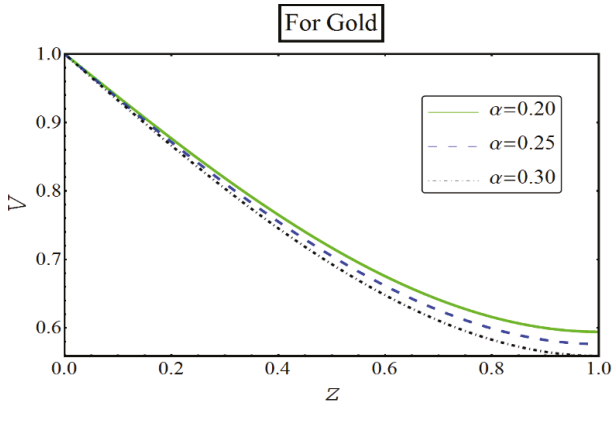

Figure 16. Behavior of azimuthal velocity for the thermocapillary parameter with gold particles.

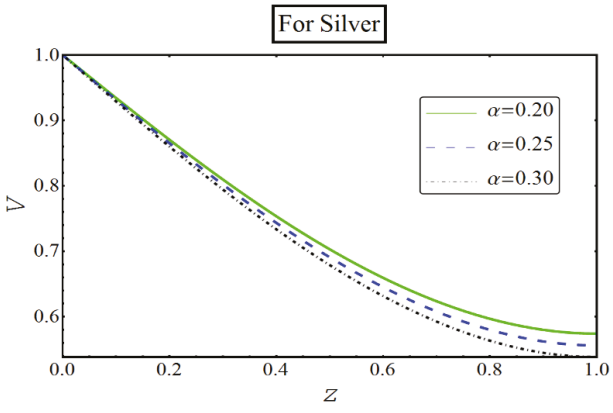

Figure 17. Behavior of azimuthal velocity for the thermocapillary parameter with silver particles.

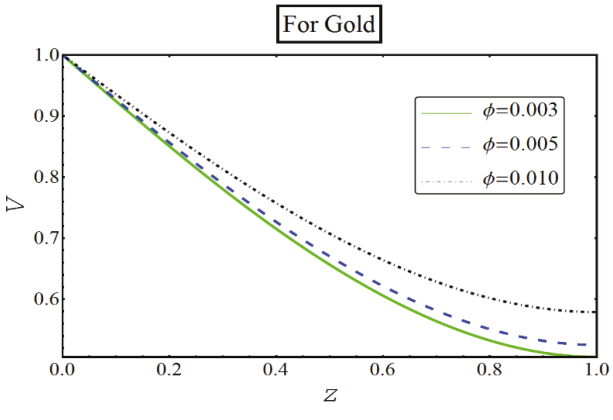

Figure 18. Effects of concentration particles on azimuthal velocity for gold.

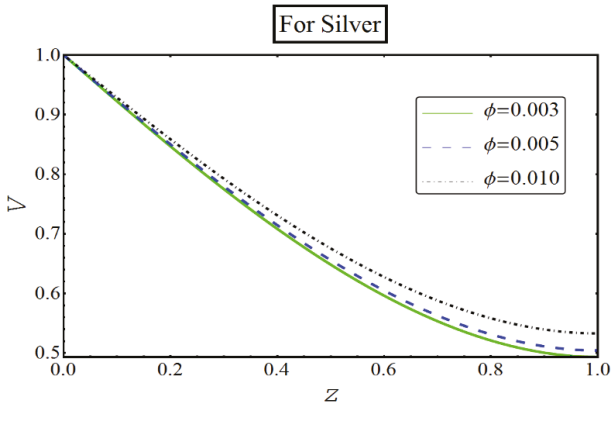

Figure 19. Effects of concentration particles suspended with ethanol on *N* for silver.

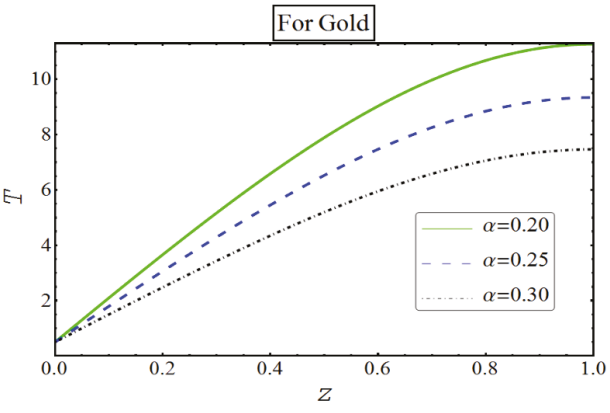

Figure 20. Temperature effects of thermocapillary parameter.

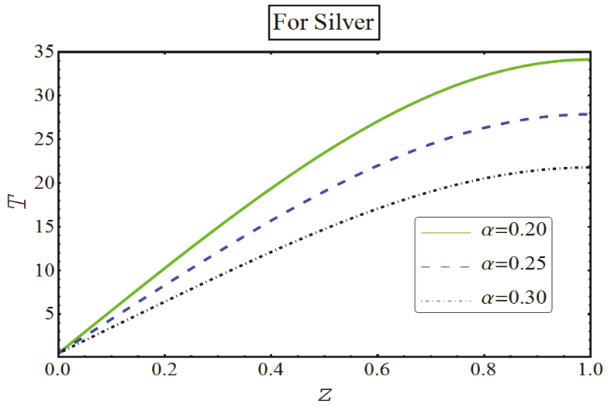

Figure 21. Temperature effects of thermocapillary parameter.

In Equations (58) and (59), $R = \frac{r}{h_0}$ is the initial thickness of the film. A similar trend in the behavior of both types of velocities is observed in the presence of silver and gold particles.

In Figures 8–19, the behavior of ethanol is quite prominent for all cases. It is observed that the radial velocity and azimuthal velocity increase for silver and gold. However, radial velocity and azimuthal velocity react quite differently for the thermocapillary parameter and the concentration of the particles. It is seen that temperature increases by increasing the values of thermocapillary parameter, as shown in Figures 20 and 21. It is in accordance with the physical expectation because radial velocity does not allow the fluid to move with full strength. However, the radial velocity is supported by the thermocapillary parameter. On the other hand, a complete reverse trend can be noted for the azimuthal velocity by varying both α and φ.

4.3. Thermal Analysis

In this section, the temperature of nanofluid was examined vertical to the disk. The mathematical relationships for temperature and temperature gradient were respectively denoted by the following relations:

$$T(z,t) = \frac{R^2}{2}\Gamma(z,t) + \tau(z,t) \tag{60}$$

$$T_z(z,t) = \frac{R^2}{2}\Gamma_z(z,t) + \tau_z(z,t) \tag{61}$$

Here smooth and organized curves are drawn in Figures 22–27. It is found that an addition of extra nanoparticles strengthens the drag force between the particles. However, thermocapillary parameter α works altogether differently by reducing the heat of the nanofluid that ultimately affirms the earlier preceding claim regarding the addition of metallic particles to the base fluid ethanol.

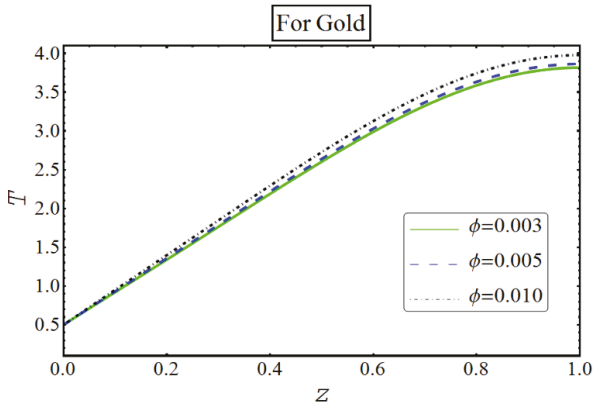

Figure 22. Temperature effects of concentration particles.

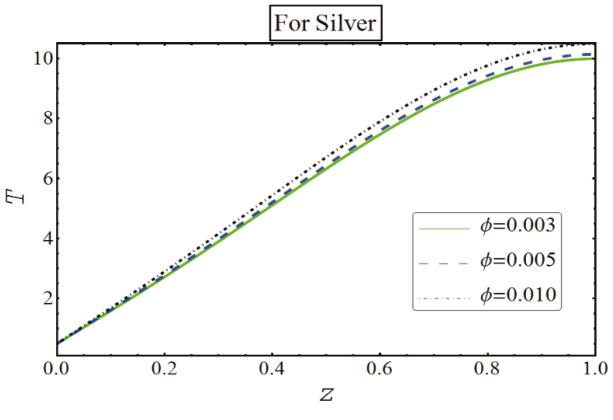

Figure 23. Temperature effects of concentration particles.

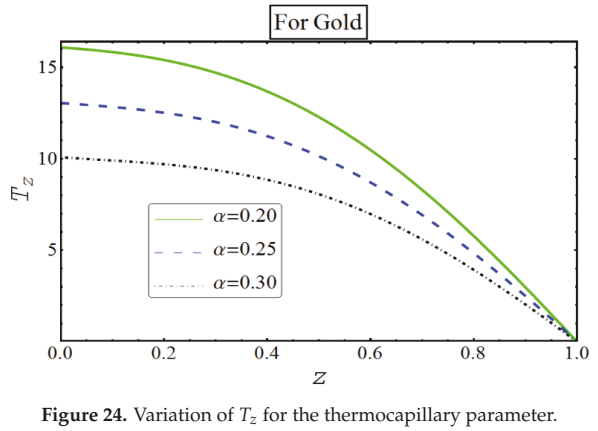

Figure 24. Variation of T_z for the thermocapillary parameter.

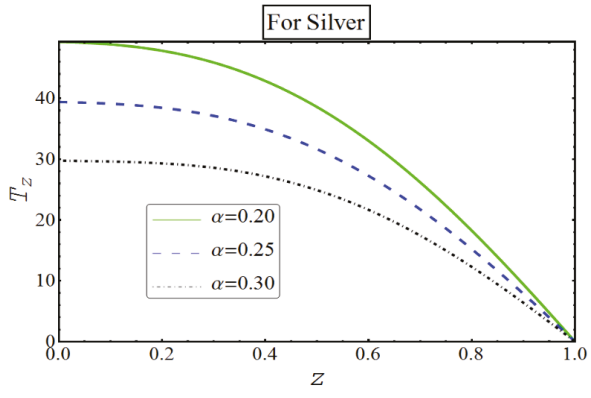

Figure 25. Variation of T_z for the thermocapillary parameter.

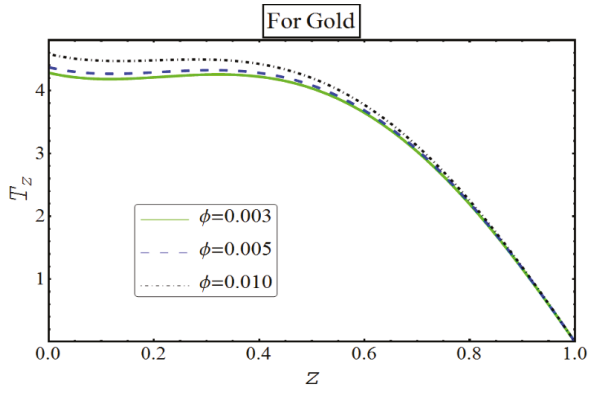

Figure 26. Variation of T_z on concentration particles.

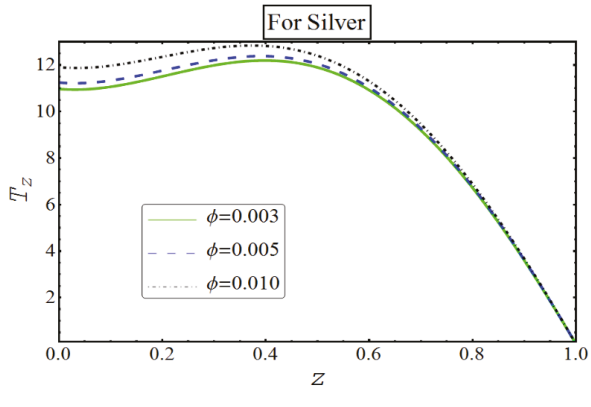

Figure 27. Variation of T_z on concentration particles.

5. Conclusions

A comparative study for silver and gold nanoparticles was comprehensively carried out to form a thin and shiny metallic layer over the surface of a rotating disk via spin coatings. Moreover, a detailed analysis of nanofluids suspended with four different types of base fluids, namely water, ethanol, methanol and ethylene-glycol has also been examined under the assumptions of nanofluids to be diluted and non-volatile. Finally, a parametric study on the basis of obtained expressions of results was made to apprehend the effects of the main parameters involved. Some significant findings are enlisted below:

- Silver metallic coating quickly settles down on the surface of the disk than to develop a gold coating.
- Thickness of the film increases with the addition of extra metallic particles.
- Radial velocity is hampered by adding more nanoparticles.
- Increase in the quantity of particles surges the thermal effects of the nanofluid.
- It is worth investigating that these results will help to choose the optimum base fluid with gold or silver particles.
- The graphical results show depletion of the fluid layer with time and one can hardly find such an evaluation in the available literature.
- Finally, it is concluded that the base fluid is the best choice for ethanol alloys with silver in the process of coating. In this way, it can be concluded that from the experimental point of view if silver alloy is used for coating then only such liquids should be considered which exhibit ethanol-like properties. Now, this effort is available for further experimental studies for those who are working in this regime for the validation of their lab results.

Author Contributions: Supervision, R.E.; Investigation, A.Z.; Methodology, F.H.; Writing-Review & Editing, T.A.

Funding: This research received no external funding.

Acknowledgments: F. Hussain gratefully thanks to FBAS to provide him administrative and technical support during his stay at IIUI as HEC indigenous scholar for the pursuance of his Ph.D. studies.

Conflicts of Interest: The authors declare no conflict of interest.

Nomenclatures

h_0	Initial film thickness
p	Pressure
t	Spinning time
U	Radial velocity component
V	Velocity
W	Axial velocity component
z	Axial coordinate
Pr	Prandtl number
Re	Reynolds number
$\overline{h}$	Film thickness
$\bar{r}$	Radial coordinate
$\overline{T}$	Temperature of nanofluid
$\overline{T}_0$	Initial room temperature
$\overline{T}_g$	Temperature in gas phase
$\overline{u}$	Radial velocity component
$\overline{v}$	Azimuthal velocity component
$\overline{w}$	Axial velocity component
k_{nf}	Thermal conductivity of nanofluid
k_f	Thermal conductivity of fluid

Greek Symbols

$\overline{\theta}$	Azimuthal coordinate of the velocity
$\overline{\Psi}$	Rotational velocity
ξ	Constant
ϕ_1	Dimensionless constant
$\overline{\rho}_p$	Density particle
$(C_P)_f$	Heat capacity of base fluid
$\overline{\mu}_{nf}$	Dynamic viscosity of nanofluid
μ	Dynamic viscosity
α	Thermocapillary parameter
$\overline{\sigma}_0$	Initial surface tension
$\overline{\sigma}$	Surface tension
ϕ	Concentration of particles
ϕ_2	Dimensionless constant
$\overline{\rho}_f$	Density of fluid
$(C_P)_f$	Heat capacity of particle
$\overline{\rho}_{nf}$	Density of nanofluid
$(\overline{\rho}C_P)_{nf}$	Heat capacity of nanofluid

Subscripts

f	Base fluid
nf	Nanofluid

Appendix A

$$f_1(t) = H + \alpha(1-\phi)^{2.5} - \frac{3H^4 Re\phi_1}{4} + \frac{3H^5 Re\phi_1}{20} - \frac{H^2 \frac{dH}{dt} Re\phi_1}{2} + \frac{131H^5 \frac{dH}{dt} Re^2\phi_1}{60} - \frac{53H^6 \frac{dH}{dt} Re^2\phi_1}{72} +$$
$$\frac{H^3\left(\frac{dH}{dt}\right)^2 Re^2\phi_1}{2} + \frac{5H^4 \frac{d^2H}{dt^2} Re^2\phi_1}{24} + \frac{H^3 \mathrm{Re}\alpha(1-\phi)^{2.5}\phi_1}{3} - \frac{5H^4 \mathrm{Re}\alpha(1-\phi)^{2.5}\phi_1}{4} - \frac{H^4 \frac{dH}{dt} \mathrm{Re}^2\alpha(1-\phi)^{2.5}\phi_1}{2} +$$
$$\frac{63H^5 \frac{dH}{dt} \mathrm{Re}^2\alpha(1-\phi)^{2.5}\phi_1}{20} + \frac{31H^7 \mathrm{Re}^2\phi_1^2}{45} - \frac{293H^8 \mathrm{Re}^2\phi_1^2}{2016} + \frac{12869H^9 \mathrm{Re}^2\phi_1^2}{90720} - \frac{3751H^{10} \mathrm{Re}^2\phi_1^2}{151200} + \frac{67H^6 \frac{dH}{dt} \mathrm{Re}^2\phi_1^2}{180} +$$
$$\frac{8H^7 \frac{dH}{dt} \mathrm{Re}^2\phi_1^2}{315} + \frac{1607H^7 \mathrm{Re}^2\alpha(1-\phi)^{2.5}\phi_1^2}{1260} - \frac{131H^8 \mathrm{Re}^2\alpha(1-\phi)^{2.5}\phi_1^2}{1120} + \frac{18679H^9 \mathrm{Re}^2\alpha(1-\phi)^{2.5}\phi_1^2}{90720} + \frac{7H^5 \frac{dH}{dt} \mathrm{Re}^2\alpha(1-\phi)^{2.5}\phi_1^2}{60} -$$
$$\frac{7H^6 \frac{dH}{dt} \mathrm{Re}^2\alpha(1-\phi)^{2.5}\phi_1^2}{72} - \frac{4H^6 \mathrm{Re}^2\alpha^2(1-\phi)^5\phi_1^2}{45} + \frac{667H^7 \mathrm{Re}^2\alpha^2(1-\phi)^5\phi_1^2}{630} - \frac{4303H^8 \mathrm{Re}^2\alpha^2(1-\phi)^5\phi_1^2}{10080} + \frac{121H^{12} \mathrm{Re}^2\phi_1^3}{1296} -$$
$$\frac{407H^{13} \mathrm{Re}^2\phi_1^3}{11340} + \frac{1369H^{14} \mathrm{Re}^2\phi_1^3}{396900} + \frac{55H^{10} \frac{dH}{dt} \mathrm{Re}^2\phi_1^3}{432} - \frac{37H^{11} \frac{dH}{dt} \mathrm{Re}^2\phi_1^3}{1512} + \frac{25H^8\left(\frac{dH}{dt}\right)^2 \mathrm{Re}^2\phi_1^3}{576} - \frac{11H^{11} \mathrm{Re}^2\alpha(1-\phi)^{2.5}\phi_1^3}{120} +$$
$$\frac{38573H^{12} \mathrm{Re}^2\alpha(1-\phi)^{2.5}\phi_1^3}{113400} - \frac{703H^{13} \mathrm{Re}^2\alpha(1-\phi)^{2.5}\phi_1^3}{11340} - \frac{H^9 \frac{dH}{dt} \mathrm{Re}^2\alpha(1-\phi)^{2.5}\phi_1^3}{16} + \frac{95H^{10} \frac{dH}{dt} \mathrm{Re}^2\alpha(1-\phi)^{2.5}\phi_1^3}{432} +$$
$$\frac{9H^{10} \mathrm{Re}^2\alpha^2(1-\phi)^5\phi_1^3}{400} - \frac{19H^{11} \mathrm{Re}^2\alpha^2(1-\phi)^5\phi_1^3}{120} + \frac{361H^{12} \mathrm{Re}^2\alpha^2(1-\phi)^5\phi_1^3}{1296};$$

$$f_2(t) = -\frac{1}{2};$$

$$f_3(t) = \frac{H^2 \mathrm{Re}\phi_1}{3} - \frac{H^3 \mathrm{Re}\phi_1}{9} + \frac{\frac{dH}{dt} \mathrm{Re}\phi_1}{6} - \frac{5H^3 \frac{dH}{dt} \mathrm{Re}^2\phi_1}{6} + \frac{7H^4 \frac{dH}{dt} \mathrm{Re}^2\phi_1}{24} - \frac{H\left(\frac{dH}{dt}\right)^2 \mathrm{Re}^2\phi_1}{6} - \frac{\mathrm{Re}^2\phi_1 H^2 \frac{d^2H}{dt^2}}{12} +$$
$$\frac{H^2 \mathrm{Re}\alpha(1-\phi)^{2.5}\phi_1}{3} + \frac{H^2 \frac{dH}{dt} \mathrm{Re}^2\alpha(1-\phi)^{2.5}\phi_1}{6} - \frac{7H^3 \frac{dH}{dt} \mathrm{Re}^2\alpha(1-\phi)^{2.5}\phi_1}{6} - \frac{8H^5 \mathrm{Re}^2\phi_1^2}{45} - \frac{H^6 \mathrm{Re}^2\phi_1^2}{108} - \frac{8H^7 \mathrm{Re}^2\phi_1^2}{315} + \frac{H^8 \mathrm{Re}^2\phi_1^2}{160} -$$
$$\frac{5H^4 \frac{dH}{dt} \mathrm{Re}^2\phi_1^2}{36} - \frac{23H^5 \mathrm{Re}^2\alpha(1-\phi)^{2.5}\phi_1^2}{90} - \frac{5H^6 \mathrm{Re}^2\alpha(1-\phi)^{2.5}\phi_1^2}{54} - \frac{11H^7 \mathrm{Re}^2\alpha(1-\phi)^{2.5}\phi_1^2}{270} - \frac{8H^5 \mathrm{Re}^2\alpha^2(1-\phi)^5\phi_1^2}{45} +$$
$$\frac{7H^6 \mathrm{Re}^2\alpha^2(1-\phi)^5\phi_1^2}{108};$$

$$f_4(t) = -\frac{H \mathrm{Re}\phi_1}{12} + \frac{H^2 \mathrm{Re}\phi_1}{12} - \frac{\mathrm{Re}\alpha(1-\phi)^{2.5}\phi_1}{12} + \frac{H \mathrm{Re}\alpha(1-\phi)^{2.5}\phi_1}{12} - \frac{H^4 \mathrm{Re}^2\phi_1^2}{12} - \frac{H^5 \mathrm{Re}^2\phi_1^2}{144} + \frac{7H^6 \mathrm{Re}^2\phi_1^2}{2160} - \frac{H^3 \frac{dH}{dt} \mathrm{Re}^2\phi_1^2}{24} -$$
$$\frac{29H^4 \mathrm{Re}^2\alpha(1-\phi)^{2.5}\phi_1^2}{144} - \frac{13H^5 \mathrm{Re}^2\alpha(1-\phi)^{2.5}\phi_1^2}{360} - \frac{H^2 \frac{dH}{dt} \mathrm{Re}^2\alpha(1-\phi)^{2.5}\phi_1^2}{24} + \frac{H^3 \mathrm{Re}^2\alpha^2(1-\phi)^5\phi_1^2}{36} - \frac{3H^4 \mathrm{Re}^2\alpha^2(1-\phi)^5\phi_1^2}{16};$$

$$f_5(t) = \frac{\mathrm{Re}\phi_1}{60} - \frac{H\mathrm{Re}\phi_1}{30} + \frac{H\frac{\mathrm{d}H}{\mathrm{d}t}\mathrm{Re}^2\phi_1}{15} - \frac{H^2\frac{\mathrm{d}H}{\mathrm{d}t}\mathrm{Re}^2\phi_1}{30} + \frac{\frac{\mathrm{d}^2H}{\mathrm{d}t^2}\mathrm{Re}^2\phi_1}{120} - \frac{\mathrm{Re}\alpha(1-\phi)^{2.5}\phi_1}{60} + \frac{H\frac{\mathrm{d}H}{\mathrm{d}t}\mathrm{Re}^2\alpha(1-\phi)^{2.5}\phi_1}{15} + \frac{H^4\mathrm{Re}^2\phi_1^2}{16} - \frac{H^5\mathrm{Re}^2\phi_1^2}{80} + \frac{H^2\frac{\mathrm{d}H}{\mathrm{d}t}\mathrm{Re}^2\phi_1^2}{24} - \frac{H^3\mathrm{Re}^2\alpha(1-\phi)^{2.5}\phi_1^2}{36} + \frac{17H^4\mathrm{Re}^2\alpha(1-\phi)^{2.5}\phi_1^2}{120} - \frac{3H^5\mathrm{Re}^2\alpha(1-\phi)^{2.5}\phi_1^2}{400} + \frac{H^2\frac{\mathrm{d}H}{\mathrm{d}t}\mathrm{Re}^2\alpha(1-\phi)^{2.5}\phi_1^2}{40} - \frac{H^3\mathrm{Re}^2\alpha^2(1-\phi)^5\phi_1^2}{60} + \frac{H^4\mathrm{Re}^2\alpha^2(1-\phi)^5\phi_1^2}{16} - \frac{9H^8\mathrm{Re}^2\phi_1^3}{320} + \frac{9H^9\mathrm{Re}^2\phi_1^3}{800} - \frac{9H^{10}\mathrm{Re}^2\phi_1^3}{8000} - \frac{3H^6\frac{\mathrm{d}H}{\mathrm{d}t}\mathrm{Re}^2\phi_1^3}{80} + \frac{3H^7\frac{\mathrm{d}H}{\mathrm{d}t}\mathrm{Re}^2\phi_1^3}{400} - \frac{H^4\left(\frac{\mathrm{d}H}{\mathrm{d}t}\right)^2\mathrm{Re}^2\phi_1^3}{80} + \frac{H^7\mathrm{Re}^2\alpha(1-\phi)^{2.5}\phi_1^3}{40} - \frac{79H^8\mathrm{Re}^2\alpha(1-\phi)^{2.5}\phi_1^3}{800} + \frac{3H^9\mathrm{Re}^2\alpha(1-\phi)^{2.5}\phi_1^3}{160} + \frac{H^5\frac{\mathrm{d}H}{\mathrm{d}t}\mathrm{Re}^2\alpha(1-\phi)^{2.5}\phi_1^3}{60} - \frac{H^6\frac{\mathrm{d}H}{\mathrm{d}t}\mathrm{Re}^2\alpha(1-\phi)^{2.5}\phi_1^3}{16} - \frac{H^6\mathrm{Re}^2\alpha^2(1-\phi)^5\phi_1^3}{180} + \frac{H^7\mathrm{Re}^2\alpha^2(1-\phi)^5\phi_1^3}{24} - \frac{5H^8\mathrm{Re}^2\alpha^2(1-\phi)^5\phi_1^3}{64};$$

$$f_6(t) = \frac{\mathrm{Re}\phi_1}{360} - \frac{\frac{\mathrm{d}H}{\mathrm{d}t}\mathrm{Re}^2\phi_1}{360} + \frac{H\frac{\mathrm{d}H}{\mathrm{d}t}\mathrm{Re}^2\phi_1}{180} + \frac{\frac{\mathrm{d}H}{\mathrm{d}t}\mathrm{Re}^2\alpha(1-\phi)^{2.5}\phi_1}{360} + \frac{H^2\mathrm{Re}^2\phi_1^2}{30} + \frac{H^3\mathrm{Re}^2\phi_1^2}{180} - \frac{H^4\mathrm{Re}^2\phi_1^2}{72} + \frac{H^5\mathrm{Re}^2\phi_1^2}{600} + \frac{H\frac{\mathrm{d}H}{\mathrm{d}t}\mathrm{Re}^2\phi_1^2}{120} - \frac{H^2\frac{\mathrm{d}H}{\mathrm{d}t}\mathrm{Re}^2\phi_1^2}{180} + \frac{H^2\mathrm{Re}^2\alpha(1-\phi)^{2.5}\phi_1^2}{12} + \frac{H^3\mathrm{Re}^2\alpha(1-\phi)^{2.5}\phi_1^2}{270} - \frac{H^4\mathrm{Re}^2\alpha(1-\phi)^{2.5}\phi_1^2}{72} + \frac{\frac{\mathrm{d}H}{\mathrm{d}t}\mathrm{Re}^2\alpha(1-\phi)^{2.5}\phi_1^2}{120} + \frac{H^2\mathrm{Re}^2\alpha^2(1-\phi)^5\phi_1^2}{20};$$

$$f_7(t) = -\frac{\mathrm{Re}^2\phi_1\frac{\mathrm{d}H}{\mathrm{d}t}}{1260} - \frac{8H^2\mathrm{Re}^2\phi_1^2}{315} + \frac{2H^3\mathrm{Re}^2\phi_1^2}{189} - \frac{17\mathrm{Re}^2\phi_1^2\frac{\mathrm{d}H}{\mathrm{d}t}}{2520} - \frac{2H\mathrm{Re}^2\alpha(1-\phi)^{2.5}\phi_1^2}{315} - \frac{11H^2\mathrm{Re}^2\alpha(1-\phi)^{2.5}\phi_1^2}{420} + \frac{13H^3\mathrm{Re}^2\alpha(1-\phi)^{2.5}\phi_1^2}{3780} - \frac{\frac{\mathrm{d}H}{\mathrm{d}t}\mathrm{Re}^2\alpha(1-\phi)^{2.5}\phi_1^2}{252} - \frac{\mathrm{Re}^2\alpha^2(1-\phi)^5\phi_1^2}{315} + \frac{H\mathrm{Re}^2\alpha^2(1-\phi)^5\phi_1^2}{315} - \frac{13H^2\mathrm{Re}^2\alpha^2(1-\phi)^5\phi_1^2}{1260} + \frac{H^6\mathrm{Re}^2\phi_1^3}{112} - \frac{H^7\mathrm{Re}^2\phi_1^3}{210} + \frac{H^8\mathrm{Re}^2\phi_1^3}{1680} + \frac{H^4\frac{\mathrm{d}H}{\mathrm{d}t}\mathrm{Re}^2\phi_1^3}{96} - \frac{29H^5\frac{\mathrm{d}H}{\mathrm{d}t}\mathrm{Re}^2\phi_1^3}{10080} + \frac{H^2\left(\frac{\mathrm{d}H}{\mathrm{d}t}\right)^2\mathrm{Re}^2\phi_1^3}{336} - \frac{H^5\mathrm{Re}^2\alpha(1-\phi)^{2.5}\phi_1^3}{252} + \frac{19H^6\mathrm{Re}^2\alpha(1-\phi)^{2.5}\phi_1^3}{756} - \frac{17H^7\mathrm{Re}^2\alpha(1-\phi)^{2.5}\phi_1^3}{2520} - \frac{H^3\frac{\mathrm{d}H}{\mathrm{d}t}\mathrm{Re}^2\alpha(1-\phi)^{2.5}\phi_1^3}{504} + \frac{3H^4\frac{\mathrm{d}H}{\mathrm{d}t}\mathrm{Re}^2\alpha(1-\phi)^{2.5}\phi_1^3}{224} - \frac{H^5\mathrm{Re}^2\alpha^2(1-\phi)^5\phi_1^3}{252} + \frac{5H^6\mathrm{Re}^2\alpha^2(1-\phi)^5\phi_1^3}{336};$$

$$f_8(t) = -\frac{\mathrm{Re}^2\phi_1^2}{360} + \frac{31H\mathrm{Re}^2\phi_1^2}{10080} - \frac{H^2\mathrm{Re}^2\phi_1^2}{840} - \frac{H^3\mathrm{Re}^2\phi_1^2}{1260} + \frac{\mathrm{Re}^2\phi_1^2\frac{\mathrm{d}H}{\mathrm{d}t}}{1008} - \frac{5\mathrm{Re}^2\alpha(1-\phi)^{2.5}\phi_1^2}{2016} - \frac{13H\mathrm{Re}^2\alpha(1-\phi)^{2.5}\phi_1^2}{5040} + \frac{H^2\mathrm{Re}^2\alpha(1-\phi)^{2.5}\phi_1^2}{1120} - \frac{\mathrm{Re}^2\alpha^2(1-\phi)^5\phi_1^2}{560} - \frac{H\mathrm{Re}^2\alpha^2(1-\phi)^5\phi_1^2}{672} - \frac{H^5\mathrm{Re}^2\phi_1^3}{640} + \frac{3H^6\mathrm{Re}^2\phi_1^3}{1600} - \frac{H^7\mathrm{Re}^2\phi_1^3}{3200} - \frac{H^3\frac{\mathrm{d}H}{\mathrm{d}t}\mathrm{Re}^2\phi_1^3}{960} + \frac{H^4\frac{\mathrm{d}H}{\mathrm{d}t}\mathrm{Re}^2\phi_1^3}{960} - \frac{H^4\mathrm{Re}^2\alpha(1-\phi)^{2.5}\phi_1^3}{1152} - \frac{41H^5\mathrm{Re}^2\alpha(1-\phi)^{2.5}\phi_1^3}{28800} + \frac{11H^6\mathrm{Re}^2\alpha(1-\phi)^{2.5}\phi_1^3}{4800} - \frac{H^2\frac{\mathrm{d}H}{\mathrm{d}t}\mathrm{Re}^2\alpha(1-\phi)^{2.5}\phi_1^3}{960} + \frac{H^3\frac{\mathrm{d}H}{\mathrm{d}t}\mathrm{Re}^2\alpha(1-\phi)^{2.5}\phi_1^3}{960} + \frac{H^3\mathrm{Re}^2\alpha^2(1-\phi)^5\phi_1^3}{1440} - \frac{19H^4\mathrm{Re}^2\alpha^2(1-\phi)^5\phi_1^3}{5760} + \frac{H^5\mathrm{Re}^2\alpha^2(1-\phi)^5\phi_1^3}{384};$$

$$f_9(t) = \frac{83\mathrm{Re}^2\phi_1^2}{90720} + \frac{H\mathrm{Re}^2\phi_1^2}{2016} + \frac{H^2\mathrm{Re}^2\phi_1^2}{2592} + \frac{127\mathrm{Re}^2\alpha(1-\phi)^{2.5}\phi_1^2}{90720} + \frac{11H\mathrm{Re}^2\alpha(1-\phi)^{2.5}\phi_1^2}{12960} + \frac{41\mathrm{Re}^2\alpha^2(1-\phi)^5\phi_1^2}{90720} - \frac{7H^4\mathrm{Re}^2\phi_1^3}{12960} + \frac{H^5\mathrm{Re}^2\phi_1^3}{194400} + \frac{H^6\mathrm{Re}^2\phi_1^3}{145800} - \frac{H^2\frac{\mathrm{d}H}{\mathrm{d}t}\mathrm{Re}^2\phi_1^3}{1620} - \frac{H^3\frac{\mathrm{d}H}{\mathrm{d}t}\mathrm{Re}^2\phi_1^3}{19440} - \frac{\left(\frac{\mathrm{d}H}{\mathrm{d}t}\right)^2\mathrm{Re}^2\phi_1^3}{5184} - \frac{H^3\mathrm{Re}^2\alpha(1-\phi)^{2.5}\phi_1^3}{9720} - \frac{23H^4\mathrm{Re}^2\alpha(1-\phi)^{2.5}\phi_1^3}{19440} - \frac{41H^5\mathrm{Re}^2\alpha(1-\phi)^{2.5}\phi_1^3}{194400} - \frac{H^2\frac{\mathrm{d}H}{\mathrm{d}t}\mathrm{Re}^2\alpha(1-\phi)^{2.5}\phi_1^3}{1080} + \frac{H^3\mathrm{Re}^2\alpha^2(1-\phi)^5\phi_1^3}{9720} - \frac{H^4\mathrm{Re}^2\alpha^2(1-\phi)^5\phi_1^3}{864};$$

$$f_{10}(t) = -\frac{41\mathrm{Re}^2\phi_1^2}{226800} - \frac{H\mathrm{Re}^2\phi_1^2}{8100} - \frac{11\mathrm{Re}^2\alpha(1-\phi)^{2.5}\phi_1^2}{64800} + \frac{H^3\mathrm{Re}^2\phi_1^3}{3600} - \frac{103H^4\mathrm{Re}^2\phi_1^3}{302400} + \frac{131H^5\mathrm{Re}^2\phi_1^3}{1512000} + \frac{H\frac{\mathrm{d}H}{\mathrm{d}t}\mathrm{Re}^2\phi_1^3}{7200} - \frac{H^2\frac{\mathrm{d}H}{\mathrm{d}t}\mathrm{Re}^2\phi_1^3}{8400} + \frac{H^2\mathrm{Re}^2\alpha(1-\phi)^{2.5}\phi_1^3}{3600} - \frac{H^3\mathrm{Re}^2\alpha(1-\phi)^{2.5}\phi_1^3}{9450} - \frac{41H^4\mathrm{Re}^2\alpha(1-\phi)^{2.5}\phi_1^3}{302400} + \frac{\mathrm{Re}^2\alpha(1-\phi)^{2.5}\phi_1^3\frac{\mathrm{d}H}{\mathrm{d}t}}{7200} - \frac{H\frac{\mathrm{d}H}{\mathrm{d}t}\mathrm{Re}^2\alpha(1-\phi)^{2.5}\phi_1^3}{7200} + \frac{H^2\mathrm{Re}^2\alpha^2(1-\phi)^5\phi_1^3}{3600} - \frac{H^3\mathrm{Re}^2\alpha^2(1-\phi)^5\phi_1^3}{3600};$$

$$f_{11}(t) = \frac{\mathrm{Re}^2\phi_1^2}{64800} - \frac{H^2\mathrm{Re}^2\phi_1^3}{14850} + \frac{53H^3\mathrm{Re}^2\phi_1^3}{356400} - \frac{19H^4\mathrm{Re}^2\phi_1^3}{356400} - \frac{\mathrm{Re}^2\phi_1^3\frac{\mathrm{d}H}{\mathrm{d}t}}{47520} + \frac{H\frac{\mathrm{d}H}{\mathrm{d}t}\mathrm{Re}^2\phi_1^3}{23760} - \frac{H\mathrm{Re}^2\alpha(1-\phi)^{2.5}\phi_1^3}{19800} + \frac{H^2\mathrm{Re}^2\alpha(1-\phi)^{2.5}\phi_1^3}{9900} + \frac{7H^3\mathrm{Re}^2\alpha(1-\phi)^{2.5}\phi_1^3}{356400} + \frac{\mathrm{Re}^2\alpha(1-\phi)^{2.5}\phi_1^3\frac{\mathrm{d}H}{\mathrm{d}t}}{47520} - \frac{\mathrm{Re}^2\alpha^2(1-\phi)^5\phi_1^3}{39600} + \frac{H\mathrm{Re}^2\alpha^2(1-\phi)^5\phi_1^3}{19800} + \frac{H^2\mathrm{Re}^2\alpha^2(1-\phi)^5\phi_1^3}{59400};$$

$$f_{12}(t) = \frac{H\mathrm{Re}^2\phi_1^3}{129600} - \frac{13H^2\mathrm{Re}^2\phi_1^3}{453600} + \frac{47H^3\mathrm{Re}^2\phi_1^3}{2721600} - \frac{\mathrm{Re}^2\phi_1^3\frac{\mathrm{d}H}{\mathrm{d}t}}{362880} + \frac{\mathrm{Re}^2\alpha(1-\phi)^{2.5}\phi_1^3}{129600} - \frac{H\mathrm{Re}^2\alpha(1-\phi)^{2.5}\phi_1^3}{32400} + \frac{H^2\mathrm{Re}^2\alpha(1-\phi)^{2.5}\phi_1^3}{56700} - \frac{\mathrm{Re}^2\alpha^2(1-\phi)^5\phi_1^3}{129600} + \frac{H\mathrm{Re}^2\alpha^2(1-\phi)^5\phi_1^3}{129600};$$

$$f_{13}(t) = -\frac{\mathrm{Re}^2\phi_1^3}{1684800} + \frac{H\mathrm{Re}^2\phi_1^3}{294840} - \frac{H^2\mathrm{Re}^2\phi_1^3}{294840} + \frac{\mathrm{Re}^2\alpha(1-\phi)^{2.5}\phi_1^3}{453600} - \frac{H\mathrm{Re}^2\alpha(1-\phi)^{2.5}\phi_1^3}{294840} - \frac{\mathrm{Re}^2\alpha^2(1-\phi)^5\phi_1^3}{1684800};$$

$$f_{14}(t) = -\frac{\mathrm{Re}^2\phi_1^3}{6350400} + \frac{H\mathrm{Re}^2\phi_1^3}{3175200} + \frac{\mathrm{Re}^2\alpha(1-\phi)^{2.5}\phi_1^3}{6350400};$$

$$f_{15}(t) = -\frac{\mathrm{Re}^2\phi_1^3}{95256000};$$

$$g_1(t) = -H^2\mathrm{Re}\phi_1 + H^3\mathrm{Re}^2\phi_1\frac{\mathrm{d}H}{dt} - H^2\mathrm{Re}\alpha(1-\phi)^{2.5}\phi_1 + H^3\mathrm{Re}^2\alpha\phi_1\frac{\mathrm{d}H}{dt}(1-\phi)^{2.5} - \frac{H^4\mathrm{Re}^2\phi_1\frac{\mathrm{d}H}{dt}}{2} + \frac{8H^5\mathrm{Re}^2\phi_1^2}{15} + \frac{H^3\mathrm{Re}\phi_1}{3} + \frac{H^6\mathrm{Re}^2\phi_1^2}{36} + \frac{8H^7\mathrm{Re}^2\phi_1^2}{105} - \frac{3H^8\mathrm{Re}^2\phi_1^2}{160} + \frac{5H^4\mathrm{Re}^2\phi_1^2\frac{\mathrm{d}H}{dt}}{12} + \frac{23H^5\mathrm{Re}^2\alpha(1-\phi)^{2.5}\phi_1^2}{30} + \frac{5H^6\mathrm{Re}^2\alpha(1-\phi)^{2.5}\phi_1^2}{18} + \frac{11H^7\mathrm{Re}^2\alpha(1-\phi)^{2.5}\phi_1^2}{90} + \frac{8H^5\mathrm{Re}^2\alpha^2(1-\phi)^5\phi_1^2}{15} - \frac{7H^6\mathrm{Re}^2\alpha^2(1-\phi)^5\phi_1^2}{36};$$

$$g_2(t) = 0;$$

$$g_3(t) = \frac{\mathrm{Re}\phi_1}{3} - \frac{H\mathrm{Re}^2\phi_1\frac{\mathrm{d}H}{dt}}{3} + \frac{H^2\mathrm{Re}^2\phi_1\frac{\mathrm{d}H}{dt}}{6} + \frac{\mathrm{Re}\alpha(1-\phi)^{2.5}\phi_1}{3} - \frac{H\mathrm{Re}^2\alpha(1-\phi)^{2.5}\phi_1\frac{\mathrm{d}H}{dt}}{3} - \frac{H^4\mathrm{Re}^2\phi_1^2}{4} + \frac{H^5\mathrm{Re}^2\phi_1^2}{20} - \frac{H^2\mathrm{Re}^2\phi_1^2\frac{\mathrm{d}H}{dt}}{6} + \frac{H^3\mathrm{Re}^2\alpha(1-\phi)^{2.5}\phi_1^2}{9} - \frac{5H^4\mathrm{Re}^2\alpha(1-\phi)^{2.5}\phi_1^2}{12};$$

$$g_4(t) = -\frac{\mathrm{Re}\phi_1}{12} - \frac{H^2\mathrm{Re}^2\phi_1^2}{6} + \frac{H^3\mathrm{Re}^2\phi_1^2}{18} - \frac{H^2\mathrm{Re}^2\alpha(1-\phi)^{2.5}\phi_1^2}{3} + \frac{H^3\mathrm{Re}^2\alpha(1-\phi)^{2.5}\phi_1^2}{18} - \frac{H^2\mathrm{Re}^2\alpha^2(1-\phi)^5\phi_1^2}{6};$$

$$g_5(t) = \frac{2H^2\mathrm{Re}^2\phi_1^2}{15} - \frac{2H^3\mathrm{Re}^2\phi_1^2}{45} + \frac{\mathrm{Re}^2\phi_1^2\frac{\mathrm{d}H}{dt}}{60} + \frac{11H^2\mathrm{Re}^2\alpha(1-\phi)^{2.5}\phi_1^2}{60} - \frac{H^3\mathrm{Re}^2\alpha(1-\phi)^{2.5}\phi_1^2}{60} + \frac{H^2\mathrm{Re}^2\alpha^2(1-\phi)^5\phi_1^2}{20};$$

$$g_6(t) = \frac{\mathrm{Re}^2\phi_1^2}{45} - \frac{H\mathrm{Re}^2\phi_1^2}{180} - \frac{H^2\mathrm{Re}^2\phi_1^2}{180} + \frac{H^3\mathrm{Re}^2\phi_1^2}{270} + \frac{7\mathrm{Re}^2\alpha(1-\phi)^{2.5}\phi_1^2}{180} + \frac{H\mathrm{Re}^2\alpha(1-\phi)^{2.5}\phi_1^2}{180} - \frac{H^2\mathrm{Re}^2\alpha(1-\phi)^{2.5}\phi_1^2}{90} + \frac{\mathrm{Re}^2\alpha^2(1-\phi)^5\phi_1^2}{45};$$

$$g_7(t) = -\frac{2\mathrm{Re}^2\phi_1^2}{105} - \frac{H\mathrm{Re}^2\phi_1^2}{630} - \frac{\mathrm{Re}^2\alpha(1-\phi)^{2.5}\phi_1^2}{35} - \frac{\mathrm{Re}^2\alpha^2(1-\phi)^5\phi_1^2}{126};$$

$$g_8(t) = \frac{17\mathrm{Re}^2\phi_1^2}{3360} + \frac{\mathrm{Re}^2\alpha(1-\phi)^{2.5}\phi_1^2}{288};$$

$$g_9(t) = -\frac{\mathrm{Re}^2\phi_1^2}{2592};$$

$$m_1(t) = -\frac{H^2\mathrm{Re}}{A_2} + \frac{H^3\mathrm{Re}}{3A_2} + \frac{2H^5\mathrm{Re}^2}{5{A_2}^2} - \frac{11H^6\mathrm{Re}^2}{36{A_2}^2} + \frac{5H^7\mathrm{Re}^2}{84{A_2}^2} + \frac{H^3\frac{d^2H}{dt^2}\mathrm{Re}^2}{{A_2}^2} - \frac{H^4\frac{d^2H}{dt^2}\mathrm{Re}^2}{2{A_2}^2} - \frac{H^2\mathrm{Re}\alpha(1-\phi)^{2.5}}{A_2} + \frac{4H^5\mathrm{Re}^2\alpha(1-\phi)^{2.5}}{5{A_2}^2} - \frac{11H^6\mathrm{Re}^2\alpha(1-\phi)^{2.5}}{36{A_2}^2} + \frac{H^3\frac{d^2H}{dt^2}\mathrm{Re}^2\alpha(1-\phi)^{2.5}}{{A_2}^2} + \frac{2H^5\mathrm{Re}^2\alpha^2(1-\phi)^5}{5{A_2}^2} + \frac{11H^6\mathrm{Re}^2\phi_1}{18A_2} - \frac{37H^7\mathrm{Re}^2\phi_1}{315A_2} + \frac{5H^4\frac{d^2H}{dt^2}\mathrm{Re}^2\phi_1}{12A_2} - \frac{3H^5\mathrm{Re}^2\alpha(1-\phi)^{2.5}\phi_1}{10A_2} + \frac{19H^6\mathrm{Re}^2\alpha(1-\phi)^{2.5}\phi_1}{18A_2};$$

$$m_2(t) = 0;$$

$$m_3(t) = \frac{\mathrm{Re}}{3A_2} - \frac{H\frac{d^2H}{dt^2}\mathrm{Re}^2}{3{A_2}^2} + \frac{H^2\frac{d^2H}{dt^2}\mathrm{Re}^2}{6{A_2}^2} + \frac{\mathrm{Re}\alpha(1-\phi)^{2.5}}{3A_2} - \frac{H\frac{d^2H}{dt^2}\mathrm{Re}^2\alpha(1-\phi)^{2.5}}{3{A_2}^2} - \frac{H^4\mathrm{Re}^2\phi_1}{4A_2} + \frac{H^5\mathrm{Re}^2\phi_1}{20A_2} - \frac{H^2\frac{d^2H}{dt^2}\mathrm{Re}^2\phi_1}{6A_2} + \frac{H^3\mathrm{Re}^2\alpha(1-\phi)^{2.5}\phi_1}{9A_2} - \frac{5H^4\mathrm{Re}^2\alpha(1-\phi)^{2.5}\phi_1}{12A_2};$$

$$m_4(t) = -\frac{\mathrm{Re}}{12A_2} - \frac{H^2\mathrm{Re}^2}{12{A_2}^2} + \frac{H^3\mathrm{Re}^2}{36{A_2}2^2} - \frac{H^2\mathrm{Re}^2\alpha(1-\phi)^{2.5}}{6{A_2}^2} + \frac{H^3\mathrm{Re}^2\alpha(1-\phi)^{2.5}}{36{A_2}^2} - \frac{H^2\mathrm{Re}^2\alpha^2(1-\phi)^5}{12{A_2}^2};$$

$$m_5(t) = \frac{H^2\mathrm{Re}^2}{30{A_2}^2} - \frac{H^3\mathrm{Re}^2}{90{A_2}^2} + \frac{H^2\mathrm{Re}^2\alpha(1-\phi)^{2.5}}{30{A_2}^2} + \frac{H^2\mathrm{Re}^2\phi_1}{30A_2} - \frac{H^3\mathrm{Re}^2\phi_1}{90A_2} + \frac{\frac{d^2H}{dt^2}\mathrm{Re}^2\phi_1}{60A_2} + \frac{H^2\mathrm{Re}^2\alpha(1-\phi)^{2.5}\phi_1}{30A_2};$$

$$m_6(t) = -\frac{\mathrm{Re}^2}{90{A_2}^2} - \frac{\mathrm{Re}^2\alpha(1-\phi)^{2.5}}{45{A_2}^2} - \frac{\mathrm{Re}^2\alpha^2(1-\phi)^5}{90{A_2}^2} - \frac{H\mathrm{Re}^2\phi_1}{180A_2} + \frac{H^2\mathrm{Re}^2\phi_1}{180A_2} - \frac{\mathrm{Re}^2\alpha(1-\phi)^{2.5}\phi_1}{180A_2} + \frac{H\mathrm{Re}^2\alpha(1-\phi)^{2.5}\phi_1}{180A_2};$$

$$m_7(t) = \frac{\mathrm{Re}^2}{252{A_2}^2} + \frac{\mathrm{Re}^2\alpha(1-\phi)^{2.5}}{252{A_2}^2} + \frac{\mathrm{Re}^2\phi_1}{1260A_2} - \frac{H\mathrm{Re}^2\phi_1}{630A_2} - \frac{\mathrm{Re}^2\alpha(1-\phi)^{2.5}\phi_1}{1260A_2};$$

$$m_8(t) = -\frac{\mathrm{Re}^2}{2016{A_2}^2} + \frac{\mathrm{Re}^2\phi_1}{10080A_2};$$

$$n_1(t) = 2H - \frac{2H^4\mathrm{Re}}{3A_2} + \frac{4H^5\mathrm{Re}}{15A_2} - \frac{H^2\frac{\mathrm{d}H}{dt}\mathrm{Re}}{A_2} + \frac{5H^7\mathrm{Re}^2}{18{A_2}^2} - \frac{97H^8\mathrm{Re}^2}{420{A_2}^2} + \frac{79H^9\mathrm{Re}^2}{1620{A_2}^2} + \frac{19H^5\frac{\mathrm{d}H}{dt}\mathrm{Re}^2}{10{A_2}^2} - \frac{44H^6\frac{\mathrm{d}H}{dt}\mathrm{Re}^2}{45{A_2}^2} + \frac{H^3\left(\frac{\mathrm{d}H}{dt}\right)^2\mathrm{Re}^2}{{A_2}^2} + \frac{5H^4\frac{d^2H}{dt^2}\mathrm{Re}^2}{12{A_2}^2} - \frac{2H^4\mathrm{Re}\alpha(1-\phi)^{2.5}}{3A_2} + \frac{5H^7\mathrm{Re}^2\alpha(1-\phi)^{2.5}}{9{A_2}^2} - \frac{97H^8\mathrm{Re}^2\alpha(1-\phi)^{2.5}}{420{A_2}^2} + \frac{19H^5\frac{\mathrm{d}H}{dt}\mathrm{Re}^2\alpha(1-\phi)^{2.5}}{10{A_2}^2} + \frac{5H^7\mathrm{Re}^2\alpha^2(1-\phi)^5}{18{A_2}^2} + \frac{137H^8\mathrm{Re}^2\phi_1}{360A_2} - \frac{1643H^9\mathrm{Re}^2\phi_1}{22680A_2} + \frac{47H^6\frac{\mathrm{d}H}{dt}\mathrm{Re}^2\phi_1}{180\mathrm{A_2}} - \frac{121H^7\mathrm{Re}^2\alpha(1-\phi)^{2.5}\phi_1}{630A_2} + \frac{239H^8\mathrm{Re}^2\alpha(1-\phi)^{2.5}\phi_1}{360A_2};$$

$$n_2(t) = -1;$$

$$n_3(t) = \frac{H^2\mathrm{Re}}{3A_2} - \frac{H^3\mathrm{Re}}{9A_2} + \frac{Re\frac{dH}{dt}}{3A_2} - \frac{2H^5\mathrm{Re}^2}{15A_2^2} + \frac{11H^6\mathrm{Re}^2}{108A_2^2} - \frac{5H^7\mathrm{Re}^2}{252A_2^2} - \frac{7H^3\frac{dH}{dt}\mathrm{Re}^2}{9A_2^2} + \frac{7H^4\frac{dH}{dt}\mathrm{Re}^2}{18A_2^2} - \frac{H\left(\frac{dH}{dt}\right)^2\mathrm{Re}^2}{3A_2^2} - \frac{H^2\frac{d^2H}{dt^2}\mathrm{Re}^2}{6A_2^2} + \frac{H^2\mathrm{Re}\alpha(1-\phi)^{2.5}}{3A_2} - \frac{4H^5\mathrm{Re}^2\alpha(1-\phi)^{2.5}}{15A_2^2} + \frac{11H^6\mathrm{Re}^2\alpha(1-\phi)^{2.5}}{108A_2^2} - \frac{7H^3\frac{dH}{dt}\mathrm{Re}^2\alpha(1-\phi)^{2.5}}{9A_2^2} - \frac{2H^5\mathrm{Re}^2\alpha^2(1-\phi)^5}{15A_2^2} - \frac{11H^6\mathrm{Re}^2\phi_1}{54A_2} + \frac{37H^7\mathrm{Re}^2\phi_1}{945A_2} - \frac{5H^4\frac{dH}{dt}\mathrm{Re}^2\phi_1}{36A_2} + \frac{H^5\mathrm{Re}^2\alpha(1-\phi)^{2.5}\phi_1}{10A_2} - \frac{19H^6\mathrm{Re}^2\alpha(1-\phi)^{2.5}\phi_1}{54A_2};$$

$$n_4(t) = -\frac{H\mathrm{Re}}{6A_2} + \frac{H^4\mathrm{Re}^2}{18A_2^2} - \frac{H^5\mathrm{Re}^2}{45A_2^2} + \frac{H^2\frac{dH}{dt}\mathrm{Re}^2}{12A_2^2} - \frac{H\mathrm{Re}\alpha(1-\phi)^{2.5}}{6A_2} + \frac{H^4\mathrm{Re}^2\alpha(1-\phi)^{2.5}}{9A_2^2} - \frac{H^5\mathrm{Re}^2\alpha(1-\phi)^{2.5}}{45A_2^2} + \frac{H^2\frac{dH}{dt}\mathrm{Re}^2\alpha(1-\phi)^{2.5}}{12A_2^2} + \frac{H^4\mathrm{Re}^2\alpha^2(1-\phi)^5}{18A_2^2} + \frac{H^5\mathrm{Re}^2\phi_1}{8A_2} - \frac{H^6\mathrm{Re}^2\phi_1}{40A_2} + \frac{H^3\frac{dH}{dt}\mathrm{Re}^2\phi_1}{12A_2} - \frac{H^4\mathrm{Re}^2\alpha(1-\phi)^{2.5}\phi_1}{18A_2} + \frac{5H^5\mathrm{Re}^2\alpha(1-\phi)^{2.5}\phi_1}{24A_2};$$

$$n_5(t) = \frac{\mathrm{Re}}{15A_2} + \frac{H\mathrm{Re}}{30A_2} - \frac{H^4\mathrm{Re}^2}{90A_2^2} + \frac{H^5\mathrm{Re}^2}{225A_2^2} + \frac{H\frac{dH}{dt}\mathrm{Re}^2}{15A_2^2} - \frac{H^2\frac{dH}{dt}\mathrm{Re}^2}{20A_2^2} + \frac{\mathrm{Re}^2\frac{d^2H}{dt^2}}{60A_2^2} + \frac{\mathrm{Re}\alpha(1-\phi)^{2.5}}{15A_2} - \frac{H^4\mathrm{Re}^2\alpha(1-\phi)^{2.5}}{90A_2^2} + \frac{H\frac{dH}{dt}\mathrm{Re}^2\alpha(1-\phi)^{2.5}}{15A_2^2} - \frac{H^4\mathrm{Re}^2\phi_1}{20A_2} + \frac{H^5\mathrm{Re}^2\phi_1}{100A_2} - \frac{H^2\frac{dH}{dt}\mathrm{Re}^2\phi_1}{30A_2} + \frac{H^3\mathrm{Re}^2\alpha(1-\phi)^{2.5}\phi_1}{45A_2} - \frac{H^4\mathrm{Re}^2\alpha(1-\phi)^{2.5}\phi_1}{12A_2};$$

$$n_6(t) = -\frac{\mathrm{Re}}{60A_2} - \frac{H^2\mathrm{Re}^2}{36A_2^2} + \frac{H^3\mathrm{Re}^2}{108A_2^2} - \frac{7\frac{dH}{dt}\mathrm{Re}^2}{180A_2^2} - \frac{H^2\mathrm{Re}^2\alpha(1-\phi)^{2.5}}{18A_2^2} + \frac{H^3\mathrm{Re}^2\alpha(1-\phi)^{2.5}}{108A_2^2} - \frac{7\frac{dH}{dt}\mathrm{Re}^2\alpha(1-\phi)^{2.5}}{180A_2^2} - \frac{H^2\mathrm{Re}^2\alpha^2(1-\phi)^5}{36A_2^2} - \frac{H^3\mathrm{Re}^2\phi_1}{90A_2} + \frac{H^4\mathrm{Re}^2\phi_1}{270A_2} - \frac{H\frac{dH}{dt}\mathrm{Re}^2\phi_1}{180A_2} - \frac{H^3\mathrm{Re}^2\alpha(1-\phi)^{2.5}\phi_1}{90A_2};$$

$$n_7(t) = \frac{H\mathrm{Re}^2}{63A_2^2} + \frac{2H^2\mathrm{Re}^2}{315A_2^2} - \frac{2H^3\mathrm{Re}^2}{945A_2^2} + \frac{11\mathrm{Re}^2\frac{dH}{dt}}{1260A_2^2} + \frac{2H\mathrm{Re}^2\alpha(1-\phi)^{2.5}}{63A_2^2} + \frac{2H^2\mathrm{Re}^2\alpha(1-\phi)^{2.5}}{315A_2^2} + \frac{H\mathrm{Re}^2\alpha^2(1-\phi)^5}{63A_2^2} + \frac{H^2\mathrm{Re}^2\phi_1}{126A_2} - \frac{H^3\mathrm{Re}^2\phi_1}{270A_2} + \frac{\frac{dH}{dt}\mathrm{Re}^2\phi_1}{315A_2} + \frac{H\mathrm{Re}^2\alpha(1-\phi)^{2.5}\phi_1}{630A_2} + \frac{H^2\mathrm{Re}^2\alpha(1-\phi)^{2.5}\phi_1}{210A_2};$$

$$n_8(t) = -\frac{\mathrm{Re}^2}{180A_2^2} - \frac{H\mathrm{Re}^2}{144A_2^2} - \frac{\mathrm{Re}^2\alpha(1-\phi)^{2.5}}{90A_2^2} - \frac{H\mathrm{Re}^2\alpha(1-\phi)^{2.5}}{144A_2^2} - \frac{\mathrm{Re}^2\alpha^2(1-\phi)^5}{180A_2^2} - \frac{H\mathrm{Re}^2\phi_1}{840A_2} + \frac{H^2\mathrm{Re}^2\phi_1}{720A_2} - \frac{\mathrm{Re}^2\alpha(1-\phi)^{2.5}\phi_1}{1008A_2} + \frac{H\mathrm{Re}^2\alpha(1-\phi)^{2.5}\phi_1}{840A_2};$$

$$n_9(t) = \frac{8\mathrm{Re}^2}{2835A_2^2} + \frac{H\mathrm{Re}^2}{1296A_2^2} + \frac{8\mathrm{Re}^2\alpha(1-\phi)^{2.5}}{2835A_2^2} + \frac{\mathrm{Re}^2\phi_1}{7560A_2} - \frac{13H\mathrm{Re}^2\phi_1}{45360A_2} - \frac{\mathrm{Re}^2\alpha(1-\phi)^{2.5}\phi_1}{7560A_2};$$

$$n_{10}(t) = -\frac{163\mathrm{Re}^2}{453600A_2^2} + \frac{\mathrm{Re}^2\phi_1}{64800A_2};$$

$$w_1(t) = 0;$$

$$w_2(t) = -1 - \alpha(1-\phi)^{2.5} + \frac{3H^4\mathrm{Re}\phi_1}{4} - \frac{3H^5\mathrm{Re}\phi_1}{20} + \frac{H^2\mathrm{Re}\phi_1\frac{dH}{dt}}{2} - \frac{131H^5\mathrm{Re}^2\phi_1\frac{dH}{dt}}{60} + \frac{53H^6\mathrm{Re}^2\phi_1\frac{dH}{dt}}{72} - \frac{H^3\mathrm{Re}^2\phi_1\left(\frac{dH}{dt}\right)^2}{2} - \frac{5H^4\frac{d^2H}{dt^2}\mathrm{Re}^2\phi_1}{24} - \frac{H^3\mathrm{Re}\alpha(1-\phi)^{2.5}\phi_1}{3} + \frac{5H^4\mathrm{Re}\alpha(1-\phi)^{2.5}\phi_1}{4} + \frac{H^4\mathrm{Re}^2\alpha(1-\phi)^{2.5}\phi_1\frac{dH}{dt}}{2} - \frac{63H^5\mathrm{Re}^2\alpha(1-\phi)^{2.5}\phi_1\frac{dH}{dt}}{20} - \frac{31H^7\mathrm{Re}^2\phi_1^2}{45} + \frac{293H^8\mathrm{Re}^2\phi_1^2}{2016} - \frac{12869H^9\mathrm{Re}^2\phi_1^2}{90720} + \frac{3751H^{10}\mathrm{Re}^2\phi_1^2}{151200} - \frac{67H^6\mathrm{Re}^2\phi_1^2\frac{dH}{dt}}{180} - \frac{8H^7\mathrm{Re}^2\phi_1^2\frac{dH}{dt}}{315} - \frac{1607H^7\mathrm{Re}^2\alpha(1-\phi)^{2.5}\phi_1^2}{1260} + \frac{131H^8\mathrm{Re}^2\alpha(1-\phi)^{2.5}\phi_1^2}{1120} - \frac{18679H^9\mathrm{Re}^2\alpha(1-\phi)^{2.5}\phi_1^2}{90720} - \frac{7H^5\mathrm{Re}^2\alpha(1-\phi)^{2.5}\phi_1^2\frac{dH}{dt}}{60} + \frac{7H^6\mathrm{Re}^2\alpha(1-\phi)^{2.5}\phi_1^2\frac{dH}{dt}}{72} + \frac{4H^6\mathrm{Re}^2\alpha^2(1-\phi)^5\phi_1^2}{45} - \frac{667H^7\mathrm{Re}^2\alpha^2(1-\phi)^5\phi_1^2}{630} + \frac{4303H^8\mathrm{Re}^2\alpha^2(1-\phi)^5\phi_1^2}{10080} - \frac{121H^{12}\mathrm{Re}^2\phi_1^3}{1296} + \frac{407H^{13}\mathrm{Re}^2\phi_1^3}{11340} - \frac{1369H^{14}\mathrm{Re}^2\phi_1^3}{396900} - \frac{55H^{10}\mathrm{Re}^2\phi_1^3\frac{dH}{dt}}{432} + \frac{37H^{11}\mathrm{Re}^2\phi_1^3\frac{dH}{dt}}{1512} - \frac{25H^8\left(\frac{dH}{dt}\right)^2\mathrm{Re}^2\phi_1^3}{576} + \frac{11H^{11}\mathrm{Re}^2\alpha(1-\phi)^{2.5}\phi_1^3}{120} - \frac{38573H^{12}\mathrm{Re}^2\alpha(1-\phi)^{2.5}\phi_1^3}{113400} + \frac{703H^{13}\mathrm{Re}^2\alpha(1-\phi)^{2.5}\phi_1^3}{11340} + \frac{H^9\mathrm{Re}^2\alpha(1-\phi)^{2.5}\phi_1^3\frac{dH}{dt}}{16} - \frac{95H^{10}\mathrm{Re}^2\alpha(1-\phi)^{2.5}\phi_1^3\frac{dH}{dt}}{432} - \frac{9H^{10}\mathrm{Re}^2\alpha^2(1-\phi)^5\phi_1^3}{400} + \frac{19H^{11}\mathrm{Re}^2\alpha^2(1-\phi)^5\phi_1^3}{120} - \frac{361H^{12}\mathrm{Re}^2\alpha^2(1-\phi)^5\phi_1^3}{1296};$$

$$w_3(t) = \tfrac{1}{3};$$

$$w_4(t) = -\frac{H^2\mathrm{Re}\phi_1}{6} + \frac{H^3\mathrm{Re}\phi_1}{18} - \frac{\mathrm{Re}\phi_1\frac{dH}{dt}}{12} + \frac{5H^3\frac{dH}{dt}\mathrm{Re}^2\phi_1}{12} - \frac{7H^4\frac{dH}{dt}\mathrm{Re}^2\phi_1}{48} + \frac{H\left(\frac{dH}{dt}\right)^2\mathrm{Re}^2\phi_1}{12} + \frac{H^2\frac{d^2H}{dt^2}\mathrm{Re}^2\phi_1}{24} - \frac{H^2\mathrm{Re}\alpha(1-\phi)^{2.5}\phi_1}{6} - \frac{H^2\frac{dH}{dt}\mathrm{Re}^2\alpha(1-\phi)^{2.5}\phi_1}{12} + \frac{7H^3\frac{dH}{dt}\mathrm{Re}^2\alpha(1-\phi)^{2.5}\phi_1}{12} + \frac{4H^5\mathrm{Re}^2\phi_1^2}{45} + \frac{H^6\mathrm{Re}^2\phi_1^2}{216} + \frac{4H^7\mathrm{Re}^2\phi_1^2}{315} - \frac{H^8\mathrm{Re}^2\phi_1^2}{320} + \frac{5H^4\frac{dH}{dt}\mathrm{Re}^2\phi_1^2}{72} + \frac{23H^5\mathrm{Re}^2\alpha(1-\phi)^{2.5}\phi_1^2}{180} + \frac{5H^6\mathrm{Re}^2\alpha(1-\phi)^{2.5}\phi_1^2}{108} + \frac{11H^7\mathrm{Re}^2\alpha(1-\phi)^{2.5}\phi_1^2}{540} + \frac{4H^5\mathrm{Re}^2\alpha^2(1-\phi)^5\phi_1^2}{45} - \frac{7H^6\mathrm{Re}^2\alpha^2(1-\phi)^5\phi_1^2}{216};$$

$$w_5(t) = \frac{H\mathrm{Re}\phi_1}{30} - \frac{H^2\mathrm{Re}\phi_1}{30} + \frac{\mathrm{Re}\alpha(1-\phi)^{2.5}\phi_1}{30} - \frac{H\mathrm{Re}\alpha(1-\phi)^{2.5}\phi_1}{30} + \frac{H^4\mathrm{Re}^2\phi_1^2}{30} + \frac{H^5\mathrm{Re}^2\phi_1^2}{360} - \frac{7H^6\mathrm{Re}^2\phi_1^2}{5400} + \frac{H^3\frac{\mathrm{d}H}{\mathrm{d}t}\mathrm{Re}^2\phi_1^2}{60} + \frac{29H^4\mathrm{Re}^2\alpha(1-\phi)^{2.5}\phi_1^2}{360} + \frac{13H^5\mathrm{Re}^2\alpha(1-\phi)^{2.5}\phi_1^2}{900} + \frac{H^2\frac{\mathrm{d}H}{\mathrm{d}t}\mathrm{Re}^2\alpha(1-\phi)^{2.5}\phi_1^2}{60} - \frac{H^3\mathrm{Re}^2\alpha^2(1-\phi)^5\phi_1^2}{90} + \frac{3H^4\mathrm{Re}^2\alpha^2(1-\phi)^5\phi_1^2}{40};$$

$$w_6(t) = -\frac{\mathrm{Re}\phi_1}{180} + \frac{H\mathrm{Re}\phi_1}{90} - \frac{H\frac{\mathrm{d}H}{\mathrm{d}t}\mathrm{Re}^2\phi_1}{45} + \frac{H^2\frac{\mathrm{d}H}{\mathrm{d}t}\mathrm{Re}^2\phi_1}{90} - \frac{\frac{\mathrm{d}^2H}{\mathrm{d}t^2}\mathrm{Re}^2\phi_1}{360} + \frac{\mathrm{Re}\alpha(1-\phi)^{2.5}\phi_1}{180} - \frac{H\frac{\mathrm{d}H}{\mathrm{d}t}\mathrm{Re}^2\alpha(1-\phi)^{2.5}\phi_1}{45} - \frac{H^4\mathrm{Re}^2\phi_1^2}{48} + \frac{H^5\mathrm{Re}^2\phi_1^2}{240} - \frac{H^2\frac{\mathrm{d}H}{\mathrm{d}t}\mathrm{Re}^2\phi_1^2}{72} + \frac{H^3\mathrm{Re}^2\alpha(1-\phi)^{2.5}\phi_1^2}{108} - \frac{17H^4\mathrm{Re}^2\alpha(1-\phi)^{2.5}\phi_1^2}{360} + \frac{H^5\mathrm{Re}^2\alpha(1-\phi)^{2.5}\phi_1^2}{400} - \frac{H^2\frac{\mathrm{d}H}{\mathrm{d}t}\mathrm{Re}^2\alpha(1-\phi)^{2.5}\phi_1^2}{120} + \frac{H^3\mathrm{Re}^2\alpha^2(1-\phi)^5\phi_1^2}{180} - \frac{H^4\mathrm{Re}^2\alpha^2(1-\phi)^5\phi_1^2}{48} + \frac{3H^8\mathrm{Re}^2\phi_1^3}{320} - \frac{3H^9\mathrm{Re}^2\phi_1^3}{800} + \frac{3H^{10}\mathrm{Re}^2\phi_1^3}{8000} + \frac{H^6\frac{\mathrm{d}H}{\mathrm{d}t}\mathrm{Re}^2\phi_1^3}{80} - \frac{H^7\frac{\mathrm{d}H}{\mathrm{d}t}\mathrm{Re}^2\phi_1^3}{400} + \frac{H^4\left(\frac{\mathrm{d}H}{\mathrm{d}t}\right)^2\mathrm{Re}^2\phi_1^3}{240} - \frac{H^7\mathrm{Re}^2\alpha(1-\phi)^{2.5}\phi_1^3}{120} + \frac{79H^8\mathrm{Re}^2\alpha(1-\phi)^{2.5}\phi_1^3}{2400} - \frac{H^9\mathrm{Re}^2\alpha(1-\phi)^{2.5}\phi_1^3}{160} - \frac{H^5\frac{\mathrm{d}H}{\mathrm{d}t}\mathrm{Re}^2\alpha(1-\phi)^{2.5}\phi_1^3}{180} + \frac{H^6\frac{\mathrm{d}H}{\mathrm{d}t}\mathrm{Re}^2\alpha(1-\phi)^{2.5}\phi_1^3}{48} + \frac{H^6\mathrm{Re}^2\alpha^2(1-\phi)^5\phi_1^3}{540} - \frac{H^7\mathrm{Re}^2\alpha^2(1-\phi)^5\phi_1^3}{72} + \frac{5H^8\mathrm{Re}^2\alpha^2(1-\phi)^5\phi_1^3}{192};$$

$$w_7(t) = -\frac{\mathrm{Re}\phi_1}{1260} + \frac{\mathrm{Re}^2\phi_1\frac{\mathrm{d}H}{\mathrm{d}t}}{1260} - \frac{H\mathrm{Re}^2\phi_1\frac{\mathrm{d}H}{\mathrm{d}t}}{630} - \frac{\mathrm{Re}^2\alpha(1-\phi)^{2.5}\phi_1\frac{\mathrm{d}H}{\mathrm{d}t}}{1260} - \frac{H^2\mathrm{Re}^2\phi_1^2}{105} - \frac{H^3\mathrm{Re}^2\phi_1^2}{630} + \frac{H^4\mathrm{Re}^2\phi_1^2}{252} - \frac{H^5\mathrm{Re}^2\phi_1^2}{2100} - \frac{H\frac{\mathrm{d}H}{\mathrm{d}t}\mathrm{Re}^2\phi_1^2}{420} + \frac{H^2\frac{\mathrm{d}H}{\mathrm{d}t}\mathrm{Re}^2\phi_1^2}{630} - \frac{H^2\mathrm{Re}^2\alpha(1-\phi)^{2.5}\phi_1^2}{42} - \frac{H^3\mathrm{Re}^2\alpha(1-\phi)^{2.5}\phi_1^2}{945} + \frac{H^4\mathrm{Re}^2\alpha(1-\phi)^{2.5}\phi_1^2}{252} - \frac{\frac{\mathrm{d}H}{\mathrm{d}t}\mathrm{Re}^2\alpha(1-\phi)^{2.5}\phi_1^2}{420} - \frac{H^2\mathrm{Re}^2\alpha^2(1-\phi)^5\phi_1^2}{70};$$

$$w_8(t) = \frac{\mathrm{Re}^2\phi_1\frac{\mathrm{d}H}{\mathrm{d}t}}{5040} + \frac{2H^2\mathrm{Re}^2\phi_1^2}{315} - \frac{H^3\mathrm{Re}^2\phi_1^2}{378} + \frac{17\frac{\mathrm{d}H}{\mathrm{d}t}\mathrm{Re}^2\phi_1^2}{10080} + \frac{H\mathrm{Re}^2\alpha(1-\phi)^{2.5}\phi_1^2}{630} + \frac{11H^2\mathrm{Re}^2\alpha(1-\phi)^{2.5}\phi_1^2}{1680} - \frac{13H^3\mathrm{Re}^2\alpha(1-\phi)^{2.5}\phi_1^2}{15120} + \frac{\frac{\mathrm{d}H}{\mathrm{d}t}\mathrm{Re}^2\alpha(1-\phi)^{2.5}\phi_1^2}{1008} + \frac{\mathrm{Re}^2\alpha^2(1-\phi)^5\phi_1^2}{1260} - \frac{H\mathrm{Re}^2\alpha^2(1-\phi)^5\phi_1^2}{1260} + \frac{13H^2\mathrm{Re}^2\alpha^2(1-\phi)^5\phi_1^2}{5040} - \frac{H^6\mathrm{Re}^2\phi_1^3}{448} + \frac{H^7\mathrm{Re}^2\phi_1^3}{840} - \frac{H^8\mathrm{Re}^2\phi_1^3}{6720} - \frac{H^4\frac{\mathrm{d}H}{\mathrm{d}t}\mathrm{Re}^2\phi_1^3}{384} + \frac{29H^5\frac{\mathrm{d}H}{\mathrm{d}t}\mathrm{Re}^2\phi_1^3}{40320} - \frac{H^2\left(\frac{\mathrm{d}H}{\mathrm{d}t}\right)^2\mathrm{Re}^2\phi_1^3}{1344} + \frac{H^5\mathrm{Re}^2\alpha(1-\phi)^{2.5}\phi_1^3}{1008} - \frac{19H^6\mathrm{Re}^2\alpha(1-\phi)^{2.5}\phi_1^3}{3024} + \frac{17H^7\mathrm{Re}^2\alpha(1-\phi)^{2.5}\phi_1^3}{10080} + \frac{H^3\frac{\mathrm{d}H}{\mathrm{d}t}\mathrm{Re}^2\alpha(1-\phi)^{2.5}\phi_1^3}{2016} - \frac{3H^4\frac{\mathrm{d}H}{\mathrm{d}t}\mathrm{Re}^2\alpha(1-\phi)^{2.5}\phi_1^3}{896} + \frac{H^5\mathrm{Re}^2\alpha^2(1-\phi)^5\phi_1^3}{1008} - \frac{5H^6\mathrm{Re}^2\alpha^2(1-\phi)^5\phi_1^3}{1344};$$

$$w_9(t) = \frac{\mathrm{Re}^2\phi_1^2}{1620} - \frac{31H\mathrm{Re}^2\phi_1^2}{45360} + \frac{H^2\mathrm{Re}^2\phi_1^2}{3780} + \frac{H^3\mathrm{Re}^2\phi_1^2}{5670} - \frac{\frac{\mathrm{d}H}{\mathrm{d}t}\mathrm{Re}^2\phi_1^2}{4536} + \frac{5\mathrm{Re}^2\alpha(1-\phi)^{2.5}\phi_1^2}{9072} + \frac{13H\mathrm{Re}^2\alpha(1-\phi)^{2.5}\phi_1^2}{22680} - \frac{H^2\mathrm{Re}^2\alpha(1-\phi)^{2.5}\phi_1^2}{5040} + \frac{\mathrm{Re}^2\alpha^2(1-\phi)^5\phi_1^2}{2520} + \frac{H\mathrm{Re}^2\alpha^2(1-\phi)^5\phi_1^2}{3024} + \frac{H^5\mathrm{Re}^2\phi_1^3}{2880} - \frac{H^6\mathrm{Re}^2\phi_1^3}{2400} + \frac{H^7\mathrm{Re}^2\phi_1^3}{14400} + \frac{H^3\frac{\mathrm{d}H}{\mathrm{d}t}\mathrm{Re}^2\phi_1^3}{4320} - \frac{H^4\frac{\mathrm{d}H}{\mathrm{d}t}\mathrm{Re}^2\phi_1^3}{4320} + \frac{H^4\mathrm{Re}^2\alpha(1-\phi)^{2.5}\phi_1^3}{5184} + \frac{41H^5\mathrm{Re}^2\alpha(1-\phi)^{2.5}\phi_1^3}{129600} - \frac{11H^6\mathrm{Re}^2\alpha(1-\phi)^{2.5}\phi_1^3}{21600} + \frac{H^2\frac{\mathrm{d}H}{\mathrm{d}t}\mathrm{Re}^2\alpha(1-\phi)^{2.5}\phi_1^3}{4320} - \frac{H^3\frac{\mathrm{d}H}{\mathrm{d}t}\mathrm{Re}^2\alpha(1-\phi)^{2.5}\phi_1^3}{4320} - \frac{H^3\mathrm{Re}^2\alpha^2(1-\phi)^5\phi_1^3}{6480} + \frac{19H^4\mathrm{Re}^2\alpha^2(1-\phi)^5\phi_1^3}{25920} - \frac{H^5\mathrm{Re}^2\alpha^2(1-\phi)^5\phi_1^3}{1728};$$

$$w_{10}(t) = -\frac{83\mathrm{Re}^2\phi_1^2}{453600} - \frac{H\mathrm{Re}^2\phi_1^2}{10080} - \frac{H^2\mathrm{Re}^2\phi_1^2}{12960} - \frac{127\mathrm{Re}^2\alpha(1-\phi)^{2.5}\phi_1^2}{453600} - \frac{11H\mathrm{Re}^2\alpha(1-\phi)^{2.5}\phi_1^2}{64800} - \frac{41\mathrm{Re}^2\alpha^2(1-\phi)^5\phi_1^2}{453600} + \frac{7H^4\mathrm{Re}^2\phi_1^3}{64800} - \frac{H^5\mathrm{Re}^2\phi_1^3}{972000} - \frac{H^6\mathrm{Re}^2\phi_1^3}{729000} + \frac{H^2\frac{\mathrm{d}H}{\mathrm{d}t}\mathrm{Re}^2\phi_1^3}{8100} + \frac{H^3\frac{\mathrm{d}H}{\mathrm{d}t}\mathrm{Re}^2\phi_1^3}{97200} + \frac{\left(\frac{\mathrm{d}H}{\mathrm{d}t}\right)^2\mathrm{Re}^2\phi_1^3}{25920} + \frac{H^3\mathrm{Re}^2\alpha(1-\phi)^{2.5}\phi_1^3}{48600} + \frac{23H^4\mathrm{Re}^2\alpha(1-\phi)^{2.5}\phi_1^3}{97200} + \frac{41H^5\mathrm{Re}^2\alpha(1-\phi)^{2.5}\phi_1^3}{972000} + \frac{H^2\frac{\mathrm{d}H}{\mathrm{d}t}\mathrm{Re}^2\alpha(1-\phi)^{2.5}\phi_1^3}{5400} - \frac{H^3\mathrm{Re}^2\alpha^2(1-\phi)^5\phi_1^3}{48600} + \frac{H^4\mathrm{Re}^2\alpha^2(1-\phi)^5\phi_1^3}{4320};$$

$$w_{11}(t) = \frac{41\mathrm{Re}^2\phi_1^2}{1247400} + \frac{H\mathrm{Re}^2\phi_1^2}{44550} + \frac{\mathrm{Re}^2\alpha(1-\phi)^{2.5}\phi_1^2}{32400} - \frac{H^3\mathrm{Re}^2\phi_1^3}{19800} + \frac{103H^4\mathrm{Re}^2\phi_1^3}{1663200} - \frac{131H^5\mathrm{Re}^2\phi_1^3}{8316000} - \frac{H\frac{\mathrm{d}H}{\mathrm{d}t}\mathrm{Re}^2\phi_1^3}{39600} + \frac{H^2\frac{\mathrm{d}H}{\mathrm{d}t}\mathrm{Re}^2\phi_1^3}{46200} - \frac{H^2\mathrm{Re}^2\alpha(1-\phi)^{2.5}\phi_1^3}{19800} + \frac{H^3\mathrm{Re}^2\alpha(1-\phi)^{2.5}\phi_1^3}{51975} + \frac{41H^4\mathrm{Re}^2\alpha(1-\phi)^{2.5}\phi_1^3}{1663200} - \frac{\frac{\mathrm{d}H}{\mathrm{d}t}\mathrm{Re}^2\alpha(1-\phi)^{2.5}\phi_1^3}{39600} + \frac{H\frac{\mathrm{d}H}{\mathrm{d}t}\mathrm{Re}^2\alpha(1-\phi)^{2.5}\phi_1^3}{39600} - \frac{H^2\mathrm{Re}^2\alpha^2(1-\phi)^5\phi_1^3}{19800} + \frac{H^3\mathrm{Re}^2\alpha^2(1-\phi)^5\phi_1^3}{19800};$$

$$w_{12}(t) = -\frac{\mathrm{Re}^2\phi_1^2}{388800} + \frac{H^2\mathrm{Re}^2\phi_1^3}{89100} - \frac{53H^3\mathrm{Re}^2\phi_1^3}{2138400} + \frac{19H^4\mathrm{Re}^2\phi_1^3}{2138400} + \frac{\frac{\mathrm{d}H}{\mathrm{d}t}\mathrm{Re}^2\phi_1^3}{285120} - \frac{H\frac{\mathrm{d}H}{\mathrm{d}t}\mathrm{Re}^2\phi_1^3}{142560} + \frac{H\mathrm{Re}^2\alpha(1-\phi)^{2.5}\phi_1^3}{118800} - \frac{H^2\mathrm{Re}^2\alpha(1-\phi)^{2.5}\phi_1^3}{59400} - \frac{7H^3\mathrm{Re}^2\alpha(1-\phi)^{2.5}\phi_1^3}{2138400} - \frac{\frac{\mathrm{d}H}{\mathrm{d}t}\mathrm{Re}^2\alpha(1-\phi)^{2.5}\phi_1^3}{285120} + \frac{\mathrm{Re}^2\alpha^2(1-\phi)^5\phi_1^3}{237600} - \frac{H\mathrm{Re}^2\alpha^2(1-\phi)^5\phi_1^3}{118800} - \frac{H^2\mathrm{Re}^2\alpha^2(1-\phi)^5\phi_1^3}{356400};$$

$$w_{13}(t) = -\frac{H\mathrm{Re}^2\phi_1^3}{842400} + \frac{H^2\mathrm{Re}^2\phi_1^3}{226800} - \frac{47H^3\mathrm{Re}^2\phi_1^3}{17690400} + \frac{\frac{\mathrm{d}H}{\mathrm{d}t}\mathrm{Re}^2\phi_1^3}{2358720} - \frac{\mathrm{Re}^2\alpha(1-\phi)^{2.5}\phi_1^3}{842400} + \frac{H\mathrm{Re}^2\alpha(1-\phi)^{2.5}\phi_1^3}{210600} - \frac{H^2\mathrm{Re}^2\alpha(1-\phi)^{2.5}\phi_1^3}{368550} + \frac{\mathrm{Re}^2\alpha^2(1-\phi)^5\phi_1^3}{842400} - \frac{H\mathrm{Re}^2\alpha^2(1-\phi)^5\phi_1^3}{842400};$$

$$w_{14}(t) = \frac{\mathrm{Re}^2\phi_1^3}{11793600} - \frac{H\mathrm{Re}^2\phi_1^3}{2063880} + \frac{H^2\mathrm{Re}^2\phi_1^3}{2063880} - \frac{\mathrm{Re}^2\alpha(1-\phi)^{2.5}\phi_1^3}{3175200} + \frac{H\mathrm{Re}^2\alpha(1-\phi)^{2.5}\phi_1^3}{2063880} + \frac{\mathrm{Re}^2\alpha^2(1-\phi)^5\phi_1^3}{11793600};$$

$$w_{15}(t) = \frac{\mathrm{Re}^2\phi_1^3}{47628000} - \frac{H\mathrm{Re}^2\phi_1^3}{23814000} - \frac{\mathrm{Re}^2\alpha(1-\phi)^{2.5}\phi_1^3}{47628000};$$

$w_{16}(t) = \frac{\mathrm{Re}^2\phi_1^3}{762048000}$;

Similarly, some constants have also been enlisted as

$A_1 = \frac{k_{nf}}{k_f}$;

$A_2 = \frac{A_1}{\mathrm{Pr}\phi_2}$;

$\phi_1 = \left(1.013 + 0.092\phi - 0.015\phi^2\right)\left[1 - \phi\left(1 + \frac{\rho_p}{\rho_f}\right)\right]$;

$\phi_2 = (1-\phi) - \phi\frac{\left(\rho C_p\right)_p}{\left(\rho C_p\right)_f}$.

References

1. Acrivos, A.; Shah, M.J.; Petersen, E.E. On the flow of a Non-Newtonian liquid on a rotating disk. *J. Appl. Phys.* **1960**, *31*, 963–968. [CrossRef]
2. Dandapat, B.S.; Maity, S.; Kitamura, A. Liquid film flow due to an unsteady stretching sheet. *Int. J. Non-Linear Mech.* **2008**, *43*, 880–886. [CrossRef]
3. Mcintryre, A.; Brush, L.N. Spin-coating of vertically stratified thin liquid films. *J. Fluid Mech.* **2010**, *647*, 265–285. [CrossRef]
4. Choi, S.U.S.; Eastman, J.A. Enhancing thermal conductivity of fluids with nanoparticles. *ASME Publ. Fed* **1995**, *231*, 99–106.
5. Buongiorno, J.; Hu, W. Nanofluid coolants for advanced nuclear power plants. In Proceedings of the ICAPP, Seoul, Korea, 15–19 May 2005; Volume 5, pp. 15–19.
6. Buongiorno, J. Convective transport in nanofluids. *J. Heat Transf.* **2006**, *128*, 240–250. [CrossRef]
7. Xu, H.; Fan, T.; Pop, I. Analysis of mixed convection flow of a nanofluid in a vertical channel with the Buongiorno mathematical model. *Int. Commun. Heat Mass Transf.* **2013**, *44*, 15–22. [CrossRef]
8. Sheikholeslami, M.; Bhatti, M.M. Active method for nanofluid heat transfer enhancement by means of EHD. *Int. J. Heat Mass Transf.* **2017**, *109*, 115–122. [CrossRef]
9. Hassan, M.; Zeeshan, A.; Majeed, A.; Ellahi, R. Particle shape effects on ferro fluid flow and heat transfer under influence of low oscillating magnetic field. *J. Magn. Magn. Mater.* **2017**, *443*, 36–44. [CrossRef]
10. Bhatti, M.M.; Abbas, T.; Rashidi, M.M.; Ali, M.E.; Yang, Z. Entropy generation on MHD Eyring-Powell nanofluid through a permeable stretching surface. *Entropy* **2016**, *18*, 224. [CrossRef]
11. Alamri, S.Z.; Ellahi, R.; Shehzad, N.; Zeeshan, A. Convective radiative plane Poiseuille flow of nanofluid through porous medium with slip: An application of Stefan blowing. *J. Mol. Liq.* **2019**, *273*, 292–304. [CrossRef]
12. Majeed, A.; Zeeshan, A.; Alamri, S.Z.; Ellahi, R. Heat transfer analysis in ferromagnetic viscoelastic fluid flow over a stretching sheet with suction. *Neural Comput. Appl.* **2018**, *30*, 1947–1955. [CrossRef]
13. Tripathi, D.; Bhushan, S.; Anwar Beg, O. Transverse magnetic field driven modification in unsteady peristaltic transport with electrical double layer effects. *Colloids Surf. A Physicochem. Eng. Asp.* **2016**, *506*, 32–39. [CrossRef]
14. Khan, W.G.; Idrees, T.; Islam, M.; Khan, S.; Dennis, L.C. Thin film Williamson nanofluid flow with varying viscosity and thermal conductivity on a time-dependent stretching sheet. *Appl. Sci.* **2016**, *6*, 334. [CrossRef]
15. Ellahi, R. Special issue on recent developments of nanofluids. *Appl. Sci.* **2018**, *8*, 192. [CrossRef]
16. Tripathi, D.; Beg, O.A. A numerical study of the oscillating peristaltic flow of generalized Maxwell viscoelastic fluids through a porous medium. *Trans. Porous Med.* **2012**, *95*, 337–348. [CrossRef]
17. Bhatti, M.M.; Rashidi, M.M. Effects of thermo-diffusion and thermal radiation on Williamson nanofluid over a porous shrinking/stretching sheet. *J. Mol. Liq.* **2016**, *221*, 567–573. [CrossRef]
18. Marin, M. An approach of a heat-flux dependent theory for micropolar porous media. *Meccanica* **2016**, *51*, 127–1133. [CrossRef]
19. Hameed, M.; Ellahi, R. Thin film flow of non-Newtonian MHD fluid on a vertically moving belt. *Int. J. Numer. Method Fluids* **2011**, *66*, 1409–1419. [CrossRef]
20. Abbasbandy, S.; Hayat, T.; Mahomed, F.M.; Ellahi, R. On comparison of exact and series solutions for thin film flow of a third grade fluid. *Int. J. Numer. Method Fluids* **2009**, *61*, 987–994. [CrossRef]

21. Hayat, T.; Ellahi, R.; Mahomed, F.M. Exact solutions for thin film flow of a third grade fluid down an inclined plane. *Chaos Solitons Fractals* **2008**, *38*, 1336–1341. [CrossRef]
22. Hayat, T.; Ellahi, R.; Mahomed, F.M. Exact solution of a thin film flow of an Oldroyd 6-constant fluid over a moving belt, Commun. *Nonlinear Sci. Numer. Simul.* **2009**, *14*, 133–139. [CrossRef]
23. Reyes, M.E.A.; Delgado, G.T.; Pérez, R.C.; Marín, J.M.; Ángel, O.Z. Optimization of the photocatalytic activity of CdO + $CdTiO_3$ coupled oxide thin films obtained by sol–gel technique. *J. Photochem. Photobiol. A Chem.* **2012**, *228*, 22–27. [CrossRef]
24. Xu, H.; Pop, I.; You, X.C. Flow and heat transfer in a nano-liquid film over an unsteady stretching surface. *Int. J. Heat Mass Transf.* **2013**, *60*, 646–652. [CrossRef]
25. Sheikholeslami, M.; Ashorynejad, H.R.; Ganji, D.D.; Yıldırım, A. Homotopy perturbation method for three-dimensional problem of condensation film on inclined rotating disk. *Sci. Iran.* **2012**, *19*, 437–442. [CrossRef]
26. Chen, X.; Dai, W.; Wu, T.; Luo, W.; Yang, J.; Jiang, W.; Wang, L. Thin film thermoelectric materials: Classification, characterization and potential for wearable applications. *Coatings* **2018**, *8*, 244. [CrossRef]
27. Osiac, M. The electrical and structural properties of nitrogen $Ge_1Sb_2Te_4$ thin film. *Coatings* **2018**, *8*, 117. [CrossRef]
28. Radwan, A.B.; Abdullah, A.M.; Mohamed, A.M.A.; Al-Maadeed, M.A. New electrospun polystyrene/Al_2O_3 nanocomposite superhydrophobic coatings; synthesis, characterization, and application. *Coatings* **2018**, *8*, 65. [CrossRef]
29. Yamamuro, H.; Hatsuta, N.; Wachi, M.; Takei, Y.; Takashiri, M. Combination of electrodeposition and transfer processes for flexible thin-film thermoelectric generators. *Coatings* **2018**, *8*, 22. [CrossRef]
30. Sheikholeslami, M.; Ellahi, R. Electrohydrodynamic nanofluid hydrothermal treatment in an enclosure with sinusoidal upper wall. *Appl. Sci.* **2015**, *5*, 294–306. [CrossRef]
31. Sheikholeslami, M.; Zia, Q.M.; Ellahi, R. Influence of induced magnetic field on free convection of nanofluid considering Koo-Kleinstreuer-Li (KKL) correlation. *Appl. Sci.* **2016**, *6*, 324. [CrossRef]
32. Rashidi, S.; Esfahani, J.A.; Ellahi, R. Convective heat transfer and particle motion in an obstructed duct with two side by side obstacles by means of DPM model. *Appl. Sci.* **2017**, *7*, 431. [CrossRef]
33. Zeeshan, A.; Ijaz, N.; Abbas, T.; Ellahi, R. The sustainable characteristic of Bio-bi-phase flow of peristaltic transport of MHD Jeffery fluid in human body. *Sustainability* **2018**, *10*, 2671. [CrossRef]
34. Hussain, F.; Ellahi, R.; Zeeshan, A. Mathematical models of electro magnetohydrodynamic multiphase flows synthesis with nanosized hafnium particles. *Appl. Sci.* **2018**, *8*, 275. [CrossRef]
35. Haq, R.U.; Soomro, F.A.; Hammouch, Z.; Rehman, S. Heat exchange within the partially heated C-shape cavity filled with the water based SWCNTs. *Int. J. Heat Mass Transf.* **2018**, *127*, 506–514. [CrossRef]
36. Usman, M.; Hamid, M.; Zubair, T.; Haq, R.U.; Wang, W. Cu-Al_2O_3/water hybrid nanofluid through a permeable surface in the presence of nonlinear radiation and variable thermal conductivity via LSM. *Int. J. Heat Mass Transf.* **2018**, *126*, 1347–1356. [CrossRef]
37. Haq, R.U.; Aman, S. Water functionalized CuO nanoparticles filled in a partially heated trapezoidal cavity with inner heated obstacle: FEM approach. *Int. J. Heat Mass Transf.* **2019**, *128*, 401–417. [CrossRef]
38. Khan, Z.; Shah, R.A.; Islam, S.; Jan, H.; Jan, B.; Rasheed, H. MHD flow and heat transfer analysis in the wirecoating process using elastic-viscous. *Coatings* **2017**, *7*, 15. [CrossRef]
39. Naghdi, S.; Rhee, K.Y.; Hui, D.; Paark, S.J. A review of conductive metal nanomaterials as conductive, Transparent, and flexible coatings, thin films, and conductive fillers: Different deposition methods and applications. *Coatings* **2018**, *8*, 278. [CrossRef]
40. Maity, S. Thermocapillary flow of thin *Cu*-water nanoliquids film during spin coating process. *Int. Nano Lett.* **2017**, *7*, 9–23. [CrossRef]
41. Khanafer, K.; Vafai, K. A critical synthesis of thermophysical characteristics of nanofluids. *Int. J. Heat Mass Transf.* **2011**, *54*, 4410–4428. [CrossRef]
42. Duangthongsuk, W.; Wongwises, S. Effect of thermophysical properties models on the predicting of the convective heat transfer coefficient for low concentration nanofluid. *Int. Commun. Heat Mass Trnasf.* **2008**, *35*, 1320–1326. [CrossRef]
43. Peyghambarzadeh, S.M.; Hashemabadi, S.H.; Hoseini, S.M.; Jamnani, M.S. Experimental study of heat transfer enhancement using water/ethylene glycol based nanofluids as a new coolant for car radiators. *Int. Commun. Heat Mass Transf.* **2011**, *38*, 1283–1290. [CrossRef]

44. Darvanjooghi, M.H.K.; Esfahany, M.N. Experimental investigation of the effect of nanoparticle size on thermal conductivity of in-situ prepared silica–ethanol nanofluid. *Int. Commun. Heat Mass Transf.* **2016**, *77*, 148–154. [CrossRef]
45. Pineda, I.T.; Lee, J.W.; Jung, I.; Kang, Y.T. CO_2 absorption enhancement by methanol-based Al_2O_3 and SiO_2 nanofluids in a tray column absorber. *Int. J. Refrig.* **2012**, *35*, 1402–1409. [CrossRef]
46. Zeeshan, A.; Ellahi, R.; Hassan, M. Magnetohydrodynamic flow of water/ethylene glycol based nanofluids with natural convection through a porous medium. *Eur. Phys. J. Plus* **2014**, *129*, 261. [CrossRef]
47. Kang, S.W.; Wei, W.C.; Tsai, S.H.; Yang, S.Y. Experimental investigation of silver nano-fluid on heat pipe thermal performance. *Appl. Therm. Eng.* **2006**, *26*, 2377–2382. [CrossRef]
48. Kumar, B.R.; Basheer, N.S.; Jacob, S.; Kurian, A.; George, S.D. Thermal-lens probing of the enhanced thermal diffusivity of gold nanofluid-ethylene glycol mixture. *J. Therm. Anal. Calorim.* **2015**, *119*, 453–460. [CrossRef]

coatings

MDPI

Article

Impact of Nonlinear Thermal Radiation and Entropy Optimization Coatings with Hybrid Nanoliquid Flow Past a Curved Stretched Surface

Dianchen Lu [1], Muhammad Ramzan [2,3,*], Shafiq Ahmad [4], Ahmad Shafee [5] and Muhammad Suleman [1]

1 Department of Mathematics, Faculty of Science, Jiangsu University, Zhenjiang 212013, China; dclu@ujs.edu.cn (D.L.); suleman@ujs.edu.cn (M.S.)
2 Department of Computer Science, Bahria University, Islamabad Campus, Islamabad 44000, Pakistan
3 Department of Mechanical Engineering, Sejong University, Seoul 143-747, Korea
4 Department of Mathematics, Quaid-i-Azam University, Islamabad 44000, Pakistan; ashafiq@math.qau.edu.pk
5 Department of Applied Science, College of Technological Studies, Public Authority of Applied Education and Training, Shuwaikh Campus, Shuwaikh 70654, Kuwait; as.zada@paaet.edu.kw
* Correspondence: mramzan@bahria.edu.pk; Tel.: +92-300-512-2700

Received: 19 September 2018; Accepted: 21 November 2018; Published: 27 November 2018

Abstract: The present investigation addresses the flow of hybrid (nickel–zinc ferrite and ethylene glycol) nanoliquid with entropy optimization and nonlinear thermal radiation coatings past a curved stretching surface. Analysis was carried out in the presence of magnetohydrodynamic, heat generation/absorption, and convective heat and mass flux conditions. Solution of the modeled problem was attained numerically using MATLAB built-in function bvp4c. Impacts of prominent parameters on betrothed distributions were depicted through graphs and were well supported by requisite discussions. Numerically calculated values of Sherwood number were established in a tabulated form and were scrutinized critically. An excellent concurrence was achieved when results of the presented model were compared with previously published result; hence, dependable results are being presented. It was observed that concentration field diminished with increasing values of curvature parameter, though the opposite trend was noticed for velocity and temperature distributions. Further, it was detected that Nusselt number decreased with augmented values of radiation and curvature parameters.

Keywords: coatings; curved stretched surface; nanoliquid; nonlinear thermal radiation; entropy generation

1. Introduction

Numerous applications of heat transfer liquids or coolants can be found in a variety of fields, such as automobiles, industry, electronics, and cooling processes. In all such industrial applications, cooling by liquids has been used for years. The process of cooling by fluids may be the single phase (where there is no phase change in the coolant) or two-phase (where coolant liquid will experience a phase change). In the latter, latent heat influences the cooling efficiency [1]. Several coolants, such as water, ethylene glycol, blend of water and glycol, propylene glycol and amalgamation of water, and propylene glycol, are used as coolants in automobiles and industrial cooling processes. In the last two decades, several researchers have devoted their efforts to increasing thermal conductivity of coolants, thereby improving heat transfer capabilities. The pioneering work of Choi et al. [2] introduced nanofluids by insertion of solid nanoparticles into liquids, thus enhancing the thermal properties of these liquids. This pioneering work has remarkably revolutionized modern engineering and the industrial world.

Nanofluids are an amalgamation of suspended solid material particles and customary liquids (ethylene glycol, water). This new type of advanced material possesses amazing capabilities that trigger the process of heat transfer and augments the thermal conductivity of the base fluid. Enhancement in the thermal conductivity and heat transfer is visualized once ferrite nanoparticles are added into the base liquid. Several examples featuring heat transfer can be quoted, including chemicals, cooling and heating system of buildings, and avionics cooling systems. Nanofluids exhibit potentially exceptional features in comparison to macrometer-sized particles. This is because nanoparticles have sufficiently larger surface area compared to micrometer-sized particles; this is the reason nanofluids possess incomparable capabilities of heat transfer [3].

In several electromagnetic applications with high permeability, e.g., electromagnetic wave absorbers and inductors, usage of nickel–zinc ferrite can be noticed. To minimize energy losses related to bulk powders, usage of nickel–zinc nanoparticles has been recommended by a number of researchers [4–6]. In addition, a majority of electronic gadgets require such materials to be compressed into outsized shapes with the required thickness, which is reasonably challenging if the size of these particles is large enough. Several methods have been proposed to get nickel–zinc ferrite, including ball milling, precipitation, and hydrothermal. Ferrofluids are colloidal fluids comprising ferromagnetic or ferrimagnetic nanoparticles suspended in an electrically insulated hauler fluid. In the current examination, ethylene glycol ($C_2H_6O_2$) was taken as a carrier fluid. The assumed ferrite nanoparticle was nickel–zinc ferrite ($NiZnFe_2O_4$) crystallize in the normal spinal structure. Typically, at room temperature, the inverted spinals are ferromagnetic and normal spinals are paramagnetic. Moreover, zinc ferrites act like antiferromagnetic in nature at low temperature. This feature makes ferromagnetic nanofluids more relevant in different real-world applications [7,8]. The ferrofluid's flow with the effect of thermal gradients and the magnetic field was discussed by Neuringer [9]. Majeed et al. [10] demonstrated the heat transfer investigation in a ferromagnetic fluid flow.

The subject of fluid flow past stretched surfaces has diverse engineering and industrial applications, including paper production, glass blowing, crystal growing, hot rolling, manufacturing of rubber sheets, annealing of copper wires, etc. The coined work of Crane [11] discussing the flow past a linearly stretching surface urged fellow researchers to discover more avenues in this exciting and interesting subject. This was followed by the remarkable work of Gupta and Gupta [12] who pondered on the flow past a spongy surface. Then, Chakrabarti and Gupta [13] examined the hydromagnetic flow past a stretched surface. Andersson et al. [14] considered the flow of power-law fluid past a surface, which was linearly stretched under the influence of magnetic forces. The flow of an Oldroyd-B fluid with the impact of generation/absorption was deliberated by Hayat et al. [15]. Muhammad et al. [16] discussed the effect of thermal stratification in the ferromagnetic fluid on a stretching sheet. Ramzan and Yousaf [17] demonstrated that the elastic viscous nanofluid finished a bi-directional stretching surface in view of Newtonian heating. Hussain et al. [18] utilized the exponentially stretching sheet to scrutinize the flow of Jeffrey nanofluid with radiation effects. Some recent explorations highlighting various fluid flows past stretched surfaces with coatings can be found in references [19–22].

In today's cutting-edge engineering technology, curved stretching has a broad relevance because of its different uses in industry, for example, in transportation and electronics. Sanni et al. [23] attained a numerical solution for the viscous fluid flow on a curved stretched channel. Sajid et al. [24] inspected the ferrofluid (Fe_3O_4) flow on a curved sheet with effects of Joule heating and magnetic forces. Rosca and Pop [25] studied time-dependent flow along a spongy curved surface. Imtiaz et al. [26] introduced the effect of homogeneous/heterogeneous reactions in ferrofluid embedded in a stretching surface. Naveed et al. [27] calculated heat transfer and used the micropolar fluid to analyze the effects over a curved surface with thermal radiation.

A literature review has specified that copious studies are available relating to nanofluids with linear/nonlinear/exponential stretching surfaces but comparatively less research work is available highlighting curved stretched surfaces. This gets even narrower when we talk about the study of hybrid nanoliquid with entropy optimization past curved surfaces. Therefore, our task here is to discuss

hybrid nanoliquid flow comprising ferromagnetic nanoparticle, i.e., nickel–zinc ferrite ($NiZnFe_2O_4$), and the base fluid, i.e., ethylene glycol ($C_2H_6O_2$), over a curved surface with entropy optimization coating. The whole analysis was performed with added impressions of nonlinear thermal radiation with entropy optimization coatings. The analysis was supported by the convective heat and mass flux boundary conditions. Numerical solution of the envisioned model was obtained by utilizing bvp4c from MATLAB. The traits of the sundry parameters on involved distributions were thoroughly discussed keeping their physical justification in mind.

2. Mathematical Formulation

We considered a 2D steady, incompressible nanoliquid flow over a curved stretching channel looped in the form of a circle with a radius R about the curvilinear directions r and x, as shown in Figure 1. Here, a higher value of R corresponds to a marginally curved surface. The stretching velocity is taken as $u = u_w$ along the x-direction. A magnetic field is applied normal to the fluid flow and along the r-direction. The electric and induced magnetic fields were overlooked owing to our assumption of small Reynolds number.

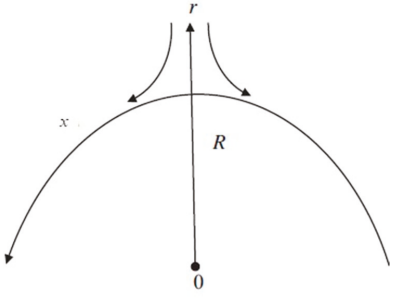

Figure 1. Flow geometry.

The assumed system is governed by the following equations:

$$\frac{\partial}{\partial r}\{(R+r)v\} + R\frac{\partial u}{\partial x} = 0 \tag{1}$$

$$\frac{u^2}{r+R} = \frac{1}{\rho_{nf}}\frac{\partial p}{\partial r} \tag{2}$$

$$v\frac{\partial u}{\partial r} + \frac{Ru}{r+R}\frac{\partial u}{\partial x} + \frac{uv}{r+R} = -\frac{1}{\rho_{nf}}\frac{R}{r+R}\frac{\partial p}{\partial x} + \frac{\mu_{nf}}{\rho_{nf}}\left(\frac{\partial^2 u}{\partial r^2} + \frac{1}{r+R}\frac{\partial u}{\partial r} - \frac{u}{(r+R)^2}\right) - \frac{\sigma}{\rho_{nf}}{B_0}^2 u \tag{3}$$

$$v\frac{\partial T}{\partial r} + \frac{Ru}{r+R}\frac{\partial T}{\partial x} = \alpha_{nf}\left(\frac{\partial^2 T}{\partial r^2} + \frac{1}{r+R}\frac{\partial T}{\partial r}\right) + \frac{Q_0}{(\rho C_p)_{nf}}(T_\infty - T) + \frac{1}{(\rho C_p)_{nf}}\frac{1}{r+R}\frac{\partial}{\partial r}(r+R)q_r \tag{4}$$

$$v\frac{\partial C}{\partial r} + \frac{Ru}{r+R}\frac{\partial C}{\partial x} = D_B\left(\frac{\partial^2 C}{\partial r^2} + \frac{1}{r+R}\frac{\partial C}{\partial r}\right) \tag{5}$$

The system of Equations (1)–(5) is supported by the following boundary conditions:

$$\begin{gathered} v|_{r=0} = 0,\ u|_{r=0} = u_w(x) = sx,\ k_f\frac{\partial T}{\partial r}\Big|_{y=0} = h^*(T_f - T),\ -D_B\frac{\partial C}{\partial r}\Big|_{r=0} = j_w \\ u|_{r\to\infty} \to 0,\ \frac{\partial u}{\partial r}\Big|_{r\to\infty} \to 0,\ T|_{r\to\infty} \to T_\infty,\ C|_{r\to\infty} \to C_\infty \end{gathered} \tag{6}$$

The thermophysical traits of the hybrid nanoliquid are appended in Table 1.

Table 1. The values of C_p, ρ, and k for ethylene glycol and $NiZnFe_2O_4$ (nickel–zinc ferrite) [28–33].

Thermo-Physical Characteristics of the Ethylene Glycol and Nickel–Zinc Ferrite	C_p (J/kg K)	ρ (kg/m^3)	k (W/mK)	Pr
ethylene glycol($C_2H_6O_2$)	2382.0	1116.6	0.2490	204.0
nickel–zinc ferrite($NiZnFe_2O_4$)	710.0	4800.0	6.3	–

The mathematical form of thermophysical properties are given as follows:

$$\mu_{nf} = \frac{\mu_f}{(1-\phi)^{2.5}},\ \alpha_{nf} = \frac{k_{nf}}{(\rho C_p)_{nf}} \tag{7}$$

$$\rho_{nf} = (1-\phi)\rho_f + \phi\rho_s,\ (\rho C_p)_{nf} = (1-\phi)(\rho C_p)_f + \phi(\rho C_p)_s \tag{8}$$

$$\frac{k_{nf}}{k_f} = \frac{(k_s+2k_f) - 2\phi(k_f-k_s)}{(k_s+2k_f) + \phi(k_f-k_s)} \tag{9}$$

In Equation (4), the nonlinear radiation heat flux term via Rosseland's approximation is given as follows:

$$q_r = \frac{4\sigma^*}{3k^*}\frac{\partial T^4}{\partial r} = \frac{16\sigma^* T^3}{3k^*}\frac{\partial T}{\partial r} \tag{10}$$

3. Solution Procedure

Here, we used the following dimensionless transformations:

$$\begin{gathered}\zeta = \sqrt{\frac{s}{\nu_f}}r,\ p = \rho_f s^2 x^2 P(\zeta),\ T = T_\infty(1+(\theta_w-1)\theta),\\ C = C_\infty + \frac{j_w}{D_B}\sqrt{\frac{\nu_f}{s}}h(\zeta),\ u = sxf'(\zeta),\ v = -\frac{R}{r+R}\sqrt{s\nu_f}f(\zeta)\end{gathered} \tag{11}$$

Here, prime denotes the derivative w, r, T, ζ and $\theta_w = T_f/T_\infty$. The above transformation Equation (11) satisfies Equation (1) identically and Equations (2)–(6) are given by the following:

$$P' = \left(1-\phi+\phi\frac{\rho_s}{\rho_f}\right)\frac{f'^2}{\zeta+K_1} \tag{12}$$

$$\begin{gathered}\frac{1}{\left(1-\phi+\phi\frac{\rho_s}{\rho_f}\right)}\frac{2K_1}{\zeta+K_1}P = \frac{1}{(1-\phi)^{25/10}\left(1-\phi+\phi\frac{\rho_s}{\rho_f}\right)}\left(f''' - \frac{f'}{(K_1+\zeta)^2} + \frac{f''}{\zeta+K_1}\right) - \frac{K_1}{\zeta+K_1}f'^2\\ + \frac{K_1}{K_1+\zeta}ff'' + \frac{K_1}{(K_1+\zeta)^2}f'f - Mf'\end{gathered} \tag{13}$$

$$\begin{gathered}\frac{1}{\Pr}\left(\frac{k_{nf}}{k_f} + R_d(1+(\theta_w-1)\theta)^3\right)\left(\theta'' + \frac{1}{\zeta+K_1}\theta'\right) + \left(1-\phi+\phi\frac{(\rho C_p)_s}{(\rho C_p)_f}\right)\left(\frac{K_1}{\zeta+K_1}f\theta'\right)\\ \lambda_1\theta + 3R_d(1+(\theta_w-1)\theta)^2\theta' = 0\end{gathered} \tag{14}$$

$$h'' + \frac{1}{\zeta+K_1}h' + S_c\left(\frac{K_1}{\zeta+K_1}\right)fh' = 0 \tag{15}$$

and

$$\begin{gathered}f(\zeta) = 0,\ f'(\zeta) = 1,\ \theta'(\zeta) = (1-\theta(\zeta))\mathrm{Bi},\ h'(\zeta) = -1,\ \text{as } \zeta = 0\\ f'(\zeta)\to 0,\ f''(\zeta)\to 0,\ \theta(\zeta)\to 0,\ h(\zeta)\to 0,\ \text{as } \zeta\to\infty\end{gathered} \tag{16}$$

Here, $K_1 = R\sqrt{\frac{s}{\nu_f}}$, $\mathrm{Bi} = \frac{h^*\sqrt{\frac{\nu_f}{s}}}{k_f}$, $S_c = \frac{\nu_f}{D_B}$, $R_d = \frac{16\sigma^* T_\infty{}^3}{3kk^*}$, $\lambda_1 = \frac{Q_0}{s(\rho C_p)_f}$, and $\Pr = \frac{\nu_f}{\alpha_f}$.

Eliminating pressure term from Equations (12) and (13) by differentiating Equation (13) with respect to ζ and then putting in Equation (12), we get the following:

$$f^{iv} + \frac{2f'''}{\zeta+K_1} - \frac{f''}{(\zeta+K_1)^2} + \frac{f'}{(\zeta+K_1)^3} + (1-\phi)^{25/10}\left(1-\phi+\phi\frac{\rho_s}{\rho_f}\right)\{\frac{K_1}{(\zeta+K_1)^2}(f'^2 - ff'') - \frac{K_1}{\zeta+K_1}(f'f'' - ff''') - \frac{K_1}{(\zeta+K_1)^3}ff'\} - (1-\phi)^{25/10}M(\frac{f'}{\zeta+K_1} + f'') = 0 \tag{17}$$

with

$$f(0) = 0,\ f'(0) = 1,\ f'(\infty) \to 0,\ f''(\infty) \to 0 \tag{18}$$

The surface drag force (C_f), Sherwood number (Sh_x), and Nu_x (Nusselt number) along x-direction are defined as follows:

$$C_f = \frac{\tau_{rx}}{\frac{1}{2}\rho u_w^2},\ \mathrm{Nu}_x = \frac{xq_w}{k_f(T_f - T_\infty)},\ \mathrm{Sh}_x = -\frac{x}{(C-C_\infty)}\frac{\partial C}{\partial r} \tag{19}$$

where

$$\tau_{rx} = \mu_{nf}(\frac{\partial u}{\partial r} - \frac{u}{r+R})_{r=0}, q_w = (q_r)_w - (\frac{\partial T}{\partial r})_{r=0} \tag{20}$$

After putting Equations (11) and (20), Equation (19) becomes the following:

$$\frac{1}{2}C_f(\mathrm{Re}_x)^{\frac{1}{2}} = f''(0) - \frac{f'(0)}{K_1},\ \mathrm{Nu}_x(\mathrm{Re}_x)^{-\frac{1}{2}} = -\left[\frac{k_{nf}}{k_f} + R_d(1+(\theta_w-1)\theta(0))^3\right]\theta'(0),\ \mathrm{Sh}_x(\mathrm{Re}_x)^{-\frac{1}{2}} = \frac{1}{h(0)} \tag{21}$$

Here, $\mathrm{Re}_x = \frac{sx^2}{v_f}$.

4. Entropy Generation

The equation of entropy generation in dimensional form is given in reference [34].

$$E_{gen}''' = \frac{k_{nf}}{T_f^2}\left[\left(\frac{\partial T}{\partial r}\right)^2 + \frac{16\sigma^* T^3}{3k_{nf}k^*}\left(\frac{\partial T}{\partial y}\right)^2\right] + \frac{\mu_{nf}}{T_f}\left(\frac{\partial u}{\partial r}\right)^2 + \frac{\sigma B_0^2}{T_f}u^2 + \frac{RD}{C_\infty}\left(\frac{\partial C}{\partial r}\right)^2 + \frac{RD}{T_f}\left(\frac{\partial C}{\partial r}\right)\left(\frac{\partial T}{\partial r}\right) \tag{22}$$

Equation (22) after applying the requisite transformations takes the following form:

$$N_G = \frac{E_{gen}'''}{E_0'''} = \mathrm{Re}_x\left[\frac{k_{nf}}{k_f} + R_d(1+\Pi\theta)^3\right]\theta'^2 + \frac{\mathrm{BrRe}_x}{\Pi^2}(f'')^2 + \frac{\mathrm{BrRe}_x}{\Pi^2}Mf'^2 + \frac{\mathrm{Re}_x\sum}{\Pi}\left(h'^2 + \frac{\theta' h'}{\Pi}\right) \tag{23}$$

where

$$\mathrm{Br} = \frac{\mu_{nf}u_w^2}{k_{nf}T_f},\ \mathrm{Re}_x = \frac{x^2 s}{\nu_f},\ \sum = \frac{C_\infty RD}{k_{nf}},\ \Pi = \theta_w - 1 \tag{24}$$

5. Results and Discussion

The MATLAB built-in function bvp4c was applied to integrate the numerical solution for the system of Equations (14), (15), and (17) with initial and boundary conditions, Equations (16) and (18), for numerous values of K_1, M, R_d, λ_1, and $\mathrm{S_c}$ graphically. For this technique, we first changed differential equations with the higher order to the equations of order one by utilizing new variables. The function bvp4c needs an initial guess for the solution and with the tolerance of 10^{-7}. The guess we chose needed to satisfy the boundary conditions (Equations (16) and (18)) and the solution. The validation of our presented results is depicted in Table 2. An excellent agreement with Sanni et al. [23] was observed when M = 1, φ = 0.0, and in the absence of temperature and concentration profile.

Table 2. Comparison of presented results for skin friction coefficient $\frac{1}{2}C_f(\mathrm{Re}_x)^{\frac{1}{2}}$ when $M = 1$ and $\varphi = 0.0$.

K_1	Sanni et al. [23]	Present Result
5	1.1576	1.15760
10	1.0734	1.07341
20	1.0355	1.03540
50	1.0140	1.01400
100	1.0070	1.00690
1000	1.0008	1.00079

Figures 2 and 3 show the impression of solid volume fraction φ on velocity and temperature profiles. Both velocity fields increased with increasing values of solid volume fraction φ. Further, the momentum and thickness of the thermal boundary layers were boosted with a larger value of φ. The values given to other parameters were $Pr = 10$, $S_c = 0.5$, $K_1 = 10$, $R_d = 0.5$, $\theta_w = 0.5$, $\lambda_1 = 0.5$, and $M = 0.1$.

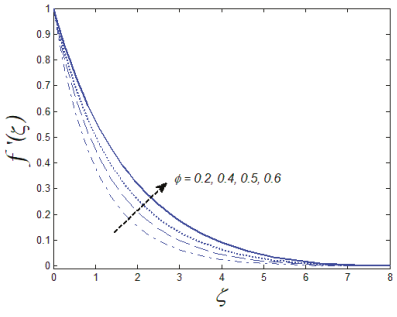

Figure 2. Upshot of φ on velocity distribution $f'(\zeta)$.

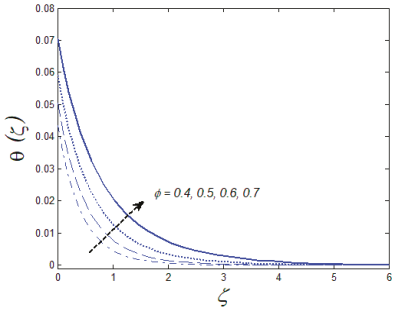

Figure 3. Upshot of φ on temperature field $\theta(\zeta)$.

The impact of the curvature parameter K_1 on velocity, concentration, and temperature profiles are depicted in Figures 4–6. Increasing values of K_1 resulted in an increase in fluid velocity and temperature field, while the concentration profile diminished. This was because of the radius of the surface augment when curvature parameter K_1 was increased. As a result, the flow increased but it offered more resistance, therefore the temperature rose. The values of other parameters were fixed as $Pr = 10$, $S_c = 0.5$, $\varphi = 0.1$, $R_d = 0.5$, $\theta_w = 0.5$, $\lambda_1 = 0.5$ and $M = 0.1$.

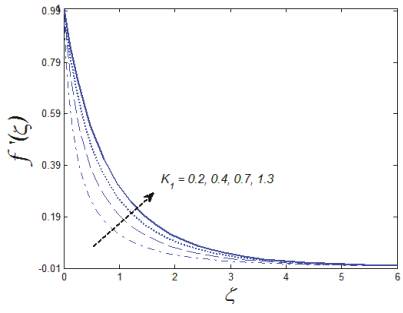

Figure 4. Upshot of K_1 on velocity profile $f'(\zeta)$.

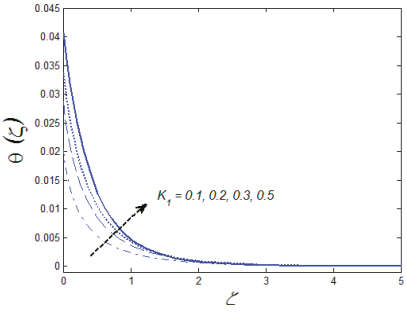

Figure 5. Upshot of K_1 on temperature profile $\theta(\zeta)$.

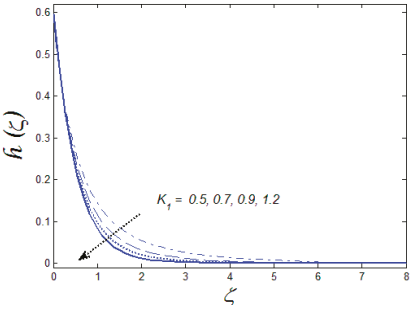

Figure 6. Upshot of K_1 on concentration field $h(\zeta)$.

Figure 7 demonstrates the variation in the velocity field for numerous estimates of magnetic parameter M. Here, increments in M led to a decline in the magnitude of fluid's velocity. This was because of the resistive force (called Lorentz force) triggered by the magnetic field, which lowered the velocity of the fluid's velocity flow. The values of the other parameters were fixed as $K_1 = 10$, $S_c = 0.5$, $\varphi = 0.1$, $R_d = 0.5$, $\theta_w = 0.5$, $\lambda_1 = 0.5$, and Bi = 0.1.

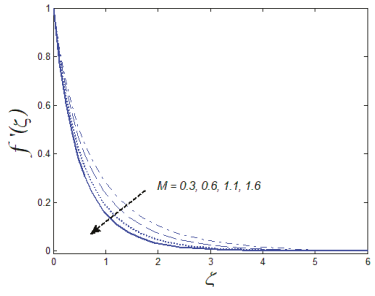

Figure 7. Upshot of M on velocity profile $f'(\zeta)$.

The characteristics of Biot number Bi and heat generation/absorption parameter λ_1 on temperature field are displayed in Figures 8 and 9, respectively. Figure 8 shows that the convective heat transfer coefficient intensified for higher estimates of Bi and the temperature subsequently rose. Figure 9 illustrates the behavior of λ_1. To increase the estimation values of heat absorption/generation parameter, the temperature profile and thermal boundary layer thickness were increased. The values of other parameters were fixed as $K_1 = 10$, $M = 0.3$, $\varphi = 0.5$, $R_d = 0.1$, $\theta_w = 0.5$, and $Pr = 10$.

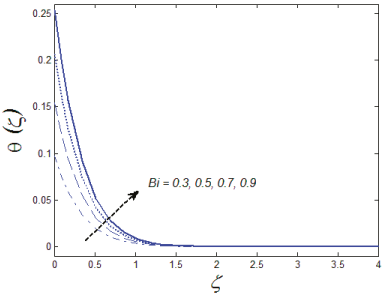

Figure 8. Upshot of Bi on temperature field $\theta(\zeta)$.

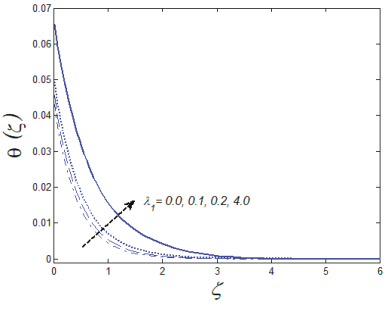

Figure 9. Upshot of λ_1 on temperature distribution $\theta(\zeta)$.

Figures 10 and 11 show the impacts of nonlinear radiation parameter R_d and Prandtl number Pr on temperature distribution, respectively. It can be seen that the temperature field fell with increasing Prandtl number Pr. As Prandtl number is linked in a reciprocal way to the thermal diffusivity, a quick augmentation in the Prandtl number Pr lessened the temperature and thickness of the thermal boundary layer. The temperature profile increased with increment in nonlinear radiation parameter R_d. Physically, the radiative heat flux increased with increasing values of R_d which ultimately boosted

the temperature of the fluid. The values assigned to other parameters were $K_1 = 10$, $M = 0.3$, $\varphi = 0.5$, Bi = 0.1, $\theta_w = 0.5$, and $S_c = 5$.

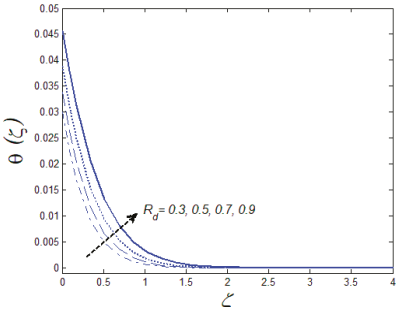

Figure 10. Upshot of R_d on temperature field θ**(ζ)**.

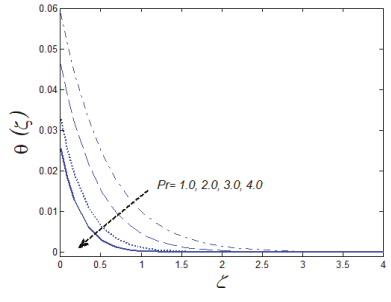

Figure 11. Upshot of Pr on temperature field θ**(ζ)**.

The impression of Schmidt number S_c on concentration distribution is portrayed in Figure 12. A decrease in concentration field was detected with increasing values of S_c. As the Schmidt number has a converse proportion with the Brownian diffusion coefficient, an increment in the S_c yielded a decay in Brownian diffusion coefficient that brought about a diminishment in concentration and its interrelated boundary layer thickness. The values allocated to other parameters were $K_1 = 10$, $M = 0.3$, $\varphi = 0.1$, Bi = 0.1, $\theta_w = 0.5$, and $R_d = 0.1$.

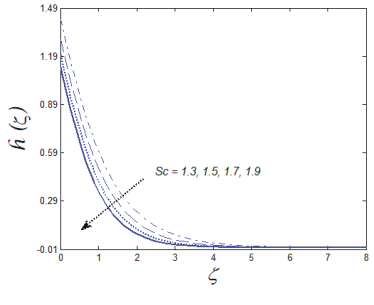

Figure 12. Upshot of S_c on concentration profile h**(ζ)**.

The influence of curvature parameter K_1 and magnetic parameter M on skin friction coefficient $-\frac{1}{2}C_f \mathrm{Re}_x^{1/2}$ is depicted in Figure 13. It can be noticed that the surface drag force diminished with increasing value of K_1. A contradictory trend was demonstrated in case of M. In Figure 14,

the consequence of magnetic parameter M and solid volume fraction φ on shear wall stress is demonstrated. The skin friction profile rose with increase in magnetic parameter M and solid volume fraction φ for fixed values of parameters Pr = 10, S_c = 0.5, R_d = 0.5, θ_w = 0.5, λ_1 = 0.5 and Bi = 0.1.

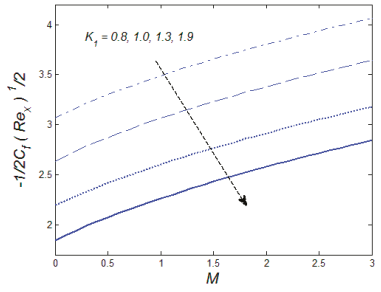

Figure 13. Upshot of K_1 and M on wall shear stress $-\frac{1}{2}C_f \mathrm{Re}_x^{1/2}$.

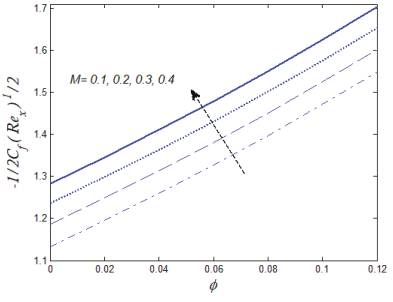

Figure 14. Upshot of M and φ on wall shear stress $-\frac{1}{2}C_f \mathrm{Re}_x^{1/2}$.

Figure 15 shows the effect of Biot number Bi and solid volume fraction φ on Nusselt number $\mathrm{Nu}_x(\mathrm{Re}_x)^{-\frac{1}{2}}$. It was detected that for higher value of Bi and φ, the surface heat transfer rate upsurged when values of parameters were given as K_1 = 10, M = 0.3, S_c = 5.0, R_d = 0.1, θ_w = 0.5, λ_1 = 0.5 and Pr = 10.

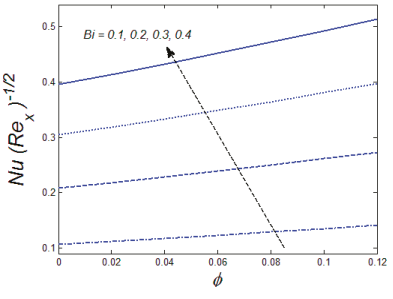

Figure 15. Upshot of Bi and on φ Nusselt number $\mathrm{NuRe}_x^{-1/2}$.

The outcome of curvature parameter K_1 and nonlinear radiation parameter R_d on Nusselt number $\mathrm{Nu}_x(\mathrm{Re}_x)^{-\frac{1}{2}}$ is examined in Figure 16. Here, a reduction in Nusselt number was noted for increasing values of curvature parameter K_1 and the opposite trend was seen for nonlinear radiation parameter R_d for fixed values of φ = 0.1, M = 0.3, S_c = 5.0, θ_w = 0.5, λ_1 = 0.5 and Pr = 10.

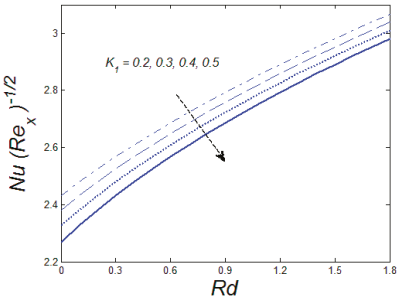

Figure 16. Upshot of K_1 and R_d on Nusselt number $\mathrm{NuRe}_x^{-1/2}$.

The impact of the Brinkman number (Br) on entropy generation is portrayed in Figure 17. From the illustration, it can be seen that entropy optimization was boosted with increasing values of (Br). The reason behind this was that more heat was generated between the layers of the fluid because of augmented values of (Br). Figure 18 displays the relationship between the magnetic parameter (M) and the entropy generation. Again, the same trait as depicted in case of (Br) was witnessed here. Higher values of (M) meant stronger Lorentz force and ultimate strengthening of the dissipation energy, and this was the main cause of irreversibility.

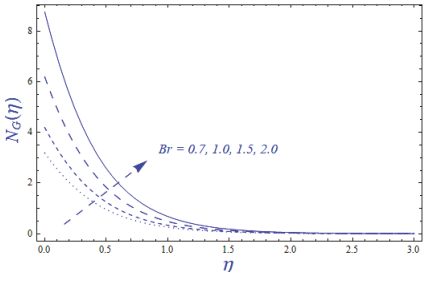

Figure 17. Upshot of Br on N_G (η).

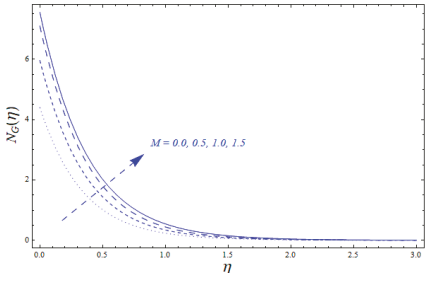

Figure 18. Upshot of M on N_G (η).

Table 3 shows the behavior of Sherwood number $\mathrm{Sh}_x(\mathrm{Re}_x)^{-\frac{1}{2}}$ for varied values of $\mathrm{S_c}$ (Schmidt number), K_1 (curvature parameter), and M (magnetic parameter). It can be seen that for snowballing values of $\mathrm{S_c}$, the Sherwood number $\mathrm{Sh}_x(\mathrm{Re}_x)^{-\frac{1}{2}}$ increased; however, it diminished for increasing value of K_1 and M.

Table 3. Numerical value of Sherwood number $\mathrm{Sh}_x(\mathrm{Re}_x)^{-\frac{1}{2}}$ for various value of parameter with fixed value of $Pr = 10$, $R_d = 0.1$, $\varphi = 0.1$, Bi = 0.1, $\theta_w = 0.5$, $\lambda_1 = 0.5\, f'(\zeta)$.

$\mathbf{S_c}$	K_1	M	$\mathbf{Sh}_x(\mathbf{Re}_x)^{-\frac{1}{2}}$
0.5	10	0.1	0.38325
1.0	–	–	0.59354
2.0	–	–	0.92268
5	5	0.1	1.60150
–	10	–	1.58090
–	50	–	1.56230
5	10	0.3	1.56270
–	–	0.5	1.54600
–	–	0.7	1.53040

6. Concluding Remarks

In this paper, the flow of nanoliquid comprising nickel–zinc ferrite–ethylene glycol ($NiZnFe_2O_4$–$C_2H_6O_2$) accompanied by entropy optimization coating past a curved stretching surface with convective heat and mass flux boundary was examined. The solution of the envisioned system of equations was found numerically by applying MATLAB built-in function bvp4c. The impact of numerous arising parameters on involved profiles was depicted via graphical illustrations with requisite discussions.

The conclusions of the current study are as follows:

- An increase in curvature parameter accounted for increasing velocity and temperature fields and diminishing concentration distribution.
- Under the considerable influence of magnetic parameter, an increased axial velocity field was attained.
- For the increasing estimates of the solid volume fraction, the temperature and velocity profiles showed increasing behavior.
- The temperature profile improved with increasing values of Biot number and heat generation/absorption parameter.
- The value of friction factor profile augmented for larger values of M and φ, but it decreased for K_1 and M.
- The Nusselt number $\mathrm{NuRe}_x^{-1/2}$ declined with increasing values of K_1 and R_d.

Author Contributions: Formal Analysis, M.R.; Funding Acquisition, D.L.; Investigation, M.R.; Methodology, D.L.; Project Administration, M.R.; Software, S.A.; Validation, M.S.; Writing—Original Draft, A.S.; Writing—Review and Editing, M.S.

Funding: This research was funded by National Natural Science Foundation China (No. 11571140 and 11671077), Faculty of Science, Jiangsu University, Zhenjiang, China.

Acknowledgments: The authors are highly thankful for exceptional support raised by the Jiangsu University, China and Bahria University, Islamabad, Pakistan.

Conflicts of Interest: Authors have no conflict of interest regarding this publication.

Nomenclature

u, v	velocity components
r, x	coordinate
R	radius of circle
P	pressure
B_0	strength of magnetic field
Q_0	volumetric rate of heat generation/absorption

q_r	nonlinear radiative heat flux
T, T_∞	temperature
C, C_w, C_∞	concentration
D_B	Brownian diffusion coefficient
T_f	convective temperature at the sheet
j_w	mass flux
u_w	stretching velocity along x-direction
k^*	mean absorption coefficient
K_1	curvature parameter
M	magnetic parameter
S	positive stretching constant
S_c	Schmidt number
R_d	radiation parameter
h^*	convective heat transfer coefficient
C_f	surface drag force
Sh_x	Sherwood number
Re_x	local Reynolds number
E_{gen}'''	volumetric rate of local entropy generation
E_0'''	characteristic entropy generation rate
N_G	entropy generation
Br	Brinkman number
Bi	Biot number
Pr	Prandtl number
Nu_x	Nusselt number
C_s	heat capacity of surface
Greek Symbols	
ρ_{nf}, ρ_f, ρ_s	density
μ_{nf}, μ_f, μ_s	dynamic viscosity
σ	electrical conductivity
σ_{nf}	modified thermal diffusivity
$(\rho C_p)_{nf}$, $(\rho C_p)_f$	heat capacity
k_f, k_{nf}, k	thermal conductivity
φ	solid volume fraction of nanofluid
ζ	a scaled boundary-layer coordinate
σ^*	Stefan–Boltzmann constant
θ_w	temperature difference
λ_1	heat generation parameter
f	dimensionless stream function,
θ	dimensionless temperature
τ_{rx}	wall's shear stress
$\sum$	a constant parameter
α	dimensionless temperature difference
Subscripts	
w	for wall surface
nf	for the nanofluid
f	for the base fluid
s	for the solid (nanoparticles)
∞	use for ambient

References

1. Das, S.K.; Choi, S.U.; Yu, W.; Pradeep, T. *Nanofluids: Science and Technology*; John Wiley & Sons Inc.: Hoboken, NJ, USA, 2007.
2. Choi, S.U.S. Enhancing Thermal Conductivity of Fluids with Nanoparticles. In *Developments and Applications of Non-Newtonian Flows*; Singer, D.A., Wang, H.P., Eds.; ASME: New York, NY, USA, 1995; Volume 66, pp. 99–105.
3. Morrison, S.A.; Cahill, C.L.; Carpenter, E.E.; Calvin, S.; Swaminathan, R.; McHenry, M.E.; Harris, V.G. Magnetic and structural properties of nickel zinc ferrite nanoparticles synthesized at room temperature. *J. Appl. Phys.* **2004**, *95*, 6392–6395. [CrossRef]
4. Naughton, B.T.; Clarke, D.R. Lattice expansion and saturation magnetization of nickel–zinc ferrite nanoparticles prepared by aqueous precipitation. *J. Am. Ceram. Soc.* **2007**, *90*, 3541–3546. [CrossRef]
5. Virden, A.E.; O'Grady, K. Structure and magnetic properties of NiZn ferrite nanoparticles. *J. Magn. Magn. Mater.* **2005**, *290*, 868–870. [CrossRef]
6. Shahane, G.S.; Kumar, A.; Arora, M.; Pant, R.P.; Lal, K. Synthesis and characterization of Ni–Zn ferrite nanoparticles. *J. Magn. Magn. Mater.* **2010**, *322*, 1015–1019. [CrossRef]
7. Sheikholeslami, M.; Ganji, D.D.; Rashidi, M.M. Ferrofluid flow and heat transfer in a semi annulus enclosure in the presence of magnetic source considering thermal radiation. *J. Taiwan Inst. Chem. Eng.* **2015**, *47*, 6–17. [CrossRef]
8. Huang, T.; Yao, J.; Huang, Z.; Yin, X.; Xie, H.; Zhang, J. Numerical simulation on ferrofluid flow in fractured porous media based on discrete-fracture model. *Open Phys.* **2017**, *15*, 370–378. [CrossRef]
9. Neuringer, J.L. Some viscous flows of a saturated ferro-fluid under the combined influence of thermal and magnetic field gradients. *Intern. J. Non-Linear Mech.* **1966**, *1*, 123–137. [CrossRef]
10. Majeed, A.; Zeeshan, A.; Ellahi, R. Unsteady ferromagnetic liquid flow and heat transfer analysis over a stretching sheet with the effect of dipole and prescribed heat flux. *J. Mol. Liquids* **2016**, *223*, 528–533. [CrossRef]
11. Crane, L.J. Flow past a stretching plate. *J. Appl. Math. Phys.* **1970**, *21*, 645–647. [CrossRef]
12. Gupta, P.S.; Gupta, A.S. Heat and mass transfer on a stretching sheet with suction or blowing. *Can. J. Chem. Eng.* **1977**, *55*, 744–746. [CrossRef]
13. Chakrabarti, A.; Gupta, A.S. Hydromagnetic flow and heat transfer over a stretching sheet. *Q. Appl. Math.* **1979**, *37*, 73–78. [CrossRef]
14. Andersson, H.I.; Bech, K.H.; Dandapat, B.S. Magnetohydrodynamic flow of a power-law fluid over a stretching sheet. *Intern. J. Non-Linear Mech.* **1992**, *27*, 929–936. [CrossRef]
15. Hayat, T.; Muhammad, T.; Shehzad, S.A.; Alsaedi, A. An analytical solution for magnetohydrodynamic Oldroyd-B nanofluid flow induced by a stretching sheet with heat generation/absorption. *Intern. J. Therm. Sci.* **2017**, *111*, 274–288. [CrossRef]
16. Muhammad, N.; Nadeem, S.; Haq, R.U. Heat transport phenomenon in the ferromagnetic fluid over a stretching sheet with thermal stratification. *Results Phys.* **2017**, *7*, 854–861. [CrossRef]
17. Ramzan, M.; Yousaf, F. Boundary layer flow of three-dimensional viscoelastic nanofluid past a bi-directional stretching sheet with Newtonian heating. *AIP Adv.* **2015**, *5*, 057132. [CrossRef]
18. Hussain, T.; Shehzad, S.A.; Hayat, T.; Alsaedi, A.; Al-Solamy, F.; Ramzan, M. Radiative hydromagnetic flow of Jeffrey nanofluid by an exponentially stretching sheet. *PLoS ONE* **2014**, *9*, e103719. [CrossRef] [PubMed]
19. Goto, Y.; Kamebuchi, Y.; Hagio, T.; Kamimoto, Y.; Ichino, R.; Bessho, T. Electrodeposition of copper/carbonous nanomaterial composite coatings for heat-dissipation materials. *Coatings* **2017**, *8*, 5. [CrossRef]
20. Park, J.E.; Jang, Y.S.; Bae, T.S.; Lee, M.H. Multi-Walled carbon nanotube coating on alkali treated TiO_2 nanotubes surface for improvement of biocompatibility. *Coatings* **2018**, *8*, 159. [CrossRef]
21. Rivero, P.; Garcia, J.; Quintana, I.; Rodriguez, R. Design of nanostructured functional coatings by using wet-chemistry methods. *Coatings* **2018**, *8*, 76. [CrossRef]
22. Ramzan, M.; Bilal, M.; Chung, J.D.; Lu, D.C.; Farooq, U. Impact of generalized Fourier's and Fick's laws on MHD 3D second grade nanofluid flow with variable thermal conductivity and convective heat and mass conditions. *Phys. Fluids* **2017**, *29*, 093102. [CrossRef]

23. Sanni, K.M.; Asghar, S.; Jalil, M.; Okechi, N.F. Flow of viscous fluid along a nonlinearly stretching curved surface. *Results Phys.* **2017**, *7*, 1–4. [CrossRef]
24. Sajid, M.; Iqbal, S.A.; Naveed, M.; Abbas, Z. Joule heating and magnetohydrodynamic effects on ferrofluid (Fe_3O_4) flow in a semi-porous curved channel. *J. Mol. Liquids* **2016**, *222*, 1115–1120. [CrossRef]
25. Roşca, N.C.; Pop, I. Unsteady boundary layer flow over a permeable curved stretching/shrinking surface. *Eur. J. Mech. B Fluids* **2015**, *51*, 61–67. [CrossRef]
26. Imtiaz, M.; Hayat, T.; Alsaedi, A. Convective flow of ferrofluid due to a curved stretching surface with homogeneous-heterogeneous reactions. *Powder Technol.* **2017**, *310*, 154–162. [CrossRef]
27. Naveed, M.; Abbas, Z.; Sajid, M. MHD flow of micropolar fluid due to a curved stretching sheet with thermal radiation. *J. Appl. Fluid Mech.* **2016**, *9*, 131–138. [CrossRef]
28. Hone, J. Carbon nanotubes: Thermal properties. *Dekker Encycl. Nanosci. Nanotechnol.* **2004**, 603–610.
29. Antar, Z.; Noel, H.; Feller, J.F.; Glouannec, P.; Elleuch, K. Thermophysical and radiative properties of conductive biopolymer composite. *Mater. Sci. Forum* **2012**, *714*, 115–122. [CrossRef]
30. Oztop, H.F.; Abu-Nada, E. Numerical study of natural convection in partially heated rectangular enclosures filled with nanofluids. *Intern. J. Heat Fluid Flow* **2008**, *29*, 1326–1336. [CrossRef]
31. Ebrahimnia-Bajestan, E.; Niazmand, H. Convective heat transfer of nanofluids flows through an isothermally heated curved pipe. *Iran. J. Chem. Eng.* **2011**, *8*, 81–97.
32. Bejan, A. *Convection Heat Transfer*; John Wiley & Sons Inc.: Hoboken, NJ, USA, 2013.
33. Zhang, Y.; Shi, Q.; Schliesser, J.; Woodfield, B.F.; Nan, Z. Magnetic and thermodynamic properties of nanosized Zn ferrite with normal spinal structure synthesized using a facile method. *Inorg. Chem.* **2014**, *53*, 10463–10470. [CrossRef] [PubMed]
34. Khorasanizadeh, H.; Nikfar, M.; Amani, J. Entropy generation of Cu-water nanofluid mixed convection in a cavity. *Eur. J. Mech.* **2013**, *37*, 143–152. [CrossRef]

coatings

MDPI

Article

Nanofluids Thin Film Flow of Reiner-Philippoff Fluid over an Unstable Stretching Surface with Brownian Motion and Thermophoresis Effects

Asad Ullah [1,2,*], Ebraheem O. Alzahrani [3], Zahir Shah [1], Muhammad Ayaz [1] and Saeed Islam [1]

[1] Department of Mathematics, Abdul Wali Khan University, Mardan 23200, Khyber Pakhtunkhwa, Pakistan; Zahir1987@yahoo.com (Z.S.); mayazmath@awkum.edu.pk (M.A.); saeedislam@awkum.edu.pk (S.I.)
[2] Department of Mathematics, Kohat University of Science & Technology, Kohat 26000, Khyber Pakhtunkhwa, Pakistan
[3] Department of Mathematics, Faculty of Science, King Abdulaziz University, P. O. Box 80203, Jeddah 21589, Saudi Arabia; eoalzahrani@kau.edu.sa
* Correspondence: asad.ullah@kust.edu.pk; Tel.: +92-300-667-7148

Received: 22 November 2018; Accepted: 27 December 2018; Published: 30 December 2018

Abstract: The current investigation is carried out on the thin film flow of Reiner-Philippoff fluid of boundary-layer type. We have analyzed the flow of thin films of Reiner-Philippoff fluid in the changeable heat transmission and radiation over a time-dependent stretching sheet in 2D. The time-dependent governing equations of Reiner-Philippoff fluid model are simplified with the help of transformation of similarity variables. To investigate the behavior of the Reiner-Philippoff fluid with variable stretching surface for different physical effects, we considered thermophoresis and Brownian motion parameters in the flow. The Homotopy Analysis Method is implemented in the reduced model to achieve a solution of the original problem. A numerical convergence of the implemented method is also analyzed. The behavior of temperature, velocity, and concentration profiles have been investigated with the variation of skin friction, Nusselt number, and Sherwood number. A comparative graphical survey is presented for the velocity gradient, under different parameters. An analytical analysis is presented for the time-dependent parameter over thin film flow. The results we obtained are better than the previously available results. For the survey, the physical representation of the embedded parameters, like, β depends on the stretching parameter ζ, and the Reiner-Philippoff fluid parameter ϵ are discussed in detail and plotted graphically. Prandtl number Pr, Brownian motion parameter Nb, thermophoretic number Nt, and Schmidt number Sc are presented by graphs and discussed in detail.

Keywords: Reiner-Phillipoff fluid; thin film; time-dependent; thermal radiation; homotopy analysis method (HAM)

1. Introduction:

In the last few decades, scientists have given great attention to thin film flow. The basic idea behind such an important concept is the applications and mechanism of thin film flow. Thin films are ubiquitous in nature and their mechanism is important to understand, because it has a wide range of practical uses. The traditional theory of Newtonian fluids is mainly focused on the linear relationship between stress and strain tensor or on their rates. Newtonian fluids are hardly pointing towards the doctrine of linear relation between the stress and strain tensor. In the same way, fluids that do not agree with the linear distribution between the stress and strain tensor are known as non-Newtonian fluids. There are two main classes of non-Newtonian fluids, visco-inelastic and visco-elastic fluids. The subsequent has great importance due its dual nature. Visco-elastic fluids, due to their viscosity, show

an elastic behavior up to some degree. In such fluids, energy is stored in the form of strain energy. One cannot ignore the strain in these types of fluids, because it is responsible to recover the original state. These fluids came under the definition of Newtonian fluids, when there is a first order derivative of all the tensor formed from the velocity field, while fluids having higher order derivative tensors present come under the definition of non-Newtonian fluids. Some of these fluids are second order, third order, and fourth order fluids. Third order liquid, which is due to its sequential nonlinear constraints, has a variety of applications.

The study of non-Newtonian fluids from a theoretical point of view is too complicated and we need a mathematical relation to briefly illuminate the relation between shear stress and the shear rate. Therefore, a variety of non-linear relations have been suggested for the study of these fluids. As a consequence, to deliberate such a categorizing demeanor, various models have been initiated and discussed in [1]. Non-Newtonian fluids are not so simple that a single mathematical relation can explain the whole scenario. Therefore, for this purpose, several models have been initiated and developed to briefly explain the nature of such fluids. Among all, Ellis fluid model, Sisko fluid model, the Carreau viscosity model, Ostwald-de Waele model, the cross-viscosity model, Carreau-Yasuda model, Powell-Eyring model, and Reiner-Philippoff fluid model are the most important models in explaining the nature of such fluids. These models have interesting properties in their own, in which the Ostwald-de Waele model is considered to be the basic model, normally known as the Power law model. The subsequent of all models discussed here is a time-independent three-parameter model, behaving like non-Newtonian fluids under intermediate shear rates and Newtonian fluids at extreme shear rates. Consequently, due to their dual nature, Reiner-Philippoff fluid has many applications in engineering sciences and other technologies.

A variety of fluids are available in nature, in which nanofluids are the most interesting fluids, due to their variety of applications. The most commonly uses of nanofluids are metal oxides, oxide ceramics and chemically stable metals, like Alumina, Silica, Zirconia, Titania, aluminum oxide, copper oxide, gold, copper and various forms of allotropes of carbon and metal carbides. Water, oils, polymeric solutions, lubricants, bio-fluids, and glycols are normally used as base fluids. Nanofluids are two-phased mixtures designed by spreading nanometer-sized particles, in which base fluid size ranging up to 100 nm. Nanoparticles play a key part in heat transfer analysis. On the other hand, applications of liquid film flow grow day by day. The most common uses of these flows are in heat exchange processes, techniques of coating, industrial and distillation processes, and many more. The applied usage of the liquid film flow is a fascinating interaction amongst fluid mechanics, structural mechanics, and technology. Some of the practical usages are polymer and metal extrusion, foodstuff processing, plastic sheets depiction, casting and fluidization of the reactor.

In the assessment of these applications, researchers have taken a keen interest in the study of liquid film flow on unstable surfaces. Stretching sheets at the beginning were treated as linear surfaces. Such a phenomenon encountered in many industrial processes, like, in cooling, extraction of polymer sheets and plastic sheets, etc. In these industrial processes the stretching sheet contacts with the fluid both mechanically and thermally. Sakiadis [2] work is considered to be the pioneering work in the study of boundary-layer flow over non-stationary and rigid surfaces. But in polymer industries stretching sheet play a key role, which is explained by Crane [3] in his famous work. After the work of Crane on stretching sheet and its numerous applications in the polymer industry, researchers have shown great interest in it. Stretching sheet problems have been investigated by different researchers under different physical parameters with their variations, like viscosity and thermal conductivity, magnetic and electric fields (MHD), thermal radiation, viscous dissipation, and chemical reactions etc.

Similar to the variations in the parameters for the stretching sheet, the same phenomenon of stretching problem is studied for different geometries and is developed from time to time. Siddiqui et al. [4,5] investigated non-Newtonian fluids on a moving built with a sloping plane in one direction for thin film flow. Tawade et al. [6] studied the effect of magnetic field upon a thin fluid stream passes over a temperamental stretching sheet with heat. They used two different numerical

approaches, Newton-Raphson and RK-Felberg. They briefly explained and provided a detailed survey of different physical parameters.

Beside all these, the implemented techniques are not to be ignored. In literature, the boundary-layer equations obtained for stretching flow are solved by different approaches. Among all, numerical and perturbation approaches have been adopted and applied by many researchers successfully. In practice, numerical techniques are too difficult to apply due to the high non-linearity of the model equations, whereas perturbation techniques are not always applicable. Perturbation techniques need a small or large parameter to be presented in the equation, which is not always available to us. To overcome this situation, some new techniques were developed and implemented by the researchers successfully. Sajid and Hayat [7] used HAM and HPM to thin film flow of Sisko fluid and Oldroyed-6 constant. The effect of thermal radiations of blending convection stream over a steeping surface in a permeable channel is studied by Bakier [8]. Nargis and Tahir [9] have given a more detailed survey of grade third fluid on a moving belt in the direction of a slanted plane. Stretching problem in permeable medium with thermal effects of a slanted plate is investigated by Moradi et al. [10]. Chaudhary et al. [11] re-examined thermal radiation impacts of liquid on exponentially extending surfaces. Eldabe et al. [12] examined convection, radiation, and synthetic effects of MHD visco-elastic fluid flow in a permeable channel on a horizontal stretching sheet. Das [13] has investigated some important properties of thermal radiation and thermophoresis of MHD blended convective flow. Recently, Hsiao [14] has examined the heat and mass trasfer effects of Maxwell fluid. MHD flow of different models, like Powell–Eyring nanofluid and other non-Newtonian fluids on stretching surfaces are briefly explained in [15–17]. Crane [3] for the first time studied the flow of gummy liquid in a stretched surface. The effect of heat exchange on an extending sheet for viscoelastic liquids is discussed by Dandapat [18]. Wang [19] for the first time studied finite liquid film on an unsteady stretching domain. The problem discussed by Wang [19] has discussed by Usha and Sridharan [20] with a survey on different parameters. For a heat transfer analysis of liquid film fluid, numerical results for different parameters were obtained by Liu and Andersson [21]. The repercussion in the thin liquid film on an unsteady stretching sheet due to the inner heat production was examined by Aziz et al. [22].

The thin liquid film flow of non-Newtonian fluids has a lot of practical features. Consequently, it becomes a common solute in engineering and other technologies. Andersson et al. [23,24] investigated the non-Newtonian thin liquid films at a time depending stretching sheet by taking the Power law model in consideration. After this pioneer investigation of Andersson, scientists have given more attention to stretching problems by using the Power law model, for more detail see [25,26]. Other models also came in discussion during this era. Megahed et al. [27] examined the thin liquid film flow of Casson liquid for viscous promulgation with slip velocity and the transmission of variable heat transition. The same scenario was discussed by Abolbashari et al. [28] for nano particles with the generation of entropy. Buongiorno's model for nano fluid thin film on a temperamental extending stretched sheet was recently investigated by Qasim et al. [29]. A steady flow of liquids through a porous medium is studied by Ariel [30]. Ariel got a high non-linear coupled boundary value problem for the geometry under consideration and applied numerical methods to obtain an appropriate solution. Sahoo et al. [31] investigated heat exchange analysis with a uniform oblique magnetic field for non-Newtonian fluids. They successfully applied finite difference and Broyden's methods for the concatenation of the field of the velocity. Aiyesimi et al. [32,33] examined the thin liquid film flow of an MHD grade third fluid and obtained some interesting results by using perturbation techniques with a brief survey impact of slip parameters and magnetic parameters. Third grade fluid and its approximate analytical solution by using OHAM for three different kinds of flow has discussed by Islam and Shah et al. [34,35]. Makinde [36] studied the same geometry with isothermal effects for hydro-dynamically third order liquid film flow. The approximate solution for velocity and temperature was obtained by a Hermitepade method. A brief discussion and explanation was given by Yao and Liu [37] of the second order fluid over flat plates for unsteady flows. Erdogan et al. [38] examined the properties of unsteady flow of the

non-Newtonian fluids, with a brief description on Poiseuille, Couette, and generalized form of Couette flow. Abdulhameed et al. [39] successfully applied Laplace transformation, perturbation techniques, and separation of variable methods for the clarity of unsteady non-Newtonian fluids over an oscillating plate. Huan was the first to settle variational rules for nano thin film-lube [40] with the help of the method of semi-inverse [41–45]. Kapitza [46], Yih [47], Krishna and Lin [48], Anderson and Dahl [49], and Cheng et al. [50] considered thin film flow problems with distinct geometric expressions. As time passes, the thin film flow applications in engineering sciences increase day by day and as a result, the researchers extended the work to a new world. Recently, coating and fiber applications of thin film flow are described and discussed in [51–54]. The geometry and other physical constraints have fixed, but some impurities have been introduced to the study as discussed in [55,56], to improve and enhance the heat transfer analysis.

An interesting and remarkable behavior of time-dependent non-Newtonian fluid is its pseoudo-plasticity, which vanishes with the expansion of shear rate. Many models have initiated as discussed earlier in the investigation of the behavior of such fluids. Among all, in Reiner-Philippoff fluid model [57], researchers have shown great interest. In 1965, Kapr and Gupta [58] have studied Reiner-Philippoff fluid two-dimensional flow in a linear channel. Different approaches have been adopted with different geometrical aspects to discuss this famous model.

In 1994, Tsung-Yen [59] investigated the boundary-layer flow problems by using this model. The basic idea of boundary-layer theory was introduced by L. Prandlt in Heidelberg, Germany, in August 1904, at the third International Congress of Mathematicians. It is the region in the fluid flow, developing at large Reynolds numbers. This region is strongly affected by inertial forces and viscous forces. Boundary layer theory is very important and has a variety of dimensions and visual perception of interest, and has been studied for a long interval of time. In 2009, this model was investigated by Yam [60] for the boundary flow past a stretching wedge. During this era Patel and Timol [61] used the technique of similarity solution for three dimensional boundary layer type equations for non-Newtonian fluids. Ahmad [62] examined the Reiner-Phillippoff fluid flow based nano-liquids past a stretching sheet. Recently, Ahmad et al. [63] discussed the same model with the same geometry with shifting and thickness in the stretching sheet.

Discussion has shown that different problems arise due to varying geometry as well as the fluid behavior, and different approaches are adopted by the researchers to meet their needs. Most of the problems that arise are highly non-linear and it is a difficult job to handle such problems with the usual available techniques in literature. Nowadays, perturbation techniques [64,65] are in the main stream for dealing with such problems. These methods work in the presence of small or large scale parameters. These parameters are not always available to us in applied sciences and we cannot apply these techniques to these types of problems. To deal with such problems, we use non-perturbative techniques like the "Lyapunov's artificial small parameter method" [66], the method of d-Expansion, and the adomians decomposition method (ADM) [67]. Various approaches have been adopted by researchers to find the solution to their problems. An exact solution in literature is very rare. This is because of the complexity of the geometry of the problem. That is why we often see numerical approaches to find the approximate solution. Among all, homotopy analysis method (HAM) [68–70] is the one by virtue of which we can find the approximate solution. In 1992, Liao [71] for the first time developed and implemented this method and found solution in the form of series in a single variable. Liao also discussed the convergence of this proposed method and found a rapid convergence. HAM has some interesting points of interest. Most importantly, this method is independent of whether a given non-linear problem contains any small or large parameters or not. In HAM, we can modify and control the region of convergence, where necessary, and is helpful in selecting distinct sets of base operations, which approximate a non-linear problem with less effort.

The goal of our current investigations is to obtain the thin liquid film flow of Reiner-Philippoff fluid over a stretching sheet with heat transfer and thermal radiations. Boundary-layer equations are obtained from the physical demonstrated geometry. Thermophoresis effects and Brownian motion

are also encircled with different physical parameters. A similarity solution is obtained with the help of new variables, due to which a complicated model is transformed into simple coupled ordinary differential equations. An analytical approach is adopted for the solution of the reduced system. HAM is implemented with initial guess as required for the implementation of the technique, due to its fast convergence. With the variation of different physical parameters, the results are plotted, tabulated, and discussed in detail. The physical significance of Sherwood number and skin friction is presented by tables.

2. Problem Formulation

Consider an electrically conducting and time-dependent thin film flow of Reiner-Philippoff fluid over spreading sheet. The elastic sheet start moving from fixed slit. The coordinates $oxyz$ are adjusted in such way that ox and the plate are equal, and oy is along the sheet. The origin is at rest in the direction of the x-axis, due to the two equal and opposite forces of the stretching sheet flow. We take the x-axis in the direction spreading sheet and has the stress velocity $U_w(x,t) = \gamma x(1-\zeta t)^{-1}$, where γ and ζ represent any fix numbers, which are vertical to y-axis as shown in Figure 1.

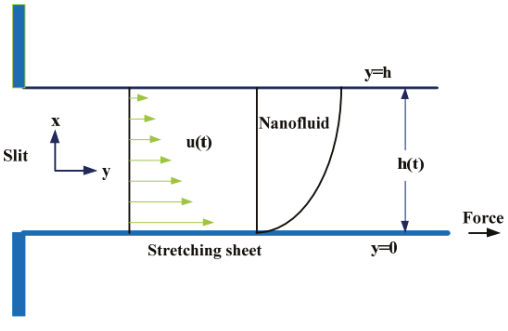

Figure 1. Geometry of the physical model.

The wall temperature [72,73] of the liquid is

$$T_w(x,t) = \left(\frac{\gamma x^2}{2(1-\zeta t)^{1.5}\nu_f}\right) T_r + T_0 \tag{1}$$

and the capacity of the nanoparticles is given by

$$C_w(x,t) = \left(\frac{\gamma x^2}{2(1-\zeta t)^{1.5}\nu_f}\right) C_r + C_0 \tag{2}$$

where ν_f denotes the fluid kinematic viscosity, T_0 and C_0 denote the temperature of the slit and volume friction of the nanoparticles, while T_r and C_r represent the reference temperature and reference volume of the nanoparticles respectively. Assume that the effects of body forces are negligible in the field of flow. In light of the previous assumptions, the equation of continuity, the basic boundary governing equations, concentration, and heat transferring equations take the following forms.

The stress deformation behavior is well explained by Reiner-Philippoff in [74], and is considered one of the classical descriptions and is given by an implicit functional way:

$$\tau_{ij} = \left[\mu_0 + \frac{\mu_\infty - \mu_0}{\frac{1}{2\tau_0^2}\left(\sum_{p=1}^{3}\sum_{q=1}^{3}\tau_{pq}\tau_{qp}\right)}\right] e_{ij} \tag{3}$$

where the parameters μ_0, μ_∞, and τ_0 are greater than zero. This model gives interesting results due to its behavior, for large or small values of the model nearly agree with Newtonian fluids. Besides this, when the values of τ_0 are in between the extremes the model agrees with non-Newtonian fluids.

The Momentum equations for two dimensional flow together with the continuity equation takes the form:

$$\frac{\partial \tilde{u}}{\partial x} + \frac{\partial \tilde{v}}{\partial y} = 0 \tag{4}$$

$$\rho\left(\frac{\partial \tilde{u}}{\partial t} + \tilde{u}\frac{\partial \tilde{u}}{\partial x} + \tilde{v}\frac{\partial \tilde{u}}{\partial y}\right) + \frac{\partial p}{\partial x} = \frac{\partial \tau_{xx}}{\partial x} + \frac{\partial \tau_{xy}}{\partial y} \tag{5}$$

$$\rho\left(\frac{\partial \tilde{v}}{\partial t} + \tilde{u}\frac{\partial \tilde{v}}{\partial x} + \tilde{v}\frac{\partial \tilde{v}}{\partial y}\right) + \frac{\partial p}{\partial y} = \frac{\partial \tau_{xy}}{\partial x} + \frac{\partial \tau_{yy}}{\partial y} \tag{6}$$

The components of stress, presented above, are difficult to present in a closed single explicit format. For this purpose, we assume a small τ_0 such that its higher powers greater than three vanishes. The stress components take the form:

$$\tau_{xy} = \tau^0_{xx} + \tau_0^2 \tau'_{xx} \tag{7}$$

with the constitutive relations defined by

$$\tau^0_{xx} = \mu_0\left(2\frac{\partial \tilde{u}}{\partial x}\right), \tau^0_{yy} = \mu_0\left(2\frac{\partial \tilde{v}}{\partial y}\right), \tau^0_{xy} = \mu_0\left(\frac{\partial \tilde{u}}{\partial y} + \frac{\partial \tilde{v}}{\partial x}\right) \tag{8}$$

where τ^0_{xx} denotes the Newtonian stress component of the fluid with μ_0, the coefficient of viscosity and τ'_{xx} is the residual contribution terms of the Reiner-Philippoff fluid, and prime should not be considered a derivative.

Using Equation (7) in Equation (3), we get

$$\tau_{ij} = \left(\mu_0 + \frac{\mu_\infty - \mu_0}{1 + \frac{1}{2\tau_0^2}(\tau^{02}_{xx} + 2\tau^{02}_{xy} + \tau^{02}_{yy} + ...)}\right) e_{ij} \tag{9}$$

Neglecting fourth and higher order terms, we get

$$\tau_{ij} = \left[\mu_0 + \frac{2(\mu_\infty - \mu_0)}{\tau^{02}_{xx} + 2\tau^{02}_{xy} + \tau^{02}_{yy}}\right] e_{ij} \tag{10}$$

Hence, τ_{ij} is explicitly related to the gradient of the velocity by the above relation.

Let us consider τ_0 as large, such that its exponent larger than three is negligible in the relation expressed below.

$$\tau_{xx} = \tau^\infty_{xx} + \frac{\tau''_{xx}}{\tau_0^2} \tag{11}$$

with the constitutive relations:

$$\tau^\infty_{xx} = \mu_\infty\left(2\frac{\partial \tilde{u}}{\partial x}\right), \tau^\infty_{yy} = \mu_\infty\left(2\frac{\partial \tilde{v}}{\partial y}\right), \tau^\infty_{xy} = \mu_\infty\left(\frac{\partial \tilde{u}}{\partial y} + \frac{\partial \tilde{v}}{\partial x}\right) \tag{12}$$

where τ^∞_{xx} denotes the Newtonian fluid stress component with the viscosity coefficient μ_∞ and τ''_{xx}, the residual contribution terms of the Reiner-Philippoff fluid, while the prime should not be considered a derivative sign.

Using Equation (11) in Equation (1), and neglecting higher exponent terms of $\frac{1}{\tau_0}$, we get

$$\tau_{ij} = \left[\mu_\infty + \frac{(\mu_0 - \mu_\infty)(\tau_{xx}^{\infty 2} + 2\tau_{xy}^{\infty 2} + \tau_{yy}^{\infty 2})}{2\tau_0^2}\right] e_{ij} \tag{13}$$

Using Equations (10) and (13) in Equations (5) and (6), we get

$$\rho\left(\frac{\partial \tilde{u}}{\partial t} + \tilde{u}\frac{\partial \tilde{u}}{\partial x} + \tilde{v}\frac{\partial \tilde{u}}{\partial y}\right) = -\frac{\partial p}{\partial x} + \frac{\partial}{\partial x}\left[2\lambda\frac{\partial \tilde{u}}{\partial x}\right] + \frac{\partial}{\partial y}\left[\lambda\left(\frac{\partial \tilde{u}}{\partial y} + \frac{\partial \tilde{v}}{\partial x}\right)\right] \tag{14}$$

$$\rho\left(\frac{\partial \tilde{v}}{\partial t} + \tilde{u}\frac{\partial \tilde{v}}{\partial x} + \tilde{v}\frac{\partial \tilde{v}}{\partial y}\right) = -\frac{\partial p}{\partial y} + \frac{\partial}{\partial y}\left[2\lambda\frac{\partial \tilde{v}}{\partial x}\right] + \frac{\partial}{\partial x}\left[\lambda\left(\frac{\partial \tilde{u}}{\partial y} + \frac{\partial \tilde{v}}{\partial x}\right)\right] \tag{15}$$

where λ represents the terms defined in the square brackets in Equations (10) and (13).

In the absence of pressure gradient, the boundary-layer equations are simplified to

$$\left(\frac{\partial \tilde{u}}{\partial t} + \tilde{u}\frac{\partial \tilde{u}}{\partial x} + \tilde{v}\frac{\partial \tilde{u}}{\partial y}\right) = \frac{1}{\rho}\left[\frac{\partial}{\partial y}\lambda\frac{\partial \tilde{u}}{\partial y}\right] \tag{16}$$

where

$$\frac{\partial \tilde{u}}{\partial y} = \frac{\tau_{ij}}{\mu_\infty + \frac{(\mu_0 - \mu_\infty)}{1+\left(\frac{\tau_{ij}}{\tau_s}\right)^2}} \tag{17}$$

$$\frac{\partial T}{\partial t} + \tilde{u}\frac{\partial T}{\partial x} + \tilde{v}\frac{\partial T}{\partial y} - \frac{K}{\rho c_p}\frac{\partial}{\partial y}\left[\frac{\partial T}{\partial y}\right] = \tau\left[D_B\left(\frac{\partial C}{\partial y}\frac{\partial T}{\partial y}\right) + \frac{D_T}{T_\infty}\left(\frac{\partial T}{\partial y}\right)^2\right] \tag{18}$$

$$\frac{1}{D_B}\left[\frac{\partial C}{\partial t} + \tilde{u}\frac{\partial C}{\partial x} + \tilde{v}\frac{\partial C}{\partial y}\right] - \frac{\partial^2 C}{\partial y^2} = \left(\frac{D_T}{T_\infty D_B}\right)\frac{\partial^2 T}{\partial y^2} \tag{19}$$

With the constraints defined at the boundaries

$$\tilde{u} = U_w, \quad \tilde{v} = 0, \quad T = T_w, \quad C = C_w \qquad \text{at} \quad y = 0, \tag{20}$$

$$\frac{\partial \tilde{u}}{\partial x} = \frac{\partial T}{\partial x} = \frac{\partial C}{\partial x} = 0, \quad \tilde{v} = \frac{dh}{dt} = 0, \quad C > 0, \qquad \text{at} \quad y = h(t) \tag{21}$$

Here, $\tilde{u}$ and $\tilde{v}$ represent the state variables, denotes the velocity components along x-axis and y-axis respectively, and ρ represents the density of the fluid, local temperature by T, and the fluid capacitance by C_p. The ratio $\frac{(\rho_c)_p}{(\rho_c)_f}$ is the characteristic ratio of the base fluid to the nanoparticles heat capacitance; D_B represents the direct Brownian diffusion constant; D_T represents thermophoretic diffusion constant, K is the thermal conductivity, and T_∞ denotes the fluid temperature far away from the slit. Introducing the succeeding similarity transformations [75,76]

$$\begin{aligned} \eta = \sqrt{\frac{\gamma}{v(1-\zeta t)}}y,\ \psi(x,y,t) = x\sqrt{\frac{v\gamma}{1-\zeta t}}f(\eta),\ \tilde{u} = \frac{\partial \psi}{\partial y} = \gamma(1-\zeta t)^{-1}f'(\eta) \\ \tilde{v} = \frac{\partial \psi}{\partial x} = -\sqrt{\frac{\gamma v}{(1-\zeta t)}}f(\eta),\ \tau_{ij} = \left[x\left(\gamma(1-\zeta t)^{-1}\right)^3\right]^{\frac{1}{2}}g(\eta) \\ h(t) = \left[\frac{v}{\gamma(1-\zeta t)^{-1}}\right]^{\frac{1}{2}}\left(T_w - T_0\right)\theta(\eta) = T - T_0,\ \left(C_w - C_0\right)\phi(\eta) = C - C_0 \end{aligned} \tag{22}$$

where prime represents the change with respect to η, $\beta = \sqrt{\frac{\zeta}{v(1-\zeta t)}}h(t)$ represents the liquid film thickness, ψ denotes the stream function, and $v = \frac{\mu}{\rho}$ is the kinematics viscosity. From the dimensionless film thickness, we can write $\frac{dh}{dt} = -\frac{c\beta}{2}\sqrt{\frac{v}{\zeta(1-\zeta t)}}$, for detail see [77,78]. With the help of the newly introduced similarity transformations, Equations (14)–(21) are reduced to the following equations, while the continuity equation is satisfied identically.

$$\frac{dg}{d\eta} - \frac{1}{\epsilon}\left[S\left(\frac{\eta}{2}\frac{d^2f}{d\eta^2} + \frac{df}{d\eta}\right) + \left(\frac{df}{d\eta}\right)^2 - f\frac{df}{d\eta}\right] = 0 \tag{23}$$

$$g - \epsilon\frac{d^2f}{d\eta^2}\left(\frac{g^2+\lambda\gamma}{g^2+\gamma}\right) = 0 \tag{24}$$

$$\frac{1}{Pr}\left(\frac{d^2\theta}{d\eta^2}\right) + f\frac{d\theta}{d\eta} - 2\theta\left(\frac{df}{d\eta}\right) - \frac{S}{2}\left(3\theta + \eta\frac{d\theta}{d\eta}\right) + Nt\left(\frac{d\theta}{d\eta}\right)^2 + Nb\left(\frac{d\theta}{d\eta}\right)\left(\frac{d\phi}{d\eta}\right) = 0 \tag{25}$$

$$\frac{d^2\phi}{d\eta^2} + Sc\left[f\frac{d\phi}{d\eta} - 2\phi\left(\frac{df}{d\eta}\right) - \frac{S}{2}\left(3\phi + \eta\frac{d\phi}{d\eta}\right)\right] + \frac{Nt}{Nb}\left(\frac{d^2\theta}{d\eta^2}\right) = 0 \tag{26}$$

The boundary constraints of the problem are:

$$f'(0) = 1, \quad f(0) = 0, \quad \theta(0) = \phi(0) = 1, \quad g(0) = 0, \quad g^{'}(0) = 1 \tag{27}$$

$$f(\beta) = \frac{S\beta}{2}, \quad f''(\beta) = 0, \quad \theta'(\beta) = \phi'(\beta) = 0, \quad g^{''}(\beta) = 0, \quad g(\beta) = \frac{S\beta}{2} \tag{28}$$

The generalized physical constraints obtained are defined as: $S = \frac{\gamma}{\epsilon}$ is the non-dimensional measure of unsteadiness, $\epsilon = \sqrt{\frac{x}{v}}$, $\lambda = \frac{\mu_0}{\mu_\infty}$ and $\gamma = \tau_s^2\left(\frac{1-\kappa t}{cx^{\frac{1}{3}}}\right)^3$ are parameters of Reiner-Philippoff fluid, $Pr = \frac{\rho v c_p}{K}$ is the Prandtl number, $Nt = \frac{\tau D_w(T_w - T_\infty)}{vT_\infty}$ represents thermophoresis constraint, $Nb = \frac{\tau D_B(C_w - C_\infty)}{v}$ represents the limitation of the Brownian motion, and $Sc = \frac{v}{D_B}$ denotes Schmidt number. All these parameters and numbers are well defined and explained briefly in literature. C_{fx} and Nu_x represent the local skin-friction coefficient and local Nusselt number respectively, and are defined as:

$$C_{fx} = \frac{(\tau)_{y=0}}{\frac{\rho\tilde{U}_w^2}{2}} \tag{29}$$

or

$$\frac{C_{fx}\sqrt{Re_x}}{2} = \tau_w\sqrt{\frac{x}{\tilde{U}_w^3}} = g(0,x) \tag{30}$$

where Re_x is known as the local Reynolds number and is defined as $Re_x = \frac{\tilde{U}_w x}{\tilde{\nu}}$ and τ_w is the value of τ on $\eta = 0$. Nu is the Nusselt number and is defined as $Nu = \frac{Q_w}{\hat{k}(T_w - T_0)}$, while Q_w denotes the heat flux and $Q_w = -\hat{k}\left(\frac{\partial T}{\partial y}\right)_{\eta=0}$. $Sh = \frac{D_B J_w}{\hat{k}(T_w - T0)}$ represents the Sherwood number in which J_w is the mass flux, where $J_w = -D_B\left(\frac{\partial c}{\partial y}\right)_{\eta=0}$.

Sherwood number Sh and Nusselt number Nu take the dimensionless forms:

$$Nu = \Theta^{'}(0), \quad Sh = -\Phi^{'}(0) \tag{31}$$

3. Solution by HAM

The approximate solution of the Equations (23)–(26) corresponding to the Equations (27) and (28) are treated with Homotopy Analysis Method (HAM). The auxiliary parameters encircled the solution which normalize and switch to conjunction of the solutions. Let us take the initial guesses:

$$\hat{f}_0(\eta) = \eta, \quad \hat{\theta}_0(\eta) = 1, \quad \hat{\phi}_0(\eta) = 1 \tag{32}$$

Let us denote the linear operators by L_f, L_θ, and L_ϕ defined as:

$$L_f(\hat{f}) = \hat{f}^{'''}, L_\theta(\hat{\theta}) = \hat{\theta}^{''}, \quad L_\phi(\hat{\phi}) = \hat{\phi}^{''} \tag{33}$$

with the property

$$L_f(\omega_1 + \omega_2\eta + \omega_3\eta^2) = 0, L_\theta(\omega_4 + \omega_5\eta) = 0, L_\phi(\omega_6 + \omega_7\eta) = 0 \tag{34}$$

where ω_j for $j \in \{1, 2, ..., 7\}$ are the general solution coefficients. The fundamental procedure of the solution by using HAM is explained in [72,73,76].

4. Results and Discussion

The current analysis is carried out on the thin film flow of Reiner-Philippoff fluid of boundary layer type over a time-dependent stretching plate. The aim of this subsection is to study the velocity distribution, temperature distribution, and concentration profile with physical effects of different embedding parameters, which are discussed in Figures 2–16.

Figure 2 demonstrates the thin film thickness β during the fluid motion. In the performance of coating, thin film thickness play a key role. Physically, the thickness of the films is directly related to the velocity. Figure 2b reflects a more rapid variations in β under smaller values of ϵ and S as compared to the results observed in part (a). The velocity of the fluid decreases with an increase in the thickness parameter β. It happens because for larger values β of the fluid viscosity increases, and as a result a gradual fall can be observe in the gradient of the velocity profile.

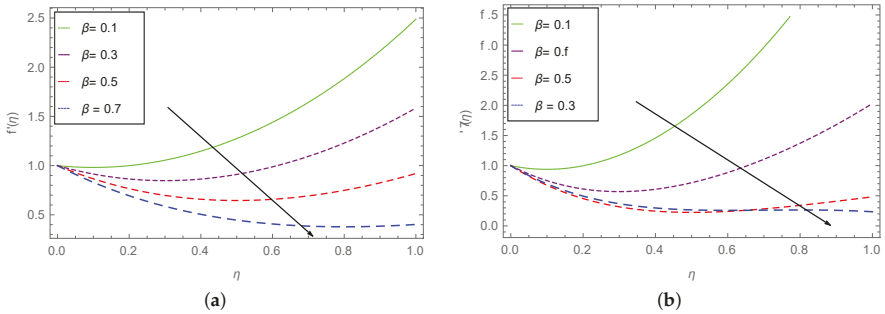

(**a**) (**b**)

Figure 2. (**a**) Impact of β on $f^{'}(\eta)$, when $\epsilon = 0.4, S = 0.2$ and (**b**) Impact of β on $f^{'}(\eta)$, when $\epsilon = 0.01, S = 0.05$.

Figure 3 illustrates the effect of the stretching parameter ϵ. The velocity profile shows an increase with the increasing values of ϵ, because the lower plate always behaves directly to the flow fluid velocity. Physically, for $\epsilon > 0$, the surface accelerating rises, $\epsilon < 0$ decelerating the surface, while $\epsilon = 0$ depict the random motion of the surface. Figure 3b reflects the sensitivity of ϵ, under smaller values of β and S.

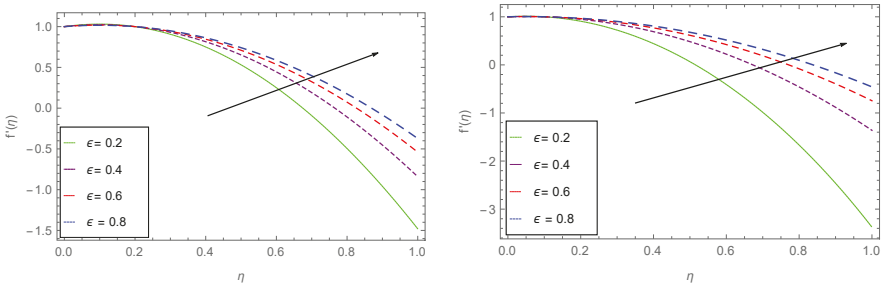

(**a**) (**b**)

Figure 3. (**a**) Impact of ϵ on $f^{'}(\eta)$, when $\beta = 0.1, S = 0.2$ and (**b**) Impact of β on $f^{'}(\eta)$, when $\beta = 0.05, S = 0.005$.

Figure 4 reveals the behavior of unsteady constraint S over $f^{'}(\eta)$ for dissimilar values of the embedded parameters. It is observed that the velocity profile $f^{'}(\eta)$ directly varies with unsteadiness parameter S. The velocity profile climes up with the increasing behavior of S. Furthermore, it is observed that the solution is possible only in the closed interval $[0, 1]$ for S. Also, the increasing values of S increases the motion of the nanofluid.

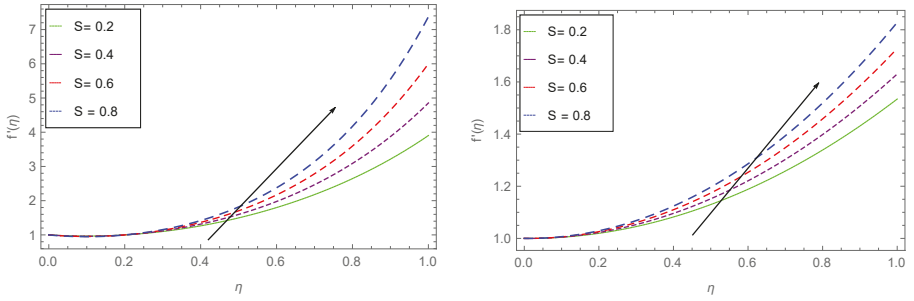

Figure 4. (**a**) Impact of S on $f^{'}(\eta)$, when $\beta = 0.1, \epsilon = 0.2$ and (**b**) Impact of β on $f^{'}(\eta)$, when $\beta = 0.01, \epsilon = 0.01$.

The impact of Pr on $\theta(\eta)$ is shown in Figure 5. An inverse relation has been observed between the temperature and the Prandlt number. Physically, for small values of Pr these fluids have larger thermal conductivity and vice versa. As a result, for larger values of Pr the thermal boundary layer declines.

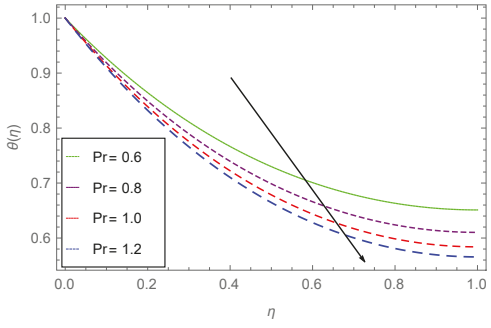

Figure 5. Impact of Pr on $\theta(\eta)$, when $S = 0.7, \beta = 1.0, \epsilon = 0.4, Nb = 0.5, Nt = 0.3, Sc = 0.7$.

The effect of the thin film thickness β on temperature profile for different values of the embedded parameters is shown in Figure 6. A similar effect in velocity profile is observed for β. The larger the thickness of the liquid film, the lesser the heat transfer. In other words, the flow of heat in the larger thickness film faces more more difficulty, as compared to a lesser thickness film.

Figure 7 illustrates the temperature distribution under Brownian motion parameter Nb. In general, due to the irregular motion of the particles, this causes a collision between these particles. An increase in heat of the fluid can be seen with the ascending order of the Brownian motion parameter Nb, consequently, free surface nanoparticle volume friction decreases.

The impact of the unsteadiness parameter S on the heat profile $\theta(\eta)$ is presented in Figure 8. It is observed that $\theta(\eta)$ varies directly with S. An increase in S increases the temperature of the fluid, which further increases the kinetic energy of the fluid, and results in increment of the liquid film motion.

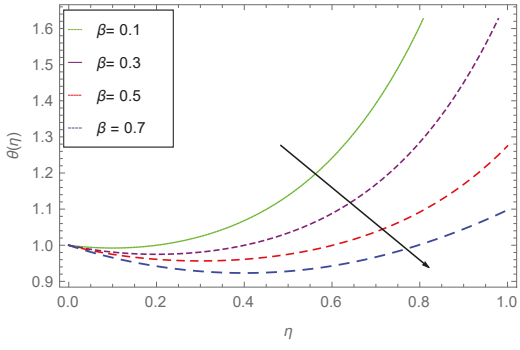

Figure 6. Impact of β on $\theta(\eta)$, when $S = 0.6, \epsilon = 0.5, Nb = 0.5, Nt = 0.3, Sc = 0.1, Pr = 0.7$.

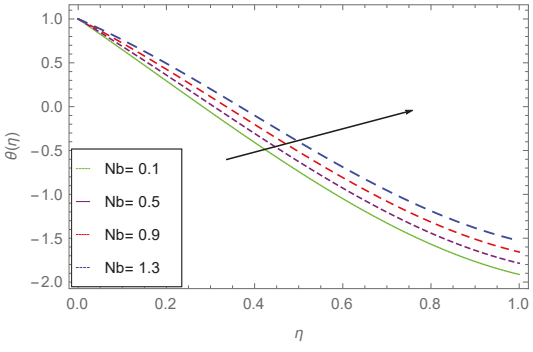

Figure 7. Impact of Nb on $\theta(\eta)$, when $S = 0.6, \epsilon = 0.5, \beta = 0.4, Nt = 0.3, Sc = 0.1, Pr = 0.7$.

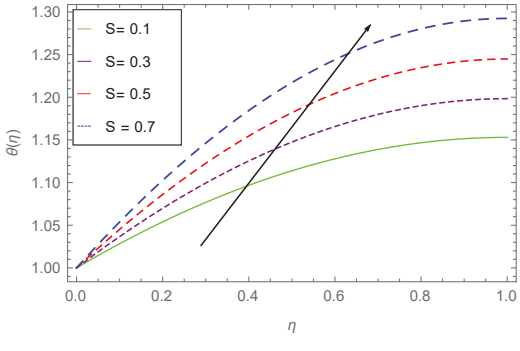

Figure 8. Impact of S on $\theta(\eta)$, when $Nb = 0.5, \epsilon = 0.5, \beta = 1.0, Nt = 0.3, Sc = 0.9, Pr = 0.6$.

Figure 9 illustrates the effect of thermophoresis parameter Nt on temperature profile. The limitations thermophoresis helps in the increase of a surface temperature. The irregularity in motion (Brownian motion), causes a temperature increase due to the kinetic energy produced by nano suspended particles, which results in thermophoretic force generation. The intensity produced by this force compels the fluid to move away from the stretching sheet. As a result, larger values of Nt cause an increase in temperature, due to which the surface temperature also increases.

Figure 10 describes the Schmidt number effect over temperature profile. Schmidt number physically relates the boundary-layer of mass transfer to the hydrodynamics layer. Increasing rate of the viscous diffusion keeping the mass flux constant increases the Schmidt number, which as a result decreases the heat profile, as shown in the figure.

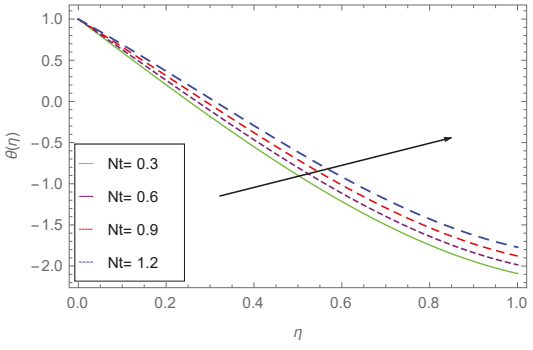

Figure 9. Impact of Nt on $\theta(\eta)$, when $Nb = 0.5, \epsilon = 0.4, \beta = 1.0, S = 0.3, Sc = 0.6, Pr = 0.5$.

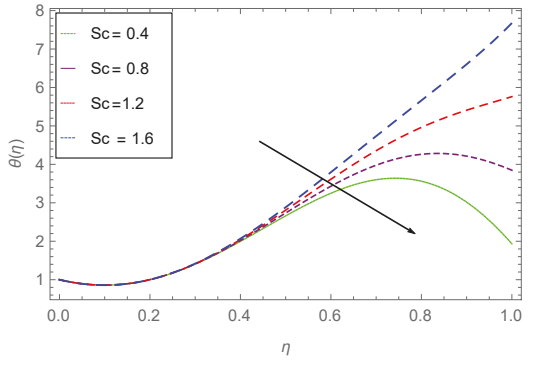

Figure 10. Impact of Sc on $\theta(\eta)$, when $Nb = 0.5, \epsilon = 0.1, \beta = 0.1, S = 0.3, Nt = 0.3, Pr = 0.6$.

The effect of Brownian motion parameter Nb on $\phi(\eta)$ is shown in Figure 11. Brownian motion is the irregular motion fluid particles. At molecular level Brownian motion of micropoler nanofluid leading the thermal conductivity of nanofluids. The figure describes an inverse relation between the concentration profile and Nb. The boundary-layer thicknesses diminishes due to an increase in Nb, which results in reducing the concentration.

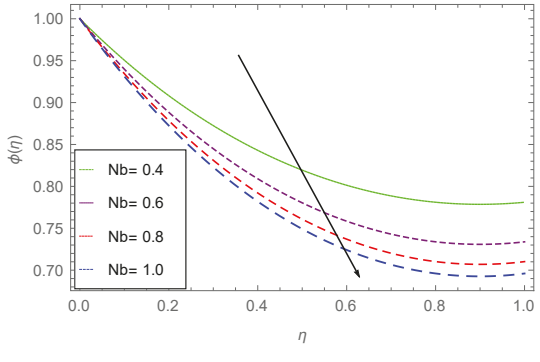

Figure 11. Impact of Nb on $\phi(\eta)$, when $Sc = 0.7, \epsilon = 0.1, \beta = 0.9, S = 0.7, Nt = 0.3, Pr = 0.6$.

Figure 12 describes the effect of thermophoresis parameter Nt on concentration field. It is clear from the figure that an increase in Nt increases the concentration field. This is because higher values of Nt increase the nanofluid molecules kinetic energy, and as a result the concentration increases.

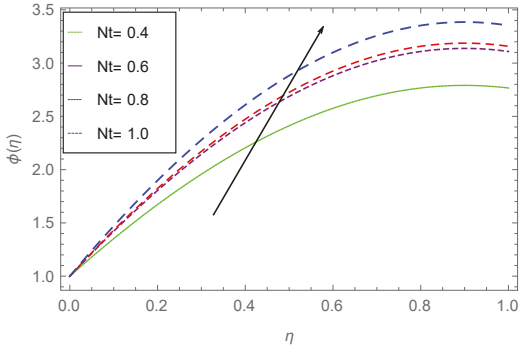

Figure 12. Impact of Nt on $\phi(\eta)$, when $Sc = 0.7, \epsilon = 0.3, \beta = 0.9, S = 0.5, Nb = 0.5, Pr = 0.6$.

The impact of Pr on ϕ is shown in Figure 13. Larger values of the Prandtl number Pr cause the concentration to falls down. The information from the figure reveals that large values of Pr cause the concentration profile to fall down. Physically, the thermal boundary-layer vanishes with greater values of Pr and as a result the concentration profile falls. The same phenomenon is observed for the heat profile.

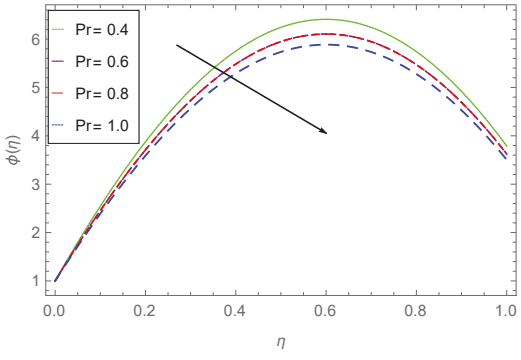

Figure 13. Impact of Pr on $\phi(\eta)$, when $Sc = 0.6, \epsilon = 0.2, \beta = 0.6, S = 0.5, Nb = 0.6, Nt = 0.6$.

Figure 14 shows the concentration profile $\phi(\eta)$ behavior, under the effect of the unsteadiness parameter S. A direct relation has been observed between the unsteadiness parameter S and $\phi(\eta)$ the concentration profile . Increasing the unsteadiness parameter S, causes an increase in the temperature to be observed, that blows the kinetic energy off the fluid, which leads to an increase in the concentration of the liquid film.

Figure 15 reveals the opposite information as discussed in the temperature distribution under different parameters. The above diagram shows that the concentration profile decreases due to an increase in Schmidt number Sc, which as a result reduces the boundary-layer thickness. This is because of the physical significance of the Schmidt number, which relates both the mass and hydrodynamic layer.

Figure 16 illustrates the effect of thin film thickness β on $\phi(\eta)$ for the different values of the embedded parameters. It is clear that the concentration profile falls with higher values of β. The same effect has been observed for β in the velocity distribution as well as in temperature distribution.

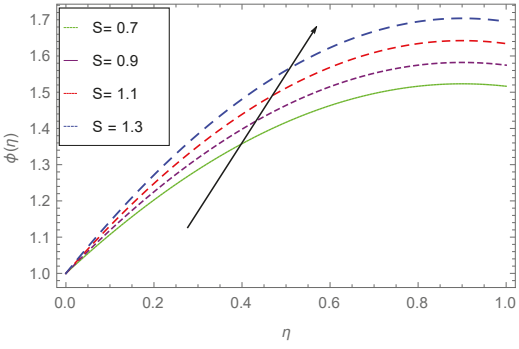

Figure 14. Impact of S on $\phi(\eta)$, when $Sc = 0.7, \epsilon = 0.8, \beta = 0.9, Pr = 0.5, Nb = 0.8, Nt = 0.4$.

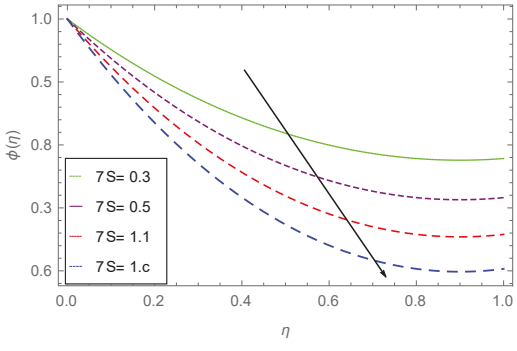

Figure 15. Impact of Sc on $\phi(\eta)$, when $S = 0.7, \epsilon = 0.8, \beta = 0.9, Pr = 0.6, Nb = 0.8, Nt = 0.4$.

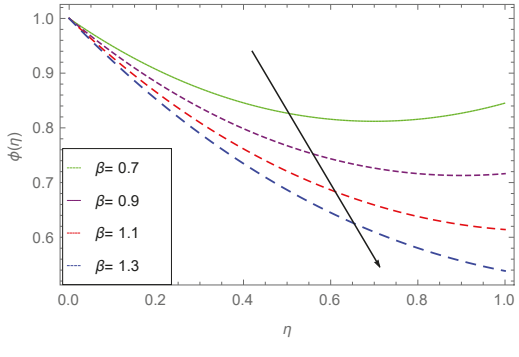

Figure 16. Impact of β on $\phi(\eta)$, when $S = 0.7, \epsilon = 0.8, Sc = 0.9, Pr = 0.6, Nb = 0.8, Nt = 0.4$.

5. Tables Discussion

Table 1 depicts the influence of Nusselt number. The effects of Nt, S, β, and Pr on $\Theta^{'}(0)$ are shown. It is clear that larger values of Nt and S decrease $\Theta^{'}(0)$, while the unsteadiness parameter S and thickness parameter β increase $\Theta^{'}(0)$. The influence of stretching parameters ϵ and λ of Reiner-Philippoff fluid and unsteadiness parameter S on skin friction C_f is presented in Table 2. It is observed that the increasing values of stretching parameters of Reiner-Philippoff fluid ϵ and λ decrease C_f, while unsteadiness parameter S increases C_f. The effects of Nb, Nt, Pr, Sc, and S on the Sherwood number $\Phi^{'}(0)$ are demonstrated in Table 3. It is observed that local Sherwood number values increases due to an increase in thermoporetic parameter Nt. Increasing values of Schmidt

number Sc decreases the Sherwood number, while increasing unsteady parameter and Prandtl number decreases the Sherwood number.

Table 1. Variation in Nusselt number with different values of the parameters Nt, Pr, β, and S.

Nt	β	S	Pr	$\Theta'(0)$
0.5	0.1	1.5	1.5	0.626541
				0.626198
				0.625771
0.1				0.625345
0.5				0.626541
1.0				0.626541
1.5	0.1			0.626541
	0.5			2.38501
	1.0			4.78618
	1.5	0.1		5.10531
		0.5		0.407137
		1.0		0.517063
		1.5	1.5	0.626541
			3.0	1.08812
			5.0	1.40251
			7.0	1.56869

Table 2. Variation in skin friction with different values of the parameters ϵ, λ, and S.

ϵ	λ	S	C_f
0.1	0.9	0.5	0.17400
0.6			0.42640
1.0			0.54710
1.8	0.95		0.11381
	0.995		0.08872
	0.9995		0.07511
	0.99995	0.5	0.06632
		1.0	1.18991
		1.5	1.981683
		2.0	2.398281

Table 3. Variation in Sherwood number with different values of the parameters Nb, Nt, Sc, S and Pr.

Nb	Nt	Sc	S	Pr	$\Phi'(0)$
0.1	0.5	1.5	1.5		−1.35820
0.5					−0.238811
1.0					−0.098888
1.5	0.1				−0.0223188
	0.5				−1.35820
	1.0				−2.75366
	1.5	0.1			−4.14542
		0.5			−1.18991
		1.0			−0.981683
		1.5	0.1		−0.398281
			0.5		−0.882057
			1.0		−1.12055
			1.5	1.5	−0.642239
				3.0	−1.21912
				5.0	−1.53875
				7.0	−1.669378

6. Conclusions

The goal of our current research is to investigate the effects of the embedded parameters on different state variables, like velocity, temperature, and the behaviour of the modeled equations under these parameters. The modeled equations are tackled with an analytical approach "homotopy analysis method" HAM. The embedded parameters and their effects are investigated and studied graphically. The motion of the suspended particles always has a great physical significance in heat transfer processes. Physically, the larger the Brownian motion parameter, the greater is the heat induction. Similar results have been observed for temperature profile with the larger values of Brownian motion. The effect of increasing values of Sc on boundary-layer thickness show a decrease in the thickness of the layer. The surface temperature increases with the increasing values of Pr, while an opposite effect is observed for unsteadiness parameter S, i.e., large values of S reduce the surface temperature. It is also observed that the temperature profile falls with large numbers of thermophoresis parameter Nt and vice versa. It is further observed that larger values of Nb reduce the mass flux, where Nt increases the mass flux. Higher values of Sc reduce the flux of mass, while it increases with increasing values of Sc. On the other hand, skin friction C_f shows a decline in its behavior with larger values of the stretching parameters ϵ and λ, while the unsteadiness parameter S increases C_f. In the solution procedure, the implemented technique convergence under the variation of physical parameters is observed numerically, which shows the reliability of our technique.

The central concluded points are as follows:

- A comparative analysis for the stretching and unsteadiness parameters for the gradient of the velocity is discussed to observe the sensitivity of these parameters.
- The temperature profile climbs up with larger values of Brownian motion parameter Nb.
- Wth larger values of S, the thermal boundary layer thickness reduces.
- Higher values of Pr increase the surface temperature, where an opposite effect is observed for unsteady parameter S, i.e., large values of S reduce the temperature of the surface.
- It is examined that the heat profile decreases with increasing values of thermophoresis parameter Nt, and increases with small numbers.
- The increasing values of Nb reduce the mass flux, where Nt increases the mass flux, while it rises with rising values of Sc.
- The effect of Prandtl number Pr on concentration and temperature profile is analyzed and a similar decline is observed in both the profiles.
- The convergence of the HAM method with the variation of the physical parameters is observed, and found its convergence more rapid as compared with other techniques.

Author Contributions: Conceptualization, S.I.; Data Curation, M.A.; Investigation, A.U., Z.S. and S.I.; Methodology, A.U., Z.S. and M.A.; Resources, A.U., Z.S. and M.A.; Software, A.U. and Z.S.; Supervision, M.A. and S.I.; Visualization, E.O.A. and M.A.; Writing–Original Draft, A.U.and Z.S.; Writing–Review and Editing, E.O.A. and S.I.

Acknowledgments: This project was funded by the Deanship of Scientific Research (DSR) at King Abdulaziz University, Jeddah. The authors, therefore, gratefully acknowledge DSR for technical and financial support.

Conflicts of Interest: The authors declare no conflict of interest.

Abbreviations

The following abbreviations and parameters with their possible dimensions stated here are used in this article:

Sh	Sherhood number
β	Film thickness parameter
Nu	Nusslet number
S	Unsteady parameter
Re	Reynold number
Pr	Prandtl number
ζ	Stretching parameter
Sc	Schmidth number
D_B	Brownian diffusion of nanofluids
$U_w(x,t)$	Stretching velocity (m/s)
Nt	Thermophoretic parameter
C_f	Skin friction coefficient
Nb	Brownian motion parameter
e_{ij}	Components of the strain rate
T	Cauchy stress tensor
T	Fluid temperature (K)
τ_{ij}	Extra stress tensor
I	Identity tensor
v	Kinematic viscosity (m^2/s)
ρ	Density (Kg/m^3)
μ	Dynamic viscosity (mPa)
c_p	Specific heat ($J\ K^{-1}\ g^{-1}\ K^{-1}$)
D_T	Thermophoretic diffusion of nanofluids
$h(t)$	Thickness of liquid
κ	Absorption coefficient
Q_w	Heat Flux (W/m^2)
Re_x	Local Reynolds number
J_w	Mass flux ($K\ g\ s^{-1}\ m^{-2}$)
f	Dimensionless velocity
∞	Condition at infinity
0	Reference condition
$\tilde{u}$	Velocity component in x-direction (m/s)
$\tilde{v}$	Velocity component in y-direction (m/s)
x,y,z	Coordinates (m)
η	Similarity variable
t	Time (s)

References

1. Bird, R.B.; Armstrong, R.C.; Hassager, O. *Dynamics of Polymeric Liquids. Volume 1: Fluid Mechanics*; John Wiley & Sons, Inc.: Hoboken, NJ, USA, 1987.
2. Sakiadis, B.C. Boundary-layer behavior on continuous solid surfaces: I. Boundary-layer equations for two-dimensional and axisymmetric flow. *AIChE J.* **1961**, *7*, 26–28. [CrossRef]
3. Crane, L.J. Flow past a stretching plate. *J. Appl. Math. Phys.* **1970**, *21*, 645–647. [CrossRef]
4. Siddiqui, A.M.; Ahmed, M.; Ghori, Q.K. Thin film flow of non-Newtonian fluids on a moving belt. *Chaos Solitons Fractals* **2007**, *33*, 1006–1016. [CrossRef]
5. Siddiqui, A.M.; Ashraf, A.; Azim, Q.A.; Babcock, B.S. Exact solutions for thin film flows of a PTT fluid down an inclined plane and on a vertically moving belt. *Adv. Stud. Theor. Phys.* **2013**, *7*, 65–87. [CrossRef]
6. Tawade, J.; Abel, M.S.; Metri, P.G.; Koti, A. Thin film flow and heat transfer over an unsteady stretching sheet with thermal radiation, internal heating in presence of external magnetic field. *Int. J. Adv. Appl. Math. Mech.* **2016**, *3*, 29–40.

7. Sajid, M.; Hayat, T.; Asghar, S. Comparison between the HAM and HPM solutions of thin film flows of non-Newtonian fluids on a moving belt. *Nonlinear Dyn.* **2007**, *50*, 27–35. [CrossRef]
8. Bakier, A.Y. Thermal radiation effect on mixed convection from vertical surfaces in saturated porous media. *Indian J. Pure Appl. Math.* **2001**, *32*, 1157–1164. [CrossRef]
9. Khan, N.; Mahmood, T. The influence of slip condition on the thin film flow of a third order fluid. *Int. J. Nonlinear Sci.* **2012**, *13*, 105–116.
10. Moradi, A.; Ahmadikia, H.; Hayat, T.; Alsaedi, A. On mixed convection—Radiation interaction about an inclined plate through a porous medium. *Int. J. Therm. Sci.* **2013**, *64*, 129–136. [CrossRef]
11. Chaudhary, S.; Singh, S.; Chaudhary, S. Thermal radiation effects on MHD boundary layer flow over an exponentially stretching surface. *Appl. Math.* **2015**, *6*, 295–303. [CrossRef]
12. Eldabe, N.T.; Elsaka, A.G.; Radwan, A.E.; Eltaweel, M.A.M. Effects of chemical reaction and heat radiation on the MHD flow of visco-elastic fluid through a porous medium over a horizontal stretching flat plate. *J. Am. Sci.* **2010**, *6*, 126–135.
13. Das, K. Effects of thermophoresis and thermal radiation on MHD mixed convective heat and mass transfer flow. *Afr. Mat.* **2013**, *24*, 511–524. [CrossRef]
14. Hsiao, K.-L. Combined electrical MHD heat transfer thermal extrusion system using Maxwell fluid with radiative and viscous dissipation effects. *Appl. Therm. Eng.* **2017**, *112*, 1281–1288. [CrossRef]
15. Hayat, T.; Sajjad, R.; Muhammad, T.; Alsaedi, A.; Ellahi, R. On MHD nonlinear stretching flow of Powell–Eyring nanomaterial. *Results Phys.* **2017**, *7*, 535–543. [CrossRef]
16. Tian, X.; Li, B.; Hu, Z. Convective stagnation point flow of a MHD non-Newtonian nanofluid towards a stretching plate. *Int. J. Heat Mass Transf.* **2018**, *127*, 768–780. [CrossRef]
17. Hsiao, K.-L. Micropolar nanofluid flow with MHD and viscous dissipation effects towards a stretching sheet with multimedia feature. *Int. J. Heat Mass Transf.* **2017**, *112*, 983–990. [CrossRef]
18. Dandapat, B.S.; Gupta, A.S. Flow and heat transfer in a viscoelastic fluid over a stretching sheet. *Int. J. Non-Linear Mech.* **1989**, *24*, 215–219. [CrossRef]
19. Wang, C. Liquid film on an unsteady stretching surface. *Quart. Appl. Math.* **1990**, *48*, 601–610. [CrossRef]
20. Usha, R.; Sridharan, R. The axisymmetric motion of a liquid film on an unsteady stretching surface. *J. Fluids Eng.* **1995**, *117*, 81–85. [CrossRef]
21. Liu, I.-C.; Andersson, H.I. Heat transfer in a liquid film on an unsteady stretching sheet. *Int. J. Therm. Sci.* **2008**, *47*, 766–772. [CrossRef]
22. Aziz, R.C.; Hashim, I.; Alomari, A.K. Thin film flow and heat transfer on an unsteady stretching sheet with internal heating. *Meccanica* **2011**, *46*, 349–357. [CrossRef]
23. Andersson, H.I.; Aarseth, J.B.; Braud, N.; Dandapat, B.S. Flow of a power-law fluid film on an unsteady stretching surface. *J. Non-Newton. Fluid Mech.* **1996**, *62*, 1–8. [CrossRef]
24. Andersson, H.I.; Aarseth, J.B.; Dandapat, B.S. Heat transfer in a liquid film on an unsteady stretching surface. *Int. J. Heat Mass Transf.* **2000**, *43*, 69–74. [CrossRef]
25. Chen, C.-H. Heat transfer in a power-law fluid film over a unsteady stretching sheet. *Heat Mass Transf.* **2003**, *39*, 791–796. [CrossRef]
26. Wang, C.; Pop, I. Analysis of the flow of a power-law fluid film on an unsteady stretching surface by means of homotopy analysis method. *J. Non-Newton. Fluid Mech.* **2006**, *138*, 161–172. [CrossRef]
27. Megahed, A.M. Effect of slip velocity on Casson thin film flow and heat transfer due to unsteady stretching sheet in presence of variable heat flux and viscous dissipation. *Appl. Math. Mech.* **2015**, *36*, 1273–1284. [CrossRef]
28. Abolbashari, M.H.; Freidoonimehr, N.; Nazari, F.; Rashidi, M.M. Analytical modeling of entropy generation for Casson nano-fluid flow induced by a stretching surface. *Adv. Powder Technol.* **2015**, *26*, 542–552. [CrossRef]
29. Qasim, M.; Khan, Z.H.; Lopez, R.J.; Khan, W.A. Heat and mass transfer in nanofluid thin film over an unsteady stretching sheet using Buongiorno's model. *Eur. Phys. J. Plus* **2016**, *131*, 16. [CrossRef]
30. Ariel, P.D. Flow of a third grade fluid through a porous flat channel. *Int. J. Eng. Sci.* **2003**, *41*, 1267–1285. [CrossRef]
31. Sahoo, B.; Poncet, S. Flow and heat transfer of a third grade fluid past an exponentially stretching sheet with partial slip boundary condition. *Int. J. Heat Mass Transf.* **2011**, *54*, 5010–5019. [CrossRef]
32. Aiyesimi, Y.M.; Okedyao, G.T.; Lawal, O.W. Unsteady MHD thin film flow of a third grade fluid with heat transfer and no slip boundary condition down an Inclined plane. *Int. J. Sci. Eng. Res.* **2013**, *4*, 420.

33. Aiyesimi, Y.M.; Okedayo, G.T.; Lawal, O.W. Effects of magnetic field on the MHD flow of a third grade fluid through inclined channel with ohmic heating. *J. Appl. Comput. Math.* **2014**, *3*, 1000153.
34. Islam, S.; Shah, R.A.; Ali, I.; Allah, N.M. Optimal homotopy asymptotic solutions of Couette and Poiseuille flows of a third grade fluid with heat transfer analysis. *Int. J. Nonlinear Sci. Numer. Simul.* **2010**, *11*, 389–400. [CrossRef]
35. Shah, R.A.; Islam, S.; Zeb, M.; Ali, I. Optimal homotopy asymptotic method for thin film flows of a third grade fluid. *J. Adv. Res. Sci. Comput.* **2011**, *3*, 1–14.
36. Makinde, O.D. Thermal criticality for a reactive gravity driven thin film flow of a third-grade fluid with adiabatic free surface down an inclined plane. *Appl. Math. Mech.* **2009**, *30*, 373–380. [CrossRef]
37. Yao, Y.; Liu, Y. Some unsteady flows of a second grade fluid over a plane wall. *Nonlinear Anal. Real World Appl.* **2010**, *11*, 4442–4450. [CrossRef]
38. Erdoğan, M.E.; Imrak, C.E. On some unsteady flows of a non-Newtonian fluid. *Appl. Math. Model.* **2007**, *31*, 170–180. [CrossRef]
39. Abdulhameed, M.; Khan, I.; Vieru, D.; Shafie, S. Exact solutions for unsteady flow of second grade fluid generated by oscillating wall with transpiration. *Appl. Math. Mech.* **2014**, *35*, 821–830. [CrossRef]
40. Nuttall, H. The flow of a viscous incompressible fluid in an inclined uniform channel, with reference to the flow on a transporter belt. *Int. J. Eng. Sci.* **1966**, *4*, 249–276. [CrossRef]
41. He, J.-H. Variational principle for nano thin film lubrication. *Int. J. Nonlinear Sci. Numer. Simul.* **2003**, *4*, 313–314. [CrossRef]
42. He, J.-H. Variational principles for some nonlinear partial differential equations with variable coefficients. *Chaos Solitons Fractals* **2004**, *19*, 847–851. [CrossRef]
43. Hao, T.-H. Application of the Lagrange multiplier method the semi-inverse method to the search for generalized variational principle in quantum mechanics. *Int. J. Nonlinear Sci. Numer. Simul.* **2003**, *4*, 311–312. [CrossRef]
44. Liu, H.-M. Variational approach to nonlinear electrochemical system. *Int. J. Nonlinear Sci. Numer. Simul.* **2004**, *5*, 95–96. [CrossRef]
45. Liu, H.-M. Generalized variational principles for ion acoustic plasma waves by He's semi-inverse method. *Chaos Solitons Fractals* **2005**, *23*, 573–576. [CrossRef]
46. Kapitza, P.L.; Kapitza, S.P. Wave flow of thin layers of viscous liquids. Part III. Experimental research of a wave flow regime. *Zhurnal Eksperimental'noi i Teoreticheskoi Fiziki* **1949**, *19*, 105–120.
47. Yih, C.-S. Stability of liquid flow down an inclined plane. *Phys. Fluids* **1963**, *6*, 321–334. [CrossRef]
48. Krishna, M.V.G.; Lin, S.P. Nonlinear stability of a viscous film with respect to three-dimensional side-band disturbances. *Phys. Fluids* **1977**, *20*, 1039–1044. [CrossRef]
49. Andersson, H.; Dahl, E.N. Gravity-driven flow of a viscoelastic liquid film along a vertical wall. *J. Phys. D Appl. Phys.* **1999**, *32*, 1557. [CrossRef]
50. Cheng, P.-J.; Lai, H.-Y.; Chen, C.-K. Stability analysis of thin viscoelastic liquid film flowing down on a vertical wall. *J. Phys. D Appl. Phys.* **2000**, *33*, 1674. [CrossRef]
51. Chen, X.; Dai, W.; Wu, T.; Luo, W.; Yang, J.; Jiang, W.; Wang, L. Thin film thermoelectric materials: Classification, characterization, and potential for wearable applications. *Coatings* **2018**, *8*, 244. [CrossRef]
52. Yamamuro, H.; Hatsuta, N.; Wachi, M.; Takei, Y.; Takashiri, M. Combination of electrodeposition and transfer processes for flexible thin-film thermoelectric generators. *Coatings* **2018**, *8*, 22. [CrossRef]
53. Khan, Z.; Shah, R.A.; Islam, S.; Jan, H.; Jan, B.; Rasheed, H.U.; Khan, A. MHD flow and heat transfer analysis in the wire coating process using elastic-vViscous. *Coatings* **2017**, *7*, 15. [CrossRef]
54. Naghdi, S.; Rhee, K.; Hui, D.; Park, S. A review of conductive metal nanomaterials as conductive, transparent, and flexible coatings, thin films, and conductive fillers: Different deposition methods and applications. *Coatings* **2018**, *8*, 278. [CrossRef]
55. Radwan, A.B.; Abdullah, A.M.; Mohamed, A.M.A.; Al-Maadeed, M.A. New electrospun polystyrene/Al_2O_3 nanocomposite superhydrophobic coatings; synthesis, characterization, and application. *Coatings* **2018**, *8*, 65. [CrossRef]
56. Osiac, M. The electrical and structural properties of nitrogen $Ge_1Sb_2Te_4$ thin film. *Coatings* **2018**, *8*, 117. [CrossRef]

57. Deshpande, A.P. Oscillatory shear rheology for probing nonlinear viscoelasticity of complex fluids: Large amplitude oscillatory shear. In *Rheology of Complex Fluids*; Krishnan, J.M., Deshpande, A.P., Sunil Kumar, P.B., Eds.; Springer: New York, NY, USA, 2010; pp. 87–110.
58. Kapur, J.; Gupta, R. Two dimensional flow of Reiner-Philippoff fluids in the inlet length of a straight channel. *Appl. Sci. Res. Sect. A* **1965**, *14*, 13–24. [CrossRef]
59. Na, T.-Y. Boundary layer flow of Reiner-Philippoff fluids. *Int. J. Non-Linear Mech.* **1994**, *29*, 871–877. [CrossRef]
60. Yam, K.S.; Harris, S.D.; Ingham, D.B.; Pop, I. Boundary-layer flow of Reiner–Philippoff fluids past a stretching wedge. *Int. J. Non-Linear Mech.* **2009**, *44*, 1056–1062. [CrossRef]
61. Patel, V.; Timol, M.G. Similarity solutions of the three dimensional boundary layer equations of a class of general non-Newtonian fluids. *Int. J. Appl. Math. Mech.* **2012**, *8*, 77–88.
62. Ahmad, A. Flow of ReinerPhilippoff based nano-fluid past a stretching sheet. *J. Mol. Liq.* **2016**, *219*, 643–646. [CrossRef]
63. Ahmad, A.; Qasim, M.; Ahmed, S. Flow of reiner–Philippoff fluid over a stretching sheet with variable thickness. *J. Braz. Soc. Mech. Sci. Eng.* **2017**, *39*, 4469–4473. [CrossRef]
64. Cole, J.D. *Perturbation Methods in Applied Mathematics*; Blaisdell Publ.: Walttham, MA, USA, 1968, p. 267.
65. He, J.-H. The homotopy perturbation method for nonlinear oscillators with discontinuities. *Appl. Math. Comput.* **2004**, *151*, 287–292. [CrossRef]
66. Lyapunov, A.M. The general problem of the stability of motion. *Int. J. Control* **1992**, *55*, 531–534. [CrossRef]
67. Adomian, G. *Solving Frontier Problems of Physics: The Decomposition Methodkluwer*; Springer: Boston, MA, USA, 1994.
68. Liao, S.-J. An explicit, totally analytic approximate solution for Blasius' viscous flow problems *Int. J. Non-Linear Mech.* **1999**, *34*, 759–778.
69. Liao, S.-J. A simple approach of enlarging convergence regions of perturbation approximations. *Nonlinear Dyn.* **1999**, *19*, 93–111. [CrossRef]
70. Liao, S.J. A uniformly valid analytic solution of two-dimensional viscous flow over a semi-infinite flat plate. *J. Fluid Mech.* **1999**, *385*, 101–128. [CrossRef]
71. Liao, S.J. The Proposed Homotopy Analysis Technique for the Solution Of Nonlinear Problems. Ph.D. Thesis, Shanghai Jiao Tong University, Shanghai, China, 1992.
72. Khan, A.S.; Nie, Y.; Shah, Z.; Dawar, A.; Khan, W.; Islam, S. Three-dimensional nanofluid flow with heat and mass transfer analysis over a linear stretching surface with convective boundary conditions. *Appl. Sci.* **2018**, *8*, 2244. [CrossRef]
73. Shah, Z.; Islam, S.; Ayaz, H.; Khan, S. Radiative heat and mass transfer analysis of micropolar nanofluid flow of casson fluid between two rotating parallel plates with effects of Hall current. *J. Heat Transf.* **2018**, *141*, 022401. [CrossRef]
74. Philippoff, W. Zur Theorie der Strukturviskosität. I. *Kolloid-Zeitschrift* **1935**, *71*, 1–16. [CrossRef]
75. Khan, N.S.; Zuhra, S.; Shah, Z.; Bonyah, E.; Khan, W.; Islam, S. Slip flow of Eyring-Powell nanoliquid film containing graphene nanoparticles. *AIP Adv.* **2018**, *8*, 115302. [CrossRef]
76. Nasir, S.; Islam, S.; Gul, T.; Shah, Z.; Khan, M.A.; Khan, W.; Khan, A.Z.; Khan, S. Three-dimensional rotating flow of MHD single wall carbon nanotubes over a stretching sheet in presence of thermal radiation. *Appl. Nanosci.* **2018**, *8*, 1361–1378. [CrossRef]
77. Shah, Z.; Islam, S.; Gul, T.; Bonyah, E.; Khan, M.A. The electrical MHD and hall current impact on micropolar nanofluid flow between rotating parallel plates. *Results Phys.* **2018**, *9*, 1201–1214. [CrossRef]
78. Jawad, M.; Shah, Z.; Islam, S.; Bonyah, E.; Khan, A.Z. Darcy-Forchheimer flow of MHD nanofluid thin film flow with Joule dissipation and Navier's partial slip. *J. Phys. Commun.* **2018**, *2*, 115014. [CrossRef]

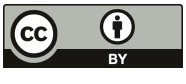

coatings

MDPI

Article

Thin Film Flow of Micropolar Fluid in a Permeable Medium

Vakkar Ali [1], Taza Gul [2], Shakeela Afridi [2], Farhad Ali [2], Sayer Obaid Alharbi [3] and Ilyas Khan [4,*]

[1] Department of Mechanical and Industrial Engineering, Majmaah University, Al Majmaah 11952, Saudi Arabia; w.ahmad@mu.edu.sa
[2] Department of mathematics, City University of Science and Information Technology (CUSIT), Peshawar 25000, Pakistan; tazatazagul@cusit.edu.pk (T.G.); shakeelaafridi@gmail.com (S.A.); farhadaliecomaths@yahoo.com (F.A.)
[3] Department of Mathematics, College of Science Al-Zulfi, Majmaah University, Al-Majmaah 11952, Saudi Arabia; so.alharbi@mu.edu.sa
[4] Faculty of Mathematics and Statistics, Ton Duc Thang University, Ho Chi Minh City, Vietnam
* Correspondence: ilyaskhan@tdt.edu.vn

Received: 9 November 2018; Accepted: 14 January 2019; Published: 6 February 2019

Abstract: The thin film flow of micropolar fluid in a porous medium under the influence of thermophoresis with the heat effect past a stretching plate is analyzed. Micropolar fluid is assumed as a base fluid and the plate is considered to move with a linear velocity and subject to the variation of the reference temperature and concentration. The latitude of flow is limited to being two-dimensional and is steadily affected by sensitive fluid film size with the effect of thermal radiation. The basic equations of fluid flow are changed through the similarity variables into a set of nonlinear coupled differential equations with physical conditions. The suitable transformations for the energy equation is used and the non-dimensional form of the temperature field are different from the published work. The problem is solved by using Homotopy Analysis Method (HAM). The effects of radiation parameter R, vortex-viscosity parameter Δ, permeability parameter Mr, microrotation parameter Gr, Soret number Sr, thermophoretic parameter τ, inertia parameter Nr, Schmidt number Sc, and Prandtl number Pr are shown graphically and discussed.

Keywords: thin film of micropolar fluid; porous medium; thermophoresis; thermal radiation; skin friction; Nusselt number and Sherwood number; variable thickness of the liquid film; HAM

1. Introduction

Fluids, generally, have a major role in many problems related to industrial and engineering applications like crystal growing, glass blowing, polymer extrusion processes, metallurgical processes, and so on. In the extrusion process, the heated liquid stretching into a cooling system, as well as the phenomenon in which the tiny sized particles are transferred from a hot surface to a cool surface, is called thermophoresis. In gasses, tiny particles like dust exert force parallel to the temperature gradient called thermophoretic force, and the motion gained by these particles is known as thermophoretic velocity. In thermophoresis, tiny particles are transferred towards cold surfaces, whereas hot surface particles also resist taking place and, as a result, a particle free layer is observed around the hot surface, as analyzed by Goldsmith and May [1]. The most important application of this phenomenon is to remove tiny particles from the path of gas particles used in turbine blades. The same phenomenon was used by Goren [2] in the study of aerosol particles, and this idea was extended by Jayaraj et al. [3] in the natural convection. The idea of mass transfer in this phenomenon was investigated by Selim et al. [4]. They analyzed the effects of physical parameters involved in the model. Chamka et al. [5,6] observed the thermophoresis effect in free convection boundary layer flow over

the permeable wall. Das [7] studied variable fluid properties with slip boundary conditions. Flow in porous media is highly important in enhanced oil recovery, geothermal energy extraction, insulation of buildings, food processing, heat storage beds, composite manufacturing, and the coating of paper and textile processes. Porous media flow describes different practical and engineering applications like oil or gaseous movement, liquid in the oil reservoir or gaseous field, the purification process of oil, gaseous wells, drilling, and the processing of carbon made substances and cosmetic material.

Generally, the study of non-Newtonian fluid flow in two- and three-dimensional problems is a tough job because of its high nonlinearity and, especially, the addition of extra terminologies such as magnetic field, porous medium, thermophoretic term, dissipation term, and so on. Despite these difficulties, efforts are being made by the researchers to solve such problems. The idea of viscous dissipation and permeable media was introduced by Al-Hadrami et al. [8]. In another paper, Al-Hadrami et al. [9] studied the combined problem of convection for both forced and free convection through a permeable channel. The micropolar fluids in two and three dimensions belong to the non-Newtonian fluids explained by Łukaszewicz [10] in his book. It is pointed out that the Navier-Stokes equation is not sufficient to handle the Cauchy stress tensor of micropolar fluid and, therefore, this fluid belongs to non-Newtonian fluids. Aouadi [11] presented a numerical solution for micropolar liquid flow over a stretched plate. The flow of second grade fluid with heat flux over a stretching surface is described in the studies of Chauhan and Olkha [12] and Cortell [13]. Dandapat and Gupta [14] observed the allied problem over a stretching sheet with some modification. The time-dependent motion of second order liquid in partially filled porous media was explored by Chuhan and Kumar [15]. Khan and Shafie [16] studied the generalized Burger's fluid including rotation in a porous medium. They observed effects of embedded parameters related to the model. Micropolar fluid is one of the important sub-class of non-Newtonian fluid. Studies related to micropolar fluids with various physical configurations with thermal radiation were presented by Abo-Eldahab and Ghonaim [17], Rashidi et al. [18,19], Heydari et al. [20], and Tripathy et al. [21]. The idea of heat and mass transfer mechanisms were described by the researchers to study the impact of various embedded parameters on the nanoparticle volume fraction. Rahman and Sattar [22] and Bakr [23] have studied the heat and mass transfer flow of micropolar fluid using the oscillatory boundary conditions. Ramzan et al. [24] have examined the Buoyancy impacts on the heat and mass transfer flow of the micropolar fluid with double stratification. Srinivasacharya and Ramreddy [25] have inspected the heat and mass transfer in micropolar fluid with thermal and mass stratification.

Recently, thin film flow has been an important subject of research. Thin film fluid is used for making different heat exchangers and tools in chemical techniques, and these applications require complete comprehension on the motion procedure. The applications comprise wire and fiber coating, polymer preparing, and so on. This motion is attached to manufacturing various types of sheets, either metallic or plastic. The quality of the final product is related to heat and mass transport and the rate of stretching. An analysis of heat transfer in Williamson nanofluid flow was conducted by Nadeem and Hussain [26] and Khan et al. [27]. Aziz et al. [28] studied heat transfer through thin film flow on an unsteady stretching sheet with internal heating. Qasim et al. [29] and Tawade et al. [30] discussed the flow of thin film using different fluids and geometries. Khan et al. [31] and Mahmood and Khan [32] investigated the effects of different variables on different fluids in their flow. According to our knowledge, there is no published work related to thermophoresis on heat transfer and thermal radiation characteristics of thin film micropolar liquid on the stretched plate under the transformations used in this research. Therefore, we have shown our interest in this paper to make an effort in discussing this new case. In this manuscript, exploration of the behavior of a steady, laminar, and two-dimensional flow of an incompressible micropolar fluid thin film into a porous medium past a stretched sheet was examined. Further, the inclusion of thermal radiation in the equation of energy is always used as a special case and, in most of the problems in the existing literature, the energy equation is used without radiation. In the papers cited above [17–20], the non-dimensional energy equation is written as $(3R + 4)\theta'' + 3R\ Pr\ f\theta' = 0$, in which R is revealed as the radiation term. Clearly, if R becomes

zero, then the energy equation is reduced to θ″ = 0, that is, the key parameter *Pr* and momentum boundary layer vanish and, therefore, the energy equation becomes meaningless. Therefore, we have tried to avoid this situation by using a transformation that is the same as in the works of [27,29,32] for the same problem as cited in the literature [17–20] with the addition of concentration. In recent research, most researchers used homotopy analysis method (HAM) to solve higher order nonlinear problems, and credit goes to Liao [33–35], who investigated such a wonderful technique to solve nonlinear higher order differential equations. Gul et al. [36,37] used the HAM method for the suitable range of parameters. Analytical solutions in series form are calculated using HAM. The effects of all parameters on velocity, microrotation, temperature, and concentration fields are shown graphically.

2. Mathematical Formulation

Consider the thin film micropolar fluid flow on a stretched plate, which is being stretched with a linear velocity $U_w = ax$. Here, $a > 0$ is a constant and shows the stretching rate and x displays the direction of the flow. The thickness δ of the thin film is chosen uniform and the medium is considered porous, as displayed in Figure 1. The stretching plate is kept at temperature T_w and concentration C_w. The temperature $T_w = T_0 - T_{ref}\left(\frac{U_w x}{2v}\right)$ and concentration $C_w = C_0 - C_{ref}\left(\frac{U_w x}{2v}\right)$ on the surface are assumed to vary with distance x from the plate. T_0 and C_0 are the temperature and concentration at the plate, while T_{ref} and C_{ref} are the constant reference temperature and concentration. Further, it is assumed that the liquid film is gripping and releasing radiation. The radiate heat flux is considered along the x-axis, while neglecting along the y-axis.

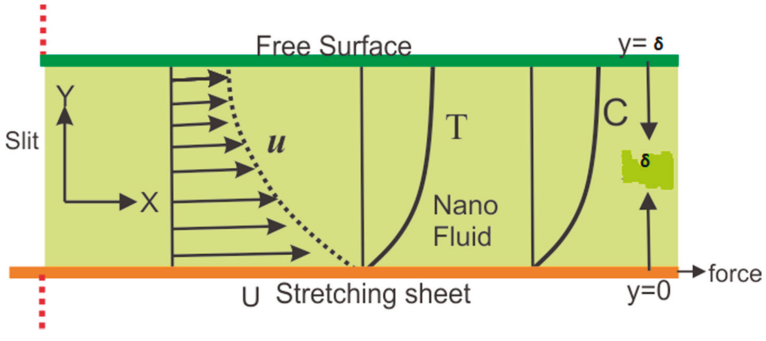

Figure 1. Physical geometry of the problem.

The basic flow equations of our proposed model are as follows:

$$u_x + v_y = 0 \tag{1}$$

$$uu_x + vu_y = vu_{xx} + k_c\sigma_y + \frac{v\varphi}{K}(U - u) + C_r\varphi(U^2 - u^2) \tag{2}$$

$$G_1\sigma_{yy} - 2\sigma - u_y = 0 \tag{3}$$

$$\rho c_p\left(uT_x + vT_y\right) = kT_{yy} - (q_r)_y \tag{4}$$

$$uC_x + vC_y = D_m C_{yy} + \frac{D_m k_T}{T_m}T_{yy} - (V_T C)_y \tag{5}$$

The modeled boundary conditions for the two-dimensional liquid film are as follows:

$$u = U_w = ax,\ v = 0,\ \sigma = 0,\ T = T_w,\ C = C_w \text{at} y = 0, \tag{6}$$

$$u_y = T_y = \sigma_y = C_y = 0,\ v = \delta_x, \text{at} y = \delta. \tag{7}$$

The Rosseland approximation is defined as follows:

$$q_r = -\frac{4\sigma^*}{3k^*}\partial_y T^4 \tag{8}$$

where q_r is radiative heat flux, σ^* is Stefan–Boltzman constant, and k^* represents the mean absorption coefficient. The flux is assumed to be small, such that T_1^5 and higher terms are ignored, as in the existing literature. After expanding by Taylor's series, T^4 is reduced to the following form:

$$T^4 = 4T_1^3 T - 3T_1^4 \tag{9}$$

T_1 is used as the temperature at the free surface. Using Equations (8) and (9), Equation (4) is reduced as follows:

$$uT_x + vT_y = \frac{k}{\rho c_p}T_{yy} + \frac{16\sigma^* T_1^3}{3\rho c_p k^*}T_{yy} \tag{10}$$

Abo-Eldahab and Ghonaim [17], Rashidi et al. [18,19] and Heydari et al. [20] introduced the following transformations:

$$\psi(x,y) = (2vU_w x)^{\frac{1}{2}} f(\eta),\ \sigma = \left(\frac{U_w}{2vx}\right)^{\frac{1}{2}} U_w g(\eta),\ \eta = \left(\frac{U_w}{2vx}\right)^{\frac{1}{2}} y,\ u_x = \psi_y \text{ and } u_y = -\psi_x \tag{11}$$

In the recent research of Khan [27] and Qasim et al. [29], the thin film flows are modeled using reference temperature and concentration for steady and unsteady problems, respectively.

$$T = T_0 - T_{ref}\left(\frac{U_w x}{2v}\right)\theta(\eta),\ C = C_0 - C_{ref}\left(\frac{U_w x}{2v}\right)\theta(\eta) \tag{12}$$

where T_0 is temperature at the stretched surface and T_{ref} is used as a constant reference temperature, such that $0 \le T_{ref} \le T_0$. Similarly, C_0 is the concentration at the stretched surface and C_{ref} is used as a constant reference concentration, such that $0 \le C_{ref} \le C_0$. Substituting Equations (11) and (12) into Equations (1)–(7), the basic governing equations of velocity, velocity rotation, and temperature with boundary conditions yield the following forms:

$$f''' + ff'' + \Delta g' + \frac{1}{Mr}(1 - f') + Nr\left(1 - (f')^2\right) = 0 \tag{13}$$

$$Gr\, g'' - 2(2g + f'') = 0 \tag{14}$$

$$\left(1 + \frac{4}{3}R\right)\theta'' - Pr(2\theta f' - f\,\theta') = 0 \tag{15}$$

$$\phi'' + Sc(Sr - \tau\phi)\theta'' + Sr(f - \tau\theta')\phi' - 2Sc\phi\, f' = 0 \tag{16}$$

$$f(0) = g(0) = 0,\ f'(0) = \theta(0) = \phi(0) = 1 \tag{17}$$

$$f''(\beta) = f(\beta) = g'(\beta) = \theta'(\beta) = \phi'(\beta) = 0 \tag{18}$$

where f is a dimensionless velocity function and g is a dimensionless microrotation angular velocity function, θ is the temperature function, ϕ is the concentration function, β is the non-dimensional thickness of the liquid film, $\Delta = \frac{k_1}{v}$ is the vortex–viscosity parameter, $Mr = \frac{Ka}{2\phi v}$ is the permeability parameter, $Nr = \frac{2\phi C_r U_w}{a}$ is the inertia coefficient parameter, $Gr = \frac{G_1 a}{v}$ represents the microrotation parameter, $Pr = \frac{\rho v c_p}{k}$ represents the Prandtl number, $R = \frac{4\sigma^* T_1^3}{k^* k}$ represents the radiation parameter, $Sc = \frac{v}{D_m}$ represents the Schmidt number, $Sr = \frac{D_m k_T (T_w - T_0)}{v T_m (C_w - C_0)}$ represents the Soret number, and $\tau = \frac{kU_w^2}{2va}$ is the thermophoretic parameter and is same as in the works of [17–20].

The important physical quantities are skin friction coefficient C_f, local Nusselt number Nu, and Sherwood number, which are defined as follows:

$$C_f = \frac{\mu(u_y)_{y=0}}{\frac{1}{2}\rho U_w^2}, Nu = \frac{-k(T_y)_{y=0}x}{k(T_w - T_0)}, Sh = \frac{-D_m(C_y)_{y=0}x}{D_m(C_w - C_0)}.$$

where $\mu(u_y)_{y=0}$, $-k(T_y)_{y=0}$, and $-D_m(C_y)_{y=0}$ are shear stress, heat, and mass fluxes at the surface, respectively. Using the variables in (11), the expressions for dimensionless skin friction, Nusselt number, and Sherwood number are obtained as follows:

$$C_f\left(\frac{\mathrm{Re}}{2}\right)^{\frac{1}{2}} = -f''(0), Nu\left(\frac{\mathrm{Re}}{2}\right)^{-\frac{3}{2}} = -\theta'(0), Sh\left(\frac{\mathrm{Re}}{2}\right)^{-\frac{3}{2}} = -\phi'(0) \tag{19}$$

Here, $\mathrm{Re} = \frac{U_w x}{v}$ represents the Reynold number based on the stretching velocity. The calculated values for the skin friction coefficient and local Nusselt number are shown in Tables 1–3.

Table 1. Values for the skin friction coefficient, when $h = -0.2, Mr = Gr = 0.8, Nr = R = \Delta = Sc = Sr = \tau = Pr = 0.3, \beta = 1$.

Δ	Mr	Nr	$-f''(0)$
0.3	0.8	0.3	1.36594
0.4	0.8	0.3	1.36571
0.5	0.8	0.3	1.36547
0.3	0.8	0.3	1.36594
0.3	0.9	0.3	1.24938
0.3	1.0	0.3	1.15533
0.3	0.8	0.3	1.36594
0.3	0.8	0.4	1.45338
0.3	0.8	0.5	1.54067

Table 2. Values of rate of heat transfer or the local Nusselt number, when $h = -0.2, Mr = Gr = 0.8, Nr = R = \Delta = Sc = Sr = \tau = Pr = 0.3, \beta = 1$.

R	Pr	$-\theta'(0)$
0.3	0.3	0.246741
0.4	0.3	0.240841
0.5	0.3	0.235105
0.3	0.3	0.246741
0.3	0.4	0.325885
0.3	0.5	0.403524

Table 3. Values of the Sherwood number, when $h = -0.2, Mr = Gr = 0.8, Nr = R = \Delta = Sc = Sr = \tau = Pr = 0.3, \beta = 1$.

Sc	Sr	τ	$-\phi'(0)$
0.3	0.3	0.3	0.265463
0.4	0.3	0.3	0.350588
0.5	0.3	0.3	0.434081
0.3	0.3	0.3	0.265463
0.3	0.4	0.3	0.264059
0.3	0.5	0.3	0.262655
0.3	0.3	0.3	0.265463
0.3	0.3	0.4	0.266868
0.3	0.3	0.5	0.268272

3. Solution Methodology

3.1. Homotopy Analysis Method

The solutions of Equations (13)–(16) with the related boundary conditions (17) and (18) are achieved using HAM. Consider that initial guesses on $f(\eta)$, $g(\eta)$, $\theta(\eta)$, and $\phi(\eta)$ satisfying the boundary conditions at $\eta = 0$ are as follows:

$$f_0(\eta) = \frac{\eta^3}{2\beta^2} - \frac{3\eta^2}{2\beta} + \eta,\ g_0(\eta) = 0, \theta_0(\eta) = 1,\ \phi_0(\eta) = 1 \tag{20}$$

The linear operators for the given functions are the following:

$$L_f(f) = f^{(iv)},\ L_g(g) = g'',\ L_\theta(\theta) = \theta'',\ L_\phi(\phi) = \phi''. \tag{21}$$

satisfying the following properties:

$$L_f\left(a_1 + a_2\eta + a_3\eta^2 + a_4\eta^3\right) = 0,\ L_g(a_5 + a_6\eta) = 0,\ L_\theta(a_7 + a_8\eta) = 0, L_\phi(a_9 + a_{10}\eta) = 0 \tag{22}$$

where $a_i (i = 1 - 10)$ are constants related to the general solution.

The corresponding nonlinear operators are as follows:

$$\begin{aligned} N_f[f(\eta;q), g(\eta;q)] = \quad & f_{\eta\eta\eta}(\eta;q) + f(\eta;q) f_{\eta\eta}(\eta;q) + \Delta g_\eta(\eta;q) \\ & + \tfrac{1}{Mr}(1 - f_\eta(\eta;q)) + Nr\left(1 - (f_\eta(\eta;q))^2\right), \end{aligned} \tag{23}$$

$$N_g[f(\eta;q), g(\eta;q)] = Gr g_{\eta\eta}(\eta;q) - 2(2g(\eta;q) + f_{\eta\eta}(\eta;q)) = 0, \tag{24}$$

$$N_\theta[f(\eta;q), \theta(\eta;q)] = \left(1 + \frac{4}{3}R\right)\theta_{\eta\eta}(\eta;q) - Pr(2\theta(\eta;q)\, f_\eta(\eta;q) - f(\eta;q)\theta_\eta(\eta;q)), \tag{25}$$

$$\begin{aligned} N_\phi[f(\eta;q), \theta(\eta;q), \phi(\eta;q)] = \phi_{\eta\eta}(\eta;q) + Sc(Sr - \tau\phi(\eta;q))\, \theta_{\eta\eta}(\eta;q) + \\ Sr(f - \tau\theta_\eta(\eta;q))\phi_\eta(\eta;q) - 2Sc\phi(\eta;q) f_\eta(\eta;q) = 0. \end{aligned} \tag{26}$$

(a) Zeroth-Order Deformation Problem

The main idea of HAM is explained in Equations (19)–(22). We formulate the zeroth-order problem from Equations (13)–(16) as follows:

$$(1 - q)L_f\{f(\eta;q) - f_0(\eta)\} = q h_f N_f\{f(\eta;q), g(\eta;q)\}, \tag{27}$$

$$(1 - q)L_g\{g(\eta;q) - g_0(\eta)\} = q h_g N_g\{f(\eta;q), g(\eta;q)\}, \tag{28}$$

$$(1 - q)L_\theta\{\theta(\eta;q) - \theta_0(\eta)\} = q h_\theta N_\theta\{f(\eta;q), \theta(\eta;q)\}, \tag{29}$$

$$(1 - q)L_\phi\{\phi(\eta;q) - \phi_0(\eta)\} = q h_\phi N_\phi\{f(\eta;q), g(\eta;q), \theta(\eta;q), \phi(\eta;q)\}, \tag{30}$$

Expanding the functions f, g, θ and ϕ by Taylor's series when $q = 0$, we have the following:

$$\begin{aligned} f(\eta;q) &= f_0(\eta) + \sum_{w=1}^{\infty} f_w(\eta)\, q^w, \\ g(\eta;q) &= g_0(\eta) + \sum_{w=1}^{\infty} g_w(\eta)\, q^w, \\ \theta(\eta;q) &= \theta_0(\eta) + \sum_{w=1}^{\infty} \theta_w(\eta)\, q^w, \\ \phi(\eta;q) &= \phi_0(\eta) + \sum_{w=1}^{\infty} \phi_w(\eta)\, q^w. \end{aligned} \tag{31}$$

where

$$f_w(\eta) = \frac{1}{w!} f_\eta^w(\eta;q)|_{q=0},\ g_w(\eta) = \frac{1}{w!} g_\eta^w(\eta;q)|_{q=0},$$
$$\theta_w(\eta) = \frac{1}{w!} \theta_\eta^w(\eta;q)|_{q=0}, \phi_w(\eta) = \frac{1}{w!} \phi_\eta^w(\eta;q)|_{q=0}. \tag{32}$$

The supporting constraints h_f, h_g, h_θ, and h_ϕ are taken such that series (33) converges at $q = 1$. Substituting $q = 1$ in (33) we get the following:

$$f(\eta) = f_0(\eta) + \sum_{w=1}^{\infty} f_w(\eta), \tag{33}$$

$$g(\eta) = g_0(\eta) + \sum_{w=1}^{\infty} g_w(\eta), \tag{34}$$

$$\theta(\eta) = \theta_0(\eta) + \sum_{w=1}^{\infty} \theta_w(\eta), \tag{35}$$

$$\phi(\eta) = \phi_0(\eta) + \sum_{w=1}^{\infty} \phi_w(\eta). \tag{36}$$

(b) w^{th} Order Deformation Problem

The following equations are satisfied by the problem of the w^{th} order.

$$L_f[f_w(\eta) - \chi_w f_{w-1}(\eta)] = h_f\ R_w^f(\eta), \tag{37}$$

$$L_g[g_w(\eta) - \chi_w g_{w-1}(\eta)] = h_g\ R_w^g(\eta), \tag{38}$$

$$L_\theta[\theta_w(\eta) - \chi_w \theta_{w-1}(\eta)] = h_\theta\ R_w^\theta(\eta), \tag{39}$$

$$L_\phi[\phi_w(\eta) - \chi_w \phi_{w-1}(\eta)] = h_\phi\ R_w^\phi(\eta). \tag{40}$$

where

$$\chi_w = \begin{cases} 0, \text{ if } q \leq 1 \\ 1, \text{ if } q > 1 \end{cases}$$

3.2. Numerical Solution

The numerical (ND solve) solution of Equations (13)–(16) with boundary conditions (17) and (18) for different values of embedded parameters are calculated and compared with HAM in Tables 4–7.

Table 4. Comparison of HAM and numerical solution for velocity when $h = -0.001, Pr = 10.6, Nr = R = Sc = Sr = \tau = \Delta = 0.5, Gr = \beta = Mr = 1$.

η	HAM Solution of $f'(\eta)$	Numerical Solution	Absolute Error
0	5.09×10^{-22}	0.000000	5.09×10^{-22}
0.1	0.099999	0.100043	4.3×10^{-5}
0.2	0.199999	0.200168	1.6×10^{-4}
0.3	0.299999	0.300364	3.6×10^{-4}
0.4	0.399999	0.400624	6.2×10^{-4}
0.5	0.499999	0.500937	9.3×10^{-4}
0.6	0.599999	0.601295	1.2×10^{-3}
0.7	0.699999	0.701689	1.6×10^{-3}
0.8	0.799999	0.802110	2.1×10^{-3}
0.9	0.899999	0.902549	2.5×10^{-3}
1	0.999999	1.002997	2.9×10^{-3}

Table 5. Comparison of HAM and numerical solution for microrotation angular velocity when $h = -0.15, Nr = R = \Delta = Sc = Sr = \tau = 0.5, Mr = \beta = 1, Gr = 5, Pr = 10.6$.

η	HAM Solution of $g(\eta)$	Numerical Solution	Absolute Error
0	−1.28767269	−0.0000000	1.2×10^{-8}
0.1	−0.0094987	−0.0088208	6.7×10^{-4}
0.2	−0.0167880	−0.0157937	9.9×10^{-4}
0.3	−0.0221826	−0.0211439	1.2×10^{-3}
0.4	−0.0259819	−0.0250914	8.9×10^{-4}
0.5	−0.0284720	−0.0278531	6.1×10^{-3}
0.6	−0.0299279	−0.0296435	2.8×10^{-4}
0.7	−0.0306156	−0.0306741	5.8×10^{-5}
0.8	−0.0307942	−0.0311543	3.6×10^{-4}
0.9	−0.0307176	−0.0312916	5.7×10^{-4}
1	−0.0306366	−0.0312919	6.5×10^{-4}

Table 6. Comparison of HAM and numerical solutions for temperature when $h = -0.33, Nr = R = \Delta = Sc = Sr = \tau = 0.5, Mr = \beta = 1, Gr = 5, Pr = 10.6$.

η	HAM Solution of $\theta(\eta)$	Numerical Solution	Absolute Error
0	0.999999989	1.000000	1.06×10^{-8}
0.1	0.924017	0.925128	1.1×10^{-3}
0.2	0.855763	0.857526	1.7×10^{-3}
0.3	0.795601	0.797495	1.8×10^{-3}
0.4	0.743742	0.745268	1.5×10^{-3}
0.5	0.700264	0.701015	7.5×10^{-4}
0.6	0.665136	0.664844	2.9×10^{-4}
0.7	0.638237	0.636805	1.4×10^{-3}
0.8	0.619370	0.616887	2.4×10^{-3}
0.9	0.608278	0.605027	3.2×10^{-3}
1	0.604656	0.601109	3.5×10^{-3}

Table 7. Comparison of HAM and numerical solutions for concentration when $h = -0.42, Nr = R = \Delta = Sc = Sr = \tau = 0.5, Mr = \beta = Gr = 1, Pr = 10.6$.

η	HAM Solution of $\phi(\eta)$	Numerical Solution	Absolute Error
0	1.000000091	1.000000	9.1×10^{-8}
0.1	0.898855	0.90411	5.2×10^{-3}
0.2	0.809875	0.81792	8.04×10^{-3}
0.3	0.733047	0.741694	8.6×10^{-3}
0.4	0.668142	0.675623	7.4×10^{-3}
0.5	0.614767	0.619828	5.1×10^{-3}
0.6	0.572423	0.57436	1.9×10^{-3}
0.7	0.540544	0.539208	1.3×10^{-3}
0.8	0.518529	0.514298	4.2×10^{-3}
0.9	0.505765	0.499496	6.2×10^{-3}
1	0.501644	0.494614	7.03×10^{-3}

4. Graphical Results and Discussion

The thin film motion of a micropolar fluid through porous media with the impact of energy radiation and thermophoresis through a stretching plate is investigated. The non-linear coupled differential Equations (13)–(16) with physical conditions (17) and (18) were determined through HAM. The effects of all the embedded constants on the dimensionless velocity field, dimensionless microrotation, dimensionless temperature field, and concentration fields—$f(\eta)$, $g(\eta)$, $\theta(\eta)$, and $\phi(\eta)$, respectively—are observed. The physical geometry of the modeled problem is demonstrated by Figure 1. Liao [33–35] presented h curves to measure the convergence of the series solution for accurate

results of the system, so suitable h-curves are drawn for the velocity profile $f(\eta)$, microrotation profile $g(\eta)$, temperature profile $\theta(\eta)$, and concentration profile $\phi(\eta)$ in range of $-2.0 \leq h_f \leq 0.1$, $-2 \leq h_g \leq 0$, $-2.1 \leq h_\theta \leq 0.1$, and $-2 \leq h_\phi \leq 0$, respectively, in Figures 2–5. The influence of permeability parameter Mr on the velocity field is described in Figure 6. The permeability parameter should be increased at a very small level because of the small thickness of the liquid film because higher values of Mr, that is , $Mr \to \infty$ correspond to the case in which there is no porous medium. The increasing values of Mr respond to the large opening of the porous space, which reduces retardation of the flow; so for increasing values of Mr, the velocity increases in this region. The larger values of the inertia coefficient parameter Nr increase the velocity of fluid as a result of its direct relation with fluid motion, deliberated in Figure 7. The influence of Δ versus motion of liquid film is represented in Figure 8. As Δ has an inverse relation with viscosity, the viscosity falls for larger values of Δ, while the velocity of the liquid film is raised. Figures 9 and 10 indicate the relationship between β with the fluid velocity profile $f(\eta)$ and microrotation profile $g(\eta)$. The fluid motion reduces with the increase in the liquid film thickness. The reason is clear, because larger values of β dominate the viscous forces and, as a result, the fluid velocity decreases. In other words, the thickness of the liquid film shows resistance to liquid flow, and fluid velocity causes retardation towards the free surface—this effect is very clear in the rotation velocity field $g(\eta)$. The microrotation profile $g(\eta)$ of the liquid film rises with the increasing microrotation Gr, as displayed in Figure 11, because the microrotation parameter has an inverse relation with the viscosity parameter. As a result, the viscosity reduces with the rising values of Gr; therefore, larger values of Gr offer low resistance to the flow and the velocity of fluid increases. Figure 12 demonstrates the variation of the inertia parameter Nr on the non-dimensional microrotation profile $g(\eta)$. It is observed that the rise in the inertia parameter Nr material parameter reduces the microrotation profile. The inclusion of thermal radiation in the equation of energy is always used as a special case and, in most of the problems in the existing literature, the energy equation is used without radiation. If the thermal radiation parameter R becomes zero, the temperature field $\theta(\eta)$ in Abo-Eldahab and Ghonaim [17], Rashidi et al. [18,19], and Heydari et al. [20] becomes meaningless, so it is not clear when the thermal radiation parameter R becomes zero in these papers. Therefore, our case of thermal radiation is reciprocal to the above published work, and is the same as Khan [27], Qasim et al. [29], and Mahmood and Khan [32]. Therefore, the temperature rises with the larger values of thermal radiation parameter, as shown in Figure 13, because the thickness of the boundary layer (thin film) is directly related to thermal radiation. Physically, the rate of energy transport increases and, as a result, the temperature of the fluid rises. The dimensionless fluid thickness β has a vital role in temperature distribution. $\theta(\eta)$ decreases with increasing values of β, which is obvious from Figure 14. The size of thin film absorbing heat, and thus the temperature of the fluid, decreases and, as a result, a cooling effect is produced. In other words, the thickness of the fluid decreases with the increasing temperature. Figure 15 represents the comparison of temperature and Prandtl number Pr. The temperature falls with growing values of Pr. In fact, the larger values of Pr enhance the viscous diffusion more than the thermal diffusion and, as a result, the temperature profile declines. Schmidt number verses concentration is deliberated in Figure 16. The rising values of Schmidt number Sc decrease the concentration field, because molecular diffusivity is inversely related to Sc. The contribution of the Soret number Sr is represented in Figure 17, showing that $\phi(\eta)$ rises when the Soret number Sr increases. In fact, the larger Soret number increases the viscosity and, therefore, $\phi(\eta)$ accelerates. Figure 18 shows the relationship between thermophoretic parameter τ and $\phi(\eta)$. They are inversely related to each other. Rising values of τ reduce the size of the boundary layer. The concentration field rises as thickness β increases, as shown in Figure 19, because of cohesive forces between molecules dominated by the increasing value of the parameter β, which result a rise in friction force and cause the fluid flow.

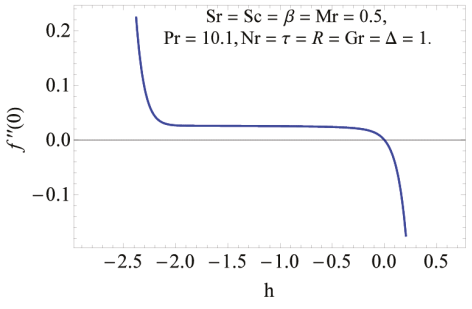

Figure 2. h_f curves for the velocity field.

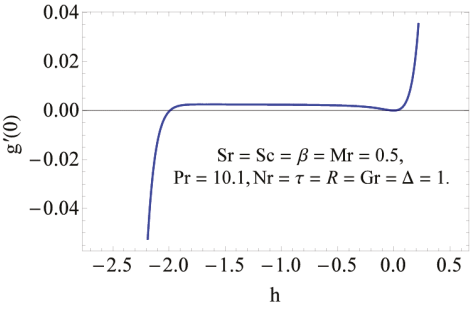

Figure 3. h_g curves for the velocity field in rotation.

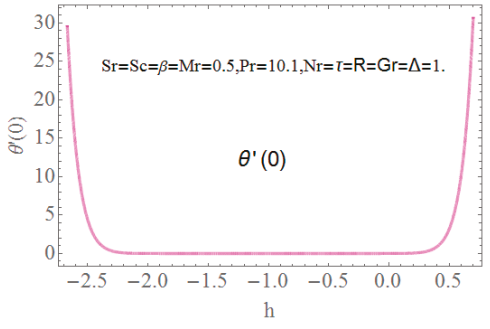

Figure 4. h_θ curves for the temperature field.

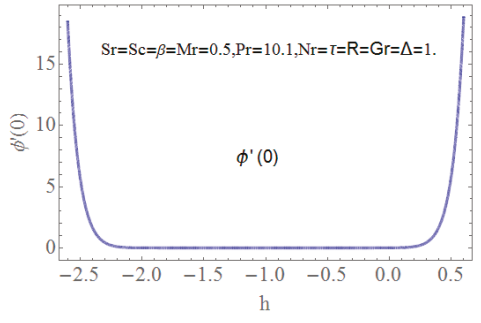

Figure 5. h_ϕ curves for the concentration field.

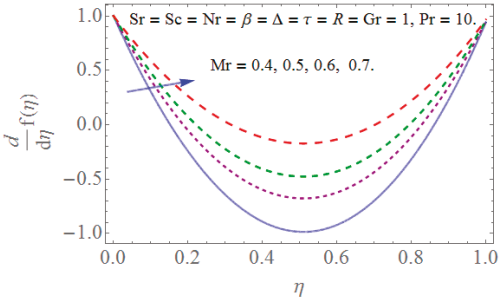

Figure 6. Effect of permeability parameter *Mr* on the velocity.

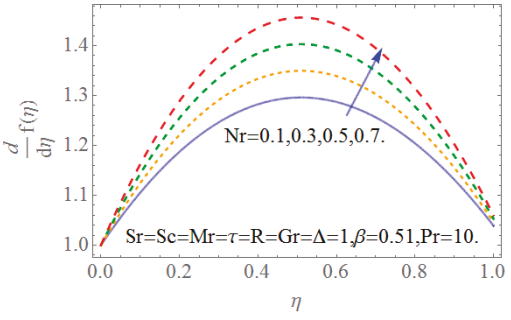

Figure 7. The comparison of dimensionless velocity with inertia coefficient parameter *Nr*.

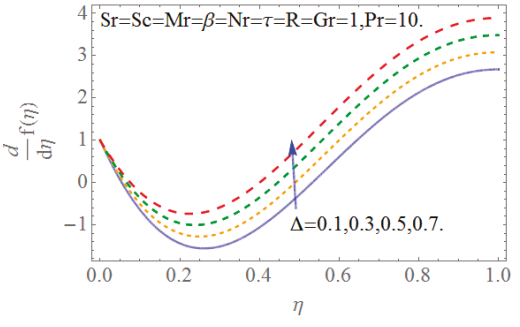

Figure 8. Velocity verses vortex–viscosity parameter Δ.

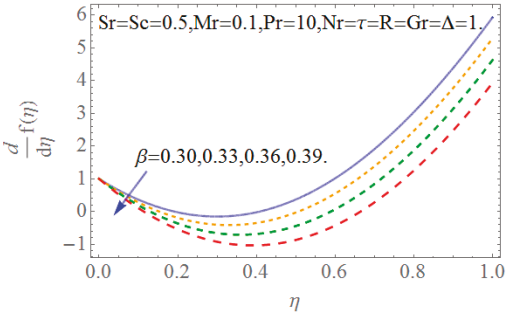

Figure 9. Variation of dimensionless velocity with dimensionless fluid thickness β.

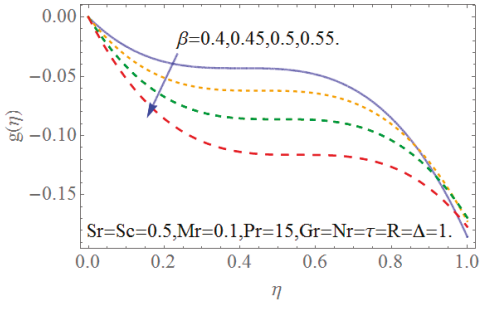

Figure 10. Variation of dimensionless microrotation profile with fluid thickness β.

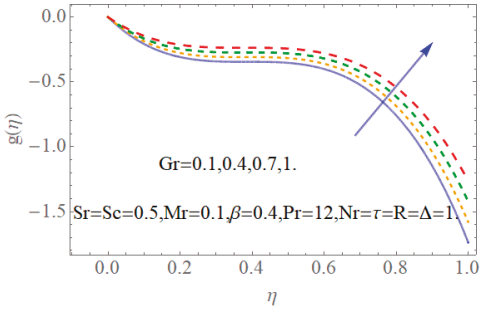

Figure 11. Microrotation profile under the effect of microrotation parameter *Gr*.

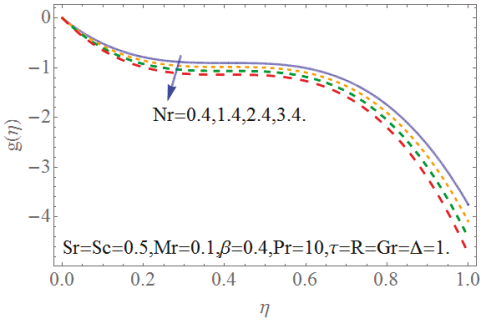

Figure 12. Variation of dimensionless microrotation profile with inertial parameter *Nr*.

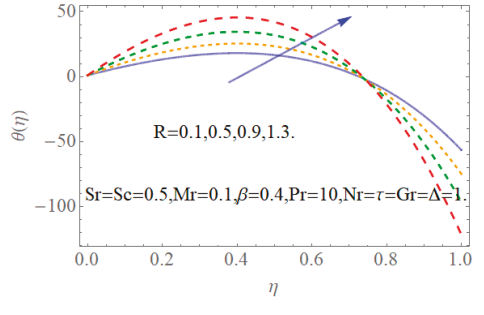

Figure 13. Temperature verses radiation parameter *R*.

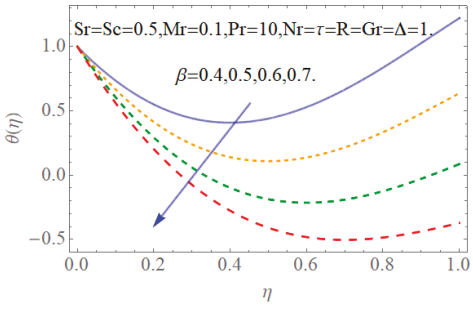

Figure 14. Temperature verses film thickness parameter β.

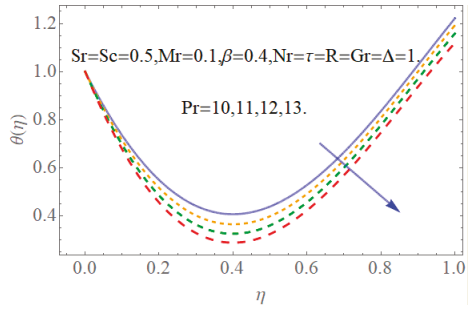

Figure 15. Temperature versus Prandtl number *Pr*.

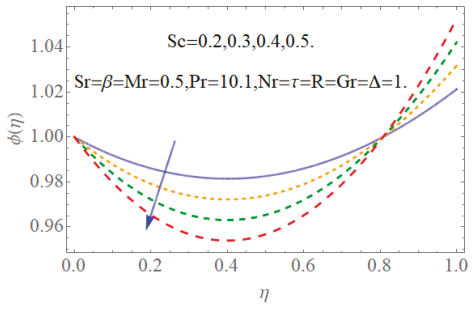

Figure 16. Variation of dimensionless concentration with Schmidt number *Sc*.

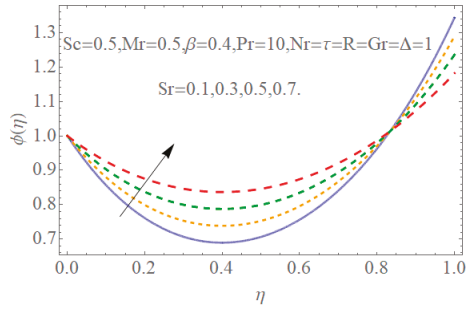

Figure 17. Variation of dimensionless concentration with Soret number *Sr*.

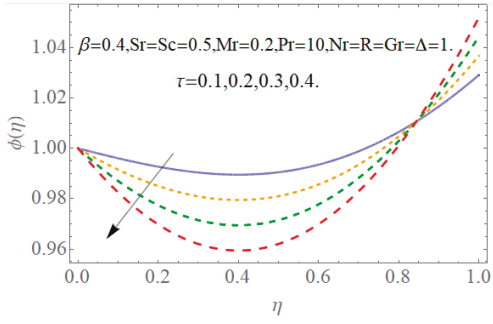

Figure 18. Concentration versus thermophoretic parameter τ.

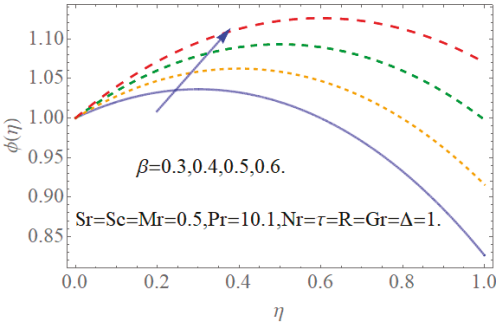

Figure 19. Variation of dimensionless concentration with dimensionless fluid thickness β.

5. Conclusions

The study of the thin film flow in a permeable medium past a stretched plate was examined. The micropolar fluid was used as a base fluid with the influence of thermal radiation and thermophoresis. Modeled non-linear coupled differential equations were tackled through HAM. The HAM solution was compared with the numerical method and close agreement was observed for the validation of the problem. The effects of the physical parameters on the velocity, temperature, and concentration profiles were displayed and discussed.

The outcomes of the problem are pointed out as follows:

- The increasing values of the thin film thickness parameter β improve the resistance force to decline the velocity and microrotation profiles, and enhance the concentration field.
- It was observed that the rise in the Soret number *Sr* enhances the concentration field $\phi(\eta)$.
- The temperature field rises with the increasing value of the thermal radiation parameter *R* because of the rate of energy and transport growth, and consequently enhances the temperature profile.
- The increase in the thickness of the thin film β reduces the temperature profile. Physically, heat transfer is larger in the thin film as compared with the thick film, while the concentration field increases as the thin film parameter β increases.
- The larger vortex–viscosity parameter Δ causes the velocity of the liquid film to rise.
- The HAM solution was validated with the numerical solution (ND-solve) and very close agreement was observed.

Author Contributions: V.A. and T.G. modelled the problem and drew the physical sketch. S.A. and F.A. introduced the similarity transformation and transformed the modeled problem into dimensionless form. S.O.A. solved the problem numerically and computed the results. I.K. discussed the results with conclusions. All the authors equally contributed in writing and revising the manuscript.

Funding: The authors would like to thank Deanship of Scientific Research, Majmaah University for supporting this work under the No. 1440-25.

Conflicts of Interest: The authors declare no conflict of interest.

Nomenclature

x, y	Cartesian coordinates
u, v	Velocity components
U_w	Stretching velocity
δ	Uniform thickness of the thin film
T_w	Wall temperature field
C_w	Surface concentration
T_{ref}	Reference temperature
C_{ref}	Reference concentration
v	Kinematic viscosity
μ	Dynamic viscosity
S	constant characteristic
C_r	Forchheimer inertia constant
k_c	coupling constant
T	Temperature field
C	Concentration field
ρ	Fluid density
$h(t)$	Liquid film thickness
q_r	Radiative heat fluctuation
σ	Stefan–Boltzmann constant
D_m	Concentration molecular diffusivity
T_m	Mean temperature
K	permeability
ψ	Stream function
β	Non-dimensional thickness of the Nano liquid film
φ	porosity parameter
Pr	Prandtl number
Sc	Schmidt number
Sr	Soret number
G_1	is the microrotation constant
R	Thermal radiation parameter
V_T	Thermophoretic velocity

References

1. Goldsmith, P.; May, F.G. *Diffusiophoresis and Thermophoresis in Water Vapour Systems*; Aerosol Science, Academic Press: London, UK, 1966; pp. 163–194.
2. Goren, S.L. Thermophoresis of aerosol particles in the laminar boundary layer on a flat plate. *J. Colloid Interface Sci.* **1977**, *61*, 77–85. [CrossRef]
3. Jayaraj, S.; Dinesh, K.K.; Pillai, K.L. Thermophoresis in natural convection with variable properties. *Heat Mass Transf.* **1999**, *34*, 469–475. [CrossRef]
4. Selim, A.; Hossain, M.A.; Rees, D.A.S. The effect of surface mass transfer on mixed convection flow past a heated vertical flat permeable plate with thermophoresis. *Int. J. Therm. Sci.* **2003**, *42*, 973–982. [CrossRef]
5. Chamkha, A.J.; Pop, I. Effect of thermophoresis particle deposition in free convection boundary layer from a vertical flat plate embedded in a porous medium. *Int. Commun. Heat Mass Transf.* **2004**, *31*, 421–430. [CrossRef]
6. Chamkha, A.J.; Al-Mudhaf, A.F.; Pop, I. Effect of heat generation or absorption on thermophoretic free convection boundary layer from a vertical flat plate embedded in a porous medium. *Int. Commun. Heat Mass Transf.* **2006**, *33*, 1096–1102. [CrossRef]

7. Das, K. Impact of thermal radiation on MHD slip flow over a flat plate with variable fluid properties. *Heat Mass Transf.* **2012**, *48*, 767–778. [CrossRef]
8. Al-Hadhrami, A.K.; Elliott, L.; Ingham, D.B. A new model for viscous dissipation in a porous media across a range of permeability values. *Transp. Porous Media* **2003**, *53*, 117–122. [CrossRef]
9. Al-Hadhrami, A.K.; Elliott, L.; Ingham, D.B. Combined free and forced convection in vertical channels of porous media. *Transp. Porous Media* **2002**, *49*, 265–289. [CrossRef]
10. Łukaszewicz, G. *Micropolar Fluids: Theory and Application*; Birkhauser: Basel, Switzerland, 1999.
11. Aouadi, M. Numerical study for micropolar flow over a stretching sheet. *Comput. Mater. Sci.* **2007**, *38*, 774–780. [CrossRef]
12. Chauhan, D.S.; Olkha, A. Slip flow and heat transfer of a second-grade fluid in a porous medium over a stretching sheet with power-law surface temperature or heat flux. *Chem. Eng. Commun.* **2011**, *198*, 1129–1145. [CrossRef]
13. Cortell, R. Similarity solutions for flow and heat transfer of a viscoelastic fluid over a stretching sheet. *Int. J. Non-Linear Mech.* **1994**, *29*, 155–161. [CrossRef]
14. Dandapat, B.S.; Gupta, A.S. Flow and heat transfer in a viscoelastic fluid over a stretching sheet. *Int. J. Non-Linear Mech.* **1989**, *24*, 215–219. [CrossRef]
15. Chauhan, D.S.; Kumar, V. Unsteady flow of a non-Newtonian second grade fluid in a channel partially filled by a porous medium. *Adv. Appl. Sci. Res.* **2012**, *3*, 75–94.
16. Khan, I.; Shafie, S. Rotating MHD flow of a generalized burgers' fluid over an oscillating plate embedded in a porous medium. *Therm. Sci.* **2015**, *19*, 183–190. [CrossRef]
17. Abo-Eldahab, E.M.; Ghonaim, A.F. Radiation effect on heat transfer of a micropolar fluid through a porous medium. *Appl. Math. Comput.* **2005**, *169*, 500–510. [CrossRef]
18. Rashidi, M.M.; Pour, S.M. A novel analytical solution of heat transfer of a micropolar fluid through a porous medium with radiation by DTM-Padé. *Heat Transf. Asian Res.* **2010**, *39*, 575–589. [CrossRef]
19. Rashidi, M.M.; Abbasbandy, S. Analytic approximate solutions for heat transfer of a micropolar fluid through a porous medium with radiation. *Commun. Nonlinear Sci. Numer. Simul.* **2011**, *16*, 1874–1889. [CrossRef]
20. Heydari, M.; Loghmani, G.B.; Hosseini, S.M. Exponential bernstein functions: An effective tool for the solution of heat transfer of a micropolar fluid through a porous medium with radiation. *Comput. Appl. Math.* **2017**, *36*, 647–675. [CrossRef]
21. Tripathy, R.S.; Dash, G.C.; Mishra, S.R.; Hoque, M.M. Numerical analysis of hydromagnetic micropolar fluid along a stretching sheet embedded in porous medium with non-uniform heat source and chemical reaction. *Eng. Sci. Technol. Int. J.* **2016**, *19*, 1573–1581. [CrossRef]
22. Rahman, M.M.; Sattar, M.A. MHD free convection and mass transfer flow with oscillatory plate velocity and constant heat source in a rotating frame of reference. *Dhaka Univ. J. Sci.* **1999**, *47*, 63–73.
23. Bakr, A.A. Effects of chemical reaction on MHD free convection and mass transfer flow of a micropolar fluid with oscillatory plate velocity and constant heat source in a rotating frame of reference. *Commun. Nonlinear Sci. Numer. Simulat.* **2011**, *16*, 698–710. [CrossRef]
24. Ramzan, M.; Ullah, N.; Chung, J.D.; Lu, D.; Farooq, U. Buoyancy effects on the radiative magneto Micropolar nanofluid flow with double stratification, activation energy and binary chemical reaction. *Sci. Rep.* **2017**, *7*, 12901. [CrossRef] [PubMed]
25. Srinivasacharya, D.; Ramreddy, C. Natural convection heat and mass transfer in a micropolar fluid with thermal and mass stratification. *Int. J. Comput. Methods Eng. Sci. Mech.* **2013**, *14*, 401–413. [CrossRef]
26. Nadeem, S.; Hussain, S.T. Flow and heat transfer analysis of Williamson nanofluid. *Appl. Nanosci.* **2014**, *4*, 1005–1012. [CrossRef]
27. Khan, W.; Gul, T.; Idrees, M.; Islam, S.; Khan, I.; Dennis, L.C.C. Thin film williamson nanofluid flow with varying viscosity and thermal conductivity on a time-dependent stretching sheet. *Appl. Sci.* **2016**, *6*, 334. [CrossRef]
28. Aziz, R.C.; Hashim, I.; Alomari, A.K. Thin film flow and heat transfer on an unsteady stretching sheet with internal heating. *Meccanica* **2011**, *46*, 349–357. [CrossRef]
29. Qasim, M.; Khan, Z.H.; Lopez, R.J.; Khan, W.A. Heat and mass transfer in nanofluid thin film over an unsteady stretching sheet using Buongiorno's model. *Eur. Phys. J. Plus* **2016**, *131*, 16. [CrossRef]

30. Tawade, J.; Abel, M.S.; Metri, P.G.; Koti, A. Thin film flow and heat transfer over an unsteady stretching sheet with thermal radiation, internal heating in presence of external magnetic field. *Int. J. Adv. Appl. Math. Mech.* **2016**, *3*, 29–40.
31. Khan, Y.; Wu, Q.; Faraz, N.; Yildirim, A. The effects of variable viscosity and thermal conductivity on a thin film flow over a shrinking/stretching sheet. *Comput. Math. Appl.* **2011**, *61*, 3391–3399. [CrossRef]
32. Mahmood, T.; Khan, N. Thin film flow of a third grade fluid through porous medium over an inclined plane. *Int. J. Nonlinear Sci.* **2012**, *14*, 53–59.
33. Shijun, L. Homotopy analysis method: A new analytic method for nonlinear problems. *Appl. Math. Mech.* **1998**, *19*, 957–962. [CrossRef]
34. Liao, S. On the homotopy analysis method for nonlinear problems. *Appl. Math. Comput.* **2004**, *147*, 499–513. [CrossRef]
35. Liao, S. *Homotopy Analysis Method in Nonlinear Differential Equations*; Higher Education Press: Beijing, China, 2012; pp. 153–165.
36. Gul, T.; Haleem, I.; Ullah, I.; Khan, M.A.; Bonyah, B.; Khan, I.; Shuaib, M. The study of the entropy generation in a thin film flow with variable fluid properties past over a stretching sheet. *Adv. Mech. Eng.* **2018**, *10*, 1–15. [CrossRef]
37. Gul, T.; Nasir, S.; Islam, S.; Shah, Z.; Khan, M.A. Effective prandtl number model influences on the γAl_2O_3-H_2O and γAl_2O_3-$C_2H_6O_2$ nanofluids spray along a stretching cylinder. *Arab. J. Sci. Eng.* **2019**, *2*, 1601–1616. [CrossRef]

coatings

MDPI

Article

Manufacturing of Double Layer Optical Fiber Coating Using Phan-Thien-Tanner Fluid as Coating Material

Zeeshan Khan [1], Haroon Ur Rasheed [1], S.O. Alharbi [2], Ilyas Khan [3,*], Tariq Abbas [1] and Dennis Ling Chuan Chin [4]

[1] Department of Computer Science, Sarhad University of Science and Information Technology Peshawar, KP 25000, Pakistan; zeeshan.maths@suit.edu.pk (Z.K.); haroon.csit@suit.edu.pk (H.U.R.); tariqabbas56@yahoo.com (T.A.)

[2] Department of Mathematics, College of Science Al-Zulfi, Majmaah University, Al-Majmaah 11952, Saudi Arabia; so.alharbi@mu.edu.sa

[3] Faculty of Mathematics and Statistics, Ton Duc Thang University, C004-19 Nguyen Huu Tho Street, Tan Phong ward, District 7, Ho Chi Minh City 700000, Vietnam

[4] Fundamental and Applied Science Department Universiti Teknologi Petronas 32610, Perak, Malaysia; dennis.ling@utp.edu.my

* Correspondence: ilyaskhan@tdt.edu.vn

Received: 9 November 2018; Accepted: 14 January 2019; Published: 24 February 2019

Abstract: Modern optical fiber required a double-layer resin coating on the glass fiber to provide protection from signal attenuation and mechanical damage. The most important plastics resin used in coating of fiber optics are plasticized polyvinyle (PVC), low/high density polyethylene (LDPE/HDPE), nylon, and polysulfone. Polymer flow during optical fiber coating in a pressure type coating die has been simulated under non-isothermal conditions. The flow dependent on the wire or fiber velocity, geometry of the die, and the viscosity of the polymer. The wet-on-wet coating process is an efficient process for two-layer coating on the fiber optics. In the present study, the constitutive equation of polymer flow satisfies viscoelastic Phan-Thien-Tanner (PTT) fluid, is used to characterize rheology of the polymer melt. Based on the assumption of the fully developed incompressible and laminar flow, the viscoelastic fluid model of two-immiscible resins-layers modeled for simplified-geometry of capillary-annulus where the glass fiber drawing inside the die at high speed. The equation describing the flow of the polymer melt inside the die was solved, analytically and numerically, by the Runge-Kutta method. The effect of physical characteristics in the problem has been discussed in detail through graphs by assigning numerical values for several parameters of interest. It is observed that velocity increases with increasing values of εD_1^2, εD_2^2, X_1, and X_2. The volume flow rate increases with an increasing Deborah number. The thickness of coated fiber optic increases with increasing εD_1^2, εD_2^2, and δ. Increase in Brinkman number and Deborah number enhances the rate of heat transfer. It is our first attempt to model PTT fluid as a coating material for double-layer optical fiber coating using the wet-on-wet coating process. At the end, the present study is also compared with the published work as a particular case, and good agreement is found.

Keywords: optical fiber coating; double-layer coating; viscoelastic PTT fluid; analytic and numerical simulations

1. Introduction

The analysis of non-Newtonian fluid is often encountered in many industrial disciplines [1,2]. The applications of such non-Newtonian fluids include wire and fiber coating, extrusion process, performance of lubricants, food processing, design of various heat exchangers, ink-jet printing, polymer preparation, colloidal and additive suspension, animal blood, chemical processing equipment, paper

production, transpiration cooling, gaseous diffusion, drilling muds, heat pipes, etc. The non-Newtonian fluids [3,4] are described by a nonlinear relationship between the sear stress and the rate of deformation tensors. For this reason, several models have been proposed. There are several subclasses of non-Newtonian fluids. Phan-Thien-Tanner fluid is one of the important fluids in this category and are mostly used for the coating of wires and optical fiber. Therefore, in this problem, we used the PTT fluid as a coating material for double-layer optical fiber coating.

In 1960, the modern concept of optical fiber was introduced, which gained significant importance in the manufacturing industry. It consists of high purity silica glass fiber in which the information travels in and forms light wave signals and the polymer coatings to protect the fiber from mechanical damage. First, the fiber is dragged through to perform in the draw furnace, and then enters in the cooling system. After going through the cooling system, the fiber is passed through the double-layer coating of the polymer. The manufacturing process comes to an end as the coating is cured by an ultraviolet lamp. Recently, two-layer coatings are used on optical fiber, i.e., primary (inner coating) and secondary coatings (outer coating). The inner-coating is made of a soft coating-material to minimize the signal-attenuation due to micro bending. The secondary-coating is made of hard coating-material that protects the primary-coating from mechanical damage. The widespread-industrial success of optical-fibers as a practical-alternative to copper-cabling could be attributed to these ultraviolet-curable coatings.

Two-types of coating processes were performed for two-layer coatings on bare glass fiber. These are called wet-on-dry (WOD) and wet-on-wet (WOW) coating processes. In the WOD coating process, fiber enters the primary coating die, followed by an ultraviolet lamp. Then, this cured fiber coating enters the secondary coating die, again followed by an ultraviolet lamp. While in the wet-on-wet process, the bare glass fiber passes through primary and secondary coating die and then cured by an ultraviolet lamp. Recently, the WOW process gained significant importance in the production industry. Herein, the WOW process is applied for the optical fiber coating.

Wire-coating (an extrusion procedure) is generally utilized as part of the polymer industry for insulation and it protects the wire from mechanical damage. In this procedure, an exposed preheated fiber or wire is dipped and dragged through the melted polymer. This procedure can also be accomplished by extruding the melted polymer over a moving wire. Typical wire coating equipment is composed of five distinct units: Pay-off tool, wire pre-heating tool, an extruder, and a cooling and takeoff tool, as shown in Figure 1. The most common dies used for coatings are: Tubing-type dies and pressure type dies. The later one is normally used for wire-coating and seems like annulus. That is why flows through such die are similar to the flows through the annular area formed by a couple of coaxial cylinders. One of the two cylinders (inner cylinder) moves in the direction of the axial, while the second (external cylinder) is fixed. Preliminary efforts done by several researchers [5–10] used power-law and Newtonian models to reveal the rheology of the polymer melt flow.

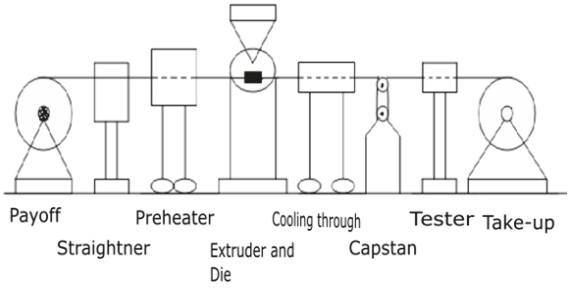

Figure 1. Optical fiber coating process.

At present, the Phan-Thein-Tranner (PTT) model, a third-grade visco-elastic fluid model, is the most commonly used model for wire-coating. The high-speed wire-coating process for polymer

melts in the elastic constitutive model was analyzed by Binding in Reference [11]. It also discussed the shortcomings of the realistic modeling approach. Mutlu et al., in Reference [12], provided the wire-coating analysis based on the tube-tooling die. Kasajima and Ito, in Reference [13], meanwhile analyzed the wire-coating process and examined the post-treatment of the polymer extruded. They also discussed the impacts of heat transfer on the cooling coating. Afterward, Winter, in References [14,15], investigated the thermal effect on die, both from inside and outside perspectives. Recently, wire-coating in view of linear variations of temperature in the post-treatment analysis was investigated by Baag and Mishra in Reference [16].

The two-layer coatings process was also studied by many researchers. Kim et al. [17] used the WOW process for optical fiber coating. Zeeshan et al. [18,19] used pressure coating die for the two-layer coating in optical fiber analysis using the PTT fluid model. The same author discussed viscoelastic fluid for the two-layer coating in the fiber coating [20]. The Sisko fluid model was used for fiber coating by adopting the WOW process [21] in the presence of pressure type coating die.

In the present study, two-layer analysis is performed using viscoelastic fluid for optical fiber coating phenomenon in the presence of pressure type coating die. Moreover, the computation of heat transfer in fiber coating has significant effects on the operating variables in coating analysis. The heat transfer also provides information to the die designers about the thermal variables that are important in obtaining better product quality and achieving optimum operating conditions [22–25]. The closed form solution for velocity field, thickness of the coated fiber optics, and temperature distribution has been obtained in the first case. In the second case, the numerical solution has been obtained. The results of both cases are compared and explained in detail. Finally, the recent result are also compared with the published work reported by Kim et al. [17], as a particular case and good agreement is found.

2. Analysis

The WOW-type coating process is illustrated in Figure 2. The glass fiber is pulled with constant velocity U through the primary coating die, which is filled with a primary coating resin. Afterwards, the uncured coated fiber optics enters the secondary coating die, which is filled with a secondary resin. After the secondary die the fiber leaves the system with two-coated layers, as displayed in Figure 2. At the end these coated-layers, they are cured by ultraviolet lamps. Where R_w, R, and R_d are the radius of the fiber optics, interface radius location, and radius of the die, L is the length of the die. The present study is investigated under the assumption that the flow is incompressible, laminar, length of the die is sufficient large, the fiber optics moves along the centerline with constant speed, negligible small radial flow, as compared to the axial flow, because of high viscosity of the polymer-melt, the viscous impacts are dominant, as compared to the inertial effects, axial heat conduction is negligible, and the thermal conductivity, specific heat, melt density do not depend on the temperature and neglect the gravitational effect. To analyze the flow, the cylindrical coordinate system (r, θ, z) is used in which r is the radial coordinate and z is the axial coordinate of the wire means centerline of the die.

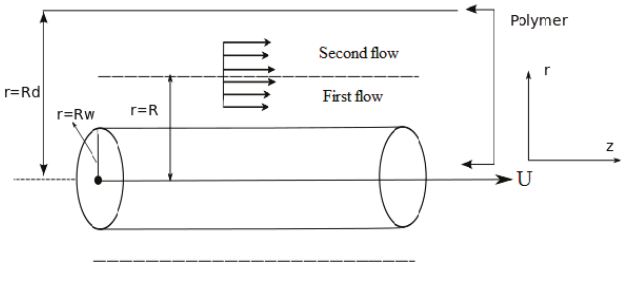

Figure 2. Geometry of double-layer optical fiber coating in wet-on-wet coating process [17].

The basic equations governing the flow of incompressible fluids are:

$$\nabla.u = 0 \tag{1}$$

$$\rho\frac{\mathrm{d}u}{\mathrm{d}t} = \nabla.\mathrm{T} \tag{2}$$

$$\rho c_p\frac{\mathrm{d}\Theta}{\mathrm{d}t} = k\nabla^2\Theta + \Phi \tag{3}$$

$$f(trS)\mathrm{S} + \lambda\dot{\mathrm{S}} = \eta\mathrm{A} \tag{4}$$

where ρ is the density of the fluid, T is the shear stress tensor, c_p is the the specific heat, D/Dt denotes the material derivative, k is the thermal conductivity, Θ is the fluid temperature, Φ is the dissipation function, trS is the trace of extra stress tensor, $\dot{\mathrm{S}}$ is the upper contra-variant convicted tensor, μ is the viscosity of the fluid, and A is the deformation rate tensor.

The shear stress tensor is given in Equation (2) and the deformation rate tensor is given in Equation (4), defined as:

$$\mathrm{T} = -p\mathrm{I} + \mathrm{S} \tag{5}$$

$$\mathrm{A} = L^T + L \tag{6}$$

where I is the identity tensor and the superscript, T stands for the transpose of a matrix, and $L = \nabla u$.

The upper contra-variant convicted tensor $\dot{\mathrm{S}}$ in Equation (4) is given by

$$\dot{\mathrm{S}} = \frac{\mathrm{dS}}{\mathrm{d}t} - \left[(\nabla u)^T\mathrm{S} + \mathrm{S}(\nabla u)\right] \tag{7}$$

The function $f(tr\mathrm{S})$ is given by Tanner [19–21],

$$f(trS) = 1 + \frac{\varepsilon\lambda}{\eta}(tr\mathrm{S}) \tag{8}$$

In Equation (8), $f(tr\mathrm{S})$ is the stress function in which ε is related to the elongation behavior of the fluid. For ε = 0, the model reduces to the well-known Maxwell model and for λ = 0, the model reduces to a Newtonian one.

With the above frame of reference and assumptions the fluid velocity, extra stress tensor and temperature filed are considered as

$$u = (0, 0, w(r)), \mathrm{S} = \mathrm{S}(r), \Theta = \Theta(r) \tag{9}$$

Using assumptions and Equation (9), the continuity Equation (1) satisfied identically and from Equations (2–8), we arrive at:

$$\frac{\partial p}{\partial r} = 0 \tag{10}$$

$$\frac{\partial p}{\partial \theta} = 0 \tag{11}$$

$$\frac{\partial p}{\partial z} = \frac{1}{r}\frac{\mathrm{d}}{\mathrm{d}r}(rS_{\mathrm{rz}}) \tag{12}$$

$$k\left(\frac{\mathrm{d}^2}{\mathrm{d}r^2} + \frac{1}{r}\frac{\mathrm{d}}{\mathrm{d}r}\right)\Theta + S_{\mathrm{rz}}\frac{\mathrm{d}w}{\mathrm{d}r} = 0 \tag{13}$$

$$f(trS)S_{\mathrm{zz}} = 2\lambda S_{\mathrm{rz}}\frac{\mathrm{d}w}{\mathrm{d}r} \tag{14}$$

$$f(trS)S_{\mathrm{rz}} = \eta\frac{\mathrm{d}w}{\mathrm{d}r} \tag{15}$$

$$\Phi = S_{rz}\frac{dw}{dr} \tag{16}$$

From Equations (10) and (11), it is concluded that p is a function of z only. Assuming that the pressure gradient along the axial direction is constant. Thus, we have $dp/dz = \Omega$.

Integrating Equation (12) with respect to r, we get

$$S_{rz} = \frac{\Omega}{2}r + \frac{C}{r} \tag{17}$$

where C is an arbitrary constant of integration.

By substituting Equation (17) in Equation (15), we have

$$f(trS) = \frac{\eta\frac{dw}{dr}}{\left(\frac{\Omega}{2}r + \frac{C}{r}\right)} \tag{18}$$

Combining Equations (14), (15) and (17), we obtain the explicit expression for a normal stress component S_{zz} as:

$$S_{zz} = 2\frac{\lambda}{\eta}\left(\frac{\Omega}{2}r + \frac{C}{r}\right)^2 \tag{19}$$

From Equations (8) and (18), we have

$$\eta\frac{dw}{dr} = \left(1 + \varepsilon\frac{\lambda}{\eta}S_{zz}\right)\left(\frac{\Omega}{2}r + \frac{C}{r}\right) \tag{20}$$

Inserting Equation (19) in Equation (20), we obtain an analytical expression for axial velocity as:

$$\frac{dw_{(j)}}{dr} = \frac{1}{\eta_{(j)}}\left(\frac{\Omega}{2}r + \frac{C_{(j)}}{r}\right) + 2\varepsilon\frac{\lambda^2}{\eta^3{}_{(j)}}\left(\frac{\Omega}{2}r + \frac{C_{(j)}}{r}\right)^3 \tag{21}$$

Additionally, the temperature distribution is

$$k_{(j)}\left(\frac{d^2}{dr^2} + \frac{1}{r}\frac{d}{dr}\right)\theta_{(j)} + S_{rz_{(j)}}\frac{dw_{(j)}}{dr} = 0 \tag{22}$$

Here, $j = 1, 2$ represents the primary layer and secondary layer flow, respectively.

The boundary condition on $\theta_{(j)}$ is θ_w at the fiber optics and θ_d at the die wall. For the problem displayed in Figure 1, at the fluid interface, we utilize the assumptions that the velocity, the shear stress, and the pressure gradient along the flow direction and the temperature and the heat flux are continuous, which are given as follows.

The relevant boundary and interface conditions [17–22] on the velocity are

$$w_1 = U \text{ at } r = R_w \text{ and } w_2 = 0 \text{ at } r = R_d \tag{23}$$

$$w_1 = w_2 \text{ and } S_{rz1} = S_{rz2} \text{ at } r = R \tag{24}$$

The relevant boundary and interface conditions [17–22] on the temperature are

$$\theta_1 = \theta_w \text{ at } r = R_w \text{ and } \theta_2 = \theta_d \text{ at } r = R_d \tag{25}$$

$$\theta_1 = \theta_2 \text{ and } k_1\frac{d\theta_1}{dr} = k_2\frac{d\theta_2}{dr} \text{ at } r = R \tag{26}$$

We introduce the non-dimensional flow variables as

$$r^* = \frac{r}{R_w}, w^*_{(j)} = \frac{w_{(j)}}{U}, \theta^*_{(j)} = \frac{\theta_{(j)}-\theta_d}{\theta_d-\theta_w}, C^*_{(j)} = \frac{2C_{(j)}}{R_w^2\Omega}, Br_{(j)} = \frac{\eta_{(j)}U^2}{k_{(j)}(\theta_d-\theta_w)}, \varepsilon D^2_{(j)} = \frac{\lambda U_c}{R_w}, X_{(j)} = \frac{U_c}{U}, \quad \Gamma^* = \frac{R}{R_w}, \frac{R_d}{R_w} = \delta > 1, K = \frac{k_2}{k_1}, j = 1, 2. \tag{27}$$

$$\frac{dw_{(j)}}{dr} = -4rX_{(j)} - 4C_{(j)}X_{(j)}\frac{1}{r} - 128X_{(j)}\varepsilon D^2_{(j)}r^3 - 384X_{(j)}\varepsilon D^2_{(j)}C_{(j)}r - 384X_{(j)}C^2{}_{(j)}\varepsilon D^2_{(j)}\frac{1}{r} - 128C^3{}_{(j)}X_{(j)}\varepsilon D^2_{(j)}\frac{1}{r^3} \tag{28}$$

$$\frac{d}{dr}\left(r\frac{d\theta_{(j)}}{dr}\right) - 4Br_{(j)}X_{(j)}\left(r^2 + C_{(j)}\right)\frac{dw_{(j)}}{dr} = 0 \tag{29}$$

$$w_1(1) = 1, w_2(\delta) = 0 \tag{30}$$

$$w_1(\Gamma) = w_2(\Gamma), S_{rz1}(\Gamma) = S_{rz2}(\Gamma) \tag{31}$$

$$\theta_1(1) = 0, \theta_2(\delta) = 1, \theta_1(\Gamma) = \theta_2(\Gamma), \frac{d\theta_1(\Gamma)}{dr} = K\frac{d\theta_2(\Gamma)}{dr}. \tag{32}$$

where $U_c = -R_w^2\Gamma/8\eta_{(j)}$ is the characteristic velocity scale, and $\varepsilon D^2_{(j)}$ is the characteristic Deborah number based on velocity scale U_c, $X_{(j)}$ has physical meaning of a non-dimensional pressure gradient and $Br_{(j)}$ is the Brinkman number. Here, Γ is the dimensionless parameter that is the ratio of the radius of the liquid-liquid interface to the radius of the optical fiber and j = 1, 2 stands for primary and secondary coating layer flows, respectively.

3. Analytical Solution (Exact Solution)

Analytical solution is given in the Appendix A.

4. Numerical Solution

We shall solve the above equations numerically. For this purpose, the Runge–Kutta–Fehlberg method is employed. The computations are carried out for δ = 2. Before proceeding to the results and their discussion, we first validate our results of numerical solution for comparing them with the corresponding results based on exact solution (given in Appendix A). To this end, Figure 3 is prepared, which shows the velocity curve obtained through both numerical and exact solutions. This figure clearly demonstrates an excellent correlation between both the solutions. This establishes the confidence on both exact and numerical solutions and also on the results predicted by these solutions.

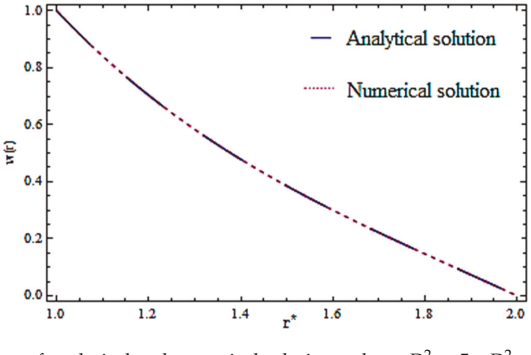

Figure 3. Comparison of analytical and numerical solutions when $\varepsilon D_1^2 = 5$, $\varepsilon D_2^2 = 10$, $X_1 = 0.5$, $X_1 = 1.0$, $\delta = 2$.

5. Results of Analysis and Discussion

This section shows the impact of different emerging parameters of interest including the Deborah numbers (viscoelastic parameter) εD_1^2 and εD_2^2 ,pressure gradient parameters X_1 and X_2, Brinkman numbers Br_1 and Br_2 and the radii ration δ on the velocity and temperature profiles, volume flow rate, thickness of the coated fiber optics, shear stress, and force required to pulling the fiber optics (later referred as force only). This purpose is achieved graphically in 4–11. Figure 4 shows the effect of dimensionless pressure gradient X_1 and X_2 on the velocity profile when $\varepsilon D_1^2 = 0.5$, $\varepsilon D_2^2 = 1$, $\delta = 2$. This figure shows that, as the pressure gradient parameter increases, the velocity profile increases. The effect of Deborah number εD_1^2 on velocity profile is shown in Figure 5. Since Deborah number is the measure of the ratio of the rate of the pressure drop in the flow to the viscosity, i.e., $\varepsilon D_{(j)}^2 = \frac{\lambda U_c}{R_w}$ where $U_c = -R_w^2 \Omega / 8\eta_{(j)}$ is the characteristic velocity and Ω is constant pressure gradient in the axial direction. That is why the velocity follows as an increasing trend with increasing Deborah number. From Figures 4 and 5, it is clear that nonlinear behavior is occurred in the velocity profiles. Since the velocity of fluid first increase up to a certain value and then decreases, which shows the shear thickening effect. For low elasticity means for low Deborah number, the velocity disparity diverges a little from the Newtonian one, however, when the Deborah number is increased, these profiles turn into a more flattened one, showing the shear-thinning effect. It can be seen that, as ε is reduced, the profiles turn to the Newtonian one and the result is therefore independent of D_1^2 and D_2^2. As $X_{(j)} = \frac{U_c}{U}$ is the pressure gradient in which $U_c = -R_w^2 \Omega / 8\eta_{(j)}$ is the characteristic velocity where U is the optical fiber velocity. That is why the velocity inside the die exceeds from the fiber optics velocity due to large values of the pressure gradient parameter.

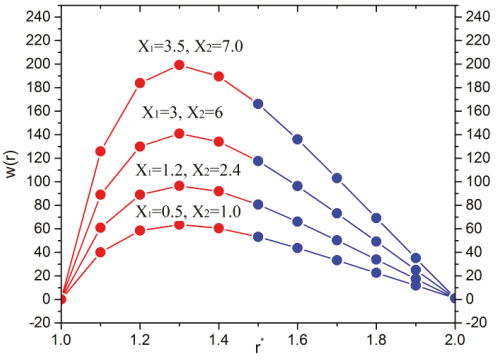

Figure 4. Effect of X_1 and X_2 on velocity when $\varepsilon D_1^2 = 5$, $\varepsilon D_2^2 = 10$, $\delta = 2$.

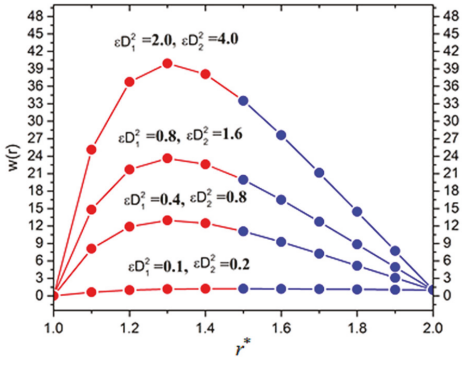

Figure 5. Effect of εD_1^2 and εD_2^2 on velocity profile when $X_1 = 0.5$, $X_1 = 1.0$, $\delta = 2$.

Figure 6 reveals that the volume flow rate increases with the increasing values of Deborah number along with increasing radii ratio δ. The dimensionless temperature profile inside the die for various values of emerging parameters is shown in Figures 7–9. Figure 7 depicts the effect of Brinkman number on temperature profile. A rise in temperature is observed with increasing the Brinkman number. Additionally, the temperature increases with an increasing Deborah number and pressure gradient parameters, as shown in Figures 8 and 9, respectively.

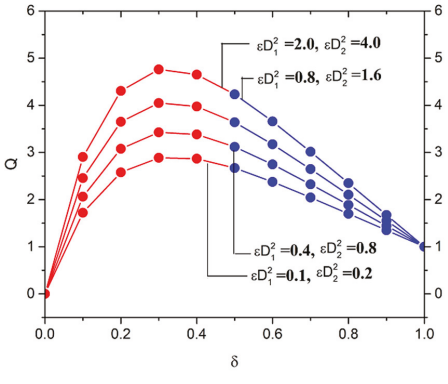

Figure 6. Effect of εD_1^2 and εD_2^2 on volume flow rate when $X_1 = 0.5$, $X_1 = 1.0$.

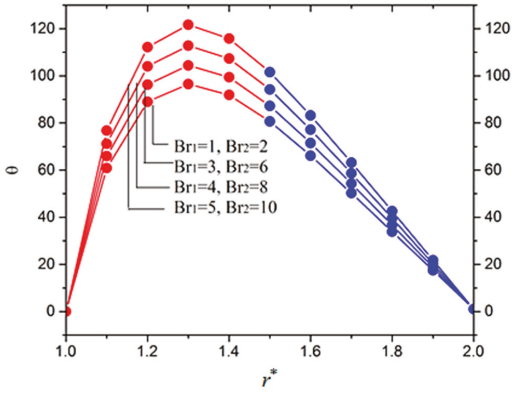

Figure 7. Effect of Br_1 and Br_2 on temperature $X_1 = 0.5$, $X_1 = 1.0$, $\varepsilon D_2^2 = 10$, $\delta = 2$.

The thickness of the coated fiber optics or coating thickness (h_c) is shown in Figures 10 and 11. It is observed that the thickness of the coated fiber optics increases with the increasing values of Deborah number and radii ratio δ, as shown in Figures 10 and 11, respectively. For the sake of validity, the present work is also compared with the published work in Reference [17] and good agreement is found by taking the non-Newtonian parameter, which tends to zero, i.e., $\lambda \to 0$.

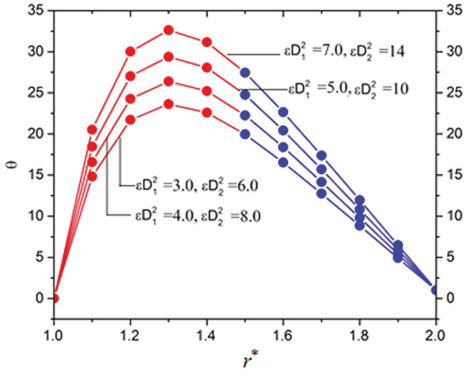

Figure 8. Effect of εD_1^2 and εD_2^2 on temperature $Br_2 = 0.5$ $X_1 = 0.5$, $X_1 = 1.0$, $\delta = 2$.

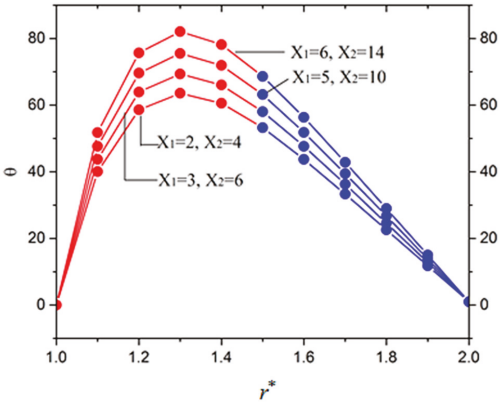

Figure 9. Effect of X_1 and X_2 on temperature $Br_2 = 0.5$, $\varepsilon D_2^2 = 10$, $\delta = 2$.

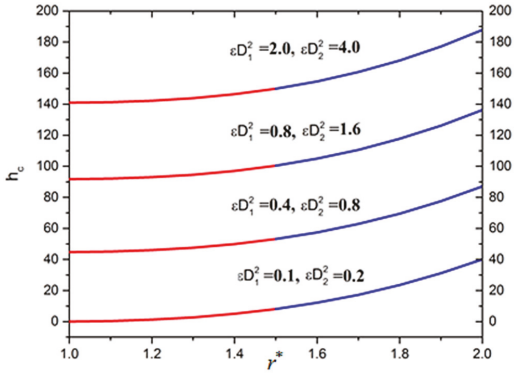

Figure 10. Effect of εD_1^2 on thickness of coated fiber optics when $X_1 = 0.5$, $X_1 = 1.0$, $\delta = 2$.

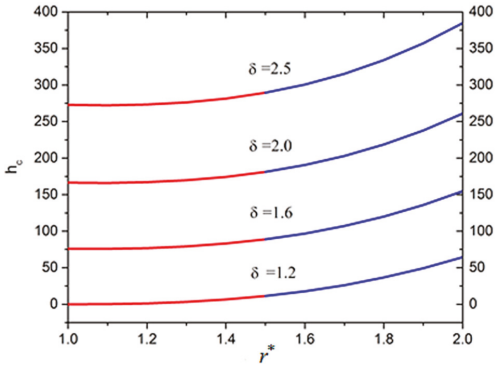

Figure 11. Effect of δ on thickness of coated fiber optics when $X_1 = 0.5$, $X_1 = 1.0$, $\varepsilon D_2^2 = 10$.

6. Conclusions

To provide protection from signal attenuation and mechanical damage, optical fibers required a double-layer resin coating on the glass fiber. Wet-on-wet coating processes are considered for double-layer coating in optical fiber manufacturing. Expressions are presented for the radial variation of axial velocity and temperature distribution analytically and numerically. Analytical expressions of velocity, volume flow rate, final radius of the coated fiber optics and force required the full fiber optics, which are reported. The effect of physical parameters such as Deborah number, dimensionless parameter, radii ratio δ and Brinkman number has been obtained numerically. It was found that velocity increases with increasing values of these parameters. The volume flow rate increases with increasing Deborah number. The thickness of coated fiber optic increase with an increase in εD_1^2, εD_2^2, and δ. The temperature depends upon Br_1, Br_2, εD_1^2, εD_1^2, X_1, and X_2, and it increases with increasing these parameters. For $\varepsilon = 0$ and $\lambda = 0$, our results respectively, reduce to Maxwell and linear viscous model. According to the best of our knowledge, there is no previous literature about the discussed problem, which is our first attempt to handle this problem with two-layer coating flows.

Author Contributions: Z.K. modelled the physical problem. H.U.R. solved it. I.K. and S.O.A. computed the results. T.A. and D.L.C.C. wrote the physical discussion of the results and conclusion. All the authors equally contributed in writing manuscript.

Acknowledgments: Authors would like to thanks YUTP 015LC0-078 for the financial support. and Deanship of Scientific Research, Majmaah University for supporting this work.

Conflicts of Interest: The authors declare no conflict of interest.

Appendix A

Analytical solution

Solutions of Equations (28) and (29) corresponding to the boundary conditions Equations (30–32) become:

$$w_1 = -2r^2X_1 - 4C_1X_1 \ln r - 32\varepsilon De_1^2 r^4 - 192X_1C_1\varepsilon De_1^2 r^2 - 384X_1{C_1}^2\varepsilon De_1^2 \ln r + 64{C_1}^3X_1\varepsilon De_1^2 \tfrac{1}{r^2} + C_3 \quad \text{(A1)}$$

$$w_2 = -2r^2X_2 - 4C_2X_2 \ln r - 32X_2\varepsilon De_2^2 r^4 - 192X_2C_{2c}\varepsilon De_2^2 r^2 - 384X_2{C_2}^2\varepsilon De_2^2 \ln r + 64{C_2}^3X_2\varepsilon De_2^2 \tfrac{1}{r^2} + C_4 \quad \text{(A2)}$$

Volume flow rates are

$$Q_1 = X_1\left(\begin{array}{l}\left(C_1 + 96{C_1}^2\varepsilon De_1^2 + \frac{1}{r}C_3\right)(\Gamma^2 - 1) - \left(\frac{1}{2} + 48C_1\varepsilon De_1^2\right)(\Gamma^4 - 1) - \frac{16}{3}\varepsilon De_1^2(\Gamma^6 - 1) + 64{C_1}^3\varepsilon De_1^2 \ln\Gamma \\ -2\left(K_a + 96{C_1}^2\varepsilon De_1^2\right)\Gamma^2 \ln\Gamma\end{array}\right) \quad \text{(A3)}$$

$$Q_2 = C_4\left(\delta^2-\Gamma^2\right)-\tfrac{1}{2}X_2\left(1+96C_2\varepsilon De_2^2\right)\left(\delta^4-\Gamma^4\right)-\tfrac{16}{3}X_2\varepsilon De_2^2\left(\delta^6-\Gamma^6\right)-2C_2X_2\left(1+192\varepsilon De_2^2\right)\times \begin{pmatrix} \delta^2\ln\delta \\ -\Gamma^2\ln\Gamma \end{pmatrix}+64{C_2}^2\varepsilon De_2^2(\ln\delta-\ln\Gamma) \tag{A4}$$

Thickness of the coated fiber optics of both layers is [17–21]

$$R_1 = \left[\left[\left[1-\tfrac{2}{15\Gamma}2\left(\begin{array}{l} 96\varepsilon De_1^2\left(-\Gamma+\Gamma^6+10(-1+\Gamma)C_1\left(\Gamma+\Gamma^2+\Gamma^3+6C_1\ln\Gamma-{C_1}^2\right)X_1\right)+ \\ 5\Gamma\left(\begin{array}{l} -3(-1+\Gamma)C_3 \\ +6\ln\left(-1+\Gamma^2\right) \\ C_1X_1+2\left(-1+\Gamma^3\right)C_1 \end{array}\right) \end{array}\right)\right]\right]^{1/2} \tag{A5}$$

$$R_2 = \left[\left[\left[1-\tfrac{1}{15\Gamma}\left[2\left(\begin{array}{l} 15\delta\Gamma(-\delta+\Gamma)C_4+6\left(\begin{array}{l} 5\Gamma\ln\delta(\delta-\Gamma)(\delta+\Gamma)C_3+ \\ 16\varepsilon De_2^2\left(\begin{array}{l} \delta^6\Gamma-\delta\Gamma^6+10(\delta-\Gamma)C_3 \\ \left(\begin{array}{l} \delta\Gamma\left(\delta^2+\delta\Gamma+\Gamma^2\right)+ \\ 6\Gamma K\ln\delta_c-{C_3}^2 \end{array}\right) \end{array}\right) \end{array}\right)X_2 \\ +10\delta\Gamma\left(\delta^3-\Gamma^3\right)X_2 \end{array}\right)\right]\right]\right]^{1/2} \tag{A6}$$

Temperature profiles for both layers are

$$\theta_1 = -4B_{r_1}X_1^2\left(\begin{array}{c} -\frac{1}{4}r^4-3K_ar^2-\frac{32}{9}\varepsilon De_1^2r^6-24K_a\varepsilon De_1^2r^4-96K_a^2\varepsilon De_1^2r^2-128K_a^3X_1\varepsilon De_1^2\ln r-4K_a^2\ln r- \\ 8\varepsilon De_1^2r^4-96K_a^2\varepsilon De_1^2r^2-384K_a^3\varepsilon De_1^2\ln r+32K_a^3\varepsilon De_1^2\frac{1}{r^2} \\ +D_1\ln r+D_2, \end{array}\right) \tag{A7}$$

$$\theta_2 = -4B_{r_2}X_2^2\left(\begin{array}{c} -\frac{1}{4}r^4-3C_3r^2-\frac{32}{9}\varepsilon De_2^2r^6-24C_3\varepsilon De_2^2r^4-96{C_3}^2\varepsilon De_2^2r^2-128{C_3}^3X_2\varepsilon De_2^2\ln r-4{C_3}^2\ln r- \\ 8\varepsilon_2De_2{}^2r^4-96{C_3}^2\varepsilon De_2^2r^2-384{C_3}^3\varepsilon De_2^2\ln r+32{C_3}^3\varepsilon De_2^2\frac{1}{r^2} \\ +D_3\ln r+D_4, \end{array}\right) \tag{A8}$$

where $K_a, K_b, K_c, K_d, D_1, D_2, D_3$ and D_4 are all constants given below:

$$C_1 = -\frac{H_1}{3}-\frac{2^{\frac{1}{3}}\left(-{H_1}^2+3H_2\right)}{3\left(-2{H_1}^3+9H_1H_2-27H_3+3\sqrt{3}\sqrt{-{H_1}^2H_2^2+4H_2^3+4H_1{}^3H_3-18H_1H_2H_3+27H_3^2}\right)^{\frac{1}{3}}}+ \frac{\left(-2{H_1}^3+9H_1H_2-27H_3+3\sqrt{3}\sqrt{-{H_1}^2H_2^2+4H_2^3+4H_1{}^3H_3-18H_1H_2H_3+27H_3^2}\right)^{\frac{1}{3}}}{32^{\frac{1}{3}}},$$

$$C_3 = 1+2_1+32\varepsilon De_1{}^2+192C_1\varepsilon De_1{}^2-64{C_1}^3X_1\varepsilon De_1{}^2, C_2 = C_3,$$

$$C_4 = 2\delta^2X_2+4C_3X_2\ln\delta+32X_2\varepsilon D_2{}^2\delta^4+192X_2C_3\varepsilon_2De_2{}^2\delta^2+384X_2{C_3}^2\varepsilon D_2{}^2\ln\delta-64{C_3}^3X_2\varepsilon D_2{}^2\frac{1}{\delta^2},$$

$$D_1 = 4B_{r_1}X_1^2(K((\ln\Gamma-\ln\delta)+\Gamma))\left(\begin{array}{c} \frac{1}{4}\Gamma^4+3{C_1}{}^2\Gamma^2+\frac{32}{9}\varepsilon De_1{}^2\Gamma^6+24{C_1}D_1{}^2\Gamma^4+96K_a^2\varepsilon De^2{}_1\Gamma^2+ \\ 128{C_1}^3\varepsilon De_1{}^2\ln\Gamma+4{C_1}^2\ln\Gamma+8\varepsilon De_1{}^2\Gamma^4+96{C_1}^2\varepsilon De_1{}^2\Gamma^2+ \\ 384{C_1}^3\varepsilon De_1\ln\Gamma-32{C_1}^3{D_1}^2\frac{1}{\Gamma^2} \end{array}\right)+$$

$$4Br_2X_2^2\left(\left(\Gamma-\left(\tfrac{1}{\Gamma}+\tfrac{1}{\Gamma^2\ln\Gamma}\right)\right)\right)\left(\begin{array}{c} \frac{1}{4}\Gamma^4+3C_3\Gamma^2+\frac{32}{9}\varepsilon De_2{}^2\Gamma^6+24C_3\varepsilon De_2{}^2\Gamma^4-96{C_3}^2\varepsilon D^2e_1\Gamma^2+ \\ 128C_b^3\varepsilon De_2{}^2\ln\Gamma+4{C_3}^2\ln\Gamma+8\varepsilon De_2{}^2\Gamma^4+96{C_3}^2\varepsilon De_2{}^2\Gamma^2+ \\ 384{C_3}^3\varepsilon D^2e_2\ln\Gamma-32{C_3}^3\varepsilon De_2{}^2\frac{1}{\Gamma^2} \end{array}\right)+$$

$$+4Br_1X_1^2\tfrac{1}{\Gamma^2\ln\delta}\left(\tfrac{1}{4}+3C_1+\tfrac{32}{9}\varepsilon De_1{}^2+32C_1\varepsilon De_1{}^2+192{C_1}^2\varepsilon De_1{}^2-32{C_1}^3\varepsilon De_1{}^2\right),$$

$$D_2 = 4Br_1X_1^2\tfrac{1}{\Gamma^2\ln\delta}\left(\tfrac{1}{4}+3C_1+\tfrac{32}{9}\varepsilon De_1{}^2+32C_1\varepsilon De_1{}^2+192{C_1}^2\varepsilon De_1{}^2-32{C_1}^3\varepsilon De_1{}^2\right),$$

$$D_3 = 4Br_1X_1^2(\Gamma(\ln\Gamma-\ln\delta))\left(\begin{array}{c} \Gamma^3+3C_1\Gamma+\frac{64}{3}\varepsilon De_1{}^2\Gamma^5+96\varepsilon De_1{}^2\Gamma^3+ \\ 192{C_1}^2\varepsilon De_1{}^2\Gamma+128{C_1}^3\varepsilon De_1{}^2\frac{1}{\Gamma}+4{C_1}^2\frac{1}{\Gamma}+ \\ 32\varepsilon De_1{}^2\Gamma^3+192{C_1}^2\varepsilon De_1{}^2\Gamma+384{C_1}^3\varepsilon De_1{}^2\frac{1}{\Gamma}+64{C_1}^2\varepsilon De_1{}^2\frac{1}{\Gamma^3} \end{array}\right)$$

$$+4Br_1X_1^2\tfrac{1}{\ln\delta}\left(\tfrac{1}{4}+3C_1+\tfrac{32}{9}\varepsilon De_1{}^2+32C_1\varepsilon De_1{}^2+192{C_1}^2\varepsilon De^2{}_1-32{C_1}^3\varepsilon De^2{}_1\right)+4Br_2X_2^2\left(\begin{array}{c} \Gamma K(\ln\Gamma-\ln\delta) \\ +\frac{1}{\ln\delta} \end{array}\right)+$$

$$\left(\begin{array}{c} \frac{1}{4}\Gamma^4+3C_3\Gamma^2+\frac{32}{9}\varepsilon De_2{}^2\Gamma^6+24C_3\varepsilon De_2{}^2\Gamma^4-96C_3^2\varepsilon De_2{}^2\Gamma^2+128C_3^3\varepsilon De_2{}^2\ln\Gamma+4C_3^2\ln\Gamma+8\varepsilon De_2{}^2\Gamma^4 \\ +96C_3^2\varepsilon De_2{}^2\Gamma^2+384C_3^3\varepsilon De_2{}^2\ln\Gamma-32C_3^3\varepsilon De_2{}^2\frac{1}{\Gamma^2} \end{array}\right)$$

$$D_4 = 4Br_2X_2^2\left(\begin{array}{c} \frac{1}{4}\Gamma^4+3C_3\Gamma^2+\frac{32}{9}\varepsilon De_2{}^2\Gamma^6+24C_3\varepsilon De_2{}^2\Gamma^4-96C_3^2\varepsilon De_2{}^2\Gamma^2+128C_3^3\varepsilon De_2{}^2\ln\Gamma+ \\ 4C_3^2\ln\Gamma+8\varepsilon De_2{}^2\Gamma^4+96C_3^2\varepsilon De_2{}^2\Gamma^2+384C_3^3\varepsilon De_2{}^2\ln\Gamma-32C_3^3\varepsilon De_2{}^2\frac{1}{\Gamma^2} \end{array}\right)-\Gamma D_3,$$

where

$$H_1 = \frac{A_2+B_2}{A_3+B_3}, H_2 = \frac{A_1+B_1}{A_3+B_3}, H_3 = \frac{G}{A_3+B_3}, A_1 = -4X_1 \ln\Gamma - 192X_2\varepsilon De_2^2 - 192X_1\varepsilon De_1^2\Gamma,$$
$$A_2 = -384X_1\varepsilon De_1^2 \ln\Gamma, A_3 = 64X_1\varepsilon De_1^2\left(\frac{1}{\Gamma^2} - 1\right), B_1 = 4X_2 \ln\Gamma + 192X_2\varepsilon De_2^2\Gamma^2,$$
$$B_2 = 384X_2\varepsilon De_2^2 \ln\delta + 192X_2\varepsilon De_2^2\Gamma^2 B_3 = -64X_2\varepsilon De_2^2\Gamma^2\left(\frac{1}{\delta^2} + \frac{1}{\Gamma^2}\right),$$
$$A_1 = -4X_1 \ln\Gamma - 192\varepsilon_1 De_1{}^2\Gamma + 192\varepsilon De_1{}^2 A_2 = -384X_1\varepsilon De_1{}^2 \ln\Gamma,$$
$$A_3 = 64X_1\varepsilon De_1{}^2\frac{1}{\Gamma} - 64X_1\varepsilon De_1{}^2, B_1 = 4X_2 \ln\Gamma + 192X_2\varepsilon De_2{}^2\Gamma^2 - 192X_2\varepsilon De_2{}^2\delta^2 - 4X_2 \ln\delta,$$
$$B_2 = -384X_2\,\varepsilon De_2{}^2 \ln\Gamma + 384X_2\varepsilon De_2{}^2 \ln\delta, B_3 = -64X_2\varepsilon De_2{}^2\frac{1}{\Gamma^2} - 64X_2\varepsilon De_2{}^2\frac{1}{\delta^2},$$
$$G = 1 + 2X_1 + 32X_1\varepsilon D_1{}^2 - 2X_2\delta^2 - 2X_1\Gamma^2 - 32X_2\varepsilon De_2{}^2\delta^4 - 32X_1\varepsilon De_1{}^2\Gamma^4 - 2X_2\Gamma^3.$$

References

1. Rajagopal, K.R. On the boundary conditions for fluids of the differential type. In *Navier-Stokes Equation and Related Non-Linear Problems*; Sequira, A., Ed.; Plenum Press: New York, NY, USA, 1995; pp. 273–278.
2. Rajagopal, K.R.; Kaloni, P.N. Some remarks on the boundary conditions for fluids of the differential type. In *Continuum Mechanics and its Applications*; Gram, G.A., Malik, S.K., Eds.; Hemisphere: Washington, DC, USA, 1989; pp. 935–941.
3. Szeri, A.Z.; Rajagopal, K.R. Flow of a non-Newtonian fluid between heated parallel plates. *Int. J. NonLinear Mech.* **1985**, *20*, 91–101. [CrossRef]
4. Makinde, O.D. Irreversibility analysis for gravitry driven non-Newtonian liquid film along an inclined isothermal plate. *Phys. Scr.* **2006**, *74*, 642–645. [CrossRef]
5. Bernhardt, E.C. *Processing of Thermoplastic Materials*; Reinhold Publishing: New York, NY, USA, 1962; pp. 263–269.
6. McKelvey, J.M. *Polymer Processing*; John Wiley and Sons: New York, NY, USA, 1962.
7. Bagley, E.B.; Storey, S.H. Processing of thermoplastic materials. *Wire Wire Prod.* **1963**, *38*, 1104–1122.
8. Han, C.D.; Rao, D. The rheology of wire coating extrusion. *Polym. Eng. Sci.* **1978**, *18*, 1019–1029. [CrossRef]
9. Carley, J.F.; Endo, T.; Krantz, W. Realistic analysis of flow in wire coating dies. *Polym. Eng. Sci.* **1979**, *19*, 1178–1187. [CrossRef]
10. Han, C.D. *Rheology and Processing of Polymeric Materials Volume 2 Polymer Processing*; Oxford University Press: Oxford, UK, 2007; pp. 235–256.
11. Binding, D.M.; Blythe, A.R.; Guster, S.; Mosquera, A.A.; Townsend, P.; Wester, M.P. Modelling polymer melt flows in wire coating process. *J. Nonnewton. Fluid Mech.* **1996**, *64*, 191–206. [CrossRef]
12. Multu, I.; Twnsend, P.; Webster, M.F. Simulation of cable-coating viscoelastic flow with coupled and de-coupled schemes. *J. Nonnewton. Fluid Mech.* **1998**, *74*, 1–23. [CrossRef]
13. Kasajima, M.; Ito, K. Post-treatment of polymer extrudate in wire coating. *Appl. Polym. Symp.* **1973**, *20*, 221–235.
14. Winter, H.H. SPE 36th ANTEC. *Tech. Pap.* **1977**, *23*, 462.
15. Symmons, G.R.; Hasmi, M.S.J.; Pervinmehr, H. Plasto-hydrodynamics die lesswire drawing theoretical treatments and experimental result. In *Progress Reports in Conference in Developments in Drawing of Metals*; North Holland: New York, NY, USA, 1992; pp. 54–62.
16. Baag, S.; Mishra, S.R. Power law model in post treatment analysis of wirecoating with linearly variable temperature. *Am. J. Heat Mass Transf.* **2015**, *2*, 89–107.
17. Kim, K.; Kwak, H.S.; Park, S.H.; Lee, Y.S. Theoretical prediction on double-layer coating in wet-on-wet optical fiber coating process. *J. Coat. Technol. Res.* **2011**, *8*, 35–44. [CrossRef]
18. Kim, K.J.; Kwak, H.S. Analytic Study of Non-Newtonian Double Layer Coating Liquid Flows in Optical Fiber Manufacturing. *Trans. Tech. Publ.* **2012**, *224*, 260–263. [CrossRef]
19. Zeeshan, K.; Shah, S.I. Double-layer Optical Fiber Coating Using Viscoelastic Phan-Thien-Tanner Fluid. *N. Y. Sci. J.* **2013**, *6*, 66–73.
20. Khan, Z.; Islam, S.; Shah, R.A.; Khan, I.; Gu, T. Exact Solution of PTT Fluid in Optical Fiber Coating Analysis using Two-layer Coating Flow. *J. Appl. Environ. Biol. Sci.* **2015**, *5*, 596–605.

21. Khan, Z.; Islam, S.; Shah, R.A. Flow and heat transfer of two immiscible fluids in double-layer optical fiber coating. *J. Coat. Technol. Res.* **2016**, *13*, 1055–1063. [CrossRef]
22. Hayat, T.; Saif, R.S.; Ellahi, R.; Taseer, M.Y.R.; Ahmad, B. Numerical study for Darcy-Forchheimer flow due to a curved stretching surface with Cattaneo-Christov heat flux and homogeneous-heterogeneous reactions. *Results Phys.* **2017**, *7*, 2886–2892. [CrossRef]
23. Hayat, T.; Saif, R.S.; Ellahi, R.; Taseer, M.Y.R.; Alsaedi, A. Simultaneous effects of melting heat and internal heat generation in stagnation point flow of Jeffrey fluid towards a nonlinear stretching surface with variable thickness. *Int. J. Therm. Sci.* **2018**, *132*, 344–354. [CrossRef]
24. Shehzad, N.; Zeeshan, A.; Ellahi, R.; Vafai, K. Convective heat transfer of nanofluid in a wavy channel: Buongiorno's mathematical model. *J. Mol. Liquids* **2016**, *222*, 446–455. [CrossRef]
25. Ellahi, R.; Riaz, A. Analytical solutions for MHD flow in a third-grade fluid with variable viscosity. *Math. Comput. Modell.* **2010**, *52*, 1783–1793. [CrossRef]

coatings

MDPI

Article

MHD Thin Film Flow and Thermal Analysis of Blood with CNTs Nanofluid

Ali Sulaiman Alsagri [1], Saleem Nasir [2], Taza Gul [3], Saeed Islam [2], K.S. Nisar [4], Zahir Shah [2] and Ilyas Khan [5,*]

[1] Mechanical Engineering Department, Qassim University, Buraydah 51431, Saudi Arabia; a.alsagri@qu.edu.sa
[2] Department of Mathematics, Abdul Wali Khan University Mardan, Mardan 23200, Pakistan; saleemnasir85@gmail.com (S.N.); saeedislam@awkum.edu.pk (S.I.); zahir1987@yahoo.com (Z.S.)
[3] Department of Mathematics, City University of Science and Information Technology (CUSIT), Peshawar 25000, Pakistan; tazagul@cusit.edu.pk
[4] Department of Mathematics, College of Arts and Science at Wadi Al-Dawaser, Prince Sattam bin Abdulaziz University, Al-Kharj 11991, Saudi Arabia; n.sooppy@psau.edu.sa
[5] Faculty of Mathematics and Statistics, Ton Duc Thang University, Ho Chi Minh 72915, Vietnam
* Correspondence: ilyaskhan@tdt.edu.vn

Received: 9 February 2019; Accepted: 25 February 2019; Published: 6 March 2019

Abstract: Our main objective in the present work is to elaborate the characteristics of heat transport and magneto-hydrodynamics (MHD) finite film flow of human blood with Carbon Nanotubes (CNTs) nanofluids over a stretchable upright cylinder. Two kinds of CNTs nanoparticles, namely (i) SWCNTs (single walled carbon nanotubes) and (ii) MWCNTs (multi walled carbon nanotubes), are used with human blood as a base liquid. In addition, a uniform magnetic field (B) has been conducted perpendicularly to the motion of nanoliquid. The transformation of the partial differential structure into a non-linear ordinary differential structure is made by using appropriate dimensionless quantities. The controlling approach of the Homotopy analysis method (HAM) has been executed for the result of the velocity and temperature. The thickness of the coating film has been kept variable. The pressure distribution under the variable thickness of the liquid film has been calculated. The impacts of different variables and rate of spray during coating have been graphically plotted. The coefficient of skin friction and Nusselt number have been presented numerically. In addition, it is noticed that the thermal field of a nanoliquid elevates with rising values of ϕ and this increase is more in SWCNTs nanofluid than MWCNTs nanofluid.

Keywords: thin film casson nanofluid; SWCNTs and MWCNTs; stretching cylinder; MHD; HAM

1. Introduction

1.1. Literature Review

Nanofluid, characterized by a significant increase in the heat and mass transfer rate compared to conventional engineered fluid (oils, lubricants, water, ethylene glycol, etc.) [1], is found to serve in a number of engineering applications, for instance, the solar energy system [2], fuel-cell industry [3], petroleum engineering [4–6], materials science [7,8], etc. Choi [9] was the first person who introduced the concept of a dilute suspension of nanoparticles with a dimension less than 100 nm (Cu, TiO_2, Al_2O_3, Ag, Fe) and their oxides in conventional fluids (oils, lubricants, water, ethylene glycol), which enhances the thermal performance of conventional fluids. Recent applications of nanofluids in the biomechanical field, such as cancer therapy, drug delivery and medicines, have produced a lot of interest in the investigation of nanofluid flows and heat transport. In view of these various applications, researchers have focused their attention on nanofluid flows. Ellahi [10] examined

the impact of MHD and thermal viscosity on the flow of non-Newtonian nanoliquid over a tube. Alshomrani and Gul [11] computed the analytical solution of magneto-hydrodynamics thin film spray of water base Al_2O_3 and CuO nanofluids on a horizontal stretchable cylinder. Asadi et al. [12,13] investigated the experimental and theoretical influence of adding MWCNTs, ZnO nanoparticles, and MgO-MWCNT hybrid nanofluids in thermal oil. Gul et al. [14] discussed the impact of an effective Prandtl number on water and ethylene glycol-based alumina nanofluid spray along a stretching cylinder.

CNTs (carbon nanotubes) have a long cylindrical profile, such as frames of carbon atoms with a diameter ranging from 0.7 nm to 50 nm. Carbon nanotubes have a specific importance in nanotechnology, conductive plastics, hardwater, air purification mechanisms, structural composite materials, sensors, display of flat panels, storage of gas, biosensors, extra-long fibers, and many other areas of science and engineering. The idea of CNTs was first discovered in 1991 by Lijima [15]. Carbon nanotubes are further classified as single wall carbon nanotubes (SWCNTs) and multi wall carbon nanotubes (MWCNTs), depending on the number of concentric layers of rolled graphene sheets. Furthermore, carbon nanotubes are predictable inventive material of the 21st century due to their special morphology; new physicochemical features; and unique thermal, electrical, and mechanical characteristics. Additionally, the existence of carbon chains in carbon nanotubes does not pose any danger to the atmosphere. Keeping the above applications, Haq et al. [16] investigated the impact of the thermal conductivity and viscosity of CNTs nanoparticles within three different base fluids (water, engine oil, and ethylene glycol) in nanofluid flowing over a stretching surface. Khan et al. [17] considered the analysis of flow and heat transport of nanofluids containing carbon nanotubes along a flat plate in the presence of the Navier slip boundary condition. Aman et al. [18] examined the effect of MHD on the flow of non-Newtonian CNTs nanofluid. They used three kinds of base liquid. Similarly, the exact solution of Maxwell nanofluid containing CNTs in four types of base fluid was investigated in [19]. Asadi et al. [20–23] conducted some experimental study on the dynamic viscosity of different nanofluids. They found that the viscosity of MWCNTs nanofluids is considerably higher than that of the base fluids. Various other important studies that have been conducted on CNTs base nanofluid can be seen via [24,25].

After the development of nanoliquids, scholars and engineers focused their concentration on examining the motion of nanofluids from various circumstances, such as stretching cylinders and sheets, rotating disks or cylinders, and parallel plates with various flow conditions. The flow problem of magneto-nanofluid through a stretching/extending surface has several practical applications in manufacturing progressions due to the mechanical property of electrically conducting liquids. A stretching surface has gained the extensive attention of scholars due to many manufacturing and technological applications, such as the fabrication and removal of polymer slips from dye, freezing of continuing filaments, lead crystal blowing, manufacture of paper, production of meals, and sketching of wires. Khan et al. [26] explored the phenomena of MHD spray scattering on a stretching cylinder using nanoparticles Al_2O_3 and CuO water-based nanoliquids. Recently, some more useful explorations of the subject associated with thin film flow have been presented in [27–30].

Non-Newtonian liquids like toothpaste, food stuff, and plastic have various uses in biochemical, pharmacological, and cosmetic industries. It is very problematic to handle this kind of liquid because the extra nonlinear term originates in the equation of motion. Thus, various liquid models are presented to describe the performance of the said materials. In the present analysis, we select the Casson model. Initially, this model was presented by [31]. It is a shear thinning fluid which is thought of as the zero-shear rate of immeasurable viscosity [32], but is the infinite shear rate at zero viscosity. Human blood, honey, jelly, and soup are examples of Casson fluid. The influence of thermal radiation on Casson fluid flow and the rate of heat exchange on a permeable extending surface have been reported [33]. Asma et al. [34] have explored the MHD flow of Casson liquid on a permeable upright plate. The impact of MHD on Casson nanofliquid flow with thermal radiation over a cylinder was studied in [35].

Among the various models of non-Newtonian time independent fluids models, one of the distinct features and a quite famous Casson model [31,36] known as the most approved is the rheological model for characterizing human blood flow [24,37,38].

In the present work, the thin film Casson nanofluid (human blood) flow comprising CNTs nanoparticles is analyzed with uniform MHD over a stretching upright cylinder. Human blood is used as the base liquid, with two varieties of SWCNTs and MWCNTs nanoparticles inside. The HAM technique [11,39–43] is performed to find the series solution of velocity and the thermal field. The physical performance of each model's parameters for SWCNTs and MWCNTs nanoparticles is presented graphically for velocity, temperature, and pressure fields. Conclusions have been established on the basis of the results.

1.2. Models of Thermophysical Properties of CNTs Nanofluids

This section demonstrates the thermophysical properties of CNTs nanofluids.

1.2.1. The Effective Density Model

ρ_{nf} is the effective density of nanofluids, which is given by [24,25]

$$\rho_{nf} = (1-\varphi)\rho_f + \varphi\,\rho_{CNT}, \tag{1}$$

Here, φ signifies the volume fraction of nanoparticles and ρ_f, ρ_{CNT} signify the density of the base fluid and CNTs, respectively.

1.2.2. The Effective Viscosity Model

μ_{nf} is the effective density of nanofluids, which is given by [24,25]

$$\mu_{nf} = \mu_f(1-\varphi)^{-2.5}, \tag{2}$$

1.2.3. The Effective Thermal Expansion Coefficient of Nanoparticles Model

$(\rho\beta^{\otimes})_{nf}$ is the effective thermal expansion coefficient of nanoparticles, which is given by [24,25]

$$(\rho\beta^{\otimes})_{nf} = (1-\varphi)(\rho\beta^{\otimes})_f + \varphi(\rho\beta^{\otimes})_{CNT}, \tag{3}$$

$(\rho\beta^{\otimes})_f, (\rho\beta^{\otimes})_{CNT}$ signify the thermal expansion coefficient of the base fluid and CNTs, respectively.

1.2.4. The Effective Specific Heat Capacity Model

$(\rho\, c_p)_{nf}$ is the effective specific heat capacity of nanofluids, which is given by [24,25]

$$(\rho\, c_p)_{nf} = (\rho\, c_p)_f \left[(1-\varphi) + \varphi\left(\frac{(\rho\, c_p)_{CNT}}{(\rho\, cp)_f}\right)\right], \tag{4}$$

$(\rho\, cp)_f, (\rho\, cp)_{CNT}$ signify the specific heat capacity of the base fluid and CNTs, respectively.

1.2.5. The Effective Electrical Conductivity Model

σ_{nf} is the effective electrical conductivity of nanofluids, which is given by

$$\sigma_{nf} = \sigma_f\left[1 + \frac{3\left(\frac{\sigma_{nf}}{\sigma_f} - 1\right)\varphi}{\left(\frac{\sigma_{nf}}{\sigma_f} + 2\right) - \left(\frac{\sigma_{nf}}{\sigma_f} - 1\right)\varphi}\right], \tag{5}$$

σ_f, σ_{CNT} signify the electrical conductivity of the base fluid and CNTs, respectively.

1.2.6. The Effective Thermal Conductivity Model

In the literature, there are several theoretical models available to calculate the thermal conductivities of carbon nanotubes (e.g., Maxwell's, Jeffery's, Davis's, Hamilton's, and crosser models), but only Xue's model [44] employs principal models, which are effective for spherical and elliptical shape particles. Xue's model was established from the Maxwell model of turning elliptical carbon nanotubes through a big axial ratio and paying the effect of the space sharing on CNTs. Here, for the thermal conductivity of nanofluid k_{nf}, Xue's model [44] has been utilized.

$$\frac{k_{nf}}{k_f} = \frac{1-\varphi+2\varphi\left(\frac{k_{CNT}}{k_{CNT}-k_f}\right)\ln\left(\frac{k_{CNT}+k_f}{2\,k_f}\right)}{1-\varphi+2\varphi\left(\frac{k_f}{k_{CNT}-k_f}\right)\ln\left(\frac{k_{CNT}+k_f}{2\,k_f}\right)}. \tag{6}$$

k_f, k_{CNT} signify the thermal conductivity of the base fluid and CNTs, respectively.

2. Description of Problem

We consider steady and incompressible two-dimensional thin film Casson nanofluids flow along a stretching upright cylinder of radius a. The z-axis represents along the surface of the cylinder and the r-axis is that taken radially, as shown in Figure 1. The cylinder is supposed to electrically conduct with constant B (magnetic field) of strength B_0. Here, $T_w = T_a$ is the surface temperature, while $T_\delta = T_b$ is the free surface temperature of the cylinder. In this scenario, the tube surface is stretching with velocity $W_w = 2s\,z$ along the z-axis. Here, $s > 0$ is used for extension of the cylinder surface, while for contraction, $s < 0$ is used. Additionally, the thermal field for the present problem is [11]

$$T = T_b - T_r\left(\frac{c\,z^2}{\upsilon_{nf}}\right)\Theta(\eta), \tag{7}$$

where T_r is the reference temperature. Furthermore, the human blood-based nanoliquid comprises two sorts of CNTs (SWCNTs and MWCNTs) [24]. Viscous dissipation and natural convection have been involved in nanofluid flow. The stress tensor of the Casson fluid model [36,37] is implemented as

$$\begin{aligned} \tau_{mn}^{sf} &= 2e_{mn}\mu_a^{df} + 2e_{mn}\frac{p_y}{\sqrt{2\pi_d}}, \text{ where } \pi_d \geq \pi_{cr}, \text{ and} \\ \tau_{mn}^{sf} &= 2e_{mn}\mu_a^{sf} + 2e_{mn}\frac{p_y}{\sqrt{2\pi_d}}, \text{ where } \pi_d \prec \pi_{cr}. \end{aligned} \tag{8}$$

In the above expression, the share stress along mth and nth components is τ_{mn}^{sf}, the deformation rate is π_d, deformation rate components mth and nth are e_{mn}, the critical value represented by π_{cr} is focused on the non- Newtonian fluid model, μ_a^{sf} is the plastic dynamic viscosity of Casson fluid, and the produce stress of the fluid is p_y.

By applying the order analysis, the suggested boundary film equations of carbon nanotubes fluid are [11]

$$\frac{\partial(ru)}{\partial\, r} + \frac{\partial(rw)}{\partial\, z} = 0, \tag{9}$$

$$\rho_{nf}\left[u\left(\frac{\partial w}{\partial r}\right) + w\left(\frac{\partial w}{\partial z}\right)\right] = \mu_{nf}\left(1+\frac{1}{\beta}\right)\left[\frac{\partial^2 w}{\partial r^2} + \frac{1}{r}\left(\frac{\partial w}{\partial r}\right)\right] + \left(\rho\beta^{\otimes}\right)_{nf}(T-T_b)g - \sigma_{nf}B_0^2 w, \tag{10}$$

$$\rho_{nf}\left[u\frac{\partial u}{\partial r} + w\frac{\partial u}{\partial z}\right] = -\frac{\partial p}{\partial r} + \mu_{nf}\left(1+\frac{1}{\beta}\right)\left(\frac{\partial^2 u}{\partial r^2} + \frac{1}{r}\frac{\partial u}{\partial r} - \frac{u}{r^2}\right), \tag{11}$$

$$\left(\rho c_p\right)_{nf}\left(u\frac{\partial T}{\partial r} + w\frac{\partial T}{\partial z}\right) = k_{nf}\left(\frac{\partial^2 T}{\partial r^2} + \frac{1}{r}\frac{\partial T}{\partial r}\right) + \mu_{nf}\left(\frac{\partial w}{\partial r}\right)^2. \tag{12}$$

Here, r, z are the radial and axial coordinates, respectively. Additionally, $u(r,z)$ and $w(r,z)$ are the velocity elements in the r and z directions. $\beta = \frac{\mu_a^{sf}\sqrt{2\pi_{cr}}}{\tau_{mn}}$ is the material parameter (Casson parameter); the local pressure and temperature are specified by p and T, respectively; the specific density of the nanofluid is ρ_{nf}; the dynamic viscosity of the nanofluid is μ_{nf}; $\beta_{nf}^{\otimes}$ is the thermal expansion coefficient of nanoparticles; the electrical conductivity of the nanofluid is σ_{nf}; the thermal conductivity of the nanofluid is k_{nf}; and the specific heat capacity of the nanofluid is $(\rho c_p)_{nf}$.

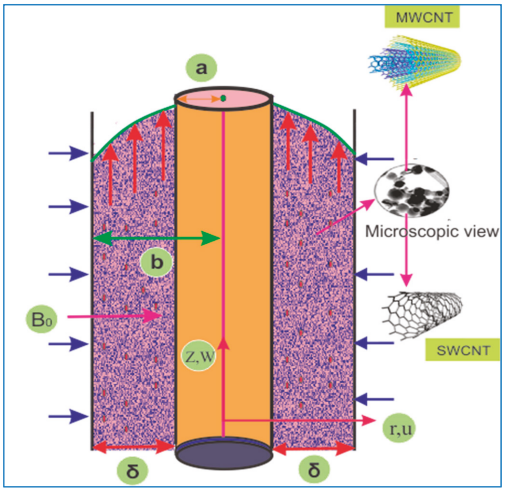

Figure 1. Schematic diagram of flow model and coordinate system.

The subjected boundary conditions for the present analysis are as follows [11]:

$$u = U_w,\ w = W_w,\ T = T_w,\ at\ r = a, \tag{13}$$

$$\mu\frac{\partial w}{\partial r} = 0,\ \frac{\partial T}{\partial r} = 0,\ u = w\frac{d\delta}{dz},\ at\ r = b. \tag{14}$$

where b is the outer radius which display the thickness of the liquid film, the expression of suction and injection velocity is U_w, and W_w is the extended velocity of the cylinder surface.

Non-Dimensional Parameters

With the aid of the following suitable conversions [11]:

$$\eta = \frac{r^2}{a^2},\ u = \frac{-sa}{\sqrt{\eta}}[f(\eta)],\ w = 2sz\left[\frac{df(\eta)}{d\eta}\right], \Theta = \frac{T - T_b}{T_a - T_b}. \tag{15}$$

The transformed equations for momentum and energy arise are

$$\begin{aligned}&\left(1+\tfrac{1}{\beta}\right)\left[\eta\left(\tfrac{d^3f(\eta)}{d\eta^3}\right)+\tfrac{d^2f(\eta)}{d\eta^2}\right]+\\&\left((1-\varphi)+\varphi\tfrac{\rho_{CNT}}{\rho_f}\right)(1-\varphi)^{2.5}\left[\mathrm{Re}\left(f(\eta)\left(\tfrac{d^2f(\eta)}{d\eta^2}\right)-\left(\tfrac{df(\eta)}{d\eta}\right)^2\right)+Gr\Theta(\eta)-Mf(\eta)\tfrac{df(\eta)}{d\eta}\right]=0,\end{aligned} \tag{16}$$

$$\begin{aligned}&\tfrac{k_{nf}}{k_f}\left(2\eta\tfrac{d^2\Theta(\eta)}{d\eta^2}+\tfrac{d\Theta(\eta)}{d\eta}\right)+\mathrm{PrRe}\left((1-\varphi)+\varphi\tfrac{(\rho c_p)_{CNT}}{(\rho c_p)_f}\right)[f(\eta)\tfrac{d\Theta(\eta)}{d\eta}-2\Theta(\eta)\tfrac{df(\eta)}{d\eta}\\&+E_c\left(\tfrac{d^2f(\eta)}{d\eta^2}\right)^2\Bigg]=0.\end{aligned} \tag{17}$$

The resultant transformed dimensionless boundary conditions are

$$f(\eta) = 1,\ \frac{df(\eta)}{d\eta} = 1, \Theta(\eta) = 1 \text{ at } \eta = 1, \tag{18}$$

$$\frac{d^2 f(\eta)}{d\eta^2} = 0,\ \frac{d\Theta(\eta)}{d\eta} = 0,\ at\ \eta = \alpha. \tag{19}$$

The solid particle volume fraction is φ, and in non-dimensional form, the variable thickness is

$$\alpha = \frac{b^2}{a^2} = \eta_b. \tag{20}$$

Here, a, b, α represent the radius of the cylinder, the external radius of the thin layer, and the dimensionless thickness of the thin layer, respectively.

$$\mathrm{Re} = \frac{sa^2}{2v_f},\ \mathrm{Pr} = \frac{\mu_f \left(c_p\right)_f}{k_f},\ M = \frac{\sigma_f B_0^2 a^2}{4\mu_f},\ Gr = \frac{a^2 g(T - T_0)(\beta\,\rho)_f}{4W_w \mu_f}, E_c = \frac{W_w^2 a^2}{\Delta T \left(c_p\right)_f}. \tag{21}$$

Re is the Local Reynolds number, Pr is the prandtl number, M is the magnetic parameter, Gr is the Grashof number, and E_c is the Eckert number in dimensionless form defined as in [11].

Evaluating the pressure distribution term from Equation (11):

$$\frac{p - p_b}{\mu c_f} = -\frac{Re}{\eta}\left((1-\varphi) + \varphi\frac{\rho_{CNT}}{\rho_f}\right)(1-\varphi)^{2.5} f^2(\eta) - 2\left(1 + \frac{1}{\beta}\right)\frac{df(\eta)}{d\eta}. \tag{22}$$

Now, the shear stress at the free surface of the fluid film is zero, which means that

$$\frac{d^2 f(\alpha)}{d\eta^2} = 0. \tag{23}$$

Also, the corresponding shear stress at the cylinder surface is

$$\tau_w = \frac{4s\ z(\rho v)_{nf}}{a}\left(1 + \frac{1}{\beta}\right)\left[\frac{d^2 f(1)}{d\eta^2}\right] = \frac{4s\ z\mu_{nf}}{a}\left(1 + \frac{1}{\beta}\right)\left[\frac{d^2 f(1)}{d\eta^2}\right]. \tag{24}$$

The non-dimensional forms of C_f, Nu (skin friction and Nesselt number, respectively) are expressed as [11]

$$\left[\frac{zRe}{a}\right]C_f = \left(1 + \frac{1}{\beta}\right)\left[\frac{d^2 f(1)}{d\eta^2}\right](1-\varphi)^{-2.5},\ Nu = -2\frac{k_{nf}}{k_f}\left[\frac{d\Theta(1)}{d\eta}\right]. \tag{25}$$

Here, $Re = \frac{sa^2}{2\,v_f}$ denotes the Reynolds number.

3. Solution Methodology

In this paper, we use the HAM technique. The HAM scheme was initially planned by Liao [32,33] and he construed the idea of Homotopy. With the help of HAM, Equations (16) and (17) are solved along with the suggested boundary condition in Equations (18) and (19). To control and improve the convergence of the problem, we used the auxiliary constant $\hbar$. A selection of initial gasses is

$$f_0(\eta) = \frac{\alpha}{2(\alpha-1)^3}\left[\eta^3 - 3\alpha\eta^2 - (3 - 6\alpha)\eta + (2 - 3\alpha)\right] + \eta,\ \Theta_0(\eta) = 1. \tag{26}$$

L_f and L_Θ are linear operators such that

$$\mathrm{L}_f = \frac{d^4 f(\eta)}{d\eta^4} \text{ and } \mathrm{L}_\Theta = \frac{d^2\Theta(\eta)}{d\eta^2}, \tag{27}$$

The general result of L_f and L_Θ is

$$\mathrm{L}_f\left\{\mathrm{K}_1 + \mathrm{K}_2\eta + \mathrm{K}_3\eta^2 + \mathrm{K}_4\eta^3\right\} = 0 \text{ and } \mathrm{L}_\Theta\{\mathrm{K}_5 + \mathrm{K}_6\eta\} = 0. \tag{28}$$

For velocity and temperature distribution, the Taylor's expansions have been applied as follows:

$$f(\eta;\rho) = f_0(\eta) + \sum_{\xi=1}^{\infty} f_\xi(\eta)\rho^\xi, \tag{29}$$

$$\Theta(\eta;\rho) = \Theta_0(\eta) + \sum_{\xi=1}^{\infty} \Theta_\xi(\eta)\rho^\xi. \tag{30}$$

But

$$f_\xi(\eta) = \frac{1}{\xi!}\frac{df(\eta;\rho)}{d\eta}\bigg|_{\rho=0} \text{ and } \Theta_\xi(\eta) = \frac{1}{\xi!}\frac{d\Theta(\eta;\rho)}{d\eta}\bigg|_{\rho=0}. \tag{31}$$

For Equations (16) and (17), the ξth order system is as follows [11]:

$$\mathrm{L}_f\left[f_\xi(\eta) - \tilde{\mathrm{N}}_\xi f_{\xi-1}(\eta)\right] = \lambda_f R_\xi^f(\eta), \tag{32}$$

$$\mathrm{L}_\Theta\left[\Theta_\xi(\eta) - \tilde{\mathrm{N}}_\xi \Theta_{\xi-1}(\eta)\right] = \lambda_\Theta R_\xi^\Theta(\eta). \tag{33}$$

where

$$\widetilde{\mathrm{N}}_\xi = \begin{cases} 1, \text{ if } \rho > 1 \\ 0, \text{ if } \rho \le 1 \end{cases}. \tag{34}$$

Onvergence of HAM

The HAM scheme has the auxiliary constants $\hbar_f$ and $\hbar_\Theta$ that constantly control and modify the solution convergence. For an appropriate value of $\hbar_f$ and $\hbar_\Theta$, we perform 18th order approximation. The appropriate region $\hbar_f$ and $\hbar_\Theta$ for SWCNTs lies between $-0.1 \le \hbar_f \le -0.5$ and $-0.2 \le \hbar_\Theta \le 1.9$, while for MWCNTs, the suitable region is between $-0.2 \le \hbar_f \le -0.8$ and $-0.1 \le \hbar_\Theta \le 1.5$.

4. Graphical Results and Discussion

In this portion, we will examine the impact of appropriate model variables on a thin layer flow of Casson nanofluid over a stretching upright cylinder. The main features of the flow, like surface drag force (coefficient of skin friction), the rate of heat transport (Nusselt number), and the rate of spray on the thin layer have been studied for both SWCNTs and MWCNTs nanofluids. The other physical parameters of interest, like the Casson parameter β, nanoparticles volume fraction φ, magnetic variable M, Grashof number Gr, Prandle number Pr, and Reynolds number Re, have been presented graphically and physically discussed for both cases of SWCNTs and MWCNTs nanoparticles. We considered the thin liquid flow and heat analysis of two kinds of CNTs (SWCNTs and MWCNTs) human blood-based nanoliquid. The schematic sketch and coordinate system of the present problem are displayed in Figure 1. The variation in the velocity field $\frac{df(\eta)}{d\eta}$, thermal field $\Theta(\eta)$, and pressure field $\frac{p-p_b}{\mu c_f}(\eta)$ of blood flow against the different emerging parameters of magnitudes $(M = 0.3, \mathrm{Pr} = 24, Ec = 1.5, \varphi = 0.01, \alpha = 1.4, Gr = 0.2, \mathrm{Re} = 0.3)$ have been portrayed in the following figures for both sorts of CNTs.

4.1. Velocity Distribution

Figure 2 depicts the behavior of $\frac{df(\eta)}{d\eta}$ by varying the magnetic parameter M and thin film thickness parameter α of both CNTs (SWCNTs and MWCNTs) nanofluids. The impacts of these quantities on $\frac{df(\eta)}{d\eta}$ are very clear during the flow of both CNTs nanofluids. It can be noted that the larger magnitude of M reduced the fluid motion in both cases (SWCNTs and MWCNTs). Physically, such a situation arises as a result of a constantly applied magnetic field B_0 that can be induced current in inductive nanoliquid. It creates resistant forces called Lorentz forces, which reduce the liquid velocity. Finally, it is clear that B_0 is used to govern the boundary layer separation. Comparatively, a rapid fall in the velocity field is perceived in the case of SWCNTs as related to the MCWNTs. In Figure 2, the effect of α (thin film nanofluid parameter) is depicted for both sorts of CNTs nanofluids. It can be observed that by increasing the value of α, the fluid motion decelerates, because in this case, the mass of the fluid is enhanced. Actually, the tiny size of the film accelerates the velocity and less energy is required for fluid motion, for example, the flow in the pipe is much easier and faster than the flow in sea water. Moreover, in the case of MWCNTs, the velocity field is dominant when compared to SWCNTs in the present study.

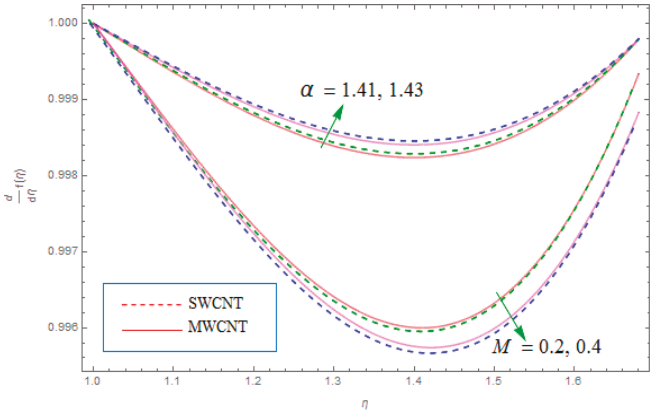

Figure 2. $\frac{df(\eta)}{d\eta}$ distribution for varying M and α.

Figure 3 presents the velocity distribution $\frac{df(\eta)}{d\eta}$ for several values of Gr using SWCNTs- and MWCNTs-based nanofluid. The velocity $\frac{df(\eta)}{d\eta}$ elevates for both CNTs by maximizing the value of Gr. Similarly, the velocity field $\frac{df(\eta)}{d\eta}$ shows the slowing behavior for both CNTs (SWCNTs and MWCNTs), reducing the value of Gr. Actually, the ratio of the thermal buoyancy force in the direction of viscous force is termed the Grashoff number Gr Therefore, the basic reason for this is that in the absenteeism of buoyancy force, there is no motion of fluid. The present outline indicates that motion of liquid is occurring due to the buoyancy force and the liquid is stationary in the absence of this force. In addition, it is clear from the figure that SWCNTs are more dominant than MWCNTs.

Figure 4 elucidates the behavior of Casson parameter β and nanoparticle volume friction φ on $\frac{df(\eta)}{d\eta}$ for both SWCNTs and MWCNTs nanofluids. For the increasing values of β, the velocity distribution $\frac{df(\eta)}{d\eta}$ in the boundary layer is shown to be declining. It can be noted that accelerating the value of β implies condensing the yield stress of Casson liquid and therefore successfully assisting the motion of boundary film flow adjacent to the stretching surface of the cylinder. Furthermore, it is found that the Casson fluid is close to Newtonian fluid for the large value of $\beta \to \infty$. Similarly, Figure 4 displays the impact of φ on the flow of nanoliquid for both nanoparticles (SWCNTs and MWCNTs). Obviously, it is perceived that the velocity distribution $\frac{df(\eta)}{d\eta}$ improves as the magnitude of φ increases

for both SWCNTs and MWCNTs nanofluids. Substantially, this occurs by inserting more particles φ in the thin fluid of the nanoliquid and increasing the strength of heat carriage and cohesive among the nanoliquid atoms, so that they become frail to halt the faster fluid flow since the heat transport in thin materials is faster than in thick materials. In addition, it is clear from the figure that the flow of SWCNTs is more dominant than MWCNTs. The velocity profiles $\frac{df(\eta)}{d\eta}$ of different magnitudes of the Reynolds number Re for both types of CNTs nanofluids are presented in Figure 5. Basically, Re is the ratio of inertial force toward the viscous force. It can be noted that the velocity profile $\frac{df(\eta)}{d\eta}$ reduces as Re increases, so the velocity tends to be zero at a certain large space from the cylinder surface. Generally, the greater value of Re controlled the inertial force, which reduced the viscous force. Hence, for the larger magnitudes of the Reynolds number Re, the velocity of nanofluids reduces and the flow of fluids declines slowly to the ambient condition. The inertial forces are more influential forces and they do not permit the liquid atoms to flow. Strong viscous forces have a strong resistance to the flow of the liquids. Boundary layer flow of fluid motion decreases with strong inertial forces.

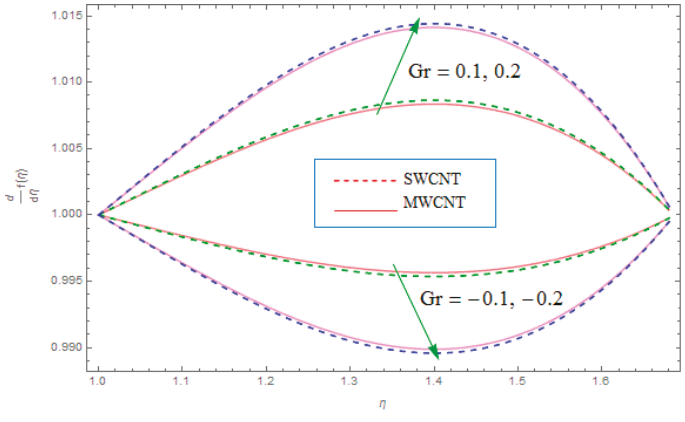

Figure 3. $\frac{df(\eta)}{d\eta}$ distribution for varying Gr.

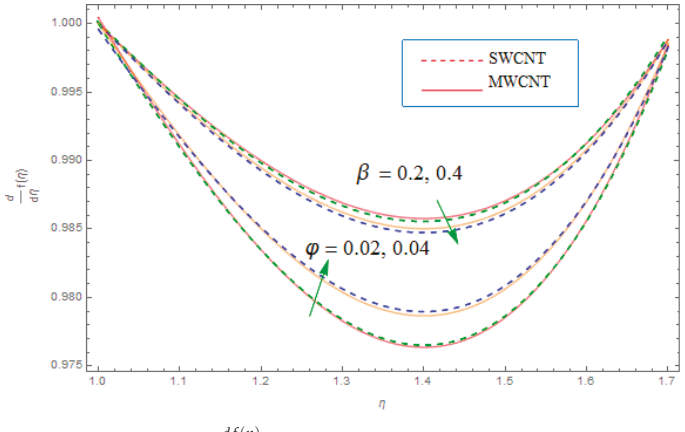

Figure 4. $\frac{df(\eta)}{d\eta}$ distribution for varying φ and β.

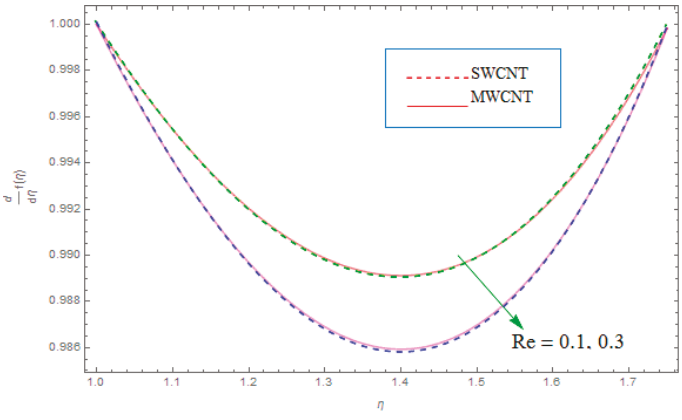

Figure 5. $\frac{df(\eta)}{d\eta}$ distribution for varying Re.

4.2. Thermal Distribution

Similarly, the next set of Figure 6, Figure 7 displays the impact of flow quantities on the thermal profile $\Theta(\eta)$. Variation in the temperature profile $\Theta(\eta)$ for both types of CNTs nanofluids with magnetic parameter M and thickness variable α is shown in Figure 6. An intensification in the thermal field $\Theta(\eta)$ is perceived with a large value of M for both nanofluids because the high estimation of M produces the Lorentz forces, which increase the fraction force between the fluid molecules for SWCNTs and MWCNTs. This force favors and supports the temperature of fluids. Since the M magnetic field is executed vertically, with the growing magnitude of M magnetic field effect, the fluid is controlled and restricted. Additionally, the greater value of α decreases $\Theta(\eta)$ as the thin liquid coating is heated up quicker than the thick liquid coating. As a result, the thermal field $\Theta(\eta)$ cools down at high values of α. The reason for this is that with the thickness of the fluid film, the mass of the fluid increases, which consumes the amount of temperature. Heat enters fluid, and as a result, the environment is cooled down. Thick film fluid needs more heat compared to thin film fluid. Figure 7 demonstrates the performance of the Reynolds number Re and Pr on the thermal filed $\Theta(\eta)$ for SWCNTs and MWCNTs. The same behavior is noted in the variation of Re and Pr for both CNTs. It is seen that a higher measure of Re denigrates $\Theta(\eta)$, explained by the basic fact that a greater magnitude of Re results in extra inertial forces arising, which tightly bonds the particles of flow nanoliquids, and greater heat is enforced to break the contacts amongst the liquid particles. Additionally, the behavior of the Prandtl number Pr on the thermal field $\Theta(\eta)$ is presented in Figure 7. From the figure, it is shown that $\Theta(\eta)$ displays a falling act for a greater magnitude of Pr for both types of CNTs nanoparticles. Generally, a greater magnitude of Pr increases the thickness of the boundary layer, which boosts the cooling efficiency of the nanomaterial. This is because Pr is the ratio of motion diffusivity to thermal diffusivity. Those fluids which have the lowest Prandtl number Pr have good thermal conductivities; therefore, thick boundary layer structures are maintained for diffusing heat.

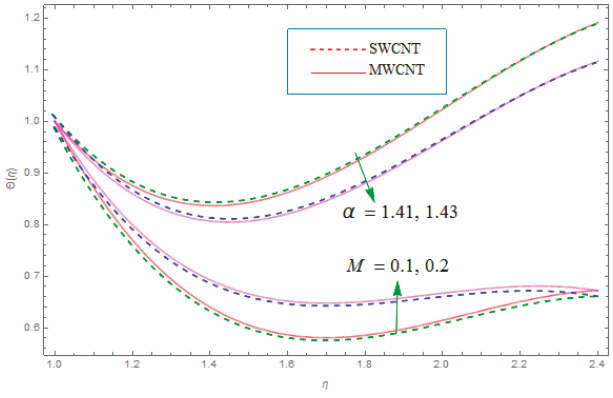

Figure 6. Distribution for varying M and α.

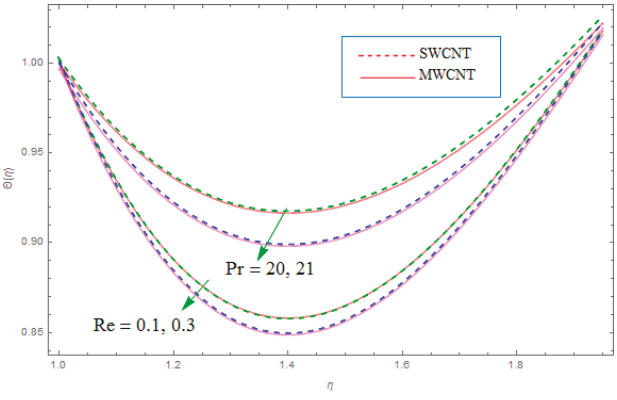

Figure 7. $\Theta(\eta)$ distribution for varying Re and Pr.

4.3. Pressure Distribution

Finally, in the set of Figures 8 and 9, we portray the variation in the key element of spray phenomena pressure distribution $\frac{p-p_b}{\mu c_f}(\eta)$ in terms of different variables for SWCNTs and MWCNTs nanofluids. The effect of φ (volume fraction) and thickness parameter α on pressure distribution $\frac{p-p_b}{\mu c_f}(\eta)$ is sketched in Figure 8. The higher values of φ lead to stronger pressure $\frac{p-p_b}{\mu c_f}(\eta)$; as a result, fraction forces are reduced and the concentration of nanoparticles is enhanced for both SWCNTs and MWCNTS nanofluids. Due to a higher concentration, the fluid becomes dense and the collision of molecules increases, exerting pressure on the wall of the cylinder. It has been noticed that the high-pressure phenomena have a vital role in blood flow, chemical reactions, and cooking easily. Furthermore, it can be observed that the pressure distribution $\frac{p-p_b}{\mu c_f}(\eta)$ is enhanced for greater values of α. The large size of the film exerts a strong pressure $\frac{p-p_b}{\mu c_f}(\eta)$ and high power is applied to diminish the stress of the thick film. The combined relationship of the film thickness and pressure created a massive force, which is compulsory for the body to move on a fluid surface. Figure 9 exhibits the effect of M and Re on $\frac{p-p_b}{\mu c_f}(\eta)$ for SWCNTs and MWCNTs. From Figure 9, it can be obviously seen that less pressure is produced by a large magnitude of M. It can be seen that the pressure distribution $\frac{p-p_b}{\mu c_f}(\eta)$ is weak due to Lorentz forces, which decrease the movement of fluid, and extra pressure is required. The magnetic field M is applied perpendicular to the flow of nanofluids. Therefore, the Lorentz forces capture the liquid in the boundary layer. To compete with the Lorentz forces due to the strong magnetic

field, the pressure must be high in order to cause motion of the fluid. Moreover, large quantities of the Reynolds number Re drop the pressure distribution $\frac{p-p_b}{\mu c_f}(\eta)$ and a strong inertial effect is produced. Due to this inertial force, the fluid particles are packed closely and inflexibly and more pressure is imposed to overcome these forces.

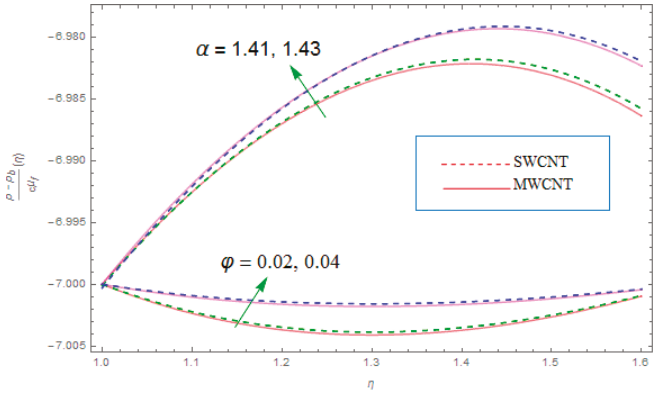

Figure 8. $\frac{p-p_b}{\mu c_f}(\eta)$ distribution for varying φ and α.

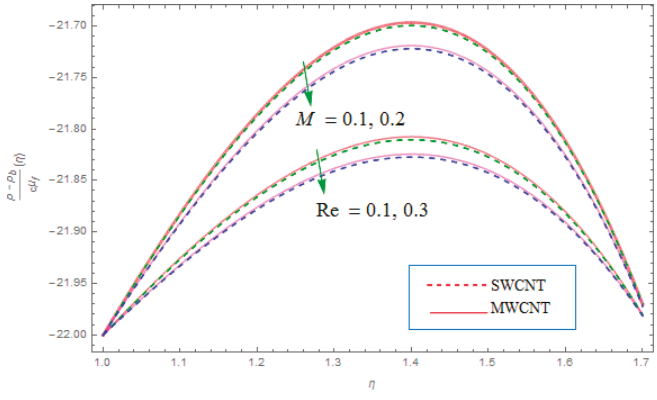

Figure 9. $\frac{p-p_b}{\mu c_f}(\eta)$ distribution for varying M and Re.

The certain mathematical values of CNTs (SWCNTs and MWCNTs) and human blood, depend on various thermo-physical characteristics, such as density ρ, thermal conductivity k_f, and specific heat c_p, as presented in Table 1. Also, Table 2 demonstrates the convergence analysis of the series solution for $f''(1)$ (velocity field) and $\Theta'(1)$ (thermal field).

Table 1. Various mathematical values of thermophysical characteristics of CNTs of three base liquids [16].

Physical Properties		k (W/mK)	ρ (kg/m^3)	c_p (J/kgK)	$\beta^{\otimes}\times10^{-5}/k$	$\sigma(Sm^{-1})$
Base fluid	Human Blood	0.492	1053	3594	0.18	0.8
Nanoparticles	SWCNT	6600	2600	425	27	10^6–10^7
	MWCNT	3000	1600	796	44	1.9×10^{-4}

Table 2. The convergence of the Homotopic results for different orders of estimation.

Order of Approximations	$f''(1)$		$-\Theta'(1)$	
	SWCNTs	**MWCNTs**	**SWCNTs**	**MWCNTs**
1	0.36550	0.31471	0.8847	0.7056
5	0.32521	0.30210	0.6667	0.5943
10	0.31063	0.24323	0.6023	0.5671
15	0.03117	0.02230	0.5931	0.5395
18	0.02325	0.04905	0.4299	0.4321
20	0.02325	0.04905	0.3385	0.4133
30	0.02325	0.04905	0.3385	0.3133
37	0.02325	0.04905	0.3385	0.3133

Table 3 demonstrates the statistical data of $f''(1)$ (surface drag force) HAM approximation at the 20th order for several values of related physical quantities, such as $M = 0.3, \mathrm{Pr} = 24, Ec = 1.5$, $\varphi = 0.01, Gr = 0.2, \alpha = 1.4, \mathrm{Re} = 0.3$ for SWCNTs/MWCNTS nanofluids. In Table 3, it is shown that the magnitude of $f''(1)$ (surface drag force) intensifies for greater values of φ, M, Re for both SWCNTs and MWCNTs. The growing thickness of the nanoparticles enhances the resistance forces, which improve skin friction. The M also governs an opposing force named the Lorentz force and a greater magnitude of M upsurges the skin friction. This drop-in influence is fast using the SWCNTs as compared to the MWCNTs.

Table 3. The numerical values of the skin friction coefficient ($f''(1)$).

φ	M	Re	$f''(1)$	
			SWCNTs	**MWCNTs**
0.01	**0.2**	0.4	0.411834	0.508077
0.02			0.700187	0.968220
0.03			0.958088	1.273380
0.01	0.3		0.40361	0.636512
	0.4		0.579942	0.674852
	0.3	0.5	0.551339	0.636271
		0.6	0.579665	0.674344

Similarly, Table 4 is organized to explain Nu at the 20th order HAM estimate for different values of relevant model variables for both SWCNTs and MWCNTs nanoliquids. From Table 4, it can be clearly observed that the value of rate of heat transport accelerates for a high magnitude of both φ, Pr and declines for a higher value of the Ec. The Ec is related to the dissipation term and a larger magnitude of Ec enhances the thermal field. Therefore, the opposite result for the higher magnitude of the Ec verses Nu is perceived.

Table 4. The numerical values of the Nusselt number ($-\Theta'(1)$).

Pr	Ec	φ	$-\Theta'(1)$	
			SWCNTs	**MWCNTs**
20	**1.5**	0.01	0.067258	0.201780
21			0.107185	0.254541
22			0.127170	0.307476
20	1.6		0.067662	0.202577
	1.7		0.068067	0.203375
	1.5	0.02	0.246752	0.517260
		0.03	0.427645	0.835803

5. Conclusions

The current study explores the effect of MHD, heat transfer, and pressure distribution of thin layer flow of Casson nanofluid over a stretching upright cylinder. Two forms of CNTs, namely SWCNTs and MWCNTs, were picked as nanoparticles to be applied in human blood base fluid. The obtained set of coupled ODEs was solved by the HAM scheme. The influence of several embedded flow variables on velocity, thermal, and pressure distribution was derived and the derived result was investigated through graphs. The salient features of the current investigation are as follows:

- Increasing the value of the Reynolds number Re and magnetic parameters M yields a reduction in the velocity field for both nanoparticles (SWCNTs and MWCNTs);
- The analysis shows that the volume fraction φ increases the velocity, thermal fields, and pressure distribution;
- The important phenomenon of pressure $\frac{p-p_b}{\mu c_f}(\eta)$ declines for a large value of M and Re, while it is enhanced by increasing α and φ;
- The thermal efficiency of nanofluid improves by increasing the dimension of a nanoparticle, as well as by increasing the magnitude of φ;
- It is observed that SWCNTs have a greater rate of heat transfer when equated to MWCNTs.

Author Contributions: A.S.A. and T.G. modelled the problem and drew the physical sketch. S.N., S.I. and Z.S. introduced the similarity transformation and transformed the modeled problem into dimensionless form. K.S.N. and I.K. solved the problem numerically and computed the results. T.G. and I.K. discussed the results with conclusions. All the authors equally contributed in writing and revising the manuscript.

Funding: No specific funding received for this work.

Conflicts of Interest: The authors declare no conflict of interest.

References

1. Sidik, N.A.; Yazid, M.N.; Mamat, R. A review on the application of nanofluids in vehicle engine cooling system. *Int. Commun. Heat Mass Transf.* **2015**, *68*, 85–90. [CrossRef]
2. Verma, S.K.; Tiwari, A.K. Progress of nanofluid application in solar collectors. *Rev. Energy Convers. Manag.* **2015**, *100*, 324–346. [CrossRef]
3. Liang, M.; Liu, Y.; Xiao, B.; Yang, S.; Wang, Z.; Han, H. An analytical model for the transverse permeability of gas diffusion layer with electrical double layer effects in proton exchange membrane fuel cells. *Int. J. Hydrog. Energy* **2018**, *43*, 17880–17888. [CrossRef]
4. Xiao, B.; Zhang, X.; Wang, W.; Long, G.; Chen, H.; Kang, H.; Ren, W. A Fractal Model For Water Flow Through Unsaturated Porous Rocks. *Fractals* **2018**, *26*, 1840015. [CrossRef]
5. Long, G.; Xu, G. The effects of perforation erosion on practical hydraulic fracturing applications. *SPE J.* **2017**, *22*, 645–659. [CrossRef]
6. Long, G.; Liu, S.; Xu, G.; Wong, S.; Chen, H.; Xiao, B. A perforation erosion model for hydraulic fracturing Applications. *SPE Prod. Oper.* **2018**, *33*, 770–783. [CrossRef]
7. Xiao, B.; Chen, H.; Xiao, S.; Cai, J. Research on Relative Permeability of Nanofibers with Capillary Pressure Effect by Means of Fractal-Monte Carlo Technique. *J. Nanosci. Nanotechnol.* **2017**, *17*, 6811–6817. [CrossRef]
8. Xiao, B.; Wang, W.; Fan, J.; Chen, H.; Hu, X.; Zhao, D.; Zhang, X.; Ren, W. Optimization of the fractal-like architecture of porous fibrous materials related to permeability, diffusivity and thermal conductivity. *Fractals* **2017**, *25*, 1750030. [CrossRef]
9. Choi, S.U.S. Enhancing Thermal Conductivity of Fluids with Nanoparticles. In *Developments and Applications of Non-Newtonian Flows*; Singer, D.A., Wang, H.P., Eds.; ASME: New York, NY, USA, 1995; Volume 66, pp. 99–105.
10. Ellahi, R. The effects of MHD and temperature dependent viscosity on the flow of a non-Newtonian nanofluid in a pipe, Analytical solution. *Appl. Math. Model.* **2013**, *37*, 1451–1457. [CrossRef]
11. Alshomrani, A.S.; Gul, T. A convective study of Al_2O_3-H_2O and Cu-H_2Onano-liquid films sprayed over a stretching cylinder with viscous dissipation. *Eur. Phys. J. Plus* **2017**, *132*, 495–512. [CrossRef]

12. Asadi, A. A guideline towards easing the decision-making process in selecting an effective nanofluid as a heat transfer fluid. *Energy Convers. Manag.* **2018**, *175*, 1–10. [CrossRef]
13. Asadi, M.; Asadi, A.; Aberoumand, S. An experimental and theoretical investigation on the effects of adding hybrid nanoparticles on heat transfer efficiency and pumping power of an oil-based nanofluid as a coolant fluid. *Int. J. Refrig.* **2018**, *89*, 83–92. [CrossRef]
14. Gul, T.; Nasir, S.; Islam, S.; Shah, Z.; Khan, M.A. Effective prandtl number model influences on the Al_2O_3-H_2O and Al_2O_3-$C_2H_6O_2$ nanofluids spray along a stretching cylinder. *Arab. J. Sci. Eng.* **2019**, *2*, 1601–1616. [CrossRef]
15. Iijima, S. Helical microtubules of graphitic carbon. *Nature* **1991**, *354*, 56. [CrossRef]
16. Haq, R.U.; Nadeem, S.; Khan, Z.H.; Noor, N.F.M. Convective heat transfer in MHD slip flow over a stretching surface in the presence of carbon nanotubes. *Phys. B Condens. Matter* **2015**, *457*, 40–47. [CrossRef]
17. Khan, W.A.; Khan, Z.H.; Rahi, M. Fluid flow and heat transfer of carbon nanotubes along a flat plate with Navier slip boundary. *Appl. Nano Sci.* **2014**, *4*, 633–641. [CrossRef]
18. Aman, S.; Khan, I.; Ismail, Z.; Salleh, M.Z.; Alshomrani, A.S.; Alghamd, M.S. Magnetic field effect on Poiseuille flow and heat transfer of carbon nanotubes along a vertical channel filled with Casson fluid. *AIP Adv.* **2017**, *7*, 1–18. [CrossRef]
19. Aman, S.; Khan, I.; Ismail, Z.; Salleh, M.Z.; Al-Mdallal, Q.M. Heat transfer enhancement in free convection flow of CNTs Maxwell nanofluids with four different types of molecular liquids. *Sci. Rep.* **2017**, *7*, 1–13. [CrossRef] [PubMed]
20. Asadi, A.; Asadi, M.; Rezaei, M.; Siahmargoi, M.; Asadi, F. The effect of temperature and solid concentration on dynamic viscosity of MWCNT/MgO (20–80)–SAE50 hybrid nano-lubricant and proposing a new correlation: An experimental study. *Int. Commun. Heat Mass Transf.* **2016**, *78*, 48–53. [CrossRef]
21. Asadi, M.; Asadi, A. Dynamic viscosity of MWCNT/ZnO-engine oil hybrid nanofluid: An experimental investigation and new correlation in different temperatures and solid concentrations. *Int. Commun. Heat Mass Transf.* **2016**, *76*, 41–45. [CrossRef]
22. Asadi, A.; Asadi, M.; Rezaniakolaei, A.; Rosendahl, L.A.; Afrand, M.; Wongwises, S. Heat transfer efficiency of Al_2O_3-MWCNT/thermal oil hybrid nanofluid as a cooling fluid in thermal and energy management applications. *Int. J. Heat Mass Transf.* **2018**, *17*, 474–486. [CrossRef]
23. Asadi, A.; Asadi, M.; Rezaniakolaei, A.; Rosendahl, L.A.; Wongwises, S. An experimental and theoretical investigation on heat transfer capability of $Mg(OH)_2$/MWCNT-engine oil hybrid nano-lubricant adopted as a coolant and lubricant fluid. *Appl. Therm. Eng.* **2018**, *129*, 577–586. [CrossRef]
24. Khalid, A.; Khan, I.; Khan, A.; Shafie, S.; Tlili, I. Case study of MHD blood flow in a porous medium with CNTS and thermal analysis. *Case Stud. Therm. Eng.* **2018**, *12*, 374–380. [CrossRef]
25. Nasir, S.; Islam, S.; Gul, T.; Shah, Z.; Khan, M.A.; Khan, W.; Khan, A.Z.; Khan, S. Three-dimensional rotating flow of MHD single wall carbon nanotubes over a stretching sheet in presence of thermal radiation. *Appl. Nanosci.* **2018**, *8*, 1361–1378. [CrossRef]
26. Khan, N.S.; Gul, T.; Islam, S.; Khan, I.; Alqahtani, A.M.; Alshomrani, A.S. Magneto- hydrodynamic Nanoliquid Thin Film Sprayed on a Stretching Cylinder with Heat Transfer. *Appl. Sci.* **2017**, *7*, 271. [CrossRef]
27. Ellahi, R.; Zeeshan, A.; Hussain, F.; Abbas, T. Study of Shiny Film Coating on Multi-Fluid Flows of a Rotating Disk Suspended with Nano-Sized Silver and Gold Particles: A Comparative Analysis. *Coatings* **2018**, *8*, 422. [CrossRef]
28. Naghdi, S.; Rhee, K.; Hui, D.; Park, S. A review of conductive metal nanomaterials as conductive, transparent, and flexible coatings, thin films, and conductive fillers: Different deposition methods and applications. *Coatings* **2018**, *8*, 278. [CrossRef]
29. Ali, V.; Gul, T.; Afridi, S.; Ali, F.; Alharbi, S.O.; Khan, I. Thin Film Flow of Micropolar Fluid in a Permeable Medium. *Coatings* **2019**, *9*, 98. [CrossRef]
30. Ullah, A.; Alzahrani, E.O.; Shah, Z.; Ayaz, M.; Islam, S. Nanofluids thin film flow of Reiner-Philippoff fluid over an unstable stretching surface with Brownian motion and thermophoresis effects. *Coatings* **2019**, *9*, 21. [CrossRef]
31. Casson, N. A Flow Equation for Pigment-Oil Suspensions of the Printing Ink Type. In *Rheology of Disperse Systems*; Pergamon Press: London, UK, 1959.

32. Dash, R.K.; Mehta, K.N.; Jayaraman, G. Casson fluid flow in a pipe filled with a homogenous porous medium. *Int. J. Eng. Sci.* **1996**, *34*, 1145–1156. [CrossRef]
33. Pramanik, S. Casson fluid flow and heat transfer past an exponentially porous stretching surface in presence of thermal radiation. *Ain Shams Eng. J.* **2014**, *5*, 205–212. [CrossRef]
34. Asma, K.; Khan, I.; Arshad, K.; Sharidan, S. Unsteady MHD free convection flow of Casson fluid past over an oscillating vertical plate embedded in a porous medium. *Eng. Sci. Technol. Int. J.* **2015**, *18*, 309–317.
35. Reddy, M.; Kumari, P.; Padma, P. Effect of Thermal Radiation on MHD Casson Nano Fluid Over a Cylinder. *J. Nanofluids* **2018**, *7*, 428–438. [CrossRef]
36. Fredrickson, A.G. *Principles and Applications of Rheology*; Prentice-Hall: Englewood Cliffs, NJ, USA, 1964.
37. Mukhopadhyay, S.; Bhattacharyya, K.; Hayat, T. Exact solutions for the flow of Casson fluid over a stretching surface with transpiration and heat transfer effects. *Chin. Phys. B* **2013**, *22*, 114701. [CrossRef]
38. Mukhopadhyay, S. Casson fluid flow and heat transfer over a nonlinearly stretching surface. *Chin. Phys. B* **2013**, *22*, 7. [CrossRef]
39. Liao, S.J. A kind of approximate solution technique which does not depend upon small parameters (II)—An application in fluid mechanics. *Int. J. Nonlinear Mech.* **1997**, *32*, 815–822. [CrossRef]
40. Liao, S.J. On the homotopy analysis method for nonlinear problems. *Appl. Math. Comput.* **2004**, *47*, 499–513. [CrossRef]
41. Ellahi, R.; Shivanian, E.; Abbasbandy, S.; Rahman, S.U.; Hayat, T. Analysis of steady flows in viscous fluid with heat/mass transfer and slip effects. *Int. J. Heat Mass Transf.* **2012**, *55*, 6384–6390. [CrossRef]
42. Gul, T.; Haleem, I.; Ullah, I.; Khan, M.A.; Bonyah, B.; Khan, I.; Shuaib, M. The study of the entropy generation in a thin film flow with variable fluid properties past over a stretching sheet. *Adv. Mech. Eng.* **2018**, *10*, 1–15. [CrossRef]
43. Gul, T. Scattering of a thin layer over a nonlinear radially extending surface with Magneto hydrodynamic and thermal dissipation. *Surf. Rev. Lett.* **2019**, *26*, 1–7. [CrossRef]
44. Xue, Q. Model for thermal conductivity of carbon nanotube-based composites. *Phys. B Condens. Matter* **2005**, *368*, 302–307. [CrossRef]

coatings

MDPI

Article

Analysis of Unsteady Flow and Heat Transfer of Nanofluid Using Blasius–Rayleigh–Stokes Variable

Dianchen Lu [1], Sumayya Mumtaz [2], Umer Farooq [1,2] and Adeel Ahmad [2,*]

[1] Faculty of Science, Department of Mathematics, Jiangsu University, Zhenjiang 212013, China; dclu@ujs.edu.cn (D.L.); umer_farooq@comsats.edu.pk (U.F.)
[2] Department of Mathematics, COMSATS University Islamabad, Islamabad 45550, Pakistan; sumayyamumtaz@gmail.com
* Correspondence: adeelahmed@comsats.edu.pk

Received: 11 February 2019; Accepted: 16 March 2019; Published: 25 March 2019

Abstract: This article investigates the unsteady flow and heat transfer analyses of a viscous-based nanofluid over a moving surface emerging from a moving slot. This new form of boundary layer flow resembles with the boundary layer flow over a stretching/shrinking surface depending on the motion of the moving slot. The governing partial differential equations are transformed to correct similar form using the Blasius–Rayleigh–Stokes variable. The transformed equations are solved numerically. Existence of dual solutions is observed for a certain range of moving slot parameter. The range of dual solution is strongly influenced by Brownian and thermophoretic diffusion of nanoparticles.

Keywords: unsteady flow and heat transfer; nanofluid; Blasius–Rayleigh–Stokes variable; dual solutions; numerical solution; correlation expressions

1. Introduction

The mechanism of drag and heat loss reduction [1] has been the focus of intensive analysis due to its application in the prevention of loss of mechanical energy. Drag and heat loss reduction may create energy savings, processing time reduction, enhancement in thermal rating, and make equipment more durable. Several well-known methods have been proposed by researchers to reduce the drag and heat loss in physical systems out of them utilization of stretching/shrinking surfaces [2] and enhancing the thermal conductivity of the involved fluid are famous [3].

Nanofluids, an achievement of researchers and scientists of the developing world of nanotechnology, exploit the thermal conductivity of solids to enhance the thermal conductivity of a fluid by adding nano-sized solid particles. Materials commonly used for nanoparticles include oxides such as alumina, silica, titania and copper oxide, and metals such as copper and gold. Carbon nanotubes and diamond nanoparticles have also been used to realize nanofluids. Nanoparticles vary from 1 to 100 nm in diameter. Thermal conductivity can be increased up to two times by adding small amount of nanoparticles. Popular base fluids include water and organic fluids such as ethanol and ethylene glycol. The volumetric fraction of the nanoparticles is usually below 5%.

A wide range of nanofluids exist in nature, like blood, which is a complex biological compound, made up of different nanoparticles that perform various functions at molecular level. A number of natural processes occurring in atmosphere and biosphere have wide variety of composition of different fluids and nanoparticles. Manufacturing and industrial waste materials are also composed of nanoscale particles and fluids. Various self-assembly processes for nanostructures generate from the addition of nanoparticles in base fluid. Considering the wide-ranging uses of nanofluid in industry and science, and the model of nanofluid presented by Buongiorno [4], many experimentalists and researchers have showed great interest in the study of nanofluids in the last few years [5–12].

Keeping the fact in view that the unsteady flows are more generalized, and the applications of nanofluids and stretching surfaces in drag and heat loss reduction, this article analyzes the unsteady flow of nanofluid over a moving surface. The study of flow over a linearly stretching sheet was initiated by Crane [13]. He derived the analytical solution of two-dimensional momentum equations. This notable work of Crane [13] has been studied by many researchers in many directions. Some recent works on the topic of stretching/shrinking surfaces are References [14–18] and the references given therein.

In 1997, Todd [19] introduced a new family of unsteady boundary layer flow over a moving surface emerging from a moving slot. He proposed a new set of transformations containing the Blasius–Rayleigh–Stoke variable to write the governing unsteady partial differential equations in similar form. Fang et al. [20] conducted the heat-transfer analysis for this boundary layer flow. In this article, we carry out the numerical analysis of unsteady flow of nanofluid past a movable surface emerging from a moving slot by converting the governing coupled unsteady partial differential equations into similar form using the transformation involving the Blasius–Rayleigh–Stoke variable. The results are presented graphically and the effects of nanoparticles on skin friction, Nusselt number and Sherwood number are discussed in detail. Dual solutions are observed for a specific range of moving slot parameter and are found to be altered due to the presence of nanoparticles. Furthermore, the numerical data is used to write the correlation expressions for certain important flow quantities by performing linear regression. Correlation expressions enable the readers to obtain the values of numerical results for different values of involved parameters from analytical expressions.

2. Mathematical Formulation

Consider the unsteady two-dimensional flow and heat transfer of an incompressible viscous-based nanofluid over a heated moving semi-infinite plate. The surface is emerging out along the x-axis from a moving slot (see Figure 1 for geometry of the problem). At time $t = 0$, the fluid is at rest. The governing boundary layer [21] equations are given as:

$$\frac{\partial U}{\partial X} + \frac{\partial V}{\partial Y} = 0 \tag{1}$$

$$\frac{\partial U}{\partial t} + U\frac{\partial U}{\partial X} + V\frac{\partial U}{\partial Y} = \nu\frac{\partial^2 U}{\partial Y^2}, \tag{2}$$

$$\frac{\partial T}{\partial t} + U\frac{\partial T}{\partial X} + V\frac{\partial T}{\partial Y} = \sigma\frac{\partial^2 T}{\partial Y^2} + \varepsilon\left(D_B\frac{\partial T}{\partial Y}\frac{\partial C}{\partial Y} + \frac{D_T}{T_\infty}\left(\frac{\partial T}{\partial Y}\right)^2\right), \tag{3}$$

$$\frac{\partial C}{\partial t} + U\frac{\partial C}{\partial X} + V\frac{\partial C}{\partial Y} = D_B\frac{\partial^2 C}{\partial Y^2} + \frac{D_T}{T_\infty}\frac{\partial^2 T}{\partial Y^2}, \tag{4}$$

where U and V are the velocity components in X and Y directions. T is the fluid temperature, C is the nanoparticles volume fraction, ν is the kinematic viscosity, σ is the thermal diffusivity of the fluid, ε is the ratio of heat capacities of the nanoparticles $(\rho c)_p$ and base fluid $(\rho c)_f$, D_B and D_T are the Brownian and thermophoretic diffusion coefficients respectively. For water nanofluids at room temperature with nanoparticles of 1–100 nm diameters, the Brownian diffusion coefficient ranges from 4×10^{-10} to 4×10^{-12} m^2/s. For alumina/water and copper/water $(\rho c)_p$ is 3.1 and 3.4 MJ/m^3 respectively. The thermophoretic diffusion is equal to 6×10^{-5} for aluminum/water nanofluid and 6×10^{-6} for copper/water nanofluid.

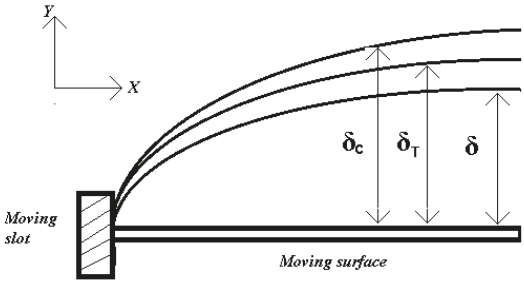

Figure 1. Systematic diagram of the problem. δ, δ_c, δ_T represent the thicknesses of momentum, thermal and nanoparticles concentration boundary layers respectively.

The corresponding boundary conditions are:

$$\begin{gathered} U(X,Y,t) = 0,\ V(X,Y,t) = 0,\ T(X,Y,t) = 0,\ C(X,Y,t) = 0\ at\ t = 0, \\ U(X,Y,t) = U_W,\ V(X,Y,t) = 0,\ T(X,Y,t) = T_W,\ C(X,Y,t) = C_W\ at\ Y = 0, \\ U(X,Y,t) \to 0,\ T(X,Y,t) \to T_\infty,\ C(X,Y,t) \to C_\infty\ as\ Y \to \infty. \end{gathered} \tag{5}$$

Since the unsteady flow is a generalized case of steady flow, Todd [19] generalized the Blasius and Rayleigh–Stokes variables to get similar equations for the boundary layer flow of viscous fluid over a moving surface, termed as the Blasius–Rayleigh–Stokes variable:

$$\eta = Y/\sqrt{\cos(\alpha)\nu t + \sin(\alpha)(\nu X/U_W)}. \tag{6}$$

This variable depicts that the slot at $Y = 0$ is moving with a constant speed $-U_w \cot\alpha$. To obtain similarity solutions for the system of Equations (1)–(5), we introduce the following similarity variables

$$\begin{gathered} \psi(x,y,t) = U_W\sqrt{\cos(\alpha)\nu t + \sin(\alpha)(\nu x/U_W)}f(\eta), \\ \theta(\eta) = \tfrac{T-T_\infty}{T_W-T_\infty},\quad \phi(\eta) = \tfrac{C-C_\infty}{C_W-C_\infty}, \end{gathered} \tag{7}$$

in the governing equations to get the following ordinary differential equations:

$$f''' + \frac{1}{2}(\cos\alpha)\eta f'' + \frac{1}{2}(\sin\alpha)ff'' = 0, \tag{8}$$

$$\theta'' + \frac{\mathrm{Pr}}{2}((\cos\alpha)\eta + (\sin\alpha)f)\theta' + N_b\theta'\phi' + N_t\theta'^2 = 0, \tag{9}$$

$$\phi'' + \frac{Le}{2}((\cos\alpha)\eta + (\sin\alpha)f)\phi' + (\frac{N_t}{N_b})\theta'' = 0, \tag{10}$$

subject to boundary conditions:

$$\begin{gathered} f(\eta) = 0,\ f'(\eta) = 1,\ \theta(\eta) = 1,\ \phi(\eta) = 1 \text{ at } \eta = 0, \\ f'(\eta) \to 0,\ \theta(\eta) \to 0,\ \phi(\eta) \to 0 \text{ as } \eta \to \infty, \end{gathered} \tag{11}$$

where prime represents the differentiation with respect to variable η. Pr is Prandtl number, N_t is thermophoresis diffusion parameter, N_b is Brownian diffusion parameter and Le is Lewis number given by the following expressions:

$$\mathrm{Pr} = \frac{\nu}{\sigma},\ N_b = \frac{\varepsilon D_B(C_W - C_\infty)}{\sigma},\ N_t = \frac{\varepsilon D_T(T_W - T_\infty)}{T_W\sigma},\ Le = \frac{\nu}{D_B}. \tag{12}$$

The range of the parameters of interest, namely thermophoresis diffusion parameter and Brownian diffusion parameter is given as: $N_b \in (0.0,\ 0.5)$ and $N_t \in [0.0,\ 0.5)$.

3. Results and Discussions

In this special case of unsteady flow, the slot is moving with constant speed $-U_w \cot(\alpha)$. For $\alpha = \pi/2$, the surface velocity is zero as in the case of Sakiadis flow [22]. For $0 < \alpha < \pi/2$, the slot is moving with the constant speed $U_w \cot(\alpha)$ in the opposite direction of stretching surface and the situation is termed as leading-edge accretion. For $\alpha \in (\alpha_L\ ,\ 0) \cup (\pi/2\ ,\ \alpha_U)$, the direction of slot motion is same as stretching sheet and the situation is termed as leading-edge ablation. As $\alpha \to 0$, the speed of slot approaches infinity in opposite direction to the stretching surface, which correspond to the Rayleigh starting-plate problem. The analytical solution for this case has been obtained using the perturbation method (see Appendix A). Since the exact analytical solution of the system (8)–(11) is not available for general α, we adopt the numerical method for the solution. In Table 1, the comparison of numerical results of skin friction with results of Fang [20] is tabulated. In Table 2, the comparison of the analytical result for $\alpha = 0$ is given with the numerical solution. Tables 1 and 2 establish the reliability of our results.

Table 1. Comparison of Fang [20] and Present study for values of different moving slot parameters.

$\alpha(^\circ)$	$-f''(0)$ (Fang [17])	Present Study
90°	0.443748	0.443872
60°	0.576684	0.576685
30°	0.613527	0.613526
0°	0.564190	0.564189
−30°	0.416304	0.416303
−48° (upper solution)	0.239052	0.239055
−48° (lower solution)	0.00150569	0.00149961

Table 2. Comparison of analytical and numerical solutions for Nusselt and Sherwood number for $\alpha = 0$.

Parameters Values	$-\theta'(0)$ (Analytical)	$-\theta'(0)$ (Numerical)	$-\phi'(0)$ (Analytical)	$-\phi'(0)$ (Numerical)
$Pr = 1$, $Le = 0.5$, $N_b = 0.01$, $N_t = 0.01$	0.5541896	0.5603877	0.0884477	0.0718526
$Pr = 1$, $Le = 0.5$, $N_b = 0.05$, $N_t = 0.0$	0.5541896	0.5532004	0.39894228	0.39894228
$Pr = 1$, $Le = 1.0$, $N_b = 0.05$, $N_t = 0.0$	0.55418958	0.5502023	0.56418958	0.56418958
$Pr = 1$, $Le = 2.0$, $N_b = 0.02$, $N_t = 0.01$	0.55418958	0.5551755	0.67603707	0.68467843

The numerical solution domain of α, $(\alpha_L < \alpha < \alpha_U)$, for the skin friction and Nusselt number mentioned by Fang [20] also hold for Sherwood number. In this study, we focus on the effects of nanoparticles on the heat transfer and behavior of nanoparticles concentration for the surface accretion and ablation.

Figure 2 demonstrates numerical solutions of velocity profile for various values of slot moving constant α ranging between $-\pi/4 < \alpha < \alpha_U$. In Figure 3 the dual solution for the velocity profile is plotted for $\alpha = -48^\circ$. The thickness of boundary layer is much greater for lower solution branch as compared to upper solution branch.

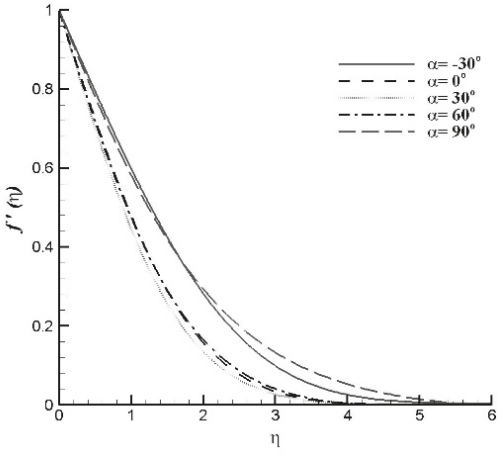

Figure 2. Velocity profiles for varying slot moving parameter α.

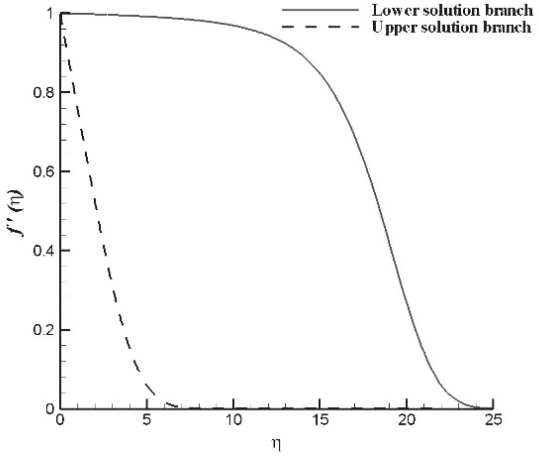

Figure 3. Profiles of velocity for different branches at $\alpha = -48°$.

Figure 4 represents the dual solution for a fixed value of moving slot parameter $\alpha = -48°$, with two distinct values of Prandtl number. For the above-mentioned values of parameters, both solutions show maximum temperature gradient which can be viewed in the region away from the wall. The change of heat transfer at the wall is less for lower solution as compared to the upper solution. The thermal layer thickness is greater for lower solution as compare to upper solution branch.

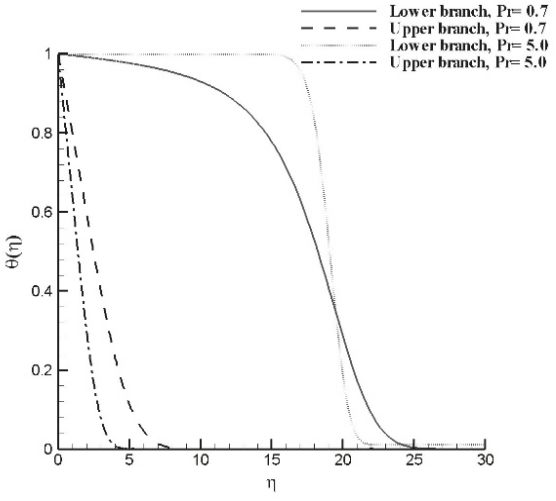

Figure 4. Temperature and its flux profiles for several branches at $\alpha = -48^{\circ}$ for varying Pr with $N_b = 0.01$ and $N_t = 0.001$.

Figures 5 and 6 illustrate the numerical solution domain of reduced Nusselt number as a function of α for different values of Brownian and thermophoretic diffusion parameters, N_b and N_t respectively. For Nusselt number, the correlation expression in the form of N_b and N_t has also been written by applying the linear regression on the set of 2401 numerical values. The values of coefficients and constant of the correlation expression in the form

$$-\theta'(0) = C + C_B N_b + C_T N_t$$

for $N_b \in (0.01,\ 0.5)$ and $N_t \in\ (0.0,\ 0.5)$ is given in Table 3 with maximum percentage error for different Prandtl number and moving slot parameter.

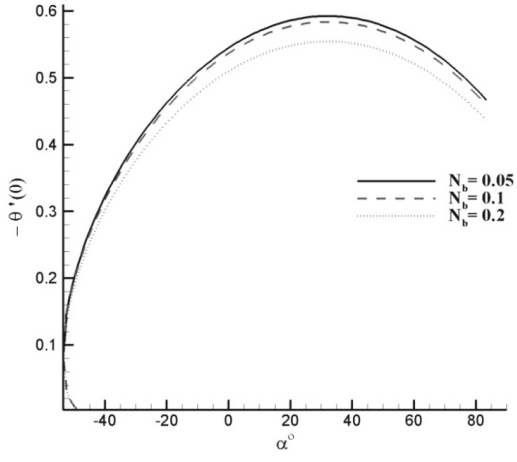

Figure 5. Effects of slot moving parameter α on reduced Nusselt number for varying N_b with $Pr = Le = 1.0$ and $N_t = 0.1$.

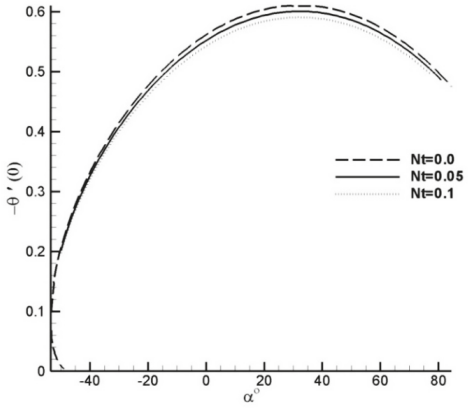

Figure 6. Effects of slot moving parameter α on reduced Nusselt number for varying N_t with $Pr = Le = 1.0$ and $N_b = 0.1$.

Table 3. Correlation expression for reduced Nusselt number and maximum percentage error defined for varying Prandtl number and moving slot parameter considering values of Brownian and thermophoresis diffusion parameters in the interval (0.01, 0.5).

Pr	*Le*	α	*C*	C_B	C_T	Max. % Error	Solution Curve
0.5	1.5	30	0413	−0.226	−0.132	2.60%	–
1.0	1.0	30	0.605	−0.261	−0.168	1.760%	–
1.0	1.0	0.0	0.601	−0.253	−0.161	2.650%	–
2.0	1.5	30	0.877	−0.305	−0.21	0.986%	–
1.0	1.0	−49	0.235	−0.101	−0.075	2.430%	Upper Solution
1.0	1.0	−49	0.004	−0.002	−0.002	7.970%	Lower Solution

It is observed that the Nusselt number decreases with an increase in parameters N_b and N_t, since higher temperatures correspond to higher Brownian and thermophoretic diffusion which resultantly reduces the surface heat flux. The same observation can be made from the correlation expressions since the coefficients of N_b and N_t are negative for all value of Pr and α. Furthermore, it is seen that dual solutions exist for a certain interval of slot moving parameter α and that interval can be viewed in Figures 5 and 6. The important observation is that the range of α reduces dramatically with an increase of N_t and the duality of solution vanishes for $N_t = 0.05$. For this reason, the correlation expression for $\alpha = -49^o$ is derived for $N_t \in (0.0,\ 0.01)$. The variation of N_b has no effect on the duality of the solution.

For a fixed value of moving slot parameter $\alpha = -49^o$, Figures 7 and 8 show the dual solution for the variation of N_b and N_t. The thickness of concentration boundary layer is greater for the smaller solution branch. As the value of N_b increases, the concentration boundary layers become thinner for upper as well as for lower solution domains. The concentration thickness of boundary layer is less for the lower solution branch. As the value of N_t increases, the concentration boundary layers become thicker for upper and lower solution domains. In Figures 9–11, the effects of Lewis number, thermophoretic diffusion and Brownian diffusion on the nanoparticles concentration flux at the surface are plotted. The Sherwood number is plotted against the moving slot parameter α. Dual solution for Sherwood number is observed in the interval $(-53^\circ, -49.5^\circ)$. Figure depicts that Sherwood number is growing function of α in the interval $(-49.5^\circ, 30^\circ)$, and decreasing function in the interval $(30^\circ, \alpha_U)$. As Le increases, i.e., the dominancy of viscous diffusion increases over the Brownian diffusion, the mass flux at the surface increases. Similar effects of Brownian diffusion and opposite effects of thermophoretic diffusion on Sherwood number are observed. In dual solution range, the effects of thermophoretic and Brownian diffusions on Sherwood number are found negligible.

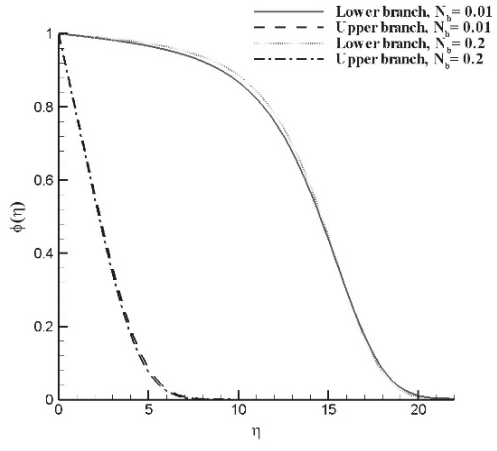

Figure 7. Dual solutions of nanoparticles concentration profile for $\alpha = -49^{\circ}$ and varying N_b, with $Pr = Le = 1.0$, $N_t = 0.001$.

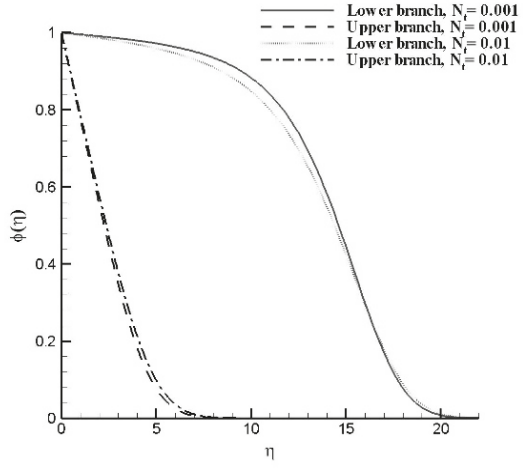

Figure 8. Dual solutions of nanoparticles concentration profile for $\alpha = -49^{\circ}$ and varying N_t, with $Pr = Le = 1.0$, $N_b = 0.05$.

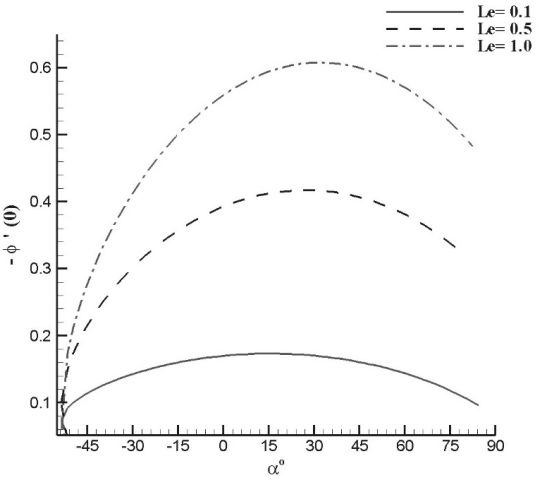

Figure 9. Effects of slot moving parameter α on reduced Sherwood number for varying Le with $Pr = 1.0$, $N_b = 0.05$, $N_t = 0.001$.

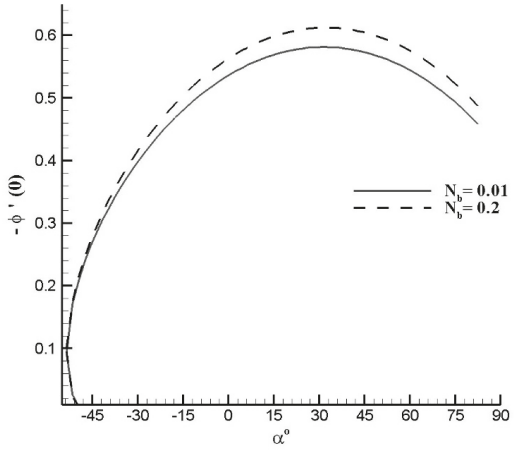

Figure 10. Effects of slot moving parameter α on reduced Sherwood number for varying N_b with $Pr = Le = 1.0$, $N_t = 0.001$.

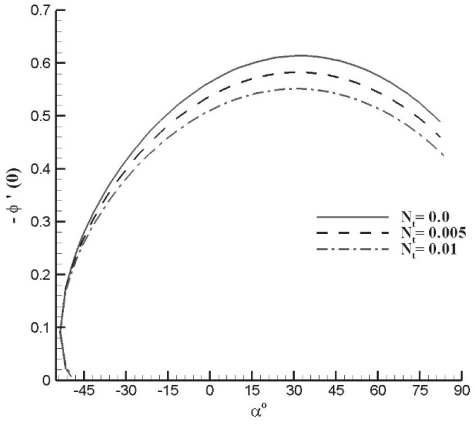

Figure 11. Effects of slot moving parameter α on reduced Sherwood number for varying N_t with $Pr = Le = 1.0$, $N_b = 0.05$.

4. Conclusions

In this work, the unsteady flow and heat transfer of a viscous-based nanofluid over a moving surface emerging from a moving slot has been considered. The effects of involved parameters on the temperature and concentration profiles are illustrated graphically. Furthermore, the variation of reduced Nusselt and Sherwood numbers with the involved parameters; namely Lewis number, Brownian motion parameter and thermophoretic diffusion parameter; are presented graphically.

The obtained results are concluded as follows:

- With the increase in the value of Brownian diffusion parameter N_b, the temperature enhances while the nanoparticles volume fraction decreases.
- By increasing the thermophoretic diffusion parameter N_t, both temperature and nanoparticles concentration are increased.
- Concentration of nanoparticles reduces with the enhancement of Lewis number Le.
- Dual solutions exist for both thermal and concentration boundary layers. The mass flux rate attains the maximum value of slot moving parameter α, as the Lewis number is increased.
- Heat flux at the surface $-\theta'(0)$ reduces with the increase of N_b and N_t in the upper solution branch. The reduced Sherwood number $-\phi'(0)$ is enhanced when N_b is increased, whereas it reduces with increasing N_t.

Author Contributions: Conceptualization and Supervision, A.A.; Methodology, S.M.; Writing—Original Draft Preparation, D.L., S.M. and A.A.; Writing—Review and Editing, U.F. and A.A.; Funding Acquisition, D.L. and U.F.

Funding: This research was funded by China Postdoctoral Science foundation (No. 189607).

Acknowledgments: Adeel Ahmad would like to acknowledge the support by the CIIT Research Grant Program of COMSATS University Islamabad, Pakistan (No. 16-68/CRGP/CIIT/ISB/17/71141).

Conflicts of Interest: The authors declare no conflict of interest.

Nomenclatures

U	Velocity component in X direction
V	Velocity component in Y direction
U_w	Plate velocity
ψ	Stream function
T	Temperature
T_∞	Ambient temperature
T_W	Wall temperature
C	Nanoparticles concentration
C_∞	Ambient nanoparticles concentration
C_W	Wall nanoparticles concentration
η	Similarity variable
α	Moving slot parameter
D_B	Brownian diffusion coefficient
D_T	Thermophoretic diffusion coefficient
Le	Lewis number
N_b	Brownian diffusion parameter
N_t	Thermophoretic diffusion parameter
Pr	Prandtl number
ϕ	Nondimensional nanoparticles concentration
θ	Nondimensional temperature
ν	Kinematic viscosity
σ	Thermal diffusivity
ε	Ratio of heat capacities of the nanoparticles
$\rho c)_f$	Heat capacity of fluid
$(\rho c)_p$	Heat capacity of nanoparticles

Appendix A

For $\alpha = 0$, the governing equations reduce to

$$f''' + \frac{1}{2}\eta f'' = 0, \tag{A1}$$

$$\theta'' + \frac{\mathrm{Pr}}{2}\eta\theta' + N_b\theta'\phi' + N_t\theta'^2 = 0, \tag{A2}$$

$$\phi'' + \frac{Le}{2}\eta\phi' + \frac{N_t}{N_b}\theta'' = 0. \tag{A3}$$

We derive the analytical expressions for the skin friction, Nusselt number and Sherwood number subject to the boundary conditions in Equation (A1). The exact solution of Equation (A1) is:

$$f'(\eta) = 1 - erf\left(\frac{1}{2}\eta\right) \tag{A4}$$

It is noted that the magnitude of thermophoretic and Brownian diffusion parameters for nanoparticles is very small [1,9], therefore we consider N_b and N_t of $O(\varepsilon)$, $\varepsilon \to 0$. We expand θ and ϕ in small parameter ε and write

$$\begin{aligned} \theta &= \theta_o + \varepsilon\theta_1 + \ldots \\ \phi &= \phi_o + \varepsilon\phi_1 + \ldots \end{aligned} \tag{A5}$$

By substituting the expressions in Equation (A5) in Equations (A2) and (A3), the leading order boundary value problem is given by

$$\theta_o'' + \frac{\mathrm{Pr}}{2}\eta\theta_o' = 0, \tag{A6}$$

$$\phi_o'' + \frac{Le}{2}\eta\phi_o' + \frac{\tau}{\beta}\theta'' = 0, \tag{A7}$$

where β and τ are constants of $O(1)$ such that $N_b = \beta\varepsilon$ and $N_t = \tau\varepsilon$. The solution of above boundary value problem can be written as

$$\begin{array}{c} \theta_o'(y) = \frac{\sqrt{\Pr}}{\sqrt{\pi}} e^{-\frac{1}{4}\Pr\eta^2}, \\ \phi_o'(y) = -\frac{\tau\Pr\left(\sqrt{\Pr} e^{-\frac{1}{4}\Pr\eta^2} - \sqrt{Le}\, e^{-\frac{1}{4}Le\eta^2}\right) + \beta(Le-\Pr)\sqrt{Le}\, e^{-\frac{1}{4}Le\eta^2}}{\sqrt{\pi}\beta(Le-\Pr)}. \end{array} \tag{A8}$$

The first order system can be written as

$$\frac{\partial^2\theta_1}{\partial y^2} + \frac{1}{2}\Pr\eta\frac{\partial\theta_1}{\partial y} + \beta\frac{\partial\theta_o}{\partial y}\frac{\partial\phi_o}{\partial y} + \tau\left(\frac{\partial\theta_o}{\partial y}\right)^2 = 0 \tag{A9}$$

$$\frac{\partial^2\phi_1}{\partial y^2} + \frac{1}{2}Le\eta\frac{\partial\phi_1}{\partial y} + \frac{\tau}{\beta}\frac{\partial^2\theta_1}{\partial y^2} = 0 \tag{A10}$$

with the boundary conditions

$$\begin{array}{c} \theta_1 = 0,\ \phi_1 = 0 \text{ at } \eta = 0 \\ \theta_1 = 0,\ \phi_1 = 0 \text{ as } \eta \to \infty \end{array} \tag{A11}$$

For the above boundary value problem, the exact solution is given by

$$\theta_1'(\eta) = e^{-\frac{1}{4}\Pr\eta^2}\left(1 - \frac{\sqrt{\Pr}}{\sqrt{\pi}}\beta\operatorname{erf}\left(\frac{1}{2}\sqrt{Le}\eta\right) - \frac{\sqrt{\Pr}}{\sqrt{\pi}}\frac{\tau}{Le-\Pr}\left(Le\operatorname{erf}\left(\frac{1}{2}\sqrt{\Pr}\eta\right) - \Pr\operatorname{erf}\left(\frac{1}{2}\sqrt{Le}\eta\right)\right)\right) \tag{A12}$$

$$\begin{array}{l} \phi_1'(\eta) = \frac{\tau}{\beta\sqrt{\pi}(Le-\Pr)} e^{-\frac{1}{4}Le\eta^2}\left(\Pr\sqrt{\pi}e^{-\frac{1}{4}(\Pr-Le)\eta^2} + \frac{\tau\Pr Le\ \operatorname{erf}\left(\frac{1}{2}\sqrt{2\Pr-Le}\eta\right)}{\sqrt{2\Pr-Le}} - \right. \\ \sqrt{\Pr^3}\left(\frac{(Le-\Pr)\beta-\Pr\tau}{Le-\Pr}\right)\left(\operatorname{erf}\left(\frac{1}{2}\sqrt{Le}\eta\right)e^{-\frac{1}{4}(\Pr-Le)\eta^2} - \frac{\sqrt{Le}}{\sqrt{\Pr}}\operatorname{erf}\left(\frac{1}{2}\sqrt{\Pr}\eta\right)\right) + ((Le-\Pr)\beta - \tau\Pr) \\ \left.\sqrt{Le}\operatorname{erf}\left(\frac{1}{2}\sqrt{\Pr}\eta\right) - \tau\frac{\sqrt{Le^3\Pr^3}}{Le-\Pr}\left(\sqrt{Le}\operatorname{erf}\left(\frac{1}{2}\sqrt{\Pr}\eta\right)e^{-\frac{1}{4}(\Pr-Le)\eta^2} - \sqrt{\Pr}\operatorname{erfi}\left(\frac{1}{2}\sqrt{Le}\,\eta\right)\right)\right), \end{array} \tag{A13}$$

where erf is the error function and erfi is the imaginary error function.

References

1. Singh, R.P. "Drag Reduction". In *Encyclopedia of Polymer Science and Technology*; John Wiley & Sons, Inc.: Hoboken, NJ, USA, 2004.
2. Zhao, H.; Wu, J.Z.; Luo, J.S. Turbulent drag reduction by traveling wave of flexible wall. *Fluid Dyn. Res.* **2004**, *34*, 175–198. [CrossRef]
3. Gyr, A.; Bewersdorff, H.W. *Drag Reduction of Turbulent Flow by Additives*; Academic Publishers: Dordrecht, The Netherlands, 1995.
4. Buongiorno, J. Convective transport in nanofluids. *J. Heat Transf.* **2006**, *128*, 240–250. [CrossRef]
5. Khan, W.A.; Pop, I. Boundary-layer flow of a nanofluid past a stretching sheet. *Int. J. Heat Mass Transf.* **2010**, *53*, 2477–2483. [CrossRef]
6. Das, K. Nanofluid flow over a shrinking sheet with surface slip. *Microfluid. Nanofluid.* **2014**, *16*, 391–401. [CrossRef]
7. Bashirnezhad, K.; Bazri, S.; Safaei, M.R. Viscosity of nanofluids: A review of recent experimental studies. *Int. Commun. Heat Mass Transf.* **2016**, *73*, 114–123. [CrossRef]
8. Ahmad, A. Flow of ReinerPhilippoff based nano-fluid past a stretching sheet. *J. Mol. Liquids* **2016**, *219*, 643–646. [CrossRef]
9. Sheremet, M.A.; Groşanc, T.; Pop, I. Steady-state free convection in right-angle porous trapezoidal cavity filled by a nanofluid: Buongiorno's mathematical model. *Eur. J. Mech. B/Fluids* **2015**, *53*, 241–250. [CrossRef]
10. Sheremet, M.A.; Pop, I. Free convection in a porous horizontal cylindrical annulus with a nanofluid using Buongiorno's model. *Comput. Fluids* **2015**, *118*, 182–190. [CrossRef]
11. Sheremet, M.A.; Cimpean, D.S.; Pop, I. Free convection in a partially heated wavy porous cavity filled with a nanofluid under the effects of Brownian diffusion and thermophoresis. *Appl. Therm. Eng.* **2017**, *113*, 413–418. [CrossRef]

12. Afridi, M.I.; Qasim, M.; Wakif, A.; Hussanan, A. Second law analysis of dissipative nanofluid flow over a curved surface in the presence of Lorentz force: Utilization of the Chebyshev–Gauss–Lobatto spectral method. *Nanomaterials* **2019**, *9*, 195. [CrossRef] [PubMed]
13. Crane, L.J. Flow past a stretching plate. *Zeitschrift für angewandte Mathematik und Physik ZAMP* **1970**, *21*, 645–647. [CrossRef]
14. Magyari, E.; Keller, B. Heat and mass transfer in the boundary layers on an exponentially stretching continuous surface. *J. Phys. D Appl. Phys.* **1999**, *32*, 577. [CrossRef]
15. Liao, S. A new branch of solutions of boundary-layer flows over an impermeable stretched plate. *Int. J. Heat Mass Transf.* **2005**, *48*, 2529–2539. [CrossRef]
16. Fang, T. Flow over a stretchable disk. *Phys. Fluids* **2007**, *19*, 128105. [CrossRef]
17. Ramesh, G.K.; Gireesha, B.J.; Bagewadi, C.S. Heat transfer in MHD dusty boundary layer flow over an inclined stretching sheet with non-uniform heat source/sink. *Adv. Math. Phys.* **2012**, *2012*, 657805. [CrossRef]
18. Imran, S.M.; Asghar, S.; Mushtaq, M. Mixed Convection Flow over an Unsteady Stretching Surface in a Porous Medium with Heat Source. *Math. Probl. Eng.* **2012**, *2012*, 485418. [CrossRef]
19. Todd, L. A family of laminar boundary layers along a semi-infinite flat plate. *Fluid Dyn. Res.* **1997**, *19*, 235–249. [CrossRef]
20. Fang, T.; Zhang, J.; Yao, S. A new family of unsteady boundary layers over a stretching surface. *Appl. Math. Comput.* **2010**, *217*, 3747–3755. [CrossRef]
21. Pritchard, P.J.; Mitchell, J.W. *Fox and McDonald's Introduction to Fluid Mechanics*, 9th ed.; Wiley: Hoboken, NJ, USA, 2011.
22. Sakiadis, B.C. Boundary layer behavior on continuous solid surfaces: I. Boundary-layer equations for two-dimensional and axisymmetric flow. *AIChE J.* **1961**, *7*, 26–28. [CrossRef]

coatings

MDPI

Article

Three-Dimensional Casson Nanofluid Thin Film Flow over an Inclined Rotating Disk with the Impact of Heat Generation/Consumption and Thermal Radiation

Anwar Saeed [1], Zahir Shah [1], Saeed Islam [1], Muhammad Jawad [1], Asad Ullah [2], Taza Gul [3] and Poom Kumam [4,5,6,*]

1 Department of Mathematics, Abdul Wali Khan University Mardan, Mardan 23200, KP, Pakistan; anwarsaeed769@gmail.com (A.S.); zahir1987@yahoo.com (Z.S.); saeedislam@awkum.edu.pk (S.I.); muhammadjawad175@yahoo.com (M.J.)
2 Institute of Numerical Sciences, Kohat University of Science and Technology, Kohat 26000, KP, Pakistan; asad.ullah@kust.edu.pk
3 Department of Mathematics, City University of Science and Information Technology (CUSIT), Peshawar 25000, Pakistan; tazagul@cusit.edu.pk
4 KMUTT-Fixed Point Research Laboratory, Room SCL 802 Fixed Point Laboratory, Science Laboratory Building, Department of Mathematics, Faculty of Science, King Mongkut's University of Technology Thonburi (KMUTT), 126 Pracha-Uthit Road, Bang Mod, Thrung Khru, Bangkok 10140, Thailand
5 KMUTT-Fixed Point Theory and Applications Research Group, Theoretical and Computational Science Center (TaCS), Science Laboratory Building, Faculty of Science, King Mongkut's University of Technology Thonburi (KMUTT), 126 Pracha-Uthit Road, Bang Mod, Thrung Khru, Bangkok 10140, Thailand
6 Department of Medical Research, China Medical University Hospital, China Medical University, Taichung 40402, Taiwan
* Correspondence: poom.kum@kmutt.ac.th; Tel.: +66-2-4708-994

Received: 13 March 2019; Accepted: 10 April 2019; Published: 15 April 2019

Abstract: In this research, the three-dimensional nanofluid thin-film flow of Casson fluid over an inclined steady rotating plane is examined. A thermal radiated nanofluid thin film flow is considered with suction/injection effects. With the help of similarity variables, the partial differential equations (PDEs) are converted into a system of ordinary differential equations (ODEs). The obtained ODEs are solved by the homotopy analysis method (HAM) with the association of MATHEMATICA software. The boundary-layer over an inclined steady rotating plane is plotted and explored in detail for the velocity, temperature, and concentration profiles. Also, the surface rate of heat transfer and shear stress are described in detail. The impact of numerous embedded parameters, such as the Schmidt number, Brownian motion parameter, thermophoretic parameter, and Casson parameter (Sc, Nb, Nt, γ), etc., were examined on the velocity, temperature, and concentration profiles, respectively. The essential terms of the Nusselt number and Sherwood number were also examined numerically and physically for the temperature and concentration profiles. It was observed that the radiation source improves the energy transport to enhance the flow motion. The smaller values of the Prandtl number, Pr, augmented the thermal boundary-layer and decreased the flow field. The increasing values of the rotation parameter decreased the thermal boundary layer thickness. These outputs are examined physically and numerically and are also discussed.

Keywords: Casson fluid; rotating disk; condensation film; heat generation/consumption; thermal radiation; HAM

1. Introduction

Energy is a requirement of production for every industry and is used in every engineering field. Important sources of energy are gas turbines, exchange membrane, and fuel cells [1], hydraulic-fracturing [2,3], etc. Suspensions of nanoparticles in fluids show a vital enrichment of their possessions at modest nanoparticle concentrations. Numerous researchers have worked on nanofluids and studied their role in heat transfer analysis, like nuclear reactors and other transportations. Nanofluids are smart fluids, where heat transfer can be decreased or increased in the base fluids. This research work focuses on investigating the vast range of uses that involve nanofluids, emphasizing their enriched heat transfer possessions, which are governable, and the defining features that these nanofluids preserve that make them suitable for such uses. Moreover, nanofluids are a new kind of energy transference fluid that are the suspension of base fluids and nanoparticles. For cooling requirements, usual heat transfer liquids cannot be used, due to their lesser thermal conductivity. By implanting nanoparticles into normal fluids, their thermal enactment can be enriched considerably. Choi [4] is widely accepted as the first publication that introduces the concept of nanofluids. He clarifies nano liquids as a liquid containing smaller scale particles known as nanoparticles about 1 to 100 nm in measure.

Bhatti et al. [5] explored the simultaneous impacts of the varying magnetic field of Jeffrey nanofluid. They examined the impact of physical parameters over the flow field. Xiao et al. [3] examined the relative permeability of nanofibers with the capillary pressure effect using the Fractal-Monte Carlo technique. They observed the impact of the embedding parameters with applications. Ellahi et al. [6] investigated the MHD non-Newtonian nanofluid with a temperature dependent viscosity flow through a pipe. The microchannel heat sink flow exploration cooled by a Cu water nanofluid by applying the least square method and the porous media approach was observed by Hatami et al. [7]. Hatami et al. [8] explored nanofluid laminar flow between rotating disks with heat transfer. Srinivas Acharya et al. [9] investigated nanofluid mixed convection flow with ion slip and Hall effects between two concentric cylinders. Khan et al. [10] investigated boundary-layer nanofluid flow through a stretching surface. Khanafer et al. [11] described two-dimensional Buoyancy driven flow with enhanced heat transfer enclosure utilizing nanofluids. Mahanthesh et al. [12] investigated unsteady MHD three-dimensional Eyring-Powell nanofluid flow with thermal radiation through a stretching sheet. Rashidi et al. [13] explored nanofluid with entropy generation and MHD flow on a steady porous rotating disk. Rashidi et al. [14] investigated 3-D film condensation on a steady inclined rotating disk.

Gul et al. [15] studied the heat and mass transfer analysis of a liquid film over an inclined plane. They compared integer and non-integer order results under the influence of embedded parameters. Saleh et al. [16] studied carbon-nanotubes suspended nanofluid flow with convective conditions using the Laplace transform. Sheikholeslami et al. [17] examined nanofluid flow in a semi-annulus enclosure with heat transfer and MHD effects. Sheikholeslami et al. [18] investigated flow in a semi-porous channel of MHD nanofluid with an analytical investigation. Later, these investigators [19] deliberated unsteady nanofluid flow through a stretching surface. Hayat et al. [20] explored the boundary layer flow of Maxwell nanofluid. Malik et al. [21] explored MHD flow through a stretching Erying-Powell nanofluid. Nadeem et al. [22] examined the flow of Maxwell liquid with nanoparticles through a vertical stretching surface. Raju et al. [23] examined flow with free convective heat transfer through a cone of MHD nano liquid. Rokni et al. [24] explored flow with the heat transfer of nanofluids through plates. Nadeem et al. [25] investigated flow on a stretching sheet of nano non-Newtonian liquid. Shehzad et al. [26] investigated the convective boundary conditions of Jaffrey nanoliquid flow with an MHD effect. Sheiholeslami et al. [27] explored flow with a magnetic field and heat transfer of nano liquid. Mahmoodi et al. [28] examined flow for cooling applications of nanonfluid with heat transfer. Recently, Shah et al. [29–32] investigated a rotating system in the effects of hall current and thermal radiations of nanofluid flow. Further theoretical investigations were examined by Sheikholeslami using different phenomena for nanofluids, with present usages and possessions with applications of numerous methods, can be found in [33–37]. Pour and Nassab [38] examined the convectional flow of

nanofluids using the numerical technique. The influence of the physical parameters was observed in their study.

The exploration of thin film has achieved substantial presentation due to its frequent usages in the field of technology, industry, and engineering in a short interval of time. The investigation of thin liquid flow is necessary, due to its practical uses, such as cable and fibber undercoat. Several well-known uses of thin film are the fluidization of devices, elastic sheet drawing, and constant formation. Regarding their uses, it is vital that scientists develop research on the stretching sheet of liquid films. Sandeep et al. [39] studied non-Newtonian nanoliquids' thin films' fluid flow with heat transfer. Wang [40] detected an unsteady flow of thin film fluid through a stretching sheet. Usha et al. [41] investigated unsteadily finite thin liquid past a stretching sheet. Liu et al. [42] investigated thin film flow with heat transfer on a stretching surface. Aziz et al. [43] perceived the flow on a stretching sheet of a thin fluid film for the production of heat inside. Tawade et al. [44] examined fluid flow with thermal radiation and heat transmission of a thin film. Fluid film flow on a stretching sheet with heat transfer was investigated by Andersson et al. [45]. Also, investigators [46–51] examined the flow of liquid film on a stretching surface for further dissimilar cases. Hatami et al. [52] examined 3-D nanofluid flow on a steady rotating disk. A similar related study about nanofluid can be seen in [52–56]. Jawad et al. [57] examined Darcy-Forchheimer nanofluid thin film flow with Joule dissipation and Navier's partial slip of the MHD effect. Jawad et al. [58] studied 3-D single-wall carbon nanotubes rotating flow with the impact of nonlinear thermal radiation and viscous dissipation in the presence of aqueous suspensions. Other related work can be seen in [59–63].

In view of the above important discussion, the aim of the current study is to investigate liquid film flow over an inclined plane. The momentum, thermal, and concentration boundary-layers under the influence of physical constraints for heat and mass transfer analysis will be examined physically and numerically.

2. Problem Formulation

Consider a steady three-dimensional Casson nanofluid thin-film flow over a rotating disk. The rotation of the disk is due to the angular velocity (Ω) in its own plane as displayed in Figure 1. An angle, β, is made by the inclined disk with the horizontal axis. Also, h denotes the film thickness of the nanofluid, and W represents the spraying velocity. The radius of the disk is very large as compared to the liquid film thickness and hence the termination influence is unnoticed. $\overline{g}$ is gravitational acceleration, T_0 is the temperature at the film surface, while T_w represents the surface temperature of the disk. Likewise, C_0 and C_h are the concentration on the film and on the disk surfaces, respectively. Pressure is a function of the z-axis only and the ambient pressure (P_0) at the sheet of the film is kept constant. The equations of continuity, momentum, concentration, and energy for a steady state are shown in Equations (1) to (6) [8–10]:

$$u_x + u_y + u_z = 0 \tag{1}$$

$$\rho_{nf}\left(uu_x + vu_y + wu_z\right) = \left(1 + \frac{1}{\gamma}\right)\mu_{nf}\left(u_{xx} + u_{yy} + u_{zz}\right) + \overline{g}\sin\beta \tag{2}$$

$$uv_x + vv_y + wv_z = \left(1 + \frac{1}{\gamma}\right)\frac{\mu_{nf}}{\rho_{nf}}\left(v_{xx} + v_{yy} + v_{zz}\right) \tag{3}$$

$$uw_x + vw_y + ww_z = \left(1 + \frac{1}{\gamma}\right)\frac{\mu_{nf}}{\rho_{nf}}\left(w_{xx} + w_{yy} + w_{zz}\right) - \overline{g}\cos\frac{\beta}{\Omega'} - \frac{P_z}{\rho_{nf}} \tag{4}$$

$$uT_x + vT_y + wT_z = \frac{k_{nf}}{\left(\rho_{cp}\right)_{nf}}\left(T_{xx} + T_{yy} + T_{zz}\right) \tag{5}$$

$$uC_x + vC_y + wC_z = D_\beta\left(C_{xx} + C_{yy} + C_{zz}\right) + \left(\frac{D_T}{T_0}\right)\left(T_{xx} + T_{yy} + T_{zz}\right) \tag{6}$$

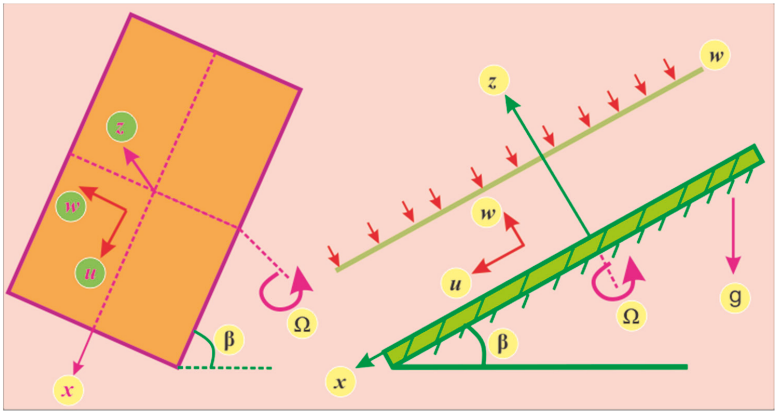

Figure 1. Geometry of the problem.

In the above equations, u, v, and w represent the velocity components in the x, y, and z axis, respectively.

The boundary conditions are as follows:

$$\begin{array}{l} u = -\Omega y, v = \Omega x, w = 0, T = T_w, C = C_h \quad at\ z = 0 \\ u_z = v_z = 0, w = 0, T = T_w, C = C_0, P = P_0 \quad at\ z = h \end{array} \tag{7}$$

Consider the similarity transformations of the form:

$$\begin{array}{c} u = -\Omega y g(\eta) + \Omega x f'(\eta) + \overline{g} k(\eta) \sin \frac{\beta}{\Omega'} \\ v = \Omega x g(\eta) + \Omega y f'(\eta) + \overline{g} s(\eta) \sin \frac{\beta}{\Omega'} \\ w = -2\sqrt{\Omega v_{nf}} f(\eta),\ T = (T_0 - T_w)\theta(\eta) + T_w \\ \eta\phi(\eta) = \frac{C - C_w}{C_0 - C_w},\ \eta = z\sqrt{\frac{\Omega}{v_{nf}}} \end{array} \tag{8}$$

The transformations introduced in Equation (8) are implemented in Equations (2) to (7). Equation (1) is proved identically and Equations (2) to (6) are obtained in the forms:

$$\left(1 + \frac{1}{\gamma}\right) f''' - f'^2 + g^2 + 2ff'' = 0 \tag{9}$$

$$\left(1 + \frac{1}{\gamma}\right) k'' + gs - kf' + 2kf = 0 \tag{10}$$

$$\left(1 + \frac{1}{\gamma}\right) g'' - 2gf' + 2g'f = 0 \tag{11}$$

$$\left(1 + \frac{1}{\gamma}\right) s'' - kg - sf' + 2s'f = 0 \tag{12}$$

If θ(η) and ϕ(η) are a function of z only, Equations (5) and (6) take the forms:

$$\left(1 - \frac{4}{3}R\right)\theta'' + 2\mathrm{Pr}\frac{A_2A_3}{A_1A_4}(I_1 f' + j_1)\theta = 0 \tag{13}$$

$$\phi'' + 2Scf\phi' + \frac{Nt}{Nb}\theta'' = 0 \tag{14}$$

$$\begin{gathered} f(0) = 0,\ f'(0) = 0,\ f''(\delta) = 0,\ \phi(0) = 0,\ \phi(\delta) = 1 \\ g(0) = 0,\ g'(\delta) = 0,\ k(0) = 0,\ k'(\delta) = 0 \\ s(0) = 0,\ s'(\delta) = 0,\ \theta(0) = 0,\ \theta'(\delta) = 1. \end{gathered} \tag{15}$$

Physical parameters and other dimensionless numbers of interest are defined as:

$$\begin{gathered} \mathrm{Pr} = \frac{v_f}{\alpha_f},\ Sc = \frac{\mu}{\rho f D},\ Nb = \frac{(\rho c)_p D_b(C_h)}{(\rho c)_f \alpha} \\ Nt = \frac{(\rho c)_p D_T(T_H)}{(\rho c)_f \alpha T_c},\ S = \frac{\alpha}{\Omega} \end{gathered} \tag{16}$$

Here, *Pr* is the Prandtl number, *Sc* is the Schmidt number, *Nb* is the Brownian motion parameter, and *Nt* is the thermophoretic parameter.

Where the normalized thickness constant is presented as:

$$\delta = h\sqrt{\frac{\Omega}{v_{nf}}} \tag{17}$$

The condensation velocity is defined as:

$$f(\delta) = \frac{W}{2\sqrt{\Omega v}} = \alpha \tag{18}$$

The pressure can be attained by the integration of Equation (4).

For the exact solution, let *Pr* = 0 and using θ(δ) = 1, the exact solution is:

$$\theta'(0) = \frac{1}{\delta} \tag{19}$$

An asymptotic limit for small, δ, is defined in Equation (17). The reduction of θ′(0) for rising δ is not monotonic. So, *Nu* is defined as:

$$Nu = \frac{k_{nf}}{k_f}\frac{(T_z)_w}{(T_0 - T_w)} = A_4\delta\theta'(0) \tag{20}$$

The Sherwood number is defined as:

$$Sh = \frac{(C_z)_w}{C_0 - C_w} = \delta\phi'(0) \tag{21}$$

3. Solution by Homotopy Analysis Method

The optimal approach is used for the solution process. Equations (9) to (14) with boundary conditions (15) are solved by HAM. Mathematica software is used for this aim. The basic derivation of the model equation through HAM is given in detail below.

Linear operators are denoted as $L_{\hat{f}}$, $L_{\hat{\theta}}$ and $L_{\hat{\phi}}$ is represented as

$$\begin{gathered} L_{\hat{f}}(\hat{f}) = \hat{f}''', L_{\hat{k}}(\hat{k}) = \mathrm{k}'', L_{\hat{g}}(\hat{g}) = \mathrm{g}'', \\ L_{\hat{s}}(\hat{s}) = \mathrm{s}'', L_{\theta}\left(\hat{\theta}\right) = \hat{\theta}'',\ L_{\hat{\phi}}\left(\hat{\phi}\right) = \phi'' \end{gathered} \tag{22}$$

The modelled Equations (9) to (14) with boundary conditions (15) are solved analytically as well as numerically. The comparison between the analytical and numerical solution is shown graphically as well as numerically in Tables 1–6 for the velocities, temperature, and concentration profiles. From these tables, an excellent agreement between the HAM and numerical (ND-Solve Techniques) methods is obtained.

Table 1. Comparison of HAM and numerical solution for $f(\eta)$.

$f(\eta)$	HAM Solution	Numerical Solution	Absolute Error
0.0	0.000000	$-2.812710 \times 10^{-10}$	2.812710×10^{-10}
0.1	0.003258	0.003258	5.703240×10^{-8}
0.2	0.012408	0.012408	2.280140×10^{-7}
0.3	0.026573	0.026573	5.104210×10^{-7}
0.4	0.044948	0.044948	8.995600×10^{-7}
0.5	0.066795	0.066793	1.388520×10^{-6}
0.6	0.091431	0.091429	1.965710×10^{-6}
0.7	0.118224	0.118221	2.615740×10^{-6}
0.8	0.146586	0.146583	3.327870×10^{-6}
0.9	0.175966	0.175962	4.078740×10^{-6}
1.0	0.205842	0.205837	4.847430×10^{-6}

Table 2. Comparison of HAM and numerical solution for $k(\eta)$.

$k(\eta)$	HAM Solution	Numerical Solution	Absolute Error
0.0	0.000000	3.431260×10^{-8}	3.431260×10^{-8}
0.1	0.082367	0.082366	2.022930×10^{-7}
0.2	0.155134	0.155134	4.388100×10^{-7}
0.3	0.218705	0.218705	6.667190×10^{-7}
0.4	0.273439	0.273438	8.749510×10^{-7}
0.5	0.319620	0.319619	1.071030×10^{-6}
0.6	0.357437	0.357436	1.231030×10^{-6}
0.7	0.386981	0.386980	1.356500×10^{-6}
0.8	0.408247	0.408246	1.432420×10^{-6}
0.9	0.421138	0.421137	1.471570×10^{-6}
1.0	0.425484	0.425483	1.467400×10^{-6}

Table 3. Comparison of HAM and numerical solution for $g(\eta)$.

$g(\eta)$	HAM Solution	Numerical Solution	Absolute Error
0.0	1.000000	1.000000	1.286450×10^{-8}
0.1	0.950141	0.950139	2.377450×10^{-6}
0.2	0.903441	0.903436	4.705070×10^{-6}
0.3	0.860810	0.860803	6.954740×10^{-6}
0.4	0.822957	0.822948	9.080750×10^{-6}
0.5	0.790417	0.790406	0.000011
0.6	0.763566	0.763553	0.000013
0.7	0.742641	0.742627	0.000014
0.8	0.727756	0.727740	0.000015
0.9	0.718908	0.718892	0.000016
1.0	0.715997	0.715981	0.000016

Table 4. Comparison of HAM and numerical solution for $s(\eta)$.

$s(\eta)$	HAM Solution	Numerical Solution	Absolute Error
0.0	0.000000	-7.170820×10^{-9}	7.170820×10^{-9}
0.1	−0.019540	−0.019539	1.154300×10^{-6}
0.2	−0.038351	−0.038349	2.304890×10^{-6}
0.3	−0.055850	−0.055846	3.427710×10^{-6}
0.4	−0.071593	−0.071588	4.501730×10^{-6}
0.5	−0.085251	−0.085246	5.509380×10^{-6}
0.6	−0.096596	−0.096590	6.416000×10^{-6}
0.7	−0.105479	−0.105471	7.187270×10^{-6}
0.8	−0.111819	−0.111811	7.792270×10^{-6}
0.9	−0.115595	−0.115587	8.183170×10^{-6}
1.0	−0.116839	−0.116831	8.326040×10^{-6}

Table 5. Comparison of HAM and numerical solution for θ(η).

θ(η)	HAM Solution	Numerical Solution	Absolute Error
0.0	0.000000	-1.777730×10^{-9}	1.777730×10^{-9}
0.1	0.116628	0.116628	1.151200×10^{-7}
0.2	0.232964	0.232964	2.309850×10^{-7}
0.3	0.348690	0.348690	3.439950×10^{-7}
0.4	0.463468	0.463469	4.517690×10^{-7}
0.5	0.576946	0.576946	5.526490×10^{-7}
0.6	0.688763	0.688763	6.424670×10^{-7}
0.7	0.798558	0.798559	7.163620×10^{-7}
0.8	0.905975	0.905976	7.751320×10^{-7}
0.9	1.010670	1.010670	8.130730×10^{-7}
1.0	1.112300	1.112300	8.304690×10^{-7}

Table 6. Comparison of HAM and numerical solution for ϕ(η).

ϕ(η)	HAM Solution	Numerical Solution	Absolute Error
0.0	0.000000	-2.935480×10^{-9}	2.935480×10^{-9}
0.1	0.109309	0.109309	8.676730×10^{-8}
0.2	0.218448	0.218448	1.752770×10^{-7}
0.3	0.327225	0.327226	2.613220×10^{-7}
0.4	0.435439	0.435440	3.434820×10^{-7}
0.5	0.542882	0.542883	4.241530×10^{-7}
0.6	0.649351	0.649352	4.969910×10^{-7}
0.7	0.754655	0.754656	5.581250×10^{-7}
0.8	0.858619	0.858620	6.055710×10^{-7}
0.9	0.961090	0.961091	6.356540×10^{-7}
1.0	1.061940	1.061940	6.465200×10^{-7}

4. Results and Discussion

The three-dimensional flow of the liquid film through a steady rotating inclined surface with mass and heat transmission was examined. The influence of the embedded parameters, magnetic field, M, Casson parameter, γ, Schmidt number, Sc, Brownian motion parameter, Nb, and thermophoretic parameter, Nt, was investigated for the axial velocity, $f(\eta)$, radial velocity, $k(\eta)$, drainage flow, $g(\eta)$, and induced flow, $s(\eta)$, temperature field, $\theta(\eta)$, and concentration profile, $\phi(\eta)$, respectively. Figures 2–5 display the influence of the Casson fluid parameter, γ, on $f(\eta)$, $k(\eta)$, $g(\eta)$, and $s(\eta)$. Rising γ generates resistance in the flow path and decreases the flow motion of nanoparticles. It is observed that an increase of the Casson fluid parameter, γ, leads to a decrease of $f(\eta)$, $k(\eta)$, $g(\eta)$, and $s(\eta)$. The opposite trend is found in case of the z-direction, that is the enormous value of γ decreases the $f(\eta)$, $k(\eta)$, $g(\eta)$, and $s(\eta)$. The influence of Pr on $\theta(\eta)$ is displayed in Figure 6. It is interesting to note that $\theta(\eta)$ decreases with large values of Pr and increases with smaller values. In fact, the thermal diffusivity of nanofluids has greater values by reducing Pr, and this effect is inconsistent for larger Pr. Hence, the greater values of Pr drop the thermal boundary layer. The influence of the radiation parameter, R, on $\theta(\eta)$ is presented in Figure 7. It is observed that if R increases, then the boundary layer area $\theta(\eta)$ is augmented. The effect of Nb on $\theta(\eta)$ is displayed in Figure 8. The converse influence was created for $\phi(\eta)$ and $\theta(\eta)$, which means augmented Nb decreases the concentration profile, $\phi(\eta)$. The concentration boundary layer thickness decreased due to the rising values of Nb and as a result, the concentration field, $\phi(\eta)$, declined. The features of the thermophoretic parameter, Nt, on the concentration profile, $\phi(\eta)$, are presented in Figure 9. The enhancement of Nt increases $\phi(\eta)$. Thus, Nt depends on the temperature gradient of the nanofluids. The kinetic energy of the nanofluids rises with the increasing value of Nt, and as a result, $\phi(\eta)$ increases. Figure 10 identifies the influence of Sc. The dimensionless number, Sc, is stated as the ratio of momentum and mass diffusivity. It is obvious that the amassed Sc reduces the $\phi(\eta)$ and as a result, the boundary layer thickness is decreased.

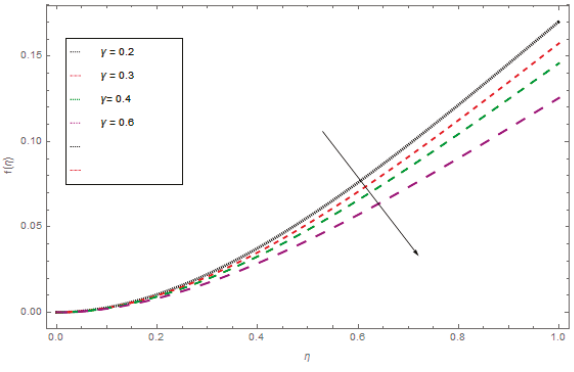

Figure 2. The influence of γ on $f(\eta)$ when Ω = 1, ρ = 1, σ = 0.5, k = 1, M = 1.

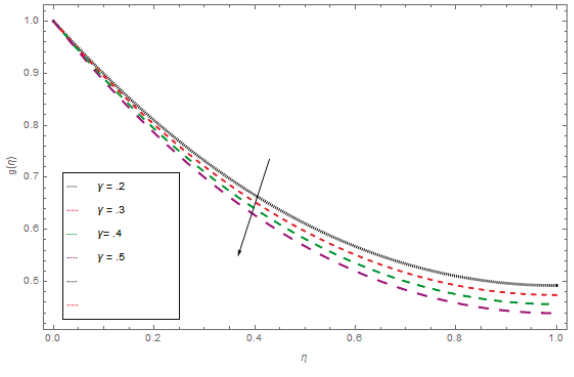

Figure 3. The influence of γ on $g(\eta)$ when Ω = 1, ρ = 1, σ = 0.5, k = 1, M = 1.

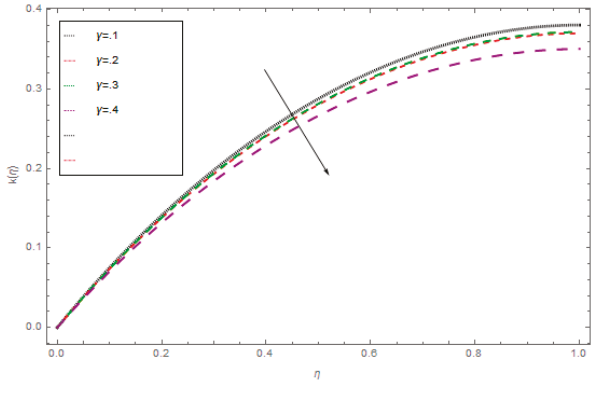

Figure 4. The influence of γ on $k(\eta)$ when Ω = 1, ρ = 1, σ = 0.5, k = 1, M = 1.

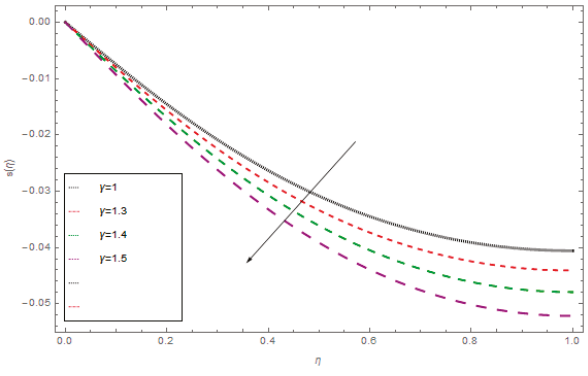

Figure 5. The influence of γ on *s*(η) when Ω = 1, ρ = 1, σ = 0.5, *k* = 1, *M* = 1.

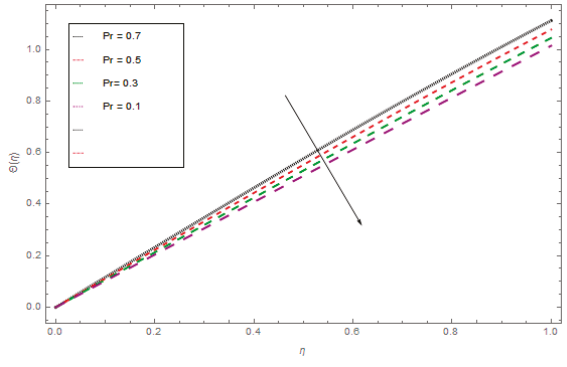

Figure 6. The influence of *Pr* on θ(η) when Ω = 1, ρ = 1, σ = 0.5, *k* = 1, *M* = 1.

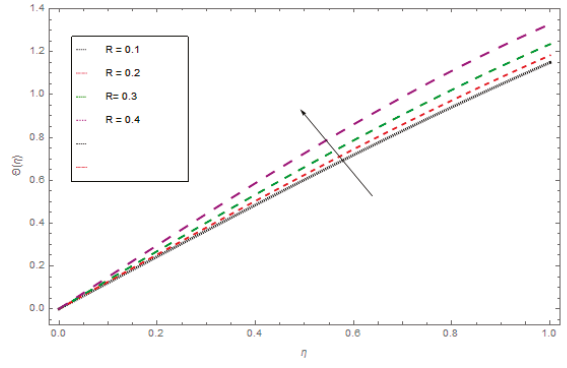

Figure 7. The influence of *R* on θ(η) when Ω = 1, ρ = 1, σ = 0.5, *k* = 1, *M* = 1.

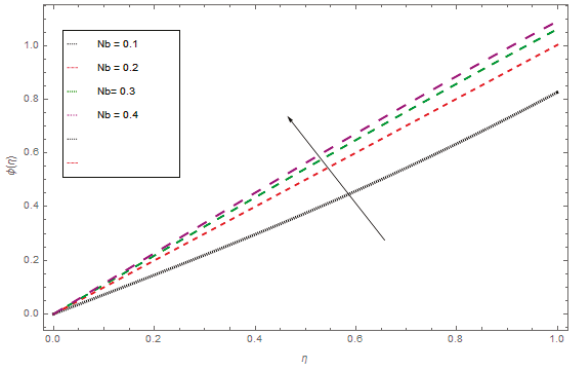

Figure 8. The effect of *Nb* on ϕ(η) when *Nt* = 0.6, *Sc* = 0.6, *S* = 0.7.

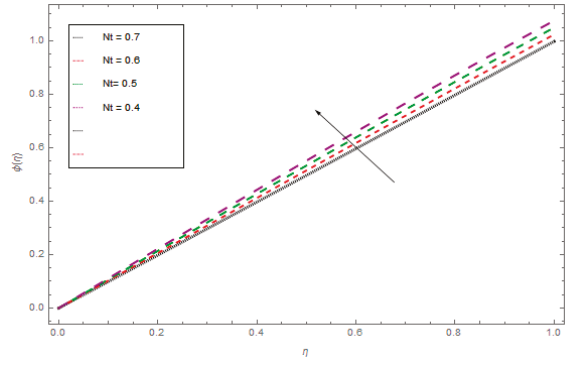

Figure 9. The influence of *Nt* on ϕ(η) when *Nb* = 0.6, *Sc* = 0.7, *S* = 0.7.

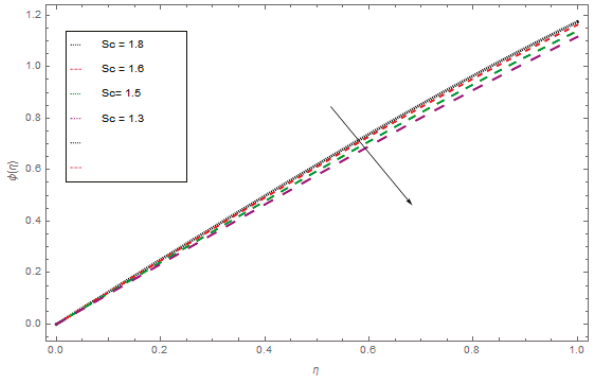

Figure 10. The influence of the Schmidt number (*Sc*) on ϕ(η) when *Nb* = 0.6, *Nt* = 0.5.

Figures 11 and 12 demonstrate the effects of *Pr* and *R*. It can be seen that rising values of *Pr* and *R* increase *Nu*. In fact, the coaling phenomenon is enhanced with increased values of these parameters. Figure 13 identifies that *Nu* reduces for the amassed values of *k*.

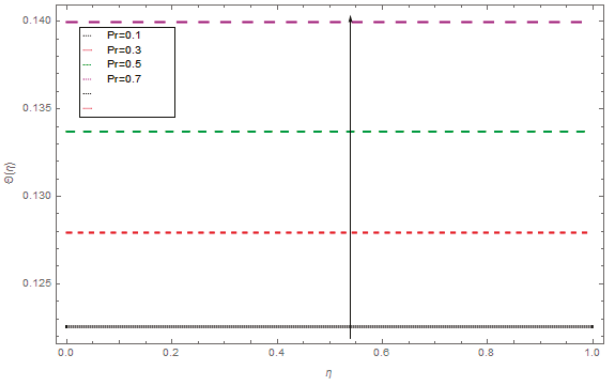

Figure 11. The impact of the Prandtl number (*Pr*) on the Nusselt number.

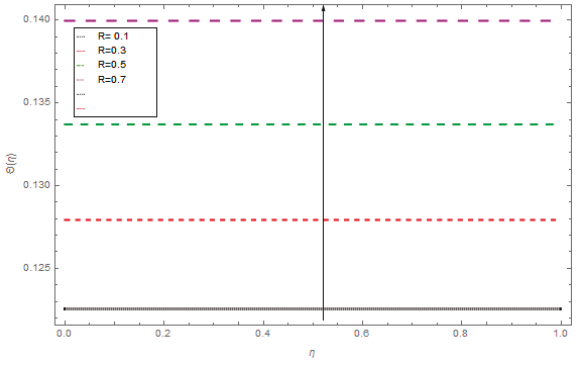

Figure 12. The influence of radiation parameter (*R*) on the Nusselt number.

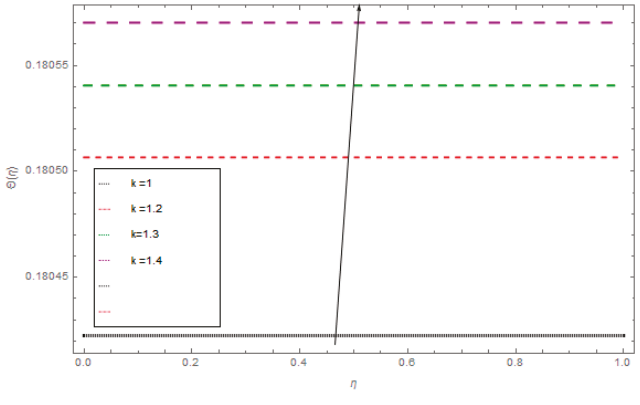

Figure 13. The influence of *k* on the Nusselt number.

5. Conclusions

In this article, the three-dimensional thin-film Casson fluid flow over an inclined steady rotating plane was examined. The thin film flow was thermally radiated and the suction/injection effect was also considered. By the similarity variables, the PDEs were converted into ODES. The obtained ODEs

were solved by the HAM with association of the MATHEMATICA program. The main features of the study are highlighted as:

- Smaller values of the Prandtl number enhance the thermal boundary layer.
- An increasing value of the magnetic field stops the fluid motion.
- Larger amounts of the thermal radiation parameter and thermophoretic parameter enhances the thermal boundary layer.
- The Casson fluid parameter produces a resistance force and its increasing value decreases the fluid motion.

Author Contributions: A.S., Z.S. and S.I. modeled the problem and wrote the manuscript. P.K. and T.Z. thoroughly checked the mathematical modeling and English corrections. A.S., M.J. and A.U. solved the problem using Mathematica software, S.I., T.G. and P.K. contributed to the results and discussions. All authors finalized the manuscript after its internal evaluation.

Funding: This research was funded by the Center of Excellence in Theoretical and Computational Science (TaCS-CoE), KMUTT.

Acknowledgments: This project was supported by the Theoretical and Computational Science (TaCS) Center under Computational and Applied Science for Smart Innovation Research Cluster (CLASSIC), Faculty of Science, KMUTT.

Conflicts of Interest: The authors declare no conflict of interest.

Nomenclature

Nb	Brownian motion parameter
T	Cauchy stress tensor
C	Concentration of the fluid
h	Film thickness
M	Magnetic parameter
Nu	Nusselt number
Pr	Prandtl number
Nt	Thermoporetic parameter
R	Radiation parameter
x, y, z	Rectangular coordinates
Re	Reynold number
Sh	Sherwood number
C_f	Skin friction coefficient
W	Spraying velocity
T_∞	Temperature of the fluid at large distance
f	Transformed dependent variable
u	Velocity component in x-direction
v	Velocity component in y-direction
μ	Coefficient of viscosity
γ	Casson fluid parameter
ϱ	Density of the fluid
p	Fluid pressure
I	Identity tensor chord
v	Kinematic viscosity
Ω	Rotation parameter
τ	Shearing stress
ψ	Stream function
β	Thickness of the fluid
η	Transformed independent variable
∞	Condition at infinity

References

1. Liang, M.; Liu, Y.; Xiao, B.; Yang, S.; Wang, Z.; Han, H. An analytical model for the transverse permeability of gas diffusion layer with electrical double-layer effects in proton exchange membrane full cells. *Int. J. Hydrogen Energy* **2018**, *43*, 17880–17888. [CrossRef]
2. Long, G.; Liu, S.; Xu, G.; Wong, S.W.; Chen, H.; Xiao, B.A. Perforation-erosion model for hydraulic-fracturing applications. *SPE. Prod. Oper.* **2018**, *33*, 770–783. [CrossRef]
3. Xiao, B.; Wang, W.; Zhang, X.; Long, G.; Chen, H.; Cai, H.; Deng, L.A. Novel fractal model for relative permeability of gas diffusion layer in proton exchange membrane fuel cell with capillary pressure effect. *Fractals* **2019**, *27*, 1950012. [CrossRef]
4. Choi, S.; Eastman, J. Enhancing thermal conductivity of fluids with nanoparticles. In Proceedings of the ASME International Mechanical Engineering Congress and Exposition, San Francisco, CA, USA, 12–17 November 1995.
5. Bhatti, M.M.; Zeeshan, A.; Ellah, R. Simultaneous effects of coagulation and variable magnetic field on peristaltically induced motion of Jeffrey nanofluid containing gyrotactic microorganism. *Microvasc. Res.* **2017**, *110*, 32–42. [CrossRef]
6. Ellahi, R. The effects of MHD and temperature dependent viscosity on the flow of non-Newtonian nanofluid in a pipe: Analytical solutions. *Appl. Math. Model.* **2013**, *37*, 1451–1467. [CrossRef]
7. Hatami, M.; Ganji, D.D. Thermal and flow analysis of microchannel heat sink (MCHS) cooled by Cu water nanofluid using porous media approach and least square method. *Energy Convers. Manag.* **2014**, *78*, 347–358. [CrossRef]
8. Hatami, M.; Sheikholeslami, M.; Ganji, D.D. Laminar flow and heat transfer of nanofluid between contracting and rotating disks by least square method. *Powder Technol.* **2014**, *253*, 769–779. [CrossRef]
9. Srinivasacharya, D.; Shafeeurrahman, M. Hall and ion slip effects on mixed convection flow of nanofluid between two concentric cylinders. *J. Assoc. Arab Univ. Basic Appl. Sci.* **2017**, *24*, 223–231. [CrossRef]
10. Khan, W.; Pop, I. Boundary-layer flow of a nanofluid past a stretching sheet. *Int. J. Heat Mass Transf.* **2010**, *53*, 2477–2483. [CrossRef]
11. Khanafer, K.; Vafai, K.; Lightstone, M.; Buoyancydriven. Heat transfer enhancement in a two-dimensional enclosure utilizing nanofluids. *Int. J. Heat Mass Transf.* **2003**, *46*, 3639–3653. [CrossRef]
12. Mahanthesh, B.; Gireesha, B.J.; Gorla, R.S.R. Unsteady three-dimensional MHD flow of a nano Eyring-Powell fluid past a convectively heated stretching sheet in the presence of thermal radiation, viscous dissipation and Joule heating. *J. Assoc. Arab Univ. Basic Appl. Sci.* **2017**, *23*, 75–84. [CrossRef]
13. Rashidi, M.M.; Abelman, S.; Mehr, N.F. Entropy generation in steady MHD flow due to a rotating porous disk in a nanofluid. *Int. J. Heat Mass Transf.* **2013**, *62*, 515–525. [CrossRef]
14. Rashidi, M.M.; Dinarvand, S. Purely analytic approximate solutions for steady three-dimensional problem of condensation film on inclined rotating disk by homotopy analysis method. *Nonlinear Anal. Real World Appl.* **2009**, *10*, 2346–2356. [CrossRef]
15. Gul, T.; Khan, M.A.; Khan, A.; Shuaib, M. Fractional-order three-dimensional thin-film nanofluid flow on an inclined rotating disk. *Eur. Phys. J. Plus* **2018**, *133*, 500–5011. [CrossRef]
16. Saleh, H.; Alali, E.; Ebaid, A. Medical applications for the flow of carbon-nanotubes suspended nanofluids in the presence of convective condition using Laplace transform. *J. Assoc. Arab Univ. Basic Appl. Sci.* **2017**, *24*, 206–212. [CrossRef]
17. Sheikholeslami, M.; Gorji-Bandpy, M.; Ganji, D.D. Numerical investigation of MHD effects on Al_2O_3-water nanofluid flow and heat transfer in a semi-annulus enclosure using LBM. *Energy* **2013**, *60*, 501–510. [CrossRef]
18. Sheikholeslami, M.; Hatami, M.; Ganji, D.D. Analytical investigation of MHD nanofluid flow in a semi-porous channel. *Powder Technol.* **2013**, *246*, 327–336. [CrossRef]
19. Abolbashari, M.H.; Freidoonimehr, N.; Rashidi, M.M. Analytical modeling of entropy generation for Casson nano-fluid flow induced by a stretching surface. *Entropy* **2015**, *6*, 542–552. [CrossRef]
20. Hayat, T.; Muhammad, T.; Shehzad, S.A.; Alsaed, A. Three-dimensional boundary layer flow of Maxwell nanofluid. *Appl. Math. Mech. Engl. Ed.* **2015**, *36*, 747–762. [CrossRef]
21. Malik, M.Y.; Khan, I.; Hussain, A.; Salahuddin, T. Mixed convection flow of MHD Erying-Powell nanofluid over a stretching sheet. A numerical study. *AIP Adv.* **2015**, *5*, 117–118. [CrossRef]

22. Nadeem, S.; Haq, R.U.; Khan, Z.H. Numerical study of MHD boundary layer flow of a Maxwell fluid past a stretching sheet in the presence of nanoparticles. *J. Taiwan Inst. Chem. Eng.* **2014**, *45*, 121–126. [CrossRef]
23. Raju, C.S.K.; Sandeep, N.; Malvandi, A. Free convective heat and mass transfer of MHD non-Newtonian nanofluids over a cone in the presence of non-uniform heat source/sink. *J. Mol. Liq.* **2016**, *221*, 101–115. [CrossRef]
24. Rokni, H.B.; Alsaad, D.M.; Valipour, P. Electro hydrodynamic nanofluid flow and heat transfer between two plates. *J. Mol. Liq.* **2016**, *216*, 583–589. [CrossRef]
25. Nadeem, S.; Rizwan, U.H.; Khan, Z.H. Numerical solution of non-Newtonian nanofluid flow over a stretching sheet. *J. Appl. Nano Sci.* **2014**, *5*, 625–631. [CrossRef]
26. Shehzad, S.A.; Hayat, A.; Alsaedi, A. MHD flow of Jeffrey nanofluid with convective boundary conditions. *Braz. Soc. Mech. Sci. Eng.* **2014**, *3*, 873–883. [CrossRef]
27. Sheikholeslami, M.; Hatami, H.M.; Ganji, D.D. Nanofluid flow and heat transfer in a rotating system in the presence of a magnetic field. *J. Mol. Liq.* **2014**, *190*, 112–120. [CrossRef]
28. Mahmoodi, M.; Kandelousi, S.H. Kerosene–alumina nanofluid flow and heat transfer for cooling application. *J. Cent. South Univ.* **2016**, *23*, 983–990. [CrossRef]
29. Shah, Z.; Islam, S.; Ayaz, H.; Khan, S. Radiative heat and mass transfer analysis of micropolar nanofluid flow of casson fluid between two rotating parallel plates with effects of hall current. *ASME J. Heat Transf.* **2019**, *141*, 022401. [CrossRef]
30. Shah, Z.; Islam, S.; Gul, T.; Bonyah, E.; Khan, M.A. Three dimensional third grade nanofluid flow in a rotating system between parallel plates with Brownian motion and thermophoresis effects. *Results Phys.* **2018**, *10*, 36–45. [CrossRef]
31. Shah, Z.; Islam, S.; Gul, T.; Bonyah, E.; Khan, M.A. The electrical MHD and hall current impact on micropolar nanofluid flow between rotating parallel plates. *Results Phys.* **2018**, *9*, 1201–1214. [CrossRef]
32. Shah, Z.; Gul, T.; Khan, A.M.; Ali, I.; Islam, S. Effects of hall current on steady three dimensional non Newtonian nanofluid in a rotating frame with Brownian motion and thermophoresis effects. *J. Eng. Technol.* **2017**, *6*, 280–296.
33. Sheikholeslami, M. CuO-water nanofluid flow due to magnetic field inside a porous media considering Brownian motion. *J. Mol. Liq.* **2018**, *249*, 921–929. [CrossRef]
34. Sheikholeslami, M.; Shah, Z.; Tassaddiq, A.; Shafee, A.; Khan, I. Application of electric field transfer in an enclosure including double for augmentation of ferrofluid heat moving walls. *IEEE Access* **2019**, *7*, 21048–21056. [CrossRef]
35. Sheikholeslami, M.; Shah, Z.; Shafi, A.; khan, I.; Itili, I. Uniform magnetic force impact on water based nanofluid thermal behavior in a porous enclosure with ellipse shaped obstacle. *Sci. Rep.* **2019**. [CrossRef]
36. Sheikholeslami, M. Fe_3O_4-Ethylene glycol nanofluid forced convection inside a porous enclosure in existence of Coulomb force. *J. Mol. Liq.* **2018**, *249*, 429–437. [CrossRef]
37. Pour, M.; Nassab, S. Numerical investigation of forced laminar convection flow of nanofluids over a backward facing step under bleeding condition. *J. Mech.* **2012**, *28*, N7–N12. [CrossRef]
38. Nasir, S.; Islam, S.; Gul, T.; Shah, Z.; Khan, M.A.; Khan, W.; Khan, A.Z.; Khan, S. Three-dimensional rotating flow of MHD single wall carbon nanotubes over a stretching sheet in presence of thermal radiation. *Appl. Nano Sci.* **2018**, *8*, 1361–1378. [CrossRef]
39. Sandeep, N.; Malvandi, A. Enhanced heat transfer in liquid thin film flow of non-Newtonian nanofluids embedded with graphene nanoparticles. *Adv. Powder Technol.* **2016**, *27*, 2448–2456. [CrossRef]
40. Wang, C.Y. Liquid film on an unsteady stretching surface. *Q. Appl. Math.* **1990**, *84*, 601–610. [CrossRef]
41. Usha, R.; Sridharan, R. On the motion of a liquid film on an unsteady stretching surface. *ASME Fluids Eng.* **1993**, *150*, 43–48. [CrossRef]
42. Liu, I.C.; Andersson, I.H. Heat transfer in a liquid film on an unsteady stretching sheet. *Int. J. Therm. Sci.* **2008**, *47*, 766–772. [CrossRef]
43. Aziz, R.C.; Hashim, I.; Alomari, A.K. Thin film flow and heat transfer on an unsteady stretching sheet with internal heating. *Meccanica* **2011**, *46*, 349–357. [CrossRef]
44. Tawade, L.; Abel, M.; Metri, P.G.; Koti, A. Thin film flow and heat transfer over an unsteady stretching sheet with thermal radiation internal heating in presence of external magnetic field. *Int. J. Adv. Appl. Math. Mech.* **2016**, *3*, 29–40.

45. Anderssona, H.I.; Aarseth, J.B.; Dandapatb, B.S. Heat transfer in a liquid film on an unsteady stretching. *Int. J. Heat Mass Transf.* **2000**, *43*, 69–74. [CrossRef]
46. Gul, T.; Haleem, I.; Ullah, I.; Khan, M.A.; Bonyah, E.; Khan, I.; Shuaib, M. The study of the entropy generation in a thin film flow with variable fluid properties past over a stretching sheet. *Adv. Mech. Eng.* **2018**, *10*, 1–15. [CrossRef]
47. Gul, T. Scattering of a thin layer over a nonlinear radially extending surface with Magneto hydrodynamic and thermal dissipation. *Surf. Rev. Lett.* **2019**, *26*, 1850123. [CrossRef]
48. Alsagri, A.S.; Nasir, S.; Gul, T.; Islam, S.; Nisar, K.S.; Shah, K.S.; Khan, I. MHD thin film flow and thermal analysis of blood with CNTs nanofluid. *Coatings* **2019**, *9*, 175. [CrossRef]
49. Shah, Z.; Bonyah, E.; Islam, S.; Khan, W.; Ishaq, M. Radiative MHD thin film flow of Williamson fluid over an unsteady permeable stretching. *Heliyon* **2018**, *4*, e00825. [CrossRef]
50. Ullah, A.; Alzahrani, E.O.; Shah, Z.; Ayaz, M.; Islam, S. Nanofluids thin film flow of reiner-philippoff fluid over an unstable stretching surface with brownian motion and thermophoresis effects. *Coatings* **2019**, *9*, 21. [CrossRef]
51. Khan, A.S.; Nie, Y.; Shah, Z. Impact of thermal radiation and heat source/sink on MHD time-dependent thin-film flow of Oldroyed-B, Maxwell, and Jeffry Fluids over a stretching surface. *Processes* **2019**, *7*, 191. [CrossRef]
52. Chen, C.H. Heat transfer in a power-law liquid film over a unsteady stretching sheet. *J. Heat Mass Transf.* **2003**, *39*, 791–796. [CrossRef]
53. Chen, C.H. Effect of viscous dissipation on heat transfer in a non-Newtonian liquid film over an unsteady stretching sheet. *J. Non-Newton. Fluid Mech.* **2006**, *135*, 128–135. [CrossRef]
54. Wang, C.; Pop, L. Analysis of the flow of a power-law liquid film on an unsteady stretching surface by means of homotopy analysis method. *J. Non-Newton. Fluid Mech.* **2006**, *138*, 161–172. [CrossRef]
55. Mahmoud, M.A.A. On flow and heat transfer in a thin liquid film over an unsteady stretching sheet with variable fluid properties and radiation. *Open Sci. J. Math. Appl.* **2015**, *3*, 14–18.
56. Hatami, M.; Jing, D.; Majeed, A.Y. Three-dimensional analysis of condensation nanofluid film on an inclined rotating disk by efficient analytical methods. *Arab. J. Basic Appl. Sci.* **2018**, *25*, 28–37. [CrossRef]
57. Jawad, M.; Shah, Z.; Islam, S.; Bonyah, E.; Khan, Z.A. Darcy-Forchheimer flow of MHD nanofluid thin film flow with Joule dissipation and Navier's partial slip. *J. Phys. Commun.* **2018**, *11*, 115014. [CrossRef]
58. Jawad, M.; Shah, Z.; Islam, S.; Majdoubi, J.; Tlili, I.; Khan, W.; Khan, I. Impact of nonlinear thermal radiation and the viscous dissipation effect on the unsteady three-dimensional rotating flow of single-wall carbon nanotubes with aqueous suspensions. *Symmetry* **2019**, *11*, 207. [CrossRef]
59. Nasir, S.; Shah, Z.; Islam, S.; Khan, W.; Bonyah, E.; Ayaz, M.; Khan, A. Three dimensional Darcy-Forchheimer radiated flow of single and multiwall carbon nanotubes over a rotating stretchable disk with convective heat generation and absorption. *AIP Adv.* **2019**, *9*, 035031. [CrossRef]
60. Feroz, N.; Shah, Z.; Islam, S.; Alzahrani, E.O.; Khan, W. Entropy generation of carbon nanotubes flow in a rotating channel with hall and ion-slip effect using effective thermal conductivity model. *Entropy* **2019**, *21*, 52. [CrossRef]
61. Alharbi, S.O.; Dawar, A.; Shah, Z.; Khan, W.; Idrees, M.; Islam, S.; Khan, I. Entropy generation in MHD eyring–powell fluid flow over an unsteady oscillatory porous stretching surface under the impact of thermal radiation and heat source/sink. *Appl. Sci.* **2018**, *8*, 2588. [CrossRef]
62. Nasir, S.; Shah, Z.; Islam, S.; Khan, W.; Khan, S.N. Radiative flow of magneto hydrodynamics single-walled carbon nanotube over a convectively heated stretchable rotating disk with velocity slip effect. *Adv. Mech. Eng.* **2019**, *11*, 1–11. [CrossRef]
63. Khan, A.S.; Nie, Y.; Shah, Z.; Dawar, A.; Khan, W.; Islam, S. Three-dimensional nanofluid flow with heat and mass transfer analysis over a linear stretching surface with convective boundary conditions. *Appl. Sci.* **2018**, *8*, 2244. [CrossRef]

coatings

MDPI

Article

A Thin Film Flow of Nanofluid Comprising Carbon Nanotubes Influenced by Cattaneo-Christov Heat Flux and Entropy Generation

Dianchen Lu [1], Muhammad Ramzan [2,3,*], Mutaz Mohammad [4,*], Fares Howari [5] and Jae Dong Chung [3]

1 Department of Mathematics, Faculty of Science, Jiangsu University, Zhenjiang 212013, China; dclu@ujs.edu.cn
2 Department of Computer Science, Bahria University, 44000 Islamabad, Pakistan
3 Department of Mechanical Engineering, Sejong University, Seoul 143-747, Korea; jdchung@sejong.edu
4 Department of Mathematics and Statistics, College of Natural and Health Sciences, Zayed University, 144543 Abu Dhabi, UAE
5 College of Natural and Health Sciences, Zayed University, 144543 Abu Dhabi, UAE; fares.howari@zu.ac.ae
* Correspondence: mramzan@bahria.edu.pk (M.R.); mutaz.mohammad@zu.ac.ae (M.M.); Tel.: +92-30-05-122-700 (M.R.); +971-2-599-3496 (M.M.)

Received: 30 March 2019; Accepted: 24 April 2019; Published: 1 May 2019

Abstract: This study aims to scrutinize the thin film flow of a nanofluid comprising of carbon nanotubes (CNTs), single and multi-walled i.e., (SWCNTs and MWCNTs), with Cattaneo-Christov heat flux and entropy generation. The time-dependent flow is supported by thermal radiation, variable source/sink, and magneto hydrodynamics past a linearly stretched surface. The obtained system of equations is addressed by the numerical approach bvp4c of the MATLAB software. The presented results are validated by comparing them to an already conducted study and an excellent synchronization in both results is achieved. The repercussions of the arising parameters on the involved profiles are portrayed via graphical illustrations and numerically erected tables. It is seen that the axial velocity decreases as the value of film thickness parameter increases. It is further noticed that for both types of CNTs, the velocity and temperature distributions increase as the solid volume fraction escalates.

Keywords: thin liquid film flow; carbon nanotubes; Cattaneo-Christov heat flux; variable heat source/sink; entropy generation

1. Introduction

The flow and heat transfer phenomenon in thin fluid film past stretched surfaces has promising applications including continuous casting, extrusion of plastic sheets, drawing of polymer surfaces, foodstuff processing, annealing and tinning of copper wires, and cooling of metallic plates [1]. The maintenance of the extrudes' surface is vital in the extrusion process smooth surface with minimum friction and enough strength is necessary for the coating procedure. Additionally, all this highly rely on the flow and heat transfer properties of the thin film over stretched surfaces. Because of this, the analysis in such cases is quite essential. Wang's [2] pioneering work by deliberating the hydrodynamics of time-dependent thin fluid film flow past a stretching sheet invited researchers to work in this attractive industry-oriented theme. Andersson et al. [3] further developed Wang's idea for heat transfer analysis. This case is further presented in a more generalized form by Chung and Andersson [4]. The solution to the same problem is discussed analytically by Wang [5]. The thin film flow is later analyzed in various scenarios like magnetic impact [6,7], thermo-capillary impacts [8], and non-Newtonian fluids [9–12].

The above-mentioned studies on thin liquid films are limited to Newtonian and non-Newtonian fluids in the absence of nanofluids. In recent years, the subject of nanofluids, owing to their amazing characteristic of high thermal conductivity, has gained much attention of researchers and scientists. The seminal work by Choi and Eastman [13] introducing "nanofluids" has revolutionized the heat transfer processes. A nanofluid is an amalgamation of the solid metallic particles called "Nanoparticles" with a size of 1–100 nm and ordinary liquids. Nanofluids are the finest coolants with amazing applications including microelectronics, optical manufacturing and transportation [14]. There are studies that emphasize the thin film liquid flow of nanofluids. Lin et al. [15] numerically scrutinized the thin film Pseudo-plastic nano liquid flow with the impact of internal heat generation by utilizing R–K scheme and Newton's method. Later, Lin et al. [16] extended this study to the impacts of viscous dissipation and temperature reliant thermal conductivity. The nano-liquid thin film flow comprising graphene nanoparticles under the influence of aligned magnetic effect is discussed by Sandeep [17]. Zhang et al. [18] studied the Oldroyd-B nanofluid thin film flow analytically with two types of nanoparticles, i.e., silver and copper and found that nanofluid containing silver nanoparticles has a better thermal conductivity in comparison to the copper nanoparticles. Zhang et al. [19] also deliberated the power law nano liquid thin film flow with the slip using the differential transform method. The problem of nanofluid thin films flowing past an elastic stretched sheet is solved using the least square method (LSM) by Fakour et al. [20]. Ishaq et al. [21] deliberated the analytical solution of Powell-Eyring nano liquid thin film flow with thermal radiation past a permeable stretched surface. The flow of Darcy-Forchheimer nanofluid thin film comprising SWCNTs past an unsteady stretched surface is studied by Nasir et al. [22].

There are numerous applications of heat transfer in industrial and engineering processes. These include cooling towers, fuel cells, microelectronics, and nuclear reactors. The fundamental essence in all these processes is that the value of thermal conductivity is presumed to be a constant. However, this value varies with temperature and other factors. Pal [23] and Vajravelu et al. [24] observed that the thermal conductivity varies linearly as the temperature is altered from 0° to 400° F. Initially, the Fourier law of heat conduction has been used in the modeling of heat transfer applications but the system encounters an initial disturbance due to the "parabolic energy equation" which is referred to as "paradox in heat conduction". This shortcoming in the Fourier's model was addressed by Cattaneo [25] who introduced the thermal relaxation time in the Fourier law of heat conduction. Cattaneo's act helped to represent the temperature profile via the hyperbolic energy equation and heat transport propagation using thermal waves with a controlled speed. This heat transport mechanism is employed in diverse practical scenarios, ranging from nano-liquid flow models to skin burn injury models [26]. Moreover, several materials possess a large thermal relaxation time, such as biological tissues having a relaxation time of 91–100 s and sand of 21 s. To uphold the material invariant formulation, Christov altered the Maxwell-Cattaneo model by swapping the time derivative with Oldroyd's upper convected derivative. This improved version is nowadays being termed as the Cattaneo-Christov (C-C) heat flux model. Later, Han et al. [27] introduced an analytical solution for the viscoelastic material including the velocity slip boundary along with the C-C heat flux. Mustafa [28] analyzed the rotating flow of the Maxwell fluid with an upper convected derivative and C-C heat flux over a linearly stretched surface using both the analytical and numerical methods. A similar case was examined by Khan et al. [29] considering an exponentially stretched surface. The squeezed flow of the C-C heat flux with CNTs between two parallel disks is studied by Lu et al. [30]. Ramzan et al. [31] studied the flow of the Williamson fluid flow numerically with C-C heat flux associated with the convective boundary condition and homogeneous-heterogeneous reactions. The flow of the magnetohydrodynamics (MHD) second-grade fluid over a stretched cylinder with C-C heat flux is discussed by Alamri et al. [32]. Ramzan et al. [33,34] deliberated the Maxwell and third-grade fluid flows with homogeneous-heterogeneous reactions and C-C heat flux. The flow of aqueous based nanotubes with homogeneous-heterogeneous reactions past a Darcy-Forchheimer three-dimensional flow is studied by Alshomrani and Ullah [35]. Saleem et al. [36] discussed the

squeezing three-dimensional nanofluid flow comprising of nanotubes in a Darcy-Forchheimer medium with thermal radiation and heat generation/absorption. There are numerous explorations that discuss on the flow of nanofluid amalgamated with carbon nanotubes in various scenarios but there are fewer that address the thin film flow. Some more explorations focusing on carbon nanotube or nanofluid flow may be found in References [37–40] and many therein.

The literature review reveals that the flow of a thin film with the Newtonian/non-Newtonian fluids is scarce in the literature and this subject gets even narrower if we talk about the thin film flows of nanofluids. Very few explorations are available that discuss the thin film flows of nanofluid-comprising nanotubes. Keeping in mind the importance of hydrodynamic flows, the idea of nanoliquid thin films in comparatively new and fewer explorations are available in the literature (see Table 1). This presented model is solved numerically and will present an estimated solution. The other limitation of the flow is that it is discussed in 2D and can be extended to 3D with some more novel effects like homogeneous-heterogeneous reactions, etc. The model presented here is an amalgamation of C-C heat flux and entropy generation in the thin film flows of the nanofluids comprising of both types of nanotubes (SWCNTs/MWCNTs) and has not yet been discussed in the literature. The numerical solution of the problem is achieved. A comparison with an already established result in the limiting case is also given and an excellent agreement between both is found. This corroborates our presented results. The graphical illustrations and numerically calculated values of the physical parameters are also added to the problem.

Table 1. The studies on nanoliquid film flow.

Authors	Nanofluid Models	Film Thickness	Nanotubes SWCNTs/MWCNTs	C-C Heat Flux
Lin et al. [15]	Tiwari and Das	√	×	×
Sandeep [17]	Tiwari and Das	√	×	×
Nasir et al. [22]	Tiwari and Das	√	SWCNTs	×
Narayana and Sibanda [41]	Tiwari and Das	√	×	×
Xu et al. [42]	Tiwari and Das	√	×	×
Qasim et al. [43]	Buongiorno's	√	×	×
Present	Tiwari and Das	√	√	√

(√) means effect is present and (×) means effect is absent.

2. Mathematical Modeling

Let us assume a thin film flow of a nanoliquid flow comprising CNTs past a time dependent linearly stretched surface. The elastic sheet emerges from a slender slit at the Cartesian coordinate system's origin (Figure 1). The surface moves along the x-axis ($y = 0$) with a velocity $u_w(x,t) = \frac{bx}{(1-\alpha t)}$, with b and a being the constants in the y-direction and temperature $T_w(x, y)$. The stream function ξ is considered such that $u = \xi_y$, and $v = -\xi_x$.

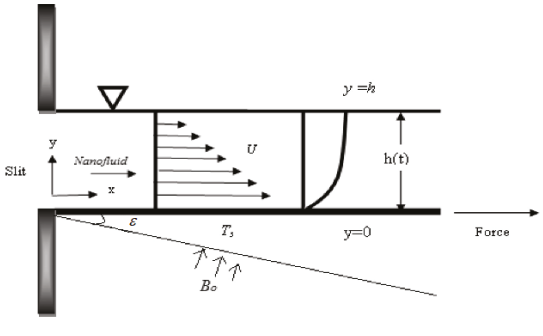

Figure 1. The flow geometry of the model.

The thin film is of width $h(x, y)$. The flow is laminar and incompressible. A magnetic field $B(x,t) = B_o(1-at)^{-\frac{1}{2}}$, is employed normal to the extended surface. The governing unsteady conservation equations [17] under the aforementioned assumptions are appended as follows:

$$\frac{\partial^2 \xi}{\partial x \partial y} - \frac{\partial^2 \xi}{\partial y \partial x} = 0 \tag{1}$$

$$\frac{\partial^2 \xi}{\partial t \partial y} - \frac{\partial \xi}{\partial y}\frac{\partial^2 \xi}{\partial x \partial y} - \frac{\partial \xi}{\partial x}\frac{\partial^2 \xi}{\partial y^2} = v_{nf}\frac{\partial^3 \xi}{\partial y^3} + \frac{\sigma_{nf}}{\rho_{nf}}B^2(t)\frac{\partial \xi}{\partial y}\cos^2 \varepsilon, \tag{2}$$

$$(\rho C_p)_{nf}\left(\frac{\partial T}{\partial t} + \frac{\partial \xi}{\partial y}\frac{\partial T}{\partial x} - \frac{\partial \xi}{\partial x}\frac{\partial T}{\partial y}\right) + \lambda_2 \Omega_2 = \left(k_{nf} + \frac{16 T_\infty{}^3 \sigma^*}{3k^*}\right)\frac{\partial^2 T}{\partial y^2} + q''' \tag{3}$$

With the following corresponding boundary conditions

$$\begin{array}{l} -\xi_x = 0,\ \xi_y = u_w,\ T = T_s, \quad \text{at} \quad y = 0, \\ \xi_{yy} = 0,\ -\xi_x = h_t,\ T = 0, \quad \text{as} \quad y = h(t). \end{array} \tag{4}$$

The Cattaneo-Christov term is defined as

$$\begin{array}{l} \Omega_2 = \frac{\partial^2 T}{\partial t^2} + \frac{\partial u}{\partial t}\frac{\partial T}{\partial x} + 2\frac{\partial \xi}{\partial y}\frac{\partial^2 T}{\partial t \partial x} - 2\frac{\partial \xi}{\partial x}\frac{\partial^2 T}{\partial t \partial y} + \frac{\partial v}{\partial t}\frac{\partial T}{\partial y} + \frac{\partial \xi}{\partial y}\frac{\partial^2 \xi}{\partial x \partial y}\frac{\partial T}{\partial x} + \frac{\partial \xi}{\partial x}\frac{\partial^2 \xi}{\partial y \partial x}\frac{\partial T}{\partial y} \\ + \left(\frac{\partial \xi}{\partial y}\right)^2\frac{\partial^2 T}{\partial x^2} + \left(\frac{\partial \xi}{\partial x}\right)^2\frac{\partial^2 T}{\partial y^2} - 2\frac{\partial \xi}{\partial y}\frac{\partial \xi}{\partial x}\frac{\partial^2 T}{\partial x \partial y} - \frac{\partial \xi}{\partial y}\frac{\partial^2 \xi}{\partial x^2}\frac{\partial T}{\partial y} - \frac{\partial \xi}{\partial x}\frac{\partial^2 \xi}{\partial y^2}\frac{\partial T}{\partial x} \end{array} \tag{5}$$

The heat source/sink "q'''" is represented by

$$q''' = \frac{k_f u_w (T_s - T_0)}{x \nu_f}\left(A^* f' + B^* \frac{(T - T_0)}{(T_s - T_0)}\right) \tag{6}$$

The thermophysical attributes (specific heat C_p, density ρ and thermal conductivity k) of the base fluid (H_2O) and carbon nanotubes (SWCNTs /MWCNTs) are appended in Table 2.

Table 2. The thermophysical physiognomies of the fluid and CNTs [30].

Physical Characteristics	Conventional Fluid	Nano Particles	
–	H_2O	SWCNTs	MWCNTs
C_p (J/kg K)	4179	425	796
ρ (kg/m^3)	997	2600	1600
k (W/mK)	0.613	6600	3000

The hypothetical relations are characterized as follows:

$$\mu_{nf} = \frac{\mu_f}{(1-\phi)^{2.5}},\ v_{nf} = \frac{\mu_{nf}}{\rho_{nf}}, \tag{7}$$

$$\rho_{nf} = (1-\phi)\rho_f + \phi\rho_{CNT},\ \alpha_{nf} = \frac{k_{nf}}{\rho_{nf}(c_p)_{nf}} \tag{8}$$

$$\frac{\sigma_{nf}}{\sigma_f} = 1 + \frac{3\sigma\phi - 3\phi}{\sigma + 2 - \sigma\phi + \phi}, \sigma = \frac{\sigma_{CNT}}{\sigma_f}, \tag{9}$$

$$\frac{k_{nf}}{k_f} = \frac{(1-\phi) + 2\phi\frac{k_{CNT}}{k_{CNT}-k_f}\ln(\frac{k_{CNT}+k_f}{2k_f})}{(1-\phi) + 2\phi\frac{k_f}{k_{CNT}-k_f}\ln(\frac{k_{CNT}+k_f}{2k_f})} \tag{10}$$

Using the similarity transformations

$$\begin{array}{l}\eta = \frac{1}{\beta}\left(\frac{b}{\nu_f(1-at)}\right)^{\frac{1}{2}} y,\ \Psi = \beta\left(\frac{b\nu_f}{(1-at)}\right)^{\frac{1}{2}} x f(\eta), \theta = \frac{T-T_0}{T_s-T_0} \\ T = T_0 - T_r\left(\frac{bx^2}{2\nu_f}\right)(1-at)^{-1.5}\theta(\eta),\end{array} \tag{11}$$

The requirement of Equation (1) is fulfilled undoubtedly and Equations (2) and (3) yield

$$f''' + (1-\phi)^{2.5}(1-\phi+\phi\frac{\rho_{CNT}}{\rho_f})\lambda\left\{ff'' - f'^2 - S\left(f' + \frac{1}{2}\eta f''\right)\right\} - (1-\phi)^{2.5}\frac{\sigma_{nf}}{\sigma_f}Mf'\cos^2\varepsilon = 0 \tag{12}$$

$$\begin{array}{l}\frac{\left(\frac{k_{nf}}{k_f}+\frac{4}{3}R\right)}{P_r\left[1-\phi+\phi\frac{(\rho C_p)_{CNT}}{(\rho C_p)_f}\right]}\theta'' - \lambda\left[2f'\theta - f\theta' + \frac{S}{2}(3\theta+\eta\theta')\right] + \frac{1}{P_r\left[1-\phi+\phi\frac{(\rho C_p)_{CNT}}{(\rho C_p)_f}\right]}(A^* f' + B^*\theta) \\ +\gamma\left\{\begin{array}{l} -\frac{15}{2}S^2\theta - \frac{7}{2}S^2\eta\theta' - \frac{1}{4}S^2\eta^2\theta'' - 8Sf'\theta - \eta Sf''\theta - \frac{3}{2}\eta Sf'\theta' \\ +\frac{9}{2}Sf\theta' + S\eta f\theta'' - 4f'^2\theta + 3ff'\theta' - f'^2\theta'' + 2ff''\theta \end{array}\right\} = 0,\end{array} \tag{13}$$

Additionally, the boundary conditions of Equation (4) become

$$f(0) = 0,\ f'(0) = 1,\ \theta(0) = 1,\ f(1) = \frac{S}{2},\ f''(1) = 0, \theta'(1) = 0 \tag{14}$$

The values of various non-dimensional parameters are defined as follows:

$$P_r = \frac{\upsilon_f}{\alpha_f}, S = \frac{\alpha}{b}, R = \frac{4\sigma^* {T_0}^3}{k^* k_f}, M = \frac{\sigma_f {B_0}^2}{b\rho_f}, \gamma = \frac{\lambda_2 b}{1-\alpha t}, \lambda = \beta^2 \tag{15}$$

Physical quantities like the Skin friction coefficient and the local Nusselt number are given as

$$\begin{array}{c} Nu_x = \frac{x q_w(x)}{k_f(T_s-T_0)}, C_f = \frac{\tau_w}{\rho_f {u_w}^2}, \\ q_w(x) = -k_{nf}\left(\frac{\partial T}{\partial y}\right)_{y=0}, \tau_w = \mu_{nf}\left(\frac{\partial u}{\partial y}\right)_{y=0},\end{array} \tag{16}$$

Additionally, in dimensionless form, as follows:

$$\begin{array}{c} {C_f Re_x}^{1/2} = \frac{1}{\beta(1-\phi)^{2.5}} f''(0), \\ Nu_x {Re_x}^{-1/2} = -\frac{1}{\beta}\left(\frac{k_{nf}}{k_f} + \frac{4}{3}R\right)\theta'(0)\end{array} \tag{17}$$

3. Entropy Generation

The entropy generation under the aforementioned assumptions is given as below:

$${E_{gen}}''' = \frac{k_f}{{T_0}^2}\left[\frac{k_{nf}}{k_f} + \frac{16{T_\infty}^3\sigma^*}{3k^* k_f}\right]\left(\frac{\partial T}{\partial y}\right)^2 + \frac{\mu_{nf}}{T_0}\left(\frac{\partial u}{\partial y}\right)^2 + \frac{\sigma_{nf}}{T_0}B^2(t)u^2\cos^2\varepsilon \tag{18}$$

where all terms defined in Equation (15) portray the usual meaning. The entropy generation N_G is defined as

$$N_G = \left(\frac{k_{nf}}{k_f} + \frac{4}{3}R\right){Re_x}\theta'^2 + \frac{1}{(1-\phi)^{2.5}}\frac{BrRe_x}{\alpha}f''^2 + \frac{BrM}{\alpha}\frac{\sigma_{nf}}{\sigma_f}\cos^2\varepsilon f'^{22} \tag{19}$$

where S_0''' and S_{gen}''' are the characteristic entropy generation rate and the entropy generation rate. The parameters defined in the above equation are given as

$$\alpha = \frac{\Delta T}{T_{w0}}, Br = \frac{\mu_f {u_w}^2}{k_f \Delta T}, Re_x = \frac{u_w x}{\nu_f} \tag{20}$$

4. Results and Discussion

This section is devoted to witnessing the impression of numerous parameters on the involved profiles whilst keeping in view their physical significance. The MATLAB built-in function bvp4c is utilized to address the differential Equations (9), (10), and (16) with the associated boundary conditions of Equation (11). To solve these, first we have converted the 2nd and 3rd order differential equations to the 1st order by introducing new parameters. The tolerance for the existing problem is fixed as 10^{-6}. The initial guess we yield must satisfy the boundary conditions asymptotically and the solution as well. The results show the influence of solid volume fraction (φ), dimensionless film thickness (λ), magnetic parameter (M), unsteadiness parameter (S), radiation parameter (R), thermal relaxation parameter (γ), and non-uniform heat source/sink parameter on the velocity, temperature and entropy generation profiles. Further, the numerical values for the Skin friction and Nusselt number are given in Tables 3 and 4 for different parameters. The numerical values of the parameters are fixed as $\varphi = 0.1$, $A^* = B^* = \lambda = \gamma = 0.5 = S$, $R = 1.0 = M$, and $P_r = 6.2$. Figures 2 and 3 display the impact of solid volume fraction (φ) on axial velocity and temperature distribution. For incremented values of the solid volume fraction (φ), the velocity and temperature profiles enhance in case of both SWCNTs and MWCNTs. Actually, the convective flow and the solid volume fraction are directly proportionate with each other and this is the main reason behind the enhancement of axial velocity and the temperature of the fluid.

Table 3. The comparison table of $-\theta'(0)$ with Sandeep [17] for varied estimates of S when $R = M = \gamma = 0$, $P_r = 1.0$.

S	$\varphi = 0$	
	Sandeep [17]	**Present Result**
1.0	2.6772221621	2.677222
1.2	1.9995914260	1.999591
1.4	1.4477543611	1.447754
1.6	0.9566978443	0.956697
1.8	0.4845366320	0.484536

Table 4. The numerical value of the Skin friction with $P_r = 6.2$.

φ	S	λ	M	$-C_f Re_x^{\frac{1}{2}}$	
–	–	–	–	SWCNTs	MWCNTs
0.1	0.1	0.1	1.0	0.53775	0.52995
0.2	–	–	–	0.57083	0.55402
0.3	–	–	–	0.60395	0.57701
–	0.1	–	–	0.53775	0.52995
–	0.2	–	–	0.54610	0.53761
–	0.3	–	–	0.55442	0.54524
–	–	0.1	–	0.53775	0.52995
–	–	0.2	–	0.62530	0.61054
–	–	0.3	–	0.70792	0.68693
–	–	–	0.0	0.12194	0.11183
–	–	–	0.5	0.34094	0.33214
–	–	–	1.0	0.53775	0.52995

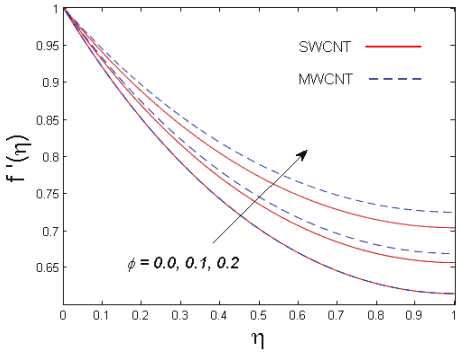

Figure 2. The illustration of φ versus $f'(\eta)$.

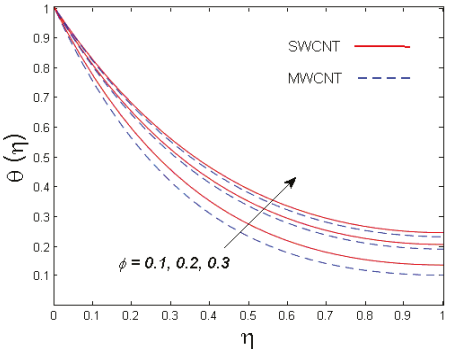

Figure 3. The illustration of φ versus θ(η).

Figures 4 and 5 depict the behavior of axial velocity and the temperature field for the growth estimates of the film thickness parameter λ. It is found that both velocity and temperature profiles diminish for increasing values of the film thickness parameter λ. In fact, the more the film thickness, the lesser the fluid motion. This is because of the fact that higher values of film thickness dominate the viscous forces, eventually diminishing the fluid velocity. Similar behavior is observed for the temperature field.

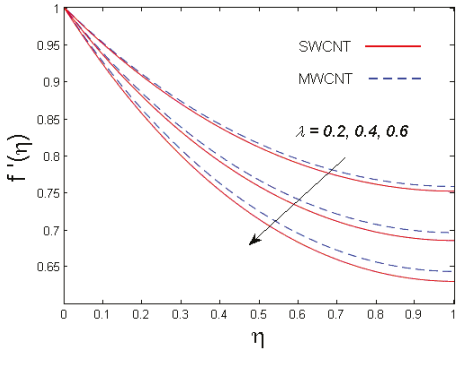

Figure 4. The illustration t of λ versus $f'(\eta)$.

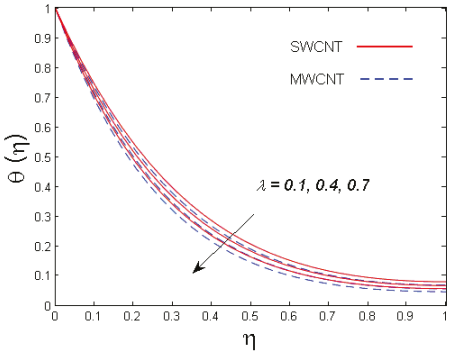

Figure 5. The illustration t of λ versus θ(η).

The effect of the magnetic parameter *M* on the velocity and temperature fields can be visualized in Figures 6 and 7. Figure 6 displays the impact of the magnetic parameter *M* on axial velocity. The is the axial velocity of the declining function of the magnetic parameter *M*. Physically, by enhancing the magnetic parameter *M*, the Lorentz force is strengthened in the flow, which has a tendency to resist the fluid's motion and slow it down. This force also creates heat energy in the flow. Consequently, the temperature distribution increases both the SWCNTs and MWCNTs, which is displayed in Figure 7.

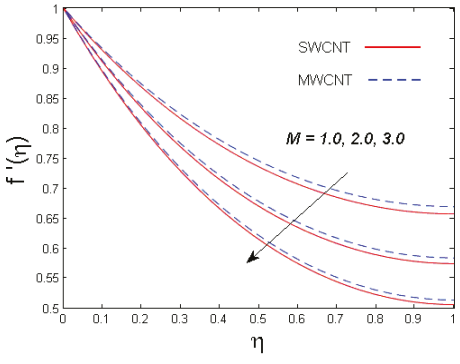

Figure 6. The illustration of *M* versus $f'(\eta)$.

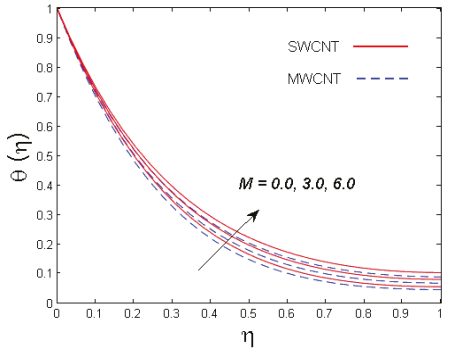

Figure 7. The illustration of *M* versus θ(η).

Figures 8 and 9 show the effect of the unsteadiness parameter *S* on the velocity and temperature distributions. It is found that with the increase of the unsteadiness parameter *S*, the axial velocity

diminishes. Physically, the bouncy effect acts on the flow and diminishes it due to the increase in the unsteadiness parameter S. Therefore, the thermal and momentum boundary layer thicknesses decrease.

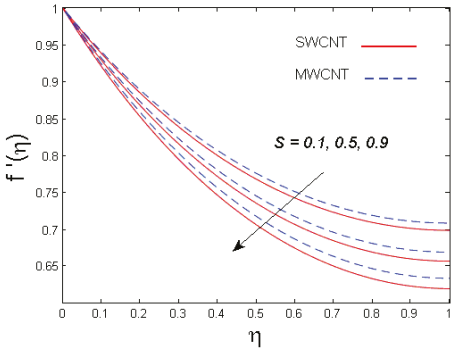

Figure 8. The illustration of S versus $f'(\eta)$.

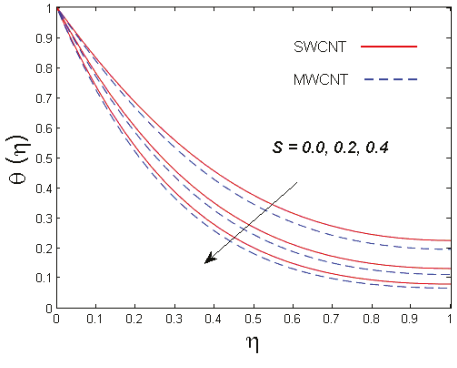

Figure 9. The illustration of S versus $\theta(\eta)$.

Figure 10 determines the consequence of the thermal relaxation parameter γ on the temperature of the fluid. It is concluded that the temperature diminishes for increased values of the thermal relaxation parameter γ. The temperature tends to be sharper near the boundary as the value of γ is higher than the points on the growth in the wall slope of the temperature profile.

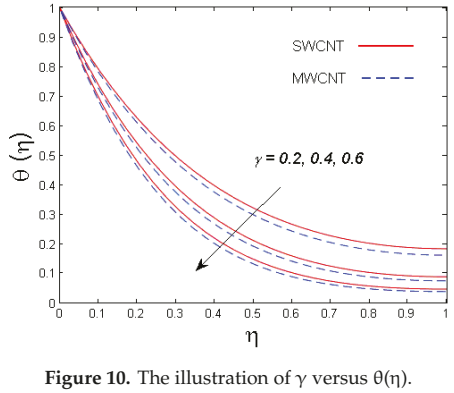

Figure 10. The illustration of γ versus $\theta(\eta)$.

Figure 11 demonstrates the impact of the radiation parameter R on the temperature profile. It is comprehended that the temperature field is an increasing function of the radiation parameter R. It is also concluded that the thermal boundary layer thickness for both carbon nanotubes is increased. In fact, larger estimates of the radiation parameter reduce the mean absorption coefficient and enhance the radiative heat flux's divergence. Due to this, the temperature of the fluid is upsurged.

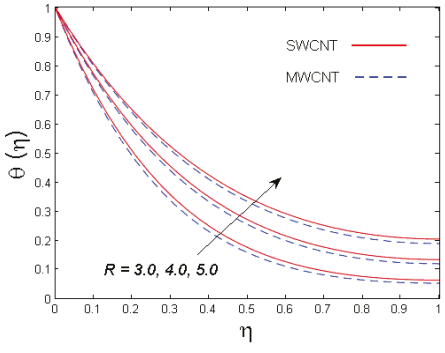

Figure 11. The illustration of R versus θ(η).

The influence of non-uniform heat source/sink parameters A^* and B^* on the temperature distribution is shown in Figures 12 and 13. It can be understood that the temperature profile augments the boosted estimates of non-uniform heat source/sink parameters.

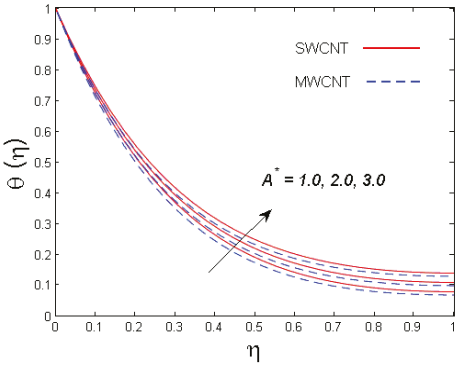

Figure 12. The illustration of A^* versus θ(η).

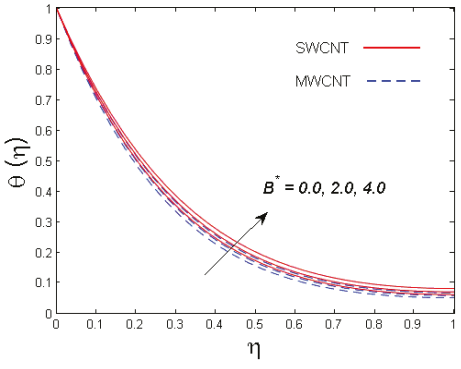

Figure 13. The illustration of B^* versus θ(η).

The effect of Brinkman number (B_r), magnetic parameter (M) and Reynolds number (Re_x) on the averaged entropy generation number is demonstrated in Figures 14–16. It is concluded that the entropy generation number increases for mounting estimations of Brinkman number (B_r), magnetic parameter (M) and Reynolds number (Re_x) for both SWCNT and MWCNT.

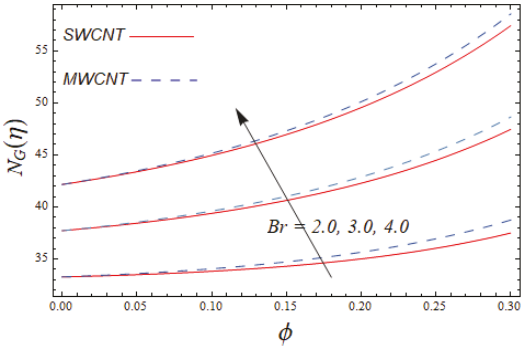

Figure 14. The illustration of B_r versus $N_G(\eta)$.

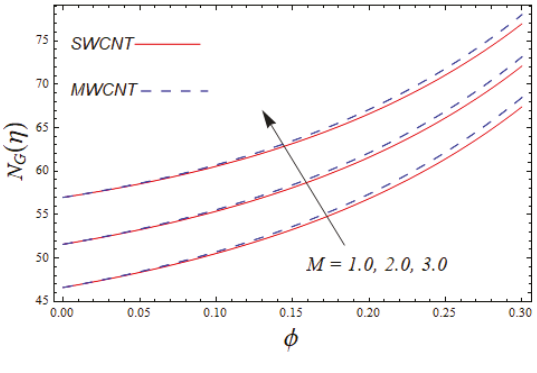

Figure 15. The illustration of M versus $N_G(\eta)$.

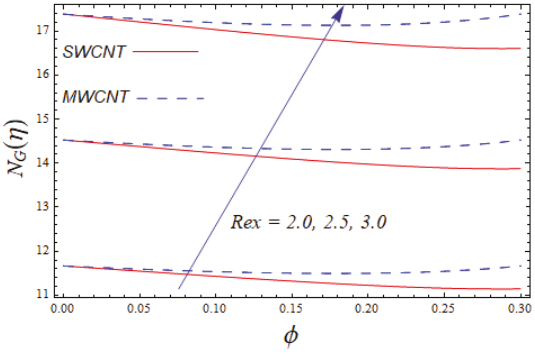

Figure 16. The illustration of Re_x versus $N_G(\eta)$.

Table 3 is erected to envision the precision of the presented model by comparing it with Sandeep [17] who discusses the flow of nanofluids past a thin film under the influence of the magnetic field. To make a comparison, we have neglected the impacts of the volume fraction, electrical conductivity, and thermal relaxation parameters. Excellent alignment is achieved between both results.

Table 4 shows the estimates of the Skin friction coefficient for different parameters. It is seen that the Skin friction coefficient increases for growing values of the magnetic parameter, solid volume fraction, unsteadiness parameter, and film thickness. Table 5 demonstrates the numerical values of Nusselt number for numerous parameters. It is determined that the Nusselt number increases with augmented values of the dimensionless film thickness, radiation parameter, solid volume fraction, and unsteadiness parameter, while it diminishes for growing values of non-uniform heat source/sink.

Table 5. The numerical value of the Nusselt number with $\gamma = 0.1$, $P_r = 6.2$.

Λ	R	φ	A^*	B^*	S	$Nu_x Re_x^{-\frac{1}{2}}$	
–	–	–	–	–	–	SWCNTs	MWCNTs
0.1	0.1	0.1	0.1	0.1	0.1	2.11090	2.06990
0.2	–	–	–	–	–	3.27730	3.16440
0.3	–	–	–	–	–	4.46510	4.24750
–	0.1	–	–	–	–	2.36350	2.06990
–	0.3	–	–	–	–	2.36770	2.07060
–	0.5	–	–	–	–	2.37230	2.07130
–	–	0.1	–	–	–	2.11090	2.06990
–	–	0.2	–	–	–	2.59370	2.54840
–	–	0.3	–	–	–	2.84440	2.84000
–	–	–	0.1	–	–	2.11800	2.06990
–	–	–	0.3	–	–	1.93540	1.89220
–	–	–	0.5	–	–	1.75270	1.71440
–	–	–	–	0.1	–	2.11800	2.06990
–	–	–	–	0.3	–	1.88910	1.85770
–	–	–	–	0.5	–	1.66430	1.25340
–	–	–	–	–	0.1	2.11090	2.06990
–	–	–	–	–	0.2	2.81360	2.72250
–	–	–	–	–	0.3	3.66060	3.48490

5. Conclusions

The thin film flow of nanofluid comprising of CNTs of both types (SWCNTs/MWCNTs) is studied whilst keeping in view the important applications of CNTs in many engineering applications. The flow is supported by the additional effects like C-C heat flux and entropy generation. The model is solved numerically with the support of the MATLAB software function bvp4c. The highlights of the existing study are

- Velocity and temperature distributions are mounting functions of the solid volume fraction for both types of CNTs in case of the thin film flow.
- For growing estimates of the thin film thickness parameter, the axial velocity diminishes.
- The velocity and temperature distributions show an opposite trend for the strong magnetic field in a thin film flow model.
- Larger estimates of heat source/sink parameter lead to an increase in the temperature of the fluid.
- The temperature of the fluid is decreased for higher values of the thermal relaxation parameter.
- With an increase in the estimates of film thickness, the magnetic parameter and the Skin friction coefficient show mounting behavior.
- The Nusselt number shows declining behavior for growing values of non-uniform heat source/sink.
- Entropy generation in the case of thin film flow is higher for larger estimates of the Brinkman number and the magnetic parameter.

Author Contributions: Data Curation, D.L.; Funding Acquisition, F.H.; Investigation, M.M.; Project Administration, M.R.; F.H.; Resources, D.L.; Software, M.M.; Supervision, M.M.; Validation, F.H.; Visualization, J.D.C.; Writing—Original Draft, J.D.C.

Funding: This research was funded by Zayed University research fund, Abu Dhabi, UAE.

Conflicts of Interest: The authors declare no conflict of interest.

Nomenclature

u, v	velocity components	B_0	magnetic field of strength
x, y	coordinate axis	P_r	Prandtl number
ξ	stream function	C_f	skin friction coefficient
B	magnetic field	Nu_x	Nusselt number
T_w	constant surface temperature	S	squeezing parameter
T	temperature	α	thermal diffusivity
Ω_2	Cattaneo-Christov parameter	Re_x	local reynolds number
q	heat source/sink	S_0	characteristic entropy generation
C_p	specific heat	S_{gen}	entropy generation rate
ρ	density	k_0	thermal conductivity near from the surface
λ_2	relaxation time of the heat flux	k_f	thermal conductivity of water
T_∞	ambient fluid temperature	ε	thermal conductivity parameter
u_w	stretching velocity along x-direction	N_G	entropy generation number
Greek Symbols			
ρ_{CNT}, ρ_f	density of nanofluid	f	dimensionless stream function
σ^*	Stephan-Boltzmann constant	θ	dimensionless temperature
μ_{nf}, μ_f	dynamic viscosity	γ	thermal relaxation parameter
k^*	viscoelastic parameter	λ	relaxation time of heat flux
α_{nf}	modified thermal diffusivity	σ_{nf}, σ_f	electrical conductivity of nanofluid and base fluid
$(\rho C_p)_{nf}$, $(\rho C_p)_f$	heat capacity	ν_{nf}, ν_f	kinematic viscosity of nanofluid
k, k_{nf}	thermal conductivity	ΔT	temperature difference
φ	solid volume fraction of nanofluid	τ_w	shear stress
η	a scaled boundary-layer coordinate	T_w	temperature on the interface
Ψ	stream function	B_r	brinkmann number
$q_w(x)$	the surface heat flux of nanoliquid film	M	hartmann number
β	thermal expansion coefficient	R	conduction radiation parameter
A^*, B^*	non-uniform heat source/sink parameters		

References

1. Aziz, R.C.; Hashim, I.; Alomari, A.K. Thin film flow and heat transfer on an unsteady stretching sheet with internal heating. *Meccanica* **2011**, *46*, 349–357. [CrossRef]
2. Wang, C.Y. Liquid film on an unsteady stretching surface. *Q. Appl. Math.* **1990**, *48*, 601–610. [CrossRef]
3. Andersson, H.I.; Aarseth, J.B.; Dandapat, B.S. Heat transfer in a liquid film on an unsteady stretching surface. *Int. J. Heat Mass Transf.* **2000**, *43*, 69–74. [CrossRef]

4. Liu, I.C.; Andersson, H.I. Heat transfer in a liquid film on an unsteady stretching sheet. *Int. J. Therm. Sci.* **2008**, *47*, 766–772. [CrossRef]
5. Wang, C. Analytic solutions for a liquid film on an unsteady stretching surface. *Heat Mass Transf.* **2006**, *42*, 759–766. [CrossRef]
6. Abel, M.S.; Mahesha, N.; Tawade, J. Heat transfer in a liquid film over an unsteady stretching surface with viscous dissipation in presence of external magnetic field. *Appl. Math. Model.* **2009**, *33*, 3430–3441. [CrossRef]
7. Noor, N.F.M.; Abdulaziz, O.; Hashim, I. MHD flow and heat transfer in a thin liquid film on an unsteady stretching sheet by the homotopy analysis method. *Int. J. Numer. Methods Fluids* **2010**, *63*, 357–373. [CrossRef]
8. Dandapat, B.S.; Santra, B.; Andersson, H.I. Thermocapillarity in a liquid film on an unsteady stretching surface. *Int. J. Heat Mass Transf.* **2003**, *46*, 3009–3015. [CrossRef]
9. Wang, C.; Pop, I. Analysis of the flow of a power-law fluid film on an unsteady stretching surface by means of homotopy analysis method. *J. Non-Newton. Fluid Mech.* **2006**, *138*, 161–172. [CrossRef]
10. Chen, C.H. Effect of viscous dissipation on heat transfer in a non-Newtonian liquid film over an unsteady stretching sheet. *J. Non-Newton. Fluid Mech.* **2006**, *135*, 128–135. [CrossRef]
11. Chen, C.H. Marangoni effects on forced convection of power-law liquids in a thin film over a stretching surface. *Phys. Lett. A* **2007**, *370*, 51–57. [CrossRef]
12. Abbas, Z.; Hayat, T.; Sajid, M.; Asghar, S. Unsteady flow of a second-grade fluid film over an unsteady stretching sheet. *Math. Comput. Model.* **2008**, *48*, 518–526. [CrossRef]
13. Choi, S.U.; Eastman, J.A. *Enhancing Thermal Conductivity of Fluids with Nanoparticles*; No. ANL/MSD/CP-84938; CONF-951135-29; Argonne National Lab.: DuPage County, IL, USA, 1995.
14. Sheikholeslami, M.; Ganji, D.D. Nanofluid flow and heat transfer between parallel plates considering Brownian motion using DTM. *Comput. Methods Appl. Mech. Eng.* **2015**, *283*, 651–663. [CrossRef]
15. Lin, Y.; Zheng, L.; Zhang, X.; Ma, L.; Chen, G. MHD pseudo-plastic nanofluid unsteady flow and heat transfer in a finite thin film over stretching surface with internal heat generation. *Int. J. Heat Mass Transf.* **2015**, *84*, 903–911. [CrossRef]
16. Lin, Y.; Zheng, L.; Chen, G. Unsteady flow and heat transfer of pseudo-plastic nanoliquid in a finite thin film on a stretching surface with variable thermal conductivity and viscous dissipation. *Powder Technol.* **2015**, *274*, 324–332. [CrossRef]
17. Sandeep, N. Effect of aligned magnetic field on liquid thin film flow of magnetic-nanofluids embedded with graphene nanoparticles. *Adv. Powder Technol.* **2017**, *28*, 865–875. [CrossRef]
18. Zhang, Y.; Zhang, M.; Bai, Y. Flow and heat transfer of an Oldroyd-B nanofluid thin film over an unsteady stretching sheet. *J. Mol. Liq.* **2016**, *220*, 665–670. [CrossRef]
19. Zhang, Y.; Zhang, M.; Bai, Y. Unsteady flow and heat transfer of power-law nanofluid thin film over a stretching sheet with variable magnetic field and power-law velocity slip effect. *J. Taiwan Inst. Chem. Eng.* **2017**, *70*, 104–110. [CrossRef]
20. Fakour, M.; Rahbari, A.; Khodabandeh, E.; Ganji, D.D. Nanofluid thin film flow and heat transfer over an unsteady stretching elastic sheet by LSM. *J. Mech. Sci. Technol.* **2018**, *32*, 177–183. [CrossRef]
21. Ishaq, M.; Ali, G.; Shah, Z.; Islam, S.; Muhammad, S. Entropy generation on nanofluid thin film flow of Eyring–Powell fluid with thermal radiation and MHD effect on an unsteady porous stretching sheet. *Entropy* **2018**, *20*, 412. [CrossRef]
22. Nasir, S.; Shah, Z.; Islam, S.; Bonyah, E.; Gul, T. Darcy Forchheimer nanofluid thin film flow of SWCNTs and heat transfer analysis over an unsteady stretching sheet. *AIP Adv.* **2019**, *9*, 015223. [CrossRef]
23. Pal, D.; Chatterjee, S. Soret and Dufour effects on MHD convective heat and mass transfer of a power-law fluid over an inclined plate with variable thermal conductivity in a porous medium. *Appl. Math. Comput.* **2013**, *219*, 7556–7574. [CrossRef]
24. Vajravelu, K.; Prasad, K.V.; Ng, C.O. Unsteady convective boundary layer flow of a viscous fluid at a vertical surface with variable fluid properties. *Nonlinear Anal. Real World Appl.* **2013**, *14*, 455–464. [CrossRef]
25. Cattaneo, C. Sulla conduzione del calore. *Atti Sem. Mat. Fis. Univ. Modena* **1948**, *3*, 83–101.
26. Tibullo, V.; Zampoli, V. A uniqueness result for the Cattaneo-Christov heat conduction model applied to incompressible fluids. *Mech. Res. Commun.* **2011**, *38*, 77–79. [CrossRef]
27. Han, S.; Zheng, L.; Li, C.; Zhang, X. Coupled flow and heat transfer in viscoelastic fluid with Cattaneo-Christov heat flux model. *Appl. Math. Lett.* **2014**, *38*, 87–93. [CrossRef]

28. Mustafa, M. Cattaneo-Christov heat flux model for rotating flow and heat transfer of upper-convected Maxwell fluid. *AIP Adv.* **2015**, *5*, 047109. [CrossRef]
29. Khan, J.A.; Mustafa, M.; Hayat, T.; Alsaedi, A. Numerical study of Cattaneo-Christov heat flux model for viscoelastic flow due to an exponentially stretching surface. *PLoS ONE* **2015**, *10*, e0137363.
30. Lu, D.; Li, Z.; Ramzan, M.; Shafee, A.; Chung, J.D. Unsteady squeezing carbon nanotubes based nano-liquid flow with Cattaneo-Christov heat flux and homogeneous–heterogeneous reactions. *Appl. Nanosci.* **2019**, *9*, 169–178. [CrossRef]
31. Ramzan, M.; Bilal, M.; Chung, J.D. MHD stagnation point Cattaneo-Christov heat flux in Williamson fluid flow with homogeneous–heterogeneous reactions and convective boundary condition—A numerical approach. *J. Mol. Liq.* **2017**, *225*, 856–862. [CrossRef]
32. Alamri, S.Z.; Khan, A.A.; Azeez, M.; Ellahi, R. Effects of mass transfer on MHD second grade fluid towards stretching cylinder: A novel perspective of Cattaneo-Christov heat flux model. *Phys. Lett. A* **2019**, *383*, 276–281. [CrossRef]
33. Ramzan, M.; Bilal, M.; Chung, J.D. Influence of homogeneous-heterogeneous reactions on MHD 3D Maxwell fluid flow with Cattaneo-Christov heat flux and convective boundary condition. *J. Mol. Liq.* **2017**, *230*, 415–422. [CrossRef]
34. Ramzan, M.; Bilal, M.; Chung, J.D. Effects of MHD homogeneous-heterogeneous reactions on third grade fluid flow with Cattaneo-Christov heat flux. *J. Mol. Liq.* **2016**, *223*, 1284–1290. [CrossRef]
35. Alshomrani, A.S.; Ullah, M.Z. Effects of homogeneous–heterogeneous reactions and convective condition in Darcy–Forchheimer flow of carbon nanotubes. *J. Heat Transf.* **2019**, *141*, 012405. [CrossRef]
36. Nasir, S.; Shah, Z.; Islam, S.; Khan, W.; Bonyah, E.; Ayaz, M.; Khan, A. Three dimensional Darcy-Forchheimer radiated flow of single and multiwall carbon nanotubes over a rotating stretchable disk with convective heat generation and absorption. *AIP Adv.* **2019**, *9*, 035031. [CrossRef]
37. Shah, Z.; Tassaddiq, A.; Islam, S.; Alklaibi, A.M.; Khan, I. Cattaneo-Christov heat flux model for three-dimensional rotating flow of SWCNT and MWCNT nanofluid with Darcy–Forchheimer porous medium induced by a linearly stretchable surface. *Symmetry* **2019**, *11*, 331. [CrossRef]
38. Gul, T.; Khan, M.A.; Noman, W.; Khan, I.; Abdullah Alkanhal, T.; Tlili, I. Fractional order forced convection carbon nanotube nanofluid flow passing over a thin needle. *Symmetry* **2019**, *11*, 312. [CrossRef]
39. Khan, A.S.; Nie, Y.; Shah, Z. Impact of thermal radiation and heat source/sink on MHD time-dependent thin-film flow of Oldroyed-B, Maxwell, and Jeffry fluids over a stretching surface. *Processes* **2019**, *7*, 191. [CrossRef]
40. Jinkins, K.R.; Chan, J.; Jacobberger, R.M.; Berson, A.; Arnold, M.S. Substrate-wide confined shear alignment of carbon nanotubes for thin film transistors. *Adv. Electron. Mater.* **2019**, *5*, 1800593. [CrossRef]
41. Narayana, M.; Sibanda, P. Laminar flow of a nanoliquid film over an unsteady stretching sheet. *Int. J. Heat Mass Transf.* **2012**, *55*, 7552–7560. [CrossRef]
42. Xu, H.; Pop, I.; You, X.C. Flow and heat transfer in a nano-liquid film over an unsteady stretching surface. *Int. J. Heat Mass Transf.* **2013**, *60*, 646–652. [CrossRef]
43. Qasim, M.; Khan, Z.H.; Lopez, R.J.; Khan, W.A. Heat and mass transfer in nanofluid thin film over an unsteady stretching sheet using Buongiorno's model. *Eur. Phys. J. Plus* **2016**, *131*, 16. [CrossRef]

coatings

MDPI

Article

Thermally Charged MHD Bi-Phase Flow Coatings with Non-Newtonian Nanofluid and Hafnium Particles along Slippery Walls

Rahmat Ellahi [1,2,*], Ahmed Zeeshan [2], Farooq Hussain [2,3] and Tehseen Abbas [4]

1 Center for Modeling & Computer Simulation, Research Institute, King Fahd University of Petroleum & Minerals, Dhahran 31261, Saudi Arabia
2 Department of Mathematics & Statistics, Faculty of Basic and Applied Sciences (FBAS), International Islamic University (IIUI), Islamabad 44000, Pakistan; ahmad.zeeshan@iiu.edu.pk (A.Z.); farooq.hussain@buitms.edu.pk (F.H.)
3 Department of Mathematics, Faculty of Arts and Basic Sciences (FABS), Balochistan University of Information Technology, Engineering, and Management Sciences (BUITEMS), Quetta 87300, Pakistan
4 Department of Mathematics, University of Education Lahore, Faisalabad Campus, Faisalabad 38000, Pakistan; tehseen.abbas@ue.edu.pk
* Correspondence: rellahi@alumni.ucr.edu

Received: 19 March 2019; Accepted: 29 April 2019; Published: 2 May 2019

Abstract: The present study is about the pressure-driven heated bi-phase flow in two slippery walls. The non-Newtonian couple stress fluid is suspended with spherically homogenous metallic particles. The magnetic susceptibility of Hafnium allures is taken into account. The rough surface of the wall is tackled by lubrication effects. The nonlinear coupled partial differential equations along with the associated boundary conditions are first reduced into a set of ordinary differential equations by using appropriate transformations and then numerical results were obtained by engaging the blend of Runge–Kutta and shooting techniques. The sway of physical quantities are examined graphically. An excellent agreement within graphical illustration and numerical results is achieved.

Keywords: heated bi-phase flow; couple stress fluid; lubrication effects; slippery walls; magnetohydrodynamics

1. Introduction

The most common fundamental type of flow through a channel is known as "Poiseuille flow." The Poiseuille flow has gained notable attention of various researchers due to its significant industrial applications. As an example, Siddiqui et al. [1] studied the plane Poiseuille flow with heat transfer. Alamri et al. [2] examined the plane Poiseuille flow with simultaneous effects of heat, magnetohydrodynamics (MHD) and second-order slip. They reported that the Stefan blowing prominently influenced on velocity and temperature distributions. Babic [3] has numerically investigated unsteady granular flows, namely transient Couette flow and cyclic Couette flow. In the first case velocity of the wall varies from one constant to another while in the second case the velocity is a harmonic function of time.

Moreover, non-Newtonian fluids have tremendous applications in the textile industry. Among the different models of non-Newtonian fluids, couple stress fluid has only lubricant viscosity. Consequently, in the absence of microstructure, couple stress in fluid arises which creates rotation without translation. Devakar et al. [4] investigated the couple stress fluid for three different cases. Ilani et al. [5] presented the unsteady nature of couple stress fluid between two parallel plates. Srinivasacharya et al. [6] discussed the laminar flow of couple stress fluid by means of quasi-linearization technique. Murthy and Nagaraju [7] conducted a study of couple stresses on the surface of a cylinder. The rotation of the

container generates the flow employing super adherence condition. All reported studies on couple stress eventually concluded that velocity always slows down in the fluid due to couple stresses by all means. Significant contributions on couple stress fluid can be seen in [8–10].

Furthermore, it is a well-known fact that most of the chemical and mechanical processes are of multiphase types. Consequently, several investigations have been performed up until now. In near past, different physical aspects of bi-phase flows were investigated by numerous researchers, such as Wu et al. [11], who discussed granular flow between opposite inclined plates for second-grade fluid containing spherical particles. Bognar et al. [12] offered flow analysis of non-Newtonian fluid on an oblique plane with material properties. Latz and Schmidt [13] presented numerical solutions for fast-moving and very slow-moving granular flows. Latz and Schmidt [14] provided numerical solutions for fast-moving and very slow-moving granular flows. The constitutive relations at small and intermediate densities were equivalent to those derived from the kinetic theory of granular flow which nevertheless recovers many aspects of dense granular flow. Two-phase fluids are inspected by Armanini [15]. The article provides full detail as to how granular fluid mechanics work. Interaction of solid–fluid for particulate flow with heat transfer is analyzed by Dan et al. [15]. Distributed Lagrange multipliers are used to obtain the expressions for velocity and temperature fields. The Boussinesq approximation is used for temperature and flow fields. The positioning of the particle is tracked by using the discrete element method.

In addition, the performance of lubricated coatings with magnetic, nanoparticles, heat transfer, and slip is very much ubiquitous in daily life. For instance, dish washing, replacement of lubricated cardiac valves, and industrial dye, as well as blood pressure control of a patient, are some common examples of slip and magnetization combination. Wang et al. [16] reported the effects of CeO_2 nanoparticles on laser cladding of Ti-based ceramic coatings. Wang et al. [17] studied nanostructure with heating treatment on thin carbon films. Ellahi et al. [18] conducted a comparative study on shiny film coating on multi-fluid flows suspended with nano-sized particles. Khan et al. [19] have used double-layer optical fiber using Phan-Thien-Tanner fluid as a coating material. Lu et al. [20] inspected nonlinear thermal radiation and entropy optimization coatings with hybrid nanoliquid flow. Riaz et al. [21] proposed a model on mass transport peristaltic flow coated with Synovial fluid. Khan [22] has analyzed the effects of slip on MHD flow of a nanofluid in a vertical channel. Bhatti et al. [23] have investigated nanofluid influenced by externally applied magnetic fields. A new slip model is proposed by Zhu and Ye [24]. They used modeling approaches for submicrometer gas-phase heat conduction over a broad pressure range. Zhang et al. [25] rectified the classical second-order boundary condition for the fundamental flows. A list of core investigations on coatings [26,27], MHD [28,29], and nanoparticles [30–37] related to proposed is given for readers to get detail understating.

Unlike all the cited literature, this article addresses a biphasic flow that has yet not been reported. Much has been done with couple stress fluid; suspension of nanoparticles, slip, and magnetic fields, but the current innovative idea, which reflects the mechanism of industrial and geophysical multiphase flows is missed. Theory of couple stress fluid which is based upon the polarity of fluid entices to incorporate metallic particles that display high magnetic susceptibility. Therefore, no choice is left other than the suspension of Hafnium particles that fit the best. An additional contribution of lubrication and heating wall distinguish the present work by changing the morpho-hydrodynamics of bi-phase flow, which is, so far, a new and different prospect in the relevant field.

2. Mathematical Analysis

The particulate couple stress fluid containing Hafnium particles of spherical shape between two flat plates apart from each other at distance h is considered. Flow is generated by the constant pressure gradient, as shown in Figure 1.

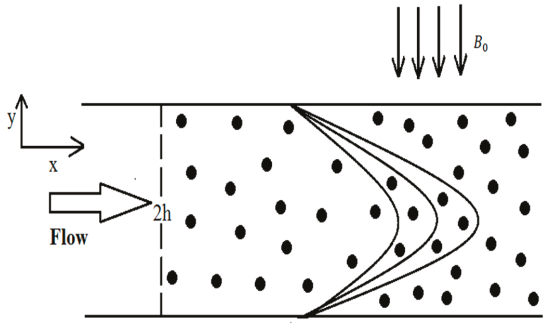

Figure 1. Particulate flow through slippery plates.

2.1. Governing Equations

The governing equations, such as continuity, momentum, and energy describing the particulate flow of couple stress, are given as:

- Conservation of mass

$$\overrightarrow{\nabla V} = 0 \tag{1}$$

- Conservation of momentum

$$\rho \frac{\overrightarrow{dV}}{dt} = \nabla T + \frac{CS}{(1-C)}\left(\overrightarrow{V}_p - \overrightarrow{V}_f\right) + \frac{\rho \overrightarrow{f}}{(1-C)} \tag{2}$$

where T denotes the Cauchy stress tensor and is defined by

$$T = -pI + s \tag{3}$$

where I is a unit tensor and s is an extra stress tensor. This can be obtained by the product of Rivlin–Ericksen tensor and coefficient of dynamic viscosity as follows:

$$s = \mu_s A_1 \tag{4}$$

$$A_1 = L + L^t \tag{5}$$

- Conservation of energy

$$\rho_f\left(C_p\right)\frac{d\Theta}{dt} = k\,\nabla^2 V + TL \tag{6}$$

The steady and laminar velocities flows in each phase is given by:

$$\overrightarrow{V}_f = \left[u_f(x,y)\ \ 0\ \ 0\right] \tag{7}$$

$$\overrightarrow{V}_p = \left[u_p(x,y)\ \ 0\ \ 0\right] \tag{8}$$

The flow is under the simultaneous influences of transversely applied magnetic fields. Moreover, the plates transmit the heat into the system being thermally charged by an external source; consequently, temperature factor can be written as:

$$\Theta = [\Theta(y)\ \ 0\ \ 0] \tag{9}$$

In view of Equations (7)–(9), the above governing equations (Equations (1)–(6)) take the following components forms:

$$0 = -\frac{\partial p}{\partial x} + \mu_s\left(\frac{\partial^2 u_f}{\partial y^2}\right) - \eta_1\left(\frac{\partial^4 u_f}{\partial y^4}\right) + \frac{CS}{(1-C)}\left(u_p - u_f\right) - \frac{\sigma B_0^2}{(1-C)}u_f \tag{10}$$

$$u_p = u_f - \frac{1}{S}\left(\frac{\partial p}{\partial x}\right) \tag{11}$$

$$0 = \frac{\partial^2 \Theta}{\partial y^2} + \frac{\mu_s}{k}\left(\frac{\partial u_f}{\partial y}\right)^2 - \frac{\eta_1}{k}\left(\frac{\partial u_f}{\partial y}\right)\left(\frac{\partial^3 u_f}{\partial y^3}\right) \tag{12}$$

2.2. Boundary Conditions

The set of boundary conditions that describe the interaction of lubricated walls with the bi-phase flow are:

- Boundary conditions at lower wall

$$u_f(y) = \beta\left\{\frac{\partial u_f}{\partial y} - \frac{\eta_1}{\mu_s}\left(\frac{\partial^3 u_f}{\partial y^3}\right)\right\},\ when\ y = -h \tag{13}$$

$$u''_f(y) = 0,\ when\ y = -h \tag{14}$$

$$\Theta(y) = \Theta_0,\ when\ y = -h \tag{15}$$

- Boundary conditions at upper wall

$$u_f(y) = -\beta\left\{\frac{\partial u_f}{\partial y} - \frac{\eta_1}{\mu_s}\left(\frac{\partial^3 u_f}{\partial y^3}\right)\right\},\ when\ y = h \tag{16}$$

$$u''_f(y) = 0,\ when\ y = h \tag{17}$$

$$\Theta(y) = \Theta_l,\ when\ y = h \tag{18}$$

By using the dimensionless quantities:

$$\begin{array}{l} u_f = Uu_f;\ u_p = Uu_p;\quad y = hy\ ;\ x = hx;\ p = \frac{\mu_s U}{h}\,p;\ B_r = \frac{U^2\mu_s}{k(\Theta_l - \Theta_0)};\\ \gamma^2 = \frac{h^2\mu_s}{\eta_1};\ M^2 = \frac{\sigma B_0^2\, h^2}{\mu_s};\ \beta_1 = \frac{\beta}{h};\quad m = \frac{\mu_s}{h^2 S};\quad \Theta(\Theta_l - \Theta_0) = \Theta - \Theta_0 \end{array} \tag{19}$$

Equations (10)–(12), after dropping the bars, can be obtained as:

$$\frac{1}{\gamma^2}\frac{\partial^4 u_f}{\partial y^4} - \frac{\partial^2 u_f}{\partial y^2} - \frac{C}{m(1-C)}\left(u_p - u_f\right) + \frac{M^2}{(1-C)}u_f + \frac{\partial p}{\partial x} = 0 \tag{20}$$

$$\frac{\partial^2 \Theta}{\partial y^2} = \frac{B_r}{\gamma^2}\left(\frac{\partial u_f}{\partial y}\right)\left(\frac{\partial^3 u_f}{\partial y^3}\right) - B_r\left(\frac{\partial u_f}{\partial y}\right)^2 \tag{21}$$

where

$$u_p = u_f - m\left(\frac{\partial p}{\partial x}\right) \tag{22}$$

As the original source of magnetized and heated bi-phase is on slippery walls and constant pressure gradient. Therefore, by taking of dp/dx = P, Equations (20) and (21) can be obtained as:

$$\frac{d^4u_f}{dy^4} - \gamma^2\frac{d^2u_f}{dy^2} + \frac{\gamma^2M^2}{(1-C)}u_f + \frac{\gamma^2}{(1-C)}P = 0 \tag{23}$$

$$\frac{d^2\Theta}{dy^2} + B_r\left(\frac{du_f}{dy}\right)^2 - \frac{B_r}{\gamma^2}\left(\frac{du_f}{dy}\right)\left(\frac{d^3u_f}{dy^3}\right) = 0 \tag{24}$$

Similarly, in view of Equation (19), the corresponding boundary conditions given in Equations (13)–(18) in the dimensionless form are:

$$u_f(y) = \beta_1\left\{\frac{du_f}{dy} - \frac{1}{\gamma^2}\left(\frac{d^3u_f}{dy^3}\right)\right\},\ when\ y = -1 \tag{25}$$

$$u''_f(y) = 0,\ when\ y = -1 \tag{26}$$

$$\Theta(y) = 0,\ when\ y = -1 \tag{27}$$

$$u_f(y) = -\beta_1\left\{\frac{du_f}{dy} - \frac{1}{\gamma^2}\left(\frac{d^3u_f}{dy^3}\right)\right\},\ when\ y = 1 \tag{28}$$

$$u''_f(y) = 0,\ when\ y = 1 \tag{29}$$

$$\Theta(y) = 1,\ when\ y = 1 \tag{30}$$

3. Numerical Results and Discussion

3.1. Procedure

This section is devoted to obtaining the numerical solutions of resulting Equations (23) and (24) by means of the Runge–Kutta method with a shooting technique [38] using MATLAB software. This technique is preferred for two following reasons; firstly, the thermal energy equation is nonlinearly coupled and, secondly, due to missing of condition. For missing condition, first of all, we are supposed to convert the given system of differential equations into first-order initial value problems in order to carry out systematic guessing of missing initial conditions which will continue until the desired accuracy and convergence are not achieved. The following equations explain in detail the numerical process, which is the prerequisite for the adopted numerical technique.

$$u_f = g_1 \tag{31}$$

in which of u_f is the velocity of the fluid phase. As it is an iterative scheme, in which each step has a possible error that can be successively reduced by changing higher order derivatives of u_f, in terms of first-order ordinary differential equations as follows:

$$\frac{du_f}{dy} = g'_1 = g_2 \tag{32}$$

$$\frac{d^2u_f}{dy^2} = g'_2 = g_3 \tag{33}$$

$$\frac{d^3u_f}{dy^3} = g'_3 = g_4 \tag{34}$$

where prime denoted the differentiation with respect to y. In view of Equations (31)–(34) the transformed form of Equation (23) is obtained as:

$$g_4' = \gamma^2 g_3 - \left(\frac{\gamma^2 M^2}{1-C}\right) g_1 - \left(\frac{\gamma^2}{1-C}\right) P \tag{35}$$

Similar to the preceding pattern, one finds no absurdness to convert thermal differential Equation (24) into first-order system by making the following suppositions:

$$\Theta = g_5 \tag{36}$$

$$\frac{d\Theta}{dy} = g_5' = g_6 \tag{37}$$

By using Equations (36) and (37) in Equation (24), we have:

$$g_6' = \frac{B_r}{m}(g_2)(g_4) - B_r (g_2)^2 \tag{38}$$

In view of Equations (35) and (38), the associated boundary conditions given in Equations (25)–(30) at the lower and upper plate can be obtained as:

$$\left.\begin{array}{l} (i)\ g_1 = \beta_1\left(g_2 - \frac{g_4}{\gamma^2}\right) \\ (ii)\ g_2 = c_1 \\ (iii)\ g_3 = 0 \\ (iv)\ g_4 = c_2 \\ (v)\ g_5 = 0 \\ (vi)\ g_6 = c_3 \end{array}\right\}, when\ y = -1 \tag{39}$$

In the same way given and missing conditions at the upper wall are:

$$\left.\begin{array}{l} (i)\ g_1 = -\beta_1\left(g_2 - \frac{g_4}{\gamma^2}\right) \\ (ii)\ g_2 = c_4 \\ (iii)\ g_3 = 0 \\ (iv)\ g_4 = c_5 \\ (v)\ g_5 = 1 \\ (vi)\ g_6 = c_6 \end{array}\right\}, when\ y = 1 \tag{40}$$

where $c_1, c_2, c_3, c_4, c_5,$ and c_6 are the missing conditions which can be easily determined during the routine calculation.

3.2. Validation

The numerical results for both phases are presented in Tables 1–3. Table 1 offers the variation of velocity for both phases against the slip parameter. Table 2 shows the simultaneous variations in the velocities for single- and two-phase flows at different points. Table 3 displays the thermal variation at different points within the given domain when M = 0.5, γ = 2.0, and B_r = 2.0. It is found that the results extracted numerically are compatible with the physical expectations and satisfy all the subjected conditions as shown graphically. This provides a useful check that the presented solutions are correct.

Table 1. Variation in the velocity of both phases against slip parameter.

y	$u_p(\beta_1=0.0)$	$u_p(\beta_1=0.015)$	$u_f(\beta_1=0.0)$	$u_f(\beta_1=0.015)$
−1.0	1.0000	1.0178	0	0.0178
−0.9	1.0572	1.0748	0.0572	0.0748
−0.8	1.1124	1.1297	0.1124	0.1297
−0.7	1.1638	1.1808	0.1638	0.1808
−0.6	1.2102	1.2271	0.2102	0.2271
−0.5	1.2508	1.2674	0.2508	0.2674
−0.4	1.2847	1.3012	0.2847	0.3012
−0.3	1.3116	1.3279	0.3116	0.3279
−0.2	1.3310	1.3473	0.3310	0.3473
−0.1	1.3427	1.3589	0.3427	0.3589
0.0	1.3466	1.3629	0.3466	0.3629
0.1	1.3427	1.3589	0.3427	0.3589
0.2	1.3310	1.3473	0.3310	0.3473
0.3	1.3116	1.3279	0.3116	0.3279
0.4	1.2847	1.3012	0.2847	0.3012
0.5	1.2508	1.2674	0.2508	0.2674
0.6	1.2102	1.2271	0.2102	0.2271
0.7	1.1638	1.1808	0.1638	0.1808
0.8	1.1124	1.1297	0.1124	0.1297
0.9	1.0572	1.0748	0.0572	0.0748
1.0	1.0000	1.0178	0	0.0178

Table 2. Variation in the velocities for single- and two-phase flows at different points.

y	$u_p(C=0.0)$	$u_p(C=0.5)$	$u_f\ (C=0.0)$	$u_f(C=0.5)$
−1.0	1.0142	1.0191	0.0142	0.0191
−0.9	1.0626	1.0788	0.0626	0.0788
−0.8	1.1093	1.1363	0.1093	0.1363
−0.7	1.1531	1.1897	0.1531	0.1897
−0.6	1.1928	1.2379	0.1928	0.2379
−0.5	1.2277	1.2799	0.2277	0.2799
−0.4	1.2570	1.3149	0.2570	0.3149
−0.3	1.2803	1.3426	0.2803	0.3426
−0.2	1.2972	1.3626	0.2972	0.3626
−0.1	1.3074	1.3747	0.3074	0.3747
0.0	1.3108	1.3788	0.3108	0.3788
0.1	1.3074	1.3747	0.3074	0.3747
0.2	1.2972	1.3626	0.2972	0.3626
0.3	1.2803	1.3426	0.2803	0.3426
0.4	1.2570	1.3149	0.2570	0.3149
0.5	1.2277	1.2799	0.2277	0.2799
0.6	1.1928	1.2379	0.1928	0.2379
0.7	1.1531	1.1897	0.1531	0.1897
0.8	1.1093	1.1363	0.1093	0.1363
0.9	1.0626	1.0788	0.0626	0.0788
1.0	1.0142	1.0191	0.0142	0.0191

Table 3. Thermal variation at the different points of given domain.

y	$\Theta(\beta_1=0.0)$	$\Theta(\beta_1=0.015)$	$\Theta(C=0.0)$	$\Theta\ (C=0.5)$
−1.0	0	0	0	0
−0.9	0.0928	0.0925	0.0814	0.0961
−0.8	0.1740	0.1734	0.1547	0.1794
−0.7	0.2457	0.2449	0.2212	0.2523
−0.6	0.3100	0.3090	0.2822	0.3173
−0.5	0.3687	0.3676	0.3390	0.3764
−0.4	0.4235	0.4224	0.3928	0.4314
−0.3	0.4758	0.4747	0.4446	0.4838
−0.2	0.5266	0.5255	0.4953	0.5347
−0.1	0.5768	0.5757	0.5454	0.5849
0.0	0.6268	0.6257	0.5954	0.6349
0.1	0.6768	0.6757	0.6454	0.6849
0.2	0.7266	0.7255	0.6953	0.7347
0.3	0.7758	0.7747	0.7446	0.7838
0.4	0.8235	0.8224	0.7928	0.8314
0.5	0.8687	0.8676	0.8390	0.8764
0.6	0.9100	0.9090	0.8822	0.9173
0.7	0.9457	0.9449	0.9212	0.9523
0.8	0.9740	0.9734	0.9547	0.9794
0.9	0.9928	0.9925	0.9814	0.9961
1.0	1.0000	1.0000	1.0000	1.0000

3.3. Discussion

In this section, a concise study of pertinent parameters is graphically presented in Figures 2–10. Figures 2 and 3 are plotted to examine the influence of the magnetic parameter on the motion of couple stress fluid and metallic Hafnium particles. In both graphs, a clear decline in velocities for higher values of the magnetic parameter is observed. Nevertheless, the theory of Hannes Alfven explains the same phenomenon involving the interaction of magnetic fields being induced into an electrically conducting fluid system. This phenomenon produces Alfven waves which result in clear retardation of fluid's speed. However, in Figures 4 and 5, the density of the Hafnium particles brings out a different result as compared to magnetic fields. The major push of pressure on the fluid on slippery walls, the hydro motion in both phases is supported by the addition of extra metallic particles. Consequently, velocity increases by increasing the number of particles. Such factors can be regarded as to attenuate the interaction of fluid particle or interparticle collision allowing the particles to move with least resistance. The most significant parameter which constitutes the existence of the present fluid flow is couple stress parameter γ. It is observed that the fluid particle additives, contribute to expediting the movement. This may cause obscurity and vagueness in the mind of a reader, but Equations (23), (28), and (31) provide enough clues about the inverse influence of couple stress parameter on the flow that attenuates the force of friction/drag arising from the effect base fluid's accumulation. This constitutes a size-dependent effect in the base fluid, in addition to minimizing the rotational field of the fluid particles. Hence, rapid fluid flow is observed in both Figures 6 and 7. However, the contribution of slippery walls is not negligible, as they assist the metallic particles to frisk freely in the liquid. The role of the slip parameter that supports the velocity of both phases is spotted in Figures 8 and 9. Generally, it is believed that slippery walls only snag the flow because of their behavior as a retarding force. Against all such expectations, in the present study, slip effects bring about unprecedented change by increasing the velocity of the fluid, as shown in Figure 8. This change is due to the inverse influence of γ, given in Equations (28) and (31) which rebuffs all such perception that slip parameter merely hampers the flow. The change in temperature through Brinkman number B_r is sketched in Figure 10. It is revealed that the higher values of Brinkman heat up the fluid temperature.

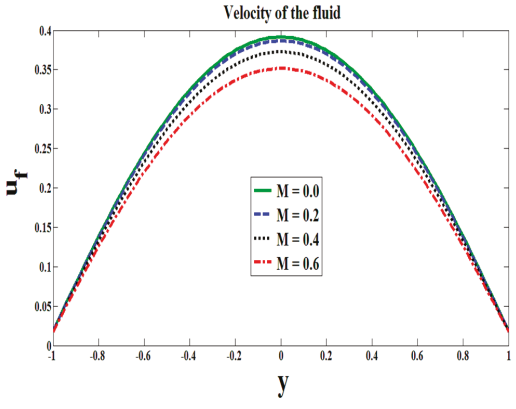

Figure 2. Effects of magnetic fields on the flow.

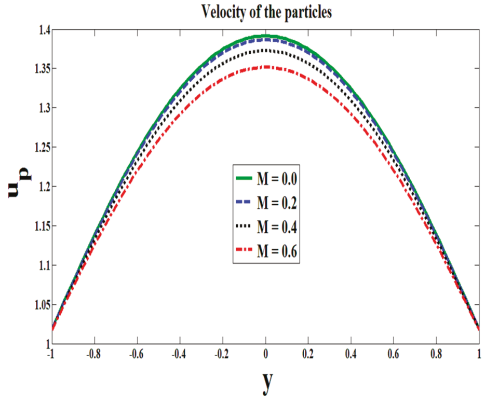

Figure 3. Effects of magnetic fields on the particles.

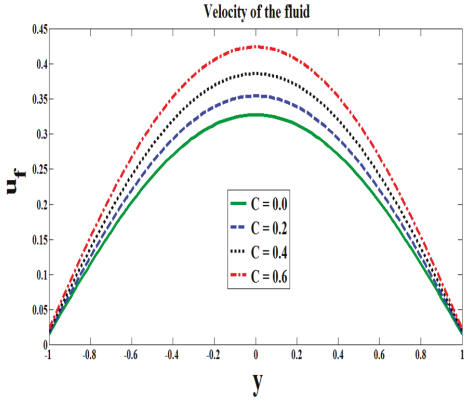

Figure 4. Effects of C on the flow.

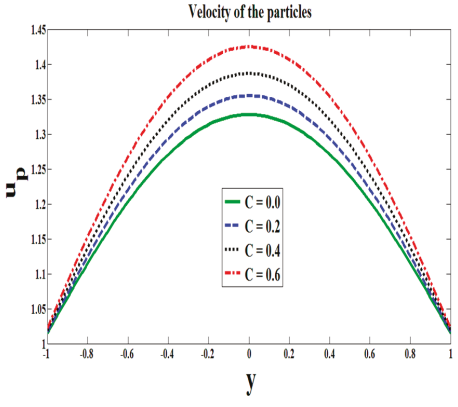

Figure 5. Effects of *C* on the particles.

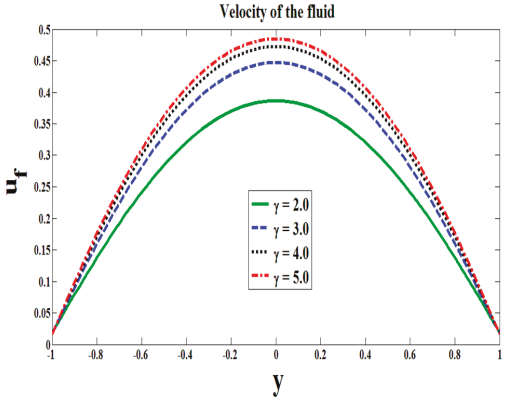

Figure 6. Couples stress parameter affecting the flow.

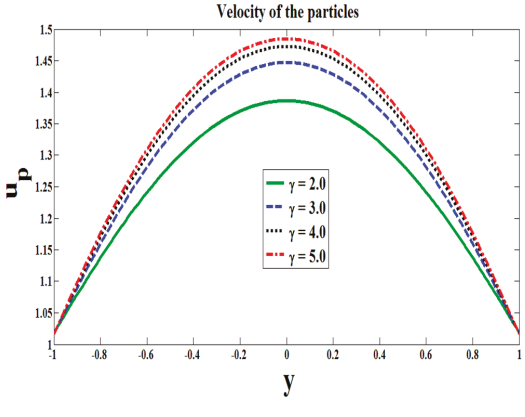

Figure 7. Couples stress parameter affecting the motion of particles.

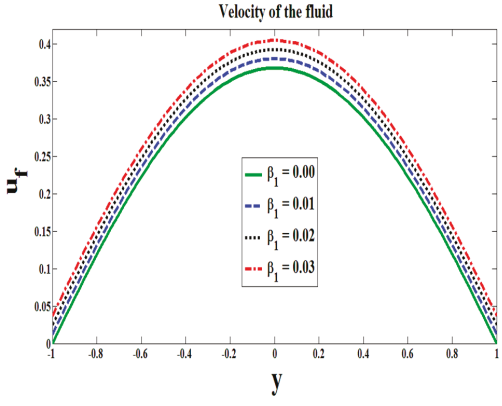

Figure 8. Effects of slip parameter on the flow.

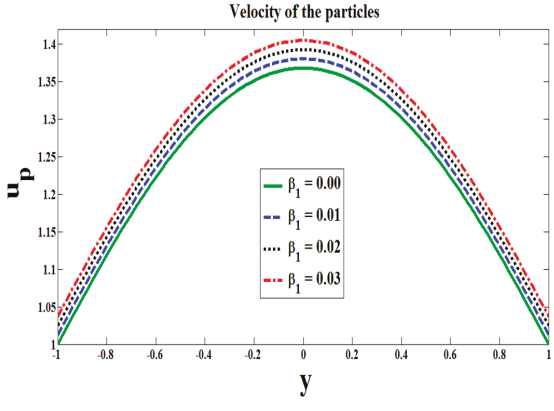

Figure 9. Effects of slip parameter on the motion of particles.

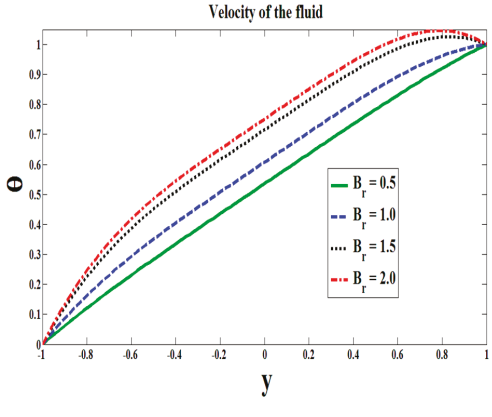

Figure 10. Role of Brinkman number on the temperature.

4. Conclusions

In this study, the heated couple stress bi-phase fluid with spherical particles of metal Hafnium is investigated. The flow bounded by two parallel plates is caused by solely the influence of pressure gradient in an axial direction. A uniform and constant magnetic field of strength B_0 snags the flow, transversely acting across the channel. Extra effects of lubrication are applied on both walls to minimize the surface roughness and to attain a smooth flow. The significant outcomes of the analysis are:

- The velocity of each phase increases due to an increase in the slip parameter.
- The magnetic field does not support the flow and ends up causing a force of resistance.
- The molecules additives of base fluid reduce the force of friction and hence velocities of both phases are galvanized.
- The temperature of the flow escalates for higher values of Brinkman number.

Author Contributions: Conceptualization, R.E.; Writing—Review and Editing, A.Z.; Methodology, F.H.; Investigation, T.A.

Funding: This research received no external funding.

Acknowledgments: Rahmat Ellahi thanks the Director Office of Research Chair Professors, King Fahd University of Petroleum and Minerals, Dhahran, Saudi Arabia, to honor him with the Chair Professor at KFUPM. Farooq Hussain also acknowledges the Higher Education Commission Pakistan to provide him the indigenous scholarship for the pursuance of his Ph.D. studies.

Conflicts of Interest: The authors declare no conflict of interest.

Nomenclature

u_f	velocity of base fluid
h	distance between plates
p	pressure
t	time
M	Hartmann number
U	reference velocity
B_0	magnetic field
C	number density of the particles
u_p	velocity of particle
$\vec{f}$	body force
f	body force
k	thermal conductivity
C_p	specific heat
m	dimensionless constant
B_r	brinkman number
S	drag force coefficient
Greek Symbols	
γ	couple stress parameter
ρ_f	density of base fluid
η_1	constant associated to couple stress fluid
Θ_0	temperature of lower wall
μ_s	viscosity
δ	electric conductivity
ρ	density of the suspension
β	slip length
Θ	dimensional temperature
Θ_1	temperature of upper wall
β_1	slip parameter

References

1. Siddiqui, A.M.; Zeb, A.; Ghori, Q.K.; Benharbit, A.M. Homotopy perturbation method for heat transfer flow of a thirdgrade fluid between parallel plates. *Chaos Solition Fract.* **2008**, *36*, 182–192. [CrossRef]
2. Alamri, S.Z.; Ellahi, R.; Shehzad, N.; Zeeshan, A. Convective radiative plane Poiseuille flow of nanofluid through porous medium with slip: An application of Stefan blowing. *J. Mol. Liq.* **2019**, *273*, 292–304. [CrossRef]
3. Babic, M. Unsteady Couette granular flows. *Phys. Fluids* **1997**, *9*, 2486–2505. [CrossRef]
4. Devakar, M.; Sreenivasu, D.; Shankar, B. Analytical solutions of couple stress fluid Flows with slip boundary conditions. *Alexandria Eng. J.* **2014**, *53*, 723–730.
5. Ilani, S.S.; Ashmawy, E.A. A time dependent slip flow of a couple stress fluid between two parallel plates through state space. *J. Taibah Univ. Sci.* **2018**, *12*, 1658–3655. [CrossRef]
6. Srinivasacharya, D.; Srinivasacharyulu, N.; Odelu, O. Flow and heat transfer of couple stress fluid in a porous channel with expanding and contracting walls. *Int. Commun. Heat Mass Transf.* **2009**, *36*, 180–185. [CrossRef]
7. Murthy, J.V.; Nagaraju, G. Flow of a couple stress fluid generated by a circular cylinder subjected to longitudinal and torsional oscillations. *Contemp. Eng. Sci.* **2009**, *2*, 451–461.
8. Hussain, F.; Ellahi, R.; Zeeshan, A.; Vafai, K. Modelling study on heated couple stress fluid peristaltically conveying gold nanoparticles through coaxial tubes: A remedy for gland tumors and arthritis. *J. Mol. Liq.* **2018**, *268*, 149–155. [CrossRef]
9. Ellahi, R.; Zeeshan, A.; Hussain, F.; Asadollahi, A. Peristaltic blood flow of couple stress fluid suspended with nanoparticles under the influence of chemical reaction and activation energy. *Symmetry* **2019**, *11*, 11–276. [CrossRef]
10. Shit, G.C.; Ranjit, N.K. Role of slip velocity on peristaltic transport of couple stress fluid through an asymmetric non-uniform channel: Application to digestive system. *J. Mol. Liq.* **2016**, *221*, 305–315. [CrossRef]
11. Wu, W.-T.; Aubry, N.; Antaki, J.F.; Massoudi, M. Normal stress effects in the gravity driven flow of granular materials. *Int. J. Nonlin. Mech.* **2017**, *92*, 84–91. [CrossRef]
12. Bognár, G.; Gombkötő, E.; Hriczó, K. Non-Newtonian fluid flow down an inclined plane. Available online: https://pdfs.semanticscholar.org/356f/347b565104a37ddb2440442a08d98ba5a057.pdf (accessed on 19 March 2019).
13. Latz, A.; Schmidt, S. Hydrodynamic modeling of dilute and dense granular flow. *Granul Matter* **2010**, *12*, 387–397. [CrossRef]
14. Armanini, A. Granular flows driven by gravity. *J. Hydraul. Res.* **2013**, *51*, 111–120. [CrossRef]
15. Dan, C.; Wachs, A. Direct Numerical Simulation of particulate flow with heat transfer. *Int. J. Heat Fluid Flow* **2010**, *31*, 1050–1057. [CrossRef]
16. Wang, H.; Chen, T.; Cong, W.; Liu, D. Laser cladding of Ti-based ceramic coatings on Ti6Al4V alloy: Effects of CeO_2 nanoparticles additive on wear performance. *Coatings* **2019**, *9*, 109. [CrossRef]
17. Wang, Z.; Gao, K.; Zhang, B.; Gong, Z.; Wei, X.; Zhang, J. Verification study of nanostructure evolution with heating treatment between thin and thick fullerene-like hydrogen carbon films. *Coatings* **2019**, *9*, 82. [CrossRef]
18. Ellahi, R.; Zeeshan, A.; Hussain, F.; Abbas, T. Study of shiny film coating on multi-fluid flows of a rotating disk suspended with nano-sized silver and gold particles: A comparative analysis. *Coatings* **2018**, *8*, 422. [CrossRef]
19. Khan, Z.; Rasheed, H.U.; Alharbi, S.O.; Khan, I.; Abbas, T.; Chin, D.L.C. Manufacturing of double layer optical fiber coating using phan-thien-tanner fluid as coating material. *Coatings* **2019**, *9*, 147. [CrossRef]
20. Lu, D.; Ramzan, M.; Ahmad, S.; Shafee, A.; Suleman, M. Impact of nonlinear thermal radiation and entropy optimization coatings with hybrid nanoliquid flow past a curved stretched surface. *Coatings* **2018**, *8*, 430. [CrossRef]
21. Riaz, A.; Al-Olayan, H.A.; Zeeshan, A.; Razaq, A.; Bhatti, M.M. Mass transport with asymmetric peristaltic propulsion coated with Synovial fluid. *Coatings* **2018**, *8*, 407. [CrossRef]
22. Khan, I. Shape effects of MoS_2 nanoparticles on MHD slip flow of molybdenum disulphide nanofluid in a porous medium. *J. Mol. Liq.* **2017**, *233*, 442–451. [CrossRef]
23. Bhatti, M.M.; Abbas, T.; Rashidi, M.M.; Ali, M.E.; Yang, Z. Entropy generation on MHD Eyring-Powell nanofluid through a permeable stretching surface. *Entropy* **2016**, *18*, 224. [CrossRef]

24. Zhu, T.; Ye, W. Theoretical and numerical studies of noncontinuum gas-phase heat conduction in micro/nano devices. *Numer. Heat Transf. Part B* **2010**, *57*, 203–226. [CrossRef]
25. Zhang, H.; Zhang, Z.; Zhang, Y.; Ye, H. Corrected second-order slip boundary condition for fluid flows in nanochannels. *Phys. Rev. E* **2010**, *81*, 066303. [CrossRef] [PubMed]
26. Jafari, R.; Mobarakeh, L.F.; Farzaneh, M. Water-repellency enhancement of nanostructured plasma-polymerized HMDSO coatings using Grey-based Taguchi method. *Nano Sci. Technol. Lett.* **2012**, *4*, 369–374. [CrossRef]
27. Radwan, A.B.; Abdullah, A.M.; Mohamed, A.M.A.; Al-Maadeed, M.A. New electrospun polystyrene/Al_2O_3 nanocomposite superhydrophobic coatings; synthesis, characterization, and application. *Coatings* **2018**, *8*, 65. [CrossRef]
28. Majid, A.; Ahmed, W.; Patil-Sen, Y.; Sen, T. Synthesis and characterisation of magnetic nanoparticles in medicine. In *Micro and Nanomanufacturing Volume II*; Jackson, M., Ahmed, W., Eds.; Springer: Cham, Switzerland, 2018; pp. 413–442.
29. Miola, M.; Ferraris, S.; Pirani, F.; Multari, C.; Bertone, E.; Rozman, K.Z.; Kostevsek, N.; Verne, E. Reductant-free synthesis of magnetoplasmonic iron oxide-gold nanoparticles. *Ceram. Int.* **2017**, *43*, 15258–15265. [CrossRef]
30. Rehman, M.A.; Ferraris, S.; Goldmann, W.H.; Perero, S.; Nawaz, Q.; Gautier, G.; Ferraris, M.; Boccaccini, A.R. Antibacterial and bioactive coatings based on RF co-sputtering of silver nanocluster-silica coatings on PEEK/bioactive glass layers obtained by electrophoretic deposition. *ACS Appl. Mater. Interfaces* **2017**, *9*, 32489–32497. [CrossRef]
31. Nasiri, H.; Jamalabadi, M.Y.A.; Sadeghi, R.; Safaei, M.R.; Nguyen, T.K.; Shadloo, M.S. A smoothed particle hydrodynamics approach for numerical simulation of nano-fluid flows. *J. Therm. Anal. Calorim.* **2019**, *135*, 1733. [CrossRef]
32. Zeeshan, A.; Shehzad, N.; Abbas, A.; Ellahi, R. Effects of radiative electro-magnetohydrodynamics diminishing internal energy of pressure-driven flow of titanium dioxide-water nanofluid due to entropy generation. *Entropy* **2019**, *21*, 236. [CrossRef]
33. Ferraris, S.; Spriano, S.; Miola, M.; Bertone, E.; Allizond, V.; Cuffini, A.M.; Banche, G. Surface modification of titanium surfaces through a modified oxide layer and embedded silver nanoparticles: Effect of reducing/stabilizing agents on precipitation and properties of the nanoparticles. *Surf. Coat. Technol.* **2018**, *344*, 177–189. [CrossRef]
34. Ali, Q.; Ahmed, W.; Lal, S.; Sen, T. Novel multifunctional carbon nanotube containing silver and iron oxide nanoparticles for antimicrobial applications in water treatment. *Mater. Today Proc.* **2017**, *4*, 57–64. [CrossRef]
35. Karimipour, A.; Orazio, A.D.; Shadloo, M.S. The effects of different nano particles of Al_2O_3 and Ag on the MHD nano fluid flow and heat transfer in a microchannel including slip velocity and temperature jump. *Phys. E* **2017**, *86*, 146–153. [CrossRef]
36. Maghsoudi, K.; Momen, G.; Jafari, R.; Farzaneh, M. Direct replication of micro-nanostructures in the fabrication of superhydrophobic silicone rubber surfaces by compression molding. *Appl. Surf. Sci.* **2018**, *458*, 619–628. [CrossRef]
37. Maghsoudi, K.; Jafari, R.; Momen, G.; Farzaneh, M. Micro-nanostructured polymer surfaces using injection molding: A review. *Mater. Today Commun.* **2017**, *13*, 126–143. [CrossRef]
38. Hossain, M.A.; Subba, R.; Gorla, R. Natural convection flow of non-Newtonian power-law fluid from a slotted vertical isothermal surface. *Int. J. Numer. Methods Heat Fluid Flow* **2009**, *19*, 835–846. [CrossRef]

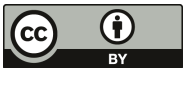

coatings

MDPI

Article

Influence of MHD on Thermal Behavior of Darcy-Forchheimer Nanofluid Thin Film Flow over a Nonlinear Stretching Disc

Abdullah Dawar [1], Zahir Shah [2], Poom Kumam [3,4,5,*], Waris Khan [6] and Saeed Islam [7]

1 Department of Mathematics, Qurtuba University of Science and Information Technology, Peshawar 25000, Pakistan
2 Center of Excellence in Theoretical and Computational Science (TaCS-CoE), SCL 802 Fixed Point Laboratory, Science Laboratory Building, King Mongkut's University of Technology Thonburi (KMUTT), 126 Pracha-Uthit Road, Bang Mod, Thrung Khru, Bangkok 10140, Thailand
3 KMUTT-Fixed Point Research Laboratory, Room SCL 802 Fixed Point Laboratory, Science Laboratory Building, Department of Mathematics, Faculty of Science, King Mongkut's University of Technology Thonburi (KMUTT), 126 Pracha-Uthit Road, Bang Mod, Thrung Khru, Bangkok 10140, Thailand
4 KMUTT-Fixed Point Theory and Applications Research Group, Theoretical and Computational Science Center (TaCS), Science Laboratory Building, Faculty of Science, King Mongkut's University of Technology Thonburi (KMUTT), 126 Pracha-Uthit Road, Bang Mod, Thrung Khru, Bangkok 10140, Thailand
5 Department of Medical Research, China Medical University Hospital, China Medical University, Taichung 40402, Taiwan
6 Department of Mathematics, Kohat University of Science and technology, Kohat 26000, KP, Pakistan
7 Department of Mathematics, Abdul Wali Khan University, Mardan 23200, Pakistan
* Correspondence: poom.kum@kmutt.ac.th; Tel.: +66-2-4708-994

Received: 5 June 2019; Accepted: 9 July 2019; Published: 17 July 2019

Abstract: The aim of this research work is to increase our understanding of the exhaustion of energy in engineering and industrial fields. The study of nanofluids provides extraordinary thermal conductivity and an increased heat transmission coefficient compared to conventional fluids. These specific sorts of nanofluids are important for the succeeding generation of flow and heat transfer fluids. Therefore, the investigation of revolutionary new nanofluids has been taken up by researchers and engineers all over the world. In this article, the study of the thin layer flow of Darcy-Forchheimer nanofluid over a nonlinear radially extending disc is presented. The disc is considered as porous. The impacts of thermal radiation, magnetic field, and heat source/sink are especially focused on. The magnetic field, positive integer, porosity parameter, coefficient of inertia, and fluid layer thickness reduce the velocity profile. The Prandtl number and fluid layer thickness reduce the temperature profile. The heat source/sink, Eckert number, and thermal radiation increase the temperature profile. The suggested model is solved analytically by the homotopy analysis method (HAM). The analytical and numerical techniques are compared through graphs and tables, and have shown good agreement. The influences of embedded parameters on the flow problem are revealed through graphs and tables.

Keywords: Darcy-Forchheimer nanofluid; nonlinear extending disc; variable thin layer; HAM and numerical method

1. Introduction

Nanoparticles less than 100 nm in size suspended into a base fluid is recognized as nanofluid. Nanofluids are used in pharmaceutical procedures, microelectronics, fuel cells, hybrid powered machines, and nanotechnology fields. Choi and Eastman [1] were the first to immerse nanoparticles into a base fluid and call it a nanofluid. Through the suspension of nanoparticles, the thermophysical

properties of the conventional fluid are enhanced. The heat transmission characteristics of a nanofluid were pointed out by Wang and Mujumdar [2]. Later on, Eastman et al. [3,4] furthered this study using different base fluids. Murshed et al. [5] experimentally showed that nanofluids that contain smaller amounts of nanoparticles have higher thermal conductivities. Furthermore, increasing the volume of the nanoparticles fraction increases the thermal conductivity of the nanofluids. Maiga et al. [6] addressed the thermal and hydrodynamic behaviors of nanofluids inside a heated tube. Nanofluid flow in a circular tube with heat flux was addressed by Bianco et al. [7]. The flow processes of nanofluids inside a heated cavity were numerically addressed by Tiwari and Das [8]. The heat transmission in nanofluid flows with Brownian and thermophoresis influences was investigated by Buongiorno [9]. The heat transmission processes of nanofluids in a porous medium were examined by Kasaeian et al. [10]. The radiative MHD flow of a nanofluid experiencing a chemical reaction under the influence of thermal radiation was addressed by Ramzan et al. [11]. The impacts of Brownian motion, magnetic field, and nanoparticles volume fraction on nanofluid flow were analyzed by Sheikholeslami and Shehzad [12]. The MHD nanofluid flow over an extending surface with the influence of viscous dissipation was addressed by Besthapu et al. [13]. The heat transmission in a nanofluid flow over an oscillatory stretching sheet with radiation impacts was addressed by Dawar et al. [14]. The same nanofluid with entropy generation and magnetic field impacts was addressed by Alharbi et al. [15]. Nanofluid flow based on four different fluids in a rotating system with a Darcyian model was addressed by Shah et al. [16]. Khan et al. [17] addressed heat transmission in MHD nanofluid flow under the influence of radiation in rotating plates.Khan et al. [18] addressed nanofluid flow over a linear extending sheet under convective conditions. The viscous dissipation impact of MHD nanofluid flow with entropy generation was determined by Dawar et al. [19]. Sheikholeslami [20] examined the radiative and heat transfer in electrohydrodynamic nanofluid flow. Sheikholeslami [21] determined the MHD nanofluid flow with Brownian influence. Dawar et al. [22] addressed the flow of nanofluid over a porous extending sheet with radiation influence. Ramzan et al. [23] examined the MHD nanofluid flow using the couple stress effect. Sajid et al. [24] examined nanofluid flow over a radially extending surface. Attia et al. [25] examined the stagnation point flow in a porous medium over a radially extending surface. But and Ali [26] scrutinized the MHD flow and heat transfer with entropy generation rate over a radially stretching surface. Zeeshan et al. [27] examined ferrofluid flow over a stretching sheet under the influence of ferromagnetism, thermal radiation, and the Prandtl number. Ellahi et al. [28] addressed the impact of a magnetic field on Carreau fluid flow. Recently, the applications and development of nanofluids were discussed by Ellahi [29]. In another article, Ellahi et al. [30] addressed differential equations with application in engineering fields. The applications of heat transfer in nanofluid flows were addressed by Abu-Nada [31]. Hayat et al. [32] discussed the MHD magnetic field impact on Powell-Eyring nanomaterial flow over a nonlinear extending sheet. Hsiao [33] examined the heat convection, conduction, and mass transfer of MHD nanofluid flow over a stretching sheet. Abu-Nada [34] addressed the heat transfer in a nanofluid flow with entropy generation. Hsiao [35] analyzed the viscous dissipation and radiative influences on MHD Maxwell nanofluid flow in a thermal extrusion system. Pour and Nassab [36] examined nanofluid flows under bleeding conditions. Tian et al. [37] addressed the MHD incompressible flow of nanofluid over an extending sheet with thermophoresis and Brownian influences. Recently, Shah et al. [38] addressed the flow of nanofluid over an extending sheet with couple stress impact. Ellahi et al. [39] examined heat transmission in a boundary layer flow with MHD and entropy generation effects. Some recent study about nanofluid flow can be seen in [39–43].

In this article, a thin layer flow of Darcy-Forchheimer nanofluid over a nonlinear radially extending disc is examined. The disc is considered as porous. The homotopy analysis method (HAM) is applied to solve the nonlinear differential equations using appropriate similarities transformations. The HAM is compared with the numerical (ND-Solve) technique through graphs and tables. Section 2 confronts with the problem of formulation. In Section 3, the modeled problem is solved by HAM. In Section 4,

the impacts of embedded parameters on the fluid flow are deliberated. Section 5 presents the concluding remarks of this research.

2. Problem Formulation

The thin layer flow of a nanofluid over a nonlinear radially extending porous disc in an axially symmetric form has been assumed. The extending disc has been kept at $z = 0$. The nanofluid thickness is regulated to the thin layer with the breadth $z = h$ where h is the thin layer thickness (Figure 1). The porous disc is stretching with a nonlinear velocity $U_w = ar^n$ where n is the integer such that $n > 0$. The applied magnetic field is assumed in a vertical direction to the flow phenomena. The pressure is considered as constant. All others assumptions for the flow phenomena are used as in [24–26]. The leading equations are considered as:

$$\frac{\partial u}{\partial r} + \frac{u}{r} + \frac{\partial w}{\partial z} = 0 \tag{1}$$

$$u\frac{\partial u}{\partial r} + w\frac{\partial u}{\partial z} = \frac{\mu}{\rho}\frac{\partial^2 u}{\partial z^2} - \frac{\sigma B_0^2}{\rho}u - \frac{1}{\rho}\left(\frac{\nu}{k} + Fu\right)u \tag{2}$$

$$u\frac{\partial T}{\partial r} + w\frac{\partial T}{\partial z} = \frac{k}{\rho c_p}\frac{\partial^2 T}{\partial z^2} + \frac{\mu}{\rho c_p}\left(\frac{\partial u}{\partial z}\right)^2 - \frac{1}{\rho c_p}\frac{\partial q_r}{\partial z} + \frac{Q_0}{\rho c_p}(T_0 - T_{\text{ref}}) \tag{3}$$

Here u, v, B_0, $F = \frac{C_b}{\sqrt{Bx}}$, C_b, q_r, Q_0, ρc_p, C_b, k, σ, ρ, μ are the components of velocity in their corresponding directions, induced magnetic strength, inertial coefficient of a permeable medium, drag coefficient, radiative heat flux, heat source/sink, effective heat capacity, thermal conductivity, kinematic viscosity, electrical conductivity, the electrical conductivity, density, and dynamic viscosity, respectively.

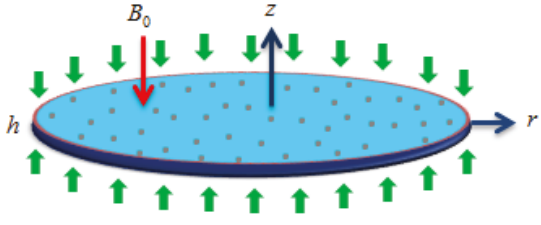

Figure 1. Geometrical illustration of the problem.

The q_r is defined as:

$$q_r = -\frac{4\sigma^*}{3k^*}\frac{\partial T^4}{\partial z} \tag{4}$$

By Taylor's expansion, T^4 can be written as:

$$T^4 = 4T_{\text{ref}}^3 T - T_{\text{ref}}^4 \tag{5}$$

In observation of Equations (4) and (5), Equation (3) is reduced as:

$$u\frac{\partial T}{\partial r} + w\frac{\partial T}{\partial z} = \frac{1}{\rho c_p}\left(k + \frac{16\sigma^* T_{\text{ref}}^3}{3k^*}\right)\frac{\partial^2 T}{\partial z^2} + \frac{\mu}{\rho c_p}\left(\frac{\partial u}{\partial z}\right)^2 + \frac{Q_0}{\rho c_p}(T_0 - T_{\text{ref}}) \tag{6}$$

The following physical conditions are defined for the nanofluid flow:

$$\begin{array}{l} u = ar^n, w = 0, \theta = \theta_w \text{ at } z = 0 \\ \mu\frac{\partial u}{\partial z} = \frac{\partial \theta}{\partial z} = 0, w = \frac{udh}{dr} \text{ at } z = h \end{array} \tag{7}$$

The $\psi(r,z) = -\frac{r^2 U_w}{\sqrt{\mathrm{Re}}} f(\eta)$ and $\eta = \frac{z}{r}\sqrt{\mathrm{Re}}$ are developed for the similarity transformations in such a way that the components of velocity (u, w) along the radial direction and axial direction have been converted as:

$$\begin{aligned} u &= -\frac{1}{r}\frac{\partial \psi(r,z)}{\partial z} = U_w f'(\eta) \\ w &= \frac{1}{r}\frac{\partial \psi(r,z)}{\partial r} = -\frac{U_w}{\sqrt{\mathrm{Re}}}\left[\left(\frac{3+n}{2}\right) f(\eta) + \left(\frac{n-1}{2}\right)\eta f'(\eta)\right] \\ T &= T_0 - T_{\mathrm{ref}}\left(\frac{U_w^2}{2a\nu_f}\right)\theta(\eta) \end{aligned} \tag{8}$$

here, $\mathrm{Re} = \frac{rU_w}{\nu_f}$ is the Reynolds number.

The transformed velocity and temperature equations are:

$$f''' + \left(\frac{3+n}{2}\right) f f'' - n(f')^2 - Mf' - (\kappa + Frf')f' = 0 \tag{9}$$

$$(1+R)\theta'' + \mathrm{Pr}\left[\left(\frac{3+n}{2}\right) f\theta' - 2n(\theta f')\right] + Ec\mathrm{Pr}(f')^2 - \gamma\theta = 0 \tag{10}$$

with boundary conditions:

$$f(0) = 0, f'(0) = 1, \theta(0) = 1, f''(\beta) = f(\beta) = \theta\prime(\beta) = 0 \tag{11}$$

In Equations (9)–(11), $\beta = \frac{h\sqrt{\mathrm{Re}}}{r}$ represents the fluid layer thickness, $M = \frac{r\sigma B_0^2}{\rho U_w}$ indicates the magnetic field parameter, $F_r = \frac{rC_b}{U_w\sqrt{Bx}}$ represents the coefficient of inertia, $\kappa = \frac{r\nu}{kU_w}$ represents the porosity parameter, $R = \frac{16r^2\sigma^* T_{\mathrm{ref}}^3 T}{3U_w^2 kk^*}$ represents the thermal radiation parameter where σ^* is the Boltzmann constant and k^* is the coefficient of absorption, $\mathrm{Pr} = \frac{\mu c_p}{k}$ indicates the Prandtl number, $\mathrm{Ec} = \frac{U_w^2}{(c_p)\Delta T}$ represents the Eckert number, and $\gamma = \frac{r^2 Q_0}{U_w^2 \rho c_p}$ represents the heat source/sink.

The skin friction and Nusselt number are defined as:

$$\begin{aligned} \frac{\sqrt{\mathrm{Re}}}{2} Cf &= -f''(0) \\ \frac{1}{\sqrt{\mathrm{Re}}} Nu &= -(1+R)\theta'(0) \end{aligned} \tag{12}$$

3. HAM Solution

The HAM technique is used to solve the modeled Equations (9) and (10) with the following procedure.

The primary guesses are picked as follows:

$$f_0(\eta) = \eta,\ \theta_0(\eta) = 1 \tag{13}$$

The L_f and L_θ are selected as:

$$L_f(f) = f''',\ L_\theta(\theta) = \theta'' \tag{14}$$

The resultant non-linear operators N_f and N_θ are specified as:

$$\begin{aligned} N_f[f(\eta;\aleph)] = \frac{\mathrm{d}^3 f(\eta;\aleph)}{\mathrm{d}\eta^3} + \left(\frac{3+n}{2}\right) f(\eta;\aleph)\frac{\mathrm{d}^2 f(\eta;\aleph)}{\mathrm{d}\eta^2} - n\left(\frac{\mathrm{d}f(\eta;\aleph)}{\mathrm{d}\eta}\right)^2 \\ -M\frac{\mathrm{d}f(\eta;\aleph)}{\mathrm{d}\eta} - \left(\kappa + Fr\frac{\mathrm{d}f(\eta;\aleph)}{d\eta}\right)\frac{\mathrm{d}f(\eta;\aleph)}{d\eta} \end{aligned} \tag{15}$$

$$N_\theta[\theta(\eta;\aleph), f(\eta;\aleph)] = (1+R)\frac{d^2\theta(\eta;\aleph)}{d\eta^2} + \Pr\left[\begin{array}{l}\left(\frac{3+n}{2}\right)f(\eta;\aleph)\frac{d\theta(\eta;\aleph)}{d\eta} \\ -2n\left(\theta(\eta;\aleph)\frac{df(\eta;\aleph)}{d\eta}\right)\end{array}\right] + \mathrm{EcPr}\left(\frac{df(\eta;\aleph)}{d\eta}\right)^2 - \gamma\theta(\eta;\aleph) \tag{16}$$

The zeroth-order problem from Equations (9) and (10) are:

$$(1-\aleph)L_f[f(\eta;\aleph) - f_0(\eta)] = \aleph\hbar_f N_f[f(\eta;\aleph)] \tag{17}$$

$$(1-\aleph)L_\theta[\theta(\eta;\aleph) - \theta_0(\eta)] = \aleph\hbar_\theta N_\theta[\theta(\eta;\aleph), f(\eta;\aleph)] \tag{18}$$

The converted boundary conditions are:

$$\begin{array}{c} f(\eta;\aleph)\big|_{\eta=0} = 0,\ \frac{df(\eta;\aleph)}{d\eta}\Big|_{\eta=0} = 1,\ \theta(\eta;\aleph)\big|_{\eta=0} = 1 \\ f(\eta;\aleph)\big|_{\beta} = \frac{df^2(\eta;\aleph)}{d\eta^2}\Big|_{\beta} = \frac{d\theta(\eta;\aleph)}{d\eta}\Big|_{\beta} = 0 \end{array} \tag{19}$$

For $\aleph = 0$ and $\aleph = 1$ we can write:

$$\begin{array}{c} f(\eta;0) = f_0(\eta),\ f(\eta;1) = f(\eta) \\ \theta(\eta;0) = \theta_0(\eta),\ \theta(h;1) = \theta(\eta) \end{array} \tag{20}$$

When $\aleph$ fluctuates form 0 to 1, the initial solutions vary to the final solutions. Then, by Taylor's series, we have:

$$\begin{array}{c} f(\eta;\aleph) = f_0(\eta) + \sum\limits_{q=1}^{\infty} f_q(\eta)\aleph^q \\ \theta(\eta;\aleph) = \theta_0(\eta) + \sum\limits_{q=1}^{\infty} \theta_q(\eta)\aleph^q \end{array} \tag{21}$$

where

$$f_q(\eta) = \frac{1}{q!}\frac{df(\eta;\aleph)}{d\eta}\Big|_{\tau=0} \text{ and } \theta_q(\eta) = \frac{1}{q!}\frac{d\theta(\eta;\aleph)}{d\eta}\Big|_{\tau=0} \tag{22}$$

The series (21) at $\aleph = 1$ converges, we obtain:

$$\begin{array}{c} f(\eta) = f_0(\eta) + \sum\limits_{q=1}^{\infty} f_q(\eta) \\ \theta(\eta) = \theta_0(\eta) + \sum\limits_{q=1}^{\infty} \theta_q(\eta) \end{array} \tag{23}$$

The $q^{th}-$ order gratifies the succeeding:

$$\begin{array}{c} L_f\Big[f_q(\eta) - \chi_q f_{q-1}(\eta)\Big] = \hbar_f V_q^f(\eta) \\ L_\theta\Big[\theta_q(\eta) - \chi_q \theta_{q-1}(\eta)\Big] = \hbar_\theta V_q^\theta(\eta) \end{array} \tag{24}$$

with boundary conditions:

$$\begin{array}{c} f_q(0) = f_q'(0) = 0, \theta_q(0) = 0 \\ f_q''(\beta) = f_q(\beta) = \theta_q'(\beta) = 0 \end{array} \tag{25}$$

here

$$V_q^f(\eta) = f_{q-1}''' + \left(\frac{3+n}{2}\right)\sum_{k=0}^{q-1} f_{q-1-k}f_k'' - n\left(f_{q-1}'\right)^2 - Mf_{q-1}' - \left(\kappa + Frf_{q-1}'\right)f_{q-1}' \tag{26}$$

$$V_q^\theta(\eta) = (1+R)\theta_{q-1}'' + \Pr\left[\left(\frac{3+n}{2}\right)\sum_{k=0}^{q-1} f_{q-1-k}\theta_k' - 2n\left(\sum_{k=0}^{q-1}\theta_{q-1-k}f_k'\right)\right] + \mathrm{EcPr}\left(f_{q-1}'\right)^2 - \gamma\theta_{q-1} \tag{27}$$

where

$$\chi_q = \begin{cases} 0, \text{ if } \aleph \leq 1 \\ 1, \text{ if } \aleph > 1 \end{cases} \tag{28}$$

4. Results and Discussion

In this section impact of physical parameters on velocity and temperature profiles are discuses. In Figure 2, h-curve for velocity and temperature profiles are displayed. In Figures 3–7, the physical influence of the embedded parameters on the thin layer flow of Darcy-Forchheimer nanofluid over a nonlinear radially extending porous disc is presented. Figure 3 depicts the impacts of positive integer n and magnetic parameter M on $f'(\eta)$. It is determined here that both parameters show a declining behavior in the velocity profile.The nonlinearity stretching phenomena of the thin film flow reduced the thin layer with the escalation in n, because the bulky magnitude of n produced an opposing force to reduce the fluid motion. Therefore, the fluid velocity was reduced with the escalated n. Moreover, the large amount of M decreased the fluid velocity. Basically, the Lorentz force says that the resists the fluid motion on the liquid boundary which, in result, diminishes the velocity of the fluid. Figure 4 reveals the impacts of κ and F_r on $f'(\eta)$. The porous medium performed a key role during fluid flow occurrences. Significantly, the porosity parameter disturbed the boundary layer flow of liquid which, as a result, produced opposition to the fluid flow and, hereafter, a decline the velocity of the fluid. Furthermore, F_r diminished the fluid flow at the surface of the radially extending disc. This behavior occurred because the porous medium was added to the flow phenomena which decreased the coefficient of inertia, and consequently, the fluid velocity was decreased. The influence of fluid layer thickness β on $f'(\eta)$ and $\theta(\eta)$ is shown in Figure 5. Physically, the resistive force to fluid flow increased with the increase in fluid layer thickness β. The increased fluid layer thickness increased the velocity and a smaller amount of energy was needed for the motion of the fluid. Consequently, the velocity profile was reduced with an increase in fluid layer thickness. Similarly, the increase in fluid layer thickness was reduced $\theta(\eta)$. Figure 6 reveals the influences of γ and R on $\theta(\eta)$. Physically, γ acted like a heat producer which increased the boundary layer thickness and released heat to the fluid flow phenomena. Therefore, the increase in γ increased $\theta(\eta)$. The increase in R increased $\theta(\eta)$. The upsurge in R enhanced the thermal boundary layer temperature of the fluid flow; consequently, increased behaviour in $\theta(\eta)$ is observed. The impact of Pr and Ec is revealed in Figure 7. The increased Eckert number increased the temperature of the thin film flow. Actually, the Eckert number produced viscous resistance due to the presence of a dissipation term which increased the nanofluid thermal conductivity to increase the temperature field. The enhanced Prandtl number Pr reduced the temperature of the thin film flow. The higher Pr numbers (e.g.,$\Pr = 7.0$) possess lower thermal conductivity which result in a decline in temperature of the boundary layer flow. Conversely, the lower Pr numbers possess higher thermal conductivity which consequently increases the temperature of the boundary layer flow.

Figures 8 and 9 display a comparison of the homotopy analysis method (HAM) and numerical (ND-Solve) techniques $f'(\eta)$ and $\theta(\eta)$. The agreement of the HAM and numerical techniques is observed here.

The influence of entrenched parameters on Cf and Nu are displayed in Tables 1 and 2. The increasing fluid layer thickness increases the opposing force to fluid flow which, as a result, improves the Cf of the thin film flow. The escalating magnetic field increases the Cf. This influence is due to the increasing magnetic field which boosts the resistive force to the flow of fluid, called Lorentz force. The κ and Fr increase the Cf. The porosity parameter disturbs the boundary layer flow of the thin film flow which increases the resistive force to the fluid. The coefficient of inertia is directly proportional to the porosity parameter. The increase in the porosity parameter increases the coefficient of inertia which, in result, boosts the opposing force to fluid flow. The increasing positive integer boosts the nonlinearity which produces resistance to the fluid and increases the Cf. The increase in R increases the Nu. The thermal boundary layer temperature of the fluid flow increases with the increase in R which increases the heat transfer of the thin film flow. The increase in Pr increases the Nu. Usually, the large amount

of Pr reduces the nanofluid thermal conductivity. Therefore, the Nu increases with the increase in Pr. The larger amount of γ increases the Nu. This effect is due to the fact that the γ increases the boundary layer thickness of the nanofluid which, in result, increases the Nu. The increasing values of Ec reduces the Nu. The Eckert number is usually composed of the nanofluid thermal conductivity term to increase the temperature profile which, in turn, gives the opposite influence for cooling processes. The escalating positive integer increases the Nu.

Tables 3 and 4 display the assessment of the homotopy analysis method (HAM) and numerical (ND-Solve) techniques for $f'(\eta)$ and $\theta(\eta)$. The agreement of the HAM and numerical techniques is observed here.

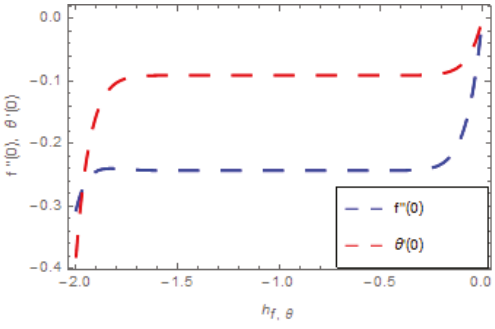

Figure 2. $\hbar$-curves for $f'(\eta)$ and $\theta(\eta)$.

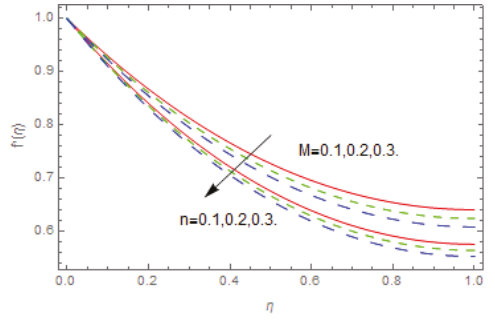

Figure 3. Impression of n and M on $f'(\eta)$.

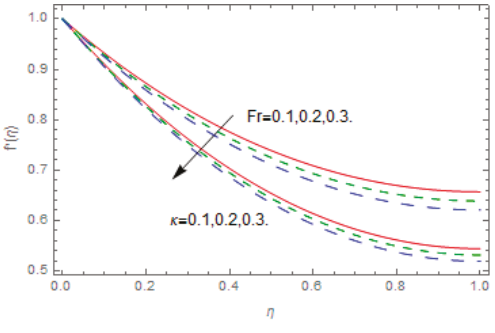

Figure 4. Impression of κ and F_r on $f'(\eta)$.

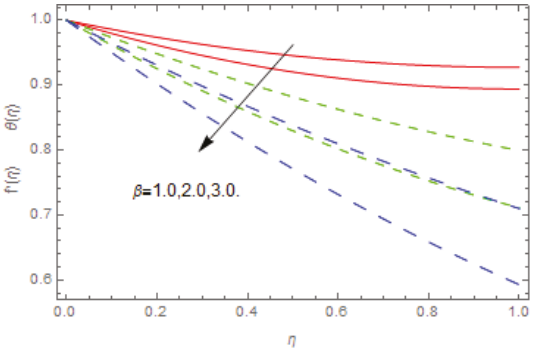

Figure 5. Impression of β on $f'(\eta)$ and $\theta(\eta)$.

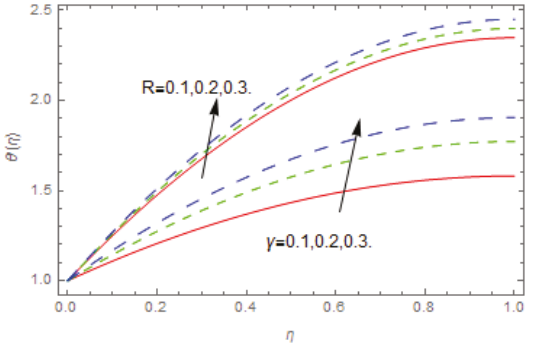

Figure 6. Impression of γ and R on $\theta(\eta)$.

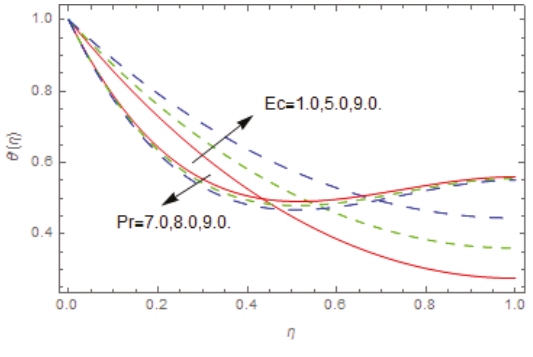

Figure 7. Impression of Pr and Ec on $\theta(\eta)$.

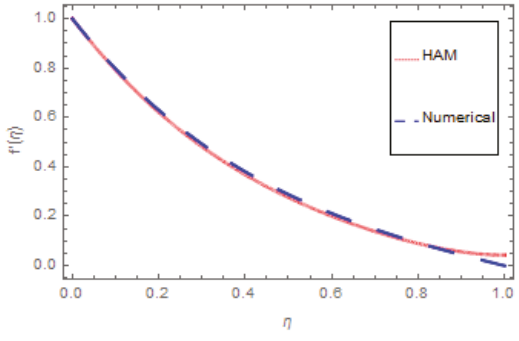

Figure 8. The assessment of HAM and ND-Solve for $f'(\eta)$.

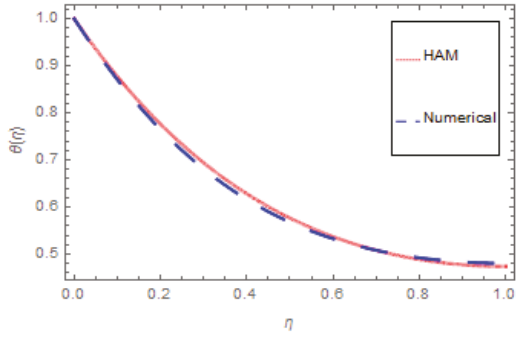

Figure 9. The assessment of HAM and ND-Solve for $\theta(\eta)$.

Table 1. The effect of embedded parameters on *Cf* at 15th order approximations of the homotopy analysis method (HAM).

β	*M*	κ	F_r	*n*	*Cf*
0.2	0.6	0.1	0.1	2.0	0.534624
0.3					0.761014
0.4					0.950758
	0.7				0.553042
	0.8				0.571415
	0.9				0.589744
		0.2			0.552042
		0.3			0.571415
		0.4			0.589744
			0.2		0.607370
			0.4		0.642203
			0.6		0.676780
				3.0	0.847565
				4.0	1.012080

Table 2. The effect of embedded parameters on *Nu* at 15th order approximations of the HAM.

R	Pr	γ	Ec	*n*	*Nu*
0.5	1.0	0.1	0.1	2.0	2.394070
0.6					2.553680
0.7					2.713280
	1.1				2.955850
	1.2				3.194332
	1.3				3.428861
		0.3			2.763659
		0.5			2.813816
		0.7			2.863768
			0.2		2.827741
			0.3		2.811727
			0.6		2.785875
				3.0	4.552986
				4.0	6.435682

Table 3. The assessment of the HAM and ND-Solve for $f'(\eta)$.

η	HAM	Numerical
0.0	1.000000	0.000000
0.1	0.961455	0.961589
0.2	0.945490	0.945568
0.3	0.931736	0.931656
0.4	0.920188	0.920156
0.5	0. 910827	0.910817
0.6	0.903656	0.903699
0.7	0.899547	0.899635
0.8	0.890117	0.890124
0.8	0.889466	0.883445
1.0	0.887864	0.887895

Table 4. The assessment of the HAM and ND-Solve for $\theta(\eta)$.

η	HAM	Numerical
0.0	1.000000	1.000000
0.1	0.993277	0.993900
0.2	0.986997	0.965800
0.3	0.981248	0.988250
0.4	0.976111	0.983133
0.5	0.971651	0.978612
0.6	0.967931	0.974732
0.7	0.964988	0.971530
0.8	0.962865	0.969025
0.9	0.961583	0.967233
1.0	0.961154	0.966158

5. Conclusions

The thin layer flow of Darcy-Forchheimer nanofluid over a nonlinear radially extending disc has been examined in this study. The nonlinear disc with a variable thickness of the nanofluid has been varied with the help of positive integer n. The magnetic field has been executed in a direction vertical to the nanofluid flow. The influences of magnetic field parameter, positive integer, porosity parameter, coefficient of inertia, fluid layer thickness, Prandtl number, heat source/sink, thermal radiation, and Eckert number on the fluid flow problem have been observed in this study. The key findings can be stated as follows:

- Increasing the magnetic field parameter, positive integer, porosity parameter, coefficient of inertia, and fluid layer thickness reduces the velocity profile.
- Increasing the Prandtl number and fluid layer thickness reduces the temperature profile.
- Increasing the heat source/sink, thermal radiation, and Eckert number increases the temperature profile.
- Increasing the fluid layer thickness, magnetic field parameter, porosity parameter, coefficient of inertia, and positive integer increases the skin friction coefficient.
- Increasing the heat source/sink, thermal radiation, Eckert number, and positive integer increases the local Nusselt number.
- Increasing the Eckert number reduces the local Nusselt number.
- An agreement between the HAM and numerical techniques is observed here.

Author Contributions: Conceptualization, A.D. and Z.S.; Methodology, A.D., Z.S. and W.K.; Software, A.D., Z.S. and S.I.; Validation, A.D. and W.K.; Resources, P.K.; Writing—Original Draft Preparation, A.D.; Writing—Review & Editing, A.D., Z.S., W.K. and S.I.; Visualization, Z.S., P.K. and S.I.

Funding: This research was funded by the Center of Excellence in Theoretical and Computational Science (TaCS-CoE), KMUTT.

Acknowledgments: This project was supported by the Theoretical and Computational Science (TaCS) Center under Computational and Applied Science for Smart Innovation Research Cluster (CLASSIC), Faculty of Science, KMUTT.

Conflicts of Interest: The author declares that they have no competing interests.

Nomenclature

a	Stretching parameter
B_0	Magnetic field (N m A^{-1})
c_P	Specific heat (J kg^{-1} K^{-1})
k	Thermal conductivity (W m^{-1} K^{-1})
n	Positive integer
Q_0	Heat flux (W m^{-2})
q_r	Radioactive heat flux (J)
u, v	Velocity components (m s^{-1})
ρ	Dynamic viscosity (MPa)
σ	Electrical conductivity (S m^{-1})
$\hbar$	Assisting parameter
Cf	Skin friction coefficient
Pr	Prandtl number
κ	Porosity parameter
β	Fluid layer thickness parameter
Ec	Eckert number
F	Permeability (m^2)
h	Thin layer thickness
k^*	Stefan Boltzmann constant
T	Fluid temperature (K)
T_{ref}	Reference temperature
Uw	Stretching velocity (m s^{-1})
η	Similarity variable
v	Kinematic viscosity (m^2 s^{-1})
σ*	Absorption coefficient
M	Magnetic field parameter
Nu	Nusselt number
R	Thermal Redation parameter
γ	Heat source/sink parameter
F_r	Coefficient of inertia parameter

References

1. Choi, S.U.S.; Estman, J.A. Enhancing thermal conductivity of fluids with nanoparticles. *ASME Publ. Fed.* **1995**, *231*, 99–106.
2. Wang, X.Q.; Mujumdar, A.S. Heat transfer characteristics of nanofluids: A review. *Int. J. Therm. Sci.* **2007**, *46*, 1–19. [CrossRef]
3. Eastman, J.A.; Phillpot, S.R.; Choi, S.U.S.; Keblinski, P. Thermal transport in nanofluids. *Annu. Rev. Mater. Res.* **2004**, *34*, 219–246. [CrossRef]
4. Eastman, J.A.; Choi, S.U.S.; Li, S.; Yu, W.; Thompson, L.J. Anomalously increased effective thermal conductivities of ethylene glycol-based nanofluids containing copper nanoparticles. *Appl. Phys. Lett.* **2001**, *78*, 718–720. [CrossRef]
5. Murshed, S.M.S.; Leong, K.C.; Yang, C. Enhanced thermal conductivity of TiO_2—Water based nanofluids. *Int. J. Therm. Sci.* **2005**, *44*, 367–373. [CrossRef]
6. Maïga, S.E.B.; Nguyen, C.T.; Galanis, N.; Roy, G. Heat transfer behaviours of nanofluids in a uniformly heated tube. *Superlattices Microstruct.* **2004**, *35*, 543–557.
7. Bianco, V.; Chiacchio, F.; Manca, O.; Nardini, S. Numerical investigation of nanofluids forced convection in circular tubes. *Appl. Therm. Eng.* **2009**, *29*, 3632–3642. [CrossRef]
8. Tiwari, R.K.; Das, M.K. Heat transfer augmentation in a two-sided lid-driven differentially heated square cavity utilizing nanofluids. *Int. J. Heat Mass Transf.* **2007**, *50*, 2002–2018. [CrossRef]
9. Buongiorno, J. Convective transport in nanofluids. *J. Heat Transf.* **2006**, *128*, 240–250. [CrossRef]
10. Kasaeian, A.; Azarian, R.D.; Mahian, O.; Kolsi, O.; Chamkha, A.J.; Wongwises, S.; Pop, I. Nanofluid flow and heat transfer in porous media: A review of the latest developments. *Int. J. Heat Mass Transf.* **2017**, *107*, 778–791. [CrossRef]
11. Ramzan, M.; Chung, J.D.; Ullah, N. Radiative magnetohydrodynamic nanofluid flow due to gyrotactic microorganisms with chemical reaction and non-linear thermal radiation. *Int. J. Mech. Sci.* **2017**, *130*, 31–40. [CrossRef]
12. Sheikholeslami, M.; Shehzad, S.A. Magnetohydrodynamic nanofluid convective flow in a porous enclosure by means of LBM. *Int. J. Heat Mass Transf.* **2017**, *113*, 796–805. [CrossRef]
13. Besthapu, P.; Haq, R.U.; Bandari, S.; Al-Mdallal, Q.M. Mixed convection flow of thermally stratified MHD nanofluid over an exponentially stretching surface with viscous dissipation effect. *J. Taiwan Inst. Chem. Eng.* **2017**, *71*, 307–314. [CrossRef]
14. Dawar, A.; Shah, Z.; Idress, M.; Khan, W.; Islam, S.; Gul, T. Impact of thermal radiation and heat source/sink on Eyring–Powell Fluid Flow over an unsteady oscillatory porous stretching surface. *Math. Comput. Appl.* **2018**, *23*, 20. [CrossRef]
15. Alharbi, S.O.; Dawar, A.; Shah, Z.; Khan, W.; Idrees, M.; Islam, S.; Khan, I. Entropy generation in MHD Eyring–Powell fluid flow over an Unsteady oscillatory porous stretching surface under the impact of thermal radiation and heat source/sink. *Appl. Sci.* **2018**, *8*, 2588. [CrossRef]
16. Shah, Z.; Dawar, A.; Islam, S.; Khan, I.; Ching, D.L.C. Darcy-Forchheimer flow of radiative carbon nanotubes with microstructure and inertial characteristics in the rotating frame. *Stud. Therm. Eng.* **2018**, *12*, 823–832. [CrossRef]
17. Khan, A.; Shah, Z.; Islam, S.; Dawar, A.; Bonyah, E.; Ullah, H.; Khan, A. Darcy-Forchheimer flow of MHD CNTs nanofluid radiative thermal behaviour and convective non uniform heat source/sink in the rotating frame with microstructure and inertial characteristics. *AIP Adv.* **2018**, *8*, 125024. [CrossRef]
18. Khan, A.S.; Nie, Y.; Shah, Z.; Dawar, A.; Khan, W.; Islam, S. Three-Dimensional nanofluid flow with heat and mass transfer analysis over a linear stretching surface with convective boundary conditions. *Appl. Sci.* **2018**, *8*, 2244. [CrossRef]
19. Dawar, A.; Shah, Z.; Khan, W.; Idrees, M.; Islam, S. Unsteady squeezing flow of magnetohydrodynamic carbon nanotube nanofluid in rotating channels with entropy generation and viscous dissipation. *Adv. Mech. Eng.* **2019**, *11*, 1–18. [CrossRef]
20. Sheikholeslami, M. Numerical investigation of nanofluid free convection under the influence of electric field in a porous enclosure. *J. Mol. Liq.* **2018**, *249*, 1212–1221. [CrossRef]
21. Sheikholeslami, M. CuO-water nanofluid flow due to magnetic field inside a porous media considering Brownian motion. *J. Mol. Liq.* **2018**, *249*, 921–929. [CrossRef]

22. Dawar, A.; Shah, Z.; Khan, W.; Islam, S.; Idrees, M. An optimal analysis for Darcy-Forchheimer 3-D Williamson nanofluid flow over a stretching surface with convective conditions. *Adv. Mech. Eng.* **2019**, *11*, 1–15. [CrossRef]
23. Ramzan, M.; Sheikholeslami, M.; Saeed, M.; Chung, J.D. On the convective heat and zero nanoparticle mass flux conditions in the flow of 3D MHD Couple Stress nanofluid over an exponentially stretched surface. *Sci. Rep.* **2019**, *9*, 562. [CrossRef] [PubMed]
24. Sajid, M.; Hayat, T.; Asghar, S. Non-similar solution for the axisymmetric flow of a third-grade fluid over a radially stretching sheet. *Acta Mech.* **2007**, *189*, 193–205. [CrossRef]
25. Attia, H.A.; Ewis, K.M.; Abdeen, M.A.M. Stagnation point flow through a porous medium towards a radially stretching sheet in the presence of uniform suction or injection and heat generation. *J. Fluids Eng.* **2012**, *134*, 081202. [CrossRef]
26. But, A.S.; Ali, A. Effects of Magnetic Field on entropy generation in flow and heat transfer due to a radially stretching surface. *Phys. Lett.* **2013**, *30*, 024701. [CrossRef]
27. Zeeshan, A.; Majeed, A.; Ellahi, R. Effect of magnetic dipole on viscous ferro-fluid past a stretching surface with thermal radiation. *J. Mol. Liq.* **2016**, *215*, 215–549. [CrossRef]
28. Ellahi, R.; Mubeshir Bhatti, M.; Khalique, C.M. Three-dimensional flow analysis of Carreau fluid model induced by peristaltic wave in the presence of magnetic field. *J. Mol. Liq.* **2017**, *241*, 1059–1068. [CrossRef]
29. Ellahi, R. Special Issue on recent developments of nanofluids. *Appl. Sci.* **2018**, *8*, 192. [CrossRef]
30. Ellahi, R.; Fetecau, C.; Sheikholeslami, M. Recent advances in the application of differential equations in mechanical engineering problems. *Math. Probl. Eng.* **2018**, *2018*, 1584930. [CrossRef]
31. Abu-Nada, E. Application of nanofluids for heat transfer enhancement of separated flows encountered in a backward facing step. *Int. J. Heat Fluid Flow* **2008**, *29*, 242–249. [CrossRef]
32. Hayat, T.; Sajjad, R.; Muhammad, T.; Alsaedi, A.; Ellahi, R. On MHD nonlinear stretching flow of Powell—Eyring nanomaterial. *Results Phys.* **2017**, *7*, 535–543. [CrossRef]
33. Hsiao, K.-L. Stagnation electrical MHD nanofluid mixed convection with slip boundary on a stretching sheet. *Appl. Therm. Eng.* **2016**, *98*, 850–886. [CrossRef]
34. Abu-Nada, E. The present research investigates second law analysis of laminar flow over a backward facing step (BFS). Entropy generation due to separation, reattachment, recirculation and heat transfer is studied numerically. *Entropy* **2005**, *7*, 234–252. [CrossRef]
35. Hsiao, K.-L. Combined electrical MHD heat transfer thermal extrusion system using Maxwell fluid with radiative and viscous dissipation effects. *Appl. Therm. Eng.* **2017**, *112*, 1281–1288. [CrossRef]
36. Pour, M.; Nassab, S. Numerical investigation of forced laminar convection flow of nanofluids over a backward facing step under bleeding condition. *J. Mech.* **2012**, *28*, N7–N12. [CrossRef]
37. Tian, X.-Y.; Li, B.W.; Hu, Z.-M. Convective stagnation point flow of a MHD non-Newtonian nanofluid towards a stretching plate. *Int. J. Heat Mass Transf.* **2018**, *127*, 768–780. [CrossRef]
38. Shah, Z.; Dawar, A.; Alzahrani, E.; Kumam, P.; Khan, A.J.; Islam, S. Hall Effect on couple stress 3D nanofluid flow over an exponentially stretched surface with Cattaneo Christov heat flux model. *IEEE Access* **2019**, *7*, 64844–64855. [CrossRef]
39. Ellahi, R.; Alamri, S.Z.; Basit, A.; Majeed, A. Effects of MHD and slip on heat transfer boundary layer flow over a moving plate based on specific entropy generation. *J. Taibah Univ. Sci.* **2018**, *12*, 476–482. [CrossRef]
40. Khan, A.S.; Nie, Y.; Shah, Z. Impact of thermal radiation on magnetohydrodynamic unsteady thin film flow of Sisko fluid over a stretching surface. *Processes* **2019**, *7*, 369. [CrossRef]
41. Ullah, A.; Alzahrani, E.O.; Shah, Z.; Ayaz, M.; Islam, S. Nanofluids thin film flow of Reiner-Philippoff fluid over an unstable stretching surface with brownian motion and thermophoresis effects. *Coatings* **2019**, *9*, 21. [CrossRef]
42. Alsagri, A.S.; Nasir, S.; Gul, T.; Islam, S.; Nisar, K.S.; Shah, Z.; Khan, I. MHD thin film flow and thermal analysis of blood with CNTs nanofluid. *Coatings* **2019**, *9*, 175. [CrossRef]
43. Saeed, A.; Shah, Z.; Islam, S.; Jawad, M.; Ullah, A.; Gul, T.; Kumam, P. Three-dimensional casson nanofluid thin film flow over an inclined rotating disk with the impact of heat generation/consumption and thermal radiation. *Coatings* **2019**, *9*, 248. [CrossRef]

coatings

MDPI

Article

Effect of the Variable Viscosity on the Peristaltic Flow of Newtonian Fluid Coated with Magnetic Field: Application of Adomian Decomposition Method for Endoscope

Safia Akram [1,*], Emad H. Aly [2,3], Farkhanda Afzal [1] and Sohail Nadeem [4]

1 MCS, National University of Sciences and Technology, Islamabad 44000, Pakistan
2 Department of Mathematics, Faculty of Science, University of Jeddah, Jeddah 21589, Saudi Arabia
3 Department of Mathematics, Faculty of Education, Ain Shams University, Roxy, Cairo 11757, Egypt
4 Department of Mathematics, Quaid-i-Azam University 45320, Islamabad 44000, Pakistan
* Correspondence: drsafiaakram@gmail.com

Received: 20 July 2019; Accepted: 13 August 2019; Published: 16 August 2019

Abstract: In the present analysis, peristaltic flow was discussed for MHD Newtonian fluid through the gap between two coaxial tubes, where the viscosity of the fluid is treated as variable. In addition, the inner tube was considered to be at rest, while the outer tube had the sinusoidal wave traveling down its motion. Further, the assumptions of long wave length and low Reynolds number were taken into account for the formulation of the problem. A closed form solution is presented for general viscosity using the Adomian decomposition method. Numerical illustrations that show the physical effects and pertinent features were investigated for different physical included phenomenon. It was found that the pressure rise increases with an increase in Hartmann number, and frictional forces for the outer and inner tube decrease with an increase in Hartmann number when the viscosity is constant. It was also observed that the size of the trapping bolus decreases with an increase in Hartmann number, and increases with an increase in amplitude ratio when the viscosity is parameter.

Keywords: peristaltic flow; an endoscope; variable viscosity; Adomian solutions; different wave forms

1. Introduction

The study of peristaltic mechanism has gained considerable attention during the past few decades [1–10]. Peristaltic mechanism involves certain physiological phenomena, like swallowing food through the esophagus, vasomotion of small blood vessels, transport of urine from kidney to bladder, chyme motion in the gastrointestinal tract, and movement of spermatozoa in human reproductive tract.

Peristaltic pumping is a form of liquid transport that occurs when a progressive wave of area contraction or expansion propagates along the length of distensible duct. There are many engineering processes in which peristaltic pumps are used to handle a wider range of fluids, particularly in the chemical and pharmaceutical industries. This mechanism is also used in the transport of slurries, sanitary fluids, and noxious fluids in the nuclear industry [11–13]. Extensive analytical, numerical, and experimental studies have been undertaken involving such flows. Important studies to the present topic include the works done by [14–19]. In all previous studies, fluid viscosity is assumed to be constant. There are few attempts in which the variable viscosity in peristaltic phenomena has been used. Mention may be made of the works by [20–22].

There are various analytical techniques to solve the differential equations arising in physics and engineering. Thus, various perturbation and non perturbation techniques are in use. Recently, Adomian decomposition has acquired great credence in tackling the linear and non-linear problems, and sometimes gives the closed form solution in the form of general functions like trigonometric

functions, Bessel functions, and so on. The impressive bibliography of the work done by the Adomian decomposition method has been presented in papers by [23–30].

The intent of the paper is to present an integrated solution for different facets of the problem. These include application of endoscopy in a viscous fluid with the variable viscosity and closed form Adomian solutions, which are presented for unknown (general $\mu(r)$) variable viscosity. In Section 2, mathematical formulation of the present problem is described. Section 3 deals with the solution of the problem using the Adomian decomposition method. Three typical examples were chosen and their closed form solutions were presented, and comparison is given with the existing literature. In Section 4, graphical results are presented to gauge the effects of certain physical parameters. Finally, streamlines for the flow problems are also drawn.

2. Mathematical Formulation

Consider the magnetohydrodynamic flow of an electrically conducting viscous fluid through the gap between two coaxial tubes. It is assumed that a uniform magnetic field B_0 is applied transversely to the flow. Further, considering that the magnetic Reynolds number is small, the induced magnetic field is negligible. A schematic diagram of the geometry of the problem under consideration is shown in Figure 1.

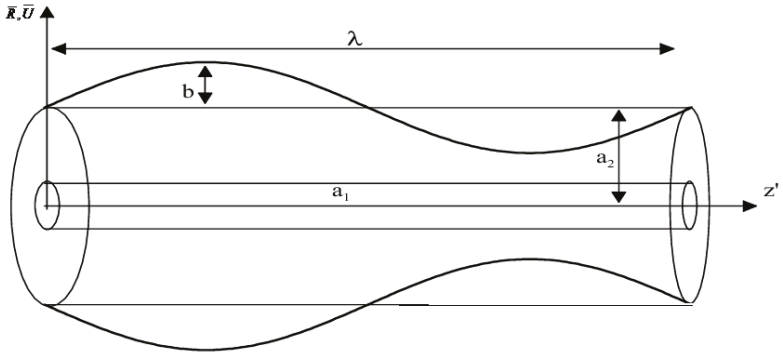

Figure 1. Effects of an endoscope on peristaltic motion.

The geometry of the wall surface is described as

$$\overline{R}_1 = a_1 \tag{1}$$

$$\overline{R}_2 = a_2 + b\cos\frac{2\pi}{\lambda}(\overline{Z} - c\bar{t}) \tag{2}$$

where a_1, and a_2 are the radii of the inner and the outer tubes, respectively; b is the amplitude of the wave; λ is the wavelength; c is the propagation velocity; and $\bar{t}$ is the time.

In the laboratory frame $(\overline{R},\ \overline{Z})$, the flow is unsteady, but, by introducing a wave frame $(\bar{r}\ ,\ \bar{z})$ moving with velocity c away from the fixed frame, the flow can be treated as steady [10]. The coordinate frames are related by the transformations.

$$\bar{z} = \overline{Z} - c\bar{t},\ \bar{r} = \overline{R},\ \overline{w} = \overline{W} - c,\ \overline{u} = \overline{U} \tag{3}$$

where $(\overline{u},\ \overline{w})$ and $\left(\overline{U},\ \overline{W}\right)$ are the velocity components in radial and axial directions in moving and fixed coordinates, respectively. Using the transformations (3), the equations that govern the flow are

$$\frac{\partial\overline{u}}{\partial\overline{r}} + \frac{\partial\overline{w}}{\partial\overline{z}} + \frac{\overline{u}}{\overline{r}} = 0 \tag{4}$$

$$\begin{aligned}\rho\Big[\overline{u}\frac{\partial\overline{u}}{\partial\overline{r}}+\overline{w}\frac{\partial\overline{u}}{\partial\overline{z}}\Big]= &-\frac{\partial\overline{p}}{\partial\overline{r}}+\frac{\partial}{\partial\overline{r}}\Big(2\mu(\overline{r})\ \frac{\partial\overline{u}}{\partial\overline{r}}\Big)\\ &+\frac{2\mu(\overline{r})}{\overline{r}}\Big[\frac{\partial\overline{u}}{\partial\overline{r}}-\frac{\overline{u}}{\overline{r}}\Big]\\ &+\frac{\partial}{\partial\overline{z}}\Big(\mu(\overline{r})\ \Big(\frac{\partial\overline{u}}{\partial\overline{z}}+\frac{\partial\overline{w}}{\partial\overline{r}}\Big)\Big)\end{aligned} \tag{5}$$

$$\begin{aligned}\rho\Big[\overline{u}\frac{\partial\overline{w}}{\partial\overline{r}}+\overline{w}\frac{\partial\overline{w}}{\partial\overline{z}}\Big]= &-\frac{\partial\overline{p}}{\partial\overline{z}}+\frac{\partial}{\partial\overline{z}}\Big(2\mu(\overline{r})\ \frac{\partial\overline{w}}{\partial\overline{z}}\Big)\\ &+\frac{1}{\overline{r}}\frac{\partial}{\partial\overline{r}}\Big(\overline{r}\mu(\overline{r})\ \Big(\frac{\partial\overline{u}}{\partial\overline{z}}+\frac{\partial\overline{w}}{\partial\overline{r}}\Big)\Big)\\ &-\sigma B_0^2(\overline{w}+c)\end{aligned} \tag{6}$$

where $\overline{u}$ and $\overline{w}$ are the velocity components in the $\overline{r}$ and $\overline{z}$ directions, respectively; ρ is the density; σ is the electrically conductivity of the fluid; and μ is the variable viscosity. The governing equations can be dimensionalized by the following non-dimensional parameters.

$$\begin{gathered}r=\frac{\overline{r}}{a_2},\ z=\frac{\overline{z}}{\lambda},\ w=\frac{\overline{w}}{c},\ u=\frac{\lambda\overline{u}}{a_2c},\ p=\frac{a_2^2\overline{p}}{\lambda c\mu},\ r_1=\frac{\overline{r}_1}{a_2},\ \delta=\frac{a_2}{\lambda}\\ r_2=\frac{\overline{r}_2}{a_2}=1+\varphi\cos(2\pi z),\ \mathrm{Re}=\frac{\rho ca_2}{\mu},\ M=\sqrt{\frac{\sigma}{\mu}}B_0a_2\end{gathered} \tag{7}$$

where ϕ is the amplitude ratio, Re is the Reynolds number, δ is the dimensionless wave number, and M is the magnetic parameter.

Using the above non-dimensional parameters in Equations (4)–(6), the following system of equations is obtained.

$$\frac{1}{r}\frac{\partial(ru)}{\partial r}+\frac{\partial w}{\partial z}=0 \tag{8}$$

$$\begin{aligned}\mathrm{Re}\delta^3\Big[u\frac{\partial u}{\partial r}+w\frac{\partial u}{\partial z}\Big]= &-\frac{\partial p}{\partial r}+\delta^2\frac{\partial}{\partial r}\Big(2\mu(r)\ \frac{\partial u}{\partial r}\Big)+\delta^2\Big(\frac{2\mu(r)}{r}\Big(\frac{\partial u}{\partial r}-\frac{u}{r}\Big)\Big)\\ &+\delta^2\Big(\frac{\partial}{\partial z}\Big(\mu(r)\ \Big(\frac{\partial u}{\partial z}\delta^2+\frac{\partial w}{\partial r}\Big)\Big)\Big)\end{aligned} \tag{9}$$

$$\begin{aligned}\delta\mathrm{Re}\Big[u\frac{\partial w}{\partial r}+w\frac{\partial w}{\partial z}\Big]=&-\frac{\partial p}{\partial z}+\delta^2\frac{\partial}{\partial z}\Big(2\mu(r)\ \frac{\partial w}{\partial z}\Big)\\ &+\frac{1}{r}\frac{\partial}{\partial r}\Big(r\mu(r)\ \Big(\frac{\partial u}{\partial z}\delta^2+\frac{\partial w}{\partial r}\Big)\Big)-M^2w\end{aligned} \tag{10}$$

Using the long wavelength approximation and dropping terms of order δ and higher, the above equations reduce to

$$\frac{\partial p}{\partial r}=0 \tag{11}$$

$$\frac{1}{r}\frac{\partial}{\partial r}\Big(r\mu(r)\ \frac{\partial w}{\partial r}\Big)=\frac{\partial p}{\partial z}+M^2w \tag{12}$$

The relevant boundary conditions in new parameters are

$$\begin{aligned}w=-1\quad at\quad r=r_1\\ w=-1\quad at\quad r=r_2\end{aligned} \tag{13}$$

3. Solution by Adomian Decomposition Method

In this section, the Adomian solution is determined for the velocity field. According to the Adomian decomposition method, Equation (12) can be written in the operator form as

$$L_rw=\frac{\mathrm{d}p}{\mathrm{d}z}+M^2w \tag{14}$$

where the differential operator L_r is defined in the form

$$L_r = \frac{1}{r}\frac{\partial}{\partial r}\left(r\mu(r)\,\frac{\partial}{\partial r}\right) \tag{15}$$

and the inverse operator L_r^{-1} is defined by

$$L_r^{-1}(.) = \int\left[\frac{1}{r\mu(r)}\int r(.)\,\mathrm{d}r\right]\mathrm{d}r \tag{16}$$

Applying the inverse operator, Equation (12) takes the form

$$\begin{array}{c} w(r,\,z) = L_r^{-1}\left[\frac{\mathrm{d}p}{\mathrm{d}z} + M^2 w\right] + c_1 r + c_2 \\ w(r,\,z) = \frac{\mathrm{d}p}{\mathrm{d}z} I(r) + L_r^{-1}\left(M^2 w\right) + c_1 r + c_2 \end{array} \tag{17}$$

in which

$$L_r^{-1}\left(\frac{\mathrm{d}p}{\mathrm{d}z}\right) = \int\left[\frac{1}{r\mu(r)}\int r\left(\frac{\mathrm{d}p}{\mathrm{d}z}\right)\mathrm{d}r\right]\mathrm{d}r = \frac{\mathrm{d}p}{\mathrm{d}z} I(r) \tag{17a}$$

and $I(r)$ is given by

$$I(r) = \int \frac{r}{2\mu(r)}\mathrm{d}r \tag{18}$$

According to Adomian decomposition, it can be written as

$$w = \sum_{n=0}^{\infty} w_n \tag{19}$$

Using the Adomian decomposition method, the solution $w(r,\,z)$ can be elegantly computed by the recurrence relation

$$\begin{array}{rcl} w_0 & = & c_1 r + c_2 \\ w_1 & = & \frac{\mathrm{d}p}{\mathrm{d}z} I(r) + M^2 L_r^{-1}(w_0) \\ w_{n+2} & = & M^2 L_r^{-1}(w_{n+1}),\ n \geq 0 \end{array} \tag{20}$$

The above equations give

$$w_n = M^{2n-2}\left(\frac{\mathrm{d}p}{\mathrm{d}z} + M^2 c_2\right)\left(L_r^{-1}\right)^{n-1} I(r) + M^{2n} c_1 \left(L_r^{-1}\right)^{n-1} I_1(r),\ n \geq 1 \tag{21}$$

in which

$$I_1(r) = \int \frac{r^2}{3\mu(r)}\mathrm{d}r \tag{22}$$

With the help of Equations (20) and (21), the closed form of w can be written as

$$\begin{array}{c} w(r,\,z) = w_0 + \sum\limits_{n=1}^{\infty} w_n \\ w(r,\,z) = c_1\chi(r) + c_2\chi_1(r) + \frac{\mathrm{d}p}{\mathrm{d}z}\chi_2(r) \end{array} \tag{23}$$

Using the boundary conditions (13), the values of constants c_1 and c_2 can be written as

$$\begin{array}{l} c_1 = \frac{\chi_1(r_1) - \chi_1(r_2)}{\chi(r_1)\,\chi_1(r_2) - \chi(r_2)\,\chi_1(r_1)} - \frac{\mathrm{d}p}{\mathrm{d}z}\left[\frac{\chi_2(r_1)\,\chi_1(r_2) - \chi_2(r_2)\,\chi_1(r_1)}{\chi(r_1)\,\chi_1(r_2) - \chi(r_2)\,\chi_1(r_1)}\right] \\ c_2 = -\frac{1}{\chi_1(r_2)} - \frac{\mathrm{d}p}{\mathrm{d}z}\frac{\chi_2(r_2)}{\chi_1(r_2)} - c_1\frac{\chi(r_2)}{\chi_1(r_2)} \end{array} \tag{24}$$

where these χ_s' are defined in Appendix A.

The closed form solution (13) is represented in terms of integrals for any kind of general variable viscosity. These integrals can be computed for particular values of variable viscosity μ. Here, three cases of variable viscosity are taken into account, $\mu(r) = 1, r$, and $\frac{1}{r}$.

3.1. Case 1 (When μ = 1)

With the help of Equations (16), (18) and (22), the following are obtained:

$$I(r) = \frac{r}{2}\mathrm{d}r = \frac{r^2}{4} \tag{25}$$

$$\left(L_r^{-1}\right)^n I(r) = \frac{\left(\frac{r}{2}\right)^{2n+2}}{[(n+1)!]^2},\ n \geq 1,\ 2,\ 3,\ldots \tag{26}$$

$$\left(L_r^{-1}\right)^n I(r) = \frac{\left(\frac{r}{2}\right)^{2n+2}}{[(n+1)!]^2},\ n \geq 1,\ 2,\ 3,\ldots \tag{27}$$

$$I_1(r) = \int \frac{r^2}{3}\mathrm{d}r = \frac{r^3}{3^2},$$

$$\left(L_r^{-1}\right)^n I_1(r) = \sum_{n=0}^{\infty} \frac{r^{2n+3}}{3^2.5^2.7^2\ldots.(2n+3)^2} \tag{28}$$

The closed form of $w(r,\ z)$ can be written as

$$w(r,\ z) = c_1\chi_3(r) + c_2 I_0(Mr) + \frac{1}{M^2}\frac{\mathrm{d}p}{\mathrm{d}z}(-1 + I_0(Mr)) \tag{29}$$

Using boundary conditions (13), the solution of (29) can be written as

$$w(r,\ z) = a_{14}\chi_3(r) + a_{15}I_0(Mr) + \frac{1}{M^2}\frac{\mathrm{d}p}{\mathrm{d}z}\left(-1 - a_{15}I_0(Mr) - a_{14}\chi_3(r)\right) \tag{30}$$

The constants appearing in the above equations are defined in the equations and I_0 are the modified Bessel functions, with the first kind of order 0.

3.1.1. Volume Flow Rate and Pressure Rise

The instantaneous volume flow rate $\overline{Q}(z)$ is given by

$$\overline{Q}(z) = \int_{r_1}^{r_2} rw(r,\ z)\ \mathrm{d}r = \frac{\mathrm{d}p}{\mathrm{d}z}a_{22} + a_{20} + a_{21} \tag{31}$$

From Equation (31), the following is obtained:

$$\frac{\mathrm{d}p}{\mathrm{d}z} = \frac{1}{a_{22}}\left(\overline{Q}(z) - a_{20} - a_{21}\right) \tag{32}$$

The volume flow Q over a period is obtained as

$$Q = \overline{Q}(z) + \left(1 + \frac{\varphi^2}{2}\right) - r_1^2 \tag{33}$$

and

$$\frac{\mathrm{d}p}{\mathrm{d}z} = \frac{1}{a_{22}}\left(Q - \left(1 + \frac{\varphi^2}{2}\right) + r_1^2 - a_{20} - a_{21}\right) \tag{34}$$

The pressure rise Δp and the friction force (at the wall) on the outer and inner tubes are $F^{(0)}$ and $F^{(1)}$, respectively, are

$$\Delta p = \int_0^1 \frac{\mathrm{d}p}{\mathrm{d}z}\mathrm{d}z \tag{35}$$

$$\begin{aligned} F^{(0)} &= \int_0^1 r_2^2\left(-\tfrac{\mathrm{d}p}{\mathrm{d}z}\right)\mathrm{d}z \\ F^{(1)} &= \int_0^1 r_1^2\left(-\tfrac{\mathrm{d}p}{\mathrm{d}z}\right)\mathrm{d}z \end{aligned} \tag{36}$$

3.1.2. Stream Function

The corresponding stream function $\left(u = -\frac{1}{r}\frac{\partial \Psi}{\partial z}\right.$ and $\left. w = \frac{1}{r}\frac{\partial \Psi}{\partial r}\right)$ can be written as

$$\Psi = a_{14}g(r) - \frac{1}{M^2}\frac{\mathrm{d}p}{\mathrm{d}z}\left(a_{14}g(r) + \frac{r^2}{2} + a_{15}\frac{r}{M}I_1(Mr)\right) + a_{15}\frac{r}{M}I_1(Mr) \tag{37}$$

where the constants appears in the above equations are defined in Appendix A; I_1 is a modified Bessel functions of the first order; and a_{14}, a_{15} are defined in Appendix A.

3.2. Case 2 (When $\mu = r$)

Using Equations (16), (18), and (22), the following is implied for $\mu = r$:

$$I(r) = \int \frac{r}{2.r}\mathrm{d}r = \frac{r}{2!} \tag{38}$$

$$\left(L_r^{-1}\right)^n I(r) = \sum_{n=0}^{\infty} \frac{r^{n+1}}{(n+2)!(1.2.3.4\ldots.(n+1))} \tag{39}$$

$$I_1(r) = \int \frac{r^2}{3.r}\mathrm{d}r = \frac{r^2}{3!} \tag{40}$$

$$\left(L_r^{-1}\right)^n I_1(r) = \frac{r^2}{3!} + \sum_{n=1}^{\infty} \frac{r^{n+2}}{(n+3)!(3.4.5\ldots.(n+2))} \tag{41}$$

With the help of these values, and using boundary conditions, the closed form of $w(r, z)$ can be written as

$$w(r, z) = b_{14}\chi_4(r) + b_{18}\chi_5(r) + \frac{\mathrm{d}p}{\mathrm{d}z}\left(\chi_6(r) + b_{19}\chi_5(r) - b_{15}\chi_4(r)\right) \tag{42}$$

The constants appearing in the above equations are defined in Appendix A.

3.2.1. Volume Flow Rate and Pressure Rise

The instantaneous volume flow rate $\overline{Q}(z)$ is given by

$$\overline{Q}(z) = \frac{\mathrm{d}p}{\mathrm{d}z}b_{29} + b_{27} + b_{25} \tag{43}$$

The volume flow rate and the pressure gradient can be calculated as

$$Q = \overline{Q}(z) + \left(1 + \frac{\varphi^2}{2}\right) - r_1^2 \tag{44}$$

The pressure rise Δp and the friction force (at the wall) on the outer and inner tubes $F^{(0)}$ and $F^{(1)}$ can be computed using (35) and (36).

$$\frac{dp}{dz} = \frac{1}{b_{29}}\left(Q - \left(1 + \frac{\varphi^2}{2}\right) + r_1^2 - b_{25} - b_{27}\right) \tag{45}$$

The constants appearing in the above equations are defined in Appendix A

3.2.2. Stream Function

Stream function, in this case, is defined as

$$\Psi = b_{14}g_0(r) + b_{18}g_1(r) + \frac{dp}{dz}(g_2(r) + b_{19}g_1(r) - b_{15}g_0(r)) \tag{46}$$

3.3. Case 3 (When $\mu = \frac{1}{r}$)

Using the similar procedure as discussed in previous sections, it can be written as

$$w(r,\, z) = d_{16}\chi_7(r) + d_{18}\chi_8(r) + \frac{dp}{dz}\left(\chi_9(r) + d_{19}\chi_8(r) - d_{17}\chi_7(r)\right) \tag{47}$$

The constants appearing in the above equations are defined in Appendix A.

3.3.1. Volume Flow Rate and Pressure Rise

The instantaneous volume flow rate $\overline{Q}(z)$ is given by

$$\overline{Q}(z) = \frac{dp}{dz}d_{27} + d_{26} + d_{25} \tag{48}$$

The volume flow Q over a period is obtained as

$$Q = \overline{Q}(z) + \left(1 + \frac{\varphi^2}{2}\right) - r_1^2 \tag{49}$$

The pressure rise Δp and the friction force $F^{(0)}$ and $F^{(1)}$ can be computed using (35) and (36).

$$\frac{dp}{dz} = \frac{1}{d_{27}}\left(Q - \left(1 + \frac{\varphi^2}{2}\right) + r_1^2 - d_{25} - d_{26}\right) \tag{50}$$

3.3.2. Stream Function

Stream function for this case is

$$\Psi = d_{16}h(r) + d_{18}h_1(r) + \frac{dp}{dz}(h_2(r) + h_1(r)d_{19} - h(r)\, d_{17}) \tag{51}$$

The constants appearing in the above equations are defined in Appendix A.

4. Results and Discussion

The objective of the current analysis is to present the closed form solutions of MHD Newtonian fluid with variable viscosity. The expression for pressure rise per wavelength and frictional forces are difficult to integrate analytically; therefore, numerical integration is used to evaluate the integrals. Figures 2–4 are plotted for pressure rise and friction force against flow rate Q when viscosity is constant. In Figure 2, it is observed that pressure rise increases with an increase of M up to $Q < 1.7$, after which the curves intersect each other and, finally, it gives an opposite behavior. The effects M on $F^{(0)}$(for outer tube) and $F^{(1)}$ (for inner tube) are presented in Figures 3 and 4. It is depicted from Figures 3

and 4 that with an increase in M, both $F^{(0)}$ and $F^{(1)}$ decrease M for small Q and, finally, the behavior is reversed at the end. A comparison of the velocity field for constant viscosity case is made between the Adomian decomposition solution and perturbation solutions obtained by [6]. (see Figure 5). Figures 6–9 are prepared when (viscosity) $\mu = r$. It is observed from Figure 6 that in the retrograde $(\Delta p > 0,\ Q < 0)$ and peristaltic pumping $(\Delta p > 0,\ Q > 0)$ regions, the pressure rise decreases with an increase in amplitude ratio φ. Figures 7 and 8 show that $F^{(0)}$ and $F^{(1)}$ give an opposite behavior as compared with Δp. The velocity field increases with the increase in M and the maximum value of the velocity is at the center (see Figure 9). Figures 10–13 are prepared when the viscosity $\mu = \frac{1}{r}$. It is observed from Figure 10 that with an increase in r_1, the pressure rise decreases in the retrograde $(\Delta p > 0,\ Q < 0)$, peristaltic pumping $(\Delta p > 0,\ Q > 0)$, and copuming $(\Delta p < 0,\ Q > 0)$ regions. It is depicted from Figures 11 and 12 that with an increase in r_1, both $F^{(0)}$ and $F^{(1)}$ decrease for small Q and, finally, the behavior is reversed at the end. The velocity profile for different values of M for the case when viscosity is $\mu = \frac{1}{r}$ is shown in Figure 13. It is observed from Figure 13 that the magnitude value of the velocity profile decreases with an increase in M.

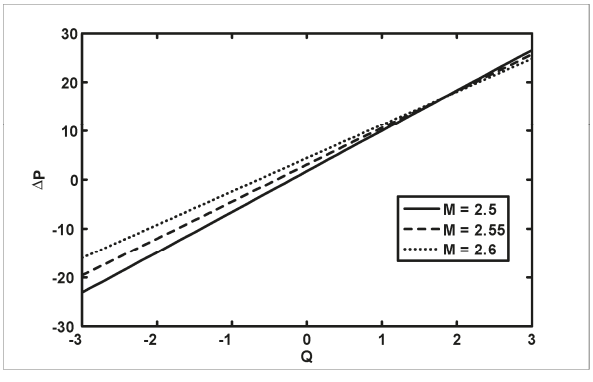

Figure 2. The variation of Δp with Q for different values of M at $r_1 = 0.4,\ \varphi = 0.4$, when $\mu = 1$.

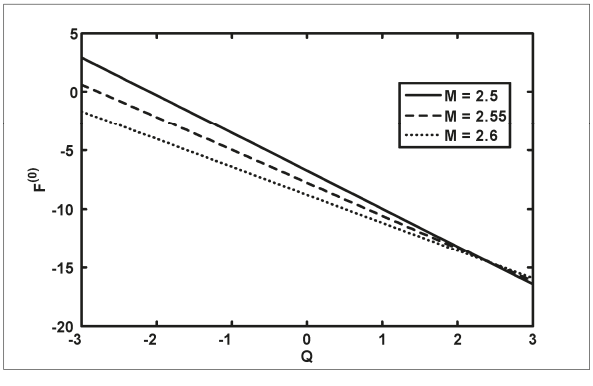

Figure 3. The variation of friction force $F^{(0)}$ (outer tube) with Q for different values of M at $r_1 = 0.4, \varphi = 0.4$, when $\mu = 1$.

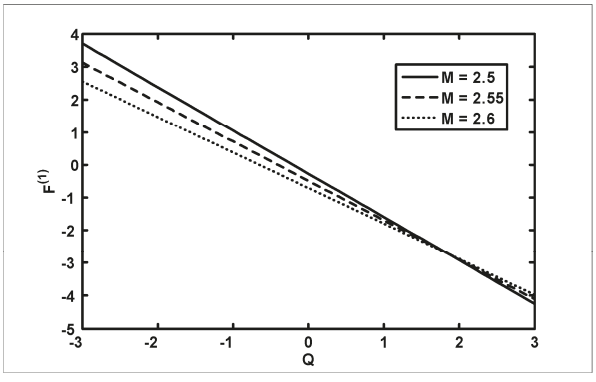

Figure 4. The variation of friction force $F^{(1)}$ (inner tube) with Q for different values of M at $r_1 = 0.4, \phi = 0.4$, when $\mu = 1$.

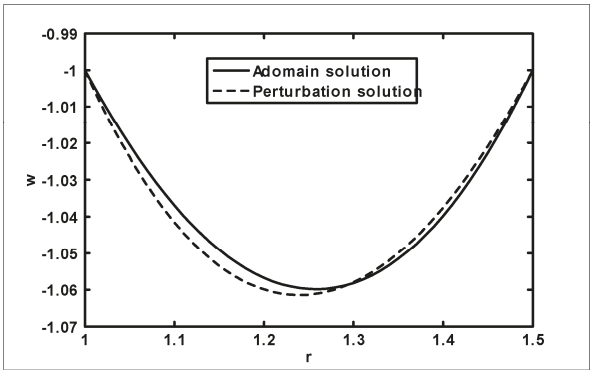

Figure 5. Comparison with the existing literature.

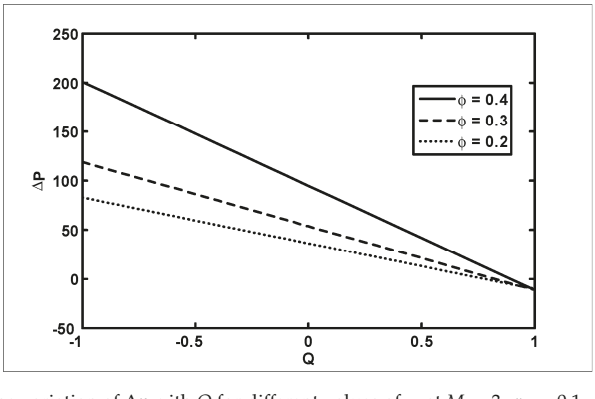

Figure 6. The variation of Δp with Q for different values of φ at $M = 3$, $r_1 = 0.1$, when $\mu = r$.

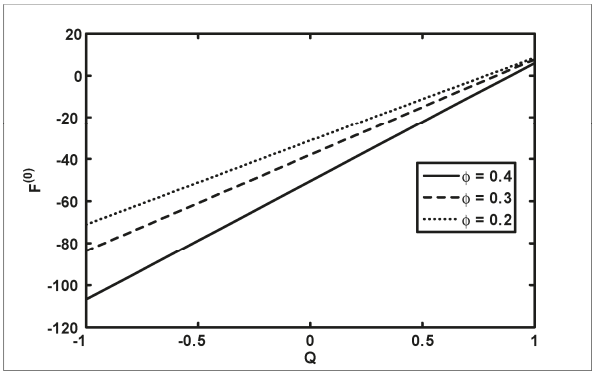

Figure 7. The variation of friction force $F^{(0)}$ (outer tube) with Q for different values of ϕ at $r_1 = 0.1, M = 3$, when $\mu = r$.

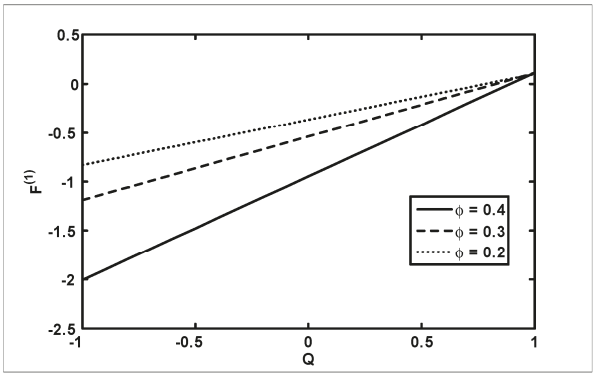

Figure 8. The variation of friction force $F^{(1)}$ (inner tube) with Q for different values of φ at $r_1 = 0.1, M = 3$, when $\mu = r$.

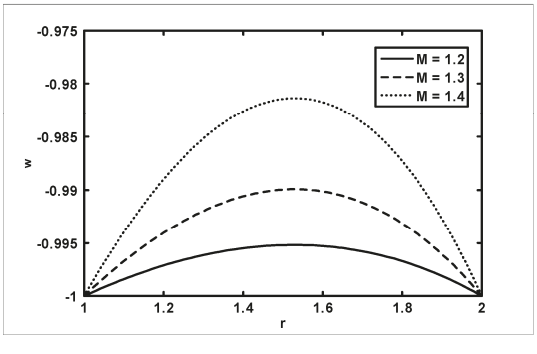

Figure 9. Velocity profiles for different values of M at $t = 1$, $z = 1, \varphi = 1$, when $\mu = r$.

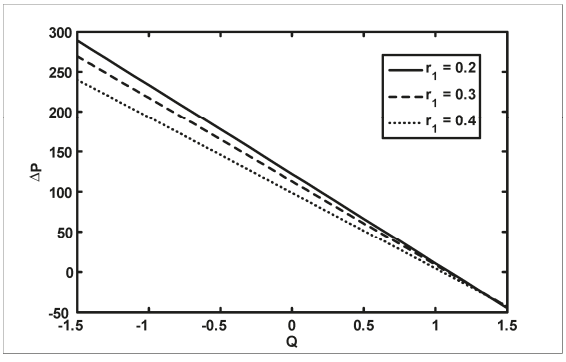

Figure 10. The variation of Δp with Q for different values of r_1 at $M = 3,\ \varphi = 0.4$, when $\mu = \frac{1}{r}$.

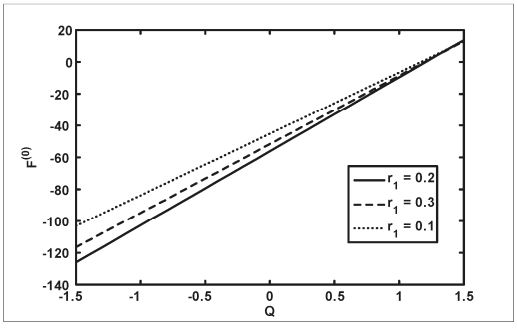

Figure 11. The variation of friction force $F^{(0)}$ (outer tube) with Q for different values of r_1 at $\varphi = 0.4,\ M = 3$, when $\mu = \frac{1}{r}$.

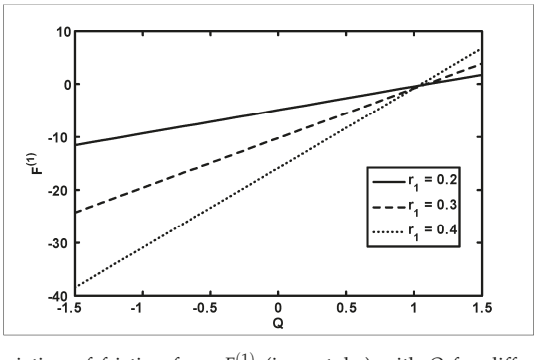

Figure 12. The variation of friction force $F^{(1)}$ (inner tube) with Q for different values of r_1 at $\varphi = 0.4,\ M = 3$, when $\mu = \frac{1}{r}$.

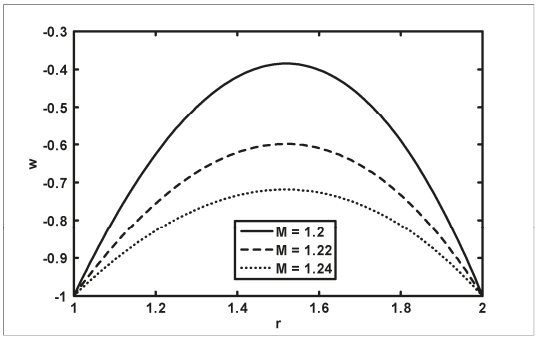

Figure 13. Velocity profiles for different values of M at $t = 1,\ z = 1,\ \varphi = 1$, when $\mu = \frac{1}{r}$.

Trapping Phenomenon

The trapping phenomenon is an interesting phenomenon in peristaltic motion, which is discussed in Figures 14–18 for the case when $\mu = 1$, $\mu = r$, and $\mu = \frac{1}{r}$. Stream lines for different values of φ for the case when $\mu = 1$ are shown in Figure 14. It is observed from Figure 6 that with an increase in amplitude ratio φ, the size of the trapping bolus increases. Stream lines for different values of M and φ for the case when $\mu = r$ are shown in Figures 15 and 16. It is observed from Figure 15 that the size of the trapping bolus decreases with an increase in Hartmann number M. The size of the trapping bolus increases with an increase in amplitude ratio φ (see Figure 16). Stream lines for different values of M and φ for the case when $\mu = \frac{1}{r}$ are shown in Figures 17 and 18. It is observed from the Figures that the size of the trapping bolus increases with an increase in Hartmann number M and amplitude ratio φ.

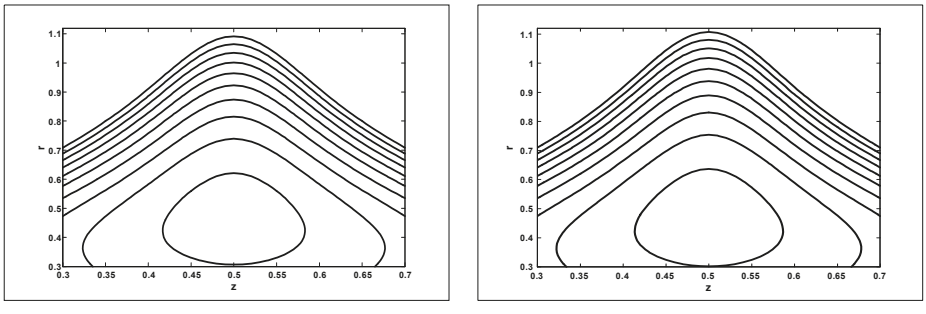

(a) (b)

Figure 14. Streamlines for two different values of φ for (**a**) $\varphi = 0.1$ and (**b**) $\varphi = 0.101$. The other parameters are chosen as $M = 2$, $Q = 0.41$, $r_1 = 0.65$ when $\mu = 1$.

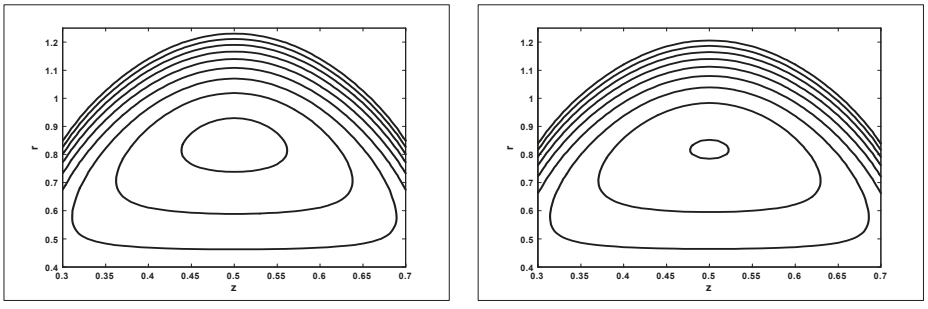

(a) (b)

Figure 15. Streamlines for two different values of M for (**a**) $M = 1$ and (**b**) $M = 0.6$. The other parameters are chosen as $\varphi = 0.2$, $Q = 0.45$, $r_1 = 1$ when $\mu = r$.

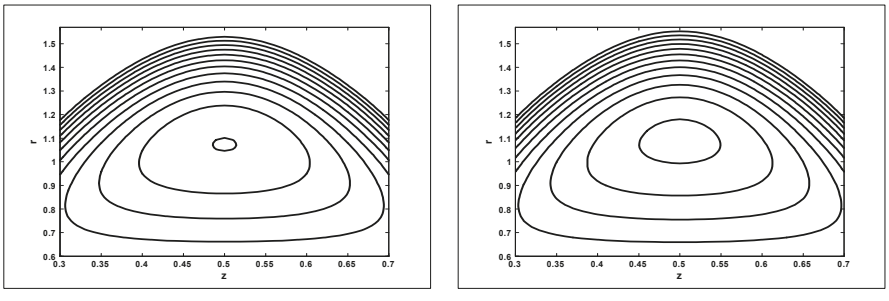

(a) (b)

Figure 16. Streamlines for two different values of φ for (**a**) $\varphi = 0.29$ and (**b**) $\varphi = 0.3$. The other parameters are chosen as $M = 1$, $Q = 0.45$, $r_1 = 1.1$ when $\mu = r$.

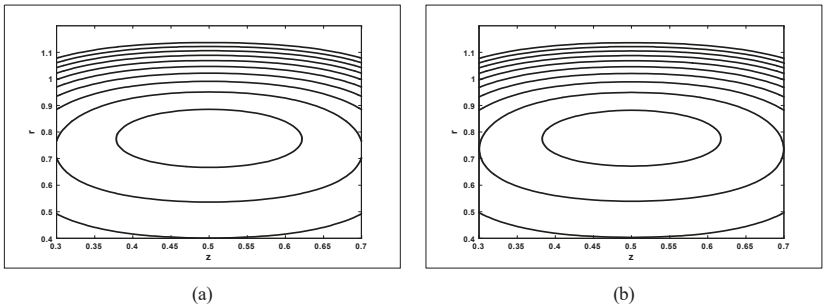

(a) (b)

Figure 17. Streamlines for two different values of M for (**a**) $M = 0.2$ and (**b**) $M = 0.1$. The other parameters are chosen as $\varphi = 0.1$, $Q = 0.4$, $r_1 = 1.1$ when $\mu = \frac{1}{r}$.

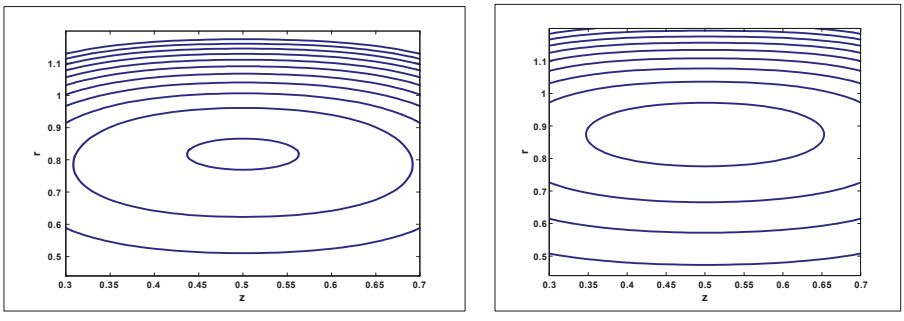

(a) (b)

Figure 18. Streamlines for two different values of r_1 for (**a**) $r_1 = 1.11$ and (**b**) $r_1 = 1.13$. The other parameters are chosen as $M = 0.2$, $Q = 0.4$, $\varphi = 0.1$ when $\mu = \frac{1}{r}$.

5. Conclusions

In the present analysis, peristaltic flow was discussed for MHD Newtonian fluid through the gap between two coaxial tubes, where the fluid viscosity was treated as variable. In addition, the inner tube was considered to be at rest, while the outer tube has the sinusoidal wave travelling down its motion. Further, the governing equations are simplified under the assumptions of long wavelength and low Reynolds number. The solution of the problem under discussion is computed analytically using the Adomian decomposition method. The results of the proposed problem are discussed through graphs. The main findings are summarized as follows:

- It was found that the pressure rise increases with an increase in Hartmann number M and frictional forces for the outer $F^{(0)}$ and inner tube $F^{(1)}$ decreases with an increase in M when viscosity $\mu = 1$.
- It was also found that the pressure rise decreases with an increase in amplitude ratio φ in the retrograde $(\Delta p > 0,\ Q < 0)$ and peristaltic pumping $(\Delta p > 0,\ Q > 0)$ regions and frictional forces give opposite behavior as compared with pressure rise when viscosity $\mu = r$.
- The pressure rise decreases in the retrograde $(\Delta p > 0,\ Q < 0)$, peristaltic pumping $(\Delta p > 0,\ Q > 0)$ and copuming $(\Delta p < 0,\ Q > 0)$ regions with an increase in r_1, and frictional forces decrease for small values of volume flow rate Q with an increase in r_1 when viscosity $\mu = \frac{1}{r}$.
- It was also noticed that the size of the trapping bolus increases with an increase in amplitude ratio φ when viscosity $\mu = 1$, while it increases with an increase in Hartmann number M and amplitude ratio φ when viscosity $\mu = \frac{1}{r}$. However, it decreases with an increase in Hartmann number M and increases with an increase in amplitude ratio φ when viscosity $\mu = r$.

Author Contributions: Conceptualization, S.A. and E.H.A.; Methodology, S.A. and F.A.; Software, S.A. and E.H.A., F.A.; Validation, S.A., F.A. and S.N.; Formal Analysis, E.H.A.; Investigation, S.A.; Resources, S.N.; Data Curation: F.A.; Writing—Original Draft Preparation, S.A.; Writing—Review and Editing: S.A. and F.A.; Visualization, E.H.A.; Supervision, S.N.; Project Administration, S.A. and F.A.; Funding Acquisition, S.A. and F.A.

Funding: This research received no external funding.

Conflicts of Interest: The authors declare no conflict of interest.

Nomenclature

a_1 and a_2	radii of the inner and the outer tubes
b	amplitude of the wave
λ	wavelength
c	propagation velocity
$\bar{t}$	Time

$(\overline{u},\ \overline{w})$	velocity components in radial and axial directions in moving coordinates
$\left(\overline{U},\ \overline{W}\right)$	velocity components in radial and axial directions in fixed coordinates
ρ	density
σ	electrically conductivity of the fluid
μ	variable viscosity
φ	amplitude ratio
Re	Reynolds number
δ	dimensionless wave number
M	magnetic parameter
Q	volume flow rate
a'_s and χ'_s	constants used to simplify the problem

Appendix A

$$\chi(r_1) = \left[r + \sum_{n=0}^{\infty} M^{2n+2}\left(L_r^{-1}\right)^n I_1(r)\right]_{r=r_1},$$

$$\chi(r_2) = \left[r + \sum_{n=0}^{\infty} M^{2n+2}\left(L_r^{-1}\right)^n I_1(r)\right]_{r=r_2},$$

$$\chi_1(r_1) = \left[1 + \sum_{n=0}^{\infty} M^{2n+2}\left(L_r^{-1}\right)^n I(r)\right]_{r=r_1},$$

$$\chi_1(r_2) = \left[1 + \sum_{n=0}^{\infty} M^{2n+2}\left(L_r^{-1}\right)^n I(r)\right]_{r=r_2},$$

$$\chi_2(r_1) = \left[\sum_{n=0}^{\infty} M^{2n}\left(L_r^{-1}\right)^n I(r)\right]_{r=r_1},$$

$$\chi_2(r_2) = \left[\sum_{n=0}^{\infty} M^{2n}\left(L_r^{-1}\right)^n I(r)\right]_{r=r_2},$$

$$\chi_3(r_1) = \left[r + \sum_{n=0}^{\infty} M^{2n+2}\frac{r^{2n+3}}{3^2.5^2.7^2....(2n+3)^2}\right]_{r=r_1},$$

$$\chi_3(r_2) = \left[r + \sum_{n=0}^{\infty} M^{2n+2}\frac{r^{2n+3}}{3^2.5^2.7^2....(2n+3)^2}\right]_{r=r_2},$$

$$\chi_4(r_1) = \left[r + M^2\frac{r^2}{3!} + \sum_{n=1}^{\infty} M^{2n+2}\frac{r^{n+2}}{(n+3)!(3.4.5....(n+2))}\right]_{r=r_1},$$

$$\chi_4(r_2) = \left[r + M^2\frac{r^2}{3!} + \sum_{n=1}^{\infty} M^{2n+2}\frac{r^{n+2}}{(n+3)!(3.4.5....(n+2))}\right]_{r=r_2},$$

$$\chi_5(r_1) = \left[1 + \sum_{n=0}^{\infty} M^{2n+2}\frac{r^{n+1}}{(n+2)!(1.2.3.4....(n+1))}\right]_{r=r_1},$$

$$\chi_5(r_2) = \left[1 + \sum_{n=0}^{\infty} M^{2n+2}\frac{r^{n+1}}{(n+2)!(1.2.3.4....(n+1))}\right]_{r=r_2},$$

$$\chi_6(r_1) = \left[\sum_{n=0}^{\infty} M^{2n}\frac{r^{n+1}}{(n+2)!(1.2.3.4....(n+1))}\right]_{r=r_1},$$

$$\chi_6(r_2) = \left[\sum_{n=0}^{\infty} M^{2n}\frac{r^{n+1}}{(n+2)!(1.2.3.4....(n+1))}\right]_{r=r_2},$$

$$\chi_7(r_1) = \left[r + \sum_{n=0}^{\infty} M^{2n+2}\frac{r^{3n+4}}{12.42.90....(3n+3)\ (3n+4)}\right]_{r=r_1},$$

$$\chi_7(r_2) = \left[r + \sum_{n=0}^{\infty} M^{2n+2}\frac{r^{3n+4}}{12.42.90....(3n+3)\ (3n+4)}\right]_{r=r_2},$$

$$\chi_8(r_1) = \left[1 + M^2\frac{r^3}{3!} + \sum_{n=1}^{\infty} M^{2n+2}\frac{r^{3n+3}}{3!(30.72.132....(3n+3)\ (3n+2))}\right]_{r=r_1},$$

$$\chi_8(r_2) = \left[1 + M^2\frac{r^3}{3!} + \sum_{n=1}^{\infty} M^{2n+2}\frac{r^{3n+3}}{3!(30.72.132....(3n+3)\ (3n+2))}\right]_{r=r_2},$$

$$\chi_9(r_1)=\left[\frac{r^3}{3!}+\sum_{n=1}^{\infty}M^{2n}\frac{r^{3n+3}}{3!(30.72.132....(3n+3)\ (3n+2))}\right]_{r=r_1},$$

$$\chi_9(r_2)=\left[\frac{r^3}{3!}+\sum_{n=1}^{\infty}M^{2n}\frac{r^{3n+3}}{3!(30.72.132....(3n+3)\ (3n+2))}\right]_{r=r_2},$$

$$g(r)=\frac{r^3}{3}+\sum_{n=0}^{\infty}\frac{\left(M^{2n+2}r^{2n+5}\right)}{(2n+5)\ \left(3^2.5^2.7^2...(2n+3)^2\right)},$$

$$g_0(r)=\frac{r^3}{3}+\frac{M^2r^4}{4!}+\sum_{n=1}^{\infty}\frac{M^{2n+2}r^{n+4}}{(n+4)\ (n+3)!(3.4.5...(n+2))},$$

$$g_0(r)=\frac{r^3}{3}+\frac{M^2r^4}{4!}+\sum_{n=1}^{\infty}\frac{M^{2n+2}r^{n+4}}{(n+4)\ (n+3)!(3.4.5...(n+2))},$$

$$g_1(r)=\frac{r^2}{2}+\sum_{n=0}^{\infty}\frac{M^{2n+2}r^{n+3}}{(n+3)\ (n+2)!(1.2.3.4...(n+1))},$$

$$g_2(r)=\sum_{n=0}^{\infty}\frac{M^{2n}r^{n+3}}{(n+3)\ (n+2)!(1.2.3.4...(n+1))},$$

$$h(r)=\frac{r^3}{3}+\sum_{n=0}^{\infty}\frac{M^{2n+2}r^{3n+6}}{(3n+6)\ (12.42.90...(3n+3)\ (3n+4))},$$

$$h_1(r)=\frac{r^2}{2}+\frac{M^2r^5}{3!5}+\sum_{n=1}^{\infty}\frac{M^{2n+2}r^{3n+5}}{(3n+5)\ 3!(30.72.132...(3n+3)\ (3n+2))},$$

$$h_2(r)=\frac{r^5}{3!}+\sum_{n=1}^{\infty}\frac{M^{2n}r^{3n+5}}{(3n+5)\ 3!(30.72.132...(3n+3)\ (3n+2))},$$

$$a_{11}=I_0(Mr_1)-I_0(Mr_2),\ a_{12}=\chi_3(r_1)I_0(Mr_2)-\chi_3(r_2)I_0(Mr_1),$$

$$a_{13}=\chi_3(r_2)-\chi_3(r_1),\ a_{14}=\frac{a_{11}}{a_{12}},\ a_{15}=\frac{a_{13}}{a_{12}},\ a_{16}=\frac{r_2^3-r_1^3}{3},$$

$$a_{17}=\sum_{n=0}^{\infty}M^{2n+2}\frac{\left(r_2^{2n+5}-r_1^{2n+5}\right)}{(2n+5)\ \left(3^2.5^2.7^2....(2n+3)^2\right)},$$

$$a_{18}=\frac{r_2I_1(Mr_2)-r_1I_1(Mr_1)}{M},\ a_{19}=\frac{r_2^2-r_1^2}{2},\ a_{20}=a_{14}(a_{16}+a_{17}),$$

$$a_{21}=a_{15}a_{18},\ a_{22}=-\frac{(a_{19}+a_{20}+a_{21})}{M^2},$$

$$b_{11}=\chi_5(r_1)-\chi_5(r_2),\ b_{12}=\chi_4(r_1)\ \chi_5(r_2)-\chi_4(r_2)\ \chi_5(r_1),$$

$$b_{13}=\chi_6(r_1)\ \chi_5(r_2)-\chi_6(r_2)\ \chi_5(r_1),\ b_{14}=\frac{b_{11}}{b_{12}},\ b_{15}=\frac{b_{13}}{b_{12}},$$

$$b_{16}=\chi_4(r_2)-\chi_4(r_1),\ b_{17}=\chi_6(r_1)\ \chi_4(r_2)-\chi_6(r_2)\ \chi_4(r_1),$$

$$b_{18}=\frac{b_{16}}{b_{12}},\ b_{19}=\frac{b_{17}}{b_{12}},\ b_{20}=\frac{M^2\left(r_2^4-r_1^4\right)}{4!},$$

$$b_{21}=\sum_{n=1}^{\infty}M^{2n+2}\frac{\left(r_2^{n+4}-r_1^{n+4}\right)}{(n+4)\ (n+3)!(3.4.5....(n+2))},$$

$$b_{22}=\sum_{n=0}^{\infty}M^{2n+2}\frac{\left(r_2^{n+3}-r_1^{n+3}\right)}{(n+3)\ (n+2)!(1.2.3.4...(n+1))},$$

$$b_{23}=a_{16}+b_{20}+b_{21},\ b_{24}=b_{22}+a_{19},\ b_{25}=b_{14}b_{23},$$

$$b_{27}=b_{18}b_{24},\ b_{28}=b_{19}b_{24},\ b_{29}=\frac{b_{22}}{M^2}+b_{28}-b_{26},$$

$$d_{11}=\chi_8(r_1)-\chi_8(r_2),\ d_{12}=\chi_8(r_2)\ \chi_7(r_1)-\chi_7(r_2)\ \chi_8(r_1),$$

$$d_{13}=\chi_9(r_1)\ \chi_8(r_2)-\chi_9(r_2)\ \chi_8(r_1),\ d_{14}=\chi_9(r_1)\ \chi_7(r_2)-\chi_9(r_2)\ \chi_7(r_1),$$

$$d_{15}=\chi_7(r_2)-\chi_7(r_1),\ d_{16}=\frac{d_{11}}{d_{12}},\ d_{17}=\frac{d_{13}}{d_{12}},\ d_{18}=\frac{d_{15}}{d_{12}},\ d_{19}=\frac{d_{14}}{d_{12}},$$

$$d_{20}=\sum_{n=0}^{\infty}M^{2n+2}\frac{\left(r_2^{3n+4}-r_1^{3n+4}\right)}{(3n+6)\ (12.42.90....(3n+3)\ (3n+4))},\ d_{21}=M^2\frac{\left(r_2^5-r_1^5\right)}{30},$$

$$d_{22}=\sum_{n=1}^{\infty}M^{2n+2}\frac{\left(r_2^{3n+5}-r_1^{3n+5}\right)}{(3n+5)\ 3!(30.72.132...(3n+3)\ (3n+2))},$$

$$d_{23}=a_{16}+d_{20},\ d_{24}=a_{19}+d_{21}+d_{22},\ d_{25}=d_{16}d_{23},$$

$$d_{26}=d_{18}d_{24},\ d_{27}=\frac{5}{M^2}d_{21}+\frac{d_{22}}{M^2}+d_{19}d_{24}-d_{17}d_{23}.$$

References

1. Abd El Naby, A.H.; El Misiery, A.E.M. Effects of an endoscope and generalized Newtonian fluid on peristaltic motion. *Appl. Math. Comput.* **2002**, *128*, 19–35. [CrossRef]

2. Mekheimer, K.S. Non-linear peristaltic transport of magneto-hydrodynamic flow in an inclined planar channel. *Arab. J. Sci. Eng.* **2003**, *28*, 183–202.
3. Elshahed, M.; Haroun, M.H. Peristaltic transport of Johnson-Segalman fluid under effect of a magnetic field. *Math. Probl. Eng.* **2005**, *6*, 663–677. [CrossRef]
4. Ellahi, R.; Bhatti, M.; Pop, I. Effects of hall and ion slip on MHD peristaltic flow of Jeffrey fluid in a non-uniform rectangular duct. *Int. J. Numer. Methods Heat Fluid Flow* **2016**, *26*, 1802–1820. [CrossRef]
5. Haroun, M.H. Effect of Deborah number and phase difference on peristaltic transport in an asymmetric channel. *Commun. Non-Linear Sci. Numer. Simul.* **2007**, *12*, 1464–1480. [CrossRef]
6. Mekheimer, K.S.; AbdElmaboud, Y. Influence of heat transfer and magnetic field on peristaltic transport of a Newtonian fluid in a vertical annulus. Application of an endoscope. *Phys. Lett. A* **2008**, *372*, 1657–1665. [CrossRef]
7. Ellahi, R.; Zeeshan, A.; Hussain, F.; Asadollahi, A. Peristaltic blood flow of couple stress fluid suspended with nanoparticles under the influence of chemical reaction and activation energy. *Symmetry* **2019**, *11*, 276. [CrossRef]
8. Nadeem, S.; Akram, S. Peristaltic transport of a hyperbolic tangent fluid model in an asymmetric channel. *Z. Nat. A* **2009**, *64*, 559–567. [CrossRef]
9. Ellahi, R.; RiazANadeem, S. A theoretical study of Prandtlnanofluid in a rectangular duct through peristaltic transport. *Appl. Nanosci.* **2014**, *4*, 753–760. [CrossRef]
10. Siddiqui, A.M.; Farooq, A.A.; Rana, M.A. Study of MHD effects on the cilia-induced flow of a Newtonian fluid through a cylindrical tube. *Magnetohydrodynamics* **2014**, *50*, 249–261.
11. Radhakrishnamacharya, G.; Murthy, V.R. Heat transfer to peristaltic transport in a non-uniform channel. *Def. Sci. J.* **1993**, *43*, 275–280. [CrossRef]
12. Radhakrishnamacharya, G.; Srinivasulu, C. Influence of wall properties on peristaltic transport with heat transfer. *C. R. Mec.* **2007**, *335*, 369–373. [CrossRef]
13. Prakash, J.; Tripathi, D.; Tiwari, A.K.; Sait, S.M.; Ellahi, R. Peristaltic Pumping of Nanofluids through a Tapered Channel in a Porous Environment: Applications in Blood Flow. *Symmetry* **2019**, *11*, 868. [CrossRef]
14. Shapiro, A.H.; Jaffrin, M.Y.; Weinberg, S.L. Peristaltic pumping with long wave length at low Reynolds number. *J. Fluid Mech.* **1969**, *37*, 799–825. [CrossRef]
15. Jaffrin, M.Y.; Shaprio, A.H. Peristaltic pumping. *Annu. Rev. Fluid Mech.* **1971**, *3*, 13–36. [CrossRef]
16. Eberhart, R.C.; Shitzer, A. *Heat Transfer in Medicine and Biology*, 1st ed.; Springer: Berlin/Heidelberg, Germany, 1985.
17. Pozrikidis, C. A study of peristaltic flow. *J. Fluid Mech.* **1987**, *180*, 515–527. [CrossRef]
18. Eytan, O.; Elad, D. Analysis of intra-uterine fluid motion induced by uterine contractions. *Bull. Math. Biol.* **1999**, *61*, 221–238. [CrossRef] [PubMed]
19. Riaz, A.; Al-Olayan, H.A.; Zeeshan, A.; Razaq, A.; Bhatti, M.M. Mass Transport with Asymmetric Peristaltic Propulsion Coated with Synovial Fluid. *Coatings* **2018**, *8*, 407. [CrossRef]
20. Abd El Naby, A.; El Misery, A.E.M.; El Shamy, I.I. Effects of an endoscope and fluid with variable viscosity on peristaltic motion. *Appl. Math. Comput.* **2004**, *158*, 497–511. [CrossRef]
21. Mekheimer, K.S.; AbdElmaboud, Y. Simultaneous effects of variable viscosity and thermal conductivity on peristaltic flow in a vertical asymmetric channel. *Can. J. Phys.* **2014**, *92*, 1541–1555. [CrossRef]
22. Husseny, S.Z.A.; AbdElmaboud, Y.; Mekheimer, K.S. The flow separation of peristaltic transport for Maxwell fluid between two coaxial tubes. *Abstr. Appl. Anal.* **2014**, *2014*, 269151. [CrossRef]
23. Adomian, G. *Non-Linear Stochastic Operator Equations*; Academic Press: Orlando, FL, USA, 1986.
24. Adomian, G. *Solving Frontier Problems of Physics: The Decomposition Method*; Kluwer Academic Publishers: Boston, MA, USA, 1994.
25. Eldabe, N.T.; Elghazy, E.M.; Ebaid, A. Closed form solution to a second order boundary value problem and its application in fluid mechanics. *Phys. Lett. A* **2007**, *363*, 257–259. [CrossRef]
26. Wazwaz, A.M. Exact solutions to nonlinear diffusion Equations obtained by the decomposition method. *Appl. Math. Comput.* **2001**, *123*, 109–122. [CrossRef]
27. Wazwaz, A.M. A new method for solving singular initial value problems in the second order ordinary differential Equations. *Appl. Math. Comput.* **2002**, *128*, 47–57. [CrossRef]
28. Wazwaz, A.M. *Partial Differential Equations, Method and Applications*; Balkema Publishers: Avereest, The Netherlands, 2002.

29. Wazwaz, A.M. Adomian decomposition method for a reliable treatment of the Emden-Fowler equationuation. *Appl. Math. Comput.* **2005**, *161*, 543–560.
30. AbdElmaboud, Y.; Mekheimer, K.S.; Abdelsalam, S.I. Study of nonlinear variable viscosity in finite-length tube with peristalsis. *Appl. Bionics Biomech.* **2014**, *11*, 197–206. [CrossRef]

coatings

MDPI

Article

Triple Local Similarity Solutions of Darcy-Forchheimer Magnetohydrodynamic (MHD) Flow of Micropolar Nanofluid Over an Exponential Shrinking Surface: Stability Analysis

Liaquat Ali Lund [1,2], Dennis Ling Chuan Ching [3], Zurni Omar [1], Ilyas Khan [4,*] and Kottakkaran Sooppy Nisar [5]

1 School of Quantitative Sciences, Universiti Utara Malaysia, Sintok 06010, Kedah, Malaysia
2 KCAET Khairpur Mirs, Sindh Agriculture University, Tandojam Sindh 70060, Pakistan
3 Fundamental and Applied Science Department, Universiti Teknologi Petronas, Perak 32610, Malaysia
4 Faculty of Mathematics and Statistics, Ton Duc Thang University, Ho Chi Minh City 72915, Vietnam
5 Department of Mathematics, College of Arts and Science, Prince Sattam bin Abdulaziz University, Wadi Al-Dawaser 11991, Saudi Arabia
* Correspondence: ilyaskhan@tdtu.edu.vn

Received: 26 April 2019; Accepted: 28 May 2019; Published: 20 August 2019

Abstract: In this paper, the MHD flow of a micropolar nanofluid on an exponential sheet in an Extended-Darcy-Forchheimer porous medium have been considered. Buongiorno's model is considered in order to formulate a mathematical model with different boundary conditions. The governing partial differential equations (PDEs) of the nanofluid flow are changed into a third order non-linear quasi-ordinary differential equation (ODE), using the pseudo-similarity variable. The resultant ODEs of the boundary value problems (BVPs) are renewed into initial value problems (IVPs) using a shooting method, and then the IVPs are solved by a fourth order Runge-Kutta (RK) method. The effects of various physical parameters on the profiles of velocity, temperature, microrotation velocity, concentration, skin friction, couple stress coefficients, heat, and concentration transfer are demonstrated graphically. The results reveal that triple solutions appear when $S \geq 2.0337$ for $K = 0.1$ and $S \geq 2.7148$ for $K = 0.2$. A stability analysis has been performed to show the stability of the solutions; only the first solution is stable and physically possible, whereas the remaining two solutions are not stable.

Keywords: pseudo-similarity variable; micropolar nanofluid; darcy forchheimer model; MHD flow; triple solution; stability analysis

1. Introduction

Micropolar fluid is a polar fluid which contains rigid randomly oriented or spherical particles. It can be defined as a fluid with micro structures and belongs to the nonsymmetric stress tensor [1]. Furthermore, this fluid model is employed to analyze the behavior of liquid crystals and exotic polymeric fluid or lubricant colloidal suspensions. Ariman et al. [2,3], Eringen [4–6], and Lukaszewicz [7] discussed the properties and applications of the micropolar fluid in details. The concept of the electrically conducting fluids motion in the presence of a magnetic field is called magnetohydrodynamics, or MHD for short. The word MHD is the combination of the words magneto, hydro, and dynamics, which mean magnetic, fluid and motion, respectively. MHD is also known as magnetofluid dynamics and hydromagnetic, which can be defined as the study of the dynamics of the electromagnetic field and the electrically conducting fluids. Recently, Kumar et al. [8] examined the MHD flow of micropolar fluid with a porous medium. Micropolar fluid with an MHD effect on a shrinking sheet along a weak

concentration has been considered by Gupta et al. [9]. Turkyilmazoglu [10] found the exact solution of micropolar fluid within the existence of the MHD effect. The MHD flow of micropolar fluids with a porous medium had been considered by many researchers, such as Sheikh et al. [11], Akhter et al. [12], Siddiq et al. [13], Dero et al. [14], Hayat et al. [15,16], Ahmed et al. [17], and Waqas et al. [18].

In the last couple of years, the use of nanofluid as a convectional fluid, in order to increase the heat transfer rate, has pulled in extensive consideration among researchers. Research demonstrated that dissolving different sorts of nanoparticles, such as nonmetal, polymeric and metal mixed in the base fluids, provides good thermal properties [19,20]. The term nanofluid, which was introduced by Choi and Eastman in 1995 [21], can be defined as a fluid that is a mixture of regular (base) fluids with nano-meter sized particles (less than 100 nm). These particles may contain oxides, carbon nanotubes, and metals. On the other hand, oil, ethylene glycol, and water are generally considered to be the base fluids. These fluids have different physical and chemical properties from regular fluids [22]. There are two approaches to study nanofluids, namely the experimental and numerical one. Many researchers considered the numerical approach to understand the behavior of nanofluids and introduced new concepts to understand them. Khanafer et al. [23] built up a model to contemplate the heat transfer improvement of Cu-water nanofluid in a two-dimensional enclosure. Meanwhile, Buongiorno [24] constructed a new non-homogeneous model in which velocity of base fluids and nanoparticles are not equal to zero. This model consists of seven slip parameters, which are Brownian diffusion, diffusiophoresis, gravity settling, fluid drainage, inertia, thermophoresis, and the Magnus effect. The references of the development of nanofluids can be found in the book by Nield and Bejan [25] and also in the published review articles on nanofluid, such as Mahian et al. [26–28] and Wong and Leon [29]. Recently, a few researchers have considered nanoparticles with non-Newtonian base fluid in the presence of MHD effects, such as Mahdy [30], Rehman et al. [31], Hamid et al. [32], Eid et al. [33], and Prabhakar et al. [34].

It can be observed from previously published literature that not much work has been done on the Extended-Darcy-Forchheimer porous medium, due to the fact that the governing equations cannot be reduced to self-similarity solutions through the use of a similarity transformation, particularly when using exponential similarity variables. Similarly, the MHD flow of micropolar nanofluid over an exponential shrinking surface has also not been considered because the equation of the angular velocity cannot be transformed into a self-similarity solution. Keeping in view these drawbacks, we attempt to employ a new approach which is a pseudo-similarity variable in the governing equations of fluid flow in order to obtain a local similar solution, as adopted by a few researchers in their studies [35–38]. The key objective of the present work is to consider the MHD flow of micropolar nanofluid over an exponential shrinking surface in an Extended-Darcy-Forchheimer porous medium. The resultant equations, after performing the pseudo-similarity variable in the form of a third-order non-linear quasi-ordinary differential equation, have been solved using the shooting method with the RK-method; we found triple solutions. When multiple solutions exist in any problem, it is necessary to conduct a stability analysis in order to determine the stable solutions. Consequently, this analysis is also taken into account in this research.

2. Problem Description and Formulation

The steady incompressible two-dimensional MHD flow of a micropolar nanofluid on an exponentially shrinking surface in an Extended-Darcy-Forchheimer porous medium is considered by adding $-\frac{1}{\sqrt{K}}\left(\frac{\vartheta}{\sqrt{K}}+bu\right)u$ in the Navier Stokes equation. The velocity of the shrinking surface in the form of exponential terms is given by $U_w(x) = U_0 e^{\frac{2x}{\ell}}$, while the uniform magnetic field of the strength B_0 has been normally applied to it (Figure 1). Due to a small value of the magnetic Reynolds number, the induced magnetic field is ignored. Under the consideration of the mentioned assumptions, the

boundary layer equations of motion for the micropolar nanofluid, heat and concentration equations are expressed as:

$$\frac{\partial u}{\partial x} + \frac{\partial v}{\partial y} = 0 \tag{1}$$

$$u\frac{\partial u}{\partial x} + v\frac{\partial u}{\partial y} = \left(\vartheta + \frac{\kappa}{\rho}\right)\frac{\partial^2 u}{\partial y^2} + \frac{\kappa}{\rho}\frac{\partial N}{\partial y} - \frac{\vartheta}{K}u - \frac{b}{\sqrt{K}}u^2 - \frac{\sigma B^2 u}{\rho} \tag{2}$$

$$u\frac{\partial N}{\partial x} + v\frac{\partial N}{\partial y} = \frac{1}{\rho j}\left[\gamma\frac{\partial^2 N}{\partial y^2} - \kappa\left(2N + \frac{\partial u}{\partial y}\right)\right] \tag{3}$$

$$u\frac{\partial T}{\partial x} + v\frac{\partial T}{\partial y} = \alpha\frac{\partial^2 T}{\partial y^2} + \tau_1\left[D_B\frac{\partial C}{\partial y}\frac{\partial T}{\partial y} + \frac{D_T}{T_\infty}\left(\frac{\partial T}{\partial y}\right)^2\right] \tag{4}$$

$$u\frac{\partial C}{\partial x} + v\frac{\partial C}{\partial y} = D_B\frac{\partial^2 C}{\partial y^2} + \frac{D_T}{T_\infty}\frac{\partial^2 T}{\partial y^2} \tag{5}$$

subject to the following boundary conditions:

$$\begin{aligned} &v = \sqrt{\frac{\vartheta U_0}{2l}}e^{\frac{x}{2l}}\, S; u = -U_w(x) + B^*\vartheta\frac{\partial u}{\partial y}; N = -m\frac{\partial u}{\partial y};\ T = T_w; C = C_w \ \ at y = 0 \\ &u \to 0;\ N \to 0;\ T \to T_\infty;\ C \to C_\infty \ \ as\ y \to \infty. \end{aligned} \tag{6}$$

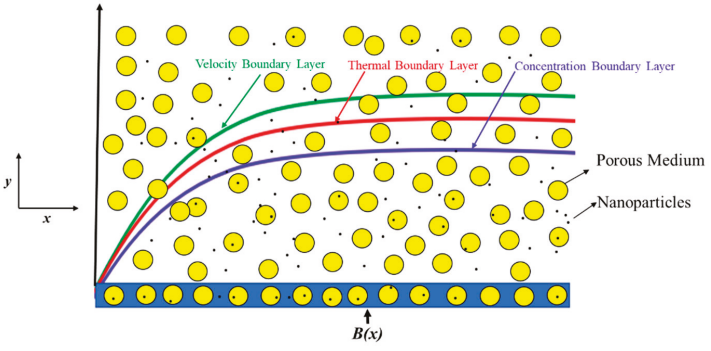

Figure 1. Physical model of the flow.

We considered the following similarity transformations, as adopted by Sanjayanand and Khan [39], to solve Equations (1)–(5), with boundary condition (6):

$$\begin{aligned} &\psi = \sqrt{2\vartheta l U_0}e^{\frac{x}{2l}}f(x,\eta), N = U_0 e^{\frac{3x}{2l}}\sqrt{\frac{U_0}{2\vartheta l}}g(x,\eta),\ \theta(x,\eta) = \frac{(T-T_\infty)}{(T_w-T_\infty)}, \\ &\varnothing(x,\eta) = \frac{(C-C_\infty)}{(C_w-C_\infty)},\ \eta = y\sqrt{\frac{U_0}{2\vartheta l}}e^{\frac{x}{2l}} \end{aligned} \tag{7}$$

where $u = \frac{\partial \psi}{\partial y}$ and $v = -\frac{\partial \psi}{\partial x}$ are components of the velocity along the directions x and y respectively,ρ is the fluid density, ϑ is the kinematic viscosity, σ is the electrical conductivity of the fluid, $B = B_0 e^{\frac{x}{2l}}$ is the magnetic field with a constant magnetic strength B_0, K_1 is the permeability of the porous medium, b is the local inertia coefficient, κ is the vortex viscosity, N is the microrotation, γ indicates the spin gradient viscosity, j is the ratio of the micro inertia and unit mass, T is the fluid temperature, and α is the thermal diffusivity of the micropolar nanofluid. Furthermore, $\tau_1 = \frac{(\rho c)_p}{(\rho c)_f}$ is the ratio between the effective heat capacity of the nanoparticle material and the capacity of the fluid, D_B is the Brownian diffusion coefficient, D_T is the thermophoretic diffusion coefficient, T_w is the temperature of the wall,

T_∞ is the ambient temperature, C_w is the concentration of the wall C_∞ is the ambient concentration, and $B^* = B_1 e^{\frac{-x}{2l}}$ is the velocity slip factor. It might be mentioned that the range of m is $0 \le m \le 1$; however, m is constant. In the case of $m = 0$, we have $N = 0$, which indicates that the strong concentration and micro-elements are near to the wall and are not rotatable. Furthermore, $m = 0.5$ shows a weak concentration, which causes the anti-symmetric part of the stress tensor to vanish. On the other hand, $m = 1$ indicates the turbulent boundary layer flows modeling (see [40,41]).

Using Equation (7) in Equations (2)–(5), we get the following partial differential equations:

$$(1+K)f_{\eta\eta\eta} + ff_{\eta\eta} + Kg_\eta - 2\left(f_\eta\right)^2 - F_S\left(f_\eta\right)^2 - K_1 f_\eta - Mf_\eta = 2l\left(f_\eta f_{\eta x} - f_{\eta\eta} f_x\right) \tag{8}$$

$$\left(1+\frac{K}{2}\right)g_{\eta\eta} + fg_\eta - 3gf_\eta - 2Kg - Kf_{\eta\eta} = 2l\left(f_\eta g_x - g_\eta f_x\right) \tag{9}$$

$$\frac{1}{Pr}\theta_{\eta\eta} + f\theta_\eta + N_b\theta_\eta \varnothing_\eta + N_t\left(\theta_\eta\right)^2 = 2l\left(f_\eta\theta_x - \theta_\eta f_x\right) \tag{10}$$

$$\varnothing_{\eta\eta} + Scf\varnothing_\eta + \frac{N_t}{N_b}\theta_{\eta\eta} = 2{\cdot}Sc{\cdot}l\left(f_\eta\varnothing_x - \varnothing_\eta f_x\right) \tag{11}$$

Furthermore, many authors considered $\gamma = \left(\mu + \frac{\kappa}{2}\right)j = \mu\left(1+\frac{K}{2}\right)j$, where $\kappa = \mu K$ is the material parameter [41] in their work. In our problem, the terms of the Extended-Darcy-Forchheimer porous medium $K_1 = \frac{lv}{2U_0 K\, e^{\frac{x}{l}}}$ and $\gamma = \mu\left(1+\frac{K}{2}\right)\frac{2\vartheta l e^{\frac{-x}{l}}}{U_0}$ do not allow it to have self-similar solutions. For this reason, by using the pseudo-similarity variable, a local similarity solution can be obtained by equating the derivative of the functions of f, g, θ and $\varnothing$ with respect to x being equal to zero. This implies that $f(x,\eta) = f(\eta); g(x,\eta) = g(\eta); \theta(x,\eta) = \theta(\eta)$ and $\varnothing(x,\eta) = \varnothing(\eta)$ [39]. As a result, all the terms on the right-hand side become zero, and we get the following third-order non-linear quasi-ordinary differential equation:

$$(1+K)f''' + ff'' + Kg' - 2f'^2 - F_S f'^2 - K_1 f' - Mf' = 0 \tag{12}$$

$$\left(1+\frac{K}{2}\right)g'' + fg' - 3gf' - 2\delta Kg - \delta Kf'' = 0 \tag{13}$$

$$\frac{1}{Pr}\theta'' + f\theta' + N_b\varnothing'\theta' + N_t(\theta')^2 = 0 \tag{14}$$

$$\varnothing'' + Scf\varnothing' + \frac{N_t}{N_b}\theta'' = 0 \tag{15}$$

subject to the boundary conditions below:

$$\begin{gathered} f(0) = S;\ f'(0) = -1 + \lambda f''(0);\ g(0) = -mf''(0);\ \theta(0) = 1; \varnothing(0) = 1 \\ f'(\eta) \to 0;\ g(\eta) \to 0;\ \theta(\eta) \to 0; \varnothing(\eta) \to 0 \quad as\ \eta \to \infty. \end{gathered} \tag{16}$$

Here, prime stands for the differentiation with respect to the new independent variable η, $K = \frac{\kappa}{\mu}$ is the non-Newtonian parameter, K_1 is the permeability parameter, $F_S = \frac{2lb}{\sqrt{K}}$ is the Forchheimmer parameter, $M = \frac{2l\sigma(B_0)^2}{\rho U_0}$ is the Hartmann number, $Pr = \frac{\vartheta}{\alpha}$ is the Prandtl number, $N_t = \frac{\tau_1 D_T(T_w - T_\infty)}{\nu T_\infty}$ is the thermophoresis parameter, $N_b = \frac{\tau_1 D_B(C_w - C_\infty)}{\nu}$ is the parameter of Brownian motion, $Sc = \frac{\vartheta}{D_B}$ is the Schmidt number, $\lambda = B_1\sqrt{\frac{\vartheta U_0}{2l}}$ is the velocity slip, and $S < 0$ and $S > 0$ are the mass injunction and suction parameter, respectively.

The physical quantities of interest are the coefficient of the skin friction, the local Nusselt number and local Sherwood number, which are given by:

$$\begin{gathered} C_f = \frac{\left[(\mu+\kappa)\frac{\partial u}{\partial y}+\kappa N\right]_{y=0}}{\rho U_0^2};\ N_u = \frac{-x\left(\frac{\partial T}{\partial y}\right)_{y=0}}{(T_w-T_\infty)};\ S_h = \frac{-x\left(\frac{\partial C}{\partial y}\right)_{y=0}}{(C_w-C_\infty)};\\ C_f(Re_x)^{\frac{1}{2}} = \sqrt{2}(1+(1-\mathrm{m})K)f''(0); N_u(Re_x)^{-\frac{1}{2}} = -\frac{1}{\sqrt{2}}\theta'(0); S_h(Re_x)^{-\frac{1}{2}} = -\frac{1}{\sqrt{2}}\varnothing'(0) \end{gathered} \tag{17}$$

where $Re_x = lu_w/\vartheta$ is the local Reynolds number.

3. Stability Analysis

Weidman et al. [42] initiated a study of the stability analysis of multiple solutions. Since then, some researchers, such as Rosca and Pop [43] and Lund et al. [44,45], performed stability analyses in their studies on multiple solutions of fluid flow problems. They found that only the first or upper solution has a physical meaning, while all of the remaining solutions (second or third) are not physically relevant or, in other words, are said to be unstable solutions. The first step in finding the stability of the solutions is to change the momentum, heat, and concentration equations into an unsteady form by considering a new variable τ. In our case, we have $\tau = \frac{U_0}{2l}e^{\frac{x}{l}}\cdot t$, as defined in the paper of Rehman et al. [46]:

$$\frac{\partial u}{\partial t}+u\frac{\partial u}{\partial x}+v\frac{\partial u}{\partial y} = \left(\vartheta+\frac{K_1}{\rho}\right)\frac{\partial^2 u}{\partial y^2}+\frac{\kappa}{\rho}\frac{\partial N}{\partial y}-\frac{\vartheta}{K}u-\frac{b}{\sqrt{K}}u^2-\frac{\sigma B^2 u}{\rho} \tag{18}$$

$$\frac{\partial N}{\partial t}+u\frac{\partial N}{\partial x}+v\frac{\partial N}{\partial y} = \frac{1}{\rho j}\left[\gamma\frac{\partial^2 N}{\partial y^2}-\kappa\left(2N+\frac{\partial u}{\partial y}\right)\right] \tag{19}$$

$$\frac{\partial T}{\partial t}+u\frac{\partial T}{\partial x}+v\frac{\partial T}{\partial y} = \alpha\frac{\partial^2 T}{\partial y^2}+\tau_1\left[D_B\frac{\partial C}{\partial y}\frac{\partial T}{\partial y}+\frac{D_T}{T_\infty}\left(\frac{\partial T}{\partial y}\right)^2\right] \tag{20}$$

$$\frac{\partial C}{\partial t}+u\frac{\partial C}{\partial x}+v\frac{\partial C}{\partial y} = D_B\frac{\partial^2 C}{\partial y^2}+\frac{D_T}{T_\infty}\frac{\partial^2 T}{\partial y^2} \tag{21}$$

The presence of τ is associated with initial value problems of the stable solution. Equating the derivative of functions with respect to x being equal to zero leads to the new similarity transfer variables in the presence of τ and η, which can be expressed as:

$$\begin{gathered} \psi = \sqrt{2\vartheta l U_0}e^{\frac{x}{2l}}f(\eta,\tau); N = U_0 e^{\frac{3x}{2l}}\sqrt{\frac{U_0}{2\vartheta l}}g(\eta,\tau);\ \theta(\eta,\tau) = \frac{(T-T_\infty)}{(T_w-T_\infty)};\\ \varnothing(\eta,\tau) = \frac{(C-C_\infty)}{(C_w-C_\infty)};\ \eta = y\sqrt{\frac{U_0}{2\vartheta l}}\,e^{\frac{x}{2l}};\ \tau = \frac{U_0}{2l}e^{\frac{x}{l}}\cdot t \end{gathered} \tag{22}$$

By applying Equation (22) in Equations (18)–(21), we get:

$$(1+K)\frac{\partial^3 f}{\partial\eta^3}+f\frac{\partial^2 f}{\partial\eta^2}+K\frac{\partial g}{\partial\eta}-2\left(\frac{\partial f}{\partial\eta}\right)^2-F_S\left(\frac{\partial f}{\partial\eta}\right)^2-K_1\frac{\partial f}{\partial\eta}-M\frac{\partial f}{\partial\eta}-\frac{\partial^2 f}{\partial\tau\partial\eta} = 0 \tag{23}$$

$$\left(1+\frac{K}{2}\right)\frac{\partial^2 g}{\partial\eta^2}+f\frac{\partial g}{\partial\eta}-3g\frac{\partial f}{\partial\eta}-2Kg-K\frac{\partial^2 f}{\partial\eta^2}-\frac{\partial g}{\partial\tau} = 0 \tag{24}$$

$$\frac{1}{Pr}\frac{\partial^2\theta}{\partial\eta^2}+f\frac{\partial\theta}{\partial\eta}+N_b\frac{\partial\varnothing}{\partial\eta}\frac{\partial\theta}{\partial\eta}+N_t\left(\frac{\partial\theta}{\partial\eta}\right)^2-\frac{\partial\theta}{\partial\tau} = 0 \tag{25}$$

$$\frac{\partial^2\varnothing}{\partial\eta^2}+Scf\frac{\partial\varnothing}{\partial\eta}+\frac{N_t}{N_b}\frac{\partial^2\theta}{\partial\eta^2}-Sc\frac{\partial\varnothing}{\partial\tau} = 0 \tag{26}$$

subject to the boundary conditions:

$$\begin{gathered} f(0,\tau)=S;\frac{\partial f(0,\tau)}{\partial \eta}=-1+\lambda\frac{\partial^2 f(0,\tau)}{\partial \eta^2};g(0,\tau)=-m\frac{\partial^2 f(0,\tau)}{\partial \eta^2};\theta(0,\tau)=1;\varnothing(0,\tau)=1 \\ \frac{\partial f(\eta,\tau)}{\partial \eta}\to 0;\ g(\eta,\tau)\to 0;\ \theta(\eta,\tau)\to 0;\varnothing(\eta,\tau)\to 0 \quad as\ \eta\to\infty \end{gathered} \tag{27}$$

In order to indicate the solution stability of $f(\eta)=f_0(\eta)$, $g(\eta)=g_0(\eta)$, $\theta(\eta)=\theta_0(\eta)$ and $\varnothing(\eta)=\varnothing_0(\eta)$, which satisfy the equation of the boundary value problem (23)–(26) with boundary condition (27), we follow the suggestion of Rehman et al. [46] by introducing the following functions:

$$\begin{gathered} f(\eta,\tau)=f_0(\eta)+e^{-\varepsilon\tau}F(\eta,\tau) \\ g(\eta,\tau)=g_0(\eta)+e^{-\varepsilon\tau}G(\eta,\tau) \\ \theta(\eta,\tau)=\theta_0(\eta)+e^{-\varepsilon\tau}H(\eta,\tau) \\ \varnothing(\eta,\tau)=\varnothing_0(\eta)+e^{-\varepsilon\tau}S(\eta,\tau) \end{gathered} \tag{28}$$

where $F(\eta,\tau)$, $G(\eta,\tau)$, $H(\eta,\tau)$ and $S\ (\eta,\tau)$ are small relative to $f_0(\eta)$, $g_0(\eta)$, $\theta_0(\eta)$ and $\varnothing_0(\eta)$ of the steady state solutions. It should be noted that the range of these functions are $0<F(\eta,\tau)<1$, $0<G(\eta,\tau)<1$, $0<H(\eta,\tau)<1$ and $0<S(\eta,\tau)<1$. Furthermore, ε is an unknown eigenvalue parameter, which needs to be found. Substituting the values of the functions and their derivatives from Equation (28) in Equations (23)–(26) with the boundary condition (27), we have:

$$(1+K)F_0'''+f_0F_0''+F_0f_0''+KG_0'-4f_0'F_0'-2F_Sf_0'F_0'-K_1F_0'-MF_0'+\varepsilon F_0'=0 \tag{29}$$

$$\left(1+\frac{K}{2}\right)G_0''+f_0G_0'+F_0g_0'-3g_0F_0'-3g_0F_0'-2K\delta G_0-K\delta F_0''+\varepsilon G_0=0 \tag{30}$$

$$\frac{1}{Pr}H_0''+f_0H_0'+F_0\theta_0'+Nb\varnothing_0'H_0'+NbS_0'\theta_0'+2Nt\theta_0'H_0'+\varepsilon H_0=0 \tag{31}$$

$$S_0''+Sc\left(f_0\varnothing_0'+F_0S_0'\right)+\frac{Nt}{Nb}H_0''+Sc\cdot\varepsilon S_0=0 \tag{32}$$

subject to the boundary conditions:

$$\begin{gathered} F_0(0)=0,F_0'(0)=\lambda F_0''(0),G_0(0)=-mF_0''(0),\ H_0(0)=0,\ S_0(0)=0 \\ F_0'(\eta)\to 0,\ G_0(\eta)\to 0,H_0(\eta)\to 0,S_0(\eta)\to 0,\ \ as\ \eta\to\infty \end{gathered} \tag{33}$$

We assumed $\tau=0$ for Equations (23)–(26) in order to calculate the initial growth and decay of the solution of Equation (28), as recommended by Alarifi et al. [47]. Under these circumstances, $F(\eta,\tau)$, $G(\eta,\tau)$, $H(\eta,\tau)$ and $S\ (\eta,\tau)$ can be written as $F_0(\eta)$, $G_0(\eta)$, $H_0(\eta)$ and $S_0(\eta)$, respectively.

It is stated in the studies of Lund et al. [44,45] and Haris et al. [48] that eigenvalues can be determined if and only if the boundary condition of any one function of the following functions $F_0(\eta)$, $G_0(\eta)$, $H_0(\eta)$ and $S_0(\eta)$ can be relaxed into the initial condition by differentiating that function one more time. In this study, we relaxed $F_0(\eta)\to 0$ as $\eta\to\infty$ and then solved the system of Equations (29)–(32) subject to Equation (33) along with the new relaxed boundary condition $F''_0(0)=1$. It is worth mentioning that the sign of the smallest eigenvalues (ε) determines the stability of the solutions. The smallest eigenvalue is negative (positive), which indicates that the solution of the flow is unstable (stable) and that there is an initial growth (decay) of disturbances.

4. Results and Discussion

In order to fully understand the considered fluid flow model, the numerical study has been carried out for various important physical parameters, such as the magnetic parameter M, permeability parameter K_1, Forchheimmer parameter F_S, non-Newtonian parameter K, thermophoresis parameter N_t, Brownian motion parameter N_b, etc. The highly non-linear system of the quasi-ordinary differential Equations (12)–(15), along with the boundary conditions (16), have been solved by using the shooting

method, and triple solutions were found. The value of η_∞ is chosen from 4 to 8, and it is worth noting that the value of η_∞ increases until the profiles of the velocity, temperature, and concentration converge asymptotically to the momentum, temperature, and concentration boundary layers, respectively.

Figure 2 was drawn to analyze the effect of the material parameter K on the velocity profiles. The thickness of the velocity boundary layer increases when the micropolar parameter K is increased in the first and the second solutions, due to the fact that the material parameter reduced the drag force and that the hydrodynamic boundary layer therefore rose. We noted that when $K = 0$ (Newtonian fluid), the second solution did not exist. On the other hand, the dual nature of the velocity profile was observed in the third solution. Figure 3 depicts the variation of the velocity profiles for the different values of the Forchheimmer parameter F_S. We observed that, due to increments in F_S, the resistant force occurred when the fluid flow was flowing on the porous surface, and hence the velocity of the flow declined in the third solutions. The dual behavior of the velocity profile was noticed in the second solution. However, no change could be seen in the first solution when F_S was increased. The velocity and thickness of the momentum boundary layers are inversely (directly) proportional to K_1 and M in the first (third) solution. On the other hand, the dual behavior of the velocity profile was seen in the second solution, as illustrated in Figures 4 and 5. The effect of the slip parameters λ and m on the velocity profiles are shown in Figures 6 and 7. In the first solution, the velocity boundary thickness was reduced as λ and m increased; this was due to the fact that the velocity of the fluid and surface have a big difference when the velocity slip factor is enhanced. For the second (third) solution, the velocity profiles decreased (increased) initially after they inclined (declined) when λ and m improved. The dual nature of the flow in some sense indicates that there is an initial growth of disturbance. Initially, the microrotation profile was reduced and then started to rise with increasing values of the micropolar parameter in the first solution, as shown in Figure 8. The thickness of the microrotation boundary layer was enhanced (reduced) as K was enhanced in the third (second) solution. The dual behavior of the microrotation profile was been observed in all solutions except the first solution when the value of m increased. The thickness of the microrotation boundary layer increased with increasing values of m in the first solution, as demonstrated in Figure 9. Figure 10 was drawn to analyze the variation of the temperature profiles for different values of the Prandtl number Pr. The thermal boundary layer thickness and temperature were incrementally reduced in the values of the Prandtl number Pr for all of the solutions, as expected. This is due to the fact that a high Prandtl number causes the thermal conductivity of nanofluid to diminish, and as a result the temperature is reduced. The variation of the temperature profiles for different values of the Brownian motion parameter N_b is shown in Figure 11. It was observed in all solutions of the temperature profiles that the temperature and thermal layer thickness were enhanced with increasing values of N_b. This is due to fact that the Brownian motion N_b increases the kinetic energy of the nanofluid; thus, the temperature of the nanofluid increases. The temperature profile, with an effect resulting from the thermophoresis parameter N_t, is illustrated in Figure 12. In all three solutions of the nanofluid flow problem, we noted that as the thermophoresis parameter N_t rose, the temperature and thickness of the thermal layer increased. This is because the thermophoretic force is generated by N_t and the temperature gradient, which pushes the flow of the nanofluid far from the boundary layer as a resulting thickness of the thermal boundary layer increases. The thickness of the concentration boundary layer declined with increasing values of the Brownian motion parameter N_b in all solutions in Figure 13, which was expected. This was physically justified by the fact that Brownian motion is generated when nanoparticle and base fluid are mixed together in a nanofluid system. Since Brownian diffusion shows the conduction of heat under those circumstances, the thickness of the concentration boundary layer decreases. Figure 14 was sketched to examine the effect of N_t on the concentration profile of nanoparticles. In all three solutions, the thickness of the concentration boundary layer was enhanced when thermophoresis increased.

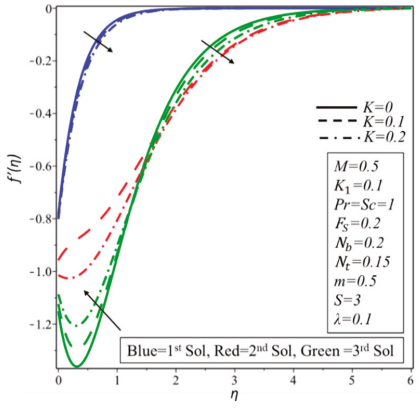

Figure 2. Profiles of the velocity for increasing values of K.

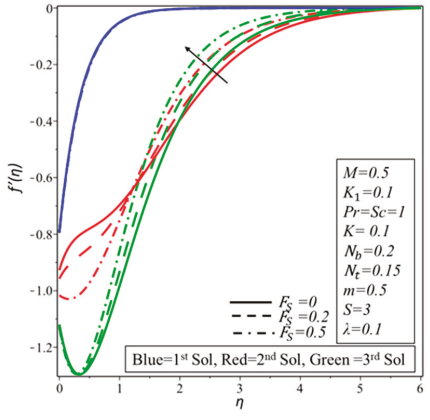

Figure 3. Profiles of the velocity for increasing values of F_S.

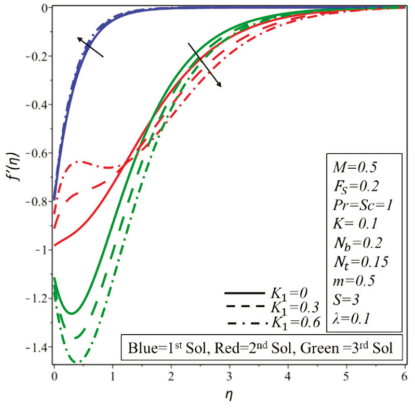

Figure 4. Profiles of the velocity for increasing values of K_1.

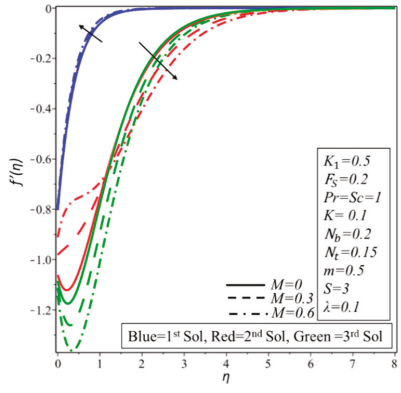

Figure 5. Profiles of the velocity for increasing values of M.

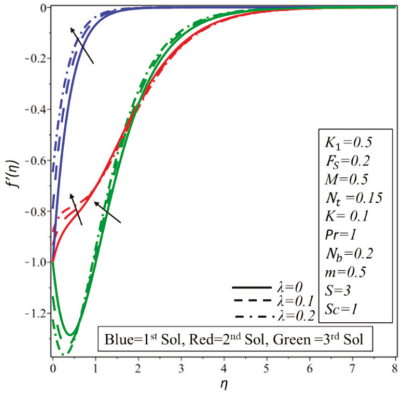

Figure 6. Profiles of the velocity for increasing values of λ.

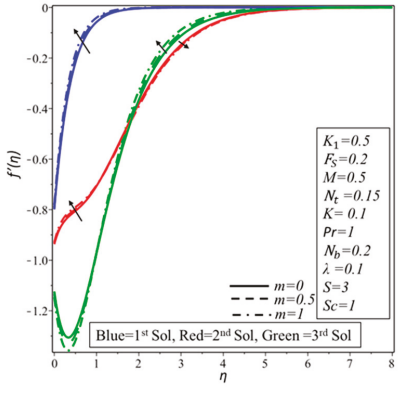

Figure 7. Profiles of the velocity for increasing values of m.

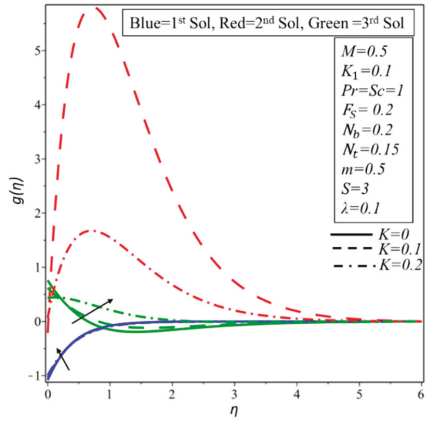

Figure 8. Microrotation profiles for increasing values of *K*.

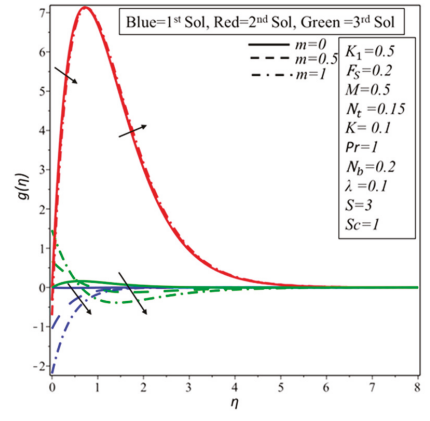

Figure 9. Microrotation profiles for increasing values of *m*.

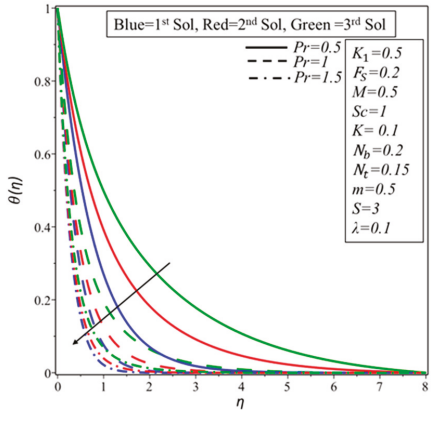

Figure 10. Temperature profiles for increasing values of *Pr*.

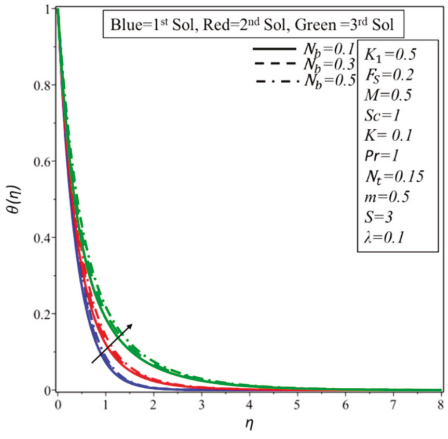

Figure 11. Temperature profiles for increasing values of N_b.

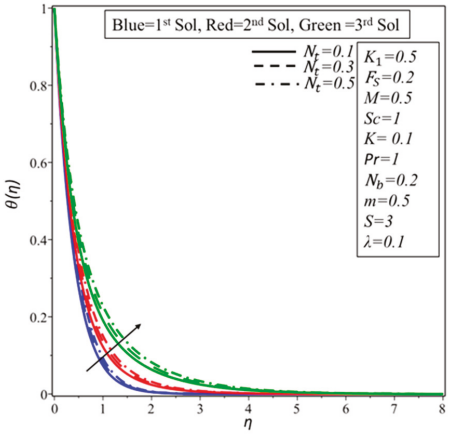

Figure 12. Temperature profiles for increasing values of N_t.

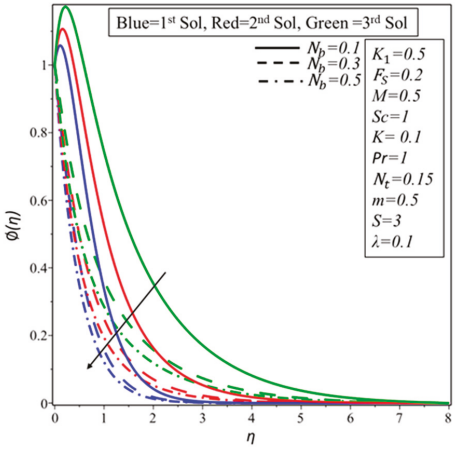

Figure 13. Nanoparticle concentration profiles for increasing values of N_b.

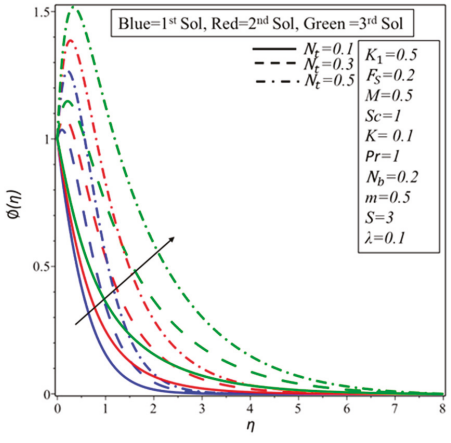

Figure 14. Nanoparticle concentration profiles for increasing values of N_t.

Wang [49] and many researchers also stated in their studies that the similarity solution of the fluid flow problems over the shrinking surface is possible to obtain when sufficient wall mass suction is applied. The flow of Newtonian fluid is different from that of non-Newtonian fluid; it is observed for micropolar nanofluid that when the value of the micropolar parameter K increases, a strong mass suction is required to obtain the solution. In this study, we discovered that there exist two regions for similarity solutions, namely multiple solutions and single solution, depending on the mass suction parameter. For $K = 0.1(K = 0.2)$ there is a range of triple solutions when $S \geq 2.0337(S \geq 2.7148)$, and a single similarity solution exists, $S < 2.0337(S < 2.7148)$, as shown in Figure 15. When the suction is enhanced, the skin friction increases in the first solution and decreases in the second and the third solutions. Figures 16–18 were drawn to examine the effect of the suction S and micropolar parameter K on the couple stress coefficient, and the heat and concentration transfer rate, respectively. In all graphs, when the suction is increased, the couple stress coefficient, heat, and concentration transfer rate are enhanced for all of the solutions.

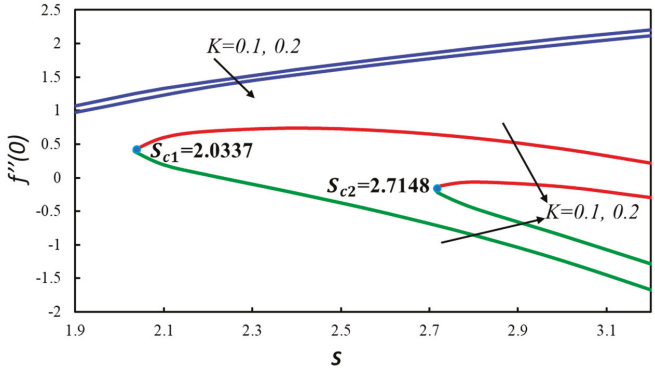

Figure 15. Coefficient of the skin friction with various values of S.

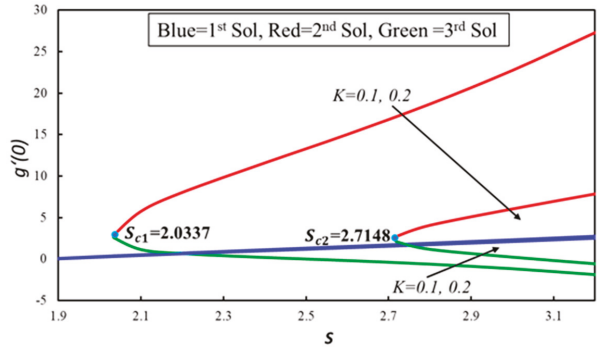

Figure 16. Couple stress coefficient with various values of *S*.

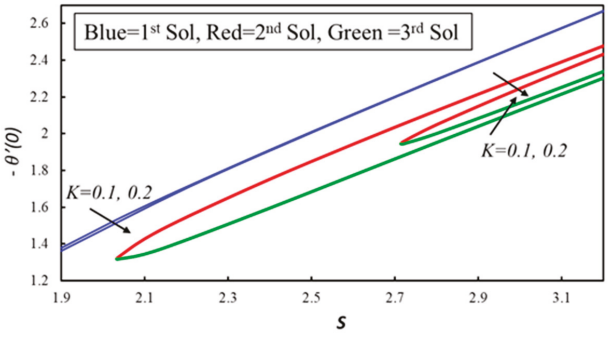

Figure 17. Heat transfer rate with various values of *S*.

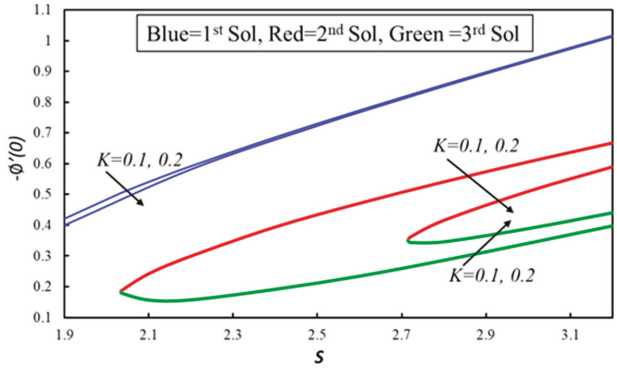

Figure 18. Concentration transfer rate with various values of *S*.

By performing a stability analysis, the stability of the fluid flow solutions is achieved in this research. We need to perform a stability analysis when more than one solution exists in the flow problem. The main focus of this analysis is to determine which solution is stable and physically possible and which one is unstable. It is worth noting that the stability of the solution depends on the sign of the smallest eigenvalue. The value of the smallest eigenvalue is determined through Equation (24), for which we have to solve Equations (25)–(28), along with the boundary conditions (29). The smallest eigenvalues ε are demonstrated in Table 1 for different values of the suction and non-Newtonian parameters. It is clear from Table 1 that the negative (positive) values of the smallest eigenvalue ε

indicate an initial growth (decay) of the disturbance that will interrupt (resume) the boundary layer separation and flow from becoming unstable (stable). It is worth mentioning that the stable solution always provides a good physical meaning which can be realized.

Table 1. Smallest eigenvalues for different values of K and S when $M = 0.5$, $Pr = Sc = 1$, $m = 0.5$, $K_1 = 0.1$, $F_S = 0.2$, $\lambda = 0.1$, $N_b = 0.2$ and $N_t = 0.15$.

K	S	ε		
		1st Solution	**2nd Solution**	**3rd Solution**
0.1	2.5	1.4309	−1.2683	−0.9436
	3	1.7854	−1.3162	−1.2053
0.2	3	0.9831	−0.4392	−0.3518
	3.5	1.2165	−0.6431	−0.5382

5. Conclusions

In this research, the MHD flow of micropolar nanofluid over an exponentially shrinking surface was considered with the effect of the porous and velocity slip. Exponential similarity variables were used to convert the partial differential equations into quasi-ordinary differential equations. The resultant equations were converted from BVPs to IVPs using a shooting method, after which the IVPs were solved by an RK-4th order method. After the findings of multiple solutions of nanofluid flow, a stability analysis was performed in order to indicate the stable solution by using the BVP4C solver in MATLAB software. The main summary findings of our research are as follow:

- Triple solutions exist when $S \geq 2.0337$ for $K = 0.1$ and when $S \geq 2.7148$ for $K = 0.2$.
- Dual solutions exist for the Newtonian case $K = 0$.
- The study of critical points acknowledges the range of multiple solutions and single solutions.
- The study of the stability analysis indicates that only the first solution is stable and that the remaining two solutions are unstable.
- The thickness of the momentum boundary layer decreases with increasing values of K_1 and M in the first solution.
- Increasing values of thermophoresis and Brownian motion parameters are caused by the thickness of the thermal boundary layer.

Author Contributions: L.A.L. and D.L.C.C. modelled the problem. Z.O. and K.S.N. numerically computed results and wrote the manuscript. I.K. discussed the results physically and proof read it.

Funding: No specific funding received for this work.

Acknowledgments: Authors would like to thank YUTP 015LCO-078 for the financial support. The authors would also like to thank Universiti Utara Malaysia (UUM) for the moral and financial support in conducting this research.

Conflicts of Interest: The authors declare no conflict of interest.

Nomenclature

u, v	velocity components
U_w	surface velocity
N	microrotation
K	material parameter
M	a constant
T	temperature
T_0	a constant
T_w	variable temperature at the sheet
T_∞	ambient temperature
C	concentration

C_0	a constant
C_∞	ambient concentration
ϑ	kinematic viscosity
κ	vortex viscosity
γ	spin gradient viscosity
j	microinertia per unit mass
α	thermal diffusivity
K^*	thermal conductivity
ψ	stream function
η	transformed variable
$B(x)$	magnetic field
b	local inertia coefficient
M	Hartmann number
Pr	Prandtl number
D_B	Brownian diffusion
D_T	thermophoretic diffusion
v_w	suction/injection velocity
K_1	permeability of the porous medium
C_w	variable concentration at the sheet
N_t	thermophoresis parameter
Sc	Schmidt number
λ	Velocity slip
S	injunction/suction parameter
C_f	skin friction coefficient
N_u	local Nusselt number
N_b	Brownian motion parameter
S_h	local Sherwood number
Re	local Reynolds number
ε	unknown eigen value
τ	Stability transformed variable

References

1. Dero, S.; Rohni, A.M.; Saaban, A. MHD micropolar nanofluid flow over an exponentially stretching/shrinking surface: Triple solutions. *J. Adv. Res. Fluid Mech. Therm. Sci.* **2019**, *56*, 165–174.
2. Ariman, T.T.N.D.; Turk, M.A.; Sylvester, N.D. Microcontinuum fluid mechanics—A review. *Int. J. Eng. Sci.* **1973**, *11*, 905–930. [CrossRef]
3. Ariman, T.T.N.D.; Turk, M.A.; Sylvester, N.D. Applications of microcontinuum fluid mechanics. *Int. J. Eng. Sci.* **1974**, *12*, 273–293. [CrossRef]
4. Eringen, A.C. Theory of micropolar fluids. *J. Math. Mech.* **1966**, *16*, 1–18. [CrossRef]
5. Eringen, A.C. Theory of thermomicrofluids. *J. Math. Anal. Appl.* **1972**, *38*, 480–496. [CrossRef]
6. Eringen, A.C. *Microcontinuum Field Theories: I. Foundations and Solids*; Springer: Heidelberg, Germany, 2012.
7. Lukaszewicz, G. *Micropolar Fluids: Theory and Applications*; Springer: Cambridge, MA, USA, 1999.
8. Kumar, G.C.; Reddy, K.J.; Konijeti, R.K.; Reddy, M.N. Non-uniform heat source/sink and joule heating effects on chemically radiative MHD mixed convective flow of micropolar fluid over a stretching sheet in porous medium. *Defect Diffus. Forum* **2018**, *388*, 281–302. [CrossRef]
9. Gupta, D.; Kumar, L.; Bég, O.A.; Singh, B. Finite element analysis of MHD flow of micropolar fluid over a shrinking sheet with a convective surface boundary condition. *J. Eng. Thermophys.* **2018**, *27*, 202–220. [CrossRef]
10. Turkyilmazoglu, M. Mixed convection flow of magnetohydrodynamic micropolar fluid due to a porous heated/cooled deformable plate: Exact solutions. *Int. J. Heat Mass Transf.* **2017**, *106*, 127–134. [CrossRef]
11. Sheikh, N.A.; Ali, F.; Khan, I.; Saqib, M.; Khan, A. MHD flow of micropolar fluid over an oscillating vertical plate embedded in porous media with constant temperature and concentration. *Math. Probl. Eng.* **2017**, *2017*, 9402964. [CrossRef]

12. Akhter, S.; Ashraf, M.; Ali, K. MHD flow and heat transfer analysis of micropolar fluid through a porous medium between two stretchable disks using quasi-linearization method. *Iran. J. Chem. Chem. Eng.* **2017**, *36*, 155–169.
13. Siddiq, M.; Rauf, A.; Shehzad, S.; Abbasi, F.; Meraj, M. Thermally and solutally convective radiation in mhd stagnation point flow of micropolar nanofluid over a shrinking sheet. *Alex. Eng. J.* **2018**, *57*, 963–971. [CrossRef]
14. Dero, S.; Uddin, M.J.; Rohni, A.M. Stefan blowing and slip effects on unsteady nanofluid transport past a shrinking sheet: Multiple solutions. *Heat Transf. Asian Res.* **2019**. [CrossRef]
15. Hayat, T.; Sajjad, R.; Ellahi, R.; Alsaedi, A.; Muhammad, T. Homogeneous-heterogeneous reactions in MHD flow of micropolar fluid by a curved stretching surface. *J. Mol. Liq.* **2017**, *240*, 209–220. [CrossRef]
16. Hayat, T.; Saif, R.S.; Ellahi, R.; Muhammad, T.; Ahmad, B. Numerical study for darcy-forchheimer flow due to a curved stretching surface with cattaneo-christov heat flux and homogeneous-heterogeneous reactions. *Results Phys.* **2017**, *7*, 2886–2892. [CrossRef]
17. Ahmed, B.; Javed, T.; Ali, N. Numerical study at moderate Reynolds number of peristaltic flow of micropolar fluid through a porous-saturated channel in magnetic field. *AIP Adv.* **2018**, *8*, 015319. [CrossRef]
18. Waqas, M.; Farooq, M.; Khan, M.I.; Alsaedi, A.; Hayat, T.; Yasmeen, T. Magnetohydrodynamic (MHD) mixed convection flow of micropolar liquid due to nonlinear stretched sheet with convective condition. *Int. J. Heat Mass Transf.* **2016**, *102*, 766–772. [CrossRef]
19. Das, S.K.; Choi, S.U.; Yu, W.; Pradeep, T. *Nanofluids: Science and Technology*; John Wiley & Sons: Hoboken, NJ, USA, 2007.
20. Dero, S.; Rohni, A.M.; Saaban, A. The dual solutions and stability analysis of nanofluid flow using tiwari-das modelover a permeable exponentially shrinking surface with partial slip conditions. *J. Eng. Appl. Sci.* **2019**, *14*, 4569–4582. [CrossRef]
21. Choi, S.U.; Eastman, J.A. Enhancing thermal conductivity of fluids with nanoparticles. *ASME Publ. Fed* **1995**, *231*, 99–106.
22. Oztop, H.F.; Abu-Nada, E. Numerical study of natural convection in partially heated rectangular enclosures filled with nanofluids. *Int. J. Heat Fluid Flow* **2008**, *29*, 1326–1336. [CrossRef]
23. Khanafer, K.; Vafai, K.; Lightstone, M. Buoyancy-driven heat transfer enhancement in a two-dimensional enclosure utilizing nanofluids. *Int. J. Heat Mass Transf.* **2003**, *46*, 3639–3653. [CrossRef]
24. Buongiorno, J. Convective transport in nanofluids. *J. Heat Transf.* **2006**, *128*, 240–250. [CrossRef]
25. Nield, D.A.; Bejan, A. *Convection in Porous Media*; Springer: New York, NY, USA, 2006.
26. Mahian, O.; Kolsi, L.; Amani, M.; Estellé, P.; Ahmadi, G.; Kleinstreuer, C.; Marshall, J.S.; Siavashi, M.; Taylor, R.A.; Niazmand, H. Recent advances in modeling and simulation of nanofluid flows-part I: Fundamental and theory. *Phys. Rep.* **2019**, *790*, 1–48. [CrossRef]
27. Mahian, O.; Kolsi, L.; Amani, M.; Estellé, P.; Ahmadi, G.; Kleinstreuer, C.; Marshall, J.S.; Taylor, R.A.; Abu-Nada, E.; Rashidi, S. Recent advances in modeling and simulation of nanofluid flows-part II: Applications. *Phys. Rep.* **2019**, *791*, 1–59. [CrossRef]
28. Mahian, O.; Kianifar, A.; Kalogirou, S.A.; Pop, I.; Wongwises, S. A review of the applications of nanofluids in solar energy. *Int. J. Heat Mass Transf.* **2013**, *57*, 582–594. [CrossRef]
29. Wong, K.V.; De Leon, O. Applications of nanofluids: Current and future. *Adv. Mech. Eng.* **2010**, *2*, 519659. [CrossRef]
30. Mahdy, A. Simultaneous impacts of mhd and variable wall temperature on transient mixed casson nanofluid flow in the stagnation point of rotating sphere. *Appl. Math. Mech.* **2018**, *39*, 1327–1340. [CrossRef]
31. Rehman, K.U.; Malik, M.; Zahri, M.; Tahir, M. Numerical analysis of MHD casson navier's slip nanofluid flow yield by rigid rotating disk. *Results Phys.* **2018**, *8*, 744–751. [CrossRef]
32. Hamid, M.; Usman, M.; Khan, Z.; Haq, R.; Wang, W. Numerical study of unsteady MHD flow of williamson nanofluid in a permeable channel with heat source/sink and thermal radiation. *Eur. Phys. J. Plus* **2018**, *133*, 527. [CrossRef]
33. Eid, M.R.; Mahny, K.L.; Muhammad, T.; Sheikholeslami, M. Numerical treatment for carreau nanofluid flow over a porous nonlinear stretching surface. *Results Phys.* **2018**, *8*, 1185–1193. [CrossRef]
34. Prabhakar, B.; Bandari, S.; Reddy, C.S. A revised model to analyze MHD flow of maxwell nanofluid past a stretching sheet with nonlinear thermal radiation effect. *Int. J. Fluid Mech. Res.* **2019**, *46*, 151–165. [CrossRef]

35. Guedda, M.; Hammouch, Z. On similarity and pseudo-similarity solutions of falkner–skan boundary layers. *Fluid Dyn. Res.* **2006**, *38*, 211–223. [CrossRef]
36. Minkowycz, W.; Sparrow, E. Local nonsimilar solutions for natural convection on a vertical cylinder. *J. Heat Transf.* **1974**, *96*, 178–183. [CrossRef]
37. Ming-Jer, H.; Cha'o-Kuang, C. Local similarity solutions of free convective heat transfer from a vertical plate to non-newtonian power law fluids. *Int. J. Heat Mass Transf.* **1990**, *33*, 119–125. [CrossRef]
38. Zhang, Z. Normal solutions of a boundary-value problem arising in free convection boundary-layer flows in porous media. *Appl. Math. Comput.* **2018**, *339*, 367–373. [CrossRef]
39. Sanjayanand, E.; Khan, S.K. On heat and mass transfer in a viscoelastic boundary layer flow over an exponentially stretching sheet. *Int. J. Therm. Sci.* **2006**, *45*, 819–828. [CrossRef]
40. Jena, S.K.; Mathur, M. Similarity solutions for laminar free convection flow of a thermomicropolar fluid past a non-isothermal vertical flat plate. *Int. J. Eng. Sci.* **1981**, *19*, 1431–1439. [CrossRef]
41. Ishak, A.; Nazar, R.; Pop, I. Heat transfer over a stretching surface with variable heat flux in micropolar fluids. *Phys. Lett. A* **2008**, *372*, 559–561. [CrossRef]
42. Weidman, P.; Kubitschek, D.; Davis, A. The effect of transpiration on self-similar boundary layer flow over moving surfaces. *Int. J. Eng. Sci.* **2006**, *44*, 730–737. [CrossRef]
43. Roşca, A.V.; Pop, I. Flow and heat transfer over a vertical permeable stretching/shrinking sheet with a second order slip. *Int. J. Heat Mass Transf.* **2013**, *60*, 355–364. [CrossRef]
44. Ali Lund, L.; Omar, Z.; Khan, I.; Raza, J.; Bakouri, M.; Tlili, I. Stability analysis of darcy-forchheimer flow of casson type nanofluid over an exponential sheet: Investigation of critical points. *Symmetry* **2019**, *11*, 412. [CrossRef]
45. Lund, L.A.; Omar, Z.; Khan, I. Analysis of dual solution for MHD flow of Williamson fluid with slippage. *Heliyon* **2019**, *5*, e01345. [CrossRef]
46. Rahman, M.; Rosca, A.V.; Pop, I. Boundary layer flow of a nanofluid past a permeable exponentially shrinking surface with convective boundary condition using buongiorno's model. *Int. J. Numer. Methods Heat Fluid Flow* **2015**, *25*, 299–319. [CrossRef]
47. Alarifi, I.M.; Abokhalil, A.G.; Osman, M.; Lund, L.A.; Ayed, M.B.; Belmabrouk, H.; Tlili, I. MHD flow and heat transfer over vertical stretching sheet with heat sink or source effect. *Symmetry* **2019**, *11*, 297. [CrossRef]
48. Harris, S.D.; Ingham, D.B.; Pop, I. Mixed convection boundary-layer flow near the stagnation point on a vertical surface in a porous medium: Brinkman model with slip. *Transp. Porous Media* **2009**, *77*, 267–285. [CrossRef]
49. Wang, C. Liquid film on an unsteady stretching surface. *Q. Appl. Math.* **1990**, *48*, 601–610. [CrossRef]

coatings

MDPI

Article

Numerical Investigation of Multiple Solutions for Caputo Fractional-Order-Two Dimensional Magnetohydrodynamic Unsteady Flow of Generalized Viscous Fluid over a Shrinking Sheet Using the Adams-Type Predictor-Corrector Method

Liaquat Ali Lund [1,2], Zurni Omar [1], Sayer O. Alharbi [3], Ilyas Khan [4,*] and Kottakkaran Sooppy Nisar [5]

1 School of Quantitative Sciences, Universiti Utara Malaysia, 06010 Sintok, Kedah
2 KCAET Khairpur Mir's Sindh Agriculture University, Tandojam Sindh 70060, Pakistan
3 Department of Mathematics, College of Science Al-Zulfi, Majmaah University, Al-Majmaah 11952, Saudi Arabia
4 Faculty of Mathematics and Statistics, Ton Duc Thang University, Ho Chi Minh City 758307, Vietnam
5 Department of Mathematics, College of Arts and Science, Prince Sattam bin Abdulaziz University, Wadi Al-Dawaser 11991, Saudi Arabia
* Correspondence: ilyaskhan@tdtu.edu.vn

Received: 29 April 2019; Accepted: 13 June 2019; Published: 27 August 2019

Abstract: In this paper, magnetohydrodynamic (MHD) flow over a shrinking sheet and heat transfer with viscous dissipation has been studied. The governing equations of the considered problem are transformed into ordinary differential equations using similarity transformation. The resultant equations are converted into a system of fractional differential boundary layer equations by employing a Caputo derivative which is then solved numerically using the Adams-type predictor-corrector method (APCM). The results show the existence of two ranges of solutions, namely, dual solutions and no solution. Moreover, the results indicate that dual solutions exist for a certain range of specific parameters which are in line with the results of some previously published work. It is also observed that the velocity boundary layer decreases as the suction and magnetic parameters increase.

Keywords: APCM; Caputo derivative; dual solutions; unsteady flow; MHD; shrinking surface

1. Introduction

The theory of fluid flow on a shrinking surface has numerous applications in real-life problems, such as shrinking film. Additionally, it has capillary effects in small pores, the shrinking-swell behavior of a rising shrinking balloon, and hydraulic properties of agricultural clay soils [1], fuel-cells [2,3], porous materials [4,5], and petroleum engineering [6,7]. Viscous fluid on a shrinking surface has been examined for the first time by Miklavčič and Wang [8], and they discovered that the flow over a shrinking surface did not exist unless sufficient mass suction was applied. It is worth mentioning that the fluid flow on shrinking and stretching surfaces have different characteristics. Gupta et al. [9] examined the magnetohydrodynamic (MHD) flow of micropolar fluid on a shrinking surface with the effect of mixed convection parameter. Meanwhile, Naveed et al. [10] considered the MHD flow of viscous fluid on a curved shrinking sheet. In order to model this problem, a curvilinear coordinates system was employed and the dual solutions were obtained. The MHD flow of nanofluid over a nonlinear stretching/shrinking wedge was considered by Khan et al. [11]. Soid et al. [12] investigated the unsteady MHD stagnation point flow over a shrinking surface and found dual solutions. Likewise,

Zaib et al. [13] considered the unsteady flow of the Williamson nanofluid over a shrinking surface and found dual solutions by using the shooting method. Lund et al. [14] analyzed the Darcy–Forchheimer flow of the Casson nanofluid with the impact of the slip condition on the shrinking surface and expressed that the existence of dual solutions relies upon the suction parameter. The slip effects on the nanofluid by utilizing the Buongiorno model has been examined by Dero et al. [15]. They found dual solutions by implementations of the shooting method and stated that it was due to the unsteadiness of the parameter. Similarly, Alarifi et al. [16] considered the stagnation point flow and found dual solutions for an opposing case. Triple solutions of micropolar nanofluid over a shrinking surface have been obtained by employing the shooting method [17]. Moreover, Lund et al. [18] performed a stability analysis by using the three-stage Lobatto IIIa formula and concluded only first solution to be stable. To the best of our knowledge, most of the studies and investigations of fluid flow have not used the Caputo fractional derivatives for multiple solutions. Therefore, the main objective of this work is to consider Caputo fractional derivatives, solve the governing equations by using the Adams-type predictor-corrector method, and find multiple solutions.

From published literature, it can be concluded that the possibility of the existence of multiple solutions of boundary layer flow on a shrinking surface is greater than on a stretching sheet. It is also discovered that the solution of fluid flow over a shrinking surface is possible only in the presence of high suction [19]. In other words, the solution is possible only on permeable surfaces. According to Mishra et al. [20], multiple solutions depend on the non-linearity in governing equations of fluid flow and other factors. Moreover, the existence of multiple solutions also depends on the values of different physical parameters such as magnetic, Reynold numbers, Prandtl numbers, and suction parameters, as claimed by Schlichting [21]. This claim complies with the findings of other researchers who discovered that the ranges of multiple solutions, single solutions, and no solutions depend on the values, such as the magnetic parameter [18], suction parameter [14], and surface velocity parameter [22]. Fang and Zhang [23] examined the steady MHD flow of viscous fluid over a shrinking surface and found dual solutions analytically. They concluded that dual and single solutions exist when $0 < M < 1$ and $M \geq 1$, respectively. Previous researchers attempted to determine multiple solutions using various analytical and numerical methods. Rana et al. [24] used the homotopy analysis method to find the multiple solutions. Rohni et al. [25] and Ishak et al. [26] found multiple solutions by using the Keller-box method. Fang et al. [27] employed an analytical approach to find multiple solutions of viscous fluid in exact form and Raza et al. [28] considered the shooting method with the Runge–Kutta of the fourth order method to find the multiple solutions of fluid flow. The objective of this paper is to extend the work of Fang and Zhang [23] under the consideration of unsteady flow and heat equation with viscous dissipation using the new approach with the Caputo derivative to reduce the governing equations to the first order ordinary differential equations, which are then solved by the Adams-type predictor-corrector method.

The MHD field was initiated by Hannes Alfvén (1908–1995) who was a famous Swedish physicist. Interest in the MHD flow started to gain attention when Hartmann invented the electromagnetic pump in 1918 [29]. In recent years, the study of non-uniform transverse-magnetic field effects is applied in many engineering problems. For example, electrically-conducting fluids that flow along with magnetic field have significant applications in oil exploration, cooling nuclear reactors, boundary layer control in the aerodynamics field, extraction of geothermal energy, and MHD generators and plasma studies. Due to the important applications of MHD flow, many researchers, mathematicians, and engineers considered MHD flow-related problems in their studies [30–32]. Ellahi et al. [33] considered the effect of MHD on Couple Stress Fluid. Makinde et al. [34] examined nanofluid under the influence of MHD and found that the hydrodynamic boundary layer is a decreasing function for higher values of magnetic parameters. This article is presented as follows: Section 2 discusses the problem formulation, in which governing equations are derived, and also gives some useful definitions and properties using solution methodology. In Section 3, numerical are presented numerically and graphically. Finally, Section 4 concludes this study by giving key findings and remarks.

2. Problem Formulation

2.1. Boundary Layer Governing Equations

The MHD flow of two-dimensional incompressible viscous fluid over a continuously unsteady shrinking surface is considered. The velocity of mass transfer and the shrinking surface are assumed to be v_w (x, t) and u_w (x, t), respectively, where t is the time and x is the coordinate measured with the shrinking surface. Under these assumptions with viscous dissipation, the governing Navier–Stokes (NS) equations of this problem are given by:

$$\frac{\partial u}{\partial x} + \frac{\partial v}{\partial y} = 0 \tag{1}$$

$$\frac{\partial u}{\partial t} + u\,\frac{\partial u}{\partial x} + v\,\frac{\partial u}{\partial y} = -\frac{1}{\rho}\frac{\partial P}{\partial x} + \vartheta\left(\frac{\partial^2 u}{\partial x^2} + \frac{\partial^2 u}{\partial y^2}\right) - \frac{\sigma^* B^2 u}{\rho} \tag{2}$$

$$\frac{\partial v}{\partial t} + u\,\frac{\partial v}{\partial x} + v\,\frac{\partial v}{\partial y} = -\frac{1}{\rho}\frac{\partial P}{\partial x} + \vartheta\left(\frac{\partial^2 v}{\partial x^2} + \frac{\partial^2 v}{\partial y^2}\right) \tag{3}$$

$$\frac{\partial T}{\partial t} + u\,\frac{\partial T}{\partial x} + v\,\frac{\partial T}{\partial y} = \alpha\left(\frac{\partial^2 T}{\partial x^2} + \frac{\partial^2 T}{\partial y^2}\right) + \frac{\mu}{\rho c_p}\left[\left(\frac{\partial u}{\partial x}\right)^2 + \left(\frac{\partial u}{\partial y}\right)^2\right] \tag{4}$$

Subject to the following boundary conditions:

$$t < 0:\ u = v = 0,\ T = T_\infty \text{ for all } x;\ y$$

$$t \geq 0:\ u = u_w(x,t) = -\frac{cx}{1-\gamma t},\ v = v_w(x,t) = -\sqrt{\frac{\vartheta_f c}{1-\gamma t}} f(0) = S, T = T_w(x,t) = T_\infty + \frac{bx^m}{1-\gamma t} \text{ at } y = 0$$

$$u \to 0;\ \ T \to T_\infty \text{ as } y \to \infty \tag{5}$$

where the pressure of fluid is denoted by P, velocity components along the x and y directions are represented by u and v, respectively, temperature of fluid is T, kinematic viscosity of the fluid is ϑ, density of the fluid is ρ, thermal diffusivity of the fluid is α, $B = \frac{B_0}{(1-\gamma t)^{1/2}}$ is the transverse magnetic field of strength which is applied with the normal surface direction, and b, c, and m are all positive constants. It is worth mentioning that $m = 1$ and $m = 0$ indicate linear and constant variation with x of the wall of temperature, respectively.

Now, we introduce the similarity variables for Equations (1)–(5) as follows:

$$u = \frac{cx}{(1-\gamma t)} f'(\eta);\ v = -\sqrt{\frac{cv}{(1-\gamma t)}}\, f(\eta),\ \theta(\eta) = \frac{T - T_\infty}{T_w - T_\infty} \tag{6}$$

Substituting (6) into Equations (2)–(4) yields the following system of ordinary differential equations

$$f''' + ff'' - (f')^2 - A\left(\frac{\eta}{2} f'' + f'\right) - Mf' = 0 \tag{7}$$

$$\frac{1}{Pr}\theta'' + f\theta' - mf'\theta - A\left(\frac{\eta}{2}\theta' + \theta\right) + Ec(f'')^2 = 0 \tag{8}$$

with reduced boundary conditions

$$f(0) = S;\ f'(0) = -1;\ \theta(0) = 1$$

$$f'(\eta) \to 0;\ \theta(\eta) \to 0 \text{ as } \eta \to \infty \tag{9}$$

where $A = \frac{\gamma}{c}$ is the unsteadiness parameter, $M = \frac{\sigma(B_0)^2}{\rho c}$ is the magnetic parameter, $Ec = \frac{U_w^2}{C_p(T_w - T_\infty)}$ is the Eckert number, and $Pr = \frac{\vartheta}{\alpha}$ is the Prandtl number. In our problem, we consider a decelerating shrinking surface ($A < 0$) as assumed in [35,36].

2.2. Preliminaries on the Caputo Fractional Derivatives

In this section, the definition of the Caputo fractional derivative and its main properties are introduced.

Definition 1. *Let $t >, a > 0, a, \alpha, t \epsilon \Re$. The Caputo fractional derivative of the order α of function $f \epsilon C^n$ is expressed as:*

$$ {}_a^C D_t^\alpha f(t) = \frac{1}{\Gamma(n-\alpha)} \int_a^t \frac{f^n(\xi)}{(t-\xi)^{\alpha+1-n}} d\xi, \; n-1 < \alpha < n \in N \tag{10} $$

Property 1. *Let $f(t), g(t) : [a, b] \to \Re$ be such that ${}_a^C D_t^\alpha f(t)$ and ${}_a^C D_t^\alpha g(t)$ exist almost everywhere, and let $c_1, c_2 \epsilon \Re$. Then ${}_a^C D_t^\alpha \{c_1 f(t) + c_2 g(t)\}$ exists almost everywhere and*

$$ {}_a^C D_t^\alpha \{c_1 f(t) + c_2 g(t)\} = c_1 {}_a^C D_t^\alpha f(t) + c_2 {}_a^C D_t^\alpha g(t) \tag{11} $$

Property 2. *If f(t) = c is a constant function then the fractional derivative of the function is equal to 0, and mathematically it can be expressed as:*

$$ {}_a^C D_t^\alpha c = 0 \tag{12} $$

We considered the general fractional differential equation involving the Caputo derivative below

$$ {}_a^C D_t^\alpha x(t) = f(t, x(t)), \; \alpha \epsilon (0,1) \tag{13} $$

with initial conditions $x_0 = x(t_0)$.

Definition 2. *The constant x^* is an equilibrium point of the Caputo fractional dynamic system (13) if, and only if, $f(t, x^*) = 0$.*

Here, we introduce the new fractional Atangana–Baleanu derivatives along the non-local and non-singular kernel [37,38].

Definition 3. *Let $f \epsilon H^1(a,b), \; b > a, \; \alpha \epsilon [0,1]$, then the new fractional derivatives of the Caputo behavior can be expressed as:*

$$ D_t^\alpha (f(t)) = \frac{B(\alpha)}{1-\alpha} \int_a^t f(x) exp\left(-\alpha \frac{t-x}{1-\alpha}\right) dx $$

where B(α) denotes a normalization function obeying B(0) = B(1) = 1.

In the case when the function does not belong to H^1 (*a*,*b*), the derivative is given by

$$ D_t^\alpha (f(t)) = \frac{\alpha B(\alpha)}{1-\alpha} \int_a^t (f(t) - f(x)) exp\left(-\alpha \frac{t-x}{1-\alpha}\right) dx $$

Furthermore, if $\sigma = \frac{1-\alpha}{\alpha} \epsilon [0, \infty)$, and $\alpha = \frac{1}{1-\sigma} \epsilon [0, \; 1]$, then the above Equation becomes

$$ D_t^\sigma (f(t)) = \frac{N(\sigma)}{\sigma} \int_a^t f(x) exp\left(-\frac{t-x}{\sigma}\right) dx, \quad N(0) = N(\infty) = 1 $$

2.3. Solution Methodology

Choosing different variables below

$$y_1 = \eta,\ y_2 = f,\ y_3 = f', y_4 = f'', y_5 = \theta, y_6 = \theta' \tag{14}$$

Equations (7) and (8) can be transformed into a system of first-order differential equations. Then, the Caputo fractional-order derivative is applied to the resultant system to produce a fractional-order system of the following form:

$$\begin{cases} D_\eta^\alpha y_1 = 1, D_\eta^\alpha y_2 = y_3,\ D_\eta^\alpha y_3 = y_4;\ D_\eta^\alpha y_4 = (y_3)^2 - y_2 y_4 + A\left(y_3 + \frac{y_1 y_4}{2}\right) + M y_3 \\ D_\eta^\alpha y_5 = y_6, D_\eta^\alpha y_6 = Pr\left\{m y_3 y_5 - y_2 y_6 + A\left(y_5 + \frac{y_1 y_6}{2}\right) - Ec(y_4)^2\right\} \end{cases} \tag{15}$$

with boundary conditions below:

$$y_1 = 0,\ y_2 = S,\ y_3 = -1,\ y_4 = u_1,\ y_5 = 1,\ y_6 = u_2 \tag{16}$$

Now, the Adams types predictor-corrector method has been applied to get the solution of fractional differential equations. The error of this method is of the order h^5, where h is the grid size.

3. Results and Discussion

The governing Equation (15) with initial conditions (16) is solved using the Adams-type predictor-corrector method, and dual solutions are found depending on the suction parameter. It is worth mentioning that when an unsteady parameter is equal to 0, our equation of momentum is reduced to an equation obtained in [23], which is the major reference of our work. Furthermore, the results of the coefficient of skin friction in our problem are in good agreement with their work. According to our results, the coefficient of skin friction is equal to $f''(0) = \frac{S \pm \sqrt{S^2 - 4 + 4M}}{2}$. For details on the comparison, please refer to Table 1. From the table, we can conclude that only the first solution of our problem is a physical realizable solution, since $f''(0) > 0$, whereas the second solution is unstable because most of the values of $f''(0)$ are less than 0. It is worth mentioning that our results of the first solution are approximately equal to the result of a published article [23], which gives us confidence on our calculation (see Table 1). It should be noted that if $\alpha < 1$, multiple solutions do not exist and do not fulfill the boundary conditions asymptotically.

Table 1. Comparison $f''(0)$ of present results with [23].

M	S	Fang	Zhang [23]	Present	Results
		1st Solution	2nd Solution	1st Solution	2nd Solution
0.5	3	2.8228756	0.1771243	2.8203848	−0.3554574
	2	1.7071067	0.2928932	1.7063214	0.2845535
0	3	2.6180339	0.3819660	2.6165735	−0.2181474
	2	1	1	1.0019038	0.94503648

Figure 1 shows the effect of the suction parameter on the velocity profile. It was noticed that the thickness of the velocity boundary layer decreased as suction increased in the first solution. This occurred due to the fact that high suction produced the resistance in the fluid flow, and, as a result, the velocity and thickness of the momentum boundary layer decreased. On the other hand, the suction was proportional to the velocity profile in the second solution.

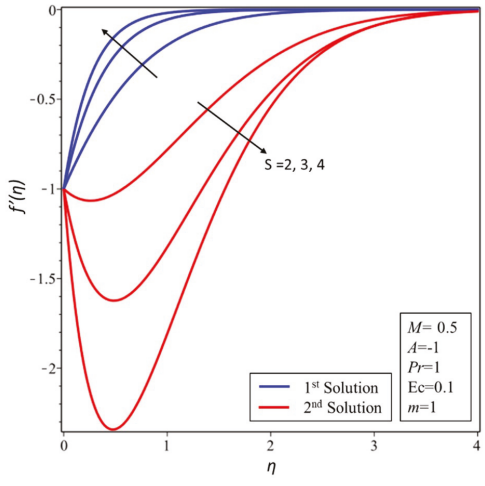

Figure 1. $f'(\eta)$ for increasing values of S.

The effect of the magnetic parameter M on the velocity is demonstrated in Figure 2. The velocity of the fluid flow decreased as magnetic parameter M increased in the first solution, as expected. This was due to the Lorentz or electromagnetic force, which can be defined as "the force which is exerted by a magnetic field on a moving fluid" [39]. We can say this force opposes the transport phenomenon. However, the opposite trend can be seen in the second solution.

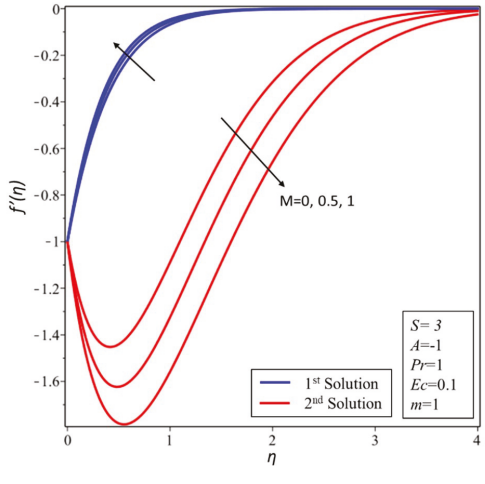

Figure 2. $f'(\eta)$ for increasing values of M and $\alpha = 1$.

Based on the results shown in Figure 3, there no change was noticed in the first solution when the magnitude of the unsteadiness parameter increased. On the other hand, the velocity layer became thicker initially and then thinner in the second solution, since deaccelerating of the unsteadiness parameter produced more drag force, which caused the thickness of the momentum boundary layer to decrease.

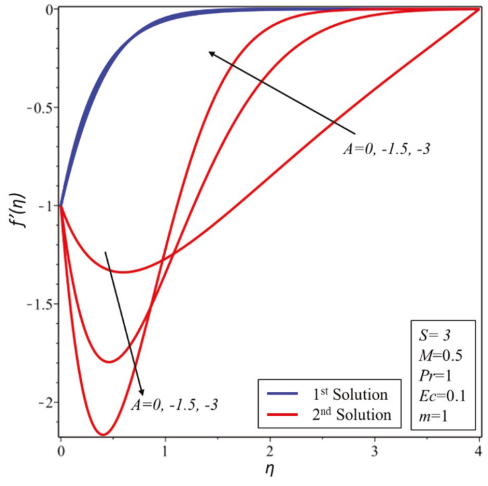

Figure 3. $f'(\eta)$ for increasing values of A and $\alpha = 1$.

The effect of the unsteadiness parameter A on a dimensionless profile of temperature is depicted in Figure 4. Both thermal boundary layer thicknesses and temperatures decreased initially and then started to increase when the unsteadiness parameter A was increased in the second solution. This behavior was expected because the momentum boundary layer declined and, therefore, the temperature increased. However, no difference could be seen in the first solution with the increasing magnitude of the unsteadiness parameter A.

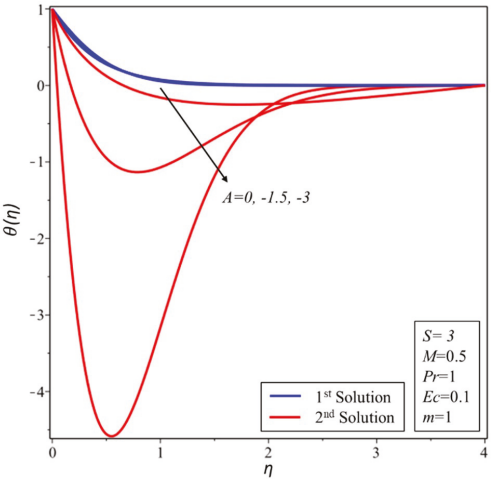

Figure 4. θ(η) for increasing values of A and $\alpha = 1$.

Figure 5 was drawn for the Prandtl number effect Pr on the profile of temperature. We can see that the temperature declined with respect to $Pr = 0.04$ to 6.7 in the first solution. This was because "fluid has relatively lower thermal conductivity for a large value of Prandtl number, which decreases the conduction and thickness of the thermal boundary layer" [40], and, consequently, the temperature reduced. This was because the "Prandtl number Pr which is the ratio of momentum diffusion to thermal" [18]. On the other hand, the thermal boundary layer thickness and temperature increase in the range of $0.04 \leq Pr \leq 3$ decreased in the range of $3 \leq Pr \leq 6.7$ in the second solution.

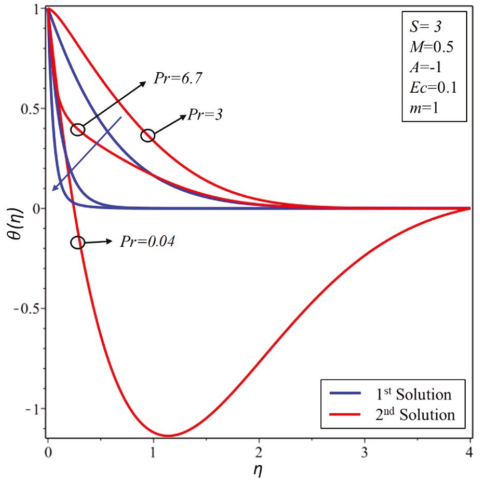

Figure 5. θ(η) for increasing values of *Pr* and α = 1.

Figure 6 indicates the temperature increase when the Ecker number was increased in the first solution. This was due to fact that an expansion in dissipation enhanced the flow of thermal conductivity, which extended the temperature and thermal boundary layer thickness. On the other hand, the Eckert number was inversely proportional to the temperature and thickness of the thermal boundary layer in the second solution.

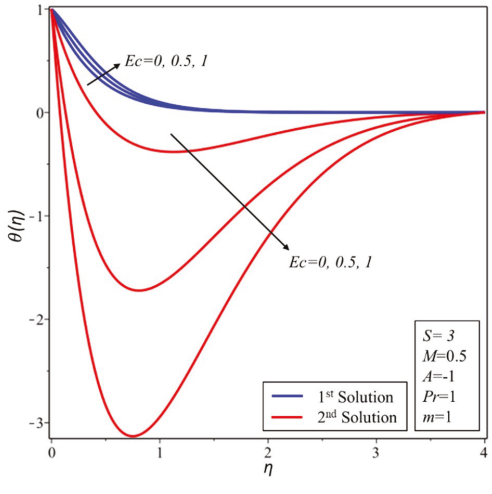

Figure 6. θ(η) for increasing values of *Ec* and α = 1.

The graph of the coefficient of skin friction for several values of *S* and different values of *A* is illustrated in Figure 7. It was observed that the skin friction coefficient increased (decreased) when suction was increased (reduced) in the first (second) solution. However, it decreased with the decreasing of the unsteady parameter *A*. Physically, resistance occurred due to increments in the suction parameter in the stable solution, while the opposite trend was seen in the unstable solution.

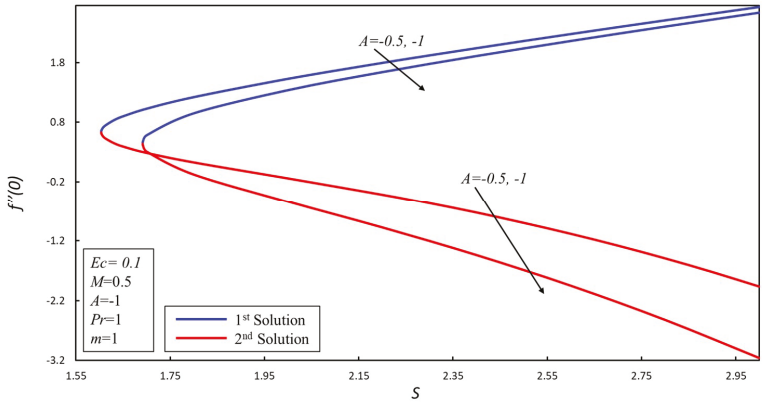

Figure 7. Coefficient of skin friction for different values of A.

Figure 8 shows the effect of α on the profile of the temperature. It was noticed that multiple solutions were difficult to be obtained when $\alpha < 1$. As α increased, the temperature of the fluid increased in the first solution and decreased in the second solution.

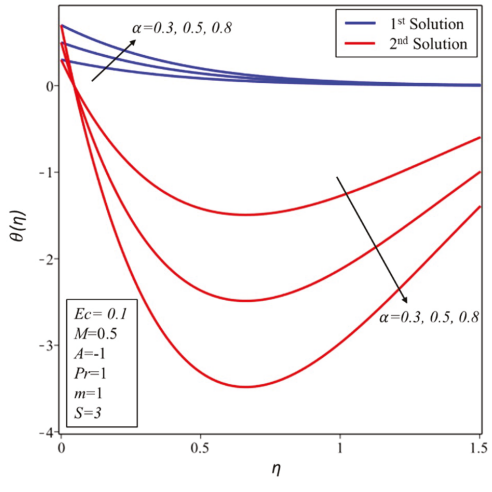

Figure 8. θ(η) for increasing values of α.

Figure 9 demonstrates the effect of α on the velocity profile. In both solutions, the velocity of the fluid decreased when α increased.

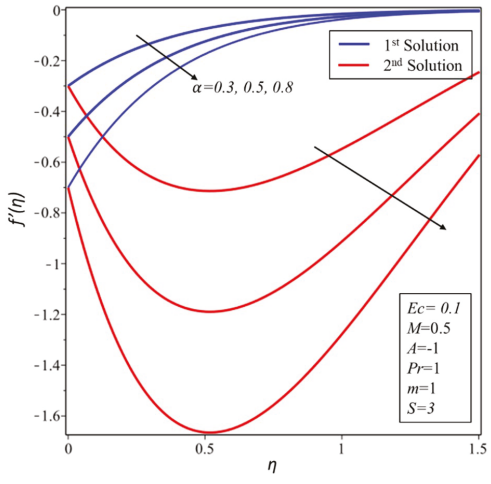

Figure 9. $f'(\eta)$ for increasing values of α.

4. Conclusion Remarks

The magnetohydrodynamic (MHD) flow over a shrinking sheet and heat transfer with viscous dissipation is numerically studied. The governing equations of the momentum and energy are transformed into the ordinary differential equations by using similarity transformation. The resultant equations have been transformed into a system of fractional differential equations by using the Caputo derivative. Fractional differential boundary layer equations, based on Caputo operators, are solved numerically by the Adams-type predictor-corrector method. We compared our result with a past published article and found it in good agreement with the first solution. Further, our results of the second solution did not concur with the published results. This was because of the heat equation and its different parameter effects on the unstable (second) solution. On the other hand, there existed two different ranges, namely, no solution and dual solutions, which depended on the magnetic and suction parameters.

Author Contributions: Z.O. and L.A.L. formulated the problem. L.A.L. and S.O.A. transformed the problem and computed the results. I.K. and K.S.N. discussed the results physically. All the authors equally contributed in writing the manuscript.

Funding: This research received no external funding.

Acknowledgments: The authors would like to thank Deanship of Scientific Research, Majmaah University for supporting this work.

Conflicts of Interest: The authors declare no conflict of interest.

References

1. Rohni, A.M.; Ahmad, S.; Pop, I. Flow and heat transfer at a stagnation-point over an exponentially shrinking vertical sheet with suction. *Int. J. Therm. Sci.* **2014**, *75*, 164–170. [CrossRef]
2. Xiao, B.; Wang, W.; Zhang, X.; Long, G.; Chen, H.; Cai, H.; Deng, L. A novel fractal model for relative permeability of gas diffusion layer in proton exchange membrane fuel cell with capillary pressure effect. *Fractals* **2019**, *27*, 1950012. [CrossRef]
3. Liang, M.; Liu, Y.; Xiao, B.; Yang, S.; Wang, Z.; Han, H. An analytical model for the transverse permeability of gas diffusion layer with electrical double layer effects in proton exchange membrane fuel cells. *Int. J. Hydrog. Energy* **2018**, *43*, 17880–17888. [CrossRef]

4. Xiao, B.; Wang, W.; Zhang, X.; Long, G.; Fan, J.; Chen, H.; Deng, L. A novel fractal solution for permeability and Kozeny-Carman constant of fibrous porous media made up of solid particles and porous fibers. *Powder Technol.* **2019**, *349*, 92–98. [CrossRef]
5. Liang, M.; Fu, C.; Xiao, B.; Luo, L.; Wang, Z. A fractal study for the effective electrolyte diffusion through charged porous media. *Int. J. Heat Mass Transf.* **2019**, *137*, 365–371. [CrossRef]
6. Long, G.; Liu, S.; Xu, G.; Wong, S.W.; Chen, H.; Xiao, B. A perforation-erosion model for hydraulic-fracturing applications. *SPE Prod. Oper.* **2018**, *33*, 770–783. [CrossRef]
7. Long, G.; Xu, G. The effects of perforation erosion on practical hydraulic-fracturing applications. *SPE J.* **2017**, *22*, 645–659. [CrossRef]
8. Miklavčič, M.; Wang, C.Y. Viscous flow due to a shrinking sheet. *Q. Appl. Math.* **2006**, *14*, 283–290. [CrossRef]
9. Gupta, D.; Kumar, L.; Bég, O.A.; Singh, B. Finite Element Analysis of MHD Flow of Micropolar Fluid over a Shrinking Sheet with a Convective Surface Boundary Condition. *J. Eng. Thermophys.* **2018**, *27*, 202–220. [CrossRef]
10. Naveed, M.; Abbas, Z.; Sajid, M.; Hasnain, J. Dual solutions in hydromagnetic viscous fluid flow past a shrinking curved surface. *Arab. J. Sci. Eng.* **2018**, *43*, 1189–1194. [CrossRef]
11. Khan, U.; Ahmed, N.; Mohyud-Din, S.T.; Bin-Mohsin, B. Nonlinear radiation effects on MHD flow of nanofluid over a nonlinearly stretching/shrinking wedge. *Neural Comput. Appl.* **2017**, *28*, 2041–2050. [CrossRef]
12. Soid, S.K.; Ishak, A.; Pop, I. Unsteady MHD flow and heat transfer over a shrinking sheet with ohmic heating. *Chin. J. Phys.* **2017**, *55*, 1626–1636. [CrossRef]
13. Zaib, A.; Haq, R.U.; Chamkha, A.J.; Rashidi, M.M. Impact of nonlinear radiative nanoparticles on an unsteady flow of a Williamson fluid towards a permeable convectively-heated shrinking sheet. *World J. Eng.* **2018**, *15*, 731–742. [CrossRef]
14. Lund, L.A.; Omar, Z.; Khan, I.; Raza, J.; Bakouri, M.; Tlili, I. Stability analysis of Darcy-Forchheimer flow of Casson type nanofluid over an exponential sheet: Investigation of critical points. *Symmetry* **2019**, *11*, 412. [CrossRef]
15. Dero, S.; Uddin, M.J.; Rohni, A.M. Stefan blowing and slip effects on unsteady nanofluid transport past a shrinking sheet: Multiple solutions. *Heat Transf.—Asian Res.* **2019**, *48*, 1149–1544. [CrossRef]
16. Alarifi, I.M.; Abokhalil, A.G.; Osman, M.; Lund, L.A.; Ayed, M.B.; Belmabrouk, H.; Tlili, I. MHD flow and heat transfer over vertical stretching sheet with heat sink or source effect. *Symmetry* **2019**, *11*, 297. [CrossRef]
17. Dero, S.; Rohni, A.M.; Saaban, A. MHD micropolar nanofluid flow over an exponentially stretching/shrinking surface: Triple solutions. *J. Adv. Res. Fluid Mech. Therm. Sci.* **2019**, *56*, 165–174.
18. Lund, L.A.; Omar, Z.; Khan, I. Analysis of dual solution for MHD flow of Williamson fluid with slippage. *Heliyon* **2019**, *5*, e01345. [CrossRef]
19. Bhattacharyya, K.; Banerjee, A.; Zaib, A.; Mahato, S.K. MHD mixed convection flow of a non-Newtonian Powell-Erying fluid over a permeable exponentially shrinking sheet. *FHMT* **2018**, *10*, 30. [CrossRef]
20. Mishra, S.; DebRoy, T. A computational procedure for finding multiple solutions of convective heat transfer equations. *J Phys. D Appl. Phys.* **2005**, *38*, 2977. [CrossRef]
21. Schlichting, H. *Boundary-Layer Theory*; McGraw-Hill: New York, NY, USA, 1968.
22. Rahman, M.M.; Rosca, A.V.; Pop, I. Boundary layer flow of a nanofluid past a permeable exponentially shrinking surface with convective boundary condition using Buongiorno's model. *Int. J. Numer. Methods Heat Fluid Flow* **2015**, *25*, 299–319. [CrossRef]
23. Fang, T.; Zhang, J. Closed-form exact solutions of MHD viscous flow over a shrinking sheet. *Commun. Nonlinear Sci. Numer. Simul.* **2009**, *14*, 2853–2857. [CrossRef]
24. Rana, P.; Shukla, N.; Gupta, Y.; Pop, I. Homotopy analysis method for predicting multiple solutions in the channel flow with stability analysis. *Commun. Nonlinear Sci. Numer. Simul.* **2018**, *66*, 183–193. [CrossRef]
25. Rohni, A.M.; Ahmad, S.; Pop, I. Boundary layer flow over a moving surface in a nanofluid beneath a uniform free stream. *Int. J. Numer. Methods Heat Fluid Flow* **2011**, *21*, 828–846. [CrossRef]
26. Ishak, A.; Nazar, R.; Pop, I. Mixed convection boundary layer flow adjacent to a vertical surface embedded in a stable stratified medium. *Int. J. Heat Mass Transf.* **2008**, *51*, 3693–3695. [CrossRef]
27. Fang, T.; Yao, S.; Zhang, J.; Aziz, A. Viscous flow over a shrinking sheet with a second order slip flow model. *Commun. Nonlinear Sci. Numer. Simul.* **2010**, *15*, 1831–1842. [CrossRef]

28. Raza, J.; Rohni, A.M.; Omar, Z. Rheology of micropolar fluid in a channel with changing walls: Investigation of multiple solutions. *J. Mol. Liq.* **2016**, *223*, 890–902. [CrossRef]
29. Mutuku-Njane, W.N. Analysis of Hydromagnetic Boundary Layer Flow and Heat Transfer of Nanofluids. Ph.D. Thesis, Cape Peninsula University of Technology, Cape Town, South Africa, 2014.
30. Sheikholeslami, M.; Ellahi, R. Three dimensional mesoscopic simulation of magnetic field effect on natural convection of nanofluid. *Int. J. Heat Mass Transf.* **2015**, *89*, 799–808. [CrossRef]
31. Kandelousi, M.S.; Ellahi, R. Simulation of ferrofluid flow for magnetic drug targeting using the lattice Boltzmann method. *Z. Für Naturforschung A* **2015**, *70*, 115–124. [CrossRef]
32. Zeeshan, A.; Shehzad, N.; Abbas, T.; Ellahi, R. Effects of radiative electro-magnetohydrodynamics diminishing internal energy of pressure-driven flow of Titanium dioxide—Water nanofluid due to entropy generation. *Entropy* **2019**, *21*, 236. [CrossRef]
33. Ellahi, R.; Zeeshan, A.; Hussain, F.; Abbas, T. Two-phase Couette flow of couple stress fluid with temperature dependent viscosity thermally affected by magnetized moving surface. *Symmetry* **2019**, *11*, 647. [CrossRef]
34. Makinde, O.D.; Mabood, F.; Khan, W.A.; Tshehla, M.S. MHD flow of a variable viscosity nanofluid over a radially stretching convective surface with radiative heat. *J. Mol. Liq.* **2016**, *219*, 624–630. [CrossRef]
35. Tie-Gang, F.; Ji, Z.; Shan-Shan, Y. Viscous flow over an unsteady shrinking sheet with mass transfer. *Chin. Phys. Lett.* **2009**, *26*, 014703. [CrossRef]
36. Rohni, A.M.; Ahmad, S.; Pop, I. Flow and heat transfer over an unsteady shrinking sheet with suction in nanofluids. *Int. J. Heat Mass Transf.* **2012**, *55*, 1888–1895. [CrossRef]
37. Atangana, A.; Baleanu, D. New fractional derivatives with non-local and non-singular kernel: Theory and application to heat transfer model. *J. Therm. Sci.* **2016**, *20*, 763–769. [CrossRef]
38. Baleanu, D.; Mousalou, A.; Rezapour, S. On the existence of solutions for some infinite coefficient-symmetric Caputo-Fabrizio fractional integro-differential equations. *Bound. Value Probl.* **2017**, *2017*, 145. [CrossRef]
39. Sheikholeslami, M.; Chamkha, A.J. Influence of Lorentz forces on nanofluid forced convection considering Marangoni convection. *J. Mol. Liq.* **2017**, *225*, 750–757. [CrossRef]
40. Lund, L.A.; Omar, Z.; Khan, I.; Dero, S. Multiple solutions of Cu–$C_6H_9NaO_7$ and Ag–$C_6H_9NaO_7$ nanofluids flow over nonlinear shrinking surface. *J. Cent. South Univ.* **2019**, *26*, 1283–1293. [CrossRef]

coatings

MDPI

Article

Convective Heat Transfer and Magnetohydrodynamics across a Peristaltic Channel Coated with Nonlinear Nanofluid

Arshad Riaz [1,*], Hanan Alolaiyan [2] and Abdul Razaq [1]

[1] Department of Mathematics, Division of Science and Technology, University of Education, Lahore 54770, Pakistan; makenqau@gmail.com
[2] Department of Mathematics, King Saud University, Riyadh 11451, Saudi Arabia; holayan@ksu.edu.sa
* Correspondence: arshad-riaz@ue.edu.pk

Received: 28 October 2019; Accepted: 28 November 2019; Published: 2 December 2019

Abstract: The aim of the current study is to present an analytical and numerical treatment of a two-dimensional peristaltic channel along with the coating of laminar layers of nanoparticles with non-Newtonian (Williamson) base liquid. In addition to this, convective heat transfer and magnetic field effects also take into consideration. The geometry is considered as an asymmetric two dimensional channel experiencing sinusoidal waves propagating across the walls. The walls are supposed to have heat convection at the upper wall and the lower wall is having no temperature gradient. The problem is manufactured under the theory of lubrication approach. The mathematical models are evolved by using appropriate transformations. The obtained nonlinear differential equations are solved analytically. Graphical features are presented to find the influence of emerging physical parameters on the stream function, velocity of the nanofluid, heat transfer, nanoparticles concentration, pressure gradient, and pressure increase. It is found that the velocity decreases in the lower part while increasing in the upper side of the channel in the presence of nanoparticles. The temperature is becoming large with increasing amount of nanoparticles and heat convection at the boundaries. It is also observed that nanoparticle concentration is getting higher with Brownian motion parameter, but fluid becomes less thermal against thermophoresis parameter. The streamlines phenomenon clearly reflects the asymmetry of the channel. The characteristics of viscous fluid can be recovered by switching the Weissenbureg number (We) to zero.

Keywords: nanofluid; Williamson model; peristaltic pumping; convective boundary conditions; asymmetric channel; analytic solutions

1. Introduction

Nanofluids attract current predilection because of its heat conduction attributes. Changing the flow geometry, boundary conditions, or thermal conductivity of liquids can improve convective heat transfer. Over the years, researchers have tried to increase the thermal conductivity of liquids. For this purpose, with the idea of Maxwell [1] solid metal particles are introduced into the base liquid. The large micro-sized particles are used to make suspensions because the conductivity of solids is greater than that of liquids, but these particles tend to produce greater resistance to the flow of base fluid. Modern nanotechnology tends to take a new direction in this field. In 1995, Choi [2] proposed a liquid with nano-sized particles suspended in a base liquid to eliminate the disadvantages of micro-sized particles. These liquids have efficient convective heat transfer compared to pure liquids. Recently, the idea of nanofluid in peristalsis has been studied by some researchers [3–10].

Peristalsis is characterized as the extension and the arrival of a substance into a liquid that improves the formative waves that broaden the length of the conduit, blending and shipping the liquid

toward the wave spread. It is a mechanism that is available in numerous organs of the human body. In some specific instruments—for example heart–lung machines, implantation gadgets, and other pumping apparatus—such types of processes are utilized. It is of specific significance in many species and especially in human body that the transportation of many tissues of the body under various conditions, for example, the sucking of blood by leaches, the heap from the kidneys to the bladder through filtration, transport of the spermatozoa to the male genital tract, the development of the bosom in the Fallopian tubes, vasomotion of little veins, just as the blending and transport of gastrointestinal entry material.

The use of heat is of particular importance in the field due to its wide scope in engineering and biomechanics. In addition, the common relationship of heat stress and peristalsis can be observed during the oxygenation process with the patient. The assessment of magnetic resonance in biological tissues has aroused great interest among researchers regarding physical problems such as blood.

The assessment of heat transfer is related to the conditions of convection used in processes such as thermal conductivity, mechanical properties, chemical reactions, and so on. Aziz [11] presented a similarity solution to incorporate the convective walls conditions for thermal boundary layer on a smooth plate. In another article, Makinde and Aziz [12] developed the MHD mixed model on a flat surface in a concise way in terms of compatibility. Makinde [13] also discussed the flow of the MHD component with the temperature and the mechanical evaluation of a plate on a flat surface with extended conditions. Merkin and Pop [14] considered the analysis of heat transfer by dynamically simulating the flow of a uniform current on a flat surface with a horizontal displacement. According to them, the heat flux near the main edge is dominated by the surface heat flux.

After knowing the significance of the above discussed phenomena, authors are keen to develop a series solution of peristaltic flow of nanofluid with Williamson fluid model as a base liquid with convective boundary conditions travelling through asymmetric channel. At least we know that this study has not been yet explored in the literature. This study will be a good base for the engineers to utilize the results in procedures like thermal energy storage, gas turbines, nuclear workshops, etc. The problem is modeled under the induction of lubrication approach. The series solutions of stream function, temperature distribution, and nanoparticle concentration are achieved by using a well-known converging method the homotopy perturbation method. The important features are analyzed more specifically by sketching graphs to estimate the impact of pertinent constant physical factors.

2. Mathematical Modeling

The incompressible Williamson model is chosen as a base fluid for nanofluid in between an asymmetric channel experiencing heat convection at the peristaltic type surfaces. The width of the channel is taken as $(d_{11} + d_{12})$. Flow is initiated due to the propagation of curved waves travelling with uniform speed c towards the flow. The exchange of heat is recognized by imposing temperatures T_0 and T_1 at the lower and upper areas, correspondingly. To discuss nano particle phenomenon, we have taken the nanoparticle concentration C_0 and on the lower side and upper one, accordingly (see Figure 1).

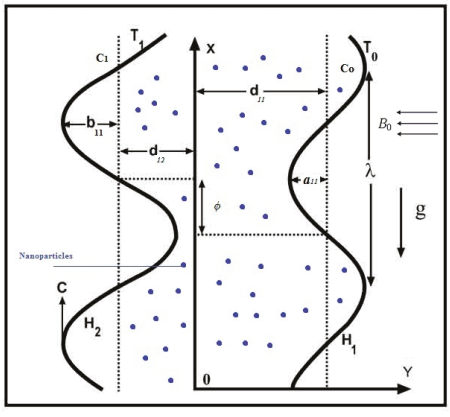

Figure 1. Geometry of the channel.

The magnetic field B_0 is exerted orthogonally. The wall surfaces are taken as

$$Y = H_1 = d_{11} + a_{11}\cos[2\pi\lambda X'] \tag{1}$$

$$Y = H_2 = -d_{12} - b_{11}\cos[2\pi\lambda X' + \overline{\varphi}],\ \text{where}\ X' = X - ct \tag{2}$$

In upper defined equations, a_{11} and b_{11} represent the wave amplitudes, λ gives the wavelength, t suggests the time, X depicts the wave's direction, and Y is placed normally to X. The range of phase variance $\overline{\varphi}$ alters as $0 \le \overline{\varphi} \le \pi$. If $\overline{\varphi} = 0$, we meant that a symmetric dimensional channel is having waves located out of the phase and $\overline{\varphi} = \pi$, suggest the waves within the phase. Moreover a_{11}, b_{11}, d_{11}, d_{12} and $\overline{\varphi}$ overcome the following relation

$$a_{11}^2 + b_{11}^2 + 2a_{11}b_{11}\cos\overline{\varphi} \le (d_{11} + d_{12})^2 \tag{3}$$

The mathematical models of the considered problem given as

$$\nabla \cdot \widehat{V} = 0 \tag{4}$$

$$\rho\left(\frac{\partial \widehat{V}}{\partial t} + \widehat{V}\cdot\nabla\widehat{V}\right) = -\nabla\overline{P} + \nabla\cdot\mathbf{S} + \rho_f\mathbf{g}\alpha_f\left(\widetilde{T} - T_0\right) + \rho_f\mathbf{g}\alpha_f\left(\widetilde{C} - C_0\right) + \mathbf{J}\times\mathbf{B} \tag{5}$$

$$(\rho c)_f\left(\frac{\partial \widetilde{T}}{\partial t} + \widehat{V}\cdot\nabla\widetilde{T}\right) = \nabla\cdot K\nabla\widetilde{T} + \mathbf{S}\cdot\nabla\widehat{V} + (\rho c)_p\left(D_B\left(\nabla\widetilde{C}\cdot\nabla\widetilde{T}\right) + \frac{D_T}{T_m}(\nabla\widetilde{T}\cdot\nabla\widetilde{T})\right) \tag{6}$$

$$\frac{\partial \widetilde{C}}{\partial t} + \hat{V}\cdot\nabla\widetilde{C} = \nabla\cdot\left(D_B\nabla\widetilde{C} + D_T\frac{\nabla\widetilde{T}}{T_o}\right) \tag{7}$$

where $\mathbf{g}$ is the gravitational body force and α_f represents the volumetric volume distension nanofluid's coefficient. In above relations, $(\rho c)_f$ denotes the fluid's heat capacity, $(\rho c)_p$ accounts for effective nanoparticles heat capacity, $\mathbf{J} = \sigma(\widehat{V}\times\overline{\mathbf{B}})$ reveals the current density, $\overline{\boldsymbol{B}} = (0, B_0)$ notifies the external magnetic field, and $\mathbf{S}$ is placed for the Cauchy stress tensor for Williamson fluid and is determined as

$$\boldsymbol{\tau} = \left(\mu_\infty + (\mu_0 + \mu_\infty)\left(1 - \Gamma\dot{\boldsymbol{\gamma}}\right)^{-1}\right)\dot{\overline{\boldsymbol{\gamma}}} \tag{8}$$

where $\dot{\overline{\gamma}}$ comprises the subsequent value

$$\dot{\overline{\gamma}} = \sqrt{\frac{1}{2}\sum_i \sum_j \dot{\gamma}_{ij}\dot{\gamma}_{ji}} = \sqrt{\frac{1}{2}\overline{\Pi}} \tag{9}$$

Here $\overline{\Pi}$ is the strain tensor. The velocity profile for the given problem is considered as $\widehat{V} = (U', V')$. Introducing a wavy frame we introduce the following transformations

$$x = X',\ y = Y,\ u = U' - c,\ v = V',\ p(x) = \overline{P}(X,\ t) \tag{10}$$

We suggest the following dimensionless parameters to be used in the above expressions

$$\begin{gathered} \overline{x} = \tfrac{2\pi x}{\lambda},\ \overline{y} = \tfrac{y}{d_{11}},\ \overline{u} = \tfrac{u}{c},\ \overline{v} = \tfrac{v}{c\delta},\ \delta = \tfrac{d_{11}}{\lambda},\ d = \tfrac{d_{12}}{d_{11}},\ \overline{p} = \tfrac{d_{11}^2 p}{\mu c \lambda},\ h_{11} = \tfrac{H_{11}}{d_{11}},\ h_{12} = \tfrac{H_{12}}{d_{12}}, \\ a_{12} = \tfrac{a_{11}}{d_{11}},\ Br = Ec\mathrm{Pr},\ b = \tfrac{b_{11}}{d_{11}},\ \mathrm{Re} = \tfrac{\rho c d_{11}}{\mu},\ \overline{\psi} = \tfrac{\psi}{c d_{11}},\ \theta = \tfrac{\overline{T} - T_0}{T_1 - T_0},\ Ec = \tfrac{c^2}{c_p(T_1 - T_0)}, \\ \mathrm{Pr} = \tfrac{\rho \nu c}{K},\ \overline{S} = \tfrac{S d_{11}}{\mu c},\ We = \tfrac{\Gamma c}{d_{11}},\ \varphi = \tfrac{\overline{C} - C_0}{C_1 - C_0},\ G_r = \tfrac{\rho_f g \alpha_f d^2 (T_1 - T_0)}{c\mu},\ G_c = \tfrac{\rho_f g \alpha_f d^2 (C_1 - C_0)}{c\mu}, \\ N_b = \tfrac{\tau D_B (C_1 - C_0)}{\nu},\ N_t = \tfrac{\tau D_T (T_1 - T_0)}{\tau T_m}, M = \sqrt{\tfrac{\sigma}{\mu}} B_0 d_{11}, We = \tfrac{\Gamma c}{d_{11}} \end{gathered} \tag{11}$$

where $M, We, Br,$ Pr, N_b, N_t, G_r, and G_c represent the Hartman number, Weissenberg number, Brinkman number, Prandtl number, Brownian motion parameter, thermophoresis parameter, local temperature Grashof number, and local nanoparticle Grashof number, accordingly. After incorporating the above structured parameters and applying the conditions of large wavelength along with small Reynolds number in a wavy frame coordinates we have the final form of Equations (4)–(7)

$$\begin{gathered} \tfrac{\partial u}{\partial x} + \tfrac{\partial v}{\partial y} = 0 \\ \tfrac{dp}{dx} = \tfrac{\partial}{\partial y}\left[\tfrac{\partial^2 \psi}{\partial y^2} - M^2 \psi + We\left(\tfrac{\partial^2 \psi}{\partial y^2}\right)^2\right] + G_r \theta + G_c \varphi \end{gathered} \tag{12}$$

or

$$\frac{\partial^2}{\partial y^2}\left[\frac{\partial^2 \psi}{\partial y^2} + We\left(\frac{\partial^2 \psi}{\partial y^2}\right)^2 - M^2 \psi\right] + G_r \frac{\partial \theta}{\partial y} + G_c \frac{\partial \varphi}{\partial y} = 0 \tag{13}$$

$$\mathrm{Pr}\left[N_b \frac{\partial \varphi}{\partial y}\frac{\partial \theta}{\partial y} + N_t\left(\frac{\partial \theta}{\partial y}\right)^2\right] + \frac{\partial^2 \theta}{\partial y^2} + Br\left[\left(\frac{\partial^2 \psi}{\partial y^2}\right)^2 + We\left(\frac{\partial^2 \psi}{\partial y^2}\right)^3\right] = 0 \tag{14}$$

$$\frac{\partial^2 \varphi}{\partial y^2} + \frac{N_t}{N_b}\frac{\partial^2 \theta}{\partial y^2} = 0 \tag{15}$$

where ψ is stream function satisfying the relations $u = \partial\delta/\partial y$ and $v = -\delta\partial\psi/\partial x$, The no-slip boundary conditions for velocity u and nanoparticles fraction φ and convective boundaries are taken into consideration for temperature θ which have the following dimensionless form in the wave frame [15]

$$\left.\begin{gathered} \psi = \tfrac{F}{2},\ \tfrac{\partial \psi}{\partial y} = -1,\ \text{ at } y = h_{11},\ \ \psi = -\tfrac{F}{2},\ \tfrac{\partial \psi}{\partial y} = -1,\ \text{ at } y = h_{12}, \\ \tfrac{\partial \theta}{\partial y} - B_i \theta = -B_i \text{ at } y = h_{11} \text{ and } \theta = 0 \text{ at } y = h_{12}\Big) \\ \varphi = 1 \qquad \text{at } y = h_{11,} \ \text{ and } \ \varphi = 0 \text{ at } y = h_{12}, \end{gathered}\right\} \tag{16}$$

where $h_{11} = 1 + a_{12}\cos x$ and $h_{12} = -d - b\cos(x + \varphi)$. Also $Bi = h_f d_{11}/K$ is the Biot number, h_f stands for the coefficient of convective thermal transport. The mean flow rate in dimensionless format is elaborated as

$$Q = F + 1 + d \tag{17}$$

3. Solution of the Problem

The above obtained Equations (12)–(15) display the nonlinear ordinary differential equations in which ψ, θ, and φ are mutually dependent. Such types of problems cannot be handled by exact techniques. Therefore, we chose a more appropriate solution procedure, the homotopy perturbation method (HPM) [16,17] to solve the current highly complicated boundary value problems. The deformation equations for ψ, θ, and φ can be constructed as

$$(1-q')\mathcal{L}_1\left(\hat{\psi}-\psi_0\right)+q'\left[\frac{\partial^2}{\partial y^2}\left(\frac{\partial^2\hat{\psi}}{\partial y^2}+We\left(\frac{\partial^2\hat{\psi}}{\partial y^2}\right)^2-M^2\hat{\psi}\right)+G_r\frac{\partial\hat{\theta}}{\partial y}+G_c\frac{\partial\hat{\varphi}}{\partial y}\right]=0, \tag{18}$$

$$(1-q')\mathcal{L}_2\left(\hat{\theta}-\theta_0\right)+q'\left[N_b\frac{\partial\hat{\theta}}{\partial y}\frac{\partial\hat{\varphi}}{\partial y}+N_t\left(\frac{\partial\hat{\theta}}{\partial y}\right)^2+\frac{\partial^2\hat{\theta}}{\partial y^2}+Br\left(\frac{\partial^2\hat{\psi}}{\partial y^2}\right)^2+We\left(\frac{\partial^2\hat{\psi}}{\partial y^2}\right)^3\right]=0, \tag{19}$$

$$(1-q')\mathcal{L}_2(\hat{\varphi}-\varphi_0)+q'\left[\frac{\partial^2\hat{\varphi}}{\partial y^2}+\frac{N_t}{N_b}\frac{\partial^2\hat{\theta}}{\partial y^2}\right]=0, \tag{20}$$

where $£_1$ and $£_2$ are linear operators which are picked as £

$$£_1=\frac{\partial^4}{\partial y^4}\text{ and }£_2=\frac{\partial^2}{\partial y^2} \tag{21}$$

and $\widehat{\psi_0}$, $\widehat{\theta_0}$, and $\widehat{\varphi_0}$ are the initial approximations which must satisfy the boundary conditions as well as differential operator. The initial approximations for ψ, θ, and φ are elected as

$$\widehat{\psi_0}=\frac{(h_{11}-h_{12}-2y)\ (-2(h_{11}-h_{12})\ (h_{11}-y)\ (h_{12}-y))}{2(h_{11}-h_{12})^2}+F\left(\frac{h_{11}^2-4h_{11}h_{12}+h_{12}^2+2(h_{11}+h_{12})\ y-2y^2}{2(h_{11}-h_{12})^2}\right) \tag{22}$$

$$\widehat{\theta_0}=\frac{B_ih_{12}-B_iy}{1-B_ih_{11}+B_ih_{12}} \tag{23}$$

$$\widehat{\varphi_0}=\frac{-h_{12}+y}{h_{11}-h_{12}} \tag{24}$$

Applying perturbation on small embedding parameters $F\in[0,\ 1]$, we suggest the following series solutions

$$\widehat{\psi}=\psi_0+q'\psi_1+q'^2\psi_2\ldots \tag{25}$$

$$\widehat{\theta}=\theta_0+q'\theta_1+q'^2\theta_2\ldots \tag{26}$$

$$\widehat{\varphi}=\varphi_0+q'\varphi_1+q'^2\varphi_2\ldots \tag{27}$$

After substituting the above series solutions in Equations (18)–(20), we get the two systems for ψ, θ, and φ.

- Zeroth Order System

$$\left.\begin{array}{c}£_1\left[\psi_0-\widehat{\psi_0}\right]=0,\\ \psi_0=\frac{F}{2},\ \frac{\partial\psi_0}{\partial y}=-1,\text{ at }y=h_1,\ \psi_0=-\frac{F}{2},\ \frac{\partial\psi_0}{\partial y}=-1,\text{ at }y=h_2,\end{array}\right\} \tag{28}$$

$$\left.\begin{array}{c}£_2\left[\theta_0-\widehat{\theta_0}\right]=0,\\ \theta_0(h_1)-B_i\theta_0(h_1)=-B_i\text{ at }y=h_i\text{ and }\theta_0=0\text{ at }y=h_2\end{array}\right\} \tag{29}$$

$$\left.\begin{array}{c} \pounds_2\left[\varphi_0-\widehat{\varphi_0}\right]=0, \\ \varphi_0=1,\ \text{ at } y=h_1 \text{ and } \varphi_0=0 \text{ at } y=h_2, \end{array}\right\} \tag{30}$$

- First Order System

$$\left.\begin{array}{c} \pounds_1[\psi]+\frac{\partial^2}{\partial y^2}\left[\frac{\partial^2\psi_0}{\partial y^2}+We\left(\frac{\partial^2\psi_0}{\partial y^2}\right)^2-M^2\psi_0\right]+G_r\frac{\partial\theta_0}{\partial y}+G_c\frac{\partial\varphi_0}{\partial y}=0, \\ \psi_1=0,\ \frac{\partial\psi_1}{\partial y}=0,\ \text{ at } y=h_1 \text{ and } \psi_1=0,\ \frac{\partial\psi_1}{\partial y}=0,\ \text{ at } y=h_2, \end{array}\right\} \tag{31}$$

$$\left.\begin{array}{c} \pounds_2(\theta_1)+N_b\left[\frac{\partial\varphi_0}{\partial y}\cdot\frac{\partial\theta_0}{\partial y}\right]+N_t\left(\frac{\partial\theta_0}{\partial y}\right)^2+\frac{\partial^2\theta_0}{\partial y^2}+Br\left[\left(\frac{\partial^2\psi_0}{\partial y^2}\right)^2+We\left(\frac{\partial^2\psi_0}{\partial y^2}\right)^3\right]=0, \\ \theta_1'(h_1)-B_i\theta_1(h_1)=0 \text{ at } y=h_1 \text{ and } \theta_1=0 \text{ at } y=h_2 \end{array}\right\} \tag{32}$$

$$\left.\begin{array}{c} \pounds_2(\varphi_1)+\frac{\partial^2\varphi_0}{\partial y^2}+\frac{N_t}{N_b}\frac{\partial^2\theta_0}{\partial y^2}=0, \\ \varphi_1=0,\ at\ y=h_1,\ \varphi_1=0\ at\ y=h_2, \end{array}\right\} \tag{33}$$

- Zeroth Order Solutions

By solving zeroth order systems by built-in technique in mathematical software, we obtain

$$\psi_0=\widehat{\psi_0}=\frac{(h_{11}+h_{12}-2y)\ (-2(h_{11}-h_{12})\ (h_{11}-y)\ h_{12}-y)}{2(h_{11}-h_{12})}+\frac{F\left(h_{11}^2-4h_{11}h_{12}+h_{12}^2+2(h_{11}+h_{12})\ y\right)-2y}{2(h_{11}-h_{12})^2} \tag{34}$$

$$\theta_0=\widehat{\theta_0}=\frac{B_ih_2-B_iy}{1-B_ih_1+B_ih_2} \tag{35}$$

$$\varphi_0=\widehat{\varphi_0}=\frac{-h_{12}+y}{h_{11}-h_{12}} \tag{36}$$

- First Order Solutions

The first order system has acquired the following general solutions

$$\begin{array}{c} \psi_1=\frac{-1}{6\left(-1+B_i(h_{11}-h_{12})^7\right)}[1/4G_c(-1+B_i(h_{11}-h_{12})^6-6(F+h_{11}-h_{12})(-h_{11}M^2+2h_{11}^3 \\ h_{12}M^2-2h_{11}h_{12}^3M^2+h_{12}^4M^2+48We(F+h_{11}-h_{12})+B_i(h_{11}-h_{12})(G_r(h_{11}-h_{12})^5+ \\ 6(F+h_{11}-h_{12})\left(-h_{11}^4M^2+2h_{11}^3h_{12}M^2++h_{12}^4M^2+48We(F+h_{11}-h_{12})\right)))y^4+ \\ \frac{3}{5}\left(-1+B_i(h_{11}-h_{12})^4(F+h_{11}-h_{12})\ M^2y^5\right)]+L_{11}+yL_{12}+y^2L_{13}+y^3L_{14} \end{array} \tag{37}$$

$$\begin{array}{c} \theta_1=\frac{1}{(-1+B_i(h_{11}-h_{12}))^2(h_{11}-h_{12})^9}[1/2B_i(h_{11}-h_{12})^8((-1+B_i(h_{11}-h_{12}))\ N_b+ \\ B_i(h_{11}-h_{12})\ N_t)\mathrm{Pr}+36Br(-1+B_i(h_{11}-h_{12}))^2(F+h_{11}-h_{12})^2(h_{11}-h_{12})^2(h_{11}^3- \\ 3h_{12}^2(h_{12}-2We)+3h_{11}\left(h_{12}^2+2FWe\right)-h_{12}\left(h_{12}^2-6We+6h_{12}We\right)))y^2-24Br \\ (-1+B_i(h_{11}-h_{12}))^2(F+h_{11}-h_{12})^2(h_{11}+h_{12})\ h_{11}^3-3h_{11}^2(h_{12}-3We)+3h_{12} \\ \left(h_{12}^2+3FWe\right)(-h_{12}(h_{12}^2-9FWe+9h_{12}We))y^3+12Br(-1+B_i(h_{11}-h_{12}))^2(F+ \\ h_{11}-h_{12})^2(h_{11}^3-3h_{11}^2(h_{12}-6We)+3h_{11}\left(h_{12}^2+6FWe\right)-h_{12}(h_{12}^2-18FWe+18 \\ h_{12}We))y^4)]-\frac{432}{5}Br\left(-1+B_i(h_{11}-h_{12})\ (F+h_{11}-h_{12})^2\right)^3Wey^5+L_{15}+yL_{16} \end{array} \tag{38}$$

$$\begin{gathered}\varphi_1 = \frac{1}{(-1+B_i(h_{11}-h_{12}))^2(h_{11}-h_{12})^9 N_b} N_t[1/3B_i(h_{11}-h_{12})^8((-1+B_i(h_{11}-h_{12}))\,N_b+ \\ B_i(h_{11}-h_{12})\,N_t)\mathrm{Pr}+36Br(-1+B_i(h_{11}-h_{12}))^2(F+h_{11}-h_{12})^2(h_{11}-h_{12})^2(h_{11}^3 \\ -3h_{11}^2\left(h_{12}-2We+3h_1\left(h_{12}^2+2FWe\right)-h_{12}\left(h_{12}^2-6FWe+6h_{12}We\right)\right))Y^2-24Br(-1 \\ +B_i(h_{11}-h_{12}))^2(F+h_{11}-h_{12})^2(h_{11}+h_{12})\,h_{11}^3-3h_{12}^2(h_{12}-3We)+h_{11}\left(h_{12}^2+3FWe\right) \\ \left(-h_{12}\left(h_{12}^2-9FWe\right)+9h_2We\right)Y^3+12G_c(-1+B_i(h_{11}-h_{12})^2(F+h_{11}-h_{12})^2 \\ \left(h_{11}^3-3h_{11}^2(h_{12}-6We)+3h_{11}^2(h_{12}-6We)+3h_{11}\left(h_{12}^2+6FWe\right)-h_{12}\left(h_{12}^2-18FWe\right)\right) \\ y^4]-\left(\tfrac{432}{5}Br(-1+B_i(h_{11}-h_{12}))^2(F+h_{11}-h_{12})^2\right)^3 Wey^5+L_{17}+yL_{18}\end{gathered} \tag{39}$$

The final solutions according to the concept of HPM are given by using $q \to 1$ in Equations (2)–(27).

$$\psi = \psi_0 + \psi_1 + \ldots \tag{40}$$

$$\theta = \theta_0 + \theta_1 + \ldots \tag{41}$$

$$\varphi = \varphi_0 + \varphi_1 + \ldots \tag{42}$$

where constants L_{ij}, $i = 1,\ j = 1-8$ can be found by routine calculation. The complete solutions of ψ, θ, and φ can be obtained by supposed solutions. The solution for pressure gradient dp/dx can be found by simply substituting the values in Equation (12). The mathematical formula for the pressure increase function Δp can been visualized in next equation that has been solved numerically by built-in technique numerical integration on Mathematica.

$$\Delta p = \int_0^1 \left(\frac{dp}{dx}\right) dx \tag{43}$$

4. Results and Discussion

This portion comprises of graphical results and discussion of obtained results for velocity, temperature, nanoparticles, pressure gradient, and stream functions. The numerical data of the pressure rise function Δp is also sketched against the domain of flow rate and found the effects of physical parameters separately. Figures 2 and 3 are sketched for the velocity profile with varying the values of (G_r) and (G_c), respectively in corresponding order. From Figure 2, it is clearly visible that velocity is decreasing in lower part and increasing in upper part of the channel and enhances its maximum peak at the center under the effect of G_r. One can see the similar behavior by taking increasing values of G_c but here the difference is that the velocity is not varying much under the effect of G_c in Figure 3. Figures 4–6 contain correspondingly the alteration of temperature profile θ with the variability of Biot number (B_i), Brinkman number (Br), and the Prandtl number (Pr). From Figure 4, one can notice that the temperature profile is stretched vertically with the increase in magnitudes of B_i. It depicts that heat convection at the boundaries enhances the temperature of the Williamson nanofluid. It is also notable here that the temperature is maximum at lower wall and minimum at the lower surface and there is much variation in temperature level at upper region as compared to lower side. Figure 5 reflects the observation that temperature is an increasing function of Br and the temperature gradients are prominent at the lower portions as equated with the upper ones, but the extent of heat is similar at both the surfaces as was observed for B_i. It can be received from Figure 6 that temperature profile is increasing in linear fashion for numerically increasing magnitudes of Pr but the change in heat is calculated more significantly in the central parts of the enclosure which is the totally different result than we have achieved in Figures 4 and 5. Figures 7 and 8 are presented to see the behavior of nanoparticles volume fraction φ with increasing magnitudes of (N_b) and (N_t). Figure 7 shows that φ is getting higher when someone increases N_b. It is also explicit here that nanoparticles are dispersed in the region between the lower and upper surfaces. On the other hand, Figure 8 revels different story, the increase in N_t decreases the nanoparticles concentration. Figure 9 is plotted for

pressure gradient dp/dx for N_b. It is seen that dp/dx is increasing as we increase N_b and gets maximum height at the center of the domain, i.e., $x = 0.5$. From Figure 10, we can see that pressure gradient is varying quite opposite manner for the parameter N_t. It can also be noticed from Figures 9 and 10 that pressure gradient gets positive values only in the central part and remains negative at the corners. Figures 11 and 12 are displaced to see the effects of parameters M and We on pressure rise Δp. Here the whole area is broken into three zones, namely Region I–III. The Region I is recognized by the portion where $Q > 0,\ \Delta p > 0$. Region II is named the place where $Q > 0$ and $\Delta p < 0$ while Region III is composed of the part $Q,\ \Delta p < 0$. Figure 11 shows that Δp curves are increasing in Region I and II while decreasing in Region III with the variation of M. Also, the free pumping exists at $Q \approx 1.5$. In Figure 12, it is observed that in Region I and II, Δp is increasing and in Region III, it is decreasing. Also, the peristaltic pumping occurs in Regions I and II between the interval $(-1.7,\ 0.5)$. The streamlines are drawn in Figures 13–15 for the parameters G_c, We, and M, respectively. From Figure 13, it is clear that the number of boluses is increasing, but size of the trapped bolus is decreasing in lower part of the channel, while in upper portion, the situation is totally reflected in opposite ways. Figure 14 gives the streamlines variation under the different values of We. It is attained here that, in the lower part, the number of boluses is increasing but size is changing randomly. The stream function for M has been sketched in Figure 15 and it is noted in both the lower and upper parts, the size of bolus in increasing while number is decreasing. It is also admitted by Figures 13–15 that trapped boluses are displaced towards left from upper to lower side due to asymmetric dimensions of the channel which can be made symmetric by imposing $\overline{\varphi} = 0$.

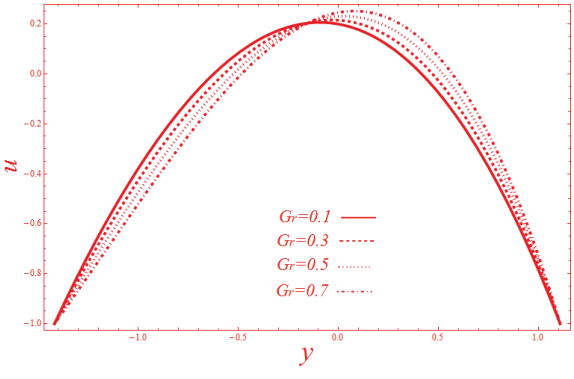

Figure 2. Modification of velocity profile against G_r for $x = 1,\ F = 2,\ a = 0.2,\ b = 0.1,\ d = 1.5,\ \varphi = 1.5,\ G_c = 0.3,\ We = 0.01,\ M = 0.1,\ B_i = 0.5$.

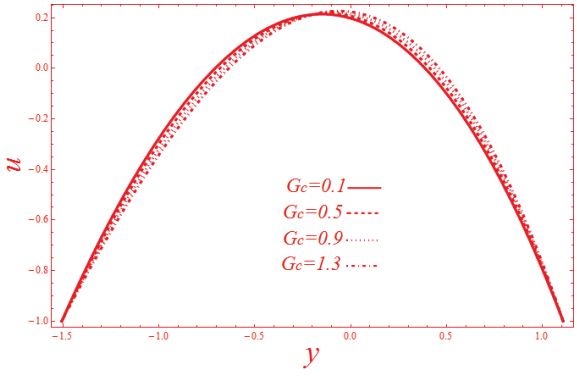

Figure 3. Modification of velocity profile against G_c for $x = 1$, $F = 2$, $a = 0.2$, $b = 0.1$, $d = 1.5$, $\varphi = 1.5$, $G_r = 0.1$, $We = 0.01$, $M = 0.1$, $B_i = 0.5$.

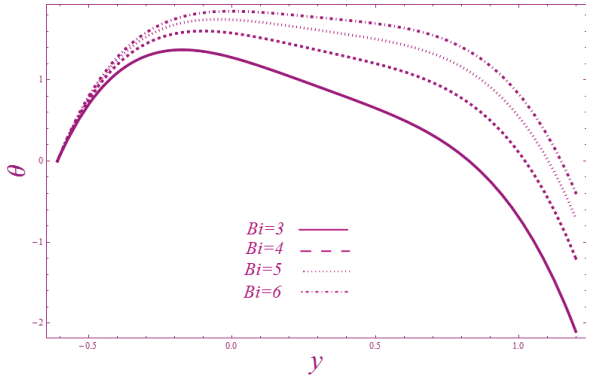

Figure 4. Modification of temperature profile against B_i for, $n = 2$, $x = 0.1$, $F = 5$, $a = 0.2$, $b = 0.1$, $d = 0.51$, $\varphi = 0.01$, $W = 0.01$, $M = 0.1$, $G_c = 0.9$, $G_r = 4$, $G_c = 0.3$, $N_b = 0.5$, Pr $= 0.4$, $N_t = 0.2$.

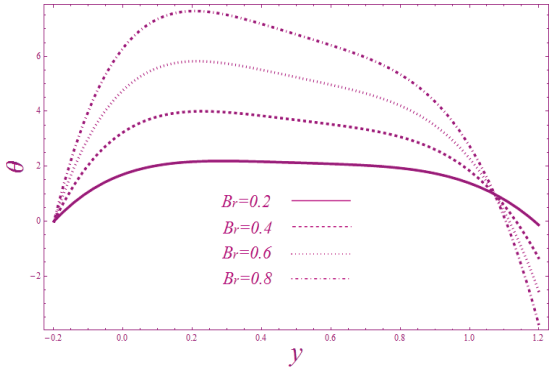

Figure 5. Modification of temperature profile against Br for $n = 2$, $x = 0.1$, $F = 5$, $a = 0.2$, $b = 0.1$, $d = 0.1$, $\varphi = 0.1$, $We = 0.01$, $G_c = 0.9$, $G_r = 1$, $B_i = 10$, $N_b = 0.5$, Pr $= 0.4$, $N_t = 0.2$.

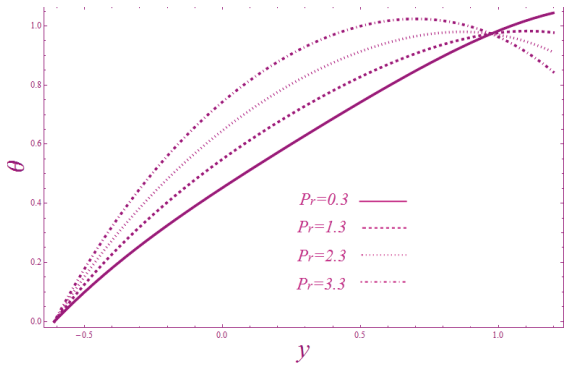

Figure 6. Modification of temperature profile against Pr for $n = 2$, $x = 0.1$, $F = 5$, $a = 0.2$, $b = 0.1$, $d = 0.51$, $\varphi = 0.1$, $We = 0.01$, $G_c = 0.9$, $G_r = 1$, $B_i = 5$, $N_b = 0.5$, $G_c = 0.01$, $N_t = 0.2$.

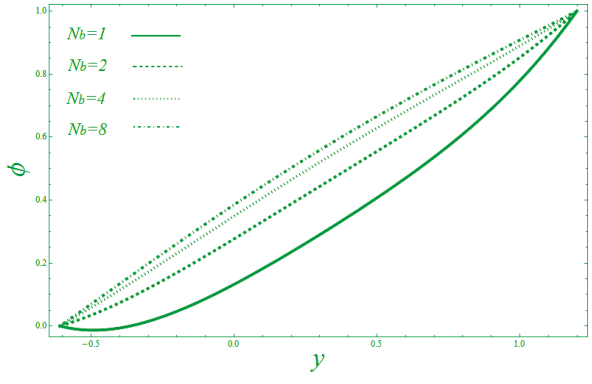

Figure 7. Modification of nanoparticles concentration against N_b for $n = 2$, $x = 0.1$, $F = 5$, $a = 0.2$, $b = 0.1$, $d = 0.51$, $\varphi = 0.01$, $We = 0.01$, $G_c = 0.9$, $G_r = 4$, $B_i = 0.5$, $\mathrm{Pr} = 0.4$, $G_c = 0.1$, $N_t = 0.2$.

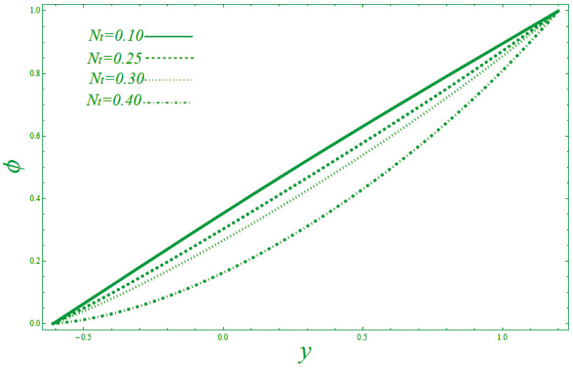

Figure 8. Modification of nanoparticles concentration against N_t for, $n = 2$, $x = 0.1$, $F = 2$, $a = 0.2$, $b = 0.1$, $d = 0.51$, $\varphi = 0.01$, $We = 0.01$,, $G_c = 0.9$, $G_r = 4$, $B_i = 0.5$, $\mathrm{Pr} = 0.4$, $G_c = 0.1$, $N_t = 0.2$.

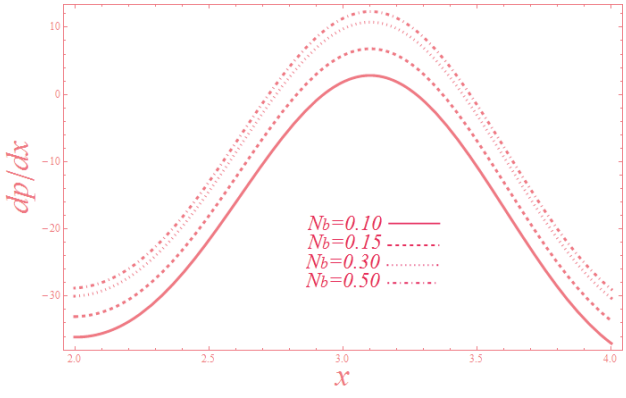

Figure 9. Modification of pressure gradient against N_b for $n = 2$, $y = 0.1$, $F = 10$, $a = 0.2$, $b = 0.1$, $d = 0.51$, $\varphi = 0.01$, $We = 0.1$, $G_c = 0.9$, $G_r = 4$, $B_i = 0.5$, $\mathrm{Pr} = 0.4$, $G_c = 0.1$, $M = 1.5$, $N_t = 0.2$.

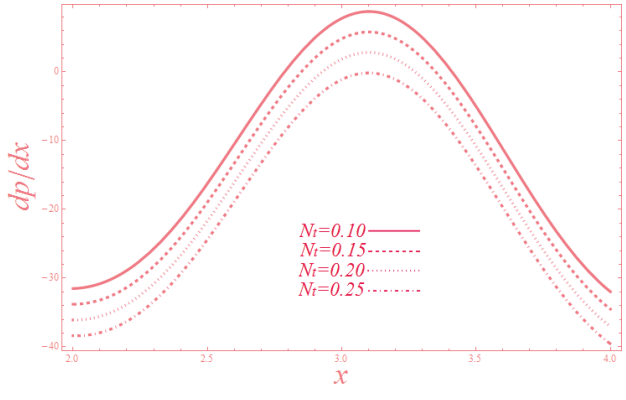

Figure 10. Modification of pressure gradient against N_t for, $n = 2$, $y = 0.1$, $F = 10$, $a = 0.2$, $b = 0.1$, $d = 0.51$, $\varphi = 0.01$, $We = 0.1$, , $G_c = 0.9$, $G_r = 4$, $B_i = 0.09$, $\mathrm{Pr} = 0.4$, $G_c = 0.3$, $M = 1.5$, $N_b = 0.1$.

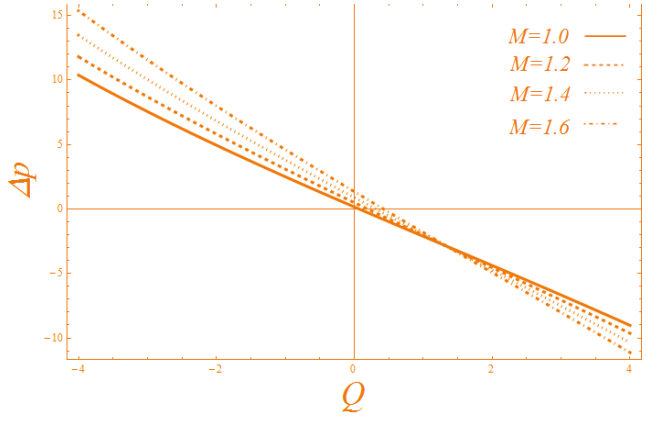

Figure 11. Modification of pressure rise against M for, $n = 2$, $y = 0.1$, $F = 10$, $a = 0.2$, $b = 0.3$, $d = 0.5$, $\varphi = 0.01$, $M = 1.3$, $G_c = 0.3$, $G_r = 0.1$, $B_i = 0.3$, $\mathrm{Pr} = 0.4$, $G_c = 0.3$, $N_b = 0.3$, $N_t = 0$.

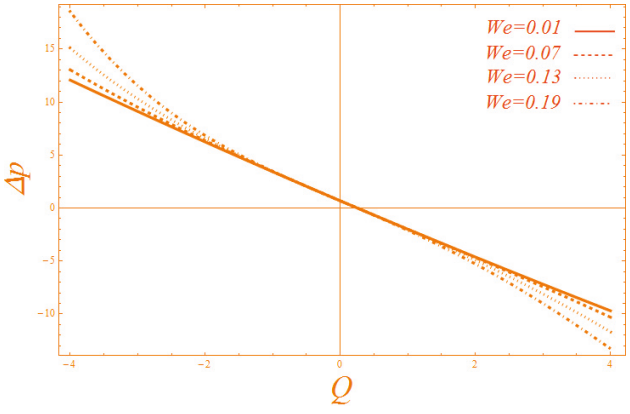

Figure 12. Modification of pressure rise against *We* for, $n = 0.1$, $y = 0.1$, $a = 0.2$, $b = 0.3$, $d = 0.5$, $\varphi = 0.01$, $M = 1.3$, $G_c = 0.3$, $G_r = 0.1$, $B_i = 0.3$, $\mathrm{Pr} = 0.4$, $G_c = 0.3$, $N_b = 0.3$, $N_t = 0.2$.

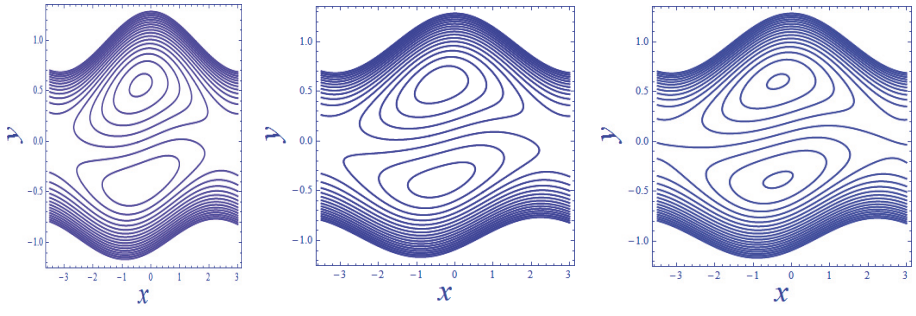

Figure 13. Modification of streamlines for $G_c = \{0.1, 0.5, 0.9\}$ when $n = 0.1$, $y = 0.1$, $F = 5$, $a = 0.3$, $b = 0.2$, $d = 0.1$, $\varphi = 0.01$, $M = 0.1$, $We = 0.1$, $G_r = 4$, $B_i = 0.09$, $\mathrm{Pr} = 0.4$, $Br = 0.9$, $N_b = 0.5$, $N_t = 0.2$.

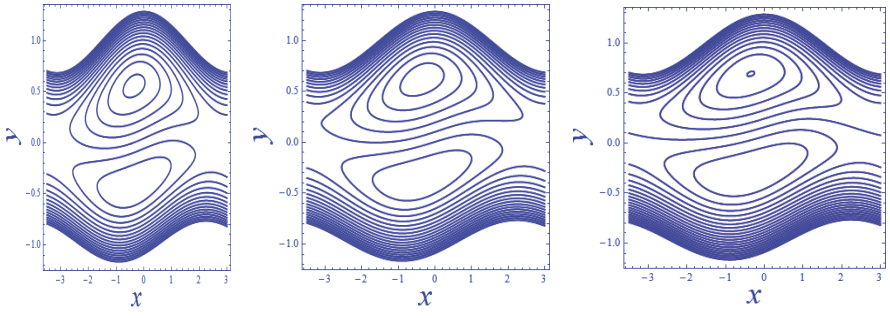

Figure 14. Modification of streamlines for $We = \{0.1, 0.2, 0.3\}$ when $n = 0.1$, $y = 0.1$, $a = 0.2$, $b = 0.3$, $d = 0.5$, $\varphi = 0.01$, $M = 0.1$, $B_i = 0.09$, $\mathrm{Pr} = 0.4$, $G_c = 0.9$, $G_r = 4$, $N_b = 0.5$, $N_t = 0.2$.

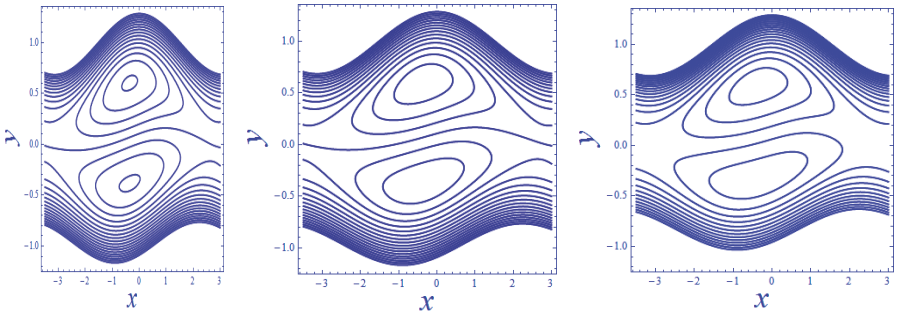

Figure 15. Modification of streamlines for $M = \{0.1, 0.9, 1.7\}$ when $n = 2$, $F = 5$, $a = 0.3$, $b = 0.2$, $d = 1$, $\varphi = 0.01$, $We = 0.1$, $G_r = 4$, $Gc = 0.1$, $B_i = 0.09$, $\mathrm{Pr} = 0.4$, $G_c = 0.9$, $N_b = 0.5$, $N_t = 0.2$.

5. Conclusions

In this article, the authors have discovered the mathematical treatment of the peristaltic flow of Williamson nanofluid coated with the walls of an asymmetric heated channel. The flow has been studied analytically and graphically through variation of some pertinent parameters. From the above discussion, the main findings are given below:

(1) The velocity of nanofluid is decreasing in the lower part while increasing in the upper side with local temperature Grashof number and local nanoparticle Grashof number.
(2) The temperature is becoming large with an increase in Biot number, Brinkman number, and Prandtl number.
(3) The nano particle concentration is getting higher when we increase Brownian motion parameter, but diminishes with thermophoresis parameter.
(4) The pressure gradient is increasing with Brownian motion parameter, but lessening for thermophoresis parameter.
(5) The peristaltic pumping fasten up with Hartman number and Weissenberg number.
(6) In the upper portion, the size of the trapped bolus is decreasing, but increasing in lower portion when we increase local nanoparticle Grashof numbers and Weissenberg numbers, but it varies in a random manner with Hartman numbers.
(7) It is important to notice that boluses are trapped by their position in lower and upper corners of the channel due to its asymmetric structure. We can recover the results of symmetric channel by neglecting the phase difference.
(8) The study of viscous nanofluid can be approached by neglecting Weissenburg number.

Author Contributions: Methodology, formal Analysis and writing—original draft preparation, A.R. (Arshad Riaz); writing—review and editing, A.R. (Abdul Razaq); funding acquisition, H.A.

Funding: This research project was supported by a grant from the Research Center of the Center for Female Scientific and Medical Colleges, Deanship of Scientific Research, King Saud University, Saudi Arabia.

Conflicts of Interest: The authors declare no conflict of interest.

References

1. Maxwell, J.C. *A Treatise on Electricity and Magnetism*, 2nd ed.; Clarendan Press: Oxford, UK, 1881.
2. Choi, S.U.S.; Eastman, J.A. *Enhancing Thermal Conductivity of Fluids with Nanoparticles*; Argonne National Lab: Du Page County, IL, USA, 1995.
3. Hassan, M.; Marin, M.; Alsharif, A.; Ellahi, R. Convective heat transfer flow of nanofluid in a porous medium over wavy surface. *Phys. Lett. A* **2018**, *382*, 2749–2753. [CrossRef]

4. Safaei, M.R.; Togun, H.; Vafai, K.; Kazi, S.N.; Badarudin, A. Investigation of heat transfer enhancement in a forward-facing contracting channel using FMWCNT nanofluids. *Numer. Heat Transf. Part A Appl.* **2014**, *66*, 1321–1340. [CrossRef]
5. Alsagri, A.S.; Nasir, S.; Gul, T.; Islam, S.; Nisar, K.S.; Shah, Z.; Khan, I. MHD Thin Film Flow and Thermal Analysis of Blood with CNTs Nanofluid. *Coatings* **2019**, *9*, 175. [CrossRef]
6. B'eg, O.A.; Tripathi, D. Mathematica simulation of peristaltic pumping with double-diffusive convection in nanofluids: A bio-nano-engineering model. *J. Nanoeng. Nanosyst.* **2011**, *225*, 99–114.
7. Akbar, N.S.; Maraj, E.N.; Butt, A.W. Copper nanoparticles impinging on a curved channel with compliant walls and peristalsis. *Eur. Phys. J. Plus.* **2014**, *129*, 183. [CrossRef]
8. Bhatti, M.M.; Rashidi, M.M. Effects of thermo-diffusion and thermal radiation on Williamson nanofluid over a porous shrinking/stretching sheet. *J. Mol. Liq.* **2016**, *221*, 567–573. [CrossRef]
9. Bhatti, M.M.; Sheikholeslami, M.; Zeeshan, A. Entropy analysis on electro kinetically modulated peristaltic propulsion of magnetized nanofluid flow through a microchannel. *Entropy* **2017**, *19*, 481. [CrossRef]
10. Prakash, J.; Tripathi, D.; Tiwari, A.K.; Sait, S.M.; Ellahi, R. Peristaltic Pumping of Nanofluids through a Tapered Channel in a Porous Environment: Applications in Blood Flow. *Symmetry* **2019**, *11*, 868. [CrossRef]
11. Aziz, A. A similarity solution for laminar thermal boundary layer over a flat plate with a convective surface boundary condition. *Commun. Nonlinear Sci. Numer. Simul.* **2009**, *14*, 1064–1068. [CrossRef]
12. Makinde, O.D.; Aziz, A. MHD mixed convection from a vertical plate embedded in a porous medium with a convective boundary condition. *Int. J. Therm. Sci.* **2010**, *49*, 1813–1820. [CrossRef]
13. Makinde, O.D. Similarity solution of hydromagnetic heat and mass transfer over a vertical plate with a convective surface boundary condition. *Int. J. Phys. Sci.* **2010**, *5*, 700–710.
14. Merkin, J.H.; Pop, I. The forced convection flow of a uniform stream over a flat surface with a convective surface boundary condition. *Commun. Nonlinear Sci. Numer. Simul.* **2011**, *16*, 602–3609. [CrossRef]
15. Akbar, N.S. Non-Newtonian fluid flow in an asymmetric channel with convective surface boundary condition: A note. *J. Power Technol.* **2014**, *94*, 34–41.
16. He, J.H. Homo topy perturbation method for solving boundary value problems. *Phys. Lett. A* **2006**, *350*, 87–88. [CrossRef]
17. He, J.H. Homotopy perturbation method: A new nonlinear analytical technique. *Appl. Math. Comput.* **2003**, *135*, 73–79. [CrossRef]

coatings

MDPI

Article

Impact of Second-Order Slip and Double Stratification Coatings on 3D MHD Williamson Nanofluid Flow with Cattaneo–Christov Heat Flux

Muhammad Ramzan [1,2], Asma Liaquet [1], Seifedine Kadry [3], Sungil Yu [4], Yunyoung Nam [5,*] and Dianchen Lu [6]

1 Department of Computer Science, Bahria University, Islamabad 44000, Pakistan; mramzan@bahria.edu.pk (M.R.); asmaabbasi323@gmail.com (A.L.)
2 Department of Mechanical Engineering, Sejong University, Seoul 143-747, Korea
3 Department of Mathematics and Computer Science, Faculty of Science, Beirut Arab University, Beirut 11072809, Lebanon; skadry@gmail.com
4 Department of ICT Convergence Rehabilitation Engineering, Soonchunhyang University, Asan 31538, Korea; rebiton@naver.com
5 Department of Computer Science and Engineering, Soonchunhyang University, Asan 31538, Korea
6 Faculty of Science, Jiangsu University, Zhenjiang 212013, China; dclu@ujs.edu.cn
* Correspondence: ynam@sch.ac.kr

Received: 1 November 2019; Accepted: 9 December 2019; Published: 11 December 2019

Abstract: The present research examines the impact of second-order slip with thermal and solutal stratification coatings on three-dimensional (3D) Williamson nanofluid flow past a bidirectional stretched surface and envisages it analytically. The novelty of the analysis is strengthened by Cattaneo–Christov (CC) heat flux accompanying varying thermal conductivity. The appropriate set of transformations is implemented to get a differential equation system with high nonlinearity. The structure is addressed via the homotopy analysis technique. The authenticity of the presented model is verified by creating a comparison with the limited published results and finding harmony between the two. The impacts of miscellaneous arising parameters are deliberated through graphical structures. Some useful tabulated values of arising parameters versus physical quantities are also discussed here. It is observed that velocity components exhibit an opposite trend with respect to the stretching ratio parameter. Moreover, the Brownian motion parameter shows the opposite behavior versus temperature and concentration distributions.

Keywords: coatings; second order slip; double stratification; Cattaneo–Christov heat flux; variable thermal conductivity; Williamson nanofluid

1. Introduction

The heat transfer phenomenon plays a vital role when the temperature varies between different bodies or parts of the same body. Heat can be transferred by three methods: convection of fluids, conduction in solids, and radiation. To examine body heat transfer, the principle of heat transfer can be applied to the human body. Here, we can quote one example: the metal pan is used to transfer heat from the stove to food. Some applications of heat transfer are cooking food over metal pots, boiling milk in metal pots, and thermal treatment of pain by a hot water bag. Straughan [1] considered the Cattaneo–Christov (CC) model for heat flux and thermal convection over a Newtonian fluid. Khan et al. [2] analyzed it numerically by engaging the bvp4c MATLAB-based function on a Sisko fluid flow accompanied by generalized Fick's and Fourier's laws over a nonlinear stretched surface. Hayat et al. [3] examined analytically the magnetohydrodynamics (MHD) flow of Jeffrey fluid past a variable thick surface via the impacts of the chemical reaction and the CC model in a

stratified medium. Waqas et al. [4] investigated the CC heat flux model for energy equation formulation rather than Fourier's law of heat conduction. It was observed that a variable thermal conductivity remains inversely proportional to a temperature profile. The Soret–Dufour effects on walls with the second-grade fluid flow between inclined parallel plain walls were inspected by Khan et al. [5]. Heat transfer characteristics of the incompressible flow of the second-grade fluid flow produced by a stretching sheet were analyzed by Ghadikolaei et al. [6]. Khan et al. [7] investigated the behavior of homogenous–heterogeneous reactions against heat transfer flow due to a stretching sheet. They noticed that homogenous–heterogeneous reactions reduce fluid concentration.

In modern engineering processes, especially in metallurgical engineering and metalworking practices, the role of MHD is fundamental for electrically conducting fluids. The magnetic field function is crucial in cooling the hot plasma inside a nuclear reactor vessel. Similarly, the magnetic field is employed for the mixing of metals inside an electrical furnace [8]. Chamkha et. al. [9] analyzed the magnetic field effect on the mixed convection unsteady flow in an ambient fluid past a cone rotating with an unsteady angular velocity. Pullepu et al. [10] analyzed the free convection flow with variable surface temperature over a nonisothermal vertical cone. Akbar et al. [11] examined the two dimensional (2D) electrically conducting flow of the hyperbolic tangent fluid past a stretching surface. They observed that an increment in the Hartmann number decelerates the fluid velocity in the domain of the stretching sheet. Seini et al. [12] d the magnetic field impact over a stretching surface accompanied by the appearance of slip velocity near the stagnation point flow. They perceived that the impact of the magnetic field is more significant on the velocity profile. Ravindran et al. [13] considered the impact of a transverse magnetic field and heat generation and absorption on time-dependent mixed convection flow over a porous cone with a chemical reaction. Boland et al. [14] simulated MHD flow of viscous fluid over a circular cylinder covered with a permeable layer. They adopted the Darcy–Brinkman–Forchheimer model to study the flow inside a porous medium. Ellahi et al. [15] investigated the influence of a Hall current on MHD Jeffrey fluid flow over a nonuniform duct. Mishra et al. [16] explored heat transfer and mass in the appearance of a magnetic field of viscoelastic fluid flow. They determined that the behavior of the magnetic field against the velocity profile is opposite to temperature distribution and concentration profiles. Hussain et al. [17] analyzed numerically the influence of the applied magnetic field on a non-Newtonian fluid flow past a stretching surface.

Nanofluids are vital in many engineering applications, such as in biomedical engineering and many chemical processes. Nanofluid is composed of nanometer-sized particles with a diameter of less than 100 nm and some conventional fluid. The basic aim of using nanofluids is to upgrade the heat transfer and thermal conductivity to attain better cooling. Khan et al. [18] d nanofluid flow over a stretching sheet. Makinde [19] extended the work of Khan et al. [18] to convective boundary condition in nanofluid flow. Nadeem et al. [20] analyzed the second-grade nanofluid (nonorthogonal stagnation point) flow in the direction of the stretching surface. The impact of the variable magnetic field on the nanofluid flow between two disks was explored by Hayami et al. [21]. They found the analytical solution via the homotopy perturbation method and observed that the temperature of the boundary layer thickness decreases with the increase of the Brownian motion parameter and thermophoretic factor. Nanofluid flow in a permeable medium over a convectively heated permeable shrinking sheet was examined by Hayat et al. [22]. Sheikholeslami et al. [23,24] considered the behavior of the magnetic field on the free and forced convection flow of nanofluids respectively by making use of the two-phase model. Hassan et al. [25] elaborated on convective transport of heat transfer in a nanofluid through a porous medium. They concluded that convective heat transfer is improved by nanoparticle concentration, and the magnetic field impacts second-order slip flow. Nayak et al. [26] focused on the numerical solution of the three-dimensional (3D) nanofluid flow with nonlinear thermal radiation with convective conditions and slip. Hosseini et al. [27] observed the nanofluid MHD flow in a microchannel heat sink via the KKL (Koo–Kleinsteuer–Li) model. They noticed that the interaction between nanoparticles and the solid phase enhances the Nusselt number. In recent years, several scientists have used nanofluid heat transfer in their studies [28–34].

Fluids are basically divided into two groups: Newtonian [35] and non-Newtonian fluids [36]. Fluids that abide by Newton's law of viscosity are termed Newtonian fluids. However, a contradiction to Newton's law of viscosity is observed in non-Newtonian fluids. Applications of non-Newtonian fluids may be found in many industrial and engineering areas, glass fiber, hot rolling, casting, and paper production. Amongst many non-Newtonian fluids, Williamson fluid possesses shear thinning property (i.e., viscosity tends to decrease when shear stress increases). Abundant articles may be found in the literature that highlight the importance of Williamson fluid in numerous scenarios. Ramzan et al. [37] examined Williamson nanofluid flow over a Riga plate. They found that with an increase in Williamson fluid parameter velocity, distribution decreases. Ramzan et al. [38] also analyzed the numerical solution of the 2D MHD stagnation point of Williamson fluid flow under the effect of homogeneous–heterogeneous reactions over a linearly stretched surface and found opposite behavior of temperature and velocity distribution against the Williamson fluid parameter. Nadeem et al. [39,40] analyzed the 2D Williamson fluid flow over a stretching sheet considering the influence of nanosized particles, also characterized as Williamson nanofluid. They studied the Williamson nanofluid peristaltic flow in a curved channel, including compliant walls.

Homotopy analysis method (HAM) was suggested by Liao [41] in 1992 to solve highly nonlinear differential equations. This technique has an edge over the rest of the contemporary techniques. HAM is one of the best and simplest technique for obtaining the convergent series solution for weakly, as well as, highly nonlinear differential equations. This technique includes the concept of homotopy from topology. HAM is used for finding a convergent series solution with high nonlinearity. Homotopy discriminates itself from other methods in the following ways:

1. Freedom to choose large or small parameters;
2. Guaranteed series solution convergence; and
3. Freedom to choose linear operators and base function.

There have been many attempts in the literature to discuss the varied fluid problems utilizing the homotopy analysis method [42–49].

A literature review discloses that copious literature may be quoted in the case of 2D non-Newtonian flows. Less work is available on 3D geometries, and this group becomes narrower if we talk about 3D Williamson nanofluid flows. The subject matter of 3D MHD flow of Williamson nanofluid over a bidirectional stretched surface with second-order slip and double stratification is even more rarely discussed. The structure of this paper is as follows: In Section 2, we present the mathematical model. In Sections 3–5, we discuss the homotopic scheme in detail with zeroth and mth order solutions. In Section 6, we address the convergence analysis. In Section 7, we present the results and discuss their physical importance, and finally, we provide concluding remarks.

2. Mathematical Modeling

Here, we consider the steady 3D Williamson nano liquid flow with velocities of $U_w = ax$ in the x-direction and $V_w = by$ in the y-direction, respectively, over a bidirectional extended sheet. While a and b are constants (Figure 1), concentration buoyancy force and thermal are used by the fluid with double stratification phenomena to study heat and mass transfers.

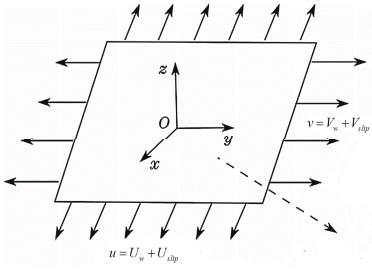

Figure 1. Schematic flow diagram.

The following are the governing boundary layer equations:

$$u_x + v_y + w_z = 0 \tag{1}$$

$$uu_x + vu_y + wu_z = \nu u_{zz} + \sqrt{2}\Gamma \nu u_z u_{zz} - \frac{\sigma B_0^2}{\rho} u + \begin{bmatrix} g[\alpha_1(T - T_\infty) + \alpha_2(T - T_\infty)^2] + \\ g[\alpha_3(\mathrm{C} - C_\infty) + \alpha_4(\mathrm{C} - C_\infty)^2] \end{bmatrix} \tag{2}$$

$$uv_x + vv_y + wv_z = \nu v_{zz} + \sqrt{2}\Gamma \nu v_z v_{zz} - \frac{\sigma B_0^2}{\rho} v \tag{3}$$

$$q + \lambda_E(q_t + V.\nabla q - q.\nabla V + (\nabla.\mathrm{V})\mathrm{q}) = -\nabla(\mathrm{kT}) \tag{4}$$

$$J + \lambda_C(\mathrm{J}_t + V.\nabla J - J.\nabla V + (\nabla.\mathrm{V})\mathrm{J}) = -D_B \nabla \mathrm{C} \tag{5}$$

$$q + \lambda_E(V.\nabla q - q.\nabla V) = -\nabla(kT) \tag{6}$$

$$J + \lambda_C(V.\nabla J - J.\nabla V) = -D_B \nabla C \tag{7}$$

under the supervision of above-mentioned consideration and the impression of thermophoresis and Brownian-motion, Equations (6) and (7) takes the form:

$$uT_x + vT_y + wT_z + \lambda_E \phi_E = \frac{1}{\rho c_p} \frac{\partial}{\partial z}(kT_z) + \tau[D_B C_z T_z + \frac{D_T}{T_\infty}(T_z)^2 \tag{8}$$

$$uC_x + vC_y + wC_z + \lambda_C \phi_C = D_B C_{zz} + \frac{D_T}{T_\infty} T_{zz} \tag{9}$$

where

$$\phi_E = u^2 T_{xx} + v^2 T_{yy} + wT_{zz} + 2uvT_{xy} + 2uwT_{xz} + 2vwT_{yz} + \begin{bmatrix} (uu_x + vu_y + wu_z)T_x + \\ (uv_x + vv_y + wv_z)T_y + \\ (uw_x + vw_y + ww_z)T_z \end{bmatrix} \tag{10}$$

$$\phi_C = u^2 C_{xx} + v^2 C_{yy} + wC_{zz} + 2uvC_{xy} + 2uwC_{xz} + 2vwC_{yz} + \begin{bmatrix} (uu_x + vu_y + wu_z)\mathrm{C}_x + \\ (uv_x + vv_y + wv_z)\mathrm{C}_y + \\ (uw_x + vw_y + ww_z)\mathrm{C}_z \end{bmatrix} \tag{11}$$

following boundary conditions supports the above-mentioned system of equations:

$$\begin{array}{l} u = U_w + U_{slip} \quad v = V_w + V_{slip} \quad w = 0 \\ T = T_w = T_0 + d_1 x \quad C = C_w = C_0 + d_2 x \qquad\qquad \text{at} \quad z = 0 \\ u \to 0 \;\; v \to 0 \;\; T \to T_\infty = T_0 + e_1 x \;\; C \to C_\infty = C_0 + e_2 x \qquad \text{as} \quad z \to \infty \end{array} \tag{12}$$

here

$$U_{slip} = \frac{2}{3}\left(\frac{3 - \alpha l^3}{\alpha} - \frac{3}{2}\frac{1 - l^2}{K_n}\right)\Lambda u_z - \frac{1}{4}\left(l^4 + \frac{2}{K_n^2}(1 - l^2)\right)\Lambda^2 u_{zz} = Au_z + Bu_{zz} \tag{13}$$

$$V_{slip} = \frac{2}{3}\left(\frac{3-\alpha l^3}{\alpha} - \frac{3}{2}\frac{1-l^2}{K_n}\right)\Lambda v_z - \frac{1}{4}\left(l^4 + \frac{2}{K_n^2}(1-l^2)\right)\Lambda^2 v_{zz} = Cv_z + Dv_{zz}, \tag{14}$$

where $A = \frac{2}{3}\left(\frac{3-\alpha l^3}{\alpha} - \frac{3}{2}\frac{1-l^2}{K_n}\right)\Lambda$, $B = -\frac{1}{4}\left(l^4 + \frac{2}{K_n^2}(1-l^2)\right)\Lambda^2$, $C = \frac{2}{3}\left(\frac{3-\alpha l^3}{\alpha} - \frac{3}{2}\frac{1-l^2}{K_n}\right)\Lambda$, $D = -\frac{1}{4}\left(l^4 + \frac{2}{K_n^2}(1-l^2)\right)\Lambda^2$, $l = \min\left[\frac{1}{K_n}, 1\right]$, α describes momentum accommodation coefficient and varies from $0 \le \alpha \le 1$ K_n denotes Knudsen number and Λ denotes molecular mean free path. On the basis of definition of l, we found for any particular estimates of K_n we own $1 \ge l \ge 0$. The molecular mean free path is always positive. Therefore, we know that B, D < 0 and C and A are positive.

To solve Equations (1),(3) and (8),(9), following similarity transformations are introduced:

$$\begin{array}{lll} u = axf\prime(\eta) & v = ayg\prime(\eta) & w = -\sqrt{av}(f(\eta)+g(\eta)) \\ \theta(\eta) = \frac{T-T_\infty}{T_w-T_\infty} & \phi(\eta) = \frac{C-C_\infty}{C_w-C_\infty} & \eta = \sqrt{\frac{a}{\nu}}z \end{array} \tag{15}$$

here, f, g, θ and ϕ are the non-dimensional form for both velocities, temperature and the concentration.

Condition for incompressibility is self-satisfied and Equations (2),(3) and (8),(9) reduce to:

$$f''' - f\prime^2 + (f+g)f'' + Wef''f''' + \lambda(1+\beta_2\theta)\theta + \lambda Nr(1+\beta_3\phi)\phi - Haf\prime = 0 \tag{16}$$

$$\mathrm{g}''' - g\prime^2 + (f+g)\mathrm{g}'' + Weg''\mathrm{g}''' - Hag\prime = 0 \tag{17}$$

$$\begin{array}{l} (1+\varepsilon\theta)\theta'' + \varepsilon\theta'^2 + \mathrm{Pr}N_b\theta\prime\phi\prime + \mathrm{Pr}N_t\theta'^2 - \mathrm{Pr}f\prime(S_1+\theta) + \\ \mathrm{Pr}(f+g)\theta\prime - \delta_t\mathrm{Pr}\left(\begin{array}{l} (f+g)^2\theta'' - 2f\prime\theta\prime(f+g) + \left(f\prime^2 - f''(f+g)\right)(S_1+\theta) \\ +(f+g)(f\prime+g\prime)\theta\prime \end{array} \right) = 0 \end{array} \tag{18}$$

$$\begin{array}{l} \phi'' + \frac{N_t}{N_b}\theta'' - \mathrm{Pr}Lef\prime(\mathrm{S}_2+\phi) + \mathrm{Pr}Le(f+g)\phi\prime - \\ \mathrm{Pr}Le\delta_c\left(\begin{array}{l} (f+g)^2\phi'' - 2f\prime(f+g)\phi\prime + \left(f\prime^2 - f''(f+g)\right)(S_2+\phi) + \\ (f+g)(f\prime+g\prime)\phi\prime \end{array} \right) \end{array} \tag{19}$$

and boundary conditions hold the form

$$\begin{array}{l} f(0) = 0 \; f\prime(0) = 1 + \gamma_1 f''(0) + \gamma_2 f'''(0) \;\; \mathrm{g}(0) = 0 \\ \mathrm{g}\prime(0) = 1 + \gamma_3 \mathrm{g}''(0) + \gamma_4 \mathrm{g}'''(0) \;\; \theta(0) = 1 - \mathrm{S}_1 \;\; \phi(0) = 1 - \mathrm{S}_2 \\ \mathrm{f}\prime(\infty) \to 0 \;\; \mathrm{g}\prime(\infty) \to 0 \; \theta(\infty) = 0 \; \phi(\infty) = 0 \qquad\qquad as \quad z \to \infty \end{array} \tag{20}$$

where the parameters given above are defined as follows:

$$\begin{array}{l} \lambda = \frac{Gr_x}{\mathrm{Re}_x^2} \;\; Gr_x = \frac{g\beta_T(T_w-T_\infty)x^3}{\nu^2} \; \mathrm{Re}_x = \frac{u_w x}{\nu} Nr = \frac{\alpha_3(C_w-C_0)}{\alpha_1(\mathrm{T}_w-T_0)} \; \mathrm{S}_1 = \frac{e_1}{d_1} \\ \gamma_1 = A\sqrt{\frac{a}{\nu}} \;\; \gamma_2 = B\frac{a}{\nu} \;\; \gamma_3 = C\sqrt{\frac{a}{\nu}} \;\; \gamma_4 = D\frac{a}{\nu} \;\; \beta_2 = \frac{\alpha_2}{\alpha_1}(T_w - T_0) \; \beta = \frac{b}{a} \\ \beta_3 = \frac{\alpha_4}{\alpha_3}(C_w - C_0) \quad \alpha_1 = \beta_T \;\; We = U_w\Gamma\sqrt{\frac{2c}{\nu}} \;\; \mathrm{Pr} = \frac{\mu c_p}{k} \; Ha = \frac{\sigma B_0^2}{\rho a} \mathrm{S}_2 = \frac{e_2}{d_2} \\ Le = \frac{\alpha}{D_B} \;\; Nt = \frac{\tau D_T(T_w-T_0)}{T_\infty\nu} \;\; Nb = \frac{\tau D_B(\mathrm{C}_w-C_0)}{T_\infty\nu} \;\; \delta_c = \lambda_C a \;\; \delta_t = \lambda_E a \end{array} \tag{21}$$

C_{fx} is the coefficients of Skin friction in x- and C_{fy} in the y-direction are represented as follows:

$$C_{fx} = \frac{\tau_{wx}}{\rho U_w^2} \quad C_{fy} = \frac{\tau_{wy}}{\rho U_w^2} \tag{22}$$

$$\text{where } \tau_{wx}|_{z=0} = u_z + \frac{\Gamma}{\sqrt{2}}(\mathrm{u}_z)^2 \;\text{ and }\; \tau_{wy}\big|_{z=0} = v_z + \frac{\Gamma}{\sqrt{2}}(\mathrm{v}_z)^2 \tag{23}$$

Coefficients of Skin friction in dimensionless forms are:

$$\begin{array}{l} C_{fx}\mathrm{Re}^{\frac{1}{2}} = [f'' + \frac{We}{2}(f'')^2]_{\eta=0} \\ C_{fy}\mathrm{Re}^{\frac{1}{2}} = [\mathrm{g}'' + \frac{We}{2}(\mathrm{g}'')^2]_{\eta=0} \end{array} \tag{24}$$

3. Homotopic Solutions

For the considered problem, $(L_f, L_g, L_\theta, L_\phi)$ are the linear operators and $(f_0, g_0, \theta_0, \phi_0)$ are the initial guesses expressed in the following form:

$$\begin{array}{l} f_0(\eta) = \frac{A}{1+\gamma_1-\gamma_2}(1-\exp(-\eta)) \quad g_0(\eta) = \frac{\beta}{1+\gamma_3-\gamma_4}(1-\exp(-\eta)) \\ \text{where} \quad 1+\gamma_1-\gamma_2 \neq 0 \; 1+\gamma_3-\gamma_4 \neq 0 \\ \theta_0(\eta) = (1-S_1)(1-\exp(-\eta)) \qquad \phi_0(\eta) = (1-S_2)(1-\exp(-\eta)) \end{array} \tag{25}$$

$$\begin{array}{ll} L_f(f) = \frac{d^3f}{d\eta^3} - \frac{df}{d\eta} & L_g(g) = \frac{d^3g}{d\eta^3} - \frac{dg}{d\eta} \\ L_\theta(\theta) = \frac{d^2\theta}{d\eta^2} - \theta & L_\phi(\phi) = \frac{d^2\phi}{d\eta^2} - \phi \end{array} \tag{26}$$

these operators satisfy the following condition:

$$\begin{array}{l} L_f[C_1 + C_2\exp(\eta) + C_3\exp(-\eta)] = 0 \\ L_g[C_4 + C_5\exp(\eta) + C_6\exp(-\eta)] = 0 \\ L_\theta[C_9\exp(\eta) + C_{10}\exp(-\eta)] = 0 \end{array} \tag{27}$$

4. Zeroth Order Deformation

The zeroth order deformation problem is defined as follows:

$$(1-p)L_f[\tilde{f}(\eta;p) - f_0(\eta)] = p\hbar_f N_f[\tilde{f}(\eta;p), \tilde{g}(\eta;p)] \tag{28}$$

$$(1-p)L_g[\tilde{g}(\eta;p) - g_0(\eta)] = p\hbar_g N_g[\tilde{f}(\eta;p), \tilde{g}(\eta;p)] \tag{29}$$

$$(1-p)L_\theta[\tilde{\theta}(\eta;p) - \theta_0(\eta)] = p\hbar_\theta N_\theta[\tilde{f}(\eta;p), \tilde{g}(\eta;p), \tilde{\theta}(\eta;p), \tilde{\phi}(\eta;p)] \tag{30}$$

$$(1-p)L_\phi[\tilde{\phi}(\eta;p) - \phi_0(\eta)] = p\hbar_\phi N_\phi[\tilde{f}(\eta;p), \tilde{g}(\eta;p), \tilde{\theta}(\eta;p), \tilde{\phi}(\eta;p)] \tag{31}$$

$$\begin{array}{llll} \tilde{f}(0;p) = 0 & \tilde{f}\prime(0;p) = 1 + \gamma_1\tilde{f}''(0;p) + \gamma_2\tilde{f}'''(0;p) & \tilde{f}\prime(\infty;p) = 0 \\ \tilde{g}(0;p) = 0 & \tilde{\mathrm{g}}\prime(0;p) = \beta + \gamma_3\tilde{\mathrm{g}}''(0;p) + \gamma_2\tilde{\mathrm{g}}'''(0;p) & \tilde{\mathrm{g}}\prime(\infty;p) = 0 \\ \tilde{\theta}(0;p) = 1 - S_1 & \tilde{\theta}(\infty;p) = 0 & \tilde{\phi}(0;p) = 1 - S_2 \qquad \tilde{\phi}(\infty;p) = 0 \end{array} \tag{32}$$

$$\begin{array}{l} N_f[\tilde{f}(\eta;p), \tilde{g}(\eta;p)] = \frac{\partial^3\tilde{f}(\eta;p)}{\partial\eta^3} - \left(\frac{\partial\tilde{f}(\eta;p)}{\partial\eta}\right)^2 + (\tilde{f}+\tilde{g})\frac{\partial^2\tilde{f}(\eta;p)}{\partial\eta^2} + \\ We\frac{\partial^2\tilde{f}(\eta;p)}{\partial\eta^2}\frac{\partial^3\tilde{f}(\eta;p)}{\partial\eta^3} + \lambda(1+\beta_2\tilde{\theta})\tilde{\theta} + \lambda Nr(1+\beta_3\tilde{\phi})\tilde{\phi} - M\frac{\partial\tilde{f}(\eta;p)}{\partial\eta} \\ N_g[\tilde{f}(\eta;p), \tilde{g}(\eta;p)] = \frac{\partial^3\tilde{g}(\eta;p)}{\partial\eta^3} - \left(\frac{\partial\tilde{g}(\eta;p)}{\partial\eta}\right)^2 + (\tilde{f}+\tilde{g})\frac{\partial^2\tilde{g}(\eta;p)}{\partial\eta^2} + \\ We\frac{\partial^2\tilde{g}(\eta;p)}{\partial\eta^2}\frac{\partial^3\tilde{g}(\eta;p)}{\partial\eta^3} - \mathrm{M}\frac{\partial\tilde{g}(\eta;p)}{\partial\eta} \end{array} \tag{33}$$

$$N_\theta[\tilde{f}(\eta;p),\tilde{g}(\eta;p),\tilde{\theta}(\eta;p),\tilde{\phi}(\eta;p)] = [(1+\varepsilon\tilde{\theta})\frac{\partial^2\tilde{\theta}(\eta;p)}{\partial\eta^2}+\varepsilon\left(\frac{\partial\tilde{\theta}(\eta;p)}{\partial\eta}\right)^2+$$
$$\Pr N_b\frac{\partial\tilde{\theta}(\eta;p)}{\partial\eta}\frac{\partial\tilde{\phi}(\eta;p)}{\partial\eta}+\Pr N_t\left(\frac{\partial\tilde{\theta}(\eta;p)}{\partial\eta}\right)^2+\Pr(\tilde{f}+\tilde{g})\frac{\partial\tilde{\theta}(\eta;p)}{\partial\eta}-$$
$$\delta_t\Pr\left(\begin{array}{l}(\tilde{f}+\tilde{g})^2\frac{\partial^2\tilde{\theta}(\eta;p)}{\partial\eta^2}-2\frac{\partial\tilde{f}(\eta;p)}{\partial\eta}\frac{\partial\tilde{\theta}(\eta;p)}{\partial\eta}(\tilde{f}+\tilde{g})+\\ \left((c)^2-\frac{\partial^2\tilde{f}(\eta;p)}{\partial\eta^2}(\tilde{f}+\tilde{g})\right)(S_1+\theta)+(\tilde{f}+\tilde{g})\left(\frac{\partial\tilde{f}(\eta;p)}{\partial\eta}\frac{\partial\tilde{g}(\eta;p)}{\partial\eta}\right)\frac{\partial\tilde{\theta}(\eta;p)}{\partial\eta}\end{array}\right) \tag{34}$$

$$N_\phi[\tilde{f}(\eta;p),\tilde{g}(\eta;p),\tilde{\theta}(\eta;p),\tilde{\phi}(\eta;p)] = \frac{\partial^2\tilde{\phi}(\eta;p)}{\partial\eta^2}+\frac{N_t}{N_b}\frac{\partial^2\tilde{\theta}(\eta;p)}{\partial\eta^2}-$$
$$\Pr\mathrm{Le}\frac{\partial\tilde{f}(\eta;p)}{\partial\eta}(S_2+\theta)+\Pr\mathrm{Le}(\tilde{f}+\tilde{g})\frac{\partial\tilde{\phi}(\eta;p)}{\partial\eta}-$$
$$\Pr\mathrm{Le}\delta_c\left(\begin{array}{l}(\tilde{f}+\tilde{g})^2\frac{\partial^2\tilde{\phi}(\eta;p)}{\partial\eta^2}-2\frac{\partial\tilde{f}(\eta;p)}{\partial\eta}(\tilde{f}+\tilde{g})\frac{\partial\tilde{\phi}(\eta;p)}{\partial\eta}+\\ \left((\frac{\partial\tilde{f}(\eta;p)}{\partial\eta})^2-\frac{\partial^2\tilde{f}(\eta;p)}{\partial\eta^2}(\tilde{f}+\tilde{g})\right)(S_2+\phi)+\\ (\tilde{f}+\tilde{g})\left(\frac{\partial\tilde{f}(\eta;p)}{\partial\eta}\frac{\partial\tilde{g}(\eta;p)}{\partial\eta}\right)\frac{\partial\tilde{\phi}(\eta;p)}{\partial\eta}\end{array}\right) \tag{35}$$

Here $p\in[0,1]$ is embedding parameter and $\hbar_f,\hbar_g,\hbar_\theta$ and $\hbar_\phi$ are the non-zero auxiliary parameters.

5. mth-Order Deformation Problems

Here, we have

$$L_f[f_m(\eta)-\chi_m f_{m-1}(\eta)] = \hbar_f R_f^n(\eta) \tag{36}$$
$$L_g[g_m(\eta)-\chi_m g_{m-1}(\eta)] = \hbar_g R_g^n(\eta) \tag{37}$$
$$L_\theta[\theta_m(\eta)-\chi_m\theta_{m-1}(\eta)] = \hbar_\theta R_\theta^n(\eta) \tag{38}$$
$$L_\phi[\phi_m(\eta)-\chi_m\phi_{m-1}(\eta)] = \hbar_\phi R_\phi^n(\eta) \tag{39}$$

$$R_f^m(\eta) = f'''_{m-1}-f'^2_{m-1}+\sum_{k=0}^{m-1}(f_{m-1-k}+g_{m-1-k})f'''_k+We\sum_{k=0}^{m-1}f''_{m-1-k}f'''_k+\lambda\theta_{m-1}+$$
$$\beta_2\lambda\sum_{k=0}^{m-1}\theta_{m-1-k}\theta_k+\lambda Nr\phi_{m-1}+\lambda Nr\beta_3\sum_{k=0}^{m-1}\phi_{m-1-k}\phi_k-Haf'_{m-1} \tag{40}$$

$$R_g^m(\eta) = g''_{m-1}-g'^2_{m-1}+\sum_{k=0}^{m-1}(f_{m-1-k}+g_{m-1-k})g''_k+We\sum_{k=0}^{m-1}g''_{m-1-k}g'''_k-Hag'_{m-1} \tag{41}$$

$$R_\theta^m(\eta) = \theta''_{m-1}+\varepsilon\sum_{k=0}^{m-1}\theta_{m-1-k}\theta''_k+\varepsilon\sum_{k=0}^{m-1}\theta'_{m-1-k}\theta'_k+\Pr N_b\sum_{k=0}^{m-1}\theta'_{m-1-k}\phi'_k+\Pr N_t\sum_{k=0}^{m-1}\theta'_{m-1-k}\theta'_k-$$
$$\Pr(S_1+\theta)f'_{m-1}+\Pr\sum_{k=0}^{m-1}(f_{m-1-k}\theta'_k+g_{m-1-k}\theta'_k)-\delta_t\Pr\sum_{k=0}^{m-1}f_{m-1-k}\sum_{l=0}^{k}f_{k-1}\theta''_1-$$
$$\delta_t\Pr\sum_{k=0}^{m-1}g_{m-1-k}\sum_{l=0}^{k}g_{k-1}\theta''_1-2\delta_t\Pr\sum_{k=0}^{m-1}f_{m-1-k}\sum_{l=0}^{k}g_{k-1}\theta''_1--2\delta_t\Pr\sum_{k=0}^{m-1}f_{m-1-k}\sum_{l=0}^{k}f'_{k-1}\theta'_1-$$
$$2\delta_t\Pr\sum_{k=0}^{m-1}g_{m-1-k}\sum_{l=0}^{k}f'_{k-1}\theta'_1-S_1\delta_t\Pr\sum_{k=0}^{m-1}f'_{m-k-1}f'_{k-1}+S_1\delta_t\Pr\sum_{k=0}^{m-1}f_{m-1-k}f''_k+$$
$$S_1\delta_t\Pr\sum_{k=0}^{m-1}g_{m-1-k}f''_k-\delta_t\Pr\sum_{k=0}^{m-1}f'_{m-k-1}\sum_{l=0}^{k}f'_{k-1}\theta_1+\delta_t\Pr\sum_{k=0}^{m-1}f_{m-1-k}\sum_{l=0}^{k}f''_{k-1}\theta_1+$$
$$\delta_t\Pr\sum_{k=0}^{m-1}g_{m-1-k}\sum_{l=0}^{k}f''_{k-1}\theta_1+\delta_t\Pr\sum_{k=0}^{m-1}f_{m-1-k}\sum_{l=0}^{k}f'_{k-1}\theta'_1+\delta_t\Pr\sum_{k=0}^{m-1}f_{m-1-k}\sum_{l=0}^{k}g'_{k-1}\theta'_1$$
$$+\delta_t\Pr\sum_{k=0}^{m-1}g_{m-1-k}\sum_{l=0}^{k}f'_{k-1}\theta'_1+\delta_t\Pr\sum_{k=0}^{m-1}g_{m-1-k}\sum_{l=0}^{k}g'_{k-1}\theta'_1 \tag{42}$$

$$
\begin{aligned}
&R_{\phi}^{m}(\eta) = \phi'_{m-1} + \frac{N_t}{N_b}\sum_{k=0}^{m-1}\theta'_{m-1-k}\theta'_k - \mathrm{PrLeS}_2 f'_{m-1} - \mathrm{PrLe}\sum_{k=0}^{m-1} f'_{m-1-k}\theta_k f'_{m-1} + \mathrm{PrLe}\sum_{k=0}^{m-1} f_{m-1-k}\phi'_k + \\
&\mathrm{PrLe}\sum_{k=0}^{m-1} g_{m-1-k}\phi'_k - \mathrm{PrLe}\delta_c\sum_{k=0}^{m-1} f_{m-1-k}\sum_{l=0}^{k} f_{k-1}\phi''_1 - \mathrm{PrLe}\delta_c\sum_{k=0}^{m-1} g_{m-1-k}\sum_{l=0}^{k} g_{k-1}\phi''_1 - \\
&2\delta_c\mathrm{PrLe}\sum_{k=0}^{m-1} f_{m-1-k}\sum_{l=0}^{k} g_{k-1}\phi''_1 - 2\delta_c\mathrm{PrLe}\sum_{k=0}^{m-1} f_{m-1-k}\sum_{l=0}^{k} f'_{k-1}\phi'_1 - \\
&2\delta_c\mathrm{PrLe}\sum_{k=0}^{m-1} g_{m-1-k}\sum_{l=0}^{k} f'_{k-1}\phi'_1 + S_2\delta_c\mathrm{PrLe}\sum_{k=0}^{m-1} f'_{m-k-1}f'_{k-1} + S_2\delta_c\mathrm{PrLe}\sum_{k=0}^{m-1} f_{m-1-k}f''_k + \\
&S_2\delta_c\mathrm{PrLe}\sum_{k=0}^{m-1} g_{m-1-k}f''_k - \mathrm{PrLe}\delta_c\sum_{k=0}^{m-1} f'_{m-k-1}\sum_{l=0}^{k} f'_{k-1}\phi_1 + \\
&\delta_c\mathrm{PrLe}\sum_{k=0}^{m-1} f_{m-1-k}\sum_{l=0}^{k} f''_{k-1}\phi_1 + \delta_c\mathrm{PrLe}\sum_{k=0}^{m-1} g_{m-1-k}\sum_{l=0}^{k} f''_{k-1}\phi_1 + \delta_c\mathrm{PrLe}\sum_{k=0}^{m-1} f_{m-1-k}\sum_{l=0}^{k} f'_{k-1}\phi'_1 + \\
&\delta_c\mathrm{PrLe}\sum_{k=0}^{m-1} f_{m-1-k}\sum_{l=0}^{k} g'_{k-1}\phi'_1 + \delta_c\mathrm{PrLe}\sum_{k=0}^{m-1} g_{m-1-k}\sum_{l=0}^{k} g'_{k-1}\phi'_1 + \delta_c\mathrm{PrLe}\sum_{k=0}^{m-1} g_{m-1-k}\sum_{l=0}^{k} g'_{k-1}\phi'_1
\end{aligned}
\tag{43}
$$

$$
\chi_m = \begin{cases} 0, & m \le 1 \\ 1, & m > 1 \end{cases} \tag{44}
$$

the final solutions can be transcribed in the subsequent forms:

$$
\begin{aligned}
f_m(\eta) &= f_m^*(\eta) + D_1 + D_2 e^{\eta} + D_3 e^{-\eta} \\
g_m(\eta) &= g_m^*(\eta) + D_4 + D_5 e^{\eta} + D_6 e^{-\eta} \\
\theta_m(\eta) &= \theta_m^*(\eta) + D_7 e^{\eta} + D_8 e^{-\eta} \\
\phi_m(\eta) &= \phi_m^*(\eta) + D_9 e^{\eta} + D_{10} e^{-\eta}
\end{aligned}
\tag{45}
$$

where $f_m, g_m, \theta_m,$ and ϕ_m symbolize the special solutions.

6. Convergence Analysis

HAM is used to obtain the solution of higher order nonlinear problems or those in series form. It gives several choices to control and modify the convergence region for the series solutions. Figure 2 represents the $\hbar-$ curves behavior of all distributions. Characteristic parameters $\hbar_f, \hbar_g, \hbar_\theta$ and $\hbar_\phi$ have permissible ranges $-1.6 \le \hbar_f \le -0.4$, $-2.15 \le \hbar_g \le -0.2$, $-2.75 \le \hbar_\theta \le -0.8$ and $-2.6 \le \hbar_\phi \le -0.6$ when $\gamma = 0.2$, Le = 1, $N_t = 0.2$, $N_b = 0.3$, Pr = 1.0, $\varepsilon = 0.3$, $\lambda = 0.002$, $\beta_1 = \beta_3 = 0.2$, $\beta = 0.1$ and M = 0.2 Table 1 represents the numerical results obtained for series solutions depicting the convergence of approximations up to the 25th order of approximations, that is, enough for series solution convergence. It can be verified that the graphical depiction in Figure 2 and the tabular results in Table 1 are in total consensus.

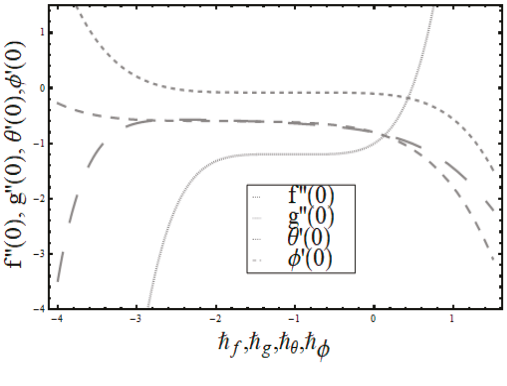

Figure 2. $\hbar-$ curves for f, g, θ and ϕ.

Table 1. Convergence analysis of series solution using different order approximations when M = 0.2, γ_1 =0.2, γ_2 = 0.2, N_b = 0.3, N_t = 0.2, λ = 0.002, Le = 1.0, Pr = 1.0 δ_t = 0.2, δ_c = 0.2, ε =0.1, β = 0.1.

Order of Approximations	$-f''(0)$	$g''(0)$	$-\theta'(0)$	$-\phi'(0)$
1	1.13509	0.07226	0.31147	0.53000
5	1.27039	0.07329	0.35690	0.46424
10	1.33592	0.07344	0.36006	0.44888
20	1.37389	0.07360	0.36099	0.44350
25	1.38731	0.07368	0.36158	0.44215
30	1.38731	0.07368	0.36158	0.44215

Table 2 was developed to validate the results obtained in the current model for skin friction in both directions by comparison with Malik et al. [50], and excellent harmony in both outcomes is achieved.

Table 2. Comparative estimates of *We* with Malik et al. [50] for skin friction along both directions in the limiting case, i.e., by considering the Hartmann number, second-order slip, temperature, and concentration profiles to zero.

We	$-[f''+\frac{We}{2}(f'')^2]_{\eta=0}$		$-[g''+\frac{We}{2}(g'')^2]_{\eta=0}$	
	[40]	Present Outcomes	[50]	Present Outcomes
0.1	1.0934	1.0933	0.4661	0.4660
0.2	1.2695	1.2695	0.4841	0.4841
0.3	1.3340	1.3341	0.5025	0.5024
0.4	1.4915	1.4916	0.5220	0.5221

7. Results and Discussion

In this section, we analyze the impact of appearing factors on particular distributions in Figures 3–21. The behavior on velocity profiles of β (ratio parameter) is described in Figures 3 and 4. It is noticed that contradictory behavior shown by both velocities ($f\prime$, $g\prime$) for an increasing rate of β. As $\beta = \frac{b}{a}$, a was smaller for higher values of β, which specified a decreasing velocity rate along the x-direction, or b with higher values specified an increasing rate along the y-direction. In Figures 5 and 6, δ_t and δ_c illustrate the influence of thermal relaxation and the concentration relaxation factor on temperature concentration and distributions. We found that both concentration and temperature fields associated with the thickness of the boundary layers were the functions of decreasing δ_c and δ_t, respectively. Furthermore, $\delta_c = 0$ and $\delta_t = 0$ existing model will transform into classical laws of Fick's and Fourier's respectively. The influence of thermal conductivity ε on the temperature distribution is described in Figure 7. For higher values of ε, an increasing rate for the thermal boundary layer is found, which in result increases the temperature distribution. In Figure 8 the impact of Lewis number Le on concentration field is described. The strength of Lewis number depends on smaller estimations of mass diffusivity than the thermal diffusivity, which shows that exhausted Brownian motion coefficient decreases nanoparticle concentration profile. Figure 9 d the influence of mixed convective factor λ on the velocity field ($g\prime$). Higher estimations of λ produce stronger buoyancy force, which indicates an increasing rate in the velocity field ($g\prime$). The behavior of Prandtl number Pr against temperature distribution is presented in Figure 10. It is inspected that heat diffusion is very slow from the heated surface for higher estimates of Pr than smaller estimations of Pr. Therefore, temperature decreases with increasing values of Pr. Figures 11 and 12 show the influence of *H*a (Hartmann number) on both velocity profiles ($f\prime$,$g\prime$). Retardation in the fluid motion is seen due to resistance effered by strong Lorentz force. This act finally points out the decreasing rate on both velocity distributions. Figures 13 and 14 demonstrate the impact of Brownian motion factor N_b on concentration and temperature distribution. For the larger estimates of N_b, fluid temperature increases and rapidly reduces the deposition of particles far away from the fluid on the stretched surface. Due to which it increases and decreases concentration. The influence of the N_t on the concentration distribution is described in Figure 15.

When the estimates of N_t are high and they are directly proportional to the temperature distribution, as a result it enhances the concentration distribution and its concentration associated with thickness of boundary layer. Figure 16 illustrates the influence of N_t on the temperature profile. When the values of N_t are higher, nanoparticles move from ambient fluid with higher temperature to the ambient fluid with lower temperature, and as a results temperature is higher in the boundary layer region. Finally, we identified the thickness of augmented thermal boundary layer. Figures 17 and 18 are drawn to display the influence of Williamson fluid parameter *We* on both velocity profiles. Increasing values of We decrease both velocities profiles. By increasing Williamson factor, relaxation time enhances. It causes to increase liquid viscosity, which results in decrease in the velocity profile. In Figure 19 the impact of stretching ratio factor β and mixed convective parameter λ on coefficient of Skin friction along x-direction is displayed. Which d that the coefficient of Skin friction shpws increasing behavior versus β and λ. Similar tendency can be observed in Hartmann number Ha and mixed convective parameter λ, against coefficient of Skin friction in x-direction, as displayed in Figure 20. Analysis of the impact of λ and Nr on Skin friction is described in Figure 21. It is noted that a thinner boundary layer is associated with larger λ, which result in higher velocity gradient near the wall. That's why Skin friction reduces against λ.

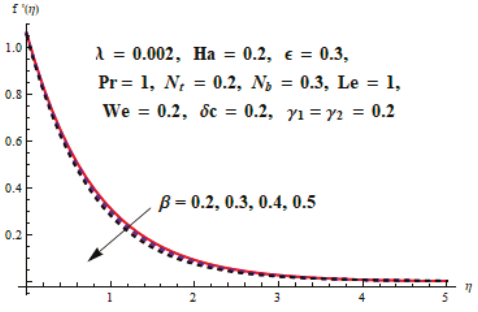

Figure 3. Impact of β against f'.

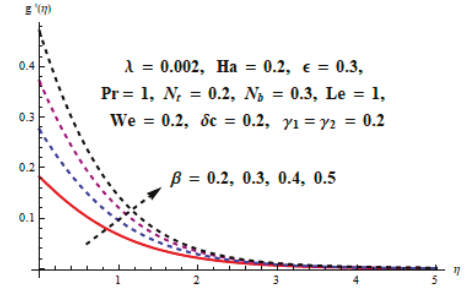

Figure 4. Impact of β against g'.

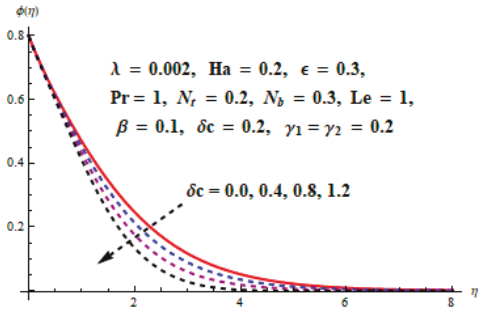

Figure 5. Impact of δc against ϕ.

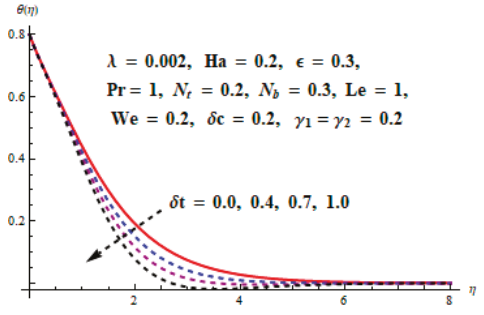

Figure 6. Impact of δ_t against θ.

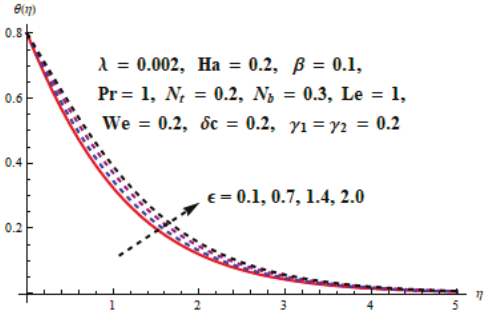

Figure 7. Impact of ∈ against θ.

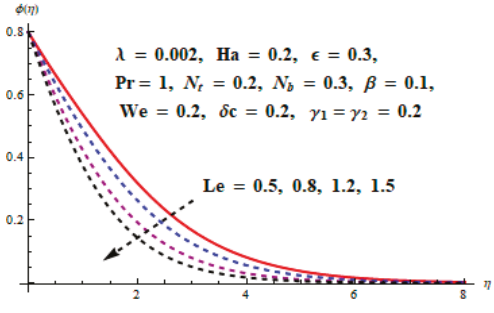

Figure 8. Impact of *Le* against ϕ.

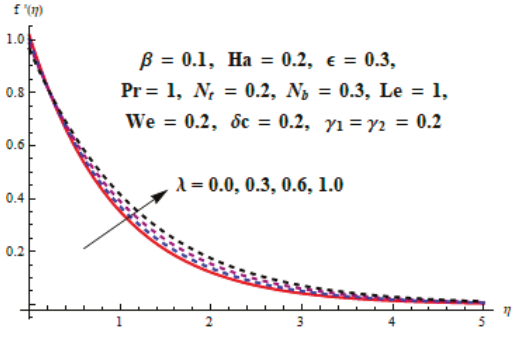

Figure 9. Impact of λ against f'.

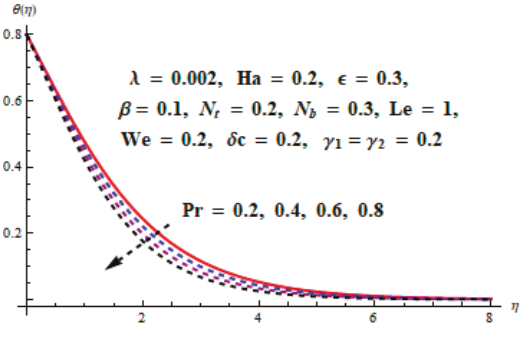

Figure 10. Impact of *P*r against θ.

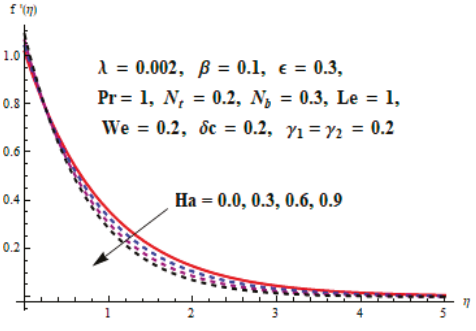

Figure 11. Impact of *Ha* against f'.

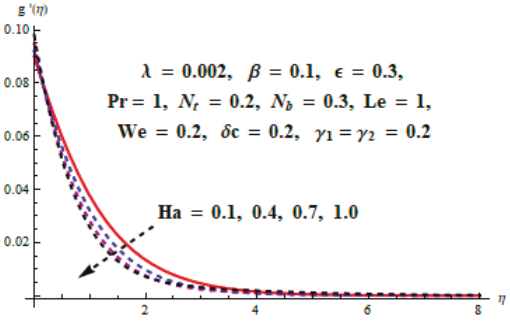

Figure 12. Impact of *Ha* against *g′*.

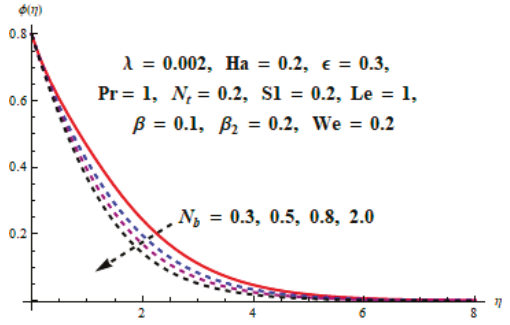

Figure 13. Impact of N_b against ϕ.

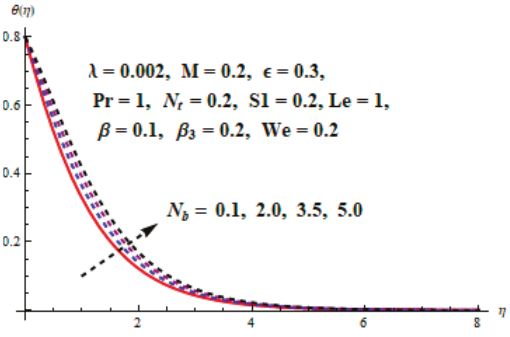

Figure 14. Impact of N_b against θ.

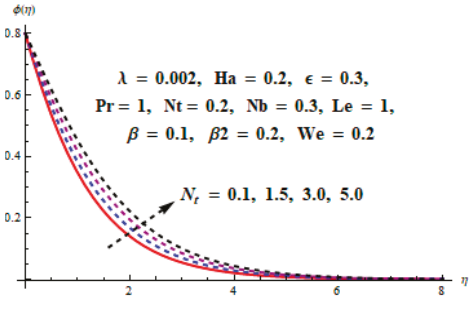

Figure 15. Impact of N_t against ϕ.

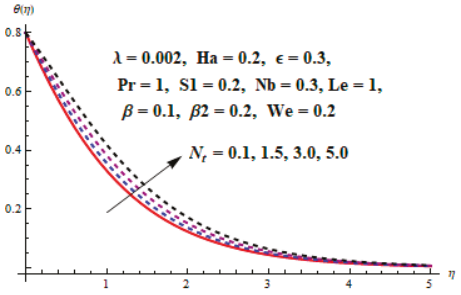

Figure 16. Impact of N_t against θ.

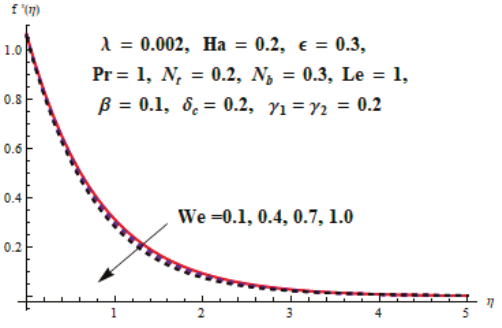

Figure 17. Impact of *We* against f'.

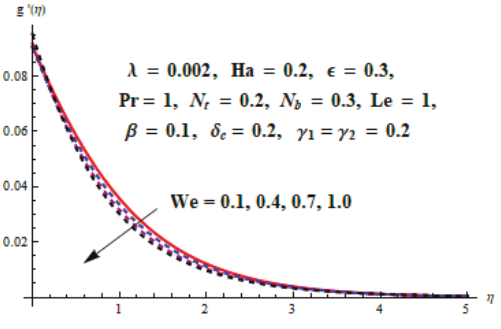

Figure 18. Impact of We against g'.

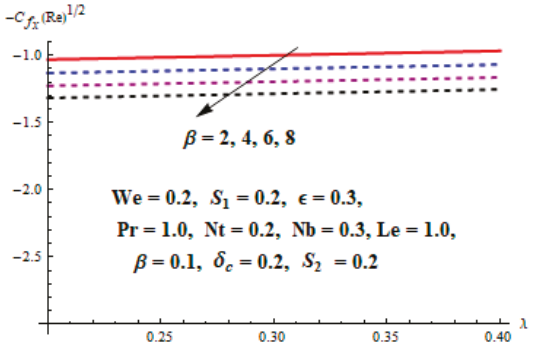

Figure 19. Impact of λ and β against Skin friction.

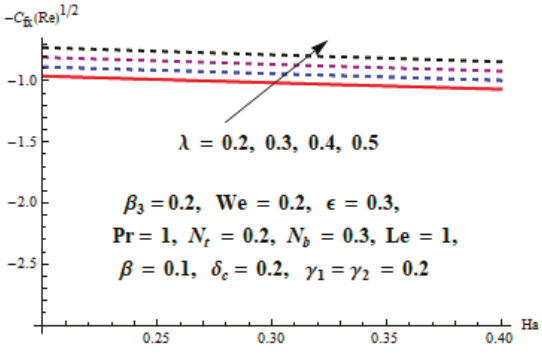

Figure 20. Impact of λ and *Ha* against Skin friction.

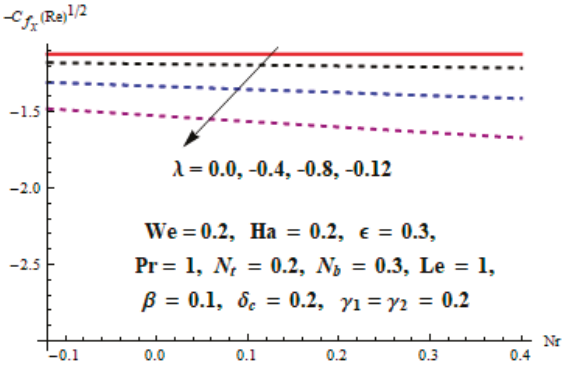

Figure 21. Impact of *Nr* and λ against Skin friction.

8. Concluding Remarks

Three-dimensional Williamson nanofluid flow was investigated considering the Cattaneo–Christov heat flux model. The originality of the envisioned mathematical model was boosted by considering the influence of double stratification and second-order slip. HAM was applied to obtain the problem solution in series form. The salient outcomes of the problem are as follows:

- The stretching ratio parameter had an opposite impact on both velocities.

- Increasing values of concentrations and temperature distributions decreased the thermal and concentration relaxation parameters, respectively.
- The higher temperature was in direct proportion with the thermal conductivity parameter.
- Velocity increased for values of the mixed convection parameter.
- For the large values of the Prandtl number, fluid temperature decreased.
- Both velocity components were decreasing functions of the Hartmann number.
- Skin friction coefficients against the x- and y- directions displayed an accelerating tendency with respect to values of the stretching ratio and mixed convection parameters.

Author Contributions: Conceptualization, M.R. and A.L.; methodology, M.R.; software, S.K.; validation, S.Y., S.N., D.L. and Y.N; funding acquisition, Y.N.

Funding: This research was supported by Basic Science Research Program through the National Research Foundation of Korea(NRF) funded by the Ministry of Education(NRF-2017R1D1A3B03028309) and also supported by the Soonchunhyang University Research Fund.

Conflicts of Interest: The authors declare no conflicts of interest regarding this publication.

Nomenclature

k_0	Elastic parameter
Re_x	Local Reynold parameter
S_1, S_2	Thermal and concentration stratification parameter
k	Thermal conductivity
C_{fy}	Skin friction coefficients in the y-direction
Ha	Hartmann number
Le	Lewis number
Nb	Brownian motion parameter
Nt	Thermophoresis parameter
We	Williamsons fluid parameter
Nr	Ratio of concentration to buoyancy forces
Gr_x	Grashof number
C_{fx}	Coefficients of skin friction in the x-direction
u, v, w	Velocity components
α_3,α_4	Linear and nonlinear coefficients of concentration expansions
J	Mass flux
T_∞	Ambient temperature
D_B	Brownian diffusion coefficient
θ	Temperature parameter
A,B,C,D	Constants
U_w	Velocity along x-axis
σ	Electrical conductivity
k_0	Elastic parameter
α_1	Normal stress moduli
γ_1, γ_3	First-order slip parameter
γ_2, γ_4	Second-order slip parameter
ν	Kinematic viscosity
β	Stretching ratio parameter
δt, δc	Thermal and concentration relaxation parameters
λ	Mixed convection parameter
ρ	Density of fluid
λ_c	Relaxation time of mass flux

λ_E	Relaxation time of heat flux
β_2,β_3	Nonlinear temperature's and concentration's convection parameter λ
α_1, α_2	Linear and nonlinear coefficients of thermal expansions
q	Normal heat flux
C_∞	Ambient concentration
D_T	Thermophoretic diffusion coefficient
f, g	Nondimensional velocity parameters
φ	Concentration parameter
ρ	Density of the fluid

References

1. Straughan, B. Thermal convection with the Cattaneo–Christov model. *Int. J. Heat Mass Transf.* **2010**, *53*, 95–98. [CrossRef]
2. Khan, W.A.; Khan, M.; Alshomrani, A.S.; Ahmad, L. Numerical investigation of generalized Fourier's and Fick's laws for Sisko fluid flow. *J. Mol. Liq.* **2016**, *224*, 1016–1021. [CrossRef]
3. Hayat, T.; Khan, M.I.; Farooq, M.; Alsaedi, A.; Waqas, M.; Yasmeen, T. Impact of Cattaneo–Christov heat flux model inflow of variable thermal conductivity fluid over a variable thicked surface. *Int. J. Heat Mass Transf.* **2016**, *99*, 702–710. [CrossRef]
4. Waqas, M.; Hayat, T.; Farooq, M.; Shehzad, S.A.; Alsaedi, A. Cattaneo-Christov heat flux model for the flow of variable thermal conductivity generalized Burgers fluid. *Int. J. Heat Mass Transf.* **2016**, *220*, 642–648. [CrossRef]
5. Khan, A.U.; Ahmed, N.; Mohyud-Din, S.T. Thermo-diffusion and diffusion-thermo effects on the flow of second-grade fluid between two inclined plane walls. *J. Mol. Liq.* **2016**, *224*, 1074–1082.
6. Ghadikolaei, S.S.; Hosseinzadeh, K.; Yassari, M.; Sadeghi, H.; Ganji, D.D. Analytical and numerical solution of non-Newtonian second-grade fluid flow on a stretching sheet. *Therm. Sci. Eng. Prog.* **2018**, *5*, 309–316. [CrossRef]
7. Khan, I.; Malik, M.Y.; Salahuddin, T.; Khan, M.; Rehman, K.U. Homogenous–heterogeneous reactions in MHD flow of Powell–Eyring fluid over a stretching sheet with Newtonian heating. *Neural Comput. Appl.* **2018**, *30*, 3581–3588. [CrossRef]
8. Ibrahim, W.; Shankar, B.; Nandeppanavar, M.M. MHD stagnation point flow and heat transfer due to nanofluid towards a stretching sheet. *Int. J. Heat Mass Transf.* **2013**, *56*, 1–9. [CrossRef]
9. Chamkha, A.J.; Al-Mudhaf, A. Unsteady heat and mass transfer from a rotating vertical cone with a magnetic field and heat generation or absorption effects. *Int. J. Therm. Sci.* **2005**, *44*, 267–276. [CrossRef]
10. Pullepu, B.; Chamkha, A.J.; Pop, I. Unsteady laminar free convection flows past a non-isothermal vertical cone in the presence of a magnetic field. *Chem. Eng. Commun.* **2012**, *199*, 354–367. [CrossRef]
11. Akbar, N.S.; Nadeem, S.; Haq, R.U.; Khan, Z.H. Numerical solutions of Magnetohydrodynamic boundary layer flow of tangent hyperbolic fluid towards a stretching sheet. *Indian J. Phys.* **2013**, *87*, 1121–1124. [CrossRef]
12. Seini, I.Y.; Makinde, O.D. Boundary layer flow near stagnation-points on a vertical surface with a slip in the presence of the transverse magnetic field. *Int. J. Numer. Methods Heat Fluid Flow* **2014**, *24*, 643–653. [CrossRef]
13. Ravindran, R.; Ganapathirao, M.; Pop, I. Effects of chemical reaction and heat generation/absorption on unsteady mixed convection MHD flow over a vertical cone with non-uniform slot mass transfer. *Int. J. Heat Mass Transf.* **2014**, *73*, 743–751. [CrossRef]
14. Bovand, M.; Rashidi, S.; Esfahani, J.A.; Saha, S.C.; Gu, Y.T.; Dehesht, M. Control of flow around a circular cylinder wrapped with a porous layer by magnetohydrodynamic. *J. Magn. Magn. Mater.* **2016**, *401*, 1078–1087. [CrossRef]
15. Ellahi, R.; Bhatti, M.M.; Pop, I. Effects of the hall and ion slip on MHD peristaltic flow of Jeffrey fluid in a non-uniform rectangular duct. *Int. J. Numer. Methods Heat Fluid Flow* **2016**, *26*, 1802–1820. [CrossRef]
16. Mishra, S.R.; Pattnaik, P.K.; Bhatti, M.M.; Abbas, T. Analysis of heat and mass transfer with MHD and chemical reaction effects on viscoelastic fluid over a stretching sheet. *Indian J. Phys.* **2017**, *91*, 1219–1227. [CrossRef]

17. Hussain, A.; Malik, M.Y.; Awais, M.; Salahuddin, T.; Bilal, S. Computational and physical aspects of MHD Prandtl-Eyring fluid flow analysis over a stretching sheet. *Neural Comput. Appl.* **2019**, *31*, 425–433. [CrossRef]
18. Khan, W.A.; Pop, I. Boundary-layer flow of a nanofluid past a stretching sheet. *Int. J. Heat Mass Transf.* **2010**, *53*, 2477–2483. [CrossRef]
19. Makinde, O.D.; Aziz, A. Boundary layer flow of a nanofluid past a stretching sheet with a convective boundary condition. *Int. J. Therm. Sci.* **2011**, *50*, 1326–1332. [CrossRef]
20. Nadeem, S.; Mehmood, R.; Akbar, N.S. Non-orthogonal stagnation point flow of a nano non-Newtonian fluid towards a stretching surface with heat transfer. *Int. J. Heat Mass Transf.* **2013**, *57*, 679–689. [CrossRef]
21. Hatami, M.; Jing, D.; Song, D.; Sheikholeslami, M.; Ganji, D.D. Heat transfer and flow analysis of nanofluid flow between parallel plates in the presence of a variable magnetic field using HPM. *J. Magn. Magn. Mater.* **2015**, *396*, 275–282. [CrossRef]
22. Hayat, T.; Imtiaz, M.; Alsaedi, A. MHD 3D flow of a nanofluid in the presence of convective conditions. *J. Mol. Liq.* **2015**, *212*, 203–208. [CrossRef]
23. Sheikholeslami, M.; Ganji, D.D.; Javed, M.Y.; Ellahi, R. Effect of thermal radiation on magnetohydrodynamics nanofluid flow and heat transfer by means of a two-phase model. *J. Magn. Magn. Mater.* **2015**, *374*, 36–43. [CrossRef]
24. Sheikholeslami, M.; Rokni, H.B. Nanofluid two-phase model analysis in the existence of induced magnetic field. *Int. J. Heat Mass Trans.* **2017**, *107*, 288–299. [CrossRef]
25. Hassan, M.; Marin, M.; Alsharif, A.; Ellahi, R. Convective heat transfer flow of a nanofluid in a porous medium over wavy surface. *Phys. Lett. A* **2018**, *382*, 2749–2753. [CrossRef]
26. Nayak, M.K.; Shaw, S.; Pandey, V.S.; Chamkha, A.J. Combined effects of slip and convective boundary condition on MHD 3D stretched flow of nanofluid through porous media inspired by non-linear thermal radiation. *Indian J. Phys.* **2018**, *92*, 1–12. [CrossRef]
27. Hosseini, S.R.; Sheikholeslami, M.; Ghasemian, M.; Ganji, D.D. Nanofluid heat transfer analysis in a microchannel heat sink (MCHS) under the effect of a magnetic field by means of the KKL model. *Powder Technol.* **2018**, *324*, 36–47. [CrossRef]
28. Lu, D.; Ramzan, M.; Mohammad, M.; Howari, F.; Chung, J.D. A Thin Film Flow of Nanofluid Comprising Carbon Nanotubes Influenced by Cattaneo-Christov Heat Flux and Entropy Generation. *Coatings* **2019**, *9*, 296. [CrossRef]
29. Li, Z.; Shafee, A.; Ramzan, M.; Rokni, H.B.; Al-Mdallal, Q.M. Simulation of natural convection of Fe 3 O 4-water ferrofluid in a circular porous cavity in the presence of a magnetic field. *Eur. Phys. J. Plus* **2019**, *134*, 77. [CrossRef]
30. Suleman, M.; Ramzan, M.; Ahmad, S.; Lu, D.; Muhammad, T.; Chung, J.D. A Numerical Simulation of Silver–Water Nanofluid Flow with Impacts of Newtonian Heating and Homogeneous–Heterogeneous Reactions Past a Nonlinear Stretched Cylinder. *Symmetry* **2019**, *11*, 295. [CrossRef]
31. Lu, D.; Li, Z.; Ramzan, M.; Shafee, A.; Chung, J.D. Unsteady squeezing carbon nanotubes based nano-liquid flow with Cattaneo–Christov heat flux and homogeneous–heterogeneous reactions. *Appl. Nanosci.* **2019**, *9*, 169–178. [CrossRef]
32. Ramzan, M.; Sheikholeslami, M.; Saeed, M.; Chung, J.D. On the convective heat and zero nanoparticle mass flux conditions in the flow of 3D MHD Couple Stress nanofluid over an exponentially stretched surface. *Sci. Rep.* **2019**, *9*, 562. [CrossRef] [PubMed]
33. Li, Z.; Sheikholeslami, M.; Shafee, A.; Ramzan, M.; Kandasamy, R.; Al-Mdallal, Q.M. Influence of adding nanoparticles on solidification in a heat storage system considering radiation effect. *J. Mol. Liq.* **2019**, *273*, 589–605. [CrossRef]
34. Farooq, U.; Lu, D.C.; Munir, S.; Suleman, M.; Ramzan, M. Flow of Rheological Nanofluid over a Static Wedge. *J. Nanofluids* **2019**, *8*, 1362–1366. [CrossRef]
35. Qayyum, S.; Khan, M.I.; Hayat, T.; Alsaedi, A. Comparative investigation of five nanoparticles in flow of viscous fluid with Joule heating and slip due to rotating disk. *Phys. B Condens. Matter* **2018**, *534*, 173–183. [CrossRef]
36. Nguyen, T.; van der Meer, D.; van den Berg, A.; Eijkel, J.C. Investigation of the effects of time periodic pressure and potential gradients on viscoelastic fluid flow in circular narrow confinements. *Microfluid. Nanofluid.* **2017**, *21*, 37. [CrossRef]

37. Ramzan, M.; Bilal, M.; Chung, J.D. Radiative Williamson nanofluid flow over a convectively heated Riga plate with chemical reaction-A numerical approach. *Chin. J. Phys.* **2017**, *55*, 1663–1673. [CrossRef]
38. Ramzan, M.; Bilal, M.; Chung, J.D. MHD stagnation point Cattaneo–Christov heat flux in Williamson fluid flow with homogeneous–heterogeneous reactions and convective boundary condition—A numerical approach. *J. Mol. Liq.* **2017**, *225*, 856–862. [CrossRef]
39. Nadeem, S.; Hussain, S.T. Flow and heat transfer analysis of Williamson nanofluid. *Appl. Nanosci.* **2014**, *4*, 1005–1012. [CrossRef]
40. Nadeem, S.; Maraj, E.N.; Akbar, N.S. Investigation of peristaltic flow of Williamson nanofluid in a curved channel with compliant walls. *Appl. Nanosci.* **2014**, *4*, 511–521. [CrossRef]
41. Liao, S.J. *Beyond Perturbation*; Chapman & Hall/CRC Press: Boca Raton, FL, USA, 2003.
42. Jafarimoghaddam, A. On the Homotopy Analysis Method (HAM) and Homotopy Perturbation Method (HPM) for a nonlinearly stretching sheet flow of Eyring-Powell fluids. *Eng. Sci. Technol. Int. J.* **2019**, *22*, 439–451. [CrossRef]
43. Freidoonimehr, N.; Rostami, B.; Rashidi, M.M. Predictor homotopy analysis method for nanofluid flow through expanding or contracting gaps with permeable walls. *Int. J. Biomath.* **2015**, *8*, 1550050. [CrossRef]
44. Ray, A.K.; Vasu, B.; Bég, O.A.; Gorla, R.S.; Murthy, P.V.S.N. Homotopy semi-numerical modeling of non-Newtonian nanofluid transport external to multiple geometries using a revised Buongiorno Model. *Inventions* **2019**, *4*, 54. [CrossRef]
45. Shukla, N.; Rana, P.; Bég, O.A.; Singh, B.; Kadir, A. Homotopy study of magnetohydrodynamic mixed convection nanofluid multiple slip flow and heat transfer from a vertical cylinder with entropy generation. *Propuls. Power Res.* **2019**, *8*, 147–162. [CrossRef]
46. Shqair, M. Solution of different geometries reflected reactors neutron diffusion equation using the homotopy perturbation method. *Results Phys.* **2019**, *12*, 61–66. [CrossRef]
47. Ramzan, M.; Farooq, M.; Alsaedi, A.; Hayat, T. MHD three-dimensional flow of couple stress fluid with Newtonian heating. *Eur. Phys. J. Plus* **2013**, *128*, 49. [CrossRef]
48. Hussain, T.; Shehzad, S.A.; Hayat, T.; Alsaedi, A.; Al-Solamy, F.; Ramzan, M. Radiative hydromagnetic flow of Jeffrey nanofluid by an exponentially stretching sheet. *PLoS ONE* **2014**, *9*, e103719. [CrossRef]
49. Ramzan, M.; Yousaf, F. Boundary layer flow of three-dimensional viscoelastic nanofluid past a bi-directional stretching sheet with Newtonian heating. *AIP Adv.* **2015**, *5*, 057132. [CrossRef]
50. Malik, M.Y.; Bilal, S.; Salahuddin, T.; Rehman, K.U. Three-dimensional Williamson fluid flow over a linearly stretching surface. *Math. Sci. Lett.* **2017**, *6*, 53–61. [CrossRef]

coatings

MDPI

Article

Impact of Velocity Second Slip and Inclined Magnetic Field on Peristaltic Flow Coating with Jeffrey Fluid in Tapered Channel

Najma Saleem [1], Safia Akram [2,*], Farkhanda Afzal [2], Emad H. Aly [3,4] and Anwar Hussain [5]

[1] College of Sciences and Human Studies, Prince Mohammad Bin Fahd University, Alkhobar 31952, Saudi Arabia; nsaleem@pmu.edu.sa
[2] MCS, National University of Sciences and Technology, Islamabad, Pakistan; farkhanda@mcs.edu.pk
[3] Department of Mathematics, Faculty of Science, University of Jeddah, Jeddah 21598, Saudi Arabia; efarag@uj.edu.sa
[4] Department of Mathematics, Faculty of Education, Ain Shams University, Roxy 11757, Cairo, Egypt
[5] DBS&H CEME, National University of Sciences and Technology, Islamabad, Pakistan; ah29919@gmail.com
* Correspondence: drsafiaakram@gmail.com

Received: 28 October 2019; Accepted: 17 December 2019; Published: 1 January 2020

Abstract: The peristaltic flow of velocity second slip boundary conditions and inclined magnetic field of Jeffrey fluid by means of heat and mass transfer in asymmetric channel was inspected in the present study. Leading equations described the existing flow were then simplified under lubrication approach. Therefore, exact solutions of stream function, concentration and temperature were deduced. Further, the numerical solutions of pressure rise and pressure gradient were computed using Mathematica software. Furthermore, the effect of the second slip parameter was argued via graphs. It has been depicted that this kind of slip is mandatory and very imperative to foresee the physical model. On the other hand, false results will be obtained.

Keywords: velocity second slip; wave forms; peristaltic flow; exact solutions; magnetic field; heat and mass transfer

1. Introduction

The peristaltic motion induced by channel or tube boundaries has a main role of fluid transport in living organisms and industrial pumping. Additionally, it has attracted attention in the fields of engineering and physiology. This transport is a means of fluid flow in an elastic path by the processes of contraction and expansion. In particular, such flows of viscous and non-Newtonian fluids are widely familiar in several biological systems including the human body in the transport of urine from the kidney to the bladder; chyme movement in the gastrointestinal tract, bile ducts, ureter, esophagus; spermatozoa in ducts efferent of the male reproductive tract; blood circulation in blood vessels; and movement of ovum in female fallopian tubes. Technical roller and finger pumps also function under this type of mechanism. In addition, with the existing of heat transfer, peristalsis is imperative in many processes such as oxygenation and hemodialysis. Further, heat transfer is also noteworthy in the treatment of diseased tissues in cancer. The cram of magnetohy drodynamic (MHD) peristaltic flow is useful as it is used in the reduction of bleeding during surgeries, targeted transfer of drugs via magnetic particles as drug carries, and MRI (magnetic resonance imaging) to diagnose diseases. It also has a pivotal role in the motion of physiological fluids including blood and blood pump machines. Furthermore, mass transfer in peristaltic flow occurs during the chemical breakdown of food, amalgamation of gastric juices with food, diffusive and ionic flows by means of membrane channels, diffusive oxygen transmission in tissue, drug delivery inside the body, and in other digestion processes.

There area lot of models for non-Newtonian fluids due to the complexity of fluids behaviour, like Carreau [1–3], Herschel [4,5], Oldroyd [6,7], Williamson [8], Johnson [9–11], Casson [12], Couette [13] and further as in [14–21]. Amongst these, the Jeffrey fluid model is considered as the simplest linear model that presents non-Newtonian fluid properties in a way which may enable the researchers to attain exact and analytical solutions. See, for example [22–25]. Kothandapani and Srinivas [26] have investigated peristaltic transport for Jeffrey fluid under consequences of a magnetic field in an asymmetric channel under the premise of a low Reynolds number and a long wavelength. Tripathi et al. [27] studied MHD peristaltic flow of Jeffrey fluid by means of a finite length cylindrical tube. Further, Nadeem et al. [28] examined the peristaltic flow of MHD Jeffrey fluid in eccentric cylinders. Khan et al. [29] investigated peristaltic transport for Jeffrey fluid with variable viscosity via a porous medium in an asymmetric channel. Srinivas and Pushparaj [30] have presented non-linear peristaltic flow in an inclined asymmetric channel.

In 1827, Navier [31] stated that shear stress at surface is linearly proportional to slip at surface. Fluids revealing slip effects are vital in polishing internal cavities and artificial heart valves. In particular, the application of this condition in peristaltic flows has perfect relevance in the field of polymers and physiology. Studies towards this point of research have been recently taken into account and a wide range of analytical and numerical studies have been reported in [32,33] and [34]. In a porous channel, effects of wall slip conditions and heat transfer on peristaltic transport of MHD Newtonian fluid with elastic wall properties have been discussed by Sirinivas et al. [35]. Hayat et al. [36] introduced a mathematical model in order to study the slip effects of heat and mass transfer on peristaltic transport of MHD power-law fluid and second grade fluid in the channel by flexible walls. Further, Hayat et al. [37] and [38] examined the influence of slip conditions and wall properties in the planar channel on MHD peristaltic flow of Maxwell fluid, and Williamson fluid in the non-uniform channel by heat and mass transfer, respectively. Nadeem and Akram [39] presented effects of partial slip on peristaltic flow of MHD Newtonian fluid in an asymmetric channel. They obtained the solutions using the method of Adomian decomposition and showed that trapping reduces with an increase of the velocity slip parameter, while pressure rise increases with an increase in the slip parameter. Hayat et al. [40,41] have analyzed effects of the slip condition on peristaltic flow of Phan-Thien-Tanner and of an Oldroyd 6-constant fluid, respectively. Mishra and Rao [42] investigated the effects of peristaltic flow of Newtonian fluid in an asymmetric channel. Akram and Nadeem [43] studied consequences with different waveforms of partial slip and nanofluid on peristaltic transport of non-Newtonian fluid. Recently, Hina et al. [44] investigated the peristaltic flow of pseudoplastic fluid with wall properties in a curved channel by heat or mass transfer.

In their important study, Roşca and Pop [45] showed that the second order slip flow model is essential to predict flow characteristics precisely. Very recently, Aly [46,47] and Aly and Vajravelu [48] have studied the effect of second velocity slip on fluid flow. In these studies, it was reported that these type of boundary conditions is compulsory and should be taken into consideration, otherwise, false results will be gained. As mentioned above, there are a considerable number of published papers regarding the effect of the first slip parameter, however, very less consideration has been given to peristaltic flows in the presence of the velocity second slip condition. Recently, Aly and Ebaid [49] presented an exact solution for the outcome of second slip on peristaltic flow of nanofluid in an asymmetric channel.

The intent of the current study is, therefore, to examine the effect of velocity second slip in non-Newtonian fluids by heat and mass transfer in the presence of an inclined magnetic field over an inclined tapered asymmetric channel, as many researchers have recently givenconsiderable attention to this geometry, for example [50–52]. As per our knowledge, no effort has been reported yet to discuss this multidimensional analysis, even in the absence of heat and mass transfer; hence, this study may be helpful in this direction of research. The present governing equations for motion, concentration and energy are simplified by assumptions of long wavelength approximation. Then, exact solutions

of reduced equations are outlines. Therefore, with help of Mathematica software, many graphical outcomes are plotted and reported for various involved physical parameters of interest.

2. Mathematical Formulation

The peristaltic motion of non-Newtonian incompressible fluid in a vertical tapered asymmetric channel, under effects of a constant magnetic field is considered. It is assumed that a wave train is moving with velocity c along non-uniform walls. In addition, we also assume that the channel andmagnetic field are inclined at angles α and Θ, respectively. Further, upper and lower walls of the channel are sustained at temperature T_0 and T_1, respectively. For the present flow, U and V are velocities in X and Y directions, respectively, in fixed frame. The upper and lower walls H_1 and H_2, respectively, of tapered asymmetric channel in fixed frame are defined as:

$$\begin{array}{rcl} Y & = & H_1 \;=\; d_1 + k^*X + a_1\cos\left[\frac{2\pi}{\lambda}(X-ct)\right] \\ Y & = & H_2 \;=\; -d_2 - k^*X - b_1\cos\left[\frac{2\pi}{\lambda}(X-ct)+\varphi\right] \end{array} \tag{1}$$

where a_1 and b_1 are amplitudes of waves; λ is wave length; $d_1 + d_2$ is width of channel; $k^*(k^* << 1)$ is non-uniform parameter; c is velocity of propagation; t is time; phase difference ϕ varies in range $0 \le \varphi \le \pi$; $\varphi = 0$ corresponds to symmetric channel by waves out of phase and $\phi = \pi$ waves are in phase; and further, a_1, b_1, d_1, d_2 and ϕ satisfy the condition [24].

$$a_1^2 + b_1^2 + 2a_1b_1\cos\phi \le (d_1+d_2)^2.$$

An equation that governs flow in the presence of gravity consequences and an inclined magnetic field are defined as [25].

$$\frac{\partial U}{\partial X} + \frac{\partial V}{\partial Y} \;=\; 0 \tag{2}$$

$$\begin{array}{c} \rho\left(\frac{\partial U}{\partial t} + U\frac{\partial U}{\partial X} + V\frac{\partial U}{\partial Y}\right) \;=\; -\frac{\partial p}{\partial X} + \frac{\partial}{\partial X}(S_{XX}) + \frac{\partial}{\partial Y}(S_{XY}) - \sigma B_0^2\cos\theta(U\cos\theta - V\sin\theta) \\ +\rho g\sin\alpha \end{array} \tag{3}$$

$$\begin{array}{c} \rho\left(\frac{\partial V}{\partial t} + U\frac{\partial V}{\partial X} + V\frac{\partial V}{\partial Y}\right) \;=\; -\frac{\partial p}{\partial Y} + \frac{\partial}{\partial X}(S_{YX}) + \frac{\partial}{\partial Y}S_{YY} + \sigma B_0^2\sin\Theta(U\cos\Theta - V\sin\Theta) \\ -\rho g\cos\alpha \end{array} \tag{4}$$

$$\begin{array}{c} C_p\left(\frac{\partial T}{\partial t} + U\frac{\partial T}{\partial X} + V\frac{\partial T}{\partial Y}\right) \;=\; \frac{K_1}{\rho}\left(\frac{\partial^2 T}{\partial X^2} + \frac{\partial^2 T}{\partial Y^2}\right) + \upsilon\left(\frac{1}{1+\lambda_1}\left(1 + \lambda_2\left(\frac{\partial}{\partial t} + U\frac{\partial}{\partial X} + V\frac{\partial}{\partial Y}\right)\right)\right. \\ \left.\left(2\left(\frac{\partial U}{\partial X}\right)^2 + 2\left(\frac{\partial V}{\partial Y}\right)^2 + \left(\frac{\partial U}{\partial Y} + \frac{\partial V}{\partial X}\right)^2\right)\right) \end{array} \tag{5}$$

$$\frac{\partial C}{\partial t} + U\frac{\partial C}{\partial X} + V\frac{\partial C}{\partial Y} \;=\; D_m\left(\frac{\partial^2 C}{\partial X^2} + \frac{\partial^2 C}{\partial Y^2}\right) + \frac{D_m K_T}{T_m}\left(\frac{\partial^2 T}{\partial X^2} + \frac{\partial^2 T}{\partial Y^2}\right) \tag{6}$$

where ρ, p, ν, σ, g, K_1, C_p, T, D_m, T_m, K_T and C represent constant density, pressure, kinematic viscosity, electrical conductivity, acceleration caused by gravity, thermal conductivity, specific heat, temperature, coefficient of mass diffusivity, mean temperature, thermal diffusion ratio and concentration of fluid, respectively.

For the Jeffrey fluid model, extra stress tensor **S** is given as [26].

$$\mathbf{S} \;=\; \frac{\mu}{1+\lambda_1}\left(\dot{\boldsymbol{\gamma}} + \lambda_2\ddot{\boldsymbol{\gamma}}\right) \tag{7}$$

where λ_1 is ratio of relaxation to retardation times; $\dot{\gamma}$ is shear rate; μ is viscosity of fluid; λ_2 is retardation time; and dots indicate differentiation with respect to time. Extra stress tensor **S** in component form is defined as:

$$\begin{aligned} S_{XX} &= \tfrac{2\mu}{1+\lambda_1}\Big(1+\lambda_2\Big(\tfrac{\partial}{\partial t}+(U\tfrac{\partial}{\partial X}+V\tfrac{\partial}{\partial Y})\Big)\Big)\tfrac{\partial U}{\partial X} \\ S_{XY} &= \tfrac{\mu}{1+\lambda_1}\Big(1+\lambda_2\Big(\tfrac{\partial}{\partial t}+(U\tfrac{\partial}{\partial X}+V\tfrac{\partial}{\partial Y})\Big)\Big)\Big(\tfrac{\partial U}{\partial Y}+\tfrac{\partial V}{\partial X}\Big) \\ S_{YY} &= \tfrac{2\mu}{1+\lambda_1}\Big(1+\lambda_2\Big(\tfrac{\partial}{\partial t}+(U\tfrac{\partial}{\partial X}+V\tfrac{\partial}{\partial Y})\Big)\Big)\tfrac{\partial V}{\partial Y} \end{aligned}$$

Furthermore, we know that the wave frame (x,y) and fixed frame (X,Y) are related by the following transformations:

$$x = X - ct,\ y = Y,\ u = U - c,\ v = V,\ \text{and}\ p(x) = p(X,t). \tag{8}$$

Let us define the following non-dimensional quantities:

$$\begin{aligned} &\bar{x} = \tfrac{x}{\lambda}, \bar{y} = \tfrac{y}{d_1}, \bar{u} = \tfrac{u}{c}, \bar{v} = \tfrac{v}{c}, \delta = \tfrac{d_1}{\lambda}, d = \tfrac{d_2}{d_1}, \bar{p} = \tfrac{d_1^2 p}{\mu c \lambda}, \bar{t} = \tfrac{ct}{\lambda}, h_1 = \tfrac{H_1}{d_1}, \\ &h_2 = \tfrac{H_2}{d_2}, a = \tfrac{a_1}{d_1}, b = \tfrac{b_1}{d_1}, Re = \tfrac{cd_1}{\nu}, \bar{\Psi} = \tfrac{\Psi}{cd_1}, Fr = \tfrac{c^2}{gd_1}, \theta = \tfrac{T-T_0}{T_1-T_0}, \\ &Sr = \tfrac{\rho D_m K_t (T_1-T_0)}{T_m \mu (C_1-C_0)}, Sc = \tfrac{\mu}{\rho D_m}, Ec = \tfrac{c^2}{C_p(T_1-T_0)}, Pr = \tfrac{\rho \nu C_p}{K_1}, \bar{S} = \tfrac{Sd_1}{\mu c}, \\ &M = \sqrt{\tfrac{\sigma}{\mu}} B_0 d_1,\ \Phi = \tfrac{C-C_0}{C_1-C_0} \end{aligned} \tag{9}$$

where Re is Reynolds number; *Fr* is Froude number; *Sr* is Soret number; *Sc* is Schmidt number; *Ec* is Eckret number; Pr is Prandtl number; *M* is Hartmann number; θ is temperature of fluid in dimensionless form; and Φ is concentration of fluid in dimensionless form.

With the help of Equations (7) and (8), Equations (2)–(6), in terms of stream function Ψ (dropping the bars, $u = \frac{\partial \Psi}{\partial y}, v = -\delta \frac{\partial \Psi}{\partial x}$), take following form:

$$\begin{aligned} Re\delta\Big(\Psi_y\Psi_{xy} - \Psi_x\Psi_{yy}\Big) &= -\tfrac{\partial p}{\partial x} + \delta\tfrac{\partial}{\partial x}(S_{xx}) + \tfrac{\partial}{\partial y}\Big(S_{xy}\Big) - \\ &M^2\cos\Theta\Big(\Big(\Psi_y+1\Big)\cos\Theta + \delta\Psi_x\sin\Theta\Big) + \tfrac{Re}{Fr}\sin\alpha \end{aligned} \tag{10}$$

$$\begin{aligned} Re\delta^3\Big(-\Psi_y\Psi_{xx} + \Psi_x\Psi_{xy}\Big) &= -\tfrac{\partial p}{\partial y} + \delta^2\tfrac{\partial}{\partial x}\Big(S_{yx}\Big) + \delta\tfrac{\partial}{\partial y}\Big(S_{yy}\Big) + \\ &M^2\delta\sin\Theta\Big(\Big(\Psi_y+1\Big)\cos\Theta + \delta\Psi_x\sin\Theta\Big) - \delta\tfrac{Re}{Fr}\cos\alpha \end{aligned} \tag{11}$$

$$\begin{aligned} Re\delta\Big(\Psi_y\theta_x - \Psi_x\theta_y\Big) &= \tfrac{1}{Pr}\Big(\theta_{yy} + \delta^2\theta_{xx}\Big) + \tfrac{Ec}{(1+\lambda_1)}\Big(1 + \tfrac{\lambda_2 c\delta}{d_1}\Big(\Psi_y\tfrac{\partial}{\partial x} - \Psi_x\tfrac{\partial}{\partial y}\Big)\Big) \\ &\Big(4\delta^2\Psi_{xy}^2 + \Big(\Psi_{yy} - \delta^2\Psi_{xx}\Big)^2\Big) \end{aligned} \tag{12}$$

$$Re\delta\Big(\Psi_y\Phi_x - \Psi_x\Phi_y\Big) = \frac{1}{Sc}\Big(\delta^2\Phi_{xx} + \Phi_{yy}\Big) + Sr\Big(\delta^2\theta_{xx} + \theta_{yy}\Big) \tag{13}$$

where extra stress tensor forJeffrey fluid in component form is defined as:

$$\begin{aligned} S_{xx} &= \tfrac{2\delta}{1+\lambda_1}\Big(1 + \tfrac{\lambda_2 c\delta}{d_1}\Big(\Psi_y\tfrac{\partial}{\partial x} - \Psi_x\tfrac{\partial}{\partial y}\Big)\Big)\Psi_{xy} \\ S_{xy} &= \tfrac{1}{1+\lambda_1}\Big(1 + \tfrac{\lambda_2 c\delta}{d_1}\Big(\Psi_y\tfrac{\partial}{\partial x} - \Psi_x\tfrac{\partial}{\partial y}\Big)\Big)\Big(\Psi_{yy} - \delta^2\Psi_{xx}\Big) \\ S_{yy} &= -\tfrac{2\delta}{1+\lambda_1}\Big(1 + \tfrac{\lambda_2 c\delta}{d_1}\Big(\Psi_y\tfrac{\partial}{\partial x} - \Psi_x\tfrac{\partial}{\partial y}\Big)\Big)\Psi_{xy} \end{aligned} \tag{14}$$

Using Equation (14) and assumptions of long wavelength approximation, Equations (10)–(13) reduce in the form:

$$-\frac{\partial p}{\partial x}+\frac{\partial}{\partial y}\left(\frac{1}{1+\lambda_1}\frac{\partial^2\Psi}{\partial y^2}\right)-M^2\cos^2\Theta\left(\Psi_y+1\right)+\frac{\mathrm{Re}}{Fr}\sin\alpha \;=\; 0 \tag{15}$$

$$-\frac{\partial p}{\partial y} \;=\; 0 \tag{16}$$

$$\frac{1}{\mathrm{Pr}}\frac{\partial^2\theta}{\partial y^2}+\frac{Ec}{(1+\lambda_1)}\left(\frac{\partial^2\Psi}{\partial y^2}\right)^2 \;=\; 0 \tag{17}$$

$$\frac{1}{Sc}\frac{\partial^2\Phi}{\partial y^2}+Sr\frac{\partial^2\theta}{\partial y^2} \;=\; 0. \tag{18}$$

Elimination of pressure from Equation (15) to (16) gives:

$$\frac{\partial^2}{\partial y^2}\left(\frac{1}{1+\lambda_1}\frac{\partial^2\Psi}{\partial y^2}\right)-M^2\cos^2\Theta\frac{\partial^2\Psi}{\partial y^2} \;=\; 0 \tag{19}$$

$$\frac{1}{\mathrm{Pr}}\frac{\partial^2\theta}{\partial y^2}+\frac{Ec}{(1+\lambda_1)}\left(\frac{\partial^2\Psi}{\partial y^2}\right)^2 \;=\; 0 \tag{20}$$

$$\frac{1}{Sc}\frac{\partial^2\Phi}{\partial y^2}+Sr\frac{\partial^2\theta}{\partial y^2} \;=\; 0. \tag{21}$$

The system of PDEs given above in Equation (19) through (21) is solved subject to the following boundary conditions:

$$\begin{array}{l}
\Psi \;=\; \frac{F}{2}\ \text{at}\ y \;=\; h_1 \;=\; 1+kx+a\cos 2\pi x\\
\Psi \;=\; -\frac{F}{2}\ \text{at}\ y \;=\; h_2 \;=\; -d-kx-b\cos(2\pi x+\varphi)\\
\frac{\partial\Psi}{\partial y} \;=\; -\frac{\eta_1^*}{(1+\lambda_1)}\frac{\partial^2\Psi}{\partial y^2}-\frac{\eta_2^*}{(1+\lambda_1)}\frac{\partial^3\Psi}{\partial y^3}-1\ \text{at}\ y \;=\; h_1\\
\frac{\partial\Psi}{\partial y} \;=\; \frac{\eta_1^*}{(1+\lambda_1)}\frac{\partial^2\Psi}{\partial y^2}+\frac{\eta_2^*}{(1+\lambda_1)}\frac{\partial^3\Psi}{\partial y^3}-1\ \text{at}\ y \;=\; h_2
\end{array} \tag{22}$$

$$\begin{array}{c}
\theta+\beta\frac{\partial\theta}{\partial y} \;=\; 0\ \text{at}\ y \;=\; h_1\\
through(13)\theta-\beta\frac{\partial\theta}{\partial y} \;=\; 1\ \text{at}\ y \;=\; h_2
\end{array} \tag{23}$$

$$\begin{array}{c}
\Phi+\gamma\frac{\partial\Phi}{\partial y} \;=\; 0\ \text{at}\ y \;=\; h_1\\
through(13)\Phi-\gamma\frac{\partial\Phi}{\partial y} \;=\; 1\ \text{at}\ y \;=\; h_2
\end{array} \tag{24}$$

where F is flux in wave frame; η_1^*,$\eta_{l_2}^*$,β and γ represent 1st-order slip parameter, 2nd-order slip parameter, thermal slip parameter, and concentration slip parameter, respectively; h_1 and h_2 are thedimensionless form of surfaces of peristaltic walls.

3. Exact Solution of Problem

Exact solution of Equation (19) satisfying boundary conditions (22) can be deduced as:

$$\begin{aligned}\Psi = \; & \tfrac{1}{L_\infty}\Big(2\cosh((h_1-h_2)\,m)\Big((-h_1-h_2+2y)\left(F\eta_1 m^2+1\right)-\eta_2 m^2(F+h_1-h_2)\Big)\\ & +2(\eta_2 m^2(F-h_2)(\cosh(m(y-h_1))+\cosh(m(y-h_2))-1)-F\eta_1 m(\sinh(m(y-h_1))\\ & +\sinh(m(y-h_2)))+F\cosh(m(y-h_1))-F\cosh(m(y-h_2))+h_1(\eta_2 m^2(\cosh(m(y-h_1))\\ & +\cosh(m(y-h_2))-1)-\eta_1 m(\sinh(m(y-h_1))+\sinh(m(y-h_2)))+\cosh(m(y-h_1))\\ & -\cosh(m(y-h_2))+1)+h_2(\eta_1 m(\sinh(m(y-h_1))+\sinh(m(y-h_2)))-\cosh(m(y-h_1))\\ & +\cosh(m(y-h_2))+1)-2y)+m(h_1+h_2-2y)(F\eta_2^2 m^4-\eta_1\left(F\eta_1 m^2+2\right)\\ & -F)\sinh((h_1-h_2)\,m),\end{aligned} \tag{25}$$

where $m = M\cos\Theta$, $\eta_1 = \frac{\eta_1^*}{(1+\lambda_1)}$, $\eta_2 = \frac{\eta_1^*}{(1+\lambda_1)}$ and L_∞ is a function of x defined in the Appendix A.

Now making use of Equation (25) in Equation (20), the exact solution of Equation (20) is derived as:

$$\begin{aligned}\theta = \; & \tfrac{m^2\mathrm{Pr}Ec\left(F+h_1-h_2\right)^2}{L_0}\Big(2\Big(2m^2y^2(\cosh((h_1-h_2)\,m)-1)+\cosh(m(-h_1-h_2+2y))\Big)\\ & +m(\eta_1(\eta_1 m(4m^2y^2(\cosh((h_1-h_2)\,m)+1)-\cosh(2m(y-h_1))-\cosh(2m(y-h_2))\\ & -2\cosh(m(-h_1-h_2+2y)))+2(4m^2y^2\sinh((h_1-h_2)\,m)+\sinh(2m(y-h_1))\\ & -\sinh(2m(y-h_2))))+\eta_2^2m^3(-(2(2m^2y^2(\cosh((h_1-h_2)\,m)+1)\\ & +\cosh(m(-h_1-h_2+2y)))+\cosh(2m(y-h_1))+\cosh(2m(y-h_2))))\\ & +2\eta_2 m(\eta_1 m(\sinh(2m(y-h_1))+\sinh(2m(y-h_2))+2\sinh(m(-h_1-h_2+2y)))\\ & -\cosh(2m(y-h_1))+\cosh(2m(y-h_2))))-\cosh(2m(y-h_1))\\ & -\cosh(2m(y-h_2)))+A_1y+A_0,\end{aligned} \tag{26}$$

where A_0,A_1 are functions of x and their values are computed by means of Equation (23) as:

$$\begin{aligned}A_0 = \; & \tfrac{1}{8\left(2\beta+h_1-h_2\right)\left(\lambda_1+1\right)}(8(\beta+h_1)\left(\lambda_1+1\right)+\\ & \tfrac{1}{L_5}(m^2Ec\mathrm{Pr}(F+h_1-h_2)^2L_9{L_6}^2-2m^2Ec\mathrm{Pr}L_{11}(\beta-h_2)\left(F+h_1-h_2\right)^2L_6L_4\\ & +m^2Ec\mathrm{Pr}(F+h_1-h_2)^2L_{10}{L_4}^2)),\end{aligned} \tag{27}$$

$$\begin{aligned}A_1 = \; & \tfrac{4m^4Ec\mathrm{Pr}\left(F+h_1-h_2\right)^2}{8\left(\lambda_1+1\right)\left(2\beta+h_1-h_2\right)L_8}\Big(\eta_2^2(h_1+h_2)\,m^4(2\beta+h_1-h_2)\left(\cosh((h_1-h_2)\,m)+1\right)\\ & -2(h_1+h_2)\left(2\beta+h_1-h_2\right)(\eta_1 m\cosh(\tfrac{1}{2}(h_1-h_2)\,m)+\sinh(\tfrac{1}{2}(h_1-h_2)\,m))^2\\ & -4\eta_2\cosh(\tfrac{1}{2}(h_1-h_2)\,m)(2\beta m\cosh((h_1-h_2)\,m)+\sinh((h_1-h_2)\,m))\\ & (\eta_1 m\cosh(((h_1-h_2)\,m))+\sinh(\tfrac{1}{2}(h_1-h_2)\,m)))-\tfrac{8(\lambda_1+1)}{8\left(\lambda_1+1\right)\left(2\beta+h_1-h_2\right)}.\end{aligned} \tag{28}$$

With the help of Equation (26), exact solution of the concentration profile in Equation (21) is concluded as:

$$\begin{aligned}\Phi = \; & \tfrac{m^2\mathrm{PrScSr}Ec\left(F+h_1-h_2\right)^2}{L_0}\Big(-2(2m^2y^2(\cosh((h_1-h_2)\,m)-1)+\cosh(m(-h_1-h_2+2y)))\\ & +m(\eta_1(\eta_1 m(2(\cosh(m(-h_1-h_2+2y))-2m^2y^2(\cosh((h_1-h_2)\,m)+1))+\cosh(2m(y-h_1))\\ & +\cosh(2m(y-h_2)))-2(4m^2y^2\sinh((h_1-h_2)\,m)+\sinh(2m(y-h_1))-\sinh(2m(y-h_2))))\\ & +\eta_2^2m^3(2(2m^2y^2(\cosh((h_1-h_2)\,m)+1)+\cosh(m(-h_1-h_2+2y)))+\cosh(2m(y-h_1))\\ & +\cosh(2m(y-h_2)))-2\eta_2 m(\eta_1 m(\sinh(2m(y-h_1))+\sinh(2m(y-h_2))\\ & +2\sinh(m(-h_1-h_2+2y)))-\cosh(2m(y-h_1))+\cosh(2m(y-h_2))))\\ & +\cosh(2m(y-h_1))+\cosh(2m(y-h_2)))+A_3y+A_2\end{aligned} \tag{29}$$

where A_2,A_3 are functions of x and their values are computed by means of Equation (24) as:

$$\begin{aligned}A_2 = \; & \tfrac{1}{8\left(2\gamma+h_1-h_2\right)\left(\lambda_1+1\right)}(8(\gamma+h_1)\left(\lambda_1+1\right)+\tfrac{1}{L_5}\Big(m^2\mathrm{PrScSr}Ec(F+h_1-h_2)^2L_2{L_4}^2\\ & +m^2\mathrm{PrScSr}Ec(F+h_1-h_2)^2L_1L_6^2-2m^2\mathrm{PrScSr}EcL_7(F+h_1-h_2)^2L_3L_4))\end{aligned} \tag{30}$$

$$\begin{aligned} A_3 = \; & \frac{4m^4 \mathrm{PrScSr}Ec\left(F+h_1-h_2\right)^2}{8\left(\lambda_1+1\right)\left(2\gamma+h_1-h_2\right)L_8}\Big(\eta_2^2(h_1+h_2)\,m^4(2\gamma+h_1-h_2)\,(-(\cosh((h_1-h_2)\,m)+1)) \\ & +2(h_1+h_2)\,(2\gamma+h_1-h_2)(\eta_1 m\cosh(\tfrac{1}{2}(h_1-h_2)\,m)+\sinh(\tfrac{1}{2}(h_1-h_2)\,m))^2 \\ & +4\eta_2\cosh(\tfrac{1}{2}(h_1-h_2)\,m)(2\gamma m\cosh((h_1-h_2)\,m)+\sinh((h_1-h_2)\,m)) \\ & (\eta_1 m\cosh(\tfrac{1}{2}(h_1-h_2)\,m)+\sinh(\tfrac{1}{2}(h_1-h_2)\,m))) - \frac{8\left(\lambda_1+1\right)}{8\left(\lambda_1+1\right)\left(2\gamma+h_1-h_2\right)}. \end{aligned} \tag{31}$$

It should be noted that $L_0 - L_{11}$ appeared in Equation (26) through (31) and are functions of x defined in the Appendix A.

4. Different Wave Shapes

Non-dimensional expressions for six considered wave forms are given as [43]. Expressions for sinusoidal, multisinsoidal, triangular, square, trapezoidal and sawtooth waves are derived from the Fourier series.

Sinusoidal wave:

$$h_1(x) \;=\; 1+kx+a\sin 2\pi x,\; h_2(x) \;=\; -d-kx-b\sin(2\pi x+\varphi)$$

Multisinsoidal wave:

$$h_1(x) \;=\; 1+kx+a\sin 2n\pi x,\; h_2(x) \;=\; -d-kx-b\sin(2n\pi x+\varphi)$$

Triangular wave:

$$\begin{aligned} h_1(x) &= 1+kx+a\left[\frac{8}{\pi^3}\sum_{m=1}^{\infty}\frac{(-1)^{m+1}}{(2m-1)^2}\sin(2\pi(2m-1)\,x)\right] \\ h_2(x) &= -d-kx-b\left[\frac{8}{\pi^3}\sum_{m=1}^{\infty}\frac{(-1)^{m+1}}{(2m-1)^2}\sin(2\pi(2m-1)\,x+\varphi)\right] \end{aligned}$$

Trapezoidal wave:

$$\begin{aligned} h_1(x) &= 1+kx+a\left[\frac{32}{\pi^2}\sum_{m=1}^{\infty}\frac{\sin\frac{\pi}{8}(2m-1)}{(2m-1)^2}\sin(2\pi(2m-1)\,x)\right] \\ h_2(x) &= -d-kx-b\left[\frac{32}{\pi^2}\sum_{m=1}^{\infty}\frac{\sin\frac{\pi}{8}(2m-1)}{(2m-1)^2}\sin(2\pi(2m-1)\,x+\varphi)\right] \end{aligned}$$

Square wave:

$$\begin{aligned} h_1(x) &= 1+kx+a\left[\frac{4}{\pi}\sum_{m=1}^{\infty}\frac{(-1)^{m+1}}{(2m-1)}\cos(2(2m-1)\,\pi x)\right] \\ h_2(x) &= -d-kx-b\left[\frac{4}{\pi}\sum_{m=1}^{\infty}\frac{(-1)^{m+1}}{(2m-1)}\cos(2(2m-1)\,\pi x+\varphi)\right] \end{aligned}$$

Sawtooth wave:

$$\begin{aligned} h_1(x) &= 1+kx+a\left[\frac{8}{\pi^3}\sum_{m=1}^{\infty}\frac{\sin(2\pi mx)}{m}\right] \\ h_2(x) &= -d-kx-b\left[\frac{8}{\pi^3}\sum_{m=1}^{\infty}\frac{\sin((2\pi mx)+\varphi)}{m}\right] \end{aligned}$$

5. Special Cases

If $\eta_1 = \eta_2 = \beta = \gamma = k = 0$, results of Nadeem and Akram [24] can be recovered as a special case for present study. In addition to the vanishing of these values and in absence of heat and mass transfer, the following results can be obtained as further special cases:

- Kothandapani and Srinivas [26], when $\Theta = \alpha = 0$,
- Srinivas and Pushparaj [30], for $\Theta = \lambda_1 = 0$ and
- Mishra and Rao [42], at $\Theta = M = \alpha = \lambda_1 = 0$.

6. Results and Discussion

In the proceeding section, numerical results of current problems are conferred through graphs. Mathematica software is utilized to analyze expressions for pressure gradient and pressure rise numerically.

Figures 1–4 are displayed to observe behaviour of pressure rise for diverse values of Jeffrey parameter λ_1, non-uniform parameter k, Reynolds number Re and inclination angle Θ. It is noted from Figure 1; Figure 2 that behaviour of pressure rise decreases in retrograde pumping ($\Delta p > 0$, $Q < 0$), peristaltic pumping ($\Delta p > 0$, $Q > 0$) and free pumping ($\Delta p = 0$) regions with an increase in λ_1 and k, whereas the behaviour of pressure rise is quite opposite in the co-pumping region ($\Delta p < 0$, $Q > 0$). In this region, with an increase in λ_1 and k, pressure rise increases. Figure 3 presents the behaviour of pressure rise for diverse values of Re. From this figure, we depicted that pressure rise increases in all pumping regions with an increase in values of Re. It is shown from Figure 4 that in the retrograde pumping ($\Delta p > 0$, $Q < 0$) region, pressure rise increases with an increase in Θ, whereas in the co-pumping region ($\Delta p < 0$, $Q > 0$), behaviour of pressure rise decreases with an increase in Θ.

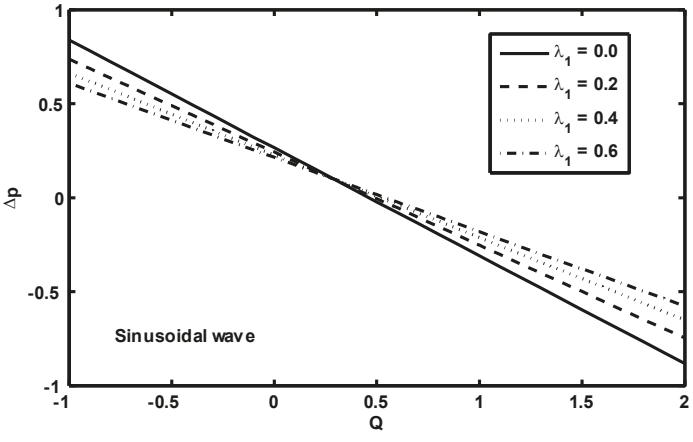

Figure 1. Variation of Δp with Q for different values of λ_1 for fixed $a = 0.7, \alpha = 0.2, b = 0.7, d = 1.5$, $\Theta = \frac{\pi}{6}, M = 0.5$, Re $= 0.4, \varphi = \frac{\pi}{4}, Fr = 0.6, \eta_1 = 0.3, \eta_2 = 0.4, k = 0.5$.

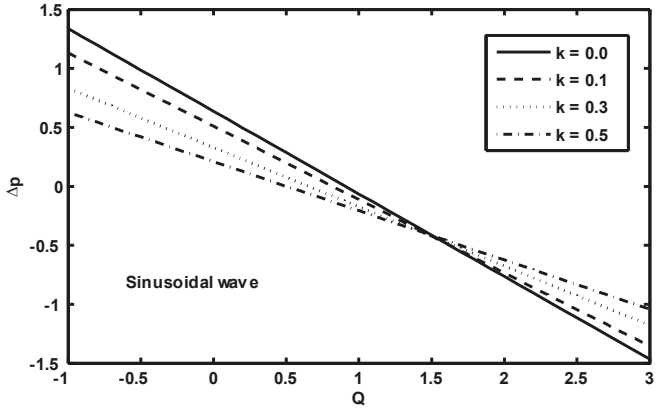

Figure 2. Variation of Δp with Q for different values of k for fixed $a = 0.7, \alpha = 0.2, b = 0.7, d = 1.5, \Theta = \frac{\pi}{6}, M = 0.5, \mathrm{Re} = 0.4, \varphi = \frac{\pi}{4}, Fr = 0.6, \eta_2 = 0.4, \eta_1 = 0.5, \lambda_1 = 0.1$.

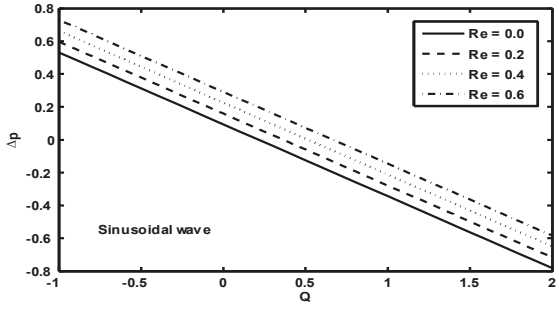

Figure 3. Variation of Δp with Q for different values of Re for fixed $a = 0.7, \alpha = 0.2, b = 0.7, d = 1.5, \Theta = \frac{\pi}{6}, \lambda_1 = 0.4, M = 0.5, \varphi = \frac{\pi}{4}, Fr = 0.6, \eta_1 = 0.3, \eta_2 = 0.4, k = 0.5$.

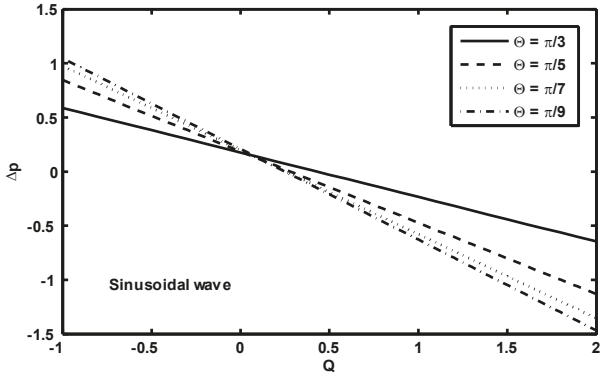

Figure 4. Variation of Δp with Q for different values of Θ for fixed $a = 0.7, \alpha = 0.2, b = 0.7, d = 1.5, \lambda_1 = 0.7, M = 1, R = 0.3, \varphi = \frac{\pi}{4}, Fr = 0.6, \eta_1 = 0.3, \eta_2 = 0.4, k = 0.5$.

Figures 5–8 are plotted in order to notice the behaviour of pressure gradient for various values of α, Jeffrey parameter λ_1, Hartmann number M and non-dimensional slip parameters η_1 and η_2. It is illustrated that for $x \in [0, 0.2]$ and $x \in [0.8, 1]$, the pressure gradient is small so that flow can easily pass without the compulsion of a large pressure gradient, whereas in region $x \in [0.2, 0.8]$, the pressure

gradient increases with an increase in α, and it decreases with an increase in λ_1, M, η_1 and η_2, so more pressure gradient is necessary to maintain the flux to pass. Figure 9 shows the behaviour of the pressure gradient for diverse wave forms. It has been observed from Figure 9 that pressure gradient is maximum for square waves.

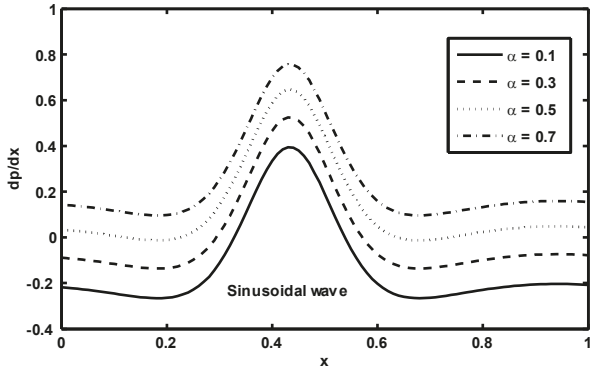

Figure 5. Variation of dp/dx with x for different values of α for fixed $a = 0.7$, $b = 0.7$, $d = 1.5$, $Fr = 0.6$, $\Theta = \frac{\pi}{3}$, $M = 0.5$, $\mathrm{Re} = 0.4$, $\varphi = \frac{\pi}{4}$, $\eta_1 = 0.4\,\eta_2 = 0.5$, $\lambda_1 = 0.3$, $k = 0.1$, $Q = 1$.

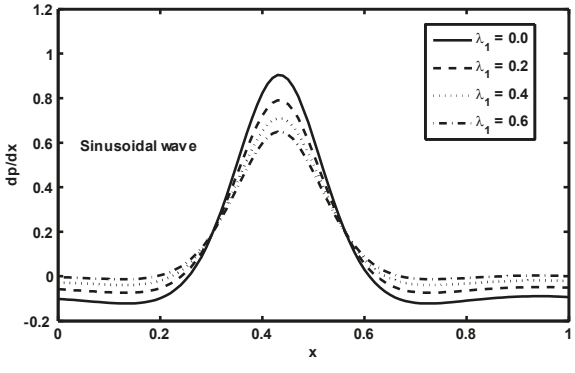

Figure 6. Variation of dp/dx with x for different values of λ_1 for fixed $a = 0.7$, $\alpha = 0.3$, $b = 0.7$, $d = 1.5$, $\Theta = \frac{\pi}{3}$, $\mathrm{Re} = 0.4$, $\varphi = \frac{\pi}{4}$, $Fr = 0.6$, $\eta_1 = 0.5$, $\eta_2 = 0.4$, $k = 0.1$, $M = 0.5$, $Q = 0.8$..

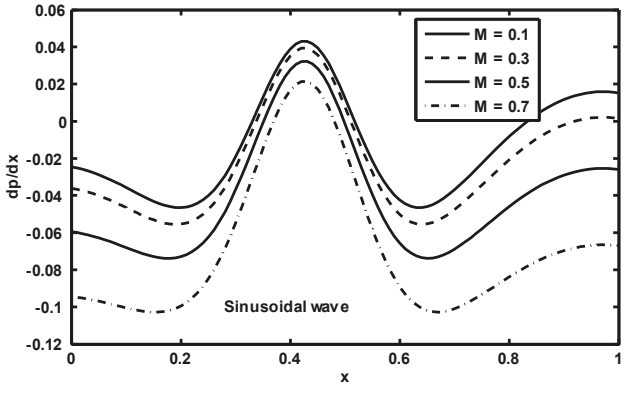

Figure 7. Variation of dp/dx with x for different values of M for fixed $a = 0.7, \alpha = 0.3, b = 0.5, d = 1.8, \Theta = \frac{\pi}{3}, \mathrm{Re} = 0.4, \varphi = \frac{\pi}{4}, Fr = 0.6, \eta_1 = 0.5, \eta_2 = 0.4, k = 0.5, \lambda_1 = 0.1, Q = 1$.

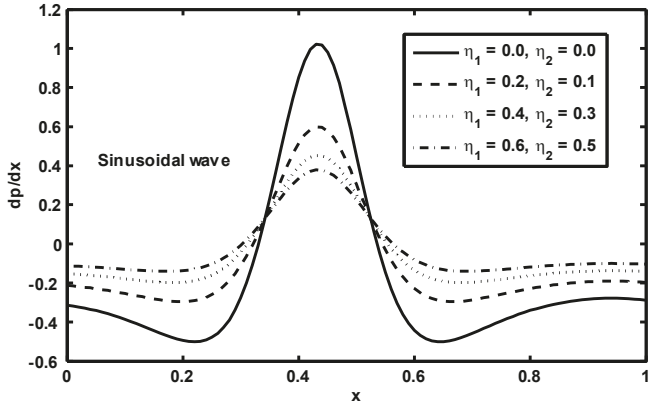

Figure 8. Variation of dp/dx with x for different values of η_1 and η_2 for fixed $a = 0.7, \alpha = 0.2, b = 0.7, d = 1.5, Fr = 0.6, \Theta = \frac{\pi}{3}, M = 0.5, \mathrm{Re} = 0.4, \varphi = \frac{\pi}{4}, \lambda_1 = 0.3, k = 0.1, Q = 1$.

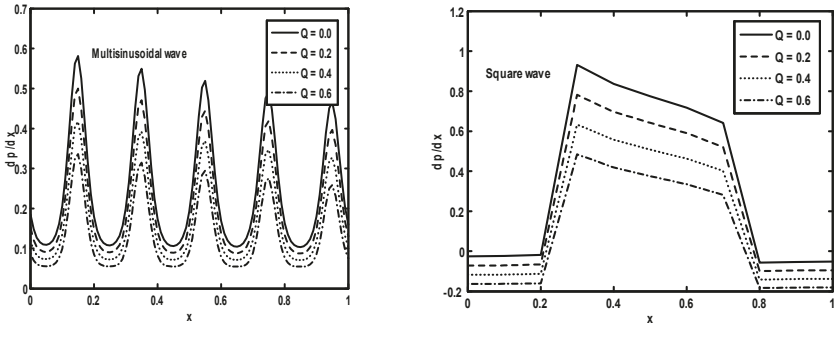

Figure 9. *Cont.*

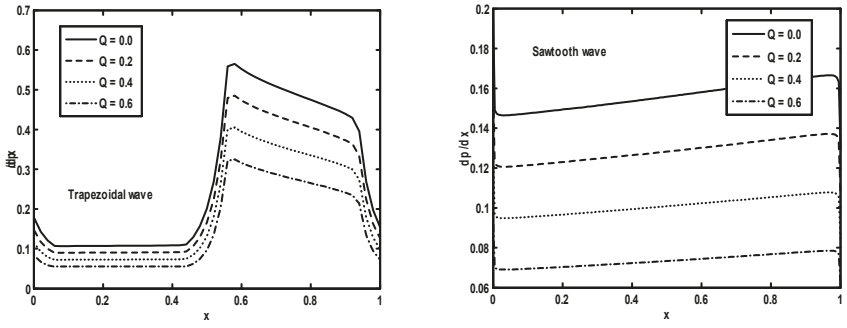

Figure 9. Variation of dp/dx with x for different wave forms for fixed $a = 0.9$, $\alpha = 0.3$, $b = 0.1$, $d = 2$, $\Theta = \frac{\pi}{3}$, $M = 0.5$, Re $= 0.4$, $\varphi = \frac{\pi}{4}$, $Fr = 0.6$, $\eta_1 = 0.5$, $\eta_2 = 0.4$, $\lambda_1 = 0.5$, $k = 0.1$.

The behaviour of temperature profiles for diverse values of Ec, λ_1 and Pr are shown in Figures 10–12. It has been observed from Figure 10 that the temperature profile increases with an increase in Ec. This phenomena is physically valid as Ec shows a direct connection with temperature profile. Figure 11 depicts variation of the temperature profile for diverse values of λ_1. It has been observed from Figure 11 that the temperature profile decreases with an increase in λ_1. It has been observed from Figure 12 that the temperature profile increases with an increase in values of Pr. This happens due to the direct relation of Pr with the temperature profile.

Figures 13–15 demonstrate theconcentration profile for diverse values of Ec, λ_1, Sr and Sc. It has been observed from Figure 13, Figure 14 that concentration profiles show opposite behaviour in comparison with the temperature profile. This observable fact physically holds as the temperature profile shows its inverse relationship with the concentration profile. It has been observed from Figure 13 that the concentration profile decreases with an increase in values of Ec. It has been depicted from Figure 14 that with an increase in λ_1 that the concentration profile increases. Figure 15 shows the concentration profile for diverse values of Sr and Sc. It has been shown in Figure 15 that the concentration profile decreases with an increase in Sr and Sc.

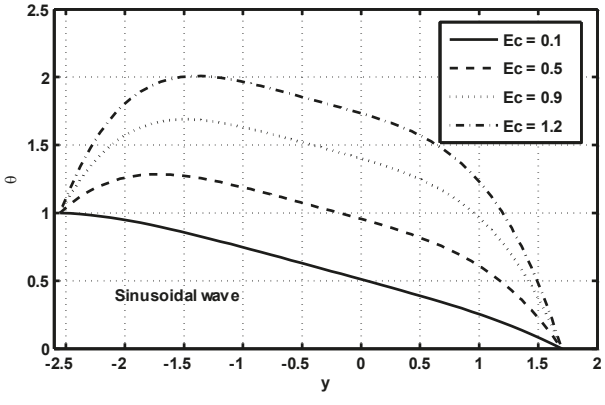

Figure 10. Temperature profile for different values of Ec for fixed $a = 0.5$, $b = 1.2$, $d = 1.5$, $\varphi = \frac{\pi}{4}$, $\beta = 0.0009$, $\eta_1 = 0.009$, $\eta_2 = 0.001$, $k = 0.2$, $\lambda_1 = 0.2$, $M = 0.1$, Pr $= 1$, $Q = 4$, $x = 1$.

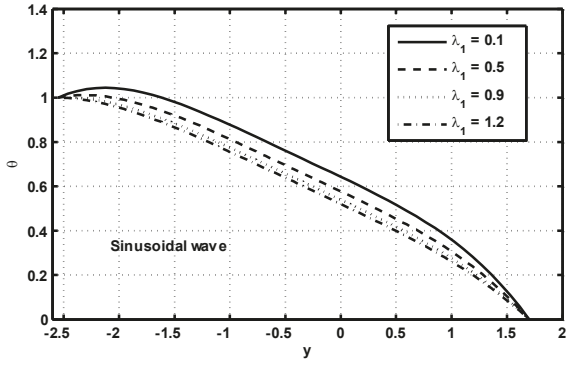

Figure 11. Temperature profile for different values of λ_1 for fixed $a = 0.5, b = 1.2, d = 1.5, \varphi = \frac{\pi}{4}$, $\beta = 0.0009, \eta_1 = 0.009, \eta_2 = 0.001, k = 0.2, M = 0.1, \Pr = 1, Q = 4, Ec = 0.2, x = 1$.

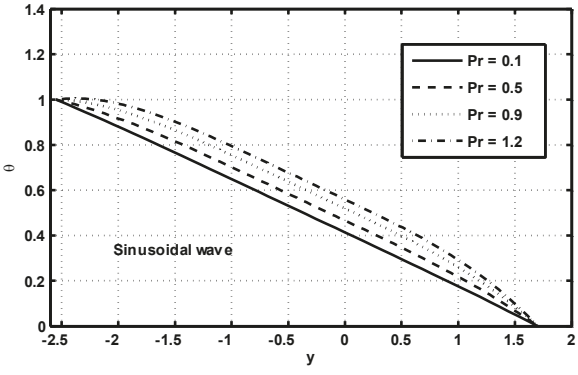

Figure 12. Temperature profile for different values of Pr for fixed $a = 0.5, b = 1.2, d = 1.5, \varphi = \frac{\pi}{4}$, $\beta = 0.0009, \eta_1 = 0.009, \eta_2 = 0.001, \lambda_1 = 1, k = 0.2, M = 0.1, Q = 4, Ec = 0.2, x = 1$.

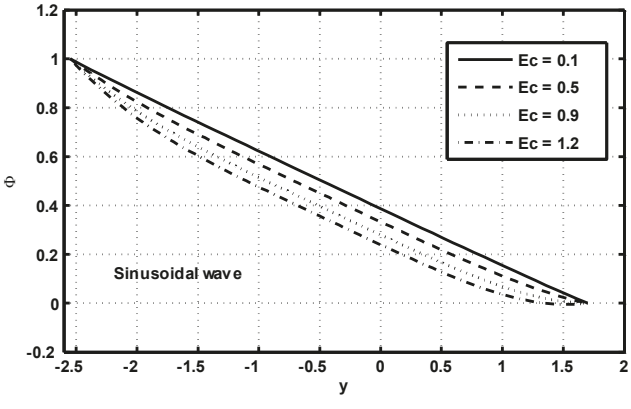

Figure 13. Concentration profile for different values of *Ec* for fixed $a = 0.5, b = 1.2, d = 1.5, \varphi = \frac{\pi}{4}$, $\gamma = 0.0009, \eta_1 = 0.009, \eta_2 = 0.001, k = 0.2, \lambda_1 = 0.2, M = 0.1, \Pr = 1, Q = 4, Sc = 0.3$, $Sr = 0.4, x = 1$.

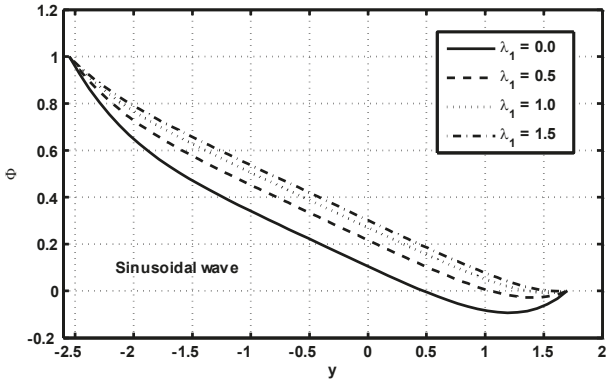

Figure 14. Concentration profile for different values of λ_1 for fixed $a = 0.5, b = 1.2, d = 1.5, \varphi = \frac{\pi}{4}$, $\gamma = 0.0009, \eta_1 = 0.009, \eta_2 = 0.001, k = 0.2, M = 0.9$, Pr $= 1, Q = 5, Sc = 0.6, Sr = 0.4$, $Ec = 0.8, x = 1$.

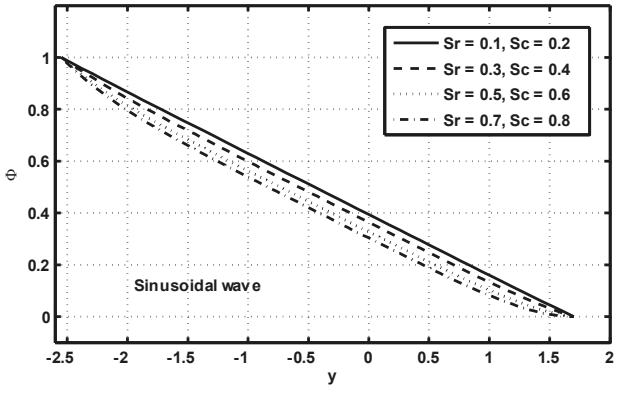

Figure 15. Concentration profile for different values of Sr and Sc for fixed $a = 0.5, b = 1.2, d = 1.5$, $\varphi = \frac{\pi}{4}, \gamma = 0.0009, \eta_1 = 0.009, \eta_2 = 0.001, \lambda_1 = 0.9, k = 0.2, M = 0.8$, Pr $= 0.5, Q = 5$, $Ec = 0.8, x = 1$.

In addition, an interesting observable fact in peristaltic flow is trapping. This is basically a pattern of an internally circulating bolus of fluid via closed stream lines. The trapping phenomena is discussed for different values of λ_1, M, η_1 and η_2. It has been observed from Figures 16–18 that the size of the trapping bolus decreases with an increase in values of λ_1, M, η_1 and η_2. Figure 19 shows the behaviour of stream lines for diverse wave forms. It has been observed that in all considered wave forms that the trapped bolus increases in size and its size is smaller in the case of the triangular wave when compared with the other three wave forms. Figure 20 shows comparison of the present work with existing literature. It is observed in this figure that the exact solution of the present work and existing literature satisfies the boundary conditions. Moreover, the magnitude value of the velocity profile is maximum in the case of the present work and Nadeem and Akram [24]. In order to show the comparison of the present work with existing literature in tabular form, Table 1 is constructed.

Table 1. Shows the comparison of the present work with existing literature in tabular form.

y	Present Work	Nadeem andAkram [24]	Kothandapani and Srinivas [26]	Srinivas and Pushparaj [30]	Mishra and Rao [42]
−1.109	−1.000	−1.000	−1.000	−1.000	−1.000
−1.009	−0.932753	−0.714278	−0.678228	−0.757937	−0.862651
−0.909	−0.8743	−0.505606	−0.459713	−0.565103	−0.736612
−0.809	−0.825682	−0.352378	−0.310456	−0.410812	−0.621188
−0.709	−0.785355	−0.239918	−0.208522	−0.287568	−0.516378
−0.609	−0.752035	−0.157452	−0.138929	−0.189381	−0.422183
−0.509	−0.724664	−0.097082	−0.0914497	−0.11148,	−0.338602
−0.409	−0.702372	−0.0530242	−0.0591067	−0.0500785	−0.265636
−0.309	−0.684449	−0.0210585	−0.0371466,	−0.00219338	−0.203285
−0.209	−0.670326	0.00187701	−0.0223419	0.0345026	−0.151548
−0.109	−0.659554	0.0179793	−0.0125168	0.0617927	−0.110426
−0.009	−0.65179	0.0287909	−0.00622739	0.081003	−0.0799192
0.091	−0.646787	0.0353474	−0.00254937	0.0930671	−0.0600266
0.191	−0.644387	0.0382767	−0.000942165	0.0985713	−0.0507487
0.291	−0.644513	0.0378597	−0.00116958	0.0977831	−0.0520854
0.391	−0.647169	0.0340561	−0.00326504	0.0906641	−0.0640367
0.491	−0.65244	0.0265019	−0.00753651	0.0768684	−0.0866028
0.591	−0.660492	0.0144732	−0.0146117	0.0557255	−0.119783
0.691	−0.671583,	−0.00318205	−0.0255305	0.0262081	−0.163579
0.791	−0.686065	−0.0281551	−0.0418976	−0.0131183	−0.217989
0.891	−0.704397	−0.0628381	−0.0661183	−0.0641648	−0.283014
0.991	−0.727164	−0.110553	−0.101752	−0.129412	−0.358653
1.091	−0.755089	−0.175871	−0.154037	−0.212031	−0.444907
1.191	−0.789059	−0.265049	−0.230655	−0.316035	−0.541775
1.291	−0.830155	−0.386629	−0.342868	−0.446481	−0.649259
1.391	−0.879684	−0.552257	−0.507167	−0.609706	−0.767357
1.491	−0.939219	−0.777798	−0.747697	−0.813642	−0.896069
1.591	−1.000	−1.000	−1.000	−1.000	−1.000

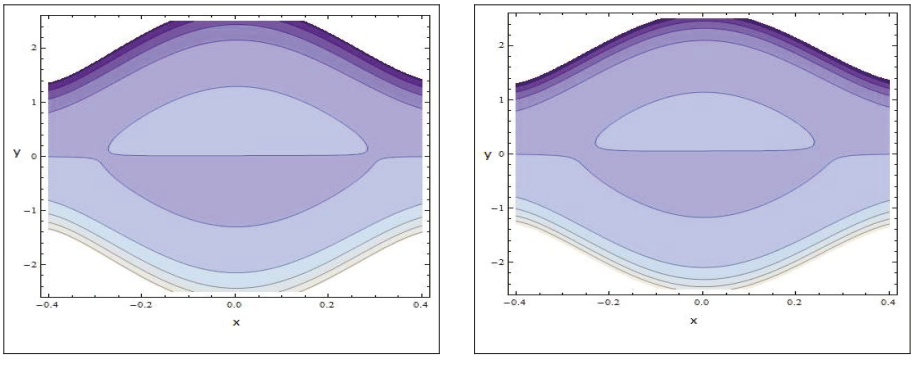

(a) (b)

Figure 16. Stream lines for different values of λ_1. (**a**) for $\lambda_1 = 0.1$, (**b**) for $\lambda_1 = 1.6$. The other parameters are $a = 0.7, b = 0.7, d = 1, \Theta = \frac{\pi}{5}, M = 2.2, \varphi = 0.01, \eta_1 = 0.009, \eta_2 = 0.001, k = 0.1, Q = 1.5$.

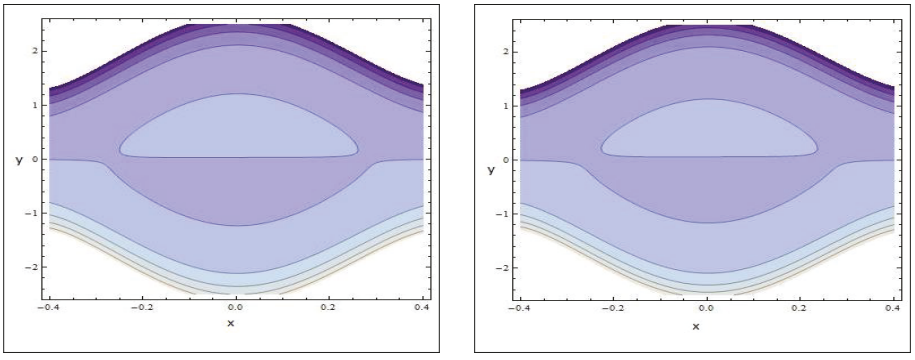

(a) (b)

Figure 17. Stream lines for different values of M. (**a**) for $M = 2.2$. (**b**) for $M = 2.54$. The other parameters are $a = 0.7, b = 0.7, d = 1, \Theta = \frac{\pi}{5}, M = 2.2, \varphi = 0.01, \eta_1 = 0.009, \eta_2 = 0.001, \lambda_1 = 1, k = 0.1, Q = 1.5$.

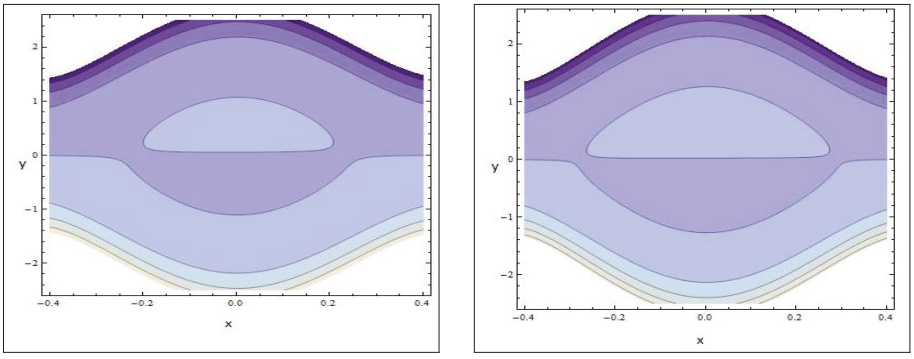

(a) (b)

Figure 18. Stream lines for different values of η_1 and η_2.(**a**) for $\eta_1 = 0.01$ and $\eta_2 = 0.001$,(**b**) for $\eta_1 = 0.09$ and $\eta_2 = 0.002$. The other parameters are $a = 0.7, b = 0.7, d = 1, \Theta = \frac{\pi}{5}, M = 1.8, \varphi = 0.01, \lambda_1 = 1.2, k = 0.1, Q = 1.5$.

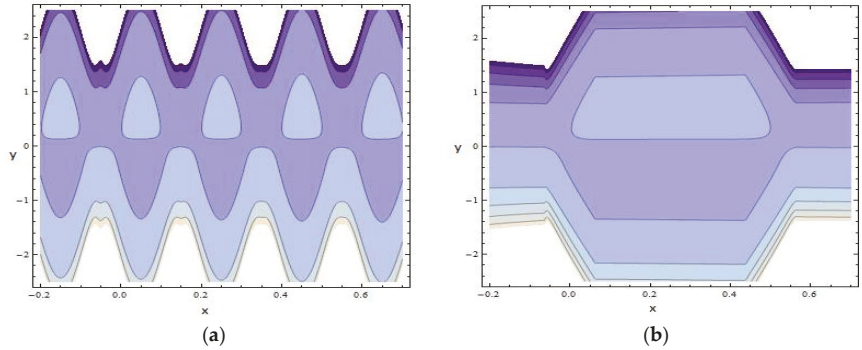

(**a**) (**b**)

Figure 19. *Cont.*

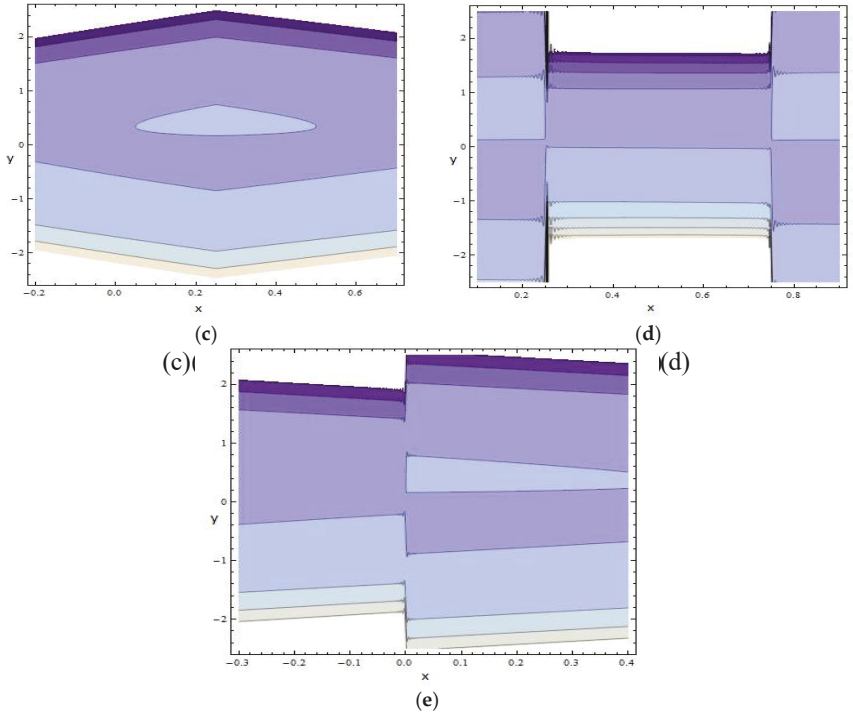

Figure 19. Stream lines fordifferent wave forms. (**a**) for multisinsoidal wave, (**b**) for trapezoidal wave, (**c**) for triangular wave, (**d**) for square wave, (**e**) for sawtooth wave, for fixed $a = 0.9, \alpha = 0.3, b = 0.1, d = 2, \Theta = \frac{\pi}{3}, M = 0.5\,\mathrm{Re} = 0.4, \varphi = \frac{\pi}{4}, Fr = 0.6, \eta_1 = 0.5, \eta_2 = 0.4, \lambda_1 = 0.5, k = 0.1$.

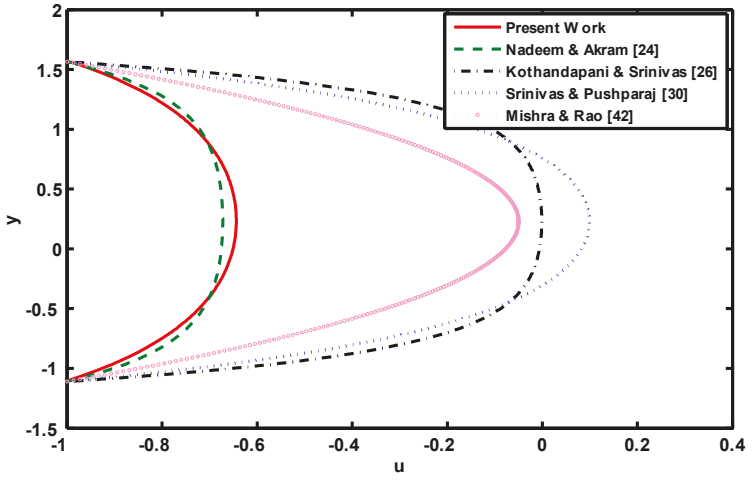

Figure 20. Comparison of the present work with existing literature.

7. Conclusions

In this research, we have investigated the effect of velocity second slip on non-Newtonian fluids by heat and mass transfer in the presence of an inclined magnetic field over an inclined tapered

asymmetric channel. Governing equations of motion, energy and concentration were simplified via assumptions of long wavelength approximation. Then, exact solutions of reduced equations were calculated. Graphical results were plotted and reported for various involved physical parameters of concern. The main results can be typified as:

- The results presented in [24,26,30,42] were considered as special cases of the present work.
- The pressure rise decreases in retrograde, peristaltic and free pumping regions and increases in co-pumping regions, with an increase in relaxation to retardation times λ_1 and non-uniform parameter k.
- The pressure rise increases in all pumping regions with an increase in Reynolds number Re.
- The pressure gradient increases with an increase in α and decreases with an increase in λ_1, Hartmann number M, slip parameter η_1 and η_2.
- The temperature profile increases with an increase in values of Eckret number Ec and decreases with an increase in relaxation to retardation times λ_1.
- The concentration profile decreases with an increase in Soret number Sr and Schmidt number Sc.
- The size of the trapping bolus decreases with an increase in values of relaxation to retardation times λ_1, Hartmann number M, slip parameter η_1 and η_2.

Author Contributions: Conceptualization, S.A. and E.H.A.; methodology, S.A.; software, N.S.; validation, S.A., N.S. and F.A.; formal analysis, A.H.; investigation, N.S.; resources, S.A.; data curation, E.H.A.; writing—original draft preparation, S.A.; writing—review and editing, E.H.A.; visualization, F.A.; supervision, S.A.; project administration, A.H.; funding acquisition, N.S. All authors have read and agreed to the published version of the manuscript.

Funding: This research received no external funding.

Acknowledgments: The authors would like to acknowledge the support provided by the Deanship of Scientific Research (DSR) at the Prince Mohammad Bin Fahd University (PMU) for funding this work.

Conflicts of Interest: The authors declare no conflict of interest.

Nomenclature

U , V	Velocities in X and Y directions in fixed frame	Fr	Froude Number
P	Pressure	Sr	Soret number
a_1 and b_1	amplitudes of waves	$d_1 + d_2$	width of channel
$k^*(k^* << 1)$	non-uniform parameter	λ	wavelength
λ_1	ratio of relaxation to retardation times	λ_2	retardation time
b	amplitude of the wave	Sc	Schmidt number
Re	Reynolds number	Ec	Eckret number
δ	dimensionless wave number	Pr	Prandtl number
M	Hartmann number	μ	viscosity
Q	volume flow rate	Ψ	Stream function
ν	kinematic viscosity	Φ	concentration of fluid in dimensionless form
θ	temperature of fluid in dimensionless form	C	Concentration of fluid
σ	electrical conductivity	K_T	thermal diffusion ratio
K_1	thermal conductivity	C_p	specific heat
T_m	mean temperature	D_m	coefficient of mass diffusivity

Appendix A

$$
\begin{aligned}
L_{\infty} = {} & 4\left(\eta_1 (h_1 - h_2) m^2 - 1\right) \cosh((h_1 - h_2) m) - 2m(2\eta_1 + h_1\left(\eta_2^2 m^4 - \eta_1^2 m^2 - 1\right) + h_2(-\eta_2^2 m^4 \\
& + \eta_1^2 m^2 + 1))\sinh((h_1 - h_2) m) + 4 \\
L_0 = {} & 8(\lambda_1 + 1)(2\left(\eta_1 (h_2 - h_1) m^2 + 1\right) \cosh((h_1 - h_2) m) - 2 + m(2\eta_1 + h_1\left(\eta_2^2 m^4 - \eta_1^2 m^2 - 1\right) \\
& + h_2\left(-\eta_2^2 m^4 + \eta_1^2 m^2 + 1\right))\sinh((h_1 - h_2) m))^2 \\
L_1 = {} & -2m^2(\gamma + h_1) h_2^2 + \left(2h_1(4\gamma + h_1) m^2 + 2\gamma(2m\gamma + \sinh(2mh_1)) m + \cosh(2mh_1)\right) h_2 \\
& - \gamma(\cosh(2mh_1) + \cosh(2mh_2) + 2m\gamma(\sinh(2mh_1) - \sinh(2mh_2))) - h_1(2\gamma(2\gamma + h_1) m^2 \\
& - 2\gamma\sinh(2mh_2) m + \cosh(2mh_2))
\end{aligned}
$$

$$
\begin{aligned}
L_2 = {} & 2m^2(\gamma + h_1) h_2^2 + \left(-2h_1(4\gamma + h_1) m^2 + 2\gamma(\sinh(2mh_1) - 2m\gamma) m + \cosh(2mh_1)\right) h_2 \\
& - \gamma(\cosh(2mh_1) + \cosh(2mh_2) + 2m\gamma(\sinh(2mh_1) - \sinh(2mh_2))) + h_1(2\gamma(2\gamma + h_1) m^2 \\
& + 2\gamma\sinh(2mh_2) m - \cosh(2mh_2)) \\
L_3 = {} & m(\sinh(mh_1) + \sinh(mh_2)) \eta_1 + \cosh(mh_2) \left(m^2\eta_2 - 1\right) + \cosh(mh_1) \left(\eta_2 m^2 + 1\right) \\
L_4 = {} & \left(m(\cosh(mh_1) + \cosh(mh_2)) \eta_1 + \sinh(mh_2) \left(m^2\eta_2 - 1\right) + \sinh(mh_1) \left(\eta_2 m^2 + 1\right)\right) \\
L_5 = {} & (2\cosh(m(h_1 - h_2)) \left((h_2 - h_1) \eta_1 m^2 + 1\right) + m\sinh(m(h_1 - h_2))(2\eta_1 + h_1(\eta_2^2 m^4 - \eta_1^2 m^2 \\
& - 1) + h_2\left(-\eta_2^2 m^4 + \eta_1^2 m^2 + 1\right)) - 2)^2
\end{aligned}
$$

$$
\begin{aligned}
L_6 = {} & m(\sinh(mh_1) + \sinh(mh_2)) \eta_1 + \cosh(mh_2) \left(m^2\eta_2 - 1\right) + \cosh(mh_1) \left(\eta_2 m^2 + 1\right) \\
L_7 = {} & 2m\gamma \cosh(2mh_2) (\gamma + h_1) - \sinh(2mh_2) (\gamma + h_1) - (2m\gamma \cosh(2mh_1) + \sinh(2mh_1)) (\gamma - h_2) \\
L_8 = {} & (2\left(\eta_1 (h_2 - h_1) m^2 + 1\right) \cosh((h_1 - h_2) m) + m(2\eta_1 + h_1\left(\eta_2^2 m^4 - \eta_1^2 m^2 - 1\right) + h_2(-\eta_2^2 m^4 \\
& + \eta_1^2 m^2 + 1))\sinh((h_1 - h_2) m) - 2)^2 \\
L_9 = {} & 2m^2(\beta + h_1) h_2^2 - \left(2h_1(4\beta + h_1) m^2 + 2\beta(2m\beta + \sinh(2mh_1)) m + \cosh(2mh_1)\right) h_2 \\
& + \beta(\cosh(2mh_1) + \cosh(2mh_2) + 2m\beta(\sinh(2mh_1) - \sinh(2mh_2))) + h_1(2\beta(2\beta + h_1) m^2 \\
& - 2\beta\sinh(2mh_2) m + \cosh(2mh_2))
\end{aligned}
$$

$$
\begin{aligned}
L_{10} = {} & -2m^2(\beta + h_1) h_2^2 + \left(2\left(2\beta^2 + 4h_1\beta + h_1^2\right) m^2 - 2\beta\sinh(2mh_1) m - \cosh(2mh_1)\right) h_2 \\
& + \beta(\cosh(2mh_1) + \cosh(2mh_2) + 2m\beta(\sinh(2mh_1) - \sinh(2mh_2))) + h_1(-2\beta(2\beta \\
& + h_1) m^2 - 2\beta\sinh(2mh_2) m + \cosh(2mh_2)) \\
L_{11} = {} & -2m\beta \cosh(2mh_2) (\beta + h_1) + \sinh(2mh_2) (\beta + h_1) + (2m\beta \cosh(2mh_1) + \sinh(2mh_1)
\end{aligned}
$$

References

1. Hayat, T.; Saleem, N.; Ali, N. Effect of induced magnetic field on peristaltic transport of a Carreau fluid. *Commun. Nonlinear Sci. Numer. Simul.* **2010**, *15*, 2407–2423. [CrossRef]
2. Ellahi, R.; Riaz, A.; Nadeem, S.; Ali, M. Peristaltic flow of Carreau fluid in a rectangular duct through a porous medium. *Math. Probl. Eng.* **2012**, *2012*, 329639. [CrossRef]
3. Vajravelu, K.; Sreenadh, S.; Saravana, R. Combined influence of velocity slip, temperature and concentration jump conditions on MHD peristaltic transport of a Carreau fluid in a non-uniform channel. *Appl. Math. Comput.* **2013**, *225*, 656–676. [CrossRef]
4. Vajravelu, K.; Sreenadh, S.; Babu, V.R. Peristaltic transport of a Hershel-Bulkley fluid in an inclined tube. *Int. J. Non Linear Mech.* **2005**, *40*, 83–90. [CrossRef]
5. Sankar, D.S.; Hemalatha, K. Pulsatile flow of Herschel—Bulkley fluid through catheterized arteries—A mathematical model. *Appl. Math. Model.* **2007**, *31*, 1497–1517. [CrossRef]
6. Tripathi, D. A mathematical model for the peristaltic flow of chyme movement in small intestine. *Math. Biosci.* **2011**, *233*, 90–97. [CrossRef]
7. Khan, A.A.; Ellahi, R.; Gulzar, M.M.; Sheikholeslami, M. Effects of heat transfer on peristaltic motion of Oldroyd fluid in the presence of inclined magnetic field. *J. Magn. Magn. Mater.* **2014**, *372*, 97–106. [CrossRef]
8. Nadeem, S.; Akram, S. Peristaltic flow of a Williamson fluid in ana symmetric channel. *Commun. Nonlinear Sci. Numer. Simul.* **2010**, *15*, 1705–1716. [CrossRef]
9. Hayat, T.; Wang, Y.; Siddiqui, A.M.; Hutter, K. Peristaltic motion of a Johnson—Segalman fluid in a plannar channel. *Math. Probl. Eng.* **2003**, *1*, 1–23. [CrossRef]

10. Hayat, T.; Javed, M.; Asghar, S. MHD peristaltic motion of Johnson—Segalman fluid in a channel with compliant walls. *Phys. Lett.* **2008**, *372*, 5026–5036. [CrossRef]
11. Akbar, N.S.; Nadeem, S.; Hayat, T. Simulation of thermal and velocity slip on the peristaltic flow of a Johnson—Segalman fluid in an inclined asymmetric channel. *Int. J. Heat Mass Transf.* **2012**, *55*, 5495–5502. [CrossRef]
12. Akbar, N.S. Influence of magnetic field on peristaltic flow of a Casson fluid in an asymmetric channel: Application in crude oil refinement. *J. Magn. Magn. Mater.* **2015**, *378*, 463–468. [CrossRef]
13. Ellahi, R.; Wang, X.; Hameed, M. Effects of heat transfer and nonlinear slip on the steady flow of Couette fluid by means of chebyshev spectral method. *Z. Fur Nat. A* **2014**, *69*, 1–8. [CrossRef]
14. Ellahi, R.; Zeeshan, A.; Hussain, F.; Asadollahi, A. Peristaltic blood flow of couple stress fluid suspended with nanoparticles under the influence of chemical reaction and activation energy. *Symmetry* **2019**, *11*, 276. [CrossRef]
15. Abbas, M.A.; Bai, Y.Q.; Bhatti, M.M.; Rashidi, M.M. Three dimensional peristaltic flow of hyperbolic tangent fluid in non-uniform channel having flexible walls. *Alex. Eng. J.* **2016**, *55*, 653–662. [CrossRef]
16. Ellahi, R.; Hassan, M.; Zeeshan, A.; Khan, A.A. The shape effects of nanoparticles suspended in HFE-7100 over wedge with entropy generation and mixed convection. *Appl. Nanosci.* **2016**, *6*, 641–651. [CrossRef]
17. Abbas, M.A.; Bai, Y.; Rashidi, M.M.; Bhatti, M.M. Analysis of entropy generation in the flow of peristaltic nanofluids in channels with compliant walls. *Entropy* **2016**, *18*, 90. [CrossRef]
18. Ellahi, R.; Hussain, F.; Ishtiaq, F.; Hussain, A. Peristaltic transport of Jeffrey fluid in a rectangular duct through a porous medium under the effect of partial slip: An application to upgrade industrial sieves/filters. *Pramana* **2019**, *93*, 34. [CrossRef]
19. Mekheimer, K.S.; Abdelmaboud, Y. Peristaltic flow of a couple stress fluid in an annulus: Application of an endoscope. *Phys. A Stat. Mech. Appl.* **2008**, *2403*, 387. [CrossRef]
20. Ellahi, R.; Rahman, S.U.; Nadeem, S.; Vafai, K. A Mathematical Study of Non-Newtonian Micropolar Fluid in Arterial Blood Flow through Composite Stenosis. *J. Appl. Math. Inf. Sci.* **2014**, *8*, 1–7. [CrossRef]
21. Abd-Alla, A.M.; Abo-Dahab, S.M.; El-Shahrany, H.D. Effects of rotation and initial stress on peristaltic transport of fourth grade fluid with heat transfer and induced magnetic field. *J. Magn. Magn. Mater.* **2014**, *49*, 268–280. [CrossRef]
22. Akram, S.; Nadeem, S. Influence of induced magnetic field and heat transfer on the peristaltic motion of a Jeffrey fluid in an asymmetric channel: Closed form solutions. *J. Magn. Magn. Mater.* **2013**, *328*, 11–20. [CrossRef]
23. Hussain, Q.; Asghar, S.; Hayat, T.; Alsaedi, A. Heat transfer analysis in peristaltic flow of MHD Jeffrey fluid with variable thermal conductivity. *Appl. Math. Mech. Engl. Ed.* **2015**, *36*, 499–516. [CrossRef]
24. Nadeem, S.; Akram, S. Influence of inclined magnetic field on peristaltic flow of a Jeffrey fluid with heat and mass transfer in an inclined symmetric or asymmetric channel. *Asia Pac. J. Chem. Eng.* **2012**, *7*, 33–44. [CrossRef]
25. Akram, S.; Aly, E.H.; Nadeem, S. Effects of metachronal wave on biomagnetic Jeffery fluid with inclined magnetic field. *Rev. Téc. Ing. Univ. Zulia.* **2015**, *38*, 18–28.
26. Kothandapani, M.; Srinivas, S. Peristaltic transport of a Jeffrey fluid under the effect of magnetic field in an asymmetric channel. *Int. J. Non Linear Mech.* **2008**, *43*, 915. [CrossRef]
27. Tripathi, D.; Ali, N.; Hayat, T.; Chaube, M.K.; Hendi, A.A. Peristaltic flow of MHD Jeffrey fluid through finite length cylindrical tube. *Appl. Math. Mech.* **2011**, *32*, 1231–1244. [CrossRef]
28. Nadeem, S.; Riaz, A.; Ellahi, R.; Mushtaq, M. Series solutions of magnetohydrodynamic peristaltic flow of a Jeffrey fluid in eccentric cylinders. *J. Appl. Math. Inf. Sci.* **2013**, *7*, 1441–1449.
29. Khan, A.A.; Ellahi, R.; Vafai, K. Peristaltic transport of a Jeffrey fluid with variable viscosity through a porous medium in an asymmetric channel. *Adv. Math. Phys.* **2012**, *2012*. [CrossRef]
30. Srinivas, S.; Pushparaj, V. Non-linear peristaltic transport in an inclined asymmetric channel. *Commun. Nonlinear Sci. Numer. Simul.* **2008**, *13*, 1782–1795. [CrossRef]
31. Navier, C.L.M.H. Sur les lois du mouvement des fluids. *Mem. Acad. R. Sci. Inst. Fr.* **1827**, *6*, 389–440.
32. Saleem, N.; Hayat, T.; Alsaedi, A. Effects of induced magnetic field and slip condition on peristaltic transport with heat and mass transfer in a non-uniform channel. *Int. J. Phys. Sci.* **2012**, *7*, 191–204.

33. Ebaid, A.; Aly, E.H. Exact analytical solution of the peristaltic nanofluids flow in an asymmetric channel with flexible walls and slip condition: Application to the cancer treatment. *Comput. Math. Meth. Med.* **2013**, 8. [CrossRef] [PubMed]
34. Aly, E.H.; Ebaid, A. Exact analytical solution for the peristaltic flow of nanofluids in an asymmetric channel with slip effect of the velocity, temperature and concentration. *J. Mech.* **2014**, *30*, 411–422. [CrossRef]
35. Srinivas, S.; Gayathri, R.; Kothandapani, M. The influence of slip conditions, wall properties and heat transfer on MHD peristaltic transport. *Comput. Phys. Commun.* **2009**, *180*, 2115–2122. [CrossRef]
36. Hayat, T.; Hina, S.; Hendi, A.A. Peristaltic motion of power-law fluid with heat and mass transfer. *Chin. Phys. Lett.* **2011**, *28*, 084707. [CrossRef]
37. Hayat, T.; Hina, S. The influence of wall properties on the MHD peristaltic flow of a Maxwell fluid with heat and mass transfer. *Nonlinear Anal. Real World Appl.* **2010**, *11*, 3155–3169. [CrossRef]
38. Hayat, T.; Hina, S. Effects of heat and mass transfer on peristaltic flow of Williamson fluid in a non-uniform channel with slip conditions. *Int. J. Numer. Methods Fluids* **2011**, *67*, 1590–1604. [CrossRef]
39. Nadeem, S.; Akram, S. Heat transfer in a peristaltic flow of MHD fluid with partial slip. *Commun. Nonlinear Sci. Numer. Simul.* **2010**, *15*, 312–321. [CrossRef]
40. Hayat, T.; Noreen, S.; Hendi, A.A. Peristaltic motion of Phan-Thien-Tanner fluid in the presence of slip condition. *J. Biorheol.* **2011**, *25*, 8–17. [CrossRef]
41. Hayat, T.; Khan, M.; Ayub, M. The effect of the slip condition on flows of an Oldroyd 6-constant fluid. *J. Comput. Appl. Math.* **2007**, *202*, 402–413. [CrossRef]
42. Mishra, M.; Rao, A.R. Peristaltic transport of a Newtonian fluid in an asymmetric channel. *ZAMP* **2003**, *54*, 532–550. [CrossRef]
43. Akram, S.; Nadeem, S. Significance of nanofluid and partial slip on the peristaltic transport of a non-Newtonian fluid with different waveforms. *IEEE Trans. Nanotechnol.* **2014**, *13*, 375–385. [CrossRef]
44. Hina, S.; Mustafa, M.; Hayat, T.; Alotaibi, N. On peristaltic motion of pesudoplastic fluid in a curved channel with heat/mass transfer and wall properties. *Appl. Math. Comput.* **2015**, *263*, 378–391.
45. Roşca, A.V.; Pop, I. Flow and heat transfer over a vertical permeable stretching/shrinking sheet with a second order slip. *Int. J. Heat Mass Transf.* **2013**, *60*, 355–364. [CrossRef]
46. Aly, E.H. Radiation and MHD boundary layer stagnation—point of nanofluid flow towards a stretching sheet embedded in a porous medium: Analysis of suction/injection and heat generation/absorption with effect of the slip model. *Math. Probl. Eng.* **2015**, *2015*. Available online: www.Hindawi.com/Journals/mpe/aip/563647 (accessed on 8 May 2015). [CrossRef]
47. Aly, E.H. Effect of the velocity slip boundary condition on the flow and heat transfer of nanofluids over a stretching sheet. *J. Comput. Theor. Nanosci.* **2015**, in press. [CrossRef]
48. Aly, E.H.; Vajravelu, K. Exact and numerical solutions of MHD nano boundary-layer flows over stretching surfaces in porous medium. *Appl. Math. Comput.* **2014**, *232*, 191–204. [CrossRef]
49. Aly, E.H.; Ebaid, A. Effect of the velocity second slip boundary condition on the peristaltic flow of nanofluids in an asymmetric channel: Exact solution. *Abstr. Appl. Anal.* **2014**, *2014*. [CrossRef]
50. Kothandapani, M.; Prakash, J. Effects of thermal radiation parameter and magnetic field on the peristaltic motion of Williamson nanofluids in a tapered asymmetric channel. *Int. J. Heat Mass Transf.* **2015**, *81*, 234–245. [CrossRef]
51. Kothandapani, M.; Prakash, J. Effect of radiation and magnetic field on peristaltic transport of nanofluids through a porous space in a tapered asymmetric channel. *J. Magn. Magn. Mater.* **2015**, *378*, 152–163. [CrossRef]
52. Kothandapani, M.; Prakash, J.; Srinivas, S. Peristaltic transport of a MHD Carreau fluid in a tapered asymmetric channel with permeable walls. *Int. J. Biomath.* **2015**, *8*. [CrossRef]

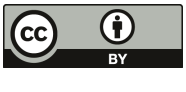

coatings

MDPI

Article

Numerical Analysis of Carbon Nanotube-Based Nanofluid Unsteady Flow Amid Two Rotating Disks with Hall Current Coatings and Homogeneous–Heterogeneous Reactions

Muhammad Ramzan [1,2,*], Saima Riasat [1], Seifedine Kadry [3], Pin Kuntha [4], Yunyoung Nam [5,*] and Fares Howari [6]

1 Department of Computer Science, Bahria University, Islamabad 44000, Pakistan; saimaqau@live.com
2 Department of Mechanical Engineering, Sejong University, Seoul 143-747, Korea
3 Department of Mathematics and Computer Science, Faculty of Science, Beirut Arab University, Beirut 115020, Lebanon; skadry@gmail.com
4 Department of ICT Convergence Rehabilitation Engineering, Soonchunhyang University, Asan 31538, Korea; pin.kuntha145@gmail.com
5 Department of Computer Science and Engineering, Soonchunhyang University, Asan 31538, Korea
6 College of Natural and Health Sciences, Zayed University, Abu Dhabi 144543, UAE; Fares.Howari@zu.ac.ae
* Correspondence: mramzan@bahria.edu.pk (M.R.); ynam@sch.ac.kr (Y.N.)

Received: 20 November 2019; Accepted: 4 January 2020; Published: 5 January 2020

Abstract: In the present exploration, our objective is to investigate the importance of Hall current coatings in the establishment of Cattaneo–Christov (CC) heat flux model in an unsteady aqueous-based nanofluid flow comprising single (SWCNTs) and multi-walled (MWCNTs) carbon nanotubes (CNTs) amid two parallel rotating stretchable disks. The novelty of the presented model is strengthened with the presence of homogeneous-heterogeneous (HH) reactions and thermal stratification effects. The numerical solution of the system of coupled differential equations with high nonlinearity is obtained by applying the bvp4c function of MATLAB software. To corroborate the authenticity of the present envisioned mathematical model, a comparison table is added to this study in limiting case. An excellent harmony between the two results is obtained. Effects of numerous parameters on involved distributions are displayed graphically and are argued logically in the light of physical laws. Numerical values of coefficient of drag force and Nusselt number are also tabulated for different parameters. It is observed that tangential velocity (function of rotation parameter) is increasing for both CNTs. Further, the incremental values of thermal stratification parameter cause the decrease in fluid temperature parameter.

Keywords: coatings; Hall current; Catttaneo-Christov heat flux; carbon nanotubes; homogeneous–heterogeneous reactions

1. Introduction

Nanofluids consist of solid particles called nanoparticles with higher thermal characteristics suspended in some base fluid. Moreover, convective heat transfer through nanoparticles has motivated many researchers for its industrial applications, pharmaceutical processes, domestic refrigerators, chillers, heat exchangers, electronic cooling system, and radiators, etc., [1]. Nanofluids are considered as the finest coolants for its various industrial applications. Nanofluids exhibit promising thermos-physical properties e.g., they have small viscosity and density and large thermal conductivity and specific heat [2]. As far as transportation of energy is concerned, the ideal features of nanofluids are the high thermal conduction and low viscosity [3]. Choi and Eastman [4] primarily examined the upsurge in thermal

conductivity by submerging nanoparticles into the ordinary fluid. Because of these thermos-physical characteristics, nanofluids are considered as the finest coolants that can work at various temperature ranges [5]. Sheikholeslami et al. [6] found a numerical solution ferrofluid flow under the influence of applied magnetic field in a hot elliptic cylinder. It is examined by them that strong Lorentz force is a source in declining the temperature of the fluid. The water-based nanofluid flow with numerous magnetite nanoparticles amid two stretchable rotating disks is numerically studied by Haq et al. [7]. Khan et al. [8] numerically addressed the water and ethylene glycol based nanofluid flow containing copper nanoparticles with suction/injection effect between parallel rotating stretchable disks. Saidi and Tamim [9] examined the pressure drop and heat transfer properties of nanofluid flow induce amid parallel stretchable disks in rotation by considering thermophoresis effects. Hayat et al. [10] also found a series solution of Jeffrey nanofluid flow between two coaxial rotating stretchable disks having convective boundary condition. Pourmehran et al. [11] numerically simulated the nanofluid flow between coaxial stretchable rotating disks.

Molecules of carbon atoms arranged in a cylindrical shape to form a structure called carbon nanotubes (CNTs). This arrangement of the molecule may be by rolling up of single sheet or by multiple sheets of graphene [12]. The novel properties of CNTs are light weight and high thermal conductivity, which make them potentially useful. CNTs are not dangerous to the environment as they are composed of carbon atoms [13]. The CNTs are the most desirous materials of the twenty-first century. Modern applications of CNTs are in microfabrication technique, pancreatic cancer test, and tissue engineering, etc., [14]. The flow of nanofluid containing both types CNTs with thermal radiation and convective boundary condition effects is examined analytically by Imtiaz et al. [15]. The water-based nanofluid flow containing CNTs of both categories under the impact of magneto-hydrodynamics (MHD) amid two parallel disks is studied by Haq et al. [16]. Mosayebidorcheh et al. [17] did heat transfer analysis with thermal radiation impacts of CNTs-based nanofluid squeezing flow between two parallel disks numerically via the least square method. Effects of thermal radiation in a magnetic field comprising both types of CNTs aqueous based nanofluid flow by two rotating stretchable disks are debated by Jyothi et al. [18]. Transparent carbon nanotubes coating to obtain conductive transparent coating is analyzed by Kaempgen [19]. Keefer et al. [20] studied carbon nanotube-coated electrodes to improve the current electrophysiological techniques. Enzyme-coated carbon nanotube as a single molecule biosensor was reported by Besteman et al. [21]. Some recent investigations featuring Carbon nanotubes amalgamated fluid flow may be found in [22–30] and many therein.

Thermal energy transformation possesses significant importance in engineering applications such as fuel cell efficiency, biomedical applications including cooling of electronic devices, heat conduction in tissues, energy production, heat exchangers, and cooling towers etc., [31]. Classical Fourier law of heat conduction was employed to describe the mechanism of heat transfer. But this model gives parabolic energy equation that is medium encountered initial disturbance instantly which is called "heat conduction paradox." Cattaneo [32] tackled this enigma by introducing the time needed for the conduction of heat via thermal waves at a limited speed which is known as thermal relaxation time. The modification in Fourier law gives hyperbolic energy equation for temperature profile. Christov [33] further inserted Oldroyd's upper convective derivative to maintain material invariant formulation. This upgraded model is known as Cattaneo- Christov heat flux model. The aqueous fluid flow by two rotating disks with the impact of CC heat flux is studied by Hayat et al. [34]. Dogonchi et al. [35] scrutinized the squeezed flow of nanofluid encompassing CC heat flux and thermal radiation effects. Lu et al. [36] discussed the unsteady squeezing nanofluid flow between parallel disks comprising CNTs with CC heat flux model and HH reactions. The recent advance studies on CC heat flux is done by many researchers [37–40].

The aforementioned literature survey (Table 1) reveals that unsteady nanofluid flow containing CNTs with CC heat flux under the influence of hall current between two rotating stretchable disks is not yet discussed. Additional impacts like HH reactions and thermal stratification of the presented

mathematical model may be considered as added features toward the novelty of the problem. The problem is solved numerically by using the bvp4c function of MATLAB software.

Table 1. A comparison table depicting uniqueness of presented mathematical model.

Author	CC Heat Flux	HH Reactions	Nanofluid with CNTs	Hall Effect	Thermal Stratification	Rotating Parallel Disks
Hayat et al. [10]	×	×	×	×	×	√
Imtiaz et al. [15]	×	×	√	×	×	√
Hayat et al. [34]	√	×	√	×	×	√
Lu et al. [36]	√	√	√	×	×	√
Present	√	√	√	√	√	√

(×) shows effect is absent and (√) shows the presence of effect.

2. Problem Formulation

Consider an axisymmetric unsteady MHD water base nanofluid flow between continuously stretchable disks with hall current effect amid non-conducting rotating disks at $z = 0$ and $z = h$. The disks rotate at constant angular velocities Ω_1 and Ω_2 about its axis. Magnetic field B_0 that is uniformly distributed is applied in the normal direction of the disks (Figure 1). Furthermore, the stretching rates of the disks are a_1 and a_2. Temperature $T_2 = T_0 + \frac{Br}{1-ct}$ refers to the temperature of upper disk while the disk's temperature at $z = h$ is $T_1 = T_0 + \frac{Ar}{1-ct}$ in a thermally stratified medium.

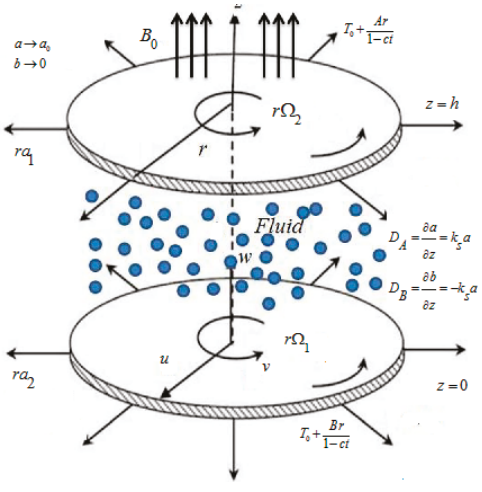

Figure 1. Schematic picture of the fluid flow.

For isothermal cubic autocatalysis, a model for homogeneous and heterogeneous reactions with reactants as chemical species are $A^*$and B^* and was proposed by Merkin and Chaudary [41] and is given by:

$$A^* + 2B^* \to 3B^*, rate = K_c = ab^2, \tag{1}$$

$$A^* \to B^*, \ rate = K_s a, \tag{2}$$

The continuity equation is

$$\nabla.\vec{V} = 0, \tag{3}$$

The momentum equations are

$$\frac{\partial u}{\partial t} + (\vec{V}.\nabla)u = \frac{-1}{\rho_{nf}}p_r^* + \frac{\mu_{nf}}{\rho_{nf}}(\nabla^2 u) - \frac{\sigma_{nf}}{\rho_{nf}}\frac{{B_O}^2}{1+m^2}(u - mv), \tag{4}$$

$$\frac{\partial v}{\partial t} + (\vec{V}.\nabla)v = \frac{\mu_{nf}}{\rho_{nf}}(\nabla^2 v) - \frac{\sigma_{nf}}{\rho_{nf}}\frac{{B_O}^2}{1+m^2}(v + mu), \tag{5}$$

$$\frac{\partial w}{\partial t} + (\vec{V}.\nabla)w = \frac{-1}{\rho_{nf}}p_z^* + \frac{\mu_{nf}}{\rho_{nf}} + \nabla^2 w, \tag{6}$$

The relevant energy equation is

$$(\rho C_p)_{nf}(\vec{V}.\nabla)T = -\nabla.\vec{q}, \tag{7}$$

where T represents the temperature, C_p the specific heat and $\vec{q}$ the heat flux. Heat flux in perspective of Cattaneo–Christov expression is satisfied.

$$\vec{q} + \epsilon_1(\frac{\partial \vec{q}}{\partial t} + \vec{V}.(\nabla\vec{q}) - \vec{q}.(\nabla\vec{V}) + (\nabla.\vec{V})\vec{q}) - k\nabla T. \tag{8}$$

Here, ϵ_1 is the thermal relaxation time and k is the thermal conductivity. Utilizing the incompressibility condition, we arrive at

$$\vec{q} + \epsilon_1(\frac{\partial \vec{q}}{\partial t} + \vec{V}.(\nabla\vec{q}) - \vec{q}.\nabla\vec{V}) - k\nabla T. \tag{9}$$

Eliminating $\vec{q}$ from Equations (9) and (7), we get

$$\begin{array}{l} T_t + uT_r + wT_z + \epsilon_1(T_{tt} + u_tT_r + 2uT_{tr} + 2wT_{tz} + w_tT_z + uu_rT_r + ww_zT_z \\ +uw_rT_r + wT_rT_z + 2uwT_{tz} + u^2w_{rr} + w^2T_{zz} = \frac{K_{nf}}{(\rho C_p)_{nf}}\Big(\nabla^2 T\Big). \end{array} \tag{10}$$

As $\vec{V} = (u, v, w)$ is the velocity vector, we obtain the following governing equations after applying the boundary layer theory:

$$u_r + \frac{u}{r} + w_z = 0, \tag{11}$$

$$u_t + uu_r + wu_z - \frac{v^2}{r} = \frac{-1}{\rho_{nf}}p_r^* + \frac{\mu_{nf}}{\rho_{nf}}(u_{rr} + \frac{1}{r}u_r - \frac{u}{r^2} + u_{zz}) - \frac{\sigma_{nf}}{\rho_{nf}}\frac{{B_O}^2}{1+m^2}(u - mv), \tag{12}$$

$$v_t + uv_r + wv_z + \frac{uv}{r} = \frac{\mu_{nf}}{\rho_{nf}}(v_{rr} + \frac{1}{r}v_r - \frac{v}{r^2} + v_{zz}) - \frac{\sigma_{nf}}{\rho_{nf}}\frac{{B_O}^2}{1+m^2}(v + mu), \tag{13}$$

$$w_t + uw_r + ww_z - \frac{v^2}{r} = \frac{-1}{\rho_{nf}}p_z^* + \frac{\mu_{nf}}{\rho_{nf}}\Big(w_{rr} + \frac{1}{r}w_r + w_{zz}\Big), \tag{14}$$

$$\begin{array}{l} T_t + uT_r + wT_z + \epsilon_1(T_{tt} + u_tT_r + 2uT_{tr} + 2wT_{tz} + w_tT_z + uu_rT_r + ww_zT_z \\ +uw_rT_r + wT_rT_z + 2uwT_{tz} + u^2w_{rr} + w^2T_{zz} = \frac{K_{nf}}{(\rho C_p)_{nf}}\Big(T_{rr} + \frac{1}{r}T_r + T_{zz}\Big), \end{array} \tag{15}$$

$$a_t + ua_r + wa_z = D_A\Big(a_{rr} + \frac{1}{r}a_r + a_{zz}\Big) - K_c a b^2, \tag{16}$$

$$b_t + ub_r + wb_z = D_B\Big(b_{rr} + \frac{1}{r}b_r + b_{zz}\Big) + K_c a b^2. \tag{17}$$

The associated boundary conditions are

$$\begin{gathered} u = \frac{ra_1}{1-ct},\ v = \frac{r\Omega_1}{1-ct}, w = 0, T = T_1(r) = T_0 + \frac{Ar}{1-ct}, \\ D_A\frac{\partial a}{\partial z} = K_s a, D_B\frac{\partial b}{\partial z} = -K_s a, \text{at } z = 0, \end{gathered} \tag{18}$$

$$u = \frac{ra_2}{1-ct},\ v = \frac{r\Omega_2}{1-ct}, w = 0, T = T_2(r) = T_0 + \frac{Br}{1-ct},\ a \to a_0\ , b \to 0,\ z = h. \tag{19}$$

Here, T_0 is the reference temperature. A and B are the dimensional constant with dimension $[\mathrm{T}\cdot\mathrm{L}^{-1}]$.

Thermo-physical properties of CNTS are represented in mathematical form as follows:

$$A = \frac{\mu_{nf}}{\mu_f} = \frac{1}{(1-\phi)^{2.5}}, \tag{20}$$

$$B = \frac{\rho_{nf}}{\rho_f} = (1-\phi) + \frac{\rho_{CNT}}{\rho_f}\phi, \tag{21}$$

$$C = \frac{(\rho C_p)_{nf}}{(\rho C_p)_f} = (1-\phi) + \frac{(\rho C_p)_{CNT}}{(\rho C_p)_f}\phi, \tag{22}$$

$$D = \frac{k_{nf}}{k_f} = \frac{(1-\phi) + 2\phi\frac{k_{CNT}}{k_{CNT}-k_f} ln\frac{k_{CNT}+k_f}{2k_f}}{(1-\phi) + 2\phi\frac{k_f}{k_{CNT}-k_f} ln\frac{k_{CNT}+k_f}{2k_f}}, \tag{23}$$

$$\frac{\sigma_{nf}}{\sigma_f} = 1 + \frac{3\phi\left(\frac{\sigma_{CNT}}{\sigma_f} - 1\right)}{\left(\frac{\sigma_{CNT}}{\sigma_f} + 2\right) - \left(\frac{\sigma_{CNT}}{\sigma_f} - 1\right)}. \tag{24}$$

Table 2 represents the thermos-physical characteristics of CNTs and H_2O.

Table 2. Thermo-physical properties of water and carbon nanotubes.

Physical Properties	Base Fluid (H_2O)	MWCNTs	SWCNTs
$C_p(\frac{J}{kg}\mathrm{k})$	4179	796	425
$\rho\left(\frac{kg}{m^3}\right)$	997.1	1600	2600
$k\left(\frac{W}{m\mathrm{k}}\right)$	0.613	3000	6600

Following transformation are used to convert the above nonlinear partial differential equations to dimensionless ordinary differential equations.

$$\begin{gathered} u = \frac{r\Omega_1}{1-ct}f'(\eta),\ v = \frac{r\Omega_1}{1-ct}g(\eta),\ w = \frac{2h\Omega_1}{\sqrt{1-ct}}f(\eta), \theta = \frac{T-T_2}{T_1-T_o}, \\ p^* = \frac{\rho\Omega_1\nu}{(1-ct)^2}\left(P(\eta) + \frac{r^2}{2h^2}\varepsilon\right),\ \eta = \frac{z}{h\sqrt{1-ct}},\ a = c_0\widetilde{\varphi}, b = c_0\widetilde{l}. \end{gathered} \tag{25}$$

Equation (11) is satisfied automatically, Equations (12) to (17) are transformed into the following form:

$$A_1\left(f' + \frac{\eta}{2}f''\right) + Re\left(f'^2 - 2ff'' - g^2\right) + \varepsilon - \frac{\sigma_{nf}}{\sigma_f}\frac{MRe(f' - mg)}{B(1+m^2)} = \frac{A}{B}f''', \tag{26}$$

$$\frac{B}{A}Re\left[\left(g + \frac{1}{2}\eta g'\right)A_1 + 2(f'g - fg')\right] - \frac{\sigma_{nf}}{\sigma_f}\frac{MRe(g + mf')}{A(1+m^2)} = g'', \tag{27}$$

$$\frac{\partial p^*}{\partial z} = (A_1(f + \eta f') - 4ff')B(1-ct)Re - 2\frac{(1-ct)}{A}f'', \tag{28}$$

$$\begin{array}{l} A_1\left(s+\theta+\frac{1}{2}\eta\theta'\right)+(s+\theta)f'-2f\theta'+\gamma[\left(s+\theta+\frac{7}{8}\eta\theta'\right)+ \\ f'\left(f'+\frac{1}{2}\eta f''\right)(s+\theta)+2f'\left(s+\theta+\frac{1}{2}\eta\theta'\right)-4f\left(\frac{1}{2}\eta\theta''+\frac{3}{2}\theta'\right)+ \\ (f+\eta f')\theta'+f'^2(s+\theta)-\frac{4}{A_1}f'\theta'-2ff''(s+\theta)+\frac{4}{A_1}f^2\theta''-\frac{4}{A_1}ff'\theta' \\ =\frac{D}{C}\left(\frac{1}{\mathrm{Pr}Re}\theta''+\frac{1}{\mathrm{Pr}}(s+\theta)\right), \end{array} \tag{29}$$

$$\frac{1}{2}\eta\widetilde{\varphi}'-\frac{2}{A_1}f\widetilde{\varphi}'-\frac{1}{Sc}\widetilde{\varphi}''+k1\widetilde{\varphi}l^2=0, \tag{30}$$

$$\frac{1}{2}\eta\widetilde{l'}-\frac{2}{A_1}f\widetilde{l'}-\frac{\delta}{Sc}\widetilde{l''}-k1\widetilde{\varphi}l^2=0, \tag{31}$$

with transformed boundary conditions

$$\begin{array}{c} f(0)=0, f(1)=0, f'(0)=\gamma_1, f'(1)=\gamma_2, g(0)=1, \\ g(1)=\Omega, \theta(0)=1-s, \theta(1)=0, P(0)=0, \end{array} \tag{32}$$

where

$$\begin{array}{c} M=\frac{\sigma_f B_O{}^2(1-ct)}{\rho_f}, A_1=\frac{c}{\Omega_1},\ \gamma_1=\frac{a_1}{\Omega_1}, \gamma_2=\frac{a_2}{\Omega_2}, Sc=\frac{h^2c}{D_A}, Pr=\frac{\upsilon_f(\rho C_p)_f}{k_f}, \Omega=\frac{\Omega_2}{\Omega_1}, \\ k1=\frac{K_c c_0^2(1-ct)}{c}, k2=\frac{k_s h(1-ct)^{1/2}}{D_A}\delta=\frac{D_B}{D_A}, \gamma=\frac{c\epsilon_1}{1-ct},\ D=\frac{k_{nf}}{k_f}, B=\frac{(\rho C_p)_{nf}}{(\rho C_p)_f}. \end{array} \tag{33}$$

By assuming the chemical species alike, we take diffusion coefficient of both species equal, so that $\delta=1$. And thus we have $\widetilde{l}(\eta)+\breve{\varphi}(\eta)=1$, we get from Equations (30) and (31)

$$\frac{1}{Sc}\widetilde{\varphi}''-\frac{1}{2}\eta\widetilde{\varphi}'+\frac{2}{A_1}f\widetilde{\varphi}'-\mathrm{k1}(1-\widetilde{\varphi})^2\widetilde{\varphi}=0, \tag{34}$$

$$\widetilde{\varphi}'(0)=K2\widetilde{\varphi}'(0),\ \widetilde{\varphi}\prime(1)\to 1, \tag{35}$$

Differentiating Equation (26), we get

$$A_1\left(\frac{3}{2}f''+\frac{\eta}{2}f'''\right)+Re(2ff'''-2gg')-\frac{\sigma_{nf}}{\sigma_f}\frac{MRe(f''-mg')}{B(1+m^2)}=\frac{A}{B}f'''', \tag{36}$$

3. Skin Friction and Local Nusselt Number

Shear stresses at lower disk in radial and tangential directions are τ_{zr} and $\tau_{z\theta}$

$$\tau_{zr}=\mu_{nf}u_z|_{z=0}=\frac{\mu_f r\Omega_1 f''(0)}{h(1-\phi)^{2.5}}, \tau_{z\theta}=\mu_{nf}u_z|_{z=0}=\frac{\mu_f r\Omega_1 g'(0)}{h(1-\phi)^{2.5}}, \tag{37}$$

The total shear stress is

$$\tau_w=\left({\tau_{zr}}^2+{\tau_{z\theta}}^2\right)^{1/2}, \tag{38}$$

Coefficients of drag force at $z=0,$ and $z=h$ for the disk are

$$\begin{array}{l} C_{f_1}=\frac{\tau_w|_{z=0}}{\rho_f(r\Omega_1)^2}=\frac{1}{Re_r(1-\phi)^{2.5}}\left[(f''(0))^2+(g'(0))^2\right]^{1/2}, \\ C_{f_2}=\frac{\tau_w|_{z=h}}{\rho_f(r\Omega_2)^2}=\frac{1}{Re_r(1-\phi)^{2.5}}\left[(f''(1))^2+(g'(1))^2\right]^{1/2}, \end{array} \tag{39}$$

Here, Re_r represents local Reynolds number.
The dimensional form of Nu (the local Nusselt number) is

$$Nu=\frac{k_{nf}(\rho c_p)_f}{\rho_f k_f}, \tag{40}$$

By using transformation given in Equations (25), Equation (40) becomes

$$(1-ct)^{1/2}Nu_1 = -\frac{k_{nf}}{k_f}\theta'(0), (1-ct)^{1/2}Nu_2 = -\frac{k_{nf}}{k_f}\theta'(1), \tag{41}$$

4. Numerical Method

In current model, MATLAB built-in-function bvp4c is used to solve coupled ordinary differential equations (ODE's) (Equations (26–36)) with mentioned boundary conditions (32). The computational purpose of the infinite domain is restricted to $\eta = 4$ which is enough to indicate the asymptotic behavior of the solution. The theme numerical scheme needs initial approximation with tolerance 10^{-6}. The initial taken estimation must meet the boundary conditions without interrupting the solution technique. We obtain a system comprising three first-order differential equations given below:

$$\begin{array}{l}
f\prime = y_2, \\
f'' = y_3, \\
f''' = y_4 \\
f'''' = yy_1 \\
yy1 = \frac{B}{A}(A_1\left(\frac{3}{2}y_3 + \frac{\eta}{2}y_4\right) + Re(2y_1y_4 - 2y_5y_6) - \frac{\sigma_{nf}}{\sigma_f}\frac{MRe(y_3 - my_6)}{B(1+m^2)}), \\
g = y_5, \\
g\prime = y_6, \\
yy_2 = \frac{B}{A}Re\left[\left(y_5 + \frac{1}{2}\ \eta y_6\right)A_1 + 2(y_2y_5 - y_1y_6)\right] - \frac{\sigma_{nf}}{\sigma_f}\frac{MRe(y_5 + my_2)}{A(1+m^2)}, \\
\theta = y_7, \\
\theta\prime = y_8 \\
yy3 = \frac{1}{\frac{D}{C}\frac{1}{\mathrm{PrRe}} - \frac{4}{A_1}(y_1)^2 - 2\eta y_1}(A_1\left(s + y_7 + \frac{1}{2}\eta y_8\right) + (s + y_7)y_2 - 2y_1y_8 + \\
\gamma[\left(s + y_7 + \frac{7}{8}\eta y_8\right) + y_2\left(y_2 + \frac{1}{2}\eta y_3\right)(s + y_7) + 2y_2\left(s + y_7 + \frac{1}{2}\eta y_8\right) - \\
6y_1y_8 + (y_1 + \eta y_2)\theta' + (y_2)^2(s + y_7) - \frac{4}{A_1}y_2y_8 - 2y_1y_3(s + y_7) - \frac{D}{\mathrm{CPr}}(s + y_7)),
\end{array} \tag{42}$$

With suitable boundary condition

$$\begin{array}{l}
y_1(0) = 0, y_2(0) = \gamma_1, y_5(0) = 1, y_7(0) = 1 - s, \\
y_1(1) = 0, y_2(1) = \gamma_2, y_5(1) = \Omega, y_7(1) = 0
\end{array} \tag{43}$$

5. Outcomes with Discussion

In this section the impact of different parameters on velocity and temperature profile, drag force coefficient, and Nusselt number is described in the form of graphs and tables. In order to acquire the required outcome we fix the different flow parameters such as $M = 0.7, A_1 = 0.5, \gamma_1 = 0.1$, $\gamma_2 = 0.5, Sc = 1, Pr = 6.7, \gamma = 0.5, k1 = 0.1, \Omega = 0.1$.

5.1. Radial and Axial Velocity Profile

In Figures 2–9, the radial velocity $f'(\eta)$ and axial velocity profiles $f(\eta)$ is depicted for *Re*, parameters, scaled Stretching γ_1 and γ_2 and nanoparticle volume fraction ϕ. The solid line ( ) and the dashed line (—-) represent the single wall carbon nanotubes and multiwall carbon nanotubes respectively. Figures 2 and 3 show that the magnitude of radial $f'(\eta)$ and axial velocity $f(\eta)$ reduces for incremental value of *Re*. The fact is that for increasing values of Reynolds number causes the increase in resistive forces which reduces the motion of fluid. Magnitude of $f'(\eta)$ and $f(\eta)$ for multiwall carbon nanotubes is higher as compared with single wall carbon nanotubes. $f(\eta)$ takes on negative values near the lower disks because upper disks are moving faster than the lower disks. Figure 4 depicts that $f'(\eta)$ escalates in the vicinity of the lower disk and declines in the vicinity of the upper disks by enhancing the value of γ_1, while the behavior of $f(\eta)$ remain same throughout the system as shown

in Figure 5. But by the increase in the value of γ_2, $f'(\eta)$ increases in the vicinity of the lower disks and decreases in the vicinity of the upper disks, (see Figure 6), and $f(\eta)$ shows decrease in magnitude throughout the system, (see Figure 7). Figure 8 shows that $f(\eta)$ reduces by the increase of nanoparticle volume fraction and magnitude of $f(\eta)$ is smaller for MWCNTs. $f'(\eta)$ is decreasing near the lower disk and enhancing near the upper disks by increasing ϕ, while the amplitude of $f'(\eta)$ is higher for MWCNTs than SWCNTs. This effect is shown in Figure 9.

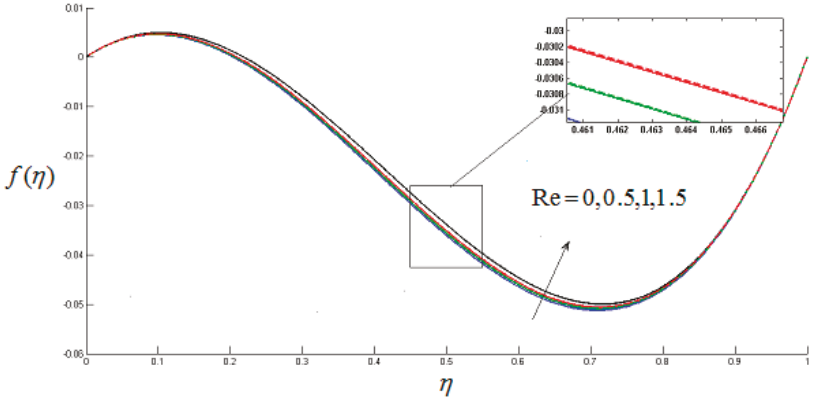

Figure 2. Axial velocity profile $f(\eta)$ for *Re*.

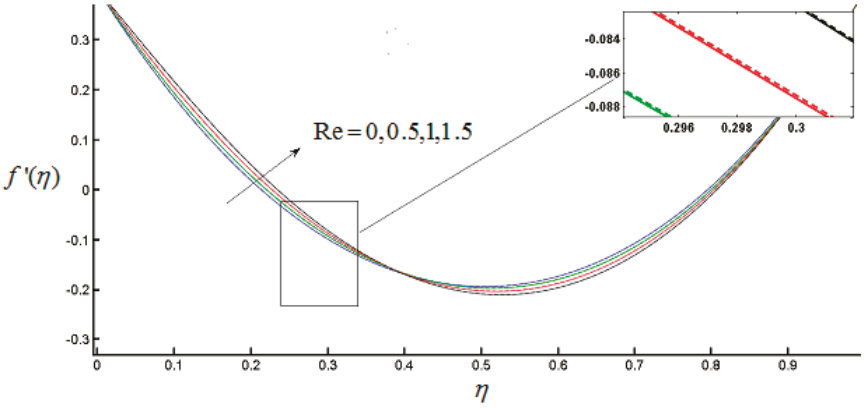

Figure 3. Radial velocity profile $f'(\eta)$ for *Re*.

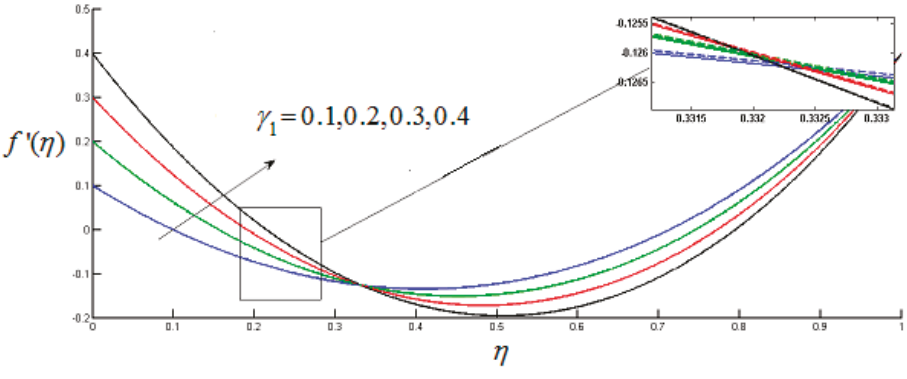

Figure 4. Radial velocity profile $f'(\eta)$ for γ_1.

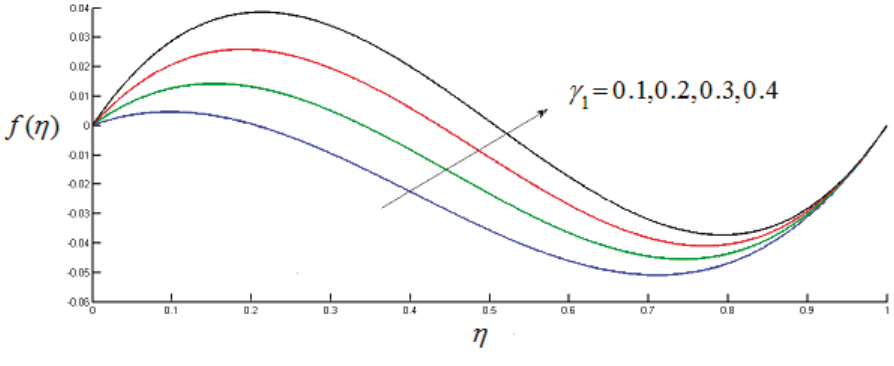

Figure 5. Axial velocity profile $f(\eta)$ for γ_1.

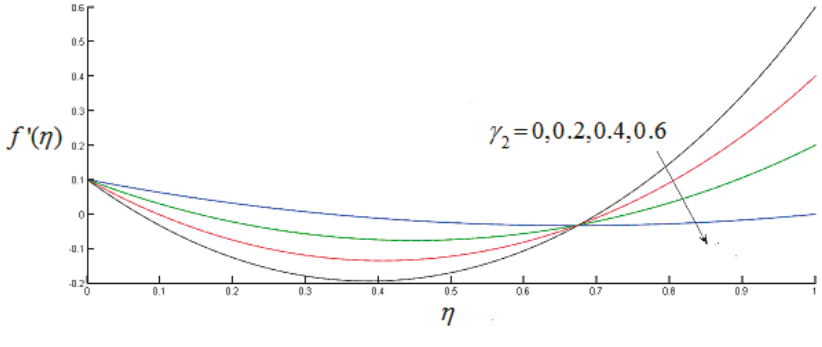

Figure 6. Radial velocity profile $f'(\eta)$ for γ_2.

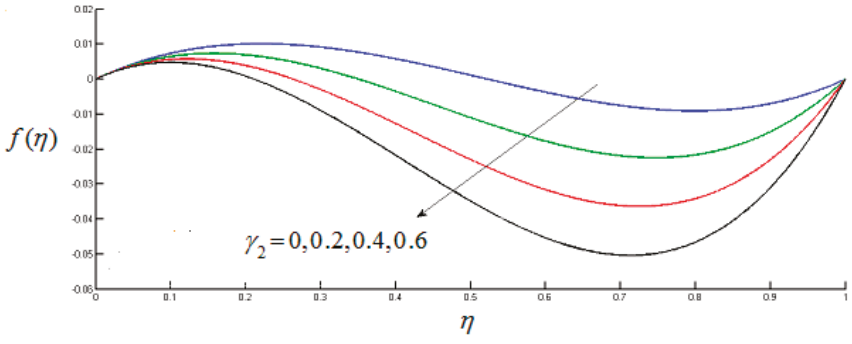

Figure 7. Axial velocity profile $f(\eta)$ for γ_2.

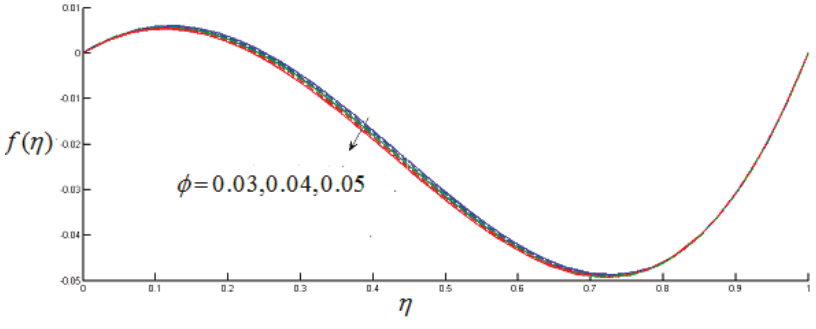

Figure 8. Radial velocity profile $f(\eta)$ for ϕ.

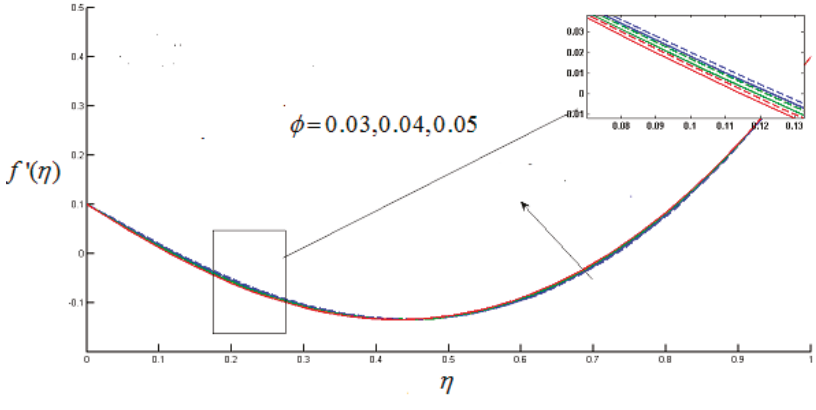

Figure 9. Axial velocity profile $f\prime(\eta)$ for ϕ.

5.2. Tangential Velocity Profile

Tangential velocity $g(\eta)$ decreases by escalating the value of M because increasing magnetic field exerts a retarding force which slows the motion of the particles within the fluid. Figure 10 depicts that the tangential velocity has smaller magnitude for MWCNTs as compared to SWCNTs. Figure 11 depicts that tangential velocity decreases for increasing value of A_1 and its value is smaller for MWCNTs. Figure 12 shows that as stretching rate increases at the upper disk it causes a decrease of tangential

velocity. $g(\eta)$ increases for incremental values of hall current parameter m and magnitude of tangential velocity profile is more increasing for MWCNTs as compared with SWCNTs as shown in Figure 13. Figure 14 depicts the relationship between Ω and $g(\eta)$. It represents that the tangential velocity is an escalating function of rotation parameter. Figures 15 and 16 depict that for increasing ϕ the amplitude of $g(\eta)$ increases and it decreases for increasing Reynolds number.

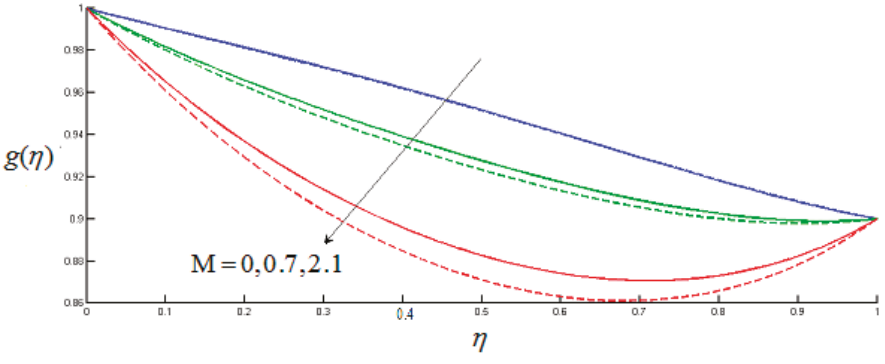

Figure 10. Tangential velocity profile for M.

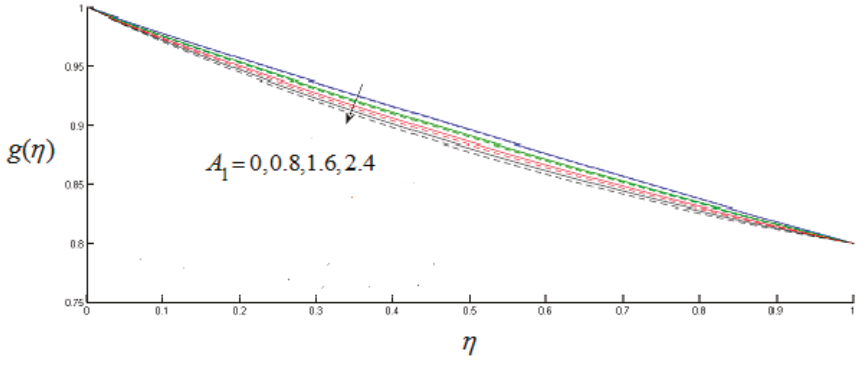

Figure 11. Tangential velocity profile for A_1.

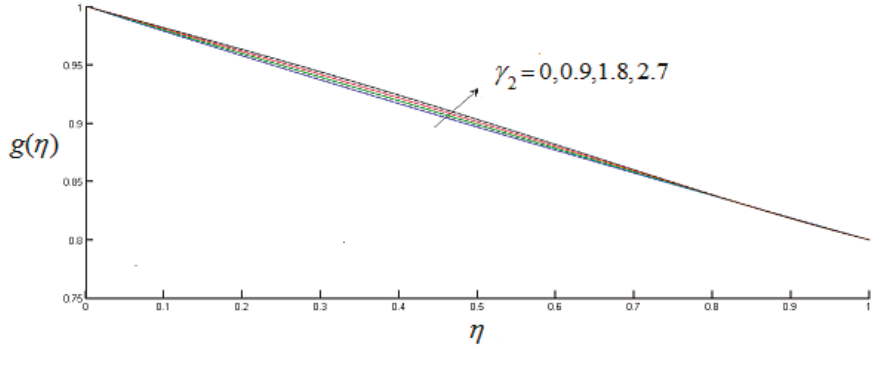

Figure 12. Tangential velocity profile for γ_2.

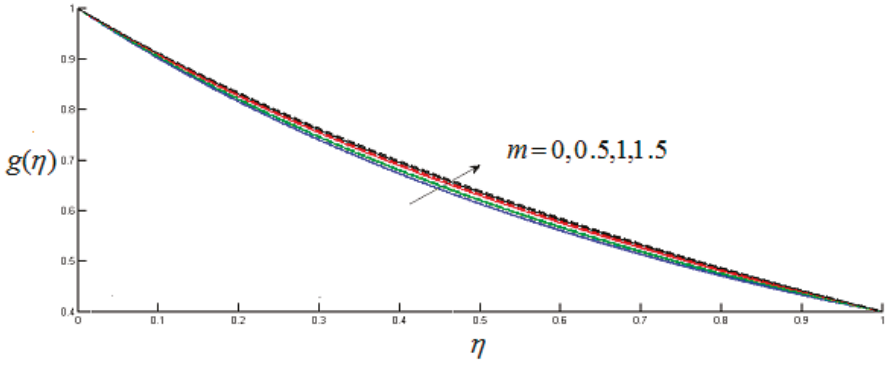

Figure 13. Tangential velocity profile for m.

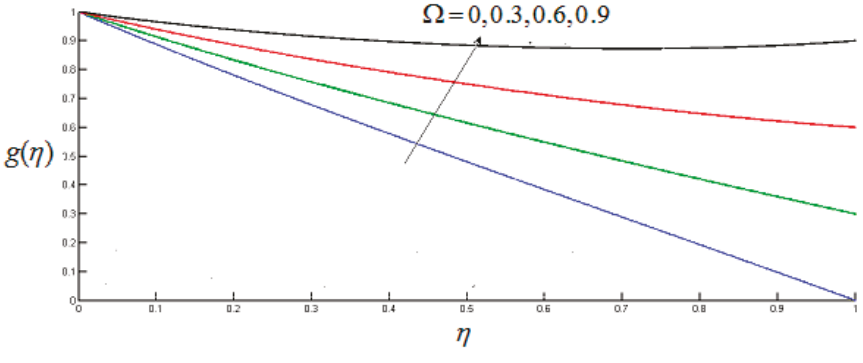

Figure 14. Tangential velocity profile for Ω.

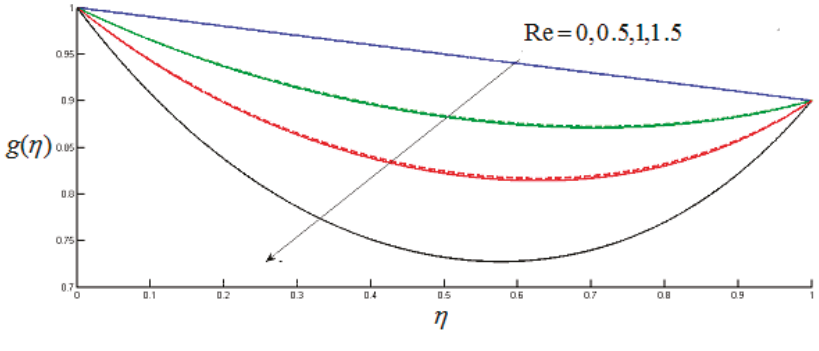

Figure 15. Tangential velocity profile for Re.

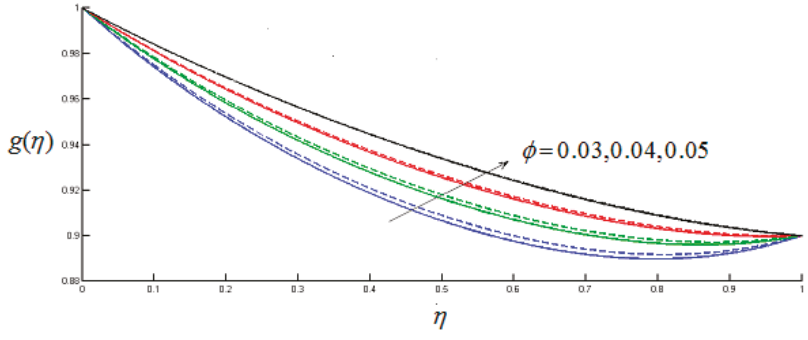

Figure 16. Tangential velocity profile for ϕ.

5.3. Dimensionless Temperature Distribution

The dimensionless temperature distribution for different values of relaxation parameter is depicted for both MWCNTs and SWCNTs in Figure 17. The figure shows that higher rate of thermal relaxation parameter causes the increase in temperature profile. Results shows that temperature profile is more increasing for MWCNTs than SWCNTs. Figure 18 shows that temperature decreases by increasing nanoparticle volume fraction and temperature profile shows more decreasing behavior for MWCNTS as compared to SWCNTs. Effect of Reynolds number, Prandtl number, stratification parameter, unsteadiness parameter A_1, stretching parameter γ_1 at lower disk on temperature profile is shown in Figures 19–23. Results are plotted both for MWCNTs and MWCNTs. Figure 19 shows that for positive values of *Re* there is an increase in temperature profile, and it shows that multi-walled carbon nanotubes have higher temperature distribution for increasing Reynolds number as compared to single-walled carbon nanotubes. Similarly, graph is plotted for negative values of Reynolds number. It is revealed that on decreasing the value of Reynolds number, temperature profile also decreases and shows more decreasing behavior for MWCNTs than SWCNTs. Figures 20–22 portray the variation of temperature profile which decreases for incremental values of s, A_1, and γ_1 this decreasing behavior is observed more for SWCNTs as compared with MWCNTs. Figure 23 depicts for increasing value of Prandtl number temperature profile decreases. The decrease in temperature by augmentation of Prandtl number is consistent with the physical expectation, as by increasing Prandtl number fluid possesses lower thermal diffusivity which causes the thickness of thermal boundary layer to decrease.

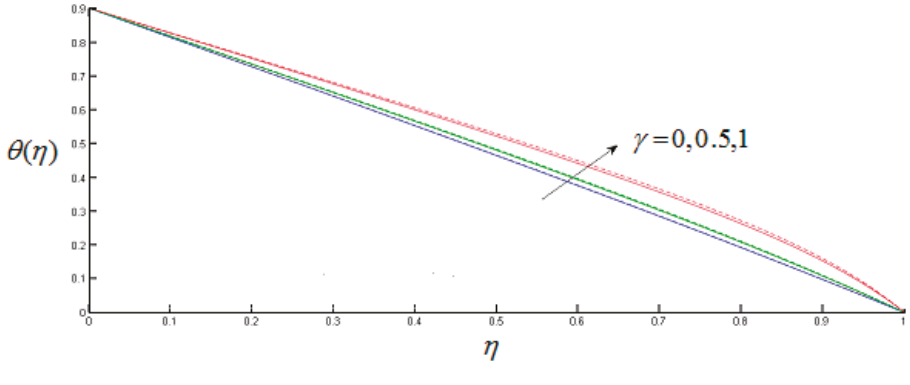

Figure 17. Temperature profile for γ.

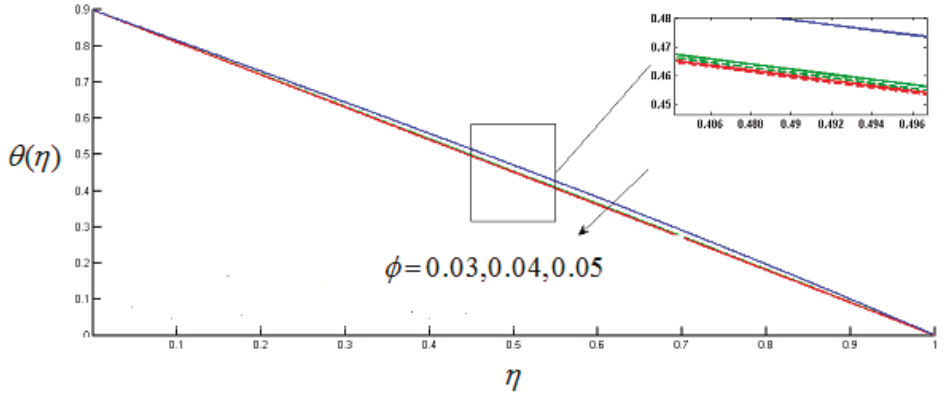

Figure 18. Temperature profile for ϕ.

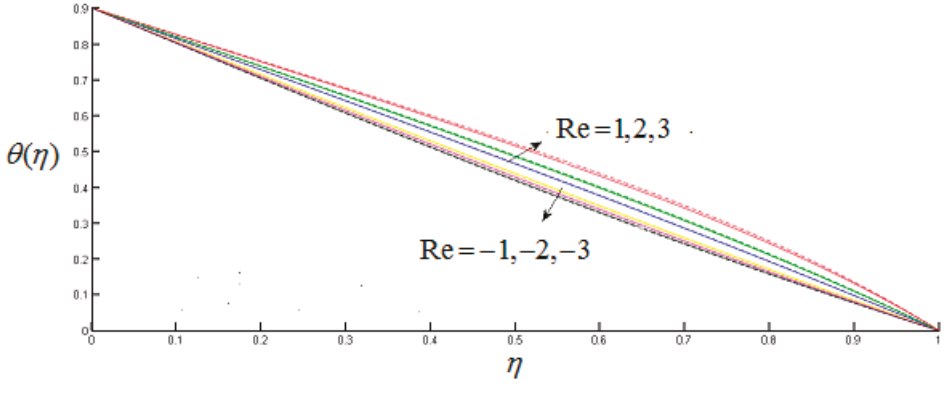

Figure 19. Temperature profile for *Re*.

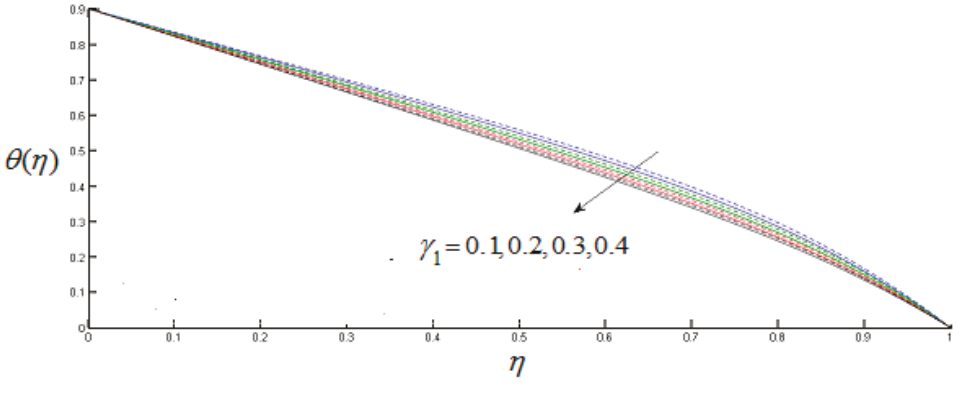

Figure 20. Temperature profile for γ_1.

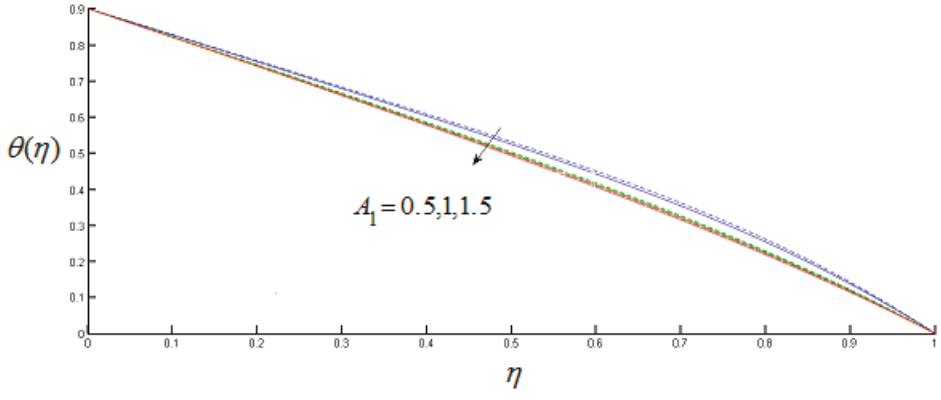

Figure 21. Temperature profile for A_1.

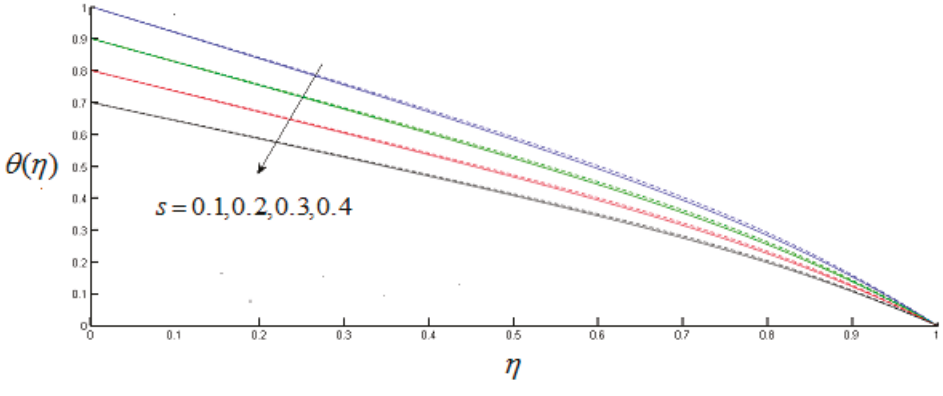

Figure 22. Temperature profile for s.

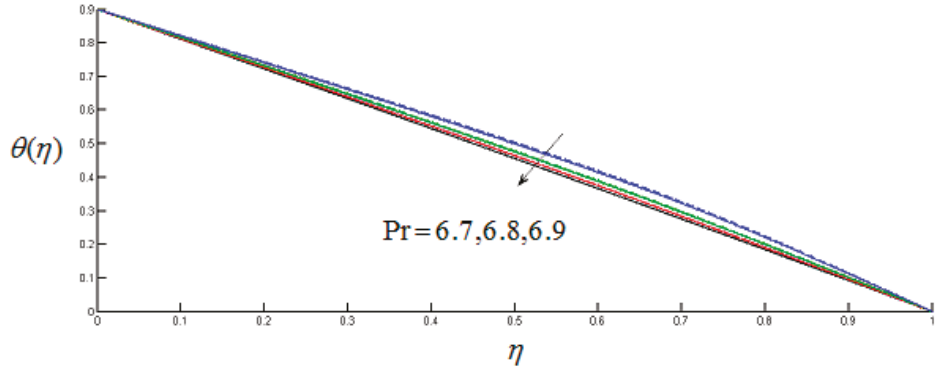

Figure 23. Temperature profile for Pr.

5.4. Concentration Profile

Figure 24 demonstrate the analysis of concentration profile. For various estimates of homogeneous reaction parameter $k1$ there is decay in concentration profile. Similar results are obtained for heterogeneous reaction parameter $k2$ in Figure 25. Concentration field is observed for Schmidt

number in Figure 26. As it is momentum to mass diffusivity ratio, so smaller the value of mass diffusivity, stronger the value of Schmidt number, which causes the reduction of the concentration of the fluid.

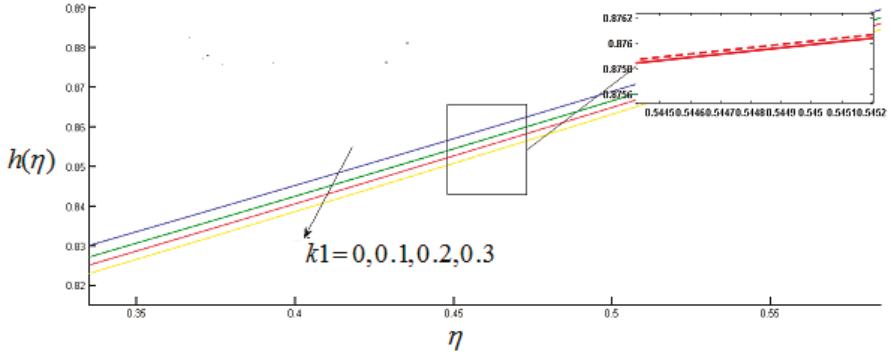

Figure 24. Concentration profile for $k1$.

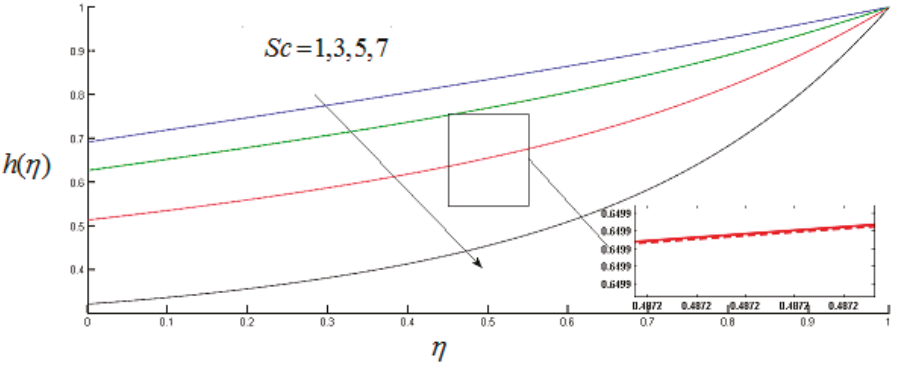

Figure 25. Concentration profile for Sc.

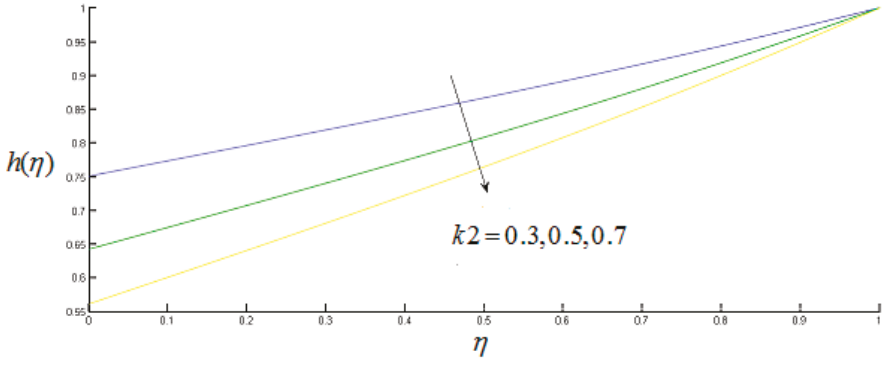

Figure 26. Concentration profile for $k2$.

Comparison of $f''(0)$ and $g'(0)$ with Stewartson [42] for several estimates of Ω by considering all extra terms as zero is depicted in Table 3. An excellent synchronization is achieved in this case. This substantiates our mathematical model and presented results.

Table 3. Comparison of $f''(0)$ and $g'(0)$ for numerous estimates of Ω with Stewartson [42].

Ω	$f''(0)$	Present	$-g'(0)$	Present
−1.0	0.06666	0.06665	2.00095	2.00096
−0.8	0.08394	0.08394	1.80259	1.80259
−0.3	0.10395	0.10396	1.30442	1.30443
0.0	0.09997	0.09998	1.00428	1.00429
0.5	0.06663	0.06664	0.50261	0.50262

5.5. Drag Force Coefficient and Heat Transfer Rate

Influence of Hartmann number M, Hall current parameter m, stretching parameter γ_1 and γ_2, and Reynolds number on Skin friction coefficients for MWCNTs and SWCNTs at both disks is portrayed in Table 4. Skin coefficient friction decrease by increasing the value of Hall current parameter m and Hartmann number M at lower and upper disk for both MWCNTs and SWCNTs, while increasing behavior for Re and scaled stretching parameter γ_1 for disk at $z = 0$ and stretching parameter γ_2 for the disk at $z = h(t)$ for both MWCNTs and SWCNTs.

Table 4. Numerical values of drag force coefficient at lower and upper disk for SWCNTs and MWCNTs when $A_1 = 0.5$, $\mathrm{Pr} = 6.7$, $\Omega = 0.5$, $S = 0.4$, $k1 = 0.1$, $k2 = 0.1$, $m = 0.5$, $Sc = 1$.

m	M	Re	γ_1	γ_2	SWCNTs C_1	MWCNTs C_1	SWCNTs C_2	MWCNTs C_2
0	0	–	–	–	5.03411	5.03457	6.04242	6.04063
–	0.5	–	–	–	5.02568	5.02466	6.04163	6.0397
–	1	–	–	–	5.01732	5.01486	6.04091	6.03888
0.5	0	–	–	–	5.03411	5.03457	6.04242	6.04063
–	0.5	–	–	–	5.02896	5.02852	6.04023	6.03805
–	1	–	–	–	5.02385	5.02253	6.03808	6.03553
0.5	0.5	0.5	–	–	4.13561	4.14261	5.58341	5.59479
–	–	1	–	–	4.2427	4.48904	5.984181	6.19988
–	–	1.5	–	–	5.15702	6.33493	7.14381	8.20049
–	–	0.1	0.1	–	2.94098	2.94399	4.87809	4.86666
–	–	–	0.2	–	3.60549	3.60836	5.22787	5.21623
–	–	–	0.1	0.6	2.94098	2.94399	4.87809	4.86666
–	–	–	–	0.8	3.553583	3.56223	6.32921	6.31152

Table 5 is erected to depict the impact of numerous parameters on heat transfer rate. It is gathered that rate of heat transfer is a decreasing function of unsteadiness parameter and Prandtl number at lower disk for both MWCNTS and SWCNTs, while it is a decreasing function of Reynolds number at lower disk and increasing function of Reynolds number at upper disk for both MWCNTs and SWCNTs.

Table 5. Numerical values of heat transfer rate at lower and upper disk for SWCNTs and MWCNTs when $\Omega = 0.5$, $\gamma_1 = 0.1$, $\gamma_2 = 0.4$, $k1 = 0.1$, $k2 = 0.1$, $m = 0.5$, $Sc = 1$.

S	Pr	Re	A_1	SWCNTs $-\frac{k_{nf}}{k_f}\theta'(0)$	MWCNTs $-\frac{k_{nf}}{k_f}\theta'(0)$	SWCNTs $-\frac{k_{nf}}{k_f}\theta'(1)$	MWCNTs $-\frac{k_{nf}}{k_f}\theta'(1)$
0.2	–	–	–	4.14135	3.83131	4.49696	4.16193
0.4	–	–	–	3.10577	2.87324	3.37182	3.12053
0.6	–	–	–	2.01701	1.91516	2.24668	2.07914
0.7	–	–	–	1.5524	1.43613	1.68411	1.55844
0.2	3.9	–	–	4.12824	3.81806	4.51945	4.18466
–	5.2	–	–	4.12164	3.81139	4.530861	4.19621
–	1.3	0.2	–	4.13503	3.82486	4.50794	4.17309
–	–	0.5	–	4.11594	3.81839	4.54154	4.18437
–	–	0.1	0.6	4.10289	3.79571	4.593021	4.25082
–	–	–	0.7	4.05746	3.75367	4.705941	4.35533
–	–	–	0.8	4.00509	3.7052	4.83659	4.47624

6. Conclusions

Unsteady axisymmetric MHD flow and transfer of heat with water-based carbon nanotubes amid two stretchable rotating disks is explored in the present study. Results for arising parameters for both SWCNTs and MWCNTs are illustrated. Main findings of our observations are as follows.

- Radial velocity increases and declines in the vicinity of the lower and the upper disks respectively.
- Radial and axial velocity profile is increasing for stretching parameter γ_1 and decreasing behavior γ_2 near the lower disks for both types of walls.
- Tangential velocity increases with increasing Hall current parameter and decreases with increasing Hartmann number in case of SWCNTs and MWCNTs.
- Temperature increases for thermal relaxation parameter, and decreases for nanoparticle volume fraction.
- In H-H reactions the concentration profile decreases for both types of CNTs.
- For incremental value of thermal stratification parameters temperature profile decreases.

Author Contributions: Conceptualization, M.R.; Methodology, S.R.; software, S.K.; Validation, P.K. and Y.N.; Formal Analysis, S.R.; Investigation, F.H.; X.X.; Writing—Original Draft Preparation, S.R.; Writing—Review and Editing, M.R.; visualization, S.K.; Supervision, M.R.; Project Administration, M.R.; Funding Acquisition, P.K. and Y.N.; All authors have read and agreed to the published version of the manuscript.

Funding: This research was funded by the Bio & Medical Technology Development Program of the NRF funded by the Korean government, MSIP(NRF-2015M3A9D7067219) and also supported by the Soonchunhyang University Research Fund.

Conflicts of Interest: Authors have no conflict of interest regarding this publication.

Nomenclature

Symbols	Description
$\vec{V} = \vec{V}(u, v, w)$	Velocity of the fluid (m/s)
M	Hartmann number
T	Temperature (K)
T_0	Reference temperature (K)
A, B	The dimensional constant $K.m^{-1}$
γ_1	Scale stretching parameters at lower disk
γ_2	Scale stretching parameters at upper disk
Ω_1	Angular velocity of the lower disk $(\sec^{-1})$
Ω_2	Angular velocity of the upper disk $(\sec^{-1})$

Symbols	Description
C_p	Specific heat $(\frac{J}{kg}\mathrm{k})$
A_1	Unsteadiness parameter
ε_1	Thermal relaxation time (sec)
B_0	Applied magnetic field (Tesla)
σ_{nf}	Thermal conductivity of nanofluid (S/m)
σ_f	Thermal conductivity of the fluid (S/m)
$k1$	Measure of strength of homogeneous reaction
$\mathbf{\Omega}$	Rotation parameter
Sc	Schmidt number
D_A	Diffusion coefficient of chemical species A^* (cm^2/s)
s	Thermal stratification parameter
$k2$	Measure of strength of heterogeneous reaction
Re	Reynolds number
μ_f	Dynamic viscosity of fluid $(Pa.s)$
μ_{nf}	Dynamic viscosity of nanofluid $(Pa.s)$
ρ_f	Density of the fluid (kgm^{-3})
k_{nf}	Thermal conductivity of the nanofluid $(W/m\mathrm{k})$
ρ_{nf}	Density of the nanofluid (kgm^{-3})
k_{CNT}	Thermal conductivity of carbon nanotubes $(W/m\mathrm{k})$
k_f	Thermal conductivity of the fluid $(W/m\mathrm{k})$
δ	Ratio of diffusion coefficients
D_B	Diffusion coefficient of chemical species B^* (cm^2/s)
Pr	**Prandtl number**
ε	Pressure parameter

References

1. Suleman, M.; Ramzan, M.; Ahmad, S.; Lu, D.; Muhammad, T.; Chung, J.D. A Numerical Simulation of Silver–Water Nanofluid Flow with Impacts of Newtonian Heating and Homogeneous–Heterogeneous Reactions Past a Nonlinear Stretched Cylinder. *Symmetry* **2019**, *11*, 295. [CrossRef]
2. Wang, X.Q.; Mujumdar, A.S. Heat transfer characteristics of nanofluids: A review. *Int. J. Therm. Sci.* **2007**, *46*, 1–19. [CrossRef]
3. Alawi, O.A.; Sidik, N.A.C.; Xian, H.W.; Kean, T.H.; Kazi, S.N. Thermal conductivity and viscosity models of metallic oxides nanofluids. *Int. J. Heat Mass Transf.* **2018**, *116*, 1314–1325. [CrossRef]
4. Choi, S.U.; Eastman, J.A. *Enhancing Thermal Conductivity of Fluids with Nanoparticles*; (No. ANL/MSD/CP-84938; CONF-951135-29); Argonne National Lab.: Lemont, IL, USA, 1995.
5. Ali, N.; Teixeira, J.A.; Addali, A. A review on nanofluids: Fabrication, stability, and thermophysical properties. *J. Nanomater.* **2018**. [CrossRef]
6. Sheikholeslami, M.; Ellahi, R.; Vafai, K. Study of Fe3O4-water nanofluid with convective heat transfer in the presence of magnetic source. *Alex. Eng. J.* **2018**, *57*, 565–575. [CrossRef]
7. Haq, R.U.; Noor, N.F.M.; Khan, Z.H. Numerical simulation of water based magnetite nanoparticles between two parallel disks. *Adv. Powder Technol.* **2016**, *27*, 1568–1575. [CrossRef]
8. Khan, Z.H.; Hussain, S.T.; Hammouch, Z. Flow and heat transfer analysis of water and ethylene glycol based Cu nanoparticles between two parallel disks with suction/injection effects. *J. Mol. Liq.* **2016**, *221*, 298–304.
9. Saidi, M.H.; Tamim, H. Heat transfer and pressure drop characteristics of nanofluid in unsteady squeezing flow between rotating porous disks considering the effects of thermophoresis and Brownian motion. *Adv. Powder Technol.* **2016**, *27*, 564–574. [CrossRef]
10. Hayat, T.; Javed, M.; Imtiaz, M.; Alsaedi, A. Convective flow of Jeffrey nanofluid due to two stretchable rotating disks. *J. Mol. Liq.* **2017**, *240*, 291–302. [CrossRef]
11. Pourmehran, O.; Sarafraz, M.M.; Rahimi-Gorji, M.; Ganji, D.D. Rheological behaviour of various metal-based nano-fluids between rotating discs: A new insight. *J. Taiwan Inst. Chem. Eng.* **2018**, *88*, 37–48. [CrossRef]

12. Herlem, G.; Picaud, F.; Girardet, C.; Micheau, O. Carbon Nanotubes: Synthesis, Characterization, and Applications in Drug-Delivery Systems. In *Nanocarriers for Drug Delivery*; Elsevier: Amsterdam, The Netherlands, 2019; pp. 469–529.
13. Ong, Y.T.; Ahmad, A.L.; Zein, S.H.S.; Tan, S.H. A review on carbon nanotubes in an environmental protection and green engineering perspective. *Braz. J. Chem. Eng.* **2010**, *27*, 227–242. [CrossRef]
14. Simon, J.; Flahaut, E.; Golzio, M. Overview of Carbon Nanotubes for Biomedical Applications. *Materials* **2019**, *12*, 624. [CrossRef]
15. Imtiaz, M.; Hayat, T.; Alsaedi, A.; Ahmad, B. Convective flow of carbon nanotubes between rotating stretchable disks with thermal radiation effects. *Int. J. Heat Mass Transf.* **2016**, *101*, 948–957. [CrossRef]
16. Haq, R.U.; Hammouch, Z.; Khan, W.A. Water-based squeezing flow in the presence of carbon nanotubes between two parallel disks. *Therm. Sci.* **2016**, *20*. [CrossRef]
17. Mosayebidorcheh, S.; Hatami, M. Heat transfer analysis in carbon nanotube-water between rotating disks under thermal radiation conditions. *J. Mol. Liq.* **2017**, *240*, 258–267. [CrossRef]
18. Jyothi, K.; Reddy, P.S.; Reddy, M.S. Influence of magnetic field and thermal radiation on convective flow of SWCNTs-water and MWCNTs-water nanofluid between rotating stretchable disks with convective boundary conditions. *Powder Technol.* **2018**, *331*, 326–337. [CrossRef]
19. Kaempgen, M.; Duesberg, G.S.; Roth, S. Transparent carbon nanotube coatings. *Appl. Surf. Sci.* **2005**, *252*, 425–429. [CrossRef]
20. Keefer, E.W.; Botterman, B.R.; Romero, M.I.; Rossi, A.F.; Gross, G.W. Carbon nanotube coating improves neuronal recordings. *Nat. Nanotechnol.* **2008**, *3*, 434. [CrossRef]
21. Besteman, K.; Lee, J.O.; Wiertz, F.G.; Heering, H.A.; Dekker, C. Enzyme-coated carbon nanotubes as single-molecule biosensors. *Nano Lett.* **2003**, *3*, 727–730. [CrossRef]
22. Lu, D.; Ramzan, M.; Mohammad, M.; Howari, F.; Chung, J.D. A Thin Film Flow of Nanofluid Comprising Carbon Nanotubes Influenced by Cattaneo-Christov Heat Flux and Entropy Generation. *Coatings* **2019**, *9*, 296. [CrossRef]
23. Ramzan, M.; Gul, H.; Kadry, S. Onset of Cattaneo-Christov Heat Flux and Thermal Stratification in Ethylene-Glycol Based Nanofluid Flow Containing Carbon Nanotubes in a Rotating Frame. *IEEE Access* **2019**, *7*, 146190–146197. [CrossRef]
24. Khan, U.; Ahmad, S.; Ramzan, M.; Suleman, M.; Lu, D.; Inam, S. Numerical Simulation of Darcy–Forchheimer 3D Unsteady Nanofluid Flow Comprising Carbon Nanotubes with Cattaneo–Christov Heat Flux and Velocity and Thermal Slip Conditions. *Processes* **2019**, *7*, 687. [CrossRef]
25. Ramzan, M.; Mohammad, M.; Howari, F. Magnetized suspended carbon Nanotubes based nanofluid flow with bio-convection and entropy generation past a vertical cone. *Sci. Rep.* **2019**, *9*, 1–15. [CrossRef]
26. Bilal, M.; Ramzan, M. Hall current effect on unsteady rotational flow of carbon nanotubes with dust particles and nonlinear thermal radiation in Darcy–Forchheimer porous media. *J. Therm. Anal. Calorim.* **2019**, *138*, 3127–3137. [CrossRef]
27. Ramzan, M.; Shaheen, N. Thermally stratified Darcy–Forchheimer nanofluid flow comprising carbon nanotubes with effects of Cattaneo–Christov heat flux and homogeneous–heterogeneous reactions. *Phy. Scr.* **2019**, *95*, 015701. [CrossRef]
28. Ramzan, M.; Mohammad, M.; Howari, F.; Chung, J.D. Entropy analysis of carbon nanotubes based nanofluid flow past a vertical cone with thermal radiation. *Entropy* **2019**, *21*, 642. [CrossRef]
29. Hayat, T.; Haider, F.; Muhammad, T.; Ahmad, B. Darcy–Forchheimer flow of carbon nanotubes due to a convectively heated rotating disk with homogeneous–heterogeneous reactions. *J. Therm. Anal. Calorimetry* **2019**, *137*, 1939–1949. [CrossRef]
30. Ramzan, M.; Sheikholeslami, M.; Chung, J.D.; Shafee, A. Melting heat transfer and entropy optimization owing to carbon nanotubes suspended Casson nanoliquid flow past a swirling cylinder-A numerical treatment. *AIP Adv.* **2018**, *8*, 115130. [CrossRef]
31. Mahian, O.; Kianifar, A.; Kalogirou, S.A.; Pop, I.; Wongwises, S. A review of the applications of nanofluids in solar energy. *Int. J. Heat Mass Transf.* **2013**, *57*, 582–594. [CrossRef]
32. Cattaneo, C. *Sulla Conduzione del Calore*; Atti Sem. Mat. Fis. Univ: Modena, Italy, 1948; Volume 3, pp. 83–101.
33. Christov, C.I. On frame indifferent formulation of the Maxwell–Cattaneo model of finite-speed heat conduction. *Mech. Res. Commun.* **2009**, *36*, 481–486. [CrossRef]

34. Hayat, T.; Qayyum, S.; Imtiaz, M.; Alsaedi, A. Flow between two stretchable rotating disks with Cattaneo-Christov heat flux model. *Results Phys.* **2017**, *7*, 126–133. [CrossRef]
35. Dogonchi, A.S.; Chamkha, A.J.; Seyyedi, S.M.; Ganji, D.D. Radiative nanofluid flow and heat transfer between parallel disks with penetrable and stretchable walls considering Cattaneo–Christov heat flux model. *Heat Transf. Asian Res.* **2018**, *47*, 735–753. [CrossRef]
36. Lu, D.; Li, Z.; Ramzan, M.; Shafee, A.; Chung, J.D. Unsteady squeezing carbon nanotubes based nano-liquid flow with Cattaneo–Christov heat flux and homogeneous–heterogeneous reactions. *Appl. Nanosci.* **2019**, *9*, 169–178. [CrossRef]
37. Ramzan, M.; Liaquet, A.; Kadry, S.; Yu, S.; Nam, Y.; Lu, D. Impact of Second-Order Slip and Double Stratification Coatings on 3D MHD Williamson Nanofluid Flow with Cattaneo–Christov Heat Flux. *Coatings* **2019**, *9*, 849. [CrossRef]
38. Ramzan, M.; Gul, H.; Sheikholeslami, M. Effect of second order slip condition on the flow of tangent hyperbolic fluid—A novel perception of Cattaneo–Christov heat flux. *Phys. Scr.* **2019**, *94*, 115707. [CrossRef]
39. Alebraheem, J.; Ramzan, M. Flow of nanofluid with Cattaneo–Christov heat flux model. *Appl. Nanosci.* **2019**, 1–11. [CrossRef]
40. Lu, D.; Ramzan, M.; Ahmad, S.; Chung, J.D.; Farooq, U. Upshot of binary chemical reaction and activation energy on carbon nanotubes with Cattaneo-Christov heat flux and buoyancy effects. *Phys. Fluids* **2017**, *29*, 123103. [CrossRef]
41. Chaudhary, M.A.; Merkin, J.H. A simple isothermal model for homogeneous-heterogeneous reactions in boundary-layer flow. II Different diffusivities for reactant and autocatalyst. *Fluid Dyn. Res.* **1995**, *16*, 335. [CrossRef]
42. Stewartson, K. On the flow between two rotating coaxial disks. In *Mathematical Proceedings of the Cambridge Philosophical Society*; Cambridge University Press: Cambridge, UK, 1953; Volume 49, pp. 333–341.

coatings

MDPI

Article

On Magnetohydrodynamic Flow of Viscoelastic Nanofluids with Homogeneous–Heterogeneous Reactions

Metib Alghamdi

Department of Mathematics, College of Science, King Khalid University, Abha 61413, Saudi Arabia; malgamdy@kku.edu.sa

Received: 5 December 2019; Accepted: 2 January 2020; Published: 9 January 2020

Abstract: This article explores magnetohydrodynamic stretched flow of viscoelastic nanofluids with heterogeneous–homogeneous reactions. Attention in modeling has been specially focused to constitutive relations of viscoelastic fluids. The heat and mass transport process is explored by thermophoresis and Brownian dispersion. Resulting nonlinear systems are computed for numerical solutions. Findings for temperature, concentration, concentration rate, skin-friction, local Nusselt and Sherwood numbers are analyzed for both second grade and elastico-viscous fluids.

Keywords: viscoelastic fluids; nanoparticles; magnetohydrodynamics; heterogeneous–homogeneous reactions; numerical solution

1. Introduction

It is now acknowledged that non-Newtonian fluids in industrial, physiological and technological processes are more significant than viscous fluids. Few examples of such fluids may include silicon oils, printer ink, mud, ice cream, egg yolk, blood at low shear rate, shampoo, gypsum paste, polymer solutions, nail polish, sand in water, ketchup etc. Rheological properties of such fluids are different and thus all these cannot be explained employing one constitutive relationship between shear rate and rate of strain. The modelled expressions for the non-Newtonian liquids are more tedious and of higher order than Navier–Stokes expressions for viscous fluids. Researchers in the field face challenges in modelling, analysis and computations from different quarters. Through different non-Newtonian fluids, the objective here is to explore second grade and elastico-viscous fluids [1–8].

Nanofluids are described by carbon nanotubes (CNTs) [9–11], Buongiorno [12] and Tiwari and Das [13] models. Therefore, the information is very significant about flows involving thermophoresis aspects. Impact of slip in flow of copper-water nanoliquid over an extendable surface is examined by Pandey and Kumar [14]. Flow of couple stress nanomaterial bound by an oscillatory stretchable surface is analyzed by Khan et al. [15]. Turkyilmazoglu [16] discussed free and circular jets in view of single phase nanomaterial. Few relevant investigatons for nanoliquids can be seen in studies [17–45].

According to previous literature, it is found that magnetohydrodynamic stretched flow of viscoelastic nanofluids with heterogeneous–homogeneous reactions has not been reported yet. Attention in modeling has been specially focused on constitutive relations of viscoelastic fluids. Heat and mass transport process is explored by thermophoresis and Brownian dispersion. Adequate transformations are considered to dimensionless the governing system. Numerical solutions of the resulting system are obtained by employing the shooting method. Contributions of numerous sundary variables on flow fields are interpreted through plots and numerical data.

2. Problem Formulation

Two-dimensional (2D) steady magnetohydrodynamic flow of incompressible viscoelastic nanoliquids by a linear stretchable surface with heterogeneous–homogeneous reactions is analyzed. Second grade and elastico-viscous liquids are considered. Attention in modeling has been specially focused on constitutive relations of viscoelastic fluids. Heat and mass transport process is explored by thermophoresis and Brownian dispersion. Let $u_w(x) = cx$ denotes wall velocity along x-axis (see Figure 1). Homogeneous-reaction for cubic catalysis is [37]:

$$A + B \to 3B,\ rate = k_c ab^2. \tag{1}$$

At catalyst surface heterogeneous-reaction is [37]:

$$A \to B,\ rate = k_s a. \tag{2}$$

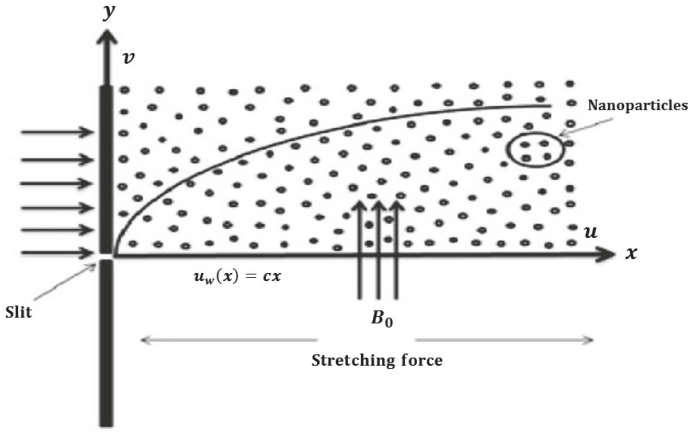

Figure 1. Flow configuration.

In above relations rate constants are described by k_s and k_c and chemical species B and A have concentrations b and a separately. Relevant equations for 2D flow satisfy [5,7]:

$$div\mathbf{V} = 0, \tag{3}$$

$$\rho\frac{d\mathbf{V}}{dt} = div\boldsymbol{\sigma} + \rho\mathbf{b}. \tag{4}$$

Cauchy stress tensor of second-order fluid is

$$\boldsymbol{\sigma} = -p\mathbf{I} + \mu\mathbf{A}_1 + \alpha_1\mathbf{A}_2 + \alpha_2\mathbf{A}_1^2, \tag{5}$$

in which $\mathbf{A}_1$ and $\mathbf{A}_2$ stand for 1st and 2nd Rivlin-Ericksen tensors respectively i.e.,

$$\mathbf{A}_1 = (grad\mathbf{V})^* + (grad\mathbf{V}), \tag{6}$$

$$\mathbf{A}_2 = \frac{d\mathbf{A}_1}{dt} + (grad\mathbf{V})^*\mathbf{A}_1 + \mathbf{A}_1(grad\mathbf{V}), \tag{7}$$

where α_1 and α_2 stand for material constants, **b** for body force, $\frac{d}{dt}$ for material derivative and p for pressure. Material moduli satisfy following relationships for second grade fluid:

$$\alpha_1 \geq 0,\ \mu \geq 0,\ \alpha_1 + \alpha_2 = 0, \tag{8}$$

in which $*$ stands for matrix transpose and velocity distribution **V** is

$$\mathbf{V} = [u(x,y), v(x,y), 0]. \tag{9}$$

The governing expressions for 2D stretching flow of viscoelastic nanofluids are [5,7,37]:

$$\frac{\partial u}{\partial x} + \frac{\partial v}{\partial y} = 0, \tag{10}$$

$$u\frac{\partial u}{\partial x} + v\frac{\partial u}{\partial y} = \nu\frac{\partial^2 u}{\partial y^2} - k_0\left(u\frac{\partial^3 u}{\partial x \partial y^2} + v\frac{\partial^3 u}{\partial y^3} + \frac{\partial u}{\partial x}\frac{\partial^2 u}{\partial y^2} - \frac{\partial u}{\partial y}\frac{\partial^2 u}{\partial x \partial y}\right) - \frac{\sigma B_0^2}{\rho}u, \tag{11}$$

$$u\frac{\partial T}{\partial x} + v\frac{\partial T}{\partial y} = \alpha\frac{\partial^2 T}{\partial y^2} + \frac{(\rho c)_p}{(\rho c)_f}\left(D_B^*\left(\frac{\partial T}{\partial y}\frac{\partial C}{\partial y}\right) + \frac{D_T}{T_\infty}\left(\frac{\partial T}{\partial y}\right)^2\right), \tag{12}$$

$$u\frac{\partial C}{\partial x} + v\frac{\partial C}{\partial y} = D_B^*\left(\frac{\partial^2 C}{\partial y^2}\right) + \frac{D_T}{T_\infty}\left(\frac{\partial^2 T}{\partial y^2}\right), \tag{13}$$

$$u\frac{\partial a}{\partial x} + v\frac{\partial a}{\partial y} = D_A\left(\frac{\partial^2 a}{\partial y^2}\right) - k_c a b^2, \tag{14}$$

$$u\frac{\partial b}{\partial x} + v\frac{\partial b}{\partial y} = D_B\left(\frac{\partial^2 b}{\partial y^2}\right) + k_c a b^2, \tag{15}$$

$$u = u_w(x) = cx,\ v = 0,\ T = T_w,\ C = C_w,\ D_A\frac{\partial a}{\partial y} = k_s a,\ D_B\frac{\partial b}{\partial y} = -k_s a \text{ at } y = 0, \tag{16}$$

$$u \to 0,\ \ T \to T_\infty,\ \ C \to C_\infty,\ \ a \to a_0,\ \ b \to 0 \text{ as } y \to \infty. \tag{17}$$

Here v and u stand for velocities in vertical and horizontal directions respectively, $(\rho c)_f$ for heat capacity of liquid, $\nu(=\mu/\rho)$ for kinematic viscosity, α_1 for normal stress moduli, μ for dynamic viscosity, T for temperature, σ for electrical conductivity, ρ for density, $k_0 = -\alpha_1/\rho$ for elastic parameter, D_T for thermophoretic factor, $\alpha = k/(\rho c)_f$ for thermal diffusivity, C for concentration, D_B^* for Brownian factor, k for thermal conductivity, $(\rho c)_p$ for effective heat capacity of nanoparticles, C_w and T_w for wall concentration and temperature respectively and C_∞ and T_∞ for ambient fluid concentration and temperature respectively. Here $k_0 < 0$ stands for second grade fluid, $k_0 > 0$ for elastico-viscous fluid and $k_0 = 0$ for Newtonian fluid. Selecting [5,7,37]:

$$\begin{gathered} u = cxf'(\zeta),\ v = -(c\nu)^{1/2}f(\zeta),\ \zeta = \left(\tfrac{c}{\nu}\right)^{1/2}y, \\ \theta(\zeta) = \tfrac{T-T_\infty}{T_w-T_\infty},\ \phi(\zeta) = \tfrac{C-C_\infty}{C_w-C_\infty},\ a = a_0 r(\zeta),\ b = a_0 h(\zeta). \end{gathered} \tag{18}$$

Expression (10) is identically verified and Equations (11)–(17) give [5,7,37]:

$$f''' + ff'' - f'^2 - k_1^*\left(2f'f''' - f''^2 - ff^{iv}\right) - M^2 f' = 0, \tag{19}$$

$$\theta'' + \Pr\left(f\theta' + N_b\theta'\phi' + N_t\theta'^2\right) = 0, \tag{20}$$

$$\phi'' + Scf\phi' + \frac{N_t}{N_b}\theta'' = 0, \tag{21}$$

$$\frac{1}{Sc_b}r'' + fr' - Krh^2 = 0, \tag{22}$$

$$\frac{\delta}{Sc_b}h'' + fh' + Krh^2 = 0, \tag{23}$$

$$f = 0,\ f' = 1,\ \theta = 1,\ \phi = 1,\ r' = K_s r,\ \delta h' = -K_s r \text{ at } \zeta = 0, \tag{24}$$

$$f' \to 0,\ \theta \to 0,\ \phi \to 0,\ r \to 1,\ h \to 0 \text{ as } \zeta \to \infty. \tag{25}$$

Here k_1^* stands for viscoelastic parameter, δ for ratio of mass diffusion coefficients, N_t for thermophoresis parameter, K for homogeneous-reaction strength, M for magnetic parameter, Sc for Schmidt number, Sc_b for Schmidt number (for heterogeneous–homogeneous reactions), N_b for Brownian motion parameter, K_s for heterogeneous-reaction strength and Pr for Prandtl number. We set these definitions as

$$\begin{gathered} k_1^* = -k_0\left(\frac{c}{\nu}\right),\ M^2 = \frac{\sigma B_0^2}{\rho c},\ \Pr = \frac{\nu}{\alpha},\ \delta = \frac{D_B}{D_A},\ K = \frac{k_c a_0^2}{u_w},\ K_s = \frac{k_s}{D_A a_0}\sqrt{\frac{c}{\nu}}, \\ Sc = \frac{\nu}{D_B^*},\ Sc_b = \frac{\nu}{D_A},\ N_b = \frac{(\rho c)_p D_B^*(C_w - C_\infty)}{(\rho c)_f \nu},\ N_t = \frac{(\rho c)_p D_T(T_w - T_\infty)}{(\rho c)_f \nu T_\infty}. \end{gathered} \tag{26}$$

Considering that $D_A = D_B$ we have $\delta = 1$ and thus

$$r(\zeta) + h(\zeta) = 1. \tag{27}$$

Now Eqsuations (22) and (23) give

$$\frac{1}{Sc_b}r'' + fr' - K(1-r)^2 r = 0, \tag{28}$$

with boundary conditions

$$r'(0) = K_s r(0),\ r(\infty) \to 1. \tag{29}$$

Coefficient of skin friction and local Sherwood and Nusselt numbers are

$$\mathrm{Re}_x^{1/2} C_f = (1 - 3k_1^*) f''(0),\ \mathrm{Re}_x^{-1/2} Sh_x = -\phi'(0),\ \mathrm{Re}_x^{-1/2} Nu_x = -\theta'(0), \tag{30}$$

in which $\mathrm{Re}_x = u_w x/\nu$ denotes the local Reynolds number.

3. Solution Methodology

By considering suitable boundary conditions on the system of equations, a numerical solution is developed using NDSolve in Mathematica. Shooting method is used via NDSolve. This method is very helpful in case of small step-size featuring negligible error. As a consequence, both x and y varied uniformly by a step-size of 0.01 [40].

4. Graphical Results and Discussion

Effects of magnetic parameter M, homogeneous-reaction strength K, Schmidt number Sc, Schmidt number (for heterogeneous–homogeneous reactions) Sc_b, thermophoresis parameter N_t, heterogeneous-reaction strength K_s, Prandtl number Pr and Brownian motion parameter N_b on concentration $\phi(\zeta)$, concentration rate $r(\zeta)$ and temperature $\theta(\zeta)$ for both second grade and elastico-viscous fluids are sketched in Figures 2–12.

Figure 2 depicts impact of magnetic parameter M on temperature $\theta(\zeta)$. Here $M \neq 0$ is for hydromagnetic flow situation and $M = 0$ corresponds to hydrodynamic flow case. Temperature $\theta(\zeta)$ is higher for hydromagnetic flow in comparison to hydrodynamic flow for both second grade and elastico-viscous fluids. Physically magnetic parameter depends upon Lorentz force. Lorentz force is an agent which resists the motion of fluid and therefore temperature $\theta(\zeta)$ enhances.

Figure 3 displays variations in temperature $\theta(\zeta)$ for increasing Prandtl number Pr. Temperature $\theta(\zeta)$ decays for larger Pr for both second grade and elastico-viscous fluids. Physically Prandtl number

involves thermal diffusivity. Larger Prandtl number corresponds to weaker thermal diffusivity which produces a decay in temperature $\theta(\zeta)$.

Figure 4 depicts impact of Brownian motion parameter N_b on temperature $\theta(\zeta)$. Larger N_b produces an increment in temperature $\theta(\zeta)$ for both second grade and elastico-viscous fluids. Larger Brownian motion parameter N_b has stronger Brownian diffusivity and weaker viscous force which increased the temperature $\theta(\zeta)$.

Figure 5 shows that larger thermophoresis parameter N_t leads to higher temperature $\theta(\zeta)$ for both second grade and elastico-viscous fluids. Larger N_t causes strong thermophoresis force which tends to shift nanoparticles from hot to cold zone and therefore temperature $\theta(\zeta)$ increases.

Impact of magnetic parameter M on concentration $\phi(\zeta)$ is displayed in Figure 6 Concentration $\phi(\zeta)$ is upgraded for increasing estimations of M for both second grade and elastico-viscous fluids. Furthermore, the concentration $\phi(\zeta)$ shows similar trend for both second grade and elastico-viscous fluids.

Figure 7 depicts that concentration $\phi(\zeta)$ is decreased for larger Schmidt number Sc for both second grade and elastico-viscous fluids. Schmidt number Sc has an inverse relation with Brownian diffusivity. Larger Schmidt number leads to weaker Brownian diffusivity which produces weaker concentration $\phi(\zeta)$.

Impact of Brownian motion N_b on concentration $\phi(\zeta)$ is shown in Figure 8 Bigger N_b produces a reduction in concentration $\phi(\zeta)$ for both second grade and elastico-viscous fluids. Physically Brownian force tries to push particles in opposite direction of concentration gradient and make nanofluid more homogeneous. Therefore, higher the Brownian force, lower the concentration gradient and more uniform concentration $\phi(\zeta)$.

Figure 9 displays that how thermophoresis N_t affects concentration $\phi(\zeta)$. Here concentration $\phi(\zeta)$ is upgraded for higher estimations of N_t for both second grade and elastico-viscous fluids. Furthermore, the concentration $\phi(\zeta)$ shows similar trend for both second grade and elastico-viscous fluids.

Figure 10 displays that how Schmidt number Sc_b affects concentration rate $r(\zeta)$. Here concentration rate $r(\zeta)$ is upgraded for higher estimations of Schmidt number Sc_b for both second grade and elastico-viscous fluids. Furthermore, the concentration rate $r(\zeta)$ shows similar trend for both second grade and elastico-viscous fluids.

From Figure 11 it is noted that larger homogeneous-reaction K displays a decay in concentration rate $r(\zeta)$ for both second grade and elastico-viscous fluids. Larger homogeneous-reaction K corresponds to higher chemical reaction which consequently decreases the concentration rate $r(\zeta)$.

Figure 12 depicts that larger heterogeneous-reaction K_s produces higher concentration rate $r(\zeta)$ for both second grade and elastico-viscous fluids. Here heterogeneous-reaction parameter K_s has an inverse relation with mass diffusivity which produces an enhancement in concentration rate $r(\zeta)$.

Table 1 displays skin-friction $-C_f \mathrm{Re}_x^{1/2}$ subject to varying k_1^* and M. Here skin-friction has higher estimations for larger M for both second grade and elastico-viscous fluids. Table 2 depicts comparison for various estimations of k_1^* with homotopy analysis method (HAM). Table 2 presents a good agreement of numerical solution with existing homotopy analysis method (HAM) solution in a limiting sense. Table 3 depicts local Nusselt number $Nu_x \mathrm{Re}_x^{-1/2}$ subject to varying k_1^*, N_b and N_t. Here larger N_b and N_t correspond to lower local Nusselt number for both second grade and elastico-viscous fluids. Table 4 shows local Sherwood number $Sh_x \mathrm{Re}_x^{-1/2}$ subject to varying k_1^*, N_b and N_t. Here larger N_t produces lower local Sherwood number while opposite trend is noted via N_b for both second grade and elastico-viscous fluids.

Table 1. Skin-friction coefficient for various estimations of viscoelastic and magnetic parameters.

M	$-C_f \mathrm{Re}_x^{1/2}$	$-C_f \mathrm{Re}_x^{1/2}$
	$k_1^* = 0.1$	$k_1^* = -0.1$
0.0	0.7379	1.2395
0.2	0.7525	1.2640
0.5	0.8250	1.3858

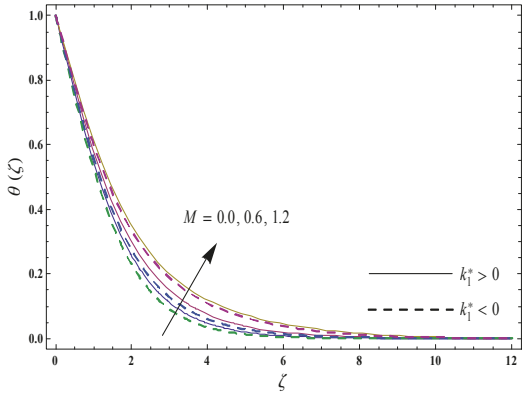

Figure 2. Variations of temperature for magnetic parameter when $N_b = 0.2$, $N_t = 0.1$ and $Sc = \Pr = 1.0$.

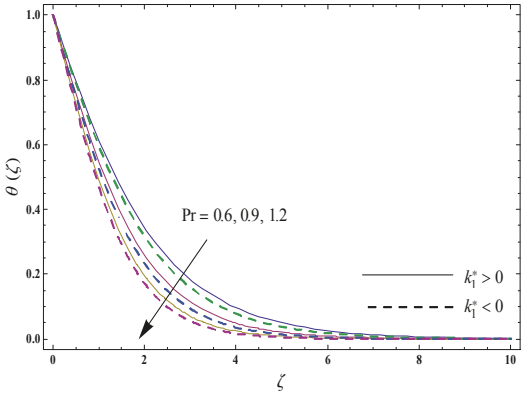

Figure 3. Variations of temperature for Prandtl number when $N_b = 0.2$, $N_t = 0.1$, $Sc = 1.0$ and $M = 0.2$.

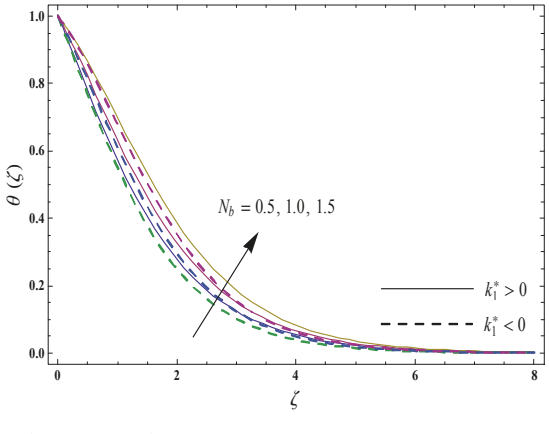

Figure 4. Variations of temperature for Brownian motion parameter when $N_t = 0.1$, $Sc = \Pr = 1.0$ and $M = 0.2$.

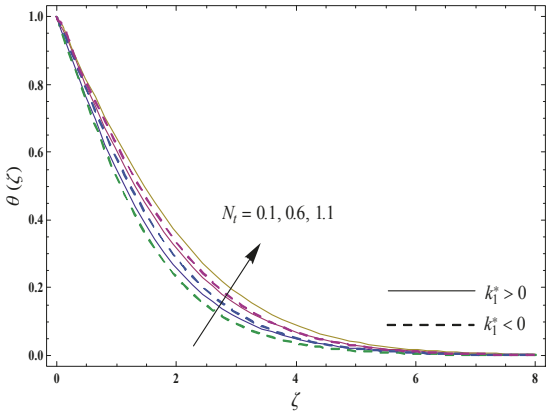

Figure 5. Variations of temperature for thermophoresis parameter when $N_b = 0.2$, $Sc = \Pr = 1.0$ and $M = 0.2$.

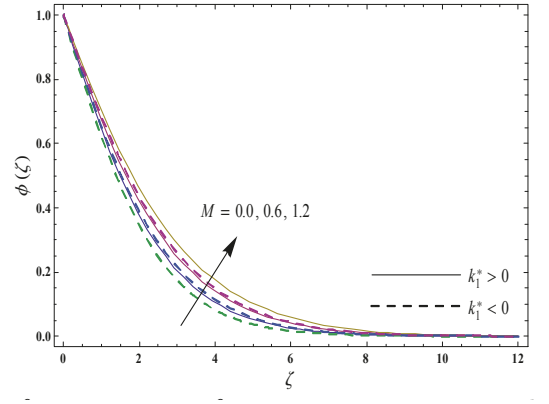

Figure 6. Variations of concentration for magnetic parameter when $N_b = 0.2$, $N_t = 0.1$ and $Sc = \Pr = 1.0$.

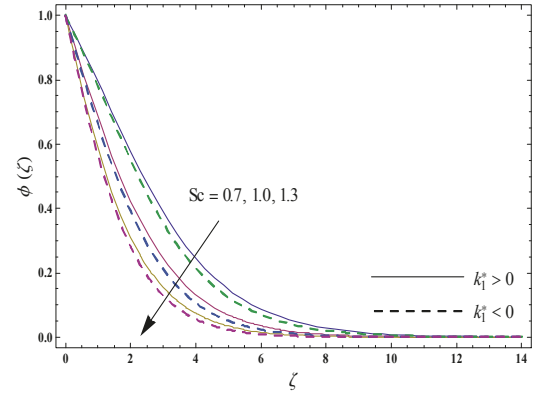

Figure 7. Variations of concentration for Schmidt number when $N_b = 0.2$, $N_t = 0.1$, $\Pr = 1.0$ and $M = 0.2$.

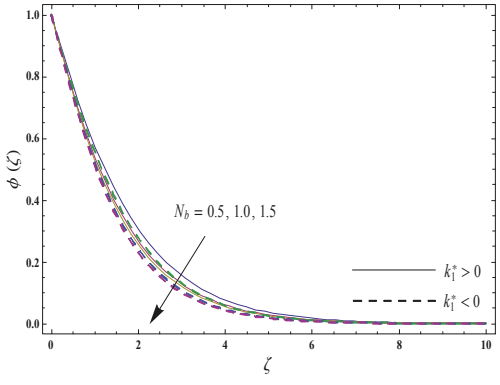

Figure 8. Variations of concentration for Brownian motion parameter when $N_t = 0.1$, $Sc = \Pr = 1.0$ and $M = 0.2$.

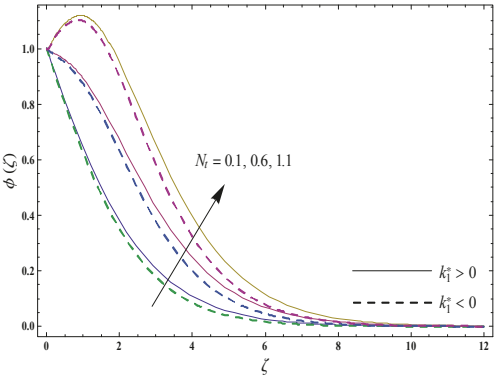

Figure 9. Variations of concentration for thermophoresis parameter when $N_b = 0.2$, $Sc = \Pr = 1.0$ and $M = 0.2$.

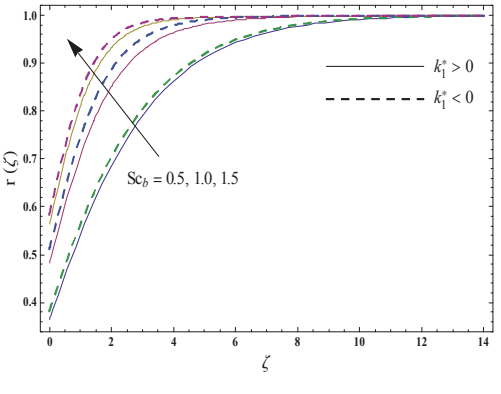

Figure 10. Variations of concentration rate for Schmidt number (for heterogeneous–homogeneous reactions) when $K = 0.2$, $K_s = 0.5$ and $M = 0.2$.

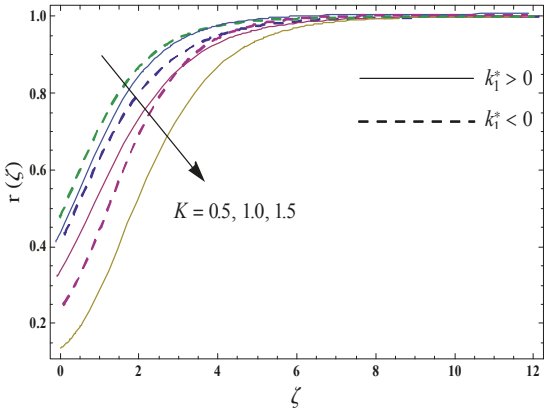

Figure 11. Variations of concentration rate for homogeneous-reaction strength when $Sc_b = 1.0$, $K_s = 0.5$ and $M = 0.2$.

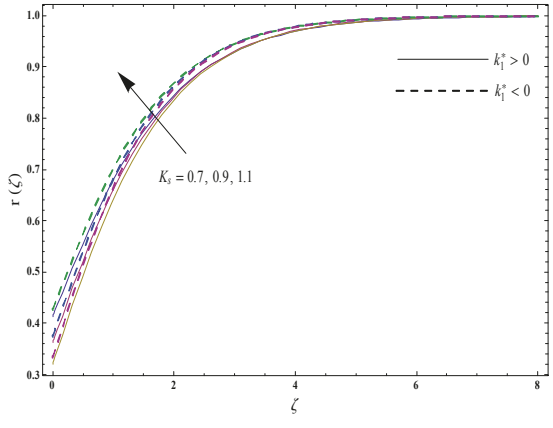

Figure 12. Variations of concentration rate for heterogeneous-reaction strength when $K = 0.2$, $Sc_b = 1.0$ and $M = 0.2$.

Table 2. Comparative data of skin-friction coefficient for various estimations of viscoelastic parameter when $M = 0$.

k_1^*	$-C_f \mathrm{Re}_x^{1/2}$	
	Numerical	**HAM [5]**
0.0	1.0000	1.00000
0.1	0.7379	0.73786
0.2	0.4472	0.44721
0.3	0.1195	0.11952

Table 3. Local Nusselt number for various estimations of viscoelastic, Brownian motion and thermophoresis parameters when $Sc = \Pr = 1.0$ and $M = 0.2$.

N_b	N_t	$Nu_x \mathrm{Re}_x^{-1/2}$	$Nu_x \mathrm{Re}_x^{-1/2}$
		$k_1^* = 0.1$	$k_1^* = -0.1$
0.1	0.1	0.5232	0.5425
0.2	-	0.4970	0.5153
0.3	-	0.4716	0.4890
0.2	0.1	0.4970	0.5153
-	0.2	0.4827	0.5002
-	0.3	0.4689	0.4856

Table 4. Local Sherwood number for various estimations of viscoelastic, Brownian motion and thermophoresis parameters when $Sc = \Pr = 1.0$ and $M = 0.2$.

N_b	N_t	$Sh_x \mathrm{Re}_x^{-1/2}$	$Sh_x \mathrm{Re}_x^{-1/2}$
		$k_1^* = 0.1$	$k_1^* = -0.1$
0.1	0.1	0.2100	0.2300
0.2	-	0.3994	0.4203
0.3	-	0.4622	0.4834
0.2	0.1	0.3994	0.4203
-	0.2	0.2435	0.2647
-	0.3	0.0982	0.1205

5. Conclusions

Magnetohydrodynamic flow of viscoelastic nanofluids bound by a linear stretchable surface with heterogeneous–homogeneous reactions are analyzed. Both concentration $\phi(\zeta)$ and temperature $\theta(\zeta)$ are enhanced via higher M. Larger Brownian motion N_b displays opposite trend for concentration $\phi(\zeta)$ and temperature $\theta(\zeta)$. Larger thermophoresis number N_t produces higher concentration $\phi(\zeta)$ and temperature $\theta(\zeta)$. Temperature $\theta(\zeta)$ is reduced when Prandtl number enhances. Prandtl number is considered to control the rate of heat transfer in engineering and industrial processes. The suitable value of Prandtl number is very essential to control the rate of heat transfer in engineering and industrial processes. Larger homogeneous-reaction K depicts a reduction in concentration rate $r(\zeta)$. Larger heterogenous-reaction K_s and Schmidt number Sc_b lead to higher concentration rate $r(\zeta)$. Skin friction is enhanced for larger magnetic parameter M. Reverse trend of local Sherwood number is seen for N_t and N_b. Local Nusselt number is decreased for thermophoresis N_t and Brownian motion N_b parameters. Furthermore, the present analysis is reduced to Newtonian fluid flow case when $k_1^* = 0$.

Funding: This research was funded by the Deanship of Scientific Research, King Khalid University, Abha, Saudi Arabia under grant number (R.G.P.2./26/40).

Acknowledgments: The author extends his appreciation to the Deanship of Scientific Research at King Khalid University for funding this work through Research Groups Program under grant number (R.G.P.2./26/40).

Conflicts of Interest: The author declares no conflict of interest.

Nomenclature

u, v	velocity components	x, y	coordinate axes
A, B	chemical species	k_c, k_s	rate constants
μ	dynamic viscosity	ρ	density of base fluid
a, b	concentrations of chemical species	k_0	elastic parameter
ν	kinematic viscosity	σ	electrical conductivity
$\mathbf{V}$	velocity distribution	B_0	magnetic field strength
$\boldsymbol{\o}$	Cauchy stress tensor	$\mathbf{b}$	body force
α_1, α_2	material constants	$\frac{d}{dt}$	material derivative
p	pressure	$\mathbf{A}_1, \mathbf{A}_2$	first and second Rivlin-Ericksen tensors
$*$	matrix transpose	D_A, D_B	mass diffusion coefficients
T	temperature	C	concentration
T_∞	ambient fluid temperature	C_∞	ambient fluid concentration
T_w	surface temperature	C_w	surface concentration
$(\rho c)_p$	effective heat capacity of nanoparticles	$(\rho c)_f$	heat capacity of fluid
α	thermal diffusivity	k	thermal conductivity
u_w	surface velocity	c	positive constant
D_B^*	Brownian diffusion coefficient	D_T	thermophoretic diffusion coefficient
ζ	similarity variable	f'	dimensionless velocity
θ	dimensionless temperature	ϕ	dimensionless concentration
r	dimensionless concentration rate	k_1^*	viscoelastic parameter
Sc	Schmidt number	M	magnetic parameter
K	homogeneous-reaction strength	Pr	Prandtl number
N_b	Brownian motion parameter	N_t	thermophoresis parameter
K_s	heterogeneous-reaction strength	Sc_b	Schmidt number
C_f	skin friction coefficient	Re_x	local Reynolds number
Nu_x	local Nusselt number	Sh_x	local Sherwood number

References

1. Ariel, P.D. On the flow of an elastico-viscous fluid near a rotating disk. *J. Comput. Appl. Math.* **2003**, *154*, 1–25. [CrossRef]
2. Tan, W.C.; Masuoka, T. Stokes' first problem for a second grade fluid in a porous half-space with heated boundary. *Int. J. Non Linear Mech.* **2005**, *40*, 515–522. [CrossRef]
3. Shadloo, M.S.; Kimiaeifar, A. Application of homotopy perturbation method to find an analytical solution for magnetohydrodynamic flows of viscoelastic fluids in converging/diverging channels. *J. Mech. Eng. Sci.* **2011**, *225*, 347–353. [CrossRef]
4. Hayat, T.; Hussain, Z.; Farooq, M.; Alsaedi, A. Effects of homogeneous and heterogeneous reactions and melting heat in the viscoelastic fluid flow. *J. Mol. Liq.* **2016**, *215*, 749–755. [CrossRef]
5. Hayat, T.; Muhammad, T.; Alsaedi, A.; Mustafa, M. A comparative study for flow of viscoelastic fluids with Cattaneo-Christov heat flux. *PLoS ONE* **2016**, *11*, e0155185. [CrossRef]
6. Hayat, T.; Aziz, A.; Muhammad, T.; Alsaedi, A. Model and comparative study for flow of viscoelastic nanofluids with Cattaneo-Christov double diffusion. *PLoS ONE* **2017**, *12*, e0168824. [CrossRef]
7. Hayat, T.; Haider, F.; Muhammad, T.; Alsaedi, A. On Darcy-Forchheimer flow of viscoelastic nanofluids: A comparative study. J. *Mol. Liq.* **2017**, *233*, 278–287. [CrossRef]
8. Sheremet, M.; Pop, I. Natural convection combined with thermal radiation in a square cavity filled with a viscoelastic fluid. *Int. J. Numer. Methods Heat Fluid Flow* **2018**, *28*, 624–640. [CrossRef]
9. Esmaeilzadeh, H.; Su, J.; Charmchi, M.; Sun, H. Effect of hydrophobicity on the water flow in carbon nanotube-A molecular dynamic study. *Theor. Appl. Mech. Lett.* **2018**, *8*, 284–290. [CrossRef]
10. Chen, J.; Han, J. Comparative performance of carbon nanotubes and nanoclays as flame retardants for epoxy composites. *Results Phys.* **2019**, *14*, 102481. [CrossRef]

11. Hayat, T.; Haider, F.; Muhammad, T.; Ahmad, B. Darcy-Forchheimer flow of carbon nanotubes due to a convectively heated rotating disk with homogeneous–heterogeneous reactions. *J. Therm. Anal. Calorimet.* **2019**, *137*, 1939–1949. [CrossRef]
12. Buongiorno, J. Convective transport in nanfluids. *Heat Transf.* **2006**, *128*, 240–250. [CrossRef]
13. Tiwari, R.K.; Das, M.K. Heat transfer augmentatics in a two aided lid-driven differentially heated square cavity utilizing nanofluid. *Int. J. Heat Mass Transf.* **2007**, *50*, 2002–2018. [CrossRef]
14. Panday, A.K.; Kumar, M. Boundary layer flow and heat transfer analysis on Cu-water nanofluid flow over a stretching cylinder with slip. *Alex. Eng. J.* **2017**, *56*, 671–677. [CrossRef]
15. Khan, S.U.; Shahzad, S.A.; Rauf, A.; Ali, N. Mixed convection flow of couple stress nanofluid over oscillatory stretching sheet with heat absorption/generation effects. *Results Phys.* **2018**, *8*, 1223–1231. [CrossRef]
16. Turkyilmazoglu, M. Free and circular jets cooled by single phase nanofluids. *Eur. J. Mech. B/Fluid* **2019**, *76*, 1–6. [CrossRef]
17. Mahian, O.; Mahmud, S.; Heris, S.Z. Analysis of entropy generation between co-rotating cylinders using nanofluids. *Energy* **2012**, *44*, 438–446. [CrossRef]
18. Goodarzi, M.; Safaei, M.R.; Vafai, K.; Ahmadi, G.; Dahari, M.; Kazi, S.N.; Jomhari, N. Investigation of nanofluid mixed convection in a shallow cavity using a twophase mixture model. *Int. J. Therm. Sci.* **2014,** *75*, 204–220. [CrossRef]
19. Hsiao, K.L. Nanofluid flow with multimedia physical features for conjugate mixed convection and radiation. *Comput. Fluids* **2014**, *104*, 1–8. [CrossRef]
20. Turkyilmazoglu, M. A note on the correspondence between certain nanofluid flows and standard fluid flows. *ASME J. Heat Transf.* **2015**, *137*, 024501. [CrossRef]
21. Malvandi, A.; Safaei, M.R.; Kaffash, M.H.; Ganji, D.D. MHD mixed convection in a vertical annulus filled with Al_2O_3–water nanofluid considering nanoparticle migration. *J. Magn. Magn. Mater.* **2015**, *382*, 296–306. [CrossRef]
22. Hayat, T.; Muhammad, T.; Alsaedi, A.; Alhuthali, M.S. Magnetohydrodynamic three-dimensional flow of viscoelastic nanofluid in the presence of nonlinear thermal radiation. *J. Magn. Magn. Mater.* **2015**, *385*, 222–229. [CrossRef]
23. Togun, H.; Ahmadi, G.; Abdulrazzaq, T.; Shkarah, A.J.; Kazi, S.N.; Badarudin, A.; Safaei, M.R. Thermal performance of nanofluid in ducts with double forward-facing steps. *J. Taiwan Inst. Chem. Eng.* **2015**, *47*, 28–42. [CrossRef]
24. Nikkhah, Z.; Karimipour, A.; Safaei, M.R.; Tehrani, P.F.; Goodarzi, M.; Dahari, M.; Wongwises, S. Forced convective heat transfer of water/functionalized multi-walled carbon nanotube nanofluids in a microchannel with oscillating heat flux and slip boundary condition. *Int. Commun. Heat Mass Transf.* **2015**, *68*, 69–77. [CrossRef]
25. Sheremet, M.A.; Pop, I.; Roşca, N.C. Magnetic field effect on the unsteady natural convection in a wavy-walled cavity filled with a nanofluid: Buongiorno's mathematical model. *J. Taiwan Inst. Chem. Eng.* **2016**, *61*, 211–222. [CrossRef]
26. Hayat, T.; Aziz, A.; Muhammad, T.; Alsaedi, A. On magnetohydrodynamic three-dimensional flow of nanofluid over a convectively heated nonlinear stretching surface. *Int. J. Heat Mass Transf.* **2016**, *100*, 566–572. [CrossRef]
27. Karimipour, A.; Taghipour, A.; Malvandi, A. Developing the laminar MHD forced convection flow of water/FMWNT carbon nanotubes in a microchannel imposed the uniform heat flux. *J. Magn. Magn. Mater.* **2016**, *419*, 420–428. [CrossRef]
28. Hayat, T.; Hussain, Z.; Muhammad, T.; Alsaedi, A. Effects of homogeneous and heterogeneous reactions in flow of nanofluids over a nonlinear stretching surface with variable surface thickness. *J. Mol. Liq.* **2016**, *221*, 1121–1127. [CrossRef]
29. Hsiao, K.L. Stagnation electrical MHD nanofluid mixed convection with slip boundary on a stretching sheet. *Appl. Therm. Eng.* **2016,** *98*, 850–861. [CrossRef]
30. Hsiao, K.L. Combined electrical MHD heat transfer thermal extrusion system using Maxwell fluid with radiative and viscous dissipation effects. *Appl. Therm. Eng.* **2017**, *112*, 1281–1288. [CrossRef]
31. Muhammad, T.; Alsaedi, A.; Shehzad, S.A.; Hayat, T. A revised model for Darcy-Forchheimer flow of Maxwell nanofluid subject to convective boundary condition. *Chin. Phys.* **2017**, *55*, 963–976. [CrossRef]

32. Hayat, T.; Sajjad, R.; Muhammad, T.; Alsaedi, A.; Ellahi, R. On MHD nonlinear stretching flow of Powell-Eyring nanomaterial. *Results Phys.* **2017**, *7*, 535–543. [CrossRef]
33. Muhammad, T.; Alsaedi, A.; Hayat, T.; Shehzad, S.A. A revised model for Darcy-Forchheimer three-dimensional flow of nanofluid subject to convective boundary condition. *Results Phys.* **2017**, *7*, 2791–2797. [CrossRef]
34. Hayat, T.; Muhammad, T.; Shehzad, S.A.; Alsaedi, A. An analytical solution for magnetohydrodynamic Oldroyd-B nanofluid flow induced by a stretching sheet with heat generation/absorption. *Int. J. Therm. Sci.* **2017**, *111*, 274–288. [CrossRef]
35. Rana, P.; Dhanai, R.; Kumar, L. MHD slip flow and heat transfer of Al_2O_3-water nanofluid over a horizontal shrinking cylinder using Buongiorno's model: Effect of nanolayer and nanoparticle diameter. *Adv. Powder Technol.* **2017**, *28*, 1727–1738. [CrossRef]
36. Hayat, T.; Muhammad, T.; Shehzad, S.A.; Alsaedi, A. On magnetohydrodynamic flow of nanofluid due to a rotating disk with slip effect: A numerical study. *Comp. Methods Appl. Mech. Eng.* **2017**, *315*, 467–477. [CrossRef]
37. Mahdy, A. Impacts of homogeneous–heterogeneous chemical reactions and inclined magnetic field on unsteady nanofluids flow. *AIP Adv.* **2018**, *8*, 115109. [CrossRef]
38. Muhammad, T.; Lu, D.C.; Mahanthesh, B.; Eid, M.R.; Ramzan, M.; Dar, A. Significance of Darcy-Forchheimer porous medium in nanofluid through carbon nanotubes. *Commun. Theor. Phys.* **2018**, *70*, 361. [CrossRef]
39. Tian, X.; Li, B.; Hu, Z. Convective stagnation point flow of a MHD non-Newtonian nanofluid towards a stretching plate. *Int. J. Heat Mass Transf.* **2018**, *127*, 768–780. [CrossRef]
40. Asma, M.; Othman, W.A.M.; Muhammad, T.; Mallawi, F.; Wong, B.R. Numerical study for magnetohydrodynamic flow of nanofluid due to a rotating disk with binary chemical reaction and Arrhenius activation energy. *Symmetry* **2019**, *11*, 1282. [CrossRef]
41. Maleki, H.; Safaei, M.R.; Alrashed, A.A.; Kasaeian, A. Flow and heat transfer in non-Newtonian nanofluids over porous surfaces. *J. Therm. Anal. Calorim.* **2019**, *135*, 1655–1666. [CrossRef]
42. Saif, R.S.; Hayat, T.; Ellahi, R.; Muhammad, T.; Alsaedi, A. Darcy-Forchheimer flow of nanofluid due to a curved stretching surface. *Int. J. Numer. Methods Heat Fluid Flow* **2019**, *29*, 2–20. [CrossRef]
43. Riaz, A.; Alolaiyan, H.; Razaq, A. Convective heat transfer and magnetohydrodynamics across a peristaltic channel coated with nonlinear nanofluid. *Coatings* **2019**, *9*, 816. [CrossRef]
44. Mahanthesh, B.; Gireesha, B.J.; Animasaun, I.L.; Muhammad, T.; Shashikumar, N.S. MHD flow of SWCNT and MWCNT nanoliquids past a rotating stretchable disk with thermal and exponential space dependent heat source. *Phys. Scr.* **2019**, *94*, 085214. [CrossRef]
45. Eid, M.R.; Mahny, K.L.; Dar, A.; Muhammad, T. Numerical study for Carreau nanofluid flow over a convectively heated nonlinear stretching surface with chemically reactive species. *Phys. A Stat. Mech. Appl.* **2020**, *540*, 123063. [CrossRef]

coatings

MDPI

Article

Significance of Arrhenius Activation Energy and Binary Chemical Reaction in Mixed Convection Flow of Nanofluid Due to a Rotating Disk

Metib Alghamdi

Department of Mathematics, College of Science, King Khalid University, Abha 61413, Saudi Arabia; malgamdy@kku.edu.sa

Received: 10 December 2019; Accepted: 16 January 2020; Published: 20 January 2020

Abstract: This article addresses mixed convective 3D nanoliquid flow by a rotating disk with activation energy and magnetic field. Flow was created by a rotating disk. Velocity, concentration and temperature slips at the surface of a rotating disk were considered. Impacts of Brownian diffusion and thermophoretic were additionally accounted for. The non-linear frameworks are simplified by suitable variables. The shooting method is utilized to develop the numerical solution of resulting problem. Plots were prepared just to explore that how concentration and temperature are impacted by different pertinent flow parameters. Sherwood and Nusselt numbers were additionally plotted and explored. Furthermore, the concentration and temperature were enhanced for larger values of Hartman number. However, the heat transfer rate (Nusselt number) diminishes when the thermophoresis parameter enlarges.

Keywords: rotating disk; mixed convective flow; MHD; binary chemical reaction; nanoparticles; arrhenius activation energy

1. Introduction

A nanoparticle of size under 100 nm deferred into a standard fluid is then named a nanofluid. The essentialness of a nanofluid is expected from its distinctive thermophysical qualities. Nanofluids show enormous capacity to lead power and heat, so they have a critical impact in industry. Nanoliquids have attracted extraordinary enthusiasm for their wide applications; for example, electronic chip cooling, hybrid powered machines, progressed atomic frameworks, solar liquid heating, microchips, excessively proficient magnets and optoelectronics. Thus, Choi [1] exhibited the term nanoparticle inundated into a standard fluid. Buongiorno [2] presented a mathematical model for heat transport in nanoliquid by considering the impacts of Brownian diffusion and thermophoretic dispersion. Further examinations on nanofluids can be seen through the attempts [3–28].

The flow due to a rotating disk plays vital roles in numerous mechanical processes, encompassing psychologist fits, rotors and flywheels. Recently rotating disks became very significant in thermal power creating frameworks, electric-control generation, stopping mechanisms, rotating sawing machines, etc. Fluid flow by a rotating disk is initiated by the Von Karman effect [29]. Turkyilmazoglu and Senel [30] explored the impacts of mass and heat transport because of the porous disk subject to rotating frame. Entropy generation in MHD flow by the rotation of porous disk subject to slip and variable properties is examined by Rashidi et al. [31]. Nanofluid flow because of revolution of disk is discussed by Turkyilmazoglu [32]. Hatami et al. [33] investigated the impacts of contracting rotating disk on nanofluids. They utilized least square technique for solution development. Mustafa et al. [34] analyzed three dimensional nanofluid flow over a stationary disk. Sheikholeslami et al. [35] constructed numerical solutions of nanofluid by a rotating surface. Micropolar liquid flow by a turning disk is explored by Doh and Muthtamilselvan [36]. Aziz et al. [37] provided a numerical report to

nanofluid flow by rotation of disk subject to slip impacts and thermal absorption/generation. Third-grade nanofluid flow over a stretchable rotating surface with heat generation is examined by Hayat et al. [38]. Radiative flow in the presence of nanoparticles and gyrotactic microorganism by the variable-in-thickness surface of a pivoting disk is explained by Qayyum et al. [39]. Hayat et al. [40] provided a numerical solution for radiative flow of carbon nanotubes by the revolution of disk subject to partial slip.

The aim of the present paper is to generalize the analysis of study [11] into four directions. Firstly, to examine magnetohydrodynamic flow of viscous nanofluid due to the rotation of disk. Attention is mainly given to Brownian diffusion and thermophoresis. Secondly, to utilize thermal, concentration and velocity slips at the surface of rotating disk. Thirdly, to consider the effect of mixed convection. Fourth, to analyze the Arrhenius activation energy and binary chemical reaction. The resulting scientific framework is solved numerically via the shooting method. Concentration, temperature and Sherwood and Nusselt numbers are also explored via graphs.

2. Problem Description

Let us examine a mixed convective 3D nanoliquid flow by a pivoting disk with slip features. Arrhenius activation energy, magnetic field and binary chemical reaction are also accounted for. A disk at $z = 0$ rotates with constant angular velocity Ω (see Figure 1). Brownian dispersion and thermophoretic impacts are additionally present. The velocities are (u, v, w) in the headings of expanding (r, φ, z) respectively. The associated boundary-layer equations are [11,37]:

$$\frac{\partial u}{\partial r} + \frac{u}{r} + \frac{\partial w}{\partial z} = 0, \tag{1}$$

$$u\frac{\partial u}{\partial r} - \frac{v^2}{r} + w\frac{\partial u}{\partial z} = \nu\left(\frac{\partial^2 u}{\partial z^2} + \frac{\partial^2 u}{\partial r^2} + \frac{1}{r}\frac{\partial u}{\partial r} - \frac{u}{r^2}\right) - \frac{\sigma B_0^2}{\rho_f}u + g^*(\beta_T(T - T_\infty) + \beta_C(C - C_\infty)), \tag{2}$$

$$u\frac{\partial v}{\partial r} + \frac{uv}{r} + w\frac{\partial v}{\partial z} = \nu\left(\frac{\partial^2 v}{\partial z^2} + \frac{\partial^2 v}{\partial r^2} + \frac{1}{r}\frac{\partial v}{\partial r} - \frac{v}{r^2}\right) - \frac{\sigma B_0^2}{\rho_f}v, \tag{3}$$

$$u\frac{\partial w}{\partial r} + w\frac{\partial w}{\partial z} = \nu\left(\frac{\partial^2 w}{\partial r^2} + \frac{\partial^2 w}{\partial z^2} + \frac{1}{r}\frac{\partial w}{\partial r}\right), \tag{4}$$

$$\begin{aligned} u\frac{\partial T}{\partial r} + w\frac{\partial T}{\partial z} &= \alpha_m\left(\frac{\partial^2 T}{\partial r^2} + \frac{\partial^2 T}{\partial z^2} + \frac{1}{r}\frac{\partial T}{\partial r}\right) \\ &+ \frac{(\rho c)_p}{(\rho c)_f}\left(D_B\left(\frac{\partial T}{\partial r}\frac{\partial C}{\partial r} + \frac{\partial T}{\partial z}\frac{\partial C}{\partial z}\right) + \frac{D_T}{T_\infty}\left(\left(\frac{\partial T}{\partial z}\right)^2 + \left(\frac{\partial T}{\partial r}\right)^2\right)\right), \end{aligned} \tag{5}$$

$$\begin{aligned} u\frac{\partial C}{\partial r} + w\frac{\partial C}{\partial z} &= D_B\left(\frac{\partial^2 C}{\partial r^2} + \frac{\partial^2 C}{\partial z^2} + \frac{1}{r}\frac{\partial C}{\partial r}\right) \\ &+ \frac{D_T}{T_\infty}\left(\frac{\partial^2 T}{\partial r^2} + \frac{\partial^2 T}{\partial z^2} + \frac{1}{r}\frac{\partial T}{\partial r}\right) - k_r^2(C - C_\infty)\left(\frac{T}{T_\infty}\right)^n \exp\left(-\frac{E_a}{\kappa T}\right), \end{aligned} \tag{6}$$

$$u = L_1\frac{\partial u}{\partial z},\ v = r\Omega + L_1\frac{\partial v}{\partial z},\ w = 0,\ T = T_w + L_2\frac{\partial T}{\partial z},\ C = C_w + L_3\frac{\partial C}{\partial z} \text{ at } z = 0, \tag{7}$$

$$u \to 0,\quad v \to 0,\quad T \to T_\infty,\quad C \to C_\infty \quad \text{as } z \to \infty. \tag{8}$$

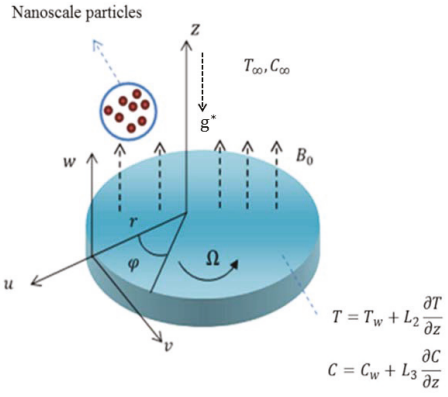

Figure 1. Schematic diagram of the problem.

Here u, v and w stand for velocity components in directions of r, φ and z; ρ_f, μ and $\nu = \mu/\rho_f$ are for fluid density, dynamic and kinematic viscosities, respectively. L_1 stands for velocity slip factor; C_∞ for ambient concentration; g^* for acceleration due to gravity; T_∞ for ambient temperature; β_T for thermal expansion factor; $(\rho c)_p$ for effective heat capacity of nanoparticles; σ for electrical conductivity; E_a for activation energy; L_3 for concentration slip factor; $(\rho c)_f$ for heat capacity of liquid; β_C for concentration expansion factor, C for concentration; L_2 for thermal slip factor; n for fitted rate constant; D_T for thermophoretic factor, $\alpha_m = k/(\rho c)_f$ and k for thermal diffusivity and thermal conductivity, respectively; k_r for reaction rate; T for fluid temperature; D_B for Brownian factor; and κ for Boltzmann constant. Selecting [37]:

$$\left.\begin{array}{c} u = r\Omega f'(\zeta),\ w = -(2\Omega\nu)^{1/2} f(\zeta),\ \theta(\zeta) = \frac{T-T_\infty}{T_w-T_\infty}, \\ \phi(\zeta) = \frac{C-C_\infty}{C_w-C_\infty},\ \zeta = \left(\frac{2\Omega}{\nu}\right)^{1/2} z,\ v = r\Omega g(\zeta). \end{array}\right\} \tag{9}$$

Equation (1) is now verified while Equations (2)–(8) yield [11,37]:

$$2f''' + 2ff'' - f'^2 + g^2 - (Ha)^2 f' + \lambda_T(\theta + \lambda_C\phi) = 0, \tag{10}$$

$$2g'' + 2fg' - 2f'g - (Ha)^2 g = 0, \tag{11}$$

$$\frac{1}{\mathrm{Pr}}\theta'' + f\theta' + N_b\theta'\phi' + N_t\theta'^2 = 0, \tag{12}$$

$$\frac{1}{Sc}\phi'' + f\phi' + \frac{1}{Sc}\frac{N_t}{N_b}\theta'' - \sigma(1+\delta\theta)^n \phi \exp\left(-\frac{E}{1+\delta\theta}\right) = 0, \tag{13}$$

$$f(0) = 0,\ f'(0) = \alpha f''(0),\ g(0) = 1 + \alpha g'(0),\ \theta(0) = 1 + \beta\theta'(0),\ \phi(0) = 1 + \gamma\phi'(0), \tag{14}$$

$$f'(\infty) \to 0,\ g(\infty) \to 0,\ \theta(\infty) \to 0,\ \phi(\infty) \to 0. \tag{15}$$

Here λ_T stands for thermal buoyancy number, N_t for thermophoresis parameter, α for velocity slip parameter, Pr for Prandtl number, λ_C for concentration buoyancy number, Sc for Schmidt parameter, Ha for Hartman number, β for thermal slip parameter, σ for chemical reaction number, N_b for Brownian parameter, δ for temperature difference parameter, γ for concentration slip parameter and E for non-dimensional activation energy. These parameters are defined by

$$\left.\begin{array}{c}(Ha)^2=\frac{\sigma B_0^2}{\Omega\rho_f},\ \mathrm{Pr}=\frac{\nu}{\alpha_m},\ \alpha=L_1\sqrt{\frac{2\Omega}{\nu}},\ \gamma=L_3\sqrt{\frac{2\Omega}{\nu}},\\ N_t=\frac{(\rho c)_p D_T(T_w-T_\infty)}{(\rho c)_f \nu T_\infty},\ Sc=\frac{\nu}{D_B},\ N_b=\frac{(\rho c)_p D_B(C_w-C_\infty)}{(\rho c)_f \nu},\ \lambda_T=\frac{\delta^*\beta_T\beta_T(T_w-T_\infty)}{\Omega},\\ \lambda_C=\frac{\beta_C(C_w-C_\infty)}{\beta_T(T_w-T_\infty)},\ \beta=L_2\sqrt{\frac{2\Omega}{\nu}},\ \sigma=\frac{k_r^2}{\Omega},\ \delta=\frac{T_w-T_\infty}{T_\infty},\ E=\frac{E_a}{\kappa T_\infty}.\end{array}\right\} \quad (16)$$

The coefficients of skin friction and Sherwood and Nusselt numbers are

$$\mathrm{Re}_r^{1/2}C_f=f''(0),\ \mathrm{Re}_r^{1/2}C_g=g'(0),\ \mathrm{Re}_r^{-1/2}Sh=-\phi'(0),\ \mathrm{Re}_r^{-1/2}Nu=-\theta'(0), \quad (17)$$

where $\mathrm{Re}_r=2(\Omega r)r/\nu$ depicts local rotational Reynolds number.

3. Solution Methodology

By employing suitable boundary conditions on the system of equations, a numerical solution was constructed considering NDSolve in Mathematica. The shooting method was employed via NDSolve. This method is very helpful in the situation of a smaller step-size featuring negligible error. As a consequence, both the z and r varied uniformly by a step-size of 0.01 [20].

4. Graphical Results and Discussion

This segment displays variations of various physical flow parameters, such as the thermophoresis parameter N_t, Hartman number Ha, thermal slip parameter β, chemical reaction parameter σ, Brownian motion parameter N_b, concentration slip parameter γ and activation energy E, on concentration $\phi(\zeta)$ and temperature $\theta(\zeta)$ distributions. Figure 2a displays the effect of Hartman number Ha on temperature $\theta(\zeta)$. Temperature $\theta(\zeta)$ is enhanced for higher estimations of Ha. The effect of thermal slip β on temperature $\theta(\zeta)$ is shown in Figure 2b. Greater β shows diminishing trend of $\theta(\zeta)$ and associated warmth layer. The impact of N_t on temperature $\theta(\zeta)$ is explored in Figure 2c. An increment in N_t leads to stronger temperature field $\theta(\zeta)$. Figure 2d depicts change in temperature $\theta(\zeta)$ for varying Brownian motion number N_b. Physically, the Brownian motion of nanoparticles is enhanced by increasing Brownian motion number N_b. Therefore dynamic vitality is altered into thermal vitality, which depicts an increment in temperature $\theta(\zeta)$ and the respective warmth layer. Figure 3a shows that how the Hartman number Ha influences concentration $\phi(\zeta)$. For a greater Hartman number Ha, both concentration $\phi(\zeta)$ and the concentration layer are upgraded. Figure 3b displays that concentration $\phi(\zeta)$ is weaker for a greater concentration slip. Figure 3c demonstrates how thermophoresis N_t influences concentration $\phi(\zeta)$. By improving the thermophoresis parameter N_t, the concentration $\phi(\zeta)$ and associated layer are upgraded. Figure 3d depicts effect of Brownian motion N_b on concentration $\phi(\zeta)$. It is noted that higher concentration $\phi(\zeta)$ is developed by utilizing greater Brownian parameter N_b. Figure 3e explains effect of non-dimensional activation energy E on concentration $\phi(\zeta)$. An increment in E rots change Arrhenius work $\left(\frac{T}{T_\infty}\right)^n \exp\left(-\frac{E_a}{\kappa T}\right)$, which inevitably builds up a generative synthetic reaction due to which concentration $\phi(\zeta)$ increases. Figure 3f introduces the fact that an increment in chemical response number σ causes a rot in concentration $\phi(\zeta)$. Figure 4a,b displays the effects of N_t and N_b on $\mathrm{Re}_r^{-1/2}Nu$. It is noted that $\mathrm{Re}_r^{-1/2}Nu$ decreases for greater N_t and N_b. Contributions of N_t and N_b on $\mathrm{Re}_r^{-1/2}Sh$ are explored in Figure 5a,b. Here $\mathrm{Re}_r^{-1/2}Sh$ is increasing the factor of N_b while it is decreasing the factor of N_t.

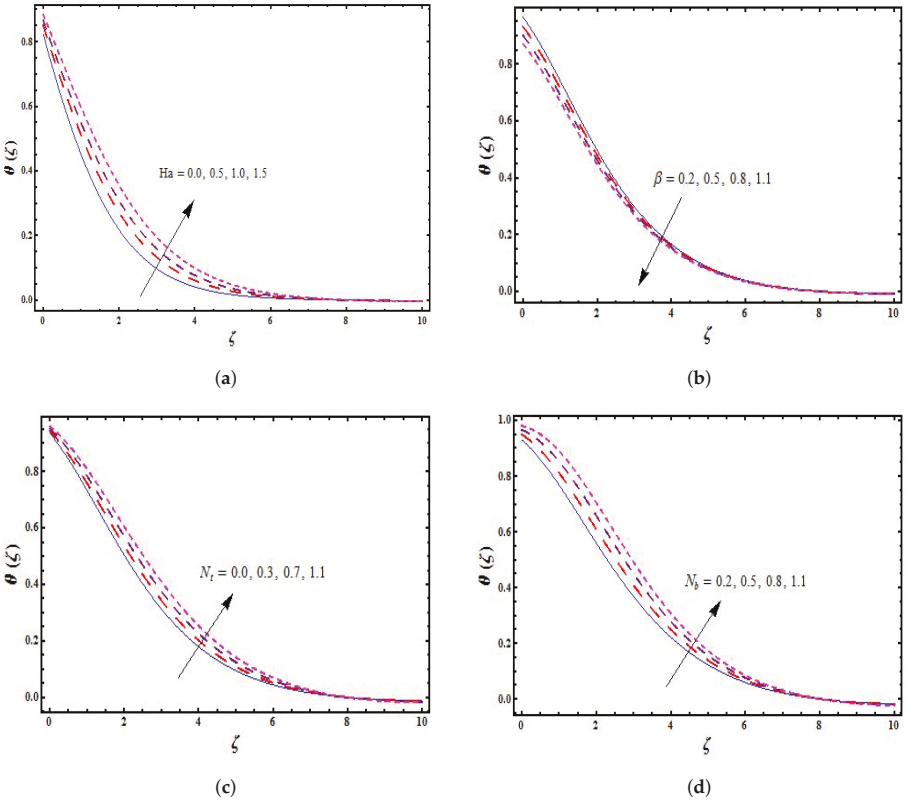

Figure 2. (**a**) Variations of temperature distribution $\theta(\zeta)$ for Hartman number *Ha*; (**b**) variations of temperature distribution $\theta(\zeta)$ for thermal slip parameter β; (**c**) variations of temperature distribution $\theta(\zeta)$ for thermophoresis parameter N_t; (**d**) variations of temperature distribution $\theta(\zeta)$ for Brownian motion parameter N_b.

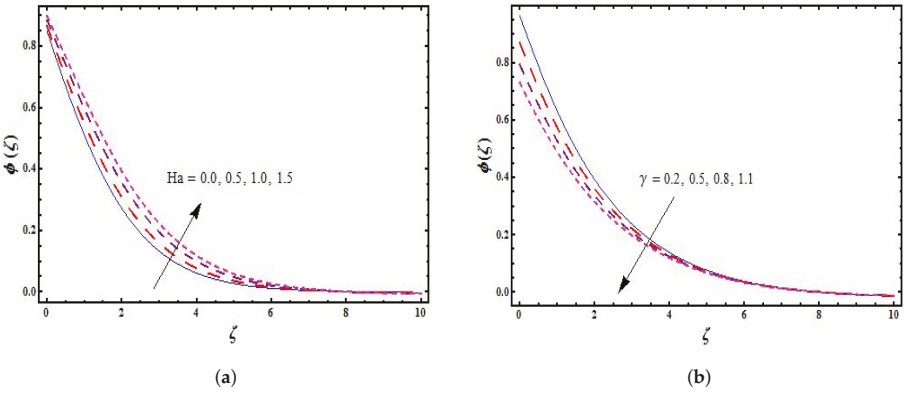

Figure 3. *Cont.*

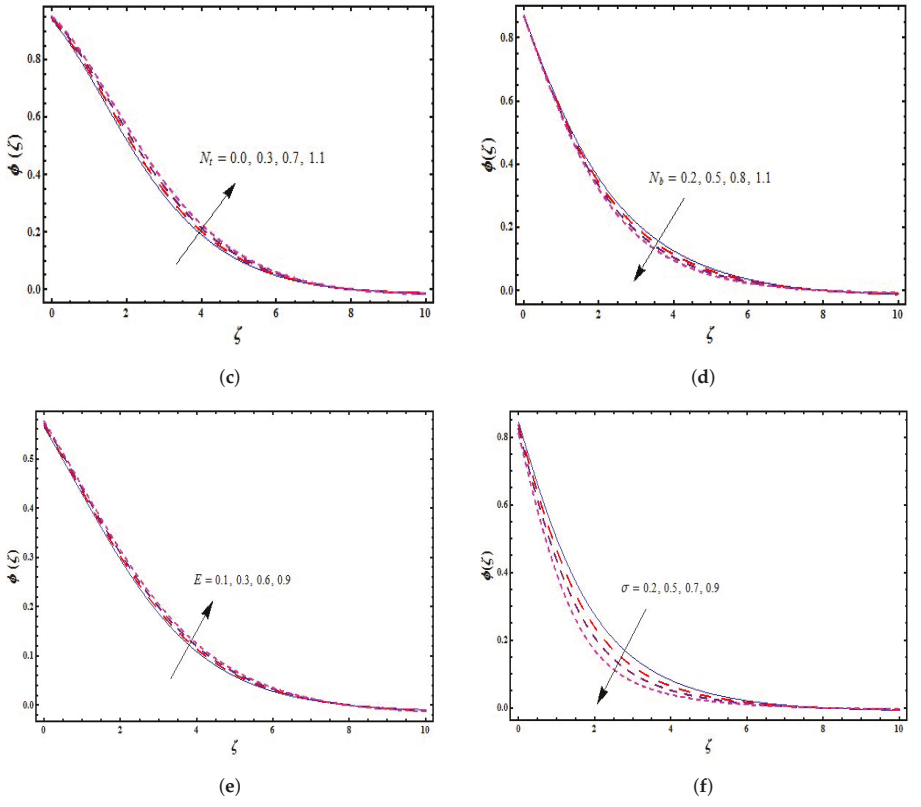

Figure 3. (**a**) Variations of concentration distribution $\phi(\zeta)$ for Hartman number Ha; (**b**) variations of concentration distribution $\phi(\zeta)$ for concentration slip parameter γ; (**c**) variations of concentration distribution $\phi(\zeta)$ for thermophoresis parameter N_t; (**d**) variations of concentration distribution $\phi(\zeta)$ for Brownian motion parameter N_b; (**e**) variations of concentration distribution $\phi(\zeta)$ for activation energy E; (**f**) variations of concentration distribution $\phi(\zeta)$ for chemical reaction parameter σ.

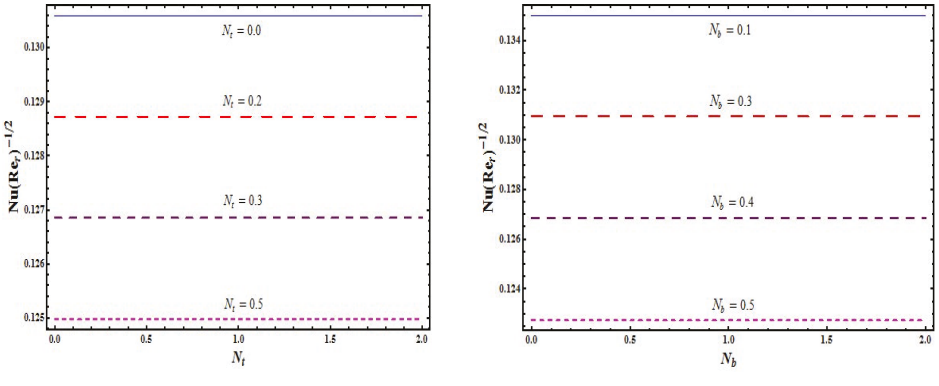

Figure 4. (**a**) Variations of Nusselt number $\mathrm{Re}_r^{-1/2}\,Nu$ for thermophoresis parameter N_t; (**b**) variations of Nusselt number $\mathrm{Re}_r^{-1/2}\,Nu$ for Brownian motion parameter N_b.

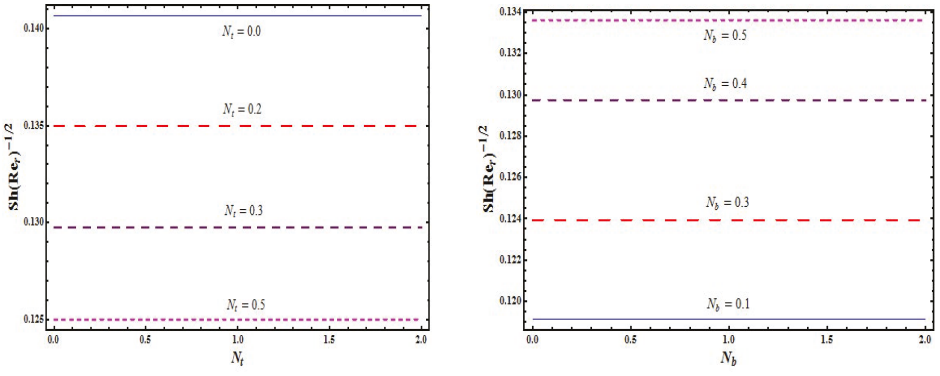

(**a**) (**b**)

Figure 5. (**a**) Variations of Sherwood number $\mathrm{Re}_r^{-1/2}\,Sh$ for thermophoresis parameter N_t; (**b**) variations of Sherwood number $\mathrm{Re}_r^{-1/2}\,Sh$ for Brownian motion parameter N_b.

5. Conclusions

Mixed convective 3D nanoliquid flow by a rotating disk subject to activation energy, magnetohydrodynamics and a binary chemical reaction was studied. Here, the flow field was considered to contain the chemically reacting species. Moreover, the mass transport mechanism was developed via modified Arrhenius function for the activation energy. Activation energy is the minimum quantity of energy needed by reactants to examine a chemical reaction. The source of the activation energy needed to initiate a chemical reaction is typically heat energy from the surroundings. Furthermore, the scientific system obtained was solved numerically via shooting method. A stronger temperature distribution was seen for N_b and N_t. Both the concentration and temperature display increasing behavior for greater Ha. Higher γ exhibits a decreasing trend for concentration field. Concentration $\phi(\zeta)$ depicts decreasing behavior for larger σ. Higher activation energy E shows stronger concentration $\phi(\zeta)$. Concentration $\phi(\zeta)$ displays reverse behavior for N_b and N_t.

Funding: This research was funded by the Deanship of Scientific Research, King Khalid University, Abha, Saudi Arabia under grant number (R.G.P.2./26/40).

Acknowledgments: The author extends his appreciation to the Deanship of Scientific Research at King Khalid University for funding this work through Research Groups Program under grant number (R.G.P.2./26/40).

Conflicts of Interest: The author declares no conflict of interest.

Nomenclature

u, v, w	velocity components	r, φ, z	coordinate axes
σ	electrical conductivity	B_0	magnetic field strength
μ	dynamic viscosity	ρ_f	density of base fluid
β_T	thermal expansion coefficient	β_C	concentration expansion coefficient
ν	kinematic viscosity	g^*	acceleration due to gravity
L_1	velocity slip coefficient	L_2	temperature slip coefficient
L_3	concentration slip coefficient	Ω	constant angular velocity
T	temperature	C	concentration
T_w	wall temperature	C_w	wall concentration
T_∞	ambient fluid temperature	C_∞	ambient fluid concentration
α_m	thermal diffusivity	k	thermal conductivity
$(\rho c)_p$	effective heat capacity of nanoparticles	$(\rho c)_f$	heat capacity of fluid
D_B	Brownian diffusion coefficient	D_T	thermophoretic diffusion coefficient
E_a	activation energy	n	fitted rate constant

k_r	reaction rate	κ	Boltzmann constant
ζ	similarity variable	f', g	dimensionless velocities
θ	dimensionless temperature	ϕ	dimensionless concentration
Sc	Schmidt number	Ha	Hartman number
λ_T	thermal buoyancy number	Pr	Prandtl number
N_b	Brownian motion parameter	N_t	thermophoresis parameter
λ_C	concentration buoyancy number	α	velocity slip parameter
β	thermal slip parameter	γ	concentration slip parameter
E	dimensionless activation energy	δ	temperature difference parameter
C_f, C_g	skin friction coefficients	Re_r	local rotational Reynolds number
Nu	Nusselt number	Sh	Sherwood number

References

1. Choi, S.U.S. *Enhancing Thermal Conductivity of Fluids With Nanoparticles*; FED 231/MD; Argonne National Lab.: Lemont, IL, USA, 1995; Volume 66, pp. 99–105.
2. Buongiorno, J. Convective transport in nanofluids. *J. Heat Transf.* **2006**, *128*, 240–250.
3. Eastman, J.A.; Choi, S.U.S.; Li, S.; Yu, W.; Thompson, L.J. Anomalously increased effective thermal conductivities of ethylene glycol-based nanofluids containing copper nanoparticles. *Appl. Phys. Lett.* **2001**, *78*, 718–720.
4. Tiwari, R.K.; Das, M.K. Heat transfer augmentation in a two-sided lid-driven differentially heated square cavity utilizing nanofluid. *Int. J. Heat Mass Transf.* **2007**, *50*, 2002–2018.
5. Abu-Nada, E.; Oztop, H.F. Effects of inclination angle on natural convection in enclosures filled with Cu-water nanofluid. *Int. J. Heat Fluid Flow* **2009**, *30*, 669–678.
6. Mansur, S.; Ishak, A. Three-dimensional flow and heat transfer of a nanofluid past a permeable stretching sheet with a convective boundary condition. *AIP Conf. Proc.* **2014**, *1614*, 906–912.
7. Hayat, T.; Muhammad, T.; Alsaedi, A.; Alhuthali, M.S. Magnetohydrodynamic three-dimensional flow of viscoelastic nanofluid in the presence of nonlinear thermal radiation. *J. Magn. Magn. Mater.* **2015**, *385*, 222–229. [CrossRef]
8. Mahanthesh, B.; Gireesha, B.J.; Gorla, R.S.R. Nonlinear radiative heat transfer in MHD three-dimensional flow of water based nanofluid over a non-linearly stretching sheet with convective boundary condition. *J. Niger. Math. Soc.* **2016**, *35*, 178–198. [CrossRef]
9. Hayat, T.; Aziz, A.; Muhammad, T.; Alsaedi, A. On magnetohydrodynamic three-dimensional flow of nanofluid over a convectively heated nonlinear stretching surface. *Int. J. Heat Mass Transf.* **2016**, *100*, 566–572.
10. Muhammad, T.; Alsaedi, A.; Shehzad, S.A.; Hayat, T. A revised model for Darcy-Forchheimer flow of Maxwell nanofluid subject to convective boundary condition. *Chin. J. Phys.* **2017**, *55*, 963–976.
11. Hayat, T.; Muhammad, T.; Shehzad, S.A.; Alsaedi, A. On magnetohydrodynamic flow of nanofluid due to a rotating disk with slip effect: A numerical study. *Comp. Methods Appl. Mech. Eng.* **2017**, *315*, 467–477. [CrossRef]
12. Sheikholeslami, M.; Kataria, H.R.; Mittal, A.S. Radiation effects on heat transfer of three dimensional nanofluid flow considering thermal interfacial resistance and micro mixing in suspensions. *Chin. J. Phys.* **2017**, *55*, 2254–2272. [CrossRef]
13. Muhammad, T.; Alsaedi, A.; Hayat, T.; Shehzad, S.A. A revised model for Darcy-Forchheimer three-dimensional flow of nanofluid subject to convective boundary condition. *Results Phys.* **2017**, *7*, 2791–2797. [CrossRef]
14. Hayat, T.; Sajjad, R.; Muhammad, T.; Alsaedi, A.; Ellahi, R. On MHD nonlinear stretching flow of Powell-Eyring nanomaterial. *Results Phys.* **2017**, *7*, 535–543. [CrossRef]
15. Ellahi, R.; Zeeshan, A.; Hussain, F.; Abbas, T. Study of shiny film coating on multi-fluid flows of a rotating disk suspended with nano-sized silver and gold particles: A comparative analysis. *Coatings* **2018**, *8*, 422. [CrossRef]
16. Selimefendigil, F.; Oztop, H.F. Mixed convection of nanofluids in a three dimensional cavity with two adiabatic inner rotating cylinders. *Int. J. Heat Mass Transf.* **2018**, *117*, 331–343. [CrossRef]

17. Muhammad, T.; Lu, D.C.; Mahanthesh, B.; Eid, M.R.; Ramzan, M.; Dar, A. Significance of Darcy-Forchheimer porous medium in nanofluid through carbon nanotubes. *Commun. Theoret. Phys.* **2018**, *70*, 361. [CrossRef]
18. Suleman, M.; Ramzan, M.; Ahmad, S.; Lu, D.; Muhammad, T.; Chung, J.D. A numerical simulation of silver-water nanofluid flow with impacts of Newtonian heating and homogeneous-heterogeneous reactions past a nonlinear stretched cylinder. *Symmetry* **2019**, *11*, 295. [CrossRef]
19. Asma, M.; Othman, W.A.M.; Muhammad, T. Numerical study for Darcy-Forchheimer flow of nanofluid due to a rotating disk with binary chemical reaction and Arrhenius activation energy. *Mathematics* **2019**, *7*, 921. [CrossRef]
20. Asma, M.; Othman, W.A.M.; Muhammad, T.; Mallawi, F.; Wong, B.R. Numerical study for magnetohydrodynamic flow of nanofluid due to a rotating disk with binary chemical reaction and Arrhenius activation energy. *Symmetry* **2019**, *11*, 1282. [CrossRef]
21. Saif, R.S.; Hayat, T.; Ellahi, R.; Muhammad, T.; Alsaedi, A. Darcy-Forchheimer flow of nanofluid due to a curved stretching surface. *Int. J. Numer. Methods Heat Fluid Flow* **2019**, *29*, 2–20. [CrossRef]
22. Ellahi, R.; Zeeshan, A.; Hussain, F.; Abbas, T. Thermally charged MHD bi-phase flow coatings with non-Newtonian nanofluid and Hafnium particles along slippery walls. *Coatings* **2019**, *9*, 300. [CrossRef]
23. Moradikazerouni, A.; Hajizadeh, A.; Safaei, M.R.; Afrand, M.; Yarmand, H.; Zulkifli, N.W.B.M. Assessment of thermal conductivity enhancement of nano-antifreeze containing single-walled carbon nanotubes: Optimal artificial neural network and curve-fitting. *Phys. A* **2019**, *521*, 138–145. [CrossRef]
24. Asadi, A.; Aberoumand, S.; Moradikazerouni, A.; Pourfattah, F.; Żyła, G.; Estelle, P.; Mahian, O.; Wongwises, S.; Nguyen, H.M.; Arabkoohsar, A. Recent advances in preparation methods and thermophysical properties of oil-based nanofluids: A state-of-the-art review. *Powder Technol.* **2019**, *352*, 209–226. [CrossRef]
25. Alsarraf, J.; Moradikazerouni, A.; Shahsavar, A.; Afrand, M.; Salehipour, H.; Tran, M.D. Hydrothermal analysis of turbulent boehmite alumina nanofluid flow with different nanoparticle shapes in a minichannel heat exchanger using two-phase mixture model. *Phys. A* **2019**, *520*, 275–288. [CrossRef]
26. Vo, D.D.; Alsarraf, J.; Moradikazerouni, A.; Afrand, M.; Salehipour, H.; Qi, C. Numerical investigation of γ-AlOOH nano-fluid convection performance in a wavy channel considering various shapes of nanoadditives. *Powder Technol.* **2019**, *345*, 649–657. [CrossRef]
27. Ranjbarzadeh, R.; Moradikazerouni, A.; Bakhtiari, R.; Asadi, A.; Afrand, M. An experimental study on stability and thermal conductivity of water/silica nanofluid: Eco-friendly production of nanoparticles. *J. Clean. Prod.* **2019**, *206*, 1089–1100. [CrossRef]
28. Ma, Y.; Shahsavar, A.; Moradi, I.; Rostami, S.; Moradikazerouni, A.; Yarmand, H.; Zulkifli, N.W.B.M. Using finite volume method for simulating the natural convective heat transfer of nano-fluid flow inside an inclined enclosure with conductive walls in the presence of a constant temperature heat source. *Phys. A* **2019**, 123035. [CrossRef]
29. Von Karman, T. Uber laminare and turbulente Reibung. *ZAMM Z. Angew. Math. Mech.* **1921**, *1*, 233–252. [CrossRef]
30. Turkyilmazoglu, M.; Senel, P. Heat and mass transfer of the flow due to a rotating rough and porous disk. *Int. J. Thermal Sci.* **2013**, *63*, 146–158. [CrossRef]
31. Rashidi, M.M.; Kavyani, N.; Abelman, S. Investigation of entropy generation in MHD and slip flow over rotating porous disk with variable properties. *Int. J. Heat Mass Transf.* **2014**, *70*, 892–917. [CrossRef]
32. Turkyilmazoglu, M.; Nanofluid flow and heat transfer due to a rotating disk. *Comput. Fluids* **2014**, *94*, 139–146. [CrossRef]
33. Hatami, M.; Sheikholeslami, M.; Gangi, D.D. Laminar flow and heat transfer of nanofluids between contracting and rotating disks by least square method. *Powder Technol.* **2014**, *253*, 769–779. [CrossRef]
34. Mustafa, M.; Khan, J.A.; Hayat, T.; Alsaedi, A. On Bödewadt flow and heat transfer of nanofluids over a stretching stationary disk. *J. Mol. Liq.* **2015**, *211*, 119–125. [CrossRef]
35. Sheikholeslami, M.; Hatami, M.; Ganji, D.D. Numerical investigation of nanofluid spraying on an inclined rotating disk for cooling process. *J. Mol. Liq.* **2015**, *211*, 577–583. [CrossRef]
36. Doh, D.H.; Muthtamilselvan, M. Thermophoretic particle deposition on magnetohydrodynamic flow of micropolar fluid due to a rotating disk. *Int. J. Mech. Sci.* **2017**, *130*, 350–359. [CrossRef]
37. Aziz, A.; Alsaedi, A.; Muhammad, T.; Hayat, T. Numerical study for heat generation/absorption in flow of nanofluid by a rotating disk. *Results Phys.* **2018**, *8*, 785–792. [CrossRef]

38. Hayat, T.; Ahmad, S.; Khan, M.I.; Alsaedi, A. Modeling and analyzing flow of third grade nanofluid due to rotating stretchable disk with chemical reaction and heat source. *Phys. B* **2018**, *537*, 116–126. [CrossRef]
39. Qayyum, S.; Imtiaz, M.; Alsaedi, A.; Hayat, T. Analysis of radiation in a suspension of nanoparticles and gyrotactic microorganism for rotating disk of variable thickness. *Chin. J. Phys.* **2018**, *56*, 2404–2423. [CrossRef]
40. Hayat, T.; Khalid, H.; Waqas, M.; Alsaedi, A. Numerical simulation for radiative flow of nanoliquid by rotating disk with carbon nanotubes and partial slip, Comput. *Methods Appl. Mech. Eng.* **2018**, *341*, 397–408. [CrossRef]

coatings

MDPI

Article

Buoyancy Driven Flow with Gas-Liquid Coatings of Peristaltic Bubbly Flow in Elastic Walls

Nouman Ijaz [1], Arshad Riaz [2], Ahmed Zeeshan [3], Rahmat Ellahi [3,4,5,*] and Sadiq M. Sait [6]

1 Department of Mathematics and Statistics, University of Lahore Sargodha Campus, Sargodha 40100, Pakistan; nouman.ijaz@math.uol.edu.pk
2 Department of Mathematics, Division of Science and Technology, University of Education, Lahore 54770, Pakistan; arshad-riaz@ue.edu.pk
3 Department of Mathematics & Statistics, Faculty of Basic and Applied Sciences (FBAS), International Islamic University, Islamabad 44000, Pakistan; ahmad.zeeshan@iiu.edu.pk
4 Center for Modeling and Computer Simulation, Research Institute, King Fahd University of Petroleum & Minerals, Dhahran-3126, Saudi Arabia
5 Fulbright Fellow, Department of Mechanical Engineering, University of California Riverside, Riverside, CA 92521, USA
6 Center for Communications and IT Research, Research Institute, King Fahd University of Petroleum & Minerals, Dhahran-31261, Saudi Arabia; sadiq@kfupm.edu.sa
* Correspondence: rellahi@alumni.ucr.edu

Received: 4 November 2019; Accepted: 26 January 2020; Published: 30 January 2020

Abstract: In this paper, liquid coatings of bubbly flow with peristaltic motion inside elastic walls is investigated. The proposed model is constructed using the two-fluid approach with the most distinctive collaboration among gas, fluid, pressure, and drag forces. Variation in pressure leads to a change in void fraction. The differential controlling conditions affected by the long wavelength of the peristaltic wave and the slow movement are taken into account. Analytical results of the simplified governing equations are obtained using the homotopy perturbation method (HPM). The features of the significant parameters are shown and examined graphically.

Keywords: gas-liquid coatings; bubbles; two-fluid model; peristaltic flow; phase distribution; HPM

1. Introduction

An air-pocket-incited gas-fluid stream is the premise of smooth motion in numerous compound building gadgets and applications ranging from boilers or evaporators and more than a few stage bubble segment reactors of different structures to enormous-scale vigorous (and sometimes anaerobic) sewage treatment plants. The two-phase transport hypothetical talk and test request are firmly connected. On the other hand, the amalgamation that emerges from this association creates colossal innovative potential for estimations advising and approving unique models. The subsequent innovation develops utility in an expansive range of uses, from cutting-edge atomic hardware and space motors to pharmaceutical assembling, nourishment innovation, vitality, and natural remediation. Sussman et al. [1] considered a level-set methodology for figuring out answers for a incompressible two-stage stream. Their study was about the movement of air bubbles in the water and falling water drops in the air. A single-liquid model for a two-stage stream with variable thickness to the stream-water flow was analyzed by Bankoff [2]. Zuber and Findlay [3] estimated the normal volumetric fixation in two-stage stream frameworks. In their analysis, the outcomes anticipated by the investigation were contrasted with experimental data acquired for different two-phase stream systems, with different fluid gas blends in the adiabatic, vertical stream over a wide weight territory. Picchi and Poesio [4] developed a unified model for both horizontal and slightly inclined fluid

pipes lubricated with two-phase gas/shear-thinning fluid. Sato and Sekoguchi [5] suggested the velocity distribution of liquid in two-phase bubble flow. A more precise analytical procedure was constructed that created the justified foreboding of the liquid velocity dispensation in two-phase bubble flow. Kuwagi et al. [6] investigated the oscillation of bubbly flow through a normally placed cylinder employing a tridimensional system. Picchi and Battiato [7] discussed immiscible two-phase flow in porous media and elaborated the impact of pore-scale flow. Bonzanini et al. [8] simulated 1-D slug and stratified flow in pipes. Sontti and Atta [9] investigated co-flow in microchannels to discuss the viscous effect on Taylor bubble formation. Bhatti et al. [10] broke down the heat and mass exchange of a two-phase stream with an electric twofold layer whose impacts were incited due to the peristaltic impetus within the sight of the transverse attractive field. Haider et al. [11] presented the heat transfer as well as a magnetic field investigation on the peristaltically initiated movement of tiny particles.

Moreover, the mechanism of peristalsis comprises expansion and contraction events that impel an ingredient forward. Examples of some cases of the peristaltic phenomenon are the transport of bile in the bile duct, the transport of urine from the kidney to the gallbladder, the transport of cilia, the vasomotion of small blood vessels, and the mixing of food in the digestive tract, to name a few. The peristaltic phenomenon also has several industrial applications such as in the flow in tube pumps, in the rollers and hoses in heart-lung machines, and in the dialysis process during open-heart surgery. [12,13].

Furthermore, in buoyancy-driven flows, although the difference in inertia is almost negligible, the gravity remains sufficiently strong to make the specific weight significantly different during the flow in multiphase fluids. Tripathi et al. [14] investigated buoyancy effects in the peristaltic flow of nanofluid under the influence of electro-osmosis. Animasaun and Pop [15] numerically explored the effects of buoyancy on the flow driven by catalytic surface reactions. Angirasa et al. [16] reported the buoyancy effects in a fluid saturated with a porous medium. Rashidi et al. [17] studied fluid flow in the presence of buoyancy forces.

In addition to the above, the presence of bubbles has appeared in several applications in a gas-liquid flow. Many theoretical and numerical investigations have been conducting for multiphase bubbly flows in oil, gas, and liquid. It has numerous usages, such as in optical fiber sensing applications [18], sensitive pressure measurement [19], the human bloodstream during decompression sickness, and subcooled flow boiling in macro-channels [20]. Ellhi et al. [21] examined the simulation of bubble through the nozzle of tube. Furthermore, lubricated coatings with bubbles in peristaltic motion have a lot of applications in the biomedical field, and among several of these, in the control of blood pressure. Particle coating with viscous liquids is an essential component in the industry for surface modification purposes in order to induce and improve precise functionalities. Coating with viscous liquids is usually present in very rich industrial trials, which allow the coating of particles under the shear forces exerted in a mixing device. A list of key investigations on peristaltic flows [22–24], multiphase flows [25–29], bubbly flows [30–34], coatings [35–40], elastic medium [41,42], and several other references are available, which provide a more in-depth understanding to the reader.

Due to the immense contribution of two-phase flow structures in many significant fields, this study attempts to trap the structures of gas-liquid bubbly flow inside the elastic walls under the peristaltic mechanism applied over a two-fluid model. Due to the nonlinear model, a powerful and efficient technique called the homotopy perturbation method is used for finding analytic solutions. This method works even without the need of a linearization process of nonlinear differential equations. The parameters affecting the flow prominently have been examined with the help of a graphical illustration.

2. Mathematical Formulation

We assumed a symmetric channel with flexible walls starting at the origin of a rectangular coordinate system, see Figure 1. Plates were placed parallel to the x-axis, on either side of the origin, separated by a distance of 2h. Only the upper portion of the symmetric channel was taken into

consideration. A continuous wave with long wavelength, λ, and speed, c, traveled on the plates [43] and was defined by

$$z = h(X,t) = a(1 + \eta(X,t)) \tag{1}$$

where $\eta(x,t) = \phi Sin(\frac{2\pi}{\lambda}(X - ct)), \phi = \frac{b}{a}$ having an interval of $(0,1)$.

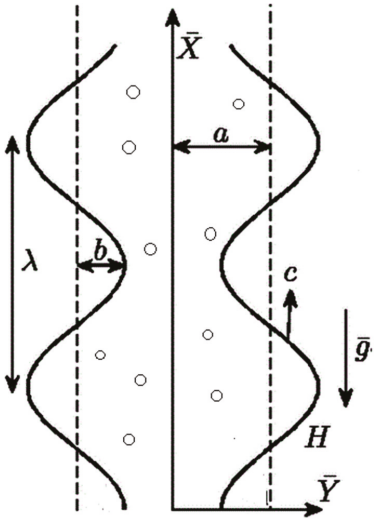

Figure 1. Geometry of the problem.

Two-Fluid Model

The two-fluid model for the flow of the gas bubbles in the Newtonian fluid with the Euler–Euler model was employed. Both phases were considered as a continuum and could be defined with the help of differential equations. A thin surface separated both the fluids and at the interphase, and consequently a jump continuity condition could be employed [44]. The bubbles were distributed homogenously in the flow and considered to be of the same spherical shape. It was assumed that no mass was transferred between the two phases and isothermal conditions were maintained. The density of the liquid was constant, whereas for the gas-phase it depended on pressure, *p*. Bubble redispersion was neglected and there was low gas holdup. With these assumptions, continuity equations for both the liquid and bubble phase were of the form [45]

$$\nabla.(U_l) = 0, \tag{2}$$

$$\frac{\partial\left(\varepsilon_g \rho_g\right)}{\partial t} + \nabla.\left(\varepsilon_g \rho_g U_g\right) = 0, \tag{3}$$

where U_l and U_b were the liquid and bubble velocities, respectively, whereas ε_g and ρ_g represented the void space and density of the gaseous phase with the closure relation constraint $\varepsilon_l + \varepsilon_g = 1$. For low gas $\varepsilon_l \approx 1$. Using ideal gas laws, $\rho_g = \frac{P}{RT_0}$, $\rho_l \approx$ constant, and because isothermal conditions were taken into account T_0 remained constant.

The momentum transfer for both the liquid and gaseous phase [46] were defined as

$$\rho_l\left(\frac{\partial U_l}{\partial t} + U_l\frac{\partial U_l}{\partial X} + V_l\frac{\partial U_l}{\partial Y}\right) = -\frac{\partial P}{\partial X} + \mu\left(\frac{\partial^2 U_l}{\partial X^2} + \frac{\partial^2 U_l}{\partial Y^2}\right) + \rho_l g - \varepsilon_g \rho_l g, \tag{4}$$

$$\rho_l\left(\frac{\partial V_l}{\partial t}+U_l\frac{\partial V_l}{\partial X}+V_l\frac{\partial V_l}{\partial Y}\right)=-\frac{\partial P}{\partial Y}+\mu\left(\frac{\partial^2 V_l}{\partial X^2}+\frac{\partial^2 V_l}{\partial Y^2}\right), \tag{5}$$

$$\varepsilon_g\rho_g\left(\frac{\partial U_g}{\partial t}+U_g\frac{\partial U_g}{\partial X}+V_g\frac{\partial U_g}{\partial Y}\right)=-\varepsilon_g\frac{\partial P}{\partial X}+\mu\varepsilon_g\left(\frac{\partial^2 U_g}{\partial X^2}+\frac{\partial^2 U_g}{\partial Y^2}\right)+\rho_g g\varepsilon_g-F_{\text{int},x}, \tag{6}$$

$$\varepsilon_g\rho_g\left(\frac{\partial V_g}{\partial t}+U_g\frac{\partial V_g}{\partial X}+V_g\frac{\partial V_g}{\partial Y}\right)=-\varepsilon_g\frac{\partial P}{\partial Y}+\mu\varepsilon_g\left(\frac{\partial^2 V_g}{\partial X^2}+\frac{\partial^2 V_g}{\partial Y^2}\right)-F_{\text{int},y}, \tag{7}$$

where F_{int} is the interaction force between the liquid and gaseous phases. These forces were able to be divided into three parts—i) force due to drag, which is incorporated in the uniform flow, ii) added mass force due to the acceleration of the bubble, and iii) lift force for the spherical bubble [47]. Mathematically this could be written as

$$F_{\text{int}}=F_d+F_{am}+F_l, \tag{8}$$

$$F_d=-C_wV_b(U_b-U_l), \tag{9}$$

$$F_{am}=-C_{am}V_b\rho_l\left(\frac{dU_{slip}}{dt}\right), \tag{10}$$

$$F_l=-C_lV_b\rho_l(U_b-U_l)\times(\nabla\times U_l), \tag{11}$$

in which C_w was a constant involving bubble diameter and drag force, V_b was the volume of the bubble, C_{am} was a constant related to the volume fraction of liquid accelerated with the bubble, U_{slip} was slip velocity defined as $U_{slip}=U_b-U_l$, and C_l was the lift coefficient. Finally, U_b was the speed of a single bubble and it was related to gas velocity by $U_g=U_b+U_{drift}$, where U_{drift} is the average drift velocity, which was proportional to the ratio of the special change in gas void fraction to total void fraction of gas.

To transform from a fixed frame to wave frame, Lorentz transformations were employed.

$$X=x*-ct,\ \mathrm{Y}=y*,\ U=u*-c,\ V=v*,p*(x*,\ y*)=P(\mathrm{X},Y,\ t). \tag{12}$$

Equations (2)-(11) became

$$\nabla.(u_l*)=0, \tag{13}$$

$$c\frac{\partial\left(\varepsilon_g\rho_g\right)}{\partial x*}+\nabla.\left(\varepsilon_g\rho_g u_g*\right)=0, \tag{14}$$

$$\rho_l\left(u_l*\frac{\partial u_l*}{\partial x*}+v_l*\frac{\partial u_l*}{\partial y*}\right)=-\frac{\partial p}{\partial x*}+\mu\left(\frac{\partial^2 u_l*}{\partial x*^2}+\frac{\partial^2 u_l*}{\partial y*^2}\right)+(1-\varepsilon_g)\rho_l g, \tag{15}$$

$$\rho_l\left(u_l*\frac{\partial v_l*}{\partial x*}+v_l*\frac{\partial v_l*}{\partial y*}\right)=-\frac{\partial p}{\partial y*}+\mu\left(\frac{\partial^2 v_l*}{\partial x*^2}+\frac{\partial^2 v_l*}{\partial y*^2}\right), \tag{16}$$

$$\varepsilon_g\rho_g\left(u_g*\frac{\partial u_g*}{\partial x*}+v_g*\frac{\partial u_g*}{\partial y*}\right)=-\varepsilon_g\frac{\partial p}{\partial x*}+\mu\varepsilon_g\left(\frac{\partial^2 u_g*}{\partial x*^2}+\frac{\partial^2 u_g*}{\partial y*^2}\right)+\rho_g g\varepsilon_g-f_{\text{int},x}, \tag{17}$$

$$\varepsilon_g\rho_g\left(u_g*\frac{\partial v_g*}{\partial x*}+v_g*\frac{\partial v_g*}{\partial y*}\right)=-\varepsilon_g\frac{\partial p*}{\partial y*}+\mu\varepsilon_g\left(\frac{\partial^2 v_g*}{\partial x*^2}+\frac{\partial^2 v_g*}{\partial y*^2}\right)-f_{\text{int},y}, \tag{18}$$

$$f_{\text{int}}=f_d+f_{am}+f_l, \tag{19}$$

$$f_d=-\mathrm{C}_wV_b(u_b*-u_l*), \tag{20}$$

$$F_{am}=-C_{am}V_b\rho_lc\left(\frac{\partial u_b*}{\partial x}-\frac{\partial u_l*}{\partial x}+(u_b*\cdot\nabla)u_b*-(u_l*\cdot\nabla)u_l*\right), \tag{21}$$

$$F_l=-C_lV_b\rho_l(u_b*-u_l*)\times(\nabla\times u_l*), \tag{22}$$

and by employing the dimensionless quantities were

$$\begin{array}{l} x = \frac{x^*}{\lambda}, y = \frac{y^*}{a}, u_{l,g} = \frac{u_{l,g}{}^*}{c}, v_{l,g} = \frac{v_{l,g}{}^*}{c}, \delta = \frac{a}{\lambda}, \mathrm{Re} = \frac{\rho c a}{\mu}, p = \frac{a^2}{\mu \lambda c} P \\ Eo = \frac{a^2}{\sigma} \rho_l g, R_{be} = \frac{ac}{\mu} \rho_l V_b, A = \frac{\mu c}{\sigma}. \end{array} \tag{23}$$

By imposing Equation (23) on Equations (12)-(22) and considering Re and δ approach zero, the corresponding expressions resulted in

$$\varepsilon_g = \frac{c_1}{\rho_g u_b}, \tag{24}$$

$$\frac{\partial p}{\partial x} = \frac{\partial^2 u_l}{\partial y^2} + \left(1 - \varepsilon_g\right) \frac{Eo}{A}, \tag{25}$$

$$A \rho_l \frac{\partial p}{\partial x} = Eo \left(\rho_g + \frac{V_b C_w}{g} \right) - R_{be} A \rho_l \left(C_l W_s \frac{\partial u_l}{\partial z} + C_{am} W_s \frac{\partial (u_b - u_l)}{\partial y} \right), \tag{26}$$

along with the consequential nondimensional boundary limitations

$$u_l(-h) = 0, u_l(h) = 0, \varepsilon_g(0) = 1. \tag{27}$$

3. Mathematical Solutions and Results

To compute the solutions of complicated nonlinear coupled equations, a powerful and efficient technique called the homotopy perturbation method (HPM) was used for finding analytic solutions. HPM is a powerful method which works even without the need of a linearization process [48–50]. It tends to reduce the nonlinear equations into a system of linear equations and generates an asymptotic solution. To serve the purpose, the initial guess was formed as

$$u_{l,0} = \frac{1}{2} \left(-2 - h^2 P + P y^2 \right) \textit{ and } u_{b,0} = 1 + Py. \tag{28}$$

The linear operators were

$$L_1 = \frac{d^2 u_l}{dy^2}, \textit{ and } L_2 = \frac{du_b}{dy}. \tag{29}$$

From Equations (22)-(23)

$$Eq1(\mathrm{x}, \mathrm{y}, \mathrm{q}) = P(\mathrm{x}, \mathrm{q}) - \frac{\partial^2 u_l}{\partial y^2}(x, y, \mathrm{q}) - \left(1 - \frac{c_1}{\rho_l u_b(\mathrm{x}, \mathrm{y}, \mathrm{q})} \right) \frac{Eo}{A}, \tag{30}$$

$$\begin{array}{l} Eq2(\mathrm{x}, \mathrm{y}, \mathrm{q}) = -A \rho_l P(\mathrm{x}, \mathrm{q}) + Eo \left(\rho_g(\mathrm{x}, \mathrm{y}, \mathrm{q}) + \frac{V_b C_w}{g} \right) - \\ R_{be} A \rho_l \left(C_l W_s \frac{\partial u_l(\mathrm{x}, \mathrm{y}, \mathrm{q})}{\partial z} + C_{am} W_s \frac{\partial (u_b(\mathrm{x}, \mathrm{y}, \mathrm{q}) - u_l(\mathrm{x}, \mathrm{y}, \mathrm{q}))}{\partial y} \right), \end{array} \tag{31}$$

Constructing the homotopy that satisfy

$$H(\mathrm{U}, \mathrm{q}) = (1 - q) \left(L_1(\mathrm{U}) - L_2(\mathrm{u}_{l,0}) \right) + q(Eq1(\mathrm{U})) = 0, \tag{32}$$

$$H(V, \mathrm{q}) = (1 - q) \left(L_2(V) - L_2(\mathrm{u}_{b,0}) \right) + q(Eq2(V)) = 0, \tag{33}$$

with $q \in (0, 1)$. When $q = 0$, the equation provided an initial guess, and for $q = 1$ the equation generated a required solution. The solution should be of the form

$$U = U_0 + pU_1 + ..., \; V = V_0 + pV_1 + ... \tag{34}$$

Setting $p = 1$ the solution will be

$$U = U_0 + U_1 + ..., \; V = V_0 + V_1 + ... \tag{35}$$

The expressions achieved up to second order were

$$\begin{aligned}
&u_f = K_5 + K_6\, y + K_7 y^2 + K_8 y^3 + K_9 y^4 - K_{10} y^5,\\
&K_5 = -1 - \tfrac{h^2 P}{2} - \tfrac{1}{12}\mathrm{Eoh}^4\mathrm{P}^2 - \tfrac{1}{24}\mathrm{C_{am}Eoh}^4\mathrm{PR_{be}W_s} + \tfrac{1}{24}\mathrm{C_l Eoh}^4\mathrm{PR_{be}W_s} - \tfrac{\mathrm{C_w Eo}^2\mathrm{h}^4\mathrm{PV_b}}{24\mathrm{g}\rho_l},\\
&K_6 = \tfrac{1}{3}\mathrm{Eo}h^2 P - \tfrac{1}{6}C_{am}\mathrm{Eo}h^2 P\mathrm{R}_{be}\mathrm{W_s} - \tfrac{C_w \mathrm{Eo}^2 h^2 \mathrm{V}_b}{3g\rho_l} - \tfrac{3C_w \mathrm{Eo}^2 h^4 PV_b}{40g\rho_l},\\
&K_7 = \tfrac{P}{2},\; K_8 = -\tfrac{\mathrm{Eo}P}{3} + \tfrac{1}{6}\mathrm{C}_{am}\mathrm{Eo}P\mathrm{W}_s + \tfrac{C_w \mathrm{Eo}^2 \mathrm{V}_b}{3g\rho_l} + \tfrac{C_w \mathrm{Eo}^2 h^2 PV_b}{12g\rho_l},\\
&K_9 = \tfrac{\mathrm{Eo}P^2}{12} + \tfrac{1}{24}\mathrm{C}_{am}\mathrm{Eo}P\mathrm{R}_{be}\mathrm{W}_s - \tfrac{1}{24}\mathrm{C}_l\mathrm{Eo}P\mathrm{R}_{be}\mathrm{W}_s + \tfrac{\mathrm{C}_w\mathrm{Eo}^2\mathrm{PV}_b}{24g\rho_l},\\
&K_{10} = \tfrac{C_w \mathrm{Eo}^2 PV_b}{120g\rho_l}
\end{aligned} \tag{36}$$

$$\begin{aligned}
&u_b = 1 + K_{11}\, y + K_{12} y^2 + K_{13} y^3 + K_{14} y^4,\\
&K_{11} = \tfrac{1}{6g\rho_l}\left(3\mathrm{C}_w\mathrm{EoV}_b\left(4 + h^2 P\right)(-2 + C_{am}\mathrm{W}_s) + gP\left(18 + \mathrm{C}_l\mathrm{Eo}h^2\mathrm{R}_{be}\mathrm{W}_s - \mathrm{C}_{am}\left(18 + \mathrm{Eo}h^2\mathrm{R}_{be}\right)\mathrm{W}_s + 6\mathrm{C}_{am}{}^2\mathrm{W}_s{}^2\right)\rho_l\right)\\
&K_{12} = \tfrac{1}{12g^2\rho_l{}^2}\left(3\mathrm{C}_w{}^2\mathrm{Eo}^2\left(4 + h^2 P\right)\mathrm{V}_b{}^2 + \mathrm{C}_w\mathrm{Eo}gP\mathrm{V}_b\left(-18 + \mathrm{Eo}h^2 + 12C_{am}\mathrm{W}_s\right)\rho 1 + 6(C_{am} - \mathrm{C}_l)g^2 P\mathrm{R}_{be}\mathrm{W}_s(-2 + C_{am}\mathrm{W}_s)\rho_l{}^2\right)\\
&\mathrm{K}_{13} = \tfrac{1}{6g^2\rho_l{}^2}\left(\mathrm{Eo}P\left(\mathrm{C}_w{}^2\mathrm{EoV}_b{}^2 + \mathrm{C}_w g\mathrm{V}_b(2 + C_{am}(-1 + \mathrm{R}_{be})\mathrm{W}_s - \mathrm{C}_l\mathrm{R}_{be}\mathrm{W}_s)\rho 1 + (C_{am} - \mathrm{C}_l)g^2\mathrm{R}_{be}\mathrm{W}_s\rho_l{}^2\right)\right)\\
&K_{14} = -\tfrac{\mathrm{C}_w\mathrm{Eo}^2\mathrm{PV}_b(\mathrm{C}_w\mathrm{V}_b + g\rho_l)}{24g^2\rho_l{}^2}.
\end{aligned} \tag{37}$$

Here, $P = \frac{\partial p}{\partial x}$. The flow rate in the fixed frame [51] was defined by

$$Q_f = \int_{-h}^{h} u_f(x,y)dy, \tag{38}$$

$$Q_g = \int_{-h}^{h} u_g(x,y)dy, \tag{39}$$

$$Q = Q_f + Q_g = \int_{-h}^{h} u_f(x,y) + u_g(x,y)dy. \tag{40}$$

Solving the equation to get P in terms of Q and x was

$$\begin{aligned}
&\tfrac{\partial p}{\partial x} = \tfrac{1}{4Eogh^5\rho_l}\left(K_1 \cdot h^5 + K_2 \cdot h^3 - \sqrt{\left(K_1 \cdot h^5 + K_2 \cdot h^3\right)^2 - \left(K_3 h^5 + K_4 h^6\right)}\right)\\
&K_1 = Eo(C_l g R_{be} W_s \rho_l - C_w A Eo V_b - C_{am} g R_{be} W_s \rho_l), K_2 = -10\tfrac{g\rho_l}{A}\\
&K3 = 120\tfrac{Eog^2\rho_l{}^2}{A}(1 - Q), K4 = 240\tfrac{g^2 h\rho_l^2 Eo}{A}
\end{aligned} \tag{41}$$

4. Discussion

To study the impact of numerous parameters, such as volume (V_b), Eotvos number (Eo), added mass coefficient (C_{am}), slip velocity (W_s), lift coefficient (C_l), and model coefficient (C_w), Figures 2–19 were plotted.

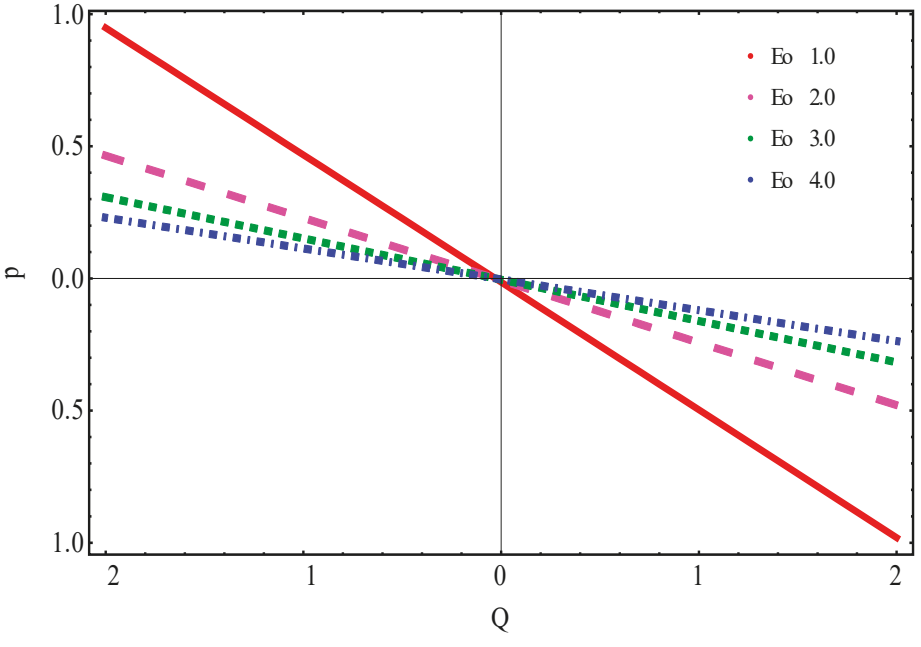

Figure 2. Pressure rise for several values of E_o.

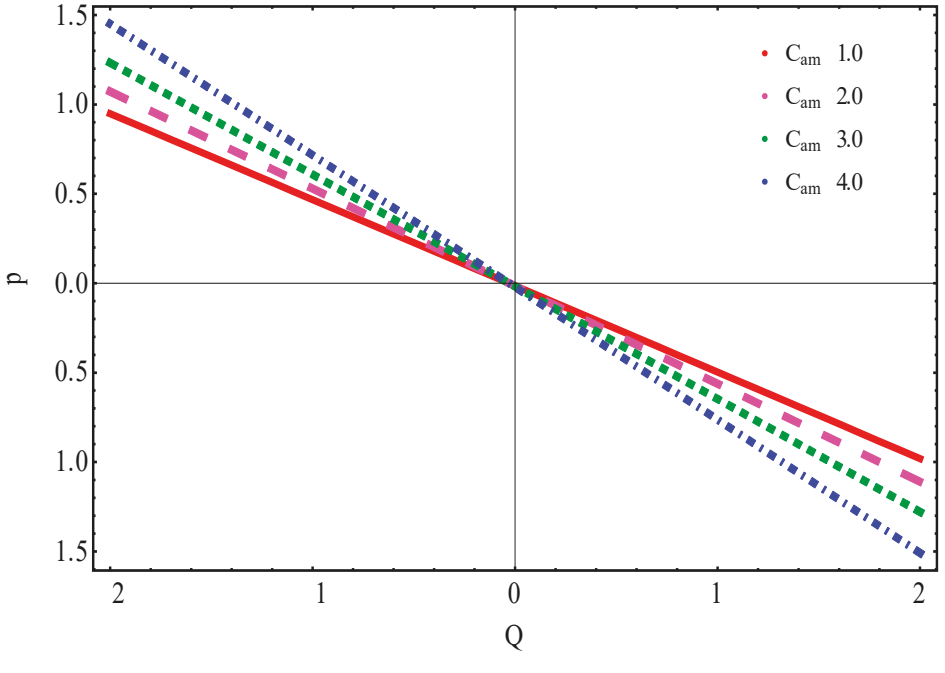

Figure 3. Pressure rise for several values of C_{am}.

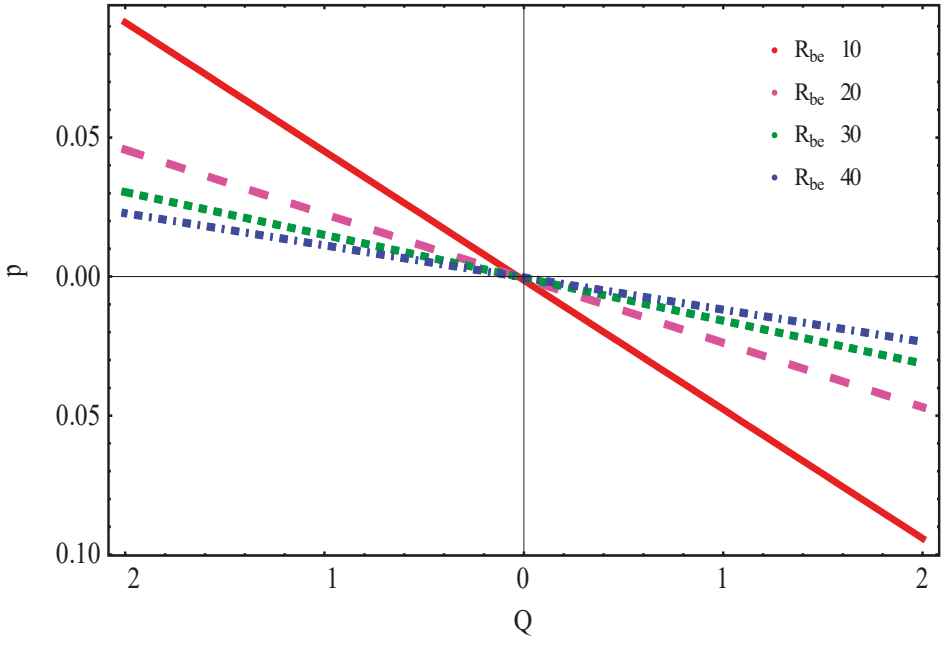

Figure 4. Pressure rise for several values of R_{be}.

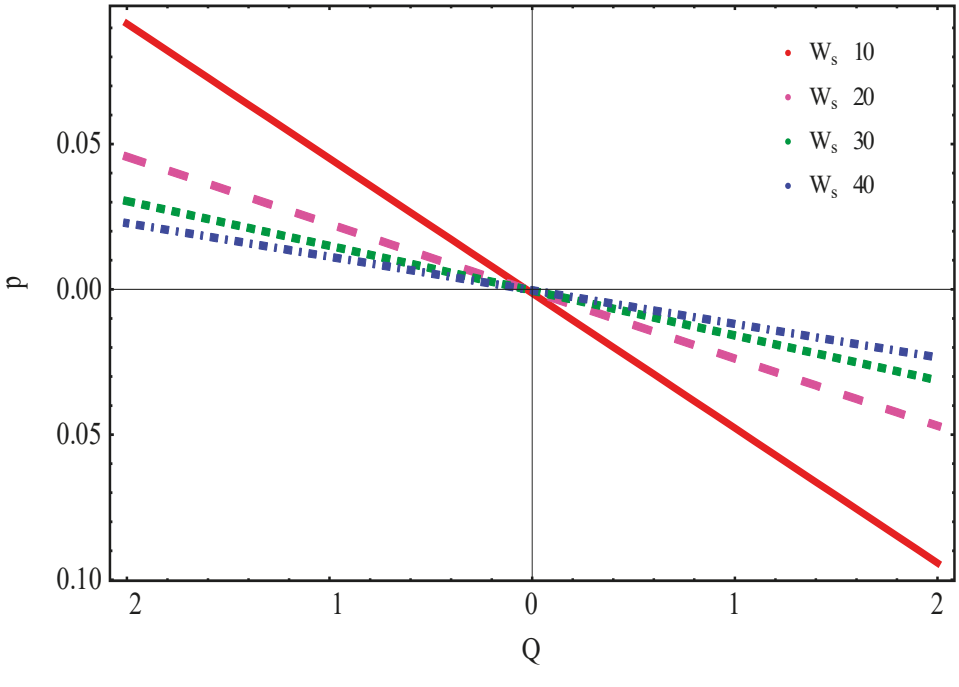

Figure 5. Pressure rise for several values of W_s.

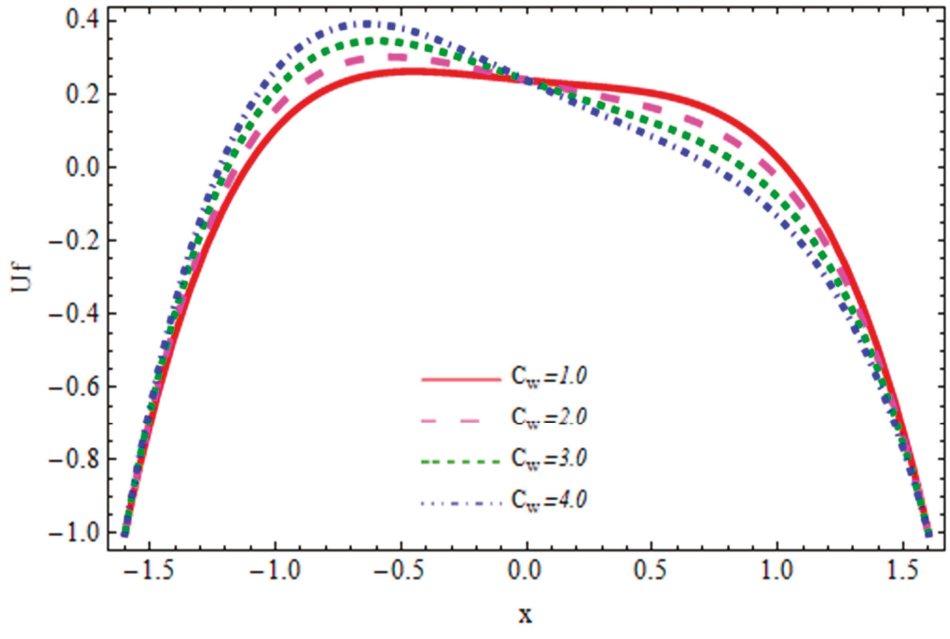

Figure 6. Fluid velocity curves for several values of C_w. $R_{be} = 10$, $V_b = 1.0$, $E_o = 1.0$, $C_{am} = 1.0$, $W_s = 10$, $C_l = 10$.

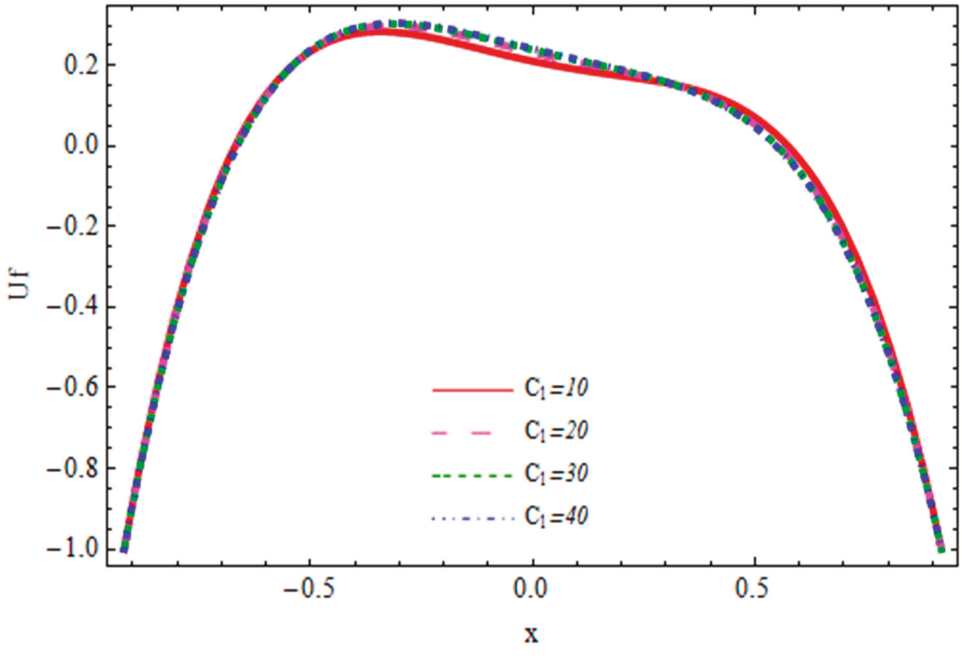

Figure 7. Fluid velocity curves for several values of C_l. $R_{be} = 10$, $V_b = 1.0$, $E_o = 1.0$, $C_{am} = 1.0$, $W_s = 10$, $C_w = 10$.

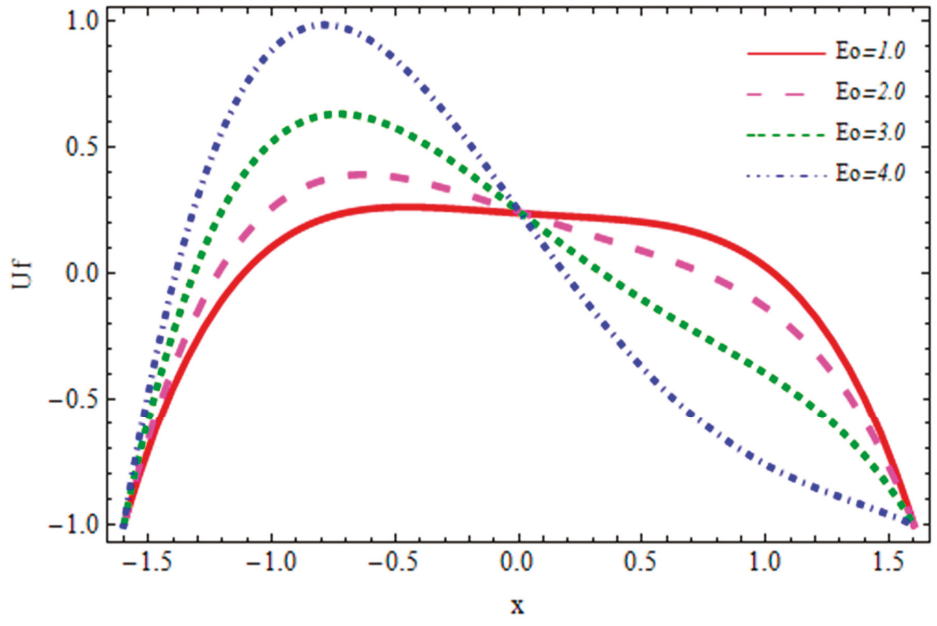

Figure 8. Fluid velocity curves for several values of E_o. $R_{be} = 10$, $V_b = 1.0$, $C_l = 10$, $C_{am} = 1.0$, $W_s = 10$, and $C_w = 1.0$.

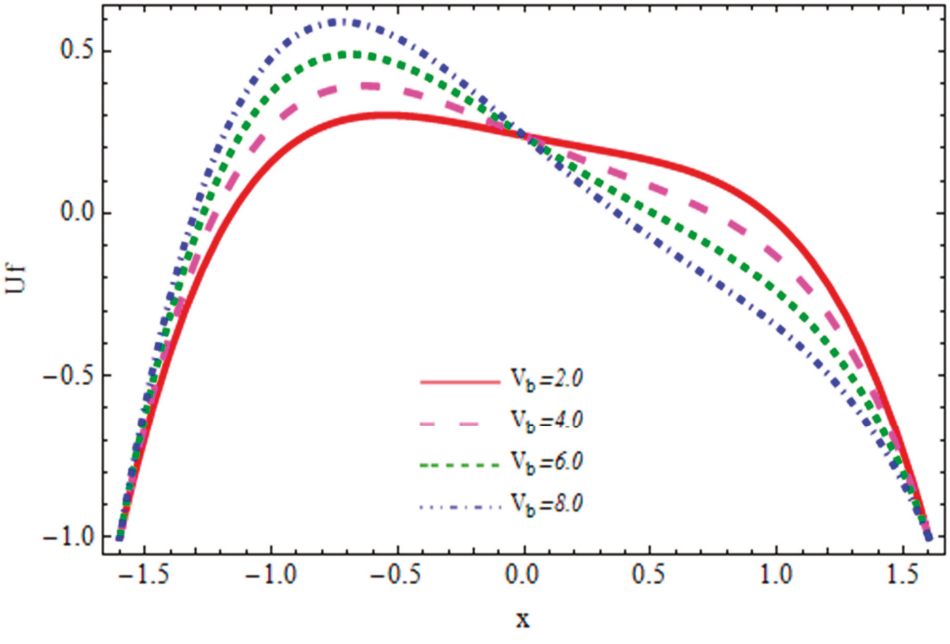

Figure 9. Fluid velocity curves for several values of V_b. $R_{be} = 10$, $E_o = 1.0$, $C_l = 10$, $C_{am} = 1.0$, $W_s = 10$, and $C_w = 1.0$.

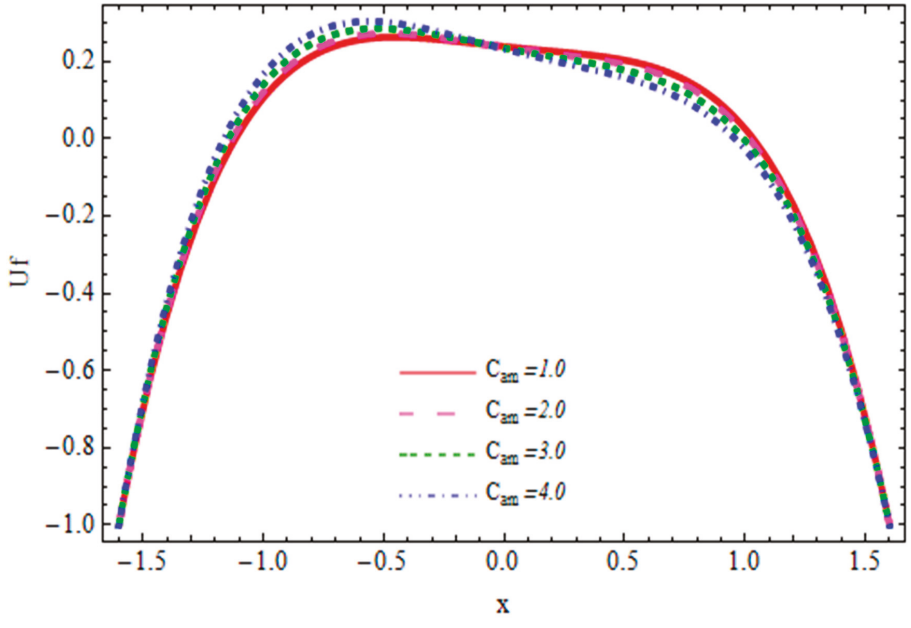

Figure 10. Fluid velocity curves for several values of C_{am}. $R_{be} = 10$, $E_o = 1.0, C_l = 10, V_b = 1.0, W_s = 10$, and $C_w = 1.0$.

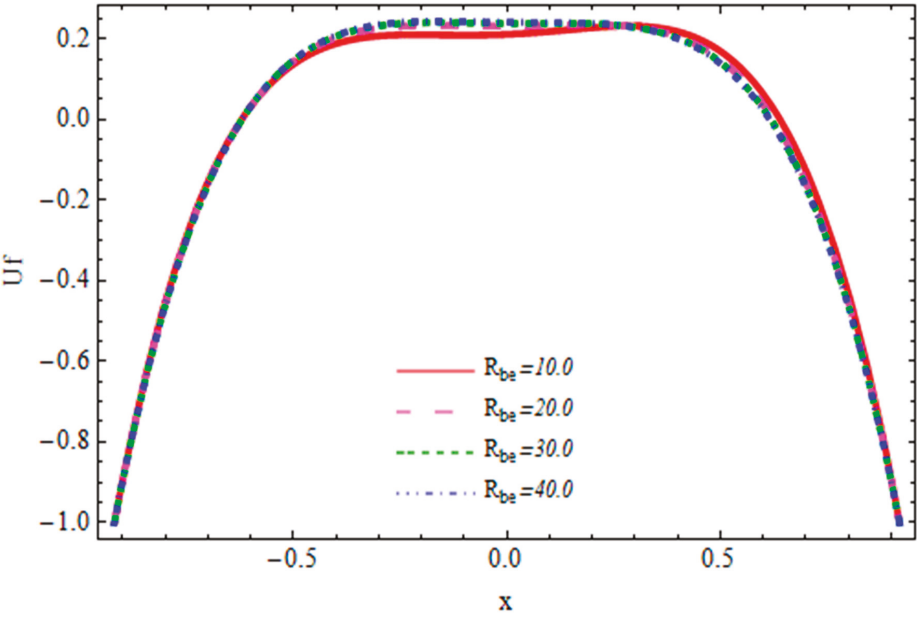

Figure 11. Fluid velocity curves for several values of R_{be}. $C_{am} = 1.0$, $E_o = 1.0$, $C_l = 10, V_b = 1.0, W_s = 10$, and $C_w = 1.0$.

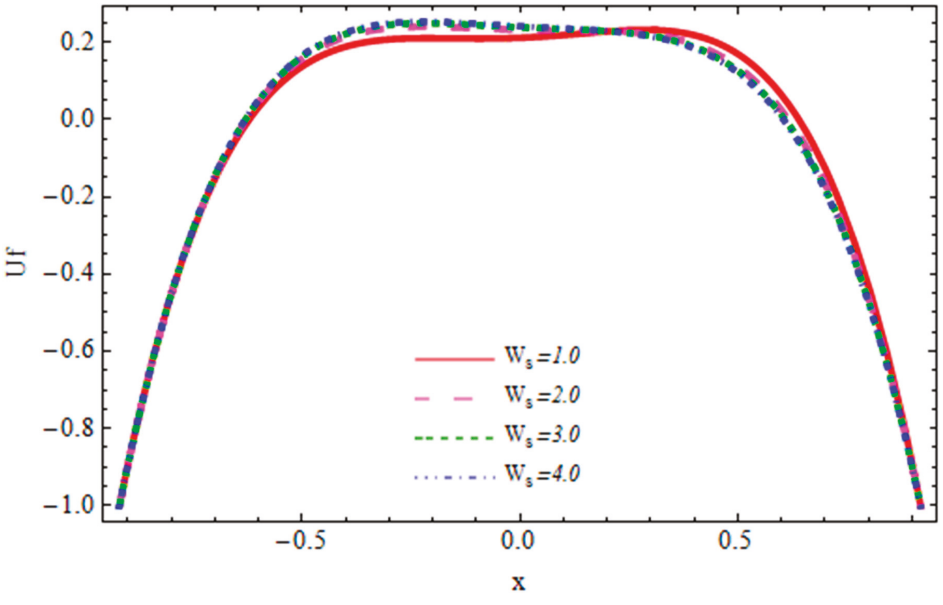

Figure 12. Fluid velocity curves for several values of W_s. $C_{am} = 1.0$, $E_o = 1.0$, $C_l = 10$, $V_b = 1.0$, $R_{be} = 10$, and $C_w = 1.0$.

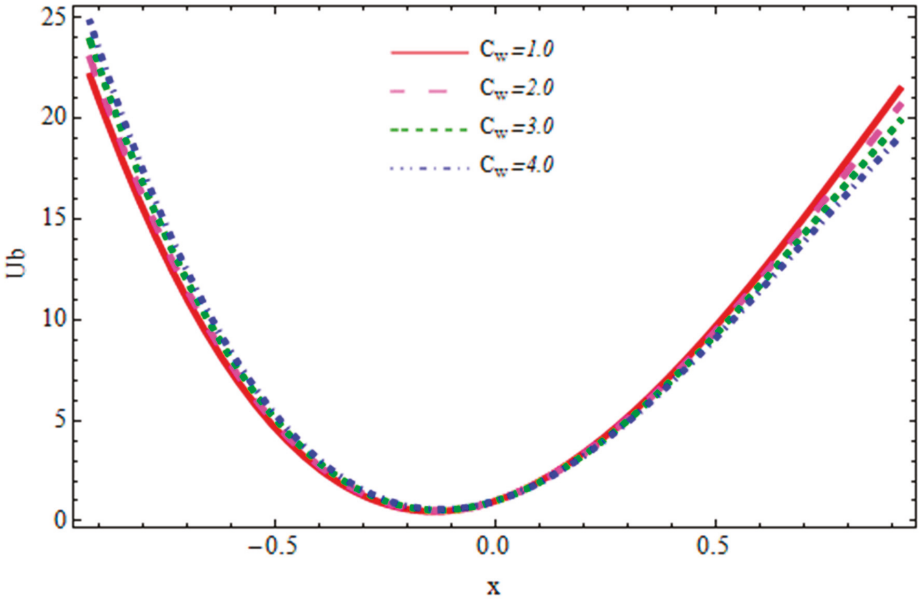

Figure 13. Bubble velocity curves for several values of C_w. $R_{be} = 10$, $V_b = 1.0$, $E_o = 1.0$, $C_{am} = 1.0$, $W_s = 10$, and $C_l = 10$.

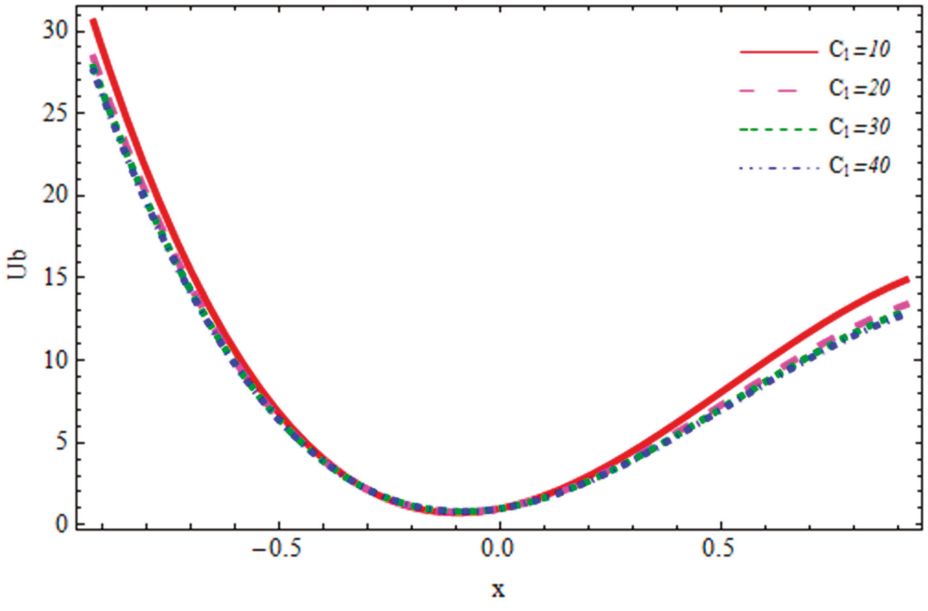

Figure 14. Bubble velocity curves for several values of C_l. $R_{be} = 10$, $V_b = 1.0$, $E_o = 1.0$, $C_{am} = 1.0$, $W_s = 10$, and $C_w = 1.0$.

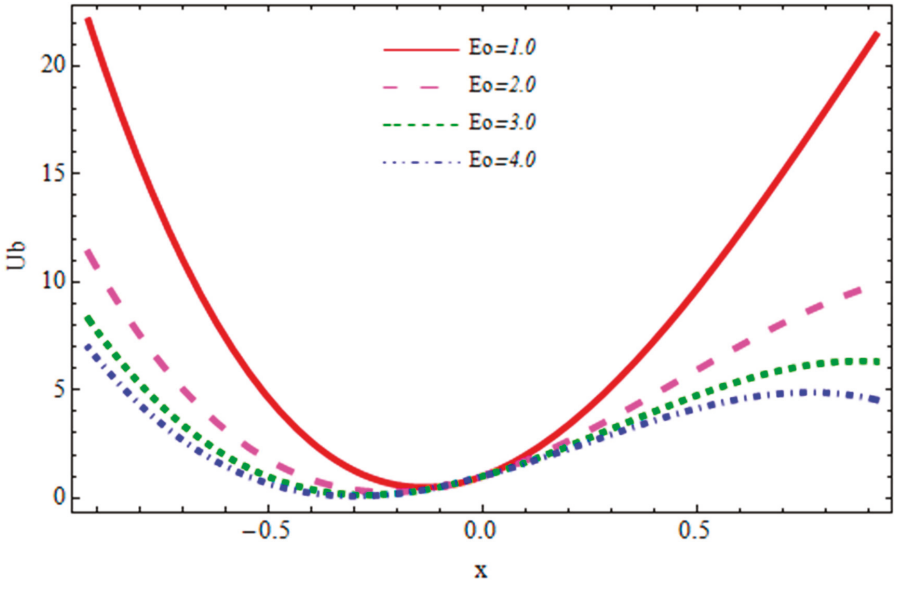

Figure 15. Bubble velocity curves for several values of E_o. $R_{be} = 10$, $V_b = 1.0$, $C_l = 10$, $C_{am} = 1.0$, $W_s = 10$, and $C_w = 1.0$.

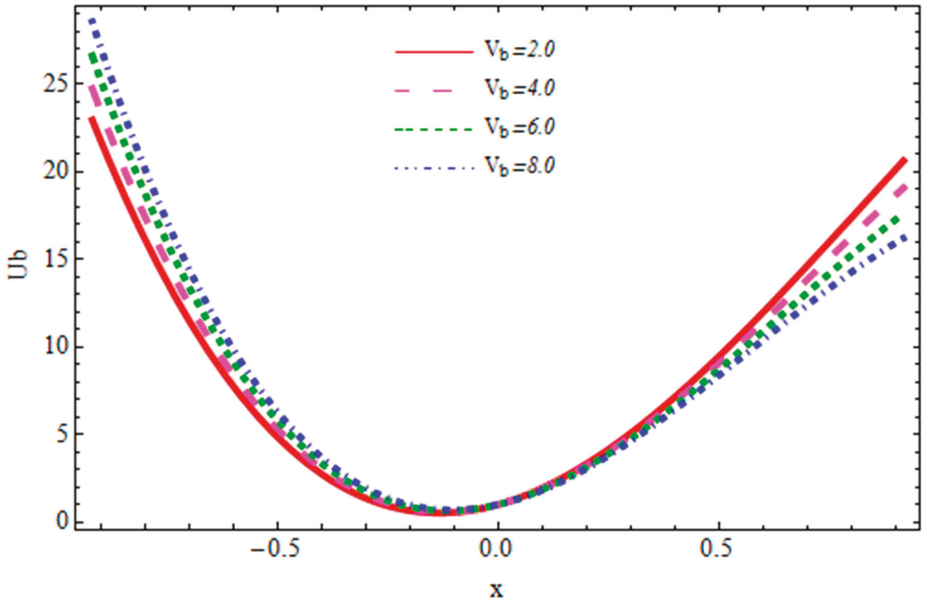

Figure 16. Bubble velocity curves for several values of V_b. $R_{be} = 10$, $E_o = 1.0$, $C_l = 10$, $C_{am} = 1.0$, $W_s = 10$, and $C_w = 1.0$.

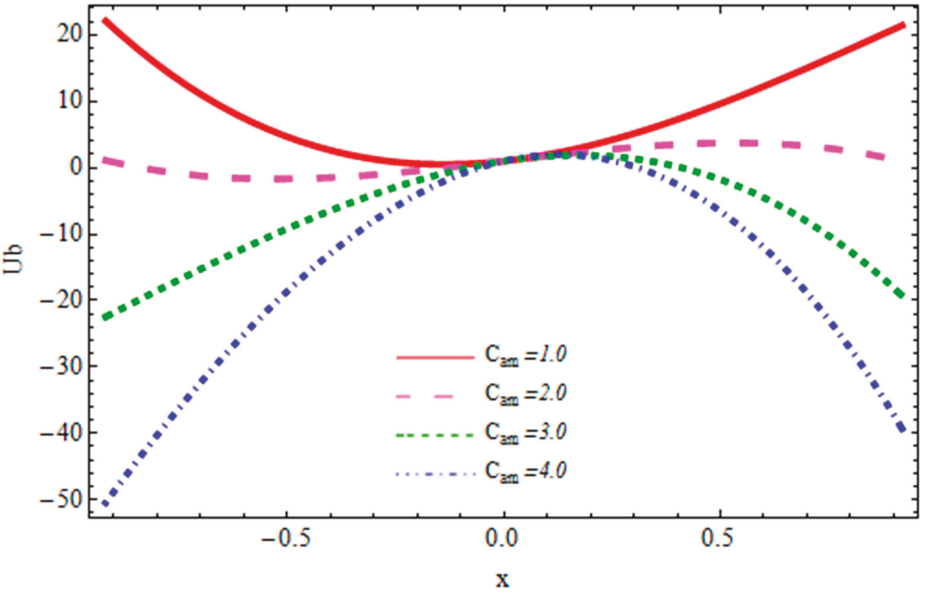

Figure 17. Bubble velocity curves for several values of C_{am}. $R_{be} = 10$, $E_o = 1.0, C_l = 10$, $V_b = 1.0$, $W_s = 10$, and $C_w = 1.0$.

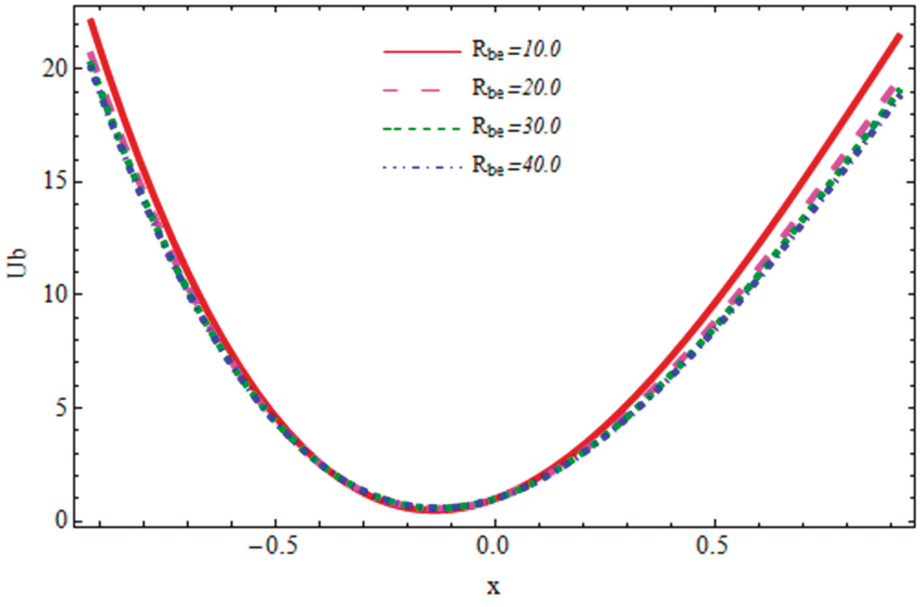

Figure 18. Bubble velocity curves for several values of R_{be}. $C_{am} = 1.0$, $E_o = 1.0, C_l = 10$, $V_b = 1.0$, $W_s = 10$, and $C_w = 1.0$.

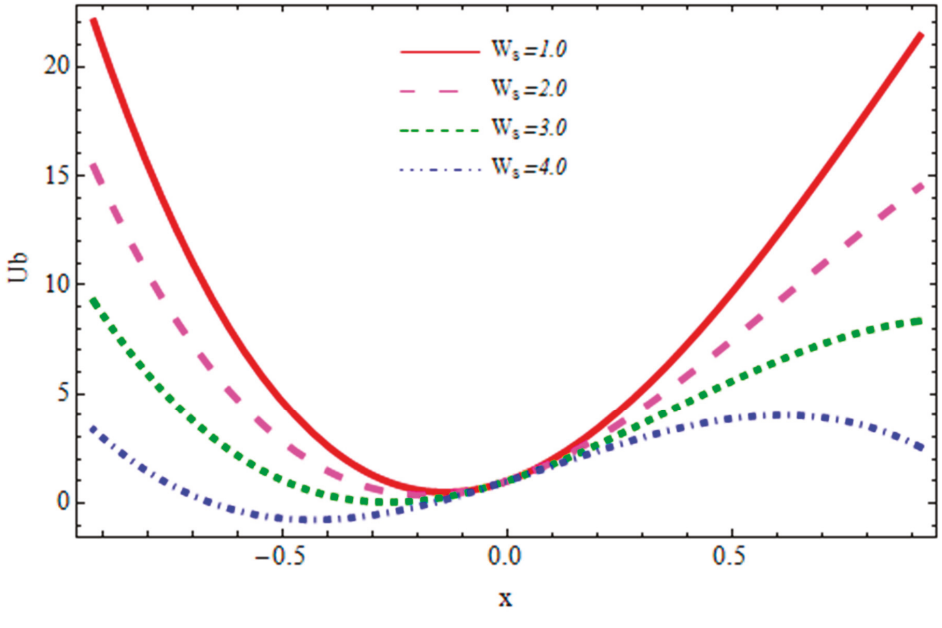

Figure 19. Bubble velocity curves for several values of W_s. $R_{be} = 10, V_b = 1.0$, $E_o = 1.0, C_{am} = 1.0$, $C_w = 10$, and $C_l = 10$.

4.1. Pressure Rising

The flow of biological fluid in peristaltic motion circulating in the human body are investigated in Figures 2–5. The pressure rise was defined as $\Delta P = \int_0^1 dx$. In Figure 2, it can be seen that by increasing the value of the Eotvos number, the pumping rate rose in the co-pumping region ($\Delta p<0$, $Q>0$), whereas the opposite behavior was seen in the retrograde pumping region ($\Delta p>0$, $Q<0$), ($\Delta p<0$, $Q<0$) and the free pumping region. From Figure 3 it is noticeable that the pumping rate dropped ($\Delta p<0$, $Q>0$) in the co-pumping region when we increased the value of the added mass coefficient and the free pumping region ($\Delta p<0$, $Q<0$). In the retrograde pumping region ($\Delta p>0$, $Q<0$) the opposite behavior was noted. It can be seen in Figure 4, that when we increased the value of Reynolds' number R_{be}, the pumping rate rose in the co-pumping region ($\Delta p\langle 0$, $Q\rangle 0$). However, the behavior was the opposite in the retrograde pumping region ($\Delta p>0$, $Q<0$) and in the free pumping region ($\Delta p<0$, $Q<0$). From Figure 5, it is noticeable that there was an upsurge in the pumping rate ($\Delta p<0$, $Q>0$) in the co-pumping region by increasing values of slip velocity and free pumping region ($\Delta p<0$, $Q<0$). In the retrograde pumping region ($\Delta p>0$, $Q<0$) the behavior was quite the opposite.

4.2. Fluid Velocity Profile

The fluid and gas velocities are examined in Figures 6–19. The effect of the model coefficient on the flow velocity was increased when we increased the value of the model coefficient, as seen in Figure 6. It is clear from Figure 7 that with increasing values of the lift coefficient, there was an upturn in the velocity of fluid. From Figure 8, it is found that the behavior of the velocity reduced with the increasing values of the Eotvos number because the Eotvos number is the ratio of gravitation force to surface tension. The larger values of *Eo* represented lesser surface tension and an increase in gravity resulted in the reduction of velocity. In Figure 9, we observed that when we increased the values of volume, the velocity reduced. Due to the rise in bubble volume, drag force increased and, hence, fluid slowed down. The fluid velocity decreased by increasing the value of the added mass coefficient as depicted in Figure 10. The added mass force increased with the rise in bubble volume because it was a drag force due to accelerating bubbles, hence the velocity of the fluid reduced. It is clear from Figure 11 that with rising values of R_{be} the velocity of the fluid was decreased. R_{be} was a parameter related to bubble volume directly, with a constant fluid density it behaved similar to V_b. From Figure 12, it was detected that the behavior of velocity reduced with increasing values of the slip velocity.

4.3. Gas Velocity Profile

The effect of the model coefficient on the flow velocity declined for higher values of the model coefficient, as displayed in Figure 13. It is clear in Figure 14 that with the increase of the lift coefficient, the velocity of fluid went up. From Figure 15, it was perceived that the behavior of the velocity rose with the increasing values of the Eotvos number. It can be perceived from Figure 16, that when we increased the values of volume, a dipping behavior of the velocity was grasped. The fluid velocity increased with increasing values of the added mass coefficient, as portrayed in Figure 17. From Figure 18, it can be concluded that with an increase in the values of R_{be}, the velocity of fluid increases. Figure 19 shows that the velocity rose with the increasing values of the slip velocity.

5. Conclusions

In this investigation, the rheological properties of the liquid influenced the coating to make dynamical behavior nonlinear. Due to nonlinearity, first the constraints of low Reynolds number and long wavelength approximations, after transforming the actual frame into a wave frame, were used, and then the nonlinear coupled equations were solved by a well-known perturbation technique. The physical effects of prominent parameters, namely volume, Eotvos number, mass coefficient, slip velocity, and model coefficients were examined and discussed.

Author Contributions: Conceptualization, R.E.; investigation, N.I.; methodology, A.R.; validation, A.Z.; writing—review and editing, S.M.S. All authors have read and agreed to the published version of the manuscript.

Funding: This research received no external funding.

Conflicts of Interest: The authors declare no conflict of interest.

References

1. Sussman, M.; Smereka, P.; Osher, S. A level set approach for computing solutions to incompressible two-phase flow. *J. Comput. Phys.* **1994**, *114*, 146–159. [CrossRef]
2. Bankoff, S.G. A variable density single-fluid model for two-phase flow with particular reference to steam-water flow. *J. Heat Transfer* **1960**, *82*, 265–270. [CrossRef]
3. Zuber, N.; Findlay, J. Average volumetric concentration in two-phase flow systems. *J. Heat Transfer* **1965**, *87*, 453–468. [CrossRef]
4. Picchi, D.; Poesio, P. A unified model to predict flow pattern transitions in horizontal and slightly inclined two-phase gas/shear-thinning fluid pipe flows. *Int. J. Multiphase Flow* **2016**, *84*, 279–291. [CrossRef]
5. Sato, Y.; Sekoguchi, K. Liquid velocity distribution in two-phase bubble flow. *Int. J. Multiphase Flow* **1975**, *2*, 79–95. [CrossRef]
6. Kuwagi, K.; Ozoe, H. Three-dimensional oscillation of bubbly flow in a vertical cylinder. *Int. J. Multiphase Flow* **1999**, *25*, 175–182. [CrossRef]
7. Picchi, D.; Battiato, I. The impact of pore-scale flow regimes on upscaling of immiscible two-phase flow in porous media. *Water Resources Res.* **2018**, *54*, 6683–6707. [CrossRef]
8. Bonzanini, A.; Picchi, D.; Ferrari, M.; Poesio, P. Shape factors inclusion in a one-dimensional, transient two-fluid model for stratified and slug flow simulations in pipes. In Proceedings of the 12th International Conference on Computational Fluid Dynamics in the Oil & Gas, Metallurgical and Process Industries, Trondheim, Norway, May/June 2017.
9. Sontti, S.G.; Atta, A. Numerical investigation of viscous effect on Taylor bubble formation in co-flow microchannel. *Comp. Aided Chem. Eng.* **2017**, *40*, 1201–1206.
10. Bhatti, M.M.; Zeeshan, A.; Ellahi, R.; Shit, G.C. Mathematical modeling of heat and mass transfer effects on MHD peristaltic propulsion of two-phase flow through a Darcy-Brinkman-Forchheimer porous medium. *Adv. Powder Technol.* **2018**, *29*, 1189–1197. [CrossRef]
11. Haider, S.; Ijaz, N.; Zeeshan, A.; Li, Y.Z. Magneto-hydrodynamics of a solid-liquid two-phase fluid in rotating channel due to peristaltic wavy movement. *Int. J. Numer. Methods Heat Fluid Flow* **2019**. [CrossRef]
12. Depner, T.A.; Rizwan, S.Y.E.D.; Stasi, T.A. Pressure effects on roller pump blood flow during hemodialysis. *ASAIO Trans.* **1990**, *36*, M456-9.
13. Haight, L.G.; Herbst, R.; Winterton, R.F.; Sorenson, J.L. Patent and Trademark Office. US Patent No. 6,234,992, 2001.
14. Tripathi, D.; Sharma, A.; Bég, O.A. Joule heating and buoyancy effects in electro-osmotic peristaltic transport of aqueous nanofluids through a microchannel with complex wave propagation. *Adv. Powder Technol.* **2018**, *29*, 639–653. [CrossRef]
15. Animasaun, I.L.; Pop, I. Numerical exploration of a non-Newtonian Carreau fluid flow driven by catalytic surface reactions on an upper horizontal surface of a paraboloid of revolution, buoyancy and stretching at the free stream. *Alexandria Eng. J.* **2017**, *56*, 647–658. [CrossRef]
16. Angirasa, D.; Peterson, G.P.; Pop, I. Combined heat and mass transfer by natural convection with opposing buoyancy effects in a fluid saturated porous medium. *Int. J. Heat Mass Transfer* **1997**, *40*, 2755–2773. [CrossRef]
17. Rashidi, M.M.; Rostami, B.; Freidoonimehr, N.; Abbasbandy, S. Free convective heat and mass transfer for MHD fluid flow over a permeable vertical stretching sheet in the presence of the radiation and buoyancy effects. *Ain Shams Eng. J.* **2014**, *5*, 901–912. [CrossRef]
18. Masud, U.; Baig, M.I.; Zeeshan, A. Automatization analysis of the extremely sensitive laser-based dual-mode biomedical sensor. *Lasers Med. Sci.* 2020. [CrossRef]
19. Liu, S.; Yang, K.; Wang, Y.; Qu, J.; Liao, C.; He, J.; Li, Z.; Yin, G.; Sun, B.; Zhou, J.; et al. High-sensitivity strin sensor based on in-fiber rectangular air bubble. *Scientif. Rep.* **2015**, *5*, 7624. [CrossRef]

20. Guo, W.; Liu, J.; Liu, J.; Wang, G.; Wang, G.; Huang, M. A Single-Ended Ultra-Thin Spherical Microbubble Based on the Improved Critical-State Pressure-Assisted Arc Discharge Method. *Coatings* **2019**, *9*, 144. [CrossRef]
21. Ellahi, R.; Zeeshan, A.; Hussain, F.; Safaei, M.R. Simulation of cavitation of spherically shaped hydrogen bubbles through a tube nozzle with stenosis. *Int. J. Numerical Methods Heat Fluid Flow* **2020**. [CrossRef]
22. Prakash, J.; Tripathi, D.; Tiwari, A.K.; Sait, S.M.; Ellahi, R. Peristaltic pumping of nanofluids through a tapered channel in a porous environment: Applications in blood flow. *Symmetry* **2019**, *11*, 868. [CrossRef]
23. Hussain, F.; Ellahi, R.; Zeeshan, A.; Vafai, K. Modelling study on heated couple stress fluid peristaltically conveying gold nanoparticles through coaxial tubes: A remedy for gland tumors and arthritis. *J. Mol. Liq.* **2018**, *268*, 149–155. [CrossRef]
24. Zeeshan, A.; Ijaz, N.; Majeed, A. Analysis of magnetohydrodynamics peristaltic transport of hydrogen bubble in water. *Int. J. Hydrogen Energy* **2018**, *43*, 979–985. [CrossRef]
25. Drew, D.A.; Lahey, R.T., Jr. Application of general constitutive principles to the derivation of multidimensional two-phase flow equations. *Int. J. Multiphase Flow* **1979**, *5*, 243–264. [CrossRef]
26. Maskaniyan, M.; Nazari, M.; Rashidi, S.; Mahian, O. Natural convection and entropy generation analysis inside a channel with a porous plate mounted as a cooling system. *Thermal Sci. Eng. Progr.* **2018**, *6*, 186–193. [CrossRef]
27. Zeeshan, A.; Hussain, F.; Ellahi, R.; Vafai, K. A study of gravitational and magnetic effects on coupled stress bi-phase liquid suspended with crystal and Hafnium particles down in steep channel. *J. Mol. Liq.* **2019**, *286*, 110898. [CrossRef]
28. Picchi, D.; Poesio, P. Stability of multiple solutions in inclined gas/shear-thinning fluid stratified pipe flow. *Int. J. Multiphase Flow* **2016**, *84*, 176–187. [CrossRef]
29. Picchi, D.; Barmak, I.; Ullmann, A.; Brauner, N. Stability of stratified two-phase channel flows of Newtonian/non-Newtonian shear-thinning fluids. *Int. J. Multiphase Flow* **2018**, *99*, 111–131. [CrossRef]
30. Suckale, J.; Qin, Z.; Picchi, D.; Keller, T.; Battiato, I. Bi-stability of buoyancy-driven exchange flows in vertical tubes. *J. Fluid Mech.* **2018**, *850*, 525–550. [CrossRef]
31. De Bertodano, M.L.; Lahey, R.T., Jr.; Jones, O.C. Phase distribution in bubbly two-phase flow in vertical ducts. *Int. J. Multiphase Flow* **1994**, *20*, 805–818. [CrossRef]
32. Tyagi, P.; Buwa, V.V. Experimental characterization of dense gas–liquid flow in a bubble column using voidage probes. *Chem. Eng. J.* **2017**, *308*, 912–928. [CrossRef]
33. Hu, D.; Han, G.; Lungu, M.; Huang, Z.; Liao, Z.; Wang, J.; Yang, Y. Experimental investigation of bubble and particle motion behaviors in a gas-solid fluidized bed with side wall liquid spray. *Adv. Powder Technol.* **2017**, *28*, 2306–2316. [CrossRef]
34. Sarafraz, M.M.; Shadloo, M.S.; Tian, Z.; Tlili, I.; Alkanhal, T.A.; Safaei, M.R.; Arjomandi, M. Convective bubbly flow of water in an annular pipe: role of total dissolved solids on heat transfer characteristics and bubble formation. *Water* **2019**, *11*, 1566. [CrossRef]
35. Ellahi, R.; Zeeshan, A.; Hussain, F.; Abbas, T. Study of shiny film coating on multi-fluid flows of a rotating disk suspended with nano-sized silver and gold particles: A comparative analysis. *Coatings* **2018**, *8*, 422. [CrossRef]
36. Khan, Z.; Ur Rasheed, H.; Alharbi, S.O.; Khan, I.; Abbas, T.; Chin, D.L.C. Manufacturing of double layer optical fiber coating using phan-thien-tanner fluid as coating material. *Coatings* **2019**, *9*, 147. [CrossRef]
37. Riaz, A.; A Al-Olayan, H.; Zeeshan, A.; Razaq, A.; Bhatti, M.M. Mass transport with asymmetric peristaltic propulsion coated with synovial fluid. *Coatings* **2018**, *8*, 407. [CrossRef]
38. Bahgat Radwan, A.; Abdullah, A.M.; Mohamed, A.; Al-Maadeed, M.A. New electrospun polystyrene/Al2O3 nanocomposite superhydrophobic coatings; synthesis, characterization, and application. *Coatings* **2018**, *8*, 65. [CrossRef]
39. Benkreira, H.; Ikin, J.B. Dissolution and growth of entrained bubbles when dip coating in a gas under reduced pressure. *Chem. Eng. Sci.* **2010**, *65*, 5821–5829. [CrossRef]
40. Ellahi, R.; Zeeshan, A.; Hussain, F.; Abbas, T. Thermally charged MHD bi-phase flow coatings with non-Newtonian nanofluid and hafnium particles along slippery walls. *Coatings* **2019**, *9*, 300. [CrossRef]
41. Marin, M. A domain of influence theorem for microstretch elastic materials. *Nonl. Analy: Real World Appl.* **2010**, *11*, 3446–3452. [CrossRef]

42. Abd-Elaziz, E.M.; Marin, M.; Othman, M.I. On the effect of Thomson and initial stress in a thermo-porous elastic solid under GN electromagnetic theory. *Symmetry* **2019**, *11*, 413. [CrossRef]
43. Akram, S.; Mekheimer, K.S.; Elmaboud, Y.A. Particulate suspension slip flow induced by peristaltic waves in a rectangular duct: effect of lateral walls. *Alexandria Eng. J.* **2018**, *57*, 407–414. [CrossRef]
44. Ishii, M.; Hibiki, T. *Thermo-Fluid Dynamics of Two-Phase Flow*; Springer: New York, NY, USA, 2010.
45. Sokolichin, A.; Eigenberger, G.; Lapin, A. Simulation of buoyancy driven bubbly flow: established simplifications and open questions. *AIChE J.* **2004**, *50*, 24–45. [CrossRef]
46. Drew, D.A. Mathematical modeling of two-phase flow. *Ann. Rev. Fluid Mech.* **1983**, *15*, 261–291. [CrossRef]
47. Auton, T.R. The lift force on a spherical body in a rotational flow. *J. Fluid Mech.* **1987**, *183*, 199–218. [CrossRef]
48. He, J.H. Linearized perturbation technique and its applications to strongly nonlinear oscillators. *Comp. Math. Appl.* **2003**, *45*, 1–8. [CrossRef]
49. He, J.H. A note on the homotopy perturbation method. *Thermal Sci.* **2010**, *14*, 565–568.
50. Dehghan, M.; Rahmani, Y.; Ganji, D.D.; Saedodin, S.; Valipour, M.S.; Rashidi, S. Convection–radiation heat transfer in solar heat exchangers filled with a porous medium: homotopy perturbation method versus numerical analysis. *Renew. Energy* **2015**, *74*, 448–455. [CrossRef]
51. Ungarish, M. *Hydrodynamics of Suspensions: Fundamentals of Centrifugal and Gravity Separation*; Springer: New York, NY, USA, 2013.

coatings

MDPI

Article

Effects of Double Diffusion Convection on Third Grade Nanofluid through a Curved Compliant Peristaltic Channel

Hanan Alolaiyan [1], Arshad Riaz [2,*], Abdul Razaq [2], Neelam Saleem [3], Ahmed Zeeshan [4] and Muhammad Mubashir Bhatti [5]

1 Department of Mathematics, King Saud University, Riyadh 11451, Saudi Arabia; holayan@ksu.edu.sa
2 Department of Mathematics, Division of Science and Technology, University of Education, Lahore 54770, Pakistan; abdul.razaq@ue.edu.pk
3 Department of Mathematics, University of Sargodha, Sargodha 40100, Pakistan; neelamsaleem34@gmail.com
4 Department of Mathematics & Statistics, Faculty of Basic and Applied Sciences (FBAS), International Islamic University (IIUI), Islamabad 44000, Pakistan; ahmad.zeeshan@iiu.edu.pk
5 College of Mathematics and Systems Science, Shandong University of Science and Technology, Qingdao 266590, China; mmbhatti@sdust.edu.cn
* Correspondence: arshad-riaz@ue.edu.pk

Received: 22 November 2019; Accepted: 26 January 2020; Published: 8 February 2020

Abstract: Nanofluids are potential heat transfer fluids with improved thermophysical properties and heat transfer performance. Double diffusion convection plays an important role in natural processes and technical applications. The effect of double convection by diffusion is not limited to oceanography, but is also evident in geology, astrophysics, and metallurgy. For such a vital role of such factors in applications, the authors have presented the analytical solutions of pumping flow of third-grade nanofluid and described the effects of double diffusion convection through a compliant curved channel. The model used for the third-grade nanofluid includes the presence of Brownian motion and thermophoresis. Additionally, thermal energy expressions suggest regular diffusion and cross-diffusion terms. The governing equations have been constructed for incompressible laminar flow of the non-Newtonian nanofluid along with the assumption of long wavelength. The obtained analytical expressions for velocity, temperature, and nanoparticle concentration have been sketched for various considerable parameters. The effects of regular buoyancy ratio, buoyancy parameter, modified Dufour parameter, and Dufour-solutal Lewis number have been analyzed along with wall properties and pumping characteristics. This study concludes that fluid becomes hotter with increase in regular buoyancy ratio and a modified Dufour parameter, but a decrease in temperature is observed for the buoyancy parameter. Moreover, the solutal concentration is behaving inversely against the Defour-Solutal Lewis number.

Keywords: double diffusion; nanofluid; curved channel; peristaltic pumping; compliant walls; analytical solutions; third grade fluid model

1. Introduction

Nanofluid has served in a number of engineering applications, for example, porous materials [1,2], fuel-cell industry [3], etc. due to its significant increase in the heat-transfer rate compared to conventional engineered fluid [4]. Nanofluids are another class of fluids made by scattering at the nanometer scale materials (nanoparticles, nanofibers, nanotubes, nanowires, nanorods, nanosheets, or nanobeads) in base fluids. As it were, nanofluids are nanoscale colloidal suspensions containing dense nanomaterial. They are two-stage frameworks with one stage (solid stage) into another (fluid stage). It was discovered that nanofluids have improved thermophysical properties, for example,

thermal conductivity, heat-diffusivity, thickness, and convective warmth move coefficients contrasted with those of base fluids, like oil or water. It has indicated incredible potential applications in numerous zones. Some investigations on nanofluid can be cited in [5–9]. Most of the human vessels are flexible in nature and the peristaltic flows exhibit such kind of geometries. The flows of such types are very useful in industry, engineering and medical. These flows have also immense applications in curing cancer cells. Abd Elnaby and Haroun [10] have studied the influence of conformal wall properties on peristaltic movement in a two-dimensional channel and produced the conclusion that the reverse pumping rate increases by rising the wall damping and reduces under the increasing magnitude of the wall elasticity as well as tension, which differs from the model used by Mittra and Prasad [11] and Srivastava and Srivastava [12]. Muthu et al. [13] analyzed the peristaltic movement of a micropolar fluid in circular cylindrical tubes with elastic wall properties. They suggested from the obtained measurement that viscous damping is affecting the mean flow reversal over the elastic surface. Nadeem et al. [14] obtained an analytical solution for pumping transport of Williamson nanofluid through a curved channel with compliant walls and offered the readings under the variation of curvature of the enclosure and heat transfer coefficient. Although a large number of studies on the peristaltic flow of conventional fluids are available, only a few articles have been reported on the peristaltic flow of nanofluids [15–18]. In this regard, Akbar et al. [19] investigated the copper nanoparticles impinging on a curved channel with compliant walls and peristalsis. They acquired analytical solutions for temperature distribution and nanoparticle concentration. Due to the importance of the effects Soret (thermal diffusion) and Dufour (diffusion-Thermo), many investigators have been studied which can be found in [20–22].

Collective forced, free convection (mixed convection stream) is occurred in large number of engineering and industrial processes, like solar central receivers attached to the wind potentials, cooling of electronic equipment through fans and nuclear reactors during emergency shutdown and heat transfers kept in lower-velocity surroundings. Heat and mass transfers accompanying effect on each other also produce a cross-diffusion influence. The temperature difference generates mass transfer which is known as Soret effect, on the other hand, the Dufour effect comes from the heat transfer produced by the concentration gradient. Due to wide range of aplications, peristaltic transport of Jeffrey fluid with double diffusion convection for nanofluids has been analyzed by Akram et al. [23] in the presence of a tilted magnetic field. Exact solutions are obtained for the breaking field of nanoparticles, the concentration field, the temperature field, the flow functions, the pressure gradient and the pressure increase with respect to the axial and transverse coordinates on the length restrictions of longwave and low Reynolds number. Akbar and Habib [24] have discussed the peristaltic flow induced by natural double-diffusive convection to achieve a nanofluid magnetic field analysis in an asymmetric porous channel and obtained solutions in a series of five coupled equations.

The feature of compliant wall in peristaltic flows is a key tool for governing muscle tension. This physical phenomenon has been revealed mathematically by a system of equations which are linked to compliant walls displacement [25,26]. Srinivasvas and Kothandapani [27] have investigated the transfer of heat and mass effects on wavy flow through a porous region experiencing compliant walls. Batti et al. [28] have introduced the wavy phenomenon of Jeffrey fluid in a non-uniform rectangular enclosure with the effects of variable magnetic field. They proposed the attributes of non-uniformity of channel on the flow with the incorporation of lubrication theory and obtained the exact solutions. Bhatt et al. [29] have published the hall current factor on peristaltic analysis of heated particle–fluid combined flow with compliant wall properties through numerical treatment. It is to be mentioned here that the analysis of double diffusion mixed convection for a wavy mechanism of viscoelastic nanofluid in a curved structured geometry has not been yet investigated.

Keeping in mind the importance of above-discussed literature and wide range of applications of mixed convection phenomenon with nanoparticles in peristaltic flows, the authors converted their attention to exploring the theoretical effects of double diffusion over peristaltic flow of nanofluid having third-grade fluid as a base fluid through a curved channel along with wall properties. Most probably, this study will be the best direction to efficiently use the achieved data in experimental

side. The equations of continuity, momentum, energy, and nanoparticle concentration have been modeled through some suitable physical conditions like low values of wavenumber and the Reynolds number. The observing equations are then solved analytically by using a perturbation method. The results are manipulated graphically and discussed in detail. The parameters affecting the phenomenon have been described individually.

2. Mathematical Modeling

The problem is to contemplate the effects of double diffusion on the peristaltic transport of an impermeable third-grade fluid in a compliant curved channel having radius R and uniform width $2d$ bent in the form around the curve with central point having the corresponding components u and v in above-mentioned sides (see Figure 1a). The walls have been structured to become wavy along the flow and have the mathematical expression as described below. The operating equations for the obstacle are [18]

$$\nabla \cdot V = 0, \tag{1}$$

$$\begin{array}{l} \rho_f(\frac{\partial v}{\partial t} + V \cdot \nabla V) = -\nabla p + \mu \nabla \cdot S \\ +(\varphi\rho_p + (1-\varphi)\rho_f(1-\beta_t(T-T_1) - \beta_c(C-C_1)))g, \end{array} \tag{2}$$

$$\begin{array}{rl} (\rho c)_f\Big[\frac{\partial T}{\partial t} + V \cdot \nabla T\Big] & = K\nabla^2 T + (\rho c)_p(D_b \nabla\varphi \cdot \nabla T + \frac{D_t}{T_1}(\nabla T \cdot \nabla T)) \\ & +(\rho c)_f D_{tc}\nabla^2 C, \end{array} \tag{3}$$

$$\frac{\partial C}{\partial t} + V \cdot \nabla C = D_s \nabla^2 C + D_{ct}\nabla^2 T, \tag{4}$$

$$\frac{\partial \varphi}{\partial t} + V \cdot \nabla]\varphi = D_b \nabla^2 \varphi + (\frac{D_t}{T_1})\nabla^2 T, \tag{5}$$

where ρ_f and ρ_p suggest the fluid and particles density in order; c stands for volumetric coefficient; V implies the velocity column; f gives the forcing factor; P delivers the pressure term; e represents the nanoparticles strength; T_0, C_0, and φ_0 describe the contextual representatives of T, C, and φ at lower wall, respectively; and T_1, C_1, and φ_1 are the correspondent at the upper wall; D_b depicts the Brownian diffusion factor; D_t the thermophoretic diffusion coefficient; β_t shows the volumetric volume expansion coefficient for the liquid; β_c is the cognate solutal coefficient; D_{ct} represents the soret diffusivity; D_s reveals the solutal diffusivity; D_{tc} directs the Dufer diffusivity; and S sweeps the fluid model tensor. We use the following dimensional quantities

$$\begin{array}{c} x^* = \frac{x}{\lambda},\ r_1^* = \frac{r_1}{d_1},\ t^* = \frac{ct}{\lambda},\ w_1^* = \frac{w_1}{d_1},\ k^* = \frac{R_1^*}{d_1}, \\ p^* = \frac{d_1^2 p}{c\lambda\mu},\ S_{ij}^* = \frac{d_1 S_{ij}}{c\mu},\ \theta = \frac{T-T_0}{T_1-T_0},\ \phi = \frac{C-C_0}{C_1-C_0}, \\ \gamma = \frac{\varphi-\varphi_0}{\varphi_1-\varphi_0},\ N_c = \frac{\beta_c C_0}{\beta_t T_0},\ N_{r_1} = \frac{\rho_p-\rho_f}{(1-\varphi_0)\rho_f\beta_t T_0},\ \tau = \frac{(\rho c)_p}{(\rho c)_f}, \end{array} \tag{6}$$

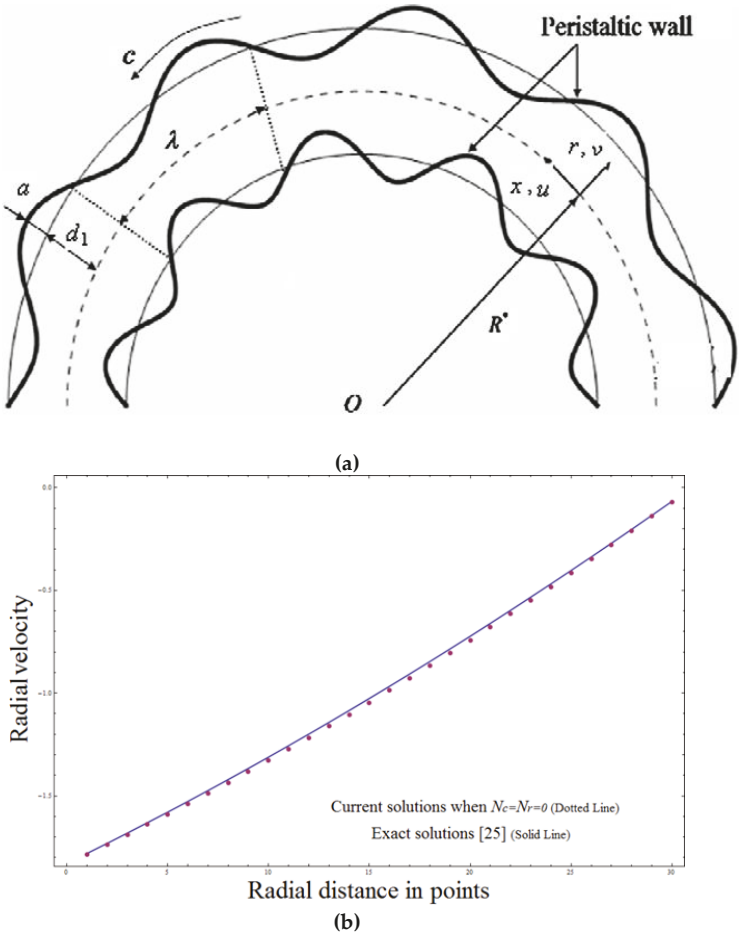

Figure 1. (**a**) Geometry of the problem. (**b**) Comparison of current work with literature [25].

The new discovered parameters like $L_d, N_b,\ N_c,\ N_d,\ N_{r1}$ and N_t take place for a Dufour Lewis number, a Brownian motion parameter, the regular double-diffusive buoyancy ratio, a modified Dufour parameter, the nanofluid buoyancy ratio, and the thermophoresis parameter, accordingly. According to the mechanism of flow, the velocity field is supposed as $\mathbf{V} = (v,\ u)$. After using above defined parameters and applying the conditions of low Reynolds number and long wavelength, the Equations (1)–(5) get the next coming form

$$-\frac{l}{r_1+k_1}\frac{\partial p}{\partial x}+\frac{1}{r_1+k_1}\frac{\partial}{\partial r_1}\Big[(r_1+k_1)^2 S_{r_1 x}\Big]+N_c\gamma+\theta-N_{r_1}\phi=0, \tag{7}$$

$$\left[\frac{\partial^2\theta}{\partial {r_1}^2}+\frac{1}{r_1+k_1}\frac{\partial\theta}{\partial r_1}+N_b\frac{\partial\phi}{\partial r_1}\frac{\partial\theta}{\partial r_1}+N_t\left(\frac{\partial\theta}{\partial r_1}\right)^2+N_d\left[\frac{\partial\gamma}{\partial r_1}+\frac{1}{r_1+k_1}\frac{\partial\gamma}{\partial r_1}\right]\right]=0, \tag{8}$$

$$\left[\frac{\partial^2}{\partial {r_1}^2}+\frac{1}{r_1+k_1}\frac{\partial}{\partial r_1}\right]\phi+\frac{N_t}{N_b}\left[\frac{\partial^2}{\partial {r_1}^2}+\frac{1}{r_1+k_1}\frac{\partial}{\partial r_1}\right]\theta=0, \tag{9}$$

$$\frac{\partial^2\gamma}{\partial r_1^2}+\frac{1}{r_1+k_1}\frac{\partial\gamma}{\partial r_1}+L_d\left[\frac{\partial^2\theta}{\partial r_1^2}+\frac{1}{r_1+k_1}\frac{\partial\theta}{\partial r_1}\right]=0, \tag{10}$$

by using the no-slip boundary conditions and compliant walls phenomenon [22,29]

$$\left.\begin{array}{c} U=c\ at\ r_1=\pm\eta=\pm(d_1+a\sin(\frac{2\pi(X-ct)}{\lambda})) \\ T=T_0\ at\ r_1=-\eta\ and\ T=T_1\ at\ r_1=\eta \\ C=C_0\ at\ r_1=-\eta\ and\ C=C_1\ at\ r_1=\eta \\ \varphi=\varphi_0\ at\ r_1=-\eta\ and\ \varphi=\varphi_1\ at\ r_1=\eta \end{array}\right],$$

After adopting wave frame phenomeno and creeping characteristics of the current ransport, we have the following conclusive form of the above-defined boundary relations in dimensionless format

$$u=0\ \text{at}\ r_1=\pm\eta=\pm(1+\varepsilon\sin 2\pi(x-t)), \tag{11}$$

$$\theta=0,\ \phi=0,\ \gamma=0\ \text{at}\ r_1=-\eta, \tag{12}$$

$$\theta=1,\ \phi=1,\gamma=1\ \text{at}\ r_1=\eta, \tag{13}$$

$$k\left[E_1\frac{\partial^3}{\partial x^3}+E_2\frac{\partial^3}{\partial x\partial t^2}+E_3\frac{\partial^2}{\partial t\partial x}\right]\eta=\frac{\partial p}{\partial x}\ \ at\ \ r_1=\pm\eta, \tag{14}$$

$$S_{r_1x}=-u_{r_1}+\frac{1}{r_1+k_1}u-2\beta(u_{r_1}+\frac{1}{r_1+k_1}u)^3. \tag{15}$$

where E_1, E_2, and E_3 are the representatives of the compliant wall properties [10].

3. Solution of the Problem

We utilize the method of series expansion to solve coupled differential equations which are given before. The deformation equations for u, θ, γ, and ϕ are defined as [30]

$$(1-q)\pounds[u-u_0]+q\left[\begin{array}{c}-\frac{l}{r_1+k_1}\frac{\partial A}{\partial x}+\frac{1}{r_1+k_1}\frac{\partial}{\partial r_1}\left[(r_1+k_1)^2S_{r_1x}\right] \\ +N_cr_1+\theta-N_{r_1}\phi\end{array}\right]=0, \tag{16}$$

$$(1-q)\pounds[\theta-\theta_0]+q\left[\begin{array}{c}\frac{\partial^2\theta}{\partial {r_1}^2}+\frac{1}{r_1+k_1}\frac{\partial\theta}{\partial r_1}+N_b\frac{\partial\varphi}{\partial r_1}\frac{\partial\theta}{\partial r_1}+N_t(\frac{\partial\theta}{\partial r_1})^2 \\ +N_d\left[\frac{\partial\gamma}{\partial r_1}+\frac{1}{r_1+k_1}\frac{\partial\gamma}{\partial r_1}\right]\end{array}\right]=0, \tag{17}$$

$$(1-q)\pounds[\varphi-\varphi_0]+q\left[\left[\frac{\partial^2}{\partial {r_1}^2}+\frac{1}{r_1+k_1}\frac{\partial}{\partial r_1}\right]\varphi+\frac{N_t}{N_b}\left[\frac{\partial^2}{\partial {r_1}^2}+\frac{1}{r_1+k_1}\frac{\partial}{\partial r_1}\right]\theta\right]=0, \tag{18}$$

$$(1-q)\pounds[\gamma-\gamma_0]+q\left[\frac{\partial^2\gamma}{\partial r_1^2}+\frac{1}{r_1+k_1}\frac{\partial\gamma}{\partial r_1}+L_d\left[\frac{\partial^2\theta}{\partial r_1^2}+\frac{1}{r_1+k_1}\frac{\partial\theta}{\partial r_1}\right]\right]=0. \tag{19}$$

where £ is the linear operator which is chosen as £ $=\frac{\partial^2}{\partial r_1^2}$. The initial guesses for u, θ, ϕ, and γ are defined as

$$\begin{array}{c}\overline{u}_0=\frac{1}{2w_1}[-2(k_1+r_1)w\ln(k_1+r_1)+(k_1-w_1)(-r_1+w_1)\ln(k_1-w_1)+ \\ (k_1+w_1)(r_1+w_1)\ln(k_1+w_1)],\end{array} \tag{20}$$

$$\begin{array}{c}\overline{\theta}_0=\frac{1}{2w_1}[-2(k_1+r_1)w_1\ln(k_1+r_1)+(k_1-w_1)(r_1+w_1)\ln(k_1-w_1)+ \\ (k_1+w_1)(r_1+w_1)\ln(k_1+w_1)],\end{array} \tag{21}$$

$$\begin{array}{c}\overline{\varphi}_0=\frac{1}{2w_1}[-2(k_1+r_1)w_1\ln(k_1+r_1)+(k_1-w_1)(-r_1+w_1)\ln(k_1-w_1)+ \\ (k_1+w_1)(r_1+w_1)\ln(k_1+w_1)],\end{array} \tag{22}$$

$$\overline{\gamma}_0 = \frac{1}{2w_1}[-2(k_1+r_1)w\ln(k_1+r_1) + (r_1-w_1)(r_1+w_1)\ln(k_1-w_1) + (k_1+w_1)(r_1+w_1)\ln(k_1+w_1)]. \tag{23}$$

Now we use the following perturbation series for u, θ, γ, and ϕ

$$\left.\begin{array}{l} u = u_0 + qu_1 + \ldots \\ \theta = \theta_0 + q\theta_1 + \ldots \\ \gamma = \gamma_0 + q\gamma_1 + \ldots \\ \varphi = \varphi_0 + q\varphi_1 + \ldots \end{array}\right\}. \tag{24}$$

After using the above series solutions in Equations (11) to (14) and comparing the coefficients of q, we get the same solutions for zeroth order terms and the first order systems found the following solutions

$$u_1 = C_1 + rC_2 - \frac{1}{4\eta^3}\left(\frac{1}{9}r\eta^2(6k(6+k+k\mathrm{N_c}-k\mathrm{N_{r1}}+6A)\eta + 3(3+5k)(1+\mathrm{N_c}-\mathrm{N_{r1}})\right.$$

$$\begin{aligned}
r\eta + (1+\mathrm{N_c}\quad & -\mathrm{N_{r1}})r^2(3+5\eta)) + \tfrac{1}{12(k+r)^3}(768(k+r)^3\beta\eta^3\mathrm{Log}[k+r]^3 \\
& -3\beta(k-\eta)^3(k+\eta)(17k^2+40kr+24r^2-6k\eta-8r\eta+\eta^2)\mathrm{Log}[k-\eta]^3 \\
& +288(k+r)^2\beta\eta^2\mathrm{Log}[k+r]^2(12(k+r)\eta+(k-\eta)(3k+4r-\eta)\mathrm{Log}[k-\eta] \\
& -(k+\eta)(3k+4r+\eta)\mathrm{Log}[k+\eta]) + \beta(k-\eta)^2(k+\eta)\mathrm{Log}[k-\eta]^2(-8(k+r)(31k+36r-5\eta)\eta \\
& +3(3k(17k^2+40kr+24r^2)\eta+(5k+8r)\eta^2-3\eta^3)\mathrm{Log}[k+\eta]) \\
& +(k+\eta)\mathrm{Log}[k+\eta](4(k+r)^2\eta^2(r^3(6+r+\mathrm{N_c}r-\mathrm{N_{r1}}r)+3(1+(1+\mathrm{N_c}-\mathrm{N_{r1}})r^3-30\beta)\eta \\
& +k(-3+90\beta+r^2(6+r+\mathrm{N_c}r-\mathrm{N_{r1}}r+3(1+\mathrm{N_c}-\mathrm{N_{r1}})\eta))) \\
& +\beta(k-\eta)(k+\eta)\mathrm{Log}[k+\eta](-8(k+r)\eta(31k+36r+5\eta) \\
& +3(k+\eta)(17k^2+40kr+24r^2+6k\eta+8r\eta+\eta^2)\mathrm{Log}[k+\eta])) \\
& -(k-\eta)\mathrm{Log}[k-\eta](4(k+r)^2\eta^2(r^3(6+r+\mathrm{N_c}r-\mathrm{N_{r1}}r)-3(1+(1+\mathrm{N_c}-\mathrm{N_{r1}})r^3-30\beta)\eta \\
& +k(-3+90\beta+\ r^2(6+r+\mathrm{N_c}r-\mathrm{N_{r1}}r-3(1+\mathrm{N_c}-\mathrm{N_{r1}})\eta))) \\
& +\beta(k+\eta)\mathrm{Log}[k+\eta](-16(k+r)\eta(31k^2kr+5\eta^2)+3(k+\eta)(3k(17k^2+40kr+24r^2) \\
& -(11k^2+32kr+24r^2)\eta+(5k+8r)\eta^2+3\eta^3)\mathrm{Log}[k+\eta])) \\
& -8(k+r)\eta\mathrm{Log}[k+r]((k+r)^2(6+(k+r)(k^2(1+\mathrm{N_c}-\mathrm{N_{r1}}) \\
& +r(6+\ r+\mathrm{N_c}r-\mathrm{N_{r1}}r)+2k(3+3A+r+\mathrm{N_c}r-\mathrm{N_{r1}}r))-936\beta)\eta^2 \\
& +6\beta(-(k-\eta)^2(7k^2+18k+12r^2-4k\eta-6r\eta+\eta^2)\mathrm{Log}[k-\eta]^2 \\
& +2(k-\eta)\mathrm{Log}[k-\eta](-6(k+r)(5k+6r-\eta)\eta \\
& +(k+\eta)(7k^2+18kr+12r^2-\eta^2)\mathrm{Log}[k+\eta]) \\
& +(k+\eta)\mathrm{Log}[k+\eta](12(k+r)\eta(5k+6r+\eta) \\
& -(k+\eta)(7k^2+18kr+12r^2+4k\eta+6r\eta+\eta^2)\mathrm{Log}[k+\eta])))),
\end{aligned} \tag{25}$$

$$\begin{aligned}
\theta_1 = C_3 + rC_4 \quad & -\tfrac{1}{4\eta^2}(2(k+r)(-1-\mathrm{Nd}+(\mathrm{N_b}+\mathrm{N_t})(k+r))\eta^2\mathrm{Log}[k+r]^2 \\
& +2(k+r)\eta+\mathrm{Log}[k+r](1+\mathrm{N_d}-(\mathrm{N_b}+\mathrm{N_t})(k+r)-2\eta \\
& -(2\mathrm{N_d}+(\mathrm{N_b}+\mathrm{N_t})(k+r))\eta+(-1-\mathrm{N_d}+(\mathrm{N_b}+\mathrm{N_t})(k \\
& +r))((k-\eta)\mathrm{Log}[k-\eta]-(k+\eta)\mathrm{Log}[k+\eta]))+\tfrac{1}{2}r((\mathrm{N_b} \\
& +\mathrm{N_t})r+2(-2(1+\mathrm{N_d})+(\mathrm{N_b}+\mathrm{N_t})(2k+r))\eta+2(4+4\mathrm{N_d} \\
& +2k(\mathrm{N_b}+\mathrm{N_t})+3(\mathrm{N_b}+\mathrm{N_t})r)\eta^2+((k-\eta)\mathrm{Log}[k-\eta]-(k \\
& +\eta)\mathrm{Log}[k+\eta])(-2(\mathrm{N_b}+\mathrm{N_t})r-2(-2(1+\mathrm{N_d})+(\mathrm{N_b} \\
& +\mathrm{N_t})(2k+r))\eta+(\mathrm{N_b}+\mathrm{N_t})r((k-\eta)\mathrm{Log}[k-\eta]-(k \\
& +\eta)\mathrm{Log}[k+\eta])))),
\end{aligned} \tag{26}$$

$$\begin{aligned}
\phi_1 = C_5 + rC_6 \quad & +\tfrac{1}{2N_b\eta}((\mathrm{N_b}+\mathrm{N_t})(k+r)(1-2\eta+\eta\mathrm{Log}[k+r]^2 \\
& +(-k+\eta)\mathrm{Log}[k-\eta]+\ (k+\eta)\mathrm{Log}[k+\eta]-\mathrm{Log}[k+r](1-2\eta \\
& +(-k+\eta)\mathrm{Log}[k-\eta]+(k+\eta)\mathrm{Log}[k+\eta])),
\end{aligned} \tag{27}$$

$$\begin{aligned}\gamma_1 = C_7 + rC_8 \quad & +\tfrac{1}{2\eta}((1+\mathrm{L_d})(k+r)(1-2\eta+\eta\mathrm{Log}[k+r]^2 \\ & +(-k+\eta)\mathrm{Log}[k-\eta]+(k+\eta)\mathrm{Log}[k+\eta]-\mathrm{Log}[k+r](1-2\eta \\ & +(-k+\eta)\mathrm{Log}[k-\eta]+(k+\eta)\mathrm{Log}[k+\eta]))),\end{aligned} \tag{28}$$

where the constants C_i, $i = 1, 2, 3, \ldots 8$ can be found by using boundary conditions are described in the Appendix A and the quantity $A(x,t)$ contains the subsequent expression

$$A(x,t) = -2\varepsilon\pi^3 k\left\{\frac{E_3}{2\pi}\sin(x-t)2\pi - (E_1+E_2)\cos(x-t)2\pi\right\}. \tag{29}$$

Therefore, the final solutions can be composed by injecting above evaluated expressions of u_0, θ_0, ϕ_0, γ_0 and u_1, θ_1, ϕ_1, γ_1 into Equation (24).

The expression for the heat transfer coefficient is described as

$$z = \eta_x \theta_r(\eta). \tag{30}$$

Hence, it is calculated as

$$\begin{aligned}z = \; & -\tfrac{1}{2+2\epsilon\mathrm{Sin}[2\pi(-t+x)]}\pi\epsilon\mathrm{Cos}[2\pi(-t+x)](5(\mathrm{Nb}+\mathrm{Nt})-4C_4+(-1+k)^2(\mathrm{Nb} \\ & +\mathrm{Nt})\mathrm{Log}[-1+k+\epsilon\mathrm{Sin}[2\pi(t-x)]]^2 \\ & +2(-1+k)\mathrm{Log}[-1+k+\epsilon\mathrm{Sin}[2\pi(t-x)]](-\mathrm{Nb}-\mathrm{Nt} \\ & +(-1+\mathrm{Nb}+k\mathrm{Nb}-\mathrm{Nd}+\mathrm{Nt}+k\mathrm{Nt})\mathrm{Log}[1+k+\epsilon\mathrm{Sin}[2\pi(-t+x)]])+\mathrm{Log}[1+k \\ & +\epsilon\mathrm{Sin}[2\pi(-t+x)]](-2(3+\mathrm{Nb}+k\mathrm{Nb}+3\mathrm{Nd}+\mathrm{Nt}+k\mathrm{Nt})+(\mathrm{Nb}+\mathrm{Nt}-3k^2\ (\mathrm{Nb} \\ & +\mathrm{Nt})-2k(-1+\mathrm{Nb}-\mathrm{Nd}+\mathrm{Nt}))\mathrm{Log}[1+k+\epsilon\mathrm{Sin}[\,2\pi(-t+x)]])+\epsilon\mathrm{Sin}[2\pi(-t \\ & +x)]\ (2(4(\mathrm{Nb}+\mathrm{Nt})-2C[2]-(-1+k)(\mathrm{Nb}+\mathrm{Nt})\mathrm{Log}[-1+k+\epsilon\mathrm{Sin}[2\pi(t-x)]]^2 \\ & -(4+\mathrm{Nb}+4\mathrm{Nd}+\mathrm{Nt})\mathrm{Log}[1+k+\epsilon\mathrm{Sin}[\,2\pi(-t+x)]]-(-1+k)(\mathrm{Nb}+\mathrm{Nt})\mathrm{Log}[1+k \\ & +\epsilon\mathrm{Sin}[2\pi(-t+x)]]^2+\mathrm{Log}[-1+k+\epsilon\mathrm{Sin}[\,2\pi(t-x)]](\mathrm{Nb}+\mathrm{Nt}+(1-2\mathrm{Nb}+\mathrm{Nd} \\ & -2\mathrm{Nt})\mathrm{Log}[1+k+\epsilon\mathrm{Sin}[\,2\pi(-t+x)]]))+(\mathrm{Nb}+\mathrm{Nt})\epsilon(4+(\mathrm{Log}[-1+k+\epsilon\mathrm{Sin}[\,2\pi(t \\ & -x)]]-\mathrm{Log}[1+k+\epsilon\mathrm{Sin}[2\pi(-t+x)]])^2)\mathrm{Sin}[2\pi(-t+x)])).\end{aligned}$$

4. Graphical Results and Discussion

The above analysis composes the effects of double diffusion on pumping flow of non-Newtonian (third order) fluid travelling through a curved channel and also described the wall properties. The formulation is carried out by introducing non-dimensional parameters and imposing the features of the lubrication approach. After achieving system of four nonlinear coupled differential equations, exact analytical solutions have been found by an appropriate analytical highly converging technique (HPM). In this segment of the study, we have included graphical treatment of various obtained quantities like comparison graph, velocity, temperature, solutal concentration, and nanoparticle phenomenon. Figure 1b is included just to validate the present results by comparing analytical solution with exact solution [25]. This graph contains the data of velocity obtained in the current study by neglecting the effects of double diffusion convection ($N_c = N_{r1} = 0$) and the data of [25]. One can find the reading that the current analytical solutions are very much in agreement with the exact solutions found by Hayat et al. [25]. In Figure 2, the velocity is displayed under the variation of the regular buoyancy ratio N_c. We conclude from this figure that the velocity of fluid is increasing with increasing quantity of N_c and become highest in the middle part of the channel. This result stresses that N_c being the ration of concentration variance to temperature gradient, when gets increased meant that concentration change is higher than the temperature difference which is actually causing the fluid to travel with greater intensity. From Figure 3, it is very clear that the velocity is showing totally opposite behavior against the buoyancy parameter N_{r1} as compared to N_c which is also prominent physically that when we increase the density of particles the fluid travels slowly. Figure 4 is portrayed to find the influence of complaint wall parameters E_1, E_2, E_3 and it can be concluded here that the velocity of the nanofluid is minimized with the complaint wall parameters. In Figure 5, the temperature profile

θ is portrayed to measure the influence of the regular buoyancy parameter N_b. According to this graph, it is noticed that the temperature is increasing with the increasing value of N_b and the highest temperature is observed at $r = 0.2$, which is near the centerline of channel. Figure 6 is showing the effect of a modified Dufour parameter N_d on temperature profile θ. This graph is emphasized that N_d is lowering the temperature throughout the geometry which represents the cooling effects due to change in nanoparticles concentration. The temperature profile θ for various values of thermophoresis parameter N_t is plotted in Figure 7. According to this figure, we can analyze that as we increase the magnitude of N_t, the temperature θ is also increased and gets higher magnitude in the central region of the channel. Figures 8 and 9 highlights the variation of nanoparticle concentration ϕ when there is an increase the values of Brownian motion parameter N_b and thermophoresis parameter N_t. It can be supposed from these figures that nanoparticle concentration is increasing with N_b but decreasing with N_t. It is also observed that nanoparticles are less in numbers in the central part and minimum quantity is at the position $r = h$. Figures 10 and 11 are drawn to manage the behavior of curvature parameter k and Defour-Solutal Lewis number L_d on solutal concentration. Figure 10 depicts that γ is increasing with the increasing values of k. It means that as we use the curved channel with large curvature, the solutal concentration will get increased. On the other hand, Figure 11 emphasizes that γ is decreasing with L_d and quite opposite behaviour is observed in this figure as we have seen from Figure 10. Figures 12–14 are captured to visualize the effects the N_b, N_d, and N_t respectively on the heat transfer coefficient z. It is found from these figures that heat transfer is decreasing with N_b and N_t on the left and right sides but increasing in the centre. It is depicted here that N_d reflects the opposite behaviour on heat transfer. It is also noted from Figures 12–14 that amount of heat transfer is maximum at the center of the channel.

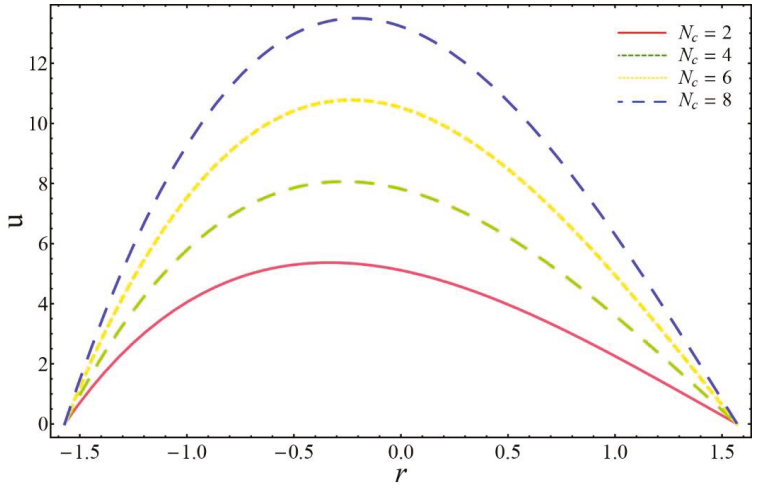

Figure 2. Alteration of N_c on u when $x = 0.2$; $t = 0$; $Q = 10$; $\beta = 0.1$; $\epsilon = 0.6$; $N_{r1} = 2$; $k = 2$; $E_1 = 0.1$; $E_2 = 0.1$; $E_3 = 0.9$.

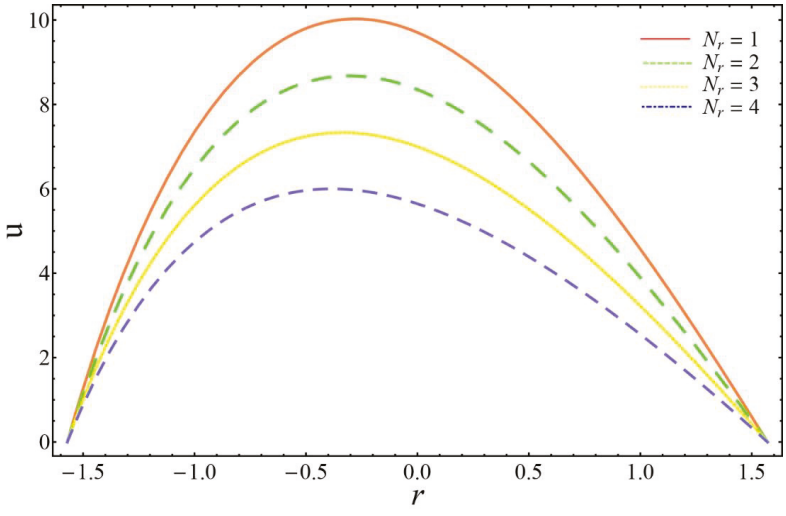

Figure 3. Alteration of N_{r1} on u when $x = 0.2$; $t = 0$; $Q = 10$; $\beta = 0.1$; $\epsilon = 0.6$; $N_c = 2$; $k = 2$; $E_1 = 0.1$; $E_2 = 0.1$; $E_3 = 0.9$.

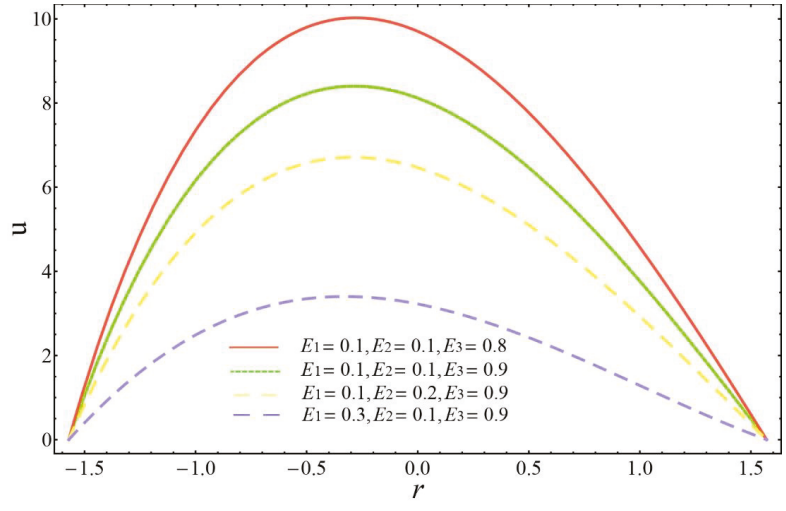

Figure 4. Variation of complaint wall parameters on u when $\epsilon = 0.6$; $\beta = 0.01$; $k = 2$; $x = 0.2$; $t = 0$; $N_c = 2$; $N_{r1} = 1$; $Q = 10$.

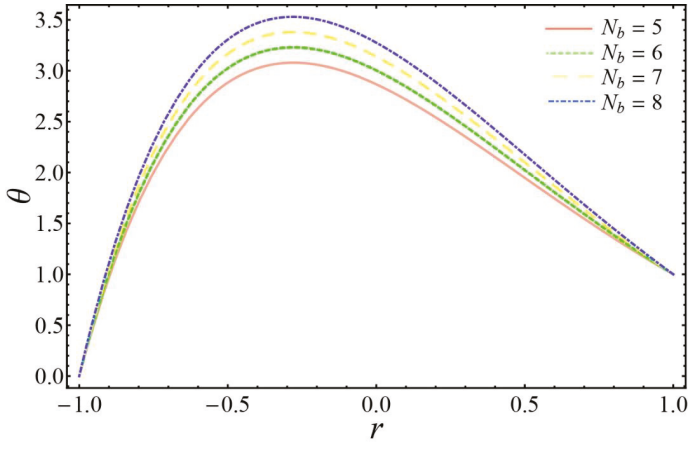

Figure 5. Alteration of N_b on θ when $x = 0.5$; $t = 0$; $Q = 10$; $\beta = 0.2$; $\epsilon = 0.6$; $N_t = 5$; $N_d = 2$; $k = 2$.

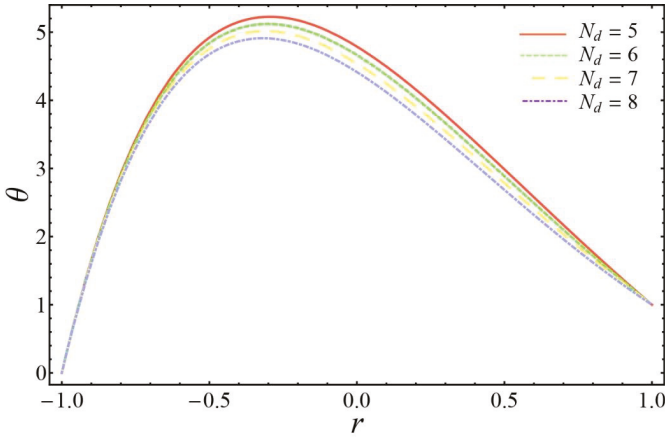

Figure 6. Alteration of N_d on θ when $x = 0.5$; $t = 0$; $Q = 10$; $\beta = 0.2$; $\epsilon = 0.6$; $N_t = 5$; $N_b = 2$; $k = 2$.

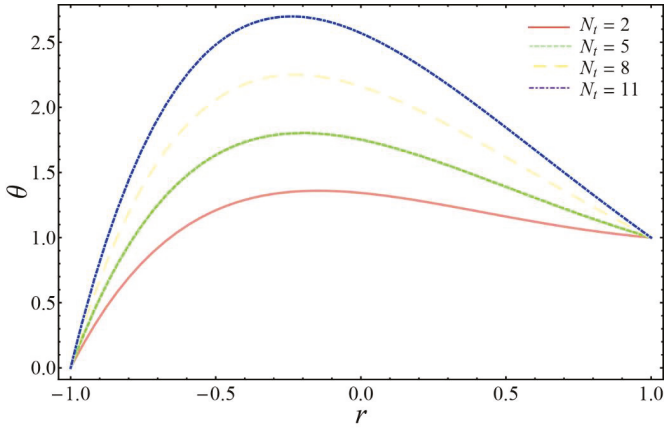

Figure 7. Alteration of N_t on θ when $x = 0.5$; $t = 0$; $Q = 10$; $\beta = 0.2$; $\epsilon = 0.2$; $N_b = 5$; $N_d = 2$; $k = 2$.

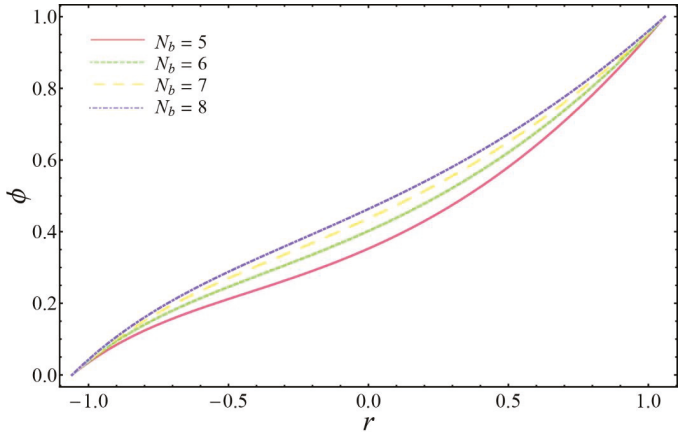

Figure 8. Alteration of N_b on ϕ when $x = 0.1$; $t = 0$; $Q = 10$; $\beta = 0.2$; $\epsilon = 0.1$; $N_t = 10$; $N_d = 2$; $k = 2$.

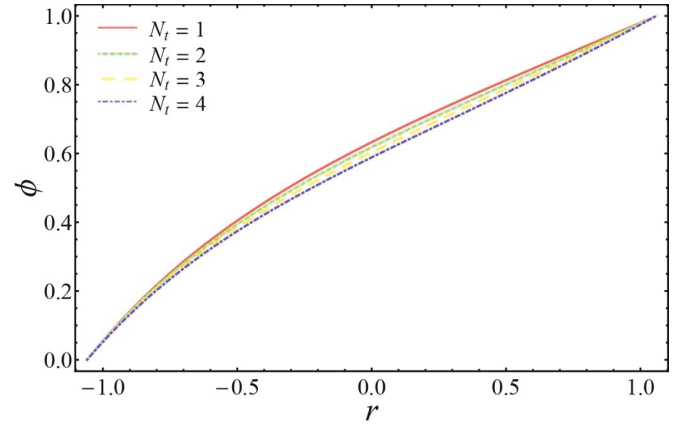

Figure 9. Alteration of N_t on ϕ when $x = 0.1$; $t = 0$; $Q = 10$; $\beta = 0.2$; $\epsilon = 0.1$; $N_b = 10$; $N_d = 2$; $k = 2$.

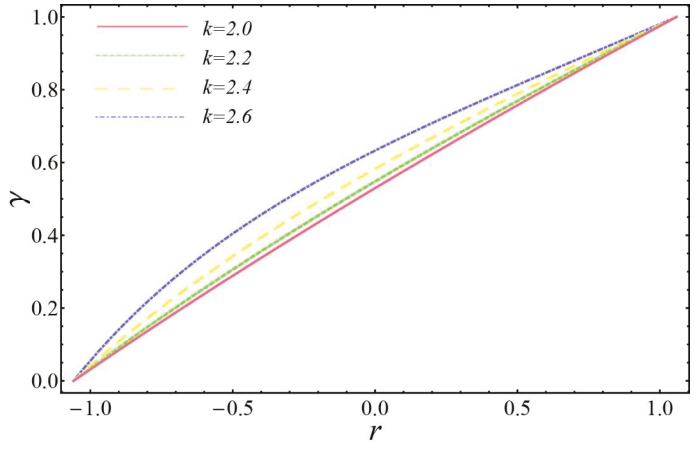

Figure 10. Alteration of k on γ when $x = 0.1$; $t = 0$; $Q = 10$; $\beta = 0.2$; $\epsilon = 0.1$; $N_b = 2$; $N_d = 1$; $L_d = 0.1$.

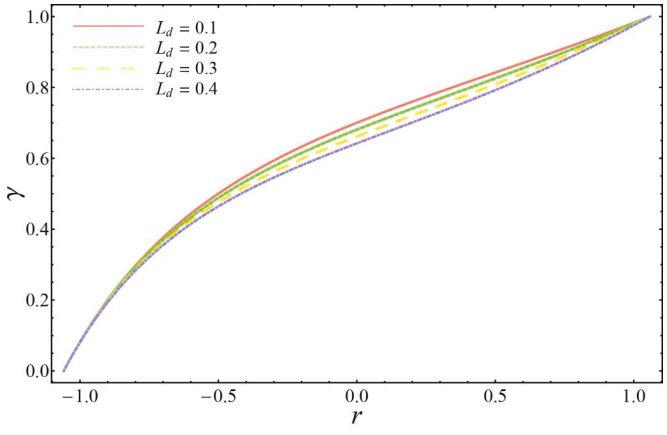

Figure 11. Alteration of L_d on γ when $x = 0.1$; $t = 0$; $Q = 10$; $\beta = 0.2$; $\epsilon = 0.1$; $N_b = 2$; $N_d = 1$; $k = 1.5$.

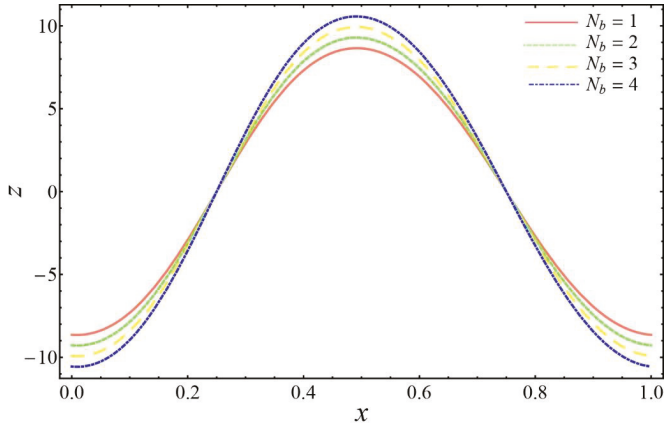

Figure 12. Alteration of N_b on z when $t = 0$; $Q = 10$; $\beta = 0.2$; $\epsilon = 0.2$; $N_t = 15$; $N_d = 2$; $k = 2$.

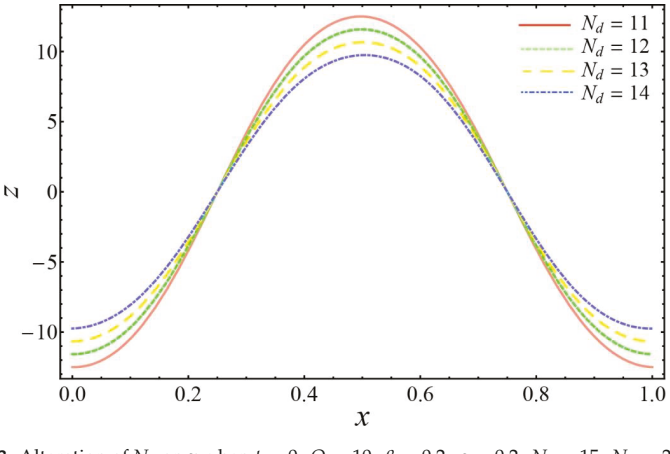

Figure 13. Alteration of N_d on z when $t = 0$; $Q = 10$; $\beta = 0.2$; $\epsilon = 0.2$; $N_t = 15$; $N_b = 20$; $k = 2$.

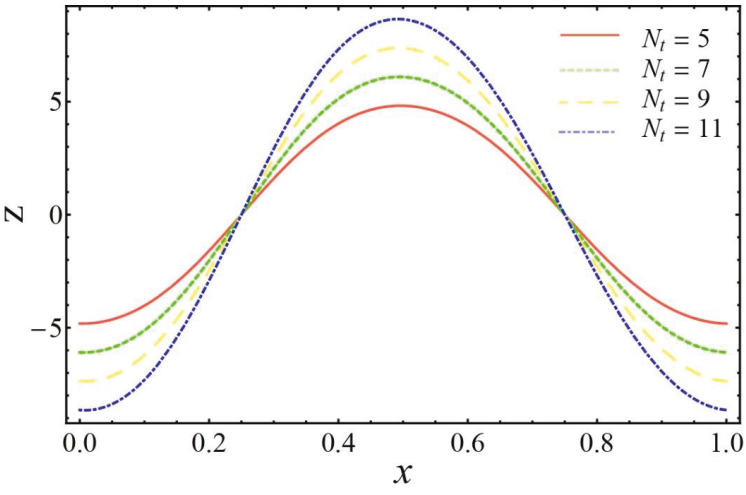

Figure 14. Alteration of N_t on z when $t = 0$; $Q = 10$; $\beta = 0.2$; $\epsilon = 0.2$; $N_b = 5$; $N_d = 2$; $k = 2$.

5. Conclusions

In the third chapter, we have presented the effect of double diffusion on the peristaltic flow of nanofluid through a curved channel. The governing equations for velocity, temperature, nanoparticles, and solutal concentration have been modified and illustrated under the suppositions of low Reynolds number and low wavelength. The solutions have been carried out by HPM. In the last section, graphical results have been sketched through figures. The major points of the study are given below:

- The velocity profile increases with an increasing regular buoyancy ratio, but buoyancy parameter and compliant walls give opposite effects on velocity.
- The temperature increases with the Brownian motion parameter and thermophoresis parameter, but decreases with the buoyancy parameter. It is also noticed that the maximum temperature is observed in the center of the channel.
- The nanoparticles increase with the variation of regular buoyancy parameter, but decrease with increasing thermophoresis parameter. Moreover, it is concluded that in the center, there are fewer numbers of nanoparticles as compared to the left side boundary.
- It is observed that as an increase in the curvature of the channel, solutal concentration is increased, but reveals opposite behavior with Defour-Solutal Lewis number.
- It is found that heat is transferred in large amounts while increasing a modified Dufour parameter, but the less heat transfer is observed in case of Brownian motion parameter and thermophoresis parameter.
- It is disclosed that current analytical study is in line with the study [25] having exact solutions by skipping the terms of double diffusion.

Author Contributions: Conceptualization, H.A.; methodology, N.S.; software, A.R. (Abdul Razaq).; validation, A.Z. & M.M.B.; formal analysis and investigation, A.R. (Arshad Riaz); writing—original draft preparation, N.S.; writing—review and editing, H.A.; funding acquisition, H.A. All authors have read and agreed to the published version of the manuscript.

Funding: The authors extend their appreciation to the Deanship of Scientific Research at King Saud University for funding this work through research group No (RG- 1440-114).

Conflicts of Interest: The authors declare no conflict of interest.

Appendix A

$$C_1 = -\frac{1}{48\eta^3}\quad (-4(3+5k)(1+N_c-N_r)\eta^5+3\beta(17k^3-96k^2\eta+51k\eta^2-32\eta^3)\mathrm{Log}[k-\eta]^3 +\beta\mathrm{Log}[k-\eta]^2(8\eta(31k^2-216k\eta+31\eta^2)-9(17k^3-32k^2\eta-77k\eta^2+32\eta^3)\mathrm{Log}[k+\eta]) +\mathrm{Log}[k-\eta](4\eta^2(3k(-1+30\beta)+(6+k^2(6+k+kN_c-kN_r+6A)\ -936\beta)\eta -3k(2+k+kN_c-kN_r+2A)\eta^2+2(1+N_c-N_r)\eta^4)+\beta\mathrm{Log}[k+\eta](-496k^2\eta +2960\eta^3+9(17k^3+32k^2\eta-77k\eta^2-32\eta^3)\mathrm{Log}[k+\eta]))+\mathrm{Log}[k+\eta](4\eta^2(k(3 -90\beta)\ +(6+k^2(6+k+kN_c-kN_r+6A)-936\beta)\eta+3k(2+k+kN_c-kN_r +2A)\eta^2-2(1+N_c-N_r)\eta^4)+\beta\mathrm{Log}[k+\eta](8\eta(31k^2+216k\eta+31\eta^2)-3(17k^3 +96k^2\eta+51k\eta^2+32\eta^3)\mathrm{Log}[k+\eta])))),$$

$$C_2 = \frac{1}{144\eta^3}\quad (4\eta^3(6k^2(1+N_c-N_r)+36k(1+A)+(1+N_c-N_r)\eta(3+5\eta))+\ 3(-45\beta\ (3k^2+\eta^2)\mathrm{Log}[k-\eta]^3 +\beta\mathrm{Log}[k-\eta]^2(-1232k\eta+135(3k^2+\eta^2)\mathrm{Log}[k+\eta])+\mathrm{Log}[k-\eta](4\eta^2(3 -846\beta+(k-\eta)(k(6+k+kN_c-kN_r+6A)-2(3+k(1+N_c-N_r))\eta))+\ \beta\mathrm{Log}[k+\eta](2464k\eta -135(3k^2+\eta^2)\mathrm{Log}[k+\eta]))+\mathrm{Log}[k+\eta](4\eta^2(-3+846\beta-(k+\eta)(6\eta+k(6+k+kN_c-kN_r +6A+2(1+N_c-N_r)\eta)))+\beta\mathrm{Log}[k+\eta](-1232k\eta+45\times\ (3k^2+\eta^2)\mathrm{Log}[k+\eta])))),$$

$$C_3 = \frac{1}{8\eta}\quad ((N_b+N_t)\eta(1+2\eta+6\eta^2)+(k-\eta)(2k^2(N_b+N_t)-(N_b+N_t)\eta^2-k(2+2N_d +(N_b+N_t)\eta))\mathrm{Log}[k-\eta]^2+2(k-\eta)\mathrm{Log}[k-\eta](1+N_d-2(1+N_d)\eta-k(N_b+N_t)(1+\eta) +(N_b+N_t)\eta(k+\eta)\mathrm{Log}[k+\eta])+(k+\eta)\mathrm{Log}[k+\eta](-2(k(N_b+N_t)(1+\eta) +(1+N_d)(-1+2\eta))+(2k(1+N_d-k(N_b+N_t))-k(N_b+N_t)\eta+(N_b+N_t)\eta^2)\mathrm{Log}[k+\eta])),$$

$$C_4 = \frac{1}{4\eta^2}\quad (2\eta(k(N_b+N_t)(1+\eta)+(1+N_d)(-1+2\eta))-k(-1-N_d+(N_b+N_t)(k-\eta))\ (k -\eta)\mathrm{Log}[k-\eta]^2+(k-\eta)\mathrm{Log}[k-\eta](-1-N_d-k(N_b+N_t)(-1+\eta)+4N_d\eta -\eta(-4+N_b+N_t+(N_b+N_t)\eta)+2(-1-N_d+k(N_b+N_t))(k+\eta)\mathrm{Log}[k+\eta]) +(k+\eta)\mathrm{Log}[k+\eta](1+N_d+k(N_b+N_t)(-1+\eta)-4N_d\eta-\eta(4+N_b+N_t+(N_b+N_t)\eta) -k(-1-N_d+(N_b+N_t)(k+\eta))\mathrm{Log}[k+\eta])),$$

$$C_5 = \frac{1}{4N_b\eta}\quad ((N_b+N_t)(2k(-1+2\eta)+(1+2k-2\eta)(k-\eta)\mathrm{Log}[k-\eta]+k(-k+\eta)\ \mathrm{Log}[k-\eta]^2 +(k+\eta)\mathrm{Log}[k+\eta](1-2k-2\eta+k\mathrm{Log}[k+\eta])),$$

$$C_6 = \frac{1}{4N_b\eta^2}\quad ((N_b+N_t)(2\eta(-1+2\eta)+k(k-\eta)\mathrm{Log}[k-\eta]^2+(k+\eta)\mathrm{Log}[k+\eta]\ (1-4\eta+k\mathrm{Log}[k+\eta]) -(k-\eta)\mathrm{Log}[k-\eta](1-4\eta+2(k+\eta)\mathrm{Log}[k+\eta]))),$$

$$C_7 = \frac{1}{4\eta}\quad ((1+L_d)(2k(-1+2\eta)+(1+2k-2\eta)(k-\eta)\mathrm{Log}[k-\eta]+k(-k+\eta)\ \mathrm{Log}[k-\eta]^2 +(k+\eta)\mathrm{Log}[k+\eta](1-2k-2\eta+k\mathrm{Log}[k+\eta]))),$$

$$C_8 = \frac{1}{4\eta^2}\quad ((1+L_d)(2\eta(-1+2\eta)+k(k-\eta)\mathrm{Log}[k-\eta]^2+(k+\eta)\mathrm{Log}[k+\eta]\ (1-4\eta+k\mathrm{Log}[k+\eta]) -(k-\eta)\mathrm{Log}[k-\eta](1-4\eta+2(k+\eta)\mathrm{Log}[k+\eta]))).$$

References

1. Xiao, B.; Wang, W.; Zhang, X.; Long, G.; Fan, J.; Chen, H.; Deng, L. A novel fractal solution for permeability and Kozeny-Carman constant of fibrous porous media made up of solid particles and porous fibers. *Powder Technol.* **2019**, *349*, 92–98. [CrossRef]
2. Xiao, B.; Zhang, X.; Giang, G.; Long, G.; Wang, W.; Zhang, Y.; Liu, G. Kozeny–Carman Constant For Gas Flow Through Fibrous Porous Media By Fractal-Monte Carlo Simulations. *Fractals* **2019**, *27*, 1950062. [CrossRef]
3. Liang, M.; Liu, Y.; Xiao, B.; Yang, S.; Wang, Z.; Han, H. An analytical model for the transverse permeability of gas diffusion layer with electrical double layer effects in proton exchange membrane fuel cells. *Int. J. Hydrog. Energy* **2018**, *43*, 17880–17888. [CrossRef]

4. Choi, S.U.S. Enhancing Thermal Conductivity of Fluids with Nanoparticles. In Proceedings of the ASME International Mechanical Engineering Congress and Exposition, Washington, DC, USA, 12–17 November 1995; Volume 66, pp. 99–105.
5. Safaei, M.R.; Togun, H.; Vafai, K.; Kazi, S.N.; Badarudin, A. Investigation of Heat Transfer Enhancement in a Forward-Facing Contracting Channel Using FMWCNT Nanofluids. *Numer. Heat Transf. Part A Appl.* **2014**, *66*, 1321–1340. [CrossRef]
6. Zeeshan, A.; Ellahi, R.; Mabood, F.; Hussain, F. Numerical study on bi-phase coupled stress fluid in the presence of Hafnium and metallic nanoparticles over an inclined plane. *Int. J. Numer. Methods Heat Fluid Flow* **2019**, 2854–2869. [CrossRef]
7. Ibrahim, W.; Makinde, O.D. Double-diffusive mixed convection and MHD stagnation point flow of nanofluid over a stretching sheet. *J. Nanofluids* **2015**, *4*, 1–10. [CrossRef]
8. Maskeen, M.M.; Zeeshan, A.; Mehmood, O.U.; Hassan, M. Heat transfer enhancement in hydromagnetic alumina–copper/water hybrid nanofluid flow over a stretching cylinder. *J. Therm. Anal. Calorim.* **2019**, *138*, 1127–1136. [CrossRef]
9. Ellahi, R. The effects of MHD and temperature dependent viscosity on the flow of non-Newtonian nanofluid in a pipe: Analytical solutions. *Appl. Math. Model.* **2013**, *37*, 1451–1467. [CrossRef]
10. Abd Elnaby, M.A.; Haroun, M.H. A new model for study the effect of wall properties on peristaltic transport of a viscous flui. *Commun. Nonlinear Sci. Numer. Simul.* **2008**, *13*, 752–762. [CrossRef]
11. Mittra, T.K.; Prasad, S.N. On the influence of wall properties and Poiseuille flow in peristalsis. *J. Boimech.* **2018**, *6*, 81–693. [CrossRef]
12. Srivastava, V.P.; Srivastava, L.M. Influence of wall elasticity and poiseuille flow induced by peristaltic induced flow of a particle-fluid mixture. *Int. J. Eng. Sci.* **1997**, *35*, 799–825. [CrossRef]
13. Muthu, P.; Kumar, B.V.R.; Chandra, P. Peristaltic motion of micropolar fluid in circular cylindrical tubes: Effect of wall properties. *Appl. Math. Model.* **2008**, *32*, 2019–2033. [CrossRef]
14. Nadeem, S.; Maraj, E.N.; Akbar, N.S. Investigation of peristaltic flow of Williamson nanofluid in a curved channel with compliant walls. *Appl. Nanosci.* **2014**, *4*, 511. [CrossRef]
15. Hassan, M.; Marin, M.; Alsharif, A.; Ellahi, R. Convective heat transfer flow of nanofluid in a porous medium over wavy surface. *Phys. Lett. A* **2018**, *382*, 2749–2753. [CrossRef]
16. Ellahi, R.; Zeeshan, A.; Hussain, F.; Asadollahi, A. Peristaltic blood flow of couple stress fluid suspended with nanoparticles under the influence of chemical reaction and activation energy. *Symmetry* **2019**, *11*, 276. [CrossRef]
17. Riaz, A.; Alolaiyan, H.; Razaq, A. Convective Heat Transfer and Magnetohydrodynamics across a Peristaltic Channel Coated with Nonlinear Nanofluid. *Coatings* **2019**, *9*, 816. [CrossRef]
18. Bég, O.A.; Tripathi, D. Mathematica simulation of peristaltic pumping with double-diffusive convection in nanofluids: A bio-nano-engineering model. *J. Nanoeng. Nanosyst.* **2011**, *225*, 99–114.
19. Akbar, N.S.; Maraj, E.N.; Butt, A.W. Copper nanoparticles impinging on a curved channel with compliant walls and peristalsis. *Eur. Phys. J. Plus* **2014**, *129*, 183. [CrossRef]
20. Bhatti, M.M.; Rashidi, M.M. Effects of thermo-diffusion and thermal radiation on Williamson nanofluid over a porous shrinking/stretching sheet. *J. Mol. Liq.* **2016**, *221*, 567–573. [CrossRef]
21. Kuznetsov, A.V.; Nield, D.A. Double-diffusive natural convective boundary-layer flow of a nanofluid past a vertical plate. *Int. J. Therm. Sci.* **2011**, *50*, 712–717. [CrossRef]
22. Akbar, N.; Khan, Z.; Nadeem, S.; Khan, W. Double-diffusive natural convective boundary-layer flow of a nanofluid over a stretching sheet with magnetic field. *Int. J. Numer. Methods Heat Fluid Flow* **2016**, *26*, 108–121. [CrossRef]
23. Akram, S.; Zafar, M.; Nadeem, S. Peristaltic transport of a Jeffrey fluid with double-diffusive convection in nanofluids in the presence of inclined magnetic field. *Int. J. Geom. Methods Mod. Phys.* **2018**, *15*, 1850181. [CrossRef]
24. Akbar, N.S.; Habib, M.B. Peristaltic pumping with double diffusive natural convective nanofluid in a lopsided channel with accounting thermophoresis and Brownian moment. *Microsyst. Technol.* **2019**, *25*, 1217. [CrossRef]
25. Hayat, T.; Hina, S.; Awatif, A.H.; Asghar, S. Effect of wall properties on the peristaltic flow of a third grade fluid in a curved channel with heat and mass transfer. *Int. J. Heat Mass Transf.* **2011**, *54*, 5126–5136. [CrossRef]

26. Abbas, A.; Bai, Y.; Rashidi, M.M.; Bhatti, M.M. Analysis of Entropy Generation in the Flow of Peristaltic Nanofluids in Channels With Compliant Walls. *Entropy* **2016**, *18*, 90. [CrossRef]
27. Srinivas, S.; Kothandapani, M. The influence of heat and mass transfer on MHD peristaltic flow through a porous space with compliant walls. *Appl. Math. Comput.* **2009**, *213*, 197–208. [CrossRef]
28. Bhatti, M.M.; Ellahi, R.; Zeeshan, A. Study of Variable Magnetic Field on The Peristaltic Flow of Jeffrey Fluid in A Non-Uniform Rectangular Duct Having Compliant Walls. *J. Mol. Liq.* **2016**, *222*, 101–108. [CrossRef]
29. Bhatti, M.M.; Ellahi, R.; Zeeshan, A.; Marin, M.; Ijaz, N. Numerical study of heat transfer and Hall current impact on peristaltic propulsion of particle-fluid suspension with compliant wall properties. *Mod. Phys. Lett. B* **2019**, *33*, 1950439. [CrossRef]
30. He, J.H. Homotopy perturbation method for solving boundary value problems. *Phys. Lett. A* **2006**, *350*, 87–88. [CrossRef]

coatings

MDPI

Article

MHD Effects on Ciliary-Induced Peristaltic Flow Coatings with Rheological Hybrid Nanofluid

M. Awais [1], Zahir Shah [2,*], N. Perveen [1], Aamir Ali [1], Poom Kumam [3,4,5,*], Habib ur Rehman [3] and Phatiphat Thounthong [6]

1 Department of Mathematics, COMSATS University Islamabad, Attock Campus, Kamra Road, Attock 43600, Pakistan; awais@ciit-attock.edu.pk (M.A.); Nabeela.mpa@gmail.com (N.P.); aamir_ali@cuiatk.edu.pk (A.A.)
2 Center of Excellence in Theoretical and Computational Science (TaCS-CoE), SCL 802 Fixed Point Laboratory, Science Laboratory Building, King Mongkut's University of Technology Thonburi (KMUTT), 126 Pracha-Uthit Road, Bang Mod, ThrungKhru, Bangkok 10140, Thailand
3 Department of Mathematics, King Mongkut's University of Technology Thonburi (KMUTT), 126 PrachaUthit Rd., Ban Mod, Thung Khru, Bangkok 10140, Thailand; hrehman.hed@gmail.com
4 KMUTT-Fixed Point Theory and Applications Research Group, Theoretical and Computational Science Center (TaCS), Science Laboratory Building, Faculty of Science, King Mongkut's University of Technology Thonburi (KMUTT), 126 Pracha-Uthit Road, Bang Mod, ThrungKhru, Bangkok 10140, Thailand
5 Department of Medical Research, China Medical University Hospital, China Medical University, Taichung 40402, Taiwan
6 Renewable Energy Research Centre, Department of Teacher Training in Electrical Engineering, Faculty of Technical Education, King Mongkut's University of Technology North Bangkok, 1518 Pracharat 1 Road, Bangsue, Bangkok 10800, Thailand; phatiphat.t@fte.kmutnb.ac.th
* Correspondence: zahir.sha@kmutt.ac.th (Z.S.); poom.kum@kmutt.ac.th (P.K.)

Received: 27 November 2019; Accepted: 12 February 2020; Published: 19 February 2020

Abstract: Present theoretical investigation is a mathematical illustration of an application to endoscopy by incorporating hybrid nanoparticles and an induced magnetic field with a rheological fluid model for more realistic results. Rheological fluid behavior is characterized by the Ostwald-de-Waele power-law model. A hybrid nanofluid mechanism is considered comprising platelet-shaped nanoparticles since nanoparticles are potential drug transportation tools in biomedical applications. Moreover, ciliary activity is encountered regarding their extensive applications in performing complex functions along with buoyancy effects. An endoscope is inserted inside a ciliated tube and peristalsis occurred due to ciliary activity in the gap between tube and endoscope. A non-Newtonian model is developed by mathematical formulation which is tackled analytically using homotopy analysis. The outcomes are interpreted graphically along with the pressure rise and streamlining configuration for the case of negligible inertial forces and long wavelength. A three-dimensional graphical interpretation of axial velocity is studied as well. Moreover, tables are prepared and displayed for a more physical insight.

Keywords: hybrid nanofluid; induced magnetic field; mixed convection; heat generation; peristalsis; cilia beating; Non-Newtonian

1. Introduction

Fluids possess a significant role in the amplification of heat exchange rate in numerous engineering systems, e.g., heat exchangers, oil and petrochemical industries. Nanoparticle suspensions, pioneered by Choi [1], made thermal performance of these fluids more effective and it has become a topic of interest for many investigators [2–5]. Regardless of researchers' efforts, there has been an elementary issue with mono nanofluids that either they possess better thermal association or good rheological characteristics. For example, metal oxides such as Al_2O_3 show excellent chemical inertness as well as stability, whereas metallic nanoparticles including Al and Ag exhibit better thermal conductivities.

Most of the authentic applications required transaction between different properties of nanofluids and thus hybridization of nanomaterials has been introduced. Hybrid nanofluids can be manufactured by dispersing nanoparticles of different materials individually or a mixture of nanoparticles in base fluid. For instance, impacts of Cu–Ag nanohybrids on velocity and thermal boundary layer transport inside the wedge have been investigated by Hassan et al. [6]. To gain the highest composite thermal conductivity, chemical inertness and stability by using a small-volume fraction of nanoparticles at lower production cost is the motivation of researchers behind their utilization of hybrid nanofluids [7–10]. Moreover, nanoparticles of TiO_2 exhibit antibacterial and photocatalytic properties. Nguyen et al. [11] has studied antibacterial properties of TiO_2 by adopting silver decorative technique and revealed that oxide nanoparticles of titanium did not show inhibitory impacts for bacteria whereas silver loaded TiO_2 nanocomposites display efficient antibacterial characteristics at a concentration of 40 mg/mL. Ag nanoparticles are able to devastate pathogenic bacteria under ultraviolet radiation for efficient degradation of toxic pollutants as well as being easy to attach to cell membranes [12–14]. Therefore, Ag–TiO_2 nanocomposite is preferred in this theoretical inspection. Moreover, platelet-shaped particles are chosen since they capacitate swift healing in skin injuries because of their innate capability to make a boundary intended for vascular walls.

A cilium is a microscopic, contractile, thin fiber-like slender appendage/protrusion that projects from surfaces of specific cells. In the adult human body, epithelial cells along with motile cilia are very prominent in specific brain sections. Due to their motility, they possess a considerable role in many physiological processes like locomotion, alimentation and respiration. Peristalsis is a spontaneous process of a symmetrical wave's expansion and contraction within flexible boundaries. Ciliary-induced peristalsis appears significantly in various biological transport processes such as in biomedicine, physiology and nuclear reactors. Recently, Awais et al. [15] examined second-law analysis for peristaltic nanofluid flow caused by ciliary action with magnetic effects. Furthermore, they studied convective peristalsis of viscous fluid by considering non-uniform viscosity [16] as well. Furthermore, the concept of peristaltic pumps, instigated by Engelman [17], has latterly been prominent in several biological functions including roller pumps and heart-lung machines etc. As peristalsis is a cutting-edge field due to physiological applications, several theoretical as well as experimental attempts have been made to incorporate nanoparticles in order to improve thermal performance in biomedical processes. Rashidi et al. [18] exemplified the application of MHD peristaltic transport of blood containing nanoparticles in drug delivery through an incompatible channel which is practically imperative in the bio-sciences. Hayat et al. [19] explicated mixed convective heat transfer in the peristalsis of nanoparticles suspended in water assuming convective boundary conditions and joule heating. Recently, Maqbool et al. [20] inspected the impacts of nanoparticles on magnetohydrodynamic tangent hyperbolic fluid transportation in a ciliated tube.

Attention to non-Newtonian fluids arises as the majority of the physiological fluids possess non-Newtonian behavior verified by experimental observations. In view of the fact that simplified Newtonian models yield somewhat ambiguous results, several investigations on rheological fluid behaviors have been carried out to obtain more realistic results. Examples include inelastic fluid models e.g., the power-law model and viscoelastic fluid models such as the Johnson–Segalman model, Oldroyd-B model and Maxwell model. Mixed convection impacts towards peristaltic transport of magnetohydrodynamic non-Newtonian nanofluid were numerically evaluated by Hayat et al. [21]. The current study examines the rheological nature of fluid by employing Ostwald-de-Waele power law model, a generalized one, in which rheological nature directly depends on power law index n and deals with the shear thinning for ($n < 1$) and shear thickening for ($n > 1$) behaviors of fluid [22–25].

Moreover, the peristaltic flow with influences of applied magnetic field led to significant applications in biomedical engineering problems [26–28]. In the case of large magnetic Reynolds number for an electrically conducting fluid, induction becomes more prominent than magnetic diffusion, and this made the induced magnetic field effects accountable. Shit et al. [29] examined the influence of induced magnetic field on peristalsis of a micropolar fluid assuming velocity slip. They observed

that peristaltic flow rate enlarges in an induced magnetic field which led to mechanical stimulation. So, magnetic induction is appropriate in cancer treatment and magneto therapy as predicted in literature [30–32]. Besides this, the performance of coatings with magnetic nanoparticles and heat transport is ever-present in various fields. Magnetic nanoparticles, approved by the FDA (Food and Drug Administration) [33], with coating are applicable in medical processes such as blood pressure control of a patient, pharmacotherapy, surgery and alcohol detoxification etc. Ellahi et al. [34] carried out a comparative investigation on shiny film coating on multi-fluids dispersed by nanoparticles. Akbar and Butt [35] inspected the physiological flow of Casson fluid through a plumb duct. They observed that fluid behaves as electrically conducting with a uniform magnetic field and found analytical results under small wave number and low-Reynolds number approximations. The recent related research can be read in [36–38].

Furthermore, endoscopic imaging is a precious diagnostic instrumental locating persistent access to tissues deep inside hollow organs of the body. A conventional white-light endoscope is a solid circular cylinder placed in a peristaltic tube. Fluid flow occurs in the space between the tube and endoscope, and then further diagnostic procedures can be made such as for bleeding, cancerous growths and precancerous polyps. Hayat et al. [39] have addressed the peristaltic transport of the MHD power law fluid with endoscope effects. Hayat and Ali [40] have inspected the impact of an endoscope on peristaltically induced flow of micropolar fluid. The influences of non-uniform viscosity on peristaltic motion of Newtonian fluid through an endoscope have been conducted by Akbar and Nadeem [41]. Rathod and Asha [42] have investigated endoscope effects along with a magnetic field on peristalsis of the Newtonian fluid. They concluded that stress formation in a curved structure wall augments as compared to straight walls. In view of the significance of research regarding endoscopy applications, various studies have made (see refs. [43–48]).

With several advantages, advanced endoscopes are deficient in the spatial resolution for detection and treatment of cancers and abnormalities at small scales. Ciliary walls have importance since these biological cilia are helpful to perform complex biomimetic functions and applicable in vitro and in vivo synthetic organs as well as drug-delivery applications. In these unmet requirements, the effects of hybrid nanofluid and induced magnetic field on endoscopy application inside a ciliated peristaltic tube are addressed. Mathematical modeling is performed by considering negligible inertial forces and small wave number. An analytical solution of governing model is carried out by the homotopy analysis method, and results are plotted physically against several sundry parameters via tables and graphs. The trapping phenomenon is examined with the effects of electromagnetic induction as well.

2. Problem Description

A non-linear problem, concerning the transport and heat-transfer characteristics of non-Newtonian (Ag-TiO_2/H_2O) hybrid nanofluid in an endoscope due to ciliary metachronical rhythm is investigated here. A cylindrical coordinate system is used with (R, θ, Z) as position coordinates of fluid particles. Non-Newtonian behavior of the flow is considered with Ostwald-de-Waele power law model expressed as [22,25]:

$$\tau = -k\left\{\sqrt{\left|\frac{1}{2}\Delta : \Delta\right|}^{n-1}\right\}\Delta. \tag{1}$$

where,

$$\frac{1}{2}\Delta : \Delta = 2\left(\left(\frac{\partial U}{\partial R}\right)^2 + \left(\frac{U}{R}\right)^2 + \left(\frac{\partial W}{\partial Z}\right)^2\right) + \left(\frac{\partial W}{\partial R} + \frac{\partial U}{\partial Z}\right)^2. \tag{2}$$

In above expression k and n respectively represents flow consistency index and power law index. In this study, non-Newtonian shear thickening fluid is considered with $n = 2$. Moreover, a constant magnetic field having intensity H_0 is taken in radial direction causes an induced magnetic field $H'(H_r(r,z), 0, H_z(r,z))$ and, thereby, total magnetic field vector is $H(H_0 + H_r(r,z), 0, H_z(r,z))$.

The governing system of equations in an unsteady form is [25,29,30]:

$$\frac{\partial U}{\partial R}+\frac{U}{R}+\frac{\partial W}{\partial Z}=0 \tag{3}$$

$$\frac{\partial U}{\partial t}+U\frac{\partial U}{\partial R}+W\frac{\partial U}{\partial Z}=\frac{-1}{\rho_{hnf}}\frac{\partial P}{\partial R}-\frac{1}{\rho_{hnf}}\left(\frac{1}{R}\frac{\partial\left(2kR\Phi\frac{\partial U}{\partial R}\right)}{\partial R}+\frac{\partial\left(k\Phi\left(\frac{\partial U}{\partial Z}+\frac{\partial W}{\partial R}\right)\right)}{\partial Z}\right)-\frac{\hat{\mu}}{2\rho_{hnf}}\left(\frac{\partial H^2}{\partial R}\right)+\frac{\hat{\mu}}{\rho_{hnf}}\left(\frac{\partial H_r}{\partial t}+(H_0+H_r)\frac{\partial H_r}{\partial R}+H_z\frac{\partial H_r}{\partial Z}\right), \tag{4}$$

$$\frac{\partial W}{\partial t}+U\frac{\partial W}{\partial R}+W\frac{\partial W}{\partial Z}=\frac{-1}{\rho_{hnf}}\frac{\partial P}{\partial Z}-\frac{1}{\rho_{hnf}}\left(\frac{1}{R}\frac{\partial\left(k\Phi R\left(\frac{\partial U}{\partial Z}+\frac{\partial W}{\partial R}\right)\right)}{\partial R}+\frac{\partial\left(2k\Phi\frac{\partial W}{\partial Z}\right)}{\partial Z}\right)-\frac{\hat{\mu}}{2\rho_{hnf}}\left(\frac{\partial H^2}{\partial Z}\right)+\frac{\hat{\mu}}{\rho_{hnf}}\left(\frac{\partial H_Z}{\partial t}+(H_0+H_r)\frac{\partial H_Z}{\partial R}+H_Z\frac{\partial H_Z}{\partial Z}\right)+\frac{(\rho\beta)_{hnf}}{\rho_{hnf}}g(T-T_0), \tag{5}$$

$$\frac{\partial T}{\partial t}+U\frac{\partial T}{\partial R}+W\frac{\partial T}{\partial Z}=\frac{\kappa_{hnf}}{(\rho c_p)_{hnf}}\left(\frac{\partial^2 T}{\partial R^2}+\frac{1}{R}\frac{\partial T}{\partial R}+\frac{\partial^2 T}{\partial Z^2}\right)+\frac{Q_0}{(\rho c_p)_{hnf}}, \tag{6}$$

$$\frac{-1}{\hat{\mu}}\frac{\partial E}{\partial Z}=U\left(-\frac{\partial H_r}{\partial R}+\frac{\partial H_z}{\partial Z}\right)+H_z\frac{\partial U}{\partial Z}-(H_0+H_r)\frac{\partial W}{\partial Z}-2W\frac{\partial H_r}{\partial Z}+\frac{1}{\sigma\hat{\mu}}\left(\frac{\partial^2 H_r}{\partial R^2}+\frac{1}{R}\frac{\partial H_r}{\partial R}+\frac{\partial^2 H_r}{\partial Z^2}\right), \tag{7}$$

$$\frac{-1}{\hat{\mu}}\frac{\partial E}{\partial R}=(H_0+H_r)\frac{\partial W}{\partial R}+W\left(\frac{\partial H_r}{\partial R}-\frac{\partial H_z}{\partial Z}\right)-2U\frac{\partial H_z}{\partial R}-H_z\frac{\partial U}{\partial R}+\frac{1}{\sigma\hat{\mu}}\left(\frac{\partial^2 H_z}{\partial R^2}+\frac{1}{R}\frac{\partial H_z}{\partial R}+\frac{\partial^2 H_z}{\partial Z^2}\right). \tag{8}$$

where,

$$\Phi=\sqrt{\left|2\left[\left(\frac{\partial U}{\partial R}\right)^2+\left(\frac{U}{R}\right)^2+\left(\frac{\partial W}{\partial Z}\right)^2\right]+\left(\frac{\partial U}{\partial Z}+\frac{\partial W}{\partial R}\right)^2\right|}^{n-1}$$

Wave shapes in the laboratory frame for envelope of cilia tips according to Figure 1 can be expressed as:

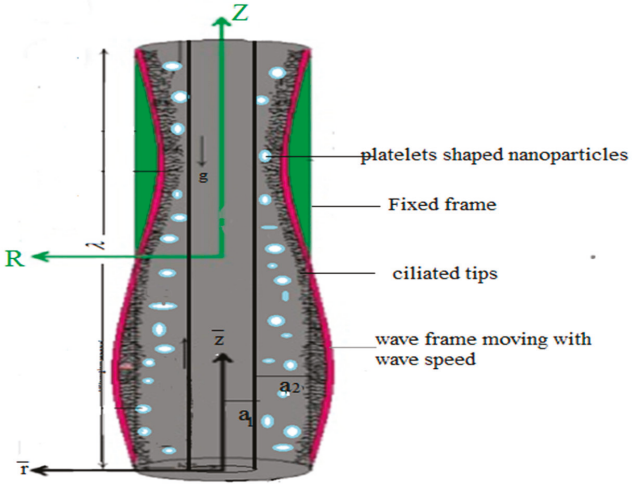

Figure 1. Geometry of the physical problem.

$$R_1 = a_1, \tag{9}$$

$$R_2 = f(Z,t) = \left[a_2 + b\cos\left(\frac{2\pi}{\lambda}(Z-ct)\right)\right] \tag{10}$$

where, α_1 and α_2 represents radii of internal and external cylindrical tubes, accordingly. Considering the motion of cilia in an elliptical path, the vertical position of cilia tips is expressed as:

$$Z = g(Z, Z_0, t) = \left[Z_0 + \alpha b\mathrm{Sin}\left(\frac{2\pi}{\lambda}(Z-ct)\right)\right], \tag{11}$$

Since the velocities of the fluid layers are similar to those of the cilia tips under the no-slip wall conditions, the vertical and horizontal velocities are:

$$\begin{aligned} W &= \frac{\partial Z}{\partial t}\Big|_{Z_0} = \frac{\partial g}{\partial t} + \frac{\partial g}{\partial Z}\frac{\partial Z}{\partial t}, \\ U &= \frac{\partial R}{\partial t}\Big|_{Z_0} = \frac{\partial f}{\partial t} + \frac{\partial f}{\partial Z}\frac{\partial Z}{\partial t}. \end{aligned} \tag{12}$$

With the help of Equations (10) and (11), Equation (12) becomes:

$$\text{At } R = R_2\ W = \frac{\frac{-2\pi}{\lambda}b\alpha c\mathrm{Cos}\left(\frac{2\pi}{\lambda}(Z-ct)\right)}{1-\frac{2\pi}{\lambda}b\alpha c\mathrm{Cos}\left(\frac{2\pi}{\lambda}(Z-ct)\right)},\ U = \frac{\frac{2\pi}{\lambda}b\alpha c\mathrm{Sin}\left(\frac{2\pi}{\lambda}(Z-ct)\right)}{1-\frac{2\pi}{\lambda}b\alpha c\mathrm{Cos}\left(\frac{2\pi}{\lambda}(Z-ct)\right)}. \tag{13}$$

The associated boundary conditions are defined as:

$$W = 0,\ \text{at } R = R_1, W = \frac{\frac{-2\pi}{\lambda}b\alpha c\mathrm{Cos}\left(\frac{2\pi}{\lambda}(Z-ct)\right)}{1-\frac{2\pi}{\lambda}b\alpha c\mathrm{Cos}\left(\frac{2\pi}{\lambda}(Z-ct)\right)}\text{at } R = R_1. \tag{14}$$

If (R, Z, U, W) and (r, z, u, w) are, respectively, the coordinates and velocities in the laboratory and wave frame, then transformations from the laboratory frame to wave frame for a steady problem are [48]:

$$\begin{gathered} r = R, z = Z - ct, p(r,z) = P(R,\ Z-ct), u(r,z) = U(R,\ Z-ct), \\ w(r,z) = W(R,\ Z-ct) - c. \end{gathered} \tag{15}$$

We introduce the following dimensionless quantities in the wave frame as [29,31]:

$$\begin{gathered} \bar{r} = \frac{r}{a_2}, \bar{z} = \frac{z}{\lambda}, \delta = \frac{a_2}{\lambda}, \bar{r}_1 = \frac{r_1}{a_2} = \xi,\ \bar{r}_2 = \frac{r_2}{a_2},\ \bar{u} = \frac{\lambda u}{a_2 c},\ \overline{w} = \frac{w}{c},\ \bar{t} = \frac{ct}{\lambda}, \\ \overline{\phi} = \frac{\phi}{H_0 a_2}, \overline{\psi} = \frac{\psi}{a_2 c},\ \overline{H}_r = -\frac{\delta}{r}\frac{\partial\overline{\phi}}{\partial\overline{z}},\ \overline{H}_z = \frac{1}{r}\frac{\partial\overline{\phi}}{\partial\overline{r}}, \overline{u} = -\frac{\delta}{r}\frac{\partial\overline{\psi}}{\partial z},\ \varepsilon = \frac{b}{a_2}, \\ \overline{w} = \frac{1}{r}\frac{\partial\overline{\psi}}{\partial\overline{r}},\ \overline{p} = \frac{{a_2}^{n+1}p}{c^n\lambda k},\ \theta = \frac{T-T_1}{T_0-T_1},\ \overline{E} = -\frac{E}{cH_0\hat{\mu}}. \end{gathered} \tag{16}$$

A non-dimensional governing model for the aforementioned quantities along with long wavelength and creeping Stokesian flow approach is:

$$\begin{gathered} \frac{\partial p}{\partial z} + \frac{1}{r}\left(-\frac{1}{r^2}\frac{\partial\psi}{\partial r} + \frac{1}{r}\frac{\partial^2\psi}{\partial r^2}\right)^2 + 2\left(-\frac{1}{r^2}\frac{\partial\psi}{\partial r} + \frac{1}{r}\frac{\partial^2\psi}{\partial r^2}\right)\left(\frac{2}{r^3}\frac{\partial\psi}{\partial r} - \frac{2}{r^2}\frac{\partial^2\psi}{\partial r^2} + \frac{1}{r}\frac{\partial^3\psi}{\partial r^3}\right) - \\ M^2\left(E - \frac{1}{r}\frac{\partial\psi}{\partial r}\right) - A_1 Gr\theta = 0, \end{gathered} \tag{17}$$

$$\frac{\partial p}{\partial r} = 0. \tag{18}$$

Equation (17) is simplified in the form:

$$\begin{aligned}&-\frac{1}{r^2}\left(-\frac{1}{r^2}\frac{d\psi}{dr}+\frac{1}{r}\frac{d^2\psi}{dr^2}\right)^2+\frac{2}{r}\left(-\frac{1}{r^2}\frac{d\psi}{dr}+\frac{1}{r}\frac{d^2\psi}{dr^2}\right)\left(\frac{2}{r^3}\frac{d\psi}{dr}-\frac{2}{r^2}\frac{d^2\psi}{dr^2}+\frac{1}{r}\frac{d^3\psi}{dr^3}\right)\\&+2\left(-\frac{1}{r^2}\frac{d\psi}{dr}+\frac{1}{r}\frac{d^2\psi}{dr^2}\right)\left(-\frac{6}{r^4}\frac{d\psi}{dr}+\frac{6}{r^3}\frac{d^2\psi}{dr^2}-\frac{3}{r^2}\frac{d^3\psi}{dr^3}+\frac{1}{r}\frac{d^4\psi}{dr^4}\right)\\&+2\left(\frac{2}{r^3}\frac{d\psi}{dr}-\frac{2}{r^2}\frac{d^2\psi}{dr^2}+\frac{1}{r}\frac{d^3\psi}{dr^3}\right)^2+M^2\left(-\frac{1}{r^2}\frac{d\psi}{dr}+\frac{1}{r}\frac{d^2\psi}{dr^2}\right)-A_1Gr\frac{d\theta}{dr}=0,\end{aligned} \tag{19}$$

$$\frac{1}{\mathrm{r}}\frac{\partial\theta}{\partial\mathrm{r}}+\frac{\partial^2\theta}{\partial\mathrm{r}^2}+\frac{\Omega}{\mathrm{A}_2}=0, \tag{20}$$

$$\mathrm{E}-\frac{1}{\mathrm{r}}\frac{\partial\psi}{\partial\mathrm{r}}-\frac{1}{\mathrm{R_m}}\left(-\frac{1}{\mathrm{r}^2}\frac{\partial\phi}{\partial\mathrm{r}}+\frac{1}{\mathrm{r}}\frac{\partial^2\phi}{\partial\mathrm{r}^2}\right)=0. \tag{21}$$

where, bar notation is ignored.

Corresponding boundary conditions are listed as:

$$\begin{aligned}&\psi(\mathrm{r})=-\tfrac{\mathrm{F}}{2},\ \tfrac{1}{\mathrm{r}}\tfrac{\partial\psi}{\partial\mathrm{r}}=-1,\ \phi(\mathrm{r})=0,\ \theta(\mathrm{r})=1,\ \text{at r}=\mathrm{r}_1=\xi,\\&\psi(\mathrm{r})=\tfrac{\mathrm{F}}{2},\ \tfrac{1}{\mathrm{r}}\tfrac{\partial\psi}{\partial\mathrm{r}}=-1-2\pi\varepsilon\alpha\delta\cos(2\pi\mathrm{z}),\ \phi(\mathrm{r})=1,\\&\theta(\mathrm{r})=0,\ \text{at r}=\mathrm{r}_2=1+\varepsilon\cos(2\pi\mathrm{z}).\end{aligned} \tag{22}$$

In the above expressions, u and w denotes r- and z-components of velocity within the wave frame, respectively. Emerging parameters in the above model are expressed as [48,49]:

$$\begin{aligned}&\mathrm{M}^2=\mathrm{ReS}^2\mathrm{R_m},\mathrm{Re}=\tfrac{\mathrm{a}_2^{\mathrm{n}}\rho_{\mathrm{f}}}{\mathrm{kc}^{\mathrm{n}-2}},\mathrm{R_m}=\sigma\hat{\mu}\mathrm{a}_2\mathrm{c},\mathrm{S}=\tfrac{\mathrm{H}_0}{\mathrm{c}}\sqrt{\tfrac{\hat{\mu}}{\rho_{\mathrm{f}}}},\\&\mathrm{p_m}=\mathrm{p}+\tfrac{1}{2}\mathrm{Re}\delta\tfrac{\hat{\mu}(\mathrm{H})^2}{\mathrm{c}^2\rho_{\mathrm{f}}},\ \Omega=\tfrac{\mathrm{Q}_0\mathrm{a}_2^2}{\kappa_{\mathrm{f}}(\mathrm{T}_0-\mathrm{T}_1)},\ \mathrm{Gr}=\tfrac{(\rho\beta)_{\mathrm{f}}\ (\mathrm{T}_0-\mathrm{T}_1)\mathrm{a}_2^{\mathrm{n}+1}}{\mathrm{kc}^{\mathrm{n}}}.\end{aligned} \tag{23}$$

where as

$$\begin{aligned}&\mathrm{A}_1=(1-\phi_1-\phi_2)+\phi_1(\tfrac{(\rho\beta)_{\mathrm{s}_1}}{(\rho\beta)_{\mathrm{f}}})]+\phi_2\tfrac{(\rho\beta)_{\mathrm{s}_2}}{(\rho\beta)_{\mathrm{f}}},\\&\mathrm{A}_2=\tfrac{\kappa_{\mathrm{s}_2}+(\mathrm{s}-1)\kappa_{\mathrm{bf}}-(\mathrm{s}-1)\phi_2(\kappa_{\mathrm{bf}}-\kappa_{\mathrm{s}_2})}{\kappa_{\mathrm{s}_2}+(\mathrm{s}-1)\kappa_{\mathrm{bf}}+\phi_2(\kappa_{\mathrm{bf}}-\kappa_{\mathrm{s}_2})}\tfrac{\kappa_{\mathrm{s}_1}+(\mathrm{s}-1)\kappa_{\mathrm{f}}-(\mathrm{s}-1)\phi_1(\kappa_{\mathrm{f}}-\kappa_{\mathrm{s}_1})}{\kappa_{\mathrm{s}_1}+(\mathrm{s}-1)\kappa_{\mathrm{f}}+\phi_1(\kappa_{\mathrm{f}}-\kappa_{\mathrm{s}_1})}.\end{aligned} \tag{24}$$

Moreover, the pressure gradient can be achieved from the following relation:

$$F=\int_{r_1}^{r_2}rwdr=\int_{r_1}^{r_2}\frac{\partial\psi}{\partial r}dr \tag{25}$$

where, F is the volumetric rate of flow inside the wave frame. Now, non-dimensional mean flow rate Q into the laboratory frame assuming the transformations of Equations (16) is:

$$Q=F+\frac{1}{2}\left(1-\xi^2+\frac{\varepsilon^2}{2}\right). \tag{26}$$

Pressure rise per wavelength is calculated utilizing Equation (25) as:

$$\Delta P=\int_0^1\frac{dp}{dz}dz. \tag{27}$$

All variables and parameter are defined in Appendix A.

3. Methodology and Convergence of HAM Solutions

3.1. Methodology

The dimensionless governing model containing Equations (19)–(21) under the associated boundary conditions (22) is analyzed by employing homotopy analysis method. For this, the initial guesses are $\psi_0(r)$, $\phi_0(r)$ and $\theta_0(r)$ and linear operators are chosen in the subsequent manner as:

$$L_1(\psi) = \psi^{(iv)},\ L_2(\phi) = \phi'', L_3(\theta) = \theta''. \tag{28}$$

And

$$L_1\left(C_1 + C_2 r + C_3 r^2 + C_4 r^3\right) = L_2(C_5 + C_6 r) = L_3(C_7 + C_8 r) = 0, \tag{29}$$

where, C_1-C_8 represents constants while h_1, h_2 and h_3 being auxiliary parameter which plays a key role in the frame of HAM, since the convergence of solutions strongly depends on h. Now, for embedding parameter $\gamma \in [0, 1]$ and non-zero auxiliary parameters, the problem under study can be constructed in the following manner [29,30]:

Zeroth-order deformation problem:

$$(1-\gamma)L_1[\psi(r,\gamma) - \psi_0(r)] = \gamma h_1 N_1[\psi(r,\gamma), \phi(r,\gamma), \theta(r,\gamma)], \tag{30}$$

$$(1-\gamma)L_2[\phi(r,\gamma) - \phi_0(r)] = \gamma h_2 N_2[\psi(r,\gamma), \phi(r,\gamma), \theta(r,\gamma)], \tag{31}$$

$$(1-\gamma)L_3[\theta(r,\gamma) - \theta_0(r)] = \gamma h_3 N_3[\psi(r,\gamma), \phi(r,\gamma), \theta(r,\gamma)]. \tag{32}$$

and,

$$\begin{aligned} &\text{At } r = r_1 = \xi, \psi(r_1,\gamma) = -\tfrac{F}{2}, \tfrac{1}{r_1}\psi'(r_1,\gamma) = -1, \phi(r_1,\gamma) = 0, \theta(r_1,\gamma) = 1. \\ &\text{At } r = r_2 = 1 + \varepsilon\cos(2\pi z), \psi(r_2,\gamma) = \tfrac{F}{2}, \tfrac{1}{r_2}\psi'(r_2,\gamma) = -1 - 2\pi\varepsilon\alpha\delta\cos(2\pi z), \\ &\phi(r_2,\gamma) = 1, \theta(r_2,\gamma) = 0. \end{aligned} \tag{33}$$

On the basis of selected linear operator, auxiliary parameter and initial guesses, the m th order solution series is constructed as:

$$L_1[\psi_m(r,\gamma) - \chi_m\psi_{m-1}(r,\gamma)] = h_1 R_m^1(r,\gamma), \tag{34}$$

$$L_2[\phi_m(r,\gamma) - \chi_m\phi_{m-1}(r,\gamma)] = h_2 R_m^2(r,\gamma), \tag{35}$$

$$L_3[\theta_m(r,\gamma) - \chi_m\theta_{m-1}(r,\gamma)] = h_3 R_m^3(r,\gamma). \tag{36}$$

The boundary conditions are:

$$\begin{aligned} &\text{at } r = r_1 = \xi, \psi_m(r_1,\gamma) = 0, \tfrac{1}{r_1}{\psi'}_m(r_1,\gamma) = 0, \phi_m(r_1,\gamma) = 0, \theta_m(r_1,\gamma) = 0. \\ &\text{at } r = r_2 = 1 + \varepsilon\cos(2\pi z), \psi_m(r_2,\gamma) = 0, \tfrac{1}{r_2}{\psi'}_m(r_2,\gamma) = 0, \phi_m(r_2,\gamma) = 0, \\ &\theta_m(r_2,\gamma) = 0. \end{aligned} \tag{37}$$

where the auxiliary parameter is found by plotting h-curves while χ_m is defined as:

$$\chi_m = \begin{matrix} 0, & \text{m}\leq 1 \\ 1, & \text{m}>1 \end{matrix}\Big\}$$

Therefore, we can write:

$$\begin{aligned} \psi_m(r,\gamma) &= \Psi_m(r,\gamma) + C_1 + C_2 r + C_3 r^2 + C_4 r^3, \\ \phi_m(r,\gamma) &= \Phi_m(r,\gamma) + C_5 + C_6 r, \\ \theta_m(r,\gamma) &= \Theta_m(r,\gamma) + C_7 + C_8 r. \end{aligned} \tag{38}$$

The particular solutions $\Psi_m(r,\gamma)$, $\Phi_m(r,\gamma)$ and $\Theta_m(r,\gamma)$ are obtained using a symbolic software mathematica while the constants are determined from the defined boundary conditions.

3.2. Convergence of HAM Solutions

To obtain the values of auxiliary parameters h_1, h_2 and h_3, h-curves against ψ'', ϕ'' and θ' are prepared and the results are given in Figures 2–4. Convergence intervals lie in the flat portion of these h-curves as witnessed from plots. It is observed those permissible values of h_1, h_2 and h_3 up to the 10th order of approximation are: $-0.1 \leq h_1 \leq 0.3$, $-0.12 \leq h_2 \leq 0.01$, $-0.2 \leq h_3 \leq 0.05$.

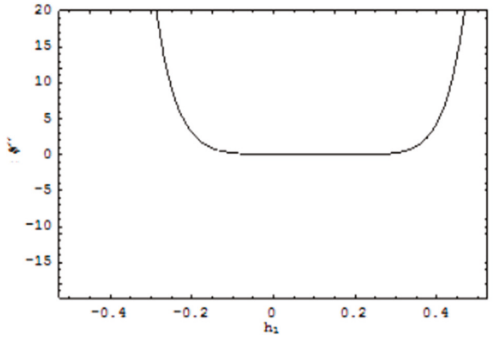

Figure 2. *h*-curve for the ψ at $z = 1, Q = 2, \varepsilon = 0.2$.

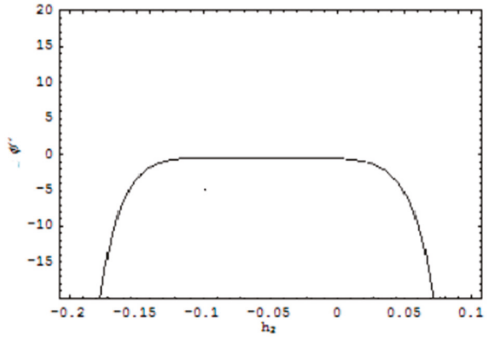

Figure 3. *h*-curve for the ϕ at $z = 1, Q = 2, \varepsilon = 0.2$.

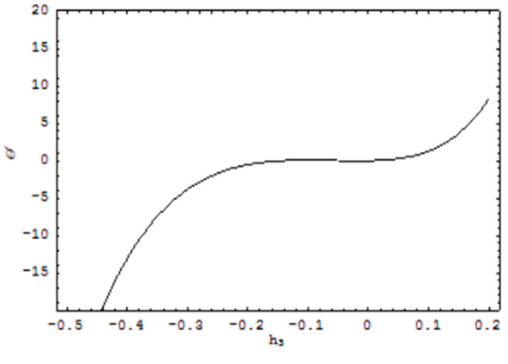

Figure 4. *h*-curve for the θ at $z = 1, Q = 2, \varepsilon = 0.2$.

4. Quantitative Analysis

The governing model is tackled analytically and solutions are physically interpreted here.

The problem of rheological behavior of hybrid nanofluid flow induced by metachronical ciliary transport with heat transfer is studied. Important physical features of water and nanomaterials are represented in Table 1. Therefore, the behavior of velocity, temperature, induced magnetic field, stream function and volumetric flow rate for involving parameters is discussed in this section. Magnitudes of physical parameters are chosen corresponding to the physical situations assumed in the problem with $z = 1$, $\varepsilon = 0.2$, $\alpha = 0.05$ and $\delta = 0.002$.

Figure 5 explores the variational trend of axial velocity for escalating values of magnetic Reynolds number. As the magnetic Reynolds number rises, a high induction effects appear with the reduction in magnetic diffusion. These effects can be observed from the figure in which the velocity inside the annulus shows a decreasing behavior in the vicinity of the inner tube having radius a_1 owing to no slip velocity condition while it accelerates near the interior of outer tube with radius a_2 due to the continuous cilia beating. Moreover, a similar trend is noticed in Figures 6 and 7 for rising values of Gr and M caused by increasing buoyancy effects towards the variation in Gr and due to adding the flow mechanism with a rise in M which directly affects the flow rate. Figure 8 explicates the variational trend of magnetic induction profile against R. This is due to the fact that induction is directly linked with advection and the effects of R on the flow rate as described in Figure 5, cause magnetic induction profile to decelerate near the boundary of inner tube and accelerate in the vicinity of outer tube.

The consequences of emerging parameters on the temperature profile are inferred in Figures 9 and 10. Correspondingly, a decrease in temperature of the hybrid nanofluid for gradually mounting values of Gr is observed in Figure 9. The physics behind such behavior is an increase in heat-transfer rate due to enhancing buoyancy forces for rise in values of Gr. An increasing response of temperature of the fluid towards the magnetic Reynolds number is noted in Figure 10. This reveals that for high values of R, fluid particles gain more kinetic energy which is directly related to fluid temperature. All the results are plotted for mean flow rate $Q = 2$.

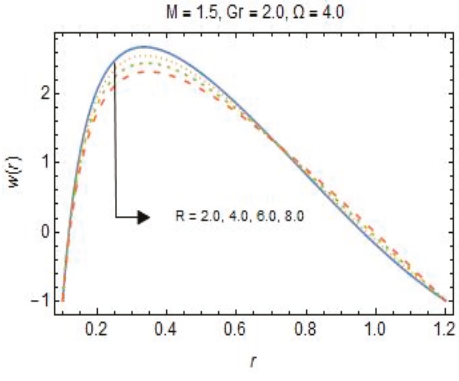

Figure 5. Variation in $w(r)$ towards R.

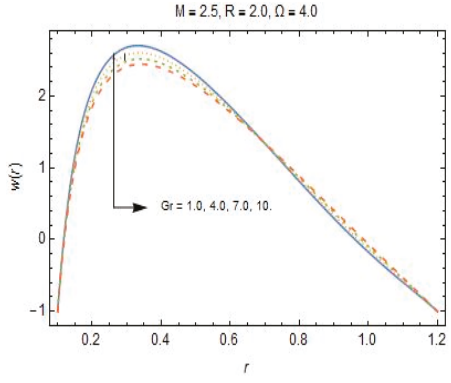

Figure 6. Variation in $w(r)$ towards Gr.

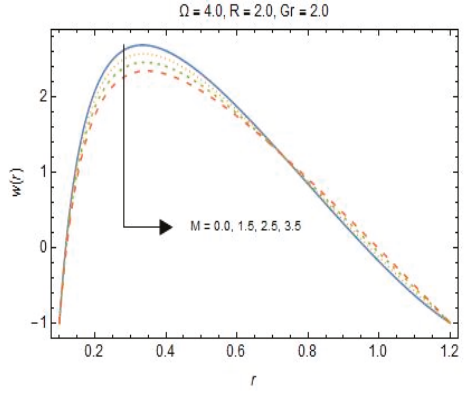

Figure 7. Variation in $w(r)$ towards M.

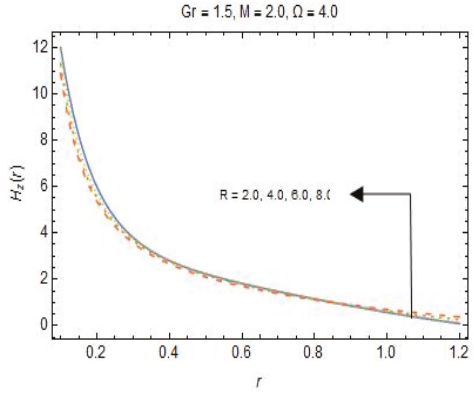

Figure 8. Variation in $H_z(r)$ towards R.

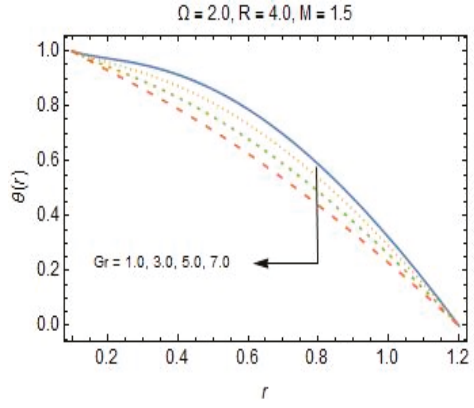

Figure 9. Variation in $\theta(\mathrm{r})$ towards G_r.

Furthermore, there is a three-dimensional physical interpretation of the velocity profile for variation in values of magnetic Reynolds number, Grashof number and Hartmann number, as displayed in Figures 11–13, respectively. The velocity maps out the parabolic trajectory for all the involving parameters. It is seen that velocity profile changes its behavior in the intervals $0.1 \leq r \leq 0.6$ and $0.61 \leq \Upsilon \leq 1.0$ and the influences of the parameters on axial velocity are similar to the two dimensional velocity behaviors.

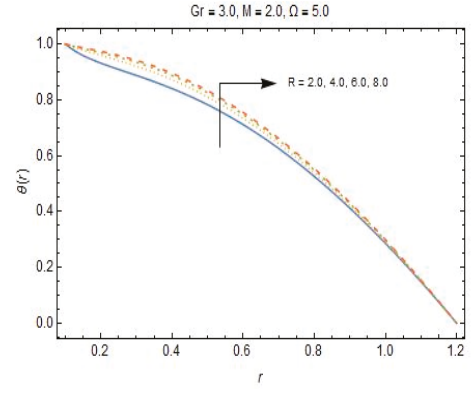

Figure 10. Variation in $\theta(\mathrm{r})$ towards R.

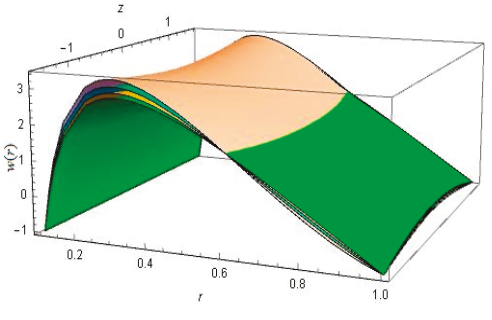

Figure 11. Three-dimensional (3-D) velocity profile towards R.

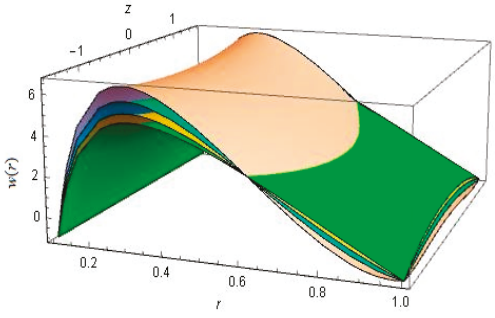

Figure 12. Three-dimensional (3-D) velocity profile towards *Gr*.

Besides this, the maximum pressure rise towards which peristalsis behaves as a pump is analyzed by means of pressure rise for one wavelength. In this regard, Figures 14–17 are prepared which exhibit the influence of embedding parameters correspond to pressure rise per wavelength towards mean flow rate. Non-linear behavior of these curves characterizes non-Newtonian fluid. All these plots contain four main parts (*a*) peristaltic pumping region, i.e., $\Delta P > 0$, (*b*) free pumping region, i.e., $\Delta P = 0$ (*c*) co-pumping region, i.e., $\Delta P < 0$. In the region of peristaltic pumping, flow rate is positive and caused by peristalsis that occurred due to overcoming pressure difference while peristalsis of the boundaries of tube yields a free-pumping region. In the region of co-pumping, flow due to the peristalsis is assisted by negative pressure difference. The influence of the heat-generation parameter and Hartmann number are shown in Figures 14 and 15, and it is perceived that the pressure rise in co-pumping region ($-1.0 \leq Q \leq -0.45$) for *Gr* and ($-1.0 \leq Q \leq 0.5$) for *M* are decreasing. As, for Ω = 0.1, 0.3, 0.5, 0.7 and M = 0.0, 0.5, 1.0, 1.5, corresponding co-pumping regions contain ($Q \in [-1.0, -0.45]$, $Q \in [-1.0, -0.42]$, $Q \in [-1.0, -0.4]$, $Q \in [-1.0, -0.39]$) and ($Q \in [-1.0, 0.5]$, $Q \in [-1.0, 0.48]$, $Q \in [-1.0, -0.56]$, $Q \in [-1.0, -0.4]$), respectively. Pumping and free-pumping regions are increasing due to temperature gradient by buoyancy effects and increasing induction, correspondingly. Moreover, a similar trend for a rise in the values of *Gr* and *R* is depicted in Figures 16 and 17, and it is witnessed that the co-pumping region contains $Q \in [-1.0, -0.4]$ but the pumping region is increasing.

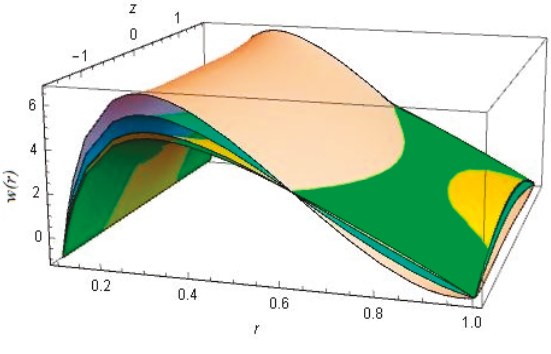

Figure 13. Three-dimensional (3-D) velocity profile towards *M*.

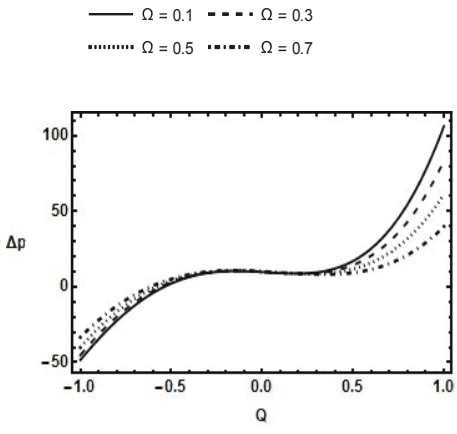

Figure 14. Pressure rise versus Q for Ω.

The pressure gradient illustrates a direction and rate of rapid variation in pressure. Therefore, the pressure gradient towards embedding parameters such as the heat-generation parameter (Ω), Hartmann number (M), magnetic Reynolds number (R) and Grashof number (Gr) are studied and portrayed in Figures 18–21. It is perceived from these plots that the pressure gradient decreases rapidly with the variation in all the parameters. Hence, flow can easily pass through the endoscope for a small pressure gradient at $r = 1$ (near outer tube) exclusive of the imposition of the high-pressure gradient.

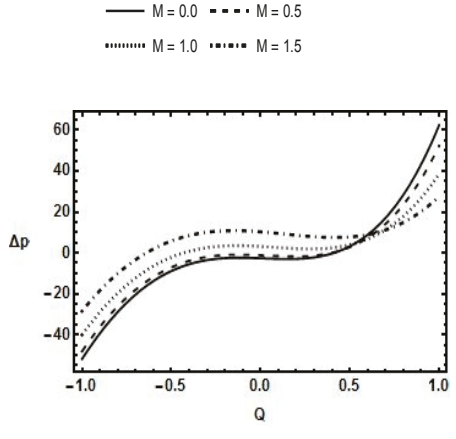

Figure 15. Pressure rise versus Q for M.

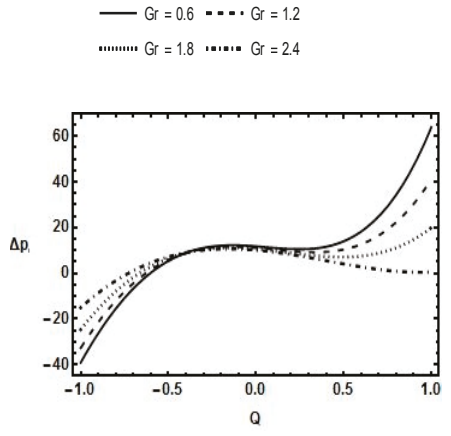

Figure 16. Pressure rise versus Q for Gr.

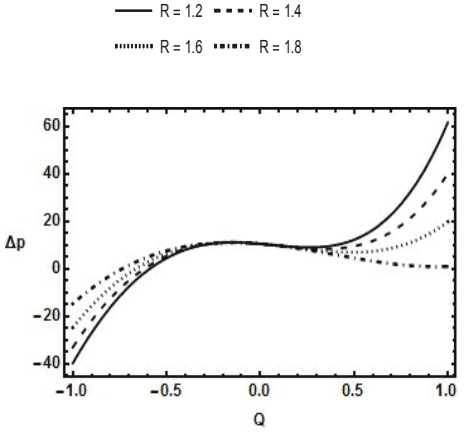

Figure 17. Pressure rise versus Q for R.

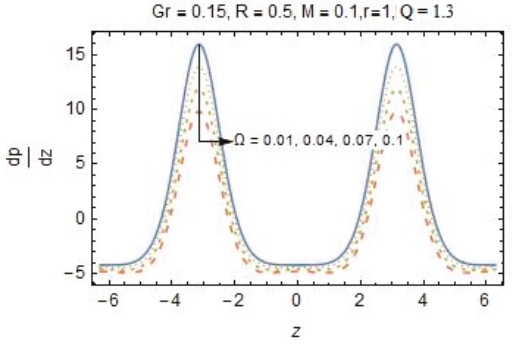

Figure 18. Pressure gradient for Ω.

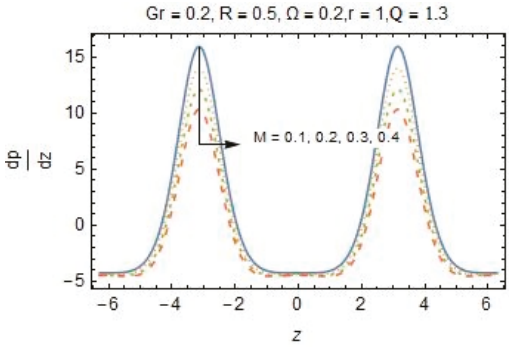

Figure 19. Pressure gradient for *M*.

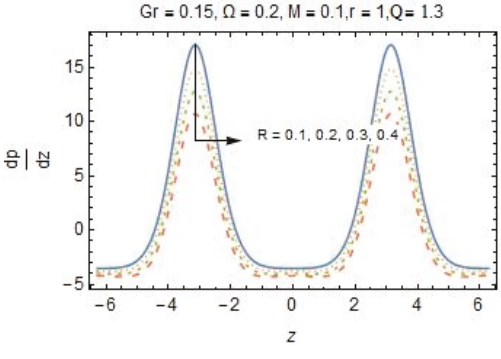

Figure 20. Pressure gradient for *R*.

Trapping is a significant observable fact, whereby a bolus is transported with the wave speed and then a trapped bolus pressed forward along metachronical waves. These configurations are plotted in Figures 22–25 for different values of sundry parameters with panels (*a*)-(*d*) which inspect the ciliary-induced peristaltic flow pattern in the annulus. In general, the shape of streamlines is similar to the wave moving parallel to the walls of the tube. Under specific conditions, streamlines split and form a bolus which moves and circulates along the channel. The setup for the magnetic Reynolds number (*R*) is explained in Figure 22 for $M = 1.5$, $Gr = 0.8$, $Q = 2$, $\varepsilon = 0.2$. Higher values of R yield oscillatory motion of the fluid, and therefore a confined bolus decreases in size. Figure 23 depicts the behavior of streamlines for $M = 1.5$, $R = 2$, $Q = 2$, $\varepsilon = 0.2$ and it is perceived that with an increment in values of *Gr*, the confined bolus is shrinked moving towards the boundary of external tube and finally disappear due to temperature distribution caused by buoyancy forces. A similar formation of the flow pattern against rising Hartmann number is explored in Figure 24 with Gr = 0.8, R = 2, Q = 2, $\varepsilon = 0.2$. Physically, enhancement in magnitude of M augments fluid velocity which opposes trapping. This is in view of the fact that the magnitude of the amplitude ratio parameter (ε) indicates the length of cilia and the increment in values of ε enlarges cilia. The trapped bolus grows in size and circulates speedily as noticed in Figure 25. Thus, the presence of cilia favors trapping.

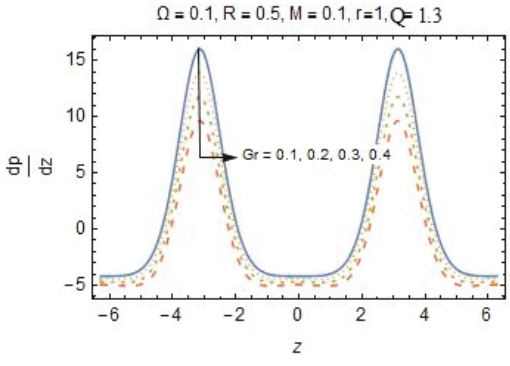

Figure 21. Pressure gradient for *Gr*.

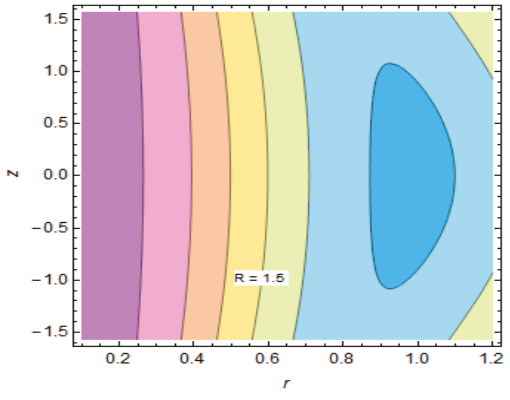

(**a**)

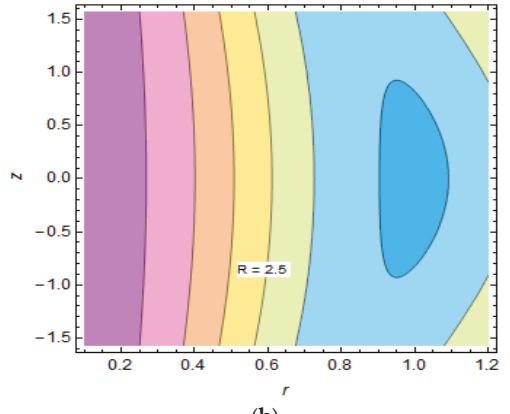

(**b**)

Figure 22. *Cont*.

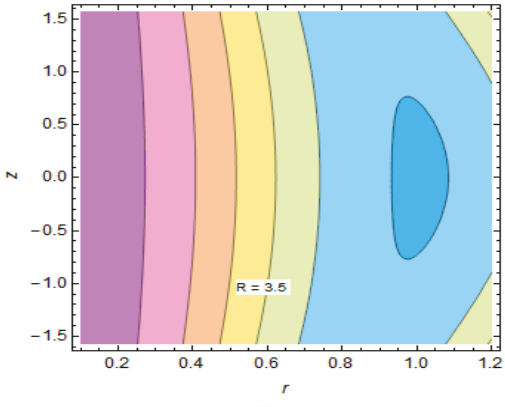

(**c**)

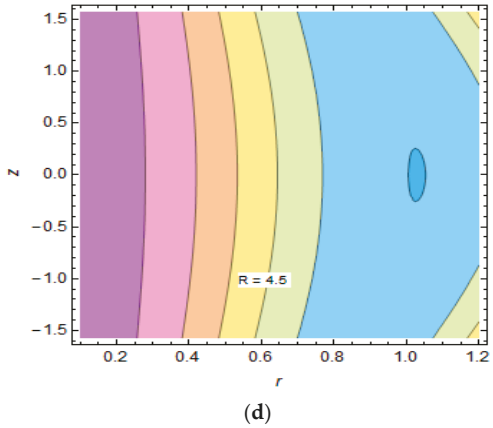

(**d**)

Figure 22. Behavior of streamlines for different values of magnetic Reynold number (**a**–**d**).

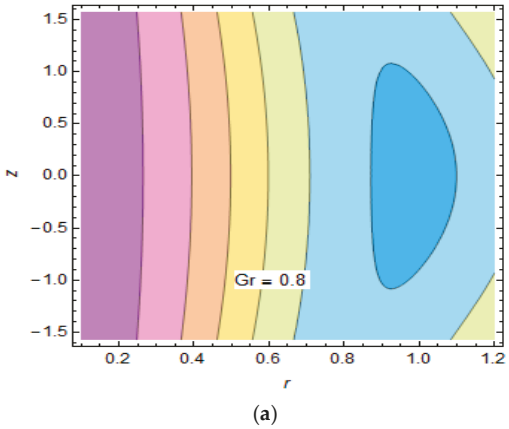

(**a**)

Figure 23. *Cont*.

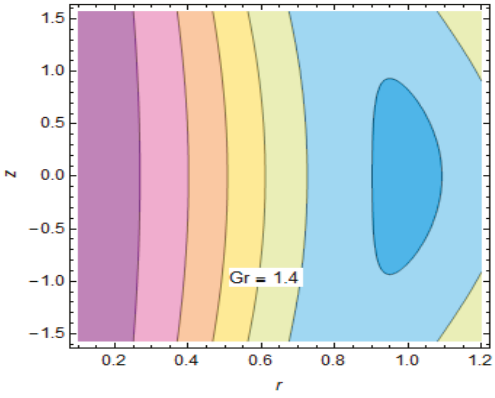

(**b**)

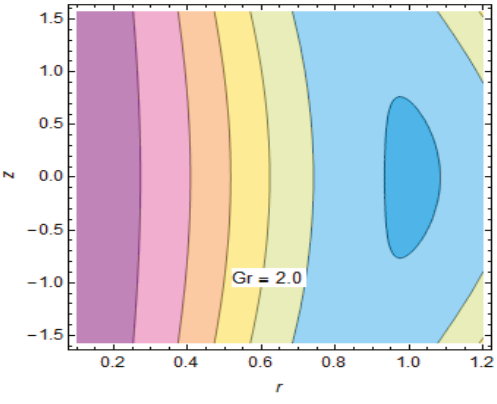

(**c**)

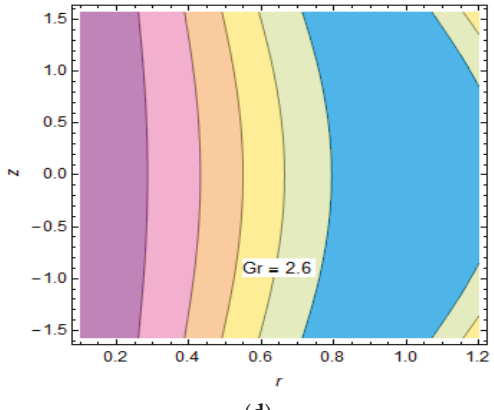

(**d**)

Figure 23. Behavior of streamlines for different values of Grashof number (**a**–**d**).

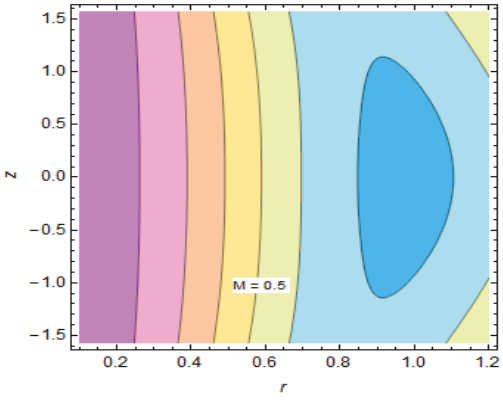

(**a**)

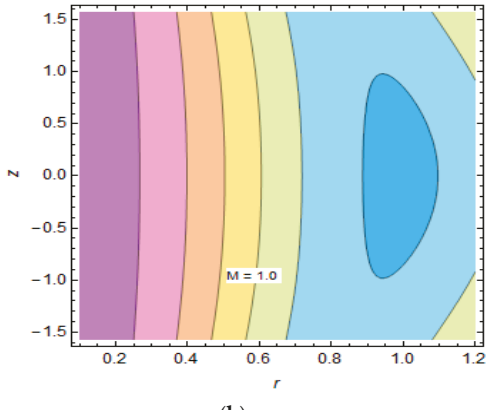

(**b**)

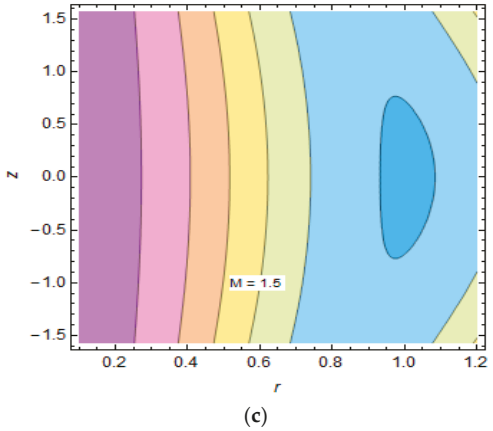

(**c**)

Figure 24. *Cont*.

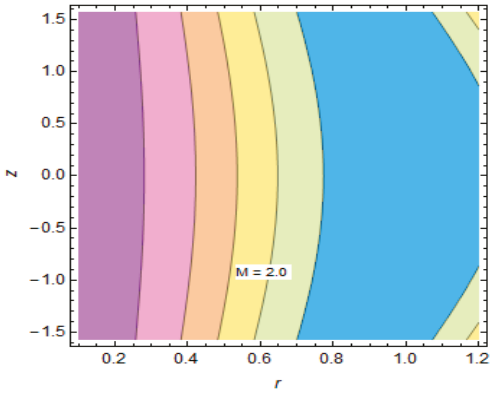

(**d**)

Figure 24. Behavior of streamlines for different values of Hartmann number (**a**–**d**).

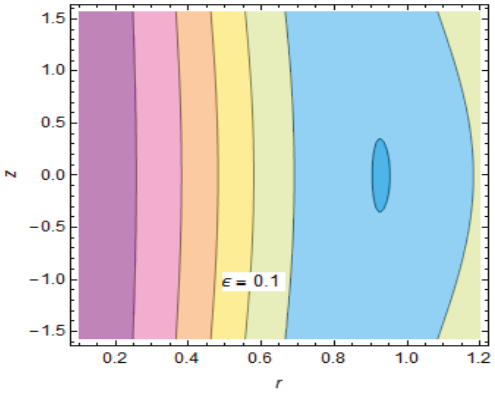

(**a**)

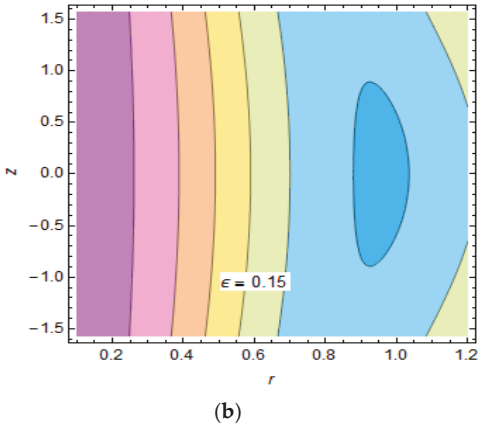

(**b**)

Figure 25. *Cont*.

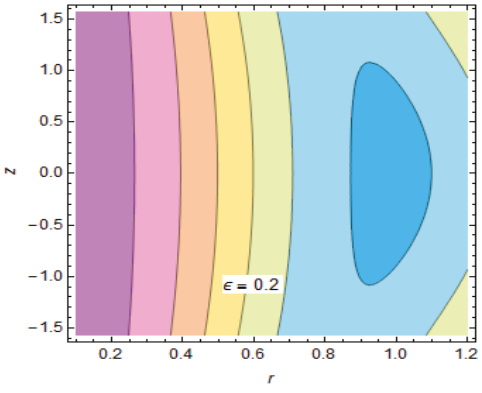

(**c**)

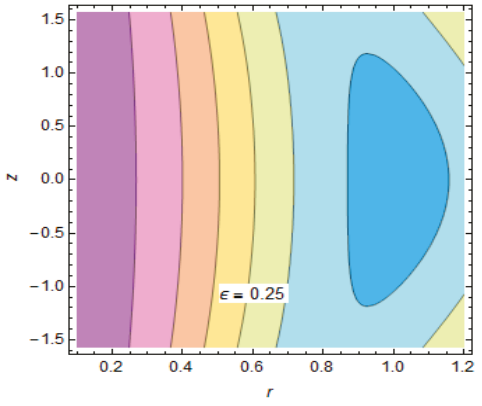

(**d**)

Figure 25. Behaviorof streamlines for different values of amplitude ratio (**a**–**d**).

Experiment-based numerical values and mathematical formulas for thermophysical characteristics of the hybrid nanofluid are expressed in Tables 1 and 2. Furthermore, the impact of engrossing parameters towards velocity and temperature profiles are presented in tabular form as shown in Tables 3 and 4. Table 3 shows that for small values of *r*, velocity decreases gradually but an increasing behavior is observed for larger radial distance against *M* and *R*. A conflicting behavior of the temperature profile towards *R* and *Gr* is depicted in Table 4. Additionally, the behaviors of velocity, temperature and magnetic induction profiles for variation in radial distance are examined and results are portrayed in Table 5. All the variations are examined for $M = 4$, $R = 2$, $Gr = 2.5$, $\Omega = 4$, $Q = 2$, $z = 1$, $\varepsilon = 0.2$.

Table 1. Numerical values of thermal characteristics of nanomaterials and base fluid at 25 °C [9,12].

Properties\Constituents	H_2O	Ag	TiO_2
Density, ρ (kg/m^3)	997	10,500	4250
Specific heat, C_p (J/kg K)	4179	235	686.2
Thermal conductivity, κ (W/m K)	0.613	429	8.95
Thermal expansion coefficient, β (10^{-5} m/(mK))	21	1.89	0.9

In addition, validation of existing results is examined by comparing them with those of Nadeem and Sadaf [50] in which an exact solution of a Newtonian Cu/blood nanofluid in the absence of magnetic induction has been studied. Table 6 shows that the two results are in good agreement. (See Table 6).

Table 2. Experimental relations for thermophysical characteristics of hybrid nanofluid [9,10].

Properties	Hybrid Nanofluid
Density	$\rho_{hnf} = \rho_f(1-\varphi_2)\left[(1-\varphi_1)+\varphi_1\left(\frac{\rho_{s_1}}{\rho_f}\right)\right]+\varphi_2\rho_{s_2}$
Heat Capacity	$\left(\rho c_p\right)_{hnf} = \left(\rho c_p\right)_f(1-\varphi_2)\left[(1-\varphi_1)+\varphi_1\left(\frac{\left(\rho c_p\right)_{s_1}}{\left(\rho c_p\right)_f}\right)\right]+\varphi_2\left(\rho c_p\right)_{s_2}$
Viscosity	$\mu_{hnf} = \frac{\mu_f}{(1-\varphi_1)^{2.5}(1-\varphi_2)^{2.5}}$
Thermal Conductivity	$\frac{\kappa_{hnf}}{\kappa_{bf}} = \frac{\kappa_{s_2}+(s-1)\kappa_{bf}-(s-1)\varphi_2\left(\kappa_{bf}-\kappa_{s_2}\right)}{\kappa_{s_2}+(s-1)\kappa_{bf}+\varphi_2\left(\kappa_{bf}-\kappa_{s_2}\right)}$, where $\frac{\kappa_{bf}}{\kappa_f} = \frac{\kappa_{s_1}+(s-1)\kappa_f-(s-1)\varphi_1\left(\kappa_f-\kappa_{s_1}\right)}{\kappa_{s_1}+(s-1)\kappa_f+\varphi_1\left(\kappa_f-\kappa_{s_1}\right)}$
Thermal Expansion Coefficient	$(\rho\beta)_{hnf} = (\rho\beta)_f[(1-\phi_1-\phi_2)+\phi_1(\frac{(\rho\beta)_{s_1}}{(\rho\beta)_f})]+\phi_2(\rho\beta)_{s_2}$,

Table 3. Numerical values of velocity profile versus *r* for variation in values of *M* and *R*.

r	w(r)					
	M=0.0	**M**=2.0	**M**=4.0	**R**=1.5	**R**=3.0	**R**=5
0.1	−1.000000	−1.000000	−1.000000	−1.000000	−1.000000	−1.000000
0.3	2.916111	2.721028	2.141469	2.721303	2.720534	2.720410
0.6	1.396253	1.358720	1.246153	1.358769	1.358632	1.358609
0.9	−0.352214	−0.235930	0.109736	−0.236095	−0.235635	−0.235561
1.2	−1.000013	−1.000013	−1.000013	−1.000013	−1.000013	−1.000013

Table 4. Numerical values of temperature profile versus r for variation in values of *R* and *Gr*.

r	θ(r)					
	R=2.0	**R**=4.0	**R**=6.0	**Gr**=0.5	**Gr**=2.0	**Gr**=3.5
0.1	1.000000	1.000000	1.000000	1.000000	1.000000	1.000000
0.3	1.074105	1.242672	1.298861	1.206081	1.140543	1.074070
0.6	0.981608	1.122851	1.169931	1.185397	1.083984	0.981587
0.9	0.501895	0.566682	0.588277	0.625917	0.564191	0.501894
1.2	0.000000	0.000000	0.000000	0.000000	0.000000	0.000000

Table 5. Variation in flow profiles for variation in radial distance *r*.

r	Velocity	Temperature	Induced Magnetic Field
0.1	−0.999999	1.000000	9.468376
0.15	1.060587	0.965941	6.306623
0.2	1.943109	0.975023	4.723305
0.25	2.349953	0.999968	3.771855
0.3	2.515741	1.028599	3.136419
0.35	2.541556	1.054529	2.681561
0.4	2.478507	1.074105	2.339547
0.45	2.355582	1.085138	2.072744
0.5	2.1907886	1.086309	1.858574
0.55	1.9962259	1.076840	1.682671
0.6	1.7806156	1.056315	1.535457
0.65	1.5506610	1.024567	1.410307
0.7	1.3118123	0.981608	1.302488

Table 5. *Cont.*

r	Velocity	Temperature	Induced Magnetic Field
0.75	1.0687020	0.927579	1.208531
0.8	0.8253723	0.862717	1.125837
0.85	0.5853391	0.787332	1.052418
0.9	0.3514943	0.701789	0.986730
0.95	0.1257983	0.606497	0.927553
0.1	−0.0913227	0.501895	0.873915
1.05	−0.3020293	0.388449	0.825024
1.1	−0.5127976	0.266646	0.780240
1.15	−0.7371672	0.136990	0.739028
1.2	−1.000013	0.000000	0.700945

Table 6. Comparison of velocity with those of Nadeem and Sadaf [50] for $n = 1, \phi_2 = 0, M = 0$ and E = 0.

r	$w(r)=\frac{1}{r}\frac{\partial \psi}{\partial r}$					
	Gr=1.0		Gr=2.0		Gr=3.0	
	Existing	[46]	Existing	[46]	Existing	[46]
0.1	−1.000000	−1.000000	−1.000000	−0.000000	−1.000000	−1.000000
0.17	−0.717905	−0.717905	−0.702637	−0.702637	−0.687369	−0.687369
0.24	−0.559148	−0.559157	−0.539095	−0.539095	−0.519033	−0.519033
0.31	−0.465611	−0.465615	−0.445894	−0.445894	−0.426172	−0.426172
0.38	−0.415011	−0.415014	−0.398441	−0.398441	−0.381868	−0.381868
0.45	−0.396309	−0.396313	−0.384359	−0.384359	−0.372405	−0.372405
0.52	−0.403142	−0.403151	−0.396393	−0.396393	−0.389636	−0.389636
0.59	−0.431481	−0.431483	−0.429839	−0.429839	−0.428195	−0.428195
0.66	−0.478539	−0.478546	−0.481408	−0.481408	−0.48427	−0.48427
0.73	−0.542336	−0.542343	−0.54867	−0.54867	−0.554997	−0.554997
0.80	−0.621365	−0.621371	−0.629747	−0.629747	−0.638123	−0.638123
0.87	−0.714447	−0.714452	−0.723131	−0.723131	−0.73181	−0.73181
0.94	−0.820564	−0.820638	−0.827574	−0.827574	−0.834509	−0.834509
1.01	−0.939132	−0.939145	−0.942016	−0.942016	−0.944887	−0.944887
1.04382	−1.00061	−1.00061	−1.00061	−1.00061	−1.00061	−1.00061

5. Conclusions

This study incorporates the effects of electromagnetic induction on a rheological model of a hybrid nanofluid in ciliary-induced peristalsis through an endoscope. The major findings are summarized as:

- Velocity of the hybrid nanofluid reduces for M and Gr near the endoscope but it increases near the external peristaltic tube having a ciliary surface due to a decreasing pressure gradient, even in creeping flow condition as observed from 2-D and 3-D plots. These results show that buoyancy effects are more prominent near the peristaltic tube and magnetic induction enhances peristalsis in presence of Ag-TiO_2 nanohybrids with 0.2% concentration.
- The magnetic induction profile displays a similar behavior as that of velocity towards the magnetic Reynolds number. An increase in values of R upgrades the flow rate and hence it is concluded that velocity and induced magnetic field relatively generate elastic oscillations. Consequently, fluid having hybrid nanoparticles can deeply interact with tumors and efficiently deliver drugs to specified section.
- The temperature of hybrid nanofluid depicts a decreasing behavior for Gr while a conflicting trend is seen for R. This trend of temperature increase of the fluid will be helpful in the removal of a cancer tumor and abnormal cells without affecting healthy parts within the body during an endoscopy.

- ❖ The behavior of the pressure rise for different parameters show that the pressure rise declines in the co-pumping region whereas it is enhanced in the pumping and free-pumping regions. Pumping rate increases for increment in radius ratio parameter which is favorable for accurate endoscopic imaging.
- ❖ The pressure gradient decreases throughout the length of the endoscope close to the ciliated peristaltic tube for $r_2 = 1$.
- ❖ Numerical values of velocity and temperature against embedding parameters explore a similar behavior as noticed in graphs. Flow profiles towards variation in radial distance are examined which satisfy the conditions of the problem.
- ❖ The presence of cilia shows a dominant effect on the behavior of the flow variables. In most cases, the sensitive interior surface of organs may be protected due to cilia as they assist velocity near the peristaltic tube.
- ❖ The peristaltic flow pattern due to ciliary activity for different parameters is displayed via streamline configuration and a reduction in the size of the trapped bolus is observed towards *R*, *M* and *Gr* but conversely enlarges for ε.
- ❖ The present work appears to be the first attempt in the literature dealing with the effects of electromagnetic induction on peristaltic transport and the heat transfer of non-Newtonian hybrid nanofluid through a ciliated tube inserted by an endoscope. Additional developments and characteristics of the problem can be examined.
- ❖ Results for Newtonian nanofluid [50] can be obtained in a limiting case.

Author Contributions: Conceptualization, M.A. and Z.S.; methodology, M.A., Z.S., P.K. and N.P.; software, A.A., P.K. and P.T.; validation, P.T. and and Z.S.; formal analysis, M.A., A.A., P.K. and N.P.; investigation, Z.S., P.K. and A.A.; resources, P.K. and P.T.; data curation, M.A.; writing—original draft preparation, M.A., Z.S. and A.A.; writing—review and editing, A.A., H.u.R.; visualization, Z.S. and H.u.R.; supervision, P.K. and A.A.; project administration, P.K., P.T. and Z.S.; funding acquisition, P.K., P.T. and Z.S. All authors have read and agreed to the published version of the manuscript.

Funding: This research was funded by the Center of Excellence in Theoretical and Computational Science (TaCS-CoE), KMUTT.

Acknowledgments: This research is supported by Postdoctoral Fellowship from King Mongkut's University of Technology Thonburi (KMUTT), Thailand.

Conflicts of Interest: The authors declare that they have no competing interests.

Nomenclature

b	Wave Amplitude in Fixed Frame Wall (m)
c	Wave speed (ms^{-1})
n	Power law index
k	Consistency index (Pa s^n)
g	Gravitational acceleration (ms^{-2})
s	Nanoparticles shape factor
E	Electric field strength (N/C)
p	Pressure (Pa)
T	Temperature (K)
T_0	Temperature of inner tube (K)
T_1	Temperature of outer tube (K)
Gr	Grashof number (dimensionless)
Q_o	Heat sink/source parameter ($Wm^{-2}K^{-1}$)
R_m	Magnetic Reynolds number
H_0	Magnetic field strength (Am^{-1})
H_r	Radial magnetic induction componentComponent (Am^{-1})
H_z	Axial magnetic induction component (Am^{-1})
c_p	Specific heat ($Jkg^{-1}K^{-1}$)
M	Hartman number

U	Radial velocity component (ms^{-1})
W	Axial velocity component (ms^{-1})
Greek Symbol	
ρ	Density (kgm^{-3})
σ	Electric conductivity (S/m)
ϕ	Magnetic force function (A^2m^{-1})
ψ	Stream function (m^2s^{-1})
β	Thermal expansion coefficient (K^{-1})
λ	Wavelength (m)
δ	Wave number (dimensionless)
$\hat{\mu}$	Magnetic Diffusivity (m^2s^{-1})
μ	Dynamic viscosity ($kgm^{-1}s^{-1}$)
ε	Wave amplitude in moving frame (m)
κ	Thermal conductivity ($Wm^{-1}K^{-1}$)
Ω	Dimensionless heat source/sink parameter
Δ	Rate of deformation tensor (s^{-1})
τ	Shear stress (Pa)
α	Measure of eccentricity
Subscript	
hnf	Hybrid Nanofluid
f	Base fluid
s_1	Solid nano particles of Ag
s_2	Solid nano particles of TiO_2

Appendix A

$$\psi_0(r) = \left(-\frac{-Fr_1^3+3Fr_1^2r_2+3Fr_1r_2^2-4r_1^3r_2^2-Fr_2^3+4r_1^2r_2^3-4\pi r_1^3r_2^2\alpha\delta\varepsilon\cos(2\pi z)+4\pi r_1^2r_2^3\alpha\delta\varepsilon\cos(2\pi z)}{2(r_1-r_2)^3}\right)+$$
$$\left(-\frac{r_1r_2\left(-6F+3r_1^2-3r_2^2+2\pi r_1^2\alpha\delta\varepsilon\cos(2\pi z)+2\pi r_1r_2\alpha\delta\varepsilon\cos(2\pi z)-4\pi r_2^2\alpha\delta\varepsilon\cos(2\pi z)\right)}{(r_1-r_2)^3}\right)r$$
$$+\left(-\frac{3Fr_1-r_1^3+3Fr_2-3r_1^2r_2+3r_1r_2^2+r_2^3-4\pi r_1^2r_2\alpha\delta\varepsilon\cos(2\pi z)+2\pi r_1r_2^2\alpha\delta\varepsilon\cos(2\pi z)+2\pi r_2^3\alpha\delta\varepsilon\cos(2\pi z)}{(r_1-r_2)^3}\right)r^2$$
$$+\left(-\frac{-2F+r_1^2-r_2^2+2\pi r_1r_2\alpha\delta\varepsilon\cos(2\pi z)-2\pi r_2^2\alpha\delta\varepsilon\cos(2\pi z)}{(r_1-r_2)^3}\right)r^3,$$

$$\phi_0(r) = \frac{1}{(r_1-r_2)}(r_1-r), \theta_0(r) = \frac{1}{(r_1-r_2)}(-r_2+r),$$

$$N_1[\psi(r,\gamma),\phi(r,\gamma),\theta(r,\gamma)]$$
$$= -\frac{1}{r^2}\left(-\frac{1}{r^2}\frac{d\psi}{dr}+\frac{1}{r}\frac{d^2\psi}{dr^2}\right)^2+\frac{2}{r}\left(-\frac{1}{r^2}\frac{d\psi}{dr}+\frac{1}{r}\frac{d^2\psi}{dr^2}\right)\left(\frac{2}{r^3}\frac{d\psi}{dr}-\frac{2}{r^2}\frac{d^2\psi}{dr^2}+\frac{1}{r}\frac{d^3\psi}{dr^3}\right)$$
$$+2\left(\frac{2}{r^3}\frac{d\psi}{dr}-\frac{2}{r^2}\frac{d^2\psi}{dr^2}+\frac{1}{r}\frac{d^3\psi}{dr^3}\right)^2+2\left(-\frac{1}{r^2}\frac{d\psi}{dr}+\frac{1}{r}\frac{d^2\psi}{dr^2}\right)\left(-\frac{6}{r^4}\frac{d\psi}{dr}+\frac{6}{r^3}\frac{d^2\psi}{dr^2}-\frac{3}{r^2}\frac{d^3\psi}{dr^3}+\frac{1}{r}\frac{d^4\psi}{dr^4}\right)$$
$$+M^2\left(-\frac{1}{r^2}\frac{d\psi}{dr}+\frac{1}{r}\frac{d^2\psi}{dr^2}\right)-A_1Gr\frac{d\theta}{dr},$$

$$N_2[\psi(r,\gamma),\phi(r,\gamma),\theta(r,\gamma)] = E-\frac{1}{r}\frac{d\psi}{dr}-\frac{1}{R_m}\left(-\frac{1}{r^2}\frac{d\phi}{dr}+\frac{1}{r}\frac{d^2\phi}{dr^2}\right),$$

$$N_3[\psi(r,\gamma),\phi(r,\gamma),\theta(r,\gamma)] = \frac{1}{r}\frac{d\theta}{dr}+\frac{d^2\theta}{dr^2}+\frac{\Omega}{A_2}.$$

$$R_m^1(r,\gamma) = 2\sum_{k=0}^{m-1}\left(\frac{1}{r^2}\psi^{(iv)}{}_{m-1-k}\psi''{}_k-\frac{1}{r^3}\psi^{(iv)}{}_{m-1-k}\psi'_k\right)+2\sum_{k=0}^{m-1}\left(\frac{1}{r^2}\psi'''{}_{m-1-k}\psi'''{}_k-\frac{6}{r^3}\psi'''{}_{m-1-k}\psi''{}_k+\frac{6}{r^4}\psi'''{}_{m-1-k}\psi'_k\right)$$
$$+15\sum_{k=0}^{m-1}\left(-\frac{2}{r^5}\psi''{}_{m-1-k}\psi'_k+\frac{1}{r^4}\psi''{}_{m-1-k}\psi''{}_k+\frac{1}{r^3}\psi'{}_{m-1-k}\psi'_k\right)+M^2\left(-\frac{1}{r^2}\psi'+\frac{1}{r}\psi''\right)-A_1Gr\theta',$$

$$R_m^2(r,\gamma) = E-\frac{1}{r}\psi'{}_{m-1}-\frac{1}{R_m}\left(-\frac{1}{r^2}\phi'{}_{m-1}+\frac{1}{r}\phi''{}_{m-1}\right),$$

$$R_m^3(r,\gamma) = r\theta''{}_{m-1}+\theta'{}_{m-1}+r\frac{\Omega}{A_2}.$$

References

1. Choi, S.U.S.; Eastman, J.A. Enhancing thermal conductivity of fluids with nanoparticles. In Proceedings of the 1995 International Mechanical Engineering Congress and Exhibition, San Francisco, CA, USA, 12–17 November 1995.
2. Awais, M.; Hayat, T.; Muqaddass, N.; Ali, A.; Awan, S.E. Nanoparticles and nonlinear thermal radiation properties in the rheology of polymeric material. *Results Phys.* **2018**, *8*, 1038–1045. [CrossRef]
3. Mehmood, A.; Zameer, A.; Ling, S.H.; Raja, M.A.Z. Design of neuro-computing paradigms for nonlinear nanofluidic system of MHD Jaffery-Hamel flow. *J. Taiwan Inst. Chem. Eng.* **2018**, *91*, 57–85. [CrossRef]
4. Shah, Z.; Sheikholeslami, M.; Kumam, P.; Shutaywi, M.; Thounthong, P. CFD simulation of water based hybrid nanofluid inside a porous enclosure employing Lorentz forces. *IEEE Access* **2019**. [CrossRef]
5. Awan, S.E.; Khan, Z.A.; Awais, M.; Rehman, S.U.; Raja, M.A.Z. Numerical treatment for hydro-magnetic unsteady channel flow of nanofluid with heat transfer. *Results Phys.* **2018**, *9*, 1543–1554. [CrossRef]
6. Qureshi, I.H.; Nawaz, M.; Shehzad, A. Numerical study of dispersion of nanoparticles in magnetohydrodynamic liquid with Hall and ion slip currents. *AIP Adv.* **2019**, *9*, 025219. [CrossRef]
7. Hassan, M.; Faisal, A.; Ali, I.; Bhatti, M.M.; Yousaf, M. Effect of Cu-Ag hybrid nanoparticles on the momentum and thermal boundary layer flow in the wedge. *Proc. Inst. Mech. Eng. Part E J. Process Mech. Eng.* **2019**. [CrossRef]
8. Shah, Z.; Alzahrani, E.O.; Alghamdi, W.; Ullah, M.Z. Influences of electrical MHD and Hall current on squeezing nanofluid flow inside rotating porous plates with viscous and joule dissipation effects. *J. Therm. Anal. Calorim.* **2020**. [CrossRef]
9. Hussain, M.; Ellahi, R.; Zeeshan, A.; Bhatti, M.M. Analysis of natural convective of non-Newtonian fluid under the effects of nanoparticles of different materials. *Proc. Inst. Mech. Eng. Part E J. Process Mech. Eng.* **2019**, *233*, 643–652. [CrossRef]
10. Rashidi, M.M.; Mohebbi, R.; Ma, Y.; Yang, Z. MHD convective heat transfer of Ag-MgO/water hybrid nanofluid in a channel with active heaters and coolers. *Int. J. Heat Mass Trans.* **2019**, *137*, 714–772.
11. Nawaz, M.; Nazir, U. An enhancement in thermal performance of partially ionized fluid due to hybrid nano-structures exposed to magnetic field. *AIP Adv.* **2019**, *9*, 085024. [CrossRef]
12. Nguyen, V.T.; Vu, V.T.; Nguyen, T.H.; Nguyen, T.A.; Tran, V.K.; Nguyen-Tri, P. Antibacterial activity of TiO_2- and ZnO-decorated with silver nanoparticles. *J. Compos. Sci.* **2019**, *3*, 61. [CrossRef]
13. Li, R.; Chen, G.; Dong, G.; Sun, X. Controllable synthesis of nanostructured TiO_2 by CTAB-assisted hydrothermal route. *New J. Chem.* **2014**, *38*, 4684–4689. [CrossRef]
14. Devi, L.G.; Kottam, N.; Murthy, B.N.; Kumar, S.G. Enhanced photocatalytic activity of transition metal ions Mn^{2+}, Ni^{2+} and Zn^{2+} doped polycrystalline titania for the degradation of aniline blue under UV/solar light. *J. Mol. Catal. A* **2010**, *328*, 44–52. [CrossRef]
15. Benkhedda, M.; Boufendi, T.; Touahri, S. Laminar mixed convective heat transfer enhancement by using Ag-TiO_2/water hybrid nanofluid in a heated horizontal annulus. *Heat Mass. Trans.* **2018**, *54*, 2799–2814. [CrossRef]
16. Abrar, M.N.; Haq, R.U.; Awais, M.; Rashid, I. Entropy analysis in a cilia transport of nanofluid under the influence of magnetic field. *Nucl. Eng. Technol.* **2017**, *49*, 1680–1688. [CrossRef]
17. Awais, M.; Bukhari, U.; Ali, A.; Yasmin, H. Convective and peristaltic viscous fluid flow with variable viscosity. *J. Eng. Phys.* **2017**, *26*, 69–78. [CrossRef]
18. Engelmann, T.W. Zur Physiologie des Ureter. *Archiv für die Gesamte Physiologie des Menschen und der Tiere* **1869**, *2*, 243–293. [CrossRef]
19. Abbas, M.A.; Bai, Y.; Rashidi, M.M.; Bhatti, M.M. Application of drug delivery in megnetohydrodynamics peristaltic blood flow of nano fluid in a non-uniform channel. *J. Mech. Med. Biol.* **2016**, *16*, 1650052. [CrossRef]
20. Hayat, T.; Nawaz, S.; Alsaedi, A.; Rafiq, M. Mixed convective peristaltic flow of water based nanofluids with Joule heating and convective boundary conditions. *PLoS ONE* **2016**, *11*, e0153537. [CrossRef]
21. Maqbool, K.; Shaheen, S.; Siddiqui, A.M. Effects of nanoparticles on MHD flow of tangent hyperbolic fluid in a ciliated tube. *Math. Biosci. Eng.* **2019**, *16*, 2927–2941. [CrossRef]
22. Hayat, T.; Farooq, S.; Alsaedi, A.; Ahmad, B. Numerical analysis for radial MHD and mixed convection effects in peristalsis of non-Newtonian nanomaterial with zero mass flux condition. *Results Phys.* **2017**, *7*, 451–458. [CrossRef]

23. Misra, J.C.; Pandey, S.K. Peristaltic flow of a multi-layered power-law fluid through a cylindrical tube. *Int. J. Eng. Sci.* **2001**, *39*, 387–402. [CrossRef]
24. Ahmad Farooq, A.; Shah, Z.; O Alzahrani, E. Heat Transfer Analysis of a Magneto-Bio-Fluid Transport with Variable Thermal Viscosity through a Vertical Ciliated Channel. *Symmetry* **2019**, *11*, 1240. [CrossRef]
25. Saeed, A.; Islam, S.; Dawar, A.; Shah, Z.; Kumam, P.; Khan, W. Influence of Cattaneo–Christov heat flux on MHD Jeffrey, Maxwell, and Oldroyd-B Nanofluids with Homogeneous-Heterogeneous reaction. *Symmetry* **2019**, *11*, 439. [CrossRef]
26. Ellahi, R.; Sait, S.M.; Shehzad, N.; Mobin, N. Numerical simulation and mathematical modeling ofElectro-Osmotic Couette–Poiseuille flow of MHD power-law nanofluid with entropy generation. *Symmetry* **2019**, *11*, 1038. [CrossRef]
27. Hayat, T.; Farooq, S.; Ahmad, B.; Alsaedi, A. Homogeneous-heterogeneous reactions and heat source/sink effects in MHD peristaltic flow of micropolar fluid with Newtonian heating in a curved channel. *J. Mol. Liq.* **2016**, *223*, 469–488. [CrossRef]
28. Bhatti, M.M.; Zeeshan, A.; Ellahi, R. Simultaneous effects of coagulation and variable magnetic field on peristaltically induced motion of Jeffrey nanofluid containing gyrotactic microorganism. *Microvasc. Res.* **2017**, *110*, 32–42. [CrossRef]
29. Rana, P.; Shukla, N. Entropy generation analysis for non-similar analytical study of nanofluid flow and heat transfer under the influence of aligned magnetic field. *Alex. Eng. J.* **2018**, *57*, 3299–3310. [CrossRef]
30. Shit, G.C.; Ranjit, N.K.; Sinha, A.; Roy, M. Effect of induced magnetic field on peristaltic transport of a micropolar fluid in the presence of slip velocity. *Int. J. Appl. Math. Mech.* **2014**, *10*, 81–107.
31. Noreen, S. Mixed convection peristaltic flow with slip conditions and induced magnetic field. *Eur. Phys. J. Plus* **2014**, *129*, 33. [CrossRef]
32. Noreen, S. Induced magnetic field effects on peristaltic flow in a curved channel. *Zeitschrift für Naturforschung A* **2015**, *70*, 3–9. [CrossRef]
33. Jha, B.K.; Aina, B. Effect of induced magnetic field on MHD mixed convection flow in vertical microchannel. *Int. J. Appl. Mech. Eng.* **2017**, *22*, 567–582. [CrossRef]
34. Eifler, A.C.; Thaxton, C.S. Nanoparticle therapeutics: FDA approval, clinical trials, regulatory pathways and case study. *Methods Mol. Biol.* **2011**, *726*, 325–338.
35. Ellahi, R.; Zeeshan, A.; Hussain, F.; Abbas, T. Study of shiny film coating on multi-fluid flows of a rotating disk suspended with nano-sized silver and gold particles: A comparative analysis. *Coatings* **2018**, *8*, 422. [CrossRef]
36. Akbar, N.S.; Butt, A.W. Physiological transportation of Casson fluid in a plumb duct. *Commun. Phys.* **2015**, *63*, 347–352.
37. Dawar, A.; Shah, Z.; Kumam, P.; Khan, W.; Islam, S. Influence of MHD on thermal behavior of Darcy-Forchheimer nanofluid thin film flow over a nonlinear stretching disc. *Coatings* **2019**, *9*, 446. [CrossRef]
38. Ellahi, R.; Zeeshan, A.; Hussain, F.; Abbas, T. Thermally charged MHD bi-phase flow coatings with non-Newtonian nanofluid and Hafnium particles through slippery walls. *Coatings* **2019**, *9*, 300. [CrossRef]
39. Hayat, T.; Momoniat, E.; Mahomed, F.M. Endoscope effects on MHD peristaltic flow of a power law fluid. *Math. Probl. Eng.* **2006**, *2006*, 84276. [CrossRef]
40. Hayat, T.; Ali, N. Effects of an endoscope on peristaltic flow of a micropolar fluid. *Math. Comput. Model.* **2008**, *48*, 721–733. [CrossRef]
41. Nadeem, S.; Akbar, N.S. Influence of temperature dependent viscosity on peristaltic transport of a Newtonian fluid: Application of an endoscope. *Appl. Math. Comput.* **2010**, *216*, 3606–3619. [CrossRef]
42. Rathod, V.P.; Asha, S.K. Effects of magnetic field and an endoscope on peristaltic motion. *J. Appl. Math.* **2011**, *2011*, 148561. [CrossRef]
43. Bhatti, M.M.; Zeeshan, A. Study of variable magnetic field and endoscope on peristaltic blood flow of particle-fluid suspension through an annulus. *Biomed. Eng. Lett.* **2016**, *6*, 242–249. [CrossRef]
44. Ramesh, K.; Devakar, M. The effects of endoscope and heat transfer on the peristaltic flow of a second grade fluid in an inclined tube. *J. Mech. Med. biol.* **2016**, *16*, 1650057. [CrossRef]
45. Ramesh, K.; Devakar, M. Magnetohydrodynamic peristaltic flow of Pseudoplastic fluid in a vertical asymmetic channel through porous medium with heat and mass transfer. *Iran. J. Sci. Technol.-Sci.* **2017**, *41*, 257–272. [CrossRef]

46. Abdellateef, A.I.; UlHaque, S.Z. Peristaltic flow of Newtonian nanofluid through an inclined annulus cylinder. *Eur. J. Pure Appl. Math.* **2016**, *9*, 266–276.
47. Ramesh, K.; Devakar, M. Effect of endoscope on the peristaltic transport of a couple stress fluid with heat transfer: Application to biomedicine. *Nonlinear Eng.* **2019**, *8*, 619–629. [CrossRef]
48. Maqbool, K.; Mann, A.B.; Siddiqui, A.M.; Shaheen, S. Fractional generalized Burgers' fluid flow due to metachronal waves of cilia in an inclined tube. *Adv. Mech. Eng.* **2017**, *9*, 1687814017715565. [CrossRef]
49. Akbar, N.S.; Tripathi, D.; Khan, Z.H.; Beg, O.A. Mathematical model for ciliary induced transport in MHD flow of Cu/H_2O nanofluids with magnetic induction. *Chin. J. Phys.* **2017**, *55*, 947–962. [CrossRef]
50. Nadeem, S.; Sadaf, H. Trapping study of nanofluids in an annulus with cilia. *AIP Adv.* **2015**, *5*, 127204. [CrossRef]

coatings

MDPI

Article

Mathematical Analysis of Entropy Generation in the Flow of Viscoelastic Nanofluid through an Annular Region of Two Asymmetric Annuli Having Flexible Surfaces

Arshad Riaz [1,*], Ayesha Gul [1], Ilyas Khan [2,*], Katta Ramesh [3], Sami Ullah Khan [4], Dumitru Baleanu [5,6,7] and Kottakkaran Sooppy Nisar [8]

1 Department of Mathematics, Division of Science and Technology, University of Education, Lahore 54770, Pakistan; ayeshagul728@gmail.com
2 Department of Mathematics, College of Science Al-Zulfi, Majmaah University, Al-Majmaah 11952, Saudi Arabia
3 Department of Mathematics, Symbiosis Institute of Technology, Symbiosis International University, Pune 412115, India; ramesh.katta@sitpune.edu.in
4 Department of Mathematics, COMSATS University Islamabad, Sahiwal 57000, Pakistan; samikhan@cuisahiwal.edu.pk
5 Department of Mathematics, Cankaya University, Ankara 06790, Turkey; dumitru@cankaya.edu.tr
6 Institute of Space Sciences, 077125 Magurele-Bucharest, Romania
7 Department of Medical Research, China Medical University Hospital, China Medical University, Taichung 40402, Taiwan; Baleanu@mail.cmuh.org.tw
8 Department of Chemistry, College of Arts and Sciences, Wadi Aldawaser, Prince Sattam bin Abdulaziz University, Al-Kharj 11991, Saudi Arabia; n.sooppy@psau.edu.sa
* Correspondence: arshad-riaz@ue.edu.pk (A.R.); i.said@mu.edu.sa (I.K.)

Received: 22 January 2020; Accepted: 25 February 2020; Published: 28 February 2020

Abstract: In this manuscript, the authors developed the mathematical model for entropy generation analysis during the peristaltic propulsion of Jeffrey nanofluids passing in a midst of two eccentric asymmetric annuli. The model was structured by implementation of lubrication perspective and dimensionless strategy. Entropy generation caused by the irreversible influence of heat and mass transfer of nanofluid and viscous dissipation of the considered liquid was taken into consideration. The governing equations were handled by a powerful analytical technique (HPM). The comparison of total entropy with the partial entropy was also invoked by discussing Bejan number results. The influence of various associated variables on the profiles of velocity, temperature, nanoparticle concentration, entropy generation and Bejan number was formulated by portraying the figures. Mainly from graphical observations, we analyzed that, in the matter of thermophoresis parameter and Brownian motion parameter, entropy generation is thoroughly enhanced while inverse readings were reported for the temperature difference parameter and the ratio of temperature to concentration parameters.

Keywords: entropy generation; Bejan number; nanoparticles; Jeffrey fluid model; peristaltic flow; analytical solutions; eccentric annuli

1. Introduction

Nanofluid, characterized by a significant increase in a number of properties compared to conventional engineered fluid [1], is found to serve in many practical applications, for example, petroleum engineering [2–5], power industry [6,7], and medical science [8,9], which has drawn particular attentions for cancer treatments in recent years. Cancer covers a huge group of diseases

which can damage any portion of the body. Nowadays, cancer is a main cause of death all over the world, around 70% of cancer deaths materialize in middle- and low-income countries. There are many treatments to cure cancer, such as surgery, radiation and chemotherapy, but these procedures may harm the normal tissue. Hanahan and Weinberg [10] have explained six cancer hallmarks, helping to differentiate features between the tumor and normal tissue, and maybe come up with better alternative therapies. These hallmarks include inducing activating invasion and metastasis, resisting cell death, angiogenesis, enabling replicative immortality, sustaining proliferative signaling, and evading growth suppressors. Based on these cancer hallmarks, latest therapies for cancer treatment have been introduced. Nowadays, nanomedicine (nanomedicine is a branch of nanotechnology, or utilization of materials less than 100 nm, applied to medicine and health sciences) is the prominent procedure for treating cancer. The nanocarriers' properties, including their targeting modifications, favorable drug release profiles, high surface-to-volume ratios, and nanoscale sizes, may authorize them to reach and target the tissue of a tumor and the deliverance of drugs in a stable and controlled manner. For cancer research, nanomaterials are available in modified shape, because to treat specific tumors, size and surface features are crucial. The size of the nanoparticle is a key attribute, which travel across the bloodstream, ensuring delivery of nanocarriers to tumor tissue. The small-scale nanoparticles can stockpile comfortably in the physiological tumor vessels and also extravagate into normal tissue. In view of many nanoparticle applications in bio-fluid flows, many researchers have concentrated their work in the field of bio-nanofluids. For instance, Prakash et al. [11] have presented the study of nanofluids which is relevant to bio-inspired nanofluid smart pump designs, which may also be exploited in smart-drug delivery. Abbas et al. [12] have provided mathematical modelling to describe the peristaltic transport of blood (blood is treated as nanofluid) and analyzed the entropy analysis. They concluded that such a study can help in analyzing blood flow in small blood vessels with elastic walls. Abdelsalam and Bhatti [13] have given a theoretical model to describe the effect of sundry variables on the feature of blood flows in the presence of nanoparticles, and suggested that Brownian motion and chemical reaction exhibit dual variation of nanoparticles' volume fraction. Shah et al. [14] have presented the theoretical study, which is applicable to the drug-delivery system, as the micro-polar nanoparticles of gold are proficient drug-delivery and drug-carrying mediums. Bhatti et al. [15] studied the two-phase flow under the effects of coagulation with peristaltic pumping through the Prandtl stress model, with magnetic field and porous medium terms. They analyzed that friction forces flourish with the altitude of clot height and particle concentration, on the other hand they are minimized with other involving factors in the problem.

It is extensively known that biological liquids, such as gastric fluids and blood, generally behave as non-Newtonian fluids. Many researchers have considered Jeffrey/viscoelastic fluid as biological (synovial, blood, gastric, chyme, and saliva) fluid. To delineate the stress relaxation effects of real fluids, the viscoelastic fluid model is appropriately competent. These effects cannot describe the usual Newtonian fluid model. In addition to this, the Jeffrey fluid model can also describe the characteristic of memory-time scale. Kahshan et al. [16] have described the Creeping flow of a viscoelastic fluid in a channel with an application to flow in a flat-plate hemodialyzer. Pandey and Tripathi [17] have explored the viscoelastic fluid flow by peristalsis in a channel in order to apply the model to the swallowing of food-bolus through the esophagus. Ellahi et al. [18] used Jeffrey fluid as bio-fluid and studied the problem of the peristaltic flow of Jeffrey fluid in a non-uniform rectangular duct, which may be applicable to modern drug delivery systems with great utility. Ramesh et al. [19] have considered Jeffery's viscoelastic formulation, which is employed in the rheology of blood. Some more studies can be seen through [20–25].

In thermodynamics, entropy is a measure of the number of specific modes in which a thermodynamic system can be organized, often called a measure of impedance or a measure of progress toward thermodynamic equilibrium. Pakdemirli and Yilbas [26] have analyzed the entropy generation mechanism of non-Newtonian fluid through a pipe. According to them, the entropy Brinkman number causes an increase in entropy generation. Entropy generation in a peristaltic

pumping problem has been presented by Souidi et al. [27]. Heat and fluid flow causing entropy generation in backward-facing step flow is suggested by Abu-Nada [28]. More studies on entropy generation in peristaltic transports are reported in [29–31], but none of these established the entropy analysis of viscoelastic nanofluids in eccentric cylinders having a peristaltic outer surface.

Keeping in mind the physiological applications of a peristaltic propulsion of viscoelastic fluids, the investigators focused on the entropy generation and Bejan number during the peristaltic transport of viscoelastic nanofluid in the annulus region of two eccentric cylinders. The equations of governing the flow are considered in the cylindrical geometry. The concerned non-dimensional system of equations is solved using optimal homotropy perturbation technique under the long wavelength and low Reynolds number assumptions. The effects of involved parameters on the pressure rise, velocity, temperature, nanoparticle concentration, entropy generation, and Bejan number are shown through graphical illustrations.

2. Mathematical Analysis

Let us analyze the entropy generation in three-dimensional flow of nanofluid with the Jeffrey model by considering the passage in a space between two eccentric annuli, with flexible outer surface along with inner rigid cylinder, going with the fluid with constant speed V. The walls of the outer annulus produce peristaltic waves along its length, which helps in pushing the fluid forward. A concentration C_0 of nanoparticles is assumed at the inner boundary, while the outer is maintained at C_1. The temperature distributions are described as T_0 and T_1 on the considered inner and lower walls accordingly (see Figure 1).

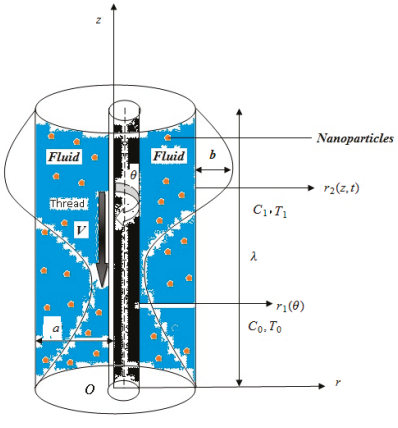

Figure 1. Diagram of flow mechanism and annuli.

The physical behavior of inner and outer layers of the annuli is manipulated mathematically as follows:

$\chi_i = \chi_j + \chi_k \cos\gamma$, for $i = 1, 2 \ldots$, where χ_1, $\chi_j = \delta$, $\chi_k = \varepsilon$, and $\gamma = \theta$ are representing the inner cylinder walls. Similarly, χ_2, $\chi_j = a$, $\chi_k = b$, and $\gamma = \frac{2\pi}{\lambda}(z - ct)$ are suggesting the same for outer annuli. Above appearing δ, a, b, λ, and c are denoting the radii of inner and outer cylinders, the amplitude of the wave, the wavelength and the wave speed, orderly.

According to the considered geometry, the velocity components are suggested as $[w_1(r, \theta, z), 0, w_2(r, \theta, z)]$. The mathematical structure of the given problem can be entertained by the following expressions based on physical laws:

$$\frac{\partial w_1}{\partial r} + \frac{\partial w_2}{\partial z} + \frac{w_1}{r} = 0, \tag{1}$$

$$\rho_f\left(\frac{\partial w_1}{\partial t}+w_1\frac{\partial w_1}{\partial r}+w_2\frac{\partial w_1}{\partial z}\right)=-\frac{\partial p}{\partial r}+\frac{\partial \Upsilon_{11}}{\partial r}+\frac{1}{r}\frac{\partial \Upsilon_{12}}{\partial \theta}+\frac{\partial \Upsilon_{13}}{\partial z}+\frac{\Upsilon_{11}}{r}-\frac{\Upsilon_{22}}{r}, \tag{2}$$

$$0=-\frac{1}{r}\frac{\partial p}{\partial \theta}+\frac{\partial \Upsilon_{12}}{\partial r}+\frac{1}{r}\frac{\partial \Upsilon_{22}}{\partial \theta}+\frac{\partial \Upsilon_{23}}{\partial z}+\frac{\Upsilon_{21}}{r}+\frac{\Upsilon_{12}}{r}, \tag{3}$$

$$\left.\begin{aligned}\rho_f\left(\tfrac{\partial w_2}{\partial t}+w_1\tfrac{\partial w_2}{\partial r}+w_2\tfrac{\partial w_2}{\partial z}\right)=&-\tfrac{\partial p}{\partial z}+\tfrac{\partial \Upsilon_{31}}{\partial r}+\tfrac{1}{r}\tfrac{\partial \Upsilon_{32}}{\partial \theta}+\tfrac{\partial \Upsilon_{33}}{\partial z}+\tfrac{\Upsilon_{31}}{r}\\&+\rho_f g\alpha(T-T_o)+\rho_f g\alpha(C-C_o),\end{aligned}\right\} \tag{4}$$

$$\left.\begin{aligned}&(\rho c)_f\left(\tfrac{\partial T}{\partial t}+w_1\tfrac{\partial T}{\partial r}+w_2\tfrac{\partial T}{\partial z}\right)=k\left(\tfrac{\partial^2 T}{\partial r^2}+\tfrac{1}{r^2}\tfrac{\partial^2 T}{\partial \theta^2}+\tfrac{\partial^2 T}{\partial z^2}+\tfrac{1}{r}\tfrac{\partial T}{\partial r}\right)+(\rho c)_p\\&\left[D_B\left(\tfrac{\partial C}{\partial r}\tfrac{\partial T}{\partial r}+\tfrac{1}{r^2}\tfrac{\partial C}{\partial \theta}\tfrac{\partial T}{\partial \theta}+\tfrac{\partial C}{\partial z}\tfrac{\partial T}{\partial z}\right)+\tfrac{D_T}{T_o}\left(\left(\tfrac{\partial T}{\partial r}\right)^2+\tfrac{1}{r^2}\left(\tfrac{\partial T}{\partial \theta}\right)^2+\left(\tfrac{\partial T}{\partial z}\right)^2\right)\right]\\&+\Upsilon_{11}\tfrac{\partial w_1}{\partial r}+\tfrac{1}{r}\Upsilon_{12}\tfrac{\partial w_1}{\partial \theta}+\Upsilon_{13}\left(\tfrac{\partial w_1}{\partial z}+\tfrac{\partial w_2}{\partial r}\right)+\tfrac{1}{r}\Upsilon_{32}\tfrac{\partial w_2}{\partial \theta}+\Upsilon_{33}\tfrac{\partial w_2}{\partial z}+\tfrac{w_1}{r}\Upsilon_{22},\end{aligned}\right\} \tag{5}$$

$$\frac{\partial C}{\partial t}+w_1\frac{\partial C}{\partial r}+w_2\frac{\partial C}{\partial z}=D_B\left(\frac{\partial^2 C}{\partial r^2}+\frac{1}{r^2}\frac{\partial^2 C}{\partial \theta^2}+\frac{\partial^2 C}{\partial z^2}+\frac{1}{r}\frac{\partial C}{\partial r}\right)+\frac{D_T}{T_o}\left(\frac{\partial^2 T}{\partial r^2}+\frac{1}{r^2}\frac{\partial^2 T}{\partial \theta^2}+\frac{\partial^2 T}{\partial z^2}+\frac{1}{r}\frac{\partial T}{\partial r}\right). \tag{6}$$

In this study, constitutive relation used for fluid is the Jeffrey mode [18], which has the following expression:

$$\boldsymbol{\Upsilon}=\frac{\mu}{1+\lambda_1}\left(\dot{\gamma}+\lambda_2\ddot{\gamma}\right). \tag{7}$$

To execute the collective effects of emerging parameters, we adopt the process of non-dimensionalization by introducing the following transformations [15,20–24]:

$$\left.\begin{aligned}&p'=\tfrac{a^2}{\mu c\lambda}p,\ w'=\tfrac{w_2}{c},\ u'=\tfrac{\lambda}{ac}w_1,\ V'=\tfrac{V}{c},\ z'=\tfrac{z}{\lambda},\ r'=\tfrac{r}{a},\ \theta'=\theta,\\&t'=\tfrac{c}{\lambda}t,\ \varphi=\tfrac{b}{a},\ \varepsilon'=\tfrac{\varepsilon}{a},\ Re=\tfrac{\rho ca}{\mu},\ \delta'=\tfrac{\delta}{a},\ \overline{\theta}=\tfrac{T-T_o}{T_1-T_o},\\&\delta_o=\tfrac{a}{\lambda},\ \sigma=\tfrac{C-C_o}{(C_1-C_o)},\ P_r=\tfrac{\mu}{\rho\alpha},\ S_c=\tfrac{\mu}{\rho D_B},\ Br=\tfrac{\rho_f g\alpha a^2}{\mu c}(T_1-T_o),\\&Gr=\tfrac{\rho_f g\alpha a^2}{\mu c}(C_1-C_o),\ Nb=\tfrac{\tau D_B}{\alpha_f}(C_1-C_o),\ Nt=\tfrac{\tau D_T}{T_o\alpha_f}(T_1-T_o),\\&\alpha_f=\tfrac{k}{(\rho c)_f},\ \tau=\tfrac{(\rho c)_p}{(\rho c)_f},\ Gc=\tfrac{\mu c^2}{K(T_1-T_o)},S'=\tfrac{\mu c}{a}.\end{aligned}\right\}$$

In light of the above manufactured relations, the Equations (1) to (6) become

$$\frac{\partial u'}{\partial r'}+\frac{\partial w'}{\partial z'}+\frac{u'}{r'}=0, \tag{8}$$

$$\mathrm{Re}\delta_o\left(\frac{\partial u'}{\partial t'}+u'\frac{\partial w'}{\partial r'}+w'\frac{\partial u'}{\partial z'}\right)=-\frac{\partial p'}{\partial r'}+\delta_o\frac{\partial S'_{11}}{\partial r'}+\delta_o\frac{1}{r'}\frac{\partial S'_{12}}{\partial \theta'}+\delta_o^2\frac{\partial S'_{13}}{\partial z'}+\delta_o\frac{S'_{11}}{r'}-\delta_o\frac{S'_{22}}{r'}, \tag{9}$$

$$0=-\frac{1}{r'}\frac{\partial p'}{\partial \theta'}+\delta_o\frac{\partial S'_{21}}{\partial r'}+\delta_o\frac{1}{r'}\frac{\partial S'_{22}}{\partial \theta'}+\delta_o^2\frac{\partial S'_{23}}{\partial z'}+\delta_o\frac{S'_{21}}{r'}+\delta_o\frac{S'_{12}}{r'}, \tag{10}$$

$$\mathrm{Re}\delta_o\left(\frac{\partial w'}{\partial t'}+u'\frac{\partial w'}{\partial r'}+w'\frac{\partial w'}{\partial z'}\right)=-\frac{\partial p'}{\partial z'}+\frac{\partial S'_{31}}{\partial r'}+\frac{1}{r'}\frac{\partial S'_{32}}{\partial \theta'}+\delta_o\frac{\partial S'_{33}}{\partial z'}+\frac{S'_{31}}{r'}+Gr\overline{\theta}+Br\sigma, \tag{11}$$

$$\left.\begin{aligned}&\delta_o\mathrm{Re}P_r\left(\tfrac{\partial \overline{\theta}}{\partial T'}+u'\tfrac{\partial \overline{\theta}}{\partial r'}+w'\tfrac{\partial \overline{\theta}}{\partial z'}\right)=\left(\tfrac{\partial^2\overline{\theta}}{\partial r'^2}+\tfrac{1}{r'^2}\tfrac{\partial^2\overline{\theta}}{\partial \theta'^2}+\delta_o^2\tfrac{\partial^2\overline{\theta}}{\partial z'^2}+\tfrac{1}{r'}\tfrac{\partial\overline{\theta}}{\partial r'}\right)\\&+Nb\left(\tfrac{\partial\sigma}{\partial r'}\tfrac{\partial\overline{\theta}}{\partial r'}+\tfrac{1}{r'^2}\tfrac{\partial\sigma}{\partial\theta'}\tfrac{\partial\overline{\theta}}{\partial\theta'}+\delta_o^2\tfrac{\partial\sigma}{\partial z'}\tfrac{\partial\overline{\theta}}{\partial z'}\right)+Nt\left(\left(\tfrac{\partial\overline{\theta}}{\partial r'}\right)^2+\tfrac{1}{r'^2}\left(\tfrac{\partial\overline{\theta}}{\partial\theta'}\right)^2\right.\\&\left.+\delta_o^2\left(\tfrac{\partial\overline{\theta}}{\partial z'}\right)^2\right)+Gc\left(\delta_o S'_{11}\tfrac{\partial u'}{\partial r'}+\delta_o\tfrac{1}{r'}S'_{12}\tfrac{\partial u'}{\partial\theta'}+S'_{13}\left(\delta_o^2\tfrac{\partial u'}{\partial z'}+\tfrac{\partial w'}{\partial r'}\right)\right.\\&\left.+\tfrac{1}{r'}S'_{32}\tfrac{\partial w'}{\partial\theta'}+\delta_o S'_{33}\tfrac{\partial w'}{\partial z'}+\delta_o\tfrac{u'}{r'}S'_{22}\right),\end{aligned}\right\} \tag{12}$$

$$\left.\begin{array}{l}\delta_o \mathrm{Re} S_c\left(\frac{\partial \sigma}{\partial t'}+u'\frac{\partial \sigma}{\partial r'}+w'\frac{\partial \sigma}{\partial z'}\right)=\left(\frac{\partial^2 \sigma}{\partial r'^2}+\frac{1}{r'^2}\frac{\partial^2 \sigma}{\partial \theta'^2}+\delta_o^2\frac{\partial^2 \sigma}{\partial z'^2}+\frac{1}{r'}\frac{\partial \sigma}{\partial r'}\right)\\ +\frac{Nt}{Nb}\left(\frac{\partial^2 \overline{\theta}}{\partial r'^2}+\frac{1}{r'^2}\frac{\partial^2 \overline{\theta}}{\partial \theta'^2}+\delta_o^2\frac{\partial^2 \overline{\theta}}{\partial z'^2}+\frac{1}{r'}\frac{\partial \overline{\theta}}{\partial r'}\right).\end{array}\right\} \tag{13}$$

Here, the quantities like Re, δ_0, Gr, Br, P_r, Nb, Nt, Gc and S_c represent the Reynolds number, wave number, local temperature Grashof number, local nanoparticle Grashof number, Prandtl number, Brownian motion parameter, thermophoresis parameter, Brinkman number, and Schmidt number, consecutively. After incorporating the theory of lubrication in this problem and disregarding the prime symbols, Equations (8) to (13) can be viewed as:

$$\frac{\partial u}{\partial r}+\frac{\partial w}{\partial z}+\frac{u}{r}=0, \tag{14}$$

$$\frac{\partial p}{\partial r}=0=\frac{\partial p}{\partial \theta}, \tag{15}$$

$$0=-\frac{\partial p}{\partial z}+\frac{\partial S_{31}}{\partial r}+\frac{1}{r}\frac{\partial S_{32}}{\partial \theta}+\frac{S_{31}}{r}+Gr\overline{\theta}+Br\sigma, \tag{16}$$

$$\left.\begin{array}{l}0=\left(\frac{\partial^2 \overline{\theta}}{\partial r^2}+\frac{1}{r^2}\frac{\partial^2 \overline{\theta}}{\partial \theta^2}+\frac{1}{r}\frac{\partial \overline{\theta}}{\partial r}\right)+Nb\left(\frac{\partial \sigma}{\partial r}\frac{\partial \overline{\theta}}{\partial r}+\frac{1}{r^2}\frac{\partial \sigma}{\partial \theta}\frac{\partial \overline{\theta}}{\partial \theta}\right)\\ +Nt\left(\left(\frac{\partial \overline{\theta}}{\partial r}\right)^2+\frac{1}{r^2}\left(\frac{\partial \overline{\theta}}{\partial \theta}\right)^2\right)+Gc\left(S_{13}\frac{\partial w}{\partial r}+\frac{1}{r}S_{32}\frac{\partial w}{\partial \theta}\right),\end{array}\right\} \tag{17}$$

$$0=\left(\frac{\partial^2 \sigma}{\partial r^2}+\frac{1}{r^2}\frac{\partial^2 \sigma}{\partial \theta^2}+\frac{1}{r}\frac{\partial \sigma}{\partial r}\right)+\frac{Nt}{Nb}\left(\frac{\partial^2 \overline{\theta}}{\partial r^2}+\frac{1}{r^2}\frac{\partial^2 \overline{\theta}}{\partial \theta^2}+\frac{1}{r}\frac{\partial \overline{\theta}}{\partial r}\right). \tag{18}$$

The dimensionless components of the stress tensor for Jeffrey model in eccentric annuli, by using cylindrical coordinates, are given by the following relations [18–20] after ignoring the prime symbols:

$$S_{11}=\frac{2\delta_o}{1+\lambda_1}\left(1+\lambda_2\delta_o\frac{c}{a}(u_{rt}+uu_{rr}+wu_{rz})\right), \tag{19}$$

$$S_{12}=\frac{\delta_o}{1+\lambda_1}\left(1+\lambda_2\delta_o\frac{c}{ar}\left(u_{t\theta}+uu_{r\theta}-r^{-1}u_\theta+wu_{z\theta}\right)\right), \tag{20}$$

$$S_{13}=\frac{1}{1+\lambda_1}\left(1+\lambda_2\delta_o\frac{c}{a}(\partial_t+u\partial_r+w\partial_z)\right)\left(\delta_o^2u_z+w_r\right), \tag{21}$$

$$S_{22}=\frac{2\delta_o}{1+\lambda_1}\left(1+\lambda_2\delta_o\frac{c}{ar}\left(u_t+uu_r-r^{-1}u+wu_z\right)\right), \tag{22}$$

$$S_{23}=\frac{1}{1+\lambda_1}\left(\frac{1}{r}w_\theta+\lambda_2\delta_o\frac{c}{ar}\left(w_{\theta t}+uw_{\theta r}-r^{-1}w_\theta+ww_{\theta z}\right)\right), \tag{23}$$

$$S_{33}=\frac{2\delta_o}{1+\lambda_1}\left(1+\lambda_2\delta_o\frac{c}{a}(w_{zt}+uw_{rz}+ww_{zz})\right). \tag{24}$$

So by switching expressions of the above stresses (after applying the constraints of long wavelength and low Reynolds number) in Equations (16)–(18), we get:

$$\frac{1}{1+\lambda_1}p_z=w_{rr}+\frac{1}{r}w_{\theta\theta}+\frac{1}{r}w_r+\left(Gr\overline{\theta}+Br\sigma\right)(1+\lambda_1), \tag{25}$$

$$\left.\begin{array}{l}0=\left(\overline{\theta}_{rr}+\frac{1}{r^2}\overline{\theta}_{\theta\theta}+\frac{1}{r}\overline{\theta}_r\right)+Nb\left(\sigma_r\overline{\theta}_r+\frac{1}{r^2}\sigma_\theta\overline{\theta}_\theta\right)+Nt\left(\overline{\theta}_r{}^2+\frac{1}{r^2}\overline{\theta}_\theta{}^2\right)\\ +Gc\left(\frac{1}{1+\lambda_1}\left(w_rw_z+\frac{1}{r^2}w_\theta{}^2\right)\right).\end{array}\right. \tag{26}$$

$$0=\left(\sigma_{rr}+\frac{1}{r^2}\sigma_{\theta\theta}+\frac{1}{r}\sigma_r\right)+\frac{Nt}{Nb}\left(\overline{\theta}_{rr}+\frac{1}{r^2}\overline{\theta}_{\theta\theta}+\frac{1}{r}\overline{\theta}_r\right). \tag{27}$$

The subscripts of $u, w, p, \partial, \theta$ and σ denote the velocity components, pressure, partial differentiation, temperature, and concentration, respectively. The non-dimensional form of radii will take the following form [32]:

$$\left.\begin{array}{l} r_1 = \delta + \varepsilon \cos\theta, \\ r_2 = 1 + \varphi \cos 2\pi(z-t). \end{array}\right\} \tag{28}$$

The respective boundary conditions may be put in the form [32]:

$$\left.\begin{array}{l} w = V, \overline{\theta} = 0, \sigma = 0 \text{ at } r = r_1, \\ w = 0, \overline{\theta} = 1, \sigma = 1 \text{ at } r = r_2. \end{array}\right\} \tag{29}$$

3. Solution Procedure

In order to solve the resulting nonlinear system of partial differential equations, we applied the fast converging analytical technique (OHPM). According to the scheme, the deformation equations for the current problem may be written as [33–37]:

$$(1-q)\left(\Im\left[\overline{w}\right] - \Im\left[\overline{w}_0\right]\right) + q\left[\Im\left[\overline{w}\right] + \frac{1}{r^2}\overline{w}_{\theta\theta} + (1+\lambda_1)\left(Br\Omega + Gr\Theta - p_z\right)\right] = 0, \tag{30}$$

$$\begin{array}{l} (1-q)\left(\Im[\Theta] - \Im\left[\overline{\theta}_0\right]\right) + q\left(\Im[\Theta] + \frac{1}{r^2}\Theta_{\theta\theta} + Nb\left(\Theta_r\Omega_r + \frac{1}{r^2}\Theta_\theta\Omega_\theta\right)\right) \\ +Nt\left(\Theta_r{}^2 + \frac{1}{r^2}\Theta_\theta{}^2\right) + Gc\left(\frac{1}{1+\lambda_1}\left(\overline{w}_z\overline{w}_r + \frac{1}{r^2}\overline{w}_\theta{}^2\right)\right)\Big) = 0, \end{array} \tag{31}$$

$$(1-q)\left(\Im[\Omega] - \Im[\overline{\sigma}_o]\right) + q\left(\Im[\Omega] + \frac{1}{r^2}\Omega_{\theta\theta} + \frac{Nt}{Nb}\left(\Theta_{rr} + \frac{1}{r}\Theta_r + \frac{1}{r^2}\Theta_{\theta\theta}\right)\right) = 0. \tag{32}$$

The linear operator is chosen as $\Im = \frac{1}{r}\partial_r(r\partial_r)$. The initial guesses for $w,\ \overline{\theta},\ \sigma$ are selected as

$$\overline{w}_o = V\ln[r/r^V](\ln[r_1/r_2])^{-1},\ \overline{\theta}_0 = \overline{\sigma}_0 = \ln[r_1/r](\ln[r_1/r_2])^{-1}. \tag{33}$$

Now we describe the following series for complete solutions.

$$w = \lim_{q\to 1}\overline{w}(r,\ \theta,\ z, t,\ q) = \lim_{q\to 1}\sum_{n=0}^{\infty} q^n\overline{w}_n, \tag{34}$$

$$\overline{\theta} = \lim_{q\to 1}\Theta(r,\ \theta,\ z, t,\ q) = \lim_{q\to 1}\sum_{n=0}^{\infty} q^n\overline{\theta}_n, \tag{35}$$

$$\sigma = \lim_{q\to 1}\Omega(r,\ \theta,\ z,\ q) = \lim_{q\to 1}\sum_{n=0}^{\infty} q^n\overline{\sigma}_n. \tag{36}$$

Making use of Equations (34)–(36) into Equations (30)–(32) and equating the coefficients of exponents of q, we gather the system of ordinary differential equations, which can be solved easily on mathematical software by built-in commands. The volume flow rate $\overline{Q}$ can be noted as [26]:

$$\overline{Q} = 2\pi\int_{r_1}^{r_2} rwdr. \tag{37}$$

The mean volume flow rate Q over one period can be written as [26,30]:

$$Q(z,\ t) = \frac{\overline{Q}}{\pi} - \frac{\varphi^2}{2} + 2\varphi\cos[2\pi(z-t)] + \varphi^2\cos^2[2\pi(z-t)]. \tag{38}$$

Now we can evaluate pressure gradient p_z by solving Equations (37) and (38). The pressure rise Δp in non-dimensional form contains the expression:

$$\Delta p = \int_0^1 (p_z) dz. \tag{39}$$

The two tables (Tables 1 and 2) are prepared through the numerical data of pressure rise Δp against flow rate Q and temperature profile θ from Equation (26), and imposing values to defined parameters on the mathematical software "Mathematica".

Table 1. Data of Δp for Q against β_1 and β_2 when $t = 0.05, \varepsilon = 0.1, \varphi = 0.1, \theta = 0.8,\ V = 0.1, \lambda_1 = 5, Br = 0.1$.

Gr	*δ*	*Q*	*Δp*
1	0.10	−1	19.3022
		−0.8	15.4814
		−0.6	11.6606
		−0.4	7.83978
		−0.2	4.01897
		0.0	0.198168
		0.2	−3.62264
		0.4	−7.44344
		0.6	−11.2642
		0.8	−15.085
		1.0	−18.9059
	0.15	−1.0	22.4955
		−0.8	18.005
		−0.6	13.5145
		−0.4	9.02408
		−0.2	4.53362
		0.0	0.0431658
		0.2	−4.44729
		0.4	−8.93775
		0.6	−13.4282
		0.8	−17.9187
		1.0	−22.4091

Table 1. *Cont.*

Gr	*δ*	*Q*	*Δp*
3	0.10	−1.0	20.7127
		−0.8	16.8919
		−0.6	13.0711
		−0.4	9.25031
		−0.2	5.42951
		0.0	1.60871
		0.2	−2.2121
		0.4	−6.0329
		0.6	−9.85371
		0.8	−13.6745
		1.0	−17.4953

Table 2. Error variation of temperature solution θ when other parameters are fixed.

Other Fixed Parameters	*r*	Residual Error
$t = 0.3$, $\varepsilon = 0.1$, $z = 0.1$, $\delta = 0.1$, $\varphi = 0.5$, $\theta = 0.8$, $V = 0.3$, $\lambda_1 = 1$, $Br = 0.5$ Nt $= 0.2$, Nb $= 0.1$.	0.169671	-1.77636×10^{-15}
	0.269671	0.00000
	0.369671	2.22045×10^{-16}
	0.469671	-2.22045×10^{-16}
	0.569671	-2.77556×10^{-16}
	0.669671	-1.66533×10^{-16}
	0.769671	-5.55112×10^{-17}
	0.869671	-2.77556×10^{-17}
	0.969671	-2.77556×10^{-17}
	1.06967	2.77556×10^{-17}
	1.16967	-3.1225×10^{-17}
	1.26967	1.73472×10^{-17}
	1.36967	-2.42861×10^{-17}

4. Entropy Generation

Entropy evaluates the anarchy of the process. Due to this most important aspect of heat and mass transfer analysis, pivot concentrations are made to analyze the entropy effects and to minimize the entropy generation. The volumetric rate of entropy generation for a Jeffrey nanofluid in three-dimensional asymmetric annuli is defined as:

$$\begin{aligned} S'_{gen} = {} & \frac{K}{T_o^2}\left(T_r{}^2 + \frac{1}{r^2}T_\theta{}^2 + T_z{}^2\right) + \frac{D_B}{C_o}\left(C_r{}^2 + \frac{1}{r^2}C_\theta{}^2 + C_z{}^2\right) + \frac{D_B}{T_o}\left(C_r T_r + \frac{1}{r^2}C_\theta T_\theta + C_z T_z\right) \\ & + \frac{1}{T_o}\left(S_{11}u_r + \frac{1}{r}S_{12}u_\theta + S_{13}(u_z + w_r) + \frac{1}{r}S_{32}w_\theta + S_{33}w_z + \frac{u}{r}S_{22}\right). \end{aligned} \tag{40}$$

From the above expression, we can assume that the entropy generation is composed of four terms: The entropy generation for heat transfer irreversibility, the entropy generation because of nanoparticles irreversibility, the entropy due to irreversibility of the combined effects of heat transfer

and nanoparticles, and the entropy in the presence of irreversibility of viscous dissipation of Jeffrey fluid, orderly. The non-dimensional parameters used in the above equation are defined as follows:

$$Ns = \frac{S'_{gen}}{S_G}, S_G = \frac{K(T_1 - T_o)^2}{a^2 T_o^2}, \Gamma = \frac{D_B T_o (C_1 - C_o)}{K(T_1 - T_o)}, \Lambda = \frac{(T_1 - T_o)}{T_o}, \Omega = \frac{(C_1 - C_o)}{C_o}\Bigg),$$

where Ns is the entropy generation number, Λ gives the temperature difference parameter, Ω represents the concentration difference parameter, Γ suggests the ratio of temperature to concentration parameters. By transforming Equation (40) into a dimensionless form without primes, we receive:

$$\begin{array}{l} Ns = \left(\overline{\theta}_r{}^2 + \frac{1}{r^2}\overline{\theta}_\theta{}^2 + \delta_o^2 \overline{\theta}_z{}^2\right) + \frac{\Gamma\Lambda}{\Omega}\left(\sigma_r{}^2 + \frac{1}{r^2}\sigma_\theta{}^2 + \delta_o^2 \sigma_z{}^2\right) + \Gamma\left(\sigma_r \overline{\theta}_r + \frac{1}{r^2}\sigma_\theta \overline{\theta}_\theta + \delta_o^2 \sigma_z \overline{\theta}_z\right) \\ + \frac{Gc}{\Omega}\left(\delta_o S_{11} u_r + \delta_o \frac{1}{r} S_{12} u_\theta + S_{13}\left(\delta_o^2 u_z + w_r\right) + \frac{1}{r} S_{32} w_\theta + \delta_o S_{33} w_z + \delta_o \frac{u}{r} S_{22}\right). \end{array} \quad (41)$$

Incorporating the lubrication approach, we achieve:

$$Ns = \left(\overline{\theta}_r{}^2 + \frac{1}{r^2}\overline{\theta}_\theta{}^2\right) + \frac{\Gamma\Lambda}{\Omega}\left(\sigma_r{}^2 + \frac{1}{r^2}\sigma_\theta{}^2\right) + \Gamma\left(\sigma_r \overline{\theta}_r + \frac{1}{r^2}\sigma_\theta \overline{\theta}_\theta\right) + \frac{Gc}{\Omega}\left(S_{13} w_r + \frac{1}{r} S_{32} w_\theta\right). \quad (42)$$

Invoking the values of S_{13} and S_{32} from Equations (21) and (23) into the above Equation (42), it becomes:

$$Ns = \left(\overline{\theta}_r{}^2 + \frac{1}{r^2}\overline{\theta}_\theta{}^2\right) + \frac{\Gamma\Lambda}{\Omega}\left(\sigma_r{}^2 + \frac{1}{r^2}\sigma_\theta{}^2\right) + \Gamma\left(\sigma_r \overline{\theta}_r + \frac{1}{r^2}\sigma_\theta \overline{\theta}_\theta\right) + \frac{Gc}{\Omega}\left(\frac{1}{1+\lambda_1}\left(w_r w_z + \frac{1}{r^2} w_\theta{}^2\right)\right). \quad (43)$$

Moreover, the Bejan number, *Be*, being the ratio of entropy generation against the heat transfer irreversibility to the total entropy generation is described mathematically as:

$$Be = \left(\overline{\theta}_r{}^2 + \frac{1}{r^2}\overline{\theta}_\theta{}^2\right)\left(\begin{array}{l} \left(\overline{\theta}_r{}^2 + \frac{1}{r^2}\overline{\theta}_\theta{}^2\right) + \frac{\Gamma\Lambda}{\Omega}\left(\sigma_r{}^2 + \frac{1}{r^2}\sigma_\theta{}^2\right) + \Gamma\left(\sigma_r \overline{\theta}_r \right. \\ \left. + \frac{1}{r^2}\sigma_\theta \overline{\theta}_\theta\right) + \frac{Gc}{\Omega}\left(\frac{1}{1+\lambda_1}\left(w_r w_z + \frac{1}{r^2} w_\theta{}^2\right)\right) \end{array}\right)^{-1}. \quad (44)$$

Bejan number, *Be*, carries the values from the interval [0,1]. If $Be < 1$, it can be observed that total entropy generation surpasses the heat transfer entropy, and for $Be = 1$, the total entropy generation approaches the entropy generation against the heat transfer irreversibility.

5. Results and Discussion

The authors obtained the quantitative analysis of nanoparticles in Jeffery fluid flowing past eccentric annuli having peristaltic waves at the outer surface. Heat and mass transfer phenomenon was also taken under consideration by the law of conservation of mass and energy. Lubrication theory was utilized to make the assumptions about laminar flow through arteries. Moreover, the effects of entropy generation and Bejan number were observed, which affect the flow due to irreversibility mechanism of temperature distribution, viscous dissipation, and nanoparticles' concentration. In this section, we describe the effects of emerging physical parameters of obtaining quantities through figures which are drawn on Mathematica and ordered in a subsequent manner. Numerical data were achieved for the expression of pressure rise by using built-in commands in mathematical software. Table 1 is placed to find the variation of pressure rise data Δp, for a flow rate domain Q from the interval $[-1, 1]$, by varying the parameters δ and Gr under the constant values of other factors. This table suggests that peristaltic pumping occurs at $Q = 0$. Figures 2 and 3 show the residual error curves, which clearly reflects the highly convergent solution of temperature distribution and nanoparticles' concentration, respectively, by keeping the rest of the quantities numerically fixed. Moreover, the values used in the graph emphasized that we can assign these numerical values of the parameters involved. Figure 4 confirms the validation of current analysis by comparing the present analysis with the study Nadeem et al. [32], which was published for viscous fluid. From this figure it is quite obvious that the current

study's results were similar to the results obtained in [32] when we neglected the non-Newtonian effects by assigning a zero value to the Jeffrey fluid parameter λ_1. It was also found from this graph that for Jeffrey fluid the radial velocity reduces. This is due to the increase in shearing stress as λ_1 grows, which was introduced into the boundary layer, which can cause loss of speed.

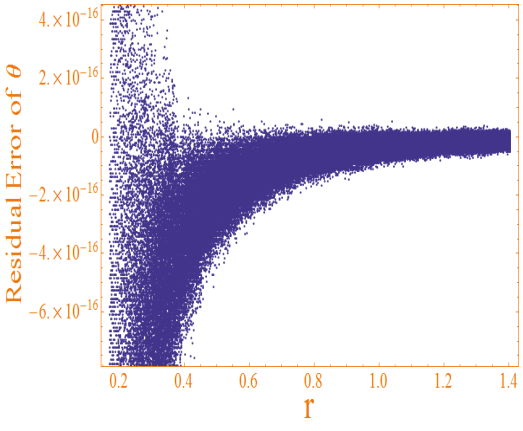

Figure 2. Residual error curves of temperature distribution θ.

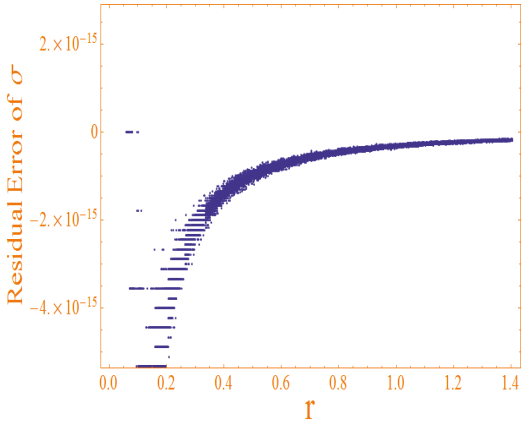

Figure 3. Residual error curves of nanoparticles' concentration σ

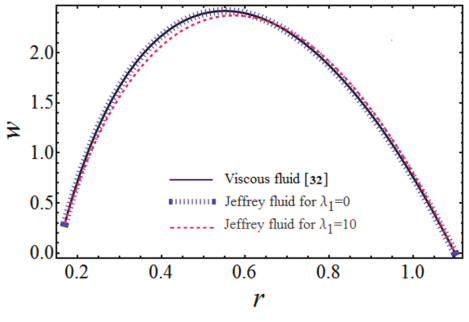

Figure 4. Comparison of present study with [32].

Figures 5–7 were plotted for pressure rise profile Δp against the flow rate domain Q. Figure 5 evaluates the effects of two parameters, the inner radius of the annuli δ, and the local temperature Grashof number Gr on peristaltic pressure rise curves. From this figure we can imagine that the lines of Δp are declining from left to right and intersecting each other at $Q = -0.2$. It can also be concluded here that pumping rate is increasing with both the parameters on the negative side of the domain, but reducing its inclination on the region of positive interval $[0, 2]$. This is due to the fact that increasing the radius of the inner cylinder exerts greater pressure on the flow on the left side, as compared to the other one, due to the eccentricity of the two annuli. Moreover, an increase in the local temperature Grashof number is produced due to the increase in outer cylinder radius, thus producing more pumping on the left side, whilst keeping the other parameters uniform. Figure 6 is sketched for Δp to estimate the influence of eccentricity parameter ε and the local nanoparticles Grashof number Br. One can observe clearly that a similar behavior is shown with ε and Br in comparison to δ and Gr. The velocity profile can be considered in Figures 7 and 8. Figure 7 discloses the variation of axial velocity w against the radial coordinate r, which is plotted for increasing numerical values of eccentricity factor ε and inner cylinder velocity V. It is shown from this graph that when we speed up the inner cylinder, the maximum velocity of fluid gets reduced near the outer annulus surface, while an increase is noticed near the walls of the inner cylinder; also, under the impact of eccentricity of two cylinders, fluid enhances its speed, but near the lower walls it becomes stable, which is very much in line with the experimental and physical results. From Figure 8, we can predict that by enlarging the nanoparticle Grashof number Gr and temperature Grashof number Br, the fluid travels rapidly in the space away from the lower surface, which is not closer to the lower boundary. Figures 9 and 10 were included to find the theoretical characteristics of temperature distribution under the alteration of Brownian motion parameter Nb and thermophoresis parameter Nt, correspondingly. It is obvious that, by raising the amount of both parameters, temperature of the liquid varied directly and the maximum temperature gradient was seen in the middle part of the space. This behavior clearly notifies that, in the presence of nanoparticles, the thermal conductivity of the fluid enhances significantly, which is also evident from the pioneer study on nanofluids [1]. This also suggests that the thermal conduction is caused by Brownian diffusion and thermophoresis diffusion in the rise of flow, which leads to an increase in flow temperature distribution.

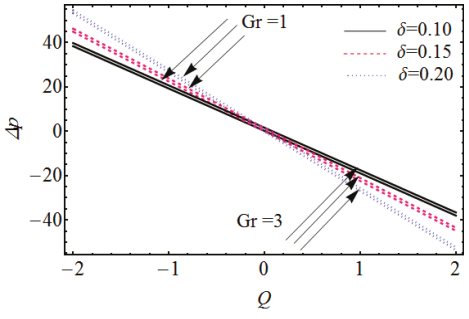

Figure 5. Variation of pressure rise Δp with δ and Gr for fixed $\theta = 0.8$, $\varphi = 0.1$, $\varepsilon = 0.1$, $Br = 0.2$, $Nb = 0.5$, $Nt = 0.2$, $\lambda_1 = 5$, $V = 0.1$, $t = 0.05$..

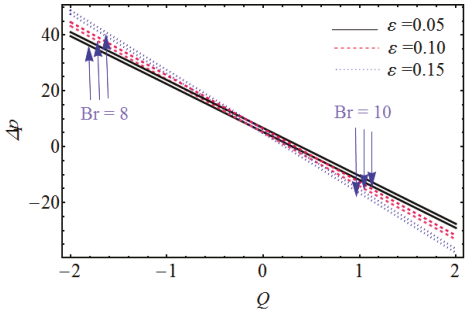

Figure 6. Variation of pressure rise Δp with ε and Br for fixed $\theta = 0.8$, $\varphi = 0.1$, $\delta = 0.1$, $Gr = 0.2$, $Nb = 0.5$, $Nt = 0.2$, $\lambda_1 = 5$, $V = 0.1$, $t = 0.05$..

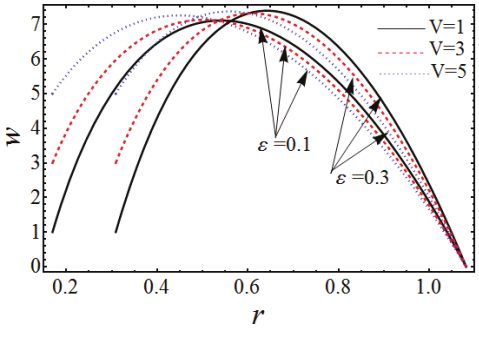

Figure 7. Variation of velocity profile w with ε and V for fixed $\theta = 0.8$, $\varphi = 0.1$, $\delta = 0.1$, $Br = 0.3$, $Gr = 1$, $\lambda_1 = 1$, $z = 0$, $t = 0.1$, $Q = 1$. .

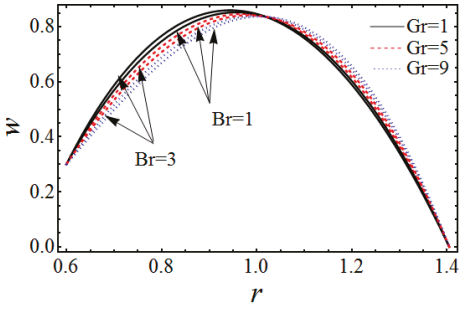

Figure 8. Variation of velocity profile w with Br and Gr for fixed $\theta = 0.1$, $\varphi = 0.5$, $\delta = 0.5$, $\varepsilon = 0.1$, $V = 0.3$, $\lambda_1 = 0.7$, $z = 0$, $t = 0.1$, $Q = 1$. .

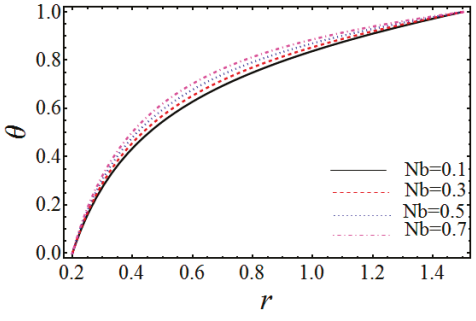

Figure 9. Variation of temperature profile $\overline{\theta}$ with Nb for fixed $\theta = 0.1,\ \varphi = 0.5,\ \delta = 0.1,\ \varepsilon = 0.1,\ V = 0.3,\ \lambda_1 = 0.7,\ z = 0,\ t = 0.3,\ Nt = 0.2,\ Br = 0.5$..

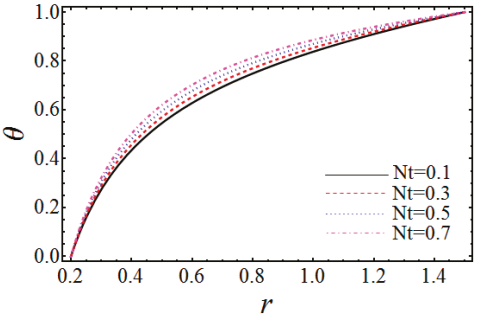

Figure 10. Variation of temperature profile $\overline{\theta}$ with Nt for fixed $\theta = 0.1,\ \varphi = 0.5,\ \delta = 0.1,\ \varepsilon = 0.1,\ V = 0.3,\ \lambda_1 = 1,\ z = 0,\ t = 0.3,\ Nb = 0.2,\ Br = 0.5$.

The profile of nanoparticles σ ismentioned in the diagrams labeled as Figures 11 and 12. In Figure 11, we can see the effects of Brownian motion parameter Nb on nanoparticles' concentration. It is clearly seen from this graph that the amount of nanoparticles is lowered with the variation of Nb. Figure 12 reflects the curves of nanoparticles' profile for the parameter Nt and it can be suggested that nanoparticles' concentration gets enlarged.

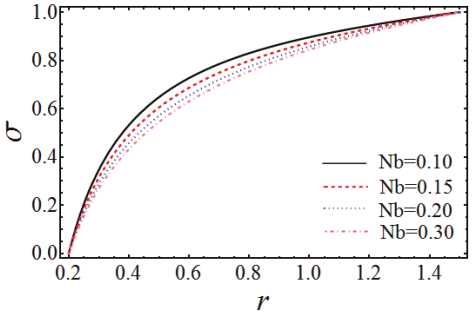

Figure 11. Variation of nanoparticles phenomenon σ with Nb for fixed $\theta = 0.1,\ \varphi = 0.5,\ \delta = 0.1,\ \varepsilon = 0.1,\ z = 0,\ t = 0.3,\ Nt = 0.2$..

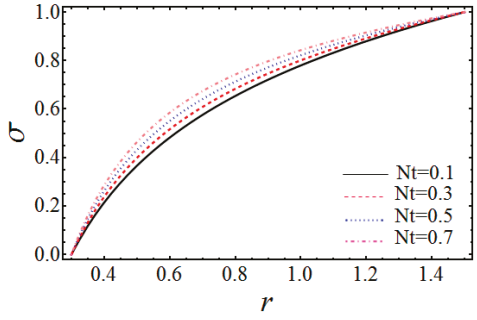

Figure 12. Variation of temperature profile σ with Nt for fixed $\theta = 0.1$, $\varphi = 0.5$, $\delta = 0.2$, $\varepsilon = 0.1$, $z = 0$, $t = 0.2$, $Nb = 0.2$..

Figures 13–18 exhibit the influence of emerging parameters on entropy function Ns. Figure 13 contains the graph of Ns against the Brinkman number Gc. This figure implies that entropy generation increases near the lower surface of the space with the increasing effects of Gc, but in the wider part it gets lowered with the varying factor. It was noticed that the entropy of the system increases with the incursion in Nb in most of the region, but near the walls it is almost stable (see Figure 14). Figure 15 concludes that the entropy shows similar characteristics with Nt, as seen for Nb, but an opposite result can be seen near the lower wall. This is because rising of N_t involves larger viscous dissipation effects, due to energy production generating more entropy. From Figure 16 it can be visualized that entropy is proportional to the concentration difference parameter Ω in the interval $r > 0.5$, but for $0 < r < 0.5$ an inverse relation is shown, but the ratio of temperature to concentration parameters Γ and the temperature difference parameter Λ showed increasing effects on the entropy generation, which can be confirmed from Figures 17 and 18, accordingly.

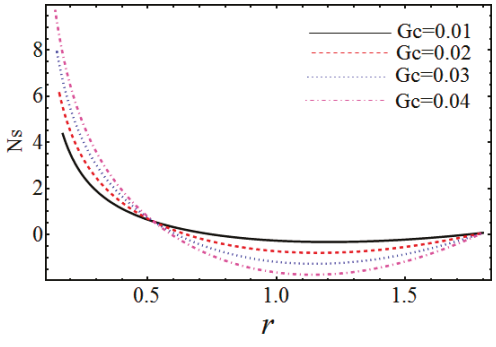

Figure 13. Curves of Ns with fixed Gc where $\theta = 0.1$, $\varphi = 0.5$, $\delta = 0.01$, $\varepsilon = 0.01$, $V = 0.3$, $\lambda_1 = 1$, $z = 0$, $t = 0.1$, $\Gamma = 0.4$, $Nb = 0.9$, $Nt = 0.5$, $Br = 1$, $Gr = 3$, $\Lambda = 0.4$, $\Omega = 0.3$, $Q = 1$. .

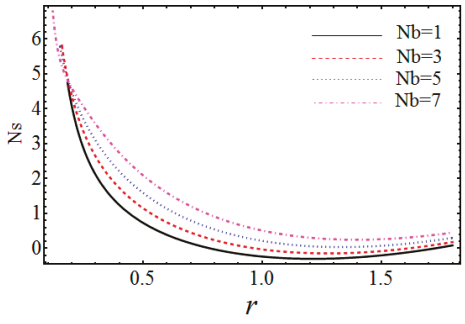

Figure 14. Curves of Ns with fixed Nb where $\theta = 0.1$, $\varphi = 0.8$, $\delta = 0.01$, $\varepsilon = 0.01$, $V = 0.3$, $\lambda_1 = 1$, $z = 0$, $t = 0.1$, $\Gamma = 0.4$, $Gc = 0.01$, $Nt = 0.9$, $Br = 1$, $Gr = 3$, $\Lambda = 1$, $\Omega = 0.3$, $Q = 1.$.

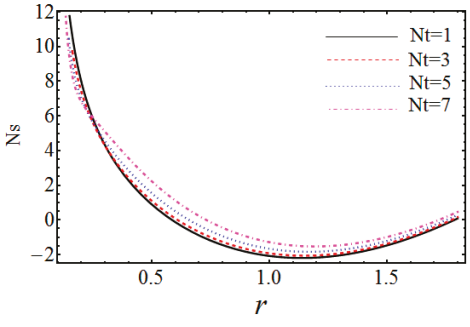

Figure 15. Curves of Ns with fixed Nt where $\theta = 0.1$, $\varphi = 0.8$, $\delta = 0.01$, $\varepsilon = 0.01$, $V = 0.3$, $\lambda_1 = 1$, $z = 0$, $t = 0.1$, $\Gamma = 0.4$, $Gc = 0.05$, $Nb = 0.9$, $Br = 1$, $Gr = 3$, $\Lambda = 1$, $\Omega = 0.3$, $Q = 1.$.

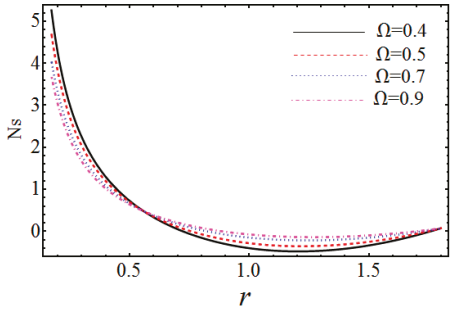

Figure 16. Curves of Ns with fixed Ω where $\theta = 0.1$, $\varphi = 0.8$, $\delta = 0.01$, $\varepsilon = 0.01$, $V = 0.3$, $\lambda_1 = 1$, $z = 0$, $t = 0.1$, $\Gamma = 0.4$, $Gc = 0.01$, $Nt = 0.5$, $Br = 1$, $Gr = 5$, $\Lambda = 1$, $Nb = 0.9$, $Q = 1.$.

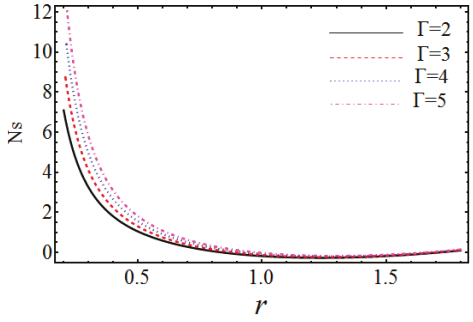

Figure 17. Curves of Ns with fixed Γ where $\theta = 0.3$, $\varphi = 0.8$, $\delta = 0.01$, $\varepsilon = 0.01$, $V = 0.3$, $\lambda_1 = 1$, $z = 0$, $t = 0.1$, $\Omega = 0.3$, $Gc = 0.01$, $Nt = 0.5$, $Br = 1$, $Gr = 3$, $\Lambda = 0.4$, $Nb = 0.9$, $Q = 1$..

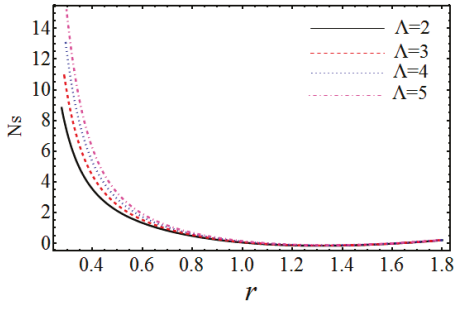

Figure 18. Curves of Ns with fixed Λ where $\theta = 0.3$, $\varphi = 0.8$, $\delta = 0.01$, $\varepsilon = 0.01$, $V = 0.3$, $\lambda_1 = 1$, $z = 0$, $t = 0.1$, $\Omega = 0.3$, $Gc = 0.01$, $Nt = 0.5$, $Br = 1$, $Gr = 3$, $\Gamma = 0.4$, $Nb = 0.9$, $Q = 1$..

Figures 19–22 are established to show the effects of physical factors on Bejan number Be, which is the ratio of two entropy generations. Figure 19 elucidates that the increase in Gc imposes an increase in Bejan number, which reflects the aspect that entropy due to heat transfer is less than that of total entropy in the lower region, but totally inverse readings are noted in the rest of the space. With the growing effects of Ω, Bejan number Be enhances through the flow domain, which can be found in Figure 20. From Figures 21 and 22 it is evident that Be decreases with increments in Γ and Λ, which indicates that the total entropy leads the same because of heat irreversibility.

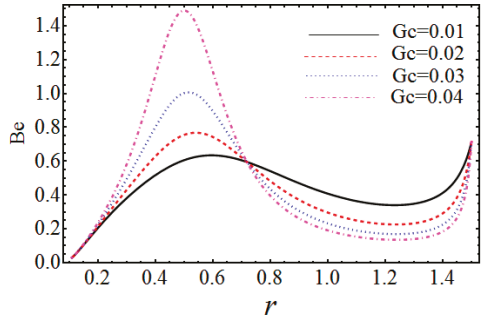

Figure 19. Curves of Be with fixed Gc where $\theta = 0.1$, $\varphi = 0.5$, $\delta = 0.1$, $\varepsilon = 0.01$, $V = 0.3$, $\lambda_1 = 0.1$, $z = 0$, $t = 0.1$, $\Omega = 0.3$, $\Lambda = 1$, $Nt = 0.5$, $Br = 1$, $Gr = 5$, $\Gamma = 0.4$, $Nb = 0.9$, $Q = 1$..

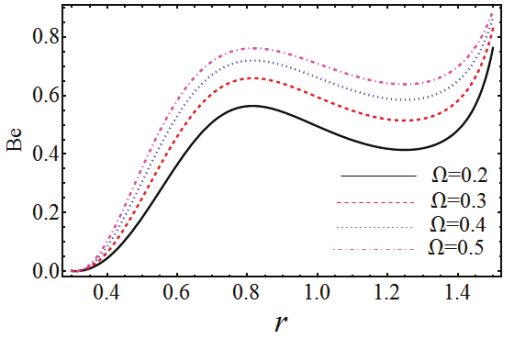

Figure 20. Curves of *Be* with fixed Ω where $\theta = 0.1$, $\varphi = 0.5$, $\delta = 0.1$, $\varepsilon = 0.2$, $V = 0.3$, $\lambda_1 = 0.1$, $z = 0$, $t = 0.1$, $Gc = 0.01$, $\Lambda = 1$, $Nt = 0.5$, $Br = 1$, $Gr = 5$, $\Gamma = 0.4$, $Nb = 0.9$, $Q = 1$..

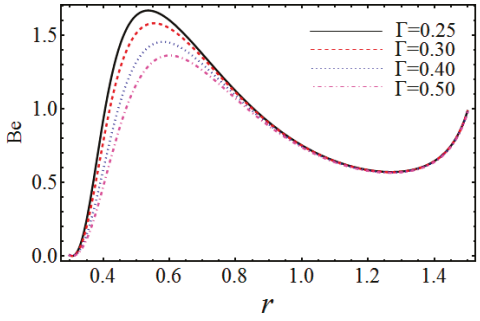

Figure 21. Curves of *Be* with fixed Γ where $\theta = 0.1$, $\varphi = 0.5$, $\delta = 0.1$, $\varepsilon = 0.2$, $V = 0.3$, $\lambda_1 = 0.1$, $z = 0$, $t = 0.1$, $Gc = 0.01$, $\Lambda = 1$, $Nt = 0.5$, $Br = 1$, $Gr = 5$, $\Omega = 0.3$, $Nb = 0.9$, $Q = 1$..

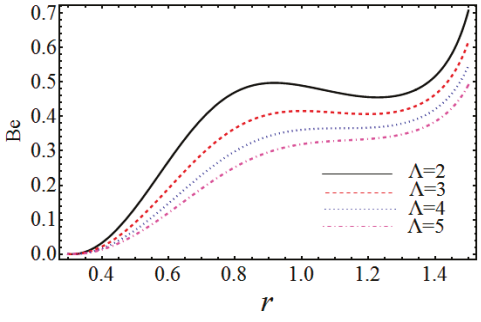

Figure 22. Curves of *Be* with fixed Λ where $\theta = 0.1$, $\varphi = 0.5$, $\delta = 0.1$, $\varepsilon = 0.2$, $V = 0.3$, $\lambda_1 = 0.1$, $z = 0$, $t = 0.1$, $Gc = 0.01$, $\Gamma = 0.4$, $Nt = 0.5$, $Br = 1$, $Gr = 5$, $\Omega = 0.3$, $Nb = 0.9$, $Q = 1$..

6. Conclusions

In the current article, entropy generation analysis and Bejan number characteristics were investigated for peristaltic propulsion of Jeffrey fluid by introducing nanoparticles passing through two eccentric asymmetric annuli. Analytical solutions for velocity, temperature, and nanoparticles' concentration were summarized. The pressure rise expression was evaluated numerically. Equations representing the laws of conservation were manipulated through the lubrication approach. The dimensionless phenomenon was also taken into account by incorporating some suitable transformations. Entropy generation number and Bejan number were achieved by substituting

the obtained values of temperature distribution, velocity profile, and nanoparticles' concentration. Effects of appertaining parameters were achieved by sketching diagrams. From the graphical features of the analysis, we gathered the following key observations:

- The pumping rate increases under the growing contribution of nanoparticles' Grashof number and temperature Grashof number.
- The fluid travels rapidly when the inner cylinders move faster, but in the upper space fluid gets slow; on the other hand, there is an opposite response evaluated for local nanoparticles' Grashof number as well as local temperature Grashof number.
- It is shown that the flow gets more heated when we increase the magnitudes of the thermophoresis parameter and the Brownian motion parameter, which also indicates the increase in thermal conductivity of the material.
- It is estimated that nanoparticles enhance with the thermophoresis parameter, but reduce under the increasing effects of the Brownian motion factor.
- It is summarized that entropy generation is raised near the inner cylinder when in relation to large values of Brinkman number; however, near the outer cylinder, observations are quite inverse; but against the thermophoresis parameter and Brownian motion parameter, entropy increased.
- From the figures of Bejan number, we showed that the temperature difference parameter and the ratio of temperature to concentration parameters degenerate the Bejan number, whereas the concentration difference parameter enhances the Bejan number; and the Brinkman number produces random results over the Bejan number profile.

Author Contributions: Conceptualization and methodology, A.R. and A.G.; software, I.K.; validation, S.U.K.; formal analysis and investigation, D.B.; writing—original draft preparation, K.S.N.; writing—review and editing, K.R.; funding acquisition, I.K. All authors have read and agreed to the published version of the manuscript.

Funding: This research received no external funding.

Acknowledgments: The authors extend their appreciation to the Deanship of Scientific Research at Majmaah University for funding this work under Project Number (RGP-2019-3).

Conflicts of Interest: The authors declare no conflicts of interest.

References

1. Choi, S.U.S. Enhancing Thermal Conductivity of Fluids with Nanoparticles. In Proceedings of the ASME International Mechanical Engineering Congress and Exposition, Washington, DC, USA, 12–17 November 1995; Volume 66, pp. 99–105.
2. Alrashed, A.A.; Gharibdousti, M.S.; Goodarzi, M.; De Oliveira, L.R.; Safaei, M.R.; Filho, E.B. Effects on thermophysical properties of carbon based nanofluids: Experimental data, modelling using regression, ANFIS and ANN. *Int. J. Heat Mass Transf.* **2018**, *125*, 920–932. [CrossRef]
3. Long, G.; Liu, S.; Xu, G.; Wong, S.-W.; Chen, H.; Xiao, B. A Perforation-Erosion Model for Hydraulic-Fracturing Applications. *SPE Prod. Oper.* **2018**, *33*, 770–783. [CrossRef]
4. Xiao, B.; Wang, W.; Zhang, X.; Long, G.; Fan, J.; Chen, H.; Deng, L. A novel fractal solution for permeability and Kozeny-Carman constant of fibrous porous media made up of solid particles and porous fibers. *Powder Technol.* **2019**, *349*, 92–98. [CrossRef]
5. Xiao, B.; Zhang, X.; Jiang, G.; Long, G.; Wang, W.; Zhang, Y.; Liu, G.; Chen, H. Kozeny–carman constant for gas flow through fibrous porous media by fractal-monte carlo simulations. *Fractals* **2019**, *27*, 27. [CrossRef]
6. Cao, Y.; Irwin, P.; Younsi, K. The future of nanodielectrics in the electrical power industry. *IEEE Trans. Dielectr. Electr. Insul.* **2004**, *11*, 797–807.
7. Imai, T.; Sawa, F.; Ozaki, T.; Shimizu, T.; Kuge, S.-I.; Kozako, M.; Tanaka, T. Approach by Nano- and Micro-filler Mixture toward Epoxy-based Nanocomposites as Industrial Insulating Materials. *IEEJ Trans. Fundam. Mater.* **2006**, *126*, 1136–1143. [CrossRef]
8. Amiri, S.; Shokrollahi, H. The role of cobalt ferrite magnetic nanoparticles in medical science. *Mater. Sci. Eng. C* **2013**, *33*, 1–8. [CrossRef]

9. Prabhu, S.; Poulose, E.K. Silver nanoparticles: Mechanism of antimicrobial action, synthesis, medical applications, and toxicity effects. *Int. Nano Lett.* **2012**, *2*, 32. [CrossRef]
10. Hanahan, U.; Weinberg, R.A. The Hallmarks of Cancer. *Cell* **2000**, *100*, 57–70. [CrossRef]
11. Prakash, J.; Siva, E.; Tripathi, D.; Kothandapani, M. Nanofluids flow driven by peristaltic pumping in occurrence of magnetohydrodynamics and thermal radiation. *Mater. Sci. Semicond. Process.* **2019**, *100*, 290–300. [CrossRef]
12. Abbas, M.A.; Bai, Y.-Q.; Rashidi, M.M.; Bhatti, M.M. Analysis of Entropy Generation in the Flow of Peristaltic Nanofluids in Channels With Compliant Walls. *Entropy* **2016**, *18*, 90. [CrossRef]
13. Abdelsalam, S.I.; Bhatti, M.M. The study of non-Newtonian nanofluid with hall and ion slip effects on peristaltically induced motion in a non-uniform channel. *RSC Adv.* **2018**, *8*, 7904–7915. [CrossRef]
14. Shah, Z.; Khan, A.; Khan, W.; Alam, M.K.; Islam, S.; Kuma, P.; Thounthong, P. Micropolar gold blood nanofluid flow and radiative heat transfer between permeable channels. *Comput. Methods Programs Biomed.* **2020**, *186*, 105197. [CrossRef] [PubMed]
15. Bhatti, M.M.; Zeeshan, A.; Ellahi, R.; Bég, O.A.; Kadir, A. Effects of coagulation on the two-phase peristaltic pumping of magnetized prandtl biofluid through an endoscopic annular geometry containing a porous medium. *Chin. J. Phys.* **2019**, *58*, 222–234. [CrossRef]
16. Kume, K. Endoscopic mucosal resection and endoscopic submucosal dissection for early gastric cancer: Current and original devices. *World J. Gastrointest. Endosc.* **2009**, *1*, 21–31. [CrossRef] [PubMed]
17. Kahshan, M.; Lu, D.; Siddiqui, A.M. A Jeffrey Fluid Model for a Porous-walled Channel: Application to Flat Plate Dialyzer. *Sci. Rep.* **2019**, *9*, 15879. [CrossRef] [PubMed]
18. Pandey, S.K.; Tripathi, D. Unsteady model of transportation of jeffrey-fluid by peristalsis. *Int. J. Biomath.* **2010**, *3*, 473–491. [CrossRef]
19. Ellahi, R.; Bhatti, M.M.; Pop, I. Effects of hall and ion slip on MHD peristaltic flow of Jeffrey fluid in a non-uniform rectangular duct. *Int. J. Numer. Methods Heat Fluid Flow* **2016**, *26*, 1802–1820. [CrossRef]
20. Ramesh, K.; Tripathi, D.; Beg, O.A.; Kadir, A. Slip and hall current effects on Jeffrey fluid suspension flow in a peristaltic hydromagnetic blood micro pump. *Iran. J. Sci. Technol. Trans. Mech. Eng.* **2019**, *43*, 675–692. [CrossRef]
21. Ranjit, N.K.; Shit, G. Entropy generation on electro-osmotic flow pumping by a uniform peristaltic wave under magnetic environment. *Energy* **2017**, *128*, 649–660. [CrossRef]
22. Ellahi, R.; Hussain, F.; Ishtiaq, F.; Hussain, A. Peristaltic transport of Jeffrey fluid in a rectangular duct through a porous medium under the effect of partial slip: An application to upgrade industrial sieves/filters. *Pramana* **2019**, *93*, 34. [CrossRef]
23. Zeeshan, A.; Ijaz, N.; Abbas, T.; Ellahi, R. The Sustainable Characteristic of Bio-Bi-Phase Flow of Peristaltic Transport of MHD Jeffrey Fluid in the Human Body. *Sustainability* **2018**, *10*, 2671. [CrossRef]
24. Ellahi, R.; Zeeshan, A.; Hussain, F.; Asadollahi, A. Peristaltic Blood Flow of Couple Stress Fluid Suspended with Nanoparticles under the Influence of Chemical Reaction and Activation Energy. *Symmetry* **2019**, *11*, 276. [CrossRef]
25. Mekheimer, K.S.; Elmaboud, Y.A.; Abdellateef, A.I. Particulate suspension flow induced by sinusoidal peristaltic waves through eccentric cylinders: Thread annular. *Int. J. Biomath.* **2013**, *6*, 1350026. [CrossRef]
26. Pakdemirli, M.; Yilbas, B.S. Entropy generation in a pipe due to non-Newtonian fluid flow: Constant viscosity case. *Sadhana* **2006**, *31*, 21–29. [CrossRef]
27. Souidi, K.F.; Ayachi, N. BenyahiaEntropy generation rate for a peristaltic pump. *J. Non Equilib. Thermodyn.* **2009**, *34*, 171–194. [CrossRef]
28. Abu-Nada, E. Entropy generation due to heat and fluid flow in backward facing step flow with various expansion ratios. *Int. J. Exergy* **2006**, *3*, 419. [CrossRef]
29. Bibi, A.; Xu, H. Entropy Generation Analysis of Peristaltic Flow and Heat Transfer of a Jeffery Nanofluid in a Horizontal Channel under Magnetic Environment. *Math. Probl. Eng.* **2019**, *2019*, 1–13. [CrossRef]
30. Rashidi, M.M.; Bhatti, M.M.; Abbas, M.A.; Ali, M. Entropy Generation on MHD Blood Flow of Nanofluid Due to Peristaltic Waves. *Entropy* **2016**, *18*, 117. [CrossRef]
31. Ellahi, R.; Raza, M.; Akbar, N.S. Study of peristaltic flow of nanofluid with entropy generation in a porous medium. *J. Porous Media* **2017**, *20*, 461–478. [CrossRef]
32. Nadeem, S.; Riaz, A.; Ellahi, R.; Akbar, N.S. Effects of heat and mass transfer on peristaltic flow of a nanofluid between eccentric cylinders. *Appl. Nanosci.* **2013**, *4*, 393–404. [CrossRef]

33. Jamalabadi, M.Y.A.; DaqiqShirazi, M.; Nasiri, H.; Safaei, M.R.; Nguyen, T.-N. Modeling and analysis of biomagnetic blood Carreau fluid flow through a stenosis artery with magnetic heat transfer: A transient study. *PLoS ONE* **2018**, *13*, e0192138.
34. Maleki, H.; Alsarraf, J.; Moghanizadeh, A.; Hajabdollahi, H.; Safaei, M.R. Heat transfer and nanofluid flow over a porous plate with radiation and slip boundary conditions. *J. Central South Univ.* **2019**, *26*, 1099–1115. [CrossRef]
35. He, J.-H. Homotopy perturbation method for solving boundary value problems. *Phys. Lett. A* **2006**, *350*, 87–88. [CrossRef]
36. Riaz, A.; Alolaiyan, H.; Razaq, A. Convective Heat Transfer and Magnetohydrodynamics across a Peristaltic Channel Coated with Nonlinear Nanofluid. *Coatings* **2019**, *9*, 816. [CrossRef]
37. Alolaiyan, H.; Riaz, A.; Razaq, A.; Saleem, N.; Zeeshan, A.; Bhatti, M.M. Effects of Double Diffusion Convection on Third Grade Nanofluid through a Curved Compliant Peristaltic Channel. *Coatings* **2020**, *10*, 154. [CrossRef]

coatings

MDPI

Article

Top Coating Anti-Erosion Performance Analysis in Wind Turbine Blades Depending on Relative Acoustic Impedance. Part 1: Modelling Approach

Luis Domenech [1], Jordi Renau [1], Asta Šakalytė [2] and Fernando Sánchez [1,*]

[1] Research Institute of Design, Innovation and Technology, University CEU Cardenal Herrera, CEU Universities, Avda. Seminario S/N, Moncada, 46115 Valencia, Spain; luis.domenech@uchceu.es (L.D.); jordi.renau@uchceu.es (J.R.)

[2] AEROX Advanced Polymers, Pobla Vallbona, 46185 Valencia, Spain; asakalyte@aerox.es

* Correspondence: fernando.sanchez@uchceu.es

Received: 10 June 2020; Accepted: 9 July 2020; Published: 16 July 2020

Abstract: Top coating are usually moulded, painted or sprayed onto the wind blade Leading-Edge surface to prevent rain erosion due to transverse repeated droplet impacts. Wear fatigue failure analysis based on Springer model has been widely referenced and validated to quantitatively predict damage initiation. The model requires liquid, coating and substrate speed of sound measurements as constant input parameters to define analytically the shockwave progression due to their relative vibro-acoustic properties. The modelling assumes a pure elastic material behavior during the impact event. Recent coating technologies applied to prevent erosion are based on viscoelastic materials and develop high-rate transient pressure build-up and a subsequent relaxation in a range of strain rates. In order to analyze the erosion performance by using Springer model, appropriate impedance characterization for such viscoelastic materials is then required and represents the main objective of this work to avoid lack of accuracy. In the first part of this research, it is proposed a modelling methodology that allows one to evaluate the frequency dependent strain-stress behavior of the multilayer coating system under single droplet impingement. The computational tool ponders the operational conditions (impact velocity, droplet size, layer thickness, etc.) with the appropriate variable working frequency range for the speed of sound measurements. The second part of this research defines in a complementary paper, the ultrasonic testing characterization of different viscoelastic coatings and the methodology validation. The modelling framework is then used to identify suitable coating and substrate combinations due to their acoustic matching optimization and to analyze the anti-erosion performance of the coating protection system.

Keywords: droplet impact modelling; impedance analysis; rain erosion; ultrasound measurements; viscoelastic modelling; wind turbine blades

1. Introduction

Rain erosion damage, caused by repeated droplet impact on wind turbine blades, is a major cause for concern, even more so at offshore locations with larger blades and higher tip speeds, see Figure 1. In most cases, since the surface protection plays a decisive role in the blade manufacture and overall performance, it has been identified as an area where a solution may be obtained. There are various protection solutions used by industry that can reduce the effect of erosion and increase the turbine expected lifetime. Four main surface protection technologies may be considered: In-mould coatings (Gel coating) applied during moulding on the entire blade surface but not specifically on the Leading Edge location where the protection is crucial; post-mould coatings specifically developed for Leading Edge Protection (LEP) and considering a multilayer system with optional configurations based on

top-coatings, filler and primer materials, depending on blade manufacturing and operational settings; tapes based on post-mould applications circumventing the issues related with liquid-based materials; shells that as tapes are manufactured in controlled conditions and applied in pre-cast solid modules over the Leading Edge surface. In order to analyze and evaluate the relative positive facts and faults of a given protection system, we will consider the common issues related with rain erosion failure for any of these technologies.

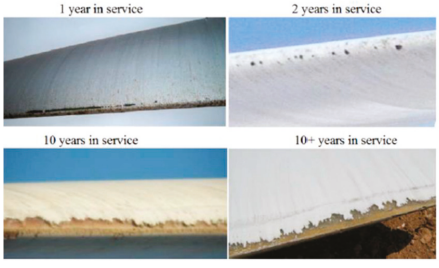

Figure 1. Examples of leading edge erosion across a range of years in service, from [1].

Industrial processes state that LEP systems can be outlined as a multi-layered system with varying layer thickness and material configurations. A particular case, used here to sketch the problem, with a post-mould coating-based LEP system is shown where the blade manufacturer includes a putty layer between the composite laminate and the coating, see Figure 2. It also can be included a primer layer under the coating and over the filler to improve adhesion mainly to avoid layer debonding and circumvent application related defects.

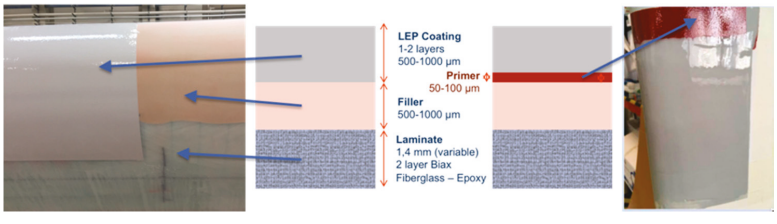

Figure 2. Leading Edge Protection (LEP) system configuration on the blade surface as a post-mould application multilayer system.

In the top coating material system, two main different types of erosion failure are mainly observed (see Figure 3) in used Rain Erosion Testing coupons: pits and cracks that progress with mass loss caused by direct impact and stress on surface and delamination indirectly caused by the interface stresses [1,2].

The analysis of erosion caused by rain droplets is considered, as first approach, a single impact event as it is shown in Figure 4. The damage is in fact a 3D dynamic consequence resulting in the propagation of shock waves [3,4]. The droplet numerical modelling has been broadly studied by different authors [5–8]. As the water droplet impinges on the surface, a longitudinal compressional normal stress wave front in the top surface material further advances towards the coating-substrate interface, where a portion of the stress wave is reflected back into the coating with a different amplitude (depending on the relative material acoustic impedance) and yields a transverse shear wave. The remaining part is transmitted to the substrate. The impact gives rise to a third wave due to the water droplet deformation itself, called the Rayleigh wave, which is confined to the surface of the top coating. Depending on the relative acoustic properties through the liquid-coating-substrate, the propagation of the stresses and, consequently, the erosion lifetime can be optimized.

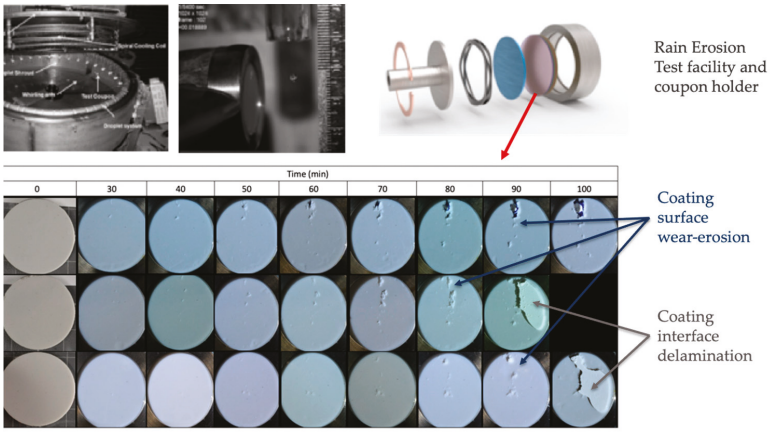

Figure 3. Two different types of erosion failure: Coating surface wear erosion with pits and cracks that progress with mass loss caused by direct impact and stress on surface and coating interface delamination indirectly caused by the coating-substrate interface stresses. The coupons were tested at Whirling arm rain erosion test facility (WARER) at University of Limerick.

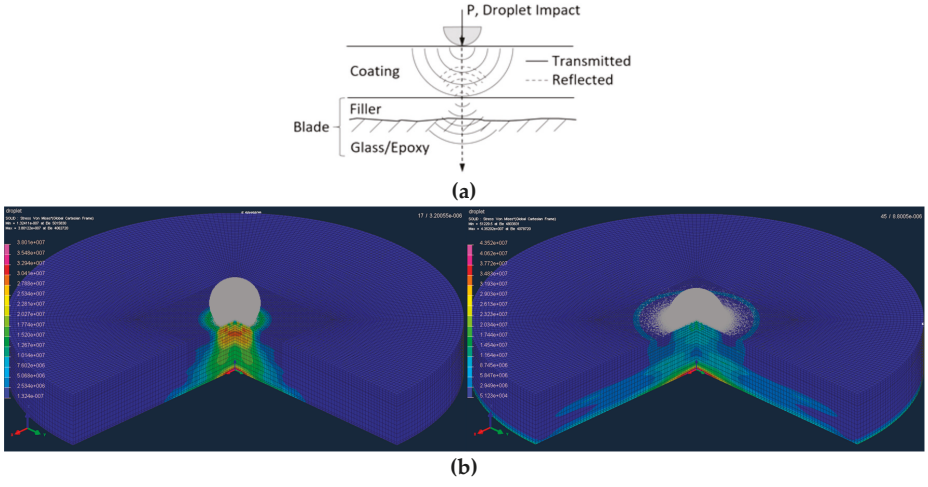

Figure 4. (**a**) Standard blade structure sketch with a filler intermediate layer showing stress wave behavior under impingement and (**b**) Liquid droplet-solid surface impact interaction depicted from numerical simulation developed by the authors.

The analysis (or design) of Leading-Edge Protection systems depends on the material properties in the configuration and the operational load to which it is designed during its realistic life, that is, it must be able to withstand accelerated loads and also fatigue field regimes [6,9]. To make a selection or design of a specific coating protection system, appropriate modelling requires to be defined [10–12]. Numerical or analytical models can be constructed with their own capabilities and limitations, [13–15].

Springer analytical model [13] has been widely referenced and industry validated [15]. The model quantitatively predicts the erosion lifetime of coated materials under the previously untested conditions. The model is limited to erosion failures such as progressive failure mode or coating wear. To use the Springer model, material test data is needed to derive the erosion performance properties of a selected system. The formulation examines the impact of a liquid droplet treating the problem only

as a pure elastic 1D tensile-compression event. This simplification is applicable since shear stresses and shear material characterization directly related with other important damage mechanisms as peeling, debonding, delamination or crack evolution are out of the wear fatigue analysis case involved.

Wear fatigue failure analysis based on Springer model requires coating and substrate speed of sound measurements as input material parameters. The model does not account for a very high-rate transient pressure build-up and the viscoelastic effects are frequency dependent for the materials involved [16–18]. The main objective of this research is to fully apply the Springer model but considering the effect of the viscoelastic stress-strain development during the impact event in the LEP multilayer system by means of the appropriate frequency range definition for the coating layer impedance characterization.

In this work, as the first part of the research, it is proposed a modelling methodology that allows one to evaluate the single droplet impingement taking into consideration the highly transient material behavior during waterdrop collisions. The computational tool ponders with different application cases the operational conditions (impact velocity, droplet size, layer thickness, etc.) with the variable working frequency range that the material develops. We will introduce in this work a complementary numerical modelling tool (developed in openmodellica [19]) including suitable material models that allow us to observe the viscoelastic behavior (with consideration for high transient strain rate deformation, and variable stiffness and damping with frequency) and not as a pure elastic event. The complete analysis is used then to define the frequency range for the corresponding impedance measurements with Ultrasonic testing. The paper is organized considering first a review of the aforementioned Springer erosion lifetime prediction modelling, then the state of the art is completed for taking into account the viscoelastic effects of the stress-strain development under single droplet impingement for elastomeric materials. In last sections, different modelling analysis cases are discussed to ponder the effect of the operational and material configurations on the frequency range definition for appropriate material properties testing.

The coating characterization is developed in a second part of the research in a complementary reference [20] for different viscoelastic coatings and the methodology validated for the input material data definition of the erosion lifetime modelling based on Springer.

In this research the model is used then to carry out studies as a computational framework that allows a parametric analysis to examine the impact of the selected coating impedance variation on the erosion performance. This provides also a guidance in the selection and modulation of coating properties and to identify suitable coating and substrate combinations due to their acoustic matching optimization. At this point, the proposed modelling methodology should reduce the scope of Rain Erosion Testing [21,22] to verify and evaluate the rain erosion resistance of coating systems.

2. Wear Erosion Lifetime Prediction Modelling from Fundamental Material Properties. A Review of Springer Model

In this section a review of the Springer model is exposed in order to be used in the next sections for wear erosion lifetime analysis depending on the material impedance measurements as input modelling data.

The progression of erosion can be experimentally measured with applicable Rain Erosion Testing. One method is in terms of the average erosion depth versus time or mass loss versus time (directly related to the number of impacts, see Figure 5). There is initially an incubation period in which damage progresses without perceptible change in the material weight loss. After a sufficient amount of fatigue degradation has accumulated, the material tends to lose mass with a constant erosion rate. This marks the end of the incubation period and a steady mass loss period begins, where the weight loss varies nearly linearly with time.

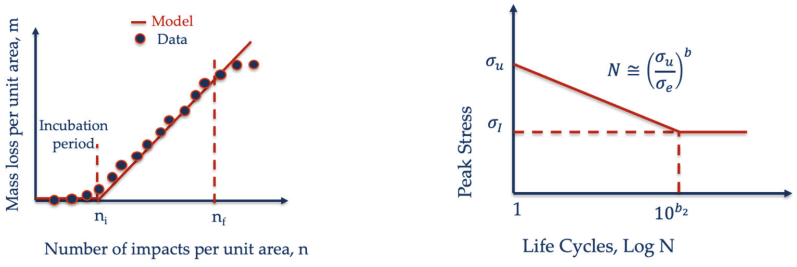

Figure 5. (**a**) Evolution of weight loss on experimental rain erosion testing coupons and lifetime prediction model defining the incubation period and mass removal rate (**b**) Springer Model based Fatigue life N approximation related with the material ultimate strength σ_u, the parameter "erosion strength", σ_e and the parameter b that includes the fatigue knee at the endurance limit σ_I. Adapted from: [13].

Springer analytical model [13] quantitatively predicts the erosion of coated materials under the previously untested conditions. The erosion evolution can be approximated by two straight lines as depicted in Figure 5 with

$$\begin{array}{c} m = 0 \quad 0 < n_{ic} \\ m = \alpha_c (n - n_{ic}) \quad n_{ic} < n < n_{fc} \end{array} \tag{1}$$

where the mass loss m produced by a given number of droplets impacts n, can be estimated once the incubation time of the coating n_{ic} and the slope of the erosion rate on the coating α_c are identified.

In order to establish these parameters, the stress history of the coating and the substrate is assessed analytically. It is affected by the shockwave progression due to the vibro-acoustic properties of each layer, and by the frequency of the repeated water droplet impacts (see Figure 6).

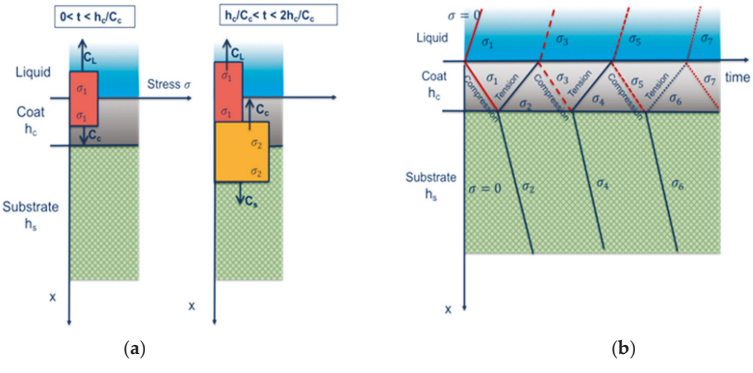

Figure 6. Stress wave pattern in the coating and in the substrate for the time intervals related with coating thickness h_c and its wave speed C_c. (**a**) Stress wave contact at interface; (**b**) Stress wave consecutive interactions.

Upon impingement on the coating, two different wave fronts travel into the liquid and coating respectively. The wave front in the coating further advances towards the coating-substrate interface, where a portion of the stress wave is reflected back into the coating and the remaining part is transmitted

to the substrate. Due to this reflection a new wave is now advancing in the coating with a different amplitude depending on the relative acoustic impedances of the coating and substrate,

$$\varphi_{Lc} = \frac{Z_L - Z_c}{Z_L + Z_c} \quad ; \quad \varphi_{sc} = \frac{Z_s - Z_c}{Z_s + Z_c} \tag{2}$$

where $Z = \rho C$ is the impedance of the material, ρ is the density and C the elastic wave speed (the speed of sound of the medium). Z_L, Z_C, and Z_S are the elastic impedances of the consecutive materials (i.e., in our problem they are the liquid ($_L$), coating ($_C$), and substrate ($_S$) layers). φ_{Lc} defines the relative impedance parameter defined on the liquid-coating interface and φ_{sc} on the substrate-coating one.

This 1D formulation, see Figure 6, examines only the normal impact of a liquid droplet with diameter d, onto a two layered structure with the first layer formed by the coating and the second layer by the substrate (assumed semi-infinite) with thickness $h_s > 2d\frac{C_s}{C_L}$, which means in fact that the reflections from a subsequent substrate additional layers are not considered in the fatigue analysis.

The magnitude of the traveling waves propagating upwards the coating-liquid interface, and traveling waves propagating downwards the coating-substrate interface, are expressed with the k number of reflections as depicted in Figure 6:

$$\begin{array}{l} \frac{\sigma_{2k}}{\sigma_1} = \frac{1+\varphi_{sc}}{1-\varphi_{sc}\varphi_{Lc}}\left[1 - (\varphi_{sc}\varphi_{Lc})^k\right] \\ \frac{\sigma_{2k-1}}{\sigma_1} = \frac{\sigma_{2k}}{\sigma_1} - \varphi_{sc}(\varphi_{sc}\varphi_{Lc})^{k-1} \end{array} \tag{3}$$

where the Water-hammer Pressure defines the initial impact pressure $\sigma_1 = P$

$$P = \frac{VZ_L\cos(\theta)}{\left(\frac{Z_L}{Z_c} + 1\right)} \tag{4}$$

That depends on the droplet impact speed V and its impact angle with $\cos(\theta)$. The stabilized stress at the interface coating-substrate can be approximated as

$$\sigma_\infty = \sigma_1 \lim_{k\to\infty} \sigma_{2k} = \sigma_1 \frac{1+\varphi_{sc}}{1-\varphi_{sc}\varphi_{Lc}} = \sigma_1 \frac{1+\frac{Z_L}{Z_c}}{1+\frac{Z_L}{Z_s}} \tag{5}$$

After a long enough period of time, the stresses at both the coating surface and the substrate interface approaches to the constant value σ_∞, which is also the stress that would occur in the substrate after impingement in the absence of the coating layer. An example on its use within the project is depicted on Figure 7. One can obtain an analytical value of the stress evolution on the coating during the droplet impact. It is an alternative simplified computation to the algorithm presented in the previous section based on a 3D numerical modelling.

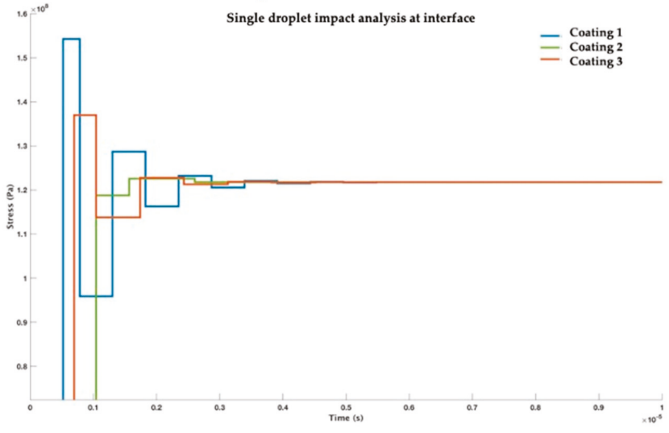

Figure 7. Variation of stress at coating-substrate interface for three different top coating LEP material candidates for the same substrate. It can be observed the capability to avoid peak values with the appropriate selection of the material impedances.

To evaluate the average stress values at the coating-liquid and coating-substrate interfaces during the duration of the impact, it is introduced a parameter k that depends on the average number of reflections in the coating layer

$$k = \frac{1 - e^{-\gamma}}{1 - \psi_{Lc}\psi_{sc}} \tag{6}$$

where the coating thickness h_c enters its computation through the parameter γ that depends on it and also on the droplet diameter d. It may be calculated as

$$\gamma = \frac{2C_c\left(\frac{Z_L}{Z_s} + 1\right)d}{C_L\left(\frac{Z_L}{Z_c} + 1\right)\left(\frac{Z_c}{Z_s} + 1\right)h_c} \tag{7}$$

Finally, the average stress on the coating surface at $x = 0$ is defined with σ_o as

$$\begin{aligned} \sigma_o &= \frac{P(\psi_{sc}+1)}{(1-\psi_{Lc}\psi_{sc})}\left(1 - \frac{(1-e^{\gamma})(\psi_{Lc}+1)\psi_{sc}}{\gamma(\psi_{sc}+1)}\right) \\ \sigma_o &= \frac{VZ_L\cos(\theta)(\psi_{sc}+1)}{\left(\frac{Z_L}{Z_c}+1\right)(1-\psi_{Lc}\psi_{sc})}\left(1 - \frac{(1-e^{\gamma})(\psi_{Lc}+1)\psi_{sc}}{\gamma(\psi_{sc}+1)}\right) \end{aligned} \tag{8}$$

If the value of the relative impedance parameter of the substrate-coating interface equals zero, $\psi_{sc} = 0$, so the coating material is considered the same as the substrate, and this expression reduces to $\sigma_o = \sigma_1 = P$ that may be used to compute the average stress for homogeneous materials.

The average stress on the coating-substrate interface at $x = h$ is defined then with σ_h as

$$\begin{aligned} \sigma_h &= \frac{P(\psi_{sc}+1)}{(1-\psi_{Lc}\psi_{sc})}\left(1 - \frac{(1-e^{\gamma})\psi_{Lc}\psi_{sc}}{\gamma}\right) \\ \sigma_h &= \frac{VZ_L\cos(\theta)(\psi_{sc}+1)}{\left(\frac{Z_L}{Z_c}+1\right)(1-\psi_{Lc}\psi_{sc})}\left(1 - \frac{(1-e^{\gamma})\psi_{Lc}\psi_{sc}}{\gamma}\right) \end{aligned} \tag{9}$$

And, as above, if the value of the relative impedance parameter of the substrate-coating interface equals zero, $\psi_{sc} = 0$, so the coating material is considered the same as the substrate, this expression reduces to $\sigma_o = \sigma_h = P$.

The incubation period of time neglecting mass loss prior the erosion develops at a given rate, as depicted in Figure 5, is analyzed with fatigue concepts. It may be estimated applying Miner's rule to

the impingement force cycles and considering the averaged stress values with the equivalent dynamic stress σ_e per unit area on the impact locations, see Figure 5c.

An approximation value for the fatigue life N is then given by a function of the equivalent dynamic stress σ_e

$$\begin{array}{c} N = \left(\frac{\sigma_{uc}}{\sigma_e}\right)^{b_c} \\ b_c = \frac{b_{2c}}{log_{10}\left(\frac{\sigma_{uc}}{\sigma_{1c}}\right)} \end{array} \tag{10}$$

where the subscript c indicates to the coating material, b_c defines the fatigue slope, b_{2c} matches to the "knee" in the fatigue curve (that may be estimated with its endurance limit σ_1) and the coating ultimate tensile strength σ_{uc} is defined for N = 1.

A parameter of the material "strength" S_c is introduced with a semi-empirical approach and depends on the poison coefficient ν_c (included to consider the location of the impact force on the radial averaged stress), and other relevant properties of both the coating material and substrate treated previously,

$$\begin{array}{c} S_c = \frac{4(b_c-1)\sigma_{uc}}{(1-2\nu_c)\left[1-\left(\frac{\sigma_{1c}}{\sigma_{uc}}\right)^{b_c-1}\right]} \cong \\ S_c = \frac{4(b_c-1)\sigma_{uc}}{(1-2\nu_c)} \end{array} \tag{11}$$

An important issue for fatigue analysis is how to consider the effect of the fatigue slope parameter for the coating b_c since it is difficult to obtain experimentally for typical LEP elastomeric materials. Equation (11) may be simplified assuming that $\sigma_{1c} < \sigma_{uc}$ and $b_c \gg 1$.

It may be stated as an equivalent erosion resistance parameter for the coating S_{ec} including the damping effect of the coating described previously by means of the average number of reflections k and the relative impedance parameter ψ_{sc} that acts on the interface wave reflections,

$$S_{ec} = \frac{4(b_c-1)\sigma_{uc}}{(1-2\nu_c)\left(2k\left|\psi_{sc}\right|+1\right)} \tag{12}$$

Fatigue life of the material is then estimated with the number of impacts during the incubation time period as

$$n_{ic}^{*} = a_1\left(\frac{S_{ec}}{\sigma_o}\right)^{a_2} \tag{13}$$

where a_1 and a_2 can be considered determined constants that may be fitted experimentally, S_{ec} represents the erosion strength of the material and depends on its fundamental properties defined in Equation (12) and the averaged stress of the coating surface during the impact event defined in Equation(8). In [1], the parameter values where defined as

$$n_{ic}^{*} = 7\times10^{-6}\left(\frac{S_{ec}}{\sigma_o}\right)^{5,7} \tag{14}$$

That may also be expressed in terms of the number impacts per site when considering the circular projected area of the droplet with a given diameter d

$$n_{ic} = \frac{8.9}{d^2}\left(\frac{S_{ec}}{\sigma_o}\right)^{5,7} \tag{15}$$

where using appropriates units allow one to predict the number of impacts per m^2 at which the coating material starts to develop erosion with a given erosion rate that may also be computed from the previous estimated parameters as

$$\alpha_c = \frac{7.3310^{-5}d^3\rho_c{\sigma_o}^4}{{S_{ec}}^4} \tag{16}$$

The equivalent analysis may be used to determine the erosion strength at interface coat-substrate instead of surface. Accordingly, Equations (11) and (15) are written introducing the fundamental properties of the substrate as

$$n_{ih} = \frac{8.9}{d^2}\left(\frac{S_{es}}{\sigma_h}\right)^{5,7}$$

$$S_{es} = \frac{4(b_s-1)\sigma_{us}}{(1-2\nu_s)\left[1-\left(\frac{\sigma_{Is}}{\sigma_{us}}\right)^{b_s-1}\right]\left(2k|\psi_{sc}|+1\right)} \cong \frac{4(b_s-1)\sigma_{us}}{(1-2\nu_s)\left(2k|\psi_{sc}|+1\right)} \quad (17)$$

As we have previously stated from [13] in order to predict the incubation time and the mass removal rate, the stress history in the coating and in the substrate has to be identified analytically or numerically. It is affected by the shockwave progression due to the vibro-acoustic properties of each layer, and by the time interval of the repeated water droplet impacts. Fatigue life of the material is then calculated, and the model can be applied to estimate the stress at different locations through the thickness, i.e., the coating surface or at the coating–substrate interface. Nevertheless, it is assumed that the bond and adhesion of the boundary interface is ideally perfect, so the modelling does not account for the microstructural imperfections and lack of adhesion of such interfaces and does not account either for the shear stresses developed on the 3D impact event.

Considering for previous assumptions, the method has been applied successfully for wear erosion damage in [15]. In that case, the erosion strength of the coating material defined in Equation (12) was empirically obtained by means of the RET (Rain Erosion Testing) testing as a unique value instead of obtaining the fundamental properties values separately.

Figure 8 shows a complete map of the liquid droplet, coating LEP and substrate (primer or filler) material impedances as input parameters of the modelling with the related equations previously stated. The impedance of the LEP thin coating and substrate materials need to be characterized and used as input data in the modelling. The appropriate variable working frequency range depending on the impact and material settings is analysed in next section and defined so the corresponding impedance characterization with Ultrasonic testing for such measurements.

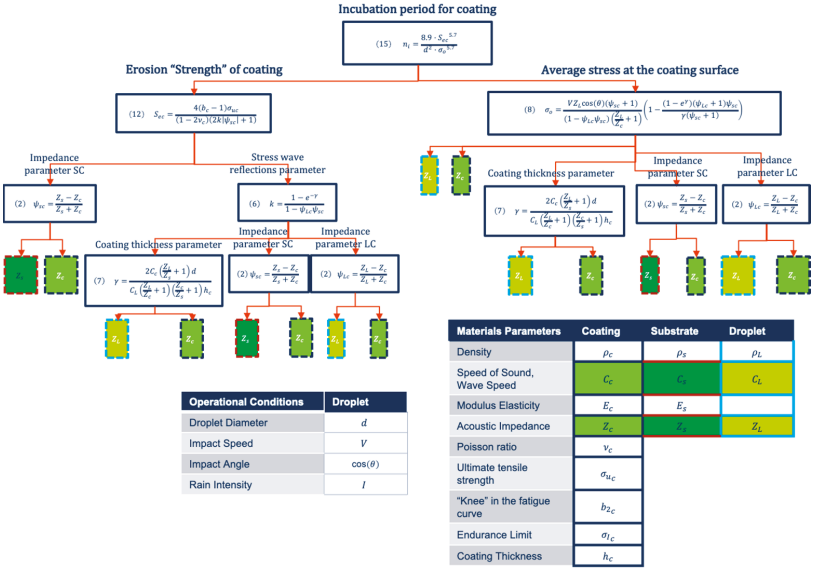

Figure 8. Diagram of liquid, coating and substrate material impedances and operational parameters affecting rain erosion performance.

3. Single Droplet Impact Modelling Considering Viscoelastic Material Characterization

3.1. Thin Coatings mechAnical Properties at High-Strain-Rates

The waterdrop impact introduces a very high-rate pressure transient build-up. The viscoelastic material experiences a very rapidly increasing stress field that leads to a distortion and a subsequent strain relaxation. The large deformation stress-strain behavior of elastomeric materials is strongly dependent on strain rate. ISO 18872 standard [23] is defined for high strain rate testing of polymeric materials. In [24–26] is analyzed for particular materials the deformation behavior over a wide range in strain rates. The problem is widely studied in the literature in regards of different mechanical properties, chemistry systems (molecular transitions and relaxations) and loading cases (considering tensile or compression). For our droplet impact analysis and modelling, it is important to note that the Ultimate Strength σ_u characterization represents an important input parameter because is directly related with the erosion strength and is exponentially related to lifetime estimation (see Equations (12) and (14) respectively). Its rate dependent value [26] is an important source of deviation on the modelling accuracy. Representative engineering stress-strain plots of a polyurethane-based polymer material under dynamic tension loading with three curves per selected strain rate level can be obtained from [26]. Characterizing LEP materials at high strain rates is difficult, even at small amplitudes because the regime of interest at a very high frequency is limited.

The highly transient material behavior during waterdrop collisions require to define the range of frequency of its data set. Stiffness of a polymer is measured as a modulus, a ratio of stress to strain at a certain stage of deformation. LEP polymers are viscoelastic materials and as a result their mechanical and acoustical property will depend very much upon measurement frequency and temperature, [27–31]. Viscoelastic variation in application of solid particle erosion analysis under high speed impact conditions is reported in [18].

This material behavior can be obtained from the frequency response data from Dynamic Mechanical Thermal Analysis (DMTA) where a sinusoidal strain is imposed on a rectangular sample as a function of temperature, see Figure 9.

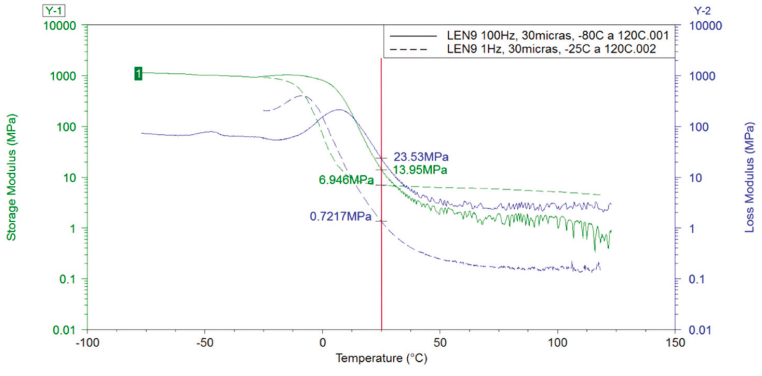

Figure 9. DMTA developed Testing for prototype LEP used in this work, only valid for low frequencies 1Hz up to 100 Hz but considering Temperature variation.

For the dynamic experiments the modulus is complex E^* and is given by $E^* = E' + iE''$ whereby E' describes the elastic or energy storage component of the modulus and E'' the loss of energy as heat in a cycle deformation. The modulus of a viscoelastic material is a function of time as well as temperature which is the basis for time-temperature superposition principles which may be used to predict the temperature-frequency behavior of a polymer.

The Dynamic Mechanical Thermal Analysis (DMTA) is the appropriate test to determine the viscoelastic properties, however, the information provided by this technique is only valid up to a frequency of 100 Hz, and therefore, it is not useful in the present context.

The Time-Temperature superposition principle may be required to determine temperature-dependent mechanical properties in a broad range of frequencies. It also may consider transforming the data from the frequency to the time domain for the computational analysis (by performing convolution calculations and inverse Fourier transform on *E′ and E″* data set).

On the other hand, Dielectric Thermal Analysis (DETA) supplies information on the molecular motion up to a frequency of 10^7 Hz by means of measuring the complex dielectric permittivity (ε^*) over the entire frequency range, so the regime of interest, see Figure 10. It gives complete information for shifts in Tg transitions depending on frequency and temperature variations, but it has a lack on the mechanical values of *E′* and *E″* since it only gives us dielectric data. Thus, it is necessary to obtain with additional time-temperature superposition the relevant mechanical data and converting it to the complex Young modulus (E^*). To that end, a series of mathematical models capable of performing such interconversion may be applied [32–34].

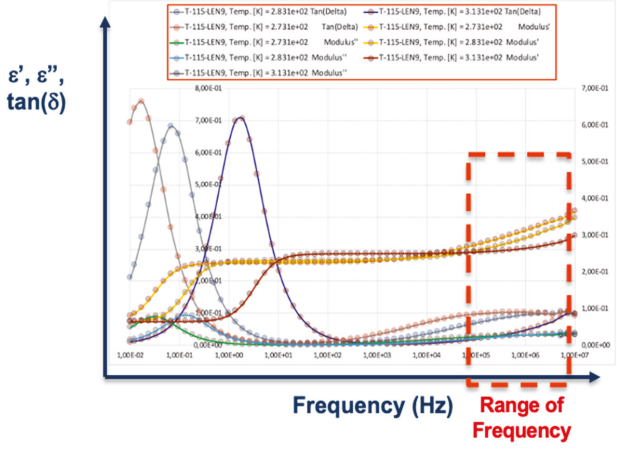

Figure 10. DETA dielectric testing was developed with 3 different temperatures for prototype LEP used in this work, valid for high frequencies up to 10 MHz but not contemplating mechanical properties definition.

A direct measurement of the required mechanical elastic properties in high frequency ranges can be obtained from Ultrasonic measurements as detailed in the literature [28–30]. There is a good correlation between the ultrasonic properties' attenuation α and sound velocity C and the elastic modulus properties:

$$E' = \rho C^2 \quad ; \quad E'' = \frac{\rho C^3}{\pi f}\alpha \tag{18}$$

The speed of sound is temperature and frequency dependent so are the acoustic impedance. In next section, further analysis is developed for better understanding the effect of most important parameters that may affect the frequency development of the stress-strain-time evolution and hence the consideration of appropriate speed of sound measurement as input modelling data.

3.2. Stress-Strain Frequency Range Analysis during Droplet Impingement

The working frequency range definition of a given single droplet impact is a complex phenomenon that needs appropriate 3D Stress-Strain analysis out of the scope of this work and depends on many operational variables. In Springer model it is simplified analytically considering the impact as a

step-like function defined by means the droplet size, the water and coating speed of sound and the impact speed (see first section of this document). In this work, the impact velocity of the droplets is defined for the conditions of the collision without differentiation of the rotor speed or the gravity effects of the rain droplets. The impact pressure is then considered through Water-hammer pressure that depends on the speed of impact and the liquid and surface impedances. The total impact duration t_L depends on the droplet diameter and the speed of sound in the liquid,

$$t_L = \frac{2d}{C_L} \tag{19}$$

It can be observed in Figure 11 this step wise force pulse definition yields a Fourier Transform decomposition with not valid frequencies due to the abrupt change on the time required to build up and down the contact forces.

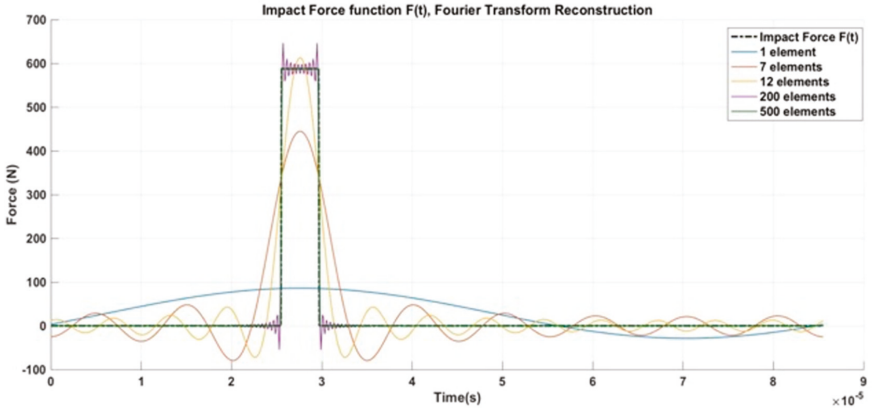

Figure 11. Impact force step wise definition and its corresponding Fourier Reconstruction (where impact duration depends on droplet diameter and the peak value depends on the velocity of droplet impact and liquid-coating relative impedances).

A first approximation of the problem would be to consider droplet with shape completely round with diameters in the range of 1–4 mm, so the corresponding duration of impacts t_L are 1.35–5.4 μs and if We assume that the time to build up and down is at least half of the impact duration time then, $\frac{1}{2}\ t_L$, give as a relation for the frequencies of that force pulse with values of 0.18–0.74 MHz, respectively.

In order to improve understanding the stress-strain development in the LEP system, we will introduce different modelling cases of analysis with alternative to Springer model assumptions:

- Including appropriate coating material models that allow us to observe the viscoelastic behaviour (with consideration for high transient strain rate deformation, and variable stiffness and damping with frequency) and not as a pure elastic event. Water droplet properties are incorporated and assumed constant in this work, but more complex material models could also be included in the developed modelling. Moreover, density variations for coating and water due temperature are also circumvented and are assumed constant during the impact event.
- Springer model undertakes a two layered structure with the substrate thickness assumed semi-infinite. We will treat the LEP system as a multilayer configuration so We will be able to observe additional wave reflections on the interfaces that affect also the surface coating. The algorithm considers water as an additional layer to allow stress wave reflections at liquid-coating interface. The initial impact conditions consider the coating as a dry surface, nevertheless, the water could also be considered as an additional thin layer from previous droplet impact but it

is neglected in this work to avoid complex liquid-coating contact modelling following Springer assumptions simplification.

- 1D formulation examines the impact of a liquid droplet treating the problem only as tensile-compression event. This simplification is applicable since shear stresses and shear material characterization are out of the scope of the fatigue analysis case involved.

The simplified model proposed that considers these assumptions, see Figure 12, has been numerically developed in Open Modellica [19]. The algorithm that includes the material models is outlined in Figure 13. This LEP configuration is defined for rain erosion testing performed at PolyTech Test & Validation A/S according to DNV-GL-RP-0171 [22], see Figure 14.

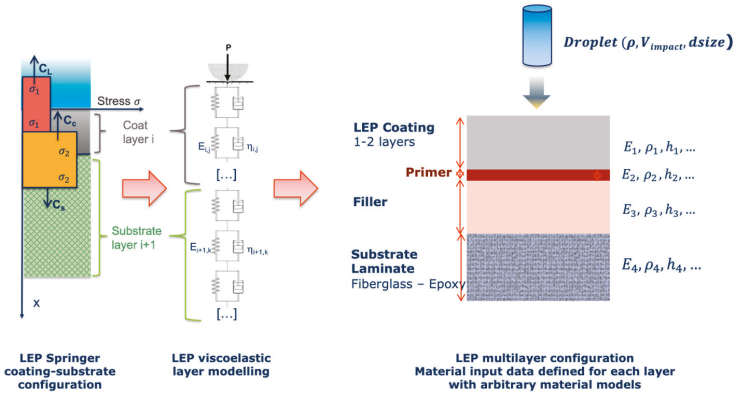

Figure 12. LEP configuration considering viscoelastic material models, multilayer and 1D droplet impact event.

Table 1. Initial Reference Input data used for the impact modelling of RET testing.

Material	Modulus E (Pa) /Viscosity (Pa s)	Speed of Sound C (m/s)	Layer Thickness /Droplet Diameter (μm)	Impact Velocity Specimen Vcenter (m/s)
Water droplet	2.19×10^9	1480.00	2000	121
Coating LEP	3.48×10^9/1.59	1733.00	500	121
Filler	4.90×10^9/3.183	1941.00	1000	121
Substrate Laminate	1.10×10^{10}	2392.00	3400	121

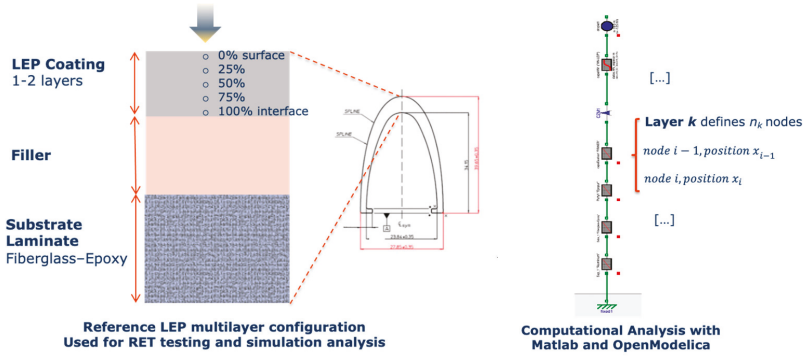

Figure 13. (**a**) Reference multilayer configuration for RET coupons. Liquid droplet and each material layer are defined by the input mechanical parameters of Table 1; (**b**) corresponding numerical configuration outline implemented in OpenModelica.

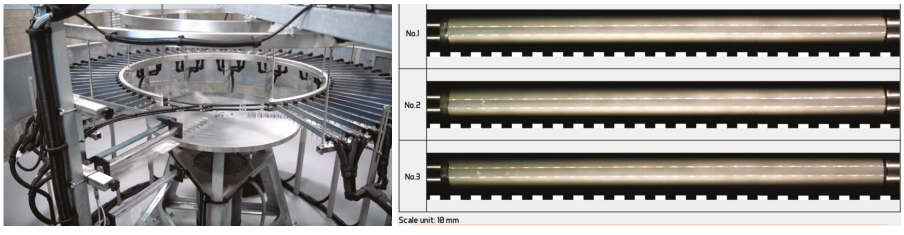

Figure 14. Rain erosion test facility and three specimens used at PolyTech Test & Validation A/S according to DNV-GL-RP-0171 [22] for the analysis and experimental validation.

The numerical procedure was implemented in a general LEP configuration according to Rain Erosion Testing coupons. Simulations of the stress-strain behavior caused in the multilayer system are computed for a given 1D discretization through the thickness position solving for a set of material nodes that belong to a particular homogenized layer. The Equilibrium equation to be accomplished for any two consecutive nodes in the multilayer system is given by

$$m_i \frac{d^2 x_i}{dt^2} = F_{i-1,i} - F_{i,i+1} \tag{20}$$

where *layer k* defines n_k nodes, *node i*−1 defines position x_{i-1} and *node i* position x_i. The material models implemented to state a given layer k give us distinctive stress-strain behavior that can be modelled as:

- Pure elastic model, where A is the impact area defined by the droplet size and E is the elastic modulus

$$F_{i-1,i} = -\frac{A \cdot E}{\left(x_i^0 - x_{i-1}^0\right)}\left(x_i - x_{i-1} - x_i^0 + x_{i-1}^0\right) \tag{21}$$

- Kelvin-Voight (KV) viscoelastic model, where η is the viscosity,

$$F_{i-1,i} = -\frac{A \cdot E}{\left(x_i^0 - x_{i-1}^0\right)}\left(x_i - x_{i-1} - x_i^0 + x_{i-1}^0\right) - \frac{A \cdot \eta}{\left(x_i^0 - x_{i-1}^0\right)}\left(\frac{dx_i}{dt} - \frac{dx_{i-1}}{dt}\right) \tag{22}$$

and considering appropriate estimation of the viscosity attenuation observed in as:

$$\begin{array}{c} \sigma_{total} = \sigma_s + \sigma_d \\ \varepsilon_{total} = \varepsilon_s = \varepsilon_d \\ E^* = E' + iE'' = E' + i2\pi f\eta \end{array} \quad \rightarrow \quad \begin{array}{c} \sigma = E\epsilon + \eta\frac{d\varepsilon}{dt} \\ \\ \eta = \frac{E''}{2\pi f} \end{array} \tag{23}$$

- Havriliak-Negami H-N viscoelastic model [32–34], where E_∞ define the unrelaxed or glassy modulus, and E_o is the relaxed rubbery modulus and τ is the relaxation time, see Figures 15 and 16.

$$F_{i-1,i} + \tau\frac{dF}{dt} = -\frac{A{\cdot}E_0}{\left(x_i^0 - x_{i-1}^0\right)}\left(x_i - x_{i-1} - x_i^0 + x_{i-1}^0\right) - \frac{A{\cdot}E_\infty}{\left(x_i^0 - x_{i-1}^0\right)}\left(\frac{dx_i}{dt} - \frac{dx_{i-1}}{dt}\right) \tag{24}$$

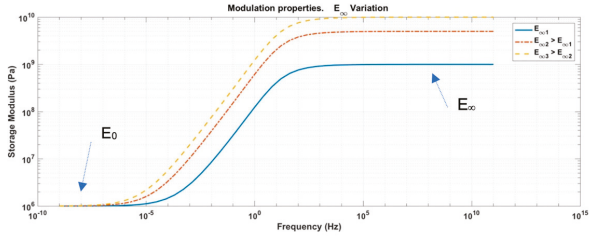

Figure 15. H-N model. Storage Modulus variation with Frequency. E_∞ unrelaxed modulus.

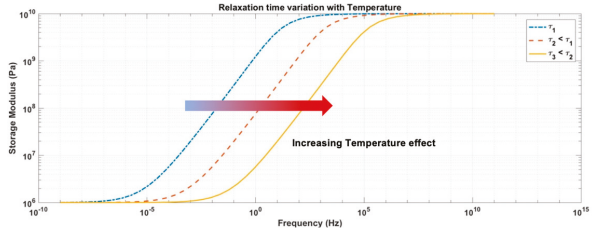

Figure 16. H-N model. Relaxation Time dependence on Temperature.

This simplified computational tool allow us to treat as parameters the material models (as pure elastic, Kelvin-Voight, Havriliak-Negami, etc.) and their related properties (density, storage modulus, loss modulus, tan delta, speed of sound, thickness, etc.), the operational variables (impact velocity, droplet diameter size, droplet density, droplet speed of sound, etc.). In order to quantify the strain rate analysis of the single droplet impact simulation, we will evaluate different cases considering the effect on variations in coating-substrate thickness, viscoelastic material properties, droplet size and droplet impact velocity from a reference configuration used in RET testing (Figure 13). The input data values for these prototype materials of Table 1 where defined initially from previous testing results and here are used for the exposed modelling procedure in order to discuss Stress-Strain frequency range analysis during droplet impingement.

The strain-stress evolution with time is evaluated at different locations of the LEP coating for appropriate comparison. The specific location of the analysis through the layer thickness is defined as variable e_x for the strain and variable s_x for the stress, where x is defined at surface x = 0, interface x = 100, or any intermediate positions with x = 25, 50 or 75 referring all to the given % of the layer thickness, see Figure 13.

A first result for the analysis of the reference testing LEP configuration is plotted in Figure 17. It is observed the strain evolution with time at the surface of the coating layer e_0 comparing two

cases: Coat_1 using a pure elastic modelling of the coating material compared with Coat_2 using a Kelvin-Voight modelling.

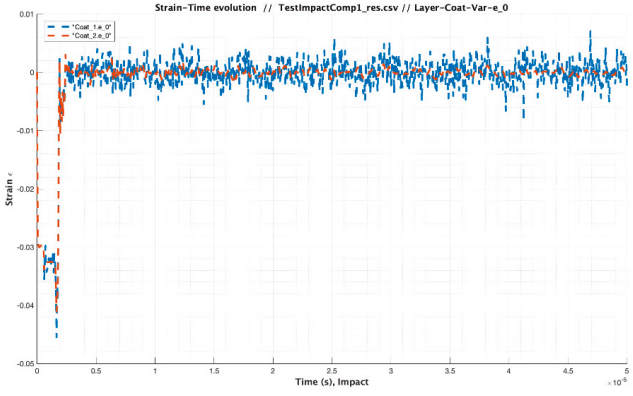

Figure 17. Strain evolution at the coating surface for the reference LEP configuration for RET coupons with input data defined in Table 1. Material models comparison.

In addition, the spectrogram of the strain evolution with time for a given location e_x is calculated with the Fourier transform applied in short-time periods though the duration of the impact analysis (0–50 μs). The strain frequency decomposition during the impact event, provide us a plot of the dominant frequency spectrum with a range of values (measured as power (dB) over Frequency (Hz)), for each time analysis period. This procedure allows us to estimate indirectly the highly transient strain-rate variations for the single droplet impact event.

Figures 18 and 19 show as a first simplified approximation, the effect of the inclusion of the attenuation consequence due to the material modelling definition. The reason for such comparison is to clarify that the material properties are frequency dependent so the input data for the modelling. This assumption is important to consider when we define the speed of sound as a constant variable in our analysis. A first conclusion for the developed case is that the most dominant frequencies occur during the first stage of the impact and that Kelvin-Voight material modelling is appropriate to avoid additional frequency noise due to the lack of attenuation when using pure elastic material models.

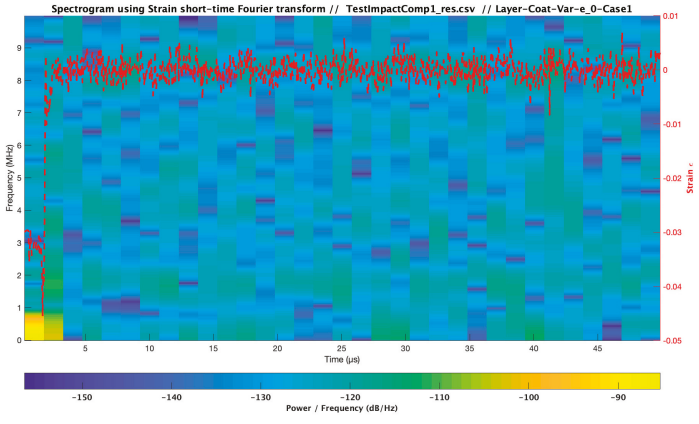

Figure 18. Spectrogram for strain evolution at the coating surface for the Reference multilayer configuration. Material models analysis for Pure elastic consideration.

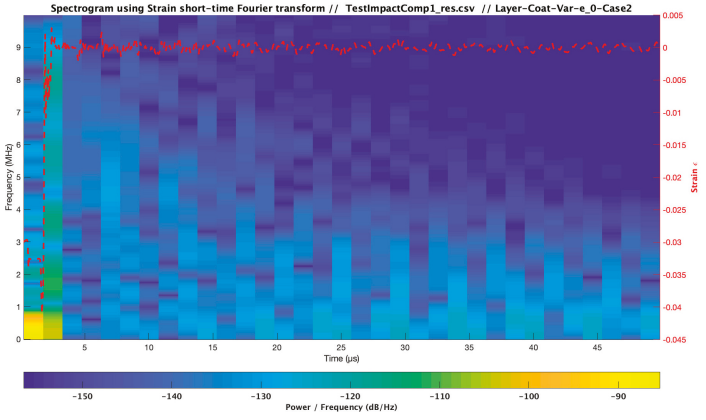

Figure 19. Spectrogram for strain evolution at the coating surface for the Reference multilayer configuration. Material models analysis for Kelvin-Voight consideration.

The computational analysis limits the frequency in a range of 0.5–2 MHz for this initial set-up conditions.

3.3. Influence of Coating-Substrate Thickness Variations

In this section, the strain-stress analysis ponders first the effect of considering a variation on the coating thickness over the reference case for the initial testing coupon of Table 1. Two cases of study are related with variations of the given parameter multiplying its value by 1,4 for Cases 1 and 2 respectively as shown in Table 2

Table 2. Modelling input data for variation cases in **Coating thickness**.

Test Impact Comparison_3 Case Analysis	Material	Modulus E (Pa) /Viscosity (Pa s)	Speed of Sound C (m/s)	Layer Thickness (μm)	Impact Velocity Specimen Vcenter (m/s)
Case 1	Coating LEP	3.48×10^9/1.59	1733.00	500	121
Case 2		3.48×10^9/1.59	1733.00	4×500	121

Figure 20 shows the influence of the Coating thickness on the stress developed at surface (s_0) and interface (s_100) for the Case 1 (reference LEP configuration). The peak values observed at interface depends also on the acoustic matching with the filler. Since the material develops different stress-strain values through its thickness, a proper layer location for comparing the strain evolution is considered to be defined at its intermediate 50% thickness location i.e., e_50, s_50. Figures 21 and 22 for Cases 1 and 2 comparison.

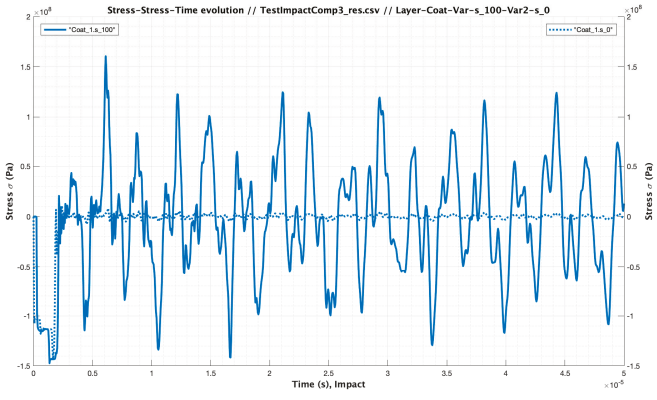

Figure 20. Stress-Time evolution for Case 1 at surface (s = 0) and interface (s = 100).

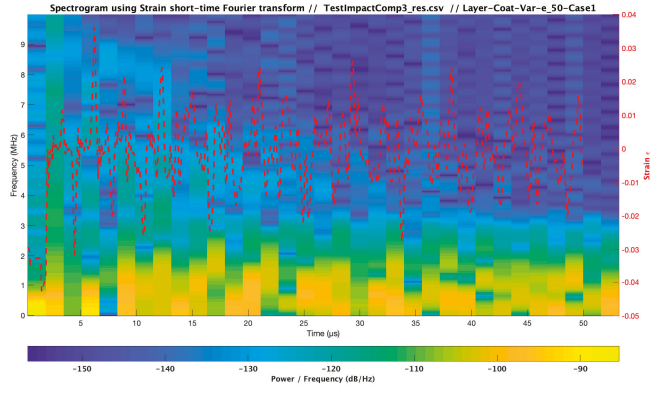

Figure 21. Spectrogram for strain evolution at the middle coating layer. Comparison for coating thickness variation respect to the reference LEP multilayer configuration (Case 1).

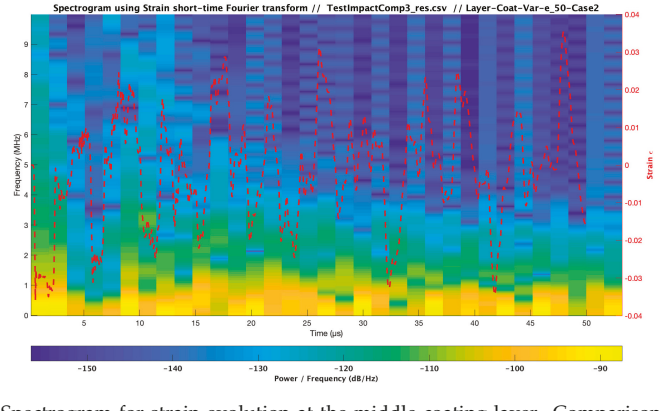

Figure 22. Spectrogram for strain evolution at the middle coating layer. Comparison for coating thickness variation respect to the reference LEP multilayer configuration (Case 2).

It is important to observe the high values of the reflection stresses developed due to the multilayer interfaces effect due to the low value of the substrate thickness of the reference LEP multilayer configuration. Springer model limits this assuming that the substrate (filler) layer has to be considered

semi-infinite, $h_s > 2d\frac{C_s}{C_L}$, which means in fact that the reflections are not considered in the fatigue analysis for computing the average stress values on surface. Other additional effect is considering very thick coatings with $h_C > 2d\frac{C_c}{C_L}$ by means of shells or tapes. Cases 1–3 analyze the effect of increasing 20 times the filler thickness and 1, 10 and 20 times the coating thickness compared to the initial reference LEP multilayer configuration of Table 1, detailed variation input data is defined on Table 3.

Table 3. Modelling input data for variation cases in semi-infinite substrates, $h_s > 2d\frac{C_s}{C_L}$, in substrate (filler) thickness and in thick coatings (shells and tapes), $h_C > 2d\frac{C_c}{C_L}$.

Test Impact Comparison_2 Case Analysis	Material	Modulus E (Pa) /Viscosity (Pa s)	Speed of Sound C (m/s)	Layer Thickness (μm)	Impact Velocity Specimen Vcenter (m/s)
Case 1	Coating LEP	3.48×10^9/1.59	1733.00	500	121
Case 2		3.48×10^9/1.59	1733.00	10×500	121
Case 3		3.48×10^9/1.59	1733.00	20×500	121
Cases 1,2,3	Filler	4.90×10^9/3.183	1941.00	20×1000	121

It is observed in Figures 23 and 24 the lower value of stress at surface (s_0) and middle location layer (s_50) due to the increment of coating thickness (so its damping capabilities). It is also appreciated the delay on wave stress reflections due to the increase on the substrate-filler thickness.

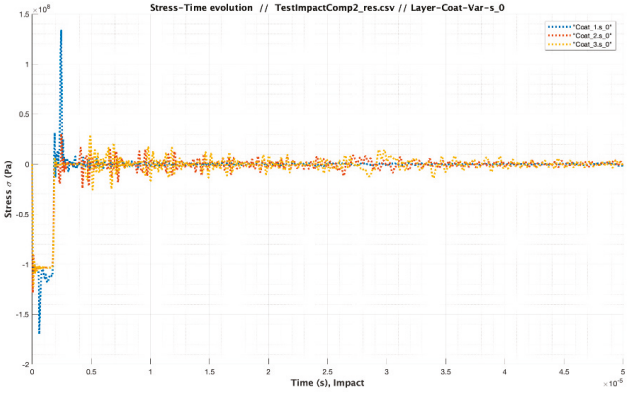

Figure 23. Stress-Time evolution for Cases 1–3 at surface, 0% of Coating thickness, considering the substrate filler as semi-infinite with increased thickness (shells, tapes).

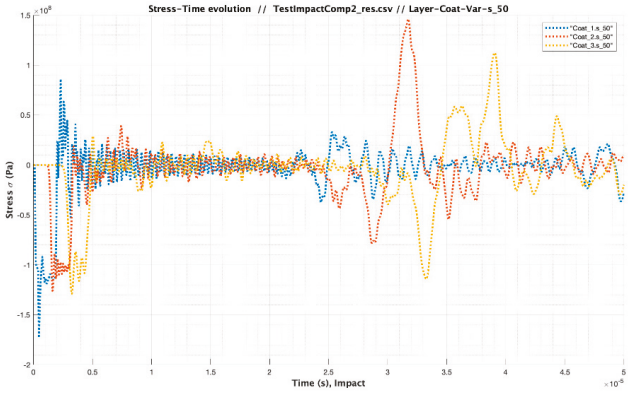

Figure 24. Stress-Time evolution for Cases 1–3 at middle coating layer, 50% thickness, considering substrate-filler as semi-infinite with increased thickness (shells, tapes).

Figures 25–27 show the corresponding influence on the strain frequency spectrum where the higher strain-rate variations are developed in the periods of time closer to the impact pulse and the wave traveling reflections.

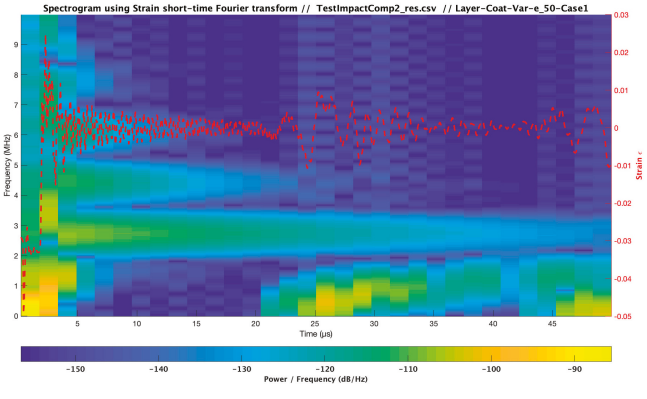

Figure 25. Spectrogram for strain evolution at the middle coating layer, 50% thickness, considering substrate-filler as semi-infinite with defined coating thickness for reference LEP configuration. Case 1.

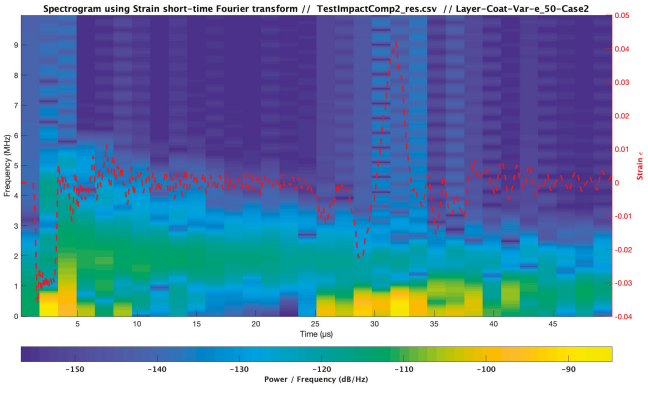

Figure 26. Spectrogram for strain evolution at the middle coating layer, 50% thickness, considering substrate-filler as semi-infinite with increased thickness (shells, tapes). Case 2.

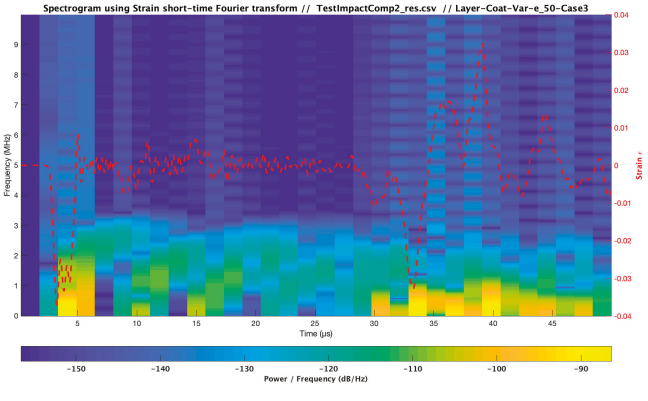

Figure 27. Spectrogram for strain evolution at the middle coating layer, 50% thickness, considering substrate-filler as semi-infinite with increased thickness (shells, tapes). Case 3.

3.4. Influence of Coating Viscoelastic Property Variations

In this section, the strain-stress analysis considers the influence of pondering a variation on the coating stiffness over the reference case for the testing coupon of Table 1. Three cases of study are related with variations of the given parameter multiplying its value by 1, 0.5 and 1.5 for Cases 1, 2, and 3, respectively as shown in Table 4.

Table 4. Modelling input data for variation cases in coating modulus (stiffness) and considering semi-infinite substrates, $h_s > 2d\frac{C_s}{C_L}$.

Test Impact Comparison_4 Case Analysis	Material	Modulus E (Pa) /Viscosity (Pa s)	Speed of Sound C (m/s)	Layer Thickness (μm)	Impact Velocity Specimen Vcenter (m/s)
Case 1	Coating LEP	3.48×10^9/1.59	1733.00	500	121
Case 2		$0.5 \times 3.48 \times 10^9$/1.59	1733.00	500	121
Case 3		$1.5 \times 3.48 \times 10^9$/1.59	1733.00	500	121
Cases 1,2,3	Filler	4.90×10^9/3.183	1941.00	20×1000	121

Figure 28 show the strain in the coating layer due to a variation on the modulus for the three different cases. It is detected an abrupt variation in the strain-rate values and its corresponding effect on the strain frequency spectrum, Figures 29 and 30. The dominant working strain frequency range is increased in the periods of time closer to the impact pulse is increased from 1 MHz, to 3–7 MHz for Cases 2 and 3.

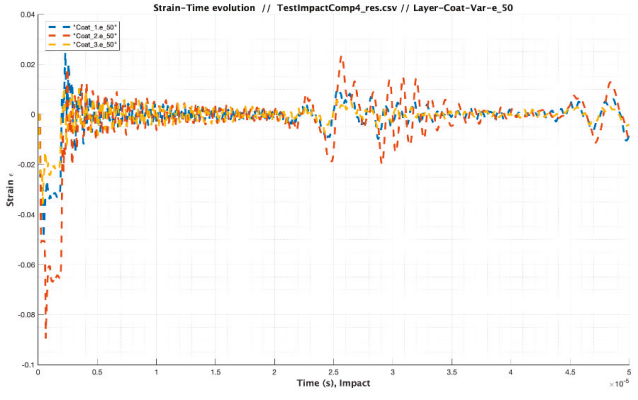

Figure 28. Strain-Time evolution for Case 1,2,3 at middle coating layer, 50% thickness, considering the substrate-filler as semi-infinite with variation in coating modulus.

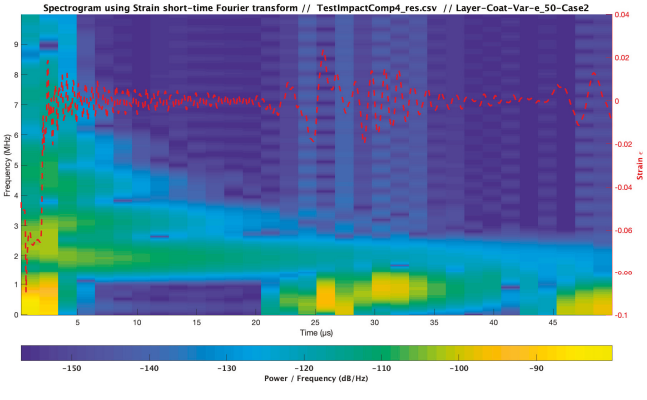

Figure 29. Spectrogram for strain evolution at the middle coating layer, 50% thickness, considering substrate-filler as semi-infinite with variation in coating modulus. Case 2.

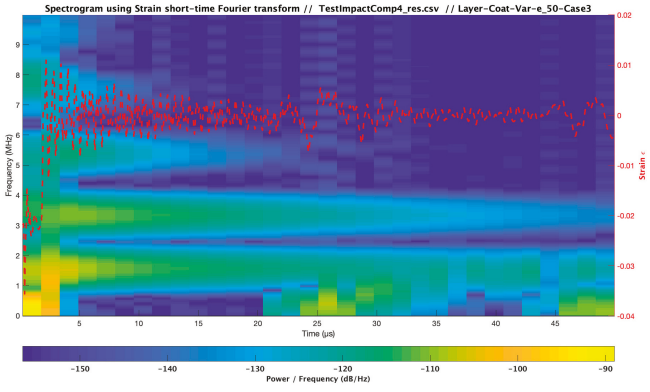

Figure 30. Spectrogram for strain evolution at the middle coating layer, 50% thickness, considering substrate-filler as semi-infinite with variation in coating modulus. Case 3.

3.5. Influence of Droplet Size Variations

The strain-stress analysis contemplates in this part the effect of pondering a distinction on the droplet diameter over the reference case for the testing coupon. Three cases of study are related with variations of the given parameter multiplying its value by 1,2 and 3 for Case 1, 2, and 3, respectively as shown in Table 5.

Table 5. Modelling input data for variation cases in droplet diameter and considering semi-infinite substrates, $h_s > 2d\frac{C_s}{C_L}$.

Test Impact Comparison_4 Case Analysis	Material	Modulus E (Pa) /Viscosity (Pa s)	Speed of Sound C (m/s)	Layer Thickness /Droplet Diameter (µm)	Impact Velocity Specimen Vcenter (m/s)
Case 1	Water droplet	2.19×10^9	1480.00	2000	121
Case 2		2.19×10^9	1480.00	2×2000	121
Case 3		2.19×10^9	1480.00	3×2000	121
Cases 1,2,3	Filler	$4.90 \times 10^9/3.183$	1941.00	20×1000	121

Figure 31 illustrates the strain evolution for the three different cases. It is noticed a delayed variation in the strain-rate values with longer periods of impact and also the equivalent effect on the strain frequency spectrum, Figures 32 and 33. The main working strain frequency range is evenly increased for bigger droplets (4–6 mm. in diameter) in the periods of time closer to the impact and the reflections with values from 1 MHz, to 3–7 MHz for Cases 2 and 3.

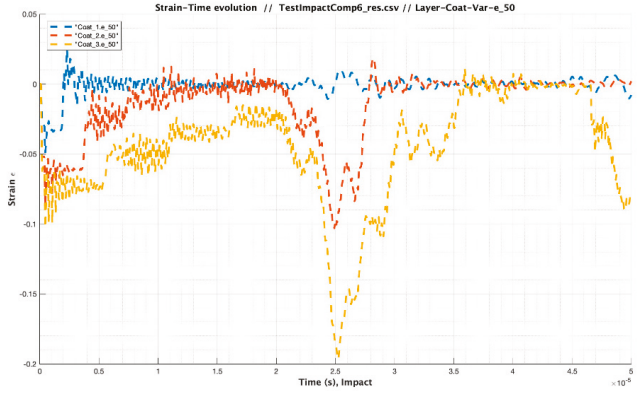

Figure 31. Strain-Time evolution for Cases 1–3 at middle coating layer, 50% thickness, considering the substrate-filler as semi-infinite with variation in droplet diameter.

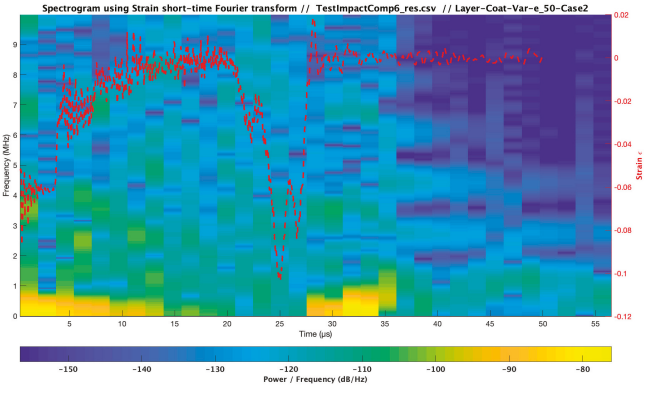

Figure 32. Spectrogram for strain evolution at the middle coating layer, 50% thickness, considering substrate-filler as semi-infinite with variation in droplet diameter. Case 2.

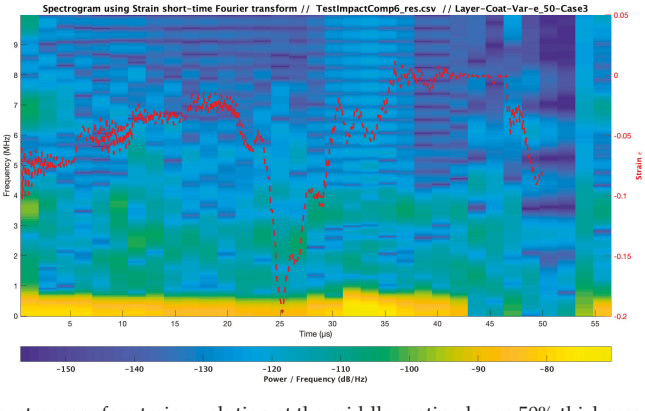

Figure 33. Spectrogram for strain evolution at the middle coating layer, 50% thickness, considering substrate-filler as semi-infinite with variation in droplet diameter. Case 3.

3.6. Influence of Droplet Impact Velocity Variations

In this section, the strain-stress analysis intends the consequence of a difference on the droplet impact velocity over the reference case for the testing coupon. Three cases of study are related with variations of the given parameter multiplying its value by 1, 0.6 and 1.4 for Cases 1, 2, and 3, respectively as shown in Table 6. It is important to note that a maximum impact velocity in operational conditions of wind turbine blades (only in offshore fields) should be defined around 170 m/s.

Table 6. Modelling input data for variation cases in droplet impact velocity and considering semi-infinite substrates, $h_s > 2d\frac{C_s}{C_L}$.

Test Impact Comparison_4 Case Analysis	Material	Modulus E (Pa)	Speed of Sound C (m/s)	Droplet Diameter (μm)	Impact Velocity Specimen Vcenter (m/s)
Case 1	Water droplet	2.19×10^9	1480.00	2000	121
Case 2		2.19×10^9	1480.00	2000	0.6×121
Case 3		2.19×10^9	1480.00	2000	1.4×121

Figure 34 clarifies the direct related variation in the strain-rate values with the impact velocity for the three different cases. The corresponding influence on the strain frequency spectrum is depicted in Figures 35 and 36. The principal working strain frequency range is evenly distributed in the periods of time closer to the impact with values from 1 to 7 MHz for Cases 2 and 3, pointing out an important influence of the impact velocity with the frequency range during impact event.

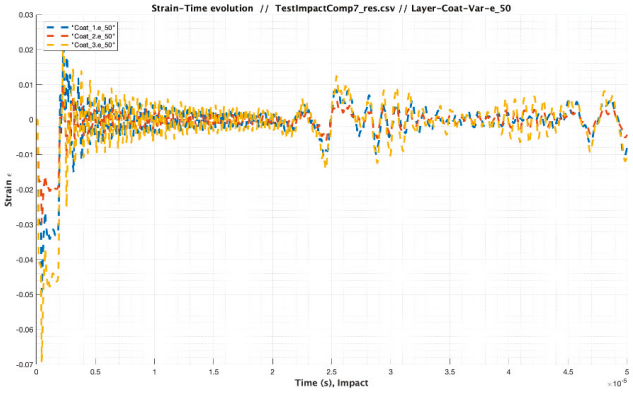

Figure 34. Strain-Time evolution for Cases 1–3 at middle coating layer, 50% thickness, considering the substrate-filler as semi-infinite with variation in droplet velocity.

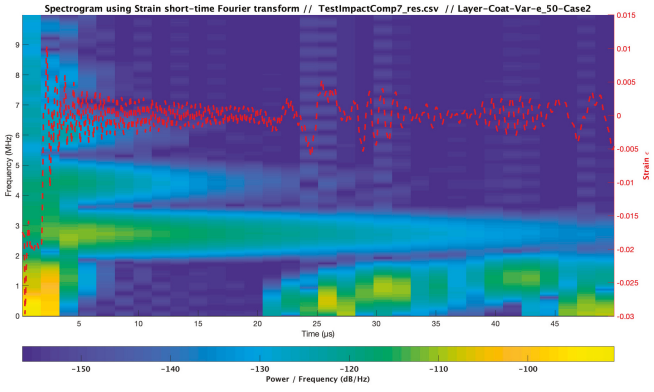

Figure 35. Spectrogram for strain evolution at the middle coating layer, 50% thickness, considering substrate-filler as semi-infinite with variation in droplet velocity. Case 2.

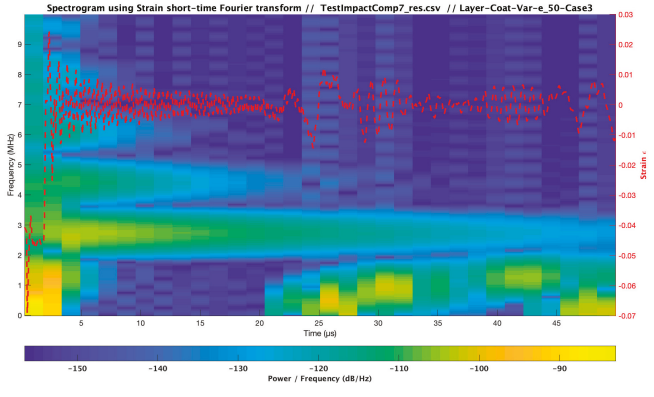

Figure 36. Spectrogram for strain evolution at the middle coating layer, 50% thickness, considering substrate-filler as semi-infinite with variation in droplet velocity. Case 3.

4. Conclusions

Numerical and analytical models have been used in this work as a tool to analyze coating LEP wear surface erosion performance. The modelling description offers a guidance in the analysis based on the material fundamental properties. It is required for a complete analysis to define criteria for identifying suitable acoustical matching of LEP coating and composite substrate interfaces.

Complex material models are considered to observe the highly transient material behavior during waterdrop collisions that require to define the range of frequency of its data set to account for strain rate dependence. The simplified single droplet impact modelling developed in this work has been implemented and its capabilities assessed. The simulated analysis pondering different operational and configuration cases used in industry has been discussed in detail and limits the working frequency in a range of 0.5–7 MHz. The analysis has been developed assuming constant values of mechanical properties during the impact event in order to imitate the Springer modelling assumptions. The upper limit of 5 MHz allows one to consider a conservative constant value for the appropriate measurement of the material impedance providing a limit on the stiffness variation of the viscoelastic response of the selected material. Then, a procedure for the measurement of acoustic impedance with a time-of-flight technique of a thin viscoelastic layer using a planar ultrasonic transducer for the frequency regime of interest can be developed. Details of such developments are reported by the authors in linked research [20].

The material impedance characterization may be obtained at the appropriate Ultrasound frequency testing for the erosion performance modelling input data to avoid lack of accuracy. The computational tool presented would allow one to define erosion performance estimators depending on the relative acoustic impedance of liquid, coating and substrate materials definition reducing the Rain Erosion Testing campaigns to evaluate the rain erosion resistance of selected top-coating systems.

Author Contributions: Designed and developed the computational tool, L.D. and J.R.; Conceived and implemented the material testing specimens, A.Š.; Determined the research program, defined the computational framework scope, its use and the interpretation of the results, supervised the work and wrote the paper, F.S. All authors have read and agreed to the published version of the manuscript.

Funding: This research has been partially funded by the DEMOWIND-2 Project "Offshore Demonstration Blade (ODB)" funded by MINECO with reference PCIN-069-2017, by the ESI-Group Chair at CEU-UCH and from the European Union's Horizon 2020 research and innovation program under grant agreement No 811473. Project "LEP4BLADES".

Conflicts of Interest: The authors declare no conflict of interest.

References

1. Cortés, E.; Sánchez, F.; O'Carroll, A.; Madramany, B.; Hardiman, M.; Young, T.M. On the material characterization of wind turbine blade coatings: Effect of the interphase adhesion on rain erosion performance. *Materials* **2017**, *10*, 1146. [CrossRef]
2. Tobin, E.F.; Young, T.M.; Raps, D.; Rohr, O. Comparison of liquid impingement results from whirling arm and water-jet erosion test facilities. *Wear* **2011**, *271*, 2625–2631. [CrossRef]
3. Gohardani, O. Impact of erosion testing aspects on current and future flight conditions. *Prog. Aerosp. Sci.* **2011**, *47*, 280–303. [CrossRef]
4. Adler, W.F. Waterdrop impact modeling. *Wear* **1995**, *186*, 341–351. [CrossRef]
5. Fang, J.; Owens, R.G.; Tacher, L.; Parriaux, A. A numerical study of the sph method for simulating transient viscoelastic free surface flows. *J. Nonnewton. Fluid Mech.* **2006**, *139*, 68–84. [CrossRef]
6. Verma, A.S.; Castro, S.G.P.; Jiang, Z.; Teuwen, J.J.E. Numerical investigation of rain droplet impact on offshore wind turbine blades under different rainfall conditions: A parametric study. *Compos. Struct.* **2020**, *241*, 112096. [CrossRef]
7. Yonemoto, Y.; Kunugi, T. Universality of Droplet Impingement: Low-to-high viscosities and surface tensions. *Coatings* **2018**, *8*, 409. [CrossRef]
8. Keegan, M.H.; Nash, D.H.; Stack, M.M. On erosion issues associated with the leading edge of wind turbine blades. *J. Phys. D Appl. Phys.* **2013**, *46*, 383001. [CrossRef]
9. Doagou-Rad, S.; Mishnaevsky, L.; Bech, J.I. Leading edge erosion of wind turbine blades: Multiaxial critical plane fatigue model of coating degradation under random liquid impacts. *Wind Energy* **2020**, *1*, 1–15. [CrossRef]
10. Mishnaevsky, L.; Fæster, S.; Mikkelsen, L.P.; Kusano, Y.; Bech, J.I. Micromechanisms of leading edge erosion of wind turbine blades: X-ray tomography analysis and computational studies. *Wind Energy* **2020**, *23*, 547–562. [CrossRef]
11. Mishnaevsky, L., Jr.; Sütterlin, J. Micromechanical model of surface erosion of polyurethane coatings on wind turbine blades. *Polym. Degrad. Stab.* **2019**, *166*, 283–289. [CrossRef]
12. Chen, J.; Geng, M.; Li, Y.; Yang, Z.; Chai, Y.; He, G. Erosion resistance and damage mechanism of TiN/ZrN nanoscale multilayer coating. *Coatings* **2019**, *9*, 64. [CrossRef]
13. Springer, G.S. *Erosion by Liquid Impact*; John Wiley and Sons: New York, NY, USA, 1976.
14. Slot, H.M.; Gelnick, E.R.M.; Rentrop, C.; van der Heide, E. Leading edge erosion of coated wind turbine blades: Review of coating life models. *Renew. Energy* **2015**, *80*, 837–848. [CrossRef]
15. Eisenberg, D.; Laustsen, S.; Stege, J. Wind turbine blade coating leading edge rain erosion model: Development and validation. *Wind Energy* **2018**, *80*. [CrossRef]
16. Elhadi Ibrahim, M.; Medraj, M. Water droplet erosion of wind turbine blades: Mechanics, testing, modeling and future perspectives. *Materials* **2020**, *13*, 157. [CrossRef]
17. Mishnaevsky, L., Jr. Toolbox for optimizing anti-erosion protective coatings of wind turbine blades: Overview of mechanisms and technical solutions. *Wind Energy* **2019**, *22*, 1636–1653. [CrossRef]

18. Arena, G.; Friedrich, K.; Ruso, P.; Padenko, E.; Acierno, D.; Filippone, G.; Wagner, J. Solid particle erosion and viscoelastic properties of thermoplastic polyurethane. *eXPRESS Polym. Lett.* **2015**, *9*, 166–176. [CrossRef]
19. OPENMODELICA. Available online: https://openmodelica.org (accessed on 6 June 2020).
20. Domenech, L.; Garcia-Peñas, V.; Šakalytė, A.; Puthukara, D.; Eskil Skoglund, F.; Sánchez, F. Top coating anti-erosion performance analysis in wind turbine blades depending on relative acoustic impedance. Part 2: Material characterization and rain erosion testing evaluation. *Coatings* **2020**, in press.
21. *Standard Test Method for Liquid Impingement Erosion Using Rotating Apparatus*; ASTM G73-10; ASTM International: West Conshohocken, PA, USA, 2017.
22. DNVGL: RP-0171. Testing of Rotor Blade Erosion Protection Systems. Recommended Practice. 2018. Available online: http://www.dnvgl.com (accessed on 1 February 2020).
23. *Plastics—Determination of Tensile Properties at High Strain Rates*; ISO 18872:2007; ISO: Geneva, Switzerland, 2007.
24. Sarva, S.S.; Deschanel, S.; Boyce, M.C.; Chen, W. Stress-strain behavior of a polyurea and a polyurethane from low to high strain rates. *Polymer* **2007**, *48*, 2208–2213. [CrossRef]
25. Roland, C.M.; Twigg, J.; van Vu, Y.; Mott, P.H. High strain rate mechanical behavior of polyurea. *Polymer* **2007**, *48*, 574–578. [CrossRef]
26. Fan, J.T.; Weerheijm, J.; Sluys, L.J. High-strain-rate tensile mechanical response of a polyurethane elastomeric material. *Polymer* **2015**, *65*, 72–80. [CrossRef]
27. Chevalier, Y.; Vinh, J.T. *Mechanics of Viscoelastic Materials and Wave Dispersion*; Wiley: Hoboken, NJ, USA, 2013.
28. Garceau, P. Characterization of Isotropic and Anisotropic Materials by Progressive Ultrasonic Waves. In *Mechanics of Viscoelastic Materials and Wave Dispersion*; Wiley: Hoboken, NJ, USA, 2013; pp. 513–554. [CrossRef]
29. Beda, T.; Esteoule, C.; Mohamed, S.; Vinh, J.T. Viscoelastic Moduli of Materials Deduced from Harmonic Responses of Beams. In *Mechanics of Viscoelastic Materials and Wave Dispersion*; Wiley: Hoboken, NJ, USA, 2013; pp. 555–597. [CrossRef]
30. Brinson, H.F.; Brinson, L.C. *Polymer Engineering Science and Viscoelasticity*; Springer: New York, NY, USA, 2010; ISBN 978-1-4899-7485-3.
31. Grate, J.W.; Wenzel, S.; White, R.M. frequency-independent and frequency-dependent polymer transitions observed on flexural plate ultrasonic wave sensors. *Anal. Chem.* **1992**, *64*, 413–423. [CrossRef]
32. Pascual, B.; Sánchez, F.; Doménech, L.; Cortés, E.; Ribes-Greus, A. Interconversion between dielectric and mechanical measurements of polymeric materials for wind turbine Blades. In Proceedings of the XI Congreso Nacional y II Internacional de Ingeniería Termodinámica, 11CNIT-XI-2018, Albacete, Spain, 12–28 June 2019.
33. Szabo, J.P.; Keough, I.A. Method for analysis of dynamic mechanical thermal analysis data using the Havriliak-Negami model. *Thermochim. Acta* **2002**, *392–393*, 1–12. [CrossRef]
34. Garcia-Bernabe, A.; Lidon-Roger, J.V.; Sanchis, M.J.; Diaz-Calleja, R.; del Castillo, L.F. Interconversion algorithm between mechanical and dielectric relaxation measurements for acetate of cis- and trans-2-phenyl-5-hydroxymethyl-1,3-dioxane. *Phys. Rev. E* **2015**, *92*, 042307. [CrossRef] [PubMed]

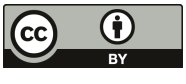

coatings

MDPI

Article

Top Coating Anti-Erosion Performance Analysis in Wind Turbine Blades Depending on Relative Acoustic Impedance. Part 2: Material Characterization and Rain Erosion Testing Evaluation

Luis Domenech [1], Víctor García-Peñas [1], Asta Šakalytė [2], Divya Puthukara Francis [3], Eskil Skoglund [3] and Fernando Sánchez [1,*]

1 Research Institute of Design, Innovation and Technology, University CEU Cardenal Herrera, CEU Universities, Avda. Seminario S/N, 46115 Moncada-Valencia, Spain; luis.domenech@uchceu.es (L.D.); vicgarpe@uchceu.es (V.G.)
2 AEROX Advanced Polymers, 46185 Pobla Vallbona-Valencia, Spain; asakalyte@aerox.es
3 Dolphitec, Studievegen 16, 2815 Gjøvik, Norway; divya@dolphitech.com (D.P.F.); eskil@dolphitech.com (E.S.)
* Correspondence: fernando.sanchez@uchceu.es

Received: 10 June 2020; Accepted: 15 July 2020; Published: 22 July 2020

Abstract: Under droplet impingement, surface leading edge protection (LEP) coating materials for wind turbine blades develop high-rate transient pressure build-up and a subsequent relaxation in a range of strain rates. The stress-strain coating LEP behavior at a working frequency range depends on the specific LEP and on the material and operational conditions, as described in this research in a previous work. Wear fatigue failure analysis, based on the Springer model, requires coating and substrate speed of sound measurements as constant input material parameters. It considers a linear elastic response of the polymer subjected to drop impact loads, but does not account for the frequency dependent viscoelastic effects for the materials involved. The model has been widely used and validated in the literature for different liquid impact erosion problems. In this work, it is shown the appropriate definition of the viscoelastic materials properties with ultrasonic techniques. It is broadly used for developing precise measurements of the speed of sound in thin coatings and laminates. It also allows accurately evaluating elastic moduli and assessing mechanical properties at the high frequencies of interest. In the current work, an investigation into various LEP coating application cases have been undertaken and related with the rain erosion durability factors due to suitable material impedance definition. The proposed numerical procedures to predict wear surface erosion have been evaluated in comparison with the rain erosion testing, in order to identify suitable coating and composite substrate combinations. LEP erosion performance at rain erosion testing (RET) technique is used widely in the wind industry as the key metric, in an effort to assess the response of the varying material and operational parameters involved.

Keywords: computational modelling; impedance analysis; rain erosion testing; ultrasound measurements; viscoelastic characterization; wind turbine blades

1. Introduction

Wind power has become a key technology to provide electricity from renewable and low-emission sources [1]. There is a need to improve existing technologies, by increasing the size of offshore wind turbines to capture more wind energy [2]. Composites use opened up great prospects in the design and manufacture of future wind turbine blades, due to the versatility offered in the material optimization and design. Nevertheless, composites perform poorly under transverse impact (i.e., perpendicular to the reinforcement direction) and are sensitive to environmental factors, such as heat, moisture,

icing, salinity and/or UV. Blade manufacturers employ surface coatings to protect the composite structure from exposure to these factors. When considering the repeated impact of rain droplets, the high required tip speed is a key contributor to surface erosion damage on the leading edges of wind turbine blades.

The leading-edge protection (LEP) coating system analyzed in this work [3] is usually molded, painted or sprayed onto the blade surface during whole blade manufacture or during a repair in-field. Industrial processes state that LEP systems can be outlined as a multi-layered system, where a putty filler layer between the laminate and the surface LEP coating is included to smooth the composite surface. A primer layer may be also integrated under the coating and over the filler layer to guarantee adhesion, circumventing delamination between layers, see Figure 1.

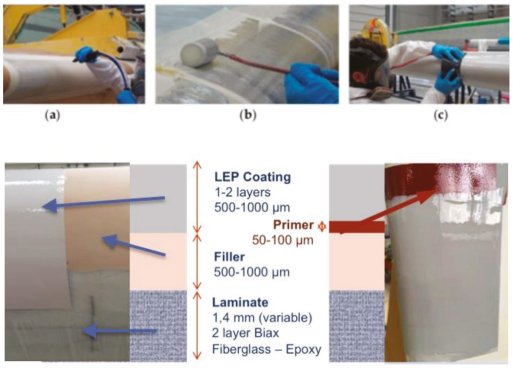

Figure 1. Leading Edge Protection (LEP) system application procedures, i.e., (**a**) spray; (**b**) roller; (**c**) trowel. Multilayer configuration.

Analytical and numerical models are commonly applied to relate top coating erosion lifetime prediction [4–6] or alternative accelerated rain erosion testing assessment is also used [7,8]. In order to identify suitable coating and composite substrate combinations based on their potential stress reduction on the surface and interface different studies are related with the droplet impact phenomena [9,10]. Recent studies treat the complexity of the single droplet impact problem with the fatigue analysis under repeated impact [11], and considering material viscoelastic approaches [12–14]. The Springer [4] model is applied and industry validated [5] for wear top-coating rain erosion lifetime assessment. It is used in this research [15] to predict wear fatigue failure analysis and as a computational tool for top-coating LEP design. In this work, its application is discussed, focusing on the required coating and substrate suitable combinations, and on the appropriate speed of sound measurements as input material parameters. The numerical model applied for the analysis of rain erosion lifetime estimation is limited to a linear elastic response of the polymer subjected to drop impact loads [4]. It is important to note that polymeric materials recently applied on the LEP systems are mainly viscoelastic materials with good properties for impact energy attenuation in erosion applications [16], that develop different mechanical response depending on temperature and on stress and strain rates [17–19]. If these parameters are not incorporated in the mechanical modeling, the predicted stresses of the coating behavior under impingement may wrongly consider the material capabilities.

In order to develop an appropriate parametric approach based on the viscoelastic material characterization, it is also necessary to consider a computational tool that allows one to design and validate the proposed modelling. In this research, a previous analysis of candidate materials in the temporal and frequency domain was developed to define applicable strain rate range for the required characterization. The simulated analysis developed in this research in a linked reference [15] limits the frequency for wind turbine rain erosion applications in a range of 0.5–7 MHz. The analysis has

been done considering the constant values of material speed of sound and density for the impedance definition, in order to reproduce the Springer modelling assumptions.

The speed of sound of viscoelastic materials is directly related with its modulus of elasticity [20]. The viscoelastic characterization of the LEP materials at the appropriate working frequency range is limited for dynamic tests based on the vibration of rods or beams [21,22] and only possible using ultrasonic waves [23–25]. Moreover, the use of the ultrasound technique in thin film applications has additional issues as coupled thickness layer determination [26–30]. Alternatively, it is well known for viscoelastic materials, that the frequency (strain rate) and temperature dependencies of polymer properties are both related. One may use the time–temperature superposition principle to generate the frequency-dependent curve, but in this case, other testing based on temperature variations are also complex and limited as described in [15]. It is important to point out here that the frequency sensitivity of ultrasound velocities is usually weak, of order tens m/s/decade, as described in [23], but since it depends mainly on the polymers relaxation and Tg, it may be a remarkable source of property variations in the performance analysis developed in this work.

The higher limit of 5 MHz proposed in [15] permits one to consider a conservative method for the suitable measurement of the material impedance, providing an upper bound limit on the stiffness variation of the viscoelastic response of the selected material, as demonstrated in [23,24], and for specific impact erosion applications in [16]. Hence, a procedure for the measurement of acoustic impedance with a time-of-flight technique of a thin viscoelastic layer using a planar ultrasonic transducer for the frequency regime of interest is done in this work, in the next section.

In the current work, impedance measurements at suitable working frequency with Ultrasonic testing are presented and developed as the input material data for the lifetime prediction based on Springer modelling exposed with different application case analysis. An investigation into various LEP coating application cases has been undertaken and related with the rain erosion durability factors. LEP erosion performance at rain erosion accelerated testing technique is used as the key metric in an effort to assess the response of changing material and processing parameters involved and to evaluate the lifetime accuracy analysis.

2. Ultrasonic Measurement of Speed of Sound of Thin Coating LEP Materials

2.1. Test Standards Used for Ultrasonic Material Characterization

The ultrasonic technique is an important procedure for viscoelastic materials' characterization at high strain rates. It is broadly used for developing precise measurements of speed of sound and attenuation. These two variables are the bases for accurately evaluating elastic moduli, and for assessing mechanical properties at high frequencies. Layer thickness and the speed of sound are important linked parameters also to account for LEP system configuration. If one of the parameters is known, the other one can be determined by simple time-of-flight (TOF) measurement of ultrasound.

An ultrasound examination is based on the propagation of ultrasonic waves in the part to be examined and the follow-up of the transmitted signal (called transmission technique), or of the signal reflected or diffracted by any surface or discontinuity (called reflection technique). Both techniques can use a single probe that acts as a transmitter and receiver, or a double probe, or separate transmitter and receiver probes. In the same way, these two techniques can involve an intermediate reflection coming from one or more surfaces of the examined object.

- The transmission technique (ISO 16823 [31] contains a more detailed description of this technique) is based on the measurement of the signal attenuation after the passage of an ultrasonic wave through the examined part.
- The reflection technique (pulse echo technique, ISO 16810 [32], and ISO 16811 [33]) uses the reflected or diffracted signal from any interface of interest inside the examined object. This signal is characterized by its amplitude and its position on the time base, the latter being a function of the distance between the reflector and the probe. The location of the reflector is determined

by knowledge of this distance, the direction of wave propagation, and the position of the probe. Contact with the test object is generally preferred over separation by a liquid buffer or immersion coupling medium. Although it is applicable, in general terms, to discontinuities in materials and applications, other techniques like the time-of-flight diffraction (TOFD, ISO 16828 [34]) can be used for both detection and sizing of discontinuities provided is performed with necessary consideration of geometry, acoustical properties of the materials, and the sensitivity of the examination.

For speed of sound measurements, the objective is to determine the exact time interval needed for a signal to travel between the front and back surface of a test object with previously known thickness. Attenuation may be calculated from the ratio of the two amplitudes measured. The pulse echo technique uses a broad band frequency range for most engineering solids, from about 300 to about 400 MHz. Preferably, the test object must have smooth, flat, parallel opposing surfaces and minimum thickness (to avoid excess of attenuation). It should meet the limitations for precise signal analysis, like the absence of discontinuities like voids or other particles. In addition, adequate force on the transducer is required to squeeze out excess coupling medium. Note that direct, normal incidence reflections may not appear even if test object shape and boundaries meet the conditions when the material is anisotropic, orthotropic or contains microstructural gradients.

2.2. Ultrasonic Speed of Sound Measurement Methodology for Thin Coating LEP Systems

Ultrasonic testing was undertaken with a Dolphitec ultrasonic system [35] using a pulse echo mode (ISO 16810 [32], and ISO 16811 [33]). This technique is based on analyzing the propagation of ultrasonic wave through the tested material. At each interface of the material, there is a spike in the ultrasonic response. This allows for the measuring the speed of sound through the material by finding the distance between the front-wall echo (spike response of the front face) and the back-wall echo and matching this to the material's actual physical measured thickness.

Ultrasonic scanning was employed to determine the acoustic impedance of neat LEP coating and filler materials. The acoustic impedance, Z can be calculated by:

$$Z = \rho C \tag{1}$$

where, ρ is the materials density and c is the speed of sound. These measurements were captured using both single crystal 2.5 and 5 MHz probes. This allowed for the measurement of material impedance at varying probe frequencies, providing information on viscoelastic response of the selected materials.

2.3. Testing Case Results

The coupons of LEP coatings, primer and filler materials for the impedance measurements were supplied by Aerox Advance Polymers [36] and the testing developed by Dolphitec [35]. The coupons prepared were of two geometries: a circular disc with a nominal diameter of 65 mm and thickness ranging for 5.5–6.3 mm on average and thin laminates of 400 µm on average, see Figure 2. The testing procedure was defined following the next steps:

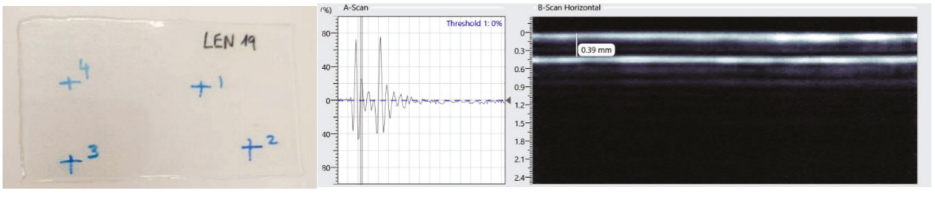

Figure 2. (Left) Thin Coating LEP used for UT coupon, (Right) Example of how a Time of Flight measurement is used in a tested coupon.

For the 2.5 and 5 MHz probes, four locations were marked on each coupon and the thickness was measured at each of these marked locations. Marks/points (starting from #1) are made on various regions on the sample coupon.

- Measurements are taken of different locations of the sample coupon using Mitutoyo Digital Vernier caliper.
- Transducer probe is placed on the coupon on the points marked region.
- The number of transmitting elements and gain of the probe is adjusted to obtain a clear image of the backwall echo with the corresponding front wall threshold.
- The crosshair line on the C scan is placed on the point of the coupon, by this the GUI shows the A scan, B scan and C scan image of the coupon at that point.
- A line measurement tool is used to define a line from the front echo to the backwall on the point on the sample. The measurement tool will display the depth, which here is the thickness of the sample.
- The velocity is adjusted in the velocity menu to obtain the measured thickness on the line measure tool, as per the Vernier caliper reading of that point/location.
- Thus, the speed of sound of that location on the coupon is recorded to obtain the impedance, with known values of density using the Equation (1).

Figure 3 shows the impedance measurements using the 2.5 MHz probes. The impendence for the coating LEP, primer and two different fillers were successfully measured in three different batches with 6 measurements developed on each material. All materials measured showed a minor reduction (5–10%) in the impedance values when measured with the 2.5 MHz probe frequency compared to the 5 MHz probe throughout all the materials tested. This would indicate a limited stiffness variation in order to develop the erosion lifetime performance analysis with Springer modelling, assuming a constant impedance value used as input data for each material and measured using the 5 MHz UT probe for all cases. Figure 4 shows the average speed of sound measurements for the 5 MHz probe.

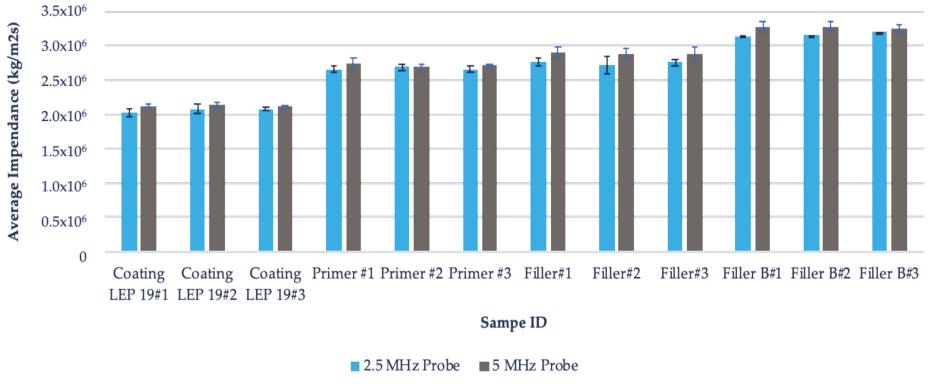

Figure 3. Average impedance measurements with the 2.5 and 5 MHz probes.

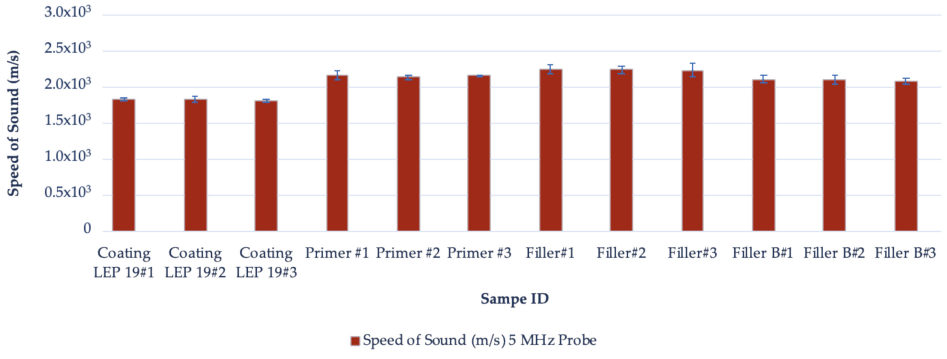

Figure 4. Average Speed of Sound measurements with the 5 MHz probe.

3. Quantitative Analysis of Relative Acoustic Impedance Characterization Affecting Rain Erosion Performance

The wear erosion lifetime prediction model used in this research was computationally evaluated and implemented [15] to link material input data definition with its performance estimation. A complete map of the liquid droplet, coating LEP and substrate (primer or filler) material impedances as input parameters of the equations defined in the modelling is proposed in Figure 5.

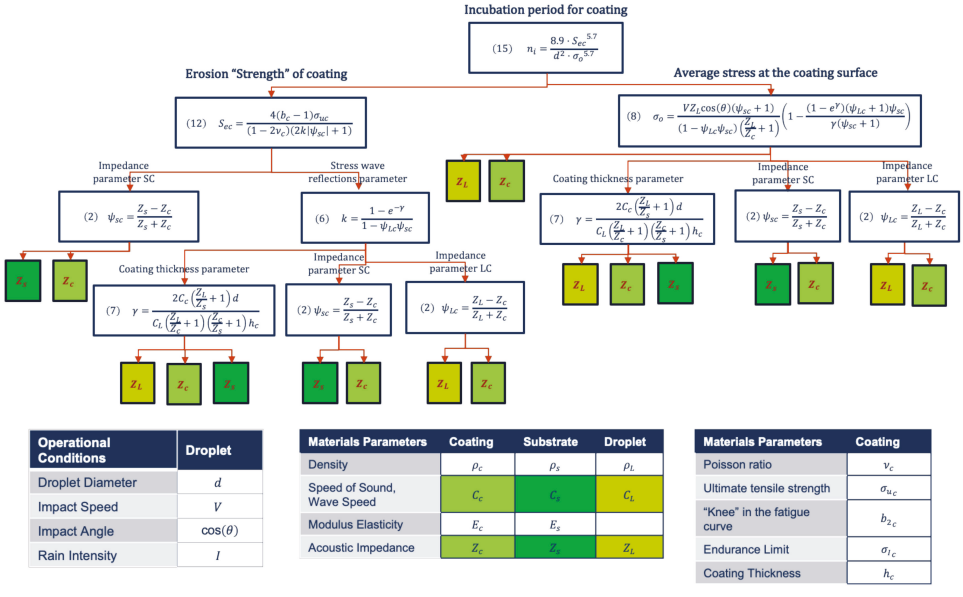

Operational Conditions	Droplet
Droplet Diameter	d
Impact Speed	V
Impact Angle	$\cos(\theta)$
Rain Intensity	I

Materials Parameters	Coating	Substrate	Droplet
Density	ρ_c	ρ_s	ρ_L
Speed of Sound, Wave Speed	C_c	C_s	C_L
Modulus Elasticity	E_c	E_s	
Acoustic Impedance	Z_c	Z_s	Z_L

Materials Parameters	Coating
Poisson ratio	ν_c
Ultimate tensile strength	σ_{u_c}
"Knee" in the fatigue curve	b_{2_c}
Endurance Limit	σ_{1_c}
Coating Thickness	h_c

Figure 5. Map of impedance values as input data for the wear erosion lifetime modelling, implemented equations in [15]. Diagram of liquid, coating and substrate material impedances and operational parameters affecting rain erosion performance.

In order to discuss assumptions and capabilities of the proposed modelling, different study cases are followed throughout this section of the document.

3.1. Case 1. Analysis of a LEP Multilayer System Rain Erosion Testing Based on ASTM G73-10

This analysis case considers the rig features used at University of Limerick based on ASTM G73-10 [37] (Figure 6), with two set of coupons comparing the inclusion of a primer layer and another one with the coating LEP application directly to the sanded filler (see [3] for details). The modelling input data are defined in Table 1.

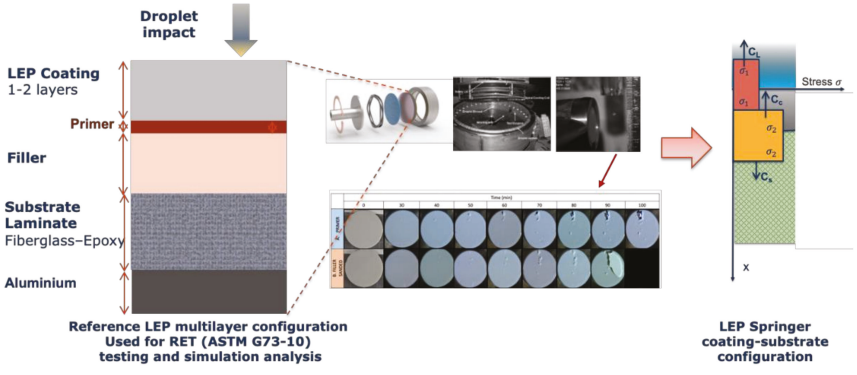

Figure 6. Reference multilayer configuration for rain erosion testing (RET) coupons (ASTM G73-10). Liquid droplet and each material layer are defined by the input mechanical parameters of Table 1.

Table 1. Reference Input data used for the Lifetime Springer modelling in Case1. ASTM G73-10.

Material	Density (gr/cm^3)	Modulus E (Pa)	Speed of Sound C (m/s)	Layer Thickness (μm)	Impact Velocity specimen Vcenter (m/s)
Water droplet	1.00	2.19×10^9	1480.00	2000 (diameter)	135
Coating LEP_1	1.160	3.48×10^9	1733.00	800	135
Primer_1	1.260	5.12×10^9	2016.00	50	135
Filler_1	1.300	4.90×10^9	1941.00	1000	135
Laminate Substrate	1.930	1.10×10^{10}	2392.00	1000	135
Aluminum support	2.700	7.1×10^{10}	5127.00	3300	135

Figure 7 shows the simulated analysis and the testing results tested at the WARER U.Limerick [3,7], comparing for two experimental batches of given top coating material prototypes, with primer and without primer, only with a filler substrate layer, as depicted in Figure 6. On the left vertical axes, one can observe the mass loss for the simulated results (in straight lines). On the right vertical axes, the box and whispers plots (in red for wear and in blue for debonding) are shown for each batch of the rain erosion testing (RET) tested coupons (developed over five coupons size batches). Horizontal axes define the incubation time for the experimental and simulated coupons. It is observed that since the primer and the filler have very similar impedance values, the expected lifetime is also comparable. Moreover, it is assumed that both materials have semi-infinite thickness (in the case of the primer, only a 50 μm thickness is applied in real). The experimental testing anticipates the wear damage showing inaccuracy on the modelling results. The simulated outcomes include important uncertainties due to fundamental properties values used as input data on the modelling. In this case, LEP top coating material ultimate strength was estimated with numerical extrapolation at high strain rates from [18].

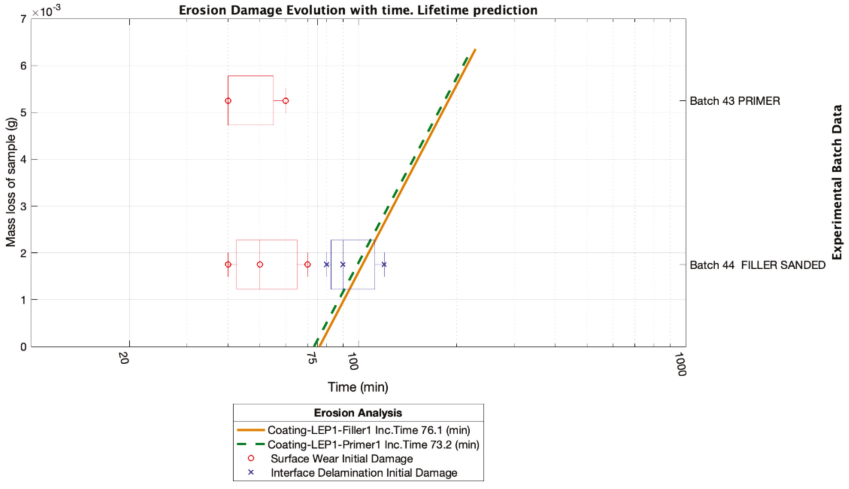

Figure 7. Rain erosion testing lifetime analysis for experimental tested and simulated material LEP configuration comparing coating LEP configuration with No-primer layer (application directly to the filler), and coating LEP configuration with intermediate primer layer.

The modelling approach nevertheless is useful to quantify how the expected lifetime of a given configuration correlates with a given fundamental property variation, as introduced in Figure 5. In Figure 8 is shown the lifetime consequence of a LEP material properties variation of 20%, such are the computation of 80% and 120% values of the reference system. In this analyzed case, the wave speed of the coating, c_c (in green dotted) and is compared with the Ultimate Strength of the coating, σ_{uc}, (in blue line). One can realize that a variation on the ultimate strength of the material influences more significantly on the expected LEP lifetime (and so its determination by appropriate testing, but out of the scope of this work). An example of that issue is quantified for the speed of sound values that the Springer modelling requires as input data used in this research.

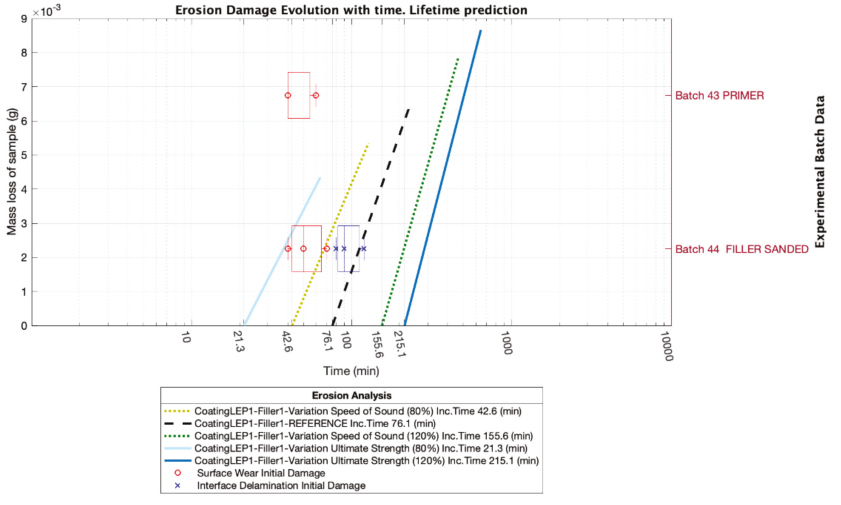

Figure 8. Lifetime analysis for experimental tested and simulated material LEP prototype comparing 20% variation of LEP Speed of Sound and Ultimate Strength.

Other analysis is due to the relative impedance values on the interfaces liquid-coating and coating-substrate that affect directly the lifetime performance results, see Figure 9. The parameters φ_{Lc} and φ_{sc} defined in Equation (2) (see Figure 5 for complete reference of the used equations), allow one to identify suitable combinations to optimize lifetime performance by means of acoustic matching.

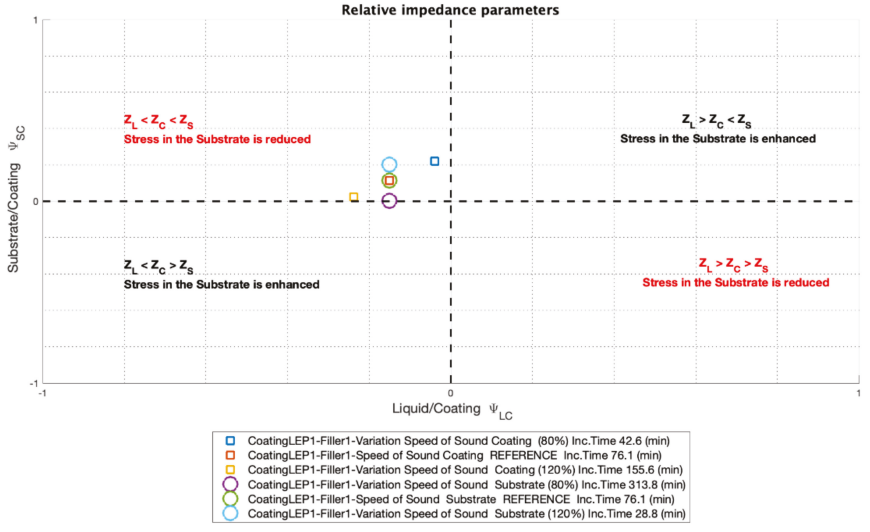

Figure 9. Relative impedance values comparing lifetime prediction due to 20% variation (computing 80% and 120% values) of the Coating c_c and Substrate c_s Speed of Sound.

It is important to note that the stress history and the criteria to consider how the stress waves affect fatigue damage is based on a simplified one-dimensional and pure elastic single impact analysis as introduced in previous section. Figure 10 shows the considered stress evolution at coating LEP surface due to consecutive reflections defined in Equations (3)–(5), introduced in [15] and depicted in Figure 5, for our reference system comparing lifetime prediction due to 50% variation of the coating speed of sound c_c (computing 50% and 150% of the reference values). The key parameter in this case is the averaged stress σ_o calculated for the estimated impact duration. It is defined as a constant value in Equation (8), introduced in [15], and directly applies in lifetime prediction with the number of impacts estimation during incubation time, Equation (15). It is observed that a reduction and an increment of the reference value reduce, in both cases, the coating LEP lifetime estimation. This is due that the coating speed of sound values affect not only the coating-substrate reflections, also the liquid-coating interface and hence to the waterhammer pressure at surface.

Figure 11 shows the equivalent analysis when the variation is due to the filler-substrate speed of sound c_s. In this case, that a 50% reduction on its value may yield and improvement of lifetime estimation and a 150% of its reference value consequences an abrupt loss on erosion lifetime. Figure 12 depicts the stress history with the same assumptions, but at the interface coating-substrate, calculating σ_h with Equation (9), introduced in [15].

The analysis allows one to define appropriate criteria for evaluate the coating LEP capability to reduce or enhance the surface and interface stress, depending on its relative coating-substrate impedance (or speed of sound). Its optimization in terms of fatigue lifetime may be coupled with another parameter analysis, as discussed later in this section. By using other numerical simulation techniques and more complex material models, the accurateness on this estimation may be also improved.

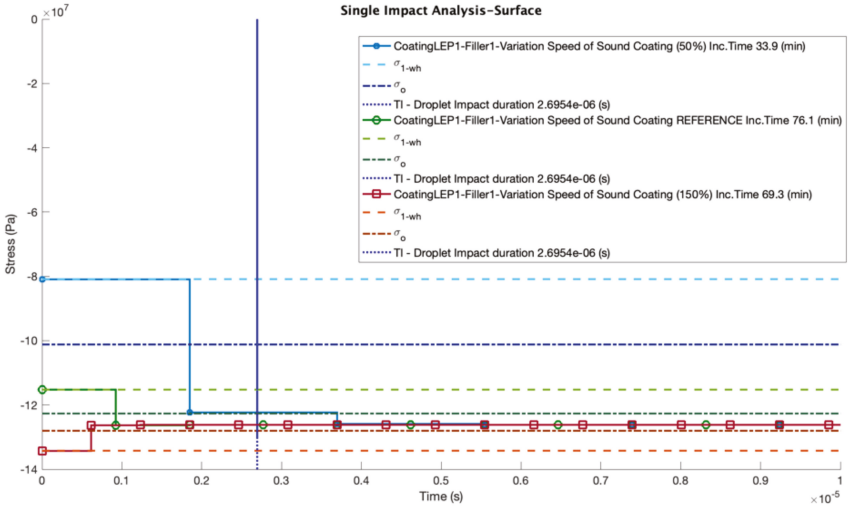

Figure 10. Surface stress evolution analysis for simulated material LEP prototype comparing 50% variation of LEP coating Speed of Sound.

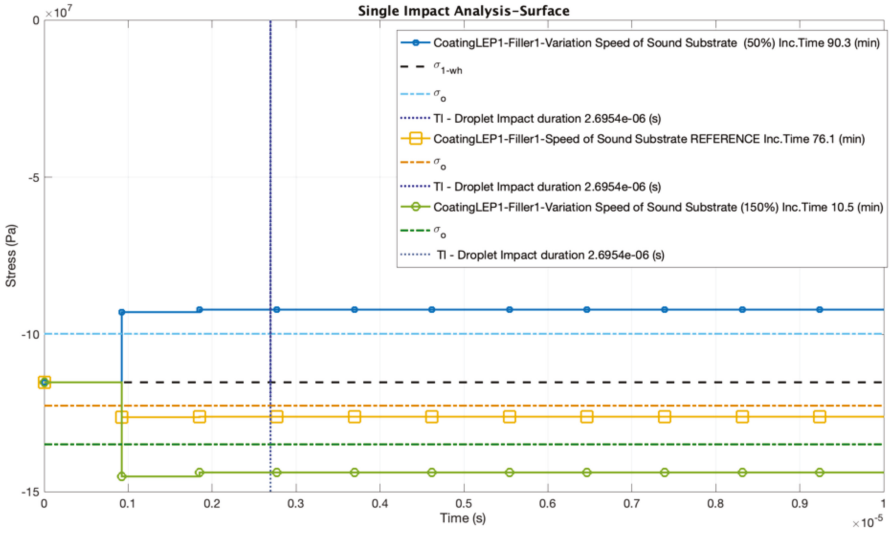

Figure 11. Surface stress evolution analysis for simulated material LEP prototype comparing 50% variation of Filler Substrate Speed of Sound.

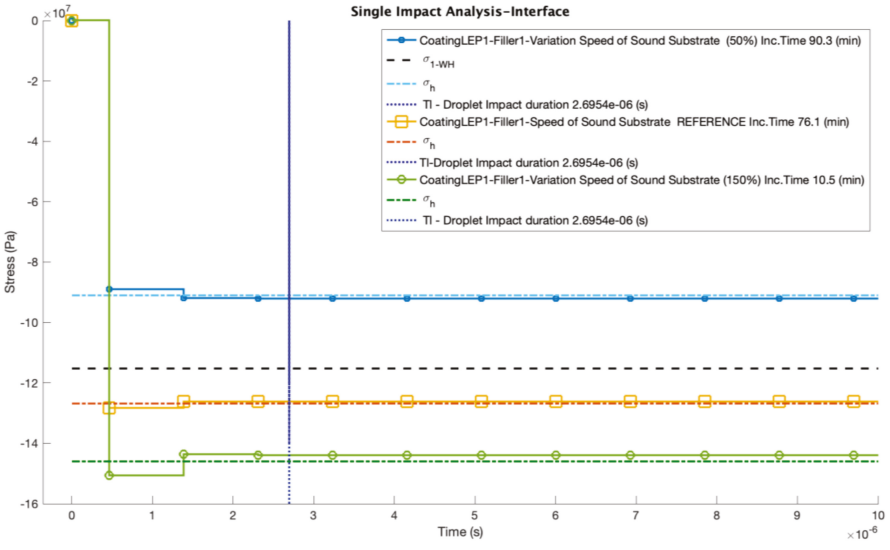

Figure 12. Interface stress evolution analysis for simulated material LEP prototype comparing 50% variation of Filler Substrate Speed of Sound.

3.2. Case 2. Relative Coating-Substrate Impedance Variability. Analysis of a LEP Multilayer System Rain Erosion Testing Based on DNVGL-RP-0171

This second case ponders a batch of three coupons with a LEP configuration definition used for testing based on DNVGL-RP-0171 [38], following the modelling introduced and implemented in [15,39] and validated at PolyTech [40], as depicted in Figures 13–15.

Table 2. Reference Input data used for the Lifetime Springer modelling in Case2. DNVGL-RP-0171.

Material	Modulus E (Pa)	Speed of Sound C (m/s)	Layer Thickness (μm)	Impact Velocity Specimen Vcenter (m/s)
Water droplet	2.19×10^9	1480.00	2000 (diameter)	121
LEP19_2.5 MHz	3.48×10^9	1733.00	500	121
LEP19_5 MHz	5.12×10^9	2016.00	500	121
Filler_5 MHz	6.53×10^9	2241.00	1000	121
Filler_2.5 MHz	5.9×10^9	2134.00	1000	121
Primer_5 MHz	5.84×10^9	2153.00	100	121
Primer_2.5 MHz	5.66×10^9	2119.00	100	121
FillerB_5 MHz	6.87×10^9	2098.00	1000	121
FillerB_2.5 MHz	6.47×10^9	2030.00	1000	121
Laminate Substrate	1.10×10^{10}	2392.00	3400	121

The modelling input data is defined in Table 2 that correspond to the speed of sound testing measurements developed for this research, in which the results are exposed in Figure 3. The objective is to validate the Springer modelling capabilities in regard to frequency-dependent speed of sound measurements.

Figure 16 shows RET testing data results tested at Polytech facilities. The two experimental coupons are configured with an intermediate primer layer to avoid delamination and to observe wear damage uniquely. It is observed the two RET test coupons (referenced S445-178R#2 and S445-178R#3) showing wear erosion damage progression at intermediate time intervals.

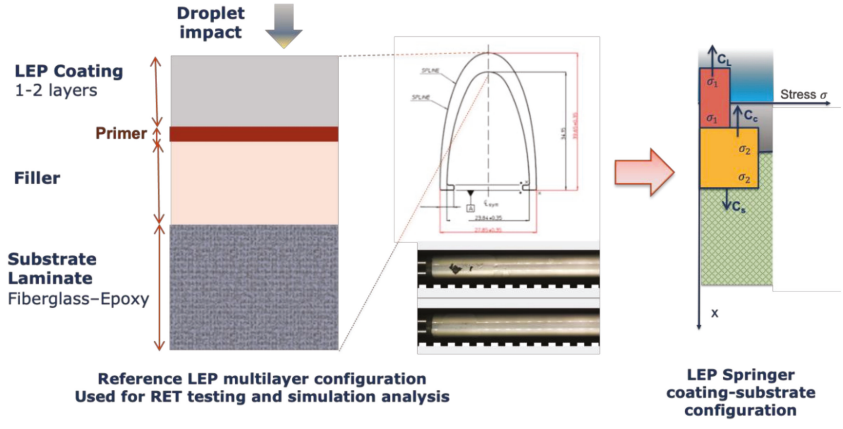

Figure 13. Reference multilayer configuration for RET coupons (DNVGL-RP-0171). Liquid droplet and each material layer are defined by the input mechanical parameters of Table 2.

Figure 14. Application execution steps of RET testing coupons used in this work (DNVGL-RP-0171).

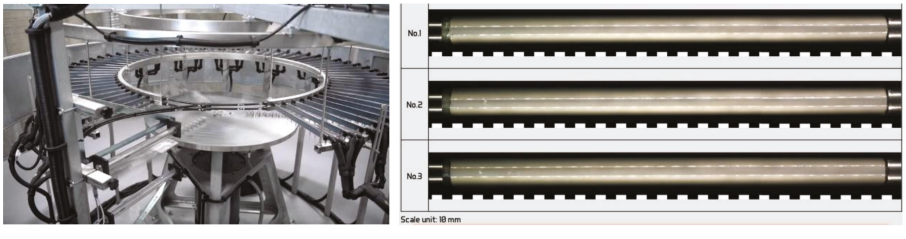

Figure 15. Rain erosion test facility and three specimens used at PolyTech Test and Validation A/S according to DNV-GL-RP-0171 [38], for the analysis and experimental validation.

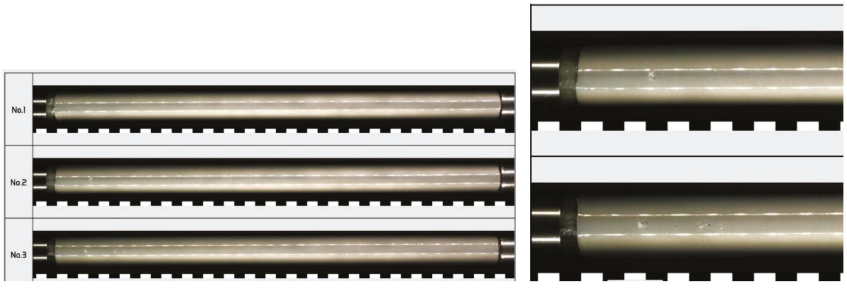

Figure 16. RET images of coupons S445-178R#2 and S445-178R#3 at intermediate testing time and zoom details to appreciate erosion damage.

The testing results data are also plotted in Figure 17 with a velocity-time representation (equivalent to V-N number of impacts until failure), where the velocity varies for each coupon depending on the location distance to the root of the rotating arm (see [38] for details on such a testing procedure) defining a slope introduced in Equation (15), from [15]. Simulated performance results are observed when using speed of sound measured values as input data at different UT frequencies of 5 or 2.5 MHz. It is detected that both cases offer the same simulated results, noting no influence on such impedance measurement deviations. The modelling results predict erosion damage earlier than RET testing. The accuracy of this modelling is reasonable, since many other material and operational parameters uncertainties are involved. Nevertheless, considering, in our problem, the unique variation due to the coating wave speed Cc, see Figure 18, the incubation time estimation (number of impacts until failure) is obtained for each simulated *Cc* value. It is observed the effect of increasing the coating speed of sound value *Cc* produces an improvement in erosion performance for a range of *Cc* values. One may also observe that, for the optimum value of *Cc*, a change in *Cc* becomes negative for this upper range values. Figure 19 shows the equivalent analysis but for a substrate speed of sound value *Cs* variation range. Both results allow one to define optimum values for material stiffness design reference. Figure 20 illustrates the limits of erosion performance deviation when considering a 10% value of its original reference for the speed of sound variation, in the coating and in the substrate. It is pointed out the stronger influence of the substrate speed of sound, mainly due to its responsibility on transferring the energy of impact to the blade laminate (in the Springer model, it is considered of semi-infinite thickness).

3.3. Case 3. Substrate Impedance Variability. Analysis of a LEP Multilayer System Rain Erosion Testing Based on DNVGL-RP-0171

This third case ponders the effect of considering different substrate materials with the same coating LEP. Figure 21 shows a blade section in reparation. It is observed different substrate material layers from the structural laminate where a filler (putty) layer between the laminate and the coating is included. Some manufacturers also include a primer layer under the coating and over the filler to improve adhesion. Depending on each industrial solution, the inclusion of interfaces may accelerate erosion by delaminating between layers. It is important in terms of repairing that the LEP configuration keeps uniform through the thickness with the appropriate substrate. In this section, the possible different erosion lifetime is analyzed due to the substrate layer impedance variation. Upon impingement, the wave front in the top coating further advances towards the coating-substrate interface, where a portion of the stress wave is reflected back into the coating with a different amplitude, depending on the relative material acoustic impedances, and the remaining part is transmitted to the substrate layer and hence to the blade.

In this worked case are used two batches of three coupons, each with two LEP configurations, as depicted in Figure 13, for rain erosion testing based on DNVGL-RP-0171. The modelling input data are defined in Table 2 that correspond to the speed of sound testing measurements developed for this research and of which the results are exposed in Figures 3 and 4. Particularly, the simulation is different to previous case 2, mainly because of the use of a different coating LEP; see Table 3 for its input data. The analysis considers RET testing results obtained at ORE-Catapult [41] with a configuration of coating LEP19B layer with a Primer layer (without filler layer) and then the laminate (glass fiver reinforced epoxy). The second test ponders the RET testing results obtained at PolyTech [40] with a configuration of coating LEP19B, primer layer and filler B as an intermediate substrate before the fourth GFRE-laminate layer.

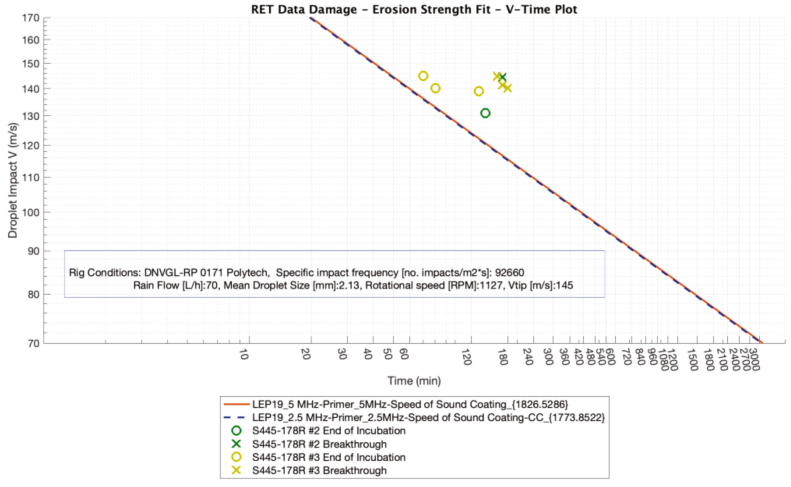

Figure 17. V-Time plot for simulated coating LEP prototype, comparing both the effect of the droplet impact velocity variations through the RET coupon from the root to the tip, according to DNVGL-RP-0171 and the comparing the simulated results when UT measuring at 2.5 and 5 MHz.

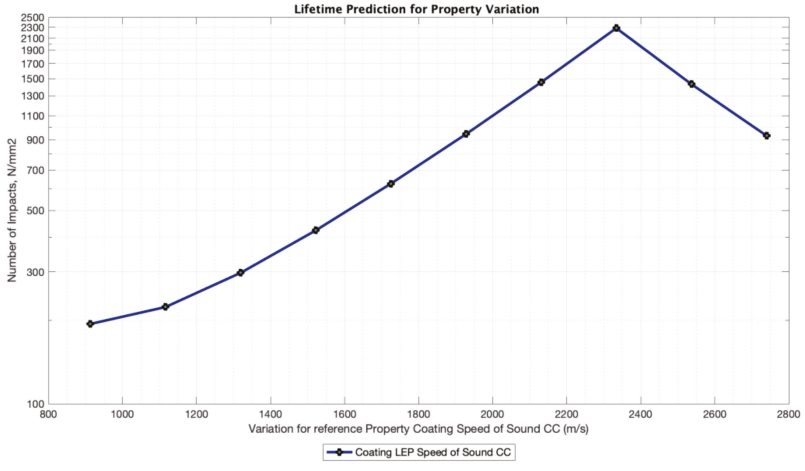

Figure 18. Incubation time estimation due to a unique variation of the coating wave speed Cc.

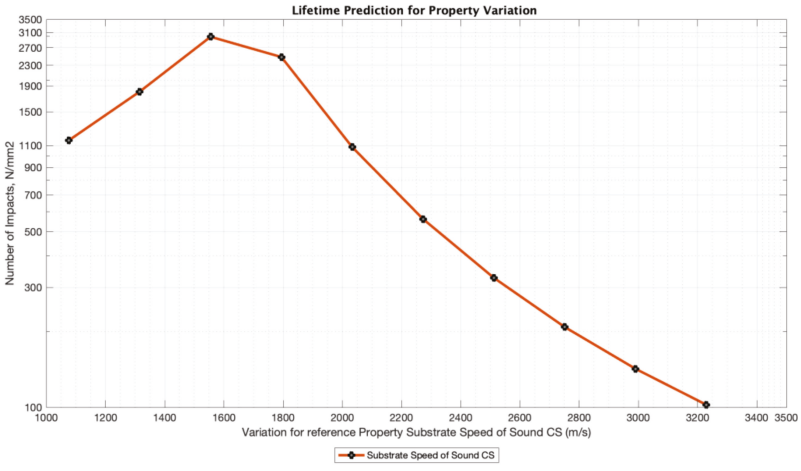

Figure 19. Incubation time estimation due to a unique variation of the substrate (primer or filler) wave speed Cs.

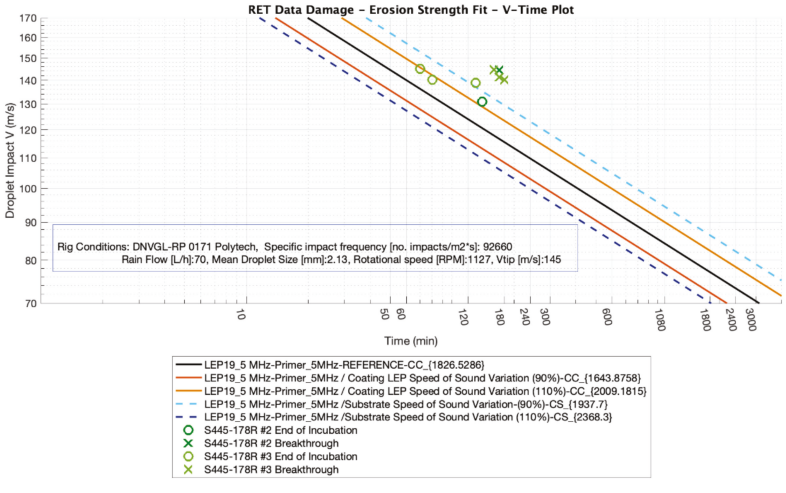

Figure 20. V-Time plot for simulated LEP prototype, comparing both the effect of a 10% variation on the coating and substrate speed of sound variations.

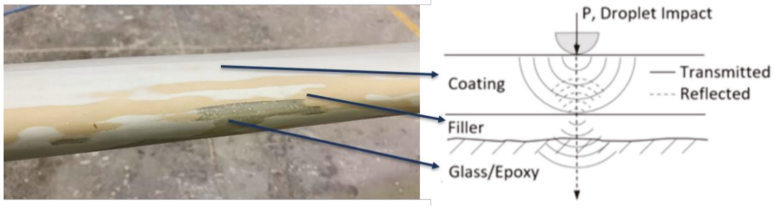

Figure 21. Blade section in reparation showing different areas with different substrates. Droplet impact reflected/transmitted stress on interface due to relative impedance.

Table 3. Reference Input data used for the Lifetime Springer modelling in Case 3. DNVGL-RP-0171.

Material	Modulus E (Pa)	Speed of Sound C (m/s)	Layer Thickness (μm)	Impact Velocity Specimen Vcenter (m/s)
Water droplet	2.19×10^9	1480.00	2000 (diameter)	121
LEP19B_5 MHz	3.05×10^9	1628.00	500	121
LEP19B_25 MHz	2.98×10^9	1609.00	500	121

Figures 22 and 23 show the RET data testing results of the two LEP configurations, evaluating the effect of using (primer-laminate) or (primer-fillerB-laminate) as substrate layers with LEP19B as the coating layer. The damage points are depicted in a V-N plot with the number of droplets impacts, until failure for each impact velocity.

We may calculate and fit the erosion strength S_{ec_fit} from the RET data as described in Equations (12) and (15), see [15] and Figure 5, in terms of number of droplet impacts N, and observed velocity. The erosion strength S_{ec_fit} of both LEP systems are derived using their RET data by matching the V_{fit} and n_{ic_fit} values for a given RET data VN plot result as

$$S_{ec\_fit} = \sigma_o \left(\frac{n_{ic\_fit}\, d^2}{8.9} \right)^{\frac{1}{5,7}} \sigma_o = V_{fit} \frac{Z_L \cos(\theta)(\psi_{sc} + 1)}{\left(\frac{Z_L}{Z_c} + 1\right)(1 - \psi_{Lc}\psi_{sc})} \left(1 - \frac{(1 - e^{\gamma})(\psi_{Lc} + 1)\psi_{sc}}{\gamma(\psi_{sc} + 1)} \right) \quad (2)$$

In our case, all the S_{ec_fit} values were obtained for all the damages (coupling V_{fit} and n_{ic_fit}) of each tested batch. The mean value of each set of initial failure points defined S_{ec_set} was obtained and plotted in a V-N curve for a complete range of V and N values with Equation (15), as introduced in [15]. See experimental RET data results in Figure 22 with V-N curve in dotted lines for the primer-laminate or primer-fillerB-laminate used as substrate layers for each configuration. Subsequent intermediate progression of damages until breakthrough are also plotted as aforementioned. It is perceived that Springer V-N curve slope obtained for the aforementioned fit erosion strength follows the experimental data for the initial damages (incubation time).

It is observed in Figure 22 for comparison and modelling accuracy validation that Springer modelling simulations from fundamental properties (filled lines) of wear damage are also plotted, considering the three cases of LEP19B as the coating layer combined with fillerB or primer or laminate as substrate layer (with labelling LEP19B-fillerB, LEP19B-primer, LEP19B-laminate, respectively). This is due to the fact that the Springer model only accounts for a semi-infinite substrate layer, and does not consider a multilayer configuration as depicted in Figure 13. Since our tested systems contemplate all a thin primer layer and then a filler or a laminate layer, the three possibilities were simulated, and the results are plotted for comparison. The modelling results predict erosion damage earlier than RET testing for the laminate and the filler B cases. In the contrary, Primer simulation shows that the RET damages occur later than predicted. These results are as expected and are justified that in reality the RET coupons have a multilayer configuration, where the primer is the first substrate layer, but only with a thickness of 500 μm. That means that the overall mechanical effect is a mixture between the thicker substrates (laminate or fillerB) and the primer. A worse performance is expected when considering a pure primer layer and better for pure laminate substrate or pure fillerB substrate (in agreement with the modelling results shown).

Figures 24 and 25 show that the incubation time estimation (number of impacts until failure) is obtained for each simulated *Cc* and *Cs* value respectively. It is observed again (as in the previous case 2) the effect of increasing the coating speed of sound value *Cc* and the substrate speed of sound value *Cs* in a variation range. Both results allow one to define the influence of the substrate material responsibility on transferring the energy of impact to the blade laminate, when considering its reparation with added filler or putty layers. We can determine that the modelling estimates well wear failure and it is

validated with the erosion strength derivation from RET testing data, which in fact is assumed to be necessary within performance estimation methodology for correct erosion analysis.

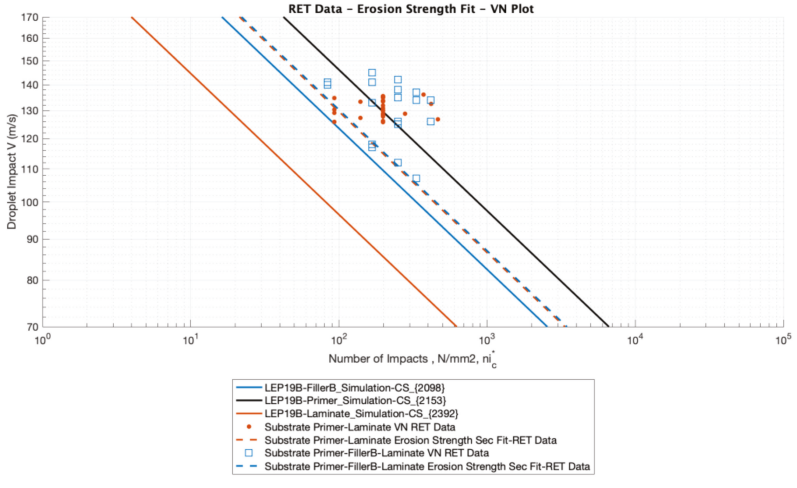

Figure 22. V-N plot for RET testing and simulated coating LEP prototype comparing both the effect of the droplet impact velocity variations though the RET coupon from the root to the tip according DNVGL-RP-0171 and comparing the simulated results when varying the substrate impedance.

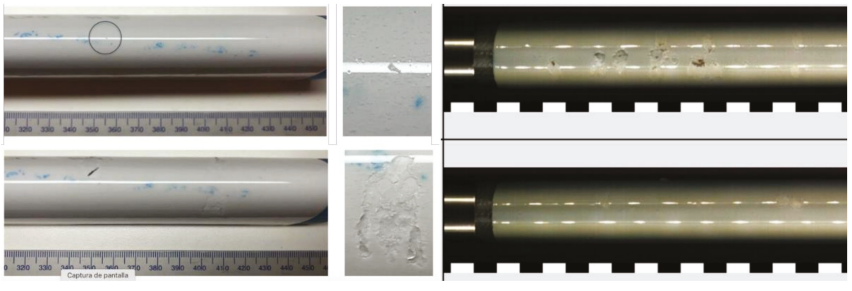

Figure 23. RET images of coupons at intermediate testing time for the two configurations: left, (LEP19B-Primer-Laminate) and right, (LEP19B-Primer-FillerB-Laminate).

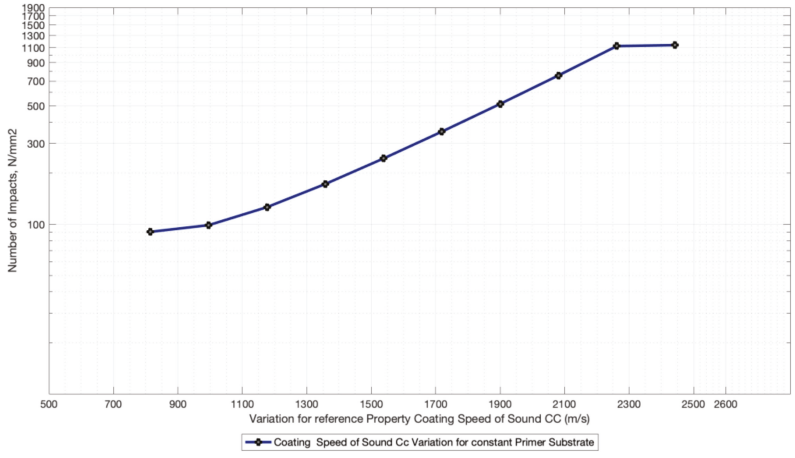

Figure 24. Incubation time (Number of impacts until failure) numerical estimation, due to a unique variation of the coating wave speed Cc when considering the Primer as the substrate layer.

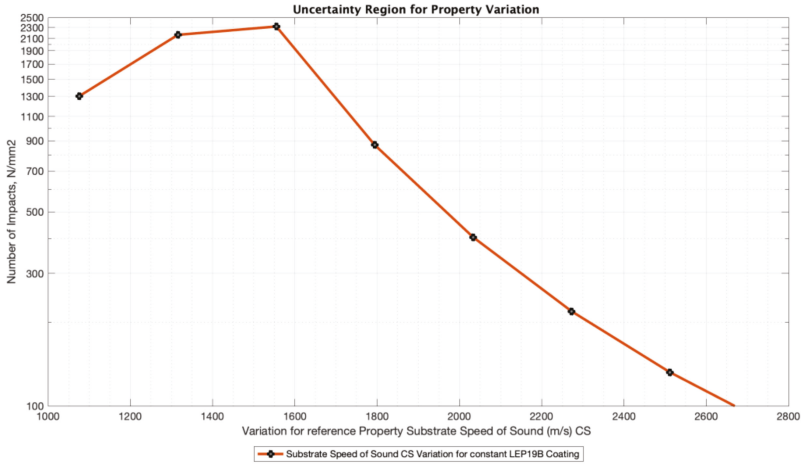

Figure 25. Incubation time (Number of impacts until failure) numerical estimation, due to a unique variation of the substrate wave speed CS when considering the LEP19B material as the substrate layer.

4. Conclusions

In the current work, an investigation into various LEP configuration cases have been undertaken and related with the rain erosion durability factors, in an effort to assess the response of changing material and processing parameters involved on its blade application.

Diverse cases are developed throughout the research work, in order to ponder the key issues on appropriate LEP system definition for its mechanical characterization, to avoid a lack of accuracy on erosion performance analysis. Viscoelastic material models are originally considered within a coating layer impedance characterization methodology, based on ultrasound measurements for the modelling input data in rain erosion lifetime applications. The computational tool has been used to define erosion performance analysis, depending on the relative acoustic impedance of liquid, coating and substrate materials. The proposed numerical procedures to predict wear surface erosion have been used to identify suitable LEP coating and composite substrate combinations. Experimental campaigns of LEP

erosion performance at rain erosion accelerated rain erosion testing (RET) technique have been used as the validation key metric to assess the response of each combined material configuration.

Author Contributions: Conceptualization, F.S.; investigation, L.D., V.G.-P., A.Š. and D.P.F.; methodology, F.S.; resources, A.Š., D.P.F., E.S. and F.S.; software, L.D. and V.G.-P; supervision, E.S. and F.S.; validation, F.S.; writing – original draft, F.S. All authors have read and agreed to the published version of the manuscript.

Funding: This research has been partially funded by the DEMOWIND-2 Project Offshore Demonstration Blade (ODB) Funded by MINECO with reference PCIN-069-2017, by the ESI-Group Chair at CEU-UCH and from the European Union's Horizon 2020 research and innovation program under grant agreement No 811473. Project "LEP4BLADES".

Conflicts of Interest: The authors declare no conflict of interest.

References

1. Eurostat Renewable Energy Statistics. Available online: https://ec.europa.eu/eurostat/statistics-explained/index.php/Renewable_energy_statistics (accessed on 9 July 2020).
2. International Energy Agency. *World Energy Outlook 2019*; IEA: Paris, France, 2019; pp. 613–614. Available online: https://www.iea.org/reports/world-energy-outlook-2019 (accessed on 9 July 2020).
3. Cortés, E.; Sánchez, F.; O'Carroll, A.; Madramany, B.; Hardiman, M.; Young, T. On the Material Characterisation of Wind Turbine Blade Coatings: The Effect of Interphase Coating–Laminate Adhesion on Rain Erosion Performance. *Materials* **2017**, *10*, 1146. [CrossRef] [PubMed]
4. Springer, G.S. *Erosion by Liquid Impact*; John Wiley and Sons: New York, NY, USA, 1976.
5. Eisenberg, D.; Laustsen, S.; Stege, J. Wind turbine blade coating leading edge rain erosion model: Development and validation. *Wind. Energy* **2018**, *21*, 942–951. [CrossRef]
6. Slot, H.; Gelinck, E.; Rentrop, C.; Van Der Heide, E. Leading edge erosion of coated wind turbine blades: Review of coating life models. *Renew. Energy* **2015**, *80*, 837–848. [CrossRef]
7. Tobin, E.F.; Young, T.; Raps, D.; Rohr, O. Comparison of liquid impingement results from whirling arm and water-jet rain erosion test facilities. *Wear* **2011**, *271*, 2625–2631. [CrossRef]
8. Ibrahim, M.E.; Medraj, M. Water Droplet Erosion of Wind Turbine Blades: Mechanics, Testing, Modeling and Future Perspectives. *Materials* **2020**, *13*, 157. [CrossRef] [PubMed]
9. Adler, W.F. Waterdrop impact modeling. *Wear* **1995**, *186*, 341–351. [CrossRef]
10. Gohardani, O. Impact of erosion testing aspects on current and future flight conditions. *Prog. Aerosp. Sci.* **2011**, *47*, 280–303. [CrossRef]
11. Doagou-Rad, S.; Jr, L.M.; Bech, J.I. Leading edge erosion of wind turbine blades: Multiaxial critical plane fatigue model of coating degradation under random liquid impacts. *Wind. Energy* **2020**, 1–15. [CrossRef]
12. Fang, J.; Owens, R.G.; Tacher, L.; Parriaux, A. A numerical study of the SPH method for simulating transient viscoelastic free surface flows. *J. Non Newtonian Fluid Mech.* **2006**, *139*, 68–84. [CrossRef]
13. Verma, A.S.; Castro, S.G.; Jiang, Z.; Teuwen, J.J. Numerical investigation of rain droplet impact on offshore wind turbine blades under different rainfall conditions: A parametric study. *Compos. Struct.* **2020**, *241*, 112096. [CrossRef]
14. Yonemoto, Y.; Kunugi, T. Universality of Droplet Impingement: Low-to-High Viscosities and Surface Tensions. *Coatings* **2018**, *8*, 409. [CrossRef]
15. Luis, D.; Jordi, R.; Asta, Š.; Fernando, S. Top coating anti-erosion performance analysis in wind turbine blades depending on relative acoustic impedance. Part 1: Modelling approach. *Coatings* **2020**, *10*, 685. [CrossRef]
16. Arena, G. Solid particle erosion and viscoelastic properties of thermoplastic polyurethanes. *Express Polym. Lett.* **2015**, *9*, 166–176. [CrossRef]
17. Sarva, S.S.; Deschanel, S.; Boyce, M.C.; Chen, W. Stress–strain behavior of a polyurea and a polyurethane from low to high strain rates. *Polymer* **2007**, *48*, 2208–2213. [CrossRef]
18. Roland, C.M.; Twigg, J.N; Vu, Y.; Mott, P.H. High strain rate mechanical behavior of polyurea. *Polymer* **2007**, *48*, 574–578. [CrossRef]
19. Fan, J.; Weerheijm, J.; Sluys, B. High-strain-rate tensile mechanical response of a polyurethane elastomeric material. *Polymer* **2015**, *65*, 72–80. [CrossRef]
20. Brinson, H.F.; Brinson, L.C. *Stress and Strain Analysis and Measurement, in Polymer Engineering Scienceand Viscoelasticity*; Springer Science+Business Media: New York, NY, USA, 2015. [CrossRef]

21. ISO 18872:2007. In *Plastics—Determination of Tensile Properties at High Strain Rates*; ISO: Geneva, Switzerland, 2007.
22. Beda, T.; Esteoule, C.; Soula, M.; Vinh, J.T. Viscoelastic Moduli of Materials Deduced from Harmonic Responses of Beams. In *Mechanics of Viscoelastic Materials and Wave Dispersion*; Wiley: Hoboken, NJ, USA, 2013; pp. 555–597. [CrossRef]
23. Sinha, M.; Buckley, D.J. Acoustic Properties of Polymers. In *Physical Properties of Polymers Handbook*; Mark, J.E., Ed.; Springer: New York, NY, USA, 2007; pp. 1021–1031.
24. Sasmita, F.; Tarigan, T.Z.S.; Judawisastra, H.; Priambodo, T.A. Study of Elastic Modulus Determination of Polymers with Ultrasonic Method. *Int. J. Adv. Sci. Eng. Inf. Technol.* **2019**, *9*, 874. [CrossRef]
25. Garceau, P. Characterization of Isotropic and Anisotropic Materials by Progressive Ultrasonic Waves. In *Mechanics of Viscoelastic Materials and Wave Dispersion*; Wiley: Hoboken, NJ, USA, 2013; pp. 513–554. [CrossRef]
26. Grate, J.W.; Wenzel, S.W.; White, R.M. Frequency-independent and frequency-dependent polymer transitions observed on flexural plate wave ultrasonic sensors. *Anal. Chem.* **1992**, *64*, 413–423. [CrossRef]
27. Lellinger, D.; Tadjbach, S.; Alig, I. Determination of the elastic moduli of polymer films by a new ultrasonic reflection method. In *Macromolecular Symposia*; Wiley-Vch Verlag: Weinheim, Germany, August 2002; Volume 184, pp. 203–214.
28. Bai, X.; Sun, Z.; Chen, J.; Ju, B.-F. A novel technique for the measurement of the acoustic properties of a thin linear-viscoelastic layer using a planar ultrasonic transducer. *Meas. Sci. Technol.* **2013**, *24*, 125602. [CrossRef]
29. Hsu, D.K.; Hughes, M.S. Simultaneous ultrasonic velocity and sample thickness measurement and application in composites. *J. Acoust. Soc. Am.* **1992**, *92*, 669. [CrossRef]
30. Kiefer, D.A.; Fink, M.; Rupitsch, S.J. Simultaneous Ultrasonic Measurement of Thickness and Speed of Sound in Elastic Plates Using Coded Excitation Signals. *IEEE Trans. Ultrason. Ferroelectr. Freq. Control.* **2017**, *64*, 1744–1757. [CrossRef] [PubMed]
31. ISO 16823:2012. In *Non-Destructive Testing—Ultrasonic Testing—Transmission Technique*; ISO: Geneva, Switzerland, 2012.
32. ISO 16810:2012. In *Non-Destructive Testing—Ultrasonic Testing—General Principles*; ISO: Geneva, Switzerland, 2012.
33. ISO 16811:2012. In *Non-Destructive Testing—Ultrasonic Testing—Sensitivity and Range Setting*; ISO: Geneva, Switzerland, 2012.
34. ISO 16828:2012. In *Non-Destructive Testing—Ultrasonic Testing—Time-of-Flight Diffraction Technique as a Method for Detection and Sizing of Discontinuities*; ISO: Geneva, Switzerland, 2012.
35. Available online: https://portal.dolphitech.com/ (accessed on 9 July 2020).
36. Available online: https://www.aerox.es/ (accessed on 9 July 2020).
37. ASTM G73-10. In *Standard Test Method for Liquid Impingement Erosion Using Rotating Apparatus*; ASTM International: West Conshohocken, PA, USA, 2017.
38. DNVGL: RP-0171. In *Testing of Rotor Blade Erosion Protection Systems*; Recommended Practice; DNV GL: Oslo, Norway, 2018; Available online: http://www.dnvgl.com (accessed on February 2020).
39. OpenModellica. Available online: https://openmodelica.org (accessed on 9 July 2020).
40. Available online: https://www.poly-tech.dk (accessed on 9 July 2020).
41. Available online: https://ore.catapult.org.uk (accessed on 9 July 2020).

MDPI
St. Alban-Anlage 66
4052 Basel
Switzerland
Tel. +41 61 683 77 34
Fax +41 61 302 89 18
www.mdpi.com

Coatings Editorial Office
E-mail: coatings@mdpi.com
www.mdpi.com/journal/coatings

MDPI
St. Alban-Anlage 66
4052 Basel
Switzerland

Tel: +41 61 683 77 34
Fax: +41 61 302 89 18

www.mdpi.com

ISBN 978-3-0365-1015-6